Published in Journals: Applied Sciences, Energies, Environments, Toxics and Water

Topic Reprint

Sustainable Environmental Technologies

Volume II

Edited by
Dibyendu Sarkar, Rupali Datta, Prafulla Kumar Sahoo and Mohammad Mahmudur Rahman

mdpi.com/topics

MDPI

Sustainable Environmental Technologies—Volume II

Sustainable Environmental Technologies—Volume II

Topic Editors

Dibyendu Sarkar
Rupali Datta
Prafulla Kumar Sahoo
Mohammad Mahmudur Rahman

MDPI

Basel • Beijing • Wuhan • Barcelona • Belgrade • Novi Sad • Cluj • Manchester

Topic Editors

Dibyendu Sarkar
Stevens Institute of Technology
Hoboken
USA

Rupali Datta
Michigan Technological University
Houghton
USA

Prafulla Kumar Sahoo
Central University of Punjab
Bathinda
India

Mohammad Mahmudur Rahman
The University of Newcastle (UON)
Callaghan
Australia

Editorial Office
MDPI AG
Grosspeteranlage 5
4052 Basel, Switzerland

This is a reprint of the Topic, published open access by the journals *Applied Sciences* (ISSN 2076-3417), *Energies* (ISSN 1996-1073), *Environments* (ISSN 2076-3298), *Toxics* (ISSN 2305-6304) and *Water* (ISSN 2073-4441), freely accessible at: https://www.mdpi.com/topics/Sustainable_Environmental_Technologies.

For citation purposes, cite each article independently as indicated on the article page online and as indicated below:

Lastname, A.A.; Lastname, B.B. Article Title. *Journal Name* **Year**, *Volume Number*, Page Range.

Volume II
ISBN 978-3-7258-3041-1 (Hbk)
ISBN 978-3-7258-3042-8 (PDF)
https://doi.org/10.3390/books978-3-7258-3042-8

Set
ISBN 978-3-7258-3037-4 (Hbk)
ISBN 978-3-7258-3038-1 (PDF)

© 2025 by the authors. Articles in this book are Open Access and distributed under the Creative Commons Attribution (CC BY) license. The book as a whole is distributed by MDPI under the terms and conditions of the Creative Commons Attribution-NonCommercial-NoDerivs (CC BY-NC-ND) license (https://creativecommons.org/licenses/by-nc-nd/4.0/).

Contents

About the Editors . . . . . **ix**

Yinyu Sun, Zhongcheng Ke, Caiyun Shen, Ruikang Sun, Qing Wei, Zihan Yin and Wei Yang
Fabrication of Carbon Aerogels Derived from Metal-Organic Frameworks/Carbon Nanotubes/Cotton Composites as an Efficient Sorbent for Sustainable Oil–Water Separation
Reprinted from: *Appl. Sci.* **2022**, *12*, 7285, https://doi.org/10.3390/app12147285 . . . . . **1**

Mirela Panainte-Lehadus, Mihai Vulpe, Valentin Nedeff, Emilian Mosnegutu, Grzegorz Przydatek, Claudia Tomozei and Dana Chitimus
Study on the Method of Household Waste Collection: Case Study
Reprinted from: *Appl. Sci.* **2022**, *12*, 7490, https://doi.org/10.3390/app12157490 . . . . . **12**

Thuane Mendes Anacleto, Betina Kozlowsky-Suzuki, Alan E. Wilson and Alex Enrich-Prast
Comprehensive Meta-Analysis of Pathways to Increase Biogas Production in the Textile Industry
Reprinted from: *Energies* **2022**, *15*, 5574, https://doi.org/10.3390/en15155574 . . . . . **22**

Junhao Qin, Xi Wang, Jidong Ying and Chuxia Lin
Biochar Is Not Durable for Remediation of Heavy Metal-Contaminated Soils Affected by Acid-Mine Drainage
Reprinted from: *Toxics* **2022**, *10*, 462, https://doi.org/10.3390/toxics10080462 . . . . . **33**

Akihiro Matsuno and Ken Kawamoto
Hydrophobicity/Oleophilicity of Autoclaved Aerated Concrete (AAC) Grains Coated with Oleic and Stearic Acids for Application as Oil/Water Separating Filtration and Adsorbent Materials in Vietnam
Reprinted from: *Environments* **2022**, *9*, 101, https://doi.org/10.3390/environments9080101 . . . **48**

John Loughrin, Philip Silva, Nanh Lovanh and Karamat Sistani
Acoustic Stimulation of Anaerobic Digestion: Effects on Biogas Production and Wastewater Malodors
Reprinted from: *Environments* **2022**, *9*, 102, https://doi.org/10.3390/environments9080102 . . . **67**

Ranganai Chidembo, Joseph Francis and Simbarashe Kativhu
Rural Households' Perceptions of the Adoption of Rooftop Solar Photovoltaics in Vhembe District, South Africa
Reprinted from: *Energies* **2022**, *15*, 6157, https://doi.org/10.3390/en15176157 . . . . . **81**

Jin You, Xiang Chen, Liang Chen, Jianghai Chen, Beibei Chai, Aiqing Kang, et al.
A Systematic Bibliometric Review of Low Impact Development Research Articles
Reprinted from: *Water* **2022**, *14*, 2675, https://doi.org/10.3390/w14172675 . . . . . **92**

Jin-Kyoung Han, Woo-Suk Jung, Jung-Min Kim, In-Hwan Park and Young-Do Kim
Analysis of Water Quality Improvement Effect of Controlled River by Multi-Functional Weir Operation
Reprinted from: *Appl. Sci.* **2022**, *12*, 8883, https://doi.org/10.3390/app12178883 . . . . . **107**

Sehad Kadiri, Serdar Dizman, Cafer M. Yeşilkanat, Hamdi Aliu and Gezim Hodolli
Radioactivity in Soils of Kosovo and Radiological Implications
Reprinted from: *Appl. Sci.* **2022**, *12*, 9520, https://doi.org/10.3390/app12199520 . . . . . **121**

Anjali Thakur, Rakesh Kumar and Prafulla Kumar Sahoo
Uranium and Fluoride Removal from Aqueous Solution Using Biochar: A Critical Review for Understanding the Role of Feedstock Types, Mechanisms, and Modification Methods
Reprinted from: *Water* **2022**, *14*, 4063, https://doi.org/10.3390/w14244063 . . . . . **134**

Sameer Neve, Dibyendu Sarkar, Zhiming Zhang and Rupali Datta
Optimized Production of Second-Generation Bioethanol from a Spent C4 Grass: Vetiver (*Chrysopogon zizanioides*)
Reprinted from: *Energies* **2022**, *15*, 9597, https://doi.org/10.3390/en15249597 . . . . . **168**

Surbhi Sharma, Mei-Ling Tsai, Vishal Sharma, Pei-Pei Sun, Parushi Nargotra, Bijender Kumar Bajaj, et al.
Environment Friendly Pretreatment Approaches for the Bioconversion of Lignocellulosic Biomass into Biofuels and Value-Added Products
Reprinted from: *Environments* **2023**, *10*, 6, https://doi.org/10.3390/environments10010006 . . . **180**

Aratrika Ghosh, Soniya Dhiman, Anirudh Gupta and Rohan Jain
Process Evaluation of Scandium Production and Its Environmental Impact
Reprinted from: *Environments* **2023**, *10*, 8, https://doi.org/10.3390/environments10010008 . . . **205**

Marta Przypis, Agata Wawoczny and Danuta Gillner
Biomass and Cellulose Dissolution—The Important Issue in Renewable Materials Treatment
Reprinted from: *Appl. Sci.* **2023**, *13*, 1055, https://doi.org/10.3390/app13021055 . . . . . **234**

Tarek Sboui, Salwa Saidi and Ahmed Lakti
A Machine-Learning-Based Approach to Predict Deforestation Related to Oil Palm: Conceptual Framework and Experimental Evaluation
Reprinted from: *Appl. Sci.* **2023**, *13*, 1772, https://doi.org/10.3390/app13031772 . . . . . **255**

Fernando García-Ávila, Angel Méndez-Heredia, Alex Trelles-Agurto, Esteban Sánchez-Cordero, Emigdio Antonio Alfaro-Paredes, Freddy Criollo-Illescas, et al.
Experimental Evaluation of Tubular Flocculator Implemented in the Field for Drinking Water Supply: Application in the Developing World
Reprinted from: *Water* **2023**, *15*, 833, https://doi.org/10.3390/w15050833 . . . . . **272**

Thais Fernandes Neulls, Paulo Leonardo Santos Gouveia, Carlos Drielson da Silva Pereira, Camilla Stephane Dias Souza, Fernanda Nayr Sena Chaves, Isabela Nascimento Souza, et al.
Comparative Study of Two Organic Wastes as Adsorbents in the Treatment of Water Rich in Nitrogen Compounds
Reprinted from: *Water* **2023**, *15*, 876, https://doi.org/10.3390/w15050876 . . . . . **303**

K. S. Shameem and P. C. Sabumon
A Review on the Stability, Sustainability, Storage and Rejuvenation of Aerobic Granular Sludge for Wastewater Treatment
Reprinted from: *Water* **2023**, *15*, 950, https://doi.org/10.3390/w15050950 . . . . . **318**

Jude A. Okolie, Toheeb Jimoh, Olugbenga Akande, Patrick U. Okoye, Chukwuma C. Ogbaga, Adekunle A. Adeleke, et al.
Pathways for the Valorization of Animal and Human Waste to Biofuels, Sustainable Materials, and Value-Added Chemicals
Reprinted from: *Environments* **2023**, *10*, 46, https://doi.org/10.3390/environments10030046 . . . **342**

Md. Monjurul Islam, Anika Amir Mohana, Md. Aminur Rahman, Mahbubur Rahman, Ravi Naidu and Mohammad Mahmudur Rahman
A Comprehensive Review of the Current Progress of Chromium Removal Methods from Aqueous Solution
Reprinted from: *Toxics* **2023**, *11*, 252, https://doi.org/10.3390/toxics11030252 . . . . . **380**

Liying Sun, Shaocheng Ge, Xi Chen and Shuo Liu
Study on Atomization and Dust Reduction Mechanisms of AEO-9-Charged Solution
Reprinted from: *Energies* **2023**, *16*, 2800, https://doi.org/10.3390/en16062800 . . . . . **423**

Jingkun Zhou, Yunkai Zhou and Xu Bai
Can Green-Technology Innovation Reduce Atmospheric Environmental Pollution?
Reprinted from: *Toxics* **2023**, *11*, 403, https://doi.org/10.3390/toxics11050403 . . . . . **437**

Jongwon Ko, Kyunghwan Kim, Ji Woo Sohn, Hongjun Jang, Hae-Seok Lee, Donghwan Kim and Yoonmook Kang
Review on Separation Processes of End-of-Life Silicon Photovoltaic Modules
Reprinted from: *Energies* **2023**, *16*, 4327, https://doi.org/10.3390/en16114327 . . . . . **458**

Antônio Cavalcante Pereira and Catherine N. Mulligan
Practices for Eutrophic Shallow Lake Water Remediation and Restoration: A Critical Literature Review
Reprinted from: *Water* **2023**, *15*, 2270, https://doi.org/10.3390/w15122270 . . . . . **478**

Maria Cristina Collivignarelli, Francesca Maria Caccamo, Stefano Bellazzi, Alessandro Abbà and Giorgio Bertanza
Assessment of the Impact of a New Industrial Discharge on an Urban Wastewater Treatment Plant: Proposal for an Experimental Protocol
Reprinted from: *Environments* **2023**, *10*, 108, https://doi.org/10.3390/environments10070108 . . **502**

João Serrano, Vasco Mau, Rodrigo Rodrigues, Luís Paixão, Shakib Shahidian, José Marques da Silva, et al.
Definition and Validation of Vineyard Management Zones Based on Soil Apparent Electrical Conductivity and Altimetric Survey
Reprinted from: *Environments* **2023**, *10*, 117, https://doi.org/10.3390/environments10070117 . . **518**

Carolina Bracho-Villavicencio, Helena Matthews-Cascon and Sergio Rossi
Artificial Reefs around the World: A Review of the State of the Art and a Meta-Analysis of Its Effectiveness for the Restoration of Marine Ecosystems
Reprinted from: *Environments* **2023**, *10*, 121, https://doi.org/10.3390/environments10070121 . . **540**

Sang-Hyun Lee, Hyun Kim, Hyunshik Moon, Hyun-Soo Kim, Sang-Sub Han and Seonghun Jeong
Effects of Wind Barrier Porosity and Inclination on Wind Speed Reduction
Reprinted from: *Appl. Sci.* **2023**, *13*, 8310, https://doi.org/10.3390/app13148310 . . . . . **560**

Vello Pallav, Tõnis Teppand, Andrus Leinpuu, Merrit Shanskiy, Mait Mets, Hugo Mändar, et al.
Stabilization of Road Embankments on Peat Soils Using Oil Shale Ash and Pozzolanic Additives
Reprinted from: *Appl. Sci.* **2023**, *13*, 8366, https://doi.org/10.3390/app13148366 . . . . . **576**

Kailin Ren, Lide Su, Yong Zhang, Xiang He and Hao Wu
Development and Evaluation of Cow Dung Composting Equipment with Ventilation and Heating
Reprinted from: *Appl. Sci.* **2023**, *13*, 8649, https://doi.org/10.3390/app13158649 . . . . . **594**

Danfeng Zhao, Tao Zhang Tianwen Chen Qi He and Dongmei Huang
Multi-Indicator Weighted Robustness Analysis of Planktonic Community Systems under Different Destructive Factors
Reprinted from: *Appl. Sci.* **2023**, *13*, 8742, https://doi.org/10.3390/app13158742 . . . . . **610**

Iain A. Struthers, Nadezda Avanessova, Anthony Gray, Miriam Noonan, R. Camilla Thomson and Gareth P. Harrison
Life Cycle Assessment of Four Floating Wind Farms around Scotland Using a Site-Specific Operation and Maintenance Model with SOVs
Reprinted from: *Energies* **2023**, *16*, 7739, https://doi.org/10.3390/en16237739 . . . . . **626**

About the Editors

Dibyendu Sarkar

Dr. Dibyendu "Dibs" Sarkar, Ph.D., is a professor of Environmental Engineering at the Department of Civil, Environmental and Ocean Engineering, Stevens Institute of Technology, Hoboken, U.S.A. He is also the Director of the Stevens Center for Sustainability. Dibs earned his Ph.D. in geochemistry from the University of Tennessee and worked as a postdoctoral researcher in soil and water chemistry at the University of Florida. He has 25 years of experience as an environmental science and engineering faculty member and has authored 3 books, 20 book chapters, more than 170 journal articles, and more than 280 technical abstracts and conference proceedings. Dibs is an elected Fellow of the Geological Society of America and Soil Science Society of America. He is the founding Editor-in-Chief of *Current Pollution Reports*, a Q1 environmental science journal, and serves as a Section Editor-in-Chief, Technical Editor, and Associate Editor of several other journals. His research interests include environmental quality and remediation, soil and water chemistry, green technology development, and risk assessment.

Rupali Datta

Dr. Rupali Datta, Ph.D., is a professor of Biological Sciences at Michigan Technological University (MTU), Michigan, U.S.A. She has a Ph.D. in Life Sciences from the University of Hyderabad, India. She completed her postdoctoral studies at the University of Niigata in Japan, the University of Florida at Gainesville, and the University of Texas at San Antonio (UTSA). Dr. Datta's primary research lies in developing green remediation technologies for environmental pollutants through the application of molecular biology and microbiology, plant biochemistry, genetics, phytoremediation, bioremediation, and plant–microbe interactions. Her current research is focused on the study of the bioavailability of metal and organic contaminants in aquatic media and the potential of using plants to remediate contaminated sites, as mediated by microbes. She has authored more than 300 publications in high-quality journals.

Prafulla Kumar Sahoo

Dr. Prafulla Kumar Sahoo, Ph.D., is an Assistant Professor in the Department of Environmental Science and Technology, Central University of Punjab, India. Dr. Sahoo received his Ph.D. degree from IIT Kharagpur. He has more than 13 years of research experience (including Ph.D. and postdoctoral) in the field of environmental geochemistry, especially for acid mine drainage, groundwater contamination, and soil and sediment geochemistry. Much of his research is focused on societal and environmental issues, including emerging toxic contaminants (such as As, U, and F) in groundwater, soils and paddy rice. The importance of his research and potential at the international level has been recognized through his selection as a BK21-postdoctoral fellow in South Korea and Young Scientist Fellow at the prestigious Brazilian Academy of Science. So far, he has authored over 100 journal articles and 10 book chapters indexed in the Scopus database. He currently serves on the Editorial Board of *Current Pollution Reports* (Springer, a Q1 environmental science journal), in addition to serving as an Associate Editor for *Soil Pollution & Remediation of Frontiers in Soil Science*.

Mohammad Mahmudur Rahman

Dr. Mohammad Mahmudur Rahman, Ph.D., is an Associate Professor in the Global Centre for Environmental Remediation (GCER), College of Engineering, Science and Environment, University

of Newcastle (UON), Australia. He is a globally recognized expert in arsenic-related research. He is also recognized as one of Australia's leading Environmental Scientists by Researcher.com. His work primarily examines the impacts of metals and metalloids on the environment and their potential risks for human health. His research encompasses varied topics, including chemistry, toxicity, bioavailability, environmental nanomaterials, environmental remediation, environmental analytical chemistry, phytoremediation, risk analysis and human health effects of arsenic, and the speciation of metals/metalloids using hyphenated techniques. Dr. Rahman's most notable achievements include publishing 242 publications in international peer-reviewed high-impact journals and refereed book chapters, underscoring his outstanding research leadership. In addition to his research, he serves as an Associate Editor for the Elsevier journal *Groundwater for Sustainable Development* and is a member of the Editorial Boards for several journals, including *Soil and Environmental Health*, *Water* (MDPI), *Journal of Sustainable Agriculture and Environment*, and *Frontiers in Nanotechnology: Environmental Nanotechnology*.

applied sciences

MDPI

Communication

Fabrication of Carbon Aerogels Derived from Metal-Organic Frameworks/Carbon Nanotubes/Cotton Composites as an Efficient Sorbent for Sustainable Oil–Water Separation

Yinyu Sun , Zhongcheng Ke *, Caiyun Shen, Ruikang Sun, Qing Wei, Zihan Yin and Wei Yang

School of Chemistry and Chemical Engineering, Huangshan University, Huangshan 245021, China; yysun_hsu@163.com (Y.S.); ascy8843@163.com (C.S.); sunruikangjnu@163.com (R.S.); wq19105591009@163.com (Q.W.); yzh20030201@163.com (Z.Y.); myxhjsn996320687@163.com (W.Y.)
* Correspondence: xiaoke1020@126.com; Tel.: +86-139-5599-7920

Abstract: Due to the continuous occurrence of water pollution problems, practical separation methods for oil–water mixtures have attracted more and more attention. To date, different kinds of materials have been developed with good hydrophobic properties and strong separation ability. Carbon aerogels, as a promising ideal adsorbent for dealing with oil-spill accidents, have received extensive attention. In this work, zeolitic imidazolate frameworks (ZIFs), nanoparticles, and carbon nanotubes (CNTs) in the three-dimensional (3D) interconnected network structure of cotton balls (CBs) were successfully prepared by a simple and scalable process. The as-prepared carbonized CBs with carbonized ZIF-8 and CNTs (CZIF-8/CNTs/CCBs) were characterized. The oil–water separation performance of the composite was also measured. The results show that the ZIF-8 clusters intercalated with abundant CNTs are fully loaded into the porous structure of the CBs after the in situ synthesis process. Additionally, ZIF-8/CNTs/CBs was carbonized in nitrogen, leading to the formation of CZIF-8/CNTs/CCBs. The prepared material possesses excellent hydrophobicity with a water contact angle of 152.7°, showing good absorption capacities Q_1 in the range of 48 to 84 times its original weight for oil and organic liquids. In addition, CZIF-8/CNTs/CCBs exhibits good recyclability in the absorption–distillation test. In summary, this study proposes a novel and simple method for the preparation of a superhydrophobic material that could have wide application in the separation of oil–water mixtures.

Keywords: zeolitic imidazolate frameworks; carbon nanotubes; cotton balls; oil–water separation

Citation: Sun, Y.; Ke, Z.; Shen, C.; Sun, R.; Wei, Q.; Yin, Z.; Yang, W. Fabrication of Carbon Aerogels Derived from Metal-Organic Frameworks/Carbon Nanotubes/Cotton Composites as an Efficient Sorbent for Sustainable Oil–Water Separation. *Appl. Sci.* **2022**, *12*, 7285. https://doi.org/10.3390/app12147285

Academic Editors: Mohammad Mahmudur Rahman, Dibyendu Sarkar, Rupali Datta and Prafulla Kumar Sahoo

Received: 21 June 2022
Accepted: 19 July 2022
Published: 20 July 2022

Publisher's Note: MDPI stays neutral with regard to jurisdictional claims in published maps and institutional affiliations.

Copyright: © 2022 by the authors. Licensee MDPI, Basel, Switzerland. This article is an open access article distributed under the terms and conditions of the Creative Commons Attribution (CC BY) license (https://creativecommons.org/licenses/by/4.0/).

1. Introduction

The frequent occurrences of oil pollution issues have become more and more alarming. It is very important to find effective strategies to solve the aforementioned issues [1–5]. Oil–water separation materials with a porous structure and a superhydrophobic surface, such as sponges [6–9], foams [10–14], carbon aerogels [15–17], and meshes [18–20], have been widely studied due to their excellent water repellency and good oil–water separation capacity. The preparation of these superhydrophobic materials is based on changing the chemical composition or the microscopic structure [21–24]. In nature, biomass materials possess many exceptional biological properties by virtue of their unique structures, and these materials are gaining significant attention [25,26]. Cotton, a typical environmentally friendly biomass material, contains abundant cellulose fibers with hydrophilic surface hydroxyl groups and a three-dimensional (3D) network structure [27–29]. The modification of cotton to produce superhydrophobic materials for the separation of water and oil has been widely investigated in recent decades [30,31]. Nevertheless, most of the preparation methods have some limitations such as a cumbersome preparation process, expensive reagents, or low oil sorption capacity. Hence, it is highly desirable to develop a facile and green method for synthesizing highly hydrophobic composites derived from cotton with

high separation capacity and low material costs, for dealing with substandard oil–water mixtures and offshore crude oil leaks.

In this study, carbon aerogels were prepared by anchoring zeolitic imidazolate frameworks (ZIFs), nanoparticles, and carbon nanotubes (CNTs) on the surface of cotton balls (CBs), followed by carbonization. The carbonized ZIF-8 and CNTs on carbonized CBs (CZIF-8/CNTs/CCBs) were examined by field emission scanning electron microscopy (FE-SEM), Fourier transform infrared spectroscopy (FTIR), X-ray photoelectron spectroscopy (XPS), energy-dispersive X-ray spectrometry (EDS), and X-ray diffraction (XRD). Furthermore, the oil–water separation performance and the reusability of the samples were also examined. The results show that the material prepared in this study has good prospects for application in the field of oil–water separation.

2. Materials and Methods

2.1. Materials

Zinc nitrate hexahydrate, 2-methylimidazole, methanol, and ethanol were supplied by Sinopharm Chemical Reagent Co., Ltd. (Shanghai, China). Industrial multiwalled carbon nanotubes were obtained from Macklin Biochemical Co., Ltd. (Shanghai, China). The commercial CBs were washed with ethanol for 1 h and dried at 80 °C for 5 h.

2.2. Preparation of CZIF-8/CNTs/CCBs

In a typical procedure, ZIF-8 and CNTs coated on CBs were successfully prepared by an in situ synthesis method. A total of 0.8 g of 2-methylimidazole was dissolved in methanol (8 mL), denoted as solution A. CBs were dipped into solution A, followed by stirring for about 1 h at room temperature. Then, 0.06 g of CNTs was dipped into the above solution under stirring for 2 h. Subsequently, 8 mL of methanol containing zinc nitrate hexahydrate (0.4 g) was added into the prepared mixture, stirring for 12 h. The as-obtained ZIF-8/CNTs/CBs was washed with deionized water and dried at 80 °C for 5 h. CZIF-8/CNTs/CCBs was prepared by carbonizing the homologous precursors in nitrogen for 2 h at 600 °C.

2.3. Physical Characterization

The surface microstructure of the samples was investigated using FE-SEM (Gemini 500, Zeiss, Oberkochen, Germany) and TEM (Tecnai G^2 F20, FEI, Ames, IA, USA). The surface chemical composition was characterized using EDS (X-Max^N 80, Oxford, UK), FTIR (Spirit-T, Shimadzu, Chiyoda-ku, Tokyo, Japan), and XPS (ESCALAB 250Xi, Thermo Fisher, Waltham, MA, USA). X-ray diffraction patterns were recorded using an XRD apparatus equipped with a Cu Kα radiation source (D8 Advance, Bruker, Karlsruhe, Germany). The water contact angles of the samples were measured using a contact angle meter (DSA100, KRUSS, Hamburg, Germany).

2.4. Oil–Water Separation Test

To evaluate the practical applications of the samples, the oil–water separation capacity was measured. In a typical test, the sample was first weighed and subsequently immersed in various organic solvents and oils for 1 min. Then, the sample was taken out for immediate weight measurement. The adsorption capacity of the sample was evaluated by Q_1 and Q_2. The adsorption capacity Q_1 was calculated through the following equation: $Q_1 = (W_2 - W_1)/W_1$, where W_1 and W_2 are the masses of the sample before and after absorption, respectively. The adsorption capacity Q_2 was assessed according to the following equation: $Q_2 = (W_2 - W_0)/W_0$, where W_0 and W_2 are the masses of the raw CBs and the sample, respectively. In the absorption–distillation test, n-heptane was sorbed by CZIF-8/CNTs/CCBs. Then, the used material was evaporated at a temperature around the boiling point (100 °C) of n-heptane. All the tests were performed under the same conditions.

3. Results and Discussion

The preparation process for CZIF-8/CNTs/CCBs involved three steps, as illustrated in the schematic diagram in Figure 1. Firstly, the 3D interconnected network structure of the CBs was fully wetted by the solution of 2-methylimidazole, which can result in active sites on the surface of the CBs for ZIF-8 growth. In this process, CBs were not only used as the support to adsorb the 2-methylimidazole but also acted as the porous structure for the loading of ZIF-8 and CNTs in the next step. Secondly, after adding a certain amount of CNTs and the solution of zinc nitrate, ZIF-8/CNTs/CBs was successfully prepared based on an in situ synthesis method, producing a color change from white to black. The addition of CNTs can not only enhance the cross-linking action of ZIF-8 but can also effectively improve the adsorption performance during the oil–water separation process. In the meantime, the prepared ZIF-8 was tightly adhered in the 3D interconnected network structure of the CBs, also improving the adsorption capacity due to its porous structure. Finally, ZIF-8/CNTs/CBs was carbonized in nitrogen at 600 °C, leading to the formation of CZIF-8/CNTs/CCBs with a superhydrophobic surface.

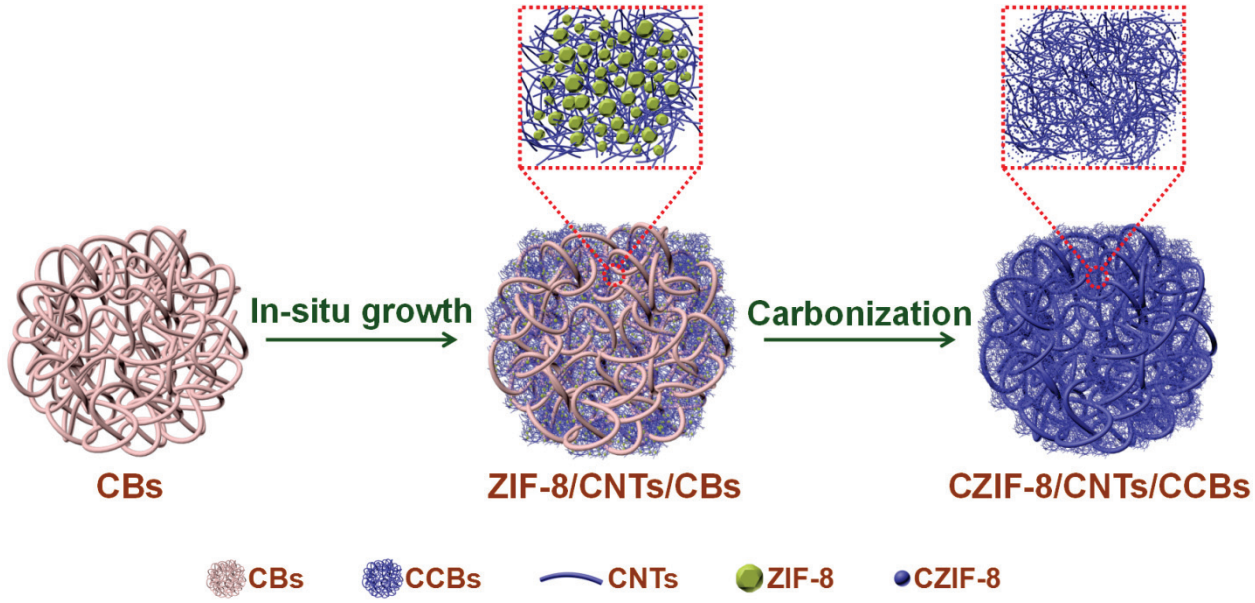


Figure 1. Schematic illustration of the preparation of CZIF-8/CNTs/CCBs.

The surface microstructure of the samples was observed using FE-SEM images of different magnifications and TEM images. As depicted in Figure 2a,d, the pristine CBs exhibit a 3D interconnected network structure and a relatively smooth surface. After the in situ synthesis process, ZIF-8 and CNTs are fully loaded into the porous structure of the CBs (Figure 2b). The ZIF-8 clusters are composed of ZIF-8 nanoparticles intercalated with abundant CNTs (Figure 2e), which is consistent with the TEM result (Figure 3a). As shown in Figure 2c,f, the ZIF-8 clusters disappear from the surface of the as-synthesized CZIF-8/CNTs/CCBs. The TEM image (Figure 3b) clearly shows that the ZIF-8 clusters are decomposed into ZIF-8 nanoparticles after carbonization.

XPS, EDS, and FTIR were used to investigate the surface chemical composition of the samples. The XPS results in Figure 4a confirm the existence of the elements C (284.8 eV), N (399.9 eV), O (532.8 eV), and Zn (1022.3 eV) in the ZIF-8/CNTs/CBs and CZIF-8/CNTs/CCBs. It is worth noting that the proportion of Zn on the surface of CZIF-8/CNTs/CCBs is clearly higher than for ZIF-8/CNTs/CBs. As can be seen from the data in Figure 4b, the XPS spectra for each element of the ZIFs/CNTs/CBs were obtained and fitted. The C 1s spectrum can be divided into four peaks at 284.5, 284.8, 285.4, and 286.6 eV, corresponding to C−C (sp^2), C−C (sp^3), C−OH, and C−N, respectively. The N 1s spectrum of ZIF-8/CNTs/CBs reveals three peaks located at 399.5, 400.0, and 401.0 eV,

ascribed to pyridinic N, pyrrolic N, and pyridine N oxide, respectively. The O 1s spectrum of ZIF-8/CNTs/CBs shows three peaks, corresponding to carboxyl C=O bonds at 532.2, and 532.8 eV and hydroxyl oxygen at 533.6 eV [32,33]. The Zn $2p^3$ spectrum of ZIF-8/CNTs/CBs contains two individual component peaks at 1022.2 and 1045.3 eV, assigned to the Zn $2p^{3/2}$ and Zn $2p^{1/2}$ electronic states, respectively. This result confirms the presence of zinc oxide, which is consistent with previous work [34]. The EDS elemental mappings shown in Figure 5a reveal that the main elements present are C and O on the surface of the CBs. After the in situ synthesis process, the elements N and Zn were detected on the surface of ZIF-8/CNTs/CBs, which corresponds to the XPS results (Figure 4a). In addition, the EDS result for CZIF-8/CNTs/CCBs reveals that the relative content of Zn showed a marked increase (Figure 4a,b). These results demonstrate that ZIF-8 particles are not only homogeneously deposited but are also abundant on the substrate. FTIR spectra were acquired to further confirm the composition of the CBs, ZIF-8/CNTs/CBs, and CZIF-8/CNTs/CCBs. As can be seen in Figure 6a, the strong broad absorption band at 3400 cm^{-1} was assigned to the abundant −OH group on the surface of the CBs. After modification with ZIF-8 and CNTs, a series of absorption bands in the range of 550−1600 cm^{-1} were found in ZIF-8/CNTs/CBs, probably caused by the imidazole ring [32]. In particular, the absorption bands at 425 and 1715 cm^{-1} are ascribed to the Zn–N stretching vibration band and the C=N stretching vibration band, respectively, which is consistent with earlier reports [35,36].

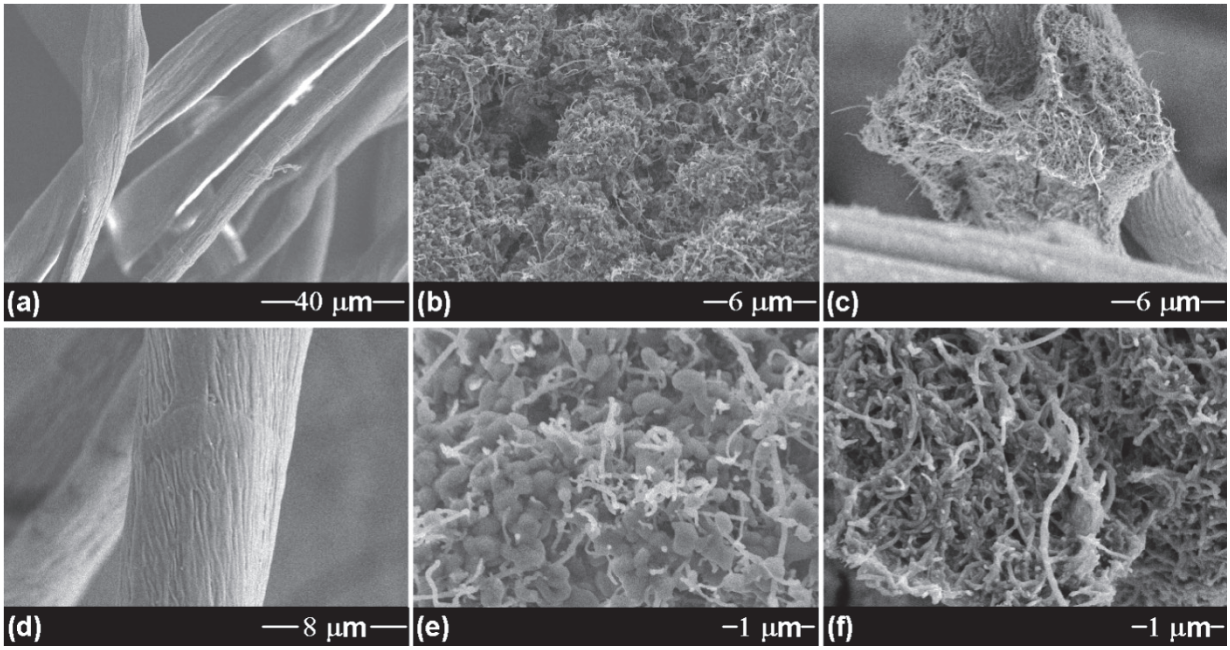


Figure 2. FE-SEM images of CBs (**a**,**d**), ZIF-8/CNTs/CBs (**b**,**e**), and C ZIF-8/CNTs/CCBs (**c**,**f**).

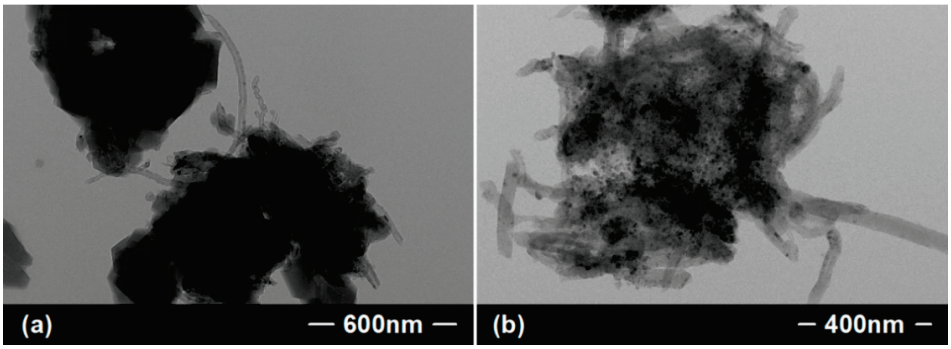


Figure 3. TEM images of ZIF-8/CNTs (**a**) and C ZIF-8/CNTs (**b**).

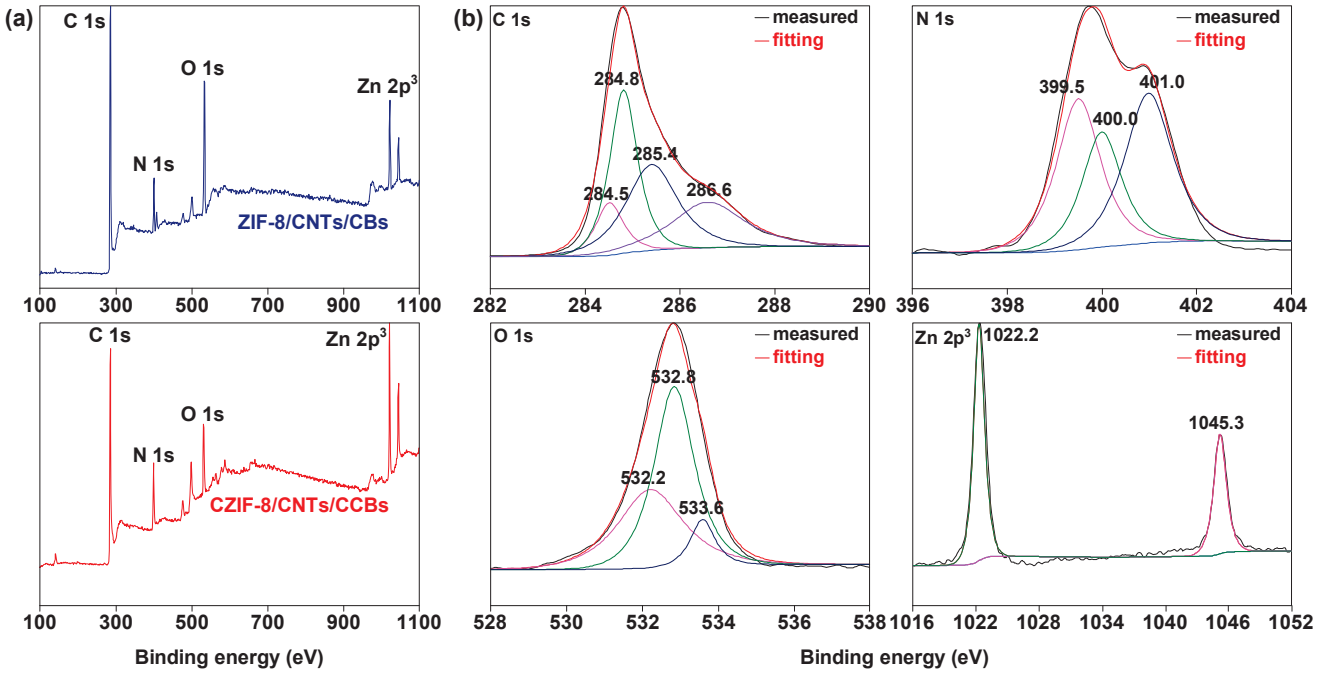


Figure 4. (**a**) XPS survey spectra of ZIF-8/CNTs/CBs and C ZIF-8/CNTs/CCBs. (**b**) C 1s, N 1s, O 1s, and Zn $2p^3$ spectra of ZIF-8/CNTs/CBs.

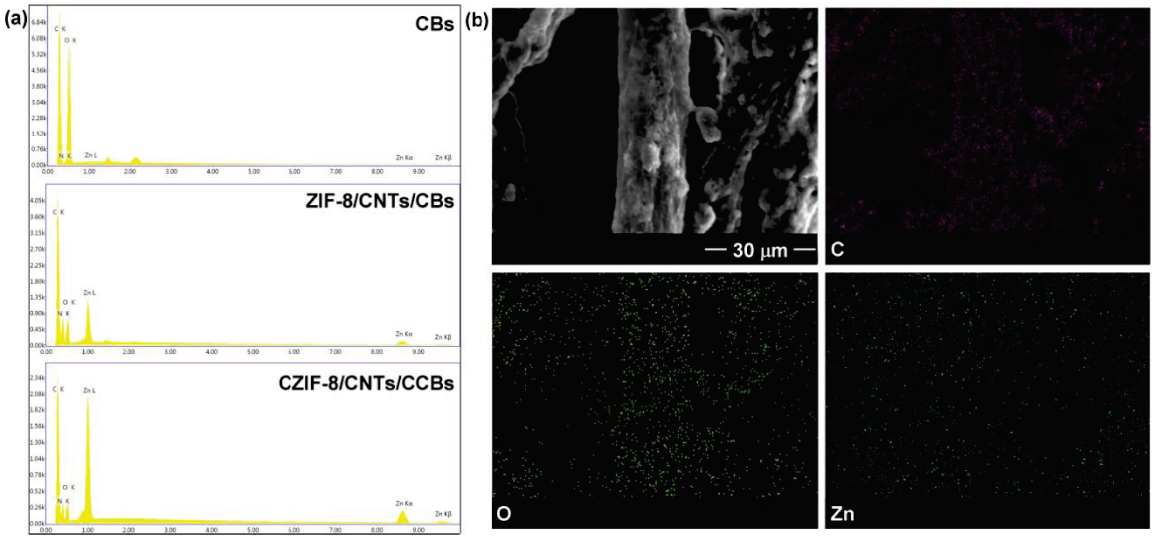


Figure 5. (**a**) Images of CBs, ZIF-8/CNTs/CBs, and CZIF-8/CNTs/CCBs EDS elemental analysis spectra. (**b**) Images of CZIF-8/CNTs/CCBs in EDS elemental mappings.

The crystalline structures of CBs, ZIF-8/CNTs/CBs, and CZIF-8/CNTs/CCBs were investigated using XRD patterns (Figure 6b). It can be seen that there are three typical diffraction peaks at 14.8°, 16.5°, and 22.9°, which were assigned to the (1–10), (110), and (200) lattice planes of cellulose in the CBs, respectively [37]. The XRD pattern of ZIF-8/CNTs/CBs shows six characteristic peaks at 7.3°, 10.4°, 12.9°, 14.7°, 16.4°, and 18.2°, which can be ascribed to the (011), (002), (112), (022), (013), and (222) lattice planes of ZIF-8, respectively [33]. Moreover, the XRD pattern of CZIF-8/CNTs/CCBs possesses only one weak and broad diffraction peak at 26.1°, corresponding to the (002) lattice plane of the graphite-structure crystallites of CCBs [38]. These XRD results further verify the successful preparation of ZIF-8 on the surface of the CBs.

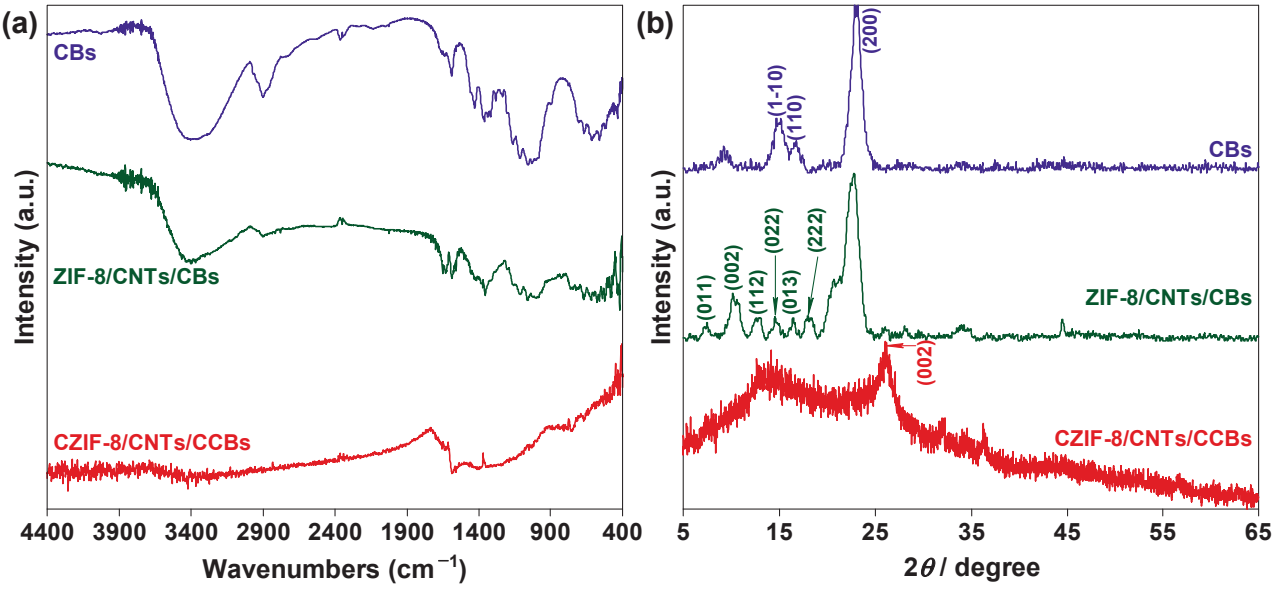


Figure 6. (**a**) FTIR spectra of CBs, ZIF-8/CNTs/CBs, and CZIF-8/CNTs/CCBs. (**b**) XRD patterns for CBs, ZIF-8/CNTs/CBs, and CZIF-8/CNTs/CCBs.

Figure 7a–c shows the water contact angles of CBs, ZIF-8/CNTs/CBs, and CZIF-8/CNTs/CCBs. CBs and ZIF-8/CNTs/CBs show good hydrophilicity, due to the existence of a hydrophilic group. After carbonization, CZIF-8/CNTs/CCBs possessed a superhydrophobic surface with a water contact angle of 152.7°. Interestingly, the water droplet descended and contacted with the surface of CZIF-8/CNTs/CCBs. However, as the water droplet continued to rise, the water droplet and the surface of the CZIF-8/CNTs/CCBs gradually separated, suggesting that the sample had an ultra-low contact-angle lag (Figure 7d). As shown in Figure 8, the absorption capability of the sample was evaluated. CZIF-8/CNTs/CCBs can quickly and completely absorb dichloromethane dyed by Oil Red O from the bottom of the water (Figure 8a). Furthermore, when CZIF-8/CNTs/CCBs contacted n-hexane dyed by Oil Red O on water, it absorbed the n-hexane in seconds (Figure 8b). These results suggest that this material has excellent oleophilic and hydrophobic properties. The oil–water separation performance of the samples was evaluated by measuring the absorption capacities for various oils and organic liquids (Figure 9a,b). CZIF-8/CNTs/CCBs showed absorption capacities Q_1 in the range of 48 to 84 times its original weight for oil and organic liquids. The absorption capacities Q_1 of CCBs were slightly higher than those of CZIF-8/CNTs/CCBs for most of the oils and organic liquids. However, it is worth noting that the absorption capacity Q_2 of CZIF-8/CNTs/CCBs was much higher than that of CCBs. The possible reason for this result is that CCBs become lighter and smaller after carbonization of the CBs. Although the absorption capacity Q_1 of CCBs for oil and organic liquids is relatively higher, the absorption capacity Q_2 is low on account of the low actual adsorption amount. Meanwhile, ZIF-8 and CNTs were loaded into the 3D interconnected network structure of CBs, and the mass of CZIF-8/CNTs/CCBs was relatively high. Therefore, the value of the absorption capacity Q_1 was lower than that of CCBs. However, the actual adsorption amount of CZIF-8/CNTs/CCBs was much higher, due to the porous structure with large volume and the loading of CZIF-8 and CNTs, resulting in a higher absorption capacity Q_2 value. Therefore, the loading of ZIF-8 and CNTs plays a critical role in improving the adsorption performance of CZIF-8/CNTs/CCBs. As shown in Table 1, the absorption capacity of CZIF-8/CNTs/CCBs is higher than that of various previously reported sorbent materials [31,39–45]. Although the sample shows lower absorption capacity than the reported materials [46–48], the precursor material is cheaper, and the preparation method is simpler. To investigate the recyclability of the sample, the absorption–distillation test was repeated up to nine times. As displayed in

Figure 9c, CZIF-8/CNTs/CCBs retained its high absorption capacity for n-heptane after nine cycles, indicating good recyclability. Based on these results, CZIF-8/CNTs/CCBs could be used as an ideal material for efficient separation of oil–water mixtures, due to its superhydrophobic properties.

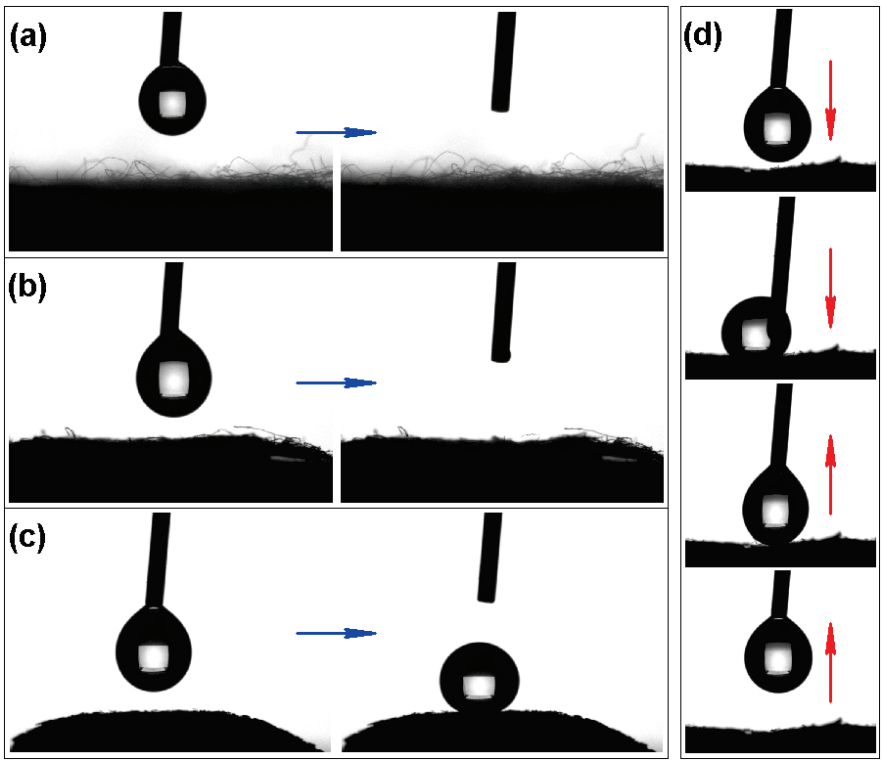


Figure 7. (**a**–**c**) The water static contact angle measurement for CBs, ZIF-8/CNTs/CBs, and CZIF-8/CNTs/CCBs. (**d**) Adhesion images of the water droplet on C ZIF-8/CNTs/CCBs.

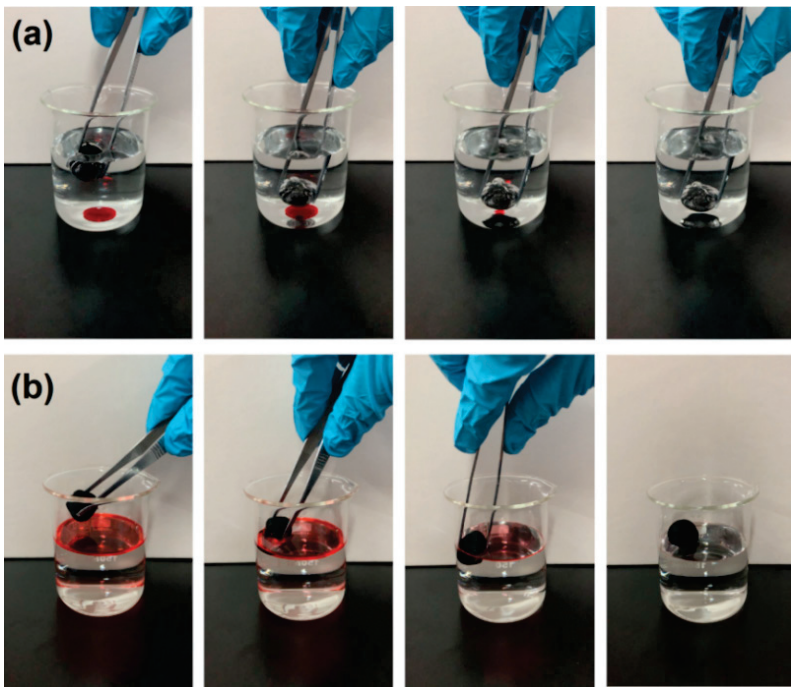


Figure 8. (**a**) Sorption process of dichloromethane (dyed with Oil Red O) by C ZIF-8/CNTs/CCBs. (**b**) Sorption process of n-hexane (dyed with Oil Red O) by C ZIF-8/CNTs/CCBs.

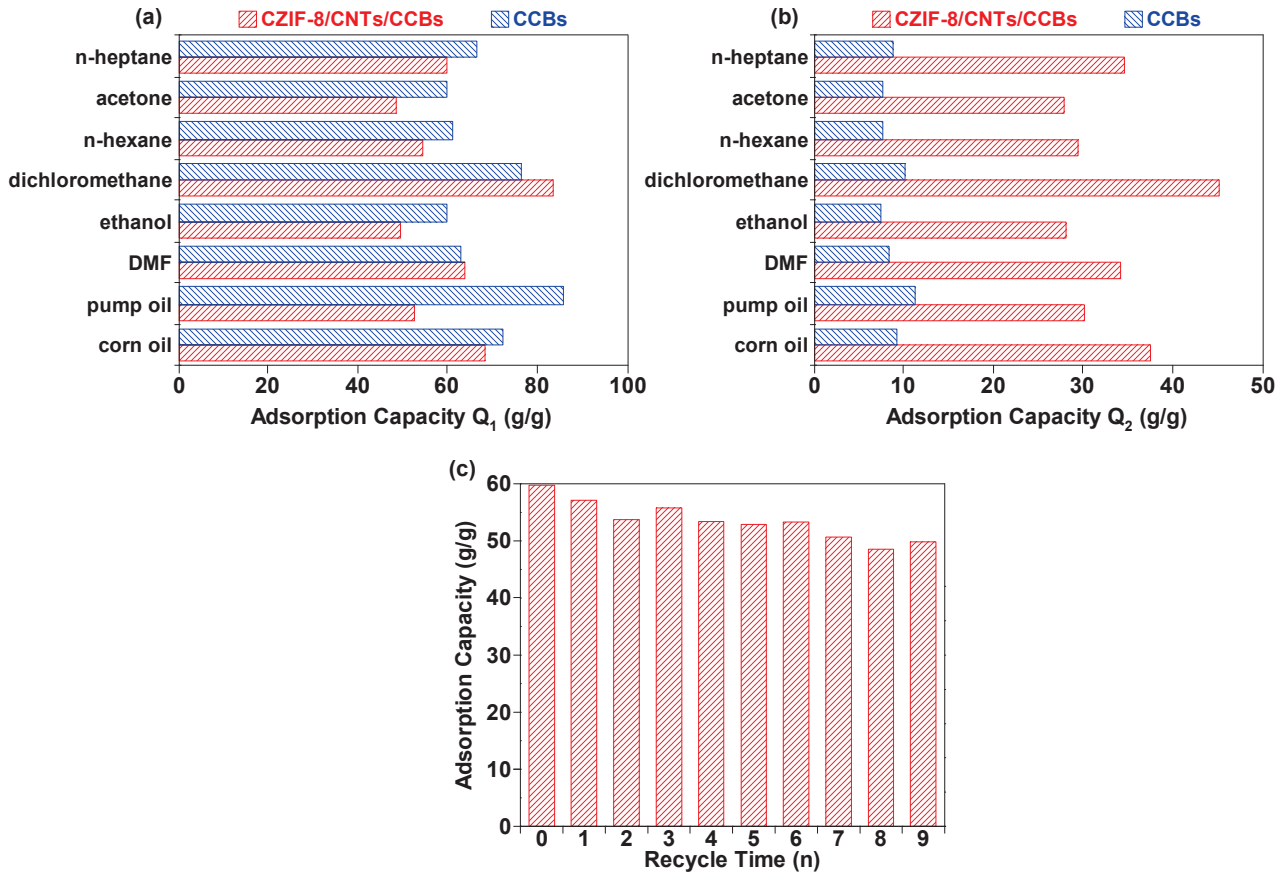


Figure 9. (**a**) Adsorption capacities Q_1 of CZIF-8/CNTs/CCBs and CCBs for oil or organic solvents. (**b**) Adsorption capacities Q_2 of CZIF-8/CNTs/CCBs and CCBs for oil or organic solvents. (**c**) Adsorption capacities of CZIF-8/CNTs/CCBs for n-heptane after 9 cycles.

Table 1. Comparison of various sorbent materials.

Sorbent Material	Absorbed Substances	Sorption Capacity ($g.g^{-1}$)	Ref.
CNT/wood aerogel	oils and organic solvents	16–39	[39]
Silylated wood sponges	oils and organic solvents	17–41	[40]
Carbon nanotube sponges	oils	49–56	[41]
Polyvinyl-alcohol-reinforced wood sponge	oils and organic solvents	4–27	[42]
Microwrinkled reduced graphene oxide	oils	36–84	[43]
Cellulose-based aerogels	oils and organic solvents	45–99	[48]
Winter melon carbon aerogel	oils and organic solvents	16–50	[45]
Carbon nanofiber aerogel	oils and organic solvents	37–87	[46]
MOF-coated cotton fiber composite	oils and organic solvents	25–48	[31]
MOF-reduced graphene oxide aerogel	oils and organic solvents	45–147	[47]
Polyimide/MXene aerogels	oils and organic solvents	18–58	[44]
CZIF-8/CNTs/CCBs	oils and organic solvents	48–84	This work

4. Conclusions

In summary, ZIF-8 and CNTs were fabricated in situ in the 3D interconnected network structure of CBs via a feasible strategy. Subsequently, carbonization treatment could effectively change the hydrophobic property of the sample. The characterization results suggested that CBs could be used as a porous structure for embedding ZIF-8 and CNTs, effectively improving the oil–water separation performance after carbonization. As an oleophilic and hydrophobic adsorbent, CZIF-8/CNTs/CCBs shows high sorption capacities of 48 to 84 times its own weight. Moreover, CZIF-8/CNTs/CCBs exhibits a stable oil

absorption capacity with reuse. This work provides a novel strategy for designing a superior adsorbent candidate for oil–water separation.

Author Contributions: Conceptualization, Y.S. and R.S.; methodology, Y.S.; validation, Z.K., C.S., and Q.W.; writing—original draft preparation, Y.S. and C.S.; writing—review and editing, Z.K., W.Y., and Z.Y. All authors have read and agreed to the published version of the manuscript.

Funding: This work was supported by Anhui Nature Science Research Program (KJHS2019B07), Anhui Provincial Nature Science Research Project (2008085MH269), Anhui Provincial Teaching Team Project (2020jxtd250), and Huangshan University Talent Introduction Funding (2018xkjq005).

Institutional Review Board Statement: Not applicable.

Informed Consent Statement: Not applicable.

Data Availability Statement: Data sharing is not applicable.

Conflicts of Interest: The authors declare no conflict of interest.

References

1. Yu, X.; Zhang, X.; Xing, Y.; Zhang, H.; Jiang, W.; Zhou, K.; Li, Y. Development of Janus Cellulose Acetate Fiber (CA) Membranes for Highly Efficient Oil-Water Separation. *Materials* **2021**, *14*, 5916. [CrossRef] [PubMed]
2. Sam, E.K.; Liu, J.; Lv, X. Surface Engineering Materials of Superhydrophobic Sponges for Oil/Water Separation: A Review. *Ind. Eng. Chem. Res.* **2021**, *60*, 2353–2364. [CrossRef]
3. Liu, H.; Geng, B.; Chen, Y.; Wang, H. Review on the Aerogel-Type Oil Sorbents Derived from Nanocellulose. *ACS Sustain. Chem. Eng.* **2016**, *5*, 49–66. [CrossRef]
4. Elhenawy, S.; Khraisheh, M.; AlMomani, F.; Hassan, M.K.; Al-Ghouti, M.A.; Selvaraj, R. Recent Developments and Advancements in Graphene-Based Technologies for Oil Spill Cleanup and Oil-Water Separation Processes. *Nanomaterials* **2021**, *12*, 87. [CrossRef]
5. Luo, W.; Sun, D.; Chen, S.; Shanmugam, L.; Xiang, Y.; Yang, J. Robust Microcapsules with Durable Superhydrophobicity and Superoleophilicity for Efficient Oil-Water Separation. *ACS Appl. Mater. Interfaces* **2020**, *12*, 57547–57559. [CrossRef]
6. Han, S.; Song, Q.; Feng, X.; Wang, J.; Zhang, X.; Zhang, Y. Flame-Retardant Silanized Boron Nitride Nanosheet-Infused Superhydrophobic Sponges for Oil/Water Separation. *ACS Appl. Nano Mater.* **2021**, *4*, 11809–11819. [CrossRef]
7. Kong, S.M.; Han, Y.; Won, N.I.; Na, Y.H. Polyurethane Sponge with a Modified Specific Surface for Repeatable Oil-Water Separation. *ACS Omega* **2021**, *6*, 33969–33975. [CrossRef]
8. Panickar, R.; Sobhan, C.B.; Chakravorti, S. Highly Efficient Amorphous Carbon Sphere-Based Superhydrophobic and Superoleophilic Sponges for Oil/Water Separation. *Langmuir* **2021**, *37*, 12501–12511. [CrossRef]
9. Wang, J.; Fan, Z.; Liu, Q.; Tong, Q.; Wang, B. Fabrication of PDMS@Fe_3O_4/MS Composite Materials and Its Application for Oil-Water Separation. *Materials* **2021**, *15*, 115. [CrossRef]
10. Ju, G.; Zhou, L.; Jiao, C.; Shen, J.; Luan, Y.; Zhao, X. One-Step Fabrication of a Functionally Integrated Device Based on Polydimethylsiloxane-Coated SiO_2 NPs for Efficient and Continuous Oil Absorption. *Materials* **2021**, *14*, 5998. [CrossRef]
11. Liu, D.; Wang, S.; Wu, T.; Li, Y. A Robust Superhydrophobic Polyurethane Sponge Loaded with Multi-Walled Carbon Nanotubes for Efficient and Selective Oil-Water Separation. *Nanomaterials* **2021**, *11*, 3344. [CrossRef] [PubMed]
12. Wu, F.; Pickett, K.; Panchal, A.; Liu, M.; Lvov, Y. Superhydrophobic Polyurethane Foam Coated with Polysiloxane-Modified Clay Nanotubes for Efficient and Recyclable Oil Absorption. *ACS Appl. Mater. Interfaces* **2019**, *11*, 25445–25456. [CrossRef] [PubMed]
13. Zhang, G.D.; Wu, Z.H.; Xia, Q.Q.; Qu, Y.X.; Pan, H.T.; Hu, W.J.; Zhao, L.; Cao, K.; Chen, E.Y.; Yuan, Z.; et al. Ultrafast Flame-Induced Pyrolysis of Poly(dimethylsiloxane) Foam Materials toward Exceptional Superhydrophobic Surfaces and Reliable Mechanical Robustness. *ACS Appl. Mater. Interfaces* **2021**, *13*, 23161–23172. [CrossRef] [PubMed]
14. Zhu, H.; Chen, D.; An, W.; Li, N.; Xu, Q.; Li, H.; He, J.; Lu, J. A Robust and Cost-Effective Superhydrophobic Graphene Foam for Efficient Oil and Organic Solvent Recovery. *Small* **2015**, *11*, 5222–5229. [CrossRef]
15. Bi, H.; Yin, Z.; Cao, X.; Xie, X.; Tan, C.; Huang, X.; Chen, B.; Chen, F.; Yang, Q.; Bu, X.; et al. Carbon fiber aerogel made from raw cotton: A novel, efficient and recyclable sorbent for oils and organic solvents. *Adv. Mater.* **2013**, *25*, 5916–5921. [CrossRef]
16. White, R.J.; Brun, N.; Budarin, V.L.; Clark, J.H.; Titirici, M.M. Always look on the "light" side of life: Sustainable carbon aerogels. *ChemSusChem* **2014**, *7*, 670–689. [CrossRef]
17. Yang, Y.; Tong, Z.; Ngai, T.; Wang, C. Nitrogen-rich and fire-resistant carbon aerogels for the removal of oil contaminants from water. *ACS Appl. Mater. Interfaces* **2014**, *6*, 6351–6360. [CrossRef]
18. Fu, C.; Gu, L.; Zeng, Z.; Xue, Q. One-Step Transformation of Metal Meshes to Robust Superhydrophobic and Superoleophilic Meshes for Highly Efficient Oil Spill Cleanup and Oil/Water Separation. *ACS Appl. Mater. Interfaces* **2020**, *12*, 1850–1857. [CrossRef]
19. Jiang, B.; Zhang, H.; Zhang, L.; Sun, Y.; Xu, L.; Sun, Z.; Gu, W.; Chen, Z.; Yang, H. Novel One-Step, In Situ Thermal Polymerization Fabrication of Robust Superhydrophobic Mesh for Efficient Oil/Water Separation. *Ind. Eng. Chem. Res.* **2017**, *56*, 11817–11826. [CrossRef]

20. Zhou, B.; Bashir, B.H.; Liu, Y.; Zhang, B. Facile Construction and Fabrication of a Superhydrophobic Copper Mesh for Ultraefficient Oil/Water Separation. *Ind. Eng. Chem. Res.* **2021**, *60*, 8139–8146. [CrossRef]
21. Lu, Z.; He, Y. Fabrication of superhydrophobic surfaces with tunable water droplet adhesion force by a two-step method. *Ceram. Int.* **2019**, *45*, 14389–14396. [CrossRef]
22. Kang, R.H.; Kim, D. Thermally Induced Silane Dehydrocoupling: Hydrophobic and Oleophilic Filter Paper Preparation for Water Separation and Removal from Organic Solvents. *Materials* **2021**, *14*, 5775. [CrossRef] [PubMed]
23. Kang, L.; Zhao, L.; Yao, S.; Duan, C. A new architecture of super-hydrophilic β-SiAlON/graphene oxide ceramic membrane for enhanced anti-fouling and separation of water/oil emulsion. *Ceram. Int.* **2019**, *45*, 16717–16721. [CrossRef]
24. Han, X.; Liu, S.; Shi, L.; Li, S.; Li, Y.; Wang, Y.; Chen, W.; Zhao, X.; Zhao, Y. ZIF-derived wrinkled Co3O4 polyhedra supported on 3D macroporous carbon sponge for supercapacitor electrode. *Ceram. Int.* **2019**, *45*, 14634–14641. [CrossRef]
25. Si, Y.; Dong, Z.; Jiang, L. Bioinspired Designs of Superhydrophobic and Superhydrophilic Materials. *ACS Cent. Sci.* **2018**, *4*, 1102–1112. [CrossRef] [PubMed]
26. Silviana, S.; Darmawan, A.; Dalanta, F.; Subagio, A.; Hermawan, F.; Milen Santoso, H. Superhydrophobic Coating Derived from Geothermal Silica to Enhance Material Durability of Bamboo Using Hexadimethylsilazane (HMDS) and Trimethylchlorosilane (TMCS). *Materials* **2021**, *14*, 530. [CrossRef]
27. Tudu, B.K.; Sinhamahapatra, A.; Kumar, A. Surface Modification of Cotton Fabric Using TiO_2 Nanoparticles for Self-Cleaning, Oil-Water Separation, Antistain, Anti-Water Absorption, and Antibacterial Properties. *ACS Omega* **2020**, *5*, 7850–7860. [CrossRef]
28. Song, C.; Zhao, J.; Li, H.; Liu, L.; Li, X.; Huang, X.; Liu, H.; Yu, Y. One-Pot Synthesis and Combined Use of Modified Cotton Adsorbent and Flocculant for Purifying Dyeing Wastewater. *ACS Sustain. Chem. Eng.* **2018**, *6*, 6876–6888. [CrossRef]
29. Ferreira, V.C.; Wise, W.R.; Monteiro, O.C. Comparative study of powder and cotton-supported BiOCl particles on the photocatalytic degradation of industrial pollutants. *Ceram. Int.* **2020**, *46*, 27508–27516. [CrossRef]
30. Yang, L.; Zhan, Y.; Yu, R.; Lan, J.; Shang, J.; Dou, B.; Liu, H.; Zou, R.; Lin, S. Facile and Scalable Fabrication of Antibacterial CO_2-Responsive Cotton for Ultrafast and Controllable Removal of Anionic Dyes. *ACS Appl. Mater. Interfaces* **2021**, *13*, 2694–2709. [CrossRef]
31. Dalapati, R.; Nandi, S.; Gogoi, C.; Shome, A.; Biswas, S. Metal-Organic Framework (MOF) Derived Recyclable, Superhydrophobic Composite of Cotton Fabrics for the Facile Removal of Oil Spills. *ACS Appl. Mater. Interfaces* **2021**, *13*, 8563–8573. [CrossRef] [PubMed]
32. Du, J.; Liu, L.; Hu, Z.; Yu, Y.; Zhang, Y.; Hou, S.; Chen, A. Raw-Cotton-Derived N-Doped Carbon Fiber Aerogel as an Efficient Electrode for Electrochemical Capacitors. *ACS Sustain. Chem. Eng.* **2018**, *6*, 4008–4015. [CrossRef]
33. Yue, Y.; Huang, Y.-L.; Bian, S.-W. Nitrogen-Doped Hierarchical Porous Carbon Films Derived from Metal–Organic Framework/Cotton Composite Fabrics as Freestanding Electrodes for Flexible Supercapacitors. *ACS Appl. Electron. Mater.* **2021**, *3*, 2178–2186. [CrossRef]
34. Singla, G.; Bhange, S.N.; Mahajan, M.; Kurungot, S. Facile synthesis of CNT interconnected PVP-ZIF-8 derived hierarchically porous Zn/N co-doped carbon frameworks for oxygen reduction. *Nanoscale* **2021**, *13*, 6248–6258. [CrossRef] [PubMed]
35. Wang, Y.; Zhang, N.; Tan, D.; Qi, Z.; Wu, C. Facile Synthesis of Enzyme-Embedded Metal-Organic Frameworks for Size-Selective Biocatalysis in Organic Solvent. *Front. Bioeng. Biotechnol.* **2020**, *8*, 714. [CrossRef] [PubMed]
36. Zhang, Y.; Jia, Y.; Li, M.; Hou, L. Influence of the 2-methylimidazole/zinc nitrate hexahydrate molar ratio on the synthesis of zeolitic imidazolate framework-8 crystals at room temperature. *Sci. Rep.* **2018**, *8*, 9597. [CrossRef]
37. Yin, W.; Li, M.; Hu, T.; Xue, Z.; Yu, J.; Chi, R. Preparation of an Adsorbent Based on Amidoxime and Triazole Modified Waste Cotton Fabrics through an Azide–Alkyne Click Reaction with Excellent Adsorption Performance toward Cu(II). *ACS Sustain. Chem. Eng.* **2018**, *7*, 1944–1955. [CrossRef]
38. Mu, J.; Shao, C.; Guo, Z.; Zhang, Z.; Zhang, M.; Zhang, P.; Chen, B.; Liu, Y. High photocatalytic activity of ZnO-carbon nanofiber heteroarchitectures. *ACS Appl. Mater. Interfaces* **2011**, *3*, 590–596. [CrossRef]
39. Zhu, Z.; Fu, S.; Lucia, L.A. A fiber-aligned thermal-managed wood-based superhydrophobic aerogel for efficient oil recovery. *ACS Sustain. Chem. Eng.* **2019**, *7*, 16428–16439. [CrossRef]
40. Guan, H.; Cheng, Z.; Wang, X. Highly compressible wood sponges with a spring-like lamellar structure as effective and reusable oil absorbents. *ACS Nano* **2018**, *12*, 10365–10373. [CrossRef]
41. Gui, X.; Zeng, Z.; Lin, Z.; Gan, Q.; Xiang, R.; Zhu, Y.; Cao, A.; Tang, Z. Magnetic and highly recyclable macroporous carbon nanotubes for spilled oil sorption and separation. *ACS Appl. Mater. Interfaces* **2013**, *5*, 5845–5850. [CrossRef] [PubMed]
42. Cai, Y.; Wu, Y.; Yang, F.; Gan, J.; Wang, Y.; Zhang, J. Wood sponge reinforced with polyvinyl alcohol for sustainable oil-water separation. *ACS Omega* **2021**, *6*, 12866–12876. [CrossRef]
43. Feng, C.; Yi, Z.; She, F.; Gao, W.; Peng, Z.; Garvey, C.J.; Dumee, L.F.; Kong, L. Superhydrophobic and superoleophilic microwrinkled reduced graphene oxide as a highly portable and recyclable oil sorbent. *ACS Appl. Mater. Interfaces* **2016**, *8*, 9977–9985. [CrossRef] [PubMed]
44. Wang, N.N.; Wang, H.; Wang, Y.Y.; Wei, Y.H.; Si, J.Y.; Yuen, A.C.Y.; Xie, J.S.; Yu, B.; Zhu, S.E.; Lu, H.D.; et al. Robust, lightweight, hydrophobic, and fire-retarded polyimide/MXene aerogels for effective oil/water separation. *ACS Appl. Mater. Interfaces* **2019**, *11*, 40512–40523. [CrossRef] [PubMed]
45. Li, Y.-Q.; Samad, Y.A.; Polychronopoulou, K.; Alhassan, S.M.; Liao, K. Carbon aerogel from winter melon for highly efficient and recyclable oils and organic solvents absorption. *ACS Sustain. Chem. Eng.* **2014**, *2*, 1492–1497. [CrossRef]

46. Ieamviteevanich, P.; Palaporn, D.; Chanlek, N.; Poo-arporn, Y.; Mongkolthanaruk, W.; Eichhorn, S.J.; Pinitsoontorn, S. Carbon nanofiber aerogel/magnetic core–shell nanoparticle composites as recyclable oil sorbents. *ACS Appl. Nano Mater.* **2020**, *3*, 3939–3950. [CrossRef]
47. Sun, T.; Hao, S.; Fan, R.; Qin, M.; Chen, W.; Wang, P.; Yang, Y. Hydrophobicity-adjustable MOF constructs superhydrophobic MOF-rGO aerogel for efficient oil-water separation. *ACS Appl. Mater. Interfaces* **2020**, *12*, 56435–56444. [CrossRef]
48. Zhang, X.; Wang, H.; Cai, Z.; Yan, N.; Liu, M.; Yu, Y. Highly compressible and hydrophobic anisotropic aerogels for selective oil/organic solvent absorption. *ACS Sustain. Chem. Eng.* **2018**, *7*, 332–340. [CrossRef]

applied sciences

MDPI

Article

Study on the Method of Household Waste Collection: Case Study

Mirela Panainte-Lehadus [1], Mihai Vulpe [1], Valentin Nedeff [1,2], Emilian Mosnegutu [1,*], Grzegorz Przydatek [3], Claudia Tomozei [1] and Dana Chitimus [1]

[1] Faculty of Engineering, "Vasile Alecsandri" University of Bacău, 600115 Bacău, Romania; mirelap@ub.ro (M.P.-L.); vulpemh@yahoo.com (M.V.); vnedeff@ub.ro (V.N.); claudia.tomozei@ub.ro (C.T.); dana.chitimus@ub.ro (D.C.)
[2] "Gheorghe Ionescu-Şişeşti" Academy of Agricultural and Forestry Sciences, 011464 București, Romania
[3] Institute of Engineering, Nowy State University of Applied Sciences Sacz, Zamenhofa 1a, 33-300 Nowy Sacz, Poland; g.przydatek@gmail.com
* Correspondence: emos@ub.ro

Abstract: This article presents research on how household waste is collected. An online survey, with 348 participants, from the Romanian region of Bacau, was conducted from October 2018 to May 2019. The online questionnaire included a set of over 40 questions, some with the aim of identifying the nature of the people participating, but most of the questions being designed to determine the collection methods for household waste. The major goal of the current study, as previously stated, was to determine the primary way of collecting household garbage from the public, while also learning various details about the participants, including their residence location, gender, age, and level of education. Referring to the means used for collecting household waste, the following items were noted: trash cans, cardboard boxes, dumpsters, and raffia bags. As a result of the study carried out, the following conclusions were drawn: it was noticed that 70 percent of those who participated in the survey came from urban areas; a larger percentage of female respondents took part in the survey (128 from 348); the majority of respondents were aged 18–29 (182); 178 respondents had a higher education level; collection of household waste in garbage bags represented 62.9 percent of the total collection methods. Following statistical processing of the data, and an overview of the main ways in which household waste was collected, a number of connections were found between the characteristics of the respondents and their household waste collection. What is noteworthy is that the characteristics of the respondents could be grouped into cumulative factors that played an important role in household waste collection: the first group formed by level of education and location of the respondents, and the second group formed by age and gender of the respondents.

Keywords: waste management; online questionnaire; household waste; statistical analysis

Citation: Panainte-Lehadus, M.; Vulpe, M.; Nedeff, V.; Mosnegutu, E.; Przydatek, G.; Tomozei, C.; Chitimus, D. Study on the Method of Household Waste Collection: Case Study. *Appl. Sci.* **2022**, *12*, 7490. https://doi.org/10.3390/app12157490

Academic Editors: Mohammad Mahmudur Rahman, Dibyendu Sarkar, Rupali Datta and Prafulla Kumar Sahoo

Received: 29 April 2022
Accepted: 22 July 2022
Published: 26 July 2022

Publisher's Note: MDPI stays neutral with regard to jurisdictional claims in published maps and institutional affiliations.

Copyright: © 2022 by the authors. Licensee MDPI, Basel, Switzerland. This article is an open access article distributed under the terms and conditions of the Creative Commons Attribution (CC BY) license (https://creativecommons.org/licenses/by/4.0/).

1. Introduction

With human progress, an increasing amount of waste is produced, resulting in waste disposal using up land, as well as contributing to global warming and having negative environmental impacts [1–3].

As a result of these factors, numerous concepts for reducing the quantity of waste created by both the public and enterprises have been developed.

Economic agents in Romania may restrict the quantity of trash created. At the European Union level, there are several legislative mechanisms that can be used to enforce existing laws. Even though the same measures apply to economic agents and to the population, the enforcement of the measures is difficult to achieve in the case of the general population.

The idea of sustainable development is more present in every aspect of human society. One of the components of this concept is the control of waste produced by both the populace and economic agents [4–15].

To create an overview of the concept of waste management as it is understood by the populace, a number of studies have been carried out by various governmental or commercial organizations [16–23]. In these studies, a precise focus is placed on aspects related to demographic parameters, the level of education of the population in the reference region, the type of housing, as well as the age of the population. The intention is to help the populace make the best waste management system choices. The choices about waste management methods are also known to be influenced by social behaviors, financial factors, cultural factors, etc. [24–37].

These studies were based on statistical analysis or real-world case analysis (for cities, institutions, areas with specific characteristics, etc.) [14,38–55].

In the future, we must ensure that people use existing waste management systems and also make use of specific systems to generate energy and material resources. To this end, people must be informed, and educational mechanisms must be established, that emphasize the importance of such ways of thinking [14,56–58].

This article describes online research on the temporary storage of household waste among the population of the Bacau region of Romania. The main purpose of this article was to identify how the population collects household waste. Whether there were statistical relationships between the different criteria used to define the group of respondents in this study and how they collect household waste was a further aim.

2. Research Methodology

Advances in software systems and current technological opportunities have made it possible to conduct targeted research on specific segments of the population at a faster rate and at a lower cost, while also providing many options for database design and interpretation.

The study presented in this paper was carried out using the Google platform, with 40-item questionnaires completed and distributed online.

This article offers the results of an analysis of part of the research. The Bacău region had a population of 742,053 in 2018.The data was provided from the responses of 348 participants who participated in the survey. Of the responses, 271 corresponded to a 90 percent confidence level [59], which, as a consequence, meant the study had a high degree of validity.

The questionnaire was distributed in an online environment and the results were obtained between 19 October 2018 and 1 May 2019.

The data flow diagram in Figure 1 shows the study's working process.

Based on the results of this study, it was decided to analyze the methods of waste collection at the generator's source, as well as the methods of waste collection by the general public, based on:

- Respondents' reference: urban area and rural area
- Gender: male and female
- Age: 15–17 years; 18–29 years; 30–39 years; 40–49 years; 50–59 years; 60–64 years; over 65 years
- Level of studies: secondary; university; postgraduate; other studies; professional

The collected material was subjected to descriptive and statistical analysis. Multi-way tables and homogeneity tests were used. The test probability value was $p < 0.05$. Frequency and multi-partition tables show the distribution of observations, due to several features at the same time. Pearson's chi-square test of independence and ML (Maximum Likelihood) for multi-way tables were used, these being used primarily in the study of the interdependence of nominal variables. In addition, hierarchical cluster analysis was applied using the agglomeration method, taking into account Ward's method and the percentage discrepancy matrix. In the article degrees of freedom (df) were tagged.

The data collected from the surveys was used to see if there were any relationships between the so-called input parameters and the home waste collection methods. Statistical analysis was performed for this purpose using two programs, namely StatSoft Poland and OriginPro.

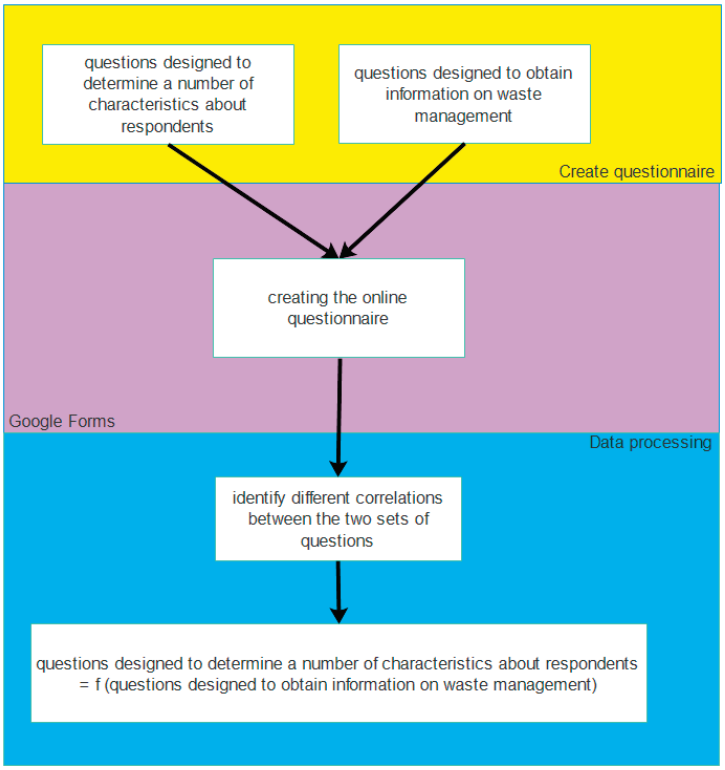


Figure 1. Working methodology.

3. Results

Following the analysis of the data obtained through the questionnaires, the following graphical representation was derived (Figure 2 and Table 1).

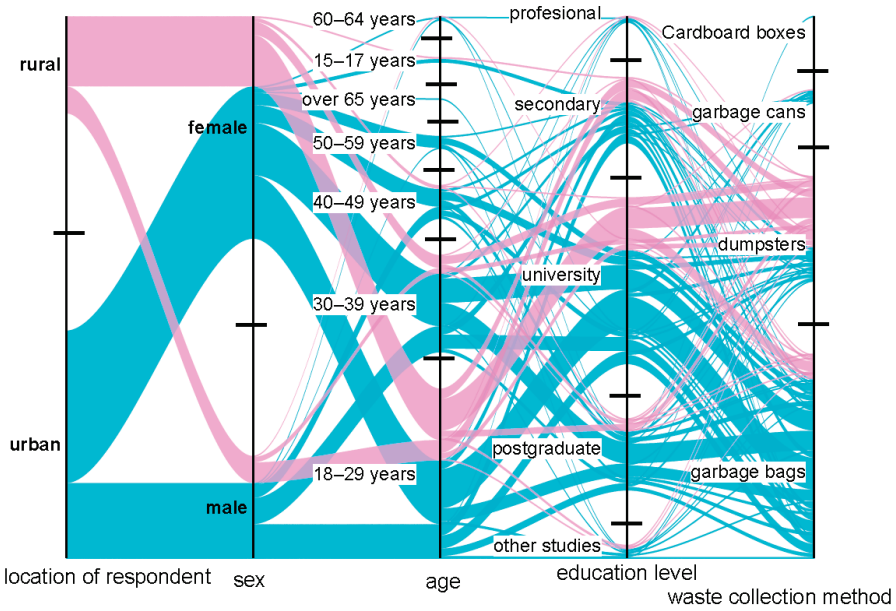


Figure 2. Distribution of the results obtained through the questionnaire.

Table 1. Table indicating the studied parameters' frequency analysis by classes, amount and waste collection method.

Class	Number	Contribution [%]
Location of respondent (pcs.)		
urban	244	70.11
rural	104	29.89
Sex (person)		
female	110	31.61
male	238	68.39
Age (person)		
18–29 years	182	52.30
30–39 years	104	29.89
40–49 years	36	10.34
50–59 years	14	4.02
15–17 years	6	1.72
60–64 years	5	1.44
above 65 years	1	0.29
Education level (person)		
university	178	51.15
postgraduate	77	22.13
secondary	71	20.40
other studies	15	4.31
professional	7	2.01
Waste collection method (pcs.)		
garbage bags	219	62.93
dumpsters	113	32.47
garbage cans	16	4.31
cardboard boxes	1	0.28

The following conclusions may be drawn from the graphic representation in Figure 2:

(a) 70% of those who participated in the survey were from urban areas, with the rest from rural areas;

(b) The number of female respondents who completed the questionnaire was determined to be 128 greater than the number of male respondents who did so;

(c) The following results were reached after evaluating the age distribution of respondents who completed the questionnaire:

- The age group 18–29 years had the most respondents (182), with 57.7% from urban areas and 42.3% from rural areas;
- People aged 30 to 39 were the second largest category, in terms of the number of respondents, with 104, more precisely 84 from urban areas, and 20 from rural areas;
- The age groups with the lowest values corresponded to intervals of more than 65 years. Six respondents were found between the ages of 15 and 17, 36 respondents were found between the ages of 40 and 49, 14 respondents were found between the ages of 50 and 59, and for the age range of 60–64 years, just one responder was found.

(d) An examination of the responses was also carried out, taking into consideration educational level of respondents. The following findings resulted from the investigation:

- There were 178 respondents with higher education, with 122 from the urban areas and 56 from the rural areas;
- There were 77 respondents with postgraduate degrees, 63 of them living in urban areas and 14 in rural areas;

- Those with a high school diploma had a score of 71, with 62% coming from urban areas and 38% living in rural areas;
- Other types of education applied to the remaining 3.73% of those who took part in the study (primary, secondary, vocational, or other).

(e) Several correlations between the characteristics of the studied group of respondents and the method of primary collection of household waste could be identified in a general analysis of the graphical representation in Figure 2. After the analysis, it was determined that:

- Many urban women between the ages of 18 and 29 and between 30 and 39 who have finished their university and postgraduate degrees collect household waste in household bags;
- Most urban men between the ages of 18 and 29 and between 30 and 39, with a high school or university degree, collect home waste in garbage bags;
- The majority of women in rural areas, between the ages of 18 and 29, with college degrees, collect household waste in landfills;
- In rural areas, most men between the ages of 18 and 29 with a high school education are responsible for collecting household waste in the trash.

In Table 1 it is noticeable that the largest share of 70.11% belonged to urban respondents. Men constituted the overwhelming share of 68.39% of the respondents. People aged 18–29 years constituted 52.30% of the respondents. It should be noted that respondents with higher education had a dominant share of 51.15%.

Next, a statistical evaluation of the data collecting method was carried out, based on the respondents' location (Table 2) and age (Table 3).

Table 2. Results of multi-partition table of method of waste collection taking into account the location of respondents.

Location of Respondent	Waste Collection Method/Contribution [%]			Total
	Garbage Bags	Dumpsters	Garbage Cans	
Urban	*79.01%*	*15.23%*	*5.76%*	70.03%
Rural	*25.96%*	*73.08%*	0.96%	29.97%
Total	63.11%	32.56%	4.32%	100.00%

Italic value of statistics means that quantity of cells > 10.

Table 3. Multi-partition table of method of waste collection taking into account respondents' age.

Age	Waste Collection Method/Contribution [%]			Total
	Garbage Bags	Dumpsters	Garbage Cans	
18–29 years	54.40%	41.21%	4.40%	52.45%
30–39 years	73.08%	23.08%	3.85%	29.97%
40–49 years	74.29%	17.14%	8.57%	10.09%
50–59 years	71.43%	28.57%	0.00%	4.03%
15–17 years	33.33%	66.67%	0.00%	1.73%
60–64 years	100.00%	0.00%	0.00%	1.44%
below 65 years	100.00%	0.00%	0.00%	0.29%
Total	63.11%	32.56%	4.32%	100.00%

Based on this analysis, it was concluded that the collection of urban household waste in household bags accounted for the biggest percentage, at 79.01%. A significantly high share was collected in dumpsters in rural areas, with the lowest share (0.96%) pertaining to collection regarding garbage cans in the rural areas.

From the studied parameters, the location of the respondents, and the method of collecting household waste, had a Chi value of Chi^2 (Table 4).

Table 4. Chi-square statistics and its components taking into account the location of the respondents and waste collection methods.

Statistic Location of Respondent × Waste Collection Method			
Statistic	**Chi2**	**df**	***p***
Chi2 Pearson	111.2061	df = 2	$p = 0.0000$
Chi2 ML	109.9521	df = 2	$p = 0.0000$

The statistically significant values for the Pearson and ML square had the same $p = 0.000$, which confirmed the significant influence of the respondents' locations on waste collection methods.

According to the analysis of the results, respondents between the ages of 40 and 49 collected the most waste into bags at 74.29%. In this mode of collecting, those aged 30–39 had a significantly lower 1.01%, and also the lowest percentage regarding use of dumpsters for waste collection.

The data from this group was subjected to analysis determining the value of the chi-square parameter (Table 5).

Table 5. Chi-square statistics and its components taking into account age and waste collection method.

Statistic Age × Waste Collection Method			
Statistic	**Chi^2**	**df**	***p***
Chi^2 Pearson	23.22422	df = 12	$p = 0.02588$
Chi^2 NW	25.98123	df = 12	$p = 0.01080$

Statistically significant values occurred when the Pearson Chi-square value did not exceed $p = 0.05$, which confirmed the influence of age on the collection method.

Next, we aimed to identify cluster correlations between the study input parameters and the output parameters.

In the beginning, a cluster analysis was performed using Ward's method. The result of this analysis is presented in Figure 3.

Based on the analysis of the two indicated clusters using Ward's method and the percentage of non-compliance matrix, it should be noted that the first cluster was dominated by rural respondents, men aged 18–29, with higher education, collecting waste, mainly in dumpsters. On the other hand, in the second group, the majority of respondents from the urban area, who also were men in the above-mentioned age group with the same level of education, collected garbage in bags.

Following this analysis, the next conclusions could be drawn:

- The highest share of used bags for segregation (79.01%) was in the urban area which underlined the importance of larger settlements in the efficiency of waste management;
- The significant influence on garbage collection method was age, which was confirmed by the highest share of 74.29% of respondents being aged 40–49 aged collecting in garbage bags;
- Men from the city and rural areas with higher education in the 18–29 age group have a significant impact on waste collection in Bacau County.

Figure 4 shows a Hierarchical Cluster Analysis. Cluster analysis was used to explain the detection of the structure in the data, taking into account the hierarchical grouping. This analysis allows the determination of the so-called tree structure of the elements of the analyzed object set.

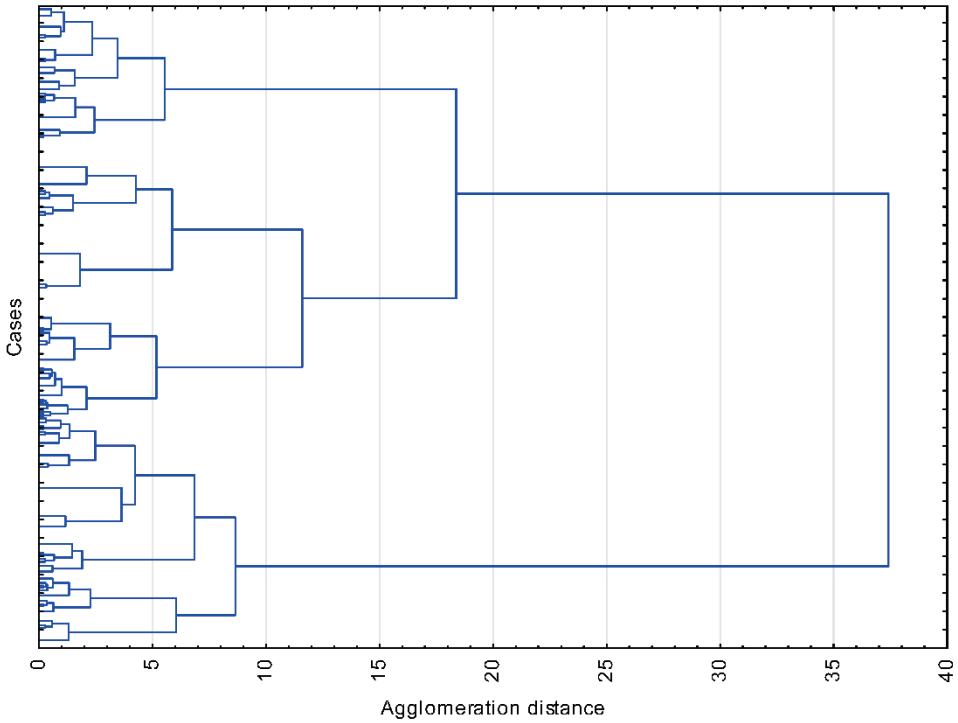


Figure 3. Agglomeration of Ward's method.

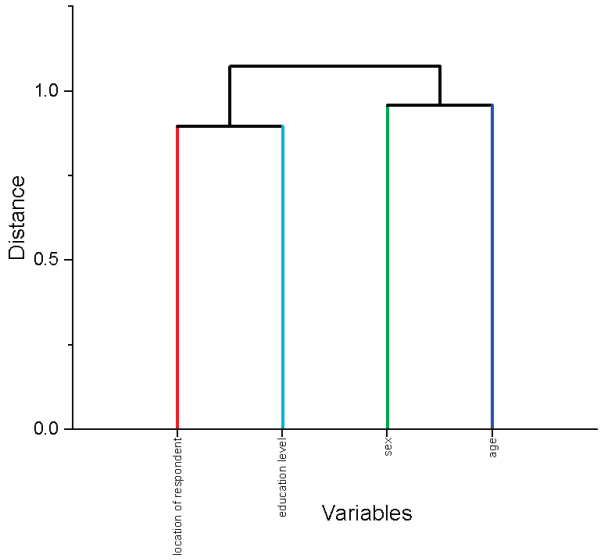


Figure 4. Analysis of hierarchical clusters.

Following this analysis, the following conclusions could be drawn:

- two clusters were identified, the first at a distance of 0.89, consisting of the level of education and location of the respondents, and the second cluster at a distance of 0.95, consisting of the respondent gender and age;
- the third cluster, which was secondary, connected the other two main clusters, the distance was 1.07;
- the last factor, with a distance of 1.08, was the location of the respondent.

4. Conclusions

This study was necessary because there are not many regional or national analyses of the solid household waste collection system which include the population that is served [47,53,54,59].

This study concentrated mostly on how the populace collects solid household waste inside the residential area. It did not consider the waste collection management system (from door to door or collection at a specified collection site) [3,11,12,19,23,28,32].

Following analysis of the results, it was found that:

- The share of respondents corresponding to the urban area was 70.1%, and the respondents from the rural area accounted for 29.9%;
- Regardless of the reference area of the respondents, the number of female respondents who participated in the study was 36.8% higher than the number of male respondents;
- The best efficiency of waste management was felt in the urban area which was confirmed by the highest share of used bags for segregation (79.01%).
- Taking into account the level of education of the respondents, 178 respondents had higher education, 77 respondents had postgraduate studies, and 71 respondents only had high school studies;
- In terms of age, in this online survey, it was found that the largest share was held by respondents aged between 18 and 29, namely 182 respondents, followed by respondents aged between 30 and 39 years, numbering 104 respondents;
- As a method of collection of household waste, it was found that the collection of waste in garbage bags accounted for 62.9%, followed by collection in dumpsters at 32.4%, and collection into garbage cans at 4.3%;
- Statistical analysis was done to find the relationships between the study's input and output parameters. For this reason, a cluster statistical analysis was used. Following these analyses, a series of correlations were identified.
- The identification of the method of primary collection of waste generated by the population aimed to achieve an overview of the understanding of the concept of collection by the population;
- Waste management was significant for young women who come from a city with higher education;
- In conclusion from the questionnaire, it can be said that the level of education and gender are the main factors that directly influence the collection of municipal waste, followed by the age of the respondent and the place where the respondent lives.

Author Contributions: Conceptualization, M.V.; methodology, V.N.; software, E.M. and G.P.; validate, V.N.; formal analysis, C.T. and D.C.; investigation, M.P.-L.; drafting—drafting the original project, M.V.; writing—review and editing, E.M. and G.P.; supervision, V.N.; project management, V.N. All authors have read and agreed to the published version of the manuscript.

Funding: This research received no external funding.

Institutional Review Board Statement: Not applicable.

Informed Consent Statement: Not applicable.

Data Availability Statement: Not applicable.

Conflicts of Interest: The authors do not declare any conflict of interest.

References

1. Abdallah, M.; Adghim, M.; Maraqa, M.; Aldahab, E. Simulation and optimization of dynamic waste collection routes. *Waste Manag. Res.* **2019**, *37*, 793–802. [CrossRef]
2. Agovino, M.; Ferrara, M.; Garofalo, A. Determinants of separate waste collection in Italy: A multidimensional analysis at the provincial level. *Environ. Dev. Sustain.* **2017**, *19*, 2297–2316. [CrossRef]
3. Rodrigues, S.; Martinho, G.; Pires, A. Waste collection systems. Part A: A taxonomy. *J. Clean. Prod.* **2016**, *113*, 374–387. [CrossRef]
4. Ulfik, A.; Nowak, S. Determinants of municipal waste management in the sustainable development of Polish regions. *Pol. J. Environ. Stud.* **2014**, *23*, 1039–1044.
5. Ianos, I.; Zamfir, D.; Stoica, I.; Cercleux, A.-L.; Schvab, A.; Pascariu, G. Solid municipal waste management for the sustainable development of the Bucharest metropolitan area. *Environ. Eng. Manag. J.* **2012**, *11*, 359–369. [CrossRef]
6. Ahmad, M.; Tri, U.; Tri, W.; Novia, R. Empowering the community in the field of waste management for sustainable development. *IOP Conf. Ser. Earth Environ. Sci.* **2019**, *281*, 012019. [CrossRef]

7. Abderrahmane, Y.; Okkacha, Y.; Hassiba, B. Sustainable solid waste management in Mecheria (western Algeria). *Energy Procedia* **2014**, *50*, 953–959.
8. Ahmed, N. Sustainable Community Waste Collection in Karachi, Pakistan. *Proc. Inst. Civ. Eng. Eng. Sustain.* **2009**, *162*, 169–176. [CrossRef]
9. Dugdhe, S.; Shelar, P.; Jire, S.; Apte, A. Efficient waste collection system. In Proceedings of the 2016 International Conference on Internet of Things and Applications (IOTA), Pune, India, 22–24 January 2016; pp. 143–147.
10. Giel, R.; Plewa, M. The evaluation method of the process of municipal waste collection. In Proceedings of the Carpathian Logistics Congress, Jesenik, Czech Republic, 4–6 November 2015; pp. 281–287.
11. Jucá, J.F.T.; Barbosa, K.R.M.; Sobral, M.C. Sustainability Indicators for Municipal Solid Waste Management: A Case Study of the Recife Metropolitan Region, Brazil. *Waste Manag. Res.* **2020**, *38*, 1450–1454. [CrossRef]
12. Laurieri, N.; Lucchese, A.; Marino, A.; Digiesi, S. Case study of a door-to-door waste collection system: A study on its sustainability and effectiveness. *Sustainability* **2020**, *12*, 5520. [CrossRef]
13. Mondal, M.M.; Speier, C.J.; Weichgrebe, D. A multi-step approach to sustainable municipal solid waste collection systems in urban areas of newly industrialized Asian countries. *Environ. Manag.* **2019**, *63*, 536–553. [CrossRef]
14. Mosnegutu, E.; Panainte-Lehadus, M.; Nedeff, F.; Tirtoaca, O.; Tomozei, C. Waste management evaluation of in the context of sustainable development. Case study Vasile Alecsandri University from Bacau. *Int. J. Conserv. Sci.* **2020**, *11*, 179–188.
15. Siu, K.W.M.; Xiao, J.X. Design and management of recycling facilities to participate in household and community recycling. *Facilities* **2016**, *34*, 350–374. [CrossRef]
16. Cole, C.; Quddus, M.; Wheatley, A.; Osmani, M.; Kay, K. The impact of local government interventions on household waste collection: A case study approach using time series modeling. *Waste Manag.* **2014**, *34*, 266–272.
17. Dahlen, L.; Vukicevic, S.; Meijer, J.E.; Lagerkvist, A. Comparison of different sorted household waste collection systems in Sweden. *Waste Manag.* **2007**, *27*, 1298–1305.
18. Dahlen, L.; Lagerkvist, A. Evaluation of recycling programs in household waste collection systems. *Waste Manag. Res.* **2010**, *28*, 577–586. [CrossRef]
19. Jouhara, H.; Czajczynska, D.; Ghazal, H.; Krzyiynska, R.; Anguilano, L.; Reynolds, K.J.; Spencer, N. Municipal household waste management systems. *Energy* **2017**, *139*, 485–506. [CrossRef]
20. Kassim, S.M.; Ali, M. Solid Waste Collection by the Private Sector: A Household Perspective - Findings from a Study in Dar es Salaam, Tanzania. *Habitat. Int.* **2006**, *30*, 769–780.
21. Lakhan, C. Assessing the effects of unit-based waste disposal systems on the collection of recyclable household materials in Ontario, Canada. *Resour. Conserv. Recy.* **2015**, *95*, 38–45.
22. Mwanza, B.G.; Mbohwa, C.; Telukdarie, A. The influence of waste collection systems on resource recovery: A Review. *Procedia Manufact.* **2018**, *21*, 846–853.
23. Warunasinghe, W.; Yapa, P.I. A survey on household solid waste management (SWM) with special reference to a suburban area (Kottawa) in Colombo. *Procedia Food Sci.* **2016**, *6*, 257–260.
24. Desa, A.; Kadir, N.B.y.A.; Yusooff, F. Waste education and awareness strategy: Towards solid waste management (SWM) program at UKM. *Procedia Soc. Behav. Sci.* **2012**, *59*, 47–50. [CrossRef]
25. Del Cimmuto, A.; Mannocci, A.; Ribatti, D.; Boccia, A.; La Torre, G. Impact on knowledge and behaviour of the general population of two different methods of solid waste management: An explorative cross-sectional study. *Waste Manag. Res.* **2014**, *32*, 556–561. [CrossRef]
26. Hirsh, J. Environmental sustainability and national personality. *J. Environ. Psychol.* **2014**, *38*, 233–240.
27. Abdelli, I.S.; Abdelmalek, F.; Djelloul, A.; Mesghouni, A.; Addou, A. GIS-based approach to optimized household waste collection in Mostaganem (Western Algeria). *Waste Manag. Res.* **2016**, *34*, 417–426. [CrossRef]
28. Arnfelser, F. Systems and installations for the collection of household waste in Vienna. *Waste Manag. Res.* **1992**, *10*, 535–541.
29. Albine, A.D.; Williams, I.D. Explaining the differences between local authorities in England and Wales in the collection and treatment of household food waste. *Waste Manag.* **2017**, *70*, 222–235.
30. Bertanza, G.; Ziliani, E.; Menoni, L. Indicators of technical-economic performance of municipal solid waste collection strategies. *Waste Manag.* **2018**, *74*, 86–97. [CrossRef]
31. Blazquez, C.; Paredes-Belmar, G. Design of the network of a household waste collection system: A case study of the commune of Renca in Santiago, Chile. *Waste Manag.* **2020**, *116*, 179–189. [CrossRef]
32. Chen, H.B.; Zhou, J.C.; Zhang, H.L.; Yang, Y. Optimizing household waste collection using the Ahp-Mea model: A case study from Kunming, China. *Environ. Eng. Manag. J.* **2017**, *16*, 2887–2899.
33. Gallardo, A.; Bovea, M.D.; Mendoza, F.J.C.; Prades, M. The evolution of sorted waste collection: A case study of Spanish cities. *Waste Manag. Res.* **2012**, *30*, 859–863. [CrossRef]
34. Hage, O.; Soderholm, P. An econometric analysis of regional differences in household waste collection: The case of plastic packaging waste in Sweden. *Waste Manag.* **2008**, *28*, 1720–1731.
35. Koushki, P.A.; Al-Duaij, U.; Al-Ghimlas, W. The cost of collecting and transporting solid household waste in Kuwait. *Waste Manag.* **2004**, *24*, 957–964. [CrossRef]
36. Shabanova, M. Separate waste collection in Russia: The level, factors and potential for citizen engagement. *Mir Rossii-Universe Russia* **2019**, *28*, 88–112.

37. Santos Moraes, L.R. Household solid waste bagging and collection and their health implications for children living in outlying urban settlements in Salvador, Bahia State, Brazil. *Cad. Saude Publica* **2007**, *23*, S643–S649. [CrossRef]
38. Oyekale, A.S. Determinants of households' involvement in waste separation and collection for recycling in South Africa. *Environ. Dev. Sustain.* **2018**, *20*, 2343–2371. [CrossRef]
39. Phu, S.T.P.; Fujiwara, T.; Minh, G.H.; Van, D.P. Solid waste management practice in a tourist destination - status and challenges: A Case study in Hoi An, Vietnam. *Waste Manag. Res.* **2019**, *37*, 1077–1088. [CrossRef]
40. Miranda, P.A.; Blazquez, C.A.; Vergara, R.; Weitzler, S. A new methodology for designing a waste collection system for island areas. *Transport. Res. E-Log.* **2015**, *77*, 227–247.
41. Mas Pertiwi, I.; Kristinayanti, W.S.; Sudiasa, W.; Andayani, K.W. Bali Badung waste management system, based on community behavior. *IOP Conf. Ser. Mater. Sci. Eng.* **2019**, *690*, 012009. [CrossRef]
42. Escortar, L.M. Study on the collection of household waste in urban communities, Cluj County. In Proceedings of the 6th International Management Conference: Approaches in Organizational Management, Buchares, Romania, 15–16 November 2012; pp. 749–755.
43. Kadir, A.A.; Sani, M. Study of solid waste composition at Taman Universities, Parit Raja, Batu Pahat. In *IOP-Materials Science and Engineering Conference Series, Proceedings of the Soft Soil Engineering International Conference 2015, Langkawi, Malaysia, 27–29 October 2015*; IOP: Bristol, UK, 2016; Volume 136.
44. Vilms, M.; Kalda, O. Introduction of a new system for sorting and collecting waste at a university. In Proceedings of the the 10th International Conference on Environmental Engineering, Vilnius, Lithuania, 27–28 April 2017.
45. Oliveira, V.; Sousa, V.; Dias-Ferreira, C. Dataset of socio-economic and waste collection indicators for Portugal at municipal level. *Data Brief* **2019**, *22*, 658–661. [CrossRef]
46. Wang, H.; El, J.; Kim, Y.; Kamata, T. Municipal solid waste management in rural areas and small counties: An economic analysis using contingent assessment to estimate willingness to pay for Yunnan, China. *Waste Manag. Res.* **2014**, *32*, 695–706. [CrossRef]
47. Vasloban, E.; Oroian, M.; Rusu, C. The integrated waste management system of Mureș County, Romania. *Technol. Chang. Manag.* **2009**, *2*, 159–161.
48. Soukopova, J.; Kalina, J.; Hrebicek, J. Mathematical and economic model of municipal waste management using Maple. In Proceedings of the 32nd International conference on Mathematical Methods in Economics, Olomouc, Czech Republic, 10–12 September 2014; pp. 938–943.
49. Reis, M.F.; Conti, M.D.; Correa, R.M. Solid waste management: Challenges and opportunities for the city of Sao Paulo. *Risus-J. Innov. Sustain.* **2015**, *6*, 77–96.
50. Liu, T.; Wu, Y.F.; Tian, X.; Gong, Y. Generation and collection of municipal solid waste in Beijing, China. *Resour. Conserv. Recy.* **2015**, *104*, 31–37.
51. Martinho, G.; Gomes, A.; Santos, P.; Ramos, M.; Cardoso, J.; Silveira, A.; Pires, A. A case study of packaging waste collection systems in Portugal - Part I: Performance and operation analysis. *Waste Manag.* **2017**, *61*, 96–107. [CrossRef]
52. Linderhof, V.; Kooreman, P.; Allers, M.; Wiersma, D. Prices based on weight in household waste collection: The case of Oostzaan. *Resour. Energy Econ.* **2001**, *23*, 359–371.
53. Vulpe, M.; Nedeff, V.; Lehadus, D.; Mosnegutu, E.F.; Cotirlet, P.C.; Barsan, N. The implication of the level of education in the perception of waste problems a case study applied to Romanian citizens. *Fresenius Environ. Bull.* **2021**, *30*, 7639–7646.
54. Vulpe, M.; Valentin, N.; Panainte-Lehadus, M.; Mosnegutu, E.F.; Barsan, N.; Tomozei, C. A study of waste management in different areas of Romania. *Fresenius Environ. Bull.* **2021**, *30*, 2686–2691.
55. Mangenda, H.H.; Nedeff, V.; Kunyima, K.; Barsan, N.; Moșneguțu, E.; Tomozei, C. Municipal waste management in Limete, Mont Amba district of Kinshasa, the Democratic Republic of the Congo. *J. Eng. Stud. Res.* **2014**, *20*, 39–45.
56. Merilainen, J.; Tukiainen, J. Public procurement versus Laissez-Faire: Evidence from Household Waste Collection. *Cesifo Econ. Stud.* **2019**, *65*, 446–463.
57. Przydatek, G. A comparative analysis of municipal waste management systems. *Pol. J. Environ. Stud.* **2016**, *25*, 2107–2112. [CrossRef]
58. Tirtoaca Irimia, O.; Grzegorz, P. Comparative analysis of the efficiency of the waste management system in some counties in Romania and Poland. *J. Eng. Stud. Res.* **2021**, *27*, 96–106.
59. Ce Este un Eșantion Reprezentativ. Available online: https://www.parintiicerschimbare.ro/ce-este-un-esantion-reprezentativ/ (accessed on 5 June 2022).

energies

MDPI

Article

Comprehensive Meta-Analysis of Pathways to Increase Biogas Production in the Textile Industry

Thuane Mendes Anacleto [1,2], Betina Kozlowsky-Suzuki [3], Alan E. Wilson [4] and Alex Enrich-Prast [2,5,6,*]

1 Programa de Pós-Graduação em Biotecnologia Vegetal e Bioprocessos, Universidade Federal do Rio de Janeiro, Rio de Janeiro 21941-901, Brazil; thuaneanacleto@gmail.com
2 Unidade Multiusuário de Análises Ambientais, Universidade Federal do Rio de Janeiro, Rio de Janeiro 21941-901, Brazil
3 Departamento de Ecologia e Recursos Marinhos, Universidade Federal do Estado do Rio de Janeiro, Rio de Janeiro 22290-240, Brazil; betinaksuzuki@unirio.br
4 School of Fisheries, Aquaculture, and Aquatic Sciences, Auburn University, Auburn, AL 36849, USA; wilson@auburn.edu
5 Department of Thematic Studies—Environmental Change and Biogas Solutions Research Center (BSRC), Linköping University, 581 83 Linköping, Sweden
6 Institute of Marine Science, Federal University of São Paulo (IMar/UNIFESP), Santos 04021-001, Brazil
* Correspondence: alex.enrich.prast@liu.se

Abstract: The textile industry is one of the largest environmental polluters in the world. Although waste management via anaerobic digestion (AD) is a sustainable strategy to transform waste into clean energy and water recovery, the efficiency of the AD process is reduced by the presence of recalcitrant materials, chemicals, and toxic contents. This study aims to investigate the performance of several chemical, physical, and biological pretreatments applied to improve the biodegradability of textile waste. We performed a meta-analysis with 117 data extracted from 13 published articles that evaluated the efficiency of pretreatments applied to textile waste prior to AD to increase biogas production measured as methane (CH_4) yield. Even though the majority of the studies have focused on the effect of chemical and physical pretreatments, our results showed that the application of biological pretreatments are more efficient and eco-friendlier. Biological pretreatments can increase CH_4 yield by up to 360% with lower environmental risk and lower operating costs, while producing clean energy and a cleaner waste stream. Biological pretreatments also avoid the addition of chemicals and favor the reuse of textile wastewater, decreasing the current demand for clean water and increasing resource circularity in the textile industry.

Keywords: textile residues; biotechnology; methane; circular economy; fibers; cotton

Citation: Anacleto, T.M.; Kozlowsky-Suzuki, B.; Wilson, A.E.; Enrich-Prast, A. Comprehensive Meta-Analysis of Pathways to Increase Biogas Production in the Textile Industry. *Energies* **2022**, *15*, 5574. https://doi.org/10.3390/en15155574

Academic Editors: Dibyendu Sarkar, Rupali Datta, Prafulla Kumar Sahoo and Mohammad Mahmudur Rahman

Received: 7 June 2022
Accepted: 30 June 2022
Published: 1 August 2022

Publisher's Note: MDPI stays neutral with regard to jurisdictional claims in published maps and institutional affiliations.

Copyright: © 2022 by the authors. Licensee MDPI, Basel, Switzerland. This article is an open access article distributed under the terms and conditions of the Creative Commons Attribution (CC BY) license (https://creativecommons.org/licenses/by/4.0/).

1. Introduction

The textile industry is one of the largest polluting sectors worldwide, with an estimated waste production of 92 million tons per year [1], including pre- (i.e., agricultural production, fiber production, wastewater, solid waste) to post-consumer (i.e., manufacturing, logistics, retail and mixtures of discarded clothing or household items) waste in the supply chain [2]. Over 8000 chemicals (e.g., dyes, suspended solids, chlorinated aromatic hydrocarbons, surfactants, and heavy metals) are used in the textile supply chain [3,4]. As a result, effluents and solid waste with high loads of hazardous chemicals are discharged, thus increasing the toxicity of the produced waste, with a high pollution risk to the environment and human health [5].

Sustainable manufacturing is crucial to reducing the environmental impact of fashion and the textile industry. Projects and policies aiming at the sustainable development of the market, such as the [6], "Strategic Agenda on Textile Waste Management and Recycling", Expert Network on Textile Recycling (ENTeR), and Conference of the Parties (COP 21), as well as the 2030 Agenda for Sustainable Development Goals (SDGs), have been important players in reframing textile production. Incentive actions for reuse are also crucial to the

implementation of the circular economy model as established by the European Union in this sector [7].

Approaches to minimizing textile waste and increasing life span such as clothing rental and repairing, the second-hand market, and reprocessing operations for the production of original or new products [7] are alternatives to manage the polluting potential. However, the advance of fast fashion follows a business model that produces large quantities of clothing and trends at low prices [1], and often of low quality. The low quality of textiles makes recycling unfeasible, restricting their use to the end of the waste management hierarchy—energy recovery—as determined in the in the Directive 2008/98/EC [8].

Anaerobic digestion (AD) is a widely applied biotechnology that has proven its effectiveness as a green solution for waste management, reducing the risk of contamination while producing energy as biogas. AD implementation in the textile industry can contribute to waste use as a resource for the generation of clean energy, as well as water reuse. However, the wide range of chemicals, organic pollutants, and recalcitrant compounds (i.e., polyacrylates, phosphonates, alkyl phenol ethoxylates, chloroform, heavy metals, and cotton-based recalcitrant material [9]) of textile waste poses challenges, reducing the efficiency of degradation if AD is applied as the only strategy [10].

Several studies have suggested that the application of pretreatments is advantageous not only to improve organic matter degradability, but also to increase the biogas yield [10–13] and further remove dyes and toxic compounds from wastewater and solid waste from aqueous solutions [4,10]. Pretreatments can be chemical, physical, biological, or combinations of these, and their performance is influenced by the chemical composition of the waste [14]. Physical pretreatments (i.e., thermal, mechanical, irradiation, ultrasound) act by disrupting cells through physical force [15]. As a result, the contact surface of the organic matter is increased by reducing the particle size, facilitating microbial attack [16]. Although physical pretreatments are advantageous since no toxic compounds are generated, some techniques (e.g., thermal) can increase energy costs, becoming unfeasible at a large-scale [16]. Chemical pretreatments (i.e., acid, alkali, organic solvents) act by breaking chemical bonds from complex structures, causing an internal increase in the surface by swelling of the cell [17]. Chemical techniques are highly efficient in degrading complex materials and are more often applied than biological and physical pretreatments [17]. However, they require extra care, since depending on the chemical reagents applied, toxic compounds can be formed. Some chemicals pretreatments such as sulphuric acid (H_2SO_4), hydrochloric acid (HCl), and nitric acid (HNO_3) can further damage operational equipment by corrosion and failure of metals [18–20]. Biological pretreatments (i.e., fungi, bacteria, microbial consortia, enzymes) act in synergy with microbial metabolism, promoting the acceleration of the degradation of organic matter [16]. Avoiding the addition and generation of harmful chemicals promotes an environmentally healthier AD system. In addition, the lower capital and energy costs compared to physical and chemical pretreatments make the application of biological techniques extremely attractive even at full-scale [19,21].

In this context, we performed a systematic review followed by a meta-analysis of the available data in the literature to evaluate the effect of pretreatments applied to textile industry waste. The aim of this study was to assess the efficiency of several pretreatments applied to textile waste prior to AD. Based on the peer-reviewed literature, we compared several physical, chemical, and biological pretreatments, as well as combinations of these, to identify the best choice in terms of the highest organic waste reduction through biogas production with the highest cost–benefit ratio.

2. Materials and Methods

The Preferred Reporting Items for Systematic Reviews and Meta-analyses (PRISMA) was used as a guide to conduct the execution of the sampling design, determining the search strategy, keywords, and exclusion/inclusion criteria for evaluating the quality of articles [22]. A systematic review followed by a meta-analysis was carried out using the Web of Science and Scopus databases and the Google Scholar search engine. We

filtered our search using keywords combined with the aid of Boolean operators (AND) and wildcards (*, $): *anaerobic digestion*, *textile*, and *pretreatment*, from 1945 to 2021, English language, with article as the type of document. The eligibility criteria to include articles in the meta-analysis were: (i) textile waste as a unique substrate for AD; (ii) application of pretreatment for biogas production; (iii) measurement of methane yield from the organic fraction; (iv) experiments with specific descriptions and measurements for control and treatment samples.

Based on Hedges et al. [23], methane production data were quantified using the natural log response ratio (RR). Thus, the mean of the pretreatment performance ($\overline{X}_T$) was compared to the mean of the control ($\overline{X}_C$), following the equation

$$RR = \ln(\overline{X}_T / \overline{X}_C) \quad (1)$$

An unweighted meta-analysis was conducted to include the largest number of studies, even those that did not report a measure of variance for the response variable [24]. Mean effect sizes and 95% confidence intervals (CI) with bias correction were conducted using R software (R Core Team, 2021) using the "metafor" package (version 3.0-2). Pretreatments were considered significant ($p < 0.05$) when their mean effect and CI did not overlap the zero line. Mean and upper CI below the zero line indicate a negative response (i.e., treatment < control or treatment less efficient than control) while mean and lower CI above the zero line represent a positive response (i.e., treatment > control or treatment more efficient than control).

We assessed the potential production of CH_4 that could be generated from cotton and polyester waste if the most appropriate pretreatment is applied. Cotton and polyester waste data from the textile industry were collected, respectively, from [25,26]. The volatile solids (VS) and total solids (TS) content for each textile waste was based on data reported in the literature [27,28] (Equations (2) and (3); Table S1). The potential production of CH_4 was estimated based on the average methane yield of untreated and pretreated cotton and polyester, considering the pretreatments with the highest increase reported in this study (Table S2) and a lower calorific value of 9.97 kWh/m^3 CH_4 [29] (Equation (4)).

$$GCW = (CW \times TS\%) \times OM_{cotton} \quad (2)$$

$$GPW = (PW \times TS\%) \times OM_{polyester} \quad (3)$$

$$CH4\ potential = GPW \times CH_4 yield \times 9.97 \quad (4)$$

where GCW is global cotton waste (million t VS/y), CW is the cotton waste (million t/y), GPW is global polyester waste (million t VS/y), PW is the polyester waste (million t/y), OM is the organic matter content in the waste (e.g., cotton, polyester) (VS%), and 9.97 is the lower calorific value of CH_4 (kWh/m^3 CH_4).

3. Results and Discussion

A total of 117 data were extracted from 13 articles (Table S3) that applied pretreatments to improve AD of textile waste (Figure S1). The solid fraction of textile waste prevailed (81%) over the liquid fraction as the type of waste that undergoes pretreatment prior to AD. Wool and pure cotton were the waste sources with the largest contribution, ca. 38% each (Figure 1).

Cotton represents a robust fraction of textile waste [30]. Its chemical composition consisting mostly of cellulose, about 80% DW (Table 1), a polymer structure with high crystallinity that requires pretreatment for successful AD [31]. Wool is a natural protein fiber highly exploited as a raw material in the textile industry due to its qualities such as high heat retention, high stain and static resistance, and good flexibility [32]. As the highest methane yield is usually observed in protein-rich substrates [33], the high protein content in wool (70% DW) indicates its potentially high energy value (Table 1). In addition, wool and cotton come originally from the agricultural sector, where AD is largely applied as a "waste-to-energy" technology promoting waste recovery and energy generation [34].

Thus, both residues are strong candidates to be explored for energy recovery, as well as to strengthen the textile supply chain from its pre-consumer phase in agricultural production.

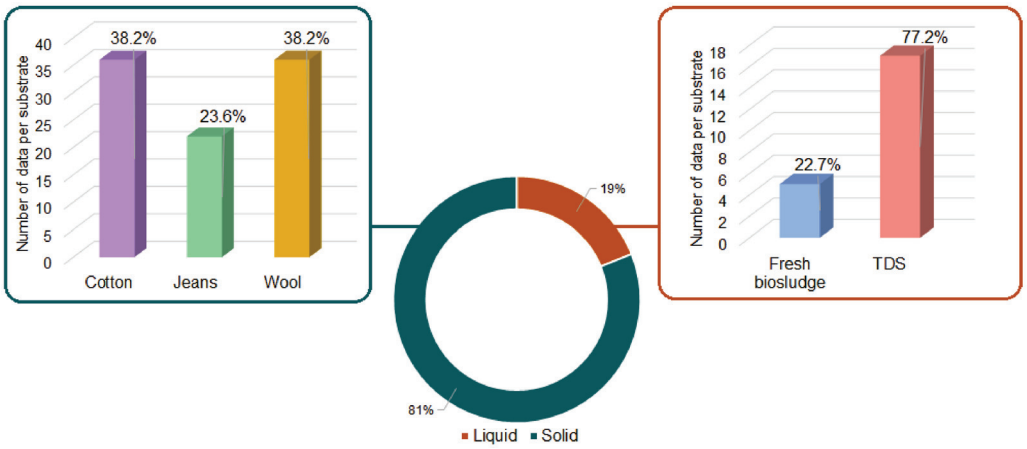


Figure 1. Different sources of textile waste used in AD reported in the literature included in the meta-analysis. TDS = textile dyeing sludge.

Table 1. Chemical characterization of different textile sources presented as averages [1].

	Cotton	Jeans	Wool	Fresh Biosludge	Textile Dye Sludge
TS (%)	93.4	98.5	37.9	14.9	4.1
VS (%TS)	84.2	61	16.6	77	52.6
pH	7.1	N.A.	7.9	8.7	7.2
Biological oxygen Demand (BOD) (mg/L)	N.A.	N.A.	N.A.	887.3	1512
Chemical oxygen demand (COD) (mg/L)	2550	N.A.	2080.2	25,215	741.3
Protein (%DW)	N.A.	N.A.	70	N.A.	N.A.
Heavy metals (mg/gSS)	N.A.	N.A.	N.A.	N.A.	Pb 0.04, Ni 0.10, Cd 0.03, Cu 0.26, Zn 0.29
Cotton (%DW)	N.A.	70	N.A.	N.A.	N.A.
Polyester (%DW)	N.A.	45	N.A.	N.A.	N.A.
Cellulose (%DW)	80	N.A.	N.A.	N.A.	N.A.

[1] References used are reported in Table S4. N.A. = not available

High consumer demand in the textile industry has driven several waste management strategies. Incineration and landfill are the main destinations of most textile waste at their end of life [1]. Although waste volume decrease by 90% is achieved via incineration and this process is viewed as an effective form of energy recovery [2,35], contaminated, damp, ripped, or stained textile waste does not contribute to energy recovery [36]. In addition, incineration can produce flue gases (e.g., sulphur dioxide (SO_2), HCI, hydrogen fluoride (HF), and nitrogen dioxide (NO_2)) that are harmful to the environment [35]. AD is, thus, the most promising technology when compared in terms of both environmental performance and energy recovery [37]. Even though it is a great challenge to stabilize the AD process since its stages are driven by microorganisms [38], the generation of clean energy and biofertilizer makes it advantageous from an environmental perspective [39].

Blue jeans waste mainly consists of cotton (70% DW) and polyester fiber (45% DW) (Table 1) and makes a large contribution to the solid fraction, representing 23% of all solid waste (Figure 1). Although the conversion of cotton to biogas through the breakdown of cellulose into simple sugars has been extensively described in the literature, its blending

with polyester is poorly described and requires further research [30,31,40]. Furthermore, as polyester represents a robust fraction of the textile sector and an increase in its production is projected due to cost-effectiveness in line with the consumption pattern of emerging countries, AD of this fraction requires attention [1]. The main challenge and bottleneck is the hydrolysis of polyester, as its large molecules hinder enzymatic attack by microorganisms, limiting the process to the surface of the material and, consequently, extending the duration of the process by months [7].

The liquid fraction of the residual organic matter represents 19% of all organic waste (Figure 1) and is mainly composed of textile dye sludge (TDS) (77.2%) and fresh sludge (22.7%) (Figure 1). Even though the liquid waste volume is much lower than the solid waste, the liquid fractions are highly toxic, with heavy metal content (Table 1), and their pollutant potential is very high [4], second only to tanneries and the pulp and paper industry [3]. High concentrations of chemical oxygen demand (COD) and biological oxygen demand (BOD), which are the analytical parameters of the degree of organic pollutants, are observed in the liquid fraction of textile waste, in the range of 741–25,215 mg/L and 887–1512 mg/L, respectively (Table 1). The amount and chemical content of textile effluents are of huge concern due to the presence of highly water-soluble chemicals. Conventional activated sludge systems or municipal sewage treatment systems are inefficient for the treatment of this residue [41], indicating a clear need for investments in water reuse and energy recovery from this waste stream. Successful pretreatment application to textile effluents has led to dye removal, decolorization of wastewater, and reduction of toxicity [4,10]. Moreover, the proper selection of the AD pretreatment results in a cost-effective and secondary treatment to alleviate environmental damage [4]. Pretreatments promote the reduction of pollutant loading, mitigating impacts on environmental and human health. Furthermore, water reuse can supply the high water demand of the textile industry itself.

Several pretreatments such as physical, chemical, biological, and combination (Figure 2, Table S2) treatments have been applied to improve AD. Pretreatments applied alone, especially physical and chemical, are the most explored, while their combinations have been less examined (Figure 2, Table S2). This could be explained by the high capital cost investment required to integrate pretreatments into the AD process, and also by the difficulty of large-scale implementation [40].

Heat application (i.e., autoclave and thermal) is the most reported treatment among physical pretreatments, alone and in combination (Figure 2). High temperatures are successful in lysing cells and increasing the solubilization of organic materials such as polysaccharides and protein, increasing soluble chemical oxygen demand in the liquid and solid fraction of the textile waste [42,43] and favoring biogas generation.

Sonication and liquid nitrogen (LN_2) are mechanical pretreatments that are highly efficient in the disruption and disintegration of complex bonds in the substrate chemical structure [44,45]. Although the application of these pretreatments has a positive effect, the increase in methane yield is limited, which may be a result of the reduction and/or inhibition of AD caused by the presence of some chemicals released from the substrate. As a result, the implementation of these pretreatments may become economically unfeasible [45].

The diversity in chemical pretreatments is the largest (Figure 2), with microaeration (n = 11) being the most applied. Oxygen addition impacts the biological microbial process and microbial electrolysis in addition to inhibiting the production of hydrogen sulfide (H_2S), promoting a more stable AD process [27]. Other chemical pretreatments such as alkaline, acids, and organic solvent additions have been shown to be highly efficient in breaking down complex structures and increasing the availability of fermentative sugars for enzymatic hydrolysis [46]. However, when applied at high doses, they can generate methanogenesis-inhibiting bioproducts such as furfural and vanillin [47].

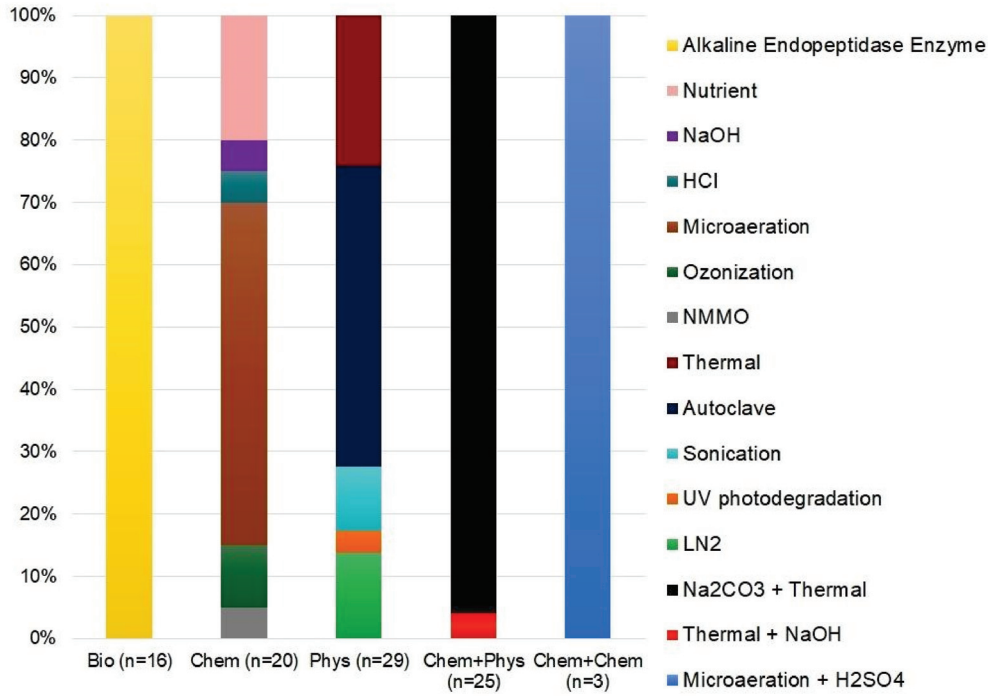


Figure 2. Diversity of methods composing the pretreatment categories applied to improve AD of textile waste reported in articles included in the meta-analysis. *Biological:* alkaline endopeptidase (n = 16); *chemical:* nutrient (n = 4), NaOH (n = 1), HCl (n = 1), microaeration (n = 11), ozonization (n = 2), N-methylmorpholine N-oxide (NMMO) (n = 1); *physical*: thermal (n = 7), autoclave (n = 14), sonication (n = 3), UV photodegradation (n = 1), liquid nitrogen (LN_2) (n = 4); *chemical + physical:* Na_2CO_3 + thermal (n = 24), thermal + NaOH (n = 1); *chemical + chemical:* microaeration + H_2SO_4 (n = 3).

Heat combined with sodium hydroxide (NaOH, n = 1) and sodium carbonate (Na_2CO_3, n = 24) were the thermochemical pretreatments reported (Figure 2). The predominance of Na_2CO_3 + thermal can be a consequence given the negative effects of sodium hydroxide such as corrosion, need for neutralization, and generation of hazardous content to the environment [31]. In contrast, sodium carbonate is successful in reducing cellulose crystallinity and consequently achieves high bioconversion of lignocellulosic content in addition to low cost [31].

As the use of enzymes provides a very selective and specific action on the organic matter [48], the predictability of its response could suggest a lower need for extensive testing, as required in other pretreatments. Therefore, the commercial enzyme alkaline endopeptidase (n = 16) was the only biological pretreatment applied to wastes from the textile industry (Figure 2, Table S2).

Biological pretreatments are the most eco-friendly, as they have a relatively low energy cost and require no addition of chemicals/inhibitory compounds. Thus, they generate less pollution and high methane yields [49]. The application of alkaline endopeptidase led to an increase in methane yield by up to 360% (RR= 1.28, 95% CI: 0.15 to 2.41, $p < 0.05$), indicating high efficiency as a pretreatment for the textile industry (Figure 3, Table S2). The use of commercial enzymes has become more attractive due to their pure nature of speeding reactions, thereby making biodegradation faster [50]. Addition of the alkaline endopeptidase enzyme shows stable performance with high protein solubilization, which improves methane production [42,50]. In fact, the success of enzyme application has led to its impressive growth in the last decade in the textile sector [48]. However, the low number of enzymes thus far investigated highlights the crucial need for more research in the area for the development of new enzymes with higher efficiencies targeting textile wastes.

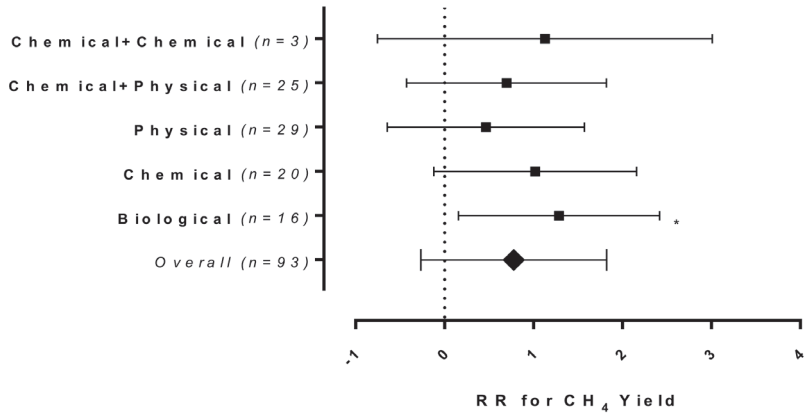


Figure 3. Effect size by natural log response ratio (RR) of methane yield with 95% confidence interval (CI) (p-value = 0.05), comparing the performance of the biological, chemical, physical, chemical + physical, and chemical + chemical pretreatments. Significant code $p \leq 0.05$ (*); n = number of effect sizes per treatment type.

Despite the superior performance of biological pretreatments (Figure 3), physical and chemical pretreatments remain the most applied on textile waste (Figure 2). This is probably due to their high performance when applied on other waste sources. However, our result (Figure 3) clearly shows that their application may not necessarily pay off and can even lead to decreases in methane yield in comparison to untreated controls, especially when applied to cotton waste (Table S2). Therefore, pretreatments should be carefully chosen before large-scale application.

The use of inappropriate pretreatments can, in fact, reduce the methane yield [51]. For instance, formation of inhibitory/toxic compounds following pretreatments, such as volatile fatty acids (VFAs) [52,53], can cause negative effects on biogas production due to the low capacity to degrade specific organic compounds and to deal with usual chemical loads in textiles such as dyes.

Chemical pretreatments used both individually and/or in combination showed a large variability over methane yield (Figure 3). This can be explained by the choice of additive (i.e., H_2SO_4, NaOH) and the concentration added, which requires care, since high doses can inhibit methanogenesis [39,47].

Even though significant results were obtained in this study, our analysis must be viewed with caution, as the application of pretreatments in textile waste is limited. Despite biological pretreatment having the highest performance (Figure 3), the same efficiency cannot be assumed for all textile wastes, as the prevailing chemical composition of the substrate is likely to have an effect on its efficiency. Therefore, careful case-by-case attention is needed to the individual performance of the different substrates subjected to pretreatments (Table S2), especially if we consider textile residues with strong environmental impacts such as cotton and polyester [31].

In fact, some textile wastes, e.g., textile dyeing sludge (TDS), have high loads of dyes, auxiliary chemicals, surfactants, and heavy metals [54]. Such chemicals can severely impair the AD microbial community, especially during hydrolysis and acidogenesis [53]. AD alone has shown CH_4 yield of 0.1 mL/gVS, which is dramatically increased after its combination with pretreatment to 56.1 mL/gVS, corresponding to an increase of 56,000% (Table S2).

Cotton and polyester represent 37% and 63% of the total fibers that are produced within the textile industry, respectively [55]. High energy demand is required for the production of those fibers and their transport to their final destination. Energy consumption is estimated at 48 kWh and 101 kWh just to produce one kilogram of cotton or polyester fiber, respectively (Figure 4A).

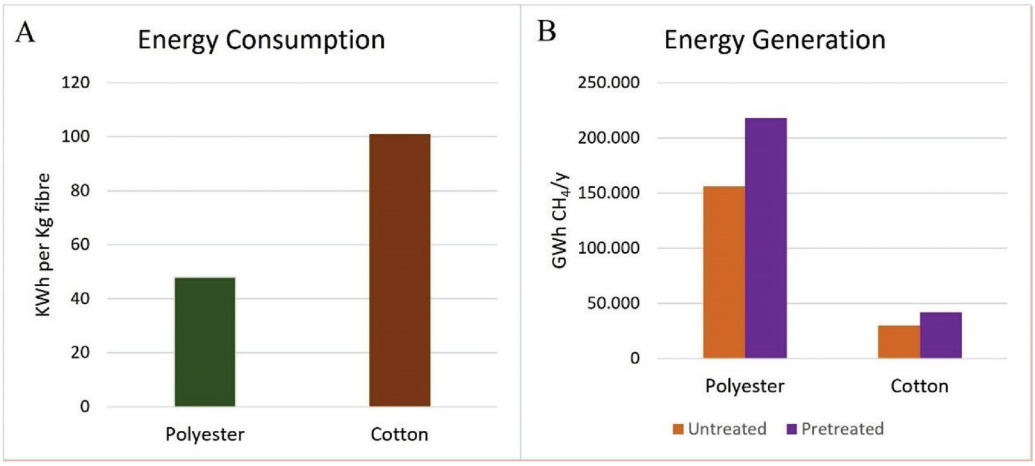


Figure 4. Consumption and generation of energy from the main textile fibers (cotton and polyester). (**A**) Energy consumption per kilogram of textile fiber produced, adapted from [1]. (**B**) Global energy generation potential from polyester and cotton untreated (orange) and pretreated (purple).

Replacing virgin cotton and polyester with second-hand clothes can save up to 65 kWh and 90 kWh of energy per kilogram of fiber reused, respectively [7]. However, the lifespan of textile products is continuously decreasing [7] and, therefore, the reuse of clothing as a strategy to reduce energy consumption is inefficient.

The destination of textile waste for AD can be a sustainable alternative for more efficient energy recovery and supply to the production chain. Considering the global annual waste production of cotton (11.7 million tons) and polyester (42 million tons) generated by the textile industry alone [25,26], we estimated a potential energy production of 155.835 GWh and 298.805 GWh from polyester and cotton, respectively (Figure 4B), which can be increased by applying the pretreatment with the best performance for those types of residues (Table S2).

4. Conclusions

Our results showed that biological pretreatments, of pretreatments commonly applied in the textile industry, promote larger biogas production via AD. In comparison with chemical and physical pretreatments, enzyme pretreatment may lead to an increase in methane yield up to 360% on average. Biological pretreatments also require no addition of chemicals and favor the reuse of textile wastewater, decreasing the current demand for clean water while increasing resource circularity in the textile industry. Moreover, biological pretreatments are very efficient in removing highly soluble chemicals that cause damage to human and environmental health, and given their lower energy demand, the cost–benefit ratio is expected to be low. The implementation of AD improved by pretreatment in the textile industry promotes adequate management of the huge amount of waste generated, converting textile residues into economic value for the industry in line with the circular economy. However, more research is crucial in the quest for new enzymes with higher efficiencies, as well as extensive screening of largely neglected residues, e.g., textile wastewater, in order to bring this sector to a more sustainable model.

Supplementary Materials: The following supporting information can be downloaded at: https://www.mdpi.com/article/10.3390/en15155574/s1, Figure S1. Flow diagram summarizing quantitatively the selection of studies from the systematic review following the Preferred Reporting Items for Systematic Reviews and Meta-analyses (PRISMA, http://www.prisma-statement.org/). *n* = number of articles; Table S1. Global production of fiber waste from the textile industry and volatile solids (VS) and total solids (TS) content; Table S2. Summary of pretreatments applied to different sources of textile waste reported in the systematic review; Table S3: Studies included in the meta-analysis.

Author Contributions: Conceptualization, T.M.A. and A.E.-P.; methodology, T.M.A.; software, T.M.A. and A.E.W.; validation, A.E.W., B.K.-S. and A.E.-P.; formal analysis, T.M.A.; investigation, T.M.A.; resources, A.E.-P.; data curation, T.M.A., A.E.W. and B.K.-S.; writing—original draft preparation, T.M.A., B.K.-S., A.E.W. and A.E.-P.; writing—review and editing, B.K.-S., A.E.W. and A.E.-P.; visualization, T.M.A., B.K.-S., A.E.W. and A.E.-P.; supervision A.E.-P.; project administration, A.E.-P.; funding acquisition, A.E.-P. All authors have read and agreed to the published version of the manuscript.

Funding: This research was funded by Swedish Energy Agency, grant number 35624-2, Formas, grant number 2021-02429. The T.M.A. was supported by the Coordenação de Aperfeiçoamento de Pessoal de Nível Superior—Brasil (CAPES)—Finance Code 001.

Institutional Review Board Statement: Not applicable.

Informed Consent Statement: Not applicable.

Data Availability Statement: Not applicable.

Acknowledgments: A.E.-P. is thankful for the support from the Biogas Solution Research Center hosted by Linköping University, Sweden. T.M.A. thanks the Coordenação de Aperfeiçoamento de Pessoal de Nível Superior—Brasil (CAPES)—Finance Code 001 for the PhD scholarship. A.E.W. thanks the Alabama Agricultural Experiment Station and the Hatch program of the National Institute of Food and Agriculture, U.S. Department of Agriculture. The authors also thank the helpful comments provided by individuals in the Meta-analysis course at Auburn University taught by A.E.W.

Conflicts of Interest: The authors declare no conflict of interest.

References

1. Niinimäki, K.; Peters, G.; Dahlbo, H.; Perry, P.; Rissanen, T.; Gwilt, A. The Environmental Price of Fast Fashion. *Nat. Rev. Earth Environ.* **2020**, *1*, 189–200. [CrossRef]
2. Stanescu, M.D. State of the Art of Post-Consumer Textile Waste Upcycling to Reach the Zero Waste Milestone. *Environ. Sci. Pollut. Res.* **2021**, *28*, 14253–14270. [CrossRef] [PubMed]
3. Nimkar, U. Sustainable Chemistry: A Solution to the Textile Industry in a Developing World. *Curr. Opin. Green Sustain. Chem.* **2018**, *9*, 13–17. [CrossRef]
4. Prabakar, D.; Manimudi, V.T.; Mathimani, T.; Kumar, G.; Rene, E.R.; Pugazhendhi, A. Pretreatment Technologies for Industrial Effluents: Critical Review on Bioenergy Production and Environmental Concerns. *J. Environ. Manag.* **2018**, *218*, 165–180. [CrossRef]
5. Sivaram, N.M.; Gopal, P.M.; Barik, D. *Toxic Waste from Textile Industries*; Elsevier Ltd.: Amsterdam, The Netherlands, 2018; ISBN 9780081025284.
6. European Clothing Action Plan (ECAP). Available online: http://www.ecap.eu.com/ (accessed on 26 June 2020).
7. Piribauer, B.; Bartl, A. Textile Recycling Processes, State of the Art and Current Developments: A Mini Review. *Waste Manag. Res. J. A Sustain. Circ. Econ.* **2019**, *37*, 112–119. [CrossRef] [PubMed]
8. European Parliament, Council. Directive 2008/98/EC of the European and of the Council of 19 November 2008 on Waste and Repealing Directives. 2008. Available online: http://www.fao.org/faolex/results/details/es/c/LEX-FAOC083580/ (accessed on 24 April 2021).
9. Chen, Y.; Cheng, J.J.; Creamer, K.S. Inhibition of Anaerobic Digestion Process: A Review. *Bioresour. Technol.* **2008**, *99*, 4044–4064. [CrossRef] [PubMed]
10. Apollo, S.; Onyango, M.S.; Ochieng, A. Integrated UV Photodegradation and Anaerobic Digestion of Textile Dye for Efficient Biogas Production Using Zeolite. *Chem. Eng. J.* **2014**, *245*, 241–247. [CrossRef]
11. Gonzalez, A.; Hendriks, A.T.W.M.; van Lier, J.B.; de Kreuk, M. Pre-Treatments to Enhance the Biodegradability of Waste Activated Sludge: Elucidating the Rate Limiting Step. *Biotechnol. Adv.* **2018**, *36*, 1434–1469. [CrossRef]
12. Chen, L.; Qin, Y.; Chen, B.; Wu, C.; Zheng, S.; Chen, R.; Yang, S.; Yang, L.; Liu, Z. Enhancing Degradation and Biogas Production during Anaerobic Digestion of Food Waste Using Alkali Pretreatment. *Environ. Res.* **2020**, *188*, 109743. [CrossRef]
13. Anacleto, T.M.; Oliveira, H.R.; Diniz, V.L.; de Oliveira, V.P.; Abreu, F.; Enrich-Prast, A. Boosting Manure Biogas Production with the Application of Pretreatments: A Meta-Analysis. *J. Clean. Prod.* **2022**, *362*, 132292. [CrossRef]
14. Mustafa, A.M.; Poulsen, T.G.; Xia, Y.; Sheng, K. Combinations of Fungal and Milling Pretreatments for Enhancing Rice Straw Biogas Production during Solid-State Anaerobic Digestion. *Bioresour. Technol.* **2017**, *224*, 174–182. [CrossRef] [PubMed]
15. Orlando, M.Q.; Borja, V.M. Pretreatment of Animal Manure Biomass to Improve Biogas Production: A Review. *Energies* **2020**, *13*, 3573. [CrossRef]
16. Abraham, A.; Mathew, A.K.; Park, H.; Choi, O.; Sindhu, R.; Parameswaran, B.; Pandey, A.; Park, J.H.; Sang, B.I. Pretreatment Strategies for Enhanced Biogas Production from Lignocellulosic Biomass. *Bioresour. Technol.* **2020**, *301*, 122725. [CrossRef] [PubMed]

17. Amin, F.R.; Khalid, H.; Zhang, H.; Rahman, S.; Zhang, R.; Liu, G.; Chen, C. Pretreatment Methods of Lignocellulosic Biomass for Anaerobic Digestion. *AMB Express* **2017**, *7*, 72. [CrossRef]
18. Pellera, F.M.; Santori, S.; Pomi, R.; Polettini, A.; Gidarakos, E. Effect of Alkaline Pretreatment on Anaerobic Digestion of Olive Mill Solid Waste. *Waste Manag.* **2016**, *58*, 160–168. [CrossRef]
19. Thompson, T.M.; Young, B.R.; Baroutian, S. Advances in the Pretreatment of Brown Macroalgae for Biogas Production. *Fuel Process. Technol.* **2019**, *195*, 106151. [CrossRef]
20. Montgomery, L.F.R.; Bochmann, G. Pretreatment of Feedstock for Enhanced Biogas Production. *IEA Bioenergy* **2014**. Available online: https://www.ieabioenergy.com/wp-content/uploads/2014/02/pretreatment_web.pdf (accessed on 13 November 2021).
21. Brémond, U.; de Buyer, R.; Steyer, J.P.; Bernet, N.; Carrere, H. Biological Pretreatments of Biomass for Improving Biogas Production: An Overview from Lab Scale to Full-Scale. *Renew. Sustain. Energy Rev.* **2018**, *90*, 583–604. [CrossRef]
22. Moher, D.; Shamseer, L.; Clarke, M.; Ghersi, D.; Liberati, A.; Petticrew, M.; Shekelle, P.; Stewart, L.A.; Estarli, M.; Barrera, E.S.A.; et al. Preferred Reporting Items for Systematic Review and Meta-Analysis Protocols (PRISMA-P) 2015 Statement. *Syst. Rev.* **2016**, *20*, 148–160. [CrossRef]
23. Hedges, L.V.; Gurevitch, J.; Curtis, P.S. *The Meta-Analysis of Response Ratios in Experimental Ecology*; Wiley: Hoboken, NJ, USA, 1999; Volume 80.
24. Cao, Y.; Wang, X.; Bai, Z.; Chadwick, D.; Misselbrook, T.; Sommer, S.G.; Qin, W.; Ma, L. Mitigation of Ammonia, Nitrous Oxide and Methane Emissions during Solid Waste Composting with Different Additives: A Meta-Analysis. *J. Clean. Prod.* **2019**, *235*, 626–635. [CrossRef]
25. Johnson, S.; Echeverria, D.; Venditti, R.; Jameel, H.; Yao, Y. Supply Chain of Waste Cotton Recycling and Reuse: A Review. *AATCC J. Res.* **2020**, *7*, 19–31. [CrossRef]
26. Our World in Data. Available online: https://ourworldindata.org/grapher/plastic-waste-polymer?tab=table (accessed on 13 November 2021).
27. Sołowski, G.; Konkol, I.; Cenian, A. Methane and Hydrogen Production from Cotton Waste by Dark Fermentation under Anaerobic and Micro-Aerobic Conditions. *Biomass Bioenergy* **2020**, *138*, 105576. [CrossRef]
28. Šerá, J.; Serbruyns, L.; De Wilde, B.; Koutný, M. Accelerated Biodegradation Testing of Slowly Degradable Polyesters in Soil. *Polym. Degrad. Stab.* **2020**, *171*, 109031. [CrossRef]
29. Ornelas-Ferreira, B.; Lobato, L.C.S.; Colturato, L.F.D.; Torres, E.O.; Pombo, L.M.; Pujatti, F.J.P.; Araújo, J.C.; Chernicharo, C.A.L. Strategies for Energy Recovery and Gains Associated with the Implementation of a Solid State Batch Methanization System for Treating Organic Waste from the City of Rio de Janeiro—Brazil. *Renew. Energy* **2020**, *146*, 1976–1983. [CrossRef]
30. Sołowski, G.; Konkol, I.; Shalaby, M.; Cenian, A. Rapid Hydrogen Generation from Cotton Wastes by Mean of Dark Fermentation. *SN Appl. Sci.* **2020**, *2*, 1–7. [CrossRef]
31. Hasanzadeh, E.; Mirmohamadsadeghi, S.; Karimi, K. Enhancing Energy Production from Waste Textile by Hydrolysis of Synthetic Parts. *Fuel* **2018**, *218*, 41–48. [CrossRef]
32. Salem Allafi, F.A.; Hossain, M.S.; Ab Kadir, M.O.; Hakim Shaah, M.A.; Lalung, J.; Ahmad, M.I. Waterless Processing of Sheep Wool Fiber in Textile Industry with Supercritical CO2: Potential and Challenges. *J. Clean. Prod.* **2021**, *285*, 124819. [CrossRef]
33. Wagner, A.O.; Lins, P.; Malin, C.; Reitschuler, C.; Illmer, P. Impact of Protein-, Lipid- and Cellulose-Containing Complex Substrates on Biogas Production and Microbial Communities in Batch Experiments. *Sci. Total Environ.* **2013**, *458–460*, 256–266. [CrossRef]
34. Dlamini, S.; Simatele, M.D.; Serge Kubanza, N. Municipal Solid Waste Management in South Africa: From Waste to Energy Recovery through Waste-to-Energy Technologies in Johannesburg. *Local Environ.* **2019**, *24*, 249–257. [CrossRef]
35. Cudjoe, D.; Acquah, P.M. Environmental Impact Analysis of Municipal Solid Waste Incineration in African Countries. *Chemosphere* **2021**, *265*, 129186. [CrossRef]
36. Expert Network on Textile Recycling (ENTeR). Strategic Agenda on Textile Waste Management and Recycling. 2016. Available online: https://www.interreg-central.eu/Content.Node/Stategic-Agenda.pdf (accessed on 20 May 2021).
37. Arafat, H.A.; Jijakli, K.; Ahsan, A. Environmental Performance and Energy Recovery Potential of Five Processes for Municipal Solid Waste Treatment. *J. Clean. Prod.* **2015**, *105*, 233–240. [CrossRef]
38. Castellano-Hinojosa, A.; Armato, C.; Pozo, C.; González-Martínez, A.; González-López, J. New Concepts in Anaerobic Digestion Processes: Recent Advances and Biological Aspects. *Appl. Microbiol. Biotechnol.* **2018**, *102*, 5065–5076. [CrossRef] [PubMed]
39. Millati, R.; Wikandari, R.; Ariyanto, T.; Putri, R.U.; Taherzadeh, M.J. Pretreatment Technologies for Anaerobic Digestion of Lignocelluloses and Toxic Feedstocks. *Bioresour. Technol.* **2020**, *304*, 122998. [CrossRef] [PubMed]
40. Patinvoh, R.J.; Osadolor, O.A.; Chandolias, K.; Sárvári Horváth, I.; Taherzadeh, M.J. Innovative Pretreatment Strategies for Biogas Production. *Bioresour. Technol.* **2017**, *224*, 13–24. [CrossRef] [PubMed]
41. Gebrati, L.; El Achaby, M.; Chatoui, H.; Laqbaqbi, M.; El Kharraz, J.; Aziz, F. Inhibiting Effect of Textile Wastewater on the Activity of Sludge from the Biological Treatment Process of the Activated Sludge Plant. *Saudi J. Biol. Sci.* **2019**, *26*, 1753–1757. [CrossRef]
42. Kabir, M.M.; Forgács, G.; Sárvári Horváth, I. Enhanced Methane Production from Wool Textile Residues by Thermal and Enzymatic Pretreatment. *Process Biochem.* **2013**, *48*, 575–580. [CrossRef]
43. Zhou, W.; Tuersun, N.; Zhang, Y.; Wang, Y.; Cheng, C.; Chen, X. Optimization and System Energy Balance Analysis of Anaerobic Co-Digestion Process of Pretreated Textile Dyeing Sludge and Food Waste. *J. Environ. Chem. Eng.* **2021**, *9*, 106855. [CrossRef]
44. Kuzmanova, E.; Zhelev, N.; Akunna, J.C. Effect of Liquid Nitrogen Pre-Treatment on Various Types of Wool Waste Fibres for Biogas Production. *Heliyon* **2018**, *4*, e00619. [CrossRef]

45. Aksu Bahçeci, H.; Sanin, S.L.; Sanin, F.D. Co-Digestion Potential of Industrial Sludges with Municipal Sludge. *Waste Biomass Valorization* **2021**, *12*, 5437–5449. [CrossRef]
46. Malik, K.; Salama, E.S.; Kim, T.H.; Li, X. Enhanced Ethanol Production by Saccharomyces Cerevisiae Fermentation Post Acidic and Alkali Chemical Pretreatments of Cotton Stalk Lignocellulose. *Int. Biodeterior. Biodegrad.* **2020**, *147*, 104869. [CrossRef]
47. Yao, Y.; Bergeron, A.D.; Davaritouchaee, M. Methane Recovery from Anaerobic Digestion of Urea-Pretreated Wheat Straw. *Renew. Energy* **2018**, *115*, 139–148. [CrossRef]
48. Liu, S.; Chen, Z.; Sun, J.; Long, J. Ecofriendly Pretreatment of Grey Cotton Fabric with Enzymes in Supercritical Carbon Dioxide Fluid. *J. Clean. Prod.* **2016**, *120*, 85–94. [CrossRef]
49. Sharma, H.K.; Xu, C.; Qin, W. Biological Pretreatment of Lignocellulosic Biomass for Biofuels and Bioproducts: An Overview. *Waste Biomass Valorization* **2019**, *10*, 235–251. [CrossRef]
50. Forgács, G.; Lundin, M.; Taherzadeh, M.J.; Horváth, I.S. Pretreatment of Chicken Feather Waste for Improved Biogas Production. *Appl. Biochem. Biotechnol.* **2013**, *169*, 2016–2028. [CrossRef] [PubMed]
51. Wang, D.; Shen, F.; Yang, G.; Zhang, Y.; Deng, S.; Zhang, J.; Zeng, Y.; Luo, T.; Mei, Z. Can Hydrothermal Pretreatment Improve Anaerobic Digestion for Biogas from Lignocellulosic Biomass? *Bioresour. Technol.* **2018**, *249*, 117–124. [CrossRef] [PubMed]
52. Saritha, M.; Arora, A. Lata Biological Pretreatment of Lignocellulosic Substrates for Enhanced Delignification and Enzymatic Digestibility. *Indian J. Microbiol.* **2012**, *52*, 122–130. [CrossRef] [PubMed]
53. Xiang, X.; Chen, X.; Dai, R.; Luo, Y.; Ma, P.; Ni, S.; Ma, C. Anaerobic Digestion of Recalcitrant Textile Dyeing Sludge with Alternative Pretreatment Strategies. *Bioresour. Technol.* **2016**, *222*, 252–260. [CrossRef]
54. Chen, X.; Xiang, X.; Dai, R.; Wang, Y.; Ma, P. Effect of Low Temperature of Thermal Pretreatment on Anaerobic Digestion of Textile Dyeing Sludge. *Bioresour. Technol.* **2017**, *243*, 426–432. [CrossRef]
55. Shirvanimoghaddam, K.; Motamed, B.; Ramakrishna, S.; Naebe, M. Death by Waste: Fashion and Textile Circular Economy Case. *Sci. Total Environ.* **2020**, *718*, 137317. [CrossRef]

toxics

MDPI

Article

Biochar Is Not Durable for Remediation of Heavy Metal-Contaminated Soils Affected by Acid-Mine Drainage

Junhao Qin [1,2], Xi Wang [1,2], Jidong Ying [1,2] and Chuxia Lin [3,*]

[1] College of Natural Resources and Environment, South China Agricultural University, Guangzhou 510642, China
[2] Key Laboratory of Agro-Environment in the Tropics, Ministry of Agriculture of China, Guangzhou 510642, China
[3] Centre for Regional and Rural Futures, Faculty of Science, Engineering and Built Environment, Deakin University, Burwood, VIC 3125, Australia
* Correspondence: chu.lin@deakin.edu.au; Tel.: +61-432-935-209

Abstract: Biochar is a soil conditioner for enhancing plant growth and reducing plants' uptake of heavy metals. However, the protonation of biochar surfaces in acid soils can weaken the capacity of biochar to reduce the phytoavailability of soil-borne heavy metals over time. The aim of this study was to test this hypothesis by performing a plant-growth experiment with five harvest cycles to examine the durability of rice-straw biochar for the remediation of an acidic-mine-water-contaminated soil. The application of the biochar significantly reduced the phytoavailability of the heavy metals and inhibited the plant uptake of cationic heavy metals but not anionic Cr. The beneficial effects of the biochar were weakened with the increasing number of harvest cycles caused by the gradual protonation of the biochar surfaces, which resulted in the desorption of the adsorbed heavy metals. The weakening capacity of the biochar to reduce the heavy-metal uptake by the vegetable plants was more evident for Cu, Zn, and Pb compared to Ni and Cd. The experimental results generally confirmed the hypothesis. It was also observed that the bioaccessible amount of various metals in the edible portion of the vegetable was also reduced as a result of the biochar application.

Keywords: heavy metal; biochar; phytoavailability; plant uptake; bioaccessibility; contaminated soil

Citation: Qin, J.; Wang, X.; Ying, J.; Lin, C. Biochar Is Not Durable for Remediation of Heavy Metal-Contaminated Soils Affected by Acid-Mine Drainage. *Toxics* **2022**, *10*, 462. https://doi.org/10.3390/toxics10080462

Academic Editors: Dibyendu Sarkar, Rupali Datta, Prafulla Kumar Sahoo and Mohammad Mahmudur Rahman

Received: 2 July 2022
Accepted: 4 August 2022
Published: 9 August 2022

Publisher's Note: MDPI stays neutral with regard to jurisdictional claims in published maps and institutional affiliations.

Copyright: © 2022 by the authors. Licensee MDPI, Basel, Switzerland. This article is an open access article distributed under the terms and conditions of the Creative Commons Attribution (CC BY) license (https://creativecommons.org/licenses/by/4.0/).

1. Introduction

The biochar produced from the pyrolysis of organic matter can be used as a soil amendment to promote plant growth and impede plants' uptake of heavy metals from contaminated soils [1–3]. This is particularly beneficial for the production of vegetables, especially leafy vegetables, which tend to easily take up heavy metals from horticultural soils, which are commonly contaminated by heavy metals due to their relatively frequent exposure to various contamination sources [4,5].

Plants can only take up heavy metals dissolved in soil solutions. The dissolution of soil-borne heavy metals is predominantly driven by soil acidification caused by the generation of either inorganic acids, such as sulfuric acid from the oxidation of sulfide minerals [6–8], or the organic acids released from plant roots [9,10]. Biochar materials frequently have an alkaline pH, which allows the neutralization of soil acidity. Biochar materials also have a large specific area due to their highly porous nature. The carboxylic, phenolic, hydroxyl, carbonyl, and quinone groups present on biochar surfaces make them capable of adsorbing heavy metals [11].

Increasing research has been undertaken to investigate the effects of biochar materials on the prevention of plants' uptake of heavy metals from soils and improvements in plant-growth performance in recent years [12]. Khan et al. [3] found that the application of poplar wood and sugarcane bagasse biochars to mine soils reduced the uptake of chromium and lead by lettuce. Sui et al. [13] showed the effects of biochar on the uptake of cadmium and

lead by wheat. Nzediegwu et al. [14] demonstrated that the levels of Cd and Zn in potato flesh were significantly reduced by soil amendment with biochar. Biochar application also increased plants' water-use efficiency and biomass production while reducing Cu concentration in *Brassica juncea* L. [15]. Medyńska-Juraszek [16] suggested that the effects of biochar on the plant uptake of heavy metals take place through interactions in the rhizosphere, where organic acids are released from plant roots. It has been shown that low-molecular-weight organic acids can alter the surface charge of biochar and affect its capacity to adsorb heavy metals [17]. So far, research work focusing on the durability of biochar materials in terms of their capacity to reduce the phytoavailability of soil-borne heavy metals is limited. This represents a knowledge gap that needs to be closed to improve the evaluation of the cost-effectiveness of using biochar to remediate contaminated soils.

The acidic water generated from mining operations involving coal and metal ores that contain sulfide minerals is a common source of heavy metals in aquatic ecosystems and agricultural lands [18,19]. For acidic-mine-water-contaminated soils, the strong acidity that is commonly encountered tends to keep a large amount of the mine-water-derived heavy metals in bioavailable forms, which can cause toxicity to plants and soil microbes, which play a crucial role in nutrient cycling [20,21]. Given its alkaline nature, biochar could be an ideal amendment for the remediation of acidic soils resulting from mine-water contamination. The soil application of biochar at a high rate for agricultural production could be cost-prohibitive [22]. Therefore, it is only practical to add biochar to contaminated soils at an economically viable application rate for the production of leafy vegetables. So far, most of the experiments aiming to examine the effects of biochar on enhancing vegetable-plant growth and reducing the plant uptake of heavy metals have been limited to a single cropping cycle for determining the suitable biochar application rate. However, when the added biochar is exposed to the H^+ present in acidic soils, the protonation of biochar surfaces can take place [23]. Protonated biochar surfaces tend not to favor the adsorption of cationic heavy metals [24,25]. It is therefore possible that the degree of biochar-surface protonation intensifies over time, resulting in the desorption of the previously adsorbed heavy metals. This could reduce the capacity of the biochar to immobilize soil-borne heavy metals and, thus, make the beneficial effects of biochar unsustainable.

It is hypothesized that biochar is not durable when its application rate is determined based on the plant-growth performance in the first cropping cycle. This study aimed to test this hypothesis by examining the performance of a selected biochar for impeding heavy-metal uptake by a vegetable plant grown in heavily contaminated soils over a period of time covering multiple harvest cycles of the above-ground plant part to evaluate the durability of the biochar for its intended beneficial use.

2. Materials and Methods

2.1. The Soil Material

A typical mine-water-contaminated soil was used for the greenhouse experiment. The area from which the soil sample was taken experienced land irrigation with river water affected by acid-mine drainage for decades [26,27]. The soil had a pH of 4.30 and contained multiple heavy metals. The concentrations of Cd, Cr, Cu, Ni, Pb, and Zn were 0.49, 58.7, 246, 15.0, 171, and 256 mg/kg, respectively. The soil contained 14.7 g/kg of organic carbon and had an EC value (electrical conductivity) of 0.723 dS/m (Table S1).

2.2. The Test-Vegetable-Plant Species

A common vegetable species, *Gynura cusimbua*, was selected as the test plant in the microcosm experiment. Seed germination and seedling development were conducted using the Murashige and Skoog (MS) basal medium prior to transplanting of the seedlings to the growth chambers.

2.3. The Biochar Material

The rice-straw-derived biochar used in the growth experiment was purchased from a commercial source. It was synthesized at 600 °C (pyrolysis temperature), according to the manufacturer's instructions. It had a pH of 9.94 and a specific surface area of 37.9 m^2/g (determined by a specific-surface-area and porosity analyzer, Gemini VII 2390, Micromeritics, Norcross, GA, USA). Details of physicochemical characteristics of the biochar material are provided in Table S1.

2.4. Microcosm Experiment

A 150-day greenhouse experiment was conducted to observe the changes in phytoavailable heavy metals in the soils and plant-tissue-borne heavy metals. Pre-experiment test suggested that an economically viable application rate of 2.5% (biochar/soil) allowed healthy growth of the test-vegetable plants from a pot trial with only one harvest. One control and one treatment were set for the multi-harvest experiment. For the treatment, 62.5 g of biochar were thoroughly incorporated into 2.5 kg of the contaminated soil. The soil without added biochar served as the control. The respective soil was placed into a plastic pot (top diameter: 27 cm; height: 20 cm). Prior to the plant-growth experiment, the soils were incubated for 15 days. Twelve plant seedlings were then transplanted to each pot. Field capacity was maintained for the soil-moisture content during the entire period of the experiment.

Five harvest cycles (30 days per cycle) were performed during the experiment. At each of the 5 harvest times, one representative plant (aerial portion plus root portion) was removed from each pot. For the remaining plants in each pot, only the aerial portion (edible part) was harvested. The plants were then allowed to re-grow for the next 30 days prior to subsequent harvest. In each pot, chemical fertilizer was added to the soil with an application rate of 4.5 g/pot at the beginning of the experiment and following the first, second, third, and fourth harvest events.

In the laboratory, the plant samples collected at each harvest time were washed with tap water, followed by deionized water. The whole plant was then separated into aerial portion and root portion. The plant portions were oven-dried to constant weight [23]. Plant powders were prepared using a pestle and mortar. For determination of bioaccesible heavy metals, the edible vegetable-plant portion was cut into small pieces and mixed thoroughly. The plant mixture was then ground with a pestle and mortar before being split into two equal parts and frozen prior to analysis.

2.5. Analytical Methods

Titratable acidity of the soils was measured by titrating an aliquot of 1:5 (soil:1 M KCl) extract using 0.01 M standardized NaOH solution. Water-extractable heavy metals and NH_4Cl-extractable heavy metals were determined from 1:5 (soil: water) extracts and 1:5 (soil: 1 M NH_4Cl) extracts, respectively. The concentrations of various heavy metals were determined by inductively coupled plasma mass spectrometry (ICP-MS, Agilent 7700). The soil-borne heavy metals were also determined by ICP-MS after digesting 0.15 g of the soil with a mixed solution of HNO_3, HF, and H_2O_2 in a microwave digester [23].

Heavy metals in the edible plant tissues were determined by ICP-MS after digestion of the oven-dried plant powder (0.10 g) with a mixed solution of HNO_3 and H_2O_2 in a microwave digester [23]. To determine the bioaccessible heavy metals in the vegetable edible portion, a modified unified BARGE method was adopted [28].

2.6. Quality Assurance and Quality Control

Certified reference materials were used for determination of various heavy metals in the soil samples (GBW07407) and the plant-tissue samples (GBW(E)100349), respectively. The recovery rates for Cr, Ni, Cu, Zn, Cd, and Pb were 86.5%, 90.6%, 105.2%, 95.7%, 89.9%, and 104.8%, respectively. Triplicated experiment was performed in this study. Repeatability analysis shows that the RSD (relative standard deviation) was 12.2%, 9.90%, 8.63%, 6.38%,

3.12%, and 9.32% for the total Cr, Ni, Cu, Zn, Cd, and Pb, respectively, in the plant tissue, 8.83%, 10.5%, 5.86%, 5.57%, 7.72%, and 8.85%, respectively, for the gastric (G) phase, and 7.82%, 6.51%, 7.69%, 5.76%, 6.26%, and 8.48%, respectively, for the gastrointestinal (GI) phase.

2.7. Statistical Analysis Method

The experimental data were analyzed using IBM SPSS® Statistics 22.0 software. Analysis of normal distribution and equal variance was performed to test whether each parameter in either the control or the treatment depended on each harvest cycle, and whether each parameter in the same harvest cycle depended on the control and the treatment. If the equal variances were assumed, one-way analysis of variance (ANOVA) with Duncan's multiple range test was used to compare the means of each parameter for the 5 harvest cycles, while significant differences between the control and the treatment for each parameter were determined by an independent sample t-test at 0.05 level or 0.01 level.

2.8. Assessment Criteria

Bioaccumulation factor (BAF) was used to evaluate the degree of heavy-metal uptake by plant root:

$$\text{BAF} = \text{HMroot}/\text{HMsoil} \quad (1)$$

The translocation of a heavy metal from root portion to aerial portion of the plant was evaluated by translocation factor (TF):

$$\text{TF} = \text{HMaerial}/\text{HMroot} \quad (2)$$

where HMsoil, HMroot, and HMaerial denote the total heavy-metal concentrations in the soil, root, and aerial portion, respectively.

The bioaccessible concentration of a heavy metal in the edible vegetable portion and the bioaccessibility of that heavy metal were calculated as follows:

$$\text{Bioaccessible heavy metal (mg/kg)} = (\text{Con} \times \text{Vol})/\text{Wt} \quad (3)$$

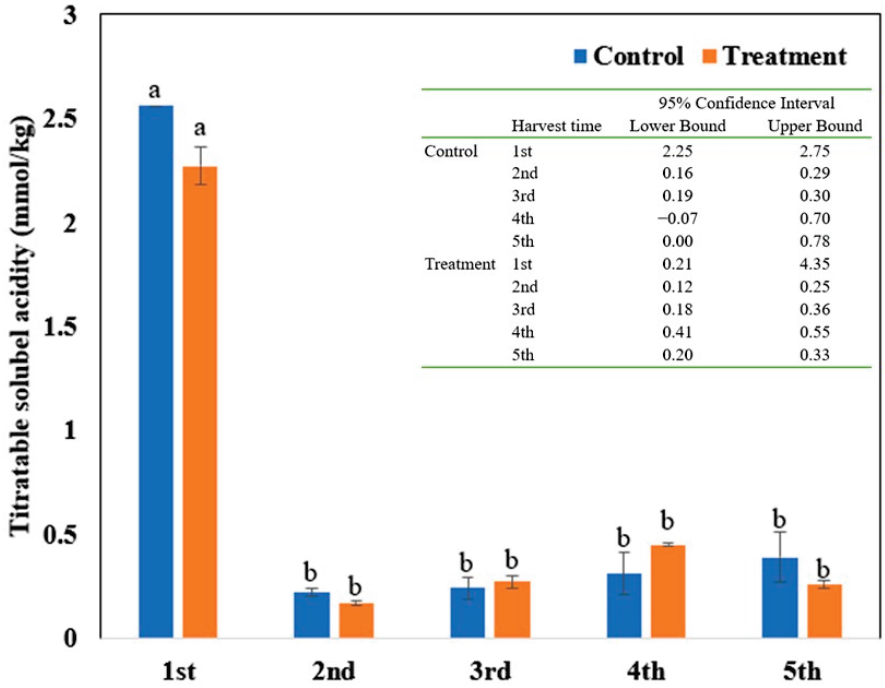
$$\text{Bioaccessibility (\%)} = \text{bioaccessible HM}/\text{total HMplant} \times 100 \quad (4)$$

where Con and Vol are the concentration (μg/mL) of a heavy metal in the simulated gastric (G) or gastrointestinal (GI) solutions and the volume (mL) of the simulated G or GI solutions, respectively. Wt (g) denotes the fresh biomass of the vegetable sample used to determine the bioassessible heavy metals (Bioaccessible HM). Total HMplant is the total heavy metal in the edible vegetable portion. Bioaccessible HM and total HMplant were all expressed on a fresh-weight basis.

3. Results

3.1. Effects of Biochar on Soil Acidity and Phytoavailable Heavy Metals

At the time of the first harvest, the titratable acidity in the soil amended with biochar (1.10 ± 0.08 mmol/kg) was significantly lower compared to the control (2.50 ± 0.00 mmol/kg). For the unamended soil, the titratable acidity tended to decrease from the first harvest time to the second harvest time and then to remain at a level below 1 mmol/kg for the later harvest times. For the amended soil, no significant difference in titratable acidity was observed among the different harvest times, except for the second harvest time, when the titratable acidity was significantly lower relative to the other harvest times (Figure 1).



	Harvest time	95% Confidence Interval Lower Bound	Upper Bound
Control	1st	2.25	2.75
	2nd	0.16	0.29
	3rd	0.19	0.30
	4th	−0.07	0.70
	5th	0.00	0.78
Treatment	1st	0.21	4.35
	2nd	0.12	0.25
	3rd	0.18	0.36
	4th	0.41	0.55
	5th	0.20	0.33

Figure 1. Temporal variation in soil titratable acidity in the control and the treatment. The data are presented as mean ± standard error (n = 3) with different letters above the bars for either the control or the treatment indicating significant differences at $p < 0.05$. The 95% confidence intervals for different harvest cycles in the control and the treatment are also provided.

No significant difference in the water-extractable Cr was observed between the unamend soil (control) and the amended soil, except at the first and third harvest times, when the amended soil had a higher water-extractable Cr concentration relative to the control soil. The NH_4Cl-extratable Cr showed no significant differences between the control soil and the amended soil either, except at the fourth harvest time, when the concentration of the NH_4Cl-extratable Cr was higher in the amended soil compared to the control soil (Table 1).

Mixed results were found for the water-extractable Ni, with the first and fourth harvest times showing a higher (significantly at $p < 0.05$) Ni concentration in the amended soil than in the unamended control soil, the second and third harvest times showing lower (significantly at $p < 0.05$) Ni concentrations in the biochar-treated soil compared to the unamended control soil, and the fifth harvest time showing no significant difference ($p > 0.05$) in Ni concentration between the unamended soil and the amended soil. For the NH_4Cl-extratable Ni, there was a significantly ($p < 0.05$) lower concentration in the biochar-treated soil than in the unamended soil at all of the five harvest times (Table 1).

For the water-extractable Cu, it was clear that the concentration in the amended soil was lower relative to the control soil for the first three harvest cycles, and the opposite was observed for the last two harvest cycles. For the NH_4Cl-extratable Cu, the concentration in the amended soil was lower compared to the unamended control soil for the first two harvest cycles, and the opposite was observed for the last two harvest cycles, with no significant difference in the NH_4Cl-extratable Cu observed between the unamended control soil and the amended soil (Table 1).

Significant differences in the water-extractable Zn were observed between the unamended control soil and the biochar-treated soil, with the first, fourth, and fifth harvest times featuring higher concentrations in the amended soil relative to the unamended control soil, while the opposite was observed for the second and third harvest cycles. There was no clear variation trend in the water-extractable Zn from the first to the fifth harvest time for both the control soil and the biochar-amended soil. For the NH_4Cl-extratable Zn, the concentration in the biochar-treated soil was always higher relative to the unamend control soil, and always at significant levels, except at the fifth harvest time (Table 1).

Table 1. Water-extractable and NH_4Cl-extratable heavy metals in the soil at different harvest times during the period of the greenhouse experiment.

		Water-Extractable		NH_4Cl-Extratable	
Element	**Harvest Time**	**Control**	**Treatment**	**Control**	**Treatment**
Cr	1st	0.004 ± 0.001a	0.015 ± 0.002a **	0.009 ± 0.000b	0.013 ± 0.002b
	2nd	0.002 ± 0.000bc	0.003 ± 0.000b	0.014 ± 0.002a	0.011 ± 0.001b
	3rd	0.001 ± 0.000c	0.004 ± 0.000b **	0.015 ± 0.001a	0.021 ± 0.004a
	4th	0.003 ± 0.000ab	0.003 ± 0.000b	0.005 ± 0.000c	0.013 ± 0.002b *
	5th	0.002 ± 0.000c	0.002 ± 0.000b	0.012 ± 0.001ab	0.010 ± 0.000b
Ni	1st	0.073 ± 0.001c	0.118 ± 0.001ab **	0.585 ± 0.012d	0.533 ± 0.008b *
	2nd	0.092 ± 0.006b	0.074 ± 0.003c *	0.648 ± 0.011c	0.602 ± 0.015a *
	3rd	0.127 ± 0.007a	0.099 ± 0.003b *	0.708 ± 0.008b	0.621 ± 0.007a **
	4th	0.086 ± 0.007bc	0.133 ± 0.011a *	0.829 ± 0.005a	0.538 ± 0.009 **
	5th	0.074 ± 0.001c	0.073 ± 0.008c	0.614 ± 0.015cd	0.530 ± 0.009b **
Cu	1st	0.443 ± 0.018b	0.257 ± 0.020bc **	7.201 ± 0.069a	5.423 ± 0.268cd **
	2nd	0.193 ± 0.083c	0.167 ± 0.016c	6.187 ± 0.312b	4.931 ± 0.110d *
	3rd	0.632 ± 0.045a	0.299 ± 0.005bc **	6.147 ± 0.263b	6.877 ± 0.228b
	4th	0.292 ± 0.004c	1.553 ± 0.097a **	4.334 ± 0.093c	8.149 ± 0.019a **
	5th	0.262 ± 0.009c	0.378 ± 0.009b **	4.022 ± 0.229c	5.597 ± 0.068c *
Zn	1st	4.191 ± 0.119b	5.613 ± 0.405b *	14.25 ± 0.230b	12.57 ± 0.372a *
	2nd	4.371 ± 0.100b	3.367 ± 0.155c **	16.66 ± 0.710b	12.61 ± 0.343a **
	3rd	6.099 ± 0.131a	5.253 ± 0.078b **	16.35 ± 1.023b	13.12 ± 0.605a *
	4th	4.039 ± 0.185b	7.629 ± 0.145a **	23.50 ± 0.808a	13.93 ± 0.069a **
	5th	3.313 ± 0.022c	4.008 ± 0.128c **	15.66 ± 1.321b	13.45 ± 0.754a
Cd	1st	0.024 ± 0.002ab	0.020 ± 0.001d	0.135 ± 0.002b	0.111 ± 0.004a **
	2nd	0.021 ± 0.001b	0.018 ± 0.001d	0.134 ± 0.009b	0.104 ± 0.006a *
	3rd	0.039 ± 0.001a	0.033 ± 0.001b	0.157 ± 0.016b	0.100 ± 0.003ab*
	4th	0.033 ± 0.011ab	0.045 ± 0.002a	0.223 ± 0.006a	0.103 ± 0.002ab **
	5th	0.020 ± 0.001b	0.027 ± 0.001c **	0.143 ± 0.006b	0.091 ± 0.003b **
Pb	1st	0.075 ± 0.006a	0.036 ± 0.001b **	22.436 ± 0.346a	18.044 ± 0.669c **
	2nd	0.052 ± 0.002bc	0.039 ± 0.002b *	19.020 ± 0.553b	18.190 ± 0.525bc
	3rd	0.077 ± 0.001a	0.050 ± 0.004b **	19.287 ± 0.151b	20.252 ± 0.642a
	4th	0.061 ± 0.004b	0.282 ± 0.021a **	11.782 ± 0.508d	19.704 ± 0.090ab **
	5th	0.047 ± 0.001c	0.060 ± 0.002b **	13.729 ± 0.158c	12.524 ± 0.332d

All values are presented as mean ± standard error (n = 3) and means with different letters in the same column for each heavy metal are significantly different ($p < 0.05$). Independent-sample t-test was used to determine whether the two mean values obtained for the control and the treatment differed significantly. "*" indicates significant difference at $p < 0.05$ between the control and the treatment for each harvest time. "**"indicates significant difference $p < 0.01$ between the control and the treatment for each harvest time.

No significant difference in the water-extractable Cd was observed, except at the fifth harvest time, when the water-extractable Cd in the amended soil was higher compared to the unamended soil. There was no clear temporal variation in the water-extractable Cd for either the unamended soil or the amended soil. For the NH_4Cl-extratable Cd, the concentration in the amended soil was significantly lower compared to the unamended control soil for all the harvest cycles. While there was no clear variation trend in the NH_4Cl-extratable Cd from the first to the fifth harvest time for the unamended soil, the NH_4Cl-extratable Cd tended to decrease with increasing numbers of harvest cycles for the biochar-treated soil (Table 1).

The water-extractable Pb in the biochar-treated soil was significantly lower compared to the control soil at the first three harvest times, but the opposite was observed for the last harvest times. There was no clear temporal variation trend in the water-extractable Pb for the unamended control soil and the biochar-treated soil. For the NH_4Cl-extratable Pb, only the first harvest cycle showed a lower Pb concentration in the biochar-treated soil compared to the unamended control soil. For the other harvest cycles, either the opposite

was the case, or no significant difference was observed in the NH_4Cl-extratable Pb between the unamended control soil and the biochar-treated soil (Table 1).

3.2. Plant-Tissue-Borne Heavy Metals at Different Harvest Times

3.2.1. Chromium

There was no significant difference in the root-borne Cr between the vegetable plant grown in the unamend soil (VP-unamended soil) and the vegetable plant grown in the amended soil (VP-amended soil), except at the third harvest time, when the root-borne Cr in the VP-amended soil was significantly lower relative to the VP-unamended soil. However, for the aerial portion, the concentration of the plant-tissue-borne Cr in the VP-amended soil was significantly lower compared to the VP-unamended soil, except at the third harvest time, when the opposite was observed (Table 2).

Table 2. Concentrations (mg/kg) of various heavy metals in the above-ground and below-ground parts of Gynura cusimbua in the growth experiment.

		Above-Ground Portion		**Below-Ground Portion**	
Element	**Harvest Time**	**Control**	**Treatment**	**Control**	**Treatment**
Cr	1st	26.88 ± 1.60a	18.47 ± 0.89bc *	61.13 ± 5.71a	70.37 ± 5.95a
	2nd	28.09 ± 3.28a	21.02 ± 0.99b *	48.93 ± 7.03a	50.24 ± 17.81a
	3rd	20.06 ± 1.48b	26.60 ± 2.47a	29.94 ± 1.53b	19.55 ± 1.91b *
	4th	16.82 ± 1.88b	15.58 ± 0.78c **	21.75 ± 2.13b	22.41 ± 0.94b
	5th	19.47 ± 0.24b	18.58 ± 0.05bc *	20.95 ± 2.64b	19.12 ± 2.45b
Ni	1st	6.80 ± 0.59b	5.25 ± 1.33b	97.50 ± 2.40a	26.25 ± 3.52a **
	2nd	8.58 ± 0.31a	5.00 ± 0.32b **	34.02 ± 1.91b	26.52 ± 0.86a *
	3rd	5.96 ± 0.52b	5.26 ± 0.94b	21.77 ± 2.74c	12.95 ± 1.73b
	4th	5.53 ± 1.78b	6.32 ± 0.10b *	13.36 ± 2.47d	8.45 ± 2.22b
	5th	6.73 ± 0.75b	18.50 ± 1.66a **	13.01 ± 1.36d	7.86 ± 0.36b *
Cu	1st	44.89 ± 4.17b	23.43 ± 2.41bc *	497.58 ± 28.61b	157.00 ± 34.61c **
	2nd	64.55 ± 3.71a	26.41 ± 0.75bc **	926.40 ± 24.22a	350.42 ± 35.91ab **
	3rd	26.60 ± 1.18c	21.78 ± 3.12c	444.27 ± 61.64b	258.80 ± 85.40bc
	4th	34.00 ± 1.85c	36.04 ± 8.33b	503.31 ± 98.12b	440.55 ± 23.05ab
	5th	44.11 ± 3.51b	52.27 ± 0.75a	484.79 ± 39.48b	493.62 ± 70.50a
Zn	1st	316.83 ± 30.43b	148.39 ± 11.63b **	408.69 ± 13.87a	340.32 ± 18.31a *
	2nd	466.71 ± 25.28a	214.41 ± 22.30ab **	377.43 ± 39.65a	248.36 ± 18.30b *
	3rd	318.68 ± 71.63b	226.72 ± 30.23ab	395.56 ± 29.92a	239.06 ± 18.06b *
	4th	273.78 ± 20.13b	339.31 ± 75.92a	257.16 ± 21.85b	200.84 ± 10.25b
	5th	387.65 ± 19.05ab	297.80 ± 58.23ab *	233.04 ± 8.81b	262.70 ± 42.50b
Cd	1st	3.94 ± 0.54b	4.41 ± 0.20bc	5.46 ± 1.08ab	6.32 ± 0.13a
	2nd	6.87 ± 0.36a	6.21 ± 0.36b	7.44 ± 2.14a	6.35 ± 0.65a
	3rd	3.91 ± 0.06b	3.95 ± 0.37c	5.13 ± 0.37ab	3.24 ± 0.29b *
	4th	5.55 ± 0.35a	8.36 ± 0.25a **	3.39 ± 0.27b	3.58 ± 0.45b
	5th	5.97 ± 0.79a	6.27 ± 1.31b	3.08 ± 0.09b	3.66 ± 0.62b
Pb	1st	8.65 ± 0.36d	3.49 ± 0.25d **	262.32 ± 28.48b	132.11 ± 25.02b *
	2nd	22.45 ± 1.21b	9.31 ± 0.05c **	392.43 ± 28.48a	176.44 ± 15.13b **
	3rd	18.70 ± 1.10c	11.34 ± 0.90bc **	226.12 ± 34.38b	165.40 ± 29.20b
	4th	15.25 ± 0.65c	14.27 ± 0.58b	288.00 ± 58.29ab	280.80 ± 16.72a
	5th	28.43 ± 1.77a	21.69 ± 2.23a	273.44 ± 24.61ab	298.00 ± 24.05a

All values are presented as mean ± standard error (n = 3) and means with different letters in the same column for each heavy metal are significantly different ($p < 0.05$). Independent-sample t-test was used to determine whether the two mean values obtained for the control and the treatment differed significantly. "*" indicates significant difference at $p < 0.05$ between the control and the treatment for each harvest time. "**" indicates significant difference $p < 0.01$ between the control and the treatment for each harvest time.

3.2.2. Nickel

The root-borne Ni in was significantly lower in the VP-amended soil than in the VP-unamended soil at any of the five harvest times. Furthermore, the root-borne Ni tended

to decrease as the number of the harvest cycle increased for both the VP-unamended soil and the VP-amended soil. For the above-ground portion, mixed results were observed: the VP-unamended soil and the VP-amended soil showed no significant difference in root-borne Ni for the first and third harvest cycles; the root-borne Ni in the VP-amended soil was significantly lower relative to the VP-unamended soil for the second harvest cycle; and at the last two harvest times, the root-borne Ni in the VP-amended soil was significantly higher relative to the VP-unamended soil (Table 2).

3.2.3. Copper

The root-borne Cu in the VP-amended soil was lower (significantly at $p < 0.05$) relative to the VP-unamended soil for the first to third harvest cycles, while the VP-unamended soil and the VP-amended soil showed no significant differences in the root-borne Cu for the last two harvest cycles. A trend was observed in which the root-borne Cu increased as the number of harvest cycles increased in the VP-amended soil, while there was no clear temporal variation in the root-borne Cu in the VP-unamended soil. For the above-ground portion, the Cu in the VP-amended soil was higher (significantly at $p < 0.05$) relative to the VP-unamended soil for the first and second harvest cycles, but the control and the treatment showed no significant difference in Cu for the last three harvest cycles (Table 2).

3.2.4. Zinc

The root-borne Zn in the VP-amended soil was lower (significantly at $p < 0.05$) compared to the VP-unamended soil for the first three harvest cycles, but the VP-unamended soil and the VP-amended soil exhibited no significant ($p > 0.05$) differences in the root-borne Zn between for the last two harvest cycles. For the above-ground portion, the Zn in the VP-amended soil was lower (significantly at $p < 0.05$) compared to the VP-unamended soil for the first two harvest cycles, but the VP-unamended soil and the VP-amended soil showed no significant differences in Zn for the last three harvest cycles (Table 2).

3.2.5. Cadmium

The VP-unamended soil and the VP-amended soil showed no significant differences in the root-borne Cd, except in the third harvest cycle, when the root-borne Cd in the VP-amended soil was significantly lower compared to the VP-unamended soil. The concentrations of the root-borne Cd tended to be higher in the earlier harvest cycles than in the later harvest cycles for both the VP-unamended and the VP-amended soils. For the above-ground portion, there was no significant difference in Cd between the VP-unamended soil and the VP-amended soil, except for the fourth harvest cycle, which showed higher plant tissue Cd in the VP-amended soil than in the VP-unamended soil. There was no clear temporal variation in the plant-tissue Cd for either the VP-unamended or the VP-unamended soils (Table 2).

3.2.6. Lead

The root-borne Pb in the VP-amended soil was lower (significantly at $p < 0.05$) compared to the VP-unamended soil for the first three harvest cycles, but the VP-unamended and VP-amended soils showed no significant differences in the root-borne Pb for the later harvest cycles. The root-borne Pb tended to increase as the number of harvest cycle increased for the VP-amended soil, while no clear trend was observed for the VP-unamended soil. For the above-ground portion, similar trends to the below-ground portion were observed; the Pb in the VP-amended soil was also significantly lower relative to the VP-unamended soil for the first three harvest cycles, but the VP-unamended soil and the VP-amended soil showed no significant differences in root-borne Pb for the later harvest cycles; the root-borne Pb tended to increase as the number of harvest cycles increased for the VP-amended soil, while no clear trend was established for the VP-unamended soil (Table 2).

3.3. Bioaccessible Heavy Metals in the Edible Vegetable Portion

The bioaccessible amounts of various heavy metals in the edible vegetable portion was lower in the VP-amended soil compared to the VP-unamended soil for the gastric phase and gastrointestinal phase ($p < 0.05$), although it was not statistically significant for the Cd at a few of the harvest times (Table 3). The concentrations of bioaccessible heavy metals varied with the harvest time but showed no clear increasing or decreasing trend with increasing numbers of harvest cycles.

Table 3. Concentration (mg/kg on a fresh weight basis) of bioaccessible heavy metals in the edible portion of *Gynura cusimbua*.

		Gastric Phase		Gastrointestinal Phase	
Element	**Harvest Time**	**Control**	**Treatment**	**Control**	**Treatment**
Cr	1st	0.14 ± 0.00b	0.03 ± 0.00c **	0.12 ± 0.01b	0.05 ± 0.00b *
	2nd	0.39 ± 0.02a	0.09 ± 0.00a **	0.72 ± 0.05a	0.05 ± 0.00b **
	3rd	0.15 ± 0.00b	0.08 ± 0.01a **	0.14 ± 0.00b	0.09 ± 0.01a **
	4th	0.14 ± 0.00b	0.06 ± 0.00b **	0.19 ± 0.01b	0.08 ± 0.00a **
	5th	0.16 ± 0.00b	0.08 ± 0.00ab **	0.11 ± 0.00b	0.09 ± 0.00a **
Ni	1st	0.30 ± 0.02b	0.09 ± 0.01b **	0.35 ± 0.02bc	0.11 ± 0.00d **
	2nd	0.39 ± 0.02a	0.24 ± 0.03a *	0.38 ± 0.00b	0.17 ± 0.01c **
	3rd	0.34 ± 0.02ab	0.20 ± 0.02a **	0.32 ± 0.01c	0.22 ± 0.01b **
	4th	0.33 ± 0.02ab	0.20 ± 0.00a **	0.35 ± 0.03bc	0.26 ± 0.01a *
	5th	0.37 ± 0.01a	0.23 ± 0.00a **	0.46 ± 0.02a	0.23 ± 0.01b **
Cu	1st	2.61 ± 0.03ab	0.54 ± 0.01d **	2.44 ± 0.03ab	0.74 ± 0.07d **
	2nd	2.55 ± 0.05ab	1.21 ± 0.06b **	2.68 ± 0.05a	0.99 ± 0.02c **
	3rd	1.26 ± 0.07c	1.01 ± 0.04c **	1.61 ± 0.05c	1.14 ± 0.09c **
	4th	1.43 ± 0.05c	1.07 ± 0.05c **	2.12 ± 0.15bc	1.45 ± 0.02b *
	5th	2.71 ± 0.22a	1.82 ± 0.02a *	2.67 ± 0.22a	1.75 ± 0.05a *
Zn	1st	14.89 ± 0.82d	4.57 ± 0.38d **	11.55 ± 0.26c	4.07 ± 0.21d **
	2nd	17.26 ± 0.53c	10.06 ± 0.12c **	21.61 ± 0.77a	8.17 ± 0.26b **
	3rd	19.32 ± 0.14b	12.52 ± 0.21bc **	11.24 ± 0.29c	9.95 ± 0.10a *
	4th	17.04 ± 0.82c	13.18 ± 0.91b *	10.12 ± 0.77c	5.65 ± 0.12c **
	5th	21.02 ± 0.12a	14.96 ± 0.35a **	16.44 ± 0.12b	8.42 ± 0.48b **
Cd	1st	0.24 ± 0.00b	0.13 ± 0.01c **	0.12 ± 0.01d	0.05 ± 0.00e **
	2nd	0.31 ± 0.00a	0.28 ± 0.01a	0.22 ± 0.00b	0.10 ± 0.01c **
	3rd	0.25 ± 0.01b	0.24 ± 0.01b	0.21 ± 0.00b	0.09 ± 0.00d **
	4th	0.31 ± 0.01a	0.22 ± 0.04b	0.19 ± 0.01c	0.14 ± 0.00b *
	5th	0.36 ± 0.01a	0.23 ± 0.00b **	0.28 ± 0.01a	0.22 ± 0.00a **
Pb	1st	0.20 ± 0.01c	0.04 ± 0.00d **	0.02 ± 0.00c	0.01 ± 0.00c *
	2nd	0.80 ± 0.00a	0.14 ± 0.00b **	0.54 ± 0.03a	0.03 ± 0.00b **
	3rd	0.19 ± 0.02c	0.11 ± 0.01c *	0.07 ± 0.00b	0.04 ± 0.00a **
	4th	0.28 ± 0.01b	0.10 ± 0.01c **	0.07 ± 0.01b	0.03 ± 0.01b **
	5th	0.81 ± 0.02a	0.46 ± 0.00a **	0.10 ± 0.00b	0.05 ± 0.00a **

All values are presented as mean ± standard error (n = 3) and means with different letters in the same column for each heavy metal are significantly different ($p < 0.05$). Independent-sample t-test was used to determine whether the two mean values obtained for the control and the treatment differed significantly. "*" indicates significant difference at $p < 0.05$ between the control and the treatment for each harvest time. "**" indicates significant difference $p < 0.01$ between the control and the treatment for each harvest time.

4. Discussion

The addition of alkaline biochar to the acidic soil caused a decrease in the titratable acidity at the first harvest time (Figure 1). This was accompanied by a reduction in the water-extractable Cu and Pb (Table 1), reflecting the immobilization of the soluble Cu and Pb, possibly through hydrolysis or adsorption by the biochar [29–32]. For example,

hydrolysis resulted in the transformation of the soluble Cu^{2+} into $Cu(OH)^{+}$ and, eventually, precipitation as insoluble $Cu(OH)_2$:

$$Cu^{2+} + OH^{-} \rightarrow Cu(OH)^{+} \quad (5)$$

$$Cu(OH)^{+} \rightarrow Cu(OH)_2 \quad (6)$$

Following the addition of the biochar to the soil, the negatively charged surfaces allowed the adsorption of cationic heavy metals to the biochar.

$$[Biochar]^{2-} + 2Cu(OH)^{+} \rightarrow [Biochar]^{2-} - 2Cu(OH)^{+} \quad (7)$$

$$[Biochar]^{2-} + Pb^{2+} \rightarrow [Biochar]^{2-} - Pb^{2+} \quad (8)$$

The application of the biochar also resulted in a decrease in the NH_4Cl-extractable heavy metals, except for the Cr. The NH_4Cl-extractable fraction of a heavy metal includes the exchangeable form of that heavy metal in addition to its soluble form. Therefore, it represents the major phytoavailable pool of heavy metals in soils [33,34]. Under the predominantly oxidizing conditions encountered in the soils in the growth experiment, Cr was likely to be present in oxyanionic forms (CrO_4^{2-} or $Cr_2O_7^{2-}$) [35,36]. Unlike cationic heavy metals, anionic Cr was not immobilized via hydrolysis or adsorption to negatively charged biochar surfaces. This explains why no reduction was observed in the soluble and exchangeable Cr from the reduced soil acidity after the biochar application. The general tendency of the concentrations of the cationic heavy metals in the amended soil, particularly Cu, Zn, and Pb, was lower compared to the unamended soil at the earlier harvest times, which suggests that the addition of the biochar had the effect of immobilizing these heavy metals. However, the protonation of the biochar surfaces took place over time, since the soil had a pH of around 4. This might have led to the replacement of the adsorbed heavy metals by H^{+}, as shown by the following example:

$$[Biochar]^{2-} - Cu^{2+} + 2H^{+} \rightarrow [Biochar]^{2-} - 2H^{+} + Cu^{2+} \quad (9)$$

This process could also have been enhanced by the generation of organic acid in the rhizosphere from plant-root exudation [23,37].

The relatively highly soluble Cu and Pb in the soil at the last two harvest times also resulted in higher concentrations of the root-borne Cu and Pb at these two harvest times, reflecting the enhanced uptake of these two heavy metals by the roots, which might have affect the growth of the plants [38–40]. From Figure 2, it can be seen that the BAF of the Cu, Zn, and Pb showed a similar pattern, in which the BAF in the unamended soil tended to be higher relative to the amended soil at the earlier harvest times, while the BAF values in the control and the biochar treatment were very close to each other at the later harvest times. This suggests that the effect of the added biochar on the prevention of the uptake of these three heavy metals was reduced over time. Unlike the three aforementioned heavy metals, the BAF of the Cr showed no clear temporal variation, and in most of the harvest times, the BAF values of the control and the biochar treatment were very close, suggesting that the added biochar had no marked effects on the uptake of the soil-borne Cr by the plant roots. This is attributable to the weak effect of the added biochar on the Cr's phytoavaibility. The BFA of the Ni in the control was higher relative to the biochar treatment for all five harvest cycles, indicating that the reduction in the plant uptake of Ni by the biochar lasted for the entire duration of the experiment. Mixed results were obtained for the BAF of the Cd, although it seems that the capacity of the added biochar to inhibit the uptake of Cd by the roots was weakened at the last two harvest times.

With regard to the root–aerial-portion translocation of the heavy metals, different distribution patterns of TF were observed for the different heavy metals across the five harvest times. The TF for a heavy metal could be higher or lower in the control than in the biochar treatment, depending on the harvest time, on a random basis (Figure 3). This suggests

that the biochar application had insignificant effects on the root–shoot translocation of the heavy metals. It is interesting to note that the Cu and Pb showed much lower TF compared to the other heavy metals. This is in agreement with the findings by Mirecki et al. [41]. By contrast, the TF in the Cd tended to be greater than in the other heavy metals. The high root–shoot translocation rate is widely recognized [42]. The variation in TF values among the different heavy metals may be attributed to the differential solubilities and tendencies toward compartmentalization of individual heavy metals in the plant vascular system [43].

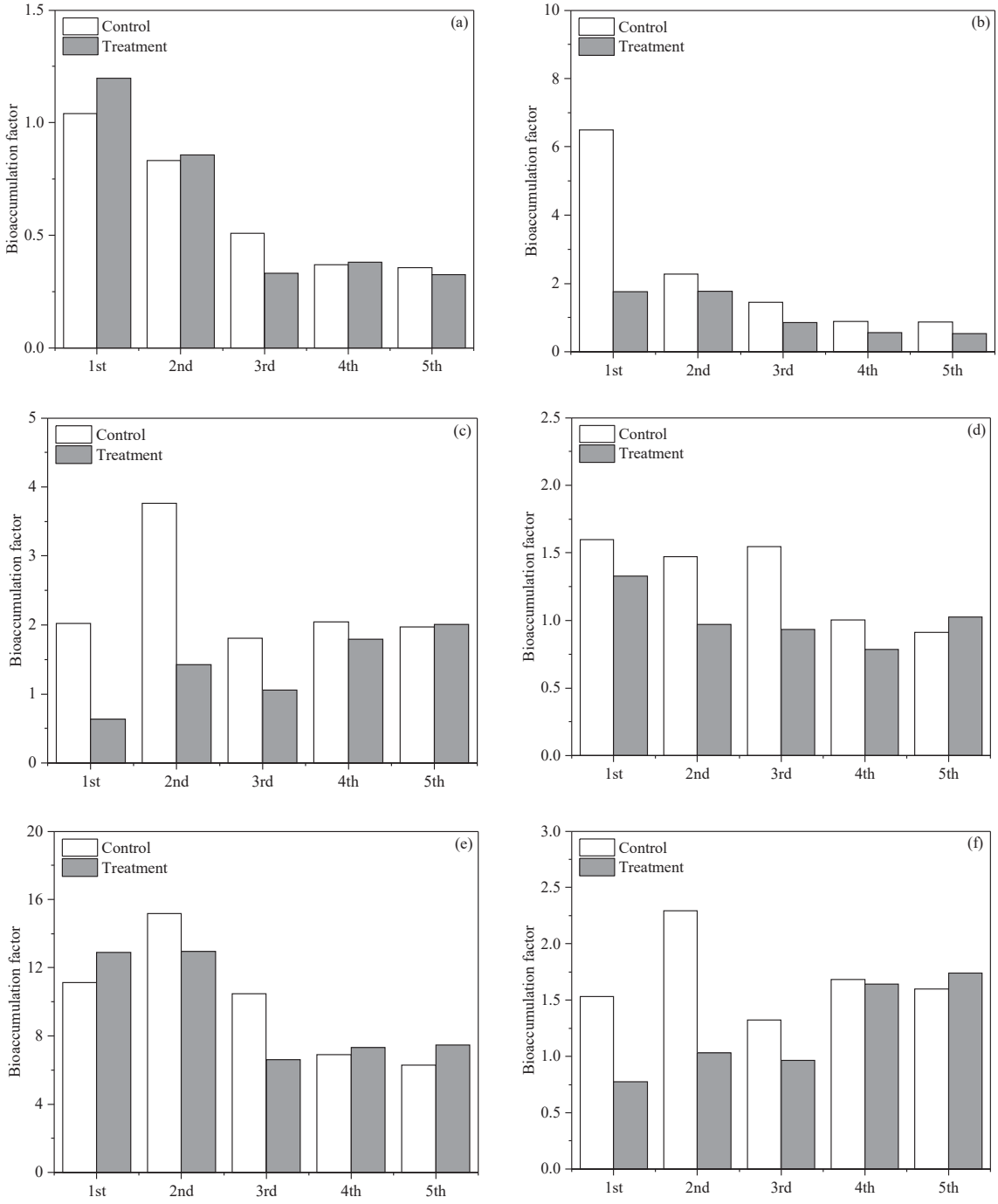


Figure 2. Bioaccumulation factor (BAF) of Cr (**a**), Ni (**b**), Cu (**c**), Zn (**d**), Cd (**e**), and Pb (**f**) for the *Gynura cusimbua* at different harvest times.

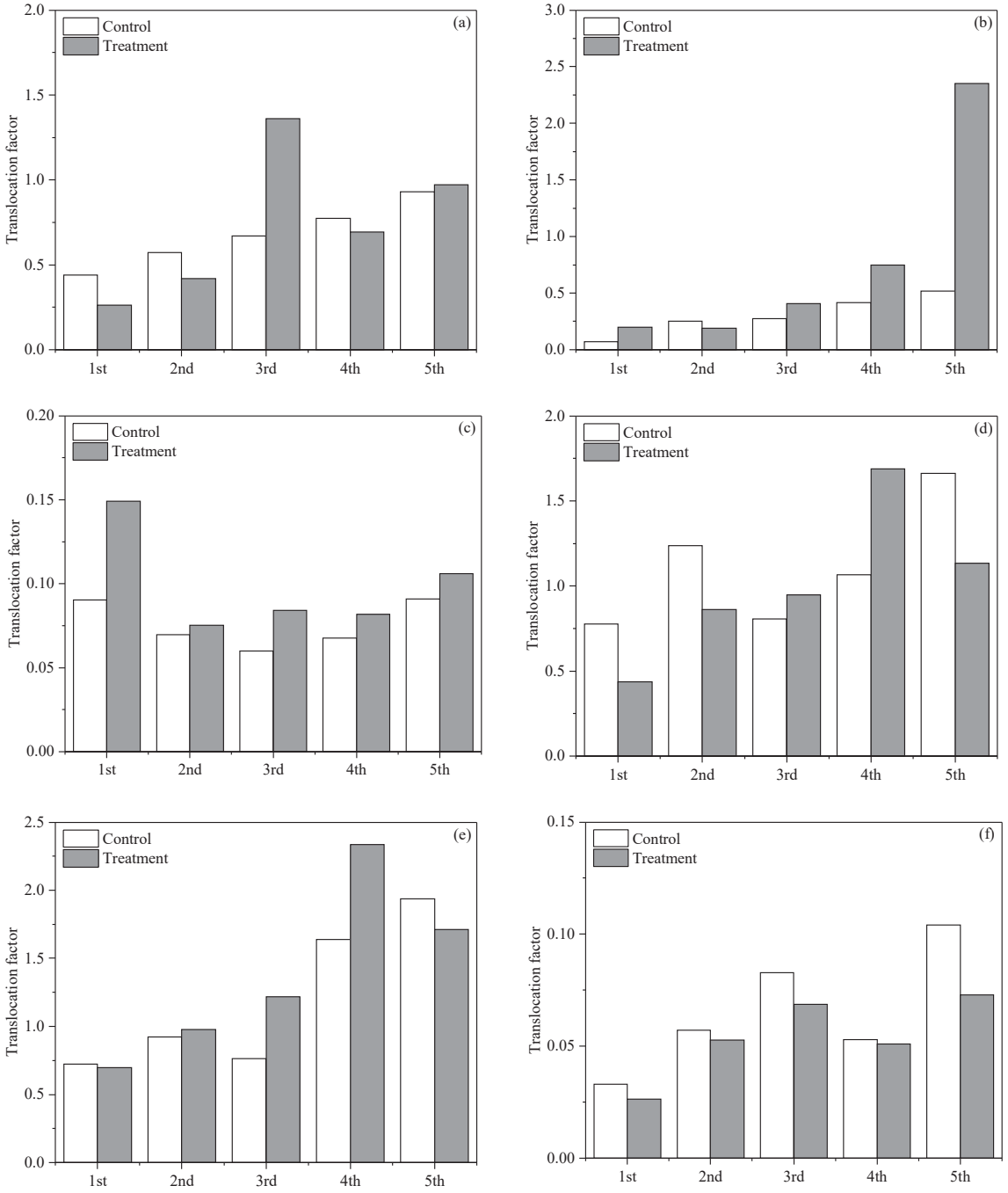


Figure 3. Translocation factor (TF) of Cr (**a**), Ni (**b**), Cu (**c**), Zn (**d**), Cd (**e**), and Pb (**f**) for the *Gynura cusimbua* at different harvest times.

While, on most occasions, the heavy-metal bioaccessibility in gastric phase was lower in the added-biochar treatment compared to the control, the opposite was observed for some occasions, which were not necessarily during the last harvest time (Figure S1). Therefore, biochar application might or might not have effects on reductions in the bioaccessibility of the edible portion of the vegetable.

There was a marked difference in bioaccessibility in the G phase among the different heavy metals, and at different times of harvest, indicating the complexity of the factors that affect the bioaccessbility of heavy metals contained in the edible vegetable portion. In general, the bioaccessibility of the plant-borne Cr and Pb was lower than that of the heavy metals, some of which displayed bioaccessibility greater than 90%.

In general, there was a high level of similarity between the G-phase bioaccessibity and the GI-phase bioaccessibility, showing that the plant-borne Cr and Pb had lower bioaccessibility than the other heavy metals (Figure S2). This appears to suggest that the intake of the heavy metals associated with consumption of the vegetable was more likely to occur during the stage of gastric digestion.

5. Conclusions

The application of biochar to the acidic-mine soil resulted in a reduction in the phytoavailability of the heavy metals, which impeded the plant uptake of cationic heavy metals, but not of the anionic Cr. However, these beneficial effects of biochar were weakened as the number of harvest cycles increased after the negatively charged surfaces of biochar were gradually protonated under acidic soil conditions. This led to the desorption of the previously adsorbed heavy metals. The weakening capacity of the biochar to impede the uptake of heavy metals by the vegetable plant was more evident for the Cu, Zn, and Pb than for the Ni and Cd. The bioaccessible amounts of heavy metals in the edible vegetable portion were also reduced due to the biochar application.

Supplementary Materials: The following supporting information can be downloaded at: https://www.mdpi.com/article/10.3390/toxics10080462/s1. Figure S1: Bioaccessibility (%) of Cr (a), Ni (b), Cu (c), Zn (d), Cd (e), and Pb (f) in the edible portion of the vegetable under simulated gastric conditions at different harvest times. Figure S2: Bioaccessibility (%) of Cr (a), Ni (b), Cu (c), Zn (d), Cd (e), and Pb (f) in the edible portion of the vegetable under simulated gastrointestinal conditions at different harvest times. Table S1: Some major physicochemical characteristics of the biochar and soil used in the greenhouse experiment.

Author Contributions: Conceptualization, J.Q. and C.L.; methodology, J.Q., X.W. and J.Y.; formal analysis, X.W. and J.Y.; investigation, X.W., J.Y. and J.Q.; data curation, X.W. and J.Y.; writing—original draft preparation, J.Q. and C.L.; writing—review and editing, C.L.; supervision, C.L.; funding acquisition, J.Q. All authors have read and agreed to the published version of the manuscript.

Funding: This work was partially supported by Natural Science Foundation of Guangdong Province, China (2021A1515011583) and the Science and Technology Program of Qingyuan, China (2020KJJH010).

Institutional Review Board Statement: Not applicable.

Informed Consent Statement: Not applicable.

Data Availability Statement: Not applicable.

Conflicts of Interest: The authors declare no conflict of interest.

References

1. Park, J.H.; Choppala, G.K.; Bolan, N.S.; Chung, J.W.; Chuasavathi, T. Biochar reduces the bioavailability and phytotoxicity of heavy metals. *Plant Soil* **2011**, *348*, 439–451. [CrossRef]
2. Puga, A.P.; Abreu, C.A.; Melo, L.C.A.; Beesley, L. Biochar application to a contaminated soil reduces the availability and plant uptake of zinc, lead and cadmium. *J. Environ. Manag.* **2015**, *159*, 86–93. [CrossRef]
3. Khan, A.Z.; Khan, S.; Ayaz, T.; Brusseau, M.L.; Khan, M.A.; Nawab, J.; Muhammad, S. Popular wood and sugarcane bagasse biochars reduced uptake of chromium and lead by lettuce from mine-contaminated soil. *Environ. Pollut.* **2020**, *263*, 114446. [CrossRef] [PubMed]
4. Beesley, L.; Moreno-Jiménez, E.; Gomez-Eyles, J.L.; Harris, E.; Robinson, B.; Sizmur, T. A review of biochars' potential role in the remediation, revegetation and restoration of contaminated soils. *Environ. Pollut.* **2011**, *159*, 3269–3282. [CrossRef]
5. Khan, A.Z.; Ding, X.; Khan, S.; Ayaz, T.; Fidel, R.; Khan, M.A. Biochar efficacy for reducing heavy metals uptake by Cilantro (*Coriandrum sativum*) and spinach (*Spinaccia oleracea*) to minimize human health risk. *Chemosphere* **2020**, *244*, 125543. [CrossRef]
6. Lin, C.; Melville, M.D. Control of soil acidification by fluvial sedimentation in an estuarine floodplain, eastern Australia. *Sediment. Geol.* **1993**, *85*, 271–284. [CrossRef]
7. Liu, Y.; Lin, C.; Ma, Y.; Lu, W.; Wu, Y.; Huang, S.; Zhu, L.; Li, J.; Chen, A. Toxic effects of two acid sulfate soils from the Dabaoshan Mine on *Corymbia citridora var.variegata* and *Daphnia carinata*. *J. Hazard. Mater.* **2009**, *166*, 1162–1168. [CrossRef] [PubMed]
8. Liao, J.; Ru, X.; Xie, B.; Zhang, W.; Wu, H.; Wu, C. Multi-phase distribution and comprehensive ecological risk assessment of heavy metal pollutants in a river affected by acid mine drainage. *Ecotox. Environ. Saf.* **2017**, *141*, 75–84. [CrossRef]

9. Montiel-Rozas, M.M.; Madejón, E.; Madejón, P. Effect of heavy metals and organic matter on root exudates (low molecular weight organic acids) of herbaceous species: An assessment in sand and soil conditions under different levels of contamination. *Environ. Pollut.* **2016**, *216*, 273–281. [CrossRef]
10. Onireti, O.O.; Lin, C.; Qin, J. Combined effects of low-molecular-weight organic acids on mobilization of arsenic and lead from multi-contaminated soils. *Chemosphere* **2017**, *170*, 161–168. [CrossRef]
11. Ahmad, M.; Rajapaksha, A.U.; Lim, J.E.; Zhang, M.; Bolan, N. Biochar as a sorbent for contaminant management in soil and water: A review. *Chemosphere* **2014**, *99*, 19–33. [CrossRef] [PubMed]
12. Chen, D.; Liu, X.; Bian, R.; Cheng, K.; Zhang, X.; Zheng, J.; Joseph, S.; Crowley, D.; Pan, G.; Li, L. Effects of biochar on availability and plant uptake of heavy metals-A me-ta-analysis. *J. Environ. Manag.* **2018**, *222*, 76–85. [CrossRef]
13. Sui, F.; Zuo, J.; Chen, D.; Li, L.; Pan, G.; Crowley, D. Biochar effects on uptake of cadmium and lead by wheat in relation to annual precipitation: A 3-year field study. *Environ. Sci. Pollut. Res.* **2018**, *25*, 3368–3377. [CrossRef] [PubMed]
14. Nzediegwu, C.; Prasher, S.; Eman, E.; Dhiman, J.; Mawof, A.; Patel, R. Effect of biochar on heavy metal accumulation in potatoes from wastewater irrigation. *J. Environ. Manag.* **2019**, *232*, 153–164. [CrossRef]
15. Gonzaga, M.; Silva, P. Biochar increases plant water use efficiency and biomass production while reducing Cu concentration in *Brassica juncea L.* in a Cu-contaminated soil. *Ecotox. Environ. Saf.* **2019**, *183*, 109557. [CrossRef]
16. Medyńska-Juraszek, A.; Rivier, P.; Rasse, D.; Joner, E. Biochar Affects Heavy Metal Uptake in Plants through Interactions in the Rhizosphere. *Appl. Sci.* **2020**, *10*, 5105. [CrossRef]
17. Achor, S.; Aravis, C.; Heaney, N.; Odion, E.; Lin, C.X. Response of organic acid-mobilized heavy metals in soils to biochar application. *Geoderma* **2020**, *378*, 114628. [CrossRef]
18. Chen, A.; Lin, C.; Lu, W.; Ma, Y.; Bai, Y.; Chen, H.; Li, J. Chemical dynamics of acidity and heavy metals in a mine water-polluted soil during decontamination using clean water. *J. Hazard. Mater.* **2010**, *175*, 638–645. [CrossRef]
19. Lin, C.; Wu, Y.; Lu, W.; Chen, A.; Liu, Y. Water chemistry and ecotoxicity of an acid mine drainage-affected stream in subtropical China during a major flood event. *J. Hazard. Mater.* **2007**, *142*, 199–207. [CrossRef]
20. Geremias, R.; Bortolotto, T.; Wilhelm-Filho, D.; Pedrosa, R.; Fáveree, V.; de Fáveree, V. Efficacy assessment of acid mine drainage treatment with coal mining waste using *Allium cepa* L. as a bioindicator. *Ecotox. Environ. Saf.* **2012**, *79*, 116–121. [CrossRef]
21. Wang, H.; Zeng, Y.; Guo, C.; Zheng, X.; Ding, C.; Lu, G.; Dang, Z. Soil rehabilitation shaped different patterns of bacterial and archaeal community in AMD-irrigated paddy soil. *Chemosphere* **2020**, *9*, 128259. [CrossRef] [PubMed]
22. Dickinson, D.; Balduccio, L.; Buysse, J.; Frederik, R.; Van Huylenbroeck, G.; Prins, W. Cost-benefit analysis of using biochar to improve cereals agriculture. *GCB Bioenergy* **2015**, *7*, 850–864. [CrossRef]
23. Qin, J.; Niu, A.; Liu, Y.; Lin, C. Arsenic in leafy vegetable plants grown on mine water-contaminated soils: Uptake, human health risk and remedial effects of biochar. *J. Hazard. Mater.* **2021**, *402*, 123488. [CrossRef] [PubMed]
24. Alozie, N.; Heaney, N.; Lin, C. Biochar immobilizes soil-borne arsenic but not cationic metals in the presence of low-molecular-weight organic acids. *Sci. Total. Environ.* **2018**, *630*, 1188–1194. [CrossRef]
25. Heaney, N.; Ukpong, E.; Lin, C. Low-molecular-weight organic acids enable biochar to immobilize nitrate. *Chemosphere* **2020**, *240*, 124872. [CrossRef]
26. Lin, C.; Lu, W.; Wu, Y. Agricultural soils irrigated with acidic mine water: Acidity, heavy metals, and crop contamination. *Aust. J. Soil. Res.* **2005**, *43*, 819–826. [CrossRef]
27. Qin, J.; Cui, X.; Yan, H.; Lu, W.; Lin, C. Active treatment of acidic mine water to minimize environmental impacts in a densely populated downstream area. *J. Clean. Prod.* **2019**, *210*, 309–316. [CrossRef]
28. Qin, J.; Nworie, O.E.; Lin, C. Particle size effects on bioaccessible amounts of ingestible soil-borne toxic elements. *Chemosphere* **2016**, *159*, 442–448. [CrossRef]
29. Trakal, L.; Komárek, M.; Száková, J.; Zemanová, V.; Tlustoš, P. Biochar application to metal-contaminated soil: Evaluating of Cd, Cu, Pb and Zn sorption behavior using single- and multi-element sorption experiment. *Plant Soil Environ.* **2011**, *57*, 372–380. [CrossRef]
30. Rizwan, M.S.; Imtiaz, M.; Huang, G.; Chhajro, M.A. Immobilization of Pb and Cu in polluted soil by superphosphate, multi-walled carbon nanotube, rice straw and its derived biochar. *Environ. Sci. Pollut. R.* **2016**, *23*, 15532–15543. [CrossRef]
31. Salam, A.; Bashir, S.; Khan, I.; Hussain, Q.; Gao, R. Biochar induced Pb and Cu immobilization, phytoavailability attenuation in Chinese cabbage, and improved biochemical properties in naturally co-contaminated soil. *J. Soils Sediments* **2019**, *19*, 2381–2392. [CrossRef]
32. Salam, A.; Shaheen, S.M.; Bashir, S.; Khan, I.; Wang, J. Rice straw- and rapeseed residue-derived biochars affect the geochemical fractions and phytoavailability of Cu and Pb to maize in a contaminated soil under different moisture content. *J. Environ. Manag.* **2019**, *237*, 5–14. [CrossRef] [PubMed]
33. Krishnamurti, G.S.R.; Smith, L.H.; Naidu, R. Method for assessing plant-available cadmium in soils. *Aust. J. Soil. Res.* **2000**, *38*, 823–836. [CrossRef]
34. Schöning, A.; Brümmer, G.W. Extraction of mobile element fractions in forest soils using ammonium nitrate and ammonium chloride. *J. Plant Nutr. Soil Sci.* **2008**, *171*, 392–398. [CrossRef]
35. Cornelis, G.; Johnson, C.A.; Gerven, T.V. Leaching mechanisms of oxyanionic metalloid and metal species in alkaline solid wastes: A review. *Appl. Geochem.* **2008**, *23*, 955–976. [CrossRef]

36. Markelova, E.; Couture, R.M.; Parsons, C.T.; Markelov, I. Speciation dynamics of oxyanion contaminants (As, Sb, Cr) in argillaceous suspensions during oxic-anoxic cycles. *Appl. Geochem.* **2018**, *91*, 75–88. [CrossRef]
37. Jones, D.L.; Dennis, P.G.; Owen, A.G.; Van Hees, P.A.W. Organic acid behavior in soils–misconceptions and knowledge gaps. *Plant Soil* **2003**, *248*, 31–41. [CrossRef]
38. John, R.; Ahmad, P.; Gadgil, K.; Sharma, S. Heavy metal toxicity: Effect on plant growth, biochemical parameters and metal accumulation by *Brassica juncea* L. *Int. J. Plant Prod.* **2009**, *3*, 65–76.
39. Kumar, V.; Singh, J.; Kumar, P. Chapter 4: Heavy metals accumulation in crop plants: Sources, response mechanisms, stress tolerance and their effects. In *Contaminants in Agriculture and Environment: Health Risks and Remediation*; Agro Environ Media, Publication Cell of AESA, Agriculture and Environmental Science Academy: Haridwar, India, 2019; pp. 39–53.
40. Shanmugaraj, B.M.; Malla, A.; Ramalingam, S. Chapter 1: Cadmium Stress and Toxicity in Plants: An Overview. In *Cadmium Toxicity and Tolerance in Plants: From Physiology to Remediation*; Academic Press: Cambridge, MA, USA, 2019; pp. 1–17.
41. Mirecki, N.; Agic, R.; Sunic, L.; Milenkovic, L. Transfer factor as indicator of heavy metals content in plants. Fresen. *Environ. Bull.* **2015**, *24*, 4212–4219.
42. Zheng, N.; Wang, Q.; Zheng, D. Health risk of Hg, Pb, Cd, Zn, and Cu to the inhabitants around Huludao Zinc Plant in China via consumption of vegetables. *Sci. Total Environ.* **2007**, *383*, 81–89. [CrossRef]
43. Kim, I.S.; Kang, K.H.; Johnson-Green, P.; Lee, E.J. Investigation of heavy metal accumulation in Polygonum thunbergii for phytoextration. *Environ. Pollut.* **2003**, *126*, 235–243. [CrossRef]

environments

Article

Hydrophobicity/Oleophilicity of Autoclaved Aerated Concrete (AAC) Grains Coated with Oleic and Stearic Acids for Application as Oil/Water Separating Filtration and Adsorbent Materials in Vietnam

Akihiro Matsuno [1,*] and Ken Kawamoto [1,2]

[1] Graduate School of Science and Engineering, Saitama University, 255 Shimo-okubo, Sakura-ku, Saitama 3388570, Japan
[2] Innovative Solid Waste Solutions (Waso), Hanoi University of Civil Engineering, No. 55 Giai Phong Street, Hai Ba Trung District, Hanoi 11616, Vietnam
* Correspondence: matsuno2017@mail.saitama-u.ac.jp; Tel.: +81-488299159

Abstract: Separation of oil and water is an effective technique to treat oily wastewater. For examining the applicability of porous grains coated with hydrophobic agents (HA) as low-cost and easily available filtration and adsorbent materials in the separation of oil and water, this study assessed the hydrophobicity/oleophilicity of porous grains made from autoclaved aerated concrete scrap coated with low-cost and harmless hydrophobic agents such as oleic and stearic acids. Tests using a sessile droplet method showed unique relationships between the contact angles (CA) of water droplets in air (CA_{wa}), oil droplets in water (CA_{ow}) and coated HA concentrations. The CA_{wa} increased linearly with increasing HA concentration and then became almost constant and/or gently increased after a specific point, indicating that a minimum coating amount gives the maximum hydrophobicity to HA-coated porous grains exists. The CA_{ow} gradually decreased exponentially with increasing HA concentration. In particular, the CA_{ow} of porous grains coated with stearic acid decreased with increasing of HA concentration in a two-step process. Furthermore, analyses of the Pearson correlation showed that both CA_{wa} and CA_{ow} correlated well with the specific surface area (SSA), implying that the SSA is a good indicator as a quick assessment of hydrophobicity/oleophilicity of HA-coated porous grains.

Keywords: hydrophobicity/oleophilicity; autoclaved aerated concrete; contact angle; sessile droplet method; oleic acid; stearic acid; oil/water separation; filtration and adsorbent materials; Vietnam

Citation: Matsuno, A.; Kawamoto, K. Hydrophobicity/Oleophilicity of Autoclaved Aerated Concrete (AAC) Grains Coated with Oleic and Stearic Acids for Application as Oil/Water Separating Filtration and Adsorbent Materials in Vietnam. *Environments* **2022**, *9*, 101. https://doi.org/10.3390/environments9080101

Academic Editor: Dino Musmarra

Received: 12 July 2022
Accepted: 8 August 2022
Published: 10 August 2022

Publisher's Note: MDPI stays neutral with regard to jurisdictional claims in published maps and institutional affiliations.

Copyright: © 2022 by the authors. Licensee MDPI, Basel, Switzerland. This article is an open access article distributed under the terms and conditions of the Creative Commons Attribution (CC BY) license (https://creativecommons.org/licenses/by/4.0/).

1. Introduction

Oil and grease in water are major pollutants of the water environment. The improper discharge and treatment of oily wastewater cause significant environmental pollution of surface and groundwater, rivers and ponds, and seawater. Especially, developing countries with rapid urbanization, industrialization, and population growth face serious water pollution by oily wastewater due to the insufficient development of wastewater treatment systems, resulting in severe impacts on human health and natural ecosystems (e.g., [1–3]). For example, Vietnam (one of the growing developing countries) reported that the inadequate treatment and improper disposal of oily wastewater as well as oil spills generated by human activities and industries such as petrochemicals, food processing, textiles, metals, mining, biopharmaceuticals, and oil and gas refineries cause serious water pollution in the whole country [4–6], and urgent actions are necessary to conserve a sound water environment and sustainable development and to prevent economic losses from improper oily wastewater treatment [1–3].

Nowadays, many technologies such as flotation, coagulation, chemical treatment, gravity separation, biological treatment, and oil/water separation have been developed and

applied to treat oily wastewater [7,8]. Among of them oil/water separation technologies using hydrophobic and oleophilic membranes/meshes/grains as filtration and adsorbent materials have been intensively developed due to their high treatment performance and cost effectiveness (e.g., [9,10]). Because the oil/water separation technologies do not need a centralized wastewater collection system and a large volume of water treatment tanks/ponds, they can be incorporated into small-scale decentralized wastewater treatment systems such as fixed-bed filtration tanks targeting domestic wastewater in rural areas (with a small number of households) and wastewater from food processing factories and craft villages [11–13]. From the viewpoint of durability and feasibility, furthermore, the filtration and/or adsorbent materials used in the oil/water separation made from easily available and environmentally sound recycled materials are desirable, particularly in Vietnam [11–13].

One of the most important characteristics to develop a high-performance oil/water separation system is the hydrophobicity/oleophilicity of the membranes/meshes/grains used as filtration and/or adsorbent materials [14–20]. The degree of hydrophobicity/oleophilicity is commonly assessed by measuring contact angles (CA) in air and/or water [21–24]. In a recent study [25], polyvinylidene fluoride (PVDF) membranes were coated with a suspension of waste brick powder (WBP) and then with sodium alginate by vacuum filtration to produce WBP-coated films. Shi et al. showed that WBP-coated membranes exhibited excellent underwater superoleophobicity, including under corrosive conditions and low adhesion to crude oil [25]. In addition, the WBP-coated membrane can separate crude oil-in-water emulsions with high separation efficiencies and permeating flux. Li et al. (2020a) showed that a TiO_2 coating applied to WBP [26] produced samples with superhydrophobic/superoleophilic properties [27], as dud Li et al. (2020b) using ZnO coating. Li et al. (2020a) and Li et al. (2020b) demonstrated that filter layers with opposite wettability exhibit high separation efficiency and flux [26,27]. On the other hand, Zhao et al. showed that a layer of waste peanut shells caused super-oleophobicity (oil contact angle of 150 ± 5) under water due to separation of immiscible oil/water mixtures by a hydrophilic substance and exhibited a desirable flux rate (2636.9 L $m^{-2} \cdot h^{-1}$) and high separation efficiency (>99.5%) for a surfactant stabilized water-in-oil emulsion [28].

As described above, many studies to assess the surface hydrophobicity/oleophilicity of filtration and/or adsorbent materials in the oil/water separation were based on the CA measurements. However, the CA measurements of hydrophobized/oleophilized surfaces in both oily water–air and oil–water systems (i.e., oil contact angles in air and water) have not been fully investigated, even though the oil contact angles in both air and water are needed to characterize the degree of hydrophobicity/oleophilicity of filtration and adsorbent materials and to assess the oil/water separation performance under both continuous (oil-in-water) and discontinuous (oily water in air) water flow conditions. Moreover, most previous studies that use hydrophobized grains for the oil/water separating materials used non-porous gains with a small specific surface area, such as quartz sands, and a limited number of studies have examined the applicability of porous grains (rich in fine pores inside and with a large specific surface area) as oil/water separating materials [29].

To encourage green practices and sustainable development, Vietnam is encouraging all economic sectors to invest in non-baked building material production and trading e.g., [30]. Among the non-baked building materials, autoclaved aerated concrete (AAC) is readily manufactured in Vietnam and widely used in many building applications [30]. AAC has a unique pore structure that consists of inner-pores (μm to nm scale) and inter-pores (mm to μm scale) [31–35]. The scrap and waste AAC has been increasing, but most AAC scrap is currently stored/dumped without reuse or recycling in many factories. Although the reuse and recycling of AAC scrap are highly desirable for sustainable consumption and production to implement the circular economy in Vietnam [36,37], till now very limited research has been done on the utilization of AAC scrap to reduce the amount that is dumped [38]. Thus, research is needed to promote development utilizing the unique porous characteristics of AAC.

Therefore, to promote low cost and high-performance oil/water separating filtration and adsorbent materials utilizing porous grains made from AAC scrap in Vietnam (VN-AAC), this research assessed the hydrophobicity (oleophilicity) of AAC grains coated with hydrophobic agents harmless to humans and the environment, such as oleic and stearic acids [39]. The specific objectives were (1) to measure the CA of water droplets in air (CA_{wa}) and the CA of oil droplets in water (CA_{ow}) of hydrophobized AAC grains in three grain sizes (0.106–0.250, 0.250–0.850, and 0.850–2.00 mm) and assess the hydrophobicity (oleophilicity) by examining the measured CA_{wa} and CA_{ow} values as a function of the amount of coated hydrophobic agents, and (2) to examine the correlations of measured CA_{wa} and CA_{ow} with physicochemical parameters such as specific surface area and organic carbon content. For comparing the tested results from AAC grains to those from non-porous grains, commercially available sands (grain sizes of 0.18–2.00 and 0.30–2.00 mm) used for sand filtration systems were also used in this research.

2. Materials and Methods

2.1. AAC Grains and Sands

Block-like AAC scrap (approximately 500 kg) was taken from Viglacera Joint Stock Company in Bac Ninh Province, Vietnam (21°11′50.8″ N, 106°00′42.8″ E) [40]. AAC is a typical lightweight cementitious material with a robust skeleton and pore structure (porous medium) and is widely used in many architectural applications worldwide due to its low density, thermal conductivity, and high heat resistance [41,42]. AAC is known to form a calcium silicate hydrate, tobermorite [$Ca_5Si_6(O, OH, F)_{18}5H_2O$], during the manufacturing process [42,43]. The block-like AAC scrap was first crushed to less than 10 mm and sieved in the laboratory to make AAC grains. Then, the AAC grains were washed gently with a low-foaming neutral detergent and rinsed thoroughly with distilled water. After being rinsed, the AAC grains were air dried and sieved again into three grain fractions, 0.106–0.250 mm (fine), 0.250–0.850 mm (middle), and 0.850–2.00 mm (coarse) [44]. For comparison of tested data from AAC grains, two commercially available sands (Nihon Genryo Materials Co., Ltd., Kanagawa, Japan) that meet the Japanese standards of filtration [45] were also used in this research. Sand with the size of 0.18–2.00 mm was used for slow filtration, and sand with the size of 0.30–2.00 mm was used for rapid filtration. The AAC grains and sands tested in this research are shown in Figure 1.

2.2. Oil

In this study, soybean oil with a high percentage of linoleic acid (53.5%) and linolenic acid (6.9%) (Wako 1st grade; Fujifilm Wako Pure Chemical Corp., Tokyo, Japan) was used. Soybean oil is a commonly consumed domestic oil in Vietnam [46] and is liquid at room temperature.

2.3. Hydrophobic Agents and Coating

Two types of hydrophobic agents (HA), stearic and oleic acids (SA and OA), were chosen to hydrophobically (oleophilically) coat the grains tested in this research [39,47–49]. Both OA and SA are harmless to humans and the environment. Olive oil is known to be rich in OA, and SA is plentiful in beef tallow and other animal and vegetable fats, materials readily available at low cost in Vietnam. In the laboratory, commercially available OA (molar mass: 282.46 g/mol, density: 0.895 g/cm^3) (Kanto Chemical Corp., Tokyo, Japan) and SA (molar mass: 284.47 g/mol, density: 0.940 g/cm^3) (Fujifilm Wako Pure Chemical Corp., Tokyo, Japan) were used. OA is a mono-unsaturated omega-9 fatty acid with the chemical formula $CH_3(CH_2)_7CH{:}CH(CH_2)_7COOH$, and SA is a saturated fatty acid with the chemical formula $CH_3(CH_2)_{16}COOH$.

The hydrophobic coating was done as follows: air-dried AAC grains and sands were soaked in a beaker along with the solvent to reach target HA concentrations (g/kg) [= M_s/M_d, where M_s is the dry mass of HA (g) and M_d is the dry mass of tested grains (kg)]. It is noted that at average room temperature, SA is a solid (powder) (melting point: 69 °C),

and OA is a liquid (melting point 13–16 °C). Therefore, considering the polarities of SA and OA, diethyl ether and ethanol were used as solvents for SA and OA, respectively. The SA and diethyl ether were thoroughly mixed using an electronic mixer before adding the sample. After volatilization of the solvent, the coated samples were stored for at least 48 h in a climate-controlled lab at 20 °C and 60% humidity to equilibrate and stored in a plastic bag after air-drying [50].

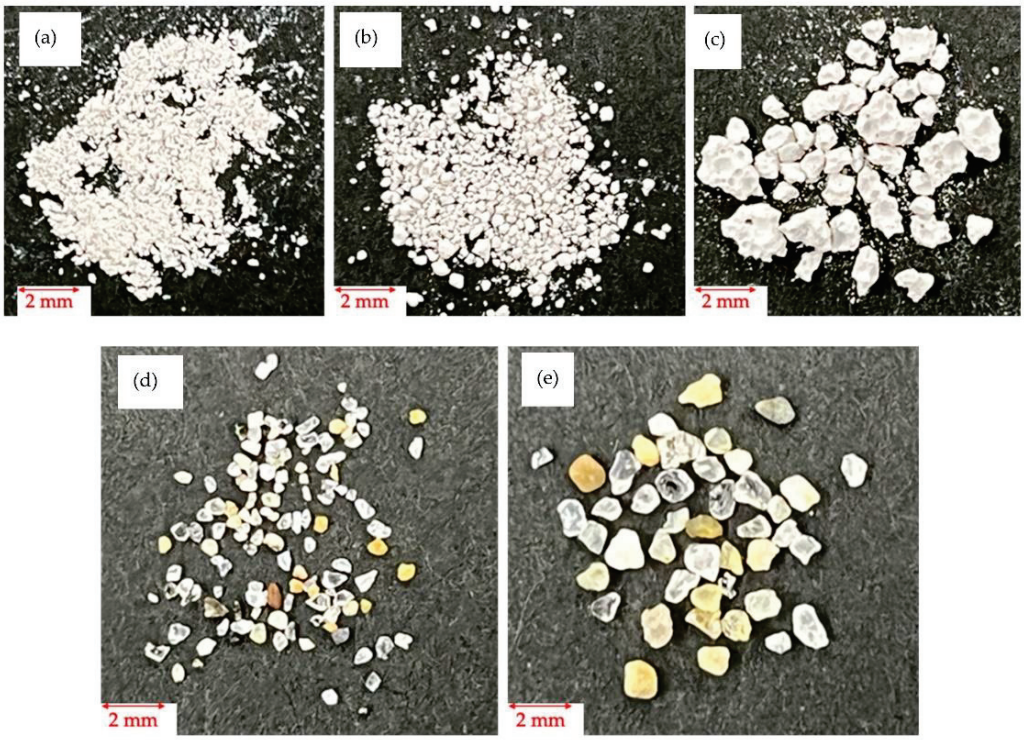


Figure 1. Samples: (**a**) VN-AAC (Grain size: 0.106–0.25 mm); (**b**) VN-AAC (Grain size: 0.25–0.85 mm); (**c**) VN-AAC (Grain size: 0.85–2.00 mm) (**d**) Sand (Grain size: 0.18–2.00 mm); (**e**) Sand (Grain size: 0.30–2.00 mm).

2.4. Measurement of Contact Angles

Contact angles of water droplets in air (CA_{wa}) for tested grains were measured by the sessile droplet method (SDM) [47,50,51] using a digital microscope (VHX-900 series, KEYENCE Japan, Tokyo, Japan). The grains were put on a smooth glass slide to which double-sided tape was attached. The glass slide was then lightly tapped to remove the excess sample, the glass slide was placed on the microscope camera stage, and a small drop of distilled water (50 ± 5 µL) was dropped onto the grains using a syringe. Horizontal microscope images were recorded to determine CA_{wa} with time, as shown in Figure 2a.

The contact angles of an oil droplet in water (CA_{ow}) were measured following the previous literature [52–54]: the test grains were placed on a smooth glass slide using a piece of double-sided tape. Then the glass slide was attached to a glass rod, and the glass rod was placed in a 2 L beaker filled with distilled water. A small drop (0.1 mL) of soybean oil was dripped from a microsyringe with the needle bent and pointing upward toward the sample attached to the underside of the slide glass. The CA_{ow} between the oil droplet and the grains is exemplified in Figure 2b.

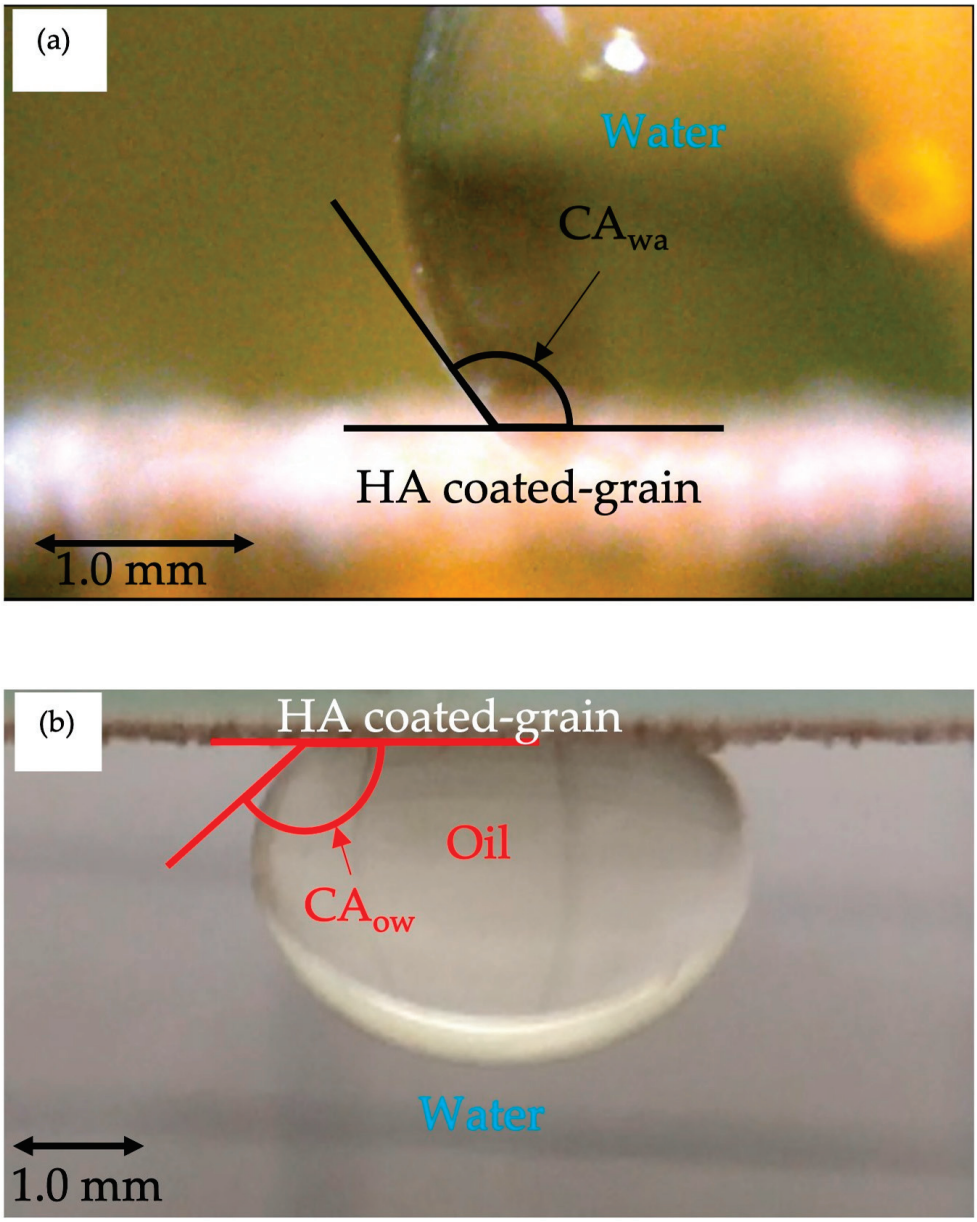


Figure 2. Sessile droplet method to measure contact angles: (**a**) Water in air (CA_{wa}); (**b**) Oil in water (CA_{ow}).

2.5. Physical and Chemical Properties of Tested Grains and Characterization of Hydrophobicity of HA-Coated Grains

Basic physical and chemical properties such as specific gravity (G_s), loss on ignition (LOI), moisture content in the air-dried condition (w_{AD}), pH, and electrical conductivity (EC) were measured [55,56]. The organic carbon (OC) content of HA-coated grains was measured by an elemental analyzer (FLASH 2000, Thermo Fisher Scientific, Inc., Waltham, MA, USA). The measured OC was also used to examine the relationships between added (mixed) HA and calculated HA based on OC (see Figure **??** in Appendix A). To characterize the surface hydrophobicity (oleophilicity) of tested grains, the A/B ratio was calculated based on the spectra measured by a Fourier transform infrared (FT-IR) spectrometer (Tensor II, Bruker Ltd., Banner Lane, UK). The FT-IR spectra focused on two absorption bands that primarily represent hydrophobic (C-H group) and hydrophilic (C=O group) functional groups. For hydrophobic methyl and methylene groups, the C-H bands occur at 2920 cm^{-1} (asymmetric stretch) and 2860 cm^{-1} (symmetric stretch) [57]. Here, both bands are combined into one band (3020–2800 cm^{-1}), which we designated as absorption band A.

Hydrophilic C=O groups occur at 1640–1615 and 1740–1720 cm^{-1} [58,59]. Here, we used slightly different bands, 1640 to 1620 and 1740 to 1710 cm^{-1}, to exclude a possible overlap with C=C and amide bands and denoted both as absorption band B. The OH bands were not considered because they could reflect differences in water content. From this, the ratio of hydrophobicity to hydrophilicity (A/B ratio) was determined [60].

The surface properties of the coated/non-coated grains were characterized by measuring the Brunauer–Emmett–Teller (BET) specific surface area (SSA in m^2/g) using a porosity analyzer (TriStar II, Micromeritics Instruments Corp., Norcross, GA, USA) [61]. The total pore volume (V_T) of non-coated grains was also measured using a porosity analyzer based on the Barrett–Joyner–Halenda method [62]. In addition, a scanning electron microscope (SEM) (TM4000plus, Hitachi High-Technologies Corp., Tokyo, Japan) and an energy dispersive X–ray spectroscope (EDS) (AZtecOne, Oxford Instruments, Abingdon, Oxon, UK) were used to investigate the morphological features and chemical compositions of HA-coated grains.

3. Results and Discussion

3.1. Physical and Chemical Characterization

Table 1 shows the physical and chemical properties of tested samples. The values of the uniformity coefficient ($U_c = D_{50}/D_{10}$) of tested samples ranged from 0.83 to 1.64, indicating that the samples were "uniform" [63]. For VN-AAC samples, the measured specific surface area (SSA) decreased with increasing grain size. The total pore volume (V_T), loss on ignition (LOI), and air-dried water content (w_{AD}) of VN-AAC, on the other hand, did not vary with grain size, and those values were one order of magnitude greater than those of sand. In particular, the high values of SSA and V_T of VN-AAC indicated that these samples were porous. VN-AAC samples were alkaline in water (pH = 8.6~9.0) and neutral in KCl solution (pH = 7.2–7.3). SEM-EDS images of OA- and SA-coated VN-AAC grains are exemplified in Figure 3. It can be seen the carbon (C) originating from coated HA materials (OA and SA) covered the tested grain surfaces well.

Table 1. Basic physical and chemical properties of tested samples in this study.

Sample	Grain Size(mm)	D_{10} (mm)	D_{50} (mm)	D_{60} (mm)	U_c (D_{50}/D_{10})	SSA (m^2/g)	V_T (cm^3/g)	LOI (%)	w_{AD} (%)	G_s (g/cm^3)	EC (mS/cm)	pH (H_2O)	pH (1 mol KCl)
VN-AAC	0.106–0.25	0.15	0.20	0.21	1.44	15.3	4.5×10^{-2}	9.2	1.44	2.57	1.04	8.90	7.27
VN-AAC	0.25–0.85	0.34	0.51	0.56	1.64	16.9	4.9×10^{-2}	9.5	2.03	2.55	0.94	8.57	7.20
VN-AAC	0.85–2.00	0.90	1.20	1.30	0.83	17.1	4.8×10^{-2}	9.4	2.01	2.46	0.83	8.97	7.33
Slow sand	0.18–2.00	0.31	0.48	0.55	1.54	3.0	6.0×10^{-3}	0.6	0.44	2.66	0.01	7.83	6.13
Rapid sand	0.30–2.00	0.62	0.79	0.83	1.28	3.5	7.0×10^{-3}	0.5	0.40	2.63	0.02	7.27	6.00

D_{10}: Grain size at 10% passing, D_{50}: Grain size at 50% passing (Median diameter), D_{60}: Grain size at 60% passing, U_c: Uniformity coefficient, SSA: Specific surface area, G_s: Specific gravity, w_{AD}: Air-dried water content, EC: Electrical conductivity, pH: Potential hydrogen was measured by using distilled water and 1 mol KCl solution (S:L = 1:2.5).

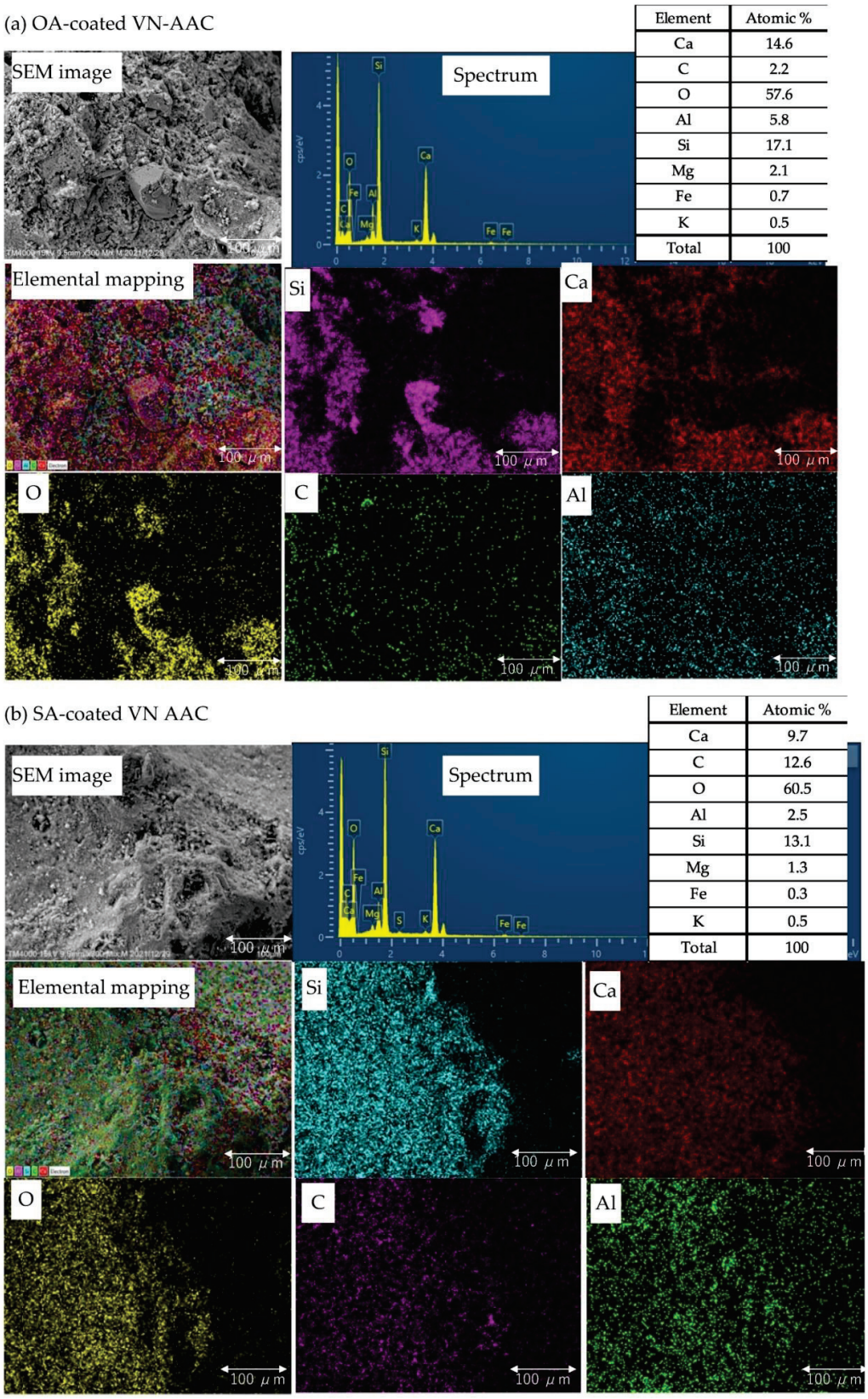


Figure 3. SEM-EDS images of (**a**) OA-coated VN-AAC grain (0.85–2.00 mm) at HA concentration = 14 g/kg and (**b**) SA-coated VN-AAC grain (0.85–2.00 mm) at HA concentration = 42 g/kg.

3.2. Contact Angles of Water in Air (CA_{wa})

Measured contact angles of water droplets in air (CA_{wa}) of tested samples as a function of the HA coating concentration are shown in Figure 4. For both OA- and SA-coated VN-AAC samples, the CA_{wa} values increased linearly with increasing HA concentration and reached 98–140°, and then became almost constant (Figure 4a,b,f) and/or gently increased (Figure 4c,g,h) after a specific point (i.e., point of intersection, hereafter labeled "PoI" and the contact angle at PoI labeled "$CA_{wa,PoI}$"). The slopes in the linear increment section (ΔS_1) and those in the gentle increment section (ΔS_2) were calculated and are given in the figure. As well, the HA concentrations corresponding to the PoI ($HA_{wa,PoI}$) and the maximum contact angles of a water droplet in air in the measured range ($CA_{wa,max}$) were read and are summarized in Table 2 For VN-AAC coated with both OA and SA, both $CA_{wa,max}$ and $CA_{wa,PoI}$ decreased with increasing grain size, indicating that a finer grain gave a higher hydrophobicity.

For both OA- and SA-coated sands, on the other hand, the CA_{wa} values increased rapidly, reached a peak, and decreased linearly with increasing HA concentration (Figure 4d,e,i,j; Table 2). The $CA_{wa,max}$ values of sands were smaller than those of VN-AAC (73–82° for OA-coated and 130–131° for SA-coated). In particular, $CA_{wa,max}$ = 73–82° of OA-coated slow sand means that the tested sand does not show hydrophobicity in air (non-water repellency).

The measured $CA_{wa,max}$, $CA_{wa,PoI}$, $HA_{wa,PoI}$, ΔS_1, and ΔS_2 in this study were compared to values of sands and glass beads reported by previous studies [39,47,64] (Table 2). Basically, the values of OA- and SA-coated sands in this study were similar to those in the previous studies and the difference in $CA_{wa,max}$ was within 10° [39,47,64]. Again, it can be found that the OA- and SA-coated AAC grains in this study gave high hydrophobicity with high values of $CA_{wa,max}$ and $CA_{wa,PoI}$.

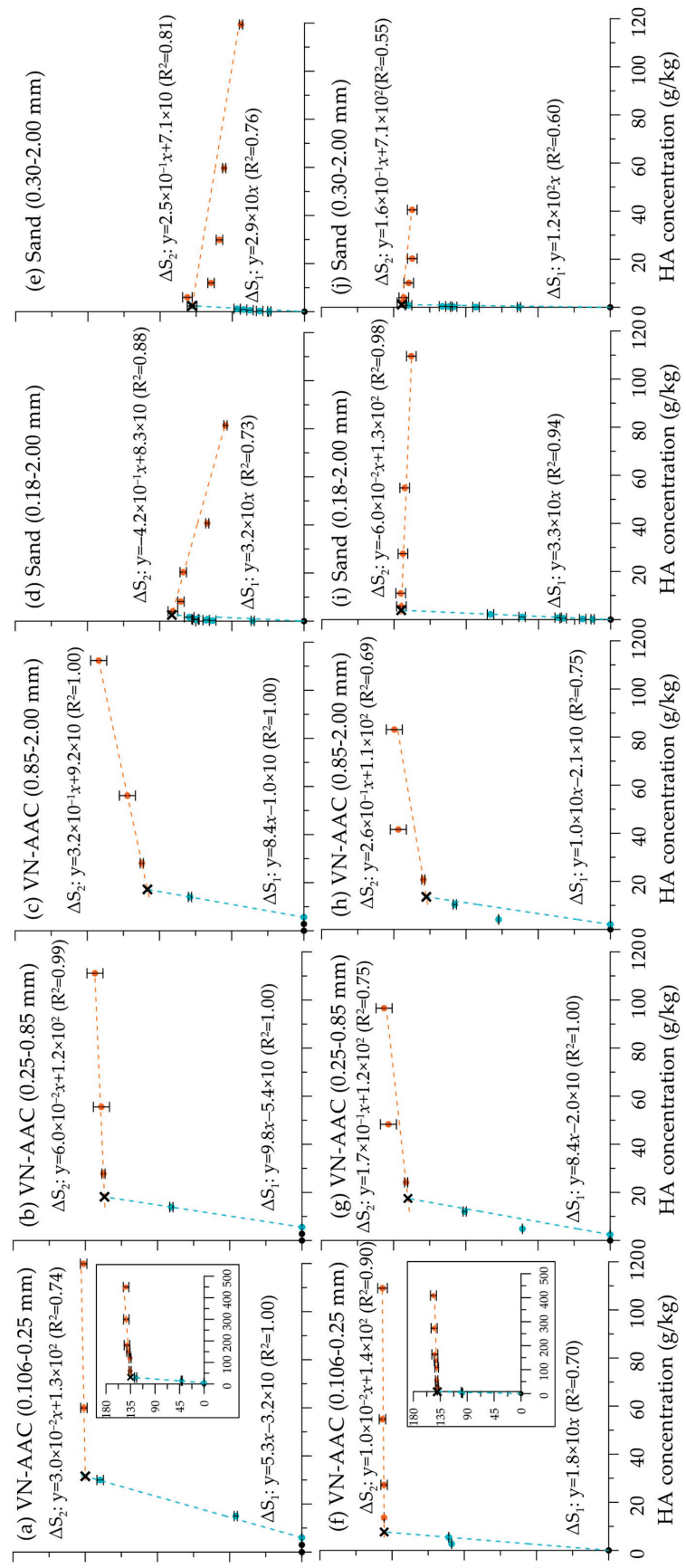


Figure 4. Relationships between CA_{wa} and HA concentrations of OA- and SA-coated VN-AAC grains and sands. OA-coated VN-AAC grains: (**a**) Grain size = 0.106–0.25 mm, (**b**) Grain size = 0.25–0.85 mm, and (**c**) Grain size = 0.85–2.00 mm. OA-coated sands: (**d**) Grain size = 0.18–2.00 mm and (**e**) Grain size = 0.30–2.00 mm. SA-coated VN-AAC grains: (**f**) Grain size = 0.106–0.25 mm, (**g**) Grain size = 0.25–0.85 mm, and (**h**) Grain size = 0.85–2.00 mm. SA-coated sands: (**i**) Grain size = 0.18–2.00 mm, and (**j**) Grain size = 0.30–2.00 mm.

Table 2. Summary of hydrophobicity/oleophilic parameters in this study and the literature.

Sample	Grain Size (mm)	Coating	CA_{wa}					CA_{ow}			Ref.
			$CA_{wa,max}$ (°)	$CA_{wa,PoI}$ (°)	$HA_{wa,PoI}$ (g/kg)	ΔS_1 (Slope)	ΔS_2 (Slope)	$CA_{ow,max}$ (°)	$CA_{ow,PoI}$ (°)	$HA_{ow,PoI}$ (g/kg)	
VN-AAC	0.106–0.25	OA	143	135	31.5	5.28	0.03	140	131	30.0	This Study
VN-AAC	0.25–0.85		129	123	18.2	9.77	0.06	130	124	13.9	
VN-AAC	0.85–2.00		128	98	17.2	8.42	0.32	124	119	28.1	
Slow sand	0.18–2.00		82	82	2.5	32.36	−0.42	138	0	20.3	
Rapid sand	0.30–2.00		73	70	2.4	28.77	−0.25	137	0	29.9	
VN-AAC	0.106–0.25	SA	146	140	7.7	18.29	0.01	138	80	54.5	
VN-AAC	0.25–0.85		141	126	17.5	8.37	0.17	130	121	12.2	
VN-AAC	0.85–2.00		135	115	13.6	9.99	0.26	124	106	20.8	
Slow sand	0.18–2.00		131	131	3.9	33.49	−0.06	138	0	27.4	
Rapid sand	0.30–2.00		130	130	1.1	115.14	−0.16	142	0	10.1	
Glass bead	0.075–0.25	OA	106	106	0.3	172.00	22.5	NA	NA	NA	Wijewardana et al., 2015 [47]
Accusand	0.105–0.25		76	76	1.0	58.00	15.1	NA	NA	NA	
Toyoura sand	0.105–0.25		97	97	0.3	388.00	0.25	NA	NA	NA	
Narita sand	0.105–0.25		94	94	1.3	86.00	0.25	NA	NA	NA	
Narita sand	0.25–0.425		93	93	1.0	93.00	0.1	NA	NA	NA	
Narita sand	0.425–0.84		79	79	1.3	89.00	0.11	NA	NA	NA	
Toyoura sand	0.105–0.25	OA	101	101	0.3	329.00	0.25	NA	NA	NA	Subedi et al., 2012 [39]
Quartz sand	0.05–0.25	SA	99	99	0.3	329.00	0.25	NA	NA	NA	González-Peñaloza et al., 2013 [64]
Quartz sand	0.25–0.5		100	100	1.0	36.00	0.06	NA	NA	NA	
Quartz sand	0.5–2.0		101	101	2.0	28.00	0.01	NA	NA	NA	

3.3. Contact Angles of Oil in Water (CA_{ow})

Measured contact angles of an oil droplet in water (CA_{ow}) of tested samples as a function of HA coating concentration are shown in Figure 5. For OA-coated VN-AAC samples (Figure 5a–c), the CA_{ow} values gradually decreased with increasing HA concentration (i.e., $CA_{ow,max}$ appeared at HA concentration = 0 g/kg). For SA-coated VN-AAC samples, on the other hand, the CA_{ow} decreased with increasing HA concentration in two steps, and a clear PoI (i.e., $HA_{ow,PoI}$) can be found. The measured values were fitted by an exponential equation in each step:

$$\text{Step 1: } y = a \exp(-bx) \quad (1)$$

$$\text{Step 2: } y = a' \exp[-b'(x - c)] \quad (2)$$

where a is the $CA_{ow,max}$ at HA concentration = 0 g/kg (°), b is the fitting parameter in Step 1, a′ is the $CA_{ow,PoI}$ at $HA_{ow,PoI}$ (°), b′ is the fitting parameter in Step 2, and c is the $HA_{ow,PoI}$ (g/kg). The measured $CA_{ow,max}$, $CA_{ow,PoI}$, and $HA_{ow,PoI}$ are also shown in Table 2.

As shown in Figure 5 and Table 2, the $CA_{ow,max}$ values of both OA- and SA-coated samples decreased with increasing grain size. The values of $CA_{ow,PoI}$ for SA-coated samples, however, were relatively constant (80–121°). The difference in the relationships between CA_{ow} and HA concentration for OA- and SA-coated VN-AAC might be attributed to characteristics of the HA coating. To understand this, the measured CA_{ow} were plotted against the measured specific surface area (SSA) and are shown in Figure 6. In the figure, the relationships between measured CA_{wa} and SSA are also shown as a reference. Compared to the relationship between CA_{wa} and SSA (Figure 6a,c,e), the relationships between CA_{ow} and SSA showed a big difference between SA- and OA-coated samples, especially in the region of Step 2 (Figure 6b,d,f). For each grain sample of VN-AAC, the SSA of SA-coated samples was higher than those of OA-coated samples. This indicates that SA coated porous grains (AAC) effectively without reducing SSA and reduced the CA_{ow} in Step 2 (oleophilicity) (Figure 5f–h) compared to OA-coated grains. In other words, the OA coating gave high CA_{ow} (oleophobicity) even when controlling the HA concentration. Considering the concept of affinity of dispersed oil and oil trap adsorbents (trapping of dispersed oil in wastewater), high oleophilic adsorbents (i.e., high hydrophobic adsorbents) are preferable for the fixed-bed grains in the oil/water separation system. Thus, an SA-coated AAC grain is likely to be more effective for oil/water separation compared to an OA-coated AAC grain.

The relationship between measured CA_{ow} as a function of HA concentration for sands, on the other hand, are shown in Figure 5d,e,j,i. The rapid linear decrease of CA_{ow} can be observed with increasing HA concentration and became $CA_{ow} = 0°$ at HA= 9.4–28.9 g/Kg (corresponding to $HA_{ow,PoI}$; see also Table 2). The rapid decrease of CA_{ow} means that coated OA and SA easily formed the grain surface oleophilicity, indicating that HA-coated sands are more suitable for oil/water separation than HA-coated AAC grains. As shown in Table 1, however, the SSA of sands are much smaller than those of AAC grains, implying that the contact area between dispersed oil in wastewater and the oleophilized grain surface area is decreased. Thus, further studies are needed to examine the efficiency of oil/water separation and trapping capacity of dispersed oil in wastewater by carrying out oil adsorption tests [65–68] and fixed-bed column experiments [69,70].

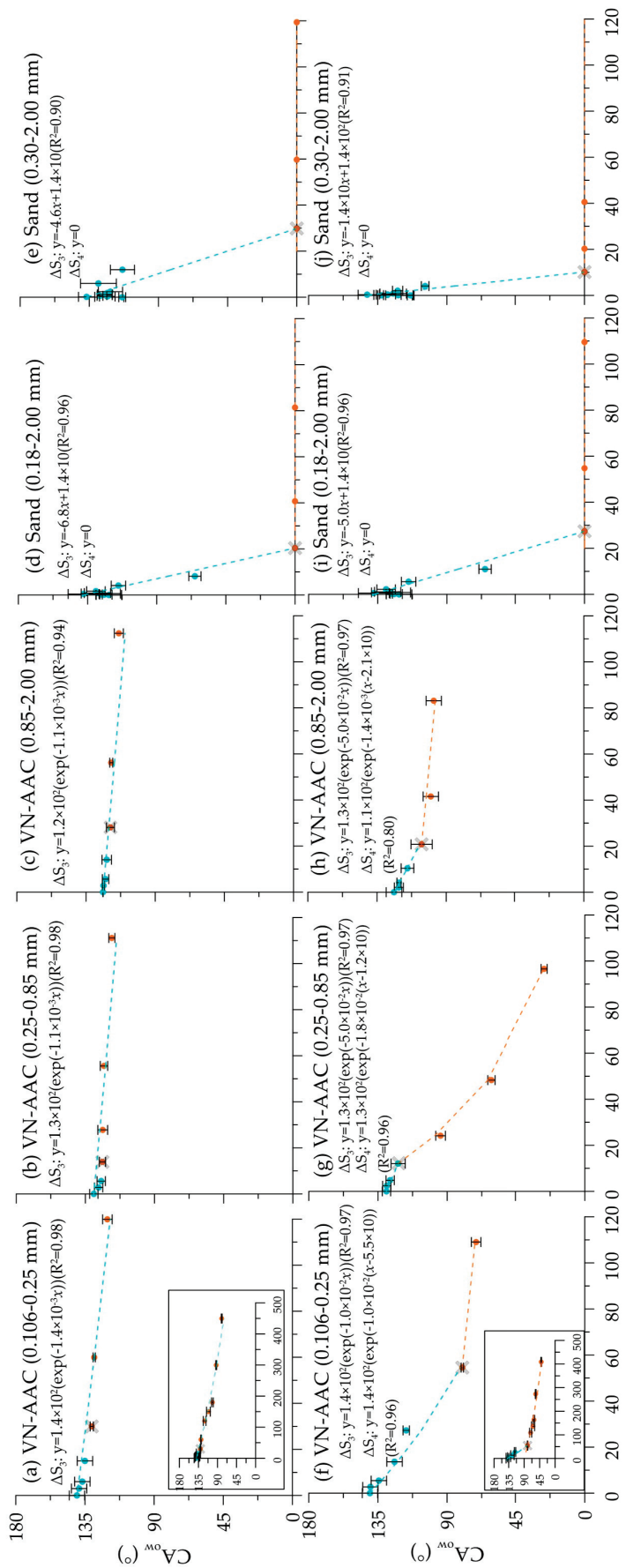


Figure 5. Relationships between CA_{ow} and HA concentration of OA- and SA-coated VN-AAC grains and sands. OA-coated VN-AAC grains: (**a**) Grain size = 0.106–0.25 mm, (**b**) Grain size = 0.25–0.85 mm, and (**c**) Grain size = 0.85–2.00 mm. OA-coated sands: (**d**) Grain size = 0.18–2.00 mm and (**e**) Grain size = 0.30–2.00 mm. SA-coated VN-AAC grains: (**f**) Grain size = 0.106–0.25 mm, (**g**) Grain size = 0.25–0.85 mm, and (**h**) Grain size = 0.85–2.00 mm. SA-coated sands: (**i**) Grain size = 0.18–2.00 mm, and (**j**) Grain size = 0.30–2.00 mm.

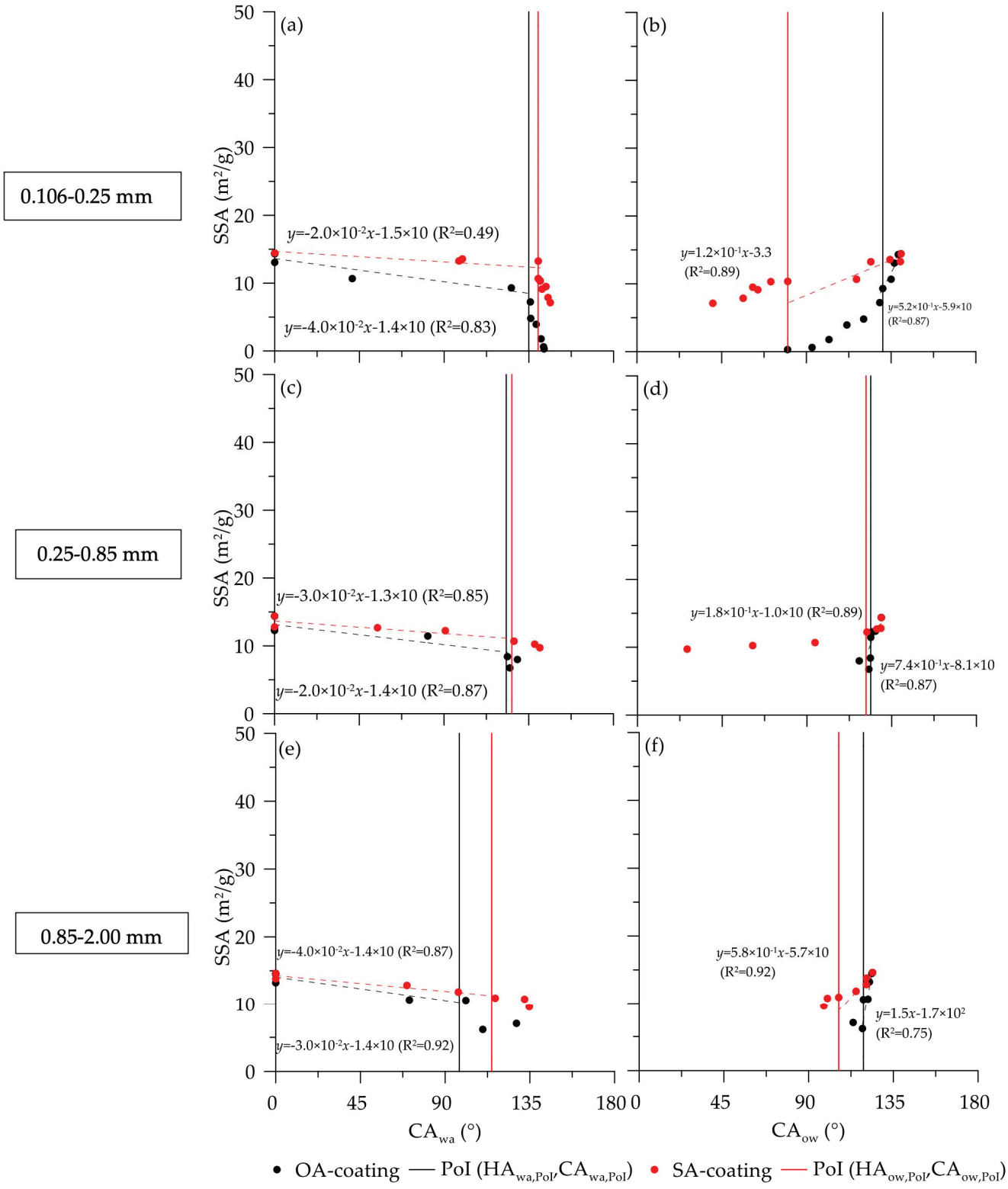


Figure 6. Relationships between SSA and CA_{wa}/CA_{ow} for OA- and SA-coated VN-AAC grains. OA-coated VN-AAC grain: (**a**,**b**) Grain size = 0.106–0.25 mm, (**c**,**d**) Grain size = 0.25–0.85 mm, and (**e**,**f**) Grain size = 0.85–2.00 mm.

3.4. Relationships between Physicochemical Properties and Measured CA_{wa} and CA_{ow}

Finally, Pearson analysis was done to examine the correlations of measured CA_{wa} and CA_{ow} with physicochemical parameters in this study. The results are shown in Table 3.

Note that data from the literature for sands [35,43,60] were also used in the analysis. The $|R^2|$ values > 0.8 are given in bold in the Table.

It can be clearly seen that the SSA correlated well with both CA_{wa} and CA_{ow} for VN-AAC grains ($|R^2| > 0.80$). The OC correlated well with CA_{wa} and CA_{ow} for OA-coated VN-AAC grains ($|R^2| = 0.72$ and 0.92); however, it gave a low correlation with CA_{wa} for SA-coated VN-AAC grains (($|R^2| = 0.50$). The A/B ratio calculated from FT-IR spectra, which are often used to characterize the hydrophobicity of soils [71–74], gave low correlations with CA_{wa} for both VN-AAC grains and sands, suggesting the A/B ratio does not characterize the hydrophobicity (i.e., contact angle of water droplet in air) for tested cementitious AAC grains and sands.

Table 3. Pearson correlation matrix of measured parameters for VN-AAC grains and sands tested in this study. Values > |0.80| are given in bold.

Sample	Coating		CA_{wa} (°)	CA_{ow} (°)	SSA (m^2/g)	OC (%)	A/B	No. of Samples
VN-AAC	OA	**CA_{wa} (°)**	1.00	−0.61	**−0.88**	0.72	0.72	25
		CA_{ow} (°)		1.00	**0.82**	**−0.92**	−0.49	
		SSA (m^2/g)			1.00	**−0.91**	−0.69	
		OC (%)				1.00	0.61	
		A/B					1.00	
	SA	**CA_{wa} (°)**	1.00	−0.66	**−0.80**	0.50	0.59	25
		CA_{ow} (°)		1.00	**0.86**	−0.75	−0.75	
		SSA (m^2/g)			1.00	**−0.81**	−0.74	
		OC (%)				1.00	0.50	
		A/B					1.00	
Sand	OA	**CA_{wa} (°)**	1.00	−0.15	−0.70	−0.01	0.59	23
		CA_{ow} (°)		1.00	0.75	−0.78	−0.61	
		SSA (m^2/g)			1.00	−0.54	**−0.82**	
		OC (%)				1.00	0.69	
		A/B					1.00	
	SA	**CA_{wa} (°)**	1.00	−0.55	**−0.91**	0.41	0.58	24
		CA_{ow} (°)		1.00	0.66	**−0.75**	−0.31	
		SSA (m^2/g)			1.00	−0.43	**−0.85**	
		OC (%)				1.00	0.29	
		A/B					1.00	

4. Conclusions

In order to develop low-cost and high-performance oil/water separating filtration media, this study assessed the hydrophobicity (oleophilicity) of porous grains made from AAC scrap coated with harmless hydrophobic agents (HA) such as oleic and stearic acids (OA and SA). For both OA- and SA-coated AAC grains, it was newly found the contact angles of water droplets in air (CA_{wa}) increased linearly with increasing HA concentration and then became almost constant and/or gently increased after a specific point (point of intersection, PoI). The HA concentration corresponding to PoI ($CA_{wa,PoI}$) can be applied to determine the minimum coating amount that gives the approximately maximum hydrophobicity of HA-coated porous grans as well as sands. The measured contact angles of an oil droplet in water (CA_{ow}) for AAC grains gave a gradual decrease exponentially with increasing HA concentration for both OA- and SA-coated AAC grains. Especially, the relationship between CA_{ow} and HA concentration for SA-coated AAC became a unique one, and the CA_{ow} decreased with increasing HA concentration in two steps. Based on Pearson correlation analysis, both CA_{wa} and CA_{ow} for HA-coated AAC grains were well correlated with the specific surface area (SSA) of tested materials, indicating that the SSA is a good indicator to quickly assessment hydrophobicity/oleophilicity (i.e., CA_{wa} and CA_{ow}) of HA-coated porous grains. Further studies are planned to quantitatively characterize oil/water separation efficiency using the HA-coated AAC grains in this study using the oil adsorption and fixed-bed column experiments.

Author Contributions: Conceptualization, A.M. and K.K.; Data curation, A.M. and K.K.; Formal analysis, A.M. and K.K.; Funding acquisition, K.K.; Investigation, A.M. and K.K.; Methodology, A.M. and K.K.; Project administration, K.K.; Resources, A.M. and K.K.; Software, A.M. and K.K.; Supervision, K.K.; Validation, K.K.; Visualization, A.M. and K.K.; Writing—original draft, A.M.; Writing—review & editing, A.M. and K.K. All authors have read and agreed to the published version of the manuscript.

Funding: This research was supported by the project of Japan Science and Technology Agency (JST), Japan International Cooperation Agency (JICA) on Science, and Technology Research Partnership for Sustainable Development (SATREPS) (no. JPMJSA1701).

Institutional Review Board Statement: Not applicable.

Informed Consent Statement: Not applicable.

Data Availability Statement: The data presented in this study are available on request from the corresponding author.

Acknowledgments: We thank the members of Hanoi University of Civil Engineering and Zafar Muhammad Junaid, a former student at Saitama University, for their support to the sample preparation in Vietnam and laboratory works.

Conflicts of Interest: The authors declare no conflict of interest.

Abbreviations

The following abbreviations are used in this manuscript:

AAC	Autoclaved aerated concrete
A/B	The ratio of hydrophobicity to hydrophilicity
BET	Brunauer Emmett Teller
CA	Contact angles
CAow	Contact angles of oil droplets in water
CAow,max	Maximum CAow of in the measured range
CAow,PoI	CAow at PoI
CAwa	Contact angles of water droplets in air
CAwa,max	Maximum CAwa of in the measured range
CAwa,PoI	CAwa at PoI
D10	Grain size at 10% passing
D50	Grain size at 50% passing (Median diameter)
D60	Grain size at 60% passing
EC	Electrical conductivity
EDS	Energy dispersive X–ray spectroscope
Gs	Specific gravity
HA	Hydrophobic agents
HAow,PoI	HA concentrations corresponding to the PoI (CAow)
HAwa,PoI	HA concentrations corresponding to the PoI (CAwa)
OA	Oleic acid
OC	Organic carbon
pH	Potential hydrogen
PoI	Point of intersection
PVDF	Polyvinylidene fluoride
SA	Stearic acid
SDM	Sessile droplet method
SEM	Scanning electron microscope
SSA	Specific surface area
Uc	The Uniformity Coefficient
VN	Vietnam
VN-AAC	AAC scrap in Vietnam
WBP	Waste brick powder

Appendix A

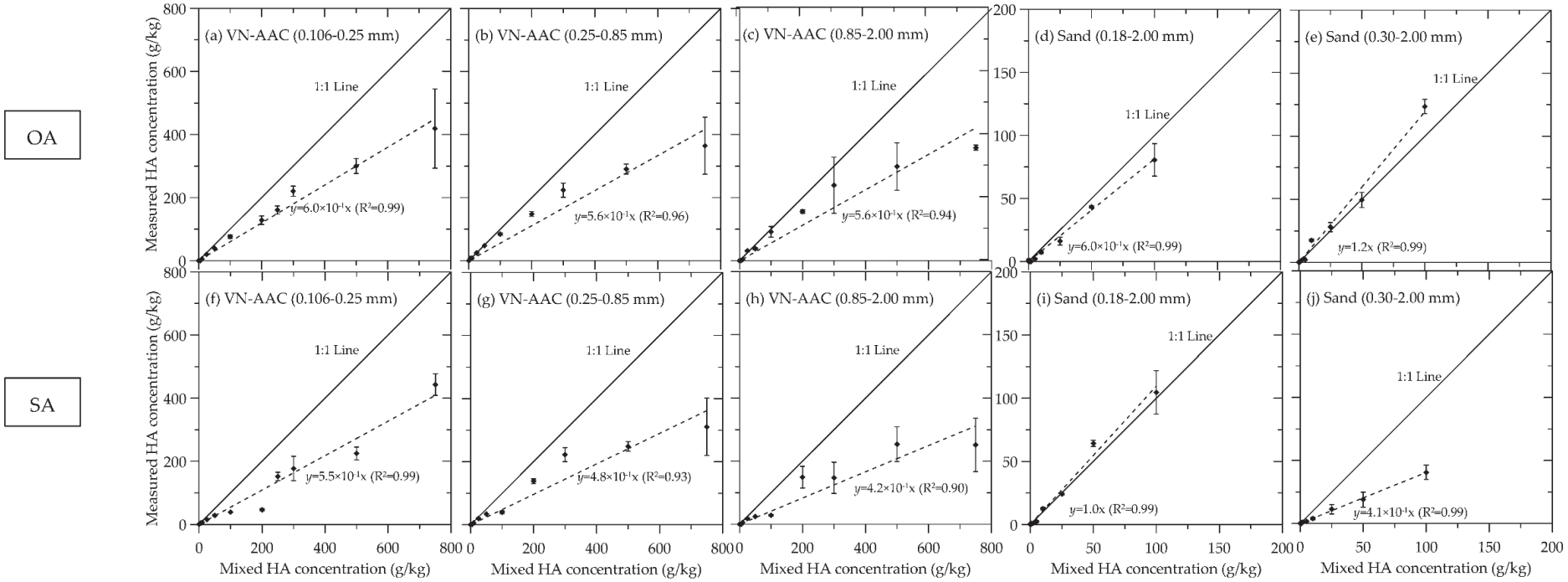


Figure A1. Relationships between measured and mixed HA concentrations for OA- and SA-coated VN AAC grains and sands. OA-coated VN-AAC grains: (**a**) Grain size = 0.106–0.25 mm, (**b**) Grain size = 0.25–0.85 mm, and (**c**) Grain size = 0.85–2.00 mm. OA-coated sands: (**d**) Grain size = 0.18–2.00 mm and (**e**) Grain size = 0.30–2.00 mm. SA-coated VN-AAC grains: (**f**) Grain size = 0.106–0.25 mm, (**g**) Grain size = 0.25–0.85 mm, and (**h**) Grain size = 0.85–2.00 mm. SA-coated sands: (**i**) Grain size = 0.18–2.00 mm and (**j**) Grain size = 0.30–2.00 mm.

References

1. Walker, A.H. Chapter 1—Oil spills and risk perceptions. In *Oil Spill Science and Technology*, 2nd ed.; Fingas, M., Ed.; Gulf Professional Publishing: Boston, MA, USA, 2017; pp. 1–70.
2. Huynh, B.Q.; Kwong, L.H.; Kiang, M.V.; Chin, E.T.; Mohareb, A.M.; Jumaan, A.O.; Basu, S.; Geldsetzer, P.; Karaki, F.M.; Rehkopf, D.H. Public health impacts of an imminent Red Sea oil spill. *Nat. Sustain.* **2021**, *4*, 1084–1091. [CrossRef] [PubMed]
3. Murawski, S.A.; Ainsworth, C.H.; Gilbert, S.; Hollander, D.J.; Paris, C.B.; Schlüter, M.; Wetzel, D.L. Introduction to the volume. In *Scenarios and Responses to Future Deep Oil Spills: Fighting the Next War*; Murawski, S.A., Ainsworth, C.H., Gilbert, S., Hollander, D.J., Paris, C.B., Schlüter, M., Wetzel, D.L., Eds.; Springer International Publishing: Cham, Switzerland, 2020; pp. 4–15.
4. Ministry of Natural Resources Environment Vietnam (MoNRE); World Bank; DANIDA. *Vietnam Environment Monitor 2003: Water*; World Bank: Washington, DC, USA, 2003.
5. Asia Pro Eco Programme. *The Risks and Consequences of Oil Pollution in Vietnam and Guidelines on Bioremediation of Oil Spills*; European Commission: Brussels, Belgium, 2006.
6. Institute for Global Environmental Strategies (IGES). Water resources management in Ho Chi Minh City. In *Sustainable Groundwater Management in Asian Cities: A Final Report of Research on Sustainable Water Management Policy*; Institute for Global Environmental Strategies: Hayama, Japan, 2006; p. 97.
7. Wang, B.; Liang, W.; Guo, Z.; Liu, W. Biomimetic super-lyophobic and super-lyophilic materials applied for oil/water separation: A new strategy beyond nature. *Chem. Soc. Rev.* **2015**, *44*, 336–361. [CrossRef] [PubMed]
8. Yong, J.; Huo, J.; Chen, F.; Yang, Q.; Hou, X. Oil/water separation based on natural materials with super-wettability: Recent advances. *Phys. Chem. Chem. Phys.* **2018**, *20*, 25140–25163. [CrossRef] [PubMed]
9. Pintor, A.M.A.; Vilar, V.J.P.; Botelho, C.M.S.; Boaventura, R.A.R. Oil and grease removal from wastewaters: Sorption treatment as an alternative to state-of-the-art technologies. A critical review. *Chem. Eng. J.* **2016**, *297*, 229–255. [CrossRef]
10. Gupta, R.K.; Dunderdale, G.J.; England, M.W.; Hozumi, A. Oil/water separation techniques: A review of recent progresses and future directions. *J. Mater. Chem. A* **2017**, *5*, 16025–16058. [CrossRef]
11. Ministry of Natural Resources Environment Vietnam (MoNRE); World Bank; DANIDA. *Vietnam Environment Monitor 2006: Water Quality in Viet Nam with a Focus on the Cau, Nhue-Day and Dong Nai River Basins*; World Bank: Washington, DC, USA, 2006.
12. Ministry of Natural Resources Environment Vietnam (MoNRE). *National State of Environment 2008: Vietnam Craft Village Environment*; Ministry of Natural Resources Environment Vietnam: Cầu Giấy, Vietnam, 2008.
13. WWF. *WWF REPORT 2018 Textile and Garment Sector in Vietnam: Water Risks and Solutions*; WWF: Gland, Switzerland, 2018.
14. Yong, J.; Chen, F.; Yang, Q.; Bian, H.; Du, G.; Shan, C.; Huo, J.; Fang, Y.; Hou, X. Oil-water separation: A gift from the desert. *Adv. Mater. Interfaces* **2016**, *3*, 1500650. [CrossRef]
15. Kong, L.H.; Chen, X.H.; Yu, L.G.; Wu, Z.S.; Zhang, P.Y. Superhydrophobic cuprous oxide nanostructures on phosphor-copper meshes and their oil-water separation and oil spill cleanup. *ACS Appl. Mater. Interfaces* **2015**, *7*, 2616–2625. [CrossRef]
16. Li, J.; Xu, C.; Guo, C.; Tian, H.; Zha, F.; Guo, L. Underoil superhydrophilic desert sand layer for efficient gravity-directed water-in-oil emulsions separation with high flux. *J. Mater. Chem. A* **2018**, *6*, 223–230. [CrossRef]
17. Ren, J.; Tao, F.; Liu, L.; Wang, X.; Cui, Y. A novel TiO_2@stearic acid/chitosan coating with reversible wettability for controllable oil/water and emulsions separation. *Carbohydr. Polym.* **2020**, *232*, 115807. [CrossRef]
18. Ezazi, M.; Shrestha, B.; Kim, S.I.; Jeong, B.; Gorney, J.; Hutchison, K.; Lee, D.H.; Kwon, G. Selective wettability membrane for continuous oil-water separation and in situ visible light-driven photocatalytic purification of water. *Glob. Chall.* **2020**, *4*, 2000009. [CrossRef]
19. Shrestha, B.; Ezazi, M.; Kwon, G. Engineered nanoparticles with decoupled photocatalysis and wettability for membrane-based desalination and separation of oil-saline water mixtures. *Nanomaterials* **2021**, *11*, 1397. [CrossRef] [PubMed]
20. Shrestha, B.; Ezazi, M.; Kwon, G. Delamination-free in-air and underwater oil-repellent filters for oil-water separation: Gravity-driven and cross-flow operations. *Energies* **2021**, *14*, 7429. [CrossRef]
21. Liu, P.; Niu, L.; Tao, X.; Li, X.; Zhang, Z.; Yu, L. Preparation of superhydrophobic-oleophilic quartz sand filter and its application in oil-water separation. *Appl. Surf. Sci.* **2018**, *447*, 656–663. [CrossRef]
22. Zhang, Y.; Zhang, Y.; Cao, Q.; Wang, C.; Yang, C.; Li, Y.; Zhou, J. Novel porous oil-water separation material with super-hydrophobicity and super-oleophilicity prepared from beeswax, lignin, and cotton. *Sci. Total Environ.* **2020**, *706*, 135807. [CrossRef]
23. Liu, J.; Zhu, X.; Zhang, H.; Wu, F.; Wei, B.; Chang, Q. Superhydrophobic coating on quartz sand filter media for oily wastewater filtration. *Colloids Surf. A Physicochem. Eng. Asp.* **2018**, *553*, 509–514. [CrossRef]
24. Shamaei, L.; Khorshidi, B.; Islam, M.A.; Sadrzadeh, M. Industrial waste lignin as an antifouling coating for the treatment of oily wastewater: Creating wealth from waste. *J. Clean. Prod.* **2020**, *256*, 120304. [CrossRef]
25. Shi, G.; Shen, Y.; Mu, P.; Wang, Q.; Yang, Y.; Ma, S.; Li, J. Effective separation of surfactant-stabilized crude oil-in-water emulsions by using waste brick powder-coated membranes under corrosive conditions. *Green Chem.* **2020**, *22*, 1345–1352. [CrossRef]
26. Li, Z.; Zhang, T.; Wang, Y.; Yue, X.; Yang, D.; Qiu, F. Waste-to-resource strategy to fabricate functionalized material from waste brick. *Sci. Total Environ.* **2020**, *703*, 135032. [CrossRef]
27. Li, Z.; Zhang, T.; Wang, M.; Qiu, F.; Yue, X.; Yang, D. Hierarchical structurized waste brick with opposite wettability for on-demand oil/water separation. *Chemosphere* **2020**, *251*, 126348. [CrossRef]

28. Zhao, B.; Ren, L.; Du, Y.; Wang, J. Eco-friendly separation layers based on waste peanut shell for gravity-driven water-in-oil emulsion separation. *J. Clean. Prod.* **2020**, *255*, 120184. [CrossRef]
29. Matsuno, A.; Junaid, Z.M.; Saito, T.; Dang, H.T.T.; Huyen, P.T.; Nga, T.T.V.; Kawamoto, K. Oil/water separation techniques using hydrophobized/oleophilized grains: A review of recent studies. *Int. J. GEOMATE* **2021**, *20*, 28–34. [CrossRef]
30. Decision No. 567/QD-TTg of Apirl 28, 2010, Approving the Program on Development of Non-Baked Building Materials through 2020. Available online: https://vanbanphapluat.co/decision-no-567-qd-ttg-approving-the-program-on-development-of-non-baked (accessed on 12 July 2022).
31. Alexanderson, J. Relations between structure and mechanical properties of autoclaved aerated concrete. *Cem. Concr. Res.* **1979**, *9*, 507–514. [CrossRef]
32. Tada, S. Microstructural approach to properties of moist cellular concrete. In *Autoclaved Aerated Concrete-Moisture and Properties*; Elsevier Science Ltd.: Amsterdam, The Netherlands, 1983.
33. Wittmann, F.H. *Autoclaved Aerated Concrete Moisture and Properties*; Elsevier Scientific Publishing, Co.: New York, NY, USA, 1983.
34. Aroni, S. *Autoclaved Aerated Concrete—Properties, Testing and Design*; CRC Press: Boca Raton, FL, USA, 2014.
35. Nguyen Trong, L.; Asamoto, S.; Matsui, K. Sorption isotherm and length change behavior of autoclaved aerated concrete. *Cem. Concr. Compos.* **2018**, *94*, 136–144. [CrossRef]
36. UNDP. *The Role of Systemic Investing in Viet Nam's Transition to a Circular Economy: A Case Study on Achieving Transformative Change in the Waste Management and Recycling System*; UNDP: New York, NY, USA, 2021.
37. Decision No. 889/QD-TTg on the National Action Program on Sustainable Production and Consumption in the 2021–2030 Period. Available online: https://vietnamcircularеconomy.vn/en/policy-library/decision-no-889-qd-ttg-on-the-national-action-program-on-sustainable-production-and-consumption-in-the-2021-2030-period-2/ (accessed on 12 July 2022).
38. Kumara, G.M.P.; Kawamoto, K. Steel slag and autoclaved aerated concrete grains as low-cost adsorbents to remove Cd^{2+} and Pb^{2+} in wastewater: Effects of mixing proportions of grains and liquid-to-solid ratio. *Sustainability* **2021**, *13*, 10321. [CrossRef]
39. Subedi, S.; Kawamoto, K.; Jayarathna, L.; Vithanage, M.; Moldrup, P.; de Jonge, L.W.; Komatsu, T. Characterizing time-dependent contact angles for sands hydrophobized with oleic and stearic acids. *Vadose Zone J.* **2012**, 11. [CrossRef]
40. Thai, H.N.; Kawamoto, K.; Nguyen, H.G.; Sakaki, T.; Komatsu, T.; Moldrup, P. Measurements and modeling of thermal conductivity of recycled aggregates from concrete, clay brick, and their mixtures with autoclaved aerated concrete grains. *Sustainability* **2022**, *14*, 2417. [CrossRef]
41. Van Boggelen, W.; van Boggelen, J. Sustainable building solutions with new generation autoclaved aerated concrete panel applications. *CE/Papers* **2018**, *2*, 513–525. [CrossRef]
42. Matsuno, A.; Ishizuka, S.; Nguyen, T.L.; Nguyen, T.D.; Nguyen, V.T.; Nguyen, H.G.; Kawamoto, K. Comparison of macropore structure and network of autoclaved aerated concrete blocks using micro-focus X-ray computed tomography. *Int. J. GEOMATE* **2020**, *19*, 160–165. [CrossRef]
43. Kikuma, J.; Tsunashima, M.; Ishikawa, T.; Matsuno, S.-Y.; Ogawa, A.; Matsui, K.; Sato, M. In situ time-resolved X-ray diffraction of tobermorite formation process under autoclave condition. *J. Am. Ceram. Soc.* **2010**, *93*, 2667–2674. [CrossRef]
44. Japanese Standards Association (JSA). *JIS Z 8801-1: 2019 Test Sieves—Part 1: Test Sieves of Metal Wire Cloth*; Japanese Standards Association (JSA): Tokyo, Japan, 2019.
45. Japan Water Works Association (JWWA). *JWWA A 103-1:2006-2 Filter Sand for Water Supply*; Japan Water Works Association (JWWA): Tokyo, Japan, 2006; 18p.
46. The Chemical Daily. *15710 Chemical Products*; The Chemical Daily Co., Ltd.: Tokyo, Japan, 2010.
47. Wijewardana, N.S.; Kawamoto, K.; Moldrup, P.; Komatsu, T.; Kurukulasuriya, L.C.; Priyankara, N.H. Characterization of water repellency for hydrophobized grains with different geometries and sizes. *Environ. Earth Sci.* **2015**, *74*, 5525–5539. [CrossRef]
48. Leelamanie, D.A.L.; Karube, J.; Yoshida, A. Characterizing water repellency indices: Contact angle and water drop penetration time of hydrophobized sand. *Soil Sci. Plant Nutr.* **2008**, *54*, 179–187. [CrossRef]
49. Karatza, Z.; Buckman, J.; Medero, G.M.; Beckett, C.T.S. Evolution of meniscus structures in hydrophobic granular systems. *J. Hydrol.* **2021**, *603*, 126954. [CrossRef]
50. Zafar, M.J. Assessment of hydrophobicity/oleophilicity for artificially coated autoclave aerated concrete grains and its applicability to treat oily wastewater. Master's Thesis, Saitama University, Saitama, Japan, 2021.
51. Bardet, J.P.; Jesmani, M.; Jabbari, N. Permeability and compressibility of wax-coated sands. *Géotechnique* **2014**, *64*, 341–350. [CrossRef]
52. Zhang, S.; Lu, F.; Tao, L.; Liu, N.; Gao, C.; Feng, L.; Wei, Y. Bio-inspired anti-oil-fouling chitosan-coated mesh for oil/water separation suitable for broad pH range and hyper-saline environments. *ACS Appl. Mater. Interfaces* **2013**, *5*, 11971–11976. [CrossRef]
53. Lu, F.; Chen, Y.; Liu, N.; Cao, Y.; Xu, L.; Wei, Y.; Feng, L. A fast and convenient cellulose hydrogel-coated colander for high-efficiency oil–water separation. *RSC Adv.* **2014**, *4*, 32544–32548. [CrossRef]
54. Fan, J.; Duan, J.; Yu, Z.; Wu, D.; Zhu, H. Oleophobicity of chitosan/micron-alumina-coated stainless steel mesh for oil/water separation. *Water Air Soil Pollut.* **2016**, *227*, 163. [CrossRef]
55. Miyazaki, T.; Nishimura, T. *Soil Physics Experimental Methods*; University of Tokyo Press: Tokyo, Japan, 2011; p. 224.
56. Japanese Geotechnical Society (JGS). *Geotechnical Test: Basics and Guidance*, 2nd ed.; Japanese Geotechnical Society (JGS): Tokyo, Japan, 2011; p. 270.

57. Capriel, P.; Beck, T.; Borchert, H.; Gronholz, J.; Zachmann, G. Hydrophobicity of the organic matter in arable soils. *Soil Biol. Biochem.* **1995**, *27*, 1453–1458. [CrossRef]
58. Celi, L.; Schnitzer, M.I.; NÈgre, M. Analysis of carboxyl groups in soil humic acids by a wet chemical method, Fourier-transform infrared spectrophotometry, and solution-state carbon-13 nuclear magnetic resonance. A comparative study. *Soil Sci.* **1997**, *162*, 189–197. [CrossRef]
59. Tasumi, M. *The Spectroscopical Society of Japan. Infrared Spectroscopy Measurement Method: Basics and Latest Methods*; S.T. Japan: Köln, Germany, 2012; p. 201.
60. Ellerbrock, R.H.; Gerke, H.H.; Bachmann, J.; Goebel, M.-O. Composition of organic matter fractions for explaining wettability of three forest soils. *Soil Sci. Soc. Am. J.* **2005**, *69*, 57–66. [CrossRef]
61. Brunauer, S.; Emmett, P.H.; Teller, E. Adsorption of gases in multimolecular layers. *J. Am. Chem. Soc.* **1938**, *60*, 309–319. [CrossRef]
62. Barrett, E.P.; Joyner, L.G.; Halenda, P.P. The determination of pore volume and area distributions in porous substances. I. Computations from nitrogen isotherms. *J. Am. Chem. Soc.* **1951**, *73*, 373–380. [CrossRef]
63. Lambe, T.W.; Whitman, R.V. *Soil Mechanics*; Wiley: Hoboken, NJ, USA, 1991.
64. González-Peñaloza, F.A.; Zavala, L.M.; Jordán, A.; Bellinfante, N.; Bárcenas-Moreno, G.; Mataix-Solera, J.; Granged, A.J.P.; Granja-Martins, F.M.; Neto-Paixão, H.M. Water repellency as conditioned by particle size and drying in hydrophobized sand. *Geoderma* **2013**, *209–210*, 31–40. [CrossRef]
65. Akhavan, B.; Jarvis, K.; Majewski, P. Hydrophobic plasma polymer coated silica particles for petroleum hydrocarbon removal. *ACS Appl. Mater. Interfaces* **2013**, *5*, 8563–8571. [CrossRef] [PubMed]
66. Qu, M.; Yuan, M.; He, J.; Xue, M.; Ma, X.; Hou, L.; Zhang, T.; Liu, X.; He, J. Substrate-versatile approach to multifunctional superamphiphobic coatings with mechanical durable property from quartz sand. *Surf. Coat. Technol.* **2018**, *352*, 191–200. [CrossRef]
67. Bigui, W.; Cheng, Y.; Jianlin, L.; Gang, W.; Liang, D.; Xiaosan, S.; Fuping, W.; Hua, L.; Qing, C. Fabrication of superhydrophilic and underwater superoleophobic quartz sand filter for oil/water separation. *Sep. Purif. Technol.* **2019**, *229*, 115808. [CrossRef]
68. Atta, A.M.; Abdullah, M.M.S.; Al-Lohedan, H.A.; Mohamed, N.H. Novel superhydrophobic sand and polyurethane sponge coated with silica/modified asphaltene nanoparticles for rapid oil spill cleanup. *Nanomaterials* **2019**, *9*, 187. [CrossRef]
69. Bigui, W.; Jianlin, L.; Gang, W.; Qing, C. Filtration of oil from oily wastewater via hydrophobic modified quartz sand filter medium. *J. Water Reuse Desalin.* **2018**, *8*, 544–552. [CrossRef]
70. Mitra, D.; Tai, M.H.; Abdullah, E.B.; Wang, C.-H.; Neoh, K.G. Facile fabrication of porous waste-derived carbon-polyethylene terephthalate composite sorbent for separation of free and emulsified oil from water. *Sep. Purif. Technol.* **2021**, *279*, 119664. [CrossRef]
71. Tarchitzky, J.; Lerner, O.; Shani, U.; Arye, G.; Lowengart-Aycicegi, A.; Brener, A.; Chen, Y. Water distribution pattern in treated wastewater irrigated soils: Hydrophobicity effect. *Eur. J. Soil Sci.* **2007**, *58*, 573–588. [CrossRef]
72. Bachmann, J.; Guggenberger, G.; Baumgartl, T.; Ellerbrock, R.H.; Urbanek, E.; Goebel, M.O.; Kaiser, K.; Horn, R.; Fischer, W.R. Physical carbon-sequestration mechanisms under special consideration of soil wettability. *J. Plant Nutr. Soil Sci.* **2008**, *171*, 14–26. [CrossRef]
73. Voelkner, A.; Holthusen, D.; Ellerbrock, R.H.; Horn, R. Quantity of hydrophobic functional CH-groups—Decisive for soil water repellency caused by digestate amendment. *Int. Agrophys.* **2015**, *29*, 247–255. [CrossRef]
74. Parolo, M.E.; Savini, M.C.; Loewy, R.M. Characterization of soil organic matter by FT-IR spectroscopy and its relationship with chlorpyrifos sorption. *J. Environ. Manag.* **2017**, *196*, 316–322. [CrossRef] [PubMed]

environments

Article

Acoustic Stimulation of Anaerobic Digestion: Effects on Biogas Production and Wastewater Malodors

John Loughrin *, Philip Silva , Nanh Lovanh and Karamat Sistani

Food Animal Environmental Systems Research Unit, Agricultural Research Service, United States Department of Agriculture, 2413 Nashville Road, Suite B5, Bowling Green, KY 42101, USA
* Correspondence: john.loughrin@usda.gov; Tel.: +1-270-781-2260

Abstract: Wastewater created from various solid wastes and agricultural residues was treated by anaerobic digestion, and the biogas and wastewater odors were quantified. One digester was exposed to low-frequency sound (<5 kHz) from underwater loudspeakers, while the other received no sonic treatment. It was hypothesized that low-frequency sound, by accelerating the breakdown of sludge via mechanisms such as cavitation induction and mechanical vibration, and enhancing biogas production, could also affect the concentrations of wastewater odors. During warm seasons, biogas production from the sound-treated digester was 29% higher than that from the control digester, and 184% higher during the cool season. Malodors—Mainly consisting of typical aromatic malodorants such as *p*-cresol and skatole, aliphatic secondary ketones, and dimethyl disulfide—were quantified. In contrast to the findings for biogas production, little difference was found in the concentrations of volatile compounds in the control and sound-treated digestates. Concentrations of dimethyl polysulfides increased over time in both the control and sound-treated digestates, likely due to the use of recycled system effluent that contained precipitated elemental sulfur. The digestate contained considerable concentrations of volatile fatty acids and ammonium, but due to the near neutral pH of the digestate it was surmised that neither made appreciable contributions to the wastewater's malodor. However, the volatile fatty acid concentrations were reduced by sonic treatment, which was not unexpected, since volatile fatty acids are precursors to methane. Therefore, although sonic treatment of the anaerobic digestate boosted biogas production, it did not markedly affect the wastewater malodors. The biosynthetic origins of wastewater malodors are discussed in this paper.

Keywords: anaerobic digestion; biogas; carbon dioxide; greenhouse gas; malodor; methane; sulfide; sonication; ultrasonication

Citation: Loughrin, J.; Silva, P.; Lovanh, N.; Sistani, K. Acoustic Stimulation of Anaerobic Digestion: Effects on Biogas Production and Wastewater Malodors. *Environments* **2022**, *9*, 102. https://doi.org/10.3390/environments9080102

Academic Editor: Manuel Soto

Received: 8 July 2022
Accepted: 10 August 2022
Published: 15 August 2022

Publisher's Note: MDPI stays neutral with regard to jurisdictional claims in published maps and institutional affiliations.

Copyright: © 2022 by the authors. Licensee MDPI, Basel, Switzerland. This article is an open access article distributed under the terms and conditions of the Creative Commons Attribution (CC BY) license (https://creativecommons.org/licenses/by/4.0/).

1. Introduction

Anaerobic digestion of wastewater and sludge is often touted for its potential for energy production and its ability to reduce greenhouse gas emissions [1]. In addition, by reducing the quantity of organic matter in waste, pollution of ground and surface waters is reduced, and nutrients such as nitrogen and phosphorus are more easily recovered to further aid in reducing eutrophication. By operating digesters at thermophilic (>50 °C) temperatures, reductions in pathogens may also be accomplished [2].

Furthermore, anaerobic digestion may be an effective means of reducing waste malodors. However, to achieve significant reductions in malodors, it is often necessary to operate digesters at elevated temperatures. For instance, Orzi et al. [3] studied 10 full-scale digesters, which achieved a 98.8% overall reduction in digestate malodor, as determined by panelists in an olfactometer analysis. Variation in hydraulic retention times (HRTs) from 20 to 70 d did not have a pronounced influence on malodor reduction, but all of the digesters were operated at 39 °C or above. Welsh et al. [4] found that anaerobic digestion at 35 °C was more effective than 25 °C in reducing the offensiveness of swine manure. Wilson et al. showed that even in thermophilic digestion (>50 °C), slight increases in temperature

reduced the concentrations of volatile sulfur compounds such as methanethiol, dimethyl sulfide, dimethyl disulfide, and dimethyl trisulfide [5]. Consequently, elevated temperature seems to be more effective in reducing wastewater malodors than long HRT. The city of Los Angeles, CA, found that operating digesters at thermophilic ranges reduced biosolids' odor content by 70% as compared to biosolids produced at mesophilic temperatures, but it was unclear whether some of the improvement was due to volatilization of the malodors, since the city of Tacoma, WA, found that potentially dangerous gas-phase concentrations of H_2S could be reduced at wastewater treatment plants by lowering the digester temperatures from 46 to 38 °C [6].

Recently, we demonstrated that the treatment of anaerobic digesters with sound at sonic frequencies (<20 kHz) could be used to accelerate biogas production and sludge degradation [7,8]. Sound was provided to 9.1 m^3 of anaerobic digestate by means of waterproofed loudspeakers on a continuous 2 h on/1 h off cycle. In a first trial, the biogas production was more than double that of a control digester, while in a second trial the biogas production was increased by 27% over that of the control during warm weather, and by 74 times that of the control in cold weather. Given that the sonic treatment seemed to some extent to substitute for wastewater heating in accelerating biogas production, this study examines whether sonic treatment of anaerobic digestate can also have a positive effect on wastewater malodors. Digestate samples collected from the primary anaerobic digesters in the previous studies were analyzed for volatile organic compounds (VOCs). Samples were collected during periods of warm weather—from May 2018 to October 2018, from June to July 2020, and from October 2019 to March 2020.

2. Materials and Methods

2.1. Digester Description

The feeding schedule of the digesters has been described previously [7,8]. In 2018, the digesters were mostly fed cracked corn, with occasional supplementation with defatted soybean meal, after initial seeding of the digesters with swine waste, chicken litter, and digestate from a commercial anaerobic digester operated at a range of 46–50 °C. Meanwhile, in 2019–2020, the digesters were fed a varying mixture of cracked corn, waste activated sludge from the Bowling Green KY municipal wastewater treatment facility, corn stover, and wastepaper/cardboard. The digesters were fed either once or twice weekly using a volume of 800–900 L. The digesters therefore had an HRT of approximately 12 weeks when fed once weekly, and about 6 weeks when fed twice weekly. The wastewater outlet from the digesters was approximately one meter above the bottom and, therefore, given the settling of solids, was designed to uncouple the sludge retention time from the wastewater retention time.

Figure 1 shows the amounts of volatile solids (VS) fed per month, along with the monthly average daily temperature and monthly average solar insolation. The digesters were fed once or twice weekly with the feed mixed with 800 L of recycled effluent from the system. The digesters were not fed from November 2018 through April 2019. Data for temperature and insolation were obtained from the Warren County Kentucky Mesonet site located on the Western Kentucky University Farm (kymesonet.org, accessed on 11 August 2022).

In 2018, the digestate was exposed to sound from waterproofed Skar Audio FSX8 8-inch (20.3 cm) 4 Ω speakers rated at 175 W RMS (root-mean-square) power (Skar Audio, Tampa, FL, USA), powered by Pyle Audio PTAU 55 stereo amplifiers rated at 120 W RMS per channel (Pyle Audio, Brooklyn, NY, USA). In 2019–2020, the speakers were replaced with Skar Audio FSX10-4 10-inch (25.4 cm) 4 W speakers rated at 200 W RMS. Details of the sound files and recording equipment used were published previously [4,5]. The stereo was operated on a 2 h on/1 h off continuous cycle.

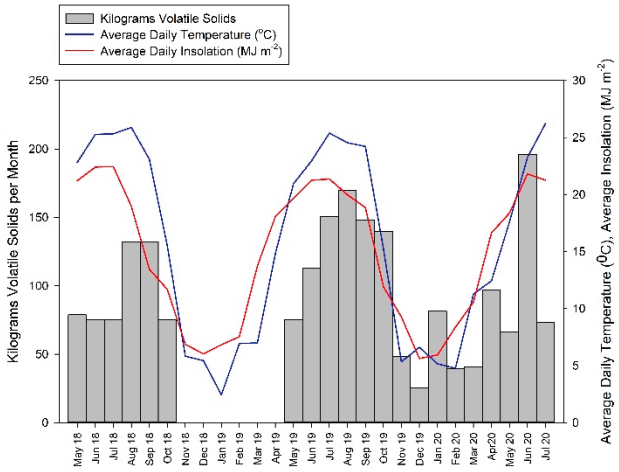


Figure 1. Amounts of volatile solids fed per month to each of the digesters, with average daily temperature and average daily insolation received for each month of the study.

2.2. Volatile Compound Extraction and Quantification

Table 1 lists the volatile compounds identified and quantified in the anaerobic digestate of the control and sound-treated digesters, along with selected physical properties. A number of other compounds—such as dimethyl trisulfide, dimethyl tetrasulfide, and dimethyl pentasulfide—were not quantified, due to a lack of authentic standards for quantification. In addition, other compounds that are important components of wastewater malodor—such as hydrogen sulfide, methyl mercaptan, and dimethyl sulfide—were not detected, due to their being too volatile for analysis by stir-bar sorptive extraction (SBSE) (with boiling points of −60.2, 5.95, and 27 °C, respectively) and/or too polar (with log octanol partition coefficients of 0.78 and 0.977 for methyl mercaptan and dimethyl sulfide, respectively).

Table 1. Selected physical properties of compounds quantified in this study (listed in elution order on a DB-5 gas chromatography column [1]).

Compound	Molecular Weight (g mol^{-1})	Boiling Point (°C)	Log P
Dimethyl disulfide	94.19	109.8	1.77
Toluene	92.14	110.6	2.73
2-Hexanone	100.16	127.6	1.38
2-Heptanone	114.18	151.0	1.98
Benzaldehyde	106.12	178.1	1.64
Oct-1-en-3-ol	128.21	175.0	2.60
Phenol	94.11	181.8	1.46
Para-Cresol	108.14	201.9	1.94
2-Nonanone	142.24	195.3	3.14
Benzyl acetate	150.18	213.0	1.96
Para-Ethylphenol	122.17	217.9	2.58
Indole	117.15	254.0	2.14
Skatole	131.18	266.0	2.60
2-Tridecanone	198.35	263.0	4.68

[1] Data obtained from The National Institutes of Health, chemidplus Advanced [9].

Digestate samples were taken from the digesters approximately 1 m above the bottom of the tank by means of a three-way valve, and stored at −20 °C until analyzed. Volatile compounds in the digestate were quantified by extraction via stir-bar sorptive extraction (SBSE) using Twister stir bars (10 mm by 0.32 mm) with a 1 mm thick polydimethylsiloxane (PDMS) coating (Gerstel, Baltimore, MD, USA), which had been preconditioned at 250 °C for 40 min under a stream of high = purity He. The stir bars were placed in sealed vessels containing 100 mL of digestate and extracted for 2 h while stirring at 150 rpm. After

extraction, the stir bars were removed, rinsed with deionized water, and blotted dry. They were then placed in 8.9 cm long by 6.35 mm o.d. thermal desorption tubes (Markes International, Sacramento, CA, USA) and desorbed as described below.

Gas chromatography-mass spectrometry (GC-MS) of semi-volatile odor compounds was performed using a Shimadzu Nexis GC-2030/QP2020 NX single-quadrupole mass spectrometer interfaced with a TD-30 thermal desorption system (Shimadzu Scientific Corp., Columbia, MD, USA). The stir bars were placed in the glass desorption tubes and desorbed at 280 °C for 5 min with a He flow rate of 30 mL min^{-1}. The cryogenic trap was maintained at −20 °C, with a transfer line temperature of 250 °C. The GC was equipped with a 30 m by 0.25 mm Rxi-5 ms (95% PDMS, 5% diphenyl polysiloxane) column with a film thickness of 0.25 μm (Restek Corp., Bellefonte, PA, USA). The GC operating conditions were an initial oven temperature of 50 °C for 1 min, then increased at 1.5 °C min^{-1} to 105 °C, and thereafter increased at 15 °C min^{-1} to 210 °C, with a final hold time of 2 min, and using a linear He flow velocity of 47.2 cm s^{-1}. The mass spectrometer used a scanning range of 35–500 m/z and a scan speed of 1666 amu s^{-1}. Identification and external calibration of compounds was based on comparison of spectra and retention times with those of authentic standards (Sigma-Aldrich Inc., St. Louis, MO, USA).

Biogas production was measured using diaphragm/bellows positive displacement meters (EKM Metering, Santa Cruz, CA, USA), and biogas quality was measured by gas chromatography (GC), as previously described [7,8]. Gas volumes were reported at ambient conditions of temperature and pressure, and CO_2 and CH_4 concentrations were quantified from samples taken by withdrawing 25 mL samples from an outlet upstream of the gas meter by means of a three-way valve and injecting the sample into a 20 mL vial equipped with a rubber septum.

Methane and CO_2 were analyzed on a Varian Model CP-3800 (Agilent Technologies, Santa Clara, CA, USA) GC modified for greenhouse gas (GHG) analysis. The GC was equipped with a model 1041 on-column injector operated at 75 °C and 263 kPa, which was connected to a 10-port gas-sampling valve and pressure-actuated solenoid valve. Half a milliliter of the vial headspace was injected using a syringe temperature of 35 °C and needle residence time of 30 s, with 250 μL of the sample transferred onto a 1.8 m by 1.6 cm o.d. column packed with 80/100 mesh Hay Sep Q (Agilent Technologies), with a He flow rate of 55 mL min^{-1}. The column was connected to a thermal conductivity detector (TCD) operated at 120 °C, and with a filament temperature of 200 °C, for CO_2 analysis. From the TCD, the sample went to a flame ionization detector operated under the following conditions: N_2 makeup gas 15 mL min^{-1}, H_2 30 mL min^{-1}, air 300 mL min^{-1}, and a detector temperature of 275 °C. The GC column oven was operated at an initial temperature of 50 °C for 4 min, and then increased at 50 °C min^{-1} to 100 °C and held at this temperature for 1 min. Four point calibrations were performed for CO_2 and CH_4.

3. Results

3.1. Biogas Production

During the first trial of the digesters in the warmer months of 2018, the digestate temperature in the control digester and sound-treated digester averaged 27.9 ± 5.3 and 26.9 ± 4.7 °C, respectively. In the second trial, from late spring 2019 to summer 2020, the average digestate temperature of the control and sound-treated digesters was 20.2 ± 9.4 and 20.4 ± 8.6 °C, respectively, with maximum temperatures of 33.6 and 31.8 °C, respectively, and minimum temperatures of 3.5 and 3.9 °C, respectively. Since the temperature range for mesophilic digestion may be considered to range from 35 to 40 °C [10], the digesters were operated at quite low temperatures.

In the year 2018, gas production was measured from mid-April to early October (Figure 2). Average weekly gas production over this period was 87% higher from the sound-treated digester (11.9 m^3 wk^{-1}) than the control digester (6.4 m^3 wk^{-1}), and the concentrations of CO_2 and CH_4 averaged 10,700 and 36,800 mmol m^{-3}, respectively, for the control digester, and 11,100 and 38,200 mmol m^{-3}, respectively, for the sound-treated

digester, from early July to mid-October [7]. Although the gas pressures in the control and sound-treated digesters were not continually monitored, the fact that the sound-treated digester produced more gas than the control digester necessarily means that the back pressure in the sound-treated digester was higher, and resulted in faster filling and emptying of the gas meter bellows. Spot checks on the digesters indicated back pressures of approximately 9–12 mm Hg (1.2–1.6 kPa). Higher back pressure on the sound-treated digester would account for higher CO_2 and CH_4 gas concentrations in the sound-treated digester as compared to the control digester. The higher gas production rate was likely a consequence of higher microbial activity in that tank due to sonic disruption of the sludge facilitating microbial colonization, as discussed below.

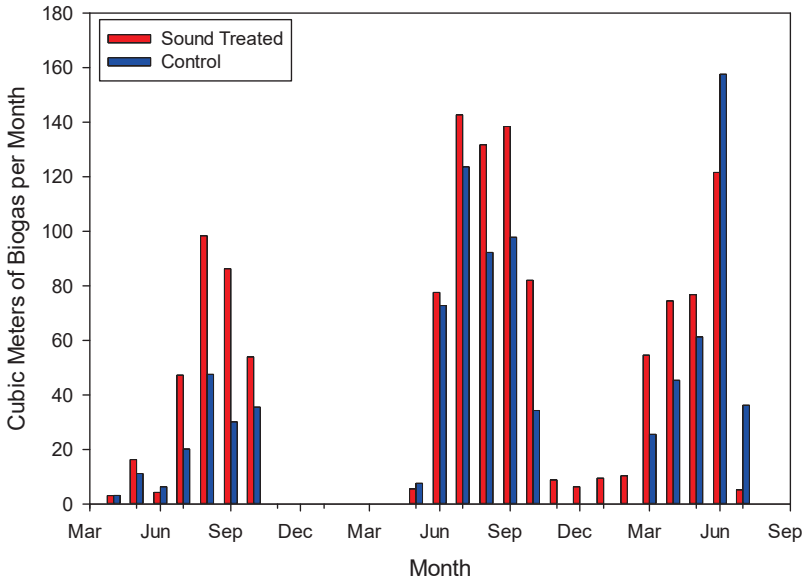


Figure 2. Average monthly gas production from the sound-treated and control anaerobic digesters.

In the second trial, lasting from late May 2019 to mid-July 2020, the average weekly gas production was 12.9 m^3 wk^{-1} and 15.7 m^3 wk^{-1} for the control and sound-treated digesters, respectively [8]. The carbon dioxide concentrations averaged 10,300 mmol m^{-3} and 10,900 mmol m^{-3} for the control and sound-treated digesters, respectively, whereas the CH_4 concentrations averaged 27,400 mmol m^{-3} and 38,900 mmol m^{-3} for the control and sound-treated digester, respectively. The CH_4 concentration percentage averaged 77.5% in 2018 and 72.7% in 2019–2020. The slightly lower average gas quality in the later evaluation period was likely due to its encompassing both warm and cool seasons, and to a more varied feedstock, which included wastepaper and waste activated sludge. From May 2018 through June 2020, monthly CH_4 production averaged 209 g kg^{-1} VS for the control digester and 326 g kg^{-1} VS for the sound-treated digester.

From June 2018 through July 2020, the mean specific biogas yields from the control and sound-treated digesters were 0.39 $\pm$ 0.31 and 0.60 $\pm$ 0.39 m^3 kg^{-1} VS, respectively. Towards the end of the evaluation period in the summer of 2020, the control digester outperformed the sound-treated digester, producing an apparent yield of 0.8 and 0.49 m^3 kg^{-1} VS in June and July, respectively whereas the sound-treated digester produced an apparent yield of only 0.62 and 0.07 m^3 kg^{-1} VS, respectively, during the same period. Given that the retention of solids was decoupled from HRT, this was doubtless due to the previous depletion of VS in the sound-treated digester. From October 2019 through April 2020, the apparent biogas yield was 0.19 $\pm$ 0.26 and 0.50 $\pm$ 0.44 m^3 kg^{-1} VS for the control and sound-treated digesters, respectively. We specifically use the phrase apparent biogas yield in that the biogas yield during any given period is not only reflective of the current feeding rate, but is also dependent on the digestion of previously accumulated feed. The sonic treatment during the cooler months enhanced gas production significantly relative to the

control digester. This necessarily meant that more VS were depleted in the sound-treated digester than in the control digester. This likely explains the lower biogas production by the sound-treated digester in the last two months of the experiment. Thus, by uncoupling the retention of solids from HRT, and retaining solids in the digesters, the sonic treatment was able to deplete VS compared to the control digester, accounting for its low gas production in the last two months of the experiment. In May 2020, it was found that sludge from the sound-treated digester contained 46.3 g VS kg^{-1} sludge, while sludge from the control digester contained 95.2 g VS kg^{-1} sludge [8].

3.2. Digestate Malodors

Fourteen odorous organic compounds were quantified from the digestate of the sound-treated and control anaerobic digesters (Table 2). Most of these compounds were selected due to their high concentrations and their status as important components of wastewater malodor [11,12]. Other compounds quantified but not occurring in high concentrations were not typical wastewater malodors. These included benzaldehyde—Which is a component of many fruit aromas such as cherry, peach, and guava [13–15]—and benzyl acetate, which is a common floral fragrance compound [16,17]. It is likely that benzaldehyde was formed by reduction of benzoic acid—A common natural product of plants. The reduction/hydrogenation of organic matter in anaerobic environments is common, and can be due to the organic matter serving as a terminal electron acceptor for anaerobic respiration [18]. A further reduction to benzyl alcohol would result in the alcohol moiety of benzyl acetate.

Table 2. Concentrations of malodorous compounds identified in anaerobic digestate [1].

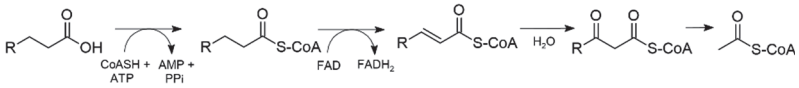
	Treatment	
Compound	**Control**	**Sound-Treated**
	Concentration (Milligrams per Liter)	
Dimethyl disulfide	171 ± 33.1	173 ± 29.6
Toluene	4.61 ± 2.1	6.0 ± 1.93
Phenol	97.5 ± 17	70.4 ± 12.4
para-Cresol	460 ± 116	435 ± 128
para-Ethylphenol	49.4 ± 25.3	50.9 ± 25.4
Indole	141 ± 30.2	104 ± 22.8
Skatole	116 ± 51.6	111 ± 17.2
	Concentration (Micrograms per Liter)	
2-Hexanone	951 ± 349	581 ± 254
2-Heptanone	835 ± 240	567 ± 161
2-Nonanone	320 ± 119	347 ± 91
2-Tridecanone	469 ± 333	717 ± 297
1-Octen-3-ol	620 ± 379	452 ± 298
Benzaldehyde	41 ± 25	29 ± 14
Benzyl acetate	19 ± 12	32 ± 14
Total identified	1043	953

[1] Data represent the mean ± standard error of the mean of 14 averaged monthly determinations encompassing May to October 2018, October 2019 to March 2020, and June to July 2020.

Oct-1-en-3-ol is a common fungal odorant, and the (*R*)- enantiomer is a characteristic impact compound responsible for the odor of mushrooms [19]. Oct-1-en-3-ol is generated via peroxidation of linoleic acid by lipoxygenase, with the hydroperoxide cleaved by hydroperoxide lyase to form 1-octen-3-ol. Lipoxygenases are common in eukaryotes, including fungi, but rare in bacteria [20].

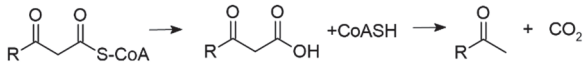
3.3. Secondary Ketones

The secondary ketones are likely synthesized by β-oxidation of free fatty acids. In β-oxidation, a fatty acid is degraded to acetyl-CoA thioesters, as well as generating the reduced coenzymes $FADH_2$ and NADH. β-Oxidation of unsaturated fatty acids requires additional enzymatic steps that are not shown in this scheme [21].



(1)

After a variable number of flavoprotein-mediated redox cycles producing acetyl-CoA and a fatty acyl-CoA thioester (1), the cycle can be terminated by a thioesterase to produce free coenzyme A (CoASH) and a β-keto acid (2). The β-keto acid is unstable, and likely spontaneously loses CO_2 to form a methyl ketone [22].



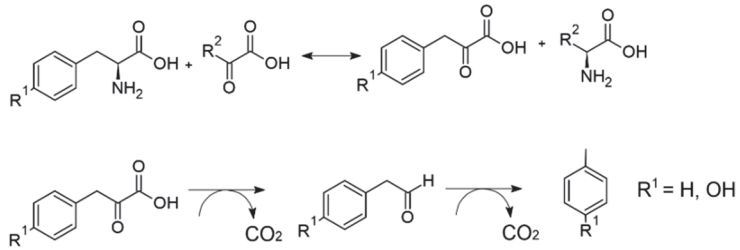
(2)

The β-oxidation of odd-numbered fatty acids could account for the presence of the odd-numbered secondary ketones [23]. Although the breakdown of fatty acids to acetyl-CoA and a fatty acyl-CoA thioester is quite efficient, the alternative pathway that results in a free β-keto acid still happens frequently, and has been enhanced in *Escherichia coli* by chromosomal deletion of the enzyme responsible for cleavage of the β-keto thioester, along with overexpression of the thioesterase responsible for the formation of the β-keto acid [22]. The engineered bacteria were capable of causing a 700-fold increase in methyl ketone production.

The secondary ketones were present at relatively low concentrations—less than 1 mg L^{-1} of digestate. Sonic treatment of the anaerobic digestate did not markedly affect the concentrations of secondary ketones, given that the concentrations of these compounds were similar in both digesters (Table 2). 2-Heptanone and 2-nonanone have low odor detection thresholds [24] (4.8 and 5.5 ppb in air, respectively), and so it is likely that these compounds had a contribution to the odor of the wastewater. During warm weather, the summed concentration of the four secondary ketones averaged 3.2 μg L^{-1} digestate in the control digester, and 2.9 μg L^{-1} in the sound-treated digestate. During cool weather, the four secondary ketones averaged 2.8 and 1.7 μg L^{-1} in the control and sound-treated digestate, respectively. The higher concentrations of secondary ketones during warm seasons were likely due to greater microbial growth during these periods.

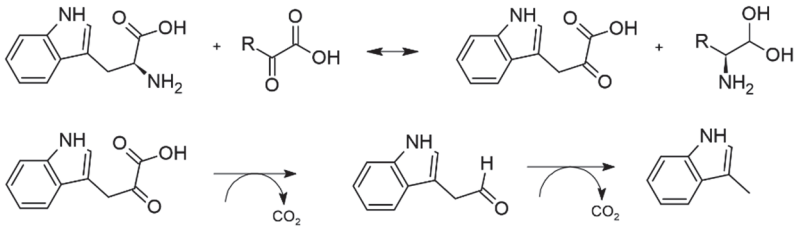
3.4. Aromatic Malodorants

Toluene and *p*-cresol are synthesized from L-phenylalanine and L-tyrosine, respectively, as shown in Equation (3). Following transamination of an acceptor, α-keto acid forms 2-oxo-3-phenylpropanoic acid or 2-oxo-3-(4-hydroxy) phenylpropanoic acid. Following decarboxylation of the 2-oxoacid, phenyl acetate (or 4-hydroxyphenylacetate) is either decarboxylated, or first reduced to the aldehyde and then decarbonylated to form the final product [25,26]:



(3)

Skatole is produced similarly from indole acetate:



(4)

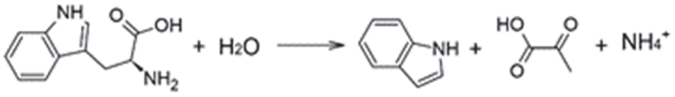
It is interesting to note that the enzymes that produce toluene, *p*-cresol, and skatole belong to the family of glycyl-radical-activating enzymes produced by facultative and strict anaerobes such as the Clostridiales, Actinomyceota, Enterobacteriaceae, and Fusobacteriaceae [25]. These enzymes are easily inactivated by oxygen [27].

Phenol is formed by bacteria such as *Clostridium tetanomorphum* via the action of L-tyrosine ammonia lyase to produce pyruvic acid and ammonium [28,29]:



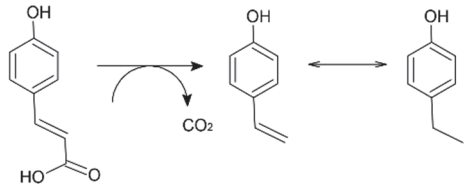
(5)

Similarly, indole is produced from tryptophan by L-tryptophanase [30]:



(6)

4-Ethylphenol has been shown to be produced by the decarboxylation of p-coumaric acid by certain yeasts and lactic acid bacteria to produce 4-vinylphenol, which is then reduced to 4-ethylphenol [31,32]:



(7)

Given the persistence of these aromatic malodorants in stored animal wastes, they have been referred to as dead-end products of amino acid catabolism—or at least as produced by intestinal bacteria [33] These aromatic malodorants have been shown to be degraded by sulfate-reducing bacteria [34]—aerobically by the purple non-sulfur bacterium *Rhodopseudomonas palustris* [35], and anaerobically by *Clostridia* spp. and by methanogenic consortia [36,37]. The intermediates in the mineralization of indole and skatole are isatin (1-H-indole-2,3-dione) and 3-methyloxindole (3-methyl-1,3-dihydroindole-2-one), respectively [37].

In the early stages of digester startup, the concentrations of aromatic malodorants were high, and in May 2018 *p*-cresol averaged 639 and 960 mg L^{-1} in the control and sound-treated digesters, respectively. By September, the concentrations of *p*-cresol had declined to 108 and 220 mg L^{-1} in the control and sound-treated digesters, respectively. Thereafter, the *p*-cresol concentrations remained low, and even during the winter of 2019–2020, when biogas production dropped, the *p*-cresol concentrations never exceeded 470 and 307 mg L^{-1} in the control and sound-treated digesters, respectively. Other aromatic malodorants behaved similarly. Since the concentrations of aromatic malodorants declined considerably after digester startup, it is likely that the aromatic malodorants were catabolized by the methanogenic consortia of the digesters.

The aromatic malodorants are major contributors to wastewater malodor. Still, the odor detection thresholds vary widely for these malodorants, ranging from 330 ppb (parts per billion) in air for toluene to 54 and 5.6 ppt (parts per trillion) in air for *p*-cresol and

skatole, respectively [38]. During warm weather, the aromatic malodors averaged 1350 and 1260 mg L^{-1} in the control and sound-treated digestates, respectively, and during cool weather they averaged 582 and 402 mg L^{-1} in the control and sound-treated digestates, respectively.

3.5. Volatile Sulfur Compounds

Dimethyl sulfide (DMS) is formed from L-methionine via dimethylsulfoniopropionate (DMSP). Although formerly thought to be exclusively produced via a largely aerobic and light-dependent process by oceanic dinoflagellates, a large number of bacteria are now known to produce DMSP and DMS, as well as methanethiol [39]. Methanethiol is a weak acid that forms methylthiolate, which is a strong nucleophile. It reacts with elemental sulfur (S_8) to form methyl polysulfide [40]:

$$CH_3S^- + S_8 \leftrightarrow CH_3S_9{}^- \quad (8)$$

Methyl polysulfides are unstable. They decompose to shorter dimethyl polysulfides and polysulfides, with $x + y = 10$:

$$CH_3S^- + CH_3S_9{}^- \leftrightarrow CH_3S_xCH_3 + S_y{}^{2-} \quad (9)$$

Jocelyn et al. found that H_2S and dimethyl disulfide (DMDS) are formed if S_8 is present in limited quantities, and that longer-chain sulfides are formed if S_8 is not limited [41]. Ver Leerdam et al. found that the reaction of methanethiol with elemental sulfur occurs under aeration [42]. In our system, wastewater from a final-stage aeration tank was mixed with feed and fed back to the digesters. Oxidation of H_2S by photosynthetic bacteria can produce octacyclic elemental sulfur [42], and wastewater gas chromatographic/mass spectral analysis of the terminal aeration tanks registered an average of 9.0×10^6 and 13×10^6 S_8 ion counts for the control and sound-treated systems, respectively, while S_8 was undetectable in the primary digesters. Although elemental sulfur did not chromatograph well on the GC column we used, this finding serves to confirm that elemental sulfur was formed in the aeration tanks.

Due to the limitations of our methodology, we were unable to quantify methanethiol and dimethyl sulfide, and did not have standards of the higher homologues of DMDS, dimethyl trisulfide (DMTS), dimethyl tetrasulfide (DMTetS), or any of the longer-chain-length sulfides. The digestates contained considerable concentrations of DMDS, and its concentration was virtually identical in the control and sound-treated digestates (Table 2). Using mass spectral total ion counts to track changes in the concentrations of the volatile disulfides (Figure 3), we found that their concentrations increased markedly in 2019–2020 as compared to their 2018 concentrations.

Since the aeration tank at the end of the system contained S_8, but the primary anaerobic digester did not, it is likely that recycling the elemental sulfur back to the system enhanced the production of dimethyl polysulfides. This finding shows that it would be desirable to remove elemental sulfur from the wastewater before recycling it back to the system, in order to reduce the concentrations of dimethyl polysulfides and H_2S.

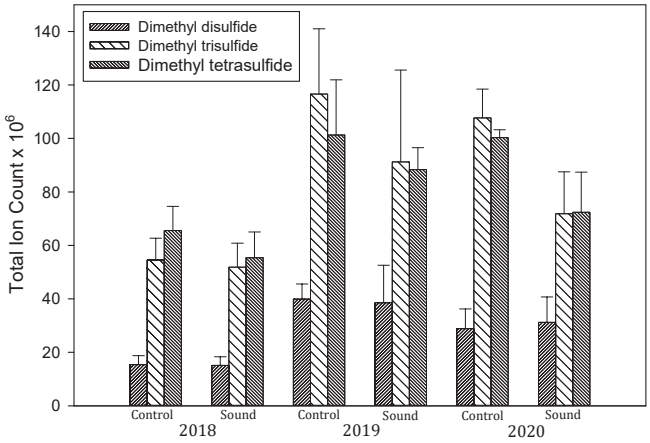


Figure 3. Averaged total ion counts for dimethyl sulfide, dimethyl trisulfide, and dimethyl tetrasulfide in anaerobic digestate, 2018–2020. Data represent the mean ± standard error of the mean.

3.6. Volatile Fatty Acids and Ammonium

Volatile fatty acids (VFAs) are largely formed via the fermentation of carbohydrates by prokaryotes to produce ATP in the absence of oxygen. Acetic acid may also be produced by acetogens via the reduction of two molecules of CO_2 with four molecules of H_2 [43]. The longer-chain VFAs are converted to acetate, and are then consumed by methanogens via cleavage of acetate to CH_4 and CO_2, whereas other methanogens produce CH_4 via reduction of CO_2 with H_2 [44].

Total VFA concentrations (acetic, propanoic, butyric, and *iso*-butyric acids) in cool weather (October 2018 through March 2019) were 44% higher in digestate from the control digester than from the sound-treated digester (6600 vs. 4600 μM), and in warm weather, total VFA concentrations were 89% higher in the control digestate than in the sound-treated digestate (1200 vs. 650 μM), reflecting consumption of VFAs by methanogens in the sound-treated digester [6]. The highest concentrations of acetate occurred during the winter of 2019–2020, when they averaged 276 mg L^{-1} in the control digester and 208 mg L^{-1} in the sound-treated digester.

During the second trial of the digesters, the pH of the control digester averaged 7.02, while the pH of the sound-treated digester averaged 7.08. However, given an average pK_a of 4.8 for the VFAs [9], over 98% of the VFAs would be in the conjugate base form, which likely limited the contribution of VFAs to the wastewater malodor (Figure 4).

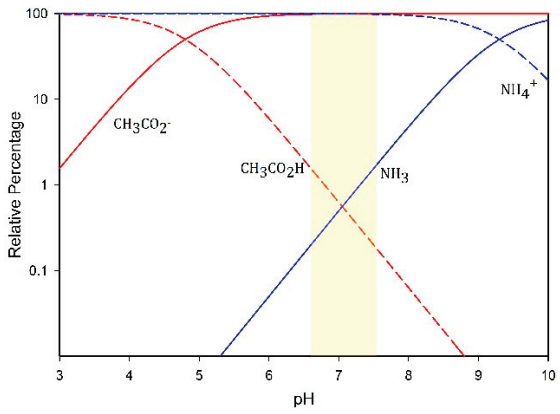


Figure 4. Bjerrum plot with the relative concentrations of acetic acid and its conjugate base, and of ammonia and its conjugate acid. The shaded area represents the mean pH of the digesters ± standard deviation of the mean.

Ammonia concentrations, on the other hand, were virtually identical in the control and sound-treated digestates, averaging 17.8 and 17.9 μM (321 and 323 mg L^{-1}), respectively.

In warm weather, the ammonium concentrations averaged 332 mg L^{-1} in the digestates for both digesters, while in cool weather the ammonium concentrations averaged 255 mg L^{-1}. The lower ammonium concentrations in the cool seasons were probably a consequence of lower feeding rates and/or lower microbial activity.

Urease activity is common in the environment. Many microorganisms hydrolyze urea intercellularly into NH_4^+ and HCO_3^-, and use the resulting proton gradient for ATP synthesis [45]. Thus, it is not surprising that the NH_4^+ concentrations in the control and sound-treated digestates were virtually identical. In the near-neutral pH range at which the digesters were operated, NH_3 would account for approximately 0.2–1.5% of the acid–base pair. Figure 4 shows a Bjerrum plot diagramming the idealized concentrations of the conjugate acid–base pairs for acetic acid and ammonia.

In any case, the odor thresholds of the VFAs and NH_3 are quite high in comparison to other malodorants of anaerobic digestate. Acetic and butyric acids have reported odor thresholds of 6 ppb and 0.19 ppb v/v, respectively, while NH_3 has a reported odor threshold of 1.5 ppm v/v. Other typical wastewater malodorants—i.e., DMS, *p*-cresol, and skatole—have reported odor thresholds of 3 ppb, 5.4×10^{-2} ppb, and 5.6×10^{-3} ppb v/v, respectively [38]. Thus, given the near-neutral pH of the digestate, neither VFAs nor NH_3 are likely to make major contributions to malodors compared to other volatile compounds, despite their relatively high concentrations.

3.7. Sonic Treatment of Anaerobic Digestate

Sonic treatment of anaerobic digestate works to increase biogas production in the same manner as ultrasonic pretreatment—that is, via sludge disruption. This occurs via various mechanisms, such as acoustic streaming inducing mass flow in the wastewater, vibrational energy imparted to the sludge, and cavitational inception and collapse, which can impart localized pressures of great amplitude [46]. Sludge disruption facilitates microbial colonization of the sludge by solubilizing nutrients and increasing the sludge's surface area [47,48]. This was evidenced by the higher background audio levels in the digester with prior sound exposure, which were likely due to greater gas production by the digester's microflora, resulting in numerous bubbles that act as acoustic resonators [46] (Supplementary Materials). Although ultrasonic pretreatment of sludge and direct sonic treatment share mechanistic similarities, they differ in sound frequency, the timing and duration of exposure, and power requirements.

Pretreatment of sludge with ultrasonic frequencies has been shown to significantly enhance the disintegration of the sludge, and thereby accelerate anaerobic digestion [49–51]. However, attenuation of sound is proportional to the sound's frequency. Largely for this reason, disintegration of waste by ultrasonication is usually conducted at relatively low frequencies—less than 100 kHz, and most often at less than 30 kHz [48]. Furthermore, lower frequencies create larger cavitation bubbles which, when they collapse, produce larger mechanical jet streams, causing greater sludge disintegration [47].

Used as a pretreatment for the disintegration of sludge prior to anaerobic digestion, ultrasonication can vary considerably in duration and intensity. For instance, Zawiega found an intensity of 4.3 W cm^{-2} for 300 s to be optimal for solubilizing WAS in treating 0.5 L sludge samples prior to digestion in a 5 L reactor for 28 d [49]. Assuming that the WAS sample was diluted to a volume of 5 L, this represents a power input of 2580 J L^{-1} of WAS. Zhao et al. [47] found optimal waste solubilization for treating WAS with 0.6 W mL^{-1} for 30 min, resulting in a power input of 1080 kJ L^{-1} sludge. Alagöz et al. used 10,000 kJ kg^{-1} VS as a pretreatment to solubilize olive and grape sludge prior to digestion [51].

In the present study, power consumption averaged about 68 W while playing music, and about 140 W when playing a 1000 Hz sine wave. This represents a power consumption of 430 and 886 J L^{-1} d^{-1} digestate, respectively. The loading rate of volatile solids averaged 97 kg $month^{-1}$. At power levels of 68 W and 140 W, this represents a power consumption of approximately 1070 and 2500 kJ kg^{-1} VS $month^{-1}$, respectively. Given the differences in the geometry of ultrasonic probes and audio speakers and the highly variable differences

in digester/reactor volumes between numerous research studies, meaningful comparisons of power consumption versus gains in biogas production are problematic. However, it is likely that the duration of sound played to the digester could be reduced considerably from the 2 h on/1 h off cycle used here to achieve increases in gas production more efficiently.

4. Conclusions

Sonic treatment of the anaerobic digestate increased biogas production by 38% compared to the control over the course of the two trial periods, but the only noticeable effect on wastewater malodorants was that sonic treatment reduced the concentration of VFAs. Given that VFAs are precursors to CH_4 production, this was not surprising.

Anaerobic digestion has the potential to greatly reduce pollution from wastewater. This is particularly true in the case of animal waste, much of which receives inadequate treatment before its release to the environment. However, anaerobic digestion is slow, and usually employs expensive heating and mixing systems to accelerate biogas production [52,53]. Sonic treatment has the potential to significantly enhance biogas production and potentially replace heating and mixing systems to some degree. However, its influence on odor control appears to be negligible.

Supplementary Materials: The following supporting information can be downloaded at: https://www.mdpi.com/article/10.3390/environments9080102/s1, MP3 file S1: 5 min control digester bottom hydrophone; MP3 file S2: 5 min sound-treated digester bottom hydrophone.

Author Contributions: Conceptualization, J.L.; methodology, J.L., P.S., N.L. and K.S.; investigation, J.L., N.L., P.S. and K.S.; writing—original draft preparation, J.L.; writing—review and editing: J.L., N.L., P.S. and K.S.; supervision, J.L.; funding acquisition, J.L. and K.S. All authors have read and agreed to the published version of the manuscript.

Funding: Funding was provided by the Agricultural Research Service (Grant No. 5040-12630-006-00D).

Data Availability Statement: The data presented in this study are available upon request to the corresponding author.

Acknowledgments: The authors thank Stacy Antle, Michael Bryant, and Zachary Berry (USDA-ARS) for technical assistance. The use of trade, firm, or corporation names in this website is for the information and convenience of the reader. Such use does not constitute an official endorsement or approval by the United States Department of Agriculture or the Agricultural Research Service of any product or service to the exclusion of others that may be suitable.

Conflicts of Interest: The authors declare no conflict of interest. The funders had no role in the design of the study; in the collection, analyses, or interpretation of data; in the writing of the manuscript; or in the decision to publish the results.

References

1. Lafratta, M.; Thorpe, R.B.; Ouki, S.K.; Shana, A.; Germain, E.; Willcocks, M.; Lee, J. Dynamic biogas production from anaerobic digestion of sewage sludge for on-demand electricity generation. *Bioresour. Technol.* **2020**, *310*, 123415. [CrossRef] [PubMed]
2. Iranpour, R.; Cox, H.H.J.; Oh, S.; Fan, S.; Kearney, R.J.; Abkian, V.; Haug, R.T. Thermophilic-Anaerobic Digestion to Produce Class A Biosolids: Initial Full-Scale Studies at Hyperion Treatment Plant. *Water Environ Res.* **2006**, *78*, 170–180. [CrossRef] [PubMed]
3. Orzi, V.; Scagglia, B.; Lonati, S.; Riva, C.; Boccasile, G.; Alborali, G.L.; Adani, F. The role of biological processes in reducing both odor impact and pathogen content during mesophilic anaerobic digestion. *Sci. Total Environ.* **2015**, *526*, 116–126. [CrossRef]
4. Welsh, F.W.; Schulte, D.D.; Kroeker, E.J.; Lapp, H.M. The Effect of anaerobic digestion upon swine manure odors. *Can. Agric. Eng.* **1977**, *19*, 122–126.
5. Wilson, C.A. The Effect of Steady-State Digestion Temperature on The Performance, Stability, and Biosolids Odor Production Associated with Thermophilic Anaerobic Digestion. Master's Thesis, Virginia Polytechnic Institute, Blacksburg, VA, USA, 8 November 2006.
6. United States Environmental Protection Agency. Biosolids Technology Fact Sheet. Multi-Stage Anaerobic Digestion. Available online: https://www.epa.gov/sites/default/files/2018-11/documents/multistage-anaerobic-digestion-factsheet.pdf (accessed on 2 August 2022).

7. Loughrin, J.; Antle, S.; Sistani, K.; Lovanh, N. In situ acoustic treatment of anaerobic digesters to improve biogas yields. *Environments* **2020**, *7*, 11. [CrossRef]
8. Loughrin, J.; Antle, S.; Simmons, J.; Sistani, K.; Lovanh, N. In situ sonification of anaerobic digestion: Extended evaluation of performance in a temperate climate. *Energies* **2020**, *13*, 5349. [CrossRef]
9. ChemIDPlus Advanced. Available online: https://chem.nlm.nih.gov/chemidplus/ (accessed on 28 June 2022).
10. Labatut, R.A.; Angenent, L.T.; Scott, N.R. Conventional mesophilic vs. thermophilic anaerobic digestion: A trade-off between performance and stability? *Water Res.* **2014**, *53*, 249–258. [CrossRef]
11. Chappuis, C.F.-J.; Niclass, Y.; Vuilleumier, C.; Starkenmann, C. Quantitative headspace analysis of selected odorants from latrines in Africa and India. *Envrion. Sci. Technol.* **2015**, *49*, 6134–6140. [CrossRef] [PubMed]
12. Jeon, E.-C.; Son, H.-K.; Sa, J.-H. Emission characteristics and factors of selected odorous compounds at a wastewater treatment plant. *Sensors* **2009**, *9*, 311–326. [CrossRef]
13. Ouaabou, R.; Ennahli, S.; Nabil, B.; Hssaini, L.; Hanine, H.; Hernández, F.; Ouhammou, M.; Mahrouz, M. Multivariate cherry quality assessment using morphological, biochemical and volatile compound traits. *Int. J. Fruit Sci.* **2020**, *20*, S1328–S1347. [CrossRef]
14. Do, J.Y.; Salunkhe, D.K.; Olson, L.E. Isolation, identification and comparison of the volatiles of peach fruit as related to harvest maturity and artificial ripening. *J. Food Sci.* **1969**, *34*, 618–621. [CrossRef]
15. Nishimura, O.; Yamaguchi, K.; Mihara, S.; Shibamoto, T. Volatile constituents of guava fruits (*Psidium guajava* L.) and canned puree. *J. Agric. Food Chem.* **1989**, *37*, 1139–1142. [CrossRef]
16. Guterman, I.; Masci, T.; Chen, X.; Negre, F.; Pichersky, E.; Dudareva, N.; Weiss, D.; Vainstein, A. Generation of phenylpropanoid pathway-derived volatiles in transgenic plants: Rose alcohol acetyltransferase produces phenylethyl acetate and benzyl acetate in petunia flowers. *Plant Mol. Biol.* **2006**, *60*, 555–563. [CrossRef]
17. Bera, P.; Kotamreddy, N.R.; Samanta, T.; Maiti, S.; Mitra, A. Inter-specific variation in headspace scent volatiles composition of four commercially cultivated jasmine flowers. *Nat. Prod. Res.* **2015**, *29*, 1328–1335. [CrossRef]
18. Wilson, R.A.; Tfaily, M.M.; Rich, V.I.; Keller, J.K.; Bridgham, S.D.; Zalman, C.M.; Meredith, L.; Hanson, P.J.; Hines, M.; Pfeifer-Meister, L.; et al. Hydrogenation of organic matter as a terminal electron sink sustains high CO2: CH4 production ratios during anaerobic decomposition. *Org. Geochem.* **2017**, *112*, 22–32. [CrossRef]
19. Mosandi, A.; Heusinger, G.; Gessner, M. Analytical and sensory differentiation of 1-octen-3-ol enantiomers. *J. Agric. Food Chem.* **1986**, *34*, 119–122. [CrossRef]
20. Goloshchapova, K.; Stehling, S.; Heydeck, D.; Blum, M.; Kuhn, H. Functional characterization of a novel arachidonic acid 12S-lipoxygenase in the halotolerant bacterium Myxococcus fulvus exhibiting complex social living patterns. *Microbiol.* **2019**, *8*, e00775. [CrossRef]
21. Schulz, H. Beta oxidation of fatty acids. *Biochim. Biophys. Acta* **1991**, *1081*, 109–120. [CrossRef]
22. Goh, E.-B.B.; Baidoo, E.E.K.; Keasling, J.D.; Beller, H.R. Engineering of bacterial methyl ketone synthesis for biofuels. *Appl. Environ. Microbiol.* **2012**, *78*, 70–80. [CrossRef]
23. Zhu, M.; Xu, X.; Li, Y.; Wang, P.; Niu, S.; Zhang, K.; Huang, X. Biosynthesis of the nematode attractant 2-heptanone and Its co-evolution between the pathogenic bacterium *Bacillus nematocida* and non-pathogenic bacterium *Bacillus subtilis*. *Front. Microbiol.* **2019**, *10*, 1489. [CrossRef]
24. Cometto-Muñiz, J.E.; Abraham, M.H.J. Olfactory psychometric functions for homologous 2-ketones. *Behav. Brain Res.* **2009**, *201*, 207–215. [CrossRef] [PubMed]
25. Zargar, K.; Saville, R.; Phelan, R.M.; Tringe, S.G.; Petzold, C.J.; Keasling, J.D.; Beller, H.R. In vitro characterization of phenylacetate decarboxylase, a novel enzyme catalyzing toluene biosynthesis in an anaerobic microbial community. *Sci. Rep.* **2016**, *6*, 31362. [CrossRef] [PubMed]
26. Liu, D.; Wei, Y.; Liu, X.; Zhou, Y.; Jiang, L.; Yin, J.; Wang, F.; Hu, Y.; Urs, A.N.N.; Liu, Y.; et al. Indoleacetate decarboxylase is a glycyl radical enzyme catalysing the formation of malodorant skatole. *Nat. Comm.* **2018**, *9*, 4224. [CrossRef] [PubMed]
27. Saito, Y.; Sato, T.; Nomoto, K.; Tsuji, H. Identification of phenol- and *p*-cresol-producing intestinal bacteria by using media supplemented with tyrosine and its metabolites. *FEMS Microb. Ecol.* **2018**, *94*, fiy125. [CrossRef]
28. Backman, L.R.F.; Funk, M.A.; Dawson, C.D.; Drennan, C.L. New tricks for the glycyl radical enzyme family. *Crit. Rev. Biochem. Mol. Biol.* **2017**, *52*, 674–695. [CrossRef]
29. Louie, G.V.; Bowman, M.E.; Moffitt, M.C.; Baiga, T.J.; Moore, B.S.; Noel, J.P. Structural Determinants and Modulation of substrate specificity in phenylalanine-tyrosine ammonia-lyases. *Chem. Biol.* **2006**, *13*, 1327–1338. [CrossRef]
30. Burns, R.O.; DeMoss, R.D. Properties of tryptophanase from Escherichia coli. *Biochem. Biophys. Acta* **1962**, *65*, 233–244. [CrossRef]
31. Couto, J.A.; Campos, F.M.; Figueiredo, A.R.; Hogg, T.A. Ability of lactic acid bacteria to produce volatile phenols. *Am. J. Enol. Vitic.* **2006**, *57*, 166–171.
32. Santamaría, L.; Reverón, I.; de Felipe, F.L.; de las Rivas, B.; Muñoz, R. Ethylphenol formation by Lactobacillus plantarum: Identification of the enzyme involved in the reduction of vinylphenols. *Appl. Environ. Microbiol.* **2018**, *84*, e0164-18. [CrossRef]
33. Ma, Q.; Meng, N.; Li, Y.; Wang, J. Occurrence, impacts, and microbial transformation of 3-methylindole (skatole): A critical review. *J. Hazard. Mater.* **2021**, *416*, 126181. [CrossRef]
34. Suflita, J.M.; Liang, L.-N.; Saxena, A. The anaerobic biodegradation of o-, m- and p-cresol by sulfate-reducing bacterial enrichment cultures obtained from a shallow anoxic aquifer. *J. Ind. Microbiol.* **1989**, *4*, 255–266. [CrossRef]

35. Sharma, N.; Doerner, K.C.; Alok, P.C.; Choudhary, M. Skatole remediation potential of Rhodopseudomonas palustris WKU-KDNS3 isolated from an animal waste lagoon. *Lett. Appl. Microbiol.* **2014**, *60*, 298–306. [CrossRef] [PubMed]
36. Kohda, C.; Ando, T.; Nakai, Y. Isolation and characterization of anaerobic indole- and skatole-degrading bacteria from composting animal wastes. *J. Gen. Appl. Microbiol.* **1997**, *43*, 249–255. [CrossRef] [PubMed]
37. Gu, J.-D.; Berry, D.F. Degradation of substituted indoles by an indole-degrading methanogenic consortium. *Appl. Environ. Microbiol.* **1991**, *57*, 2622–2627. [CrossRef] [PubMed]
38. Nagata, Y.; Takeuchi, N. Measurement of odor threshold by triangle odor bag method. *Odor Meas. Rev.* **2003**, *118*, 118–127.
39. Williams, B.T.; Martínez, A.B.; Cowles, K.; Bermejo, A.; Curson, A.R.J.; Zhang, Y.; Newton-Payne, S.; Hind, A.J.; Li, C.-Y.; Rivera, P.P.L.; et al. Bacteria are important dimethylsulfoniopropionate producers in coastal sediments. *Nat. Microbiol.* **2019**, *4*, 1815–1825. [CrossRef]
40. van Leerdam, R.C.; van den Bosch, P.L.F.; Lens, P.N.L.; Janssen, A.J.H. Reactions between methanethiol and biologically produced sulfur. *Environ. Sci. Technol.* **2011**, *45*, 1320–1326. [CrossRef]
41. Joycelyn, P.C. Chemical reactions of thiols. In *Biocehmistry of the SH Group*; Watts, D.C., Ed.; Academic Press: London, UK, 1972; pp. 85–87.
42. Pickering, I.J.; George, G.N.; Yu, E.Y.; Brune, D.C.; Tuschak, C.; Overmann, J.; Beatty, J.T.; Prince, R.C. Analysis of sulfur biochemistry of sulfur bacteria using x-ray absorption spectroscopy. *Biochemistry* **2001**, *40*, 8138–8145. [CrossRef]
43. Schuchmann, K.; Müller, V. Energetics and application of heterotrophy in acetogenic bacteria. *Appl. Environ. Microbiol.* **2016**, *82*, 4056–4069. [CrossRef]
44. Kouzuma, A.; Tsutsuumi, N.; Ishii, S.; Ueno, Y.; Abe, T.; Watanabe, K. Non-autotrophic methanogens dominate in anaerobic digesters. *Sci. Rep.* **2018**, *7*, 1510. [CrossRef]
45. Chen, Y.; Chen, H.; Chen, Z.; Hu, H.; Deng, C.; Wang, X. The benefits of autotrophic nitrogen removal from high concentration of urea wastewater through a process of urea hydrolysis and partial nitritation in sequencing batch reactor. *J. Environ. Manag.* **2021**, *292*, 112762. [CrossRef] [PubMed]
46. Brennen, C.E. *Cavitation and Bubble Dynamics*, 1st ed.; Cambridge University Press: New York, NY, USA, 2014; p. 268.
47. Tiehm, A.; Nickel, K.; Zellhorn, M.; Neis, U. Ultrasonic waste activated sludge disintegration for improving anaerobic stabilization. *Wat. Res.* **2001**, *25*, 2003–2009. [CrossRef]
48. Tyagi, V.K.; Lo, S.-L.; Appels, L.; Dewil, R. Ultrasonic treatment of waste sludge: A review on mechanisms and applications. *Crit. Rev. Environ. Sci. Technol.* **2014**, *44*, 1220–1288. [CrossRef]
49. Zawieja, I.; Wlodarczyk, R.; Kowalczyk, M. Biogas generation from sonicated excess sludge. *Water* **2019**, *11*, 2127. [CrossRef]
50. Zhao, Y.-H.; Zhang, B.; Tao, J.; Li, Q.; Lv, B. Optimization of energy consumption of the ultrasonic pretreatment on sludge disintegration. In *IOP Conference Series: Materials Science and Engineering, Proceedings of the 2nd International Conference on Manufacturing Technology, Materials and Chemical Engineering, Wuhan, China, 14–16 June 2019*; IOP Publishing: Bristol, UK, 2019; p. 012198. [CrossRef]
51. Alagöz, B.A.; Yenigün, O.; Erfinçler, A. Ultrasound assisted biogas production from co-digestion of wastewater sludges and agricultural wastes: Comparison with microwave pre-treatment. *Ultason. Sonochem.* **2017**, *40*, 193–200. [CrossRef] [PubMed]
52. Stroot, P.G.; McMahon, K.D.; Mackie, R.I.; Raskin, L. Anaerobic codigestion of municipal solid waste biosolids under various mixing conditions, I. Digester performance. *Water Res.* **2001**, *35*, 1804–1816. [CrossRef]
53. Wu, B. Integration of mixing, heat transfer, and biochemical reaction kinetics in anaerobic methane fermentation. *Biotechnol. Bioeng.* **2012**, *109*, 2864–2874. [CrossRef]

energies

MDPI

Article

Rural Households' Perceptions of the Adoption of Rooftop Solar Photovoltaics in Vhembe District, South Africa

Ranganai Chidembo *, Joseph Francis and Simbarashe Kativhu

Institute for Rural Development, Faculty of Science, Engineering & Agriculture, University of Venda, Thohoyandou 0950, South Africa

* Correspondence: chidemborg@gmail.com; Tel.: +27-76-180-6611

Abstract: Rooftop solar photovoltaics have the potential to successfully electrify rural and scattered communities worldwide. However, access to clean, high-quality, reliable and affordable energy remains elusive for several households in rural areas of the developing world. To fully comprehend, unpack and proffer meaningful solutions to this mismatch, energy sources in use and types in areas where rural electrification through solar home systems are profiled. Furthermore, grassroot communities' perceptions of rooftop solar photovoltaics (PVs) was explored. A case study design was adopted. Thirty (30) households were purposively sampled from three selected villages. Their perceptions on the adoption of solar photovoltaic home systems were analysed qualitatively using Atlas ti 8 software. Thematic network analysis was pursued. Households in the chosen villages use grid connections, paraffin, solar PV, firewood and candles to meet their energy needs. The chosen villages used energy for water heating, refrigeration, cooking, illumination, space heating, entertainment and ironing at the household level. In general, the participating households perceived solar PVs as a relatively cheap, easy-to-use, environmentally friendly alternative energy, and did not demand regular payments once installed. However, there was a discerning perception that solar was a weak technology that could not be relied on because it produces an inferior quality of energy, could be easily stolen and needed high capital investment beyond the reach of many consumers. The results obtained in this study highlight that the solar home system (SHS) rollout should be sensitive to rural communities' financial situations and be innovative in that low-income households are included. In addition, there is a need for a robust awareness programme that highlights the energy availability, reliability, quality, cost effectiveness and legal, health and safety benefits of the SHS to the rural families in the district.

Keywords: energy poverty; renewable energy; rooftop solar systems; perceptions

Citation: Chidembo, R.; Francis, J.; Kativhu, S. Rural Households' Perceptions of the Adoption of Rooftop Solar Photovoltaics in Vhembe District, South Africa. *Energies* **2022**, *15*, 6157. https://doi.org/10.3390/en15176157

Academic Editors: Dibyendu Sarkar, Rupali Datta, Prafulla Kumar Sahoo and Mohammad Mahmudur Rahman

Received: 20 July 2022
Accepted: 19 August 2022
Published: 24 August 2022

Publisher's Note: MDPI stays neutral with regard to jurisdictional claims in published maps and institutional affiliations.

Copyright: © 2022 by the authors. Licensee MDPI, Basel, Switzerland. This article is an open access article distributed under the terms and conditions of the Creative Commons Attribution (CC BY) license (https://creativecommons.org/licenses/by/4.0/).

1. Introduction

Energy poverty is a global challenge [1] that affects about 2.67 billion people who rely on traditional fuels [1–3] for cooking and heating. Most people lack access to clean and affordable energy sources in rural areas. They depend on traditional biomass [1]. Throughout the world, dependence on traditional biomass has exposed them to dangerous health hazards associated with air pollution [4,5]. To respond to this scourge, governments and other stakeholders have mounted efforts to transition rural and unelectrified communities from traditional biomass to the adoption of renewable energy resources that are much safer and cleaner [6]. However, the expensive cost of grid extension, unreliable infrastructure, lack of political will and institutional weakness [7] jeopardise these efforts. Moreover, the availability and affordability of renewable energy sources [8] have been a setback that frustrates energy transitioning. Despite all these setbacks, adopting renewable energy sources remains the only promising alternative for universal access to affordable and clean energy among the rural-poor communities in developing nations.

In South Africa, the government has committed to the socio-economic transformation of rural and marginalised communities through the provision of off-grid connections (solar home systems) [9]. In 1999, the Integrated National Electrification Programme (INEP) introduced a fee-for-service programme for 300,000 installations [9]. It was piloted in 2002 by Shell–ESKOM Joint Venture at the same time as the other six concessionaires [10]. The assumption was that a typical indigent home would require a 50 kWh for domestic services such as charging mobile phones, outdoor and indoor illumination, television, radio player and water heating. Consequently, the government has mandated a monthly supply of 50 kWh for low-income customers [9,11,12]. Overall, the programme targeted to generate 10,000 GWh by 2013 [13]. The programme missed its target [14], failing dismally [15]. The INEP initially targeted to electrify 300,000 households, but in 2012 only 46,000 were still using the systems [16]. This is a cause for concern. The programme's failure is attributed to the failure of the programme planners to factor in rural communities' views, attitudes and perceptions of the SHS. Despite the nobility of the programme, without consideration of the consumers' attitudes, the programme was bound to fail. Thus, this paper will unpack current energy sources, types and the rural communities' perceptions of using SHS as an alternative energy source in the rural communities of South Africa.

The adoption of rooftop solar home systems (SHSs) is one way for energy transitioning for rural and scattered communities of South Africa. Rooftop SHS is ideal in South Africa because the country's average solar radiation is 7 KWh.m^2 [17]. Cognisant of the challenges that compromised the INEP, solar radiation potential and energy poverty situation among the rural communities, the cabinet launched a New Household Electrification Strategy (NHES) [18]. The NHES sought to achieve universal energy access by 2025 by ensuring that only 90% of new houses will utilise the national grid. The remaining 10% will be electrified with high-quality off-grid SHS (i.e., 50 to 100 Wp stand-alone SHS recommended for off-grid electrification). This decision resulted from the realisation that rooftop solar photovoltaic systems are the most promising technology for practical rural electrification. Secondly, SHSs are proving to be a more resilient and efficient electricity system for the rural unelectrified communities [19]. Generally, there is a rapid transition from traditional centralised electricity generation and intensive use of fossils to isolated rooftop solar home systems [20]. Thus, the NHES was launched in 2013. As a result of these two crucial attempts to electrify rural villages with rooftop SHSs, rural communities in South Africa were exposed to the use of solar home systems. In an effort to understand the SHS adoption impediments, this paper profiles energy sources and types used in three selected villages in the Vhembe District (Duvhuledza, Mbahe and Tshamutilikwa) that participated in both the INEP and NHES programmes in the past. Finally, the rural households' perceptions of rooftop solar PV technology are explored.

2. Theoretical Background

(a) Energy Ladder Approach

Fuel use and choice among households are explored through the energy ladder model (ELA) [21]. The model assumes that a household's income will increase a family shifts to more modern and cleaner energy sources such as liquid petroleum gas (LPG) and electricity. In addition, the model assumes that energy consumption increases with more efficient fuels. Therefore, energy sources for most rural households are biomass, including fuelwood, charcoal and agricultural waste. According to this theory, homes move up the ladder, from biomass to paraffin and then LPG or electricity due to increased disposable income and improved lifestyles. Thus, technological advancements aimed at improving energy efficiency are only afforded and resorted to by households with disposable income. Central to the ELA is household income to move from one fuel to another in a linear trend. Many scholars have criticised this since households do not necessarily follow the energy ladder because of their financial position. Multiple fuel use approaches have debunked this approach. Due to these weaknesses of the energy ladder approach, ELA must be used alongside the multiple fuel approach.

(b) Multiple Fuel Use Approach

This approach responds directly to the shortcomings of the energy ladder approach. It postulates that poorest rural households, particularly in developing nations, do not move from one fuel to another; instead, they use multiple fuel sources found at all levels of the energy ladder. Different fuels are not switched, but fuel staking is pursued whereby fuels for cooking are added, and even the most traditional ones are not displaced or abandoned [22]. For instance, in Zimbabwe, access and availability have been identified as the driving forces for fuel choice [23]. As such, household fuel choice is not dependent on economic factors alone but on several factors that include gender, the level of education and household head [24]. Cultural and taste preferences contribute to household fuel choice [25]. Households act rationally; thus, they move up and down the ladder due to several factors which might be cultural. Understanding the factors that influence household fuel choices is essential before concentrating on shifts [26]. Thus, in this paper, a more holistic approach combining the insights of ELA and MFUA was applied to understand energy sources, types and rural communities' perceptions of renewable energy sources such as solar photovoltaics.

3. Materials and Methods

The current case study was conducted in Mbahe, Dhuvuledza and Tshamutilikwa which are in the Thulamela municipality of the Vhembe District in South Africa. The villages are found in the eastern part of the municipality towards the Kruger National Park (Figure 1). They are mainly rural with scattered households. Thirty (30) households, ten (10) per village, were selected via a case study design. Only those households that participated in the SHS Electrification Programme implemented by the Thulamela Local Municipality and Solar Vision Private Limited were purposively selected for the study. Before the actual data collection, SHS Electrification Programme beneficiaries were identified in each village. Out of the identified households, only ten were randomly selected per village. Creswell and Tashakkori (2007) contend that ten respondents constitute a large enough sample size for a phenomenological study in qualitative studies [27]. In contrast, Morse (1995) suggests that six respondents are sufficient to reach data saturation in a phenomenological study [28]. Furthermore, Bernard (2011) contends that the ideal standard for qualitative sample size is "to interview to redundancy" [29] or to interview to saturation [30]. Given the lack of consensus on the appropriate sample size in exploratory studies, this study targeted 30 respondents, far beyond the suggested sample size for explorative studies in the literature. In-depth face-to-face interviews were conducted to solicit individual households' insights on the rooftop solar home systems and the current energy uses, types and principal fuel sources. The responses were recorded using a voice recorder. In all instances where the local language (Venda) was used, it was translated into the English at transcribing stage. Transcribe data were exported to Atlast ti as a Hermeneutic Unit. It was analysed using Thematic Network Analysis (TNA) in Atlas ti version 8. The data were analysed using open coding, code by list and in vivo. The relationship and logical pattern explaining the perceived advantages and disadvantages of adopting an SHS were extracted from the data using the linking and related functions under Network View Manager.

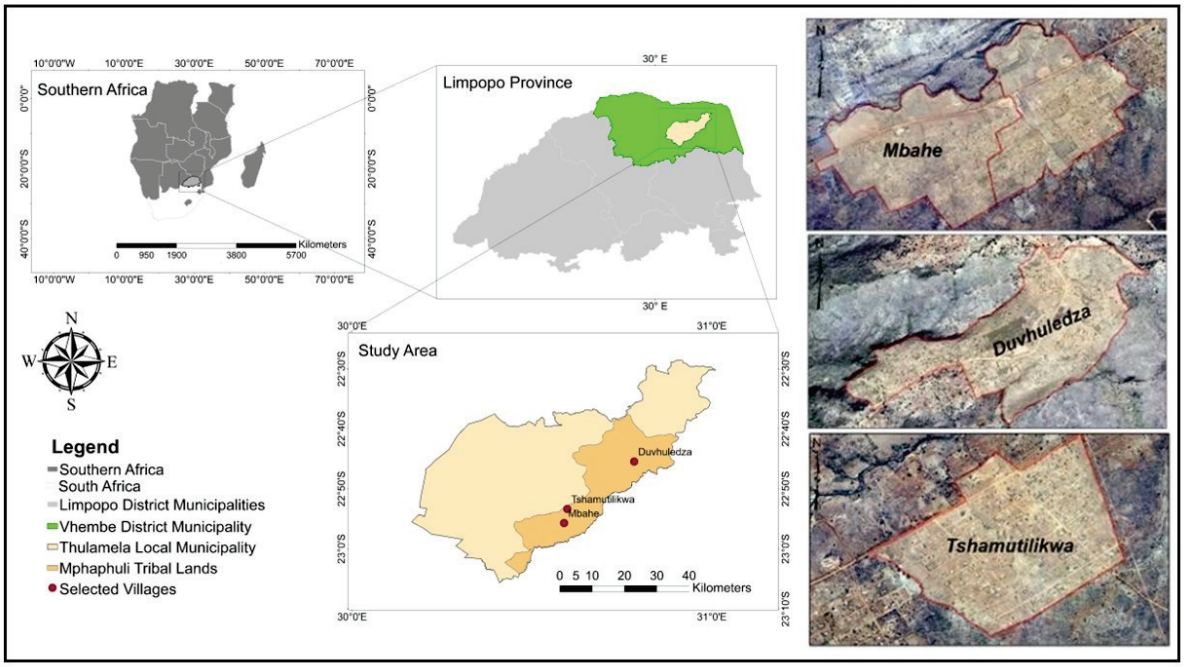


Figure 1. A map of the study site.

4. Results

4.1. Demography

Most of the study's thirty respondents (83%) were females. Almost 36% of females were residents of Tshamutilikwa. Adults aged between 36 and 60 comprised 60% of the total number of the respondents, with the elderly constituting about a third, 30% of the respondents. Youths within the 18- and 35-year-old range made up 10% of the respondents. As indicated in Table 1, in Tshamutilikwa, no youth was interviewed. Duvhuledza village had the highest number of youths (7%) participating in this study.

Table 1. Demographic characteristics of the respondents in the study on the perception of solar PV adoption.

		Mbahe	Duvhuledza	Tshamutilikwa	Total Frequency (n = 30)	Cumulative (%)
Gender	Male	2	2	1	5	16.7
	Female	8	8	9	25	83.3
Age	Youths (18–35 years)	1	2	0	3	10
	Adults (36–60 years)	6	7	5	18	60
	Elderly (61+ years)	3	1	5	9	30

4.2. Energy Types and Uses

The interviews revealed that families use various energy sources in the selected villages. The dominant prevalent energy sources in the chosen villages are grid electricity, paraffin, solar photovoltaics, firewood and candles. These sources meet household energy needs at the household level, ranging from cooking, water heating, indoor and outdoor illumination, refrigeration, ironing (straightening fabric), air conditioning, entertainment and space heating. Presented in Table 2 is how each energy source is used at the household level, as extracted by the interviews.

Table 2. Energy types and their uses in a household in the rural areas of the Vhembe District.

Domestic Energy Use	Energy Source(s)	Frequency (N = 30)	Cumulative Percentage (%)
1. Illumination	• Candles	3	10.0
	• Paraffin lamps	1	3.3
	• Battery cells	1	3.3
	• Solar photovoltaics	1	3.3
	• Grid electricity	22	73.3
	• Grid electricity	29	96.7
2. Water heating	• Solar geyser	1	3.3
	• Grid electricity	14	46.7
	• Liquefied petroleum gas	2	6.6
	• Firewood	21	70
3. Entertainment	• Battery cells	1	3.3
	• Grid electricity	28	93.3
4. Cooking	• Firewood	24	80.0
	• Electricity	17	56.7
	• Liquefied petroleum gas	2	6.6
5. Space heating	• Liquefied petroleum gas	1	3.3
	• Firewood	6	20
6. Air conditioning	• Nothing	16	53.3
	• Electricity	13	43.3
7. Ironing clothes	• Firewood	8	26.7

(a) Grid electricity

Households are using grid electricity for space heating, refrigeration, cooking, household lights, water heating, entertainment and air conditioning at the household level in the selected villages. As presented in Table 2, 29 and 28 out of 30 participants use grid electricity for refrigeration and entertainment. As shown in Table 2, 22 of the 30 that were interviewed use it for illumination compared to 17 for cooking. About half of the survey households used it for water heating and air conditioning. These findings align with Motjoadi, Bokoro and Onibonoje, who concluded that the primary purpose of electricity for rural dwellers is domestic use [31]. Many rural communities that are connected to the grid in sub-Saharan Africa are restricted to lighting, television, radio and cell phone charging [1,32]. They further posit that rural communities cannot buy electrical appliances. This view is echoed by [31], who argue that electricity affordability remains a challenge for rural communities despite being connected to the grid. Overall, grid connections in rural communities of developing countries are struggling with reliability, stability, sustainability, power quality and efficiency [33]

(b) Paraffin

As shown in Table 2, some households use paraffin as an energy source. It is mainly used for household lights. Earlier studies in South Africa have found a similar trend [34–36]. Interestingly, paraffin was only mentioned by one of the thirty households participating in this study. This is in line with the observation by [37], who observed that the reliance on paraffin for lights is not uniform across geographical areas and within individual communities. They said that only the poorest and vulnerable communities use paraffin with only limited access to other energy forms. According to the energy ladder hypothesis, the use of paraffin is one step from unclean sources such as biomass [38]. In other words,

the use of paraffin for lights is a shift from low-quality fuels such as biomass to more convenient, versatile and cleaner modern sources [21]. Despite categorising the use of paraffin as an improvement on the energy ladder, it remains an unclean energy source that is detrimental to both human health and the environment. It is worth noting that a separate study in different villages of the Vhembe District revealed that paraffin is being used for cooking [39].

(c) Solar Photovoltaics

Solar photovoltaics systems are one of the energy sources that emerged in the study. As indicated in Table 2, it is exclusively used for water heating and indoor and outdoor illumination. It is apparent from Table 2, that only one participant in the study mentioned solar PV systems. This is in line with the findings of [32], who observed that the use of solar PV systems is very minimal in Southern Africa. In South Africa, solar PV systems are for lighting and home appliances in rural communities [40]. Surprisingly, the solar module price is declining steadily [40], but there is still low uptake of the technology among the rural communities of the Vhembe District. If properly harnessed, solar PV technology would be contributing to about 14% of the total energy supply in the country by 2050 [41]. In addition, an installation of a 50 kWh/m can save ZAR 100 billion per annum and save the struggling national grid by generating 9720 GWh [42], ultimately cutting carbon dioxide emissions of about 5.8 million metric tonnes.

(d) Firewood

The use of firewood among the rural households in the Vhembe District is predominantly for ironing clothes, water heating and space heating. Table 2 reveals that 8 out of the 30 homes who partook in this research mentioned using firewood for ironing clothes. The bulk (24) of the people among the participating families use firewood for cooking, while 21 used it for water heating. Only six used it to meet their space heating needs. These findings align with the studies by [32,39], which noted that some rural and remote communities rely on burning fuelwood for cooking and heating. The South African Energy Outlook of 2019 has predicted that about 10% of the South African population will still be using fuelwood for cooking by 2030 [43]. They observed that many families in sub-Saharan Africa still use dirty fuels such as firewood for light and cooking. About 730 million rely on biomass such as firewood in sub-Saharan Africa [44]. Notably, most families in rural South Africa are not employed and do not have a stable source of income [39]. Firewood is prevalent among the poor [45,46] because they can afford this source financially.

It is worth noting that households relying on firewood spend a considerable amount of time and labour gathering from near and afar [1]. Let alone the severe threat it poses to the environment and human health [47]. At the receiving end of these activities are children and women. The results conform with the findings of Statistics South Africa, which observed that about 40% of the rural dwellers in the Limpopo Province use firewood for cooking [48]. Currently, meeting energy needs using firewood is cheaper than using any other available energy source [39]. This explains why despite almost 100% grid connection in some villages of the district and incentives for using it such as offering accessible promotional units by the service provider, families still opt for fuelwood use as the energy of choice for their cooking and water heating needs. High fuelwood usage for cooking is driven by the belief that food cooked with firewood tastes better than that cooked with electricity [39]. Household energy preferences are multifaceted and dynamic. Thus, an attempt to promote new energy technology needs thorough socio-economic, cultural and taste research.

(e) Candles

Some households were using candles for lighting purposes. Notably, as Figure 1 shows, candle usage was not that popular. Representatives of only two households were of this view. This is consistent with Rahut, Behera and Ali's findings that only 2.9% of Eastern and Southern African households used candles for illumination [32]. This finding shows that rural communities still rely on unclean energy sources to meet their household

illumination needs. Reliance on candles for lighting exposes rural families to both health and physical hazards.

4.3. Rural Communities' Perceptions of Solar Home Systems

Several rural communities' perceptions of the adoption and use of SHS among rural households in South Africa emerged and are presented in Table 3. Firstly, 23% of the rural households thought solar systems were unaffected by load shedding. As shown in Table 1, this view was shared across the villages. According to Piliso, Senzanje and Dhavu, since 2010, the South African electrical power distribution company ESKOM has struggled to provide enough electricity for the country [49]. As a result, load shedding has become perennial in the country. The prevalence and devastating effect of load shedding have been confirmed by Mabunda, who concluded that it has many stages [50]. Once effected, electricity-powered gadgets and devices switch off for hours. The households are restricted from doing or enjoying tasks and services that need electrical power. As a result, this has subjected the populace to continued bouts of load shedding. Thus, in the context of recurrent and intensifying load shedding, rural communities feel solar photovoltaic adoption has the potential to spare them from devasting effects of load shedding.

Table 3. Rural households' perceptions of solar home systems (SHSs).

Perceived Advantages of a SHS	Village Distribution	Frequency (n = 30)	Cumulative (%)	Perceived Disadvantages of Adopting a SHS	Village Distribution	Frequency (n = 30)	Cumulative (%)
A solar home system is not affected by load shedding	Duvhuledza (2) Mbahe (4) Tshamutilikwa (1)	7	23.0	A SHS does not work well during cloudy or rainy climatic conditions	Duvhuledza (4) Mbahe (7) Tshamutilikwa (6)	17	56.7
Solar technology is relatively cheap (Installation and maintenance)	Duvhuledza (3) Mbahe (4)	7	23.0	Solar equipment is expensive	Duvhuledza (1) Mbahe (11)	2	6.7
Solar technology is simple and easy to use	Duvhuledza (2)	2	6.7	Solar PV panels can be stolen easily	Duvhuledza (2) Mbahe (1) Tshamutilikwa (1)	4	13.3
The energy is derived from a renewable resource, the sun, and is environmentally friendly	Duvhuledza (1) Mbahe (1) Tshamutilikwa (2)	4	13.3	A SHS's efficiency is reduced by the presence of dust particles which are prevalent in the rural villages	Tshamutilikwa (1)	1	3.3
Once installed, the SHS does not require regular payments	Mbahe (1) Tshamutilikwa (1)	2	6.7	Solar technology produces inferior quality energy, which can power limited household appliances	Duvhuledza (2) Tshamutilikwa (1)	3	10
Solar home system adoption reduces energy supply demand on-grid connections	Tshamutshezi (1)	1	3.3				

It also emerged that 23% of the rural communities perceive solar adoption as cheap, i.e., installation and maintenance. This perception mainly came from participants from Mbahe village. Indeed, SHS installation and maintenance are relatively cheap. In Bangladesh, Momotaz and Karim posit that rural communities share the same sentiment, with over 76% indicating that the SHS cost was within the purchasing ability [51]. In Pakistan, a similar trend among rural and scattered communities was observed, where SHS was considered an affordable technology for rural and scattered communities [52]. Notably, this could be a result of the general solar financing system. According to Ngoepe et al., the pay-as-you-go billing system has demonstrated that off-grid providers go beyond promoting and providing clean and sustainable rural electrification but providing affordable financial services for profit-making [53]. Notably, about 6.7% of the participating families felt that installation and maintenance are too expensive and beyond their reach. This sentiment mainly came from Mbahe and Duvhuledza villages. In other words, the affordability of SHS is contested among rural families. Thus, as much as installation and maintenance are generally cheap, this divided perception could explain why its uptake is not encouraging in the district, as the majority are not using it.

In addition, 6.7% of rural families participating in this study believe that SHS has the propensity to help them save household financial resources. Noticeably, this view is harboured in Duvhuledza and Mbahe. This observation is in sync with the findings of [54], which concluded that SHS is a low-cost solution to rural electrification if adopted and has the potential to help in energy spending. To further bolster this perception, [55,56] have observed that the price for SHS modules has become increasingly attractive. This same sentiment is echoed by [57,58], who noted that the prices of SHS modules have drastically dropped. According to the World Bank, using SHS reduces a household's cost of lights and vulnerability to domestic health and safety hazards [3]. The SHS has become financially attractive due to heavy government subsidies [56,58].

Results have also revealed that 6.7% of the families in the selected villages perceive SHS as a simple and accessible technology. This view only emerged from Duvhuledza village. This sentiment was shared by [59] when they concluded that SHS is touted for technical quality in Bangladesh. This perception is also seen in Vietnam and Sweden [60,61]. Moreso, SHS is perceived as environmentally friendly. This is widely shared across all the participating villages. This is in sync with Missourian and Kopacek's findings which concluded that SHS is one of the environmentally friendly technologies [62]. It has also emerged that SHS, once installed, does not need regular payments. This gives this technology a comparative advantage over other technologies in the district; mainly, electricity is widely used, but people are not affording it now. Finally, the rural households believe that adopting SHS helps ease the energy supply demand from the currently overwhelmed grid connection.

As much as the rural communities in the selected villages of the Vhembe District in South Africa had positive perceptions about the technology, it needs to be highlighted that some households have negative perceptions. For instance, the majority, i.e., 56.7% of the families, believe that SHS does not work well during cloudy and rainy climatic conditions. This finding conforms with the conclusions of [63], which conclude that indigent people targeted by off-grid entrepreneurs have trust issues with the technology. In Kenya, the SHS end-users also have trust issues; however, according to Faris, the M-Kope uses local pastors to create awareness and a market for SHS [64]. Thus, all these trust issues must be dealt with for rural electrification through SHS to succeed.

Some households believe that SHS photovoltaic cells can be easily stolen. About 13% of the families participating in this study shared this view. As indicated in Table 3, two households were from Duvhuledza, each from Mbahe and Tshamutilikwa. One of the unintended results was that the participating families showed that SHS's efficiency is reduced by the accumulation of dust on the panels. A possible explanation for this result is that most of the roads in rural areas of Vhembe District are not tarred. Interestingly, system reduction due to the accumulation of dust particles was only mentioned in Tshamutilikwa, with about 3.3% of the families participating in this study. Finally, it also emerged that rural families in the Vhembe District felt that SHS does not produce adequate quality energy.

About a tenth of the respondents raised the fact that the household solar system is limited in terms of its capacity to power. They argued that an SHS could not be used to cook or iron clothes. This conforms to Taylor and So's findings, which note that solar power generation is far lower than the grid supply [65]. This reinforces the results obtained in an earlier study [20]. The latter scholars concluded that a SHS could not constantly supply power because its sources varied from one season and geographical location to another.

5. Conclusions

Even though the participating families indicated positive perceptions of solar photovoltaic technology, its proliferation in rural areas is hindered by high capital and maintenance costs. In addition, the results reveal that families in the rural communities of South Africa are still reliant on unhealthy fuels such as wood, paraffin and candles. This situation is compounded by the fact that, in Africa, more than two-fifths of the population live under USD 1.90 a day; such people are not considered for basic financial services such as

insurance, bank loans and others as they do not have a steady income, own a personal bank account and reliable credit history. Thus, SHS providers should not only leverage the financial implications of using unclean energy sources such as fossil fuels and biomass but also the financial capabilities of the end-users of the technology. Thus, Roberts suggests that solar home systems innovators need tailor-made service charges in line with the financial situation of the communities they intend to electrify.

Concisely, South African rural communities have the potential to adopt renewable energy sources, but they are not adequately harnessed. Currently, the government is subsidising more on-grid connections at the expense of off-grid connections. Central to this is the politicisation of rural electrification in South Africa. Areas earmarked for SHS encroached with grid electricity to score cheap electoral votes. Therefore, political and trade unions' interference exacerbates rural electrification challenges through SHS in South Africa. In addition, the SHS implementation programme needs to be aware of the capacity and system types. Besides the system capacity, SHS should be evaluated to improve rural communities' energy access regarding availability, reliability, quality, cost effectiveness, legal, health and safety. All this information needs should be shared with rural families who intend or who are willing to adopt an SHS. It will help decrease the prejudices harboured by the rural communities.

Author Contributions: R.C. carried out the conceptualisation, data collection, analysis and writing. J.F. and S.K. supervised and reviewed the manuscript. All authors have read and agreed to the published version of the manuscript.

Funding: This research was funded by the DST-NRF Centre of Excellence in Human Development at the University of Witwatersrand, Johannesburg, in the Republic of South Africa. Opinions expressed and the conclusion arrived at are those of the authors and not attributed to the Centre of Excellence in Human Development.

Institutional Review Board Statement: The Animal, Environment and Biosafety Research Ethics Committee under the University of Venda, Research Ethics Committee approved the study as straightforward research without ethical problems (Category 1) under ethical clearance number SARDF/21/IRD/10/1210.

Informed Consent Statement: All the research participants voluntary participated in this study. All their rights were expressed and explained clearly both in writing and verbally.

Data Availability Statement: Not applicable.

Conflicts of Interest: The authors declare no conflict of interest.

References

1. Muhumuza, R.; Zacharopoulos, A.; Mondol, J.D.; Smyth, M.; Pugsley, A. Energy consumption levels and technical approaches for supporting development of alternative energy technologies for rural sectors of developing countries. *Renew. Sustain. Energy Rev.* **2018**, *97*, 90–102. [CrossRef]
2. International Energy Agency. World Energy Outlook (WEO): Energy Access Database. 2016. Available online: https://www.iea.org/reports/world-energy-outlook-2016 (accessed on 23 May 2022).
3. World Bank. World Development Indicators. 2017. Available online: http://hdl.handle.net/10986/26447 (accessed on 3 May 2022).
4. Chafe, Z.A.; Brauer, M.; Klimont, Z.; Van Dingenen, R.; Mehta, S.; Rao, S.; Riahi, K.; Dentener, F.; Smith, K.R. Household cooking with solid fuels contributes to ambient PM2. 5 air pollution and the burden of disease. *Environ. Health Perspect.* **2014**, *122*, 1314–1320. [CrossRef]
5. Muller, C.; Yan, H. Household fuel use in developing countries: Review of theory and evidence. *Energy Econ.* **2018**, *70*, 429–439. [CrossRef]
6. Mensah, J.T.; Adu, G. An empirical analysis of household energy choice in Ghana. *Renew. Sustain. Energy Rev.* **2015**, *51*, 1402–1411. [CrossRef]
7. Yao, C.; Chen, C.; Li, M. Analysis of rural residential energy consumption and corresponding carbon emissions in China. *Energy Policy* **2012**, *41*, 445–450. [CrossRef]
8. Momodu, I.M. Domestic energy needs and natural resources conservation: The case of fuelwood consumption in Nigeria. *Mediterr. J. Soc. Sci.* **2013**, *4*, 147. [CrossRef]
9. Meyer, L.E.; Overen, O.K. Towards a sustainable rural electrification scheme in South Africa: Analysis of the Status quo. *Energy Rep.* **2021**, *7*, 4273–4287. [CrossRef]

10. Borchers, M.; Qas, N.; Guant, T.; Mavhungu, J.; Winkler, H.; Afrane-Okese, Y.; Thom, C. National Electrification Programme Evaluations: Summary Report. 2001. Available online: https://open.uct.ac.za/bitstream/handle/11427/22682/Borchers_2001.pdf?sequence=6 (accessed on 10 March 2022).
11. Kambule, N.; Yessoufou, K.; Nwulu, N.; Mbohwa, C. Exploring the driving factors of prepaid electricity meter rejection in the largest township of South Africa. *Energy Policy* **2019**, *124*, 199–205. [CrossRef]
12. Kelvin, O.O.; Edson, M.L.; Golden, M. Thermal, economic and environmental analysis of a low-cost house in Alice, South Africa. *Sustainability* **2017**, *9*, 425. [CrossRef]
13. Department of Minerals and Energy. 2003. Available online: https://www.gov.za/nso/documents/department-minerals-and-energy-annual-report-20022003 (accessed on 10 March 2022).
14. Thopil, M.S.; Bansal, R.C.; Zhang, L.; Sharma, G. A review of grid connected distributed generation using renewable energy sources in South Africa. *Energy Strategy Rev.* **2018**, *21*, 88–97. [CrossRef]
15. World Bank. Detailed Case Study: The South African Solar Home System (SHS) Concessions, Evaluation of Rural Electrification Concessions in Sub-Saharan Africa. Available online: http://documents.worldbank.org/curated/en/708211498162775424/pdf/116659-WP-PUBLIC-P150241-37p-Detailed-Case-Study-South-Africa.pdf (accessed on 10 April 2022).
16. Conway, D.; Robinson, B.; Mudimu, P.; Chitekwe, T.; Koranteng, K.; Swilling, M. Exploring hybrid models for universal access to basic solar energy services in informal settlements: Case studies from South Africa and Zimbabwe. *Energy Res. Soc. Sci.* **2019**, *56*, 101202. [CrossRef]
17. Eberhard, A.; Kolker, J.; Leigland, J. *South Africa's Renewable Energy IPP Procurement Program: Success Factors and lLessons*; World Bank Group 1202; World Bank: Washington, DC, USA, 2014; Available online: https://openknowledge.worldbank.org/handle/10986/20039 (accessed on 13 May 2022).
18. Department of Minerals and Energy. 2015. Available online: https://www.platinumiris.co.za/wp-content/uploads/doe/01/2015%20-%202016%20Department%20of%20Energy%20Annual%20Report.pdf (accessed on 12 June 2022).
19. Barrie, J.; Cruickshank, H.J. Shedding light on the last mile: A study on the diffusion of Pay as You Go Solar Home Systems in Central East Africa. *Energy Policy* **2017**, *107*, 425–436. [CrossRef]
20. Akikur, R.K.; Saidur, R.; Ping, H.W.; Ullah, K.R. Comparative study of stand-alone and hybrid solar energy systems suitable for off-grid rural electrification: A review. *Renew. Sustain. Energy Rev.* **2013**, *27*, 738–752. [CrossRef]
21. Van der Kroon, B.; Brouwer, R.; Van Beukering, P.J. The energy ladder: Theoretical myth or empirical truth? Results from a meta-analysis. *Renew. Sustain. Energy Rev.* **2013**, *20*, 504–513. [CrossRef]
22. Hoffman, H.; Uckert, G.; Reif, C.; Muller, K.; Sieber, S. Traditional biomass energy consumption and the potential introduction of firewood efficient stoves: Insight from western Tanzania. *Reg. Environ. Chang.* **2015**, *15*, 1191–1201. [CrossRef]
23. Campbell, B.M.; Vermeulen, S.J.; Mangono, J.J.; Mabugu, R. The energy transition in action: Urban domestic fuel choices in changing Zimbabwe. *Energy Policy* **2003**, *31*, 553–562. [CrossRef]
24. Uhunamure, S.E.; Nethengwe, N.S.; Tinarwo, D. Correlating the factors influencing household decisions on adoption and utilisation of biogas technology in South Africa. *Renew. Sustain. Energy Rev.* **2019**, *107*, 264–273. [CrossRef]
25. Arthur, M.; Bond, C.A.; Willson, B. Estimation of elasticities for domestic energy demand in Mozambique. *Energy Econ.* **2012**, *34*, 398–409. [CrossRef]
26. Zaku, S.G.; Abdallah, A.; Olayande, J.S.; Kabir, A.; Tukur, A. Comparative studies of household energy use in Nigeria: A case of Gwagwalada and Gwako in Gwagwalada Area Council of Abuja FCT. *Swift J. Econ. Int. Financ.* **2015**, *1*, 5–9.
27. Creswell, J.W.; Tashakkori, A. Differing perspectives on mixed methods research. *J. Mix. Methods Res.* **2007**, *1*, 303–308. [CrossRef]
28. Morse, J.M. The significance of saturation. *Qual. Health Res.* **1995**, *5*, 147–149. [CrossRef]
29. Bernard, H.R. *Research Methods in Anthropology: Qualitative and Quantitative Approaches*, 5th ed.; Rowman Altamira: New York, NY, USA, 2011.
30. LeCompte, M.D.; Schensul, J.J. *Designing and Conducting Ethnographic Research: An Introduction*; Rowman Altamira: New York, NY, USA, 2010; Volume 1.
31. Motjoadi, V.; Bokoro, P.N.; Onibonoje, M.O. A review of microgrid-based approach to rural electrification in South Africa: Architecture and policy framework. *Energies* **2020**, *13*, 2193. [CrossRef]
32. Rahut, D.; Behera, B.; Ali, A. Factors determining household use of clean and renewable energy sources for lighting in Sub-Saharan Africa. *Renew. Sustain. Energy Rev.* **2017**, *72*, 661–672. [CrossRef]
33. Ahlborg, H.; Hammar, L. Drivers and barriers to rural electrification in Tanzania and Mozambique Grid-extension, off-grid, and renewable energy technologies. *Renew. Energy* **2014**, *61*, 117–124. [CrossRef]
34. Griffin, N.J.; Banks, D.I.; Mavrandonis, J.; Shackleton, C.M.; Shackleton, S.E. *Household Energy and Wood Use in a Peripheral Rural Area of the Eastern Transvaal Lowveld*; Department of Mineral and Energy Affairs: Pretoria, South Africa, 1992.
35. Davis, M. Rural household energy consumption: The effects of access to electricity—Evidence from South Africa. *Energy Policy* **1998**, *26*, 207–217. [CrossRef]
36. Howells, M.I.; Alfstad, T.; Victor, D.G.; Goldstein, G.; Remme, U. A model of household energy services in a low-income rural African village. *Energy Policy* **2005**, *33*, 1833–1851. [CrossRef]
37. Madubansi, M.; Shackleton, C.M. Changing energy profiles and consumption patterns following electrification in five rural villages, South Africa. *Energy Policy* **2006**, *34*, 4081–4092. [CrossRef]
38. Sepp, S. *Multiple Household Fuel Use: A Balanced Choice between Firewood, Charcoal and LPG*; GIZ: Frankfurt, Germany, 2014.

39. Uhunamure, S.E.; Nethengwe, N.S.; Musyoki, A. Driving forces for fuelwood use in households in the Thulamela Municipality, South Africa. *J. Energy S. Afr.* **2017**, *28*, 25–34. [CrossRef]
40. Aliyu, A.K.; Modu, B.; Tan, C.W. A review of renewable energy development in Africa: A focus in South Africa, Egypt and Nigeria. *Renew. Sustain. Energy Rev.* **2018**, *81*, 2502–2518. [CrossRef]
41. Banks, D.; Schäffler, J. The Potential Contribution of Renewable Energy in South Africa. Johannesburg, South Africa: Sustainable Energy & Climate Change Project (SECCP). 2006. Available online: https://www.ee.co.za/wp-content/uploads/legacy/Gener%201.pdf (accessed on 13 April 2022).
42. Ab Kadir, M.Z.A.; Rafeeu, Y.; Adam, N.M. Prospective scenarios for the full solar energy development in Malaysia. *Renew. Sustain. Energy Rev.* **2010**, *14*, 3023–3031. [CrossRef]
43. South African Energy Outlook. 2019. Available online: https://www.iea.org/reports/africa-energy-outlook-2019 (accessed on 3 March 2022).
44. International Energy Agency. 2014. Available online: https://www.iea.org/reports/world-energy-outlook-2014 (accessed on 3 March 2022).
45. Das, S.; De Groote, H.; Behera, B. Determinants of household energy use in Bhutan. *Energy* **2014**, *69*, 661–672.
46. Behera, B.; Jeetendra, A.; Ali, A. Household collection and use of biomass energy sources in South Asia. *Energy* **2015**, *85*, 468–480. [CrossRef]
47. Mishra, V. Indoor air pollution from biomass combustion and acute respiratory illness in preschool age children in Zimbabwe. *Int. J. Epidemiol.* **2003**, *32*, 847–853. [CrossRef]
48. Statistics South Africa. General Household Survey 2014. Report Number P0318. Available online: http://www.statssa.gov.za/publications/P0318/P03182014.pdf (accessed on 10 April 2022).
49. Piliso, P.; Senzanje, A.; Dhavu, K. The extent, characteristics and potential of solar powered irrigation systems in South Africa. *J. Energy S. Afr.* **2021**, *32*, 26–40. [CrossRef]
50. Mabunda, N.E. Use of Photovoltaic Energy to Minimise the Impact of Load-shedding in South Africa. In Proceedings of the 2021 International Conference on Electrical 2021, Computer and Energy Technologies (ICECET), Cape Town, South Africa, 9–10 December 2021; IEEE: Piscataway, NJ, USA, 2021; pp. 1–4.
51. Momotaz, S.N.; Karim, A.M. Customer satisfaction of the solar home system service in Bangladesh. *World* **2012**, *2*, 193–210.
52. Omara, Z.M.; Kabeel, A.E.; Abdullah, A.S. A review of solar still performance with reflectors. *Renew. Sustain. Energy Rev.* **2017**, *68*, 638–649. [CrossRef]
53. Ngoepe, T.; Henriksen, T.F.; Power, A.P.; Panulo, B.; Modungwa, B.; Scholtz, L.; Gulati, M. Switching on Finance for Off-Grid Energy. Bertha Centre, WWF-SA. 2016. Available online: https://gsbberthacentre.uct.ac.za/researching/switching-on-finance-for-off-grid-energy/ (accessed on 10 April 2022).
54. IEA. *Energy Access Outlook 2017: From Poverty to Prosperity*; International Energy Agency: Paris, France, 2017. [CrossRef]
55. Mitscher, M.; Rüther, R. Economic performance and policies for grid-connected residential solar photovoltaic systems in Brazil. *Energy Policy* **2012**, *49*, 688–694. [CrossRef]
56. Urmee, T.; Harries, D. Determinants of the success and sustainability of Bangladesh's SHS program. *Renew. Energy* **2011**, *36*, 2822–2830. [CrossRef]
57. Azimoh, C.L.; Klintenberg, P.; Wallin, F.; Karlsson, B. Illuminated but not electrified: An assessment of the impact of Solar Home System on rural households in South Africa. *Appl. Energy* **2015**, *155*, 354–364. [CrossRef]
58. Waleedm, A.; Javed, M.R.; Riaz, M.T.; Virk, U.S.; Khan, S.; Mujtaba, A.; Ahmas, S.; Arshad, G. Study on Hybrid Wind-Solar System for Energy Saving Analysis in Energy Sector. In Proceedings of the 2020 3rd International Conference on Computing, Mathematics and Engineering Technologies (iCoMET), Sukkur, Pakistan, 29–30 January 2020; pp. 1–6. [CrossRef]
59. Qureshi, T.M.; Ullah, K.; Arentsen, M.J. Factors responsible for solar PV adoption at household level: A case of Lahore, Pakistan. *Renew. Sustain. Energy Rev.* **2017**, *78*, 754–763. [CrossRef]
60. Do, T.N.; Burke, P.J.; Baldwin, K.G.; Nguyen, C.T. Underlying drivers and barriers for solar photovoltaics diffusion: The case of Vietnam. *Energy Policy* **2020**, *144*, 111561. [CrossRef]
61. Palm, A. Local factors driving the diffusion of solar photovoltaics in Sweden: A case study of five municipalities in an early market. *Energy Res. Soc. Sci.* **2016**, *14*, 1–12. [CrossRef]
62. Masoumian, M.; Kopacek, P. End-of-life management of photovoltaic modules. *IFAC-PapersOnLine* **2015**, *48*, 162–167. [CrossRef]
63. Rastogi, C. M-Kopa solar: Lighting up the dark continent. *South Asian J. Bus. Manag. Cases* **2018**, *7*, 93–103. [CrossRef]
64. Faris, S.; Bloomberg. The Solar Company Making a Profit on Poor Africans. pp. 1–4. 2015. Available online: www.bloomberg.com/features/2015-mkopa-solar-in-africa/ (accessed on 1 April 2022).
65. Taylor, M.; So, E.Y. *Solar PV in Africa: Costs and Markets*; IRENA: Bonn, Germany, 2016.

water

MDPI

Review

A Systematic Bibliometric Review of Low Impact Development Research Articles

Jin You [1,2], Xiang Chen [3,4], Liang Chen [3,4], Jianghai Chen [3,4], Beibei Chai [1,2,*], Aiqing Kang [5], Xiaohui Lei [5] and Shuqian Wang [1]

[1] School of Water Conservancy and Hydroelectric Power, Hebei University of Engineering, Handan 056021, China
[2] Hebei Key Laboratory of Intelligent Water Conservancy, Hebei University of Engineering, Handan 056038, China
[3] Shanghai Investigation, Design and Research Institute Co., Ltd., Shanghai 200434, China
[4] China Three Gorges Corporation, Wuhan 430010, China
[5] State Key Laboratory of Simulation and Regulation of Water Cycle in River Basin, China Institute of Water Resources and Hydropower Research, Beijing 100038, China
* Correspondence: cbb21@163.com; Tel.: +86-153-4926-8338

Abstract: The concept of low impact development (LID) plays a crucial role in rainstorm management and non-point source pollution prevention and control. Sorting and summarizing related research through the knowledge map can objectively present the disciplinary structure, research focus, and research hotspots of the LID research. Based on 2103 LID pieces of literature in Chinese and English included in the web of science (WOS) database and China's integrated knowledge resources system (CNKI) database from 2004 to 2021, this paper aims to perform statistical analysis from three aspects: bibliometrics, keyword hotspot co-occurrence and clustering, and literature co-citation clustering. The obtained results reveal that research on LID-based issues maintains a high degree of enthusiasm in China and abroad, but their corresponding focuses are dissimilar. Foreign research essentially focuses on the environmental field with frequent interdisciplinary phenomena, combining the triple goals of water quality improvement, runoff reduction, and multi-functional expansion, and is committed to solving the impact of uncertain factors on urban stormwater management in extreme climates. Chinese research is mostly aimed at unlocking practical engineering problems, which also leads to the majority of research works in the field of building science and engineering. This is mainly due to a series of water-related problems caused by the change in land use types in China. The researchers have determined the type, quantity, location, and combination of the optimal LID measures by establishing appropriate models, using optimization algorithms, and developing multi-level analysis methods. Although the multi-dimensional results of LID in recent years have greatly expanded the framework paradigm, most of the conducted research works are still biased towards the micro-scale. The present hotspot research considers how to make a macroscopic overall layout and efficiently cooperate with the pipelines network, rivers, and lakes systems to unlock the problems pertinent to urban rainwater and non-point source pollution.

Keywords: low impact development (LID); visual analysis; CiteSpace software; research hotspots

Citation: You, J.; Chen, X.; Chen, L.; Chen, J.; Chai, B.; Kang, A.; Lei, X.; Wang, S. A Systematic Bibliometric Review of Low Impact Development Research Articles. *Water* **2022**, *14*, 2675. https://doi.org/10.3390/w14172675

Academic Editor: Dibyendu Sarkar

Received: 18 July 2022
Accepted: 26 August 2022
Published: 29 August 2022

Publisher's Note: MDPI stays neutral with regard to jurisdictional claims in published maps and institutional affiliations.

Copyright: © 2022 by the authors. Licensee MDPI, Basel, Switzerland. This article is an open access article distributed under the terms and conditions of the Creative Commons Attribution (CC BY) license (https://creativecommons.org/licenses/by/4.0/).

1. Introduction

Urbanization, industrialization, and climate change significantly affect the intensity, incidence, and duration of extreme weather events, such as floods, urban waterlogging, and nonpoint source pollution [1]. Traditional stormwater management involves the quick discharge of excess stormwater through a centralized drainage system to ensure urban water security [2]. However, the management approach is unsustainable and brings the challenges of groundwater resource depletion, unnatural redistribution of water resources, and excessive carbon emissions [3]. In view of the increasingly severe ecological and

environmental problems, the low impact development (LID) [4,5] design concept based on rain gardens was first proposed in the United States, and relative technical standards was compiled in 1999. Subsequently, various urban stormwater management concepts have been adopted, such as Australia's Water Sensitive Urban Design (WSUD) [6], Sustainable Urban Discharge System (SUDS) [7] in Europe, and China's Sponge City [8,9]. These stormwater management methodologies are aimed at achieving a healthy urban water cycle by coordinating the LID stormwater system, urban stormwater pipes and canal system, and the excess stormwater runoff discharge system. The LID is an essential part of stormwater management that emphasizes green priority and source control. Through green LID measures such as bioretention, grass trenches, and green roofs, urban stormwater can be managed from the source via infiltration, storage, regulation, transfer, and pollutant interception and purification [10]. By increasing investigations on the LID, more and more results have proved that LID lessens the total amount of runoff [11,12] and peak flood flow [13], delays the peak flood time [14], rises the infiltration rate [15], and reduce the pollution load [16]. However, it leads to obtaining synergistic benefits in terms of water environment and ecology [17].

By collecting LID-based articles published from 2004 to 2021 in Chinese and English in accordance with the WOS and CNKI databases, the information visualization analysis was performed using appropriate software entitled "CiteSpace". The main objective of exploiting this specific software is to conduct statistical analysis and visual map demonstration from various aspects. The most important ones include bibliometrics, hotspot keyword co-occurrence and clustering, and co-citation clustering, in an effort to systematically review the current LID research. While exploring the LID research by international scholars, the research status in China is also reviewed. In the context of the sponge city construction and sustainable development in China, the research is aimed at providing rational solutions for some crucial issues such as urban waterlogging, groundwater resource depletion, and urban nonpoint source pollution.

2. Method and Data Processing

In recent years, the bibliometric literature review has been broadly performed in hydrology [1,18], ecology [19], regenerative medicine [20], and other fields. Using visualization software, one can directly, clearly, and vividly diagnose the dynamic evolution, development trend, research progress, and hotspots in the research field. CiteSpace [21,22] is extensively utilized in analyzing keywords and citations of articles due to its powerful function, excellent visualization effects, and rich layouts. Keywords are direct descriptions of the content and theme of a study, and citations comprehensively display the study details and the development trend. In the keyword co-occurrence analysis, the frequency of keywords usually reveals the evolution of keyword hotspots in the field of research and the strength of individual keywords. In combination with burst terms, it can review the volatile hotspots in the research field and explore the potential applications. Keyword cluster analysis is to classify data into various groups according to the homogeneity between keywords to obtain high support directions of different categories. Co-citation analysis can be utilized to show the research content of key nodes, such that it is convenient for researchers to summarize current research clusters and analyze future research directions.

In the present scrutiny, a total of 2103 articles in the field of LID research are collected. Of which, 1053 articles written in English are retrieved from the Web of Science (WOS) database. The timeframe is between 2004 and September 2021. The keyword used in the literature search is low impact development. The literature type is limited to articles. The CNKI database is also exploited for Chinese literature retrieval, the understudy timeframe is between 2009 and September 2021, the keyword used for search is "low impact development + LID", and the literature type includes both journal publications and dissertations, and a total of 1050 articles are collected. Then, the CiteSpace5.6.R5 software (CiteSpace 5.6.R5, Chaomei Chen: Philadelphia, PA, USA) is employed to analyze the quantity, subject categories, keywords, and co-citations of the included articles. This software can summa-

rize the research status, progress, and hotspots, as well as the associated problems with those studies. Finally, research prospects are proposed and explained in some detail.

3. Bibliometric Analysis of LID-Based Research Articles

Based on the bibliometric analysis of the data derived from WOS and CNKI, the variation of the annual number of publications and the cumulative number is demonstrated in Figure 1. It can be seen from Figure 1 that the cumulative numbers of articles written in Chinese and English are generally comparable. The LID research abroad emerged in 2004, and then the annual number of articles has steadily grown. The Chinese articles on the LID originated in 2009, and the number of articles rapidly increased after 2015. The concept of LID is originally proposed by the Prince George's County Department of Environmental Resources in the US. Subsequently, on the basis of the LID concept, several other concepts are proposed globally, such as Australia's Water Sensitive Urban Design (WSUD), New Zealand's Low Impact Urban Design and Development (LIUDD) program, Sustainable Urban Drainage System (SUDS) in Europe and the Sponge Cities in China. In Graham et al. [23] published in 2004, the specific concept of "Low Impact Development" was employed for the first time, and the efficiency of the LID measures such as bioretention, green roofs, and permeable pavement was assessed through water balance simulation. In China, the construction of pilot sponge cities in 2015 can be regarded as a key time point in the LID research.

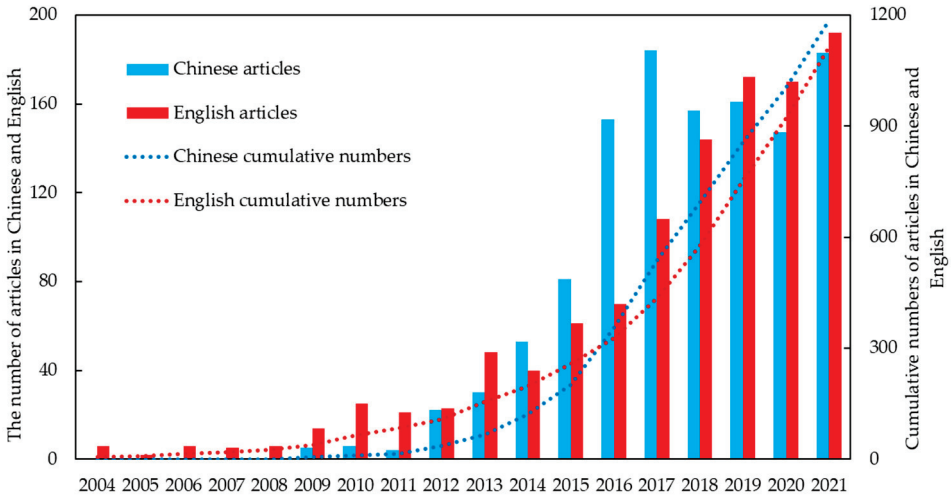


Figure 1. The number of published papers on the LID framework research from 2004 to 2021.

From the subject categories of the WOS literature as presented in Table 1, the largest categories of English articles are Environmental Sciences & Ecology, Environmental Sciences, and Water Resources. In these English-based studies, the runoff and pollution caused by heavy rainfall have been managed through source control such that the development area has a natural hydrological cycle as much as possible. Islam et al. [1] proposed the overall goals of the LID, which includes: (1) comprehensive control of the precipitation and water quality, (2) control of the runoff from the source as much as possible, (3) increasing urban hydrological processes, such as evaporation, infiltration, and storage, and (4) improving ecological benefits. In addition to the theoretically performed research, the application of LID in various fields, including engineering, civil engineering, and engineering and environment, has been examined by abroad researchers.

Table 1. The subject categories of the LID research based on the WOS database.

No.	Quantity	Centrality	Subject
1	689	0.35	Environmental Sciences & Ecology
2	637	0.11	Environmental Sciences
3	560	0.08	Water Resources
4	467	0.53	Engineering
5	232	0.16	Engineering & Civil
6	212	0.03	Engineering & Environmental

Different from of the research abroad, the largest categories of Chinese-based studies include Construction Science & Engineering and Water Conservancy & Hydropower Engineering (see Table 2). This is mainly attributed to the fact that the rapid urbanization in China is the primary challenge for urban stormwater management. The increase in urban construction land has changed rivers outside the city into inland rivers, reducing stormwater storage space, increasing impervious areas, and aggravating urban waterlogging. Moreover, urban construction has a huge impact on the ecological environment and exerts great pressure on water security. With the construction of the pilot sponge cities in 2015, Chinese scholars have conducted extensive examinations on the difficulties and demands in the construction of sponge cities, which greatly expand the application field of the LID research.

Table 2. The subject categories of the LID research based on the CNKI database.

No.	Quantity	Centrality	Subject
1	919	61.27	Construction Science & Engineering
2	357	23.80	Water Conservancy & Hydropower Engineering
3	88	5.87	Environmental Science and Resource Utilization
4	72	4.80	Road and Water Transportation
5	8	0.53	Resource Science
6	4	0.27	Gardening

4. International LID Research Progress

4.1. Keyword Co-Occurrence Analysis of Research Topics

The LID is a novel stormwater management method, and its whole evolution can be divided into the formation and development stages. According to the statistics of high-frequency keywords (see Table 3), the formation stage can be rationally considered in the time interval of 2004–2014. In this stage, the context of the LID research is finalized, and the impact on the hydrological cycle, model simulation, and practical application are discussed. The top keywords include Performance, System, as well as those representing crucial components of the hydrological cycle such as Runoff, Infiltration, and Water Quality. The SWMM is broadly utilized in the LID research due to its excellent hydrological and hydrodynamic simulation performance. In addition, Bioretention and Green Infrastructure are also repeatedly mentioned as potential application directions. The development stage of the LID started in 2015. In this stage, the focus is on the Optimization, Uncertainty, and Resilience along with Management Practice. The research content involves perfecting the LID research framework, as well as addressing new demands such as water security and water ecology brought about by global climate change.

Table 3. The high-frequency keywords of publications according to the WOS database.

Stage	Keywords (Frequency/Centrality)
Formation stage (2004–2014)	LID (503/0.04); runoff (249/0.05); performance (220/0.02); stormwater management (191/0.06); system (153/0.09); urbanization (140/0.07); bioretention (137/0.06); green infrastructure (133/0.04); water quality (113/0.04); model (107/0.03); SWMM (105/0.03); infiltration (79/0.08)
Development stage (2015–2021)	optimization (68/0.01); management practice (63/0.01); infrastructure (31/0.01); city (30/0.02); urban runoff (28/0.01); uncertainty (25/0.04); benefit (22/0.01); resilience (17/0.01); reduction (17/0.01)

It can be found based on the burst terms in English-based articles (see Table 4, red colors represent the year of the burst terms appeared) that Stormwater Management has been a research hotspot throughout the research period due to its central role in the LID-based research. The LID measures such as Porous Pavement and Bioretention emerged as short-term research hot topics. In recent years, the hotspots have shifted to Stormwater Management Model and Challenges due to global climate change.

Table 4. Keywords burst detection of publications based on the WOS database.

Keywords	Year	Strength	Begin	End	2004–2021
best management practice	2004	8.5	2004	2015	
infiltration	2004	7.22	2004	2015	
storm water management	2004	3.81	2004	2015	
storm water	2004	6.2	2005	2016	
porous pavement	2004	6.53	2007	2017	
retention	2004	4.8	2007	2016	
quantity	2004	3.82	2007	2010	
hydrology	2004	4.89	2008	2013	
stream	2004	4.42	2008	2017	
water	2004	4.47	2009	2014	
bioretention	2004	3.79	2009	2013	
North Carolina	2004	5.6	2010	2014	
pollutant removal	2004	5.53	2011	2015	
storm water management	2004	3.94	2011	2012	
land use change	2004	5.41	2015	2016	
urban runoff	2004	5.25	2015	2017	
modeling	2004	4.14	2015	2017	
rainfall	2004	5.67	2019	2021	
challenge	2004	4.49	2019	2021	
storm water management model	2004	3.85	2019	2021	

Notes: Red colors represent the year of the burst terms appeared.

4.2. Keyword Cluster Analysis

According to the keyword clustering (see Table 5) and the timeline view of clustering (see Figure 2), it is detectable that the research on Bioretention (#0) is relatively independent, and the experimental analysis and water quality improvement (contaminant removal rate) have been the focused of the clustering study. In contrast, the other LID measures such as Green Roof (#2) and Green Infrastructure (#4) focused more on the model simulation and water reduction (e.g., total runoff, peak flow, and peak flood time). Additionally, landscape ecological benefit is a performance indicator of all LID measures. Liu et al. [24] conducted a detailed investigation on the principle, design, performance, advantages, disadvantages, and costs of LID measures such as bioretention ponds, grass-planting trenches, sunken green spaces, green roofs, permeable pavements, rainwater tanks, and roof truncations.

Optimization (#3) and Climate Change (#7) are the focus of the current research, the clustering keywords such as Optimization, Uncertainty, Cost-effectiveness, Climate change, and Urbanization represent the hot topics and the leading edge of the current research. In the cluster, the cost has been considered as the objective function in some articles, and they are aimed to scrutinize the distribution strategy for reducing the total runoff, peak runoff, and pollutant load. With more and more in-depth investigations, some scholars have commenced considering the influences of externally uncertain conditions such as climate change, urbanization, and rainfall. Furthermore, the parameter optimization of the LID measures (e.g., NSGA II, PSO, MOALOA) and multi-criteria methods [25] (e.g., AHP, TOPSIS) has attracted much attention. Gogate et al. [26] employed AHP and TOPSIS multi-criteria analysis approaches to choose the best storm control measures. Li et al. [27] discovered the optimal combination of LID measures and retention tanks by combining the SWMM model with the PSO algorithm. The SWMM is the most common model exploited in the LID research. Kaykhosravi et al. [28] conducted a comprehensive analysis of eleven LID models as a function of the model characteristics, hydrology, and hydraulic modules and found that the SWMM had the best applicability.

Table 5. The keyword clustering of the publications based on the WOS database.

Cluster Name	Size	Homogeneity	Research Topic (log Likelihood Ratio/*p* Value)
#0 bioretention	112	0.616	bioretention (48.76/0.001); SWMM (31.51/0.001); stormwater (30.66/0.0001)
#1 sponge city	106	0.457	sponge city (38.37/0.0001); bioretention (18.038/0.001); urban catchment (13.75/0.001); water quality (13.68/0.001); sustainablity (13.19/0.001)
#2 green roof	69	0.669	green roof (28.95/0.0001); porous pavements (21.32/0.0001); permeable pavement (21.04/0.0001)
#3 optimization	61	0.694	optimization (37.09/0.0001); cost (17.07/0.001); management practice (16.46/0.0001); uncertainty (11.33/0.001)
#4 green infrastructure	57	0.697	green infrastructure (24.35/0.0001); stormwater management (20.31/0.001); urban hydrology (17.28/0.0001)
#5 low impace development	36	0.745	low impact development (32.02/0.0001); SWMM model (28/0.0001); LID (12.97/0.001)
#6 constant head test	34	0.829	constant head test (12/0.001); pollution (12/0.001); sensitivity analysis (10/0.005)
#7 climate change	33	0.784	climate change (35.15/0.0001); urbanization (31.45/0.05); land use (13.78/0.001)
#8 SWMM	28	0.873	SWMM (44.37/0.0001); water quality (10.5/0.005); conservation subdivision (10.17/0.005)

4.3. Co-Citation Clustering Analysis

Based on the co-citation clustering (see Table 6) and the co-citation references clustering network (see Figure 3), it can be seen that the LID research can be divided into the three major groups: optimization (#0 multi-objective optimization), principle (#1 hydrology, #2 groundwater, and #6 first flush effect), and application (#3 sponge city, #4 LID practices, #5 green roof). It can be seen from the clustering timeline (see Figure 4) that the research on the principle of the LID originated in the field of hydrology. Since 2004, a large number of investigations have been carried out on the impact of the LID measures on the hydrological processes, which demonstrate that precipitation is the main factor that affects the hydrological process of the LID measures. Qin et al. [29] systematically examined extreme rainfall events with various precipitation, duration, and peak intensity, and analyzed the performance of the LID measures due to different precipitation characteristics. Since 2012, urban hydrology and groundwater recharge have become the research hotspots. Palla and Gnecco [10] conducted a simulation examination of the LID-based systems on the urban watershed scale and validated the effectiveness of the LID measures in various rainfall return periods. In the past few years, the research on the principle of the LID

measures mostly focused on the initial scour effect, which is also the main reason for the urban nonpoint source pollution. Yang et al. [30] proposed an appropriate classification standard for multi-objective stormwater management, which is employed to select suitable bioretention facilities considering multiple performance objectives (e.g., reduction of initial scour effect, and lessening of the total runoff and peak flow).

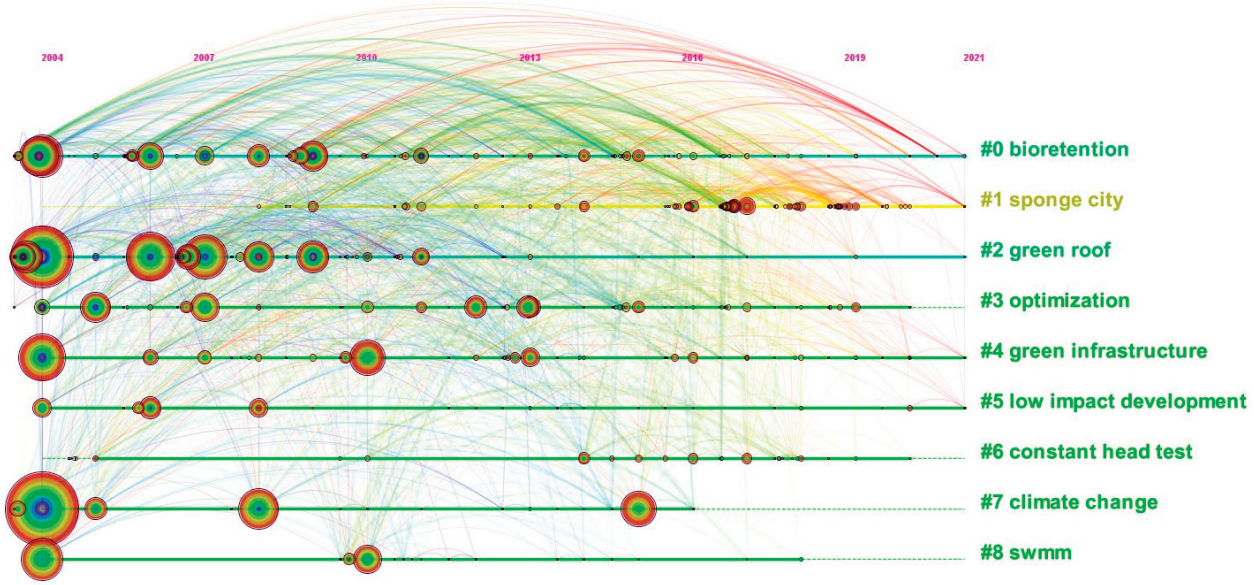


Figure 2. The time-line view of the keywords clustering based on the WOS.

Table 6. The co-citation clustering of the LID research according to the WOS.

Cluster	Size	Homogeneity	Average Year	Research Topic (log Likelihood Ratio/*p* Value)
#0 multi-objective optimization	163	0.717	2017	multi-objective optimization (11.77/0.001); optimization (10.98/0.001); SWMM (8.97/0.005); climate change (6.33/0.05); sustainable urban drainage systems (6.02/0.05); life cycle cost (5.77/0.05)
#1 hydrology	132	0.902	2008	hydrology (22.52/0.0001); bioretention (14.78/0.001); SWMM (12.47/0.001); sponge city (12.23/0.001); sustainable development (12.06/0.001)
#2 groundwater	85	0.781	2014	groundwater (9.36/0.005); urban hydrology (9.08/0.005); green infrastructure (12.47/0.001); groundwater recharge (7.95/0.005)
#3 sponge city	71	0.796	2016	sponge city (25.75/0.0001); bioretention (12.92/0.001); urban sustainability (7.81/0.01)
#4 LID practices	57	0.875	2011	LID practices (6.77/0.01)
#5 green roof	52	0.897	2013	green roof (26.31/0.0001); LID (12.2/0.001); retention (10.79/0.005)
#6 first flush effect	46	0.95	2017	first flush effect (10.22/0.0005); denitrification (10.22/0.005); stormwater runoff (8.93/0.005)
#7 sustain	30	0.921	2011	sustain (6.93/0.01); site selection (6.13/0.05); LID-BMPs (6.13/0.05)
#8 conservation subdivision	26	0.979	2007	conservation subdivision (16.32/0.0001); experimental auction (8.13/0.005)
#10 benefit cost ratios	21	0.952	2002	benefit cost ratios (10.43/0.005); conservation (10.43/0.005); water balance (7.67/0.01)

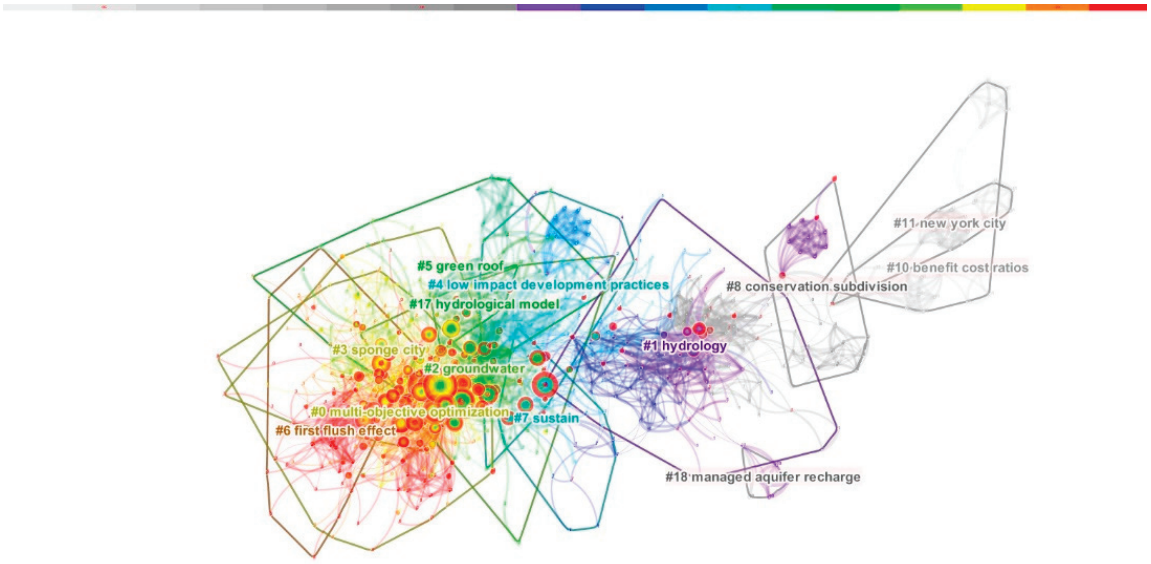


Figure 3. The co-citation references clustering network of the LID framework research based on the WOS.

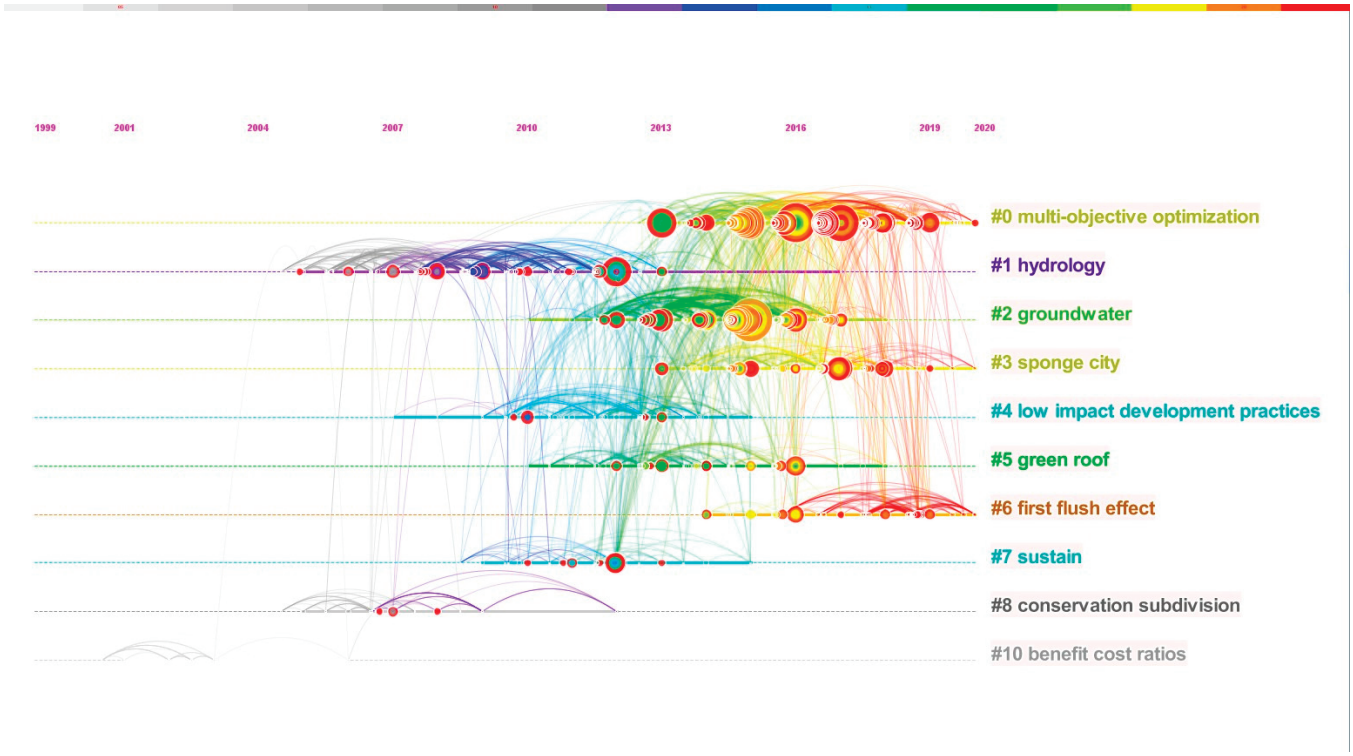


Figure 4. The time-line view of the LID framework research based on the WOS.

Table 7 presents high-cited literatures in the field of low-impact development re-search. From the perspective of literature citations, scholars in other countries have examined green infrastructure and bioretention in the early stage. However, after 2015, the performed research works have been mainly focused on the construction of sponge cities in China. For instance, Xia et al. [31] and Li et al. [32] summarized the opportunities and challenges facing the construction of sponge cities in China. LID optimization has been a hot topic since it was first mentioned in 2013. The relevant studies adopted the SWMM and optimization algorithm to solve the objective function (e.g., water quantity [33,34], water quality [35], and

cost minimization [36], thereby determining the optimal deployment of the LID measures. Some other explorations also considered uncertainties in the input parameters such as precipitation, anti-seepage coefficients, accumulation and scour coefficients, as well as changes brought about by climate change [37] and land-use type [38].

Table 7. The key publications from co-citation references clustering according to the WOS.

Frequency	Year	Author	Title
122	2017	Eckart et al. (2017) [8]	Performance and implementation of low impact development—A review
109	2015	Fletcher et al. (2015) [9]	SUDS, LID, BMPs, WSUD and more—The evolution and application of terminology surrounding urban drainage
79	2015	Palla and Gnecco (2015) [10]	Hydrologic modeling of Low Impact Development systems at the urban catchment scale
75	2016	Ahiablame and Shakya (2016) [13]	Modeling flood reduction effects of low impact development at a watershed scale
75	2016	Chui et al. (2016) [36]	Assessing cost-effectiveness of specific LID practice designs in response to large storm events
64	2013	Qin et al. (2013) [29]	The effects of low impact development on urban flooding under different rainfall characteristics
61	2012	Ahiablame et al. (2012) [5]	Effectiveness of low impact development practices: literature review and suggestions for future research
58	2015	Baek et al. (2015) [33]	Optimizing low impact development (LID) for stormwater runoff treatment in urban area, Korea: Experimental and modeling approach
51	2015	Liu et al. (2015a) [34]	Enhancing a rainfall-runoff model to assess the impacts of BMPs and LID practices on storm runoff
50	2015	Rosa et al. (2015) [39]	Calibration and verification of SWMM for low impact development
49	2017	Kong et al. (2017) [38]	Modeling stormwater management at the city district level in response to changes in land use and low impact development
47	2015	Jia et al. (2015) [40]	LID-BMPs planning for urban runoff control and the case study in China
46	2019	Li et al. (2019) [41]	Comprehensive performance evaluation of LID practices for the sponge city construction: A case study in Guangxi, China
45	2018	Eckart et al. (2018) [42]	Multiobjective optimization of low impact development stormwater controls
44	2017	Xia et al. (2017) [31]	Opportunities and challenges of the sponge city construction related to urban water issues in China
41	2015	Martin-Mikle et al. (2015) [43]	Identifying priority sites for low impact development (LID) in a mixed-use watershed
40	2017	Mao et al. (2017) [44]	Assessing the ecological benefits of aggregate LID-BMPs through modelling
40	2017	Li et al. (2017) [32]	Sponge city construction in China: A survey of the challenges and opportunities
40	2018	Zhang and Chui (2018) [45]	A comprehensive review of spatial allocation of LID-BMP-GI practices: Strategies and optimization tools
39	2015	Liu et al. (2015b) [35]	Evaluating the effectiveness of management practices on hydrology and water quality at watershed scale with a rainfall-runoff model

5. LID Research Progress in China

5.1. Keyword Co-Occurrence Analysis of Research Topics

According to the high-frequency keywords listed in Table 8, the research contents of Chinese articles in the formation stage (i.e., the time interval of 2009–2014) are basically the same as those of English articles, mainly focusing on the nature of LID and sponge cities, as well as the applications of both the SWMM and SUSTAIN models. In the development stage (i.e., the time interval of 2015-present), different from research works abroad that have focused on global climate change, China's research works have been mostly focused on solving the negative effects of urbanization, including an in-depth exploration of landscape design and sponge city construction such as rainfall gardens, LID facilities, landscaped

gardens, and sponge campuses. It is should be noticed that at this stage, the total annual runoff control is proposed as the general target of the LID design in China, and the concept of sustainable development of sponge city construction is also defined.

Table 8. The high-frequency keywords of publications according to the CNKI database.

Stage	Keywords (Frequency/Centrality)
Formation stage (2009–2014)	LID (756/1.21); Sponge city (336/0.26); SWMM mode (125/0.11); Stormwater management (57/0.03); Rainwater utilization (37/0.01); Cost-effectiveness(31/0.01); Urban waterlogging (29/0.01); Runoff control (274/0.01); Urbanization (24/0.01); Green roof(17/0.01); Non-point source pollution (16/0.00); SUSTAIN model(15/0.00)
Development stage (2015–2021)	Rainfall garden (35/0.01); Landscape design (31/0.01); LID facilities(22/0.04); Landscape garden (21/0.01); Rainwater system (20/0.01); total annual runoff control (15/0.00); Sponge campus (13/0.00); Stormwater management model (12/0.00); Sustainable development (11/0.00)

Based on the burst terms displayed in Table 9, it can be found that present China's LID research is mainly conducted in three branches: rainfall gardens, residential areas, and sponge campuses. The sponge campus is a small urban stormwater system and is a hot topic of current research, whose burst strength reaches 3.3. Additionally, a variety of approaches such as AHP and multi-objective optimization have been exploited to determine the optimal type [46], size, as well as quantity, and location [47] of the LID measures.

Table 9. The burst terms of publications according to the CNKI database.

Keywords	Year	Strength	Begin	End	2009–2021
storm water	2009	3.8	2009	2015	
cost-effectiveness	2009	3.46	2009	2014	
runoff	2009	3.42	2009	2014	
urbanization	2009	3.3	2009	2015	
green building	2009	2.59	2009	2016	
optimization algorithm	2009	2.43	2009	2014	
sponge city	2009	2.12	2009	2014	
storm-water management	2009	3.81	2012	2015	
rainwater utilization	2009	3.04	2012	2015	
rain garden	2009	2.14	2014	2016	
the amount of runoff	2009	2.1	2014	2015	
residential area	2009	2.66	2016	2018	
planning and design	2009	2.39	2017	2018	
sponge campuses	2009	3.32	2019	2021	
analytic hierarchy process	2009	2.9	2019	2021	
multi-objective optimization	2009	2.53	2019	2021	
low impact development	2009	2.23	2019	2021	
stormwater management model	2009	2.2	2019	2021	
urban road	2009	2.08	2019	2021	
stormwater regulation	2009	2.07	2019	2021	

Notes: Red colors represent the year of the burst terms appeared.

5.2. Keyword Cluster Analysis

From the keyword cluster analysis (see Table 10) and the timeline view of the clustering (see Figure 5) standpoints, the demonstrated results reveal that the cluster is relatively simple. The keywords in the Grass trenches (#2), Rainwater Utilization (#3), and Sponge

City (#4) clusters are mostly presenting the application areas. According to Figure 5, the key nodes are concentrated in the early stage. The prominent nodes are concentrated in the early stage of the introduction framework, and there are few connections between clusters, reflecting that domestic LID is mostly based on practical problems and lacks in-depth exploration of theories. Some scholars have examined the influence of external factors such as confluence relationship [48], terrain slope [49], and pre-conditions [50] on the effectiveness of LID measures, and the research results have enriched the scope of LID-based frameworks. Several investigators have also verified the effectiveness of LID-based measures in the established LID research areas such as Beijing [51], Guangxi [41], and Shenzhen [52].

Table 10. The keyword clustering of publications based on the CNKI database.

Cluster	Size	Homogeneity	Research Topic (log Likelihood Ratio/*p* Value)
#0 LID	93	0.779	LID (71.82/0.0001); Urban waterlogging (39.9/0.0001); Sustainable development (18.18/0.0001)
#1 SWMM model	70	0.719	SWMM model (69.66/0.0001); Sponge-type utility tunnel (45.16/0.0001); SUSTAIN model (45.16/0.0001)
#2 Grass trenches	53	0.841	Grass trenches (45.54/0.0001); Green roof(35.47/0.0001); permeable pavement (22.55/0.0001)
#3 Rainwater utilization	50	0.824	Rainwater utilization (43.52/0.0001); LID technologies (35.14/0.0001); Landscape design (26.85/0.0001)
#4 Sponge city	47	0.697	Sponge city (93.67/0.0001); Benefit quantification (29.77/0.0001); Optimization (29.77/0.0001); Annual runoff control rate (23.15/0.0001)

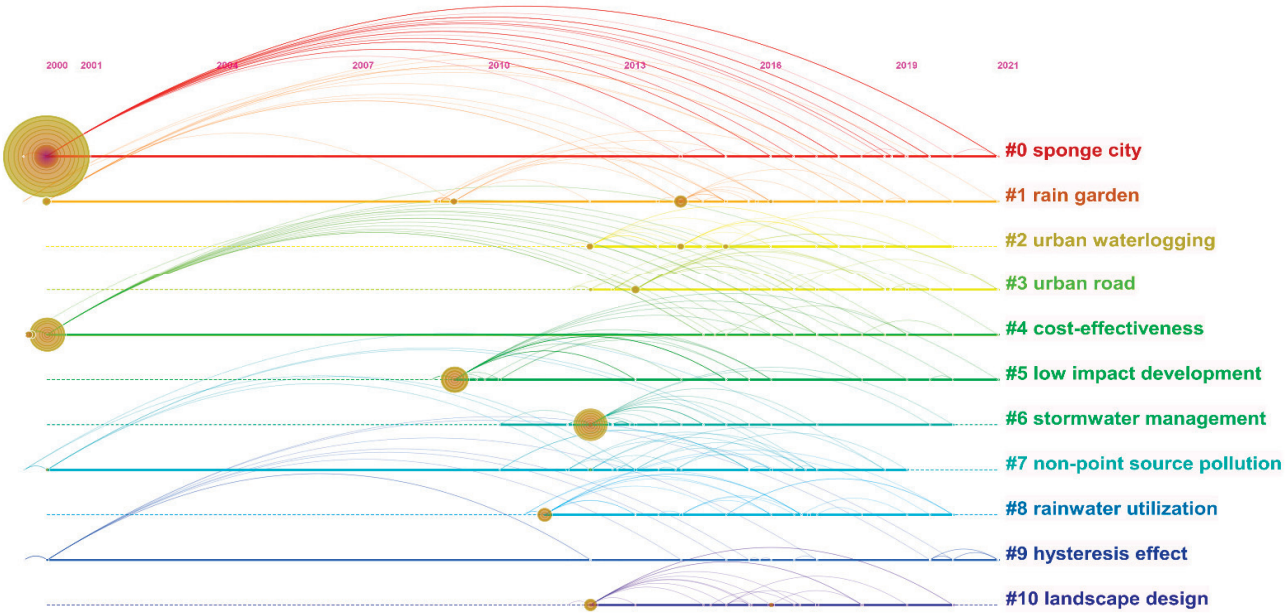


Figure 5. The time-line view of the keywords clustering of publications according to the CNKI database.

6. Conclusions

6.1. Comparison of the LID Research in China and Abroad

Research on LID-based issues has maintained a high level of interest at China and abroad, but their pertinent focuses are different. By comparing the LID research in China and abroad, the following results are obtained:

(1) Research abroad focuses on the improvement and expansion of the LID framework, while China's research emphasizes on the application of technologies associated with

the sponge city construction. From the number of publications by subject category point of view, the research field with the largest number of publications in English articles is Environmental Science, whereas the top research field in China is Architectural Science. This issue is closely related to the severe water safety as well as water ecological problems in China. Compared to the relatively mature urban stormwater management systems in foreign countries, the rapid urbanization process in China has resulted in the lack of long-term planning for urban stormwater management systems. Since the proposal of sponge city construction in 2015, the number of related Chinese articles has grown exponentially. The conducted studies not only solve the problems of urban waterlogging, groundwater resource depletion, and urban non-point source pollution in China, but also provide references for the LID application in other countries;

(2) Commonly, the research abroad emphasizes on the impact caused by global climate change, whereas China's research is mainly motivated by changes in land-use types. From the keyword clustering standpoints, research abroad basically focuses on the LID parameter optimization, modelling, and improvement of the multi-objective optimization method, uncertainty due to climate and land-use changes, and disaster resistance, while China's research emphasizes on problems encountered in sponge city construction. The advantage is that, in the context of urban waterlogging and non-point source pollution, such explorations can quickly and comprehensively analyze the problems and provide timely information for China's sponge city construction, sustainable development, water safety, and water ecology. Nevertheless, there are also some apparent shortcomings, such as high homogeneity, and lack of innovation;

(3) The research abroad focuses on optimization of the LID parameters through experimental research, while China's research emphasizes on the model simulation in order to determine the type, quantity, location, and combination of optimal LID measures. The bioretention represents the largest cluster of English articles, and Experimental Analysis and Water Quality Improvement are the focus of such investigations. However, few Chinese explorations have been carried out in the areas mentioned above. China's research mainly employs the SWMM model to simulate the LID measures with obvious water reduction effects, such as concave green space and permeable pavement, subjected to various rainfall return periods.

6.2. Research Trends

Based on the above discussion, climate change and disaster mitigation are frontier issues in the fields pertinent to the LID. However, the present literature has some limitations, which still should be discussed deeply as follows:

(1) Expand the scope of research. The LID research has achieved good results in research areas such as sponge campuses, residential areas, and urban "brownfields", but most of research works have been conducted at the micro-scale. How to extend the research scale to the scale of cities and watersheds, make a macro-level overall layout, and proficiently cooperate with the pipeline networks, rivers, and lake systems is the key to unlocking the problems of urban rainwater and non-point source pollution;

(2) Expand the breadth of research. To further strengthen the cross-coordination between various disciplines, the previous disciplines were mainly involved in the fields of water resources and the environment, and the optimization objectives and optimization functions were mostly considered as water quality and water quantity. Whether multi-objective optimization can be taken into account in the future, economic benefits, landscape benefits, and climate uncertainties are also included in the evaluation system;

(3) Carry out the original view test. The LID measure can be regarded as a small hydrological cycle system whose efficacy depends on both its corresponding factors and externally exerted conditions. Foreign scholars have accomplished a lot of experimental work on bioretention facilities to assess their performance. Prototype observation

experiments for other LID measures can be also carried out in the future, and the obtained results can be employed to validate the numerical models for the sake of enhancing the research accuracy.

Author Contributions: Conceptualization, J.Y. and B.C.; methodology, J.Y., B.C. and S.W.; validation, J.Y., X.C., L.C. and J.C.; data curation, J.Y., B.C., A.K. and X.L.; writing original draft preparation, J.Y.; writing—review and editing, B.C. and S.W. All authors have read and agreed to the published version of the manuscript.

Funding: This work was supported by the National Natural Science Foundation of China (NSFC, No. 51809283), and the Foundation of China Three Gorges Corporation (No. 202003136).

Institutional Review Board Statement: Not applicable.

Informed Consent Statement: Not applicable.

Data Availability Statement: The datasets used and/or analysed during the current study are available from the corresponding author on reasonable request.

Acknowledgments: The authors would like to express their gratitude to Hebei University of Engineering, and EditSprings (https://www.editsprings.cn, accessed on 18 March 2022) for the expert linguistic services provided.

Conflicts of Interest: The authors declare no conflict of interest.

References

1. Islam, A.; Hassini, S.; El-Dakhakhni, W. A systematic bibliometric review of optimization and resilience within low impact development stormwater management practices. *J. Hydrol.* **2021**, *599*, 126457. [CrossRef]
2. Chen, Y.; Samuelson, H.W.; Tong, Z. Integrated design workflow and a new tool for urban rainwater management. *J. Environ. Manag.* **2016**, *180*, 45–51. [CrossRef] [PubMed]
3. Qi, C.; Chang, N.-B. Integrated carbon footprint and cost evaluation of a drinking water infrastructure system for screening expansion alternatives. *J. Clean. Prod.* **2013**, *60*, 170–181. [CrossRef]
4. Dietz, M.E. Low Impact Development Practices: A Review of Current Research and Recommendations for Future Directions. *Water Air Soil Pollut.* **2007**, *186*, 351–363. [CrossRef]
5. Ahiablame, L.M.; Engel, B.A.; Chaubey, I. Effectiveness of Low Impact Development Practices: Literature Review and Suggestions for Future Research. *Water Air Soil Pollut.* **2012**, *223*, 4253–4273. [CrossRef]
6. Akhter, M.S.; Hewa, G.A. The Use of PCSWMM for Assessing the Impacts of Land Use Changes on Hydrological Responses and Performance of WSUD in Managing the Impacts at Myponga Catchment, South Australia. *Water* **2016**, *8*, 511. [CrossRef]
7. Viavattene, C.; Ellis, J.B. The management of urban surface water flood risks: SUDS performance in flood reduction from extreme events. *Water Sci. Technol. J. Int. Assoc. Water Pollut. Res.* **2013**, *67*, 99–108. [CrossRef]
8. Eckart, K.; McPhee, Z.; Bolisetti, T. Performance and implementation of low impact development—A review. *Sci. Total Environ.* **2017**, *607–608*, 413–432. [CrossRef]
9. Fletcher, T.D.; Shuster, W.; Hunt, W.F.; Ashley, R.; Butler, D.; Arthur, S.; Trowsdale, S.; Barraud, S.; Semadeni-Davies, S.; Bertrand-Krajewski, J.-L.; et al. SUDS, LID, BMPs, WSUD and more—The evolution and application of terminology surrounding urban drainage. *Urban Water J.* **2015**, *12*, 525–542. [CrossRef]
10. Palla, A.; Gnecco, I. Hydrologic modeling of Low Impact Development systems at the urban catchment scale. *J. Hydrol.* **2015**, *528*, 361–368. [CrossRef]
11. Mani, M.; Bozorg-Haddad, O.; Loáiciga, H.A. A new framework for the optimal management of urban runoff with low-impact development stormwater control measures considering service-performance reduction. *J. Hydroinform.* **2019**, *21*, 727–744. [CrossRef]
12. Zhang, P.; Chen, L.; Hou, X.; Wei, G.; Zhang, X.; Shen, Z. Detailed Quantification of the Reduction Effect of Roof Runoff by Low Impact Development Practices. *Water* **2020**, *12*, 795. [CrossRef]
13. Ahiablame, L.; Shakya, R. Modeling flood reduction effects of low impact development at a watershed scale. *J. Environ. Manag.* **2016**, *171*, 81–91. [CrossRef]
14. Xian, B.C.C.; Kang, C.W.; Ab Wahab, M.; Zainol, M.R.R.M.A.; Baharudin, F. Evaluation of low impact development and best management practices on peak flow reduction using SWMM. In *IOP Conference Series: Earth and Environmental Science*; IOP Publishing: Bristol, UK, 2021; Volume 646, p. 012045.
15. Xing, W.; Li, P.; Cao, S.-B.; Gan, L.-L.; Liu, F.-L.; Zuo, J.-E. Layout effects and optimization of runoff storage and filtration facilities based on SWMM simulation in a demonstration area. *Water Sci. Eng.* **2016**, *9*, 115–124. [CrossRef]

16. Rezaei, A.R.; Ismail, Z.; Niksokhan, M.H.; Dayarian, M.A.; Ramli, A.H.; Yusoff, S. Optimal implementation of low impact development for urban stormwater quantity and quality control using multi-objective optimization. *Environ. Monit. Assess.* **2021**, *193*, 241. [CrossRef]
17. Kong, Z.; Shao, Z.; Shen, Y.; Zhang, X.; Chen, M.; Yuan, Y.; Li, G.; Wei, Y.; Hu, X.; Huang, Y.; et al. Comprehensive evaluation of stormwater pollutants characteristics, purification process and environmental impact after low impact development practices. *J. Clean. Prod.* **2021**, *278*, 123509. [CrossRef]
18. Wu, J.; Wu, X.; Zhang, J. Development Trend and Frontier of Stormwater Management (1980–2019): A Bibliometric Overview Based on CiteSpace. *Water* **2019**, *11*, 1908. [CrossRef]
19. Zhu, Y.; Koutra, S.; Zhang, J. Zero-Carbon Communities: Research Hotspots, Evolution, and Prospects. *Buildings* **2022**, *12*, 674. [CrossRef]
20. Cheng, C.; Hu, Z.; Liu, S.; Tseng, H. Emerging trends in regenerative medicine: A scientometric analysis in CiteSpace. *Expert Opin. Biol. Ther.* **2012**, *12*, 593–608. [CrossRef]
21. Chen, C. Searching for intellectual turning points: Progressive knowledge domain visualization. *Proc. Natl. Acad. Sci. USA* **2004**, *101* (Suppl. 1), 5303–5310. [CrossRef]
22. Chen, C. Science Mapping: A Systematic Review of the Literature. *J. Data Inf. Sci.* **2017**, *2*, 1–40. [CrossRef]
23. Graham, P.; MacLean, L.; Medina, D.; Patwardhan, A.; Vásárhelyi, G. The Role of Water Balance Modelling in the Transition to Low Impact Development. *Water Qual. Res. J.* **2004**, *39*, 331–342. [CrossRef]
24. Liu, T.; Lawluvy, Y.; Shi, Y.; Yap, P.-S. Low Impact Development (LID) Practices: A Review on Recent Developments, Challenges and Prospects. *Water Air Soil Pollut.* **2021**, *232*, 344. [CrossRef]
25. Ho, H.-C.; Lin, S.-W.; Lee, H.-Y.; Huang, C.-C. Evaluation of a Multi-Objective Genetic Algorithm for Low Impact Development in an Overcrowded City. *Water* **2019**, *11*, 2010. [CrossRef]
26. Gogate, N.G.; Kalbar, P.P.; Raval, P.M. Assessment of stormwater management options in urban contexts using Multiple Attribute Decision-Making. *J. Clean. Prod.* **2017**, *142*, 2046–2059. [CrossRef]
27. Li, F.; Yan, X.-F.; Duan, H.-F. Sustainable Design of Urban Stormwater Drainage Systems by Implementing Detention Tank and LID Measures for Flooding Risk Control and Water Quality Management. *Water Resour. Manag.* **2019**, *33*, 3271–3288. [CrossRef]
28. Kaykhosravi, S.; Khan, U.T.; Jadidi, A. A Comprehensive Review of Low Impact Development Models for Research, Conceptual, Preliminary and Detailed Design Applications. *Water* **2018**, *10*, 1541. [CrossRef]
29. Qin, H.-P.; Li, Z.-X.; Fu, G. The effects of low impact development on urban flooding under different rainfall characteristics. *J. Environ. Manag.* **2013**, *129*, 577–585. [CrossRef]
30. Yang, Y.; Chui, T.F.M. Optimizing surface and contributing areas of bioretention cells for stormwater runoff quality and quantity management. *J. Environ. Manag.* **2018**, *206*, 1090–1103. [CrossRef]
31. Xia, J.; Zhang, Y.Y.; Xiong, L.H.; He, S.; Wang, L.F.; Yu, Z.B. Opportunities and challenges of the Sponge City construction related to urban water issues in China. *Sci. China Earth Sci.* **2017**, *60*, 652–658. [CrossRef]
32. Li, H.; Ding, L.; Ren, M.; Li, C.; Wang, H. Sponge City Construction in China: A Survey of the Challenges and Opportunities. *Water* **2017**, *9*, 594. [CrossRef]
33. Baek, S.-S.; Choi, D.-H.; Jung, J.-W.; Lee, H.-J.; Lee, H.; Yoon, K.-S.; Cho, K.H. Optimizing low impact development (LID) for stormwater runoff treatment in urban area, Korea: Experimental and modeling approach. *Water Res.* **2015**, *86*, 122–131. [CrossRef] [PubMed]
34. Liu, Y.; Ahiablame, L.M.; Bralts, V.F.; Engel, B.A. Enhancing a rainfall-runoff model to assess the impacts of BMPs and LID practices on storm runoff. *J. Environ. Manag.* **2015**, *147*, 12–23. [CrossRef]
35. Liu, Y.; Bralts, V.F.; Engel, B.A. Evaluating the effectiveness of management practices on hydrology and water quality at watershed scale with a rainfall-runoff model. *Sci. Total Environ.* **2015**, *511*, 298–308. [CrossRef] [PubMed]
36. Chui, T.F.M.; Liu, X.; Zhan, W. Assessing cost-effectiveness of specific LID practice designs in response to large storm events. *J. Hydrol.* **2016**, *533*, 353–364. [CrossRef]
37. Sohn, W.; Kim, J.-H.; Li, M.-H.; Brown, R. The influence of climate on the effectiveness of low impact development: A systematic review. *J. Environ. Manag.* **2019**, *236*, 365–379. [CrossRef] [PubMed]
38. Kong, F.; Ban, Y.; Yin, H.; James, P.; Dronova, I. Modeling stormwater management at the city district level in response to changes in land use and low impact development. *Environ. Model. Softw.* **2017**, *95*, 132–142. [CrossRef]
39. Rosa, D.J.; Clausen, J.C.; Dietz, M.E. Calibration and Verification of SWMM for Low Impact Development. *JAWRA J. Am. Water Resour. Assoc.* **2015**, *51*, 746–757. [CrossRef]
40. Jia, H.; Yao, H.; Tang, Y.; Yu, S.L.; Field, R.; Tafuri, A.N. LID-BMPs planning for urban runoff control and the case study in China. *J. Environ. Manag.* **2015**, *149*, 65–76. [CrossRef]
41. Li, Q.; Wang, F.; Yu, Y.; Huang, Z.C.; Li, M.T.; Guan, Y.T. Comprehensive performance evaluation of LID practices for the sponge city construction: A case study in Guangxi, China. *J. Environ. Manag.* **2019**, *231*, 10–20. [CrossRef]
42. Eckart, K.; McPhee, Z.; Bolisetti, T. Multiobjective optimization of low impact development stormwater controls. *J. Hydrol.* **2018**, *562*, 564–576. [CrossRef]
43. Martin-Mikle, C.J.; de Beurs, K.M.; Julian, J.P.; Mayer, P.M. Identifying priority sites for low impact development (LID) in a mixed-use watershed. *Landsc. Urban Plan.* **2015**, *140*, 29–41. [CrossRef]

44. Mao, X.; Jia, H.; Yu, S.L. Assessing the ecological benefits of aggregate LID-BMPs through modelling. *Ecol. Model.* **2017**, *353*, 139–149. [CrossRef]
45. Zhang, K.; Chui, T.F.M. A comprehensive review of spatial allocation of LID-BMP-GI practices: Strategies and optimization tools. *Sci. Total Environ.* **2018**, *621*, 915–929. [CrossRef] [PubMed]
46. Song, J.Y.; Chung, E.-S. A Multi-Criteria Decision Analysis System for Prioritizing Sites and Types of Low Impact Development Practices: Case of Korea. *Water* **2017**, *9*, 291. [CrossRef]
47. Kaykhosravi, S.; Abogadil, K.; Khan, U.T.; Jadidi, M.A. The Low-Impact Development Demand Index: A New Approach to Identifying Locations for LID. *Water* **2019**, *11*, 2341. [CrossRef]
48. Shen, H.; Xu, Z. Analysis and test of different confluence relationship LID rainfall control methods. *J. Hydraul. Eng.* **2019**, *50*, 578–588.
49. Hou, J.; Han, H.; Qi, W.; Guo, K.; Li, Z.; Hinkelmann, R. Experimental investigation for impacts of rain storms and terrain slopes on low impact development effect in an idealized urban catchment. *J. Hydrol.* **2019**, *579*, 124176. [CrossRef]
50. Hou, J.; Li, D.; Wang, X.; Gou, K.; Tong, Y.; Ma, Y. Simulation of the Impact of LID measures on runoff control at the building District Scale. *Adv. Water Sci.* **2019**, *30*, 45–55.
51. Shen, H.; Zhang, S.; Xu, Z. LID block allocation and runoff reduction effect monitoring in Beijing Future Science and Technology City. *J. Hydraul. Eng.* **2018**, *49*, 937–944.
52. Zhang, Y.; Xu, H.; Liu, H.; Zhou, B. The Application of Low Impact Development Facility Chain on Storm Rainfall Control: A Case Study in Shenzhen, China. *Water* **2021**, *13*, 3375. [CrossRef]

applied sciences

MDPI

Article

Analysis of Water Quality Improvement Effect of Controlled River by Multi-Functional Weir Operation

Jin-Kyoung Han [1], Woo-Suk Jung [2], Jung-Min Kim [3], In-Hwan Park [4] and Young-Do Kim [5,*]

[1] Department of Environmental Engineering, Inje University, Gimhae-si 50834, Korea
[2] Nakdong River Support Team, Presidential Water Commission, Changwon-si 51439, Korea
[3] Nakdong River Environment Research Center, National Institute of Environmental Research (NIER), Incheon 40103, Korea
[4] Department of Faculty of Civil Engineering, Seoul National University of Science and Technology, Seoul 01811, Korea
[5] Department of Civil & Environmental Engineering, Myongji University, Yongin-si 17058, Korea
* Correspondence: ydkim@mju.ac.kr

Abstract: In this study, the water quality change in a stagnant controlled river containing hard management structures due to pulsed flow was simulated. The Environmental Fluid Dynamics Code (EFDC) model was used for the water quality change simulation, and the water quality improvement effect caused by pulsed flow was simulated for multiple scenarios. Based on Case 1, in which 274.2–291.8 CMS was discharged for five hours, other scenarios, in which the gate was opened by 0.5 m and 1.0 m while the discharge time was doubled, were simulated. On comparing the water level results with the observed data, a relatively positive result of R2 = 0.82 was obtained. The water quality simulation results showed that the concentrations of Chl-a, COD, and T-P were, respectively, approximately 7.7%, 4.5%, and 4.0% higher in Case 2 than in Case 1, 24 h after the start of discharge. Cases 3 and 4, on the other hand, exhibited decreased concentrations of Chl-a, COD, and T-P 24 h after the start of discharge. These results confirm that pulsed flow leads to different water quality improvement effects depending on the discharge amount and duration. Furthermore, the water quality improvement effect was recorded at close to 0% after 72 h in all scenarios. As the water quality improvement effect due to pulsed flow appears within 24 h and almost disappears after 72 h depending on the scenario, a physical solution to this problem is required.

Keywords: controlled river; water quality; multi-functional weir; pulse discharge

Citation: Han, J.-K.; Jung, W.-S.; Kim, J.-M.; Park, I.-H.; Kim, Y.-D. Analysis of Water Quality Improvement Effect of Controlled River by Multi-Functional Weir Operation. *Appl. Sci.* **2022**, *12*, 8883. https://doi.org/10.3390/app12178883

Academic Editors: Dibyendu Sarkar, Rupali Datta, Prafulla Kumar Sahoo and Mohammad Mahmudur Rahman

Received: 10 February 2022
Accepted: 22 August 2022
Published: 4 September 2022

Publisher's Note: MDPI stays neutral with regard to jurisdictional claims in published maps and institutional affiliations.

Copyright: © 2022 by the authors. Licensee MDPI, Basel, Switzerland. This article is an open access article distributed under the terms and conditions of the Creative Commons Attribution (CC BY) license (https://creativecommons.org/licenses/by/4.0/).

1. Introduction

The concept of pulsed flow was established by the Australian Government's National Water Commission (NWC). It was reported that the water quality as well as the natural ecology of the river environment can be improved by mimicking the conditions of natural flooding by adjusting the flow rate changes in existing controlled rivers through the discharge of dams and weirs [1]. In the Nakdong River, located in the south-eastern region of South Korea, eight multifunctional weirs have been constructed to prepare for droughts and floods. Each of these consists of a fixed weir and a gate for controlling the flow rate, their purpose is to adjust the flow of the Nakdong River according to precipitation. A river in which the flow rate is managed using gates, such as the multifunctional weirs of the Nakdong River, is referred to as a "controlled river". A controlled river allows for the benefit of manipulating the flow of the river depending on its purpose. However, the sediment accumulation in the river due to the implementation of hard management and the subsequent bed slope as well as particle size change become factors that can alter the river environment [2]. Because such a change in the river environment affects the water quality of the river system, it is necessary to monitor the change in water quality due to the operation of these gates. This is especially important for the Nakdong River system as it

supplies water to nearby cities and agricultural lands, in addition to some areas without any treatment, ergo it is imperative to determine gate operation plans for improvement in water quality [3]. Weir gate operation and pulsed flow are also interconnected with the algal bloom warning system, which has classified four cyanobacteria species (Microcystis, Anabaena, Oscillatoria, and Aphanizomenon) that produce toxic substances into three warning levels depending on the population of harmful cyanobacteria: attention, alert, and outbreak. The gates are used to perform a pulsed flow from the alert step through a dam-weir link operation for the purpose of improving the water quality in the main channel of the Nakdong River.

In the case of the Murray River in Australia, the average annual flow rate was reduced by half through the use of weirs constructed upstream. Due to the decrease in the flow rate, river deformation was observed, such as the drying and exposure of some of the river beds [4,5]. In France, studies on the effect of pulsed flow on canal water quality management and algae reduction in terms of water quality management have been reported [6]. In addition, in the United States, in-lake mesocosm experiments were conducted in small bays during an outbreak of harmful algae, and the effect of reducing algae by pulsed flow was demonstrated [7]. In South Korea, the water pollution phenomenon in which algal bloom occurs due to the construction of hydraulic structures is recognized as an important issue in managed river systems. To reduce water pollution by algae, a temporary water quality improvement effect induced by the discharge of a large amount of flow from an upstream reservoir using pulsed flow is often used. To analyze the flushing effect of pulsed flow, Chung et al. explored the improvement in the Daecheong Dam reservoir water quality after pulsed flow [8]. Further, Jung et al. studied water quality improvement and algal bloom due to pulsed flow in the Seungchon Weir of the Yeongsan River [9]. The puled flow, which does not take into account the algal growth characteristics and growth rate, increases the nutrient utilization rate of the algae, which can cause side effects such as increased algae generation or accumulation in downstream weirs. Therefore, for optimal weir operation, a detailed study on the puled flow effect is required. However, these studies, which applied actual gate operation cases of a multifunctional weir for their research on water quality improvement, are not sufficient. Extensive and intensive experiments are needed to evaluate the effect of improving water quality and reducing algae according to pulsed flow.

It is difficult to evaluate the effect of pulsed flow with short-term measurement results. The reason is that the water quality concentration and algae density of rivers are the results of complex interactions between physical, chemical, and biological factors such as weather, water quantity, and water quality. Therefore, it is difficult to distinguish the effect of pulsed flow alone through experiments. The most efficient method is to use a model that can derive appropriate alternatives through analysis of various scenarios [10].

The purpose of this study is to analyze the water quality improvement effect through the pulsed flow of a multi-functional weir by modeling the hydraulic flow and water quality phenomenon using a three-dimensional EFDC model. The water quality improvement effect of pulsed flow was analyzed for the section of the Nakdong River from the Gangjeong-Goryeong Weir to the Dalseong Weir, which has become a controlled river due to the construction of multi-functional weirs. Through the analysis, changes in the concentration of variables determining the water quality were expressed as an increase or decrease rates (%). In addition, the increase and decrease periods of the concentrations due to pulsed flow were ascertained in order to arrive at measures for water quality improvement. It is intended to be used as the basic data for the multi-functional weir operation plan for water quality improvement.

2. Research Background

2.1. Pulsed Flow

Pulsed flow refers to a gate operation method that temporarily discharges a large amount of water to improve downstream water quality and river habitats [11]. Pulsed flow

is performed in the Nakdong River to improve water quality when an algal bloom occurs. The operation affects the water quality of the Nakdong River where the surface water is used as a water supply source for the neighboring regions. As multiple agricultural intake stations are distributed from the Gangjeong-Goryeong Weir to the Dalseong Weir of the Nakdong River, it is necessary to verify the operation methods of the weirs and the effect of pulsed flow on the improvement of water quality. Observation is required in order to improve the water quality using pulsed flow, but on-site verification is difficult when a large amount of flow is discharged at once. Therefore, in this study, the water quality improvement effect of pulsed flow was verified according to the operation methods of the weirs, through numerical experiments that used the Environmental Fluid Dynamics Code (EFDC).

2.2. EFDC (Environmental Fluid Dynamics Code) Overview

EFDC is a software program developed by the Virginia Institute of Marine Science and is maintained and managed by the Environmental Protection Agency (EPA) of the United States of America. It consists of a hydrodynamics model, a water quality model, and a sediment transport model. It is capable of quasi-three-dimensional (3D) hydraulic and water quality analysis in various areas, such as rivers, lakes, and coastal systems. The hydrodynamic model, which is the basis of simulation using EFDC, uses the time-averaged Navier-Stokes equation as the governing equation. It uses the curvilinear-orthogonal coordinate in the horizontal direction and the sigma coordinate in the vertical direction. The momentum equations of the hydrodynamics model in the x and y directions are as follows [12]:

$$\begin{aligned}&\frac{\partial}{\partial t}(m_x m_y H u) + \frac{\partial}{\partial x}(m_y H u u) + \frac{\partial}{\partial y}(m_x H v u) + \frac{\partial}{\partial z}(m_x m_y w u) - f_e m_x m_y H v \\ &= -m_y H \frac{\partial}{\partial x}(p + p_{atm} + \phi) + m_y\left(\frac{\partial}{\partial x} z_b^* + z\frac{\partial}{\partial x} H\right)\frac{\partial}{\partial z} p + \frac{\partial}{\partial z}\left(m_x m_y \frac{A_v}{H}\frac{\partial}{\partial z} u\right) \\ &\quad + \frac{\partial}{\partial x}\left(\frac{m_y}{m_x} H A_H \frac{\partial}{\partial x} u\right) + \frac{\partial}{\partial y}\left(\frac{m_x}{m_y} H A_H \frac{\partial}{\partial y} u\right) - m_x m_y c_p D_p \left(u^2 + v^2\right)^{1/2} u\end{aligned} \tag{1}$$

$$\begin{aligned}&\frac{\partial}{\partial t}(m_x m_y H v) + \frac{\partial}{\partial x}(m_y H u v) + \frac{\partial}{\partial y}(m_x H v v) + \frac{\partial}{\partial z}(m_x m_y w v) + f_e m_x m_y H u \\ &= -m_x H \frac{\partial}{\partial y}(p + p_{atm} + \phi) + m_x\left(\frac{\partial}{\partial y} z_b^* + z\frac{\partial}{\partial y} H\right)\frac{\partial}{\partial z} p + \frac{\partial}{\partial z}\left(m_x m_y \frac{A_v}{H}\frac{\partial}{\partial z} v\right) \\ &\quad + \frac{\partial}{\partial x}\left(\frac{m_y}{m_x} H A_H \frac{\partial}{\partial x} v\right) + \frac{\partial}{\partial y}\left(\frac{m_x}{m_y} H A_H \frac{\partial}{\partial y} v\right) - m_x m_y c_p D_p \left(u^2 + v^2\right)^{1/2} v\end{aligned} \tag{2}$$

where u, v, and w are flow velocities in the x, y, and z directions. m_x and m_y are scale factors in the x and y directions. A_H and A_V are eddy viscosities in the horizontal and vertical directions. $z_s{}^*$, $z_b{}^*$ are the physical vertical coordinates of the free surface and bed. H is the water depth, f_e is the effective Coriolis acceleration, D_p is the dimensionless projected vegetation area, and c_p is the drag coefficient. As the motion equation for the vertical direction, the following equation assuming hydrostatic pressure was used:

$$\frac{\partial}{\partial z} p = -gHb = -gH(\rho - \rho_o)\rho_o^{-1} \tag{3}$$

where ρ and ρ_o are the density and reference density, respectively, and denotes the buoyancy. In addition, the continuity equation is as follows:

$$\frac{\partial}{\partial t}(m_x m_y H) + \frac{\partial}{\partial x}(m_y H u) + \frac{\partial}{\partial y}(m_x H v) + \frac{\partial}{\partial z}(m_x m_y w) = 0 \tag{4}$$

The water quality model of EFDC calculates the spatio-temporal distribution of water quality factors using the flow calculation results of the hydrodynamics model, and utilizes the following 3D advection-diffusion equation as the governing equation.

$$\frac{\partial}{\partial t}(m_x m_y HC) + \frac{\partial}{\partial x}(m_y HuC) + \frac{\partial}{\partial y}(m_x HvC) + \frac{\partial}{\partial z}(m_x m_y wC) - \frac{\partial}{\partial z}(m_x m_y w_{sc} C) = \frac{\partial}{\partial x}\left(\frac{m_y}{m_x} HK_H \frac{\partial}{\partial x} C\right) + \frac{\partial}{\partial y}\left(\frac{m_x}{m_y} HK_H \frac{\partial}{\partial y} C\right) + \frac{\partial}{\partial z}\left(m_x m_y \frac{K_v}{H} \frac{\partial}{\partial z} C\right) + Q_c \quad (5)$$

where C is the concentration, K_v and K_H are diffusion coefficients in the vertical and horizontal directions, w_{sc} is the settling velocity, and Q_c is the source-sink term [13–15]. The water quality model considered 22 water quality factors as the calculation variables to implement the complicated interrelationships between aquatic ecosystems. Among them, four types of algae—cyanobacteria, green algae, diatom algae, and stationary algae—were included [16]. For the three variables (salinity, water temperature, and total suspended solids) required for the calculation of the 22 variables, the results derived from the hydrodynamic model were used [17]. The interaction between each water quality item is shown in Figure 1. As can be seen from the figure, it is necessary to determine appropriate parameters for the simulation of complicated interrelationships between water quality factors. In this study, parameters were corrected using the observation results of the water quality observatories located in the section between the Gangjeong-Goryeong Weir and the Dalseong Weir.

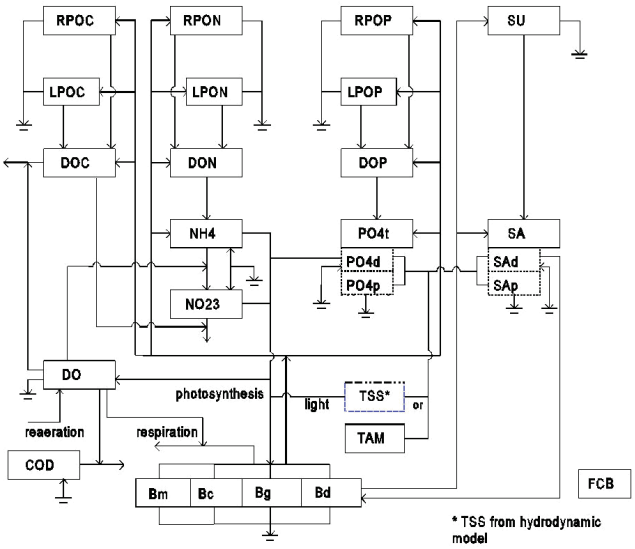


Figure 1. Schematic Diagram for The EFDC Water Column Water Quality Model (13).

3. Study Methods

2.3. Descriptions of Study Area

The section between the Gangjeong-Goryeong Weir and the Dalseong Weir, which is the target section of this study, is located in the middle and downstream areas of the Nakdong River basin (Figure 2). The length of this section is approximately 25 km, and the Geumho River confluence point is located in the downstream area of the Gangjeong-Goryeong Weir. In addition, a river island is located at the Geumho River confluence point, and complicated topographical characteristics including bends occur from the confluence point to approximately 4 km downstream. Located in this study section are two water quality measurement networks; the National Institute of Environmental Research (NIER) provides water quality observation data for these networks every eight days. Furthermore, the hourly data on the discharge amount and water level produced by the Gangjeong-

Goryeong Weir and the Dalseong Weir was used as the input data for the hydraulic and water quality simulation.

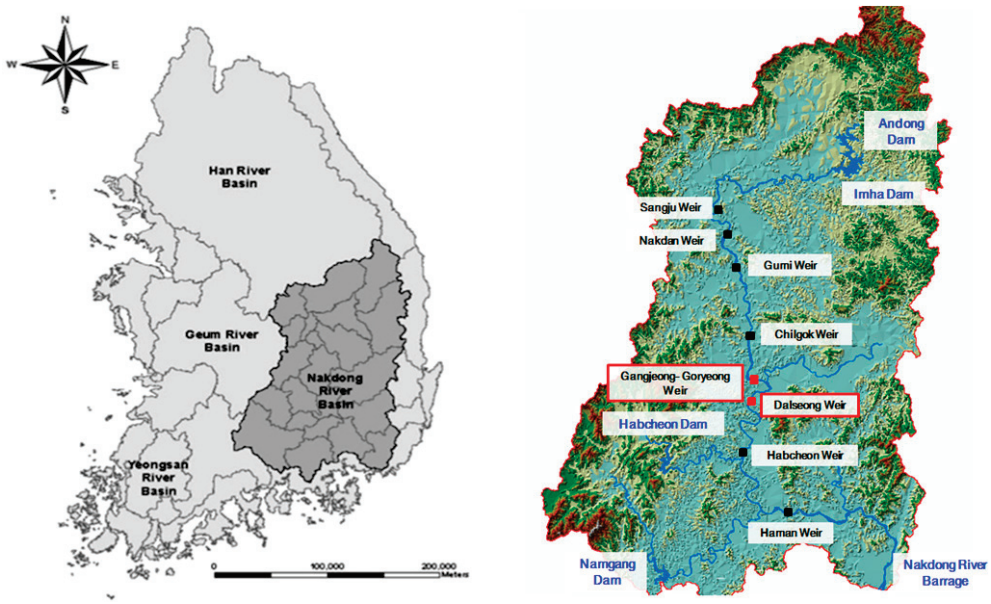


Figure 2. Gangjeong-Goryeong Weir and Dalseong Weir Section in Study Area.

2.4. Model Input Data

The flow simulation results of the hydrodynamic model were required in the water quality simulation using the water quality model, and precise topographic data and boundary conditions for the simulation section were required as input to improve the accuracy of the flow simulation results [18]. In particular, as sudden topographic changes occur in the section between the Gangjeong-Goryeong Weir and the Dalseong Weir due to the large difference in altitude between the main waterway and the floodplain, precise topographic data capable of considering such characteristics were required [19]. Therefore, in this study, the topographical information measured precisely at the intervals of 40–50 m in the longitudinal and transverse directions in the study section of the Nakdong River was used to construct computational grids [20]. By constructing an orthogonal curvilinear grid using orthogonal curvilinear coordinates, the planar shape of the stream was expressed with a high degree of accuracy with the minimum number of grids centered on the main flow. Figure 3 shows the numerical grid generated using topographic data. The grid configuration is shown in Figure 3a, which consists of 12,000 pieces. Figure 3b show the finite difference between lattice and the bed height for each lattice and the water depth for each lattice [21].

Figure 4 shows the locations of the multifunctional weirs and water quality observatories in the study section. For flow simulation using the hydrodynamics model, the discharge amount of the Gangjeong-Goryeong Weir and the inflow rate of the Geumho River were used as the upstream boundary conditions, and the inflow rate of the Dalseong Weir was used as the downstream boundary condition. The discharge amount data provided by WAMIS [22] were used for the discharge amount of the Gangjeong-Goryeong Weir, and the daily flow rate data provided by Geumho C were used for the flow rate of the Geumho River. For water quality input data of the Nakdong River, the data measured by the Dasa water quality observatory, located in the upstream area of the Gangjeong-Goryeong Weir, from 1 January to 1 December 2014 were used. For the Geumho River, the simulation was performed using the water quality data measured at Geumho River 6 during the same period.

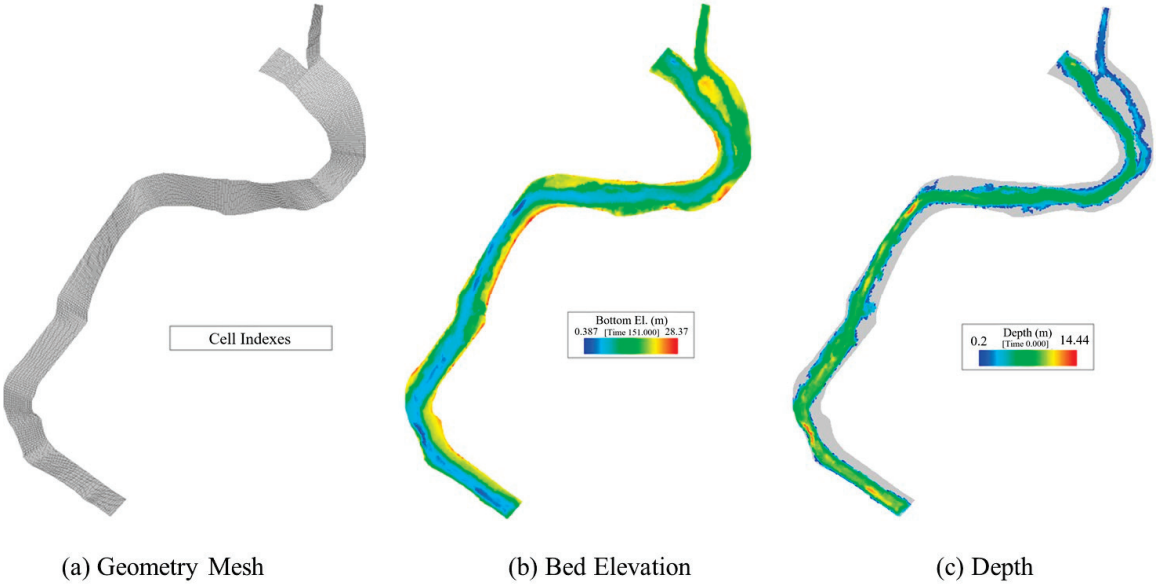


Figure 3. Test bed Section Geographic Construction.



Survey Location	Division Section Survey Location	Research institutions
Dasa	Jukgokri Dasaeup Dalsunggun, Daegu Metropolitan City	Nakdong River Enviroment Research Center
Geumho River 6	Pahodong Dalsungu, Daegu Metropolitan City	Nakdong River Enviroment Research Center
Geumho C	Pahodong Dalsungu, Daegu Metropolitan City	Nakdong River Enviroment Research Center
Hwawon naru	Hwawoneup Dalsunggun, Daegu Metropolitan City	Daegu Regional Environmental Agency
Goryeong	Samdaeri seongsanmyeon goryeongun, Gyeongsangbuk-do	Daegu Regional Environmental Agency

Figure 4. Survey Location of Water Quality Gangjeong-Goryeong Weir and Dalseong Weir Section.

2.5. Calibration & Validation of EFDC Model

To correct the errors in the parameters of the hydrodynamic model, the water level data measured from the upstream area of the Dalseong Weir from 1 January to 1 December 2014 were compared with the numerical simulation results. The parameters of the hydrodynamic model were corrected through a trial-and-error method. After correcting the parameters, the results were compared with the observation results and an R^2 of 0.82 was obtained. Flow simulation was performed using the corrected parameters, and the results were compared with the water level data measured from 1 January to 1 September 2015. Here too, an R^2 of 0.82 was obtained and it was possible to appropriately reproduce the flow of the simulated section using the corrected parameters.

For the water quality model for simulation, appropriate parameter values were selected through a comparison of the measurement results presented by NIER [23]. For parameter correction of the water quality model, the water quality data measured at the

Hwawon-naru and Goryeong water quality observatories from 1 January to 1 December 2014 were used. Figure 5 is a graph that compares the results of the water quality simulation with the corrected parameters and the measurement results of the Hwawon-naru and Goryeong water quality observatories. The five water quality factors (Chl-a, DO, COD, T-N, and T-P) measured at the Hwawon-naru and Goryeong water quality observatories showed errors of less than 20% and the daily change in each of these water quality factors could be reproduced effectively.

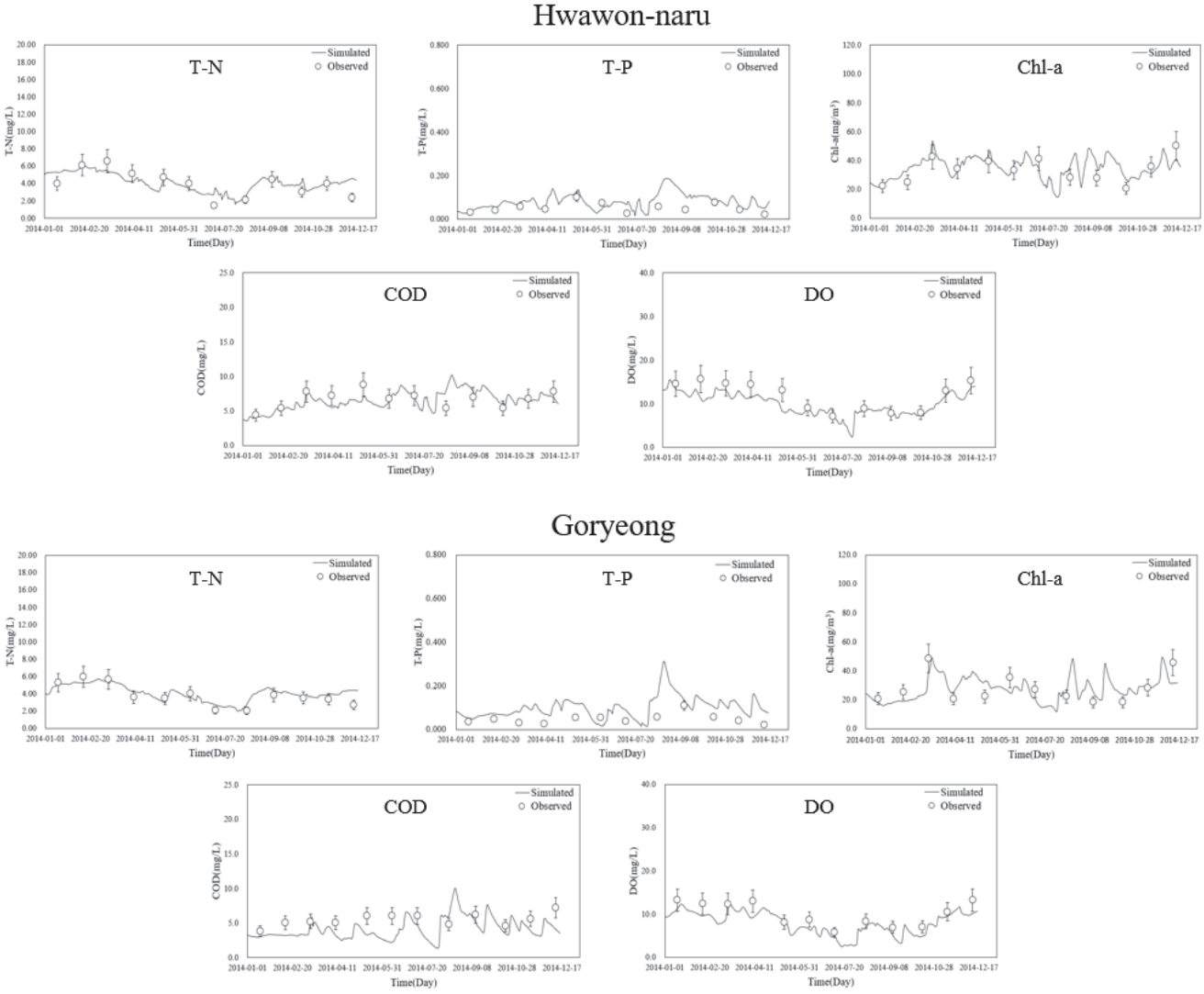


Figure 5. Water Quality Simulation Calibration (From January 2014 to December 2014).

To verify whether the corrected parameters of the water quality model could be applied to other periods, the water quality data were measured at the Hwawon-naru and Goryeong water quality observatories from 1 January to 1 September in 2015 were compared with the simulation results. Figure 6 is a graph that compares the time series data of each water quality factor with the numerical simulation results. The numerical simulation results reflected the daily change in each water quality factor, and the average error from the observation results was within approximately 20%. This indicates that the corrected parameters for the simulation section can be applied to other periods.

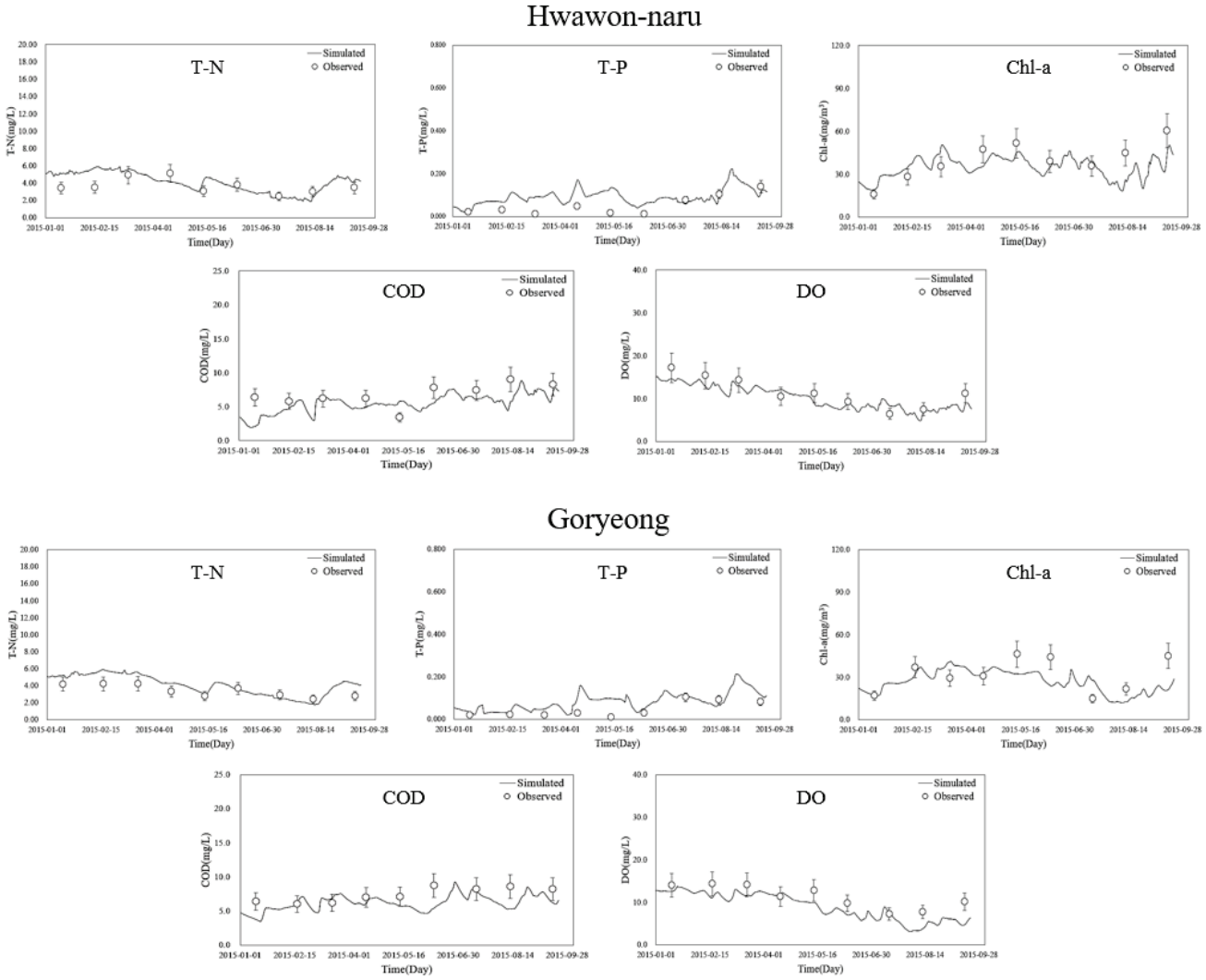


Figure 6. Water Quality Simulation Validation (From January 2015 to December 2015).

3. Results

3.1. Results of Scenario by Multi-Functional Weir Operation

Numerical simulation was performed to analyze the water quality improvement effect of pulsed flow in the section between the Gangjeong-Goryeong Weir and the Dalseong Weir. Four scenarios were considered based on the gate operation method (Table 1). First, in Case 1, the actual pulsed flow at the Gangjeong-Goryeong Weir on 16 June 2015, was reproduced through numerical simulation. In Case 1, the basic discharge amount of the Gangjeong-Goryeong Weir was 274.2 m^3/s, and a pulsed flow operation was performed to temporarily discharge up to 291.8 m^3/s for five hours from 11:00 to 16:00. In Case 2, the pulsed flow duration was doubled to 10 h, and a maximum of 291.8 m^3/s was discharged, similar to Case 1. To compare the water quality improvement effects based on the linked operations of the weirs located in the upstream and downstream areas, changes in the water quality according to the flow rate and flow velocity were compared in Cases 3 and 4 by opening the Dalseong Weir gate by 0.5 m and 1.0 m respectively, and the same pulsed flow conditions as in Case 1 were applied.

Table 1. Scenario Simulations of the Operating Weir.

		Scenario
Case 1	Real Case	16 June 2015 Pulse Discharge actual operating Weir (11:00~16:00, Discharge: 274.2 m^3/s~291.8 m^3/s)
Case 2	Real Case Discharge time extension	16 June 2015 Pulse Discharge actual operating Weir + Discharge times, twice extended
Case 3	Upstream Weir Operations	16 June 2015 Pulse Discharge + GangjeongGoryeong Weir, Dalseong Weir 0.5 m opening gate
Case 4	Upstream Weir Operations	16 June 2015 Pulse Discharge + GangjeongGoryeong Weir, Dalseong Weir 1.0 m opening gate

Figure 7 is a graph that compares water quality changes according to the weir operation scenarios in Table 1 at the Hwawon-naru water quality observatory. Each water quality concentration exhibited different variations depending on the pulsed flow scenario. In Case 1, the DO concentration increased and Chl-a, COD, T-N, and T-P showed a tendency to decrease after 11:00 when the pulsed flow was initiated. Water quality fluctuation was observed at the Hwawon-naru point in the downstream area of the Gangjeong-Goryeong Weir from the moment the pulsed flow operation began at 11:00 on 16 June 2015; flow rate and flow velocity also increased. The DO concentration increased and the concentrations of Chl-a, COD, T-N, and T-P decreased as the discharge time increased, indicating the water quality improvement effect of pulsed flow. However, the water quality fluctuation at the Goryeong point, located in the 15-km downstream area from Hwawon-naru, was smaller than that at Hwawon-naru; also, the water quality fluctuation exhibited inconsistent tendencies. Therefore, it can be concluded that the water quality improvement effect of pulsed flow at the Gangjeong-Goryeong Weir was concentrated in the upstream area and it decreased in the direction of the downtown area.

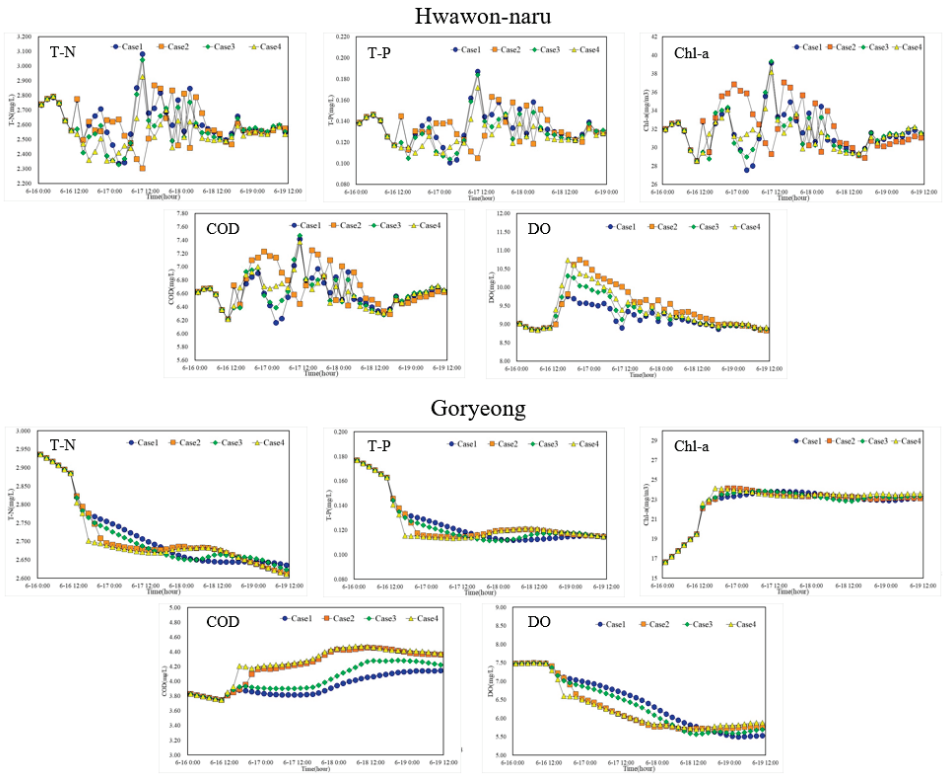


Figure 7. Scenario Comparison Results.

3.2. Analysis of Water Quality Improvement effect

To analyze the water quality improvement effect, the water quality changes in Cases 2, 3, and 4 were compared with each other based on the scenario in Case 1, in which the actual pulsed flow was performed. Figure 8 is a graph showing the time variation of the water quality decrease rate in each scenario compared to Case 1, and Table 2 summarizes the change in the decrease rate over time. In Case 2, Chl-a, COD, and T-P were, respectively, 7.68%, 4.48%, and 3.99% higher compared to Case 1 for 24 h after the start of discharge, and the water quality concentrations were found to be higher due to the change in the fluid flow caused by the pulsed flow. For the following 48 h, the decrease rates of the water quality variables, except for DO, increased, and DO gradually increased, thereby exhibiting the water quality improvement effect. After 72 h, however, the decrease rate was close to 0% and the effect of pulsed flow showed a tendency to decrease. The initial increase in organic matter is considered to be the cause of the re-floating of organic matter in the sediment deposited on the river bed according to the pulsed flow. Therefore, it is considered that the effect of sediment organic matter re-floating should be carefully considered when performing pulsed flow. Therefore, when the pulsed flow time was extended, the initial water quality concentrations temporarily increased due to the upstream influence, but the water quality concentrations slowly improved over time due to the flushing effect. However, only a temporary water quality improvement effect was observed, and it seemed that effective countermeasures were necessary to obtain a continuous water quality improvement effect.

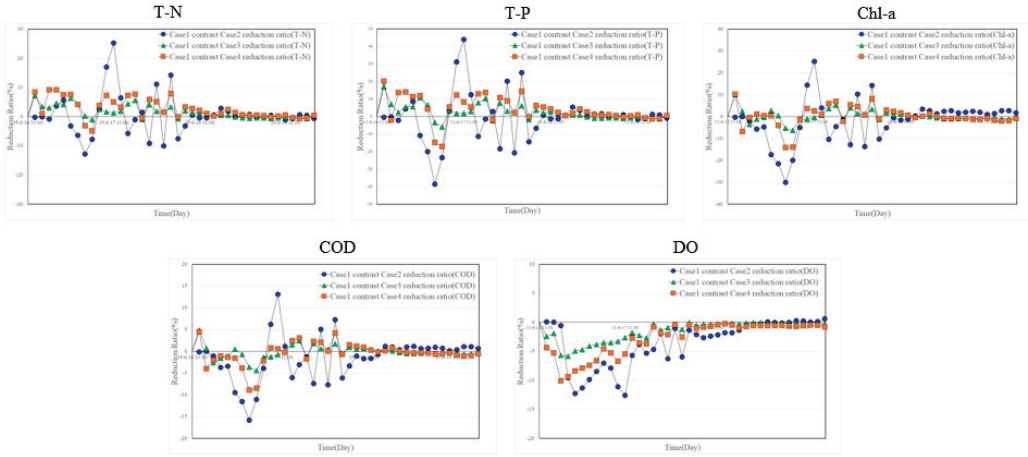


Figure 8. Case 1 Contrast Scenario Reduction Ratio.

For Cases 3 and 4, the flow velocity was found to be higher than that in Case 1 due to the opening of the gate. Therefore, the upstream water was temporarily introduced immediately after discharge, and thus the Chl-a, COD concentrations increased for 24 h after the start of pulsed flow similar to Case 2. The water quality concentrations of Case 4, in which there was a wider gap in the gate, were found to be higher than those of Case 3. T-N and T-P showed an immediate response to pulsed flow, and showed a tendency to improve compared to other water quality items due to the dilution effect as the flow rate increased. After 48 h, the flow was gradually stabilized, DO increased, and the decreased rates of Chl-a, COD, T-N, and T-P slowly increased, resulting in the improvement of water quality observed through the decrease in water quality concentrations. In addition, Case 4 exhibited a higher water quality improvement effect than Case 3. After 72 h, the decrease rate was close to 0% and the effect of pulsed flow disappeared as is seen in Case 2. These results indicate that the flushing effect is improved through the increase in the flow velocity caused by the opening of the downstream gate, and that the water quality improvement effect increased as the opening of the gate widened.

Table 2. Case 1 Contrast Scenario Reduction Ratio.

Case 1 Contrast Case 2 Reduction Ratio															
Time (hour)	Case	Chl-a (mg/m^3)	Chl-a (%)	Case	DO (mg/L)	DO (%)	Case	COD (mg/L)	COD (%)	Case	T-N (mg/L)	T-N (%)	Case	T-P (mg/L)	T-P (%)
After 24 h	1	31.2	7.68∇	1	9.4	6.49∇	1	6.57	4.48∇	1	2.57	0.22∇	1	0.126	3.99∇
	2	33.4		2	10		2	6.85		2	2.57		2	0.128	
After 48 h	1	33	0.41∇	1	9.2	4.46∇	1	6.76	0.79∇	1	2.71	1.86Δ	1	0.145	2.73Δ
	2	32.9		2	9.6		2	6.8		2	2.64		2	0.139	
After 72 h	1	30.7	1.52Δ	1	8.9	0.88∇	1	6.5	0.30Δ	1	2.56	0.48Δ	1	0.13	0.99Δ
	2	30.2		2	9		2	6.48		2	2.54		2	0.128	
Case 1 Contrast Case 3 Reduction Ratio															
Time (hour)	Case	Chl-a (mg/m^3)	Chl-a (%)	Case	DO (mg/L)	DO (%)	Case	COD (mg/L)	COD (%)	Case	T-N (mg/L)	T-N (%)	Case	T-P (mg/L)	T-P (%)
After 24 h	1	31.2	0.23∇	1	9.4	3.65∇	1	6.57	0.89∇	1	2.57	3.01Δ	1	0.126	4.28Δ
	3	31.2		3	9.8		3	6.62		3	2.49		3	0.12	
After 48 h	1	33	1.53Δ	1	9.2	1.21∇	1	6.76	0.56Δ	1	2.71	2.08Δ	1	0.145	3.67Δ
	3	32.5		3	9.3		3	6.72		3	2.65		3	0.14	
After 72 h	1	30.7	0.32∇	1	8.9	0.16∇	1	6.5	0.14∇	1	2.56	0.06Δ	1	0.13	0.16Δ
	3	30.8		3	9		3	6.51		3	2.56		3	0.129	
Case 1 Contrast Case 4 Reduction Ratio															
Time (hour)	Case	Chl-a (mg/m^3)	Chl-a (%)	Case	DO (mg/L)	DO (%)	Case	COD (mg/L)	COD (%)	Case	T-N (mg/L)	T-N (%)	Case	T-P (mg/L)	T-P (%)
After 24 h	1	31.2	2.06∇	1	9.4	6.32∇	1	6.57	2.33∇	1	2.57	4.17Δ	1	0.126	4.97Δ
	4	31.7		4	10		4	6.71		4	2.5		4	0.118	
After 48 h	1	33	3.10Δ	1	9.2	2.13∇	1	6.76	1.23Δ	1	2.71	4.08Δ	1	0.145	7.21Δ
	4	31.9		4	9.4		4	6.67		4	2.59		4	0.134	
After 72 h	1	30.7	0.17∇	1	8.9	0.57∇	1	6.5	0.05∇	1	2.56	0.85Δ	1	0.13	1.68Δ
	4	30.8		4	9		4	6.5		4	2.54		4	0.127	

4. Discussion

In this study, the water quality improvement effect of pulsed flow was analyzed for the section between the Gangjeong-Goryeong Weir and the Dalseong Weir of the Nakdong River, which became a controlled river due to the construction of multifunctional weirs. To determine an efficient pulsed flow method, the water quality improvement effects according to the upstream and downstream gate operation systems were compared via numerical simulation using the EFDC. To perform numerical simulation using EFDC, the parameters of the hydrodynamic model and water quality model were corrected through a comparison of the simulation results with the water quality observation results. The hydrodynamic model exhibited an R^2 value of 0.84, indicating that the model could effectively reproduce the flow of the target section. In addition, after correcting the parameters of the water quality model, the average error range of each water quality factor was found to be within 20% and the model accurately represented the water quality change of the target section. Various scenarios were analyzed using a physics-based water quality model. Finally, an effective multi-functional weir operation plan was attempted to improve water quality.

To analyze the water quality improvement effect of pulsed flow, a numerical simulation was performed for a total of four pulsed flow scenarios, including an actual pulsed flow case and three gate operation scenarios. Water quality improvement was observed mostly in the upstream section, and the water quality concentrations hardly changed at the 15-km downstream point. Furthermore, the water quality improvement gradually decreased with time. When the discharge time was doubled, the water quality concentrations became lower for 24–48 h. In addition, when the gates of the upstream and downstream weirs were opened instead of maintaining the discharge time, the water quality improvement effect was higher than when the discharge time was extended. In general, the pulsed flow is used as a method for controlling the algal bloom. Flow management strategies such as pulsed flows, weir drawdown, and artificial de-stratification have been proposed as means of controlling cyanobacterial blooms in regulated rivers [24]. The algal management strategy for the Murray–Darling Basin aims to reduce the frequency and intensity of algal blooms and other water quality problems associated with nutrient pollution in the basin through a framework of coordinated planning and management actions [25]. The success of pulsed flows to disperse established algal blooms has been demonstrated in the Murray Darling Basin [26–29]. The provision of pulsed flows above production targets has become part of the operating protocols for many systems including the Murray River. While the successes of pulsed flows to disperse algal blooms are numerous, there are documented cases of negative impacts. For example, the dispersal of an established bloom with pulsed flows can also create impacts in downstream reaches. In highly regulated systems such as the Menindee Lakes, blooms dispersed from upstream can simply reestablish in regulated reaches or impoundments further downstream where conducive flow conditions return [30]. The mitigation of algal bloom by pulsed flow in the Yeongsan River in Korea can be seen as an attempt to improve the efficiency with the minimum flow rate in the seasonal situation of the dry season when the flow rate is insufficient. However, it was a tool for solving problems in some sections, not macroscopically considering the condition of the downstream river. It contained limitations in controlling high concentrations of algal biomass [11]. When algal blooms occur frequently or for a long period of time, the economic loss caused by the suspension of small hydro power generation and the downstream impact of the transfer of algal blooms must be considered at the same time [1]. This indicates that managing the gate operation, for increasing the flow velocity, of the target area is essential to ensure improvement in the water quality and that a physical method for preventing stratification is also required.

5. Conclusions

In this study, water quality change according to puled flow was analyzed using a physics-based model. Recently, uncertainty about water quality variables is increasing due to changes in the river environment and the effects of climate change. Therefore,

field monitoring should be performed concurrently for precise predictive modeling. In addition, it is considered that the accumulation of monitoring data for the improvement of cyanobacteria in summer should proceed. By presenting a method to identify and predict changes in river flow and water quality according to weir operation scenarios, it is expected to be utilized as decision-making data for weir operation. Therefore, it is possible to continuously supplement and improve the quality of the results according to the actual weir operation scenario in the future. It is judged that the effect of improving water quality through efficient weir operation can be maximized in connection with the on-site monitoring results.

Author Contributions: Conceptualization, J.-K.H.; Data curation, W.-S.J.; Formal analysis, J.-K.H. and I.-H.P.; Investigation, J.-M.K.; Methodology, J.-K.H., W.-S.J., J.-M.K., I.-H.P. and Y.-D.K.; Project administration, Y.-D.K.; Writing—original draft, J.-K.H.; Writing—review & editing, Y.-D.K. All authors have read and agreed to the published version of the manuscript.

Funding: This work is supported by the Korea Agency for Infrastructure Technology Advancement (KAIA) grant funded by the Ministry of Land, Infrastructure and Transport (Grant 1615012318).

Institutional Review Board Statement: Not applicable.

Informed Consent Statement: Not applicable.

Data Availability Statement: Not applicable.

Conflicts of Interest: The authors declare no conflict of interest.

References

1. Watts, R.J.; Allan, C.; Bowmer, K.H.; Page, K.J.; Ryder, D.S.; Wilson, A.L. *Pulsed Flows: A Review of Environmental Costs and Benefits and Best Practice*; Waterlines Report; National Water Commission: Canberra, Australia, 2009; p. 16.
2. Brandt, S.A. Classification of geomorphological effects downstream of dams. *Catena.* **2000**, *40*, 375–401. [CrossRef]
3. Research on Implementing the Harmful Algal Bloom Alert System for Weir in the Nakdong River watershed, NIER RP2013-249. Available online: https://dl.nanet.go.kr/ (accessed on 1 January 2014).
4. Thoms, M.C.; Walker, K.F. Channel changes associated with two adjacent weirs on a regulated lowland alluvial river. *River Res. Appl.* **1993**, *8*, 271–284. [CrossRef]
5. Baker, P.D.; Brookes, J.D.; Burch, M.D.; Maier, H.R.; Ganf, G.G. Advection, growth and nutrient status of phytoplankton populations in the lower River Murray, South Australia. *River Res. Appl.* **2000**, *16*, 327–344. [CrossRef]
6. Mitrovic, S.M.; Chessman, B.C.; Bowling, L.C.; Cooke, R.H. Modelling suppression of cyanobacterial blooms by flow management in a Lowland River. *River Res. Appl.* **2006**, *22*, 109–114. [CrossRef]
7. Fovet, O.; Genthon, O.; Litrico, X.; Belaud, G. Managing invasive algae with flushing flows: New perspectives for canal control. In Proceedings of the World Environmental and Water Resources Congress 2012, Albuquerque, NM, USA, 20–24 May 2010; pp. 2177–2187. [CrossRef]
8. Chung, S.W.; Kim, Y.K. Impact of a flushing discharge from an upstream dam on the NH_3-N concentrations during winter seasons in Geum River. *J. Korean Soc. Water Environ.* **2005**, *21*, 609–616.
9. Chong, S.A.; Yi, H.S.; Hwang, H.S.; Kim, H.J. Modeling the Flushing Effect of Multi-purpose Weir Operation on Algae Removal in Yeongsan River. *J. Korean Soc. Environ. Eng.* **2015**, *37*, 563–572. [CrossRef]
10. Park, D.Y.; Park, H.S.; Kim, S.J.; Chung, S.W. Analysis of Water Quality Variation by Lowering of Water Level in Gangjeong-Goryong Weir in Nakdong River. *J. Environ. Impact Assess.* **2019**, *28*, 245–262. [CrossRef]
11. Shin, J.K.; Kang, B.G.; Hwang, S.J. Limnological Study on Spring-Bloom of a Green Algae, Eudorina elegans and Weirwater Pulsed-Flows in the Midstream (Seungchon Weir Pool) of the Yeongsan River, Korea. *Korean J. Ecol. Environ. Korean Soc. Limnol.* **2016**, *49*, 320–333. [CrossRef]
12. Hamrick, J.M. *A Three-Dimensional Environmental Fluid Dynamics Computer Code: Theoretical and Computational Aspects*; Special Report, 317; College of William and Mary: Williamsburg, VA, USA; Virginia Institute of Marine Science: Gloucester Point, VA, USA, 1992.
13. Hur, Y.T.; Park, J.H. Assessment of EFDC model for hydrodynamic analysis in the Nakdong River. *J. Korea Water Resour. Assoc.* **2009**, *42*, 309–317. [CrossRef]
14. James, S.C.; Shrestha, P.L.; Roberts, J.D. Modeling noncohesive sediment transport using multiple sediment size classes. *J. Coast. Res.* **2006**, *22*, 1125–1132. [CrossRef]
15. Lee, K.S. A Study on the Effect of Watershed Characteristics Change on Estuaries Using EFDC. Master's Thesis, Changwon National University, Changwon, Korea, 2013.

16. Park, K.; Kuo, A.Y.; Shen, J.; Hamrick, J.M. *A Three-Dimensional Hydrodynamic-Eutrophication Model (HEM-3D): Description of Water Quality and Sediment Process Submodels, Special Report*; Virginia Institute of Marine Science: Gloucester Point, VA, USA; College of William and Mary: Williamsburg, VA, USA, 1995.
17. Moustafa, M.Z.; Hamrick, J.M. Modeling circulation and salinity transport in the Indian River Lagoon. In *Estuarine and Coastal Modeling*; ASCE: Reston, VA, USA, 1993; pp. 381–395.
18. National Geographic Information Institute. Available online: https://ngii.go.kr (accessed on 1 January 2014).
19. Ann, J.M.; Park, I.H. An Assessment on the Hydraulic Characteristics of a Multi-dimensional Model in Response to Measurement Resolution and Spatial Interpolation Methods. *Korean Soc. Geospat. Inf. Syst.* **2012**, *20*, 43–51. [CrossRef]
20. National Institute of Environmental Research Water Information System. Available online: https://water.nier.go.kr (accessed on 1 January 2014).
21. Seo, S.H. Analysis of Hydraulic Characteristics on Geum River Using 3 Dimensional Numerical Model-Focused on the Gongju Weir. Master's Thesis, Kongju National University, Kongju, Korea, 2012.
22. Water Resources Management Information System. Available online: http://www.wamis.go.kr/. (accessed on 1 January 2014).
23. National Institute of Environmental Research. *Nakdong River Water Quality Model Factor Research*; National Institute of Environmental Research: Incheon, Korea, 2004.
24. Herath, G. Freshwater algal blooms and their control: Comparison of the European and Australian experience. *J. Environ. Manag.* **1997**, *51*, 217–227. [CrossRef]
25. Sherman, B.S.; Webster, I.T.; Jones, G.J.; Oliver, R.L. Transitions between Auhcoseira and Anabaena dominance in a turbid river weir pool. *Limnol. Oceanogr.* **1998**, *43*, 1902–1915. [CrossRef]
26. Webster, I.T.; Sherman, B.S.; Bormans, M.; Jones, G. Management strategies for cyanobacterial blooms in an impounded lowland river. *Regul. Rivers Res. Manag. Int. River Res. Manag.* **2000**, *16*, 513–525. [CrossRef]
27. Maier, H.R.; Kingston, G.B.; Clark, T.; Frazer, A.; Sanderson, A. Risk-based approach for assessing the effectiveness of flow management in controlling cyanobacterial blooms in rivers. *River Res. Appl.* **2004**, *20*, 459–471. [CrossRef]
28. Mitrovic, S.M.; Oliver, R.L.; Rees, C.; Bowling, L.C.; Buckney, R.T. Critical flow velocities for the growth and dominance of Anabaena circinalis in some turbid freshwater rivers. *Freshw. Biol.* **2003**, *48*, 164–174. [CrossRef]
29. Vink, S.; Bormans, M.; Ford, P.W.; Grigg, N.J. Quantifying ecosystem metabolism in the middle reaches of Murrumbidgee River during irrigation flow releases. *Mar. Freshw. Res.* **2005**, *56*, 227–241. [CrossRef]
30. Grace, M.; Holland, D.; Chan, T.; Roberts, S. *Lower Darling River Algal Growth Studies*; Canberra, Australia, 2004. Available online: https://www.act.gov.au/ (accessed on 1 January 2014).

applied sciences

MDPI

Article

Radioactivity in Soils of Kosovo and Radiological Implications

Sehad Kadiri [1], Serdar Dizman [2], Cafer M. Yeşilkanat [3], Hamdi Aliu [4] and Gezim Hodolli [4,*]

[1] Faculty of Radiology, AAB College, 10 000 Pristina, Kosovo
[2] Department of Physics, Faculty of Arts and Sciences, Recep Tayyip Erdogan University, 53100 Rize, Türkiye
[3] Science Teaching Department, Artvin Çoruh University, 08000 Artvin, Türkiye
[4] Faculty of Agriculture and Veterinary, University of Pristina "Hasan Prishtina", 10 000 Pristina, Kosovo
* Correspondence: g.hodolli@hotmail.com or gezim.hodolli@uni-pr.edu

Abstract: This study was carried out to determine the presence of the main radionuclides from natural and artificial radioactivity in the soil of Kosovo, using gamma-ray spectroscopy. The mean activity concentration for Ra-226, Th-232, K-40, and Cs-137 was 22.32 ± 1.41, 22.14 ± 1.31, 358.16 ± 8.85, and 12.94 ± 0.44 Bq/kg, respectively. Radium equivalent activity ranged from 47 to 100 Bq/kg. The mean of calculated values for the gamma index (I_γ), external hazard index (H_{ex}), absorbed dose rate (ADR), annual gonadal dose rate (AGDE), annual effective dose rate (AEDE), and excess lifetime cancer risk (ELCR) were 0.61, 0.22, 40 nGy/h, 275 μSv/year, 49 μSv/year, and 170, respectively. In conclusion, the radiological parameters arising from the soil samples of Kosovo belong to the normal range of radionuclides, compared to those compiled by UNSCEAR from worldwide reports; therefore, health hazards are insignificant.

Keywords: radioactivity; spatial mapping; Kosovo; soil; radiological hazard

Citation: Kadiri, S.; Dizman, S.; Yeşilkanat, C.M.; Aliu, H.; Hodolli, G. Radioactivity in Soils of Kosovo and Radiological Implications. *Appl. Sci.* **2022**, *12*, 9520. https://doi.org/10.3390/app12199520

Academic Editor: Dibyendu Sarkar

Received: 29 August 2022
Accepted: 19 September 2022
Published: 22 September 2022

Publisher's Note: MDPI stays neutral with regard to jurisdictional claims in published maps and institutional affiliations.

Copyright: © 2022 by the authors. Licensee MDPI, Basel, Switzerland. This article is an open access article distributed under the terms and conditions of the Creative Commons Attribution (CC BY) license (https://creativecommons.org/licenses/by/4.0/).

1. Introduction

Radiation is found everywhere in the earth's environment, and there is evidence that it was so from the beginning of time and will continue to be present. Therefore, all human beings are exposed to natural radiation sources and human-made sources daily. Natural background radiation comes from cosmic, terrestrial, and internal radiation. The most important source of man-made radiation exposure to the public is medical procedures, such as diagnostic X-rays, nuclear medicine, and radiation therapy. Smaller contributions to man-made radiation sources include nuclear weapons tests, nuclear reactor accidents, and nuclear power plants. The artificial radionuclide ^{137}Cs were spread to the soil of Kosovo due to fallout after the Chornobyl nuclear power accident on 26 April 1986 [1,2]. Furthermore, during the Kosovo War in 1999, the North Atlantic Treaty Organization (NATO) used depleted uranium (DU). Hence, some regions of Kosovo were radiologically contaminated [3–6].

Humans are exposed to background radiation from cosmic radiation and the gamma rays released in soils, building materials, water, food, and air. Some regions have been identified as high background radiation areas (HBRAs), and possible harmful effects on public health were detected [7]. Therefore, it is crucial to install an adequate system for health protection. In recent years, these conditions have attracted more attention from researchers, and much more researchers have been conducted on them [8–14]. Radioactivity in soil directly impacts fruits and vegetables [15–17].

The present study is carried out as there is no study on determining radioactivity levels in soil samples taken from all regions of Kosovo. In this context, the primarly purpose of this study is to detect natural and artificial radioelements ^{226}Ra, ^{232}Th, ^{40}K, and ^{137}Cs in soil samples. For the assessment of radiological hazards arising from natural radioactivity, radium equivalent activity (Ra_{eq}), gamma index ($I\gamma$), external hazard index (H_{ex}), absorbed dose rate in the air (D), annual gonadal dose rate (AGDE), the annual effective dose rate

(AEDE), and excess lifetime cancer risk (ELCR) were calculated. The results were compared with internationally recommended values.

2. Materials and Methods

2.1. Study Area

Kosovo is located in Southeast Europe, in the central part of the Balkan Peninsula. It borders Serbia, Montenegro, Albania, and North Macedonia. Kosovo extends within longitudes 41°50′58″ and 43°15′42″ and within latitudes 20°01′30″ and 21°48′02″. It covers a surface area of approximately 10,900 km^2, and it is characterized by elevations between 400 and 700 m above sea level but shows unexpected changes in relief and morphology. These morphological changes are a consequence of the geological setting. The population of Kosovo is almost 1.9 million, and the population density is 168 people per square kilometer.

2.2. Sample Collection and Preparation

For a homogeneous sampling process in the whole country, the cluster sampling method was chosen [18]. The territory of Kosovo was divided into thirty equal surface units with a rectangular shape. One cell represented around 363 km^2, and a soil sample was taken from each. A total of 30 soil samples were taken in the year 2020. Geographical sampling locations were recorded by portable GPS during sampling time. The digital map with the sampling location was prepared using free open-source QGIS. The location distributions of the sampling are illustrated in Figure 1. The soil samples, were collected using a shovel, from 0 to 5 cm in depth. The soil samples were removed from unwanted redundancies (stones, vegetation, and roots) and were placed in clean, zip-locked bags (1–2 kg). The samples were then transferred to the laboratory. They were dried in an oven at 60 °C for 48 h, grained, passed through 2 mm sieves, weighed, and transferred into uncontaminated, empty Marinelli beakers of uniform size. Finally, the samples were stored for four weeks to allow the daughter products to come into radioactive secular equilibrium with their parents, ^{226}Ra and ^{222}Rn.

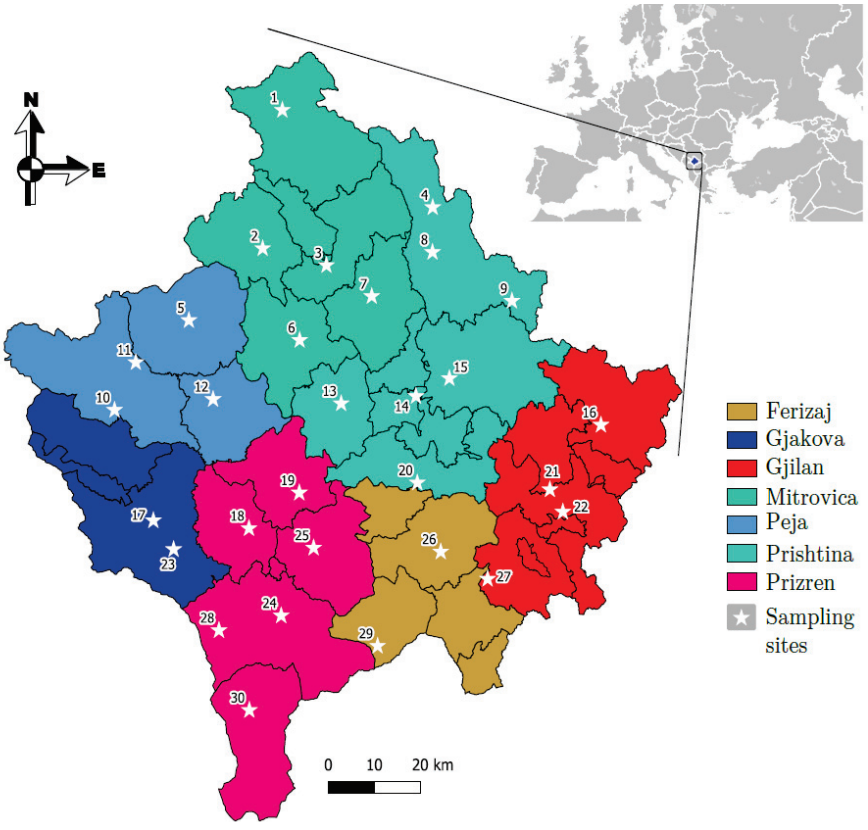


Figure 1. The map of Kosovo and the location of the sampling points.

2.3. Experimental Methods

The radioactivity levels of the samples were analyzed using gamma spectrometry, which is an equipped, high-purity germanium gamma-ray detector ORTEC, with a 55% relative efficiency and a resolution of full width at half maximum (FWHM) of 1.90 keV at 1.33 MeV of peaks for the gamma of ^{60}Co. The detector was shielded by a cylindrical lead shield, with an average thickness of 10 cm, to achieve a background level as low as possible. Efficiency and energy calibration of the detector was carried out with a ^{152}Eu calibration source (Amersham Company, Amersham, UK). As standard procedure the cylindrical geometry of samples with constant volume and distance were applied to all samples.

2.4. Activity Concentration (A)

Each of the soil samples reaching the balance were placed on the detector and counted for a period of 60.000 s. The obtained gamma spectra were analyzed using data acquisition and analysis program named Gamma Vision [19]. The activity concentration of each sample was subtracted from the activity concentration of an empty plastic container to remove the contribution of the background radiation. To calculate the activity concentrations of the soil samples by specific radionuclide (A), we used Equation (1):

$$A(\text{Bq/kg}) = \frac{C}{\varepsilon \times P \times m \times t} \quad (1)$$

where C is the net count (area) under the corresponding peak, ε is the detector efficiency at the corresponding peak energy, P is the absolute transition probability of the specific γ-ray at the corresponding peak energy, m is the mass of the sample (kg), and t is the counting time in seconds.

To measure the activity concentration of ^{226}Ra, ^{232}Th, ^{40}K, and ^{137}Cs on soil samples, we used standard methodology, based on γ-ray energies of specific elements. This procedure has been described elsewhere [20,21].

To calculate the uncertainty of the activity concentration (ΔA), we used Equation (2) [22].

$$\Delta A = A\sqrt{\left(\frac{\Delta C}{C}\right)^2 + \left(\frac{\Delta \varepsilon}{\varepsilon}\right)^2 + \left(\frac{\Delta P}{P}\right)^2 + \left(\frac{\Delta m}{m}\right)^2} \quad (2)$$

where ΔC is the uncertainty of count rate, ΔP is the uncertainty of emission probability found in the nuclear data tables, $\Delta\varepsilon$ is the uncertainty of efficiency, and Δm is the uncertainty of weighing.

To calculate the minimum detectable activity for each radionuclide, we used Equation (3) [23]:

$$\text{MDA}(\text{Bq/kg}) = \frac{1.645\sqrt{B}}{\varepsilon \times P \times m \times t} \quad (3)$$

where 1.645 is the statistical coverage factor (confidence level 95%), and B is the background for the related region of a specific radionuclide.

In addition, the accuracy of the measurements was obtained from the reference standard range of 95 to 98% for all radionuclides. The certified soil reference material (IAEA-375) checked the measurement system for accuracy with a matrix similar to the samples.

2.5. Calculation of Radiological Hazards

Radium equivalent activity (Ra_{eq}) is a widely used hazard index and was calculated through the relation given by Beretka and Mathew [24]. It was assumed that 370 Bq/kg of ^{226}Ra, 259 Bq/kg of ^{232}Th, and 4810 Bq/kg of ^{40}K produced the same gamma-ray dose rate. The calculation is shown in Equation (4):

$$\text{Ra}_{eq} = A_{\text{Ra}} + 1.43A_{\text{Th}} + 0.077A_{\text{K}} \quad (4)$$

where A_{Ra}, A_{Th}, and A_{K} are the activity concentrations of related radionuclides, respectively.

Gamma index (I_γ)—Gamma index (I_γ) was calculated by using the Equation (5):

$$I_\gamma = \frac{A_{Ra}}{150Bq/kg} + \frac{A_{Th}}{100Bq/kg} + \frac{A_K}{1500Bq/kg} \quad (5)$$

where A_{Ra}, A_{Th}, and A_K were explained in Equation (4) of this paper [25].

External hazard indices (H_{ex}) were calculated for the samples investigated using the model proposed by Krieger [26], where the external hazard index is given by:

$$H_{ex} = \frac{A_{Ra}}{370Bq/kg} + \frac{A_{Th}}{259Bq/kg} + \frac{A_K}{4810Bq/kg} < 1 \quad (6)$$

where A_{Ra}, A_{Th}, and A_K, were explained in Equation (4) of this paper

Absorbed dose rate in air (ADR) is the external terrestrial gamma radiation in the air at 1 m above ground level, due to the presence of ^{226}Ra, ^{232}Th, ^{40}K, and ^{137}Cs in the soil samples at each site. This was calculated using the following Equation (7) [27],

$$ADR = aA_{Ra} + bA_{Th} + cA_K + dA_{Cs} \quad (7)$$

where A_{Ra}, A_{Th}, and A_K, were explained in Equation (4) of this paper. The coefficients a, b, c, and d are the dose conversion factors, and their values are 0.462, 0.604, 0.042, and 0.1243 in nGy/h per Bq/kg, respectively.

The annual gonadal dose rate (AGDE)—The activity of bone marrow and bone surface cells are considered organs of interest by UNSCEAR [28]. Therefore, the AGDE, due to the activity concentrations of ^{226}Ra, ^{232}Th, and ^{40}K, was calculated using Equation (8) [29]:

$$AGDE(\mu Sv/year) = 3.09A_{Ra} + 4.18A_{Th} + 0.314A_K \quad (8)$$

where A_{Ra}, A_{Th}, and A_K, were explained in Equation (4) of this paper. The coefficients 3.09, 4.18, and 0.314 are conversion factors in (Sv/y)/(Bq/kg).

The annual effective dose rate (AEDE)—The annual effective dose equivalent is given by using Equation (9):

$$AEDE(\mu Sv/year) = D \times DCF \times OF \times 8760h/year \times 10^{-3} \quad (9)$$

where DCF is the dose conversion factor absorbed in the air (0.7 Sv/Gy), and OF is the outdoor occupancy factor (0.2) [28].

Excess lifetime cancer risk (ELCR) is given by using Equation (10):

$$ELCR = AEDE \times DL \times RF \quad (10)$$

where DL is the life span (70 years) and RF is the risk factor (Sv^{-1}), that is, mortal cancer risk per sievert. As stochastic effects, the ICRP 60 used values of 0.05 for the community [30].

2.6. Spatial Interpolation and Mapping

The distribution maps created in this study were prepared according to the SGS-ANN approach suggested by Yeşilkanat [31]. In this approach, different from the original literature, each spatial pixel (100×100 m^2) was calculated separately, using in a hybrid manner the conditional gauss simulation (SGS) and artificial neural network (ANN) methods in order to predict local changes rather than general distribution characteristics. Therefore, the population ratios and the radiological risks per pixel were calculated by weighting the population. More details about the ANN model can be found in the cited source [31].

For all calculations and maps used in the study, SP [32], GSTAT [33], RSNNS [34], and caret library files [35] were used together with the R programming language [36].

3. Results and Discussion

3.1. The Activity Concentrations of the Radionuclides

It was observed that the mean activity concentrations of these radionuclides were comparable with the worldwide average concentration [28]. In this context, all of the concentrations of ^{232}Th and ^{226}Ra were found to be below the world average. The average value of the ^{40}K concentrations in the studied soil samples was lower than the world average. However, the ^{40}K concentrations of site-1 (Leposaviq), site-2 (Zubin Potok), site-3 (Mitrovicë), site-4 (Podujevë), site-8 (Podujevë), site-10 (Pejë), site-15 (Prishtinë), site-17 (Gjakovë), and site-30 (Dragash) samples were slightly higher than the worldwide average. The difference in the activity values of the naturally occurring ^{40}K in the soil samples had been fertilized with artificial fertilizers and contained residues from animal carcasses.

^{137}Cs do not exist in soil naturally, but it is a product of fallout radioactivity. It might have been deposited in the soil of Kosovo, presumably due to the Chornobyl nuclear power accident on 26 April 1986, a nuclear weapon tests, or a reprocessing of spent nuclear fuel. The concentration of ^{137}Cs in the trace level was reported on honey samples from Kosovo [37]. The study findings were compared to the values of some works used in other literature (Table 1). As shown in Table 1, the average activity value (22.32 Bq/kg) found for ^{226}Ra in this study is lower than the reported values in Italy (79 Bq/kg) [38], Saudi Arabia (23.2 Bq/kg) [39], Lebanon (27 Bq/kg) [40], Yemen (44.4 Bq/kg) [41], Syria (29 Bq/kg) [42], Artvin (42.2 Bq/kg) [12], and Croatia (44.7 Bq/kg) [43], while less results were reported for Bolu (18.2 Bq/kg) [44], and Oman (14.4 Bq/kg) [45]. The average activity value (21.1 Bq/kg) found for ^{232}Th is higher than the reported values in Saudi Arabia (7.7 Bq/kg), Oman (9.9 Bq/kg), and Turkey (17.3 Bq/kg), yet lower than the other values. The average activity value found for ^{40}K is lower than the reported values in Italy (640 Bq/kg), Yemen (822.7 Bq/kg), and Croatia (542 Bq/kg) but higher than other values. In addition to these, the average activity value found for ^{137}Cs in the soil samples is lower than the reported values in Italy (25 Bq/kg), Lebanon (21 Bq/kg), Oman (2770 Bq/kg), Syria (27 Bq/kg), and Croatia (30.8 Bq/kg) but higher than other values.

Table 1. Comparisons of specific radionuclide concentrations by countries (Bq/kg).

Country	^{226}Ra	^{232}Th	^{40}K	^{137}Cs	References
Italy	79	48	640	25	[38]
Saudi Arabia	23.2	7.7	278.0	1.4	[39]
Lebanon	27	24	246	21	[40]
Yemen	44.4	58.2	822.7	4.8	[41]
Syria	29	21	310	27	[42]
Upper Egypt *	16.5	10.2	192	/	[46]
Turkey (Bolu)	18.2	17.3	258.3	7.5	[44]
Turkey (Artvin)	42.2	32.2	402	30.4	[12]
Croatia	44.7	42.3	542	30.8	[43]
Kosovo	22.3	21.1	358.2	12.9	Present study

* The values are presenting the average of the range.

The statistical summary information of the activity concentrations (actual data) obtained from the Kosovo soils' experimental measurement results and the simulation distributions obtained by the SGS-ANN method for each radionuclide is shown in Table 2, comparatively. According to this, for the actual data, the activity concentrations of ^{226}Ra, ^{232}Th, ^{40}K, and ^{137}Cs varied from 8 Bq/kg to 30 Bq/kg, with a mean of 22 Bq/kg; 7 Bq/kg to 31 Bq/kg, with a mean of 21 Bq/kg; 105 Bq/kg to 515 Bq/kg, with a mean of 358 Bq/kg; and <MDA to 43 Bq/kg, with a mean of 13 Bq/kg, respectively. Similarly, for the simulation data, the activity concentrations of ^{226}Ra, ^{232}Th, ^{40}K, and ^{137}Cs varied from 12 Bq/kg to 29 Bq/kg, with a mean of 23 Bq/kg; 11 Bq/kg to 29 Bq/kg, with a mean of 21 Bq/kg; 181 Bq/kg to 541 Bq/kg, with a mean of 370 Bq/kg; and 1 to 41 Bq/kg, with a mean of 10 Bq/kg, respectively.

Table 2. Statistics of the actual measurement and simulation of radionuclide activity concentrations in the soil of Kosovo.

Radionuclides	Data	Mean-SD	Median	Min–Max	Percentiles (25–75)
^{226}Ra (Bq/kg)	Actual	22 ± 5	24	8–30	19–26
	Simulation	23 ± 2	23	12–29	21–25
^{232}Th (Bq/kg)	Actual	21 ± 5	21	7–31	19–25
	Simulation	21 ± 2	21	11–29	20–22
^{40}K (Bq/kg)	Actual	358 ± 106	368	105–515	289–447
	Simulation	370 ± 48	369	181–541	337–406
^{137}Cs (Bq/kg)	Actual	13 ± 12	10	<MDA–43	3–15
	Simulation	10 ± 2	10	1–41	7–13
^{232}Th/^{226}Ra	Actual	0.95 ± 0.1	0.95	0.69–1.21	0.9–1.00
	Simulation	0.93 ± 0.07	0.93	0.68–1.33	0.88–0.97
^{40}K/^{226}Ra	Actual	16.5 ± 5.1	16.9	7.75–30.4	12.8–18.5
	Simulation	16.4 ± 2.4	16.3	9.75–29.4	14.7–17.8
^{40}K/^{232}Th	Actual	17.4 ± 5.2	18.5	7.13–29.9	13.4–20.5
	Simulation	17.6 ± 2.3	17.7	9.83–27.6	15.9–19.3

In Table 2, statistics on the proportional changes of radionuclide activities are comparatively listed for both real data and simulation data. For the actual data, the ^{232}Th/^{226}Ra ratios varied from 0.69 to 1.21, with an average of 0.95 in Kosovo. The correlation between thorium and radium is lower than the world's average (1.29). The ^{40}K/^{226}Ra ratios varied from 7.75 to 30.4, with an average of 16.5 in Kosovo. Its value is higher than the average of the world (11.77). Lastly, the ^{40}K/^{232}Th ratios varied from 7.13 to 29.9, with an average of 17.4 in Kosovo. The ratio value is greater than the world's average (9.16). Similarly, for the simulation data, the ^{232}Th/^{226}Ra, ^{40}K/^{226}Ra, and ^{40}K/^{232}Th ratios varied from 0.68 to 1.33, with a mean of 0.93; 9.75 to 29.4, with a mean of 16.4; and from 9.83 to 27.6, with a mean of 17.6, respectively.

Correlations between natural radionuclide concentrations were also examined for real and simulation data. A significantly positive and strong correlation was determined between ^{232}Th and ^{226}Ra radionuclides (Figure 2). The variance explained (R^2) between ^{232}Th, and ^{226}Ra radionuclides were calculated as 81% for actual data and 51% for simulation data. On the other hand, the correlations between ^{40}K and ^{226}Ra and ^{40}K and ^{232}Th were determined, and it was determined that there is a weak and positive relationship in both cases. The variance explained between ^{40}K and ^{226}Ra radionuclides were calculated as 14% for the actual data and 8.5% for the simulation data. Again, the variance explained between ^{40}K and ^{232}Th radionuclides were calculated as 10% for actual data and 7.3% for simulation data. The presence of a significant correlation between the activity concentrations of ^{226}Ra, ^{232}Th, and ^{40}K radionuclides shows that radionuclides in soils of the study area are derived from the same natural source.

Figure 3 comparatively shows the histograms of both actual and simulation data for the activity concentrations of ^{226}Ra, ^{232}Th, ^{40}K, and ^{137}Cs radionuclides. According to the Shapiro–Wilk normality test results, ^{232}Th and ^{40}K distributions were found to be normal ($p > 0.05$), while ^{226}Ra and ^{137}Cs distributions were log-normal ($p > 0.05$). In addition, it was determined that the distribution structures of the real measurement data and the simulation data were significantly similar ($p > 0.05$), according to the results of the two-sample Kolmogorov–Smirnov test. From all these findings, it could be seen that the simulation data, which reveal the radionuclide distribution for the entire study area, are very effective in representing real data.

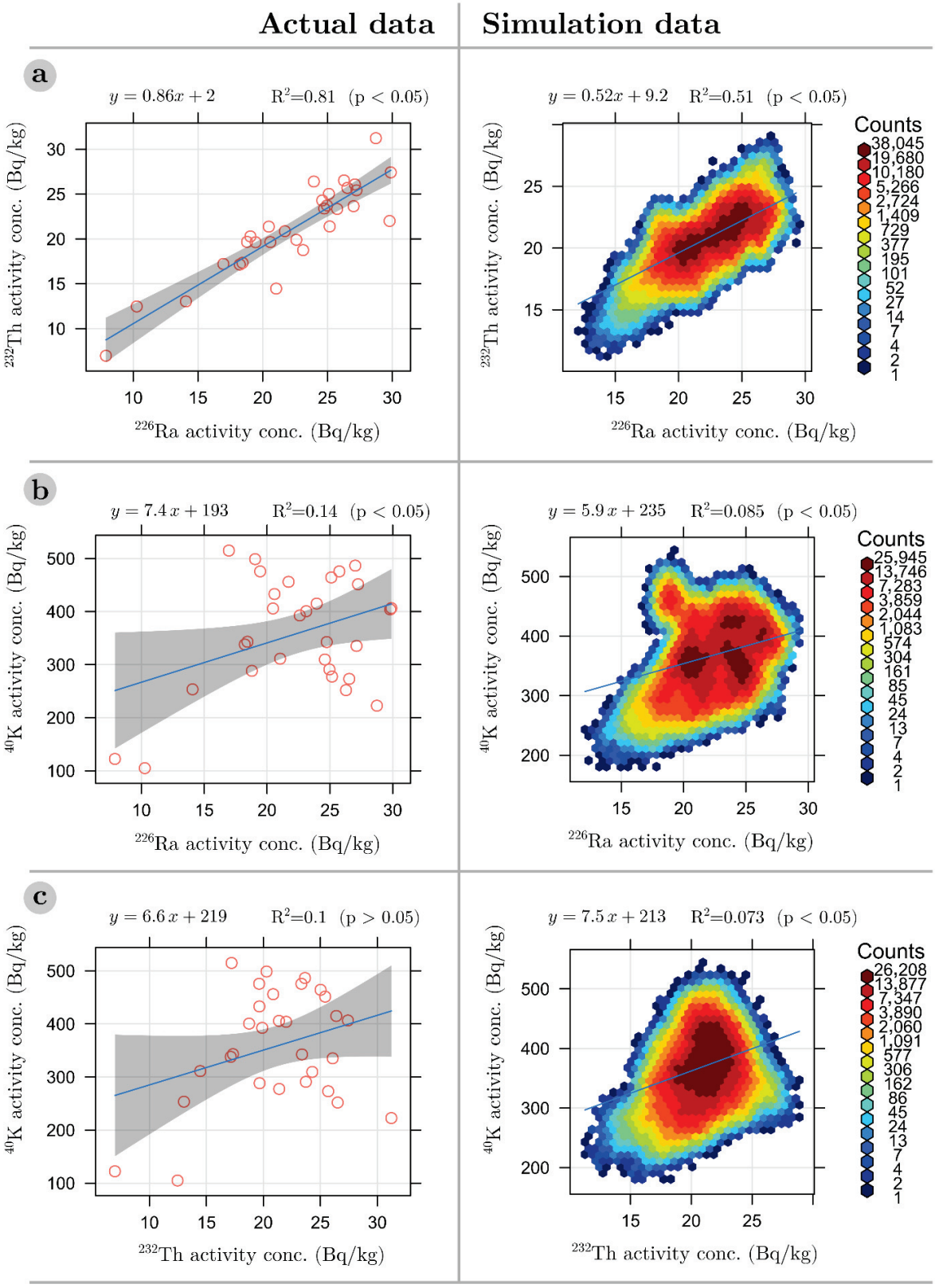


Figure 2. Correlation analysis of natural radioisotopes (^{226}Ra, ^{232}Th, ^{40}K) versus each other for actual and simulation data. (**a**) Correlation between ^{226}Ra and ^{232}Th activity concentration, (**b**) Correlation between ^{226}Ra and ^{40}K activity concentration, (**c**) Correlation between ^{232}Th and ^{40}K activity concentration.

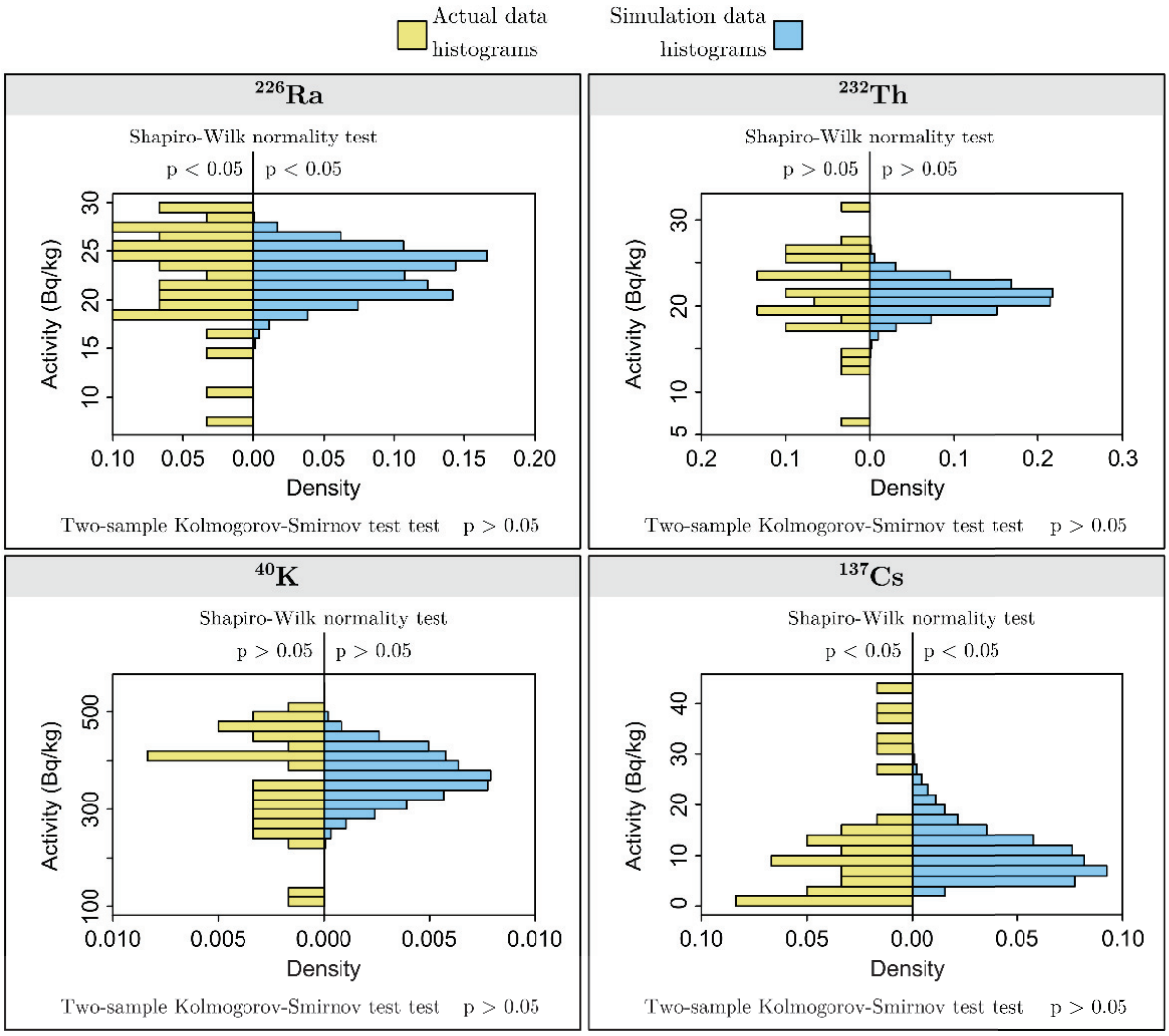


Figure 3. Frequency distributions of ^{226}Ra, ^{232}Th, ^{40}K, and ^{137}Cs concentrations for actual and simulation data.

Figure 4 shows the performance metrics of the SGS-ANN estimation results. Explanations of these performance evaluation metrics are given in the Supplementary Material. According to the results of cross-validation, the Pearson correlation coefficients (significance, MAE in Bq/kg, RMSE in Bq/kg) for ^{226}Ra, ^{232}Th, ^{40}K, and ^{137}Cs were 0.34 ($p < 0.05$, 4.2, 5.0), 0.37 ($p < 0.05$, 3.9, 4.7), 0.42 ($p < 0.05$, 78.7, 95.6), and 0.40 ($p < 0.05$, 8.7, 11.4), respectively.

Figure 5 shows the distribution maps of the activity concentrations of ^{226}Ra, ^{232}Th, ^{40}K, and ^{137}Cs for Kosovo, generated by the SGS-ANN method at 100 × 100 m spatial pixel resolution. According to these distribution maps, it is noteworthy that natural radionuclide activities are higher in the northern, southern, and western parts of Kosovo compared to the inner and eastern parts. ^{137}Cs artificial radionuclide activities are observed to be more effective in the eastern parts of the country close to Chernobyl.

3.2. Assessment of Radiological Hazards

Statistical descriptors of Ra_{eq}, I_γ, and H_{ex} radiological hazard indices were determined according to SGS-ANN simulation data for all Kosovo. The smallest and highest average Ra_{eq}, I_γ, and H_{ex} values were determined in Gjilan (Ra_{eq} = 73 Bq/kg, I_γ = 0.55, H_{ex} = 0.20) and Mitrovica (Ra_{eq} = 87 Bq/kg, I_γ = 0.66, H_{ex} = 0.24), respectively.

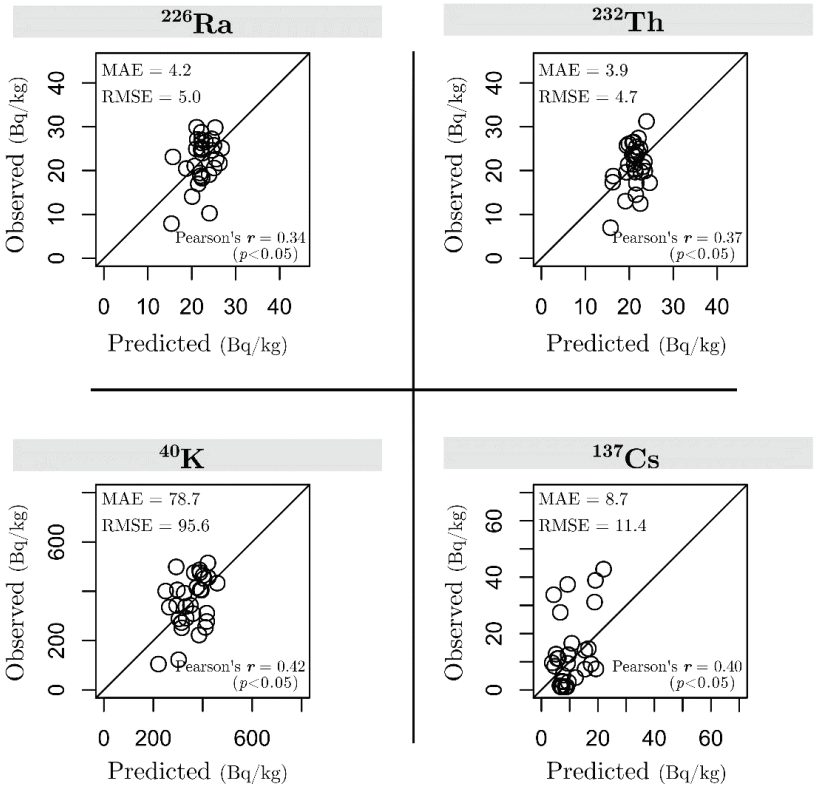


Figure 4. The cross-validation diagrams generated as a result of comparing the predicted values with the observed values for ^{226}Ra, ^{232}Th, ^{40}K, and ^{137}Cs.

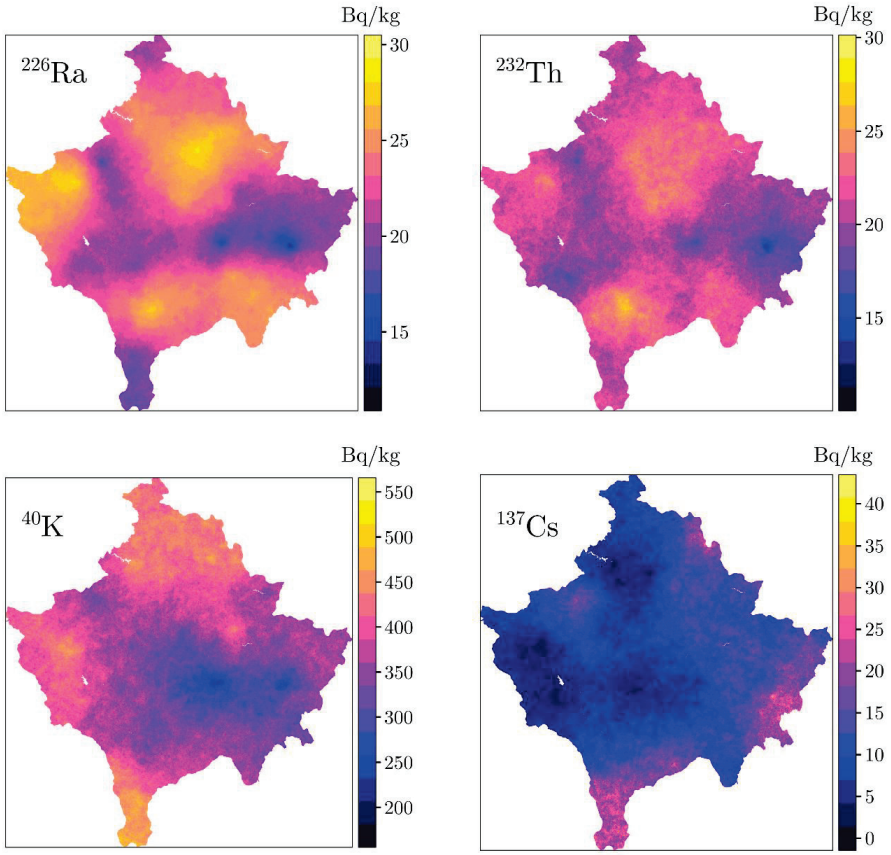


Figure 5. Distributions of radioactivity concentration for ^{226}Ra, ^{232}Th, ^{40}K, and ^{137}Cs.

In Kosovo soil samples, the mean value of Ra_{eq} was found to be 80.1 Bq/kg. This value is lower than the worldwide average of 370 Bq/kg [28]. Additionally, when the average Ra_{eq} values were compared with the values of other countries, they were found to be lower than the obtained values of 166 Bq/kg in Fırtına Valley [47], 112 Bq/kg in Artvin [12], and 232 Bq/kg in southwestern Nigeria [48]. The mean I_γ calculated for the Kosovo soil samples had a mean value of 0.61, which is less than the mean value of the world, which is 1, according to the European Commission (European Commission, 1999). The average value of Hex was found to be only 0.22, so no harmful effects to the residents can happen due to radiation hazards. Figure 6 shows distribution maps of radiological hazards for Kosovo. When these maps were examined, it was seen that radiological hazards are at low levels, especially in the province of Gjilan and in the inner parts of Prishtina. They are at high levels in the Mitrovica province, north of Prishtina, south of Prizren, and western parts of Gjakova and Peja.

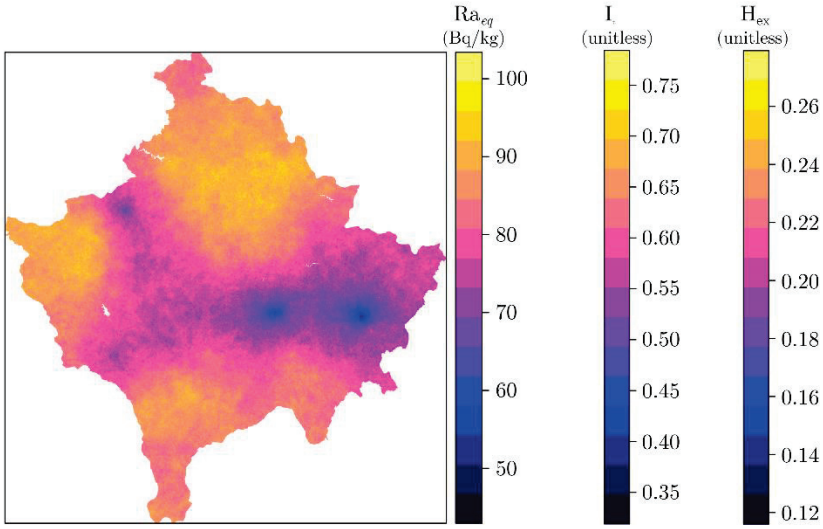


Figure 6. The values of radiological hazard parameters, based on measured and simulated data from the soil.

3.3. Assessment of Radiological Health Risks

Statistical descriptors of AGDE, ADR, AEDE, and ELCR radiological health risk levels were determined according to SGS-ANN simulation data for all of Kosovo. The smallest and highest of the mean levels of AGDE, ADR, AEDE, and ELCR were determined in the provinces of Gjilan (AGDE = 248 μSv/year, ADR = 37 nGy/h, AEDE = 46 μSv/year and ELCR = 0.16×10^{-3}) and Mitrovica (AGDE = 296 μSv/year, ADR = 43 nGy/h, AEDE = 53 μSv/year and ELCR = 0.18×10^{-3}), respectively.

The mean AGDE value was found to be 269.8 μSv/year. These values are lower than the world mean (300 μSv/year) [49]. However, the maximum values calculated in all provinces except Gjilan were found to be higher than the global average. The mean of the absorbed dose rate (ADR) in the air, at 1 m above the ground, generated from gamma radiation of ^{226}Ra, ^{232}Th, ^{40}K, and ^{137}Cs in the soil samples of Kosovo resulted in 39.3 nGy/h, and this is 27% lower than the recommended values by UNSCEAR [28].

In addition, the average AEDE of the soil samples that resulted was 48 μSv/y. It is lower than the average world value of 70 μSv/y [28]. The calculated values of the excess lifetime cancer risk (ELCR) for all soil samples ranged from 0.1×10^{-3} to 0.21×10^{-3}, with a mean of 0.17×10^{-3}. The average world value of ELCR is 0.29×10^{-3} [28]. The average ELCR acquired in this study was lower than the world's mean values. Furthermore, the distribution map of these parameters calculated for Kosovo is shown in Figure 7 and Table 3.

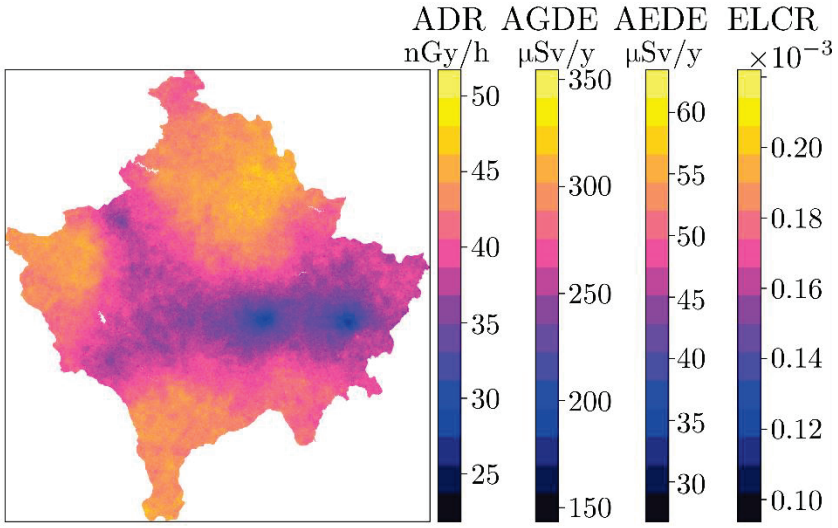


Figure 7. Distributions of radiological health risks and calculated parameters ADR, AGDE, AEDE, and ELCR.

Table 3. The values of radiologic hazard parameters calculated for the soil samples of Kosovo.

Statistics	Ra_{eq}	I_g	H_{ex}	AGDE (μSv/y)	ADR (nGy/h)	AEDE (μSv/y)	ELCR ($\times 10^{-3}$)
Minimum	27.27	0.20	0.07	91.92	13.47	16.51	0.06
Maximum	100.40	0.74	0.27	335.11	48.77	59.81	0.21
Average	80.13	0.61	0.22	269.81	39.3	48.22	0.17
World average	370	≤1	≤1	300	60	70	2.9

4. Conclusions

This study aimed to determine the levels of natural (^{226}Ra, ^{232}Th, and ^{40}K) and artificial (^{137}Cs) radioactivity of soil samples from Kosovo. It was done by using a high-purity germanium gamma-ray detector. The reported activity concentrations in the present study were within the proposed limits of international radiation protection agencies. In addition to activity measurements, the radiological hazard parameters: radium equivalent activity (Ra_{eq}), gamma index (I_γ), external hazard index (H_{ex}), absorbed dose rate in the air (D), annual gonadal dose rate (AGDE), the annual effective dose rate (AEDE), and excess lifetime cancer risk (ELCR) were calculated, and the obtained results were lower than the world means for each mentioned parameter. Therefore, radioactivity concentration in the Kosovo soils is similar to the worldwide average and represents no radiological hazard for the population. The results obtained by this study will serve as a reference for possible future changes. Also, it provides a good baseline for the setting up of natural and artificial radioactivity mapping for monitoring possible radioactivity pollution.

Supplementary Materials: The following supporting information can be downloaded at: https://www.mdpi.com/article/10.3390/app12199520/s1, ref. [50] is cited in the supplementary materials.

Author Contributions: Conceptualization, S.K., S.D. and G.H.; data curation, C.M.Y. formal analysis, C.M.Y.; investigation, S.D. and G.H.; methodology, S.D. and G.H.; project administration, S.K. and H.A.; resources, S.D. and S.K.; software, C.M.Y.; supervision, S.K.; validation, S.K. and G.H.; writing—original draft, S.D. and C.M.Y.; writing—review and editing, H.A. and G.H. All authors have read and agreed to the published version of the manuscript.

Funding: This research received no external funding.

Institutional Review Board Statement: Not applicable.

Informed Consent Statement: Not applicable.

Data Availability Statement: Not applicable.

Acknowledgments: The authors would like to thank the editor-in-chief, editor, and anonymous reviewers for their valuable reviews.

Conflicts of Interest: The authors declare no conflict of interest.

References

1. Hodolli, G.; Kadiri, S.; Dumani, S.; Halimi, Y.; Jonuzaj, A.; Xhafa, B.; Hasani, F. Variation of total beta activity in air by years on Obiliq. *J. Environ. Occup. Sci.* **2012**, *1*, 121. [CrossRef]
2. Turhan, Ş.; Köse, A.; Varinlioğlu, A.; Şahin, N.K.; Arikan, T.I.; Oğuz, F.; Yücel, B.; Özdemir, T. Distribution of terrestrial and anthropogenic radionuclides in Turkish surface soil samples. *Geoderma* **2012**, *187–188*, 117–124. [CrossRef]
3. Danesi, P.R.; Markowicz, A.; Chinea-Cano, E.; Burkart, W.; Salbu, B.; Donohue, D.; Ruedenauer, F.; Hedberg, M.; Vogt, S.; Zahradnik, P.; et al. Depleted uranium particles in selected Kosovo samples. *J. Environ. Radioact.* **2003**, *64*, 143–154. [CrossRef]
4. UNEP. *Depleted Uranium in Kosovo, Post-Conflict Environmental Assessment (No. Scientific Team Mission to Kosovo 5–19 November 2000)*; UNEP: Geneva, Switzerland, 2001.
5. Departamento de Protecção Radiológica e Segurança Nuclear. *Report of the Portuguese Scientific Mission to Kosovo and to Bosnia-Herzegovina for Assessment of Radioactive Contamination and of the Radiological Risk Due to the Use of Depleted Uranium Ammunitions*; Estrada Nacional 10, 2686–2953 Sacavém, Portugal, Relatório DPRSN-A, no 14 April 2001; MCT—Ministério da Ciência e Tecnologia: Lisbon, Portugal, 2001. Available online: http://www.ctn.tecnico.ulisboa.pt/uk/uk_reltec.htm (accessed on 13 September 2022).
6. Carvalho, F.P.; Oliveira, J.M. Uranium isotopes in the Balkan's environment and foods following the use of depleted uranium in the war. *Environ. Int.* **2010**, *36*, 352–360. [CrossRef]
7. Zlobina, A.; Farkhutdinov, I.; Carvalho, F.P.; Wang, N.; Korotchenko, T.; Baranovskaya, N.; Farkhutdinov, A. Impact of Environmental Radiation on the Incidence of Cancer and Birth Defects in Regions with High Natural Radioactivity. *Int. J. Environ. Res. Public Health* **2022**, *19*, 8643. [CrossRef]
8. Alzubaidi, G.; Hamid, F.B.S.; Abdul Rahman, I. Assessment of Natural Radioactivity Levels and Radiation Hazards in Agricultural and Virgin Soil in the State of Kedah, North of Malaysia. *Sci. World J.* **2016**, *2016*, 6178103. [CrossRef]
9. Amanjeet; Kumar, A.; Kumar, S.; Singh, J.; Singh, P.; Bajwa, B.S. Assessment of natural radioactivity levels and associated dose rates in soil samples from historical city Panipat, India. *J. Radiat. Res. Appl. Sci.* **2017**, *10*, 283–288. [CrossRef]
10. Shohda, A.M.; Draz, W.M.; Ali, F.A.; Yassien, M.A. Natural radioactivity levels and evaluation of radiological hazards in some Egyptian ornamental stones. *J. Radiat. Res. Appl. Sci.* **2018**, *11*, 323–327. [CrossRef]
11. Tabar, E.; Yakut, H.; Saç, M.M.; Taşköprü, C.; İçhedef, M.; Kuş, A. Natural radioactivity levels and related risk assessment in soil samples from Sakarya, Turkey. *J. Radioanal. Nucl. Chem.* **2017**, *313*, 249–259. [CrossRef]
12. Taşkın, H.; Yeşilkanat, C.M.; Kobya, Y.; Çevik, U. Evaluation And Mapping Of Radionuclides in The Terrestrial Environment And Health Hazard Due To Soil Radioactivity in Artvin, Turkey. *Arab. J. Geosci.* **2018**, *11*, 729. [CrossRef]
13. Yeşilkanat, C.M.; Kobya, Y.; Taşkin, H.; Çevik, U. Dose rate estimates and spatial interpolation maps of outdoor gamma dose rate with geostatistical methods; A case study from Artvin, Turkey. *J. Environ. Radioact.* **2015**, *150*, 132–144. [CrossRef] [PubMed]
14. Kobya, Y.; Taşkın, H.; Yeşilkanat, C.M.; Çevik, U. Evaluation of Outdoor Gamma Dose Rate and Cancer Risk in Artvin Province, Turkey. *Hum. Ecol. Risk Assess.* **2015**, *21*, 2077–2085. [CrossRef]
15. Ugbede, F.O.; Osahon, O.D. Soil-to-plant transfer factors of 238U and 232Th in rice from Ezillo paddy fields, Ebonyi State, Nigeria. *J. Environ. Radioact.* **2021**, *233*, 106606. [CrossRef] [PubMed]
16. Raj, P.; Padiyath, N.; Semioshkina, N.; Addad, Y.; Foulon, F.; Francis, D.; Voigt, G. Conceptualization of arid region radioecology strategies for agricultural ecosystems of the United Arab Emirates (UAE). *Sci. Total Environ.* **2022**, *832*, 154965. [CrossRef] [PubMed]
17. Uosif, M.A.M.; Alrowaili, Z.A.; Elsaman, R.; Mostafa, A.M.A. Soil–soybean transfer factor of natural radionuclides in different soil textures and the assessment of committed effective dose. *Radiat. Prot. Dosim.* **2020**, *188*, 529–535. Available online: https://academic.oup.com/rpd/article/188/4/529/5735230 (accessed on 13 September 2022). [CrossRef] [PubMed]
18. IAEA. *Technical Report Series; Guidelines on Soil and Vegetation Sampling for Radiological Monitoring*; IAEA Division of Public Information, No. 486; IAEA: Vienna, Austria, 2019.
19. GammaVision Gamma Spectroscopy. Application Software | AMETEK ORTEC. Available online: https://www.ortec-online.com/products/application-software/gammavision (accessed on 13 September 2022).
20. IAEA. *Radiation Safety*; IAEA Division of Public Information, 96-00725 IAEA; IAEA: Vienna, Austria, 1996.
21. ICRP. 1990 Recommendations of the International Commission on Radiological Protection. In *ICRP Publication 60. Ann. ICRP*; Pergamon Press: Oxford, UK, 1991.
22. Khandaker, M.U.; Jojo, P.J.; Kassim, H.A.; Amin, Y.M. Radiometric analysis of construction materials using HPGe gamma-ray spectrometry. *Radiat. Prot. Dosim.* **2012**, *152*, 33–37. [CrossRef]
23. Currie, L.A. Limits for Qualitative Detection and Quantitative Determination: Application to Radiochemistry. *Anal. Chem.* **1968**, *40*, 586–593. [CrossRef]

24. Beretka, J.; Mathew, P.J. Natural Radioactivity of Australian Building Materials. *Ind. Wastes By-Products. Health Phys.* **1985**, *48*, 87–95.
25. European Commission. *Radiation Protection 112: Radiological Protection Principles Concerning the Natural Radioactivity of Building Materials*; European Commission: Brussels, Belgium, 1999; pp. 1–16.
26. Krieger, R. Radioactivity of Construction Materials. *Betonw. Fert. Technol.* **1981**, *47*, 468–473.
27. UNSCEAR. *Sources and Effects of Ionizing Radiation*; United Nations Scientific Committee on the Effects of Atomic Radiation; United Nations Publication: New York, NY, USA, 2008.
28. UNSCEAR. *Source and Effects of Ionizing Radiation*; United Nations Scientific Committee on the Effects of Atomic Radiation, Report to the General Assembly with Annex B; United Nations Publication: New York, NY, USA, 2000.
29. Mamont-Ciesla, K.; Gwiazdowski, B.; Biernacka, M.; Zak, A. Radioactivity of Building Materials in Poland. 1982. Available online: https://inis.iaea.org/search/search.aspx?orig_q=RN:16033994 (accessed on 13 September 2022).
30. ICRP. *Recommendations of the ICRP: Annals of the ICRP (International Commission on Radiological Protection)*; Publication 103 Volume 37/2-4; ICRP: Ottawa, ON, Canada, 2007.
31. Yeşilkanat, C.M. A novel hybrid approach to the mapping and prediction of the terrestrial gamma dose rate distribution in the Central Anatolia Region of Turkey. *J. Environ. Radioact.* **2019**, *208–2009*, 106009. [CrossRef]
32. Pebesma, E.J.; Bivand, R. Classes and methods for spatial data in R. *R News* **2005**, *4*, 9–13.
33. Pebesma, E.J.; Wesseling, C.G. Gstat: A program for geostatistical modelling, prediction and simulation. *Comput. Geosci.* **1998**, *24*, 17–31. [CrossRef]
34. Bergmeir, C.; Benítez, J.M. Neural Networks in R Using the Stuttgart Neural Network Simulator: RSNNS. *J. Stat. Softw.* **2012**, *46*, 1–26. [CrossRef]
35. Kuhn, M.; Wing, J.; Weston, S.; Williams, A.; Keefer, C.; Engelhardt, A.; Cooper, T.; Mayer, Z.; Kenkel, B.; Benesty, M.; et al. caret: Classification and Regression Training. *R Packag. Version 6.0-86*. 2020. Available online: https://cran.r-project.org/web/packages/caret/index.html (accessed on 13 September 2022).
36. Ihaka, R.; Gentleman, R. R: A Language for Data Analysis and Graphics. *J. Comput. Graph. Stat.* **1996**, *5*, 299–314. [CrossRef]
37. Dizman, S.; Hodolli, G.; Kadiri, S.; Aliu, H.; Makolli, S. Radioactivity in Kosovo honey samples. *Pol. J. Environ. Stud.* **2020**, *29*, 1119–1127. [CrossRef]
38. Guidotti, L.; Carini, F.; Rossi, R.; Gatti, M.; Cenci, R.M.; Beone, G.M. Gamma-spectrometric measurement of radioactivity in agricultural soils of the Lombardia region, northern Italy. *J. Environ. Radioact.* **2015**, *142*, 36–44. [CrossRef] [PubMed]
39. Alshahri, F.; El-Taher, A. Investigation of natural radioactivity levels and evaluation of radiation Hazards in residential-area soil near a Ras Tanura refinery, Saudi Arbia. *Pol. J. Environ. Stud.* **2019**, *28*, 25–34. [CrossRef]
40. El Samad, O.; Baydoun, R.; Nsouli, B.; Darwish, T. Determination of natural and artificial radioactivity in soil at North Lebanon province. *J. Environ. Radioact.* **2013**, *125*, 36–39. [CrossRef]
41. Abd El-mageed, A.I.; El-Kamel, A.H.; Abbady, A.; Harb, S.; Youssef, A.M.M.; Saleh, I.I. Assessment of natural and anthropogenic radioactivity levels in rocks and soils in the environments of Juban town in Yemen. *Radiat. Phys. Chem.* **2011**, *80*, 710–715. [CrossRef]
42. Al-Masri, M.S.; Amin, Y.; Hassan, M.; Ibrahim, S.; Khalili, H.S. External gamma-radiation dose to Syrian population based on the measurement of gamma-emitters in soils. *J. Radioanal. Nucl. Chem.* **2006**, *267*, 337–343. [CrossRef]
43. Ivanić, M.; Fiket, Ž.; Medunić, G.; Furdek Turk, M.; Marović, G.; Senčar, J.; Kniewald, G. Multi-element composition of soil, mosses and mushrooms and assessment of natural and artificial radioactivity of a pristine temperate rainforest system (Slavonia, Croatia). *Chemosphere* **2019**, *215*, 668–677. [CrossRef] [PubMed]
44. Dizman, S.; Görür, F.K.; Keser, R.; Görür, O. The assessment of radioactivity and radiological hazards in soils of Bolu province, Turkey. *Environ. Forensics* **2019**, *20*, 211–218. [CrossRef]
45. Saleh, I.H. Radioactivity of 238U, 232Th, 40K, and 137Cs and assessment of depleted uranium in soil of the Musandam Peninsula, Sultanate of Oman. *Turk. J. Eng. Environ. Sci.* **2012**, *36*, 236–248. [CrossRef]
46. Mostafa, A.M.A.; Uosif, M.A.M.; Elsaman, R.; Alrowaili, Z.A.; Moustafa, E. The dependence of natural radioactivity levels and its radiological hazards on the texture of agricultural soil in Upper Egypt. *Environ. Earth Sci.* **2020**, *79*, 228. [CrossRef]
47. Kurnaz, A.; Küçükömeroğlu, B.; Keser, R.; Okumusoglu, N.T.; Korkmaz, F.; Karahan, G.; Çevik, U. Determination of radioactivity levels and hazards of soil and sediment samples in Firtina Valley (Rize, Turkey). *Appl. Radiat. Isot.* **2007**, *65*, 1281–1289. [CrossRef]
48. Jibiri, N.N.; Isinkaye, M.O.; Bello, I.A.; Olaniyi, P.G. Dose assessments from the measured radioactivity in soil, rock, clay, sediment and food crop samples of an elevated radiation area in south-western Nigeria. *Environ. Earth Sci.* **2016**, *75*, 107. [CrossRef]
49. Ademola, J.A. Determination of natural radionuclides content in some building materials in nigeria by gamma-ray spectrometry. *Health Phys.* **2008**, *94*, 43–48. [CrossRef]
50. Draper, N.R.; Smith, H. *Applied Regression Analysis*; Wiley: New York, NY, USA, 1998.

water

MDPI

Review

Uranium and Fluoride Removal from Aqueous Solution Using Biochar: A Critical Review for Understanding the Role of Feedstock Types, Mechanisms, and Modification Methods

Anjali Thakur [1], Rakesh Kumar [2] and Prafulla Kumar Sahoo [1,3,*]

[1] Department of Environmental Science and Technology, Central University of Punjab, V.P.O. Ghudda, Bathinda 151401, Punjab, India
[2] School of Ecology and Environment Studies, Nalanda University, Rajgir 803116, Bihar, India
[3] Instituto Tecnológico Vale (ITV), Rua Boaventura da Silva, 955, Belém 66055-090, PA, Brazil
* Correspondence: prafulla.iitkgp@gmail.com

Abstract: Uranium (U) and fluoride (F^-) are the major global geogenic contaminants in aquifers and pose serious health issues. Biochar, a potential adsorbent, has been widely applied to remediate geogenic and anthropogenic contaminants. However, there is a lack of research progress in understanding the role of different feedstock types, modifications, adsorption mechanisms on physico-chemical properties of biochar, and factors affecting the adsorption of U and F^- from aqueous solution. To fill this lacuna, the present review gives insight into the U and F^- removal from aqueous solution utilizing biochar from various feedstocks. Feedstock type, pyrolysis temperature, modifications, solution pH, surface area, and surface-charge-influenced biochar adsorption capacities have been discussed in detail. Major feedstock types that facilitated U and F^- adsorption were crop residues/agricultural waste, softwood, grasses, and animal manure. Low-to-medium pyrolyzing temperature yielded better biochar properties for U and F^- adsorption. Effective modification techniques were mainly acidic and magnetic for U adsorption, while metal oxides, hydroxides, alkali, and magnetic modification were favourable for F^- adsorption. The major mechanisms of U adsorption were an electrostatic attraction and surface complexation, while for F^- adsorption, the major mechanisms were ion exchange and electrostatic attraction. Lastly, the limitations and challenges of using biochar have also been discussed.

Keywords: biochar; uranium; fluoride; adsorption mechanism; feedstocks; aqueous solution; remediation

Citation: Thakur, A.; Kumar, R.; Sahoo, P.K. Uranium and Fluoride Removal from Aqueous Solution Using Biochar: A Critical Review for Understanding the Role of Feedstock Types, Mechanisms, and Modification Methods. *Water* **2022**, *14*, 4063. https://doi.org/10.3390/w14244063

Academic Editors: Gaurav Sharma and Saglara S. Mandzhieva

Received: 23 October 2022
Accepted: 4 December 2022
Published: 13 December 2022

Publisher's Note: MDPI stays neutral with regard to jurisdictional claims in published maps and institutional affiliations.

Copyright: © 2022 by the authors. Licensee MDPI, Basel, Switzerland. This article is an open access article distributed under the terms and conditions of the Creative Commons Attribution (CC BY) license (https://creativecommons.org/licenses/by/4.0/).

1. Introduction

Rapid industrialization, rising population, unplanned urbanization, and intense agricultural activities have severely exploited water resources. As a result, the demand for clean water has increased tremendously. According to the United Nations Children's fund (UNICEF) and World Health Organization (WHO) report, about 2.2 billion people globally and up to 600 million people in underdeveloped nations still lack access to clean water [1]. Goal 6 of the United Nations (UN) Sustainable Development Goals (SDGs) seeks to ensure access to water and sanitation for all, implying the need to improve water quality and protect water-related ecosystems. This goal points to the need for synthesizing technological advances in water research to be economically viable for developing countries [2]. Groundwater serves as the primary supply of drinking water in the majority of the developing nations due to inadequate freshwater sources. However, groundwater contamination has recently increased due to several contaminants (As, U, F^-, Cd, Cr, Zn, NO_3^-, PO_4^{3-}, etc.) via geogenic and endless anthropogenic activities [3,4]. Among them, U and F^- contamination is mainly caused by geogenic sources [5]. The intake of higher levels of U and F^- can cause serious health issues such as nephrotoxicity, dental and skeletal fluorosis, bone cancer, and brain damage [6,7]; hence, it is essential to mitigate them. Elevated levels

of U in groundwater have been reported in many parts of the world, such as Finland, Greece, Germany, Australia, Canada, and the U.S., and Southeast Asian countries such as India, Pakistan, China, and Bangladesh [8]. The WHO guideline for U in drinking water is 30 μg L^{-1} and by the Atomic Energy Regulatory Board (AERB) is 60 μg L^{-1}. Drinking water above these contamination limits can cause serious health issues. The health risk of U in groundwater is more due to its chemical toxicity than the radiotoxicity. Chemical toxicity causes damage to the kidney (nephrotoxicity), liver, reproductive system, and skeleton, whereas radiotoxicity targets the lungs, bones, and brain [8–10]. Globally, many nations, including India, China, Sri Lanka, Argentina, South Africa, UK, Pakistan, etc., have significant F^- concentrations in their groundwater [11,12]. More than 200 million individuals worldwide drink water with elevated F^- levels [13]. The World Health Organization states that 1.5 mg L^{-1} is the permissible limit for F^- in drinking water. However, excessive F^- intake causes skeletal and dental fluorosis, bone cancer, and brain damage [7].

Numerous techniques have been developed to mitigate U and F^-, namely membrane filtration methods such as nanofiltration and reverse osmosis, ion exchange, lime softening, coagulation by Fe/Al salts, and permeable reactive barriers using zerovalent iron. Adsorbents such as iron oxide, titanium dioxide, precipitation and coagulation, electrolytic defluoridation, adsorption, and electrodialysis have been utilized [14–20]. However, technologies have certain limitations, such as high installation and maintenance costs, pH dependence, high energy consumption, membrane fouling, and scaling [14,21]. Hence, these technologies are not cost-effective and cannot be applied in developing countries on a large scale. Among these methods, adsorption is the most effective and promising method for removing F^-, U, and other heavy metals from contaminated water. For F^- removal, various adsorbents have been used, such as activated alumina [22], bone char [23], activated carbon [24], metal oxides and hydroxides [25,26], zeolite [21], etc. Adsorbents, such as hematite [27], zeolite [28], activated carbon [29], diatomite [30], etc., have been applied for U removal. However, their expensive production cost makes them uneconomical. As a result, there is a huge demand for sustainable and low-cost adsorbent development.

Biochar is a solid, stable, porous, and low-cost adsorbent which is a carbonaceous material obtained from the thermal degradation of biomass, widely used for the remediation of contaminants from polluted/contaminated soil and water ecosystems [31,32]. Biochar has attained significant recognition due to its economic, sustainable, reusable, environmentally safe, and high adsorption efficiency. Evidence shows that biochar can remove various contaminants, including U and F^- [33–37]. For further enhancement in the adsorption of U and F^-, biochar has been modified with different techniques and materials, such as $MnFe_2O_4$ [38], $FeCl_3$ [39], HNO_3 [33], $Al(OH)_3$ [13], H_3PO_4 [35], $LaCl_3$ [40], etc. However, there is enough literature available on the review of contaminant removal from aqueous solution using biochar, including organic and inorganic contaminants [41–51], heavy metals [52–63], emerging contaminants [64–67], and chemical and microbial pollutants [68]. However, there is no systematic review on the role of feedstocks on U and F^- removal by biochar from aqueous solution and its comparison with respect to different raw/pristine and modified biochars. Therefore, to the best of our knowledge, this review gives a systematic idea about the role of feedstock types on biochar properties, modification techniques to enhance adsorption capacity, interactions with contaminants, and factors affecting the adsorption efficiency of U and F^- removal in aqueous solution.

The present review work aims to highlight (i) the application of biochars obtained from different feedstocks for U and F^- adsorption, (ii) the different production techniques for synthesis of the biochar and modification methods for the enhancement of adsorption efficiency of the biochar, (iii) the factors affecting the adsorption of U and F^- such as pH, biochar dosage, U and F^- concentration, co-existing ions, and temperature, (iv) adsorption mechanisms, (v) adsorption isotherms, kinetics, and thermodynamics, and (vi) challenges and limitations for real U and F^- groundwater treatment. Lastly, this paper concludes with future studies and recommendations for in-depth research on removing U and F^- using low-cost biochars.

2. Methodology

To address the objectives, extensive research was performed from scholarly databases (Scopus, ScienceDirect, and Web of Science) on U and F^- removal using biochar. The following keywords and synonyms in different combinations: 'biochar', 'sorption', 'water treatment', 'uranium', 'fluoride removal', 'pollutant/contaminant removal', 'heavy metal removal', 'aqueous solution', 'groundwater', 'adsorption', 'modification', 'mechanism', 'biomass adsorbent', 'crop residue', 'agricultural biomass', 'reusability', and 'regeneration' were used for the literature search. More than 1100 studies were identified using these keywords from three different databases. Duplicates were removed using Endnote, and studies that reported metal removal other than the ones under investigation were not considered for this review. More than 300 papers were retrieved after excluding duplicates and studies that were irrelevant. Selected articles were further scrutinized based on the abstract, and approximately 89 studies focusing on U and F^- removal from aqueous solution/wastewater/groundwater were included in this review. The papers on biochar (studies of U and F^- removal) covered the period from 2011 to 2022. Publications were distributed in order, with 37 studies on F^- removal and 52 on U removal. Prisma flowchart was used for displaying data collection, exclusion and inclusion criteria (Figure 1).

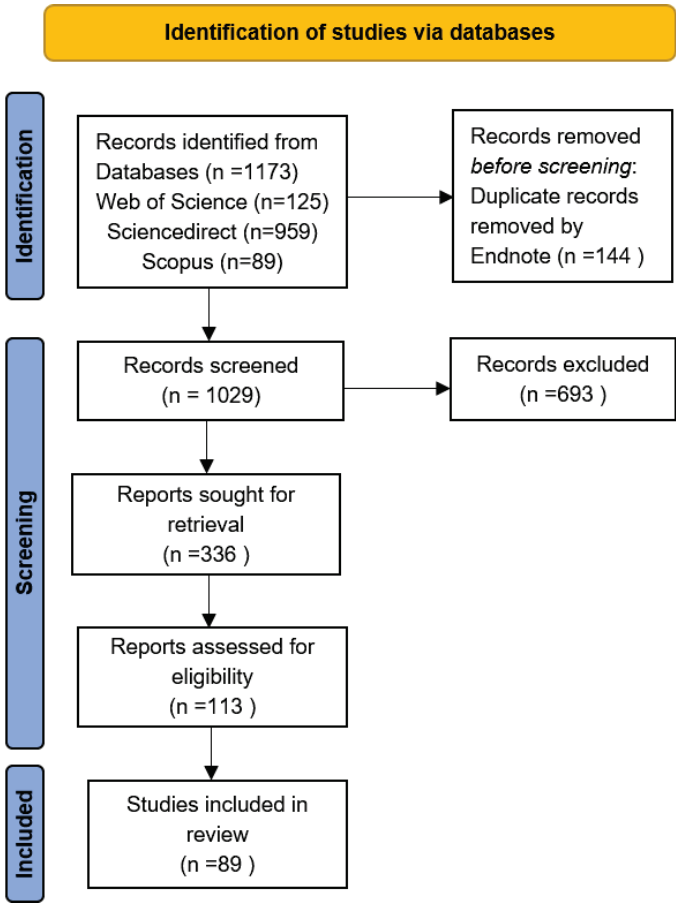


Figure 1. PRISMA flowchart showing data collection, exclusion, and inclusion criteria.

3. Results and Discussion

3.1. Role of Different Feedstock Types on Biochar Properties

Biochar has been obtained from pyrolyzing different feedstocks to remove U and F^-, due to their inherent and excellent physiochemical properties. Generally, woody biomass and crop residues are comprised of cellulose, hemicellulose, and lignin. Feedstocks such as crop residues (sugarcane bagasse, rice husk, wheat straw, rice straw, etc.), grasses, and softwood (pine) are composed of a large proportion of cellulose and hemicellulose and

degrade faster due to lower thermal resistance [69,70]. As a result, cellulose and hemicellulose degrade at lower temperatures (200–400 °C), while lignin has a wide decomposition range (200–900 °C) [57,69,71]. Hence, softwood and crop residues require low temperatures for pyrolysis. Biochar yield is less in this case because biomass with high cellulose and hemicellulose contain aliphatic carbon phases, which can easily break. Thus, they do not make stable biochar and produce low biochar yield. These feedstocks produce high-oxygen-containing functional groups such as carboxyl, carbonyl, and hydroxyl [69,70,72,73].

On the other hand, hardwoods (eucalyptus) are composed of a high fraction of lignin; therefore, they require higher temperatures for degradation. These feedstocks make stable biochar because they contain aromatic monomers and high carbon content making them thermally stable and thus producing high biochar yield [69,70]. Some feedstocks which are not plant-based/non-woody, such as animal manure and sludge, also degrade faster. Thus, they require a low temperature range for biochar preparation [70,72,74]. Biochar prepared at high temperatures is suitable for the sorption of organic contaminants, while the sorption of inorganic contaminants requires low temperatures [45,70,75] As a result, crop residues, grasses, and manure-based feedstocks are beneficial for U and F adsorption as they have oxygen-based functional groups [74,76].

3.2. Applications of Biochar in U and F^- Remediation

Biochar has gained much attention due to its widely available feedstock, making it a low-cost adsorbent, and it possesses high surface area, porosity, and oxygen-rich functional groups [77]. This section describes the application of biochar for removing U and F^- from the water and their efficiency.

U is a ubiquitous radioactive element, and its presence in water makes it unfit for drinking and causes many toxic effects on kidneys, bones, and the liver [8–10]. Various treatment technologies have been developed for U removal, such as reverse osmosis, ion exchange, coagulation, and adsorption [78,79]. Of these, adsorption by biochar is the most cost-effective method [72,80]. Several kinds of research have been performed on the bioremediation of U-contaminated water through biochar, described in this section.

Feedstocks, modification methods, and optimum operating conditions such as pyrolysis temperature, residence time, pH, and biochar dosage were employed to remediate U and F^- through biochar (Figure 2). For instance, rice husk biochar was employed for U removal, which showed a removal efficiency of 99.8% and adsorption capacity of 138.88 mg g^{-1} (Table 1) at pH 5.5 and temperature range of 303–353 K with a biochar dose of 0.38 g L^{-1} and initial U concentration of 3 mg L^{-1} [81]. Jin et al. [82] examined wheat straw biochar which exhibited a maximum sorption capacity of 355.6 mg g^{-1} at pH 4.5, temperature of 25 °C, with initial concentration of 10 mg L^{-1}. HNO_3-modified rice straw biochar significantly removed U with a sorption capacity of 242.65 mg g^{-1} (oxidized biochar) and 162.54 mg g^{-1} (raw biochar) at pH 5.5, a temperature of 25 °C, and dose of 0.01 g L^{-1}. HNO_3 oxidation increased the surface area, porosity, and oxygen-containing functional groups [33]. Pine-needles-based biochar successively removed U with a maximum adsorption capacity of 623.7 mg g^{-1} at pH 6, a temperature of 25 °C, and dosage of 5 g L^{-1} [37]. Dai et al. [34] reported U removal from corn-cob-based biochar with a sorption capacity of 163.18 mg g^{-1} at pH 6, temperature of 25 °C, and biochar dose of 5 g L^{-1}. Palm-based biochar was investigated for U removal, which showed a removal efficiency of 99.2% and maximum sorption potential of 488.7 mg g^{-1} at pH 3 and 25 °C [36]. Guo et al. [83] successfully removed U using sponge gourd biochar with a sorption capacity of 239.21 mg g^{-1} at pH 5, temperature of 30 °C, and initial concentration of U given 5 mg L^{-1}. Similarly, Ioannou et al. [84] prepared sponge gourd biochar which exhibited an excellent U sorption potential of 904 mg g^{-1} at pH 3 and 23 °C. Lingamdinne et al. [85] employed magnetically modified watermelon rind biochar which showed a U uptake of 323.56 mg g^{-1} for modified biochar and 135.86 mg g^{-1} for pristine biochar at pH 4 and 20 °C. The high sorption capacity was due to the magnetization of biochar by Fe oxide, resulting in increased surface area, porosity, and sorption potential.

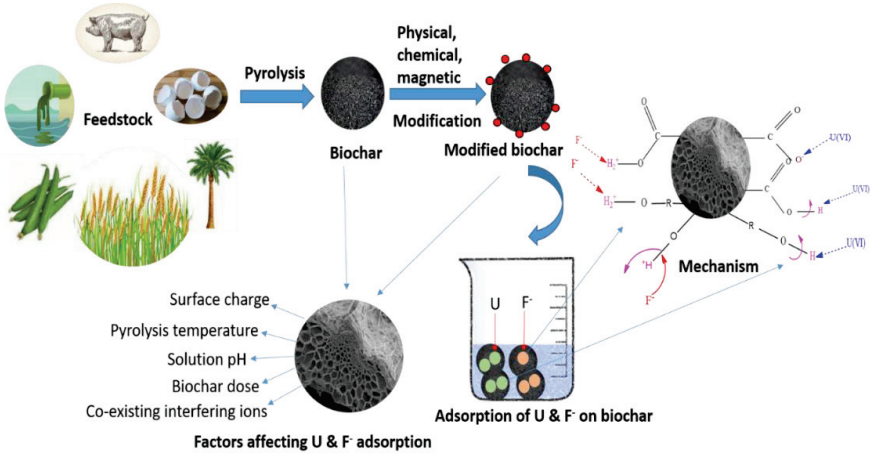


Figure 2. Schematic diagram of U and F^- adsorption on biochar.

Drinking F^--contaminated water can cause serious health issues such as skeletal fluorosis, dental fluorosis, bone cancer, and brain damage [86–88]. Various research works have been conducted on F^- removal using biochar, such as Zhou et al. [89] who prepared La/Fe/Al oxide-loaded rice straw biochar with a maximum F^- sorption capacity of 10.85 mg g^{-1} for raw biochar while 111.11 mg g^{-1} for the modified one (Table 1), in the pH range of 3 to 11 with an initial F^- concentration of 6 mg L^{-1}. Wheat-straw-derived biochar impregnated with $Al(OH)_3$ and $La(OH)_3$ was used for F^- removal from water. The prepared biochar showed 98.69% removal with a maximum F^- uptake of 51.28 mg g^{-1} at pH 7 and a temperature of 25 °C [90]. Nanoscale rice husk biochar was studied for defluoridation with a removal efficiency of 90% and maximum F^- adsorption capacity of 17.3 mg g^{-1} at pH 7 and a temperature of 30 °C [24]. Mohan et al. [91] utilized magnetic corn stover biochar, which removed F^- at pH 2, with a maximum sorption capacity of 4.11 mg g^{-1}. *Tamarix hispida*-based biochar showed 99.6% removal from synthetic water and 86.69% from real wastewater. The biochar exhibited an adsorption potential of 164.23 mg g^{-1} at pH 6 and temperature of 25 °C [40]. Coconut-derived biochar was used for defluoridation with a removal efficiency of 82.45% at pH 6.27 and a solution temperature of 30 °C [92]. Seed shells of *Camellia oleifera* (tea oil plant) were utilized for biochar production to remove F^- from aqueous solution and exhibited an adsorption capacity of 11.04 mg g^{-1} at pH 6.8 [93]. Watermelon rind biochar easily removed F^- at pH 1 with a maximum sorption capacity of 9.5 mg g^{-1} [94]. Wang et al. [95] prepared pomelo-peel-based biochar for defluoridation, which showed 100% removal efficiency with a sorption potential of 18.52 mg g^{-1} at pH 6.5. Okra stem biochar effectively removed F^- with an adsorption capacity of 20 mg g^{-1} at pH 2, a temperature of 35 °C, and with an initial concentration of 10 mg L^{-1} [96]. A biochar composite of *platanus acerifoli* leaves and eggshell showed an excellent removal efficiency of 98.53% with a maximum adsorption capacity of 308 mg g^{-1} at pH 5 and 25 °C [97].

Discussed above are some of the studies about the application of biochar in U and F^- remediation. It was observed that the adsorption capacity of biochar depends on various parameters such as feedstock, modification, pH, dose, temperature, initial concentration of U and F^- in the solution, and functional groups. The effects of these parameters are discussed in Sections 3.5 and 3.7. Table 1 summarizes the various research works carried out on U and F^- removal using biochar.

3.3. Synthesis of Biochar

The thermochemical conversion of biomass is the most common method for the production of biochar [98]. It includes pyrolysis, gasification, torrefaction, and hydrothermal carbonization [72]. For better biochar yield, parameters such as feedstock type, carbonization temperature, modification methods, heating rate, residence time, solution pH, adsorption temperature, adsorbent dosage, etc., must be optimum because of their significant

impact on the physicochemical properties of the biochar [74,99,100]. Different categories of feedstock have been utilized for the synthesis of biochar, such as crop residues (corn stover, rice straw, rice husk, wheat straw, corn cob, etc.) [73,101,102], woody biomass (pine needles, pine sawdust, bamboo, eucalyptus wood, palm tree fibres, etc.) [103–105], fruit waste (watermelon rind and orange peel) [94,106], animal waste (pig manure, horse manure, and dairy manure) [107–109], sewage sludge [110], etc. For example, Jin et al. [82] derived biochar from cow manure and wheat straw for U removal from water. It was found that cow-manure-derived biochar exhibited higher removal efficiency than wheat straw-derived biochar. Because of higher ash content, surface oxygen (which bonded with U ions) and Ca^{2+} occurred on the surface, exchanged with positively charged U ions, and provided new adsorption sites on the surface of cow-manure-derived biochar.

Furthermore, carbonization temperature is also an essential parameter for synthesis as it affects the pore volume and surface area of the biochar. For instance, Hu et al. [111] pyrolyzed bamboo sawdust at different temperatures (300, 450, and 600 °C). It was observed that surface area and pore volume were positively correlated with the pyrolysis temperature, i.e., the pore volume and surface area of the biochar were enhanced with increasing pyrolysis temperature, resulting in higher U uptake. However, Alkurdi et al. [112] pyrolyzed sheep bone to derive bone char for F^- removal at different temperatures (500, 650, 800, and 900 °C). The surface area of bone char decreased from 120.031 $m^2\ g^{-1}$ to 89.06 $m^2\ g^{-1}$; as a result, the pore volume decreased from 0.283 $m^3\ g^{-1}$ to 0.235 $m^3\ g^{-1}$, with increased pyrolyzing temperature from 500 °C to 900 °C due to pore shrinkage and pore breakage at very high temperatures.

Modification is another critical parameter in the synthesis of biochar, which is performed prior to or after the pyrolysis of raw biomass to improve the adsorption capacity, surface morphology, and physiochemical properties of the biochar. For instance, Lingamdinne et al. [85] magnetically modified watermelon rind biochar for U removal. They found that magnetization improved the surface morphology from poorly structured to a porous and ordered structure of the biochar and enhanced the surface area from 52.1 $m^2\ g^{-1}$ to 86.35 $m^2\ g^{-1}$. U uptake was enhanced from 135.86 mg g^{-1} to 323.56 mg g^{-1} after the magnetization. Different biochar modification methods are further discussed in Section 3.5. The various biochar production techniques are as follows:

3.3.1. Pyrolysis

The pyrolysis process commonly produces biochar, and this process involves the thermal degradation of biomass into solid (biochar), liquid (bio-oil), and gas (syngas) in oxygen-limited conditions at high temperatures ranging from 300 to 700 °C [113,114]. Pyrolysis is further classified into slow and fast pyrolysis based on the pyrolysis temperature, heating rate, and residence time. In slow pyrolysis, biochar is the primary product, while the major products in fast pyrolysis are bio-oil and syngas. Compared to fast pyrolysis, slow pyrolysis is better for biochar production because biochar yields decrease with an increase in temperature and heating rate [114,115].

3.3.2. Gasification

Gasification is the thermal decomposition of solid carbonaceous material derived from fossil fuels such as wood or coal into producer gas known as syngas at high temperature (>700 °C) with gasifying agents such as steam, oxygen, air, etc., to partially oxidize the feedstock [72,114,115]. During gasification, the major product is syngas, while biochar is produced as a by-product with a lower yield [72].

3.3.3. Torrefaction

Torrefaction is a pretreatment process before pyrolysis to improve the properties of the biomass. Torrefaction increases the hydrophobicity, further enhancing the biochar's storage stability, grindability, and carbon content. Reducing oxygen, water, or moisture from biomass increases the biochar yield [116]. Torrefaction is known as mild pyrolysis,

operating at low temperatures and heating rates. Biomass is pyrolyzed in the temperature range of 200–300 °C, at a heating rate of <50 °C min^{-1}, having a residence time of less than 30 min under anaerobic conditions and atmospheric pressure [116,117].

3.3.4. Hydrothermal Carbonization

Hydrothermal carbonization is used for making biochar from wet biomass. It helps improve the properties of the biomass, such as hydrophobicity, grindability, increased carbon content, and reduced oxygen content. It is specially employed for feedstock such as sewage sludge, animal and human wastes, compost, municipal wastes, etc. As biomass does not require drying before the treatment, it is better and more economical than pyrolysis and gasification [113,114].

3.4. Characteristics of Biochar

Scanning electron microscopy–electronic dispersive X-ray (SEM-EDX) analyses the biochar's surface morphology and elemental mapping. For example, Ahmed et al. [38] determined the surface morphology and elemental composition using SEM-EDS. They concluded the fibrous–porous structure of the biochar and the presence of C, O, Fe, Mn, and Na on the biochar surface, which confirmed the $MnFe_2O_4$ fabrication of the biochar. The surface area of biochar is analysed using the Brunauer–Emmett–Teller method (BET). For instance, Guilhen et al. [36] performed the BET method and found that the surface area of biochar increased from 0.8320 to 643.12 m^2 g^{-1} after CO_2 activation, resulting in a high adsorption capacity of the biochar, which confirmed that physical activation has potential to enhance U uptake using biochar.

Fourier-transform infrared spectroscopy (FTIR) is used to observe the functional groups on biochar surfaces. For example, several previous studies have utilized acid-modified biochar and found that C–O, C=O, O–H, C–H, and –COOH were the main functional groups present on the biochar surface [7,33,35,82,111,118–121]. Biochars treated with a base showed C=O, N–H, C–H, C–O, O–H, and C–OH as the major functional groups [90,122–124]. Magnetized biochars showed different functional groups such as Fe–O, C=O, C–O, O-H, C=C, C–H, C–O–C, and Si–O–Si [39,85,91,125–127]. Ahmed et al. [38] and Hu et al. [105] observed that a new peak was detected at 909 cm^{-1} and 916 cm^{-1}, which corresponded to the stretching vibration of $[U=O=U]^{2+}$ and confirmed U adsorption on the biochar surface. Similarly, Sadhu et al. [94] observed a new adsorption peak at 997 cm^{-1}, which corresponded to C–F stretching and indicated F^- adsorption.

X-ray photoelectron spectroscopy (XPS) examines the elemental composition and chemical state of atoms in a produced material and provides information about the adsorption mechanism. For example, Ding et al. (2018) found that adsorbed U was a mixture of 87% U(IV) and 13% U(VI). X-ray diffraction (XRD) is used to analyse the crystallographic structures of prepared biochar and the dominant minerals present on the biochar surface. For instance, Wei et al. [128] performed XRD and found that the crystalline size of CeO_2, which was dispersed onto the biochar surface, was 17.07 nm. Similarly, Halder et al. [92] observed several peaks which showed the presence of fluorinated compounds such as K_2MgF_4 and $KFeF_3$ and confirmed the F^- sorption onto the biochar surface.

3.5. Modification Methods

Modification is necessary to improve biochar properties such as surface area, pore structure, and functional groups [129]. Modification has four types: physical modification, chemical modification, magnetic modification, and impregnation or coating of the minerals [130]. Modification or activation can be conducted before or after pyrolysis. Figure 3 shows the different modification methods, including physical, chemical, and magnetic modification and Table 1 summarizes the effect of different modification methods on the properties of biochar for U and F^- removal.

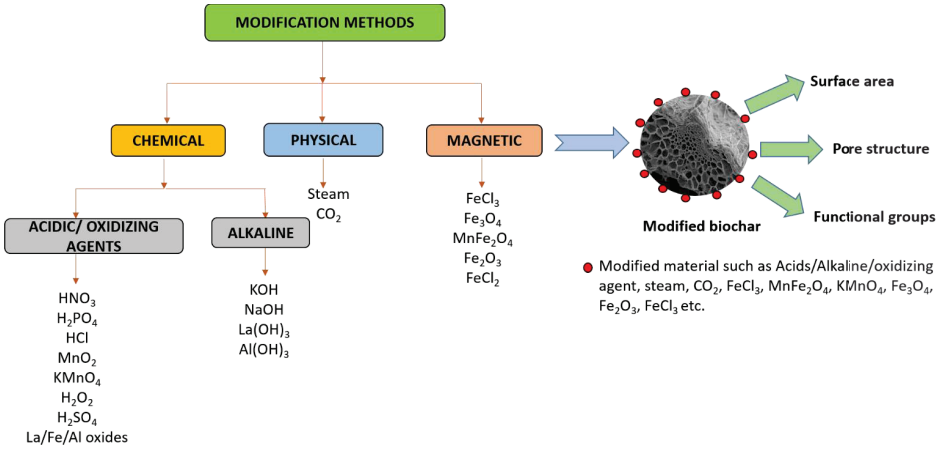


Figure 3. Schematic diagram representing different modification methods of biochar which affect the different properties of biochar, including surface area, pore structure, functional groups on biochar surface, etc.

3.5.1. Physical Modification

Physical modification involves the utilization of oxidizing agents such as CO_2, air, steam, and ozone at high temperatures above 700 °C. It is generally employed for increasing the surface area and porosity of biochar [164]. For instance, Guilhen et al. [36] removed U from aqueous solution using biochar modified with CO_2 as an activation agent at the temperature range of 700–1000 °C. The CO_2 activation increased the aromaticity and porosity of the biochar with the increase in surface area from 0.83 to 643 m^2 g^{-1} and enhanced the removal efficiency from 80.5% (primary biochar) to 99.2% (activated biochar). Activation made the adsorption sites more heterogenous and as a result created more pores of biochar. Similarly, Halder et al. [92] employed the steam activation of biochar at 900 °C for F^- removal from aqueous solution, resulting in enhanced porosity and a surface area of 1054 m^2 g^{-1}. Steam activation of the biochar resulted in an increased removal efficiency of 82.45%. Steam activation created more adsorption sites by releasing volatile compounds during the activation process.

3.5.2. Chemical Modification

Chemical modification is carried out via acids, oxidizing agents, and alkaline treatment. Acid modification enhances the surface area, improves surface morphology, pore structure, and enriches the biochar surface with oxygen-containing functional groups such as carboxylic (COO^-), hydroxyl (OH^-), carbonyl (CO), etc., resulting in a negative surface charge of the biochar and promoting enhanced adsorption of the cationic species [120,130]. For example, HNO3 modification induced negative charge on the biochar surface due to oxygen-containing functional groups and enhanced the U removal through complexation between positive U species and acidic functional groups. This modification provided high surface area, porosity, and microporous and mesoporous structure, resulting in higher stability and performance over pristine biochar (Table 1) [33,82,118–121]. Similarly, Guan et al. [35] modified pine tree sawdust biochar with the phosphoric acid–microwave method for F^- removal. The fabricated biochar showed an increase in surface area from 7.7 to 389.95 m^2 g^{-1}, a decrease in pore diameter from 17 to 0.9 Å, and an enhanced adsorption capacity of 0.885 mg g^{-1}. The modification removed some impurities from the pores of pristine biochar resulting in the availability of more active sites for F^- adsorption. The acid treatment protonated the surface functional groups such as hydroxyl and carboxyl, resulting in electrostatic attraction between F^- and protonated functional groups. De et al. [7] modified biochar with hydrochloric acid for F^- removal. This modified biochar showed increased active sites, a graphite-like carbon structure, and high carbon content resulting in higher adsorption than the raw biochar with a removal efficiency of 98.5% and adsorption potential of 1.11 mg g^{-1}.

Table 1. Effect of modification on the adsorption capacity of biochar for U and F^- removal.

Feedstock	Modification	Target Contaminant	Surface Area (m^2 g^{-1})	Pore Structure	Adsorption Capacity (mg g^{-1})/Removal Efficiency (%)		References
					Raw Biochar	Modified Biochar	
Rice straw	Hydroxyapatite–biochar nanocomposite	U	157.96	Mesoporous	110.56	428.25	[131]
Rice straw	HNO_3 oxidation	U	-	Mesoporous	162.54	242.65	[33]
Wheat straw	HNO_3 oxidation	U	290.1	-	8.7	355.6	[82]
Rice husk	Magnetization by Siderite	U	109.65	Mesoporous	-	52.63	[125]
Rice husk	Silicon containing biochar-supported iron oxide nanoparticles	U	62.88	-	-	138.88	[81]
Rice husk	Magnetic modification using Fe^{2+}/Fe^{3+} plus SO_4^{2-} solution	U	109	-	64	118	[132]
Corn cob	Thermal air treatment at 300 °C	U	-	Mesoporous	68.82	163.18	[34]
Pine needles	Magnetization of oxidised biochar (HNO_3 treated) by $FeCl_3$	U	-	-	-	623.7	[37]
Pine sawdust	MgO/biochar composite	U	51.45	Mesoporous	-	514.72	[133]
Macaúba palm	CO_2 activation	U	643.12	Microporous	-	488.7	[36]
Palm tree fibres	HNO_3 oxidation	U	-	-	-	112	[121]
Bamboo sawdust	Phytic acid	U	1298	-	16.2	229.2	[111]
Bamboo biomass	Phosphate impregnation biochar cross-linked Mg–Al layered double-hydroxide composite	U	445.17	Microporous	15.869	274.15	[134]
Cactus fibre	HNO_3 oxidation	U	<5	Microporous	-	214	[118]
Chinese banyan aerial root	$KMnO_4$ modification	U	284	Mesoporous	19.08	27.29	[135]
Puncture vine	Magnetization by $FeCl_3$	U	-	Mesoporous	-	17.24	[39]
Hydrophyte biomass	Magnetization by $FeCl_2$	U	92.43	-	52.36	54.35	[136]
Hydrophyte	Phytic acid modification	U	433	-	-	128.5	[137]
Pig manure	$KMnO_4$	U	-	-	369.9	979.3	[107]
Pig manure	H_2O_2	U	-	-	369.9	661.7	[107]
Pig manure	NaOH	U	227.9	Mesoporous	369.9	952.5	[138]
Pig manure	HCl	U	36.3	Mesoporous	369.9	53.3	[138]
Pig manure	NaOH	U	345.7	Microporous	45.8	221.4	[124]
Pig manure	H_2O_2	U	189	Microporous	45.8	145.1	[124]
Horse manure	Bismuth impregnation	U	-	-	186	516.5	[108]
Horse manure	$MgCl_2$ modification	U	-	-	-	625.8	[139]
Cow manure	HNO_3 oxidation	U	101.5	-	64	73.3	[82]
Carp fish scales	KOH activation	U	1074.73	Microporous	71.59	291.98	[122]
Sewage sludge	Thermal air treatment	U	-	Mesoporous	78.66	96.73	[34]
Sewage sludge	Air roasting–oxidation	U	623.09	Mesoporous	139.5	490.2	[140]
Winery waste (grape peels)	Chemically modification by NaOH, Na_2CO_3	U	-	-	-	255	[141]
Winery waste (grape peels)	Thermal modification at 650 °C and oxidized with HNO_3	U	165	-	-	100	[141]
Malt spent rootlets	HNO_3 oxidation	U	540	Mesoporous	547	500	[120]
Coffee espresso residue	HNO_3 oxidation	U	700	Mesoporous	547	357	[120]
Olive kernels	HNO_3 oxidation	U	510	Mesoporous	357	381	[120]
Fungi	Sulfide nano zero valent iron	U	102.7	_	-	427.9	[142]
Green algae	Mn impregnation	U	63.7	Mesoporous	-	100.2	[143]
Cyanobacteria	Magnetic modification using Fe_3O_4	U	-	-	58.05	52.06	[144]
Sponge gourd	ZnO-modified biochar hydrogel	U	-	-		239.21	[83]
Sponge gourd fibres	MnO_2 oxidation	U	<5	Microporous	95	904	[84]
Sponge gourd sponges	HNO_3 oxidation	U	-	-	-	92	[119]
Sponge gourd sponge	Salophen modification	U	-	-	-	833	[145]

Table 1. *Cont.*

Feedstock	Modification	Target Contaminant	Surface Area (m^2 g^{-1})	Pore Structure	Adsorption Capacity (mg g^{-1})/Removal Efficiency (%)		References
					Raw Biochar	Modified Biochar	
Sponge gourd residue	Functionalization by hummer method	U	-	-	-	382	[146]
Watermelon rind	Magnetization by co-precipitation	U	86.35	-	135.86	323.56	[85]
Watermelon seeds	$MnFe_2O_4$ modification	U	-	Mesoporous	21.24	27.61	[38]
Longan shell (fruit)	Nano zero valent iron	U	1168.88	Mesoporous	-	331.13	[77]
Orange peel	MnO_2 modification	U	273.25	Mesoporous	165.4	246.3	[106]
Orange peel	Hydrogel	U	-	-	-	263.2	[147]
Tea waste	Iron manganese oxide	U	12	-	-	510.8	[148]
Rice straw	La/Fe/Al oxides impregnation	F^-	95.36	Mesoporous	10.85	111.11	[89]
Wheat straw	Impregnation of aluminium and lanthanum hydroxide	F^-	-	-	-	51.28	[90]
Rice husk	Chemical modification by iron	F^-	58.98	Mesoporous	-	4.45	[149]
Rice husk	Nano-scale size reduction	F^-	-	-	-	17.3	[24]
Rice husk	Magnetic biochar anchored with Al and Mg	F^-	114	Mesoporous	-	21.59	[150]
Corn stover	Magnetization by Fe^{3+}/Fe^{2+} solution	F^-	3.61	Microporous	6.42	4.11	[91]
Chir pine	Calcium pretreated	F^-	-	-	-	16.72	[151]
Mongolian scotch pine tree sawdust	Phosphoric acid-microwave method	F^-	339	Microporous	-	0.885	[35]
Douglas fir (pine)	Magnetization by Fe_2O_3/Fe_3O_4	F^-	494	Microporous	-	9.04	[152]
Douglas fir (pine)	Iron-titanium biochar composite	F^-	576	Microporous	-	36	[153]
Reed biomass	Ce-loaded biochar beads	F^-	236.84	Mesoporous	-	34.86	[128]
Kashgar tamarisk	Lanthanum chloride	F^-	164.52	Mesoporous	-	164.23	[40]
Tea oil plant (seed shells)	Impregnation of zirconium dioxide	F^-	-	-	-	11.04	[93]
Sawdust	Chemical modification via cross-linking and protonation of the chitosan-sawdust biochar beads	F^-	57.97	Microporous	-	4.413	[154]
Pongammia pinnata seed cake	Engineered biochar by HCl solution	F^-	10.1	Microporous	-	1.11	[7]
Coconut	Steam activation	F^-	1054	Mixture of micropores and mesopores	-	82.45%	[92]
Pomelo peel	Impregnation of polypyrrole	F^-	-	-	-	18.52	[95]
Peanut shell	MgO	F^-	182.3	Mesoporous	-	83.05	[155]
Spent mushroom compost	$Al(OH)_3$ coating	F^-	28.5	-	-	36.5	[13]
Food waste	$AlCl_3$ impregnation	F^-	20.95	-	-	123.4	[156]
Tea waste	Chemical modification by H_2SO_4, $NaNO_3$, $KMnO_4$	F^-	11.833	Macroporous	-	52.5	[157]
Red algae seaweed	Spent biochar	F^-	319.47	Microporous	-	2.1	[158]
Dairy manure	Calcium modification	F^-	2.6	-	0.11	0.42	[109]
Tea waste	Magnetic modification	F^-	115.65	Mesoporous	-	18.78	[159]
Peanut hull	Nil	F^-	98.2	Mesoporous	3.665	-	[160]
Pinecone	$AlCl_3$	F^-	-	-	-	14.07	[161]
Conocarpus erectus	Nil	F^-	9.88	Microporous	205.7	-	[162]
Yak dung	$FeCl_2$	F^-	-	-	-	3.928	[163]

U: Uranium; F^-: Fluoride; -: data not available.

Oxidizing agents such as manganese oxide (MnO_2) [84,106], hydrogen peroxide (H_2O_2) [107,124], and potassium permanganate ($KMnO_4$) [107,135] were used to modify biochar for U removal, while metal oxides, such as iron oxide, aluminium oxide, and lanthanum oxide [89], were used to modify the biochar surface for F^- adsorption. These oxidizing agents showed enhanced adsorption due to a rise in surface area, porosity, and oxygenated functional groups on the biochar surface [165].

Alkaline treatment was given by metal hydroxides, such as KOH [122], NaOH [124,138], $La(OH)_3$ [90], and $Al(OH)_3$ [13]. For example, Saikia et al. [123] reported that the removal efficiency of F^- by perennial-grass-based biochar activated by adding KOH pellets was 24.8%. After activation, they observed a rise in surface area from 5.57 $m^2\ g^{-1}$ to 1248.2 $m^2\ g^{-1}$. Similarly, Chen et al. [13] observed an increased adsorption capacity of 36.5 mg g^{-1} and surface area from 3.6 to 28.5 $m^2\ g^{-1}$, and Yan et al. [90] reported increased F^- removal efficiency from 77.97% to 98.69% resulting from biochar modification with aluminium and lanthanum hydroxides. An increase in surface area was found because the coating of $Al(OH)_3$ on the biochar surface was amorphous (the presence of small particles). Amorphous materials have more active sites for sorption [166].

3.5.3. Magnetic Modification

The magnetization of biochar increases the adsorption capacity by enhancing the surface area, pore volume, surface morphology, functional groups, and stability of the biochar. In addition, magnetic biochar can be reused multiple times through the separation of contaminants from biochar using an external magnetic field [61,85]. For instance, Ahmed et al. [39] produced biochar from *Tribulus terrestris* (puncture vine) and magnetized it using $FeCl_3$ to remove U(VI) from wastewater. The magnetic biochar exhibited a layered porous structure, which provided increased surface area and enhanced adsorption capacity. After the modification, there was an increase in oxygen content resulting in oxygen-containing functional groups. FTIR analysis revealed the presence of Fe–O, C=O, C–O, and –OH functional groups after the magnetization of biochar. Another study was carried out by Philippou et al. [37] for removing U from aqueous solution through magnetic modification using Fe_3O_4-loaded pine needles biochar, which enhanced the adsorption capacity to 623.7 mg g^{-1}. Ahmed et al. [38] synthesized biochar from *Citrullus lanatus* L. (watermelon) seeds and used $MnFe_2O_4$ to magnetically modify biochar through the co-precipitation method for U(VI) removal from wastewater. It was observed that magnetic biochar exhibited a mesoporous structure, higher stability, enhanced adsorption capacity of 27.61 mg g^{-1} from 21.24 mg g^{-1} (pristine biochar), oxygenated functional groups, and increased availability of active sites on the biochar.

The impregnation of mineral salt solution increases the oxygen functional groups on the biochar surface, increasing the sorption capacity of the adsorbent. For instance, Zhou et al. [89] derived biochar from rice straw impregnated with La/Fe/Al oxides through co-precipitation for F^- removal from drinking water. Impregnation increased the production of hydroxyl groups on the biochar surface. Impregnated biochar enhanced the surface area from 2.59 $m^2\ g^{-1}$ to 95.36 $m^2\ g^{-1}$ and the adsorption capacity from 10.85 mg g^{-1} to 111.11 mg g^{-1} in a wide pH range of 3–11.

3.5.4. Thermal Air Treatment (TAT)

Dai et al. [34] applied the TAT method to modify the biochar to remove U(VI) from the aqueous solution. In this method, the biochar surface was engineered by heating biochar at 300 °C for 30 min to enhance the adsorption performance of the biochar. The adsorption capacity of the biochar increased from 68.82 mg g^{-1} to 163.18 mg g^{-1}. The resultant biochar exhibited a high O/C ratio resulting in oxygen-containing functional groups, a reduction in the average pore diameter (11.53 nm to 3.62 nm), and increased surface area (360.35 to 362.26 $m^2\ g^{-1}$), resulting in the development of a mesoporous structure, which facilitated U(VI) removal from the water. Compared to physical and chemical modification, thermal air

treatment (TAT) exhibited a lower carbonization temperature and shorter processing time resulting in elevated product yield and lower production cost and energy consumption.

3.6. Raw vs. Modified Biochar

Biochar (raw as well as modified) has been widely utilized for U and F^- removal from aqueous solution at several operating parameters such as pH, dose, temperature, initial concentration, etc. The following section discusses the comparative analysis of adsorption capacities with respect to raw and modified biochar at different experimental conditions. For example, Hu et al. [111] employed phytic-acid-modified bamboo sawdust biochar pyrolyzed at 450 °C to remediate U(VI) from synthetic water. The modified biochar showed a higher sorption capacity (229.2 mg g^{-1}) than raw biochar (16.2 mg g^{-1}) (Table 1) at pH 4 and 25 °C. Fabrication enhanced the surface area of the biochar from 8.47 m^2 g^{-1} to 157.96 m^2 g^{-1}, nearly nineteen times higher than the pristine biochar. Modification enlarged the pores due to the release of volatile matter during pyrolysis, resulting in enhanced pore volume from 0.015 cm g^{-1} (raw biochar) to 0.919 cm g^{-1} (modified biochar). Phytic acid fabrication introduced phosphate-functionalized groups on the biochar surface and improved the pore structure, which enhanced the U(VI) uptake compared with raw biochar. Similarly, Ahmed et al. [33] used HNO_3-modified rice straw biochar to remove U(VI) from aqueous solution. Oxidized biochar exhibited an adsorption capacity of 242.65 mg g^{-1}, while raw biochar showed a maximum sorption capacity of 162.54 mg g^{-1} at pH 5.5 and a temperature of 25 °C. Nitric acid enriched the carbonized surface with acidic functional groups such as carboxyl and carbonyl, thereby enhancing the adsorption ability of the biochar. Similar findings were reported by [82,118–121]. A novel adsorbent, hydroxyapatite biochar nanocomposite made from rice straw, was developed by Ahmed et al. [131] to remove U(VI) from laboratory water. The fabricated biochar exhibited an adsorption potential of 428.25 mg g^{-1}, while raw biochar showed an adsorption capacity of 110.56 mg g^{-1}. Essentially, hydroxyapatite is a calcium phosphate material which has a high tendency to remediate environmental contaminants [167]. Hence, introducing this biomaterial on the biochar surface enhanced its adsorption potential compared to raw biochar. The highest U(VI) uptake was observed at pH 5.5, a temperature of 25 °C, and initial concentration of 50 mg L^{-1} in both the adsorbents. Modified biochar showed excellent removal efficiency >90% even after five sorption–desorption cycles. Han et al. [124] examined NaOH-modified pig manure biochar for U immobilization and observed that modified biochar exhibited more significant sorption potential (221.4 mg g^{-1}) than the pristine one (45.8 mg g^{-1}). The greater U uptake was due to the enhanced surface area (from 135.7 m^2 g^{-1} to 345.7 m^2 g^{-1}), pore volume (0.032 cm^3 g^{-1} to 0.119 cm^3 g^{-1}), and carboxyl and hydroxyl functional group complexation with U. A similar study was performed using alkali (NaOH)-modified pig manure biochar for U removal which supported these results [107].

Zhou et al. [89] employed tri-metallic (La/Fe/Al oxides)-modified biochar derived from rice straw for the defluoridation of aqueous solution. The modified biochar exhibited a maximum adsorption potential of 111.11 mg g^{-1}, while pristine biochar showed 10.85 mg g^{-1} F^- uptake. The impregnation of metal oxides on the biochar surface enhanced the surface area (2.59 to 95.36 m^2 g^{-1}), pore volume (0.012 to 0.611 cm^3 g^{-1}), and pore diameter (12.01 to 12.49 nm). As La/Fe/Al oxides have a positive charge and fluoride has negative, the fabricated biochar showed a higher capacity for F^- removal through ion exchange and electrostatic interactions. Generally, biochars are negatively charged [168]; hence, the raw biochar exhibited less F^- uptake than the modified biochar. Maximum removal was observed at pH 3, with a biochar dosage of 1 g L^{-1}, with an initial concentration of 6 mg L^{-1} in both sorbents. Limited studies have compared raw and modified biochar in the case of F^-. They have determined the adsorption capacities of only modified/coated/fabricated biochars.

Based on the available literature, it was observed that less acidic or near-neutral pH (discussed in Section 3.7.1), low-to-medium (200–550 °C) pyrolyzing temperature, a

solution temperature of 25 °C, and chemical (acidic) and magnetic modification of the biochar yielded better results for U adsorption. In the case of F^-, alkali pH (see Section 3.7.1), a medium pyrolyzing temperature (450–700 °C), and a solution temperature of 30 °C, metal oxides and hydroxides, magnetization, and chemical (weak acids and alkali) modification might be more favourable for F^- removal.

3.7. Factors Affecting the Adsorption of U and F^- in Aqueous Solution

3.7.1. Influence of pH

Among various factors, the pH of the solution is one of the crucial factors which affects the adsorption of contaminants by governing their speciation and surface charge of biochar in varying-pH solution [84,107]. Speciation of U was influenced at varying pH; at pH values less than 6, U (VI) occurred in the form of uranyl species (UO_2^{2+}) and positively charged hydroxy complexes, such as $(UO_2)_3(OH)_4^{2+}$, $(UO_2)_2(OH)_2^{2+}$, $(UO_2)_3(OH)_5^{+}$, $UO_2(OH)^{+}$, $(UO_2)_4(OH)_7^{+}$, $(UO_2)_3(OH)_5^{2+}$, and $(UO_2)_2OH^{3+}$, and negatively charged species of U, i.e., $(UO_2)_2CO_3(OH)_3^-$ occurred at pH > 6 (Table 2) [169,170]. It was found that at lower pH values (3–6) (less acidic or near neutral), the biochar surface was negatively charged due to the presence of negatively charged functional groups (COO^-, OH^-) [171] and positively charged U species were present at these pH values [169]. In addition, when the solution pH > pH_{ZPC}, the surface charge on the biochar became negative, which attracted the positive U species through electrostatic attraction and complexation, resulting in a high adsorption capacity [133] (Table 2). Figure 4 summarizes how major parameters affect U and F^- adsorption.

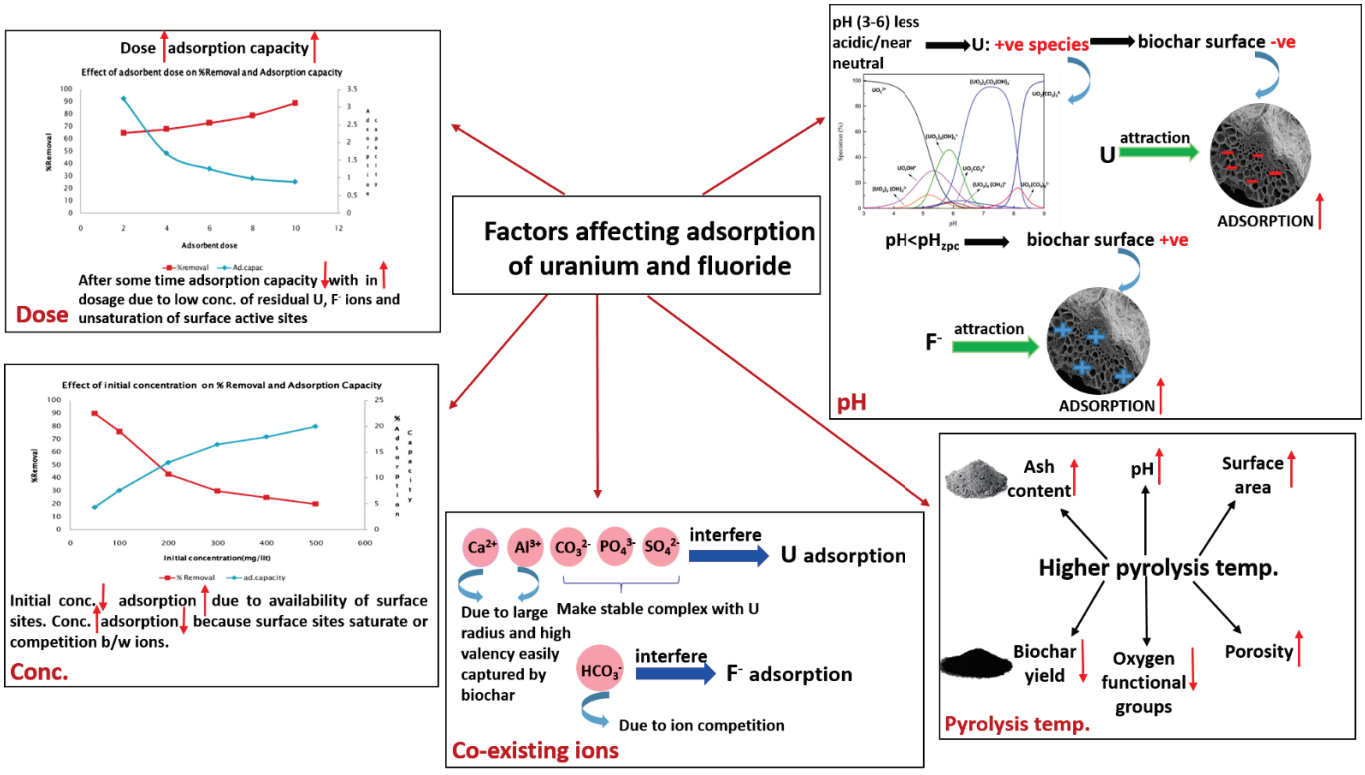


Figure 4. Effect of different parameters on the adsorption capacity and removal efficiency of U and F^-, including biochar dose, initial concentration of U and F^-, solution pH, pyrolysis temperature, and Co-existing ions.

For example, Ahmed et al. [39] have found that the adsorption of U (VI) increases with a rise in pH up to pH 6 and decreases at pH > 6 using magnetic-modified biochar. This occurred due to repulsion between negatively charged U species and the negatively

charged biochar surface at pH > 6. Hu et al. [105] examined the impact of pH on the adsorption capacity of U (VI) using bamboo shoot shell biochar at a pH ranging from 1 to 7 and found the maximum adsorption at pH 4 which decreased further with the increase in pH. This is because at pH < 4, electrostatic repulsion occurred between the positively charged biochar surface (due to protonation of functional groups—carboxyl and hydroxyl groups) and positively charged U species; hence, adsorption is less. Biochar was positively charged when the pH was highly acidic (1–2) due to the protonation of functional groups leading to repulsion between positive U species and the positive biochar surface. It was observed that slightly acidic or near-neutral pH favoured high adsorption capacities for U because of the presence of negatively charged functional groups due to the deprotonation of functional groups and smaller pH_{ZPC} values, which led to attraction between positive U species and the negative biochar surface, whereas at basic pH values, the biochar was negatively charged due to the deprotonation of functional groups resulting in repulsion between negative species of U and the negative biochar surface.

The interaction between biochar and F^- is affected by the point of zero charge ($_{PZC}$). As the solution pH is less than pH_{PZC}, it favours the adsorption of F^- electrostatically [89]. Table 3 shows the influence of the solution pH on the biochar adsorption capacity for F^- removal. For instance, Habibi et al. [40] synthesized lanthanum-chloride-activated biochar, which had a pH_{PZC} of 6.6, and reported that F^- removal increased at pH < 6.6 and gradually decreased at pH > 6.6. At varying pH, the protonation or deprotonation of functional groups on the biochar surface occurs. At low pH, the removal of anionic F^- species is favoured, as the functional groups present on the surface of the biochar are protonated [7]. At high pH, the removal of cationic species is favoured due to the deprotonation of functional groups present on the biochar surface. Sadhu et al. [94] observed a significant impact on the adsorption of F^- using watermelon rind biochar, which showed a maximum adsorption of F^- at pH 1, which was found to be 9.5 mg g^{-1}. Furthermore, a sharp decline in adsorption efficiency was observed above pH 2. Another reason for the high adsorption capacity was the electrostatic attraction between the positively charged biochar and F^- ions (Table 3). However, there are studies where F^- adsorption has occurred at higher pH values (pH > 4). This is due to ion exchange between F^- ions and the negatively charged or less positively charged biochar surface [90].

3.7.2. Effect of Biochar Dose on U and F^- Adsorption

For the optimum remediation of U and F^-, it is required to optimize the biochar dose by keeping the pH and the initial concentration of U and F^- constant. With increased biochar dosage, the adsorption capacity and removal percentage of U and F^- rose to the optimum level as the high dosage of the biochar provided many effective active sites on the biochar surface [107]. Table 4 shows the influence of biochar dosage on the adsorption capacity. For example, Yan et al. [90] observed that the F^- removal rate increased from 77.97% to 98.69% as the biochar dosage rose from 0.25 to 1 g L^{-1}. Xu et al. [176] identified that the U (VI) removal rate increased from 31.38 to 96.03% with the rise in iochar dose from 0.03 to 0.3 g L^{-1}. At the same time, a further increase in adsorbent doses decreased the adsorption capacity.

3.7.3. Influence of Initial Concentration

The initial concentration of U and F^- in aqueous solution influences the adsorption capacity of biochar. The impact of initial F^- and U concentration on biochar adsorption capacity is shown in Table 5. With low initial concentrations of U, F^-, and fixed biochar dose, the adsorption of U and F^- ions increased due to the availability of active surface sites. Furthermore, as the initial concentration of U and F^- increased, the adsorption decreased because fewer surface active sites were available, and there was more competition between the ions [13,105,118]. For instance, Goswami and Kumar [24] analysed that the removal rate of F^- declined from 90% to 68.3% with an initial F^- concentration increment from 3 to 10 mg L^{-1}, utilizing nanoscale rice husk biochar.

Table 2. Influence of solution pH on the adsorption of U.

Feedstock	Solution pH	pH_{PZC}	Target Pollutant	Speciation Adsorbed	Biochar Surface Charge	Adsorption Capacity (mg g^{-1})	References
Rice straw	5.5	2.5	U	UO_2^{2+}, $(UO_2)_3(OH)_5^+$, $(UO_2)_3(OH)_4^{2+}$, $(UO_2)_2(OH)_2^{2+}$	negative	428.25	[131]
Rice straw	5.5	2.5	U		negative	242.65	[33]
Wheat straw	6	3	U	UO_2^{2+}, $(UO_2)_3(OH)_5^+$, $(UO_2)_2(OH)_2^{2+}$, UO_2OH^+, $(UO_2)_4(OH)_7^+$	negative	355.6	[82]
Rice husk	4	3.51	U	UO_2^{2+}, UO_2OH^+, $(UO_2)_3(OH)_5^+$	negative	52.63	[125]
Rice husk	5.5	4.17	U	UO_2^{2+}, $(UO_2)_3(OH)_5^+$, $(UO_2)_2(OH)_2^{2+}$	negative	138.88	[81]
Rice husk	7	3.71	U	$UO_2(OH)^+$, $(UO_2)_2(OH)_2$, $(UO_2)_3(OH)_5^{2+}$	negative	118	[132]
Corn cob	6	_	U	$(UO_2)_3(OH)_5^+$, $(UO_2)_2(OH)_2^{2+}$, UO_2OH^+	negative	163.18	[34]
Pine needles	6	3.8	U	_	_	623.7	[37]
Pine needles	6	_	U	_	_	62.7	[172]
Pine sawdust	4	2.98	U	UO_2^{2+}, $(UO_2)_3(OH)_5^+$, $(UO_2)_2(OH)_2^{2+}$, $(UO_2)_4(OH)_7^+$	negative	514.72	[133]
Macaúba palm	3		U			488.7	[36]
Palm tree fibres	6	_	U	_	_	112	[121]
Bamboo sawdust	4	2.73	U	UO_2^{2+}, $(UO_2)_3(OH)_5^+$, $(UO_2)_2(OH)_2^{2+}$, UO_2OH^+	negative	229.2	[111]
Bamboo biomass	4	4.28	U	UO_2^{2+}, $(UO_2)_3(OH)_5^+$, $(UO_2)_2(OH)_2^{2+}$, UO_2OH^+		274.15	[134]
Bamboo	6	_	U	_	_	_	[34]
Bamboo shoot shell	4	_	U	UO_2^{2+}, $(UO_2)_2(OH)_2^{2+}$, UO_2OH^+, $(UO_2)_4(OH)_7^+$	negative	32.3	[105]
Cactus fibre	3	_	U	_	_	214	[118]
Camphor tree leaves	6.5	5.76	U	UO_2^{2+}, $(UO_2)_2(OH)_2^{2+}$, UO_2OH^+	negative	98.29	[173]
Miswak branches	4	2.79	U	UO_2^{2+}, $(UO_2)_2(OH)_2^{2+}$, UO_2OH^+	negative	85.71	[174]
Chinese banyan aerial root	4	_	U	_	_	27.29	[135]
Eucalyptus wood	5.5	_	U	$(UO_2)_2OH^{3+}$, $(UO_2)_3(OH)_5^+$, $(UO_2)_2(OH)_2^{2+}$, UO_2OH^+, $(UO_2)_4(OH)_7^+$	negative	27.2	[175]
Puncture vine	6	4	U	UO_2^{2+}, $(UO_2)_3(OH)_5^+$, $(UO_2)_3(OH)_4^{2+}$, $(UO_2)_2(OH)_2^{2+}$	negative	17.24	[39]
Water hyacinth	6	_	U	UO_2^{2+}, $(UO_2)_2(OH)_2^{2+}$, UO_2OH^+, $(UO_2)_4(OH)^{7+}$	negative	138.57	[176]
Hydrophyte biomass	3	4.2	U	UO_2^{2+}		54.35	[136]
Hydrophyte	4	2.46	U	UO_2^{2+}, $(UO_2)_3(OH)_4^{2+}$, $(UO_2)_2(OH)_2^{2+}$, UO_2OH^+	negative	128.5	[137]
Switchgrass	5.9	_	U	UO_2^{2+}, $(UO_2)_3(OH)_5^+$, $(UO_2)_2(OH)_2^{2+}$, UO_2OH^+	negative	4	[177]
Pig manure	4		U			979.3	[107]
Pig manure	4		U			661.7	[107]
Pig manure	4		U			952.5	[138]
Pig manure	4.5	_	U	UO_2^{2+},$(UO_2)_2(OH)_2^{2+}$, UO_2OH^+		221.4	[124]
Horse manure	4	9.05	U	UO_2^{2+}		516.5	[108]
Horse manure	4		U	UO_2^{2+}	negative	625.8	[139]
Cow manure	4.5	3	U	UO_2^{2+}, $(UO_2)_3(OH)_5^+$, $(UO_2)_2(OH)_2^{2+}$, UO_2OH^+, $(UO_2)_4(OH)_7^+$	negative	73.3	[82]
Carp fish scales	5	2.87	U	UO_2^{2+}, $(UO_2)_3(OH)_5^+$, $(UO_2)_2(OH)_2^{2+}$, UO_2OH^+	negative	291.98	[122]
Sewage sludge	6	_	U	$(UO_2)_3(OH)_5^+$, $(UO_2)_2(OH)_2^{2+}$, UO_2OH^+	negative	96.73	[34]
Sewage sludge	6	3	U	UO_2^{2+}, $(UO_2)_3(OH)_5^+$, $(UO_2)_2(OH)_2^{2+}$, UO_2OH^+	negative	490.2	[140]
Winery waste (grape peels)	4	_	U	UO_2^{2+}	negative	255	[141]
Winery waste (grape peels)	4	_	U	UO_2^{2+}	negative	100	[141]
Malt spent rootlets (MSR)	3	_	U	_	_	547	[120]
Coffee espresso residue	3	_	U	_	_	547	[120]
Olive kernels	3	_	U	_	_	357	[120]
Fungi	5	6.41	U		positive	427.9	[142]
Green algae	6	2.62	U	$(UO_2)_3(OH)_5^+$, $(UO_2)_2(OH)_2^{2+}$, $(UO_2)_4(OH)_7^+$	negative	100.2	[143]
Cyanobacteria	6	3.5	U	$(UO_2)_3(OH)_5^+$, $(UO_2)_2(OH)_2^{2+}$, UO_2OH^+	negative	58.05	[144]
Sponge gourd	5	_	U	$(UO_2)_3(OH)_5^+$, $(UO_2)_2(OH)_2^{2+}$, UO_2OH^+	negative	239.21	[83]

Table 2. *Cont.*

Feedstock	Solution pH	pH_{PZC}	Target Pollutant	Speciation Adsorbed	Biochar Surface Charge	Adsorption Capacity (mg g^{-1})	References
Sponge gourd fibres	3		U			904	[84]
Sponge gourd sponges	3	_	U	_	_	92	[119]
Sponge gourd sponge	5.5	_	U	_	_	833	[145]
Sponge gourd residue	6	1.8	U	UO_2^{2+}, $(UO_2)_3(OH)_5^+$, $(UO_2)_2(OH)_2^{2+}$, UO_2OH^+	negative	382	[146]
Watermelon rind	4	5.4	U	_	_	323.56	[85]
Watermelon seeds	4	2.5	U	_	_	27.61	[38]
Longan shell (fruit)	6	6.25	U			331.13	[77]
Orange peel	5.5	2.6	U	UO_2^{2+}, $(UO_2)_3(OH)_4^{2+}$, $(UO_2)_2(OH)_2^{2+}$, UO_2OH^+, $(UO_2)_2OH^{3+}$, $UO_2(OH)_2$	negative	246.3	[106]

U: Uranium; _: data not available; pH_{ZPC} = zero-point charge (pH value at which there is no charge).

Table 3. Effect of solution pH on biochar adsorption capacity for F^- removal.

Feedstock	Solution pH	pH_{PZC}	Target Pollutant	Biochar Surface Charge	Adsorption Capacity (mg g^{-1})	References
Rice straw	8	11	F^-	positive	111.11	[89]
Wheat straw	7	4.8	F^-	negative	51.28	[90]
Rice husk	4	6	F^-	positive	4.45	[178]
Rice husk	7	_	F^-	_	17.3	[24]
Rice husk	5.3		F^-		21.59	[150]
Rice husk	6	_	F^-	_	1.856	[149]
Black gram straw	2	_	F^-	_	16	[96]
Corn stover	2	1.96	F^-		4.11	[91]
Chir pine	4.5	_	F^-	_	16.72	[151]
Mongolian scotch pine tree sawdust	7	_	F^-	_	0.885	[35]
Pine bark	2	9	F^-	positive	9.77	[179]
Pine wood	2	9	F^-	positive	7.66	[179]
Douglas fir	7	11	F^-	positive	9.04	[152]
Douglas fir	6	6.4	F^-	positive	36	[153]
Reed biomass	5.5	8.26	F^-	positive	34.86	[128]
Kashgar tamarisk	6	6.6	F^-	positive	164.23	[40]
Tea oil plant (seed shells)	6.8	4.45	F^-	negative	11.04	[93]
Sawdust	7	2.2	F^-	negative	4.413	[154]
Pongammia pinnata seed cake	7	_	F^-	_	1.11	[7]
Coconut	6.5	_	F^-	_	_	[92]
Cattail	_	_	F^-	_	1.28	[180]
Pomelo peel	6.5	8.6	F^-	positive	18.52	[95]
Watermelon rind	1	2.1	F^-	positive	9.5	[94]
Okra (lady finger) stem	2	_	F^-	_	20	[96]
spent Mushroom compost	10	_	F^-	_	4.7	[13]
Food waste	7.1	_	F^-	_	123.4	[158]
Tea waste	2	_	F^-	_	52.5	[109]
Red algae seaweed	5	6.9	F^-	positive	2.1	[169]
Dairy manure	5	8.8	F^-	positive	0.42	[109]
Sheep bone	_	_	F^-	_	2.33	[112]
Bone residues (chicken, cattle, and mixed bones)	_	_	F^-	_	4.29	[181]
Eggshell and platanus acerifoli leaves (5:1)	5	_	F^-	_	308	[97]

F^-: Fluoride; _: data not available, pH_{ZPC}: zero-point charge (pH value at which there is no charge).

Table 4. Effect of biochar dosage on U and F^- adsorption.

Feedstock	Biochar Dose (g L^{-1})	Target Pollutant	Adsorption Capacity (mg g^{-1})	References
Rice straw	5 mg/50 mL	U	428.25	[131]
Rice straw	0.01g	U	242.65	[33]
Wheat straw	_	U	355.6	[82]
Rice husk	1	U	52.63	[125]
Rice husk	0.38	U	138.88	[81]
Rice husk	0.4	U	118	[132]
Corn cob	0.25	U	163.18	[34]
Pine needles	5	U	623.7	[37]
Pine needles	0.01 g/50 mL	U	62.7	[172]
Pine sawdust	0.2	U	514.72	[133]
Macaúba palm	10	U	488.7	[36]
Palm tree fibres	0.1 g	U	112	[121]
Bamboo sawdust	0.4	U	229.2	[111]
Bamboo biomass	_	U	274.15	[134]
Bamboo shoot shell	2	U	32.3	[105]
Cactus fibre	0.01	U	214	[118]
Camphor tree leaves	0.25	U	98.29	[173]
Miswak branches	1	U	85.71	[174]
Chinese banyan aerial root	1	U	27.29	[135]
Eucalyptus the Wood	5	U	27.2	[175]
Puncture vine	0.5g	U	17.24	[39]
Water hyacinth	0.2	U	138.57	[176]
Hydrophyte biomass	1	U	54.35	[136]
Hydrophyte	0.4	U	128.5	[137]
Switchgrass	0.1	U	4	[177]
Pig manure	0.3	U	979.3	[107]
Pig manure	0.3	U	661.7	[107]
Pig manure	0.1	U	952.5	[138]
Pig manure	_	U	221.4	[124]

Table 4. *Cont.*

Feedstock	Biochar Dose (g L^{-1})	Target Pollutant	Adsorption Capacity (mg g^{-1})	References
Horse manure	0.1	U	516.5	[108]
Horse manure	0.1	U	625.8	[139]
Cow manure	_	U	73.3	[82]
Carp fish scales	0.1	U	291.98	[122]
Sewage sludge	0.25	U	96.73	[34]
Sewage sludge	0.13	U	490.2	[140]
Winery waste (grape peels)	1	U	255	[141]
Winery waste (grape peels)	1	U	100	[141]
Malt spent rootlets	0.01	U	547	[120]
Coffee espresso residue	0.01	U	547	[120]
Olive kernels	0.01	U	357	[120]
Fungi	0.05	U	427.9	[142]
Green algae	0.5	U	100.2	[143]
Cyanobacteria	0.5	U	58.05	[144]
Sponge gourd	5 mg/50 mL	U	239.21	[83]
Sponge gourd fibres	_	U	904	[84]
Sponge gourd sponges	0.01 g	U	92	[119]
Sponge gourd sponge	_	U	833	[145]
Sponge gourd residue	0.4	U	382	[146]
Watermelon rind	1	U	323.56	[85]
Watermelon seeds	1	U	27.61	[38]
Longan shell (fruit)	0.1	U	331.13	[77]
Orange peel	10 mg/50 mL	U	246.3	[106]
Rice straw	1	F^-	111.11	[89]
Wheat straw	1	F^-	51.28	[90]
Rice husk	4	F^-	4.45	[178]
Rice husk	1	F^-	17.3	[24]
Rice husk	0.1	F^-	21.59	[150]
Rice husk	10	F^-	1.856	[149]
Black gram straw	2.5	F^-	16	[96]
Corn stover	5	F^-	4.11	[91]
Chir pine	2	F^-	16.72	[151]
Mongolian scotch pine tree sawdust	3.6 g/100 mL	F^-	0.885	[35]
Pine bark	10	F^-	9.77	[179]
Pine wood	10	F^-	7.66	[179]
Douglas fir (pine)	0.05 g/25 mL	F^-	9.04	[152]
Douglas fir (pine)	25 mg	F^-	36	[153]
Reed biomass	1	F^-	34.86	[128]
Kashgar tamarisk	5	F^-	164.23	[40]
Tea oil plant (seed shells)	1.6	F^-	11.04	[93]
Sawdust	5	F^-	4.413	[154]
Coconut	7	F^-	_	[92]
Cattail	_	F^-	1.28	[180]
Pongammia pinnata seed cake	10	F^-	1.11	[7]
Pomelo peel	2.5	F^-	18.52	[95]
Watermelon rind	0.2 g	F^-	9.5	[94]
Okra (lady finger) stem	2.5	F^-	20	[96]
Spent mushroom compost	2	F^-	4.7	[13]
Food waste	0.1 g/30 mL	F^-	123.4	[156]
Tea waste	10	F^-	52.5	[157]
Red algae seaweed	0.6 g/100 mL	F^-	2.1	[158]
Dairy manure	0.33	F^-	0.51	[109]
Sheep bone	1	F^-	2.33	[112]
Bone residues (chicken, cattle, and mixed bones)	1	F^-	4.29	[181]
Eggshell and platanus acerifoli leaves (5:1)	1.6	F^-	308	[97]

U: Uranium; F^-: Fluoride; _: data not available.

De et al. [7] observed F^- concentrations of 5–20 mg L^{-1} with a fixed biochar dose to examine the impact of initial concentration. The highest removal percentage of 98.5% was obtained at 10 mg L^{-1} F^- concentration. However, with a further rise in the initial concentration, the adsorption decreased drastically because of the saturation of active surface sites. Mahmoud et al. [182] determined the influence of the initial concentration of uranyl ions in the range of 30–150 mg L^{-1} at a constant pH, contact time, and dosage and found that the removal percentage increased from 81.3% to 89.5% for 30–80 mg L^{-1} uranyl

ion concentration. However, increased uranyl ion concentration from 80 to 150 mg L^{-1} decreased the removal efficiency due to more ions in the solution than the biochar surface active sites.

Table 5. Influence of initial concentration on adsorption of F^- and U.

Feedstock	Initial Conc. (mg L^{-1})	Target Pollutant	Adsorption Capacity (mg g^{-1})	References
Rice straw	6	F^-	111.11	[89]
Wheat straw	6	F^-	51.28	[90]
Rice husk	5	F^-	4.45	[178]
Rice husk	5	F^-	17.3	[24]
Rice husk	2	F^-	21.59	[150]
Rice husk	4	F^-	1.856	[149]
Black gram straw	10	F^-	16	[96]
Corn stover	100	F^-	4.11	[91]
Chir pine	50	F^-	16.72	[151]
Mongolian scotch pine tree sawdust	20	F^-	0.885	[35]
Pine bark	100	F^-	9.77	[179]
Pine wood	100	F^-	7.66	[179]
Douglas fir (pine)	10	F^-	9.04	[152]
Douglas fir (pine)	50	F^-	36	[153]
Reed biomass	10	F^-	34.86	[128]
Kashgar tamarisk	40	F^-	164.23	[40]
Tea oil plant (seed shells)	70	F^-	11.04	[93]
Sawdust	10	F^-	4.413	[154]
Coconut	10	F^-	_	[92]
Cattail	20	F^-	1.28	[180]
Pongammia pinnata seed cake	10	F^-	1.11	[7]
Pomelo peel	10	F^-	18.52	[132]
Watermelon rind	50	F^-	9.5	[94]
Okra (lady finger) stem	10	F^-	20	[96]
Spent mushroom compost	10	F^-	4.7	[13]
Food waste	300	F^-	123.4	[156]
Tea waste	50	F^-	52.5	[157]
Red algae seaweed	15	F^-	2.1	[158]
Dairy manure	5	F^-	0.42	[109]
Sheep bone	10	F^-	2.33	[112]
Bone residues (chicken, cattle and mixed bones)	10	F^-	4.29	[181]
Eggshell and platanus acerifoli leaves (5:1)	500	F^-	308	[97]
Rice straw	50	U	428.25	[131]
Rice straw	50	U	242.65	[33]
Wheat straw	10	U	355.6	[82]
Rice husk	10	U	52.63	[125]
Rice husk	3	U	138.88	[81]
Rice husk	80	U	118	[132]
Corn cob	25	U	163.18	[34]
Pine needles	11.9	U	623.7	[37]
Pine needles	50	U	62.7	[172]
Pine sawdust	10	U	514.72	[133]
Macaúba palm	5	U	488.7	[36]
Palm tree fibres	11.9	U	112	[121]
Bamboo sawdust	47.6	U	229.2	[111]
Bamboo biomass	_	U	274.15	[134]
Bamboo shoot shell	50	U	32.3	[105]
Cactus fibre	119	U	214	[118]
Camphor tree leaves	50	U	98.29	[173]
Miswak branches	60	U	85.71	[174]
Chinese banyan aerial root	30	U	27.29	[135]
Eucalyptus the Wood	300	U	27.2	[175]
Puncture vine	50	U	17.24	[39]
Water hyacinth	30	U	138.57	[176]
Hydrophyte biomass	_	U	54.35	[136]
Hydrophyte	47.6	U	128.5	[137]
Switchgrass	10	U	4	[177]
Pig manure	10	U	979.3	[107]
Pig manure	10	U	661.7	[107]
Pig manure	10	U	952.5	[138]

Table 5. *Cont.*

Feedstock	Initial Conc. (mg L^{-1})	Target Pollutant	Adsorption Capacity (mg g^{-1})	References
Pig manure	10	U	221.4	[124]
Horse manure	10	U	516.5	[108]
Horse manure	10	U	625.8	[139]
Cow manure	10	U	73.3	[82]
Carp fish scales	40	U	291.98	[122]
Sewage sludge	25	U	96.73	[34]
Sewage sludge	50	U	490.2	[140]
Winery waste (grape peels)	100	U	255	[141]
Winery waste (grape peels)	100	U	100	[141]
Malt spent rootlets	_	U	547	[120]
Coffee espresso residue	_	U	547	[120]
Olive kernels	_	U	357	[120]
Fungi	10	U	427.9	[142]
Green algae	50	U	100.2	[143]
Cyanobacteria	50	U	58.05	[144]
Sponge gourd	5	U	239.21	[83]
Sponge gourd fibres		U	904	[84]
Sponge gourd sponges	119	U	92	[119]
Sponge gourd sponge	_	U	833	[145]
Sponge gourd residue	225	U	382	[146]
Watermelon rind	20	U	323.56	[85]
Watermelon seeds	30	U	27.61	[38]
Longan shell (fruit)	23.6	U	331.13	[77]
Orange peel	50	U	246.3	[106]

U = Uranium, F^- = Fluoride, _ data not available.

3.7.4. Influence of Co-Existing Ions

Various ions from different sources, including sulphate, chloride, nitrate, carbonate, bicarbonate, phosphate, etc., are generally present in groundwater [13]. These ions were found to regulate the adsorption process by competing with U and F^- ions for interaction with the active surface sites of biochar. The presence of these anions decreased the adsorption efficiency. Liao et al. [107] reported a significant reduction in U adsorption due to the interference of Ca^{2+}, Al^{3+}, $SO_4{}^{2-}$, $CO_3{}^{2-}$, and $PO_4{}^{3-}$ ions. Due to the large radius and high valency of Ca^{2+} and Al^{3+}, U ions were easily captured by the biochar and occupied the active surface sites, leading to decreased U adsorption efficiency. $SO_4{}^{2-}$, $CO_3{}^{2-}$, and $PO_4{}^{3-}$ formed stable complexes with U resulting in the reduction in adsorption efficiency of U. Mei et al. [93] observed the effect of $SO_4{}^{2-}$, $NO_3{}^-$, Cl^-, and $HCO_3{}^-$ on the F^- adsorption, where $NO_3{}^-$, Cl^-, and $SO_4{}^{2-}$ had little impact on the F^- adsorption while $HCO_3{}^-$ reduced the F^- adsorption due to the ion competition.

However, some studies have shown that the co-existing ions (Cl^-, $NO_3{}^-$, $PO_4{}^{3-}$, and $SO_4{}^{2-}$) had little or no significant impact on the adsorption efficiency of U and F^- due to their selectivity of biochar-based materials and their modification methods [13,85]. It was observed that the major co-existing ions interfering with the adsorption of U and F^- were phosphate, sulphate, carbonate, and bicarbonate. In addition, it depends on the properties of the feedstock chosen for the biochar and the materials and methods used for its modification which highly affect the adsorption efficiency of the biochar. Hence, it is crucial to know the co-existing ions in natural groundwater to improve the selectivity of adsorbent for the U and F^- removal experiments.

3.7.5. Influence of Pyrolysis Temperature on U and F^- Adsorption

Pyrolysis temperature is an essential factor influencing the quality and yield of biochar. The pyrolysis temperature mainly affects the structure and properties of the biochar. Table 6 shows the effect of pyrolysis temperature on U and F^- adsorption. Higher temperature increases the pH, surface area, and ash content of the biochar but reduces the yield of the biochar [69,70,74,100]. Furthermore, with the rise in temperature, the porosity of the biochar increases due to the removal of volatile matter, and porosity enhances the adsorptive capacity of biochar [69,74]. Biochar produced at higher temperatures possesses

a higher stable fraction than those prepared at lower temperatures [69]. Oxygen-containing functional groups, for example, carboxyl, hydroxyl, carbonyl, ether, and lactone, on the biochar decreases with an increase in temperature [69,183].

Table 6. Effect of carbonization temperature on U and F^- adsorption.

Feedstock	Carbonization Temp. (°C)	Surface Area (m^2 g^{-1})	Target Pollutant	Adsorption Capacity (mg g^{-1})	References
Rice straw	500	157.96	U	428.25	[131]
Rice straw	500	_	U	242.65	[33]
Wheat straw	450	290.1	U	355.6	[82]
Rice husk	500	109.65	U	52.63	[125]
Rice husk	300	62.88	U	138.88	[81]
Rice husk	500	109	U	118	[132]
Corn cob	800	_	U	163.18	[34]
Pine needles	600	_	U	623.7	[37]
Pine needles	180	_	U	62.7	[172]
Pine sawdust	500	51.45	U	514.72	[133]
Macaúba palm	350	643.12	U	488.7	[36]
palm tree fibres	650	_	U	112	[121]
Bamboo sawdust	450	1298	U	229.2	[111]
Bamboo biomass	700	445.17	U	274.15	[134]
Bamboo shoot shell	500	10.93	U	32.3	[105]
Cactus fibre	600	<5	U	214	[118]
Camphor tree leaves	350	65.91	U	98.29	[173]
Miswak branches	400	9.05	U	85.71	[174]
Chinese banyan aerial root	600	284	U	27.29	[135]
Eucalyptus wood	400	20	U	27.2	[175]
Puncture vine	500	_	U	17.24	[39]
Water hyacinth	400	50.545	U	138.57	[176]
Hydrophyte biomass	700	92.43	U	54.35	[136]
Hydrophyte	500	433	U	128.5	[137]
Switchgrass	300	2.9	U	4	[177]
Pig manure	500	_	U	979.3	[107]
Pig manure	500	_	U	661.7	[107]
Pig manure	500	227.9	U	952.5	[138]
Pig manure	250	_	U	221.4	[124]
Horse manure	500	_	U	516.5	[108]
Horse manure	500	_	U	625.8	[139]
Cow manure	450	101.5	U	73.3	[82]
Carp fish scales	330	1074.73	U	291.98	[122]
Sewage sludge	500	_	U	96.73	[34]
Sewage sludge	600	623.09	U	490.2	[140]
Winery waste (grape peels)	650	_	U	255	[141]
Winery waste (grape peels)	650	165	U	100	[141]
Malt spent rootlets (MSR)	850	540	U	547	[120]
Coffee espresso residue	850	700	U	547	[120]
Olive kernels	850	510	U	357	[120]
Fungi	160	102.7	U	427.9	[142]
Green algae	180	63.7	U	100.2	[143]
Cyanobacteria	200	_	U	58.05	[144]
Sponge gourd	400	_	U	239.21	[83]
Sponge gourd fibres	650	<5	U	904	[84]
Sponge gourd sponges	650	_	U	92	[119]
Sponge gourd sponge	650	_	U	833	[145]
Sponge gourd residue	200	_	U	382	[146]
Watermelon rind	500	86.35	U	323.56	[85]
Watermelon seeds	350	_	U	27.61	[38]
Longan shell (fruit)	800	1168.88	U	331.13	[77]
Orange peel	650	273.25	U	246.3	[106]
rice straw	500	95.36	F^-	111.11	[89]
Wheat straw	_	_	F^-	51.28	[90]
Rice husk	700	58.98	F^-	4.45	[178]
Rice husk	600	_	F^-	17.3	[24]
Rice husk	600	114	F^-	21.59	[150]
Rice husk	500	2.45	F^-	1.856	[149]
Black gram straw	500	9.27	F^-	16	[96]
Corn stover	500	3.61	F^-	4.11	[91]
Chir pine	400	_	F^-	16.72	[151]
Mongolian scotch pine tree sawdust	550	339	F^-	0.885	[35]
Pine bark	450	1.88	F^-	9.77	[179]
Pine wood	450	2.73	F^-	7.66	[179]
Douglas fir (pine)	1000	494	F^-	9.04	[152]
Douglas fir (pine)	1000	576	F^-	36	[153]
Reed biomass	600	236.84	F^-	34.86	[128]
Kashgar tamarisk	350	164.52	F^-	164.23	[40]
Tea oil plant (seed shells)	400	_	F^-	11.04	[93]
Sawdust	660	57.97	F^-	4.413	[154]
Pongammia pinnata seed cake	550	10.1	F^-	1.11	[7]
Coconut	700	1054	F^-	_	[92]

Table 6. *Cont.*

Feedstock	Carbonization Temp. (°C)	Surface Area (m^2 g^{-1})	Target Pollutant	Adsorption Capacity (mg g^{-1})	References
Cattail	800	733.62	F^-	1.28	[180]
Pomelo peel	600	_	F^-	18.52	[132]
Watermelon rind	400	0.5365	F^-	9.5	[94]
Okra (lady finger) stem	600	23.52	F^-	20	[96]
Spent mushroom compost	500	28.5	F^-	4.7	[13]
Food waste	600	20.95	F^-	123.4	[156]
Tea waste	400	11.833	F^-	52.5	[157]
Red algae seaweed	450	319.47	F^-	2.1	[158]
Dairy manure	500	2.6	F^-	0.42	[109]
Sheep bone	650	113.874	F^-	2.33	[112]
Bone residues (chicken, cattle, and mixed bones)	350	_	F^-	4.29	[181]
Bone residues (chicken, cattle, and mixed bones)	700	_	F^-	2.91	[181]
Eggshell and platanus acerifoli leaves (5:1)	800	44.7	F^-	308	[97]

U = Uranium, F^- = Fluoride, _ not available.

3.7.6. Influence of Different Feedstocks on U and F^- Adsorption

Several feedstocks have been utilized to prepare biochar to remove U and F^- from aqueous solution. For example, magnetically modified rice husk biochar was prepared by Wang et al. [132] to remove U. Magnetization enhanced the biochar surface area from 52.1 m^2 g^{-1} to 109 m^2 g^{-1} and pore volume from 0.02 cm^3 g^{-1} to 0.05 cm^3 g^{-1}, thereby increasing U adsorption capacity from 64 mg g^{-1} (raw biochar) to 118 mg g^{-1} (modified biochar) (Table 1) at pH 7 and temperature of 55 °C. Similar findings were reported by [37,39,85,125,136]. Similarly, phosphate-impregnated biochar from bamboo biomass was examined for U removal. Biochar fabrication increased the surface area from 10.31 m^2 g^{-1} to 445.17 m^2 g^{-1} and pore volume from 0.031 m^3 g^{-1} to 0.236 m^3 g^{-1}, which resulted in enhanced U adsorption potential from 15.869 mg g^{-1} to 274.15 mg g^{-1} at pH 4 and a temperature of 25 °C [134]. Ying et al. [106] applied orange-peel-derived biochar modified with MnO_2 for U extraction. MnO_2 modification increased the surface area of the biochar from 165.01 m^2 g^{-1} to 273.25 m^2 g^{-1} and improved the U sorption ability of biochar from 165.4 mg g^{-1} to 246.3 mg g^{-1}. Similar results were observed by [84]. Dairy-manure-based biochar was used for the defluoridation of water. The prepared biochar was modified with calcium, and modified biochar showed 75% removal efficiency with a F^- uptake of 0.11 mg g^{-1} for pristine biochar and 0.42 mg g^{-1} for modified biochar at pH 8 and a temperature of 25 °C [109].

3.8. Adsorption Mechanism of U and F^-

The physical and chemical reactions between adsorbate (U, F^-) and adsorbent (biochar) regulate U and F^- removal from an aqueous solution. Adsorption mechanisms differ according to the type of biomass or feedstock, the presence of functional groups on biochar surface, the physicochemical properties of biochar such as the pH of the medium, and the type of target contaminants [47,57]. Figure 5 summarizes the major adsorption mechanisms of U and F^- on biochar. The possible adsorption mechanisms for U and F^- are ion exchange, surface complexation, electrostatic attraction, and precipitation.

The most probable adsorption mechanisms of F^- and U are ion exchange, electrostatic interactions, and surface complexation. Ion exchange is the interaction between the oxygen-based functional groups on the biochar surface and the target contaminant, which involves exchanging the same type of ions (cation–cation or anion–anion). In the case of F^- adsorption, ion exchange is associated with ion replacement in which F^- ions replace an ion (hydroxyl, carboxylic, and sulphate) from biochar surface [35,82,83,90,127,128,131,132]. For instance, Mei et al. [93] removed the F^- from water using zirconium dioxide biochar through ion exchange between OH^- and F^- on the zirconia particles. Wang et al. [95] used polypyrrole-modified biochar synthesized from pomelo peel to remove F^- and concluded that ion exchange (anion exchange between F^- and Cl^-) was the main adsorption mechanism.

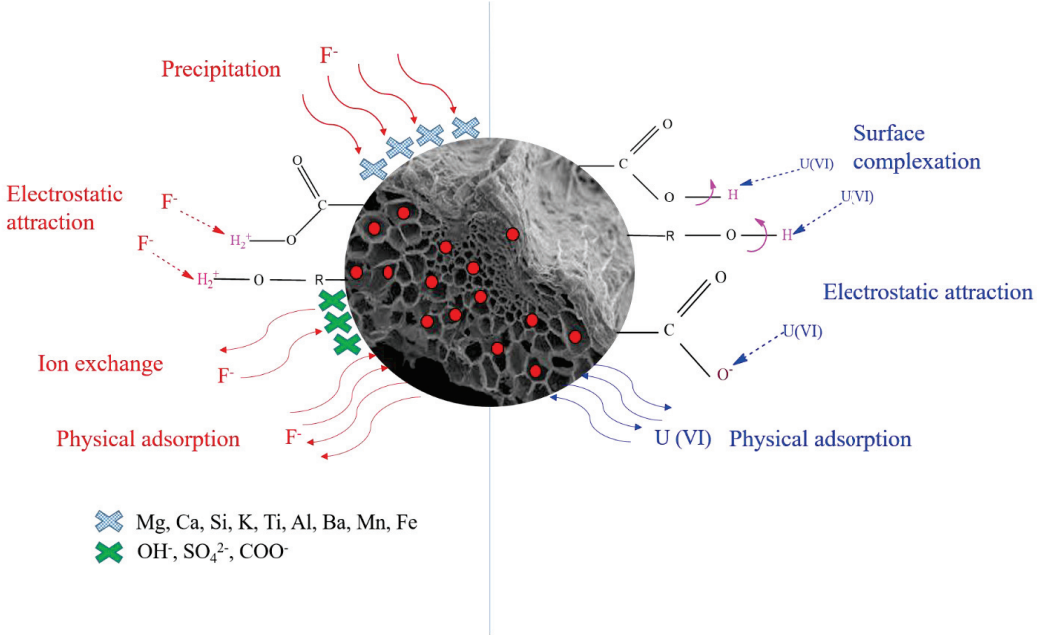


Figure 5. Schematic representation of major mechanisms of U and F^- adsorption on biochar surface.

Electrostatic interaction occurs between the oppositely charged surface of biochar and contaminants. Electrostatic interaction is related to the solution pH and the pH_{ZPC} of the biochar. When the solution pH < pH_{PZC}, the surface charge of the biochar becomes positive and binds the anionic contaminants. When the pH > pH_{PZC}, the biochar surface is negatively charged and binds the cationic contaminants [51,56]. For instance, Sadhu et al. [94] found that maximum adsorption of F^- was at pH 1 because the pH_{PZC} of biochar was at pH 2.1. Electrostatic interactions also occurred between the negative- and positive-charged biochar and U, F^- as a result of ionization of the functional groups, such as $–COOH_2^+$, $–ROH_2^+$, or $–COO^-$ [56,94,107]. Surface complexation (inner sphere and outer sphere) involves the adsorption of U and F^- through the formation of complexes with oxygen functional groups, such as carboxyl, hydroxyl, and carbonyl [31]. Many studies revealed that the dominant mechanism for U adsorption was surface complexation between U(VI) ions and the surface functional groups –COOH, –OH, –CO [33,34,37–39,85,119,132]. Metal F^- precipitation is another mechanism suggested for F^- adsorption, which involves the presence of metals, such as Ca, Mg, Si, K, Al, Mn, Ba, Fe, and Ti in biochar, and F^- ions react with these metals to form insoluble fluorides on biochar [94,97,179].

4. Adsorption Isotherms, Kinetics, and Thermodynamics

4.1. Adsorption Isotherms

The Langmuir and Freundlich isotherm models are generally used to evaluate the equilibrium adsorption capacity of U and F^-. The Langmuir isotherm shows the homogeneous adsorption process and monolayer adsorption, while the Freundlich model shows heterogeneity and multilayer adsorption. For example, Chen et al. [133] assessed the interaction between initial U concentration and equilibrium adsorption capacity. They reported that the Langmuir adsorption isotherm was more favourable for describing the U adsorption than other models and confirmed that the adsorption process is single-layer adsorption. Similarly, Meilani et al. [156] performed an isotherm study to detect the F^- adsorption and adsorption capacity of aluminium-modified food waste biochar. It was found that sorption occurred by the Langmuir adsorption isotherm, which suggested that adsorption was monolayer, homogeneous, occurred only on localized sites, and there were no interactions between the adsorbed ions. In another study, Dai et al. [34] applied the Langmuir and Freundlich isotherm models to assess the U adsorption capacity of corn cob biochar (CCB) and sewage sludge biochar (SSB). They found that the Langmuir isotherm model better

fitted U adsorption by CCB while the Freundlich isotherm model better fitted U adsorption by SSB. Since the CCB was ash-poor biochar, the surface structure was homogeneous, while SSB was ash-rich biochar; thus, the surface structure was heterogeneous.

However, in some cases, the Tempkin and Halsey adsorption isotherm model is also used. For instance, Sadhu et al. [94] applied four adsorption isotherm models (including Langmuir, Freundlich, Tempkin, and Halsey) to depict the F^- adsorption and found that experimental data were better fitted by the Freundlich model than the other three models. Halsey isotherm is appropriate for multilayer adsorption, and Tempkin isotherm is suitable for the uniform distribution of binding energies.

4.2. Adsorption Kinetics

Adsorption kinetics is used to analyse the adsorption behaviour between biochar and contaminants (U and F^-) with reference to contact time. Pseudo-first-order and pseudo-second-order kinetic models were used to investigate U and F^- adsorption on the biochar. For instance, Chen et al. [133] reported that the adsorption behaviour between U and MgO/biochar was chemisorption because the correlation coefficient (R^2) of pseudo-second-order kinetics was greater than the first-order kinetics. Similarly, Meilani et al. [156] employed pseudo-first-order and pseudo-second-order models to examine the adsorption mechanism of F^- on the surface of aluminium-modified food waste biochar. They found that the adsorption process was chemical adsorption, as pseudo-second-order kinetics fitted better with the experimental data due to the higher regression coefficient (R^2) than the pseudo-first-order model. In another study, Dai et al. [34] performed adsorption kinetics and concluded that the U adsorption process was both physical and chemical adsorption. It was found that the U adsorption process involved two steps: first, the initial phase, which contained rapid adsorption, and second, it involved a slower adsorption process. In the initial rapid phase, a higher amount of U adsorbed onto the CCB (ash-poor), and a lower amount of U adsorbed on the SSB (ash-rich) in the later slower phase. It was found that pseudo-first-order and pseudo-second-order models both fitted well for U adsorption process.

4.3. Adsorption Thermodynamics

Adsorption thermodynamics is used to analyse the adsorption process with respect to temperature. The thermodynamic factors, including enthalpy, Gibbs free energy, and entropy, provide information about the adsorption process. Negative Gibbs free energy represents that the adsorption process increases with respect to temperature and is spontaneous. Negative enthalpy indicates that adsorption capacity decreases with an increase in temperature, and the process of adsorption is heat-releasing. The positive enthalpy value shows that the adsorption potential increases with the rise in temperature, and the process is heat-absorbing. The positive entropy value represents the rise in randomness at the liquid–solid mass transfer interface. For example, Chen et al. [133] reported that the U adsorption process by MgO/biochar was spontaneous and exothermic because the adsorption capability declined with the rising temperature, which confirmed that the sorption process was exothermic and negative Gibbs free energy described the spontaneity of the process. In another study, Guan et al. [35] reported that F^- adsorption on modified Mongolian scotch pine tree sawdust biochar increased with respect to temperature (T = 308, 318, and 328 K), which indicated that the adsorption process was endothermic. Similarly, Ahmed et al. [39] examined the influence of temperature on the sorption process of U on the magnetized biochar derived from *Tribulus terrestris* plant. They found that the sorption process was spontaneous and heat-absorbing because U adsorption increased with rising temperature from 298 to 318 K with negative Gibbs free energy and positive enthalpy and entropy.

5. Regeneration of Biochar

Regeneration of biochar is the reverse of the adsorption process achieved by desorbing the contaminant from the biochar. It improves the reusability and stability of the biochar by performing sorption/desorption cycles. Desorption experiments were performed using desorbing agents, mainly acids and alkaline solutions. For instance, Mishra et al. [175] studied the desorption of the U from loaded biochar using nitric acid. They reported that acids are better eluting agents because they provide H^+ ions which tend to protonate the surface of biochar, resulting in the elution of positively charged U ions. In another investigation, Liao et al. [138] examined the reusability of pig-manure-derived biochar using ethanol, HCl, KOH, and deionized water as desorbing agents. Among them, HCl showed the effective desorption of U because, at low pH, hydronium ions have more affinity for active sites than the U(VI) species. The removal efficiency was found to be 85% after five cycles. Pang et al. [142] tested the stability and reusability of nano-zerovalent iron-based biochar. They performed five regeneration cycles using sodium bicarbonate as a desorbing agent to desorb U. They reported that the removal efficiency of biochar was 80.6% in the first cycle, which declined to 52% after five cycles.

Various U(VI) sorption–desorption cycles were performed by Philippou et al. [37], who found that the adsorption capability of the biochar for U decreased after each cycle due to the loss of biochar material. Adsorption % declined from 99.5 to 87.2%, and desorption% reduced from 99.6 to 62.6% after four cycles. Sadhu et al. [94] performed three cycles of sorption–desorption to analyse the desorption of F^- from watermelon rind biochar and concluded that the adsorption capacity of biochar was 79.54% after the first cycle, 71.99% after the second cycle, and 60.17% after the third cycle. Hence, the prepared biochar was stable and could be reused. Similarly, De et al. [7] examined the reusability of biochar using H_2SO_4 desorbing agent to desorb F^-. They performed five cycles of sorption–desorption and reported an adsorption percentage of 98.5% after the first cycle and 68% after five cycles. Ahmed et al. [39] assessed the reusability of biochar by performing five cycles of repeated adsorption of U on magnetic biochar obtained from a *Tribulus terrestris* plant. It was found that the adsorption potential of biochar slightly declined after five cycles suggesting that the biochar has the potential to extract U from water and can be reused.

6. Challenges and Limitations for Real U and F^- Groundwater Treatment

The application of biochar for treating real U and F^--contaminated groundwater is crucial for understanding the practical applicability and limitations of low-cost novel adsorbents. Lingamdinne et al. [85] have tested real groundwater spiked with 10 mg L^{-1} of U from Republic of Korea for U treatment using magnetic watermelon rind biochar. In semi-column experiments, more than 90% of U was removed with magnetic biochar in up to three cycles at pH 4. In addition, Sen et al. [81] collected groundwater from West Bengal and Jharkhand, with U concentrations in the range of 38–85 µg L^{-1}. Therefore, iron-modified biochar showed a maximum removal efficiency of 97–99.77% for U at pH 5.5–8.0 at < 1 g of biochar dose. Interestingly, in the USA, Kumar et al. [177] collected groundwater with pH 3.9 and U concentrations of 3.0 mg L^{-1}, which reported an adsorption capacity of 0.52 mg g^{-1} using switchgrass biochar in column experiments. Through batch sorption experiments, the adsorption capacity for U was observed at 2.12 mg g^{-1} at pH 3.9, whereas it increased to about 4 mg g^{-1} with increasing pH up to 5.9 [177]. From the above analysis, it has been clear that U removal from real groundwater is pH-dependent, and the effect of biochar dose, initial U concentration, and other dependent parameters is yet to be investigated.

Recently, Kumar et al. [184] have summarized practical applications and limitations in treating F^--contaminated water through raw/modified biochar. It has been investigated that most of the research has been performed at low pH to treat real or spiked groundwater using biochars. For example, Mohan et al. [91] have reported that low adsorption capacity, 4.38 and 5.37 mg L^{-1}, was observed at pH 2 using corn stover pristine biochar and magnetic biochar, respectively, for 10 mg L^{-1} fluorides-spiked groundwater collected

from Ghaziabad, India. In the context of industrial effluents, Sadhu et al. [94] have treated industrial wastewater with F^- concentrations of 5570 mg L^{-1} in multiple batch runs with increasing biochar dosage at pH 1 using watermelon rind biochar. In contrast, few studies have also treated F^--contaminated groundwater close to neutral pH (5–8) with a removal efficiency of 81–100% [92,185,186]. For example, Zhou et al. [186] observed that 100% F^- removal efficiency was removed from groundwater having 5 mg L^{-1} F^- concentrations using magnetic biochar at pH 8. Similarly, a removal efficiency of 81% was observed for F^--contaminated groundwater with 7 mg L^{-1} using shell-derived activated biochar at pH 6.5 [92]. In addition, in China, 97% of F^--contaminated groundwater (9.8 mg L^{-1}) was treated with lanthanum-modified biochar at pH 5.2 [185]. Besides adsorption, the gravity filtration method showed a removal efficiency of 92.5–94.7% for F^- ions from drinking water using iron-modified biochar [187]. Apart from this, groundwater contains various cations/anions that can significantly influence F^- removal during the treatment of real groundwater using biochar, which is yet to be investigated. Batch sorption experiments were extensively performed using raw/modified biochar at the laboratory scale; however, very few studies have reported the implication of biochars in column experiments to treat F^--contaminated water. The transport and deposition of F^- were analysed with respect to adsorbent dosage, F^- concentrations, and flow velocity, as these parameters can impact F^- adsorption. For example, the retention and transport mechanism for F^- in column experiments, using various biochars derived, such as pulse straw biochar [96], modified biochar (MgO-biochar) [155], and dairy manure-derived biochar [109].

Till now, biochar research has mostly been carried out at a small scale/laboratory scale. So, to upscale biochar for the treatment of natural groundwater/wastewater/surface water, the major limitations include controlled experimental designs in the laboratory, which is the main limiting factor while implementing biochar at a large scale. Most of the experiments are batch experiments, with limited column studies. The cost of production is one of the major factors limiting biochar application on a large scale. There are limited studies on removing U and F^- from real aquifers/surface water. There are operational challenges while designing a water treatment plant to remove U and F^- using biochar. Natural groundwater/surface waters contain co-existing ions with respect to U and F^-, which interferes with the adsorption. A risk assessment of biochar application needs to be investigated to remove U and F^- from drinking water. The toxicological impacts of biochar need to be investigated. Biochar recycling and management of the waste biochar need to be taken into consideration. There are studies related to the regeneration and reusability of biochar, but the efficiency of the biochar decreases after a few cycles. Hence, the safe disposal and alternate use of waste biochar are the concern.

7. Conclusions, Research Gaps, and Future Perspectives

The present review has summarized the recent studies for removing U and F^- from aqueous solution using raw and modified biochar prepared from different feedstocks. Different feedstocks, production techniques, modification methods, adsorption mechanisms, factors influencing the U and F^- adsorption, and experimental conditions for the optimum removal of U and F^- were reviewed in this paper. It was found that pyrolysis was the dominant biochar production technique. Low-to-medium pyrolysis temperature, cellulose, and hemicellulose-rich feedstocks such as crop residues, grasses, softwood, and manure-based biochars were effective for U and F^- removal. Acidic and magnetic modification favoured U adsorption, while metal oxides, hydroxides, and alkali modification aided F^- adsorption. The dominated adsorption mechanisms for U adsorption were surface complexation (inner-sphere complexation) and electrostatic attraction, whereas ion exchange, electrostatic attraction, and precipitation were adsorptive mechanisms for F^- ions. Different parameters affected the adsorption process, including pH, biochar dosage, initial concentration, co-existing ions, and pyrolysis temperature. It was found that alkaline pH facilitated F^- adsorption while slightly acidic and near-neutral pH favoured U adsorption. High pyrolysis temperature raised the pH of biochar and reduced the biochar yield.

Consequently, adsorption capacity decreased due to pore shrinking or pore breakage and loss of acidic functional groups. It is crucial to have knowledge about the co-existing ions in natural groundwater to improve the selectivity of adsorbent for the U and F^- removal experiments. Although several investigations have been carried out to remove U and F^- with biochar, some research gaps in the literature need to be addressed.

1. Most of the investigations have been carried out at lab scale through batch studies using synthetic water or simulated water, and limited studies have been performed using natural water. In order to scale up, column studies should be conducted for field applications, and future research should be focused on the treatment of natural water.
2. Most studies have focused on the selective removal/extraction of either U or F^- using biochar. However, actual waters contain multiple contaminants, so future research should focus on using biochar to remove multiple contaminants from water.
3. There is a lack of studies for the treatment of drinking-water sources such as natural waters and groundwater using biochar. Most of the studies have focused on the remediation of wastewater.
4. Most of the modifications are chemical modifications, and there is a need for environmentally friendly green methods/materials for modification.
5. The effect of co-existing ions has not been studied in detail. There is no detailed study on the impact of multiple components in the solution that interferes with the U and F^- adsorption.
6. Most studies have considered U as a cation (UO_2^{2+}), but in alkaline solutions, U exists as $(UO_2)_2CO_3$ $(OH)^{3-}$ (anion). So, there is no study for treating anionic U using biochar from aqueous solution.

Author Contributions: Conceptualization, A.T. and P.K.S.; methodology, A.T.; formal analysis, A.T.; investigation, data curation, A.T.; writing—original draft preparation, A.T.; writing—review and editing, P.K.S. and R.K.; supervision, P.K.S. All authors have read and agreed to the published version of the manuscript.

Funding: This research was financially supported by the University Grants Commission (UGC) in the form of Ph.D. fellowship.

Data Availability Statement: Not applicable.

Acknowledgments: The first author would like to acknowledge the University Grants Commission (UGC), India for providing financial support in the form of Ph.D. fellowship. We acknowledge the DST-FIST (Fund for Improvement of S & T Infrastructure of the Department of Science and Technology) support at the Department of Environmental Science and Technology of the Central University of Punjab for providing support to this work. PKS would also like to acknowledge the SERB Core Research Grant (CRG/2021/002567) from the Department of Science and Technology (DST), India, and the Research Seed Money Grant (GP-25) from the Central University of Punjab for technical support.

Conflicts of Interest: The authors declare no conflict of interest.

References

1. Salehi, M. Global Water Shortage and Potable Water Safety; Today's Concern and Tomorrow's Crisis. *Environ. Int.* **2022**, *158*, 106936. [CrossRef] [PubMed]
2. Hering, J.G.; Maag, S.; Schnoor, J.L. A Call for Synthesis of Water Research to Achieve the Sustainable Development Goals by 2030. *Environ. Sci. Technol.* **2016**, *50*, 6122–6123. [CrossRef] [PubMed]
3. Aravinthasamy, P.; Karunanidhi, D.; Subramani, T.; Anand, B.; Roy, P.D.; Srinivasamoorthy, K. Fluoride Contamination in Groundwater of the Shanmuganadhi River Basin (South India) and Its Association with Other Chemical Constituents Using Geographical Information System and Multivariate Statistics. *Chem. Erde* **2020**, *80*, 125555. [CrossRef]
4. Kaur, G.; Kumar, R.; Mittal, S.; Sahoo, P.K.; Vaid, U. Ground/Drinking Water Contaminants and Cancer Incidence: A Case Study of Rural Areas of South West Punjab, India. *Hum. Ecol. Risk Assess.* **2021**, *27*, 205–226. [CrossRef]
5. Coyte, R.M.; Singh, A.; Furst, K.E.; Mitch, W.A.; Vengosh, A. Co-Occurrence of Geogenic and Anthropogenic Contaminants in Groundwater from Rajasthan, India. *Sci. Total Environ.* **2019**, *688*, 1216–1227. [CrossRef]

6. Ma, M.; Wang, R.; Xu, L.; Xu, M.; Liu, S. Emerging Health Risks and Underlying Toxicological Mechanisms of Uranium Contamination: Lessons from the Past Two Decades. *Environ. Int.* **2020**, *145*, 106107. [CrossRef]
7. De, D.; Santosha, S.; Aniya, V.; Sreeramoju, A.; Satyavathi, B. Assessing the Applicability of an Agro-Industrial Waste to Engineered Bio-Char as a Dynamic Adsorbent for Fluoride Sorption. *J. Environ. Chem. Eng.* **2018**, *6*, 2998–3009. [CrossRef]
8. Balaram, V.; Rani, A.; Rathore, D.P.S. Uranium in Groundwater in Parts of India and World: A Comprehensive Review of Sources, Impact to the Environment and Human Health, Analytical Techniques, and Mitigation Technologies. *Geosystems Geoenvironment* **2022**, *1*, 100043. [CrossRef]
9. Coyte, R.M.; Jain, R.C.; Srivastava, S.K.; Sharma, K.C.; Khalil, A.; Ma, L.; Vengosh, A. Large-Scale Uranium Contamination of Groundwater Resources in India. *Environ. Sci. Technol. Lett.* **2018**, *5*, 341–347. [CrossRef]
10. Brugge, D.; Buchner, V. Health Effects of Uranium: New Research Findings. *Rev. Environ. Health* **2011**, *26*, 231–249. [CrossRef]
11. Ali, S.; Thakur, S.K.; Sarkar, A.; Shekhar, S. Worldwide Contamination of Water by Fluoride. *Environ. Chem. Lett.* **2016**, *14*, 291–315. [CrossRef]
12. Kumar, M.; Goswami, R.; Patel, A.K.; Srivastava, M.; Das, N. Scenario, Perspectives and Mechanism of Arsenic and Fluoride Co-Occurrence in the Groundwater: A Review. *Chemosphere* **2020**, *249*, 126126. [CrossRef] [PubMed]
13. Chen, G.J.; Peng, C.Y.; Fang, J.Y.; Dong, Y.Y.; Zhu, X.H.; Cai, H.M. Biosorption of Fluoride from Drinking Water Using Spent Mushroom Compost Biochar Coated with Aluminum Hydroxide. *Desalin. Water Treat.* **2016**, *57*, 12385–12395. [CrossRef]
14. Shen, J.; Schäfer, A. Removal of Fluoride and Uranium by Nanofiltration and Reverse Osmosis: A Review. *Chemosphere* **2014**, *117*, 679–691. [CrossRef] [PubMed]
15. Katsoyiannis, I.A.; Zouboulis, A.I. Removal of Uranium from Contaminated Drinking Water: A Mini Review of Available Treatment Methods. *Desalin. Water Treat.* **2013**, *51*, 2915–2925. [CrossRef]
16. Bhatnagar, A.; Kumar, E.; Sillanpää, M. Fluoride Removal from Water by Adsorption—A Review. *Chem. Eng. J.* **2011**, *171*, 811–840. [CrossRef]
17. Ghosh, D.; Sinha, M.K.; Purkait, M.K. A Comparative Analysis of Low-Cost Ceramic Membrane Preparation for Effective Fluoride Removal Using Hybrid Technique. *Desalination* **2013**, *327*, 2–13. [CrossRef]
18. Ndiaye, P.I.; Moulin, P.; Dominguez, L.; Millet, J.C.; Charbit, F. Removal of Fluoride from Electronic Industrial Effluentby RO Membrane Separation. *Desalination* **2005**, *173*, 25–32. [CrossRef]
19. Azbar, N.; Türkman, A. Defluoridation in Drinking Waters. *Water Sci. Technol.* **2000**, *42*, 403–407. [CrossRef]
20. Chaturvedi, A.K.; Yadava, K.P.; Pathak, K.C.; Singh, V.N. Defluoridation of Water by Adsorption on Fly Ash. *Water. Air. Soil Pollut.* **1990**, *49*, 51–61. [CrossRef]
21. Habuda-Stanić, M.; Ravančić, M.; Flanagan, A. A Review on Adsorption of Fluoride from Aqueous Solution. *Materials* **2014**, *7*, 6317–6366. [CrossRef] [PubMed]
22. Samarghandi, M.R.; Khiadani, M.; Foroughi, M.; Zolghadr Nasab, H. Defluoridation of Water Using Activated Alumina in Presence of Natural Organic Matter via Response Surface Methodology. *Environ. Sci. Pollut. Res.* **2016**, *23*, 887–897. [CrossRef] [PubMed]
23. Vithanage, M.; Bhattacharya, P. Fluoride in the Environment: Sources, Distribution and Defluoridation. *Environ. Chem. Lett.* **2015**, *13*, 131–147. [CrossRef]
24. Goswami, R.; Kumar, M. Removal of Fluoride from Aqueous Solution Using Nanoscale Rice Husk Biochar. *Groundw. Sustain. Dev.* **2018**, *7*, 446–451. [CrossRef]
25. Arfin, T.; Waghmare, S. Fluoride Removal from Water by Mixed Metal Oxide Adsorbent Materials: A State-of-the-Art Review. *Int. J. Eng. Sci. Res. Technol.* **2015**, *4*, 519–536.
26. Velazquez-Jimenez, L.H.; Vences-Alvarez, E.; Flores-Arciniega, J.L.; Flores-Zuñiga, H.; Rangel-Mendez, J.R. Water Defluoridation with Special Emphasis on Adsorbents-Containing Metal Oxides and/or Hydroxides: A Review. *Sep. Purif. Technol.* **2015**, *150*, 292–307. [CrossRef]
27. Shuibo, X.; Chun, Z.; Xinghuo, Z.; Jing, Y.; Xiaojian, Z.; Jingsong, W. Removal of Uranium (VI) from Aqueous Solution by Adsorption of Hematite. *J. Environ. Radioact.* **2009**, *100*, 162–166. [CrossRef]
28. Camacho, L.M.; Deng, S.; Parra, R.R. Uranium Removal from Groundwater by Natural Clinoptilolite Zeolite: Effects of PH and Initial Feed Concentration. *J. Hazard. Mater.* **2010**, *175*, 393–398. [CrossRef]
29. Alahabadi, A.; Singh, P.; Raizada, P.; Anastopoulos, I.; Sivamani, S.; Dotto, G.L.; Landarani, M.; Ivanets, A.; Kyzas, G.Z.; Hosseini-Bandegharaei, A. Activated Carbon from Wood Wastes for the Removal of Uranium and Thorium Ions through Modification with Mineral Acid. *Colloids Surf. A Physicochem. Eng. Asp.* **2020**, *607*, 125516. [CrossRef]
30. (Ölmez) Aytaş, Ş.; Akyil, S.; Aslani, M.A.A.; Aytekin, U. Removal of Uranium from Aqueous Solutions by Diatomite (Kieselguhr). *J. Radioanal. Nucl. Chem.* **1999**, *240*, 973–976. [CrossRef]
31. Inyang, M.I.; Gao, B.; Yao, Y.; Xue, Y.; Zimmerman, A.; Mosa, A.; Pullammanappallil, P.; Ok, Y.S.; Cao, X. A Review of Biochar as a Low-Cost Adsorbent for Aqueous Heavy Metal Removal. *Crit. Rev. Environ. Sci. Technol.* **2016**, *46*, 406–433. [CrossRef]
32. Ahmad, M.; Rajapaksha, A.U.; Lim, J.E.; Zhang, M.; Bolan, N.; Mohan, D.; Vithanage, M.; Lee, S.S.; Ok, Y.S. Biochar as a Sorbent for Contaminant Management in Soil and Water: A Review. *Chemosphere* **2014**, *99*, 19–33. [CrossRef] [PubMed]
33. Ahmed, W.; Mehmood, S.; Qaswar, M.; Ali, S.; Khan, Z.H.; Ying, H.; Chen, D.Y.; Núñez-Delgado, A. Oxidized Biochar Obtained from Rice Straw as Adsorbent to Remove Uranium (VI) from Aqueous Solutions. *J. Environ. Chem. Eng.* **2021**, *9*, 105104. [CrossRef]

34. Dai, L.; Li, L.; Zhu, W.; Ma, H.; Huang, H.; Lu, Q.; Yang, M.; Ran, Y. Post-Engineering of Biochar via Thermal Air Treatment for Highly Efficient Promotion of Uranium(VI) Adsorption. *Bioresour. Technol.* **2020**, *298*, 122576. [CrossRef] [PubMed]
35. Guan, X.; Zhou, J.; Ma, N.; Chen, X.; Gao, J.; Zhang, R. Studies on Modified Conditions of Biochar and the Mechanism for Fluoride Removal. *Desalin. Water Treat.* **2015**, *55*, 440–447. [CrossRef]
36. Guilhen, S.N.; Rovani, S.; de Araujo, L.G.; Tenório, J.A.S.S.; Mašek, O. Uranium Removal from Aqueous Solution Using Macauba Endocarp-Derived Biochar: Effect of Physical Activation. *Environ. Pollut.* **2021**, *272*, 116022. [CrossRef] [PubMed]
37. Philippou, K.; Anastopoulos, I.; Dosche, C.; Pashalidis, I. Synthesis and Characterization of a Novel Fe_3O_4-Loaded Oxidized Biochar from Pine Needles and Its Application for Uranium Removal. Kinetic, Thermodynamic, and Mechanistic Analysis. *J. Environ. Manage.* **2019**, *252*, 109677. [CrossRef] [PubMed]
38. Ahmed, W.; Mehmood, S.; Núñez-Delgado, A.; Ali, S.; Qaswar, M.; Khan, Z.H.; Ying, H.; Chen, D.Y. Utilization of Citrullus Lanatus L. Seeds to Synthesize a Novel $MnFe_2O_4$-Biochar Adsorbent for the Removal of U(VI) from Wastewater: Insights and Comparison between Modified and Raw Biochar. *Sci. Total Environ.* **2021**, *771*, 144955. [CrossRef]
39. Ahmed, W.; Mehmood, S.; Núñez-delgado, A.; Qaswar, M.; Ali, S.; Ying, H.; Liu, Z.; Mahmood, M.; Chen, D. Fabrication, Characterization and U (VI) Sorption Properties of a Novel Biochar Derived from Tribulus Terrestris via Two Different Approaches. *Sci. Total Environ.* **2021**, *780*, 146617. [CrossRef]
40. Habibi, N.; Rouhi, P.; Ramavandi, B. Modification of Tamarix Hispida Biochar by Lanthanum Chloride for Enhanced Fluoride Adsorption from Synthetic and Real Wastewater. *Environ. Prog. Sustain. Energy* **2019**, *38*, S298–S305. [CrossRef]
41. Liang, L.; Xi, F.; Tan, W.; Meng, X.; Hu, B.; Wang, X. Review of Organic and Inorganic Pollutants Removal by Biochar and Biochar-Based Composites. *Biochar* **2021**, *3*, 255–281. [CrossRef]
42. Mohan, D.; Sarswat, A.; Ok, Y.S.; Pittman, C.U. Organic and Inorganic Contaminants Removal from Water with Biochar, a Renewable, Low Cost and Sustainable Adsorbent—A Critical Review. *Bioresour. Technol.* **2014**, *160*, 191–202. [CrossRef] [PubMed]
43. Gwenzi, W.; Chaukura, N.; Noubactep, C.; Mukome, F.N.D. Biochar-Based Water Treatment Systems as a Potential Low-Cost and Sustainable Technology for Clean Water Provision. *J. Environ. Manage.* **2017**, *197*, 732–749. [CrossRef]
44. Sizmur, T.; Fresno, T.; Akgül, G.; Frost, H.; Moreno-Jiménez, E. Biochar Modification to Enhance Sorption of Inorganics from Water. *Bioresour. Technol.* **2017**, *246*, 34–47. [CrossRef] [PubMed]
45. Tan, X.; Liu, Y.; Zeng, G.; Wang, X.; Hu, X.; Gu, Y.; Yang, Z. Application of Biochar for the Removal of Pollutants from Aqueous Solutions. *Chemosphere* **2015**, *125*, 70–85. [CrossRef] [PubMed]
46. Abbas, Z.; Ali, S.; Rizwan, M.; Zaheer, I.E.; Malik, A.; Riaz, M.A.; Shahid, M.R.; ur Rehman, M.Z.; Al-Wabel, M.I. A Critical Review of Mechanisms Involved in the Adsorption of Organic and Inorganic Contaminants through Biochar. *Arab. J. Geosci.* **2018**, *11*, 448. [CrossRef]
47. Ambaye, T.G.; van Hullebusch, M.V.E.D.; Rtimi, A.A.S. Mechanisms and Adsorption Capacities of Biochar for the Removal of Organic and Inorganic Pollutants from Industrial Wastewater. *Int. J. Environ. Sci. Technol.* **2021**, *18*, 3273–3294. [CrossRef]
48. Zeghioud, H.; Fryda, L.; Djelal, H.; Assadi, A.; Kane, A. A Comprehensive Review of Biochar in Removal of Organic Pollutants from Wastewater: Characterization, Toxicity, Activation/Functionalization and Influencing Treatment Factors. *J. Water Process Eng.* **2022**, *47*, 102801. [CrossRef]
49. Zhang, M.; Song, G.; Gelardi, D.L.; Huang, L.; Khan, E.; Mašek, O.; Parikh, S.J.; Ok, Y.S. Evaluating Biochar and Its Modifications for the Removal of Ammonium, Nitrate, and Phosphate in Water. *Water Res.* **2020**, *186*, 116303. [CrossRef]
50. Shakoor, M.B.; Ye, Z.L.; Chen, S. Engineered Biochars for Recovering Phosphate and Ammonium from Wastewater: A Review. *Sci. Total Environ.* **2021**, *779*, 146240. [CrossRef]
51. Almanassra, I.W.; Mckay, G.; Kochkodan, V.; Ali Atieh, M.; Al-Ansari, T. A State of the Art Review on Phosphate Removal from Water by Biochars. *Chem. Eng. J.* **2021**, *409*, 128211. [CrossRef]
52. Ambika, S.; Kumar, M.; Pisharody, L.; Malhotra, M.; Kumar, G.; Sreedharan, V.; Singh, L.; Nidheesh, P.V.; Bhatnagar, A. Modified Biochar as a Green Adsorbent for Removal of Hexavalent Chromium from Various Environmental Matrices: Mechanisms, Methods, and Prospects. *Chem. Eng. J.* **2022**, *439*, 135716. [CrossRef]
53. Dai, Y.; Zhang, N.; Xing, C.; Cui, Q.; Sun, Q. The Adsorption, Regeneration and Engineering Applications of Biochar for Removal Organic Pollutants: A Review. *Chemosphere* **2019**, *223*, 12–27. [CrossRef] [PubMed]
54. Lakshmi, D.; Akhil, D.; Kartik, A.; Gopinath, K.P.; Arun, J.; Bhatnagar, A.; Rinklebe, J.; Kim, W.; Muthusamy, G. Artificial Intelligence (AI) Applications in Adsorption of Heavy Metals Using Modified Biochar. *Sci. Total Environ.* **2021**, *801*, 149623. [CrossRef]
55. Liu, T.; Lawluvy, Y.; Shi, Y.; Ighalo, J.O.; He, Y.; Zhang, Y.; Yap, P.S. Adsorption of Cadmium and Lead from Aqueous Solution Using Modified Biochar: A Review. *J. Environ. Chem. Eng.* **2022**, *10*, 106502. [CrossRef]
56. Qiu, B.; Tao, X.; Wang, H.; Li, W.; Ding, X.; Chu, H. Biochar as a Low-Cost Adsorbent for Aqueous Heavy Metal Removal: A Review. *J. Anal. Appl. Pyrolysis* **2021**, *155*, 105081. [CrossRef]
57. Sharma, P.K.; Kumar, R.; Singh, R.K.; Sharma, P.; Ghosh, A. Review on Arsenic Removal Using Biochar-Based Materials. *Groundw. Sustain. Dev.* **2022**, *17*, 100740. [CrossRef]
58. Wang, L.; Wang, Y.; Ma, F.; Tankpa, V.; Bai, S.; Guo, X.; Wang, X. Mechanisms and Reutilization of Modified Biochar Used for Removal of Heavy Metals from Wastewater: A Review. *Sci. Total Environ.* **2019**, *668*, 1298–1309. [CrossRef]
59. Zheng, C.; Yang, Z.; Si, M.; Zhu, F.; Yang, W.; Zhao, F.; Shi, Y. Application of Biochars in the Remediation of Chromium Contamination: Fabrication, Mechanisms, and Interfering Species. *J. Hazard. Mater.* **2021**, *407*, 124376. [CrossRef]

60. Zoroufchi Benis, K.; Motalebi Damuchali, A.; Soltan, J.; McPhedran, K.N. Treatment of Aqueous Arsenic—A Review of Biochar Modification Methods. *Sci. Total Environ.* **2020**, *739*, 139750. [CrossRef]
61. Godwin, P.M.; Pan, Y.; Xiao, H.; Afzal, M.T. Progress in Preparation and Application of Modified Biochar for Improving Heavy Metal Ion Removal From Wastewater. *J. Bioresour. Bioprod.* **2019**, *4*, 31–42. [CrossRef]
62. Hussin, F.; Aroua, M.K.; Szlachta, M. Biochar Derived from Fruit By-Products Using Pyrolysis Process for the Elimination of Pb(II) Ion: An Updated Review. *Chemosphere* **2022**, *287*, 132250. [CrossRef] [PubMed]
63. Li, H.; Dong, X.; da Silva, E.B.; de Oliveira, L.M.; Chen, Y.; Ma, L.Q. Mechanisms of Metal Sorption by Biochars: Biochar Characteristics and Modifications. *Chemosphere* **2017**, *178*, 466–478. [CrossRef] [PubMed]
64. Berslin, D.; Reshmi, A.; Sivaprakash, B.; Rajamohan, N.; Kumar, P.S. Remediation of Emerging Metal Pollutants Using Environment Friendly Biochar- Review on Applications and Mechanism. *Chemosphere* **2022**, *290*, 133384. [CrossRef] [PubMed]
65. Cheng, N.; Wang, B.; Wu, P.; Lee, X.; Xing, Y.; Chen, M.; Gao, B. Adsorption of Emerging Contaminants from Water and Wastewater by Modified Biochar: A Review. *Environ. Pollut.* **2021**, *273*, 116448. [CrossRef]
66. Amusat, S.O.; Kebede, T.G.; Dube, S.; Nindi, M.M. Ball-Milling Synthesis of Biochar and Biochar–Based Nanocomposites and Prospects for Removal of Emerging Contaminants: A Review. *J. Water Process Eng.* **2021**, *41*, 101993. [CrossRef]
67. Shahid, M.K.; Kashif, A.; Fuwad, A.; Choi, Y. Current Advances in Treatment Technologies for Removal of Emerging Contaminants from Water—A Critical Review. *Coord. Chem. Rev.* **2021**, *442*, 213993. [CrossRef]
68. Biswal, B.K.; Vijayaraghavan, K.; Tsen-Tieng, D.L.; Balasubramanian, R. Biochar-Based Bioretention Systems for Removal of Chemical and Microbial Pollutants from Stormwater: A Critical Review. *J. Hazard. Mater.* **2022**, *422*, 126886. [CrossRef]
69. Hassan, M.; Liu, Y.; Naidu, R.; Parikh, S.J.; Du, J.; Qi, F.; Willett, I.R. Influences of Feedstock Sources and Pyrolysis Temperature on the Properties of Biochar and Functionality as Adsorbents: A Meta-Analysis. *Sci. Total Environ.* **2020**, *744*, 140714. [CrossRef]
70. Tomczyk, A.; Sokołowska, Z.; Boguta, P. Biochar Physicochemical Properties: Pyrolysis Temperature and Feedstock Kind Effects. *Rev. Environ. Sci. Bio/Technol.* **2020**, *19*, 191–215. [CrossRef]
71. Yang, H.; Yan, R.; Chen, H.; Lee, D.H.; Zheng, C. Characteristics of Hemicellulose, Cellulose and Lignin Pyrolysis. *Fuel* **2007**, *86*, 1781–1788. [CrossRef]
72. Yaashikaa, P.R.; Kumar, P.S.; Varjani, S.; Saravanan, A. A Critical Review on the Biochar Production Techniques, Characterization, Stability and Applications for Circular Bioeconomy. *Biotechnol. Rep.* **2020**, *28*, e00570. [CrossRef] [PubMed]
73. Wijitkosum, S. Biochar Derived from Agricultural Wastes and Wood Residues for Sustainable Agricultural and Environmental Applications. *Int. Soil Water Conserv. Res.* **2022**, *10*, 335–341. [CrossRef]
74. Ippolito, J.A.; Cui, L.; Kammann, C.; Wrage-Mönnig, N.; Estavillo, J.M.; Fuertes-Mendizabal, T.; Cayuela, M.L.; Sigua, G.; Novak, J.; Spokas, K.; et al. Feedstock Choice, Pyrolysis Temperature and Type Influence Biochar Characteristics: A Comprehensive Meta-Data Analysis Review. *Biochar* **2020**, *2*, 421–438. [CrossRef]
75. Enaime, G.; Baçaoui, A.; Yaacoubi, A.; Lübken, M. Biochar for Wastewater Treatment—Conversion Technologies and Applications. *Appl. Sci.* **2020**, *10*, 3492. [CrossRef]
76. Janu, R.; Mrlik, V.; Ribitsch, D.; Hofman, J.; Sedláček, P.; Bielská, L.; Soja, G. Biochar Surface Functional Groups as Affected by Biomass Feedstock, Biochar Composition and Pyrolysis Temperature. *Carbon Resour. Convers.* **2021**, *4*, 36–46. [CrossRef]
77. Zhang, Q.; Wang, Y.; Wang, Z.; Zhang, Z.; Wang, X.; Yang, Z. Active Biochar Support Nano Zero-Valent Iron for Efficient Removal of U(VI) from Sewage Water. *J. Alloy. Compd.* **2021**, *852*, 156993. [CrossRef]
78. Saleh, T.A.; Mustaqeem, M.; Khaled, M. Water Treatment Technologies in Removing Heavy Metal Ions from Wastewater: A Review. *Environ. Nanotechnol. Monit. Manag.* **2022**, *17*, 100617. [CrossRef]
79. Dulama, M.; Iordache, M.; Deneanu, N. Treatment of Uranium Contaminated Wastewater a review. In *Proceedings of NUCLEAR 2013 the 6th Annual International Conference on Sustainable Development through Nuclear Research and Education Part 3/3*; 2013; pp. 80–87. Available online: http://inis.iaea.org/search/search.aspx?orig_q=RN:47056986 (accessed on 22 October 2022).
80. Boraah, N.; Chakma, S.; Kaushal, P. Attributes of Wood Biochar as an Efficient Adsorbent for Remediating Heavy Metals and Emerging Contaminants from Water: A Critical Review and Bibliometric Analysis. *J. Environ. Chem. Eng.* **2022**, *10*, 107825. [CrossRef]
81. Sen, K.; Mishra, D.; Debnath, P.; Mondal, A.; Mondal, N.K. Adsorption of Uranium (VI) from Groundwater by Silicon Containing Biochar Supported Iron Oxide Nanoparticle. *Bioresour. Technol. Rep.* **2021**, *14*, 100659. [CrossRef]
82. Jin, J.; Li, S.; Peng, X.; Liu, W.; Zhang, C.; Yang, Y.; Han, L.; Du, Z.; Sun, K.; Wang, X. HNO_3 Modified Biochars for Uranium (VI) Removal from Aqueous Solution. *Bioresour. Technol.* **2018**, *256*, 247–253. [CrossRef]
83. Guo, Y.; Liu, X.; Xie, S.; Liu, H.; Wang, C.; Wang, L. 3D ZnO Modified Biochar-Based Hydrogels for Removing U(VI) in Aqueous Solution. *Colloids Surf. A Physicochem. Eng. Asp.* **2022**, *642*, 128606. [CrossRef]
84. Ioannou, K.; Hadjiyiannis, P.; Liatsou, I.; Pashalidis, I. U(VI) Adsorption by Biochar Fiber–MnO2 Composites. *J. Radioanal. Nucl. Chem.* **2019**, *320*, 425–432. [CrossRef]
85. Lingamdinne, L.P.; Choi, J.S.; Angaru, G.K.R.; Karri, R.R.; Yang, J.K.; Chang, Y.Y.; Koduru, J.R. Magnetic-Watermelon Rinds Biochar for Uranium-Contaminated Water Treatment Using an Electromagnetic Semi-Batch Column with Removal Mechanistic Investigations. *Chemosphere* **2022**, *286*, 131776. [CrossRef] [PubMed]
86. Solanki, Y.S.; Agarwal, M.; Gupta, A.B.; Gupta, S.; Shukla, P. Fluoride Occurrences, Health Problems, Detection, and Remediation Methods for Drinking Water: A Comprehensive Review. *Sci. Total Environ.* **2022**, *807*, 150601. [CrossRef]

87. Nizam, S.; Virk, H.S.; Sen, I.S. High Levels of Fluoride in Groundwater from Northern Parts of Indo-Gangetic Plains Reveals Detrimental Fluorosis Health Risks. *Environ. Adv.* **2022**, *8*, 100200. [CrossRef]
88. Kashyap, S.J.; Sankannavar, R.; Madhu, G.M. Fluoride Sources, Toxicity and Fluorosis Management Techniques—A Brief Review. *J. Hazard. Mater. Lett.* **2021**, *2*, 100033. [CrossRef]
89. Zhou, N.; Guo, X.; Ye, C.; Yan, L.; Gu, W.; Wu, X.; Zhou, Q.; Yang, Y.; Wang, X.; Cheng, Q. Enhanced Fluoride Removal from Drinking Water in Wide PH Range Using La/Fe/Al Oxides Loaded Rice Straw Biochar. *Water Supply* **2022**, *22*, 779–794. [CrossRef]
90. Yan, L.; Gu, W.; Zhou, N.; Ye, C.; Yang, Y. Preparation and Characterization of Wheat Straw Biochar Loaded with Aluminium/Lanthanum Hydroxides: A Novel Adsorbent for Removing Fluoride from Drinking Water. *Environ. Technol.* **2021**, *43*, 2771–2784. [CrossRef]
91. Mohan, D.; Kumar, S.; Srivastava, A. Fluoride Removal from Ground Water Using Magnetic and Nonmagnetic Corn Stover Biochars. *Ecol. Eng.* **2014**, *73*, 798–808. [CrossRef]
92. Halder, G.; Khan, A.A.; Dhawane, S. Fluoride Sorption Onto a Steam-Activated Biochar Derived From Cocos Nucifera Shell. *CLEAN–Soil Air Water* **2016**, *44*, 124–133. [CrossRef]
93. Mei, L.; Qiao, H.; Ke, F.; Peng, C.; Hou, R.; Wan, X.; Cai, H. One-Step Synthesis of Zirconium Dioxide-Biochar Derived from Camellia Oleifera Seed Shell with Enhanced Removal Capacity for Fluoride from Water. *Appl. Surf. Sci.* **2020**, *509*, 144685. [CrossRef]
94. Sadhu, M.; Bhattacharya, P.; Vithanage, M.; Padmaja Sudhakar, P. Adsorptive Removal of Fluoride Using Biochar—A Potential Application in Drinking Water Treatment. *Sep. Purif. Technol.* **2022**, *278*, 119106. [CrossRef]
95. Wang, J.; Chen, N.; Li, M.; Feng, C. Efficient Removal of Fluoride Using Polypyrrole-Modified Biochar Derived from Slow Pyrolysis of Pomelo Peel: Sorption Capacity and Mechanism. *J. Polym. Environ.* **2018**, *26*, 1559–1572. [CrossRef]
96. Kumar, H.; Patel, M.; Mohan, D. Simplified Batch and Fixed-Bed Design System for E Ffi Cient and Sustainable Fluoride Removal from Water Using Slow Pyrolyzed Okra Stem and Black Gram Straw Biochars. *ACS Omega* **2019**, *4*, 19513–19525. [CrossRef]
97. Sha, Q.; Xie, H.; Liu, W.; Yang, D.; He, Y.; Yang, C.; Wang, N. Removal of Fluoride Using Platanus Acerifoli Leaves Biochar—An Efficient and Low-Cost Application in Wastewater Treatment. *Environ. Technol.* **2021**, 1–43. [CrossRef]
98. Jha, S.; Nanda, S.; Acharya, B.; Dalai, A.K. A Review of Thermochemical Conversion of Waste Biomass to Biofuels. *Energies* **2022**, *15*, 6352. [CrossRef]
99. Sun, Y.; Gao, B.; Yao, Y.; Fang, J.; Zhang, M.; Zhou, Y.; Chen, H.; Yang, L. Effects of Feedstock Type, Production Method, and Pyrolysis Temperature on Biochar and Hydrochar Properties. *Chem. Eng. J.* **2014**, *240*, 574–578. [CrossRef]
100. Tripathi, M.; Sahu, J.N.; Ganesan, P. Effect of Process Parameters on Production of Biochar from Biomass Waste through Pyrolysis: A Review. *Renew. Sustain. Energy Rev.* **2016**, *55*, 467–481. [CrossRef]
101. Asadi, H.; Ghorbani, M.; Rezaei-Rashti, M.; Abrishamkesh, S.; Amirahmadi, E.; Chengrong, C.; Gorji, M. Application of Rice Husk Biochar for Achieving Sustainable Agriculture and Environment. *Rice Sci.* **2021**, *28*, 325–343. [CrossRef]
102. Windeatt, J.H.; Ross, A.B.; Williams, P.T.; Forster, P.M.; Nahil, M.A.; Singh, S. Characteristics of Biochars from Crop Residues: Potential for Carbon Sequestration and Soil Amendment. *J. Environ. Manage.* **2014**, *146*, 189–197. [CrossRef] [PubMed]
103. Reguyal, F.; Sarmah, A.K.; Gao, W. Synthesis of Magnetic Biochar from Pine Sawdust via Oxidative Hydrolysis of FeCl2 for the Removal Sulfamethoxazole from Aqueous Solution. *J. Hazard. Mater.* **2017**, *321*, 868–878. [CrossRef] [PubMed]
104. Umar, M.; Amru, A.R.; Amin, N.H.M.; Zaid, H.M.; Guan, B.H. Biomass Activated Carbon from Oil Palm Shell as Potential Material to Control Filtration Loss in Water-Based Drilling Fluid. *Optim. Based Model Using Fuzzy Other Stat. Tech. Towar. Environ. Sustain.* **2020**, 55–65.
105. Hu, H.; Zhang, X.; Wang, T.; Sun, L.; Wu, H.; Chen, X. Bamboo (*Acidosasa longiligula*) Shoot Shell Biochar: Its Potential Application to Isolation of Uranium(VI) from Aqueous Solution. *J. Radioanal. Nucl. Chem.* **2018**, *316*, 349–362. [CrossRef]
106. Ying, D.; Hong, P.; Jiali, F.; Qinqin, T.; Yuhui, L.; Youqun, W.; Zhibin, Z.; Xiaohong, C.; Yunhai, L. Removal of Uranium Using MnO2/Orange Peel Biochar Composite Prepared by Activation and in-Situ Deposit in a Single Step. *Biomass Bioenergy* **2020**, *142*, 105772. [CrossRef]
107. Liao, J.; Ding, L.; Zhang, Y.; Zhu, W. Efficient Removal of Uranium from Wastewater Using Pig Manure Biochar: Understanding Adsorption and Binding Mechanisms. *J. Hazard. Mater.* **2022**, *423*, 127190. [CrossRef]
108. Liao, J.; He, X.; Zhang, Y.; Zhu, W.; Zhang, L.; He, Z. Bismuth Impregnated Biochar for Efficient Uranium Removal from Solution: Adsorption Behavior and Interfacial Mechanism. *Sci. Total Environ.* **2022**, *819*, 153145. [CrossRef]
109. Wallace, A.R.; Su, C.; Choi, Y.-K.; Kan, E.; Sun, W. Removal of Fluoride from Water Using a Calcium-Modified Dairy Manure-Derived Biochar. *J. Environ. Eng.* **2020**, *146*, 1–10. [CrossRef]
110. Xu, D.; Fan, X.; Chen, Q.; Qiao, S.; Zhang, J.; Yang, Y.; Wang, H.; Zhang, L.; Hou, J. Removal of Nitrogen and Phosphorus from Water by Sludge-Based Biochar Modified by Montmorillonite Coupled with Nano Zero-Valent Iron. *Water Sci. Technol.* **2022**, *85*, 2114–2128. [CrossRef]
111. Hu, R.; Xiao, J.; Wang, T.; Chen, G.; Chen, L.; Tian, X. Engineering of Phosphate-Functionalized Biochars with Highly Developed Surface Area and Porosity for Efficient and Selective Extraction of Uranium. *Chem. Eng. J.* **2020**, *379*, 122388. [CrossRef]
112. Alkurdi, S.S.A.; Al-juboori, R.A.; Bundschuh, J.; Bowtell, L. Effect of Pyrolysis Conditions on Bone Char Characterization and Its Ability for Arsenic and Fluoride Removal. *Environ. Pollut.* **2020**, *262*, 114221. [CrossRef] [PubMed]

113. Thúy, N.; Chi, L.; Anto, S.; Shan, T.; Kumar, S.S.; Shanmugam, S.; Samuel, M.S.; Mathimani, T.; Brindhadevi, K.; Pugazhendhi, A. A Review on Biochar Production Techniques and Biochar Based Catalyst for Biofuel Production from Algae. *Fuel* **2020**, *287*, 119411. [CrossRef]
114. Gabhane, J.W.; Bhange, V.P.; Patil, P.D.; Bankar, S.T.; Kumar, S. Recent Trends in Biochar Production Methods and Its Application as a Soil Health Conditioner: A Review. *SN Appl. Sci.* **2020**, *2*, 1307. [CrossRef]
115. Wang, J.; Wang, S. Preparation, Modification and Environmental Application of Biochar: A Review. *J. Clean. Prod.* **2019**, *227*, 1002–1022. [CrossRef]
116. Chen, D.; Zheng, Z.; Fu, K.; Zeng, Z.; Wang, J.; Lu, M. Torrefaction of Biomass Stalk and Its Effect on the Yield and Quality of Pyrolysis Products. *Fuel* **2015**, *159*, 27–32. [CrossRef]
117. Heidenreich, S.; Müller, M.; Foscolo, P.U. Chapter 3—Biomass Pretreatment. In *Advanced biomass gasification*; Heidenreich, S., Müller, M., Foscolo, P.U.B.T.-A.B.G., Eds.; Academic Press: Cambridge, MA, USA, 2016; pp. 11–17. ISBN 978-0-12-804296-0. Available online: https://www.sciencedirect.com/science/article/pii/B9780128042960000038 (accessed on 22 October 2022).
118. Hadjittofi, L.; Pashalidis, I. Uranium Sorption from Aqueous Solutions by Activated Biochar Fibres Investigated by FTIR Spectroscopy and Batch Experiments. *J. Radioanal. Nucl. Chem.* **2015**, *304*, 897–904. [CrossRef]
119. Liatsou, I.; Michail, G.; Demetriou, M.; Pashalidis, I. Uranium Binding by Biochar Fibres Derived from Luffa Cylindrica after Controlled Surface Oxidation. *J. Radioanal. Nucl. Chem.* **2017**, *311*, 871–875. [CrossRef]
120. Paschalidou, P.; Pashalidis, I.; Manariotis, I.D.; Karapanagioti, H.K. Hyper Sorption Capacity of Raw and Oxidized Biochars from Various Feedstocks for U(VI). *J. Environ. Chem. Eng.* **2020**, *8*, 103932. [CrossRef]
121. Stasi, C.; Georgiou, E.; Ioannidis, I.; Pashalidis, I. Uranium Removal from Laboratory and Environmental Waters by Oxidised Biochar Prepared from Palm Tree Fibres. *J. Radioanal. Nucl. Chem.* **2022**, *331*, 375–381. [CrossRef]
122. Xia, D.; Liu, Y.; Cheng, X.; Gu, P.; Chen, Q.; Zhang, Z. Applied Surface Science Temperature-Tuned Fish-Scale Biochar with Two-Dimensional Homogeneous Porous Structure: A Promising Uranium Extractant. *Appl. Surf. Sci.* **2022**, *591*, 153136. [CrossRef]
123. Saikia, R.; Goswami, R.; Bordoloi, N.; Senapati, K.K.; Pant, K.K.; Kumar, M.; Kataki, R. Removal of Arsenic and Fluoride from Aqueous Solution by Biomass Based Activated Biochar: Optimization through Response Surface Methodology. *J. Environ. Chem. Eng.* **2017**, *5*, 5528–5539. [CrossRef]
124. Han, L.; Zhang, E.; Yang, Y.; Sun, K.; Fang, L. Highly Efficient U(VI) Removal by Chemically Modified Hydrochar and Pyrochar Derived from Animal Manure. *J. Clean. Prod.* **2020**, *264*, 121542. [CrossRef]
125. Li, M.; Liu, H.; Chen, T.; Dong, C.; Sun, Y. Synthesis of Magnetic Biochar Composites for Enhanced Uranium(VI) Adsorption. *Sci. Total Environ.* **2019**, *651*, 1020–1028. [CrossRef] [PubMed]
126. Liao, J.; Xiong, T.; Ding, L.; Zhang, Y.; Zhu, W. Effective Separation of Uranium(VI) from Wastewater Using a Magnetic Carbon as a Recyclable Adsorbent. *Sep. Purif. Technol.* **2022**, *282*, 120140. [CrossRef]
127. Ding, L.; Tan, W.; Xie, S.; Mumford, K.; Lv, J.; Wang, H.; Fang, Q.; Zhang, X.; Wu, X.; Li, M. Uranium Adsorption and Subsequent Re-Oxidation under Aerobic Conditions by *Leifsonia* sp.—Coated Biochar as Green Trapping Agent. *Environ. Pollut.* **2018**, *242*, 778–787. [CrossRef] [PubMed]
128. Wei, Y.; Wang, L.; Wang, J. Cerium Alginate Cross-Linking with Biochar Beads for Fast Fluoride Removal over a Wide PH Range. *Colloids Surf. A Physicochem. Eng. Asp.* **2022**, *636*, 128161. [CrossRef]
129. An, Q.; Li, X.Q.; Nan, H.Y.; Yu, Y.; Jiang, J.N. The Potential Adsorption Mechanism of the Biochars with Different Modification Processes to Cr(VI). *Environ. Sci. Pollut. Res.* **2018**, *25*, 31346–31357. [CrossRef]
130. Chemerys, V.; Baltrėnaitė, E. Modified Biochar: A Review on Modifications of Biochar Towards Its Enhanced Adsorptive Properties. 2016.
131. Ahmed, W.; Núñez-Delgado, A.; Mehmood, S.; Ali, S.; Qaswar, M.; Shakoor, A.; Chen, D.Y. Highly Efficient Uranium (VI) Capture from Aqueous Solution by Means of a Hydroxyapatite-Biochar Nanocomposite: Adsorption Behavior and Mechanism. *Environ. Res.* **2021**, *201*, 111518. [CrossRef]
132. Wang, S.; Guo, W.; Gao, F.; Wang, Y.; Gao, Y. Lead and Uranium Sorptive Removal from Aqueous Solution Using Magnetic and Nonmagnetic Fast Pyrolysis Rice Husk Biochars. *RSC Adv.* **2018**, *8*, 13205–13217. [CrossRef]
133. Chen, W.; Feng, J.; Liu, S.; Zhang, J.; Cai, Y.; Lv, Z.; Fang, M.; Tan, X. A Green and Economical MgO/Biochar Composite for the Removal of U(VI) from Aqueous Solutions. *Chem. Eng. Res. Des.* **2022**, *180*, 391–401. [CrossRef]
134. Lyu, P.; Wang, G.; Wang, B.; Yin, Q.; Li, Y.; Deng, N. Adsorption and Interaction Mechanism of Uranium (VI) from Aqueous Solutions on Phosphate-Impregnation Biochar Cross-Linked MgAl Layered Double-Hydroxide Composite. *Appl. Clay Sci.* **2021**, *209*, 106146. [CrossRef]
135. Li, N.; Yin, M.; Tsang, D.C.W.; Yang, S.; Liu, J.; Li, X.; Song, G.; Wang, J. Mechanisms of U(VI) Removal by Biochar Derived from Ficus Microcarpa Aerial Root: A Comparison between Raw and Modified Biochar. *Sci. Total Environ.* **2019**, *697*, 134115. [CrossRef]
136. Hu, Q.; Zhu, Y.; Hu, B.; Lu, S.; Sheng, G. Mechanistic Insights into Sequestration of U (VI) toward Magnetic Biochar: Batch, XPS and EXAFS Techniques. *J. Environ. Sci.* **2018**, *70*, 217–225. [CrossRef] [PubMed]
137. Zhou, Y.; Xiao, J.; Hu, R.; Wang, T.; Shao, X.; Chen, G.; Chen, L.; Tian, X. Engineered Phosphorous-Functionalized Biochar with Enhanced Porosity Using Phytic Acid-Assisted Ball Milling for Efficient and Selective Uptake of Aquatic Uranium. *J. Mol. Liq.* **2020**, *303*, 112659. [CrossRef]

138. Liao, J.; Chen, H.; Zhang, Y.; Zhu, W. Pyrolysis of Animal Manure under Nitrogen Atmosphere: An Environment Protection Way to Obtain Animal Manure Biochar for High-Efficient Adsorption of Uranium (VI). *J. Anal. Appl. Pyrolysis* **2022**, *163*, 105493. [CrossRef]
139. Zheng, B.; Liao, J.; Ding, L.; Zhang, Y.; Zhu, W. High Efficiency Adsorption of Uranium in Solution with Magnesium Oxide Embedded Horse Manure-Derived Biochar. *J. Environ. Chem. Eng.* **2021**, *9*, 106897. [CrossRef]
140. Sun, Y.; Zeng, B.; Dai, Y.; Liang, X.; Zhang, L.; Ahmad, R.; Su, X. Modification of Sludge-Based Biochar Using Air Roasting-Oxidation and Its Performance in Adsorption of Uranium(VI) from Aqueous Solutions. *J. Colloid Interface Sci.* **2022**, *614*, 547–555. [CrossRef]
141. Noli, F.; Kapashi, E.; Pashalidis, I.; Margellou, A.; Karfaridis, D. The Effect of Chemical and Thermal Modifications on the Biosorption of Uranium in Aqueous Solutions Using Winery Wastes. *J. Mol. Liq.* **2022**, *351*, 118665. [CrossRef]
142. Pang, H.; Diao, Z.; Wang, X.; Ma, Y.; Yu, S.; Zhu, H.; Chen, Z.; Hu, B.; Chen, J.; Wang, X. Adsorptive and Reductive Removal of U(VI) by Dictyophora Indusiate-Derived Biochar Supported Sulfide NZVI from Wastewater. *Chem. Eng. J.* **2019**, *366*, 368–377. [CrossRef]
143. Wang, B.; Zheng, J.; Li, Y.; Zaidi, A.; Hu, Y.; Hu, B. Fabrication of δ-MnO2-Modified Algal Biochar for Efficient Removal of U(VI) from Aqueous Solutions. *J. Environ. Chem. Eng.* **2021**, *9*, 105625. [CrossRef]
144. Wang, B.; Li, Y.; Zheng, J.; Hu, Y.; Wang, X.; Hu, B. Efficient Removal of U(VI) from Aqueous Solutions Using the Magnetic Biochar Derived from the Biomass of a Bloom-Forming Cyanobacterium (*Microcystis aeruginosa*). *Chemosphere* **2020**, *254*, 126898. [CrossRef] [PubMed]
145. Liatsou, I.; Pashalidis, I.; Nicolaides, A. Triggering Selective Uranium Separation from Aqueous Solutions by Using Salophen-Modified Biochar Fibers. *J. Radioanal. Nucl. Chem.* **2018**, *318*, 2199–2203. [CrossRef]
146. Ye, T.; Huang, B.; Wang, Y.; Zhou, L.; Liu, Z. Rapid Removal of Uranium(VI) Using Functionalized Luffa Rattan Biochar from Aqueous Solution. *Colloids Surf. A Physicochem. Eng. Asp.* **2020**, *606*, 125480. [CrossRef]
147. Akl, Z.F.; Zaki, E.G.; ElSaeed, S.M. Green Hydrogel-Biochar Composite for Enhanced Adsorption of Uranium. *ACS Omega* **2021**, *6*, 34193–34205. [CrossRef] [PubMed]
148. Liu, J.; Ge, Y.; Wang, G.; Liu, Y.; Xu, X. Highly Efficient Removal of U(VI) in Aqueous Solutions by Tea Waste-Derived Biochar-Supported Iron-Manganese Oxide Composite. *J. Radioanal. Nucl. Chem.* **2021**, *330*, 871–882. [CrossRef]
149. Yadav, K.; Jagadevan, S. Effect of Pyrolysis of Rice Husk–Derived Biochar on the Fuel Characteristics and Adsorption of Fluoride from Aqueous Solution. *Bioenergy Res.* **2021**, *14*, 964–977. [CrossRef]
150. Shen, Z.; Jin, J.; Fu, J.; Yang, M.; Li, F. Anchoring Al- and/or Mg-Oxides to Magnetic Biochars for Co-Uptake of Arsenate and Fluoride from Water. *J. Environ. Manage.* **2021**, *293*, 112898. [CrossRef]
151. Yadav, T.K.; Abhishek; Prasad, B.; Singh, D.; Prasad, K.S. Calcium Pretreated Pinus Roxburghii Wood Biochar for Adsorptive Removal of Fluoride from Aqueous Solution. *Biointerface Res. Appl. Chem.* **2022**, *12*, 4307–4316. [CrossRef]
152. Bombuwala Dewage, N.; Liyanage, A.S.; Pittman, C.U.; Mohan, D.; Mlsna, T. Fast Nitrate and Fluoride Adsorption and Magnetic Separation from Water on A-Fe2O3 and Fe3O4 Dispersed on Douglas Fir Biochar. *Bioresour. Technol.* **2018**, *263*, 258–265. [CrossRef]
153. Herath, A.; Navarathna, C.; Warren, S.; Perez, F.; Pittman, C.U.; Mlsna, T.E. Iron/Titanium Oxide-Biochar (Fe_2TiO_5/BC): A Versatile Adsorbent/Photocatalyst for Aqueous Cr(VI), Pb^{2+}, F^- and Methylene Blue. *J. Colloid Interface Sci.* **2022**, *614*, 603–616. [CrossRef]
154. Rupasinghe, N.K.L.C.; Senanayake, S.M.A.E.; Nanayakkara, K.G.N. Development, Characterization and Mechanisms Study of Protonated Sawdust Biochar-Chitosan Composite Bead Biosorbent for Defluoridation of Contaminated Groundwater. *Bioresour. Technol. Rep.* **2022**, *17*, 100946. [CrossRef]
155. Wan, S.; Lin, J.; Tao, W.; Yang, Y.; Li, Y.; He, F. Enhanced Fluoride Removal from Water by Nanoporous Biochar-Supported Magnesium Oxide. *Ind. Eng. Chem. Res.* **2019**, *58*, 9988–9996. [CrossRef]
156. Meilani, V.; Lee, J.I.; Kang, J.K.; Lee, C.G.; Jeong, S.; Park, S.J. *Application of Aluminum-Modified Food Waste Biochar as Adsorbent of Fluoride in Aqueous Solutions and Optimization of Production Using Response Surface Methodology*; Elsevier Inc.: Amsterdam, The Netherlands, 2021; Volume 312, ISBN 0003212254. [CrossRef]
157. Roy, S.; Sengupta, S.; Manna, S.; Das, P. Chemically Reduced Tea Waste Biochar and Its Application in Treatment of Fluoride Containing Wastewater: Batch and Optimization Using Response Surface Methodology. *Process Saf. Environ. Prot.* **2018**, *116*, 553–563. [CrossRef]
158. Naga Babu, A.; Srinivasa Reddy, D.; Suresh Kumar, G.; Ravindhranath, K.; Krishna Mohan, G.V. Sequential Synergetic Sorption Analysis of Gracilaria Rhodophyta Biochar toward Aluminum and Fluoride: A Statistical Optimization Approach. *Water Environ. Res.* **2020**, *92*, 880–898. [CrossRef]
159. Ashraf, I.; Li, R.; Chen, B.; Al-Ansari, N.; Rizwan Aslam, M.; Altaf, A.R.; Elbeltagi, A. Nanoarchitectonics and Kinetics Insights into Fluoride Removal from Drinking Water Using Magnetic Tea Biochar. *Int. J. Environ. Res. Public Health* **2022**, *19*, 13092. [CrossRef]
160. Kumar, P.; Prajapati, A.K.; Dixit, S.; Yadav, V.L. Adsorption of Fluoride from Aqueous Solution Using Biochar Prepared from Waste Peanut Hull. *Mater. Res. Express* **2019**, *6*, 125553. [CrossRef]
161. Khan, B.A.; Ahmad, M.; Iqbal, S.; Bolan, N.; Zubair, S.; Shafique, M.A.; Shah, A. Effectiveness of the Engineered Pinecone-Derived Biochar for the Removal of Fluoride from Water. *Environ. Res.* **2022**, *212*, 113540. [CrossRef]

162. Papari, F.; Najafabadi, P.R.; Ramavandi, B. Fluoride Ion Removal from Aqueous Solution, Groundwater, and Seawater by Granular and Powdered Conocarpus Erectus Biochar. *Desalin. Water Treat.* **2017**, *65*, 375–386. [CrossRef]
163. Chunhui, L.; Jin, T.; Puli, Z.; Bin, Z.; Duo, B.; Xuebin, L. Simultaneous Removal of Fluoride and Arsenic in Geothermal Water in Tibet Using Modified Yak Dung Biochar as an Adsorbent. *R. Soc. Open Sci.* **2018**, *5*, 181266. [CrossRef]
164. Sajjadi, B.; Chen, W.Y.; Egiebor, N.O. A Comprehensive Review on Physical Activation of Biochar for Energy and Environmental Applications. *Rev. Chem. Eng.* **2019**, *35*, 735–776. [CrossRef]
165. Zhao, F.; Shan, R.; Gu, J.; Zhang, Y.; Yuan, H.; Chen, Y. Magnetically Recyclable Loofah Biochar by KMnO4Modification for Adsorption of Cu(II) from Aqueous Solutions. *ACS Omega* **2022**, *7*, 8844–8853. [CrossRef]
166. Zhai, W.; Sakthivel, T.; Chen, F.; Du, C.; Yu, H.; Dai, Z. Amorphous Materials for Elementary-Gas-Involved Electrocatalysis: An Overview. *Nanoscale* **2021**, *13*, 19783–19811. [CrossRef]
167. Su, M.; Tsang, D.C.W.; Ren, X.; Shi, Q.; Tang, J.; Zhang, H.; Kong, L.; Hou, L.; Song, G.; Chen, D. Removal of U(VI) from Nuclear Mining Effluent by Porous Hydroxyapatite: Evaluation on Characteristics, Mechanisms and Performance. *Environ. Pollut.* **2019**, *254*, 112891. [CrossRef]
168. Wang, X.; Guo, Z.; Hu, Z.; Zhang, J. Recent Advances in Biochar Application for Water and Wastewater Treatment: A Review. *PeerJ* **2020**, *8*, e9164. [CrossRef]
169. Mühr-Ebert, E.L.; Wagner, F.; Walther, C. Speciation of Uranium: Compilation of a Thermodynamic Database and Its Experimental Evaluation Using Different Analytical Techniques. *Appl. Geochem.* **2019**, *100*, 213–222. [CrossRef]
170. Kumar, A.; Tripathi, R.M.; Rout, S.; Mishra, M.K.; Ravi, P.M.; Ghosh, A.K. Characterization of Groundwater Composition in Punjab State with Special Emphasis on Uranium Content, Speciation and Mobility. *Radiochim. Acta* **2014**, *102*, 239–254. [CrossRef]
171. Tan, Z.; Yuan, S.; Hong, M.; Zhang, L.; Huang, Q. Mechanism of Negative Surface Charge Formation on Biochar and Its Effect on the Fixation of Soil Cd. *J. Hazard. Mater.* **2020**, *384*, 121370. [CrossRef]
172. Zhang, Z.B.; Cao, X.H.; Liang, P.; Liu, Y.H. Adsorption of Uranium from Aqueous Solution Using Biochar Produced by Hydrothermal Carbonization. *J. Radioanal. Nucl. Chem.* **2013**, *295*, 1201–1208. [CrossRef]
173. Li, X.; Pan, H.; Yu, M.; Wakeel, M.; Luo, J.; Alharbi, N.S.; Liao, Q.; Liu, J. Macroscopic and Molecular Investigations of Immobilization Mechanism of Uranium on Biochar: EXAFS Spectroscopy and Static Batch. *J. Mol. Liq.* **2018**, *269*, 64–71. [CrossRef]
174. Albayari, M.; Nazal, M.K.; Khalili, F.I.; Nordin, N.; Adnan, R. Biochar Derived from Salvadora Persica Branches Biomass as Low-Cost Adsorbent for Removal of Uranium(VI) and Thorium(IV) from Water. *J. Radioanal. Nucl. Chem.* **2021**, *328*, 669–678. [CrossRef]
175. Mishra, V.; Sureshkumar, M.K.; Gupta, N.; Kaushik, C.P. Study on Sorption Characteristics of Uranium onto Biochar Derived from Eucalyptus Wood. *Water. Air. Soil Pollut.* **2017**, *228*, 309. [CrossRef]
176. Xu, Z.; Xing, Y.; Ren, A.; Ma, D.; Li, Y.; Hu, S. Study on Adsorption Properties of Water Hyacinth-Derived Biochar for Uranium (VI). *J. Radioanal. Nucl. Chem.* **2020**, *324*, 1317–1327. [CrossRef]
177. Kumar, S.; Loganathan, V.A.; Gupta, R.B.; Barnett, M.O. An Assessment of U(VI) Removal from Groundwater Using Biochar Produced from Hydrothermal Carbonization. *J. Environ. Manage.* **2011**, *92*, 2504–2512. [CrossRef]
178. Yadav, K.; Jagadevan, S. Influence of Torrefaction and Pyrolysis on Engineered Biochar and Its Applicability in Defluoridation: Insight into Adsorption Mechanism, Batch Adsorber Design and Artificial Neural Network Modelling. *J. Anal. Appl. Pyrolysis.* **2021**, *154*, 105015. [CrossRef]
179. Mohan, D.; Sharma, R.; Singh, V.K.; Steele, P.; Pittman, C.U. Fluoride Removal from Water Using Bio-Char, a Green Waste, Low-Cost Adsorbent: Equilibrium Uptake and Sorption Dynamics Modeling. *Ind. Eng. Chem. Res.* **2012**, *51*, 900–914. [CrossRef]
180. Dong, Q.; Yang, D.; Luo, L.; He, Q.; Cai, F.; Cheng, S.; Chen, Y. Engineering Porous Biochar for Capacitive Fluorine Removal. *Sep. Purif. Technol.* **2021**, *257*, 117932. [CrossRef]
181. Shahid, M.K.; Kim, J.Y.; Shin, G.; Choi, Y. Effect of Pyrolysis Conditions on Characteristics and Fluoride Adsorptive Performance of Bone Char Derived from Bone Residue. *J. Water Process Eng.* **2020**, *37*, 101499. [CrossRef]
182. Mahmoud, M.E.; Khalifa, M.A.; El Wakeel, Y.M.; Header, M.S.; El-Sharkawy, R.M.; Kumar, S.; Abdel-Fattah, T.M. A Novel Nanocomposite of Liquidambar Styraciflua Fruit Biochar-Crosslinked-Nanosilica for Uranyl Removal from Water. *Bioresour. Technol.* **2019**, *278*, 124–129. [CrossRef]
183. Ahmed, N.; Rahman, M.; Won, S.; Shim, S. Biochar Properties and Eco-Friendly Applications for Climate Change Mitigation, Waste Management, and Wastewater Treatment: A Review. *Renew. Sustain. Energy Rev.* **2017**, *79*, 255–273. [CrossRef]
184. Kumar, R.; Sharma, P.; Yang, W.; Sillanpää, M.; Shang, J.; Bhattacharya, P.; Vithanage, M.; Maity, J.P. State-of-the-Art of Research Progress on Adsorptive Removal of Fluoride-Contaminated Water Using Biochar-Based Materials: Practical Feasibility through Reusability and Column Transport Studies. *Environ. Res.* **2022**, *214*, 114043. [CrossRef]
185. Wang, J.; Chen, N.; Feng, C.; Li, M. Performance and Mechanism of Fluoride Adsorption from Groundwater by Lanthanum-Modified Pomelo Peel Biochar. *Environ. Sci. Pollut. Res.* **2018**, *25*, 15326–15335. [CrossRef]
186. Zhou, J.; Liu, Y.; Han, Y.; Jing, F.; Chen, J. Bone-Derived Biochar and Magnetic Biochar for Effective Removal of Fluoride in Groundwater: Effects of Synthesis Method and Coexisting Chromium. *Water Environ. Res.* **2019**, *91*, 588–597. [CrossRef]
187. Mandoreba, C.; Gwenzi, W.; Chaukura, N. Defluoridation of Drinking Water Using a Ceramic Filter Decorated with Iron Oxide-Biochar Composites. *Int. J. Appl. Ceram. Technol.* **2021**, *18*, 1321–1329. [CrossRef]

energies

MDPI

Article

Optimized Production of Second-Generation Bioethanol from a Spent C4 Grass: Vetiver (*Chrysopogon zizanioides*)

Sameer Neve [1], Dibyendu Sarkar [1,*], Zhiming Zhang [1] and Rupali Datta [2]

[1] Department of Civil, Environmental, and Ocean Engineering, Stevens Institute of Technology, Hoboken, NJ 07030, USA
[2] Department of Biological Sciences, Michigan Technological University, Houghton, MI 49931, USA
* Correspondence: dsarkar@stevens.edu

Abstract: Vetiver grass (*Chrysopogon zizanioides*) is well-known for its contaminant phytoextraction potential and its capacity to reduce soil erosion, owing to its massive, dense root system. However, the shoots are not major contributors to either of these processes, and are either not utilized at all or they become part of the waste stream. It is well-recognized that lignocellulosic biomass can serve as a source of raw material to produce second-generation bioethanol. This study investigated the simultaneous saccharification and fermentation (SSF) of acid–alkali pretreated vetiver (VG) shoots by *Saccharomyces cerevisiae*. Vetiver shoots were obtained from three sources: (1) shoots from VG grown in clean potting soil, (2) shoots from VG used for antibiotics phytoextraction from a constructed wetland setup, and (3) shoots from VG used for lead phytoextraction during soil remediation. Bioethanol yield from the shoots from clean soil was the highest (19.58 g/L), followed by the one used for lead phytoextraction (19.50 g/L) and the one used for antibiotics phytoextraction (19.17 g/L). Bioethanol yield and quality obtained from these three VG shoots was superior or similar to other C4 grasses used for bioethanol generation. This study successfully demonstrated that spent vetiver biomass after phytoextraction applications can be repurposed to generate high-quality bioethanol.

Keywords: vetiver shoots; lignocellulosic biomass; waste reuse; dilute acid pretreatment; bioethanol

Citation: Neve, S.; Sarkar, D.; Zhang, Z.; Datta, R. Optimized Production of Second-Generation Bioethanol from a Spent C4 Grass: Vetiver (*Chrysopogon zizanioides*). *Energies* **2022**, *15*, 9597. https://doi.org/10.3390/en15249597

Academic Editor: Giuliano Dragone

Received: 19 November 2022
Accepted: 14 December 2022
Published: 17 December 2022

Publisher's Note: MDPI stays neutral with regard to jurisdictional claims in published maps and institutional affiliations.

Copyright: © 2022 by the authors. Licensee MDPI, Basel, Switzerland. This article is an open access article distributed under the terms and conditions of the Creative Commons Attribution (CC BY) license (https://creativecommons.org/licenses/by/4.0/).

1. Introduction

With tremendous energy demand and limited fossil fuel resources, the world is facing pressure to address future energy shortages. Bioenergy production could be a practical solution, which has been studied extensively for the past few decades. "First-generation" bioethanol is produced by fermenting raw materials derived from sugar, whereas "second-generation" bioethanol is produced primarily by fermenting lignocellulosic biomass. "Third-generation" bioethanol is primarily generated from marine organisms such as algae, both microalgae and macroalgae [1]. The properties of microalgae in terms of high carbohydrate and lipid contents, fast growth rate, high contribution to CO_2 mitigation, low land use, and high flexibility in cultivation media make it a well-recognized source for the "third-generation" bioethanol production [2–4]. Irrespective of feedstock sources, fermentation only yields an alcohol-lean broth, rendering it useless for use as fuel or industrial processes. Therefore, bioethanol needs to be refined. Using fractional distillation, it is possible to concentrate bioethanol to a concentration of 95.6 vol% (89.5 mol%), which corresponds to an azeotropic composition with a boiling point of 78.2 °C [5]. In several regions in the U.S., bioethanol has largely replaced methyl tertiary butyl ether as a gasoline additive and oxygenates [6]. Currently, corn starch is used to produce more than 95% of the vehicle-usage bioethanol in the U.S., while the land required for producing these energy feedstocks is considerably large [7]. Land requirement could be significantly minimized if lignocellulosic materials were used for bioenergy production.

Vetiver grass (VG, *Chrysopogon zizanioides*) is a tropical plant that can grow in various environmental conditions, possessing dense root systems which spread into the soil.

Without rhizomes or stolons, VG's root can bind soil beneath the plant to a depth of up to 3 m [8]. The shoots sprout from the bottom of the clump and are long, narrow, and rough. Vetiver also has a high efficiency in absorbing dissolved nutrients [9], so it can proliferate under low nutrient conditions and produce high biomass [10]. In Thailand, 10 types of VG consisting of cellulose (31.85–38.51%), hemicellulose (37.87–42.61%), and lignin (3.67–5.06%) were reported [11].

VG is widely used for environmental purposes. It is either used for slope stabilization or contaminant phytoextraction [12–14]. The massive and dense root system of VG is responsible for holding the soil particles together and for scavenging contaminants from soil and water [15,16]. However, because of limited translocation, the majority of the contaminants are retained in VG roots during the phytoextraction process. Hence, concentrations of contaminants in VG shoots are typically very low. The high cellulose content of VG shoot, however, makes it a viable raw material for the production of bioethanol. Briefly, cellulose is the main content of lignocellulose, which consists of a linear polymer [17] and a cellulose chain that can be converted into glucose by either chemical or enzymatic digestion. The glucose from cellulose hydrolysis is used for bioethanol fermentation by microbes. Similar to microalgae, VG has a fast growth rate and produces a large quantity of biomass, which provides a sufficient amount of feedstock for bioethanol generation. VG can also be grown in a variety of media, such as in soil, surface water, (either clean or polluted water bodies, or hydroponically, which is another distinct advantage over other feedstock [18].

Overall, bioethanol generation from VG, particularly the spent VG after phytoextraction applications, would likely minimize the use of agricultural land for generating traditional bioethanol feedstock, reduce the cost of producing conventional feedstock, and present a much preferable alternative to landfilling the spent biomass. However, the quality of bioethanol generated from VG and spent VG is unclear. Therefore, the main objective of this study was to produce bioethanol from VG from various sources (i.e., VG grown in clean soil, VG used for phytoextraction of antibiotics, VG used for phytoextraction of lead) and compare the yield and quality of the bioethanol obtained with those of other C4 grasses.

2. Materials and Methods

2.1. Biomass Sources and Preparation

Shoots of VG in this study were obtained from three different sources: shoots from fresh VG that was cultivated in potting soil in the greenhouse [19], shoots from VG that were used for the uptake of antibiotics in our previous study with a ciprofloxacin (CIP) concentration of 80 mg/kg and a tetracycline (TTC) concentration of 98 mg/kg [20], and shoots from VG that was used for the uptake of lead during phytoextraction process in our previous study, which had 11.5 mg/kg lead in their shoots [21]. All three types of VG shoots were washed, sun-dried, and chopped into 1–2 cm pieces before oven-drying (65 °C for 48 h) and milling to small particles (~0.2 mm) in a planetary ball mill following the process in Nagara et al. [22]. The extractives, cellulose, hemicellulose, and lignin content in the VG leaf samples were determined according to the methods described by Yang et al. [23].

2.2. Bioethanol Production

2.2.1. Dilute Acid-Alkali Pretreatment

The processes involved in bioethanol production used in this study are shown in Figure 1. Cellulose (40–60% of the total dry weight), hemicellulose (20–40%), and lignin (10–25%) make up the majority of lignocellulose, the primary component of plant cell walls [5]. Pretreatment comprises of delignification of the feedstock to increase cellulose accessibility at the hydrolysis stage [24]. Dilute acid pretreatment was adopted with minor modifications owing to similarities in the biomass leading to high bioethanol yield [25,26]. About 70 g of milled VG shoots were added to 1 L of 1% (v/v) sulfuric acid. The mixture was autoclaved at 130 °C and 24.5 psi (relative to atmosphere) for 45 min. After acid

pretreatment, the pH of the vetiver slurry was adjusted to 5.0 using 1 M NaOH. Then, the VG shoots were filtered, washed, and dried at 60 °C for 24 h.

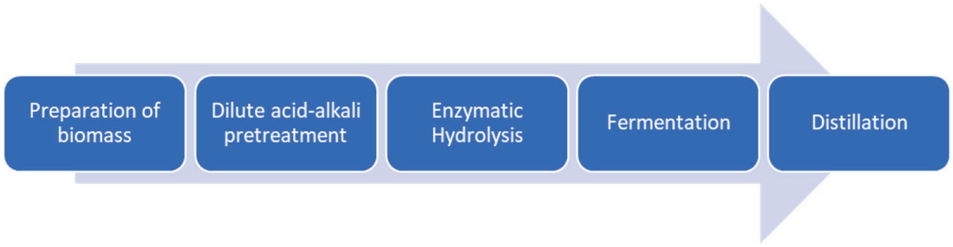


Figure 1. Bioethanol generation process from VG shoots.

2.2.2. Enzymatic Hydrolysis

Cellulase (60 U/g), β-glucosidase (120 U/g), 400 µL of 2% sodium azide (for antimicrobial activity), and 20 mL of 0.1 M sodium citrate buffer (pH 4.8) were added per gram of milled grass as per the optimized conditions discussed by Geiger et al. [25]. The samples were incubated at 30 °C and shaken at 150 rpm for 132 h. After enzymatic treatment, the reaction mixture was heated at 80 °C for 10 min to stop the enzymatic activity.

2.2.3. Bioethanol Fermentation

Yeast culture: *Saccharomyces cerevisiae* was pre-cultured in yeast extract peptone dextrose (YPD) agar plate (10 g/L yeast extract, 20 g/L peptone, 20 g/L dextrose) at 30 °C for 24 h on a rotary shaker at 150 rpm. Yeast cells were centrifuged at 3220× *g* for 10 min and washed with deionized water. For the fermentation of bioethanol, an inoculum containing 10% yeast cells (10^9 cells/mL) was utilized.

Fermentation media: 150 mL of 0.1 M sodium citrate buffer (pH 4.8) was added to acid-pretreated VG samples (10 g) in 250 mL Erlenmeyer flasks, followed by 5 g/L yeast extract, 5 g/L urea, 0.5 g/L $MgSO_4 \cdot 7H_2O$, and 1 g/L KH_2PO_4. The media were autoclaved at 120 °C for 15 min.

2.2.4. Simultaneous Saccharification and Fermentation (SSF)

The short-term commercial production of lignocellulosic bioethanol is greatly improved by fermenting C5 and C6 sugars through simultaneous saccharification and fermentation (SSF). In this study, SSF was performed in 250 mL Erlenmeyer flasks containing 150 mL fermentation medium. Cellulase (8 U/g) and β-glucosidase (120 U/g) were added for saccharification. *S. cerevisiae* was then inoculated at a cell concentration of 22% (*w*/*v*). The mixture was then incubated at 33 °C in an orbital shaker at 150 rpm. Samples were taken after 0, 12, 24, 48, 72, and 104 h, and the amounts of monosaccharides remaining, and bioethanol produced were analyzed by high-performance liquid chromatography (HPLC). All determinations were performed in three biological replications. A distillation procedure was employed to further separate and purify the bioethanol from water during a fermentation conversion based on their distinct volatilities (boiling points of 78.3 °C and 100 °C for bioethanol and water, respectively). Fractional distillation of the fermentation broth was carried out following the process described by Muhaji and Sutjahjo [27]. A Still Spirit Turbo-500 boiler and distiller setup were used to obtain refined bioethanol. Five liters of fermentation broth was continuously boiled at 80 °C, and the condensate bioethanol was collected through the condenser output. This process was continued until there was no condensate from the boiler suggesting that the fermentation broth was converted into an azeotropic mixture, where the alcohol in the vapor phase was not as concentrated as the one in the liquid phase to allow further fractional distillation [28].

Thus, bioethanol can be recovered at a 95% concentration using a condensation process. Bioethanol yield is calculated as the amount of bioethanol produced per unit of substrate utilized as described in the following formula by Zabed et al. [29]:

$$Y_{EtOH} = CV/m$$

where Y_{EtOH} is bioethanol yield (mg/g), C is bioethanol concentration (mg/L), V is the initial volume of liquid medium (L), and m is the mass of the substrate (g).

2.3. Determination of Sugars and Bioethanol

Concentrations of D-glucose, D-galactose, D-xylose, L-arabinose, and bioethanol were determined by the following separation by HPLC using a BioRad (Hercules, CA, USA) Aminex HPX-87H column (300 × 7.8 mm) at 65 °C with 5 mM H_2SO_4 as the mobile phase, at a flow rate of 0.6 mL/min and an injection volume of 10 µL (Figure S1 in Supplementary Information). Samples were appropriately diluted in deionized water prior to injection. The quality of bioethanol generated by VG from different sources was analyzed using various ASTM methods.

2.4. Quality Analysis of Bioethanol

Ethanol was extracted from the fermentation broth and then purified to assess its suitability for use as a transportation fuel. The distillate was refined via four rounds of filtration, and then ASTM procedures were used to evaluate its physicochemical qualities following the protocols by Bint-E-Naser et al. [30], Mass et al. [31], Yüksel and Yüksel [32] and Sutjahjo [27].

2.5. Statistical Analysis

All sample analysis was performed in triplicates and the data were statistically analyzed using the JMP statistical software package (JMP 10, SAS Institute Inc.). The Tukey–Kramer HSD test was carried out to test whether group mean pairs were significantly different at $\alpha = 0.05$.

3. Results and Discussion

3.1. Characterization of Vetiver Grass

Figure 2 shows the percent composition of the extractives, cellulose, hemicellulose, and lignin in VG that were obtained from three different sources. Holocellulose, including cellulose and hemicellulose, was present in much larger amounts (~70%) than extractives (~10%) and lignin (~15%). In terms of those four compositions, there was no significant difference ($p < 0.05$) among the VG from different sources, indicating that the lignocellulosic composition of VG may not be significantly affected by the accumulation of antibiotics or lead during phytoextraction processes.

Restiawaty and Dewi reported that VG shoots had high contents of hemicellulose (34.55% *w*/*w*), cellulose (31.39% *w*/*w*), and lignin (17.58% *w*/*w*) [26], which is similar to the current study. By comparing VG composition reported previously (Table 1), we found that the contents of cellulose, hemicellulose, and lignin in the VG in this study were similar to the previous studies. The overall composition was around the mean of the ranges for individual components—cellulose (30–38.51%), hemicellulose (31.5–42.61%), and lignin (3.67–17.58%) (Table 1). When VG in this study was compared to other C4 grasses, it showed higher percentages of cellulose, hemicellulose, and lignin than those in sorghum. The cellulose content of VG was similar to switchgrass and miscanthus, and lower than wheat straw. Both hemicellulose and lignin contents in VG were higher than those in sorghum, miscanthus, and wheat straw (Table 1), suggesting that VG (regardless of the source) can be employed for bioenergy production instead of being landfilled to form a circular economy model.

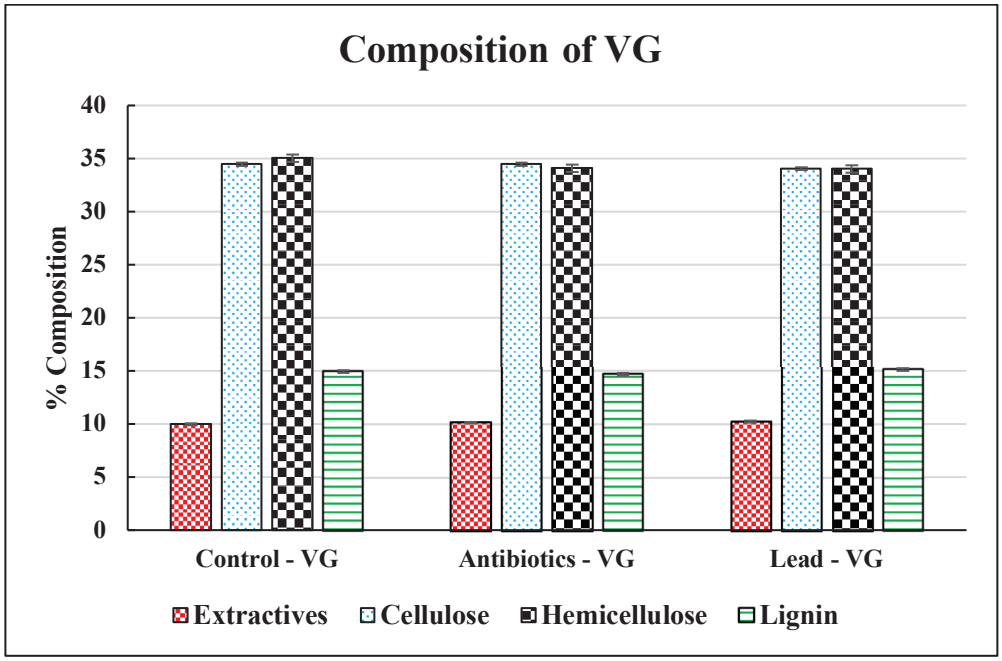


Figure 2. Lignocellulosic composition of VG from different sources.

Table 1. Comparison of the main composition of VG and other C4 grasses from previous reports.

C4 Grasses	Cellulose (%)	Hemicellulose (%)	Lignin (%)	References
Vetiver	34.48	35.07	14.34	This study
Vetiver	34.49	34.12	14.69	[20]
Vetiver	34.06	34.05	15.12	[21]
Vetiver	31.39	34.55	17.58	[26]
Vetiver	32.6	31.5	17.3	[10]
Vetiver	31.85−38.51	37.87–42.61	3.67–5.06	[11]
Vetiver	30–35	40	10	[33]
Wheat straw	49	34	6.5	[34]
Sorghum	26.3	20	7	[35]
Switchgrass	29.5–37.8	21.5–27.4	13.9–21.1	[36]
Miscanthus	32.71	34.86	8.9	[37]

3.2. Sugar Release from Vetiver Grass

Hemicellulose produces several pentoses and hexoses, and cellulose hydrolyzes to provide glucose if properly catalyzed [38]. Hemicellulase and cellulase are the two enzymes that could break down the bonds in hemicellulose and cellulose, respectively. Since high concentrations of hemicellulose (~35%, *w*/*w*) and cellulose (~35%, *w*/*w*) were present in VG from all three sources (Figure 2), sugars were produced as expected. The water-soluble fractions of the extractable monosaccharides (i.e., galactose, glucose, arabinose, and xylose) are shown in Figure 3. For all VG types, xylose was the dominating monosaccharide (44.21–47.84%), followed by arabinose (15.41–16.34%), glucose (11.08–13.56%), and galactose (6.51–7.88%). The high sugar production was probably due to the two-stage acid–alkali pretreatment, which produced higher sugar contents than the single-stage acid or alkali pretreatment [39]. The fine particle size (~0.2 mm) of the milled VG biomass utilized in this study enhanced the surface area of biomass and aided in the breakdown of hemicelluloses. The finding from sugar production indicated that hemicelluloses in VG

were dominated by arabinoxylan, a commonly found sugar in the cell walls of plants [40]. Glucose showed up in significant amounts (>10%), probably as glucan, while galactose may represent end-group residues in the samples' side chains [41].

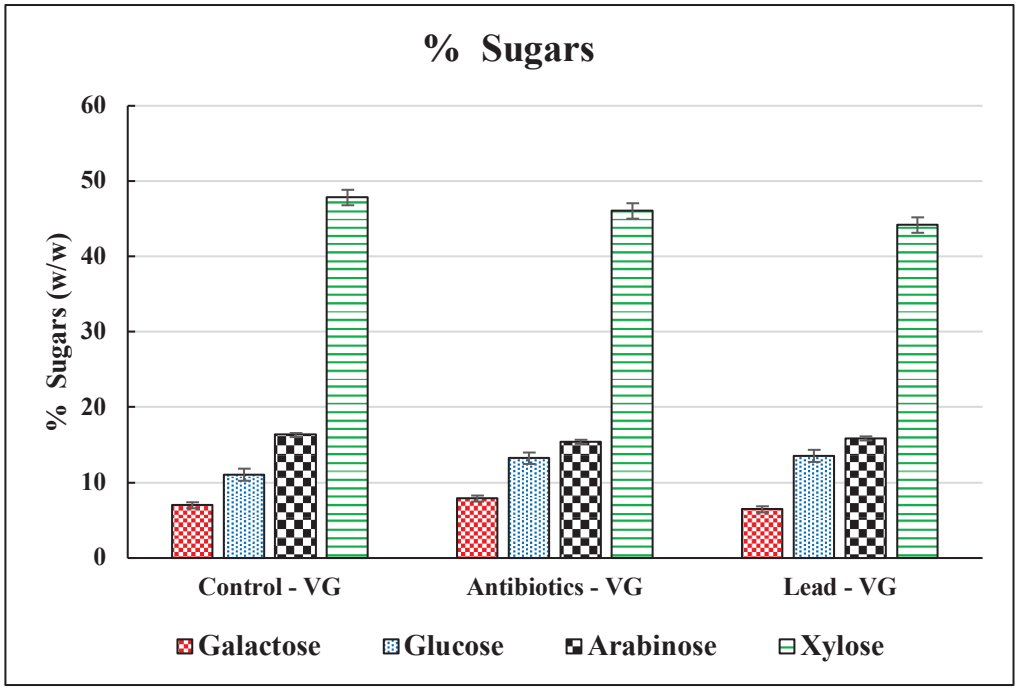


Figure 3. Reducing sugars in different sources of VG.

3.3. Bioethanol Production from Vetiver Grass

As seen in Figure 4, the time profile of the SSF exhibits a growth pattern until 72 h of fermentation, and there is a drop in the concentration of bioethanol past that up to the end of the experiment at 104 h. All three sets of VG had similar concentrations, most of the time points barring the 48 h mark. The increase in bioethanol concentration can also be attributed to the potential drop in the sugar concentrations. As suggested by Das et al. [42], there is an inverse relationship between the bioethanol and sugar content of the lignocellulosic biomass. A substantial decrease in the bioethanol concentration after 72 h was observed owing to the accumulation of reducing sugars in the fermentation media.

The findings of this study show that fresh VG shoots produced the highest bioethanol concentration (279.76 mg/g), followed by the spent VG used for lead phytoextraction (278.57 mg/g) and antibiotics phytoextraction (273.90 mg/g). This corresponded well with the holocellulose contents with the highest in fresh VG shoots (69.55%, Figure 2). Although the bioethanol production rates for the VG used for lead and antibiotic phytoextraction were slightly lower, they were not significantly different from those for fresh VG, indicating that the presence of lead or antibiotics in the biomass would not significantly affect the bioethanol production process. In this study, the average bioethanol yields from VG were higher than the bioethanol yield from dwarf Napier grass (121 mg/g) but lower than that from Kans grass (460 mg/g) (Table 2). Although *S. cerevisiae* was the common microbial species in all these cases, the higher yield in Kans grass could be associated with the independent process of saccharification and acid pretreatment. It is also observed that *S. cerevisiae* is not the highest-yielding fermentation microorganism, and better yields are observed when used in conjunction, as seen in the results of Eliana et al. [43] and Xiang et al. [44]. Genetically modified versions of *S. cerevisiae* have also proven effective in similar operating conditions [44,45].

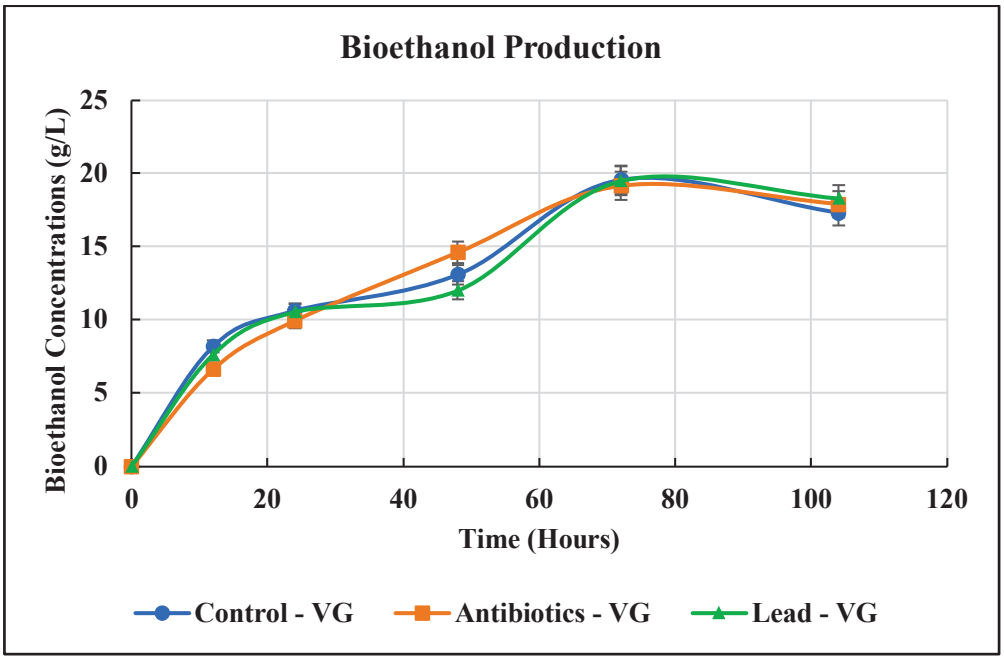


Figure 4. Bioethanol production from different sources of VG.

Table 2. Comparison of bioethanol yield of VG and other C4 grasses previously reported.

C4 Grasses	Microorganisms	Mechanisms	Bioethanol Yields	References
Vetiver (fresh)	*S. cerevisiae*	SSF	279.76 mg/g or 19.58 g/L	This study
Vetiver (antibiotics contamination)	*S. cerevisiae*	SSF	273.90 mg/g or 19.17 g/L	This study
Vetiver (lead contamination)	*S. cerevisiae*	SSF	278.57 mg/g or 19.50 g/L	This study
Dwarf Napier grass (*Schumach*)	*S. cerevisiae* NBRC 2044	SSF	121 mg/g	[46]
Kans grass (*Saccharum spontaneum*)	*S. cerevisiae*	SAF	460 mg/g	[47]
Switch grass (*Panicum virgatum*)	*S. cerevisiae* 424 A (LNH-ST)	SSCF	32.1 g/L	[45]
Elephant grass (*Pennisetun purpureum*)	*Aspergillus niger and S. cerevisiae*	SSF	23.4 g/L	[43]
Switchgrass (*Panicum virgatum*)	*Kluyveromyces marxianus IMB3*	SSF	22.5 g/L	[48]
Mission grass (*Pennisetum polystachion*)	*S. cerevisiae* TISTR 5596	SHF	16 g/L	[49]
Thatch grass (*Hyparrhenia rufa*)	*Zymomonas mobilis*	SSF	8.8 g/L	[42]

Table 2. *Cont.*

C4 Grasses	Microorganisms	Mechanisms	Bioethanol Yields	References
Sea grass (*Cymodocea serrulata*)	*S. cerevisiae*	SSF	0.047 mL/g	[50]
Cocksfoot grass (*Dactylis glomerata*)	*Pichia stipitis CBS 6054*	SSF	158 mL/kg	[51]
Giant miscanthus (*Miscanthus giganteus*)	*Scheffersomyces* (*Pichia*) *stipitis* CBS 6054	SSF	12.1 g/L	[52]
Rice grass (*Spartina* spp.)	*Trichoderma reesei* SEMCC 3.217 and *S. cerevisiae* SEMCC 2.157	SSF	28.1 g/L	[44]

SSF = Simultaneous Saccharification and Fermentation; SSCF = Simultaneous Saccharification and Co-Fermentation; SAF = Saccharification; SHF = Separate Hydrolysis and Fermentation.

The yield of bioethanol from VG was typically higher than that from microalgae, a well-recognized biomass source for "third-generation" bioethanol production. Bibi et al. [53] reported bioethanol production of 14.9 g/L using freshwater green microalgae *Closteriopsis acicularis*. Bioethanol production was reported to be 11.7 g/L for a carbohydrate-rich microalgae *Chlorella vulgaris* FSP-E [54]; a lower yield of bioethanol (3.83 g/L) was reported by Harun et al. [55].

The values of lignin content of the different grasses directly correlate with the bioethanol yield. The various pretreatment methods are responsible for breaking through the lignin, accessing the holocellulosic material, and converting it to sugars and bioethanol. As inferred from Figure 4 earlier, if fewer sugars are accumulated at the end of the process, it would favor bioethanol production. Easier digestion of VG is made possible by the increase in the surface area resulting from milling the dried shoots. In addition, a bigger mesh size would result in less sugar being produced from the breakdown of carbohydrates.

3.4. Quality Analysis of Bioethanol

Results indicated that there was no significant difference among those three sources of VG in terms of bioethanol content, density, freezing points, and all other tested parameters. Because the resulting bioethanol had no lead or antibiotics, the spent VG shoot biomass after phytoextraction applications can also be used for high-quality bioethanol generation. The values of all parameters, except the freezing point, of the bioethanol from VG were comparable to the standard bioethanol [32,56]. The ethanol contents of VG bioethanol ranged from 98.83 to 98.89%, a slightly higher value originating from the fresh VG. Although these values were slightly lower than the standard values, they were higher than those reported in the literature. Specifically, with a 4% HNO_3 pretreatment and distillation, the bioethanol contents generated from *Miscanthus sacchariflorus* (a C4 perennial grass) ranged from 89.9 to 92.5% [57]. Azeke et al. [58] reported an even lower range from 44 to 72.6% using elephant grass (*Pennisetun purpureum*) as the feedstock to produce bioethanol. The higher freezing point (i.e., −94 °C) of VG bioethanol than the standard bioethanol (i.e., −114 °C) could be induced by the impurities in the VG bioethanol. Some commonly identified impurities, such as ethyl acetate and crotonaldehyde [57], present higher freezing points (−84 and −76 °C, respectively), which increases the overall freezing point of the bioethanol. The existence of impurities also corresponds to the slightly lower bioethanol contents from VG than the standard bioethanol (Table 3). The bioethanol content in the purified form also correlates to the concentration in the fermentation media, so a better choice of fermentation media may lead to a higher yield and of higher quality.

Table 3. Comparison of bioethanol quality of VG with standards.

Parameter	ASTM Test Methods	Control—VG	Lead—VG	Antibiotics—VG	Standard
Ethanol Content (%)	ASTM D 5501	98.89	98.85	98.83	99–100
Density at 25°C (g/mL)	ASTM D 4052	0.766	0.784	0.774	0.79
Freezing Point (°C)	ASTM D 2386	−94	−94	−94	−114
Boiling Point (°C)	ASTM D 5399-09	78.3	78.4	78.4	78
Flash Point (°C)	ASTM D 93	12.8	12.7	12.7	13
API gravity (°)	ASTM D 4052	52.3	51.9	53.1	52
Calorific Value (MJ/kg)	ASTM D 2014-96	31.26	30.68	33.09	
Heat of vaporization (kJ/kg K)	ASTM E 2071	278	282	279	289
Reid vapor pressure (kPa)	ASTM D 323-99a	12.67	11.96	13.24	14.25
Viscosity (cSt)	ASTM D 88-94	1.01	1.01	1.04	1.03
Cu strip corrosion at 50 °C	ASTM D 130-04	1a	1a	1a	1a
ASTM distillation IBP (°C)	ASTM D 86-04b	80.5	80.6	81	81
Sulfur content (wt%)	ASTM D 3177-89	0.03	0.03	0.03	0.03
Water content (%)	ASTM D 95-70	1.11	1.15	1.17	0–1
ASTM color	ASTM D 1500-03	None	None	None	None
Research Octane Number	ASTM D 2699	107	108	108	108

The density of bioethanol is much lower than water's, while the American Petroleum Institute gravity (API gravity) values for all three feedstocks were in the range of 51.9–53.1, which is much higher than the value of water, indicating that the fluid can be easily transported through barrels and pipelines [30]. Viscosity is the measure of resistance to flow, and the viscosity of these VG is observed to be twice that of gasoline-based fuels. All three samples of VG gave a slight tarnish (1a) to the copper strip and were colorless overall. The Research Octane number meets the standard value of 108 and suggests that this bioethanol can be blended with traditional fluid and used as E10 fuel.

3.5. Future Perspectives

Due to the rising demand for bioethanol in the world market, it is critical to provide a consistent supply of inexpensive and plentiful feedstocks for generating high-quality bioethanol at competitive prices. By investigating the simultaneous saccharification and fermentation of acid–alkali pretreated vetiver shoots by *Saccharomyces cerevisiae*, this study demonstrated that the spent shoot biomass of VG involved in contaminant phytoextraction processes that are typically unutilized or landfilled can be used to produce bioethanol at similar production rates and quality as fresh, unspent VG biomass, which will significantly reduce the cost of bioethanol production. The combination of environmental remediation and bioenergy production can be further explored towards developing a true circular economy model. Different pretreatment methods and different microbial strains for better yields can be further investigated in the future. Strategies to reduce the overall cost of bioethanol production should be explored so it would be competitive with the conventional fuel market.

4. Conclusions

This study explored the generation of bioethanol by vetiver grass from three sources: VG grown in clean soil, VG used for phytoextraction of antibiotics from a constructed

wetland setup, and VG used for phytoextraction of lead from contaminated soils. For all three sources, the lignocellulosic compositions were similar: cellulose, 30–38.51%; hemicellulose, 31.5–42.61%; lignin, 3.67–17.58%; xylose was the dominating monosaccharide (44.21–47.84%). Bioethanol production (142–151 mg/g) was comparable with or superior to other C4 grasses. Their high quality makes them an excellent candidate for blending with fuels. Thus, VG, both fresh and spent, could be a viable candidate for second-generation biofuel feedstock. Future research may further investigate the feasibility of this novel circular economy model.

Supplementary Materials: The following supporting information can be downloaded at: https://www.mdpi.com/article/10.3390/en15249597/s1, Figure S1. A representative HPLC chromatograph showing the monosaccharide and bioethanol peaks.

Author Contributions: S.N.: Methodology, Data collection and analysis, Data curation, Visualization, Writing—original draft. D.S.: Conceptualization, Supervision, Funding acquisition, Project management, Writing—review & editing. R.D.: Conceptualization, Writing—review & editing. Z.Z.: Writing—review & editing. All authors have read and agreed to the published version of the manuscript.

Funding: This research received no external funding. S.N. is grateful for his Ph.D. assistantship provided by the Stevens Institute of Technology.

Data Availability Statement: Data presented in this study are available on request from the corresponding author.

Acknowledgments: S.N. would like to acknowledge Saumik Panja for providing the vetiver grass used for bioethanol production and assistance with the HPLC instrument.

Conflicts of Interest: The authors declare no conflict of interest.

References

1. Jambo, S.A.; Abdulla, R.; Azhar, S.H.M.; Marbawi, H.; Gansau, J.A.; Ravindra, P. A review on third generation bioethanol feedstock. *Renew. Sustain. Energy Rev.* **2016**, *65*, 756–769. [CrossRef]
2. Li, G.; Hu, R.; Wang, N.; Yang, T.; Xu, F.; Li, J.; Wu, J.; Huang, Z.; Lyu, T. Cultivation of microalgae in adjusted wastewater to enhance biofuel production and reduce environmental impact: Pyrolysis performances and life cycle assessment. *J. Clean. Prod.* **2022**, *355*, 131768. [CrossRef]
3. Huang, Z.; Zhang, J.; Pan, M.; Hao, Y.; Hu, R.; Xiao, W.; Li, G.; Lyu, T. Valorisation of microalgae residues after lipid extraction: Pyrolysis characteristics for biofuel production. *Biochem. Eng. J.* **2022**, *179*, 108330. [CrossRef]
4. Li, G.; Hao, Y.; Yang, T.; Xiao, W.; Pan, M.; Huo, S.; Lyu, T. Enhancing bioenergy production from the raw and defatted microalgal biomass using wastewater as the cultivation medium. *Bioengineering* **2022**, *9*, 637. [CrossRef] [PubMed]
5. Kang, Q.; Appels, L.; Tan, T.; Dewil, R. Bioethanol from lignocellulosic biomass: Current findings determine research priorities. *Sci. World J.* **2014**, *2014*, 298153. [CrossRef]
6. Solomon, B.D. Biofuels and sustainability. *Ann. N. Y. Acad. Sci.* **2010**, *1185*, 119–134. [CrossRef] [PubMed]
7. Ethanol explained—U.S. Energy Information Administration (EIA). Available online: https://www.eia.gov/energyexplained/biofuels/ethanol.php (accessed on 13 November 2022).
8. An Overview on the Application of the Vetiver Grass System in Asia-Pacific and Southern African Regions. Available online: https://www.vetiver.org/AUS_asiaoverview.htm (accessed on 13 November 2022).
9. Zhang, Z.; Sarkar, D.; Sidhu, V.; Warke, M.; Datta, R. Impact of EDDS Dosage on Lead Phytoextraction in Contaminated Urban Residential Soils. *Front. Sustain. Cities* **2022**, *3*, 773467. [CrossRef]
10. Raman, J.K.; Gnansounou, E. LCA of bioethanol and furfural production from vetiver. *Bioresour. Technol.* **2015**, *185*, 202–210. [CrossRef]
11. Wongwatanapaiboon, J.; Kangvansaichol, K.; Burapatana, V.; Inochanon, R.; Winayanuwattikun, P.; Yongvanich, T.; Chulalaksananukul, W. The potential of cellulosic ethanol production from grasses in Thailand. *J. Biomed. Biotechnol.* **2012**, *2012*, 303748. [CrossRef]
12. Panja, S.; Sarkar, D.; Datta, R. Removal of antibiotics and nutrients by Vetiver grass (*Chrysopogon zizanioides*) from secondary wastewater effluent. *Int. J. Phytoremediat.* **2020**, *22*, 764–773. [CrossRef]
13. Pidatala, V.R.; Li, K.; Sarkar, D.; Wusurika, R.K.; Datta, R. Identification of biochemical pathways associated with lead tolerance and detoxification in *Chrysopogon zizanioides* L. Nash (vetiver) by metabolic profiling. *Environ. Sci. Technol.* **2016**, *50*, 2530–2537. [CrossRef] [PubMed]

14. Sengupta, A.; Sarkar, D.; Das, P.; Panja, S.; Parikh, C.; Ramanathan, D.; Bagley, S.; Datta, R. Tetracycline uptake and metabolism by vetiver grass (*Chrysopogon zizanioides* L. Nash). *Environ. Sci. Pollut. Res.* **2016**, *23*, 24880–24889. [CrossRef] [PubMed]
15. Panja, S.; Sarkar, D.; Li, K.; Datta, R. Uptake and transformation of ciprofloxacin by vetiver grass (*Chrysopogon zizanioides*). *Int. Biodeterior. Biodegrad.* **2019**, *142*, 200–210. [CrossRef]
16. Attinti, R.; Barrett, K.R.; Datta, R.; Sarkar, D. Ethylenediaminedisuccinic acid (EDDS) enhances phytoextraction of lead by vetiver grass from contaminated residential soils in a panel study in the field. *Environ. Pollut.* **2017**, *225*, 524–533. [CrossRef] [PubMed]
17. Gnansounou, E.; Alves, C.M.; Raman, J.K. Multiple applications of vetiver grass—A review. *Int. J. Environ. Sci.* **2017**, *2*, 125–141.
18. Li, K.; Liu, Q.; Fang, F.; Luo, R.; Lu, Q.; Zhou, W.; Hou, S.; Cheng, P.; Liu, J.; Addy, M.; et al. Microalgae-based wastewater treatment for nutrients recovery: A review. *Bioresour. Technol.* **2019**, *291*, 121934. [CrossRef]
19. Neve, S.; Sarkar, D.; Datta, R. Effects of Pyrolysis Temperature and Residence Time on Physicochemical Properties of Biochar Derived from Spent Vetiver Roots. presented at the ASA, CSSA, SSSA International Annual Meeting, Nov. 2022. Available online: https://scisoc.confex.com/scisoc/2022am/meetingapp.cgi/Paper/142823 (accessed on 14 November 2022).
20. Panja, S.; Sarkar, D.; Zhang, Z.; Datta, R. Removal of antibiotics and nutrients by vetiver grass (*Chrysopogon zizanioides*) from a plug flow reactor based constructed wetland model. *Toxics* **2021**, *9*, 84. [CrossRef]
21. Zhang, Z.; Sarkar, D.; Sidhu, V.; Datta, R. Removal of Lead in Residential Soils of Jersey City Using Biodegradable Chelating Agent-Enhanced Phytoremediation. presented at the GSA 2020 Connects Online, Oct. 2020. Available online: https://gsa.confex.com/gsa/2020AM/webprogram/Paper356930.html (accessed on 14 November 2022).
22. Nagara, V.N.; Sarkar, D.; Elzinga, E.J.; Datta, R. Removal of heavy metals from stormwater runoff using granulated drinking water treatment residuals. *Environ. Technol. Innov.* **2022**, *28*, 102636. [CrossRef]
23. Yang, H.; Yan, R.; Chen, H.; Zheng, C.; Lee, D.H.; Liang, D.T. In-depth investigation of biomass pyrolysis based on three major components: Hemicellulose, cellulose and lignin. *Energy Fuels* **2006**, *20*, 388–393. [CrossRef]
24. Sun, Y.; Cheng, J. Hydrolysis of lignocellulosic materials for ethanol production: A review. *Bioresour. Technol.* **2002**, *83*, 1–11. [CrossRef]
25. Geiger, E.M.; Sarkar, D.; Datta, R. Evaluation of copper-contaminated marginal land for the cultivation of vetiver grass (*Chrysopogon zizanioides*) as a lignocellulosic feedstock and its impact on downstream bioethanol production. *Appl. Sci.* **2019**, *9*, 2685. [CrossRef]
26. Restiawaty, E.; Dewi, A. Comparison of Pretreatment Methods on Vetiver Leaves for Efficient Processes of Simultaneous Saccharification and Fermentation by Neurospora sp. In *Journal of Physics: Conference Series*; IOP Publishing: Bristol, UK, 2017; Volume 877, No. 1; p. 012048. [CrossRef]
27. Sutjahjo, D.H. The characteristics of bioethanol fuel made of vegetable raw materials. In *IOP Conference Series: Materials Science and Engineering*; IOP Publishing: Bristol, UK, 2018; Volume 296, No. 1; p. 012019. [CrossRef]
28. Kvaalen, E. *Alcohol Distillation: Basic Principles, Equipment, Performance Relationships, and Safety*; Purdue University, Cooperative Extension Service: West Lafayette, IN, USA, 1984.
29. Zabed, H.; Sahu, J.N.; Boyce, A.N.; Faruq, G. Fuel ethanol production from lignocellulosic biomass: An overview on feedstocks and technological approaches. *Renew. Sustain. Energy Rev.* **2016**, *66*, 751–774. [CrossRef]
30. Bint-E-Naser, S.F.; Hossain, L.; Debnath, M.; Barua, P.P.; Khan, M.S. Analyzing Physico-Chemical Properties of Bioethanol and Bioethanol-Blended Fuels. *J. Nat. Sci. Sustain. Technol.* **2017**, *11*, 331–339.
31. Maas, R.H.; Bakker, R.R.; Boersma, A.R.; Bisschops, I.; Pels, J.R.; de Jong, E.; Weusthuis, R.A.; Reith, H. Pilot-scale conversion of lime-treated wheat straw into bioethanol: Quality assessment of bioethanol and valorization of side streams by anaerobic digestion and combustion. *Biotechnol. Biofuels* **2008**, *1*, 14. [CrossRef] [PubMed]
32. Yüksel, F.; Yüksel, B. The use of ethanol–gasoline blend as a fuel in an SI engine. *Renew. Energy* **2004**, *29*, 1181–1191. [CrossRef]
33. Methacanon, P.; Chaikumpollert, O.; Thavorniti, P.; Suchiva, K. Hemicellulosic polymer from Vetiver grass and its physicochemical properties. *Carbohydr. Polym.* **2003**, *54*, 335–342. [CrossRef]
34. Sambusiti, C.; Ficara, E.; Rollini, M.; Manzoni, M.; Malpei, F. Sodium hydroxide pretreatment of ensiled sorghum forage and wheat straw to increase methane production. *Water Sci. Technol.* **2012**, *66*, 2447–2452. [CrossRef]
35. Rooney, W.L.; Blumenthal, J.; Bean, B.; Mullet, J.E. Designing sorghum as a dedicated bioenergy feedstock. *Biofuels Bioprod. Biorefining* **2007**, *1*, 147–157. [CrossRef]
36. Jung, S.J.; Kim, S.H.; Chung, I.M. Comparison of lignin, cellulose, and hemicellulose contents for biofuels utilization among 4 types of lignocellulosic crops. *Biomass Bioenergy* **2015**, *83*, 322–327. [CrossRef]
37. Qin, J.; Yang, Y.; Jiang, J.; Yi, Z.; Xiao, L.; Ai, X.; Chen, Z. Comparison of lignocellulose composition in four major species of Miscanthus. *Afr. J. Biotechnol.* **2012**, *11*, 12529–12537. [CrossRef]
38. Sarkar, N.; Ghosh, S.K.; Bannerjee, S.; Aikat, K. Bioethanol production from agricultural wastes: An overview. *Renew. Energy* **2012**, *37*, 19–27. [CrossRef]
39. Huong, V.T.T.; Atjayutpokin, T.; Chinwatpaiboon, P.; Smith, S.M.; Boonyuen, S.; Luengnaruemitchai, A. Two-stage acid-alkali pretreatment of vetiver grass to enhance the subsequent sugar release by cellulase digestion. *Renew. Energy* **2022**, *195*, 755–765. [CrossRef]
40. McCartney, L.; Marcus, S.E.; Knox, J.P. Monoclonal antibodies to plant cell wall xylans and arabinoxylans. *J. Histochem. Cytochem.* **2005**, *53*, 543–546. [CrossRef] [PubMed]

41. Sun, R.C.; Sun, X.F. Fractional and structural characterization of hemicelluloses isolated by alkali and alkaline peroxide from barley straw. *Carbohydr. Polym.* **2002**, *49*, 415–423. [CrossRef]
42. Das, S.P.; Ghosh, A.; Gupta, A.; Goyal, A.; Das, D. Lignocellulosic fermentation of wild grass employing recombinant hydrolytic enzymes and fermentative microbes with effective bioethanol recovery. *BioMed Res. Int.* **2013**, *2013*, 386063. [CrossRef] [PubMed]
43. Eliana, C.; Jorge, R.; Juan, P.; Luis, R. Effects of the pretreatment method on enzymatic hydrolysis and ethanol fermentability of the cellulosic fraction from elephant grass. *Fuel* **2014**, *118*, 41–47. [CrossRef]
44. Liang, X.; Hua, D.; Zhang, J.; Xu, H.; Li, Y.; Zhang, X.; Zhao, S. Cellulosic ethanol production using rice grass (*Spartina* spp.) with cellulase. *Asian J. Chem.* **2011**, *23*, 1815–1818.
45. Yasuda, M.; Takenouchi, Y.; Nitta, Y.; Ishii, Y.; Ohta, K. Italian ryegrass (*Lolium multiflorum* Lam) as a high-potential bio-ethanol resource. *Bioenergy Res.* **2015**, *8*, 1303–1309. [CrossRef]
46. Yasuda, M.; Ishii, Y.; Ohta, K. Napier grass (*Pennisetum purpureum* Schumach) as raw material for bioethanol production: Pretreatment, saccharification, and fermentation. *Biotechnol. Bioprocess Eng.* **2014**, *19*, 943–950. [CrossRef]
47. Kataria, R.; Ghosh, S. Saccharification of Kans grass using enzyme mixture from *Trichoderma reesei* for bioethanol production. *Bioresour. Technol.* **2011**, *102*, 9970–9975. [CrossRef]
48. Aiyejagbara, M.; Aderemi, B.; Ameh, A.; Ishidi, E.; Ibeneme, E.F.A.; Olakunle, M. Production of Bioethanol from Elephant Grass (*Pennisetum purpureum*) Stem. *Int. J. Innov. Math. Stat. Energy Policies* **2016**, *4*, 1–9.
49. Prasertwasu, S.; Khumsupan, D.; Komolwanich, T.; Chaisuwan, T.; Luengnaruemitchai, A.; Wongkasemjit, S. Efficient process for ethanol production from Thai Mission grass (*Pennisetum polystachion*). *Bioresour. Technol.* **2014**, *163*, 152–159. [CrossRef] [PubMed]
50. Ravikumar, S.; Gokulakrishnan, R.; Kanagavel, M.; Thajuddin, N. Production of biofuel ethanol from pretreated seagrass by using *Saccharomyces cerevisiae*. *Indian J. Sci. Technol.* **2011**, *4*, 1087–1089. [CrossRef]
51. Njoku, S.I.; Iversen, J.A.; Uellendahl, H.; Ahring, B.K. Production of ethanol from hemicellulose fraction of cocksfoot grass using *Pichia stipitis*. *Sustain. Chem. Processes* **2013**, *1*, 1–7. [CrossRef]
52. e Silva, C.F.L.; Schirmer, M.A.; Maeda, R.N.; Barcelos, C.A.; Pereira, N., Jr. Potential of giant reed (*Arundo donax* L.) for second generation ethanol production. *Electron. J. Biotechnol.* **2015**, *18*, 10–15. [CrossRef]
53. Bibi, F.; Yasmin, H.; Jamal, A.; Al-Harbi, M.S.; Ahmad, M.; Zafar, M.; Ahmad, B.; Samra, B.N.; Ahmed, A.F.; Ali, M.I. Deciphering role of technical bioprocess parameters for bioethanol production using microalgae. *Saudi J. Biol. Sci.* **2021**, *28*, 7595–7606. [CrossRef]
54. Ho, S.H.; Huang, S.W.; Chen, C.Y.; Hasunuma, T.; Kondo, A.; Chang, J.S. Bioethanol production using carbohydrate-rich microalgae biomass as feedstock. *Bioresour. Technol.* **2013**, *135*, 191–198. [CrossRef]
55. Harun, R.; Danquah, M.K.; Forde, G.M. Microalgal biomass as a fermentation feedstock for bioethanol production. *J. Chem. Technol. Biotechnol.* **2010**, *85*, 199–203. [CrossRef]
56. Bušić, A.; Marđetko, N.; Kundas, S.; Morzak, G.; Belskaya, H.; Ivančić Šantek, M.; Komes, D.; Šantek, B. Bioethanol production from renewable raw materials and its separation and purification: A review. *Food Technol. Biotechnol.* **2018**, *56*, 289–311. [CrossRef]
57. Skiba, E.A.; Ovchinnikova, E.V.; Budaeva, V.V.; Banzaraktsaeva, S.P.; Kovgan, M.A.; Chumachenko, V.A.; Mironova, G.F.; Kortusov, A.N.; Parmon, V.N.; Sakovich, G.V. Miscanthus bioprocessing using HNO3-pretreatment to improve productivity and quality of bioethanol and downstream ethylene. *Ind. Crops Prod.* **2022**, *177*, 114448. [CrossRef]
58. Azeke, E.M.; Eze, C.L.; Ubong, I.; Kuroshi, L. The Potential of Elephant Grass (*Pennisetum purpureum* Schum), a Nigerian Indigenous Grass. In Proceedings of the Bioethanol Production: A Decarbonization Alternative for the Maritime Industry, Southern African Transport Conference, Pretoria, South Africa, 8–11 July 2019.

environments

MDPI

Review

Environment Friendly Pretreatment Approaches for the Bioconversion of Lignocellulosic Biomass into Biofuels and Value-Added Products

Surbhi Sharma [1,†], Mei-Ling Tsai [2,†], Vishal Sharma [2,3,†], Pei-Pei Sun [2], Parushi Nargotra [2], Bijender Kumar Bajaj [1], Chiu-Wen Chen [3,4,*] and Cheng-Di Dong [3,*]

1 School of Biotechnology, University of Jammu, Jammu 180006, India
2 Department of Seafood Science, National Kaohsiung University of Science and Technology, Kaohsiung City 81157, Taiwan
3 Department of Marine Environmental Engineering, National Kaohsiung University of Science and Technology, Kaohsiung City 81157, Taiwan
4 Institute of Aquatic Science and Technology, National Kaohsiung University of Science and Technology, Kaohsiung City 81157, Taiwan
* Correspondence: cwchen@nkust.edu.tw (C.-W.C.); cddong@nkust.edu.tw (C.-D.D.)
† These authors contributed equally to this work.

Abstract: An upsurge in global population and rapid urbanization has accelerated huge dependence on petroleum-derived fuels and consequent environmental concerns owing to greenhouse gas emissions in the atmosphere. An integrated biorefinery uses lignocellulosic feedstock as raw material for the production of renewable biofuels, and other fine chemicals. The sustainable bio-economy and the biorefinery industry would benefit greatly from the effective use of lignocellulosic biomass obtained from agricultural feedstocks to replace petrochemical products. Lignin, cellulose, hemicellulose, and other extractives, which are essential components of lignocellulosic biomass, must be separated or upgraded into useful forms in order to fully realize the potential of biorefinery. The development of low-cost and green pretreatment technologies with effective biomass deconstruction potential is imperative for an efficient bioprocess. The abundance of microorganisms along with their continuous production of various degradative enzymes makes them suited for the environmentally friendly bioconversion of agro-industrial wastes into viable bioproducts. The present review highlights the concept of biorefinery, lignocellulosic biomass, and its valorization by green pretreatment strategies into biofuels and other biochemicals. The major barriers and challenges in bioconversion technologies, environmental sustainability of the bioproducts, and promising solutions to alleviate those bottlenecks are also summarized.

Keywords: integrated biorefinery; circular bioeconomy; lignocellulosic biomass; pretreatment; valorization; enzymes; biofuels; biochemicals

Citation: Sharma, S.; Tsai, M.-L.; Sharma, V.; Sun, P.-P.; Nargotra, P.; Bajaj, B.K.; Chen, C.-W.; Dong, C.-D. Environment Friendly Pretreatment Approaches for the Bioconversion of Lignocellulosic Biomass into Biofuels and Value-Added Products. *Environments* **2023**, *10*, 6. https://doi.org/10.3390/environments10010006

Academic Editor: Simeone Chianese

Received: 9 November 2022
Revised: 17 December 2022
Accepted: 21 December 2022
Published: 23 December 2022

Copyright: © 2022 by the authors. Licensee MDPI, Basel, Switzerland. This article is an open access article distributed under the terms and conditions of the Creative Commons Attribution (CC BY) license (https://creativecommons.org/licenses/by/4.0/).

1. Introduction

Global population growth and socioeconomic expansion have contributed to an enormous rise in pollution and an expedited depletion of energy resources [1–3]. The primary cause of the current global energy crisis and deterioration of the environment is the overconsumption of conventional fossil fuels, which contribute significantly to greenhouse gas emissions, global warming, acid rain, and other climatic ill-effects [4,5]. Thus, it is imperative to make enduring technological developments to supply the accelerating energy demand without imperiling the planet's finite resources [6]. The paradigm of 'take, make, and dispose of' is currently being replaced by 'reuse and recovery' of resources in order to attain 'healthy climate-healthy individuals' and socioeconomic success [7]. To produce low-carbon, long-lasting, and fossil-free fuels, the development of various

non-conventional/renewable/infinite energy resources is being explored. Lignocellulosic biomass (LCB)-based biofuels are attaining prominence as a feasible substitute for petroleum-based fuels [4,8]. LCB constituted by agricultural residues/food waste/forest products/municipal and sewage wastes represents the most promising, copious, and a low-cost carbon-based substrate, which can be extensively exploited for the production of biofuels and other commercial products in a biorefinery [5,9–11]. The sustainable bioeconomy and the biorefinery industry would benefit greatly from the effective use of lignocellulosic biomass obtained from agricultural feedstocks to replace petrochemical products.

Biorefinery is a strategy which integrates several conversion processes, such as biochemical, thermo-chemical, and microbial growth to generate energy, biofuels, chemicals, and other value-added desired industrial products from LCB [12]. However, the full-scale bioconversion of LCB to bioenergy/biofuels (biodiesel, bioethanol, biobutanol), and bio-based commodities (chemicals, feed, food) poses various significant obstacles in terms of energy input and product yield in the overall process [13]. LCB, a hetero-polysaccharide complex, is composed of a variety of polymers (cellulose, hemicellulose, and lignin), and other polar and non-polar substances [10,14–16]. The structural polysaccharides of LCB are entangled with lignin blocks in a very complicated manner, thereby imparting high rigidity and recalcitrance to the biomass structure [13]. Hence, a key bottleneck in the valorization of LCB for the production of power, fuels, or other chemicals is its structural recalcitrance, which might be successfully reduced by implementing an appropriate pretreatment approach [1,17]. Pretreatment aims to disrupt the crystalline structure of biomass by breaking the hydrogen bonds and cross-linked hydrophobic interactions between cellulose, hemicellulose, and lignin; thus, increasing the accessibility of biomass to enzyme hydrolysis [18,19]. An effective pretreatment may improve the cellulose's accessibility, pore size, and surface area while lowering its degree of polymerization (DP) and crystallinity [20,21]. The primary pretreatment regimes available for the fractionation of LCB can be categorized as physical, chemical, physicochemical, and biological techniques [7]. However, most of these methods possess several limitations such as high cost, being non-'green', generation of inhibitors/toxic substances, and many others. Therefore, in the current times, research is being focused on the development of environmentally friendly and cost-efficient pretreatment methods to achieve successful LCB fuel technology [14,16]. The choice of an appropriate pretreatment technique depends upon biomass type, its structural properties, composition, and degree of polymerization. Pretreatment is the principal capital-intensive step in LCB biorefinery; thus, it significantly affects the overall economy of a bioprocess [22].

Another crucial step in the chain of LCB fuel schemes is enzymatic saccharification of suitably pretreated biomass. The enzyme cocktail of cellulases (endo-β-1,4-glucanase, cellobiohydrolase, and β-glucosidase), and hemicellulases (xylanases, glucuronidase, glucomannanase, galactomannanase, β-xylosidase, acetylesterase) works synergistically to rupture the cellulose and hemicellulose fibers into glucose monomers during enzymatic hydrolysis [20,23]. Currently, lytic polysaccharide monooxygenases (LPMOs), manganese peroxidase, and laccases are being employed for enzymatic saccharification because they hydrolyze the polysaccharides and remove lignin; thus, improving the effectiveness of process by increasing the glucose yield and decreasing the quantity of cellulases [4,23]. However, high sensitivity, high cost, less stability, and high dosage of the enzymes hinder greatly the economic feasibility of the biofuel production process. Thus, novel approaches such as onsite enzyme production, usage of enzyme cocktails, enzyme immobilization, and others are being utilized for achieving the cost-economy of the overall process [14,24]. Besides biofuel, a variety of value-added products are also produced through enzymatic saccharification of pretreated LCB, such as xylo-oligosaccharides, xylose, psicose, tagatose, xylene, toluene, benzene, aliphatic acids, quinines, and lignin monomers including syringols, syringaldehyde, propylphenol eugenol, vanillin, aryl ethers, and many others [25]. For the production of biofuel–ethanol, butanol, lactic acid, acetone, or other end products, the reducing sugars (hexoses and pentoses) obtained are subjected to a biochemical pro-

cess named fermentation [23]. The fermentation process is intended to be optimized via pretreatment and hydrolysis techniques [26].

Based on the composition of sugary hydrolysate, specific micro-organisms (bacteria, fungi or yeasts) are required for metabolization and product formation [2]. The commonly used micro-organisms for ethanol fermentation include *Saccharomyces cerevisiae*, *Pichia stipitis*, *Zymomonas mobilis*, *Candida shehatae*, *Candida brassicae*, *Klebsiella oxytoca*, *Mucor indicus*, *Escherichia coli*, *Penicillium*, *Trichoderma*, and *Aspergillus* [9,15,18,27]. *Saccharomyces cerevisiae* is the principal yeast which has been employed extensively for the production of alcohol, mainly in wine industries and breweries [2]. Thus, valorization of lignocellulosic feedstock into biofuels, and other upgraded products, envisages the 'waste to wealth' transformation, and the growth of a biomass-based economy [28]. The current review therefore addresses the concept of biorefinery, the associated challenges, and the possible solutions that might improve bioprocessing for the development of a sustainable biorefinery. The recent trends in the different steps of bioconversion of LCB into valuable bioproducts, including pretreatment and enzymatic hydrolysis steps, are presented. Additionally, a brief description of promising physical, chemical, physicochemical, and biological pretreatment strategies and key steps involved in biofuel production processes is outlined. The review also discusses the environment sustainability of the biofuels and bioproducts, current challenges, and possible sustainable solutions to achieve the targets of integrated biorefineries.

2. Lignocellulosic Biorefinery Concept for Circular Bioeconomy

In order to boost production of green fuels and add economic value, the concept of a biorefinery was established. A biorefinery is a fundamental framework developed for the use of raw biomass (LCB, algae, other organic wastes), in which all processing methods are integrated in a systematic manner to produce sustainable bio-based products [2]. The biorefineries are essential to foster a circular bioeconomy that is knowledge-driven and environmentally sound [2,29].The idea of circular bioeconomy emphasizes the recovery of all goods from resources without any waste being discharged, and the lignocellulosic biomass utilized as a feedstock plays a vital role in the production of both bioproducts and the energy needed to power them. The primary goal of circular bioeconomy is to replace the end-of-life phase through resource recovery, the use of renewable energy, the elimination of harmful chemicals, and the zero discharge concept by altering the design of all relevant systems and business models [12]. Conventional biorefineries implement high levels of process integration and little waste output to transform biomass into a variety of products for different industrial sectors [30]. According to the International Energy Agency (IEA), biorefinery targets "the sustainable conversion of various biomasses into bioenergy and diverse bioproducts (chemicals, feed, and food), and bioenergy (power, heat, and biofuels)" [26]. Based on the literature survey [2,20,31], biorefinery can be classified into three phases on the basis of biomass, biomass processing technology, and the product:

a. Phase I biorefinery (one feed, one preset processing technology, and one main product). For example, in the European Union, vegetable oil biorefinery involves the production of biodiesel by the transesterification of rapeseed oil;
b. Phase II biorefinery (one feed, multiple processing technologies, and multiple end products). For example, in Sweden, forestry feedstock is refined to produce cellulose, lignosulphonate, and bioethanol;
c. Phase III biorefinery (multiple feedstocks, multiple processing technologies, and multiple end products). For example, lignocellulosic biomass-based biorefinery, two-platform biorefinery, green biorefinery, and others.

A successful biorefinery must be the one which produces very little or no waste, while processing. Thus, an integrated strategy which combines conversion strategies (chemical, thermochemical, and biochemical), and potent downstream strategies systematically, must be used in a zero-waste biorefinery for achieving the target of circular bioeconomy [2,12]. In this way, a sustainable and more economical approach could be developed for an ideal biorefinery, which could potentially provide a plethora of fuels, and value-added industrial

products [23]. With the basic layout of a biorefinery process, the unexplored lignocellulosic biomass can serve as a potent resource for the production of bioproducts. The ability to use various LCBs can provide a consistent supply for biorefining processes throughout the year; thus, boosting the viability of biomass waste valorization with an economic perspective [32]. The accomplishment of LCB-based second generation (2G) biorefinery is largely determined by the type, composition, and properties of biomasses as well as the conversion processes used in the process.

3. Lignocellulose Composition and Structure

Lignocellulosic biomass is the most copious, low-cost, carbon-neutral, and high-energy density organic polymer present on this earth [33]. The production of renewable fuels from LCB not only boosts global energy security, but also minimizes waste, helps rural economies, and reduces environmental problems [34]. LCB is a heterogeneous polymeric complex composed of three major components; i.e., cellulose (35–55%), hemicellulose (20–40%), and aromatic lignin (10–25%), and minor traces of protein, pectin, ash, and other extractives (inorganics, waxes, fats, resin acids, phenolics) [12,35]. Table 1 shows the cellulose, hemicellulose, and lignin content in different types of lignocellulosic feedstocks.

Table 1. Composition of different lignocellulosic biomass feedstocks.

S. No.	Lignocellulose Feedstocks	Cellulose (%)	Hemicelluloses (%)	Lignin (%)	Reference
1.	Sugarcane bagasse	38.6	20	24.68	[9]
2.	Sunflower stalks	27.22	11.94	-	[35]
3.	Oat flakes	21	38%	27	[36]
4.	Spruce sawdust	55.4	1.4% arabinose, 4.2% xylose	28.7	[37]
5.	Eucalyptus	41.58	15.85	29.40	[38]
6.	*Parthenium hysterophorus*	49.98	7.61%arabinose, 14.18% xylose	17.6	[15]
7.	*Saccharum spontaneum*	32.16	19.36	16.86	[33]
8.	Birchwood planks	54.22	28.14	11.13	[39]
9.	Oak sawdust	44.7	1.2% arabinose, 14.8% xylose	26.7	[37]
10.	Oil palm trunk	56.1	16.15	19.11	[40]
11.	Pine	36.2	23.0	32.8	[41]
12.	Cup plant	39	21	21	[42]
13.	Sun hemp fiber	75.6	10.05	10.32	[43]
14.	Watermelon rind	39.67	23.21	10.6	[44]
15.	Peanut shell	36.9% glucan	13.2% xylan, 1.5% galactan, 5.2% arabinan, 1.0% mannan,	30.2% Klason lignin, 3.9% acid-soluble lignin,	[45]
16.	Corn cob	41	22.6	14.1	[46]
17.	Barley straw	31.1 ± 0.8	27.2 ± 0.4	18.8 ± 0.2	[47]
18.	Corn stover	31.5% glucan	22.5% xylan, 2.1% galactan, 1.7% arabinan	18	[48]

The percentage composition of these polymers may differ in different biomasses due to variations in biomass type (softwood, hardwood, grasses, and farm waste), soil type, climate type, fertilizers type, growing conditions, harvesting technique, and other physical factors [1,9,16].

3.1. Cellulose

Cellulose $(C_6H_{10}O_5)_x$ is an unbranched linear polymer of β-D-glucopyranose units, joined together by β-(1,4) glycosidic linkages [49]. It is the primary component of lignocellulosic biomass, which accounts for 30–50 wt% of the whole dry mass [2]. The degree of polymerization (DP) of cellulose fibrils is approximately greater than 10,000. The uniform

structure of cellulose fibrils is formed by inter- and intramolecular hydrogen bonding as well as covalent interactions, which offers great tensile strength to cellulose and makes it resistant to various solvents [34]. Due to the presence of hydrogen bonding between hydroxyl groups in cellulose, different crystalline patterns with varying degrees of crystallinity are produced.

The cellulose polymers are separated from one another and more likely to form hydrogen bonds with other molecules in the more amorphous regions. Due to these two distinct molecular configurations, the polymer has a paracrystalline structure, where both the amorphous and crystalline portions are present [50]. Amorphous cellulose, which is easier to access, can be easily hydrolyzed by cellulase, while the harder-to-access crystalline part cannot be effectively broken down [36]. The important bio-based products obtained from the processing of cellulose include ethanol, succinic acid (SA), levulinic acid (LA), sorbitol, hydroxyacetaldehyde, and many others [2].

3.2. Hemicellulose

Hemicellulose $(C_5H_8O_4)_m$, the most rich carbohydrate polymer after cellulose, constitutes about 15–35 wt% (dry mass basis) of total biomass. It is structurally a heteropolymer with less polymerization degree and molecular weight as compared to cellulose [23,27]. It contains both branching and linear polymers that are made from a variety of anhydrous sugars (xylose, arabinose, D-glucuronic acid, L-rhamnose, and others). Since the hemicellulose components have amorphous nature, and low DP, they do not significantly increase the biomass's recalcitrance [1,49]. Thus, it can be separated rapidly, and utilized to make biofuels such as bioethanol, and other value-added products including lactic acid, xylo-oligosaccharides, xylitol, hydroxymethylfurfural (HMF), polyhydroxyalkanoates, and furfural [2]. The most prevalent hemicellulose polysaccharides are known as xylans, which have polymeric chains made up of 1,4-linked -D-xylose units [51]. Depending on its source, xylan has a different chemical makeup. Hemicellulose also contains mannan components such as glucomannan, galactomannan, glucuronic acid, and galacturonic acid. Mannose residues are connected by β-1,4-bonds, whereas galactomannan is formed when mannose residues use α-1,6-bonds to link the galactose residues.

3.3. Lignin

Lignin $[C_9H_{10}O_3(OCH_3)_{0.9–1.7}]_n$ is primarily one of the crucial components of plant cell walls that offers them stiffness and strength while guarding against microbial attack [1,52]. It is an insoluble, stiff, aromatic biopolymer made up of monolignols such assinapyl alcohol, p-coumaryl alcohol, and coniferyl alcohol [20,53]. The presence of these components varies significantly, depending on the type of plant and extraction technique, with softwood and hardwood having higher (25–31 wt%) and lower percentages (16–24 wt%) of lignin, respectively [15,17,35]. With a projected accessibility of more than 3×10^{11} tons, or around 30% of all non-fossil carbon, it is a rich organic non-fossil carbon present on the planet. Due to its abundant availability, lignin macromolecule represents a potential source for the production of fine chemicals, adsorbents, fuels, and polymer processing materials [54]. Lignin generally forms a three-dimensional cross-linked network by integrating with cellulose and hemicellulose components of LCB.

The common interunit bonds in lignin include β-aryl ether resinol, phenylcoumaran, dibenzodioxocin, β-1,4-O-5′, and α-O-4′ linkages [53]. Ether bonds, which make up roughly 60–75% of all bonding in lignin and are a common type of bond accounting for approximately 45–62% of all connection types, are the main type of bond used to connect the various structural units [1]. Lignin has long been considered a roadblock in the lignocellulosic biorefineries due to its non-productive binding with the cellulolytic enzymes [3,55]. However, the past ten years have brought a paradigm shift in lignin research so that it is now considered a bridge for biorefineries and an essential natural polymer for value addition that can achieve the targets of circular bioeconomy in future.owe

3.4. Other Components

Apart from cellulose, hemicellulose, and lignin polymers, LCB is also constituted by proteins, pectins, small amounts of extractives (5–15 wt%) such as gums, terpenoids, diterpenes, fatty acids, and chlorophyll, other phenolic substances, and mineral-rich ash (1–5 wt%) (K, Mg, Ca, Si) [34,51]. In contrast to lignocellulosic content, these components provide color and smell to the wood, serve as energy storage units, and shield the plant species from microbial invasions [22]. The non-structural parts of lignocellulosic biomass, known as extractives, can be dissolved in water or neutral organic solvents such as hexane and ethanol. Various biopolymers, including terpenes, terpenoids, proteins, fats, waxes, lipids, steroids, and phenolic substances including lignans, stilbenes, and tannins, are found in extractives [51]. Ash is a solid, inorganic residue that remains after all LCB deposits have been completely burned [56]. It contains elements and minerals such as silicates, carbonates, phosphates, calcium, magnesium, sodium, and potassium [57]. In contrast to agricultural wastes, woody biomass often has a very low ash content [51]. For the prediction of deposits that form in the boilers during gasification or incineration, it is crucial to have a thorough understanding of the physical and chemical features of lignocellulosic ashes.

4. Recent Advances in Pretreatment Technologies for Lignocellulosic Biomass

The highly complex and recalcitrant structure of lignocellulosic biomass is the biggest barrier to 2G biorefining [58]. The intermeshed matrix of LCB biopolymers (cellulose, hemicellulose, and lignin) provides resistance to various microbial and enzymatic digestions. The other variables that affect the biomass recalcitrance include the biomass's porosity, and the presence of proteins and acetyl groups [59]. Thus, fractionation of lignocellulosic components becomes essential for the extraction of monomeric sugars to produce biopolymers, biofuels, and biochemicals [1,4,33]. Pretreatment of LCB is a very significant step in a biorefinery, which enables the efficient disintegration of biomass, increasing the permeability and surface area availability of polysaccharides towards enzymatic hydrolysis. A desirable pretreatment aims to reduce biomass crystallinity, improve porosity, remove lignin, prevent inhibitor formation, avoid sugar degradation, require less energy input, and cost less [36,60]. A variety of conventional pretreatment strategies have been developed for the disruption of biomass, such as biological, physical, chemical, and physicochemical (Figure 1) [1,51]. Table 2 shows the merits and limitations of different pretreatment methods along with their effects in the valorization of LCB. The majority of these methods, however, are associated with limitations such as high operational expense, harsh operational conditions (pressure, pH, and temperature), toxic product formation, and many others [14,15,61]. Hence, novel eco-benign pretreatment techniques are needed to be developed to overcome the constraints of traditional methods.

4.1. Physical Pretreatment

Physical pretreatment techniques primarily aim to decrease the particle size of LCB, and increase the surface accessibility of polysaccharides [22,62]. Mechanical treatment (chipping, milling, and/or grinding), freezing, pyrolysis, microwave irradiation, pulsed electric field, ultrasonication, and torrefaction are several pretreatment approaches employed to destruct the lignocellulosic biomass [49,62,63]. However, most of these methods necessitate high energy/power consumption, high-cost processing instruments/equipment, and also produce hazardous chemical compounds. Thus, they are considered less attractive for industrial-scale usage [5,22,34,61]. Even so, various methods including ultrasound and microwave irradiation have been developed as very efficient in the decrystallization and solubilization of cellulose and lignin from lignocellulosic feedstock.

4.1.1. Ultrasound Pretreatment

Ultrasound irradiation assisted pretreatment includes application of high-frequency (20–500 MHz) mechanical acoustic waves that produce a high-shear force for proficient defibrillation, and degradation of lignocellulosic biomass [18]. Ultrasound pretreatment

method is based on the basic principle of the 'cavitation effect', in which the ultrasonic waves aid in breaking α-O-4 and β-O-4 lignin linkages, which results in the development of cavitation bubbles by fractionating the ligno-polysaccharides complex of biomass [7,9]. When these bubbles reach a threshold size, they rapidly collapse, causing a significant rise in temperature (2000–5000 K) and pressure (1800 atm) [23]. This also offers a number of benefits including less residence time, high levels of activation energy, and adequate mass transfer for efficient LCB deconstruction [62].

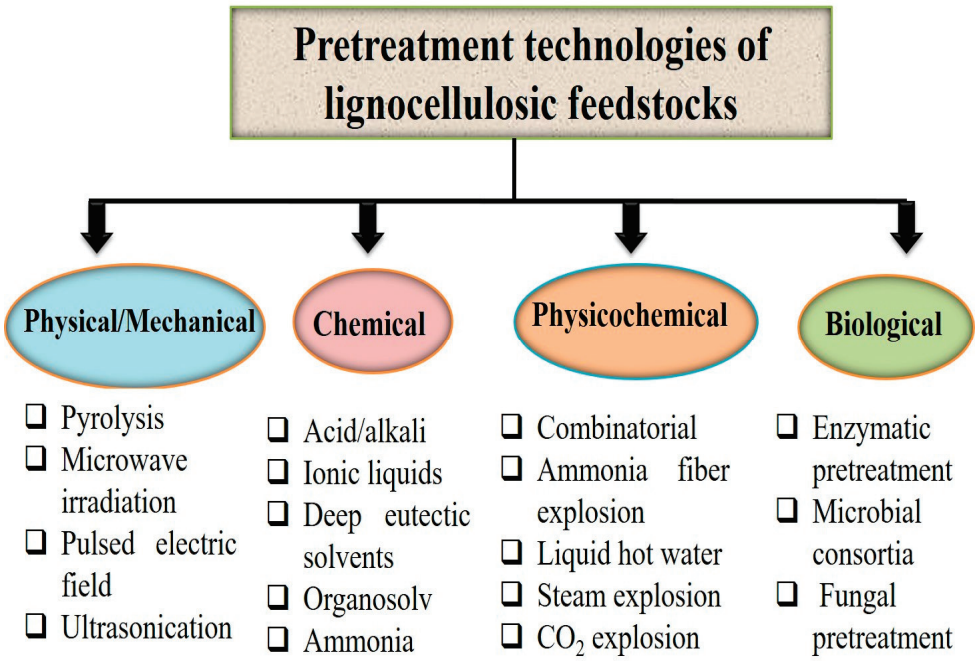


Figure 1. Different pretreatment technologies for breaking the inherent recalcitrant structure of lignocellulosic biomass.

He et al. [64] investigated the structural variations of eucalyptus wood due to ultrasound pretreatment assisted with distilled water, aqueous acetic acid, or aqueous soda solution at 28 KHz frequency and 300 W power. It was observed that the proportion of alkali metals was significantly reduced after ultrasound pretreatment. There was an increase in the crystallinity (35.5%) of wood samples after pretreatment, which indicated the successful disintegration of wood biomass. Subhedar et al. [65] reported pretreatment of pistachio shells, groundnut shells, and coconut coir using ultrasound irradiation (0.5% *w/v* biomass loading, 100W power, and 70 min pretreatment time). Compared to alkaline pretreatment, the delignification percentage of LCB was significantly higher (80–100%) in case of the ultrasound-assisted method. At optimal parameters, the sugar yield obtained through ultrasound-assisted digestion was found to be greater for pistachio shells, groundnut shells, and coconut coir, i.e., 18.4, 21.3, and 23.9 g/L, respectively, as compared to alkali hydrolysis, i.e., 8.1, 10.2, and 12.1 g/L, respectively, in similar biomass order. In another study conducted by Kunaver et al. [66], a high-frequency ultrasound irradiation approach was employed for the liquefaction of different forest wood waste residues into value-added products. The results demonstrated the high production of low-molecular-weight residual products by using short reaction time (decreased by factor 9), and less energy/power consumption. Thus, ultrasound technology (standalone/integrated) has been the top choice for effective LCB pretreatment.

4.1.2. Microwave Irradiation

This irradiation method involves non-ionizable, low-frequency electromagnetic radiation waves called microwaves produced by cycling off a dipole (two opposite and equal charges separated by a particular distance) [22]. Microwave pretreatment exhibits an

excellent potential in the bioprocessing of lignocellulosic biomass as the heat produced by the technique raises the temperature and pressure (thermal effect), throughout the biomass rather than just on its surface, demonstrating greater energy efficiency than traditional heating methods [67]. According to Mankar et al. [62], LCB acts as a good biological conductor due to the presence of non-ionic amorphous and ionic crystalline cellulose regions. Temperature, initial feedstock components, irradiation time, microwave power, and catalyst loading have a discernible impact on the microwave–physicochemical processing of biomass [68]. Application of microwave irradiation heats the polar structure of LCB, and leads to the formation of hotspots. Consequently, constant blasts occur inside the biomass structure, which accelerates the reorientation of crystalline cellulose fibrils [67]. In particular, microwave heating has a number of benefits, including short reaction time, fast and homogenous heating, low activation energy, increased product yield, few by-products, being environmentally friendly and a low-cost, energy-effective operation [68].

Nuchdang et al. [69] investigated the effect of microwave pretreatment for *Brachiara mutica* (paragrass) biomass, treated with acid and alkali. The results showed that use of microwave irradiation at 120 °C, 30 min, and 5% *w*/*w* alkali-to-biomass ratio increased the total reducing sugars significantly (137.3%), as compared to native biomass. Kainthola et al. [70] reported the highest solubilization of rice straw biomass under the influence of microwave irradiation (for 4 min, at 190 °C), resulting in a high specific yield of methane, i.e., 325.2318 mL/g/VS. A short reaction time and high heating rate reduced the production of inhibitory products, thus improving the efficacy of the pretreatment process. In another study, microwave-assisted $FeCl_3$, H_2SO_4, and NaOH pretreatment was carried out for sugarcane bagasse biomass to extract the fermentable sugars. The results demonstrated high lignin removal, and high sugar yield including removal of glucose and xylose selectively, at a short residence time of 5 to 10 min [71]. Despite the amazing advantages of microwave irradiation, the development of industrial microwave heating applications and the incorporation of microwaves into the physicochemical approach for biomass preparation are relatively limited. Additionally, the operation conditions for microwave-assisted pretreatment should be fine-tuned to extract the polymeric sugars (cellulose/hemicellulose) as efficiently as possible.

4.2. Chemical Pretreatment

This type of pretreatment involves the usage of various chemicals such as acids, alkali, deep eutectic solvents, ionic liquids, ammonia, ozone, and many others for the disruption of recalcitrant lignocellulosic biomass [1,15,33]. Chemical pretreatment aims to decrease the biomass crystallinity, increase its porosity, remove lignin, and thus, enhance the biomass surface availability towards enzymatic hydrolysis [60]. Acids (concentrated and dilute) cleave the hemicellulose fraction, and remove part of the lignin of LCB, thus providing greater cellulose access to hydrolysis by enzymes [72]. However, most acids are associated with various limitations such as sugar loss, high cost, corrosive nature, and production of inhibitors [23]. Morais et al. [73] carried out pretreatment of sugarcane bagasse with dilute phosphoric acid that under optimal pretreatment conditions (4.95% phosphoric acid, 80 °C, 375 min) yielded maximum reducing sugars (98% glucose) with higher saccharification efficiency (99%). Alkaline pretreatment leads to the delignification of biomass by cleaving aryl-ether, ester, and C-C bonds, removes hemicelluloses, and increases the surface area for efficient hydrolysis and fermentation [22,74]. However, long reaction time, and high expense for neutralization of pretreatment slurry are the major limitations of the alkaline pretreatment [62]. A mild alkali (sodium hydroxide)-mediated pretreatment of cogon grass was performed at 2% *w/v* NaOH concentration, 90 min time, and 85 °C [75]. The results showed higher saccharification efficiency (90.8%) after alkali pretreatment, which on fermentation yielded maximum ethanol (76%). Although traditional chemicals (acids/alkalis) result in improved decrystallization and cellulose accessibility in a biorefinery, they also have a number of drawbacks that prevent their usage on a large scale [76]. These pretreatment techniques' principal downsides include the high expense of recovering

the acid/alkali, the requirement for corrosive-resistant equipment, and the production of inhibitory compounds. Therefore, the pursuit of new eco-friendly solvents has been intensified in recent years.

4.2.1. Ionic Liquids (ILs)

Ionic liquids (ILs) have effectively become the most environmentally friendly and reusable organic solvents for LCB processing due to their numerous extraordinary tuneable characteristics [13,18,53]. ILs are organic salts of cationic and anionic species, have lower melting point, are non-inflammable, have high chemical and thermal stability, and low vapor pressure [59]. IL-mediated pretreatment solubilizes the polar and non-polar molecules of ligno-polysaccharides, decreases cellulose crystallinity, increases porosity, eliminates the lignin sheath, and thus provides larger cellulose accessibility to saccharification enzymes. Several imidazolium-based ionic liquids have been used for pretreatment of lignocellulosic biomass.

Alayoubi et al. [37] carried out low-temperature (45 °C) IL, 1-ethyl-3-methylimidazolium acetate pretreatment of oak sawdust, spruce sawdust, and model cellulose, which on saccharification produced a high glucose yield, i.e., 59.3%, 49.3%, and 68.2%, respectively. Dotsenko et al. [77] reported an effective delignification, and biotransformation of hardwood (hornbeam wood and spruce), and softwood biomass samples, after pretreatment with ionic liquid 1-butyl-3-methylimidazolium chloride ([Bmim]Cl). Pretreatment of sugarcane tops biomass using ionic liquid tris (2-hydroxyethyl) methylammonium-methylsulfate ([TMA]$MeSO_4$), followed by saccharification, resulted in a high sugar yield, i.e., 181.18 mg/g biomass [14]. However, expensive synthesis, potential toxicity, recycling issues, and non-biodegradability are a few limitations of ILs which limit their large-scale usage in industries [9,78].

4.2.2. Deep Eutectic Solvents (DESs)

Lately, DESs have gained a lot of interest as a green chemistry approach for the digestibility of lignocellulosic biomass [1,9]. Deep eutectic solvents primarily consist of a mixture of liquid eutectic materials that include hydrogen-bond donors and acceptors at a particular molar ratio [79]. They exist mostly in liquid form, and possess lower melting points than their single constituents [16]. They exhibit almost similar characteristics with ILs including low vapor pressure, non-flammability, high thermo-chemical stability, high miscibility, high polarity, and thus, can be efficiently used for the fractionation of LCB [62,79]. However, easy synthesis, low cost, non-toxicity, good recyclability, and increased biodegradability make them preferable solvents to ILs. DESs solubilize lignin effectively from LCB, and transform the crystalline portion of cellulose into amorphous cellulose in moderate process conditions [1]. Deep eutectic solvents' promising properties have forced and encouraged their subsequent use for successful LCB bioconversion, making them superior to diluted acids and ionic liquids.

Jing et al. [80] investigated the production of biohydrogen from corn cob biomass by using a DES (ChCl/ethanolamine) system. The pretreatment resulted in maximum removal of lignin with high percentage efficiency (83.12%). Tan et al. [81] carried out pretreatment of oil palm empty fruit bunch (EFB) biomass with a choline chloride/formic acid (CC-FA), and choline chloride/lactic acid (CC-LA) solvent system. The results demonstrated improved biomass fractionation with high delignification efficiency of 60 wt%. Thi and Lee [82] investigated the effect of three DESs (choline chloride-urea, ChCl-U; chloride-lactic acid, ChCl-LA; choline chloride-glycerol, ChCl-G) on the pretreatment of oil palm empty fruit bunch biomass. The results illustrated that ChCl-LA pretreatment followed by saccharification gave the highest sugar yield (20.7%), followed by ChCl-G and ChCl-U pretreatment, which yielded sugar content of approximately 20.0% and 16.9%, respectively. To further improve the effectiveness of the DES pretreatment and maximize the yield of reducing sugars, a thorough investigation of the operating parameters and techno-economic analysis of the process is required.

4.2.3. Organosolv Pretreatment

Organosolv pretreatment is one of the promising methods for the effective valorization of lignocellulosic biomass into value-added chemicals that could facilitate the shift towards increased use of renewable biomass substrates. Organosolv pretreatment uses organic solvents (ethanol, methanol, formic acid, acetic acid, phenol, glycerol, or acetone) or their aqueous solutions to specially extract or remove lignin from lignocellulosic feedstocks [83]. The organosolv pretreatment provides for highly efficient generation of ethanol, lignin, and other biochemicals from LCB when compared to other pretreatment techniques. In this pretreatment, LCB is added to a combination of organic solvent and water that has a solid-to-liquid ratio between 1:4 and 1:10 (w/w) and a solvent concentration of 35–70% (w/w) [84]. The rate of pretreatment reaction can also be accelerated by including a catalyst. The pretreatment causes the lignin linkages and lignin–carbohydrate bonds to hydrolyze, resulting in a solid phase primarily consisting of cellulose and hemicellulose. To avoid lignin precipitation, this prepared material must be rinsed with an organic solvent. Thereafter, the pretreated biomass is washed in distilled water to remove the organic solvent, and the solid and liquid phases are separated. The pretreated solids are subsequently enzymatically saccharified and fermented to produce value-added biochemicals, whereas the solvent is recovered from the spent liquor using the distillation process (Figure 2).

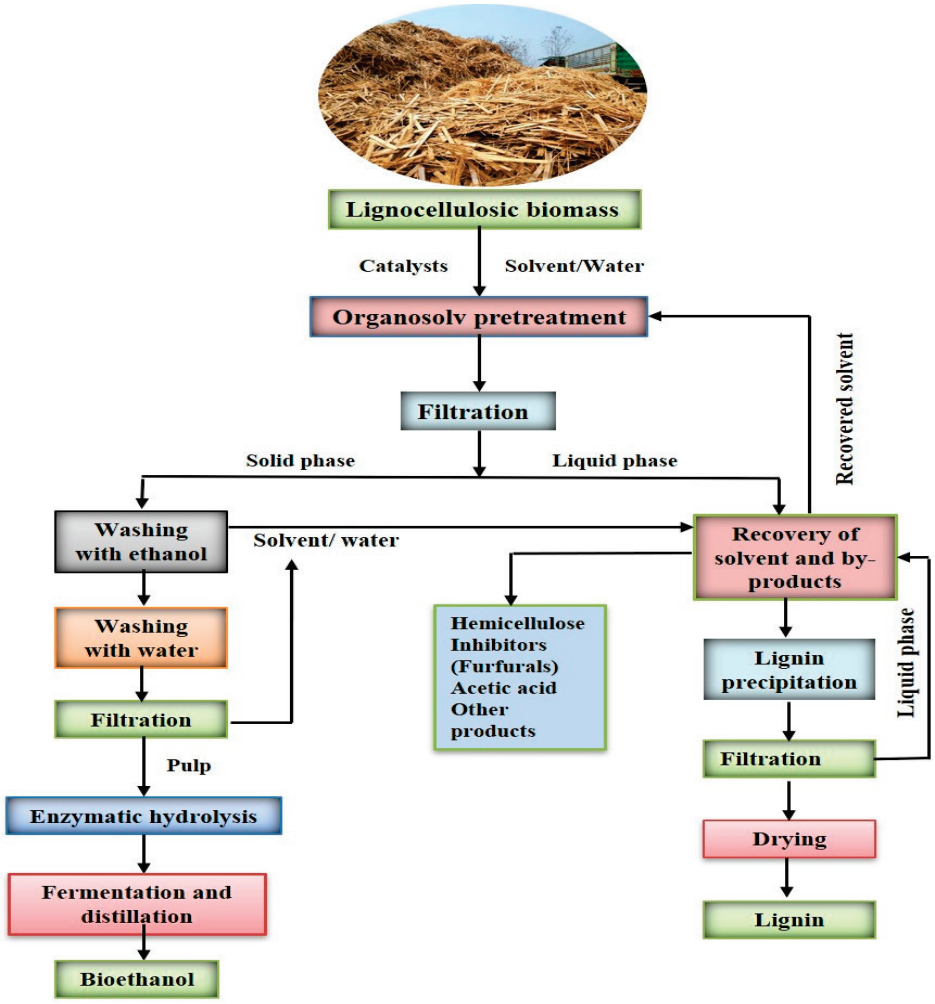


Figure 2. Schematic representation of steps in organosolv pretreatment of lignocellulosic feedstocks.

Karnaouri et al. [85] pretreated pine and beechwood biomass with mild oxidative organosolvs (tetrahydrofuran, acetone and ethanol) that produced cellulose-rich solid fractions for lactic acid production from *Lactobacillus delbrueckii* strain. A high lactic acid

production of 62 g/L was obtained from beechwood biomass compared to that obtained from pine biomass (36.4 g/L), showing that organosolv pretreatment is suited for both hardwood and softwood biomass for the production of valuable biochemicals. In another recent study [86], the sorghum biomass was pretreated by modified low-cost organosolv using glycerol solvent and ammonia as catalyst, which resulted in a significant improvement in the saccharification (reducing sugars of 421.35 mg/g biomass) and fermentation yields (36 g/L). Tang et al. [87] executed synergetic organosolv and organic amine pretreatment of corn stover biomass to produce salt-free high-quality lignin and fermentable sugars. Under optimal process conditions, maximum sugar yield of 83.2%, made up of 87.1% glucose and 75.4% xylose, was obtained with a significant delignification percentage of 81.7% by the application of aqueous ethanol (60% *v*/*v*) as a solvent, and *n*-propylamine (10mmoL/g biomass) as a catalyst.

The promising results with the organosolv pretreatment have led to the establishment of organosolv-based biorefineries in developed countries including the United states of America, Brazil, Germany, Australia, France, and Canada [84]. The further setting up of organosolv-based biorefineries would need an integration of LCB components into pretreatment processes and the reduction of pretreatment costs. This can be accomplished by lowering the volume of organic solvent used in pretreatment, raising the added value of by-products, and optimizing the entire process using statistical approaches.

4.3. Physicochemical Pretreatment

The physicochemical pretreatment technique involves the combination of both chemical and physical methods, and is believed to be more efficient in the disintegration of lignin–polysaccharide complexes under varying process conditions, i.e., temperature and pressure [88]. Various methods including carbon dioxide explosion, steam explosion, liquid hot water method, ammonia fiber explosion, wet oxidation, and different combinatorial approaches come under physicochemical methods [20,89]. Steam explosion is the most common method for LCB pretreatment in which an autohydrolysis reaction is carried out by high-pressure saturated steam, which decreases the biomass crystallinity, removes lignin, and transforms cellulose and hemicellulose into soluble oligomers [63]. In CO_2 explosion pretreatment, dissolution of LCB is caused due to the application of high-pressure supercritical carbon dioxide at high temperature. Ammonia fiber explosion and CO_2 explosion work at low temperature; thus, are considered more economical [90]. The integration of different techniques such as acids, alkali, DESs, ILs, combined with ultrasound, microwave, or other methods have been employed by various researchers to improve the effectiveness of the process [9,15,17].

Kuglarz et al. [91] carried out combined pretreatment of industrial hemp biomass with steam at 180 °C and 1% H_2SO_4, which resulted in the production of a maximum glucose yield of 73–74%, and an ethanol content of 75–79%. Nargotra et al. [35] reported an enhanced sugar yield of 63.42 mg/g biomass by the combinatorial pretreatment (ionic liquid, 1-butyl-3-methyl imidazolium chloride+ alkali, NaOH) of sunflower stalk biomass, as compared to IL (79.6 mg/g biomass), and NaOH (97.38 mg/g biomass) in standalone mode. Vaid et al. [92] reported a combined application of DES (choline chloride/glycerol) and calcium hydroxide for the pretreatment of *Saccharum spontaneum* biomass, followed by enzymatic hydrolysis under one-pot consolidated bioprocessing. The results demonstrated a maximum sugar yield of 372.3 mg/g biomass which was 4.94-fold higher than the sugar yield obtained under unoptimized conditions (75.25 mg/g biomass). In another study conducted by Hou et al. [93], eucalyptus sawdust was pretreated by combined application of microwave and IL [TBA][OH], which on hydrolysis yielded maximum sugar yield of 410.67 mg/g biomass in 48h under optimal pretreatment conditions. Vaid et al. [33] employed a novel pretreatment approach using sodium dodecylsulfate-assisted IL tris (2-hydroxyethyl) methyl- ammonium methyl sulphate for the deconstruction of *Saccharum spontaneum* biomass. Hydrolysis with IL-stable *Bacillus subtilis* G2 enzymes yielded

maximum reducing sugars of 364.24 mg/g biomass under optimized process conditions, in comparison to unoptimized (154.91 mg/g biomass).

4.4. Biological Pretreatment

Biological pretreatment entails the utilization of microorganisms, mostly fungi and bacteria, which have the ability to produce extracellular lignocellulolytic enzymes for the degradation of lignocellulosic biomass. Brown, white, and soft-rot fungi such as *Dichmitus squalens*, *Phanerochaete chrysosporium*, *Jungua separabilima*, *Phlebia radiata*, and *Rigidosporus lignosus* are generally used for the digestion of polysaccharides [20,34]. This pretreatment method is regarded as an efficient, affordable, and environmentally friendly process as it does not employ high energy inputs, and produces less harmful substances, compared to other chemical strategies [94]. However, less available surface area due to biomass structural complexity, slow digestion rate, and requirement of monitored microbial growth conditions restrict the use of biological pretreatment at commercial levels [63,95] (see Table 2).

Table 2. Different pretreatment methods with their merits, demerits, and pretreatment conditions and promising results.

Pretreatment Process	Merit	Demerit	Biomass/Pretreatment Conditions	Significant Results	Reference
Acid treatment	Hemicellulose hydrolysis, increased biomass porosity	Formation of furfurals, hydroxymethyl furfural, corrosion	Sugarcane bagasse/4.95% phosphoric acid, 80 °C, 375 min)	98% glucose yield, 99% saccharification efficiency.	[73]
			γ-Valerolactone/dilute H_2SO_4 (4:1, *v*/*v*), 120 °C, 60 min.	89.1% glucose yield	[96]
Alkali pretreatment	High lignin removal, hemicellulose hydrolysis	Formation of magnesium and calcium salts, long residence time	Date palm/20 % NH_3, 80 °C, 12 h	High biochemical methane potential (309.76 mL CH_4/g-TS)	[74]
			Giant reed biomass/20% NaOH	High glucose yield (44.9%), high H_2 yield (98.3 mL/g TS)	[97]
Ionic liquid pretreatment	Liquid at room temperature, low toxicity, low vapor pressure, high digestibility, thermal stability	Expensive and toxic to hydrolytic enzymes	Almond wood/ethanolamine acetate (15 wt % solid loading)	High glucose (24–82%) and xylose yields (14–80%); 60.8% fermentation efficiency	[98]
			Stinging nettle stems/1-butyl-3-methylimidazolium acetate (10 g biomass in 50 cm^3 IL, 120 °C, 2 h)	High ethanol concentration (7.3 g L^{-1})	[99]
Deep eutectic solvent pretreatment	Easy synthesis, low-cost, biodegradable less toxic, recyclable	High viscosity, hygroscopic	*Parthenium hysterophorus*/ChCl/sorbitol (1:5),	Higher sugar yield (148.54 mg/g biomass)	[16]
			Sugarcane bagasse/ChCl:glycerol (1:10)-ultrasound	Higher reducing sugar titer (276.8mg/g substrate)	[9]
			Banana peel waste/ChCl-based DES	High total reducing sugar yield of 72.9%	[100]
Organosolv pretreatment	Easy recovery and recycling, effective delignification	Repeated washings of pretreated LCB, expensive solvents	Pine, beechwood/mild oxidative (acetone, tetrahydrofuran, and ethanol)	High lactic acid production (beechwood: 62 g L^{-1}; pine: 36.4 g L^{-1})	[85]
			Corn stover/aqueous ethanol (60%, *v*/*v*), n-propylamine (10 mmol/g, biomass)	High sugar yield (83.2%) and delignification (83.2%)	[87]
Ultrasound pretreatment	Size reduction, proper mixing of biomass with solvent, disintegration of cell wall components, less process time, assistive technique	Low conversion efficiency	Rice straw/ultrasound-IL treatment,	Increased reducing sugar, delignification and cellulose conversion by 20.13–28.96%, 18.06–19.33% and 31.69–35.23%, respectively	[101]
			Eucalyptus wood/ultrasound-distilled water (28 KHz, 300 W)	Effective disintegration of biomass with 35.5% increase in crystallinity	[64]
Microwave pretreatment	Continuous operation, less process time and low energy input	Requires high temperature for processing, no hot spots, low efficiency for apolar materials	*Brachiara mutica* (paragrass)/ microwave-alkali (5% *w*/*w*), 120 °C, 30 min.	Increased total reducing sugars to 137.3%	[69]
			Rice straw/microwave radiation for 4 min, at 190 °C)	High specific yield of methane (325.23 mL/g/VS)	[70]

5. Enzymatic Hydrolysis as an Integral Step in Biorefineries

Enzymatic hydrolysis of pretreated lignocellulosic feedstock is the key step in the LCB-biorefinery chain, which involves the transformation of polymeric carbohydrates into simple fermentable monomers with the help of saccharification enzymes such as cellulases, hemicellulases, and ligninases [14,33,55,61]. The three major cellulolytic enzymes employed to degrade cellulose are: a) endo-1,4-β-D-glucanases (hydrolyze low-crystalline cellulose chains randomly); b) cellobiohydrolases/exoglucanases (hydrolyze cello-oligosaccharides' reducing and non-reducing ends to generate cellobiose units); and c) cellobiases/β-glucosidases (hydrolyze cellobiose to form D-glucose) [2,4,36]. All the three cellulases work simultaneously and synergistically as a mixture, thus increasing the catalytic activity of cellulase enzymes [102].

Besides cellulases, hemicellulases such as β-xylosidase, xylanases, glucomannanase, glucuronidase, galactomannanase, and acetylesterase are employed for the hydrolysis of hemicellulose polymers [23,103,104]. Xylanases solubilize β-1,4-D-xylan fractions of hemicellulose by cleaving the β-1,4-D-xylopyranosyl bond, and thus, result in the formation of oligomeric (xylo-oligosaccharides) and monomeric sugars [105,106]. Another class of enzymes named lytic polysaccharide monooxygenases (LPMO) work synergistically with cellulases, and thus boost the effectiveness of cellulose degradation [4,23]. LPMOs are copper-dependent enzymes that follow an oxidative mechanism to improve the disintegration of biomass. In the presence of cellobiose dehydrogenase and ascorbic acid (electron donors), copper ions cause reduction of oxygen, thus aiding in the cleavage of glycosidic linkages of crystalline cellulose [36,58].

Lignin, an aromatic polymer of LCB, acts as a physical barrier in the process of polysaccharides extraction [1,4,15]. It is degraded by a variety of ligninolytic enzymes such as laccases, versatile peroxidase manganese peroxidase, and lignin peroxidase [107]. Micro-organisms (fungi and bacteria) are commonly used for the production of hydrolytic enzymes. Micro-organisms such as *Bacillus velezensis*, *Bacillus paranthracis*, *Aspergillus terreus*, *Aspergillus niger*, *Trametes versicolor*, and *Phanerochaete chrysosporium* are a few of the examples that produce enzymes with cellulolytic, hemicellulolytic, and ligninolytic capabilities [2,107]. Various factors such as enzymatic activity of saccharification enzymes, enzyme loading, substrate quantity, process conditions, and inhibitors present in the post-pretreatment sugar hydrolysate [90]. However, addition of various salts/surfactants/metal ions, optimization of process parameters, and utilization of enzyme mixture increase the efficiency of enzymatic hydrolysis [108].

In a study conducted by Cai et al. [109], the addition of polyvinylpyrrolidone (1 g/L) during enzymatic saccharification of dilute acid-pretreated eucalyptus biomass increased its digestibility to 73.4% from 28.9%, as compared to other additives (bovine serum albumin, PEG, and Tween). Rocha-Martin et al. [110] reported an improvement in the glucose yield by 32, 10, and 7.5% after PEG4000-assisted hydrolysis of pretreated microcrystalline cellulose (Avicel), corn stover, and sugar cane straw biomass, respectively. Addition of PEG4000 increased the endoglucanase and beta-glucosidase catalytic activity by 60 and 20%, respectively and also decreased the liquefaction time (up to 25%).

Although enzymatic hydrolysis is a crucial step in the bio-transformation of LCB at commercial level, application of enzymes still has a number of drawbacks, including high cost, limited availability, less stability, non-recyclability, and non-reusability; thus, limiting the effectiveness of the bioprocess [111]. To circumvent these problems, immobilization of microbial enzymes on suitable matrices/support materials provides a promising solution [112]. Nanomaterials (with a size of less than 100 nm) such as nanoparticles, nanofibers, nanoflowers, nanomagnets, and many others have the potential to completely transform the production of biocatalysts and their application in the bioenergy area [4]. Nanobiocatalysts provide a number of benefits to enzymes including high surface area, increased activity, increased stability, reusability, easy synthesis, environmental friendliness, and a cost-effective nature [113,114]. Furthermore, enzyme engineering or genetic manipulation of gene coding for saccharification enzymes can improve the catalytic activity and stability

of enzymes [4]. The production of competent and resistant microorganisms, which can survive harsh environments, and development of stable enzymes require the potential application of genetic engineering tools [25].

Karnaouri et al. [115] produced an enzyme called MtEG5A expressed from the endoglucanase gene of *Myceliophthora thermophile*, a thermophilic fungus, into *Pichia pastoris*, the methylotrophic yeast. These enzymes have been found to hydrolyze birch, wheat straw, and spruce biomass, producing large quantities of cellobiose and hence increased yield of sugars. In a study, cellulases immobilized on magnetic nanoparticles were utilized for the hydrolysis of *Allamanda schottii* L. flowers pretreated with sodium hydroxide, and the highest sugar yield of 25 g/ml was observed in comparison to that with native enzyme, i.e., 18 g/mL. Fermentation of the obtained sugar hydrolysates yielded an ethanol content of 252 g/L (immobilized enzyme), and 182g/L (native enzyme), respectively [116]. Hwangbo et al. [117] investigated the combined pretreatment of NaOH and IL, 1-ethyl-3-methylimidazolium chloride of corn husks, hydrolyzed with five types of saccharifying enzymes, which were cross-linked in the presence and absence of magnetic nanoparticles called magnetite-saccharifying enzyme cross-linked enzyme aggregates, M-SE-CLEAs, and saccharifying enzyme cross-linked enzyme aggregates, SE-CLEAs. The results indicated a maximum reducing sugar yield of 250 mg/g biomass by employing SE-CLEAs. Additionally, reusability of M-SE-CLEAs was successfully achieved in up to three hydrolysis cycles.

6. Bioconversion of Lignocellulosic Biomass into Biofuels and Value-Added Materials

Carbohydrate-rich lignocellulosic biomass obtained from agricultural by-products, forestry residues, municipal wastes, and industrial emissions holds a remarkable potential for the production of green energies, i.e., biofuels (bioethanol, biohydrogen, biomethane, biobutanol, biogas), and other value-added products through various aforementioned thermochemical and biochemical conversion technologies [1,59,79]. Enzymatic digestion of polysaccharides results in the production of reducing sugars, which on fermentation produce various kinds of biofuels. A biochemical process that catalyzes the conversion of monomeric carbohydrates with the help of microorganisms under a low oxygen environment is known as fermentation [26]. Most widely employed industrial microorganisms for the fermentation process are *Schizosaccharomyces*, *Saccharomyces cerevisiae*, *Candida shehatae*, *Zymomonas mobilis*, *Pichia stipitis,* and others [90]. For microorganisms to thrive, all the internal conditions (dissolved oxygen, culture medium, and other micronutrients), and necessary parameters (pH, temperature, and sugar content) must be satisfied. They must possess high product yield, and resistance to the toxic inhibitory compounds [118]. The conventional method used for fermentation of biomass hydrolysate has a specific process in which the fermentation is carried out in several types (batch, fed-batch, solid state, consolidated bioprocessing, simultaneous saccharification and fermentation, and separate hydrolysis and fermentation) [23,27]. The processed lignocellulosic biomass after several rounds of steps, including pretreatment and enzymatic saccharification, acts as a suitable substrate for the production of bioproducts such as biofuels, bioplastics, vanillin, hydroxymethylfurfural, etc. (Figure 3) [1,4,103,119].

6.1. Bioethanol

Biofuel ethanol (C_2H_5OH) is a promising green combustible fuel compared to gasoline due to various characteristics such as higher flammability, high octane number, higher combustion efficiency, high heat of vaporization, shortened burning time, and minimum toxicity, and is less polluting than petrol. It is usually mixed with gasoline and used as fuel in the transportation industry [27,120]. India contributes only 2% to the overall global bioethanol production [121]. At present, most of the ethanol is produced from first-generation (1G) feedstocks, which are a proven and well-established method with high bioethanol productivity and output. Data from the International Energy Agency (IEA) show that 1G bioethanol production has increased globally to 104 billion liters with

a 3% yearly growth rate [122]. However, the process is linked to the controversy over the conversion of food into fuel and leads to significant environmental impacts [123]. In contrast, second-generation (2G) bioethanol production is built on the limitations of 1G bioethanol and is mostly generated from lignocellulosic feedstocks in the form of non-food crops and agricultural wastes. According to IEA reports, a 2% annual growth rate for bioethanol production is estimated, which will account for 119 billion liters of bioethanol in 2023 and might increase to 145 billion liters under favorable circumstances [122]. For the production of bioethanol, LCB is first processed into simple sugars (hexoses and pentoses), and then metabolized into ethanol by fermenting microorganisms such *Saccharomyces cerevisiae* and *Pichia stipitis* [2]. Jin et al. [124] executed ethanol fermentation of the sugary liquor obtained by hydrolysis of combinatorially (sodium hydroxide and hydroxymethylation reagents) pretreated sugarcane bagasse, and observed a maximum ethanol yield of 10.67 g/L. Vaid et al. [17] reported the highest ethanol concentration of 0.148 g/g pine needle biomass under consolidated bioprocessing of pine needle biomass pretreated with 1-ethyl-3-methylimidazolium methanesulfonate. However, despite remarkable research being done on the bioethanol production from LCB using novel biorefinery approaches, the cost of production has been a major bottleneck in the commercialization of this green fuel. Therefore, some of the limitations associated with standalone 1G and 2G processes may be resolved by integrating 1G–2G bioethanol production, which could ultimately result in a breakthrough in the creation of a workable technology for large-scale bioethanol production [123]. When compared to a standalone 2G bioethanol plant, integrated 1G–2G bioethanol production from sugar-based crops offers better productivity rates, an appealing commercial opportunity, and is more ecologically benign.

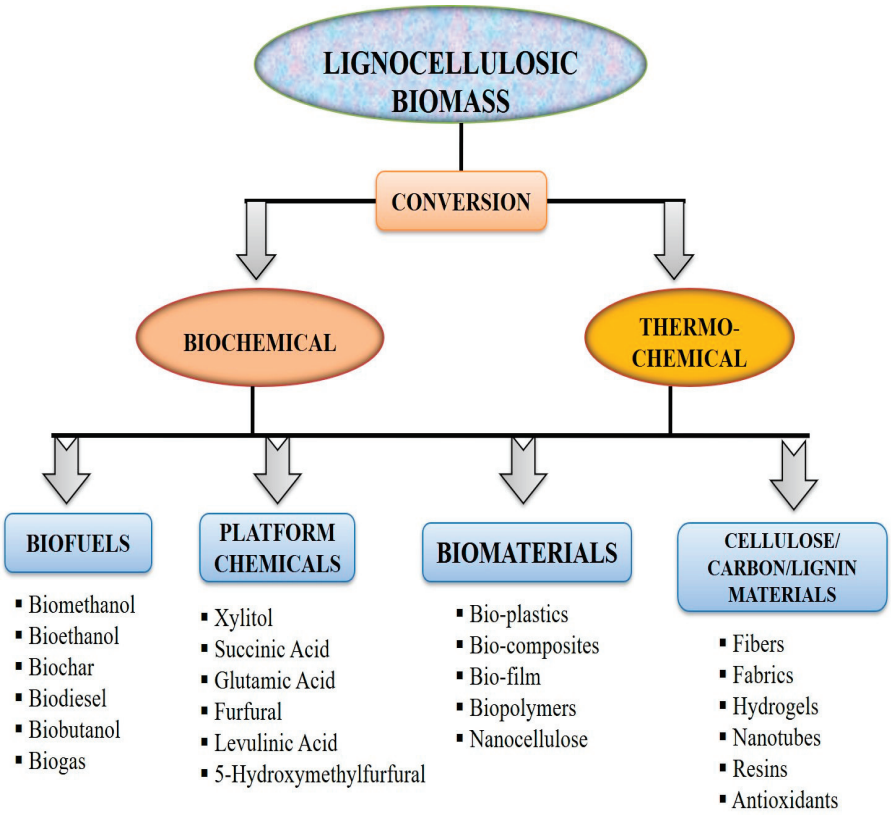


Figure 3. Biochemical and thermochemical conversion of lignocellulosic substrate into biofuels and value-added bioproducts.

6.2. Biodiesel

Another promising alternative to non-renewable fossil fuels is fatty acid methyl ester, called biodiesel due to its sustainability, biodegradability, renewability, and environmental

friendliness as compared to conventional diesel [125]. It is generally produced from edible and non-edible oils by transesterification, blending, pyrolysis, microemulsion, or other conversion processes. Biodiesel can replace the fossil-derived diesel directly without any modification in existing engines, and is non-explosive, non-inflammable, and non-toxic [126]. Wang et al. [127] reported two insect (*Tenebrio molitor* L. and *Hermetia illucens* L.)-based biorefinery processes of corn stover biomass, and observed the produced crude grease of 1.95 g yielded a significant quantity of biofertilizer (111.59 g), protein (6.55 g), and biodiesel (1.7g). Bateni et al. [128] carried out alkali pretreatment of castor plant at optimal conditions to improve the bioethanol and biodiesel yield, which was obtained to be 27.2–71% and 85.0 $\pm$ 1.0%, respectively. It was estimated that 149.6 g of biodiesel and approximately 30.1 g of bioethanol was produced from 1 kg of castor plant.

6.3. Biomethane

LCB biopolymers can be digested anaerobically by bacteria to produce an easily storable and flexible biofuel named biomethane or biogas [12]. Firstly, the complex lignopolysaccharides are processed with a suitable pretreatment strategy into simpler molecules of amino acids, sugars, and fatty acids. Acidogens (fermentative bacteria) digest these monomers to short chain fatty acids, and then convert them into acetate, hydrogen, and carbon dioxide. These end products act as substrates to produce biomethane via methanogenesis. Recently, Banu et al. [129] reported a maximum biomethane yield of 0.174 L/g COD from waste-activated sludge pretreated by bacterial pretreatment induced by mild hydrogen peroxide, as compared to methane obtained with bacterial pretreatment, i.e., 0.078 L/g COD, and control sludge, i.e., 0.02175 L/g COD.

6.4. 5-Hydroxymethylfurfural (HMF)

5-Hydroxymethylfurfural (HMF) is generally considered as a multifunctional molecule due to the presence of a furan ring structure joined with an alcohol and aromatic aldehyde [130]. 5-Hydroxymethylfurfural can produce a variety of derivatives including 2,5-diformylfuran (2,5-DFF), levulinic acid, 2,5-dimethylfuran (2,5-DMF), and 2,5-bis(hydroxymethyl) furan (2,5-BHF) [131]. These compounds have been used as precursors in the production of materials such aspolyesters, polyamides, and polyurethane [132]. Ruby and Schüth [108,133] reported 5-hydroxymethylfurfural production by fructose dehydration with the application of acid-free and metal-free heterogeneous catalytic systems. The results showed a maximum of 77% HMF yield. Zhao et al. [134] carried out as-synthesized solid acid catalyst-mediated fructose degradation to produce HMF with maximum yield of 90% under optimal process conditions.

6.5. Biohydrogen

Hydrogen is a clean fuel, which when burned in fuel cell releases water and possesses a greater combustion rate. In the recent past, several biohydrogen production methods have been investigated from a variety of lignocellulosic materials, including rice straw, wheat straw, grass, softwood, rice husk, and woody waste. The H_2 production from LCB involves a step-wise sequence of pretreatment, hydrolysis, fermentation, and gasification. The biological approach, i.e., dark fermentation, is thought to be more environmentally benign and long-lasting when compared to other modern technologies [135]. Using locally isolated facultative bacteria, *Proteus mirabilis*, the hydrogen production from the hydrolysates of acid and alkali pretreated paddy straw was explored. A maximum volume of 833.43 $\pm$ 21.72 mL H_2 was produced from acidic hydrolysate through dark fermentation, which had a higher H_2 yield than alkaline treatment method [136]. Utilizing corn silage, fruit and vegetable waste, and sugar beet pulp, dark fermentative hydrogen production was studied that produced 52 cm^3/gVS H_2 after deep eutectic solvent pretreatment of waste biomass [137]. In another study, the microwave pretreatment of switchgrass and miscanthus at various processing temperatures and dissolution in subcritical water resulted in a higher yield of hydrogen-rich gas by aqueous-phase reforming [138]. However, more

innovative strategies are required to improve the viability of lignocellulosic biohydrogen production, and integrated biorefinery platforms that may offer a viable alternative.

7. Environmental Sustainability of Biofuels and Value-Added Biochemicals from Lignocellulosics

The continuous emission of greenhouse gases (GHGs) due to combustion of fossil-derived fuels lead to an enormous increase in the global temperature, causing global warming, and other environmental problems including pollution, climate change, and oil spills [27]. An exponential rise in global population and depletion of conventional fossil resources have caused the demand for energy worldwide to soar [139]. Valorization of abundantly available lignocellulosic biomass waste into biofuels and value-added products promises an effective solution. Biofuels, which are made from non-fossilized biomass (plant products) or other organic solid wastes, offer the advantage of lowering net carbon emissions, primarily GHGs, and dependency on oil [121]. Increasing the use of biofuels would benefit several important policy goals such as energy security, fuel quality, and environmental friendliness. Biofuels can easily replace petroleum-based fuels and, in many nations, can serve as an indigenous source of transportation fuel rather than one that must be imported. However, if imported, biodiesel or ethanol will probably originate outside of OPEC (Organization of Petroleum Exporting Countries), diversifying the supply of transportation fuels on a more global scale.

The advantages of using ethanol to increase fuel octane levels have caught the attention of refiners and automakers, particularly in cases where MTBE and other possible octane enhancers are restricted or banned. Biofuels are often more environmentally benign than petroleum fuels due to their production of fewer GHG emissions across the whole fuel cycle. Vehicles powered by biofuels release less of various pollutants that exacerbate air quality issues, especially in metropolitan areas, either in their pure form or as blends with conventional petroleum fuels. Combining biofuels with conventional fuels can reduce some air pollutants while increasing others (such as NOx emissions) [140]. The bioconversion of LCB into various value-added chemicals such as formic acid, succinic acid, lactic acid, levulinic acid, 2,5-dimethylfuran (2,5-DMF), 5-hydroxymethylfurfural (5-HMF), and other aromatic compounds can be transformed into a variety of upgraded derivatives that possess remarkable potential as biopolymers, biofuels, and in solvent factories [131].

8. Current Challenges and Future Prospects

Second-generation biorefinery based on lignocellulosic feedstock is a renewable, sustainable, and eco-benign approach in view of deteriorating fossil fuel supplies, increased energy prices, and environmental ill-effects [59]. However, full-scale bio-transformation of LCB into desired chemicals is still limited due to high operational and investment costs. This challenge is ascribed to LCBs' intrinsically tough structure, which resists microbial invasion and enzyme access [13]. A comprehensive study on the characterization and composition of the lignocellulosic substrate is a prerequisite for the development of a successful biorefinery. The composition, availability, cost, production, collection, storage, and shipping are factors which are taken into consideration while selecting lignocellulosic feedstock [2]. Bioconversion processes including biomass pretreatment and enzymatic saccharification are the key steps that affect the techno-economic feasibility of a biorefinery. As the green refinery concept is put into practice, it is necessary to maximize the cost-effectiveness and quality of fractionated products. Despite improvements in a number of different pretreatment strategies, which produce high sugar yield with fewer demerits, there is still a lot of room for enhanced LCB pretreatment and detoxification-based advancements [59]. Thus, adequate and cost-efficient pretreatment methods need to be developed that can cause maximum degradation of biomass, with less chemical and energy consumption, and boost the subsequent enzymatic hydrolysis. The severity of biomass pretreatment influences the amount of enzyme required for the next step of hydrolysis [27]. Therefore, future research efforts should focus more on developing customized pretreatment techniques while con-

sidering various LCB compositions or the targeted products, as well as developing a solid understanding of the reaction mechanism underlying pretreatment.

Another major obstacle that hinders the feasibility of a biorefinery is the high operational expense of hydrolytic enzymes. The enzymatic hydrolysis step contributes about 25–30% of the total biomass processing cost, and has not yet been fully commercialized for second-generation biofuel production. Therefore, exploration and production of affordable enzyme mixtures are required for an efficient hydrolysis process [90]. Several techniques such as metagenomics, metabolic engineering, and protein engineering can be used to discover highly stable and genetically modified hydrolytic enzymes, leading to the production of various desirable products [4,25]. Immobilization of potent enzymes on nanosized materials (organic wastes, nanoparticles, nanofibers, nanotubes, and others) provides a plethora of benefits to enzymes including high stability, recyclability, reusability, and high catalytic activity, thus improving the cost effectiveness of 2G biorefinery [117]. The majority of the microorganisms involved in fermentation can metabolize only a specific class of sugars; for example, *Saccharomyces cerevisiae* can ferment only hexoses, while *Pichia stipitis* can metabolize only five carbon sugars, leaving other residues unused (lignin and unreacted substrates, among others). To boost ethanol yield and productivity, it is crucial to investigate and create genetically modified cellulolytic and fermentative microorganisms and co-culture systems. Future commercialization of biorefineries is just the tip of the iceberg. Due to the high cost of renewable energy produced by a single technology, combining various technologies on a large scale for commercial purposes would increase the yield of renewable energy and make it more economical. The integration of biorefineries to scale up the projects to close the gap between the generation and commercialization of biofuels and value-added products is the subject of extensive research. In the past decade, a number of research and review articles have been published in the literature that have provided exciting and novel low-cost methods of the valorization of lignocellulosic biomass into biological commodities including biofuels (Figure 4). An analysis of the articles published from 2013 to 2022 shows a total of 927 research and review papers (through a Scopus database search for the terms 'biomass AND lignocellulose', 'biofuels' and 'pretreatment' in the abstracts, titles, and keywords).

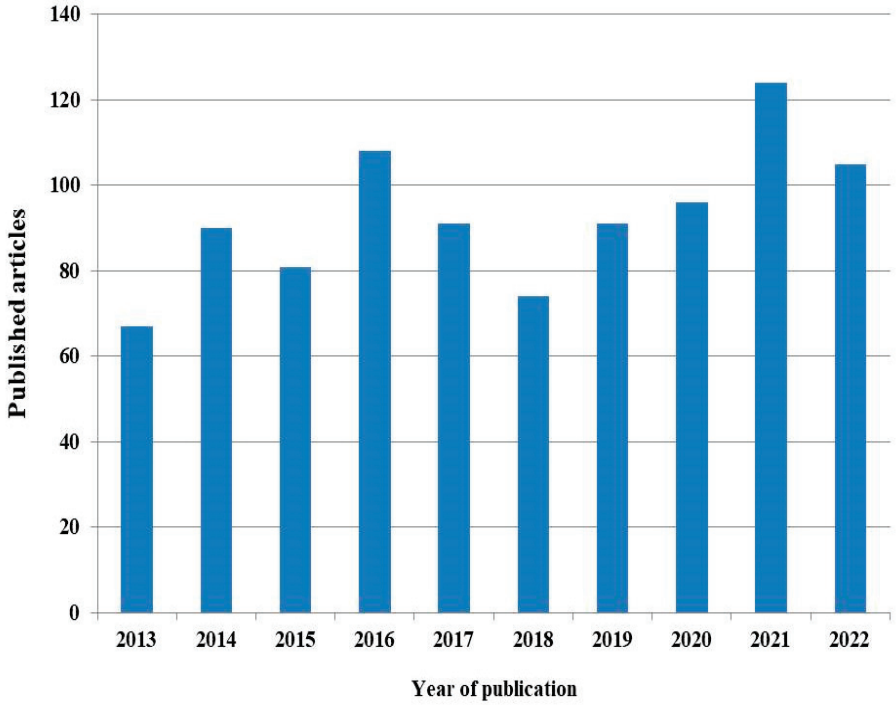


Figure 4. Number of articles published between 2013 and 2022 (Scopus database: lignocellulosic biomass/biofuel/pretreatment in the title/abstract/keyword of a research or review paper).

Over the past ten years, there has been a lot of interest in using LCB to produce fuels and value-added products, and therefore, a number of international patents have also been obtained, both at pilot and industrial scales. Patents provide both economic and technological information, and show the general tendency of markets. The United States, China, Japan, Germany, South Korea, France, Canada, and the United Kingdom have filed the highest number of patents related to biofuels [141].Different processes, techniques, and products have been developed and patented from time to time. Future research can be carried out on patent development technology with a focus on economic sustainability. In the coming years, the extensive and fruitful research on the bioconversion of LCB into 2G biofuels and value-added materials is expected to rise, ideally fulfilling the objectives of the lignocellulosic biorefineries.

9. Conclusions

The concept of lignocellulosic biorefinery is developed by valorizing lignocellulosic biomass and its constituent parts into value-added products and enhanced energy. Introduction of process-efficient and low-cost technologies is the most essential requirement for sustainable and renewable energy production. It not only minimizes the negative environmental impact, but also cuts down on carbon emissions. This review encompasses detailed information on the lignocellulosic biomass, processing technologies, merits, demerits, and challenges associated with a biorefinery. For forest-based biorefineries to be incorporated into industrial supply chains, a sustainable and ecologically friendly solution for the valorization of lignocellulosic biomass through cost-effective and sustainable processes must be developed.

Author Contributions: Conceptualization, V.S. and P.N.; validation, V.S., M.-L.T., C.-W.C., P.N. and C.-D.D.; formal analysis, V.S., B.K.B., M.-L.T., P.N. and C.-W.C.; investigation, V.S., B.K.B. and C.-D.D.; writing—original draft preparation, S.S. and V.S.; writing—review and editing, P.N. and V.S.; visualization, V.S., M.-L.T. and C.-D.D.; resources, M.-L.T.; supervision, M.-L.T., P.-P.S. and C.-D.D.; funding acquisition, C.-D.D. All authors have read and agreed to the published version of the manuscript.

Funding: This work was funded by Taiwan MOST for funding support (Ref. No. 109-2222-E-992-002).

Data Availability Statement: Not applicable.

Acknowledgments: Authors V.S. and P.N. gratefully acknowledge National Kaohsiung University of Science and Technology, Kaohsiung City, Taiwan, for providing the post-doctoral fellowship. Authors M.-L.T., C.-W.C. and C.-D.D. acknowledge Ministry of Science and Technology, Taiwan MOST for funding support (Ref. No. 109-2222-E-992-002).

Conflicts of Interest: The authors declare no conflict of interest.

References

1. Sharma, V.; Tsai, M.-L.; Chen, C.-W.; Sun, P.-P.; Patel, A.K.; Singhania, R.R.; Nargotra, P.; Dong, C.-D. Deep eutectic solvents as promising pretreatment agents for sustainable lignocellulosic biorefineries: A review. *Bioresour. Technol.* **2022**, *360*, 127631. [CrossRef]
2. Devi, A.; Bajar, S.; Kour, H.; Kothari, R.; Pant, D.; Singh, A. Lignocellulosic Biomass Valorization for Bioethanol Production: A Circular Bioeconomy Approach. *BioEnergy Res.* **2022**, *15*, 1820–1841. [CrossRef]
3. Sharma, V.; Tsai, M.-L.; Nargotra, P.; Chen, C.-W.; Sun, P.-P.; Singhania, R.R.; Patel, A.K.; Dong, C.-D. Journey of lignin from a roadblock to bridge for lignocellulose biorefineries: A comprehensive review. *Sci. Total. Environ.* **2022**, *863*, 160560. [CrossRef]
4. Sharma, V.; Tsai, M.-L.; Nargotra, P.; Chen, C.-W.; Kuo, C.-H.; Sun, P.-P.; Dong, C.-D. Agro-Industrial Food Waste as a Low-Cost Substrate for Sustainable Production of Industrial Enzymes: A Critical Review. *Catalysts* **2022**, *12*, 1373. [CrossRef]
5. Weng, Z.-H.; Nargotra, P.; Kuo, C.-H.; Liu, Y.-C. Immobilization of Recombinant Endoglucanase (CelA) from *Clostridium thermocellum* on Modified Regenerated Cellulose Membrane. *Catalysts* **2022**, *12*, 1356. [CrossRef]
6. Periyasamy, S.; Isabel, J.B.; Kavitha, S.; Karthik, V.; Mohamed, B.A.; Gizaw, D.G.; Sivashanmugam, P.; Aminabhavi, T.M. Recent advances in consolidated bioprocessing for conversion of lignocellulosic biomass into bioethanol—A review. *Chem. Eng. J.* **2022**, *453*, 139783. [CrossRef]
7. Hassan, S.S.; Williams, G.A.; Jaiswal, A.K. Emerging technologies for the pretreatment of lignocellulosic biomass. *Bioresour. Technol.* **2018**, *262*, 310–318. [CrossRef]

8. Razzak, S.A.; Lucky, R.A.; Hossain, M.M.; Delasa, H. Valorization of Microalgae Biomass to Biofuel Production: A review. *Energy Nexus* **2022**, *7*, 100139. [CrossRef]
9. Sharma, V.; Nargotra, P.; Sharma, S.; Bajaj, B.K. Efficacy and functional mechanisms of a novel combinatorial pretreatment approach based on deep eutectic solvent and ultrasonic waves for bioconversion of sugarcane bagasse. *Renew. Energy* **2020**, *163*, 1910–1922. [CrossRef]
10. Sharma, V.; Nargotra, P.; Sharma, S.; Bajaj, B.K. Efficient bioconversion of sugarcane tops biomass into biofuel-ethanol using an optimized alkali-ionic liquid pretreatment approach. *Biomass Convers. Biorefin.* **2020**, *10*, 1–14. [CrossRef]
11. Sharma, V.; Bhat, B.; Gupta, M.; Vaid, S.; Sharma, S.; Nargotra, P.; Singh, S.; Bajaj, B.K. Role of Systematic Biology in Biorefining of Lignocellulosic Residues for Biofuels and Chemicals Production. In *Sustainable Biotechnology—Enzymatic Resources of Renewable Energy*; Singh, O.V., Chandel, A.K., Eds.; Springer International Publishing: Cham, Switzerland, 2018; pp. 5–55; ISBN 978-3-319-95480-6.
12. Banu, J.R.; Preethi; Kavitha, S.; Tyagi, V.K.; Gunasekaran, M.; Karthikeyan, O.P.; Kumar, G. Lignocellulosic biomass based biorefinery: A successful platform towards circular bioeconomy. *Fuel* **2021**, *302*, 121086. [CrossRef]
13. Vu, H.P.; Nguyen, L.N.; Vu, M.T.; Johir, M.A.H.; McLaughlan, R.; Nghiem, L.D. A comprehensive review on the framework to valorise lignocellulosic biomass as biorefinery feedstocks. *Sci. Total Environ.* **2020**, *743*, 140630. [CrossRef]
14. Sharma, S.; Nargotra, P.; Sharma, V.; Bangotra, R.; Kaur, M.; Kapoor, N.; Paul, S.; Bajaj, B.K. Nanobiocatalysts for efficacious bioconversion of ionic liquid pretreated sugarcane tops biomass to biofuel. *Bioresour. Technol.* **2021**, *333*, 125191. [CrossRef]
15. Nargotra, P.; Sharma, V.; Bajaj, B.K. Consolidated bioprocessing of surfactant-assisted ionic liquid-pretreated *Parthenium hysterophorus* L. biomass for bioethanol production. *Bioresour. Technol.* **2019**, *289*, 121611. [CrossRef]
16. Nargotra, P.; Sharma, V.; Sharma, S.; Kapoor, N.; Bajaj, B.K. Development of consolidated bioprocess for biofuel-ethanol production from ultrasound-assisted deep eutectic solvent pretreated *Parthenium hysterophorus* biomass. *Biomass Convers. Biorefin.* **2020**, *12*, 5767–5782. [CrossRef]
17. Vaid, S.; Nargotra, P.; Bajaj, B.K. Consolidated bioprocessing for biofuel-ethanol production from pine needle biomass. *Environ. Prog. Sustain. Energy* **2018**, *37*, 546–552. [CrossRef]
18. Sharma, V.; Nargotra, P.; Bajaj, B.K. Ultrasound and surfactant assisted ionic liquid pretreatment of sugarcane bagasse for enhancing saccharification using enzymes from an ionic liquid tolerant *Aspergillus assiutensis* VS34. *Bioresour. Technol.* **2019**, *285*, 121319. [CrossRef]
19. Vaid, S.; Bhat, N.; Nargotra, P.; Bajaj, B.K. Combinatorial application of ammonium carbonate and sulphuric acid pretreatment to achieve enhanced sugar yield from pine needle biomass for potential biofuel–ethanol production. *Energy Ecol. Environ.* **2018**, *3*, 126–135. [CrossRef]
20. Hazeena, S.H.; Sindhu, R.; Pandey, A.; Binod, P. Lignocellulosic bio-refinery approach for microbial 2,3-Butanediol production. *Bioresour. Technol.* **2020**, *302*, 122873. [CrossRef]
21. Sharma, H.K.; Xu, C.; Qin, W. Biological Pretreatment of Lignocellulosic Biomass for Biofuels and Bioproducts: An Overview. *Waste Biomass Valoriz.* **2019**, *10*, 235–251. [CrossRef]
22. Kumar, B.; Bhardwaj, N.; Agrawal, K.; Chaturvedi, V.; Verma, P. Current perspective on pretreatment technologies using lignocellulosic biomass: An emerging biorefinery concept. *Fuel Process. Technol.* **2020**, *199*, 106244. [CrossRef]
23. Haq, I.U.; Qaisar, K.; Nawaz, A.; Akram, F.; Mukhtar, H.; Zohu, X.; Xu, Y.; Mumtaz, M.W.; Rashid, U.; Ghani, W.A.W.A.K.; et al. Advances in Valorization of Lignocellulosic Biomass towards Energy Generation. *Catalysts* **2021**, *11*, 309. [CrossRef]
24. Kumar, V.; Patel, S.K.S.; Gupta, R.K.; Otari, S.V.; Gao, H.; Lee, J.; Zhang, L. Enhanced Saccharification and Fermentation of Rice Straw by Reducing the Concentration of Phenolic Compounds Using an Immobilized Enzyme Cocktail. *Biotechnol. J.* **2019**, *14*, e1800468. [CrossRef] [PubMed]
25. Manisha; Yadav, S.K. Technological advances and applications of hydrolytic enzymes for valorization of lignocellulosic biomass. *Bioresour. Technol.* **2017**, *245*, 1727–1739. [CrossRef] [PubMed]
26. Wicker, R.J.; Kumar, G.; Khan, E.; Bhatnagar, A. Emergent green technologies for cost-effective valorization of microalgal biomass to renewable fuel products under a biorefinery scheme. *Chem. Eng. J.* **2021**, *415*, 128932. [CrossRef]
27. Toor, M.; Kumar, S.S.; Malyan, S.K.; Bishnoi, N.R.; Mathimani, T.; Rajendran, K.; Pugazhendhi, A. An overview on bioethanol production from lignocellulosic feedstocks. *Chemosphere* **2020**, *242*, 125080. [CrossRef]
28. Elegbede, J.; Ajayi, V.; Lateef, A. Microbial valorization of corncob: Novel route for biotechnological products for sustainable bioeconomy. *Environ. Technol. Innov.* **2021**, *24*, 102073. [CrossRef]
29. Awasthi, M.K.; Sarsaiya, S.; Patel, A.; Juneja, A.; Singh, R.P.; Yan, B.; Awasthi, S.K.; Jain, A.; Liu, T.; Duan, Y.; et al. Refining biomass residues for sustainable energy and bio-products: An assessment of technology, its importance, and strategic applications in circular bio-economy. *Renew. Sustain. Energy Rev.* **2020**, *127*, 109876. [CrossRef]
30. Velvizhi, G.; Balakumar, K.; Shetti, N.P.; Ahmad, E.; Pant, K.K.; Aminabhavi, T.M. Integrated biorefinery processes for conversion of lignocellulosic biomass to value added materials: Paving a path towards circular economy. *Bioresour. Technol.* **2022**, *343*, 126151. [CrossRef]
31. A Linares-Pasten, J.; Andersson, M.; NKarlsson, E. Thermostable Glycoside Hydrolases in Biorefinery Technologies. *Cur. Biotechnol.* **2014**, *3*, 26–44. [CrossRef]
32. Jin, Q.; Yang, L.; Poe, N.; Huang, H. Integrated processing of plant-derived waste to produce value-added products based on the biorefinery concept. *Trends Food Sci. Technol.* **2018**, *74*, 119–131. [CrossRef]

33. Vaid, S.; Sharma, S.; Bajaj, B.K. Chemo-enzymatic approaches for consolidated bioconversion of Saccharum spontaneum biomass to ethanol-biofuel. *Bioresour. Technol.* **2021**, *329*, 124898. [CrossRef]
34. Wagle, A.; Angove, M.J.; Mahara, A.; Wagle, A.; Mainali, B.; Martins, M.; Goldbeck, R.; Paudel, S.R. Multi-stage pre-treatment of lignocellulosic biomass for multi-product biorefinery: A review. *Sustain. Energy Technol. Assess.* **2022**, *49*, 101702. [CrossRef]
35. Nargotra, P.; Sharma, V.; Gupta, M.; Kour, S.; Bajaj, B.K. Application of ionic liquid and alkali pretreatment for enhancing saccharification of sunflower stalk biomass for potential biofuel-ethanol production. *Bioresour. Technol.* **2018**, *267*, 560–568. [CrossRef]
36. Houfani, A.A.; Anders, N.; Spiess, A.C.; Baldrian, P.; Benallaoua, S. Insights from enzymatic degradation of cellulose and hemicellulose to fermentable sugars—A review. *Biomass Bioenergy* **2020**, *134*, 105481. [CrossRef]
37. Alayoubi, R.; Mehmood, N.; Husson, E.; Kouzayha, A.; Tabcheh, M.; Chaveriat, L.; Sarazin, C.; Gosselin, I. Low temperature ionic liquid pretreatment of lignocellulosic biomass to enhance bioethanol yield. *Renew. Energy* **2020**, *145*, 1808–1816. [CrossRef]
38. Li, H.-Y.; Chen, X.; Wang, C.-Z.; Sun, S.-N.; Sun, R.-C. Evaluation of the two-step treatment with ionic liquids and alkali for enhancing enzymatic hydrolysis of Eucalyptus: Chemical and anatomical changes. *Biotechnol. Biofuels* **2016**, *9*, 166. [CrossRef]
39. Kohli, K.; Katuwal, S.; Biswas, A.; Sharma, B.K. Effective delignification of lignocellulosic biomass by microwave assisted deep eutectic solvents. *Bioresour. Technol.* **2020**, *303*, 122897. [CrossRef]
40. Zulkefli, S.; Abdulmalek, E.; Rahman, M.B.A. Pretreatment of oil palm trunk in deep eutectic solvent and optimization of enzymatic hydrolysis of pretreated oil palm trunk. *Renew. Energy* **2017**, *107*, 36–41. [CrossRef]
41. Haykir, N.I.; Soysal, K.; Yaglikci, S.; Gokce, Y. Assessing the effect of protic ionic liquid pretreatment of *Pinus radiata* from different perspectives including solvent-water ratio. *J. Wood Chem. Technol.* **2021**, *41*, 236–248. [CrossRef]
42. Klímek, P.; Meinlschmidt, P.; Wimmer, R.; Plinke, B.; Schirp, A. Using sunflower (*Helianthus annuus* L.), topinambour (*Helianthus tuberosus* L.) and cup-plant (*Silphium perfoliatum* L.) stalks as alternative raw materials for particleboards. *Ind. Crop. Prod.* **2016**, *92*, 157–164. [CrossRef]
43. Paul, S.K.; Chakraborty, S. Microwave-assisted ionic liquid-mediated rapid catalytic conversion of non-edible lignocellulosic Sunn hemp fibres to biofuels. *Bioresour. Technol.* **2018**, *253*, 85–93. [CrossRef] [PubMed]
44. Fakayode, O.A.; Akpabli-Tsigbe, N.D.K.; Wahia, H.; Tu, S.; Ren, M.; Zhou, C.; Ma, H. Integrated bioprocess for bio-ethanol production from watermelon rind biomass: Ultrasound-assisted deep eutectic solvent pretreatment, enzymatic hydrolysis and fermentation. *Renew. Energy* **2021**, *180*, 258–270. [CrossRef]
45. Ge, S.; Wu, Y.; Peng, W.; Xia, C.; Mei, C.; Cai, L.; Shi, S.Q.; Sonne, C.; Lam, S.S.; Tsang, Y.F. High-pressure CO_2 hydrothermal pretreatment of peanut shells for enzymatic hydrolysis conversion into glucose. *Chem. Eng. J.* **2020**, *385*, 123949. [CrossRef]
46. Łukajtis, R.; Rybarczyk, P.; Kucharska, K.; Konopacka-Łyskawa, D.; Słupek, E.; Wychodnik, K.; Kamiński, M. Optimization of Saccharification Conditions of Lignocellulosic Biomass under Alkaline Pre-Treatment and Enzymatic Hydrolysis. *Energies* **2018**, *11*, 886. [CrossRef]
47. Oliva, J.M.; Negro, M.J.; Manzanares, P.; Ballesteros, I.; Chamorro, M.Á.; Sáez, F.; Ballesteros, M.; Moreno, A.D. A Sequential Steam Explosion and Reactive Extrusion Pretreatment for Lignocellulosic Biomass Conversion within a Fermentation-Based Biorefinery Perspective. *Fermentation* **2017**, *3*, 15. [CrossRef]
48. Park, S.H.; Pham, T.T.H.; Kim, T.H. Effects of Additional Xylanase on Saccharification and Ethanol Fermentation of Ammonia-Pretreated Corn Stover and Rice Straw. *Energies* **2020**, *13*, 4574. [CrossRef]
49. Hoang, A.T.; Ong, H.C.; Fattah, I.M.R.; Chong, C.T.; Cheng, C.K.; Sakthivel, R.; Ok, Y.S. Progress on the lignocellulosic biomass pyrolysis for biofuel production toward environmental sustainability. *Fuel Process. Technol.* **2021**, *223*, 106997. [CrossRef]
50. Siqueira, J.G.W.; Rodrigues, C.; Vandenberghe, L.P.D.S.; Woiciechowski, A.L.; Soccol, C.R. Current advances in on-site cellulase production and application on lignocellulosic biomass conversion to biofuels: A review. *Biomass Bioenergy* **2020**, *132*, 105419. [CrossRef]
51. Okolie, J.A.; Nanda, S.; Dalai, A.K.; Kozinski, J.A. Chemistry and Specialty Industrial Applications of Lignocellulosic Biomass. *Waste Biomass Valoriz.* **2021**, *12*, 2145–2169. [CrossRef]
52. Haldar, D.; Dey, P.; Patel, A.K.; Dong, C.-D.; Singhania, R.R. A Critical Review on the Effect of Lignin Redeposition on Biomass in Controlling the Process of Enzymatic Hydrolysis. *BioEnergy Res.* **2022**, *15*, 863–874. [CrossRef]
53. Hasanov, I.; Raud, M.; Kikas, T. The Role of Ionic Liquids in the Lignin Separation from Lignocellulosic Biomass. *Energies* **2020**, *13*, 4864. [CrossRef]
54. Lobato-Peralta, D.R.; Duque-Brito, E.; Villafán-Vidales, H.I.; Longoria, A.; Sebastian, P.; Cuentas-Gallegos, A.K.; Arancibia-Bulnes, C.A.; Okoye, P.U. A review on trends in lignin extraction and valorization of lignocellulosic biomass for energy applications. *J. Clean. Prod.* **2021**, *293*, 126123. [CrossRef]
55. Singhania, R.R.; Patel, A.K.; Raj, T.; Chen, C.-W.; Ponnusamy, V.K.; Tahir, N.; Kim, S.-H.; Dong, C.-D. Lignin valorisation via enzymes: A sustainable approach. *Fuel* **2022**, *311*, 122608. [CrossRef]
56. Nanda, S.; Mohanty, P.; Pant, K.K.; Naik, S.; Kozinski, J.A.; Dalai, A.K. Characterization of North American Lignocellulosic Biomass and Biochars in Terms of their Candidacy for Alternate Renewable Fuels. *BioEnergy Res.* **2013**, *6*, 663–677. [CrossRef]
57. Vassilev, S.V.; Baxter, D.; Andersen, L.K.; Vassileva, C.G.; Morgan, T.J. An overview of the organic and inorganic phase composition of biomass. *Fuel* **2012**, *94*, 1–33. [CrossRef]
58. Yoo, C.G.; Meng, X.; Pu, Y.; Ragauskas, A.J. The critical role of lignin in lignocellulosic biomass conversion and recent pretreatment strategies: A comprehensive review. *Bioresour. Technol.* **2020**, *301*, 122784. [CrossRef]

59. Bhatia, S.K.; Jagtap, S.S.; Bedekar, A.A.; Bhatia, R.K.; Patel, A.K.; Pant, D.; Banu, J.R.; Rao, C.V.; Kim, Y.-G.; Yang, Y.-H. Recent developments in pretreatment technologies on lignocellulosic biomass: Effect of key parameters, technological improvements, and challenges. *Bioresour. Technol.* **2020**, *300*, 122724. [CrossRef]
60. Jatoi, A.S.; Abbasi, S.A.; Hashmi, Z.; Shah, A.K.; Alam, M.S.; Bhatti, Z.A.; Maitlo, G.; Hussain, S.; Khandro, G.A.; Usto, M.A.; et al. Recent trends and future perspectives of lignocellulose biomass for biofuel production: A comprehensive review. *Biomass Convers. Biorefin.* **2021**, *11*, 1–13. [CrossRef]
61. Nargotra, P.; Vaid, S.; Bajaj, B.K. Cellulase Production from Bacillus subtilis SV1 and Its Application Potential for Saccharification of Ionic Liquid Pretreated Pine Needle Biomass under One Pot Consolidated Bioprocess. *Fermentation* **2016**, *2*, 19. [CrossRef]
62. Mankar, A.R.; Pandey, A.; Modak, A.; Pant, K. Pretreatment of lignocellulosic biomass: A review on recent advances. *Bioresour. Technol.* **2021**, *334*, 125235. [CrossRef] [PubMed]
63. Srivastava, N.; Rawat, R.; Oberoi, H.S.; Ramteke, P.W. A Review on Fuel Ethanol Production From Lignocellulosic Biomass. *Int. J. Green Energy* **2015**, *12*, 949–960. [CrossRef]
64. He, Z.; Wang, Z.; Zhao, Z.; Yi, S.; Mu, J.; Wang, X. Influence of ultrasound pretreatment on wood physiochemical structure. *Ultrason. Sonochem.* **2017**, *34*, 136–141. [CrossRef] [PubMed]
65. Subhedar, P.B.; Ray, P.; Gogate, P.R. Intensification of delignification and subsequent hydrolysis for the fermentable sugar production from lignocellulosic biomass using ultrasonic irradiation. *Ultrason. Sonochem.* **2018**, *40*, 140–150. [CrossRef] [PubMed]
66. Kunaver, M.; Jasiukaitytė, E.; Čuk, N. Ultrasonically assisted liquefaction of lignocellulosic materials. *Bioresour. Technol.* **2012**, *103*, 360–366. [CrossRef] [PubMed]
67. Haldar, D.; Purkait, M.K. A review on the environment-friendly emerging techniques for pretreatment of lignocellulosic biomass: Mechanistic insight and advancements. *Chemosphere* **2021**, *264*, 128523. [CrossRef] [PubMed]
68. Hoang, A.T.; Nižetić, S.; Ong, H.C.; Mofijur, M.; Ahmed, S.; Ashok, B.; Bui, V.T.V.; Chau, M.Q. Insight into the recent advances of microwave pretreatment technologies for the conversion of lignocellulosic biomass into sustainable biofuel. *Chemosphere* **2021**, *281*, 130878. [CrossRef]
69. Nuchdang, S.; Thongtus, V.; Khemkhao, M.; Kirdponpattara, S.; Moore, E.J.; Setiabudi, H.D.B.; Phalakornkule, C. Enhanced production of reducing sugars from paragrass using microwave-assisted alkaline pretreatment. *Biomass Convers. Biorefin.* **2021**, *11*, 2471–2483. [CrossRef]
70. Kainthola, J.; Shariq, M.; Kalamdhad, A.; Goud, V.V. Enhanced methane potential of rice straw with microwave assisted pretreatment and its kinetic analysis. *J. Environ. Manag.* **2019**, *232*, 188–196. [CrossRef]
71. Zhu, Z.; Liu, Y.; Yang, X.; McQueen-Mason, S.J.; Gomez, L.D.; Macquarrie, D.J. Comparative evaluation of microwave-assisted acid, alkaline, and inorganic salt pretreatments of sugarcane bagasse for sugar recovery. *Biomass Convers. Biorefin.* **2021**, *11*, 2681–2693. [CrossRef]
72. Kundu, C.; Samudrala, S.P.; Kibria, M.A.; Bhattacharya, S. One-step peracetic acid pretreatment of hardwood and softwood biomass for platform chemicals production. *Sci. Rep.* **2021**, *11*, 11183. [CrossRef]
73. Morais, W.G.; Pacheco, T.F.; Corrêa, P.S.; Martins, A.A.; Mata, T.M.; Caetano, N.S. Acid pretreatment of sugarcane biomass to obtain hemicellulosic hydrolisate rich in fermentable sugar. *Energy Rep.* **2020**, *6*, 18–23. [CrossRef]
74. Mehrez, I.; Chandrasekhar, K.; Kim, W.; Kim, S.-H.; Kumar, G. Comparison of alkali and ionic liquid pretreatment methods on the biochemical methane potential of date palm waste biomass. *Bioresour. Technol.* **2022**, *360*, 127505. [CrossRef]
75. Goshadrou, A. Bioethanol production from Cogongrass by sequential recycling of black liquor and wastewater in a mild-alkali pretreatment. *Fuel* **2019**, *258*, 116141. [CrossRef]
76. Woiciechowski, A.L.; Neto, C.J.D.; de Souza Vandenberghe, L.P.; de Carvalho Neto, D.P.; Sydney, A.C.N.; Letti, L.A.J.; Karp, S.G.; Torres, L.A.Z.; Soccol, C.R. Lignocellulosic biomass: Acid and alkaline pretreatments and their effects on biomass recalcitrance—Conventional processing and recent advances. *Bioresour. Technol.* **2020**, *304*, 122848. [CrossRef]
77. Dotsenko, A.S.; Dotsenko, G.S.; Senko, O.V.; Stepanov, N.A.; Lyagin, I.V.; Efremenko, E.N.; Gusakov, A.V.; Zorov, I.N.; Rubtsova, E.A. Complex effect of lignocellulosic biomass pretreatment with 1-butyl-3-methylimidazolium chloride ionic liquid on various aspects of ethanol and fumaric acid production by immobilized cells within SSF. *Bioresour. Technol.* **2018**, *250*, 429–438. [CrossRef]
78. Lim, W.-L.; Gunny, A.A.N.; Kasim, F.H.; AlNashef, I.M.; Arbain, D. Alkaline deep eutectic solvent: A novel green solvent for lignocellulose pulping. *Cellulose* **2019**, *26*, 4085–4098. [CrossRef]
79. Amesho, K.T.T.; Lin, Y.-C.; Mohan, S.V.; Halder, S.; Ponnusamy, V.K.; Jhang, S.-R. Deep eutectic solvents in the transformation of biomass into biofuels and fine chemicals: A review. *Environ. Chem. Lett.* **2022**, *20*, 1–48. [CrossRef]
80. Jing, Y.; Li, F.; Li, Y.; Jiang, D.; Lu, C.; Zhang, Z.; Zhang, Q. Biohydrogen production by deep eutectic solvent delignification-driven enzymatic hydrolysis and photo-fermentation: Effect of liquid–solid ratio. *Bioresour. Technol.* **2022**, *349*, 126867. [CrossRef]
81. Tan, Y.T.; Ngoh, G.C.; Chua, A.S.M. Effect of functional groups in acid constituent of deep eutectic solvent for extraction of reactive lignin. *Bioresour. Technol.* **2019**, *281*, 359–366. [CrossRef]
82. Thi, S.; Lee, K.M. Comparison of deep eutectic solvents (DES) on pretreatment of oil palm empty fruit bunch (OPEFB): Cellulose digestibility, structural and morphology changes. *Bioresour. Technol.* **2019**, *282*, 525–529. [CrossRef] [PubMed]
83. Vaidya, A.A.; Murton, K.D.; Smith, D.A.; Dedual, G. A review on organosolv pretreatment of softwood with a focus on enzymatic hydrolysis of cellulose. *Biomass Convers. Biorefin.* **2022**, *12*, 5427–5442. [CrossRef]
84. Borand, M.N.; Karaosmanoğlu, F. Effects of organosolv pretreatment conditions for lignocellulosic biomass in biorefinery applications: A review. *J. Renew. Sustain. Energy* **2018**, *10*, 033104. [CrossRef]

85. Karnaouri, A.; Asimakopoulou, G.; Kalogiannis, K.G.; Lappas, A.; Topakas, E. Efficient d-lactic acid production by Lactobacillus delbrueckii subsp. bulgaricus through conversion of organosolv pretreated lignocellulosic biomass. *Biomass Bioenergy* **2020**, *140*, 105672. [CrossRef]
86. Joy, S.P.; Krishnan, C. Modified organosolv pretreatment for improved cellulosic ethanol production from sorghum biomass. *Ind. Crop. Prod.* **2022**, *177*, 114409. [CrossRef]
87. Tang, C.; Shan, J.; Chen, Y.; Zhong, L.; Shen, T.; Zhu, C.; Ying, H. Organic amine catalytic organosolv pretreatment of corn stover for enzymatic saccharification and high-quality lignin. *Bioresour. Technol.* **2017**, *232*, 222–228. [CrossRef] [PubMed]
88. Li, X.; Shi, Y.; Kong, W.; Wei, J.; Song, W.; Wang, S. Improving enzymatic hydrolysis of lignocellulosic biomass by bio-coordinated physicochemical pretreatment—A review. *Energy Rep.* **2022**, *8*, 696–709. [CrossRef]
89. Mockaitis, G.; Bruant, G.; Foresti, E.; Zaiat, M.; Guiot, S.R. Physicochemical pretreatment selects microbial communities to produce alcohols through metabolism of volatile fatty acids. *Biomass Convers. Biorefin.* **2022**, *12*, 1–15. [CrossRef]
90. Raud, M.; Kikas, T.; Sippula, O.; Shurpali, N. Potentials and challenges in lignocellulosic biofuel production technology. *Renew. Sustain. Energy Rev.* **2019**, *111*, 44–56. [CrossRef]
91. Kuglarz, M.; Gunnarsson, I.B.; Svensson, S.-E.; Prade, T.; Johansson, E.; Angelidaki, I. Ethanol production from industrial hemp: Effect of combined dilute acid/steam pretreatment and economic aspects. *Bioresour. Technol.* **2014**, *163*, 236–243. [CrossRef]
92. Vaid, S.; Sharma, S.; Dutt, H.C.; Mahajan, R.; Bajaj, B.K. One pot consolidated bioprocess for conversion of *Saccharum spontaneum* biomass to ethanol-biofuel. *Energy Convers. Manag.* **2021**, *250*, 114880. [CrossRef]
93. Hou, X.; Wang, Z.; Sun, J.; Li, M.; Wang, S.; Chen, K.; Gao, Z. A microwave-assisted aqueous ionic liquid pretreatment to enhance enzymatic hydrolysis of Eucalyptus and its mechanism. *Bioresour. Technol.* **2019**, *272*, 99–104. [CrossRef]
94. Hosseini Koupaie, E.; Dahadha, S.; Bazyar Lakeh, A.A.; Azizi, A.; Elbeshbishy, E. Enzymatic pretreatment of lignocellulosic biomass for enhanced biomethane production—A review. *J. Environ. Manag.* **2019**, *233*, 774–784. [CrossRef]
95. Prasad, R.K.; Chatterjee, S.; Mazumder, P.B.; Gupta, S.K.; Sharma, S.; Vairale, M.G.; Datta, S.; Dwivedi, S.K.; Gupta, D.K. Bioethanol production from waste lignocelluloses: A review on microbial degradation potential. *Chemosphere* **2019**, *231*, 588–606. [CrossRef]
96. Ni Sun, S.; Chen, X.; Tao, Y.H.; Cao, X.F.; Li, M.F.; Wen, J.L.; Nie, S.X.; Sun, R.C. Pretreatment of Eucalyptus urophylla in γ-valerolactone/dilute acid system for removal of non-cellulosic components and acceleration of enzymatic hydrolysis. *Ind. Crop. Prod.* **2019**, *132*, 21–28. [CrossRef]
97. Jiang, D.; Ge, X.; Zhang, T.; Chen, Z.; Zhang, Z.; He, C.; Zhang, Q.; Li, Y. Effect of alkaline pretreatment on photo-fermentative hydrogen production from giant reed: Comparison of NaOH and $Ca(OH)_2$. *Bioresour. Technol.* **2020**, *304*, 123001. [CrossRef]
98. Das, L.; Achinivu, E.C.; Barcelos, C.A.; Sundstrom, E.; Amer, B.; Baidoo, E.E.K.; Simmons, B.A.; Sun, N.; Gladden, J.M. Deconstruction of Woody Biomass via Protic and Aprotic Ionic Liquid Pretreatment for Ethanol Production. *ACS Sustain. Chem. Eng.* **2021**, *9*, 4422–4432. [CrossRef]
99. Smuga-Kogut, M.; Szymanowska-Powałowska, D.; Markiewicz, R.; Piskier, T.; Kogut, T. Ionic liquid pretreatment of stinging nettle stems and giant miscanthus for bioethanol production. *Sci. Rep.* **2021**, *11*, 18465. [CrossRef]
100. Manivannan, H.; Anguraj, B.L. Valorization of fruit waste using DES pretreatment and hydrolysis over a heterogeneous catalyst for bioethanol production. *Biomass Convers. Biorefin.* **2021**, *11*, 1–11. [CrossRef]
101. Zhang, W.; Liu, J.; Wang, Y.; Sun, J.; Huang, P.; Chang, K. Effect of ultrasound on ionic liquid-hydrochloric acid pretreatment with rice straw. *Biomass Convers. Biorefin.* **2021**, *11*, 1749–1757. [CrossRef]
102. Roth, J.C.G.; Hoeltz, M.; Benitez, L.B. Current approaches and trends in the production of microbial cellulases using residual lignocellulosic biomass: A bibliometric analysis of the last 10 years. *Arch. Microbiol.* **2020**, *202*, 935–951. [CrossRef] [PubMed]
103. Sharma, S.; Sharma, V.; Nargotra, P.; Bajaj, B.K. Process desired functional attributes of an endoxylanase of GH10 family from a new strain of *Aspergillus terreus* S9. *Int. J. Biol. Macromol.* **2018**, *115*, 663–671. [CrossRef] [PubMed]
104. Sharma, S.; Sharma, V.; Nargotra, P.; Bajaj, B.K. Bioprocess development for production of a process-apt xylanase with multifaceted application potential for a range of industrial processes. *SN Appl. Sci.* **2020**, *2*, 739. [CrossRef]
105. Madadi, M.; Tu, Y.; Abbas, A. Recent Status on Enzymatic Saccharification of Lignocellulosic Biomass for Bioethanol Production. *Electron J. Biotechnol.* **2017**, *13*, 135–143.
106. Alokika; Singh, B. Enhanced production of bacterial xylanase and its utility in saccharification of sugarcane bagasse. *Bioprocess Biosyst. Eng.* **2020**, *43*, 1081–1091. [CrossRef]
107. Cui, L.; Wang, Z.; Zeng, Y.; Yang, N.; Liu, M.; Zhao, Y.; Zheng, Y. Lignin Biodegradation and Its Valorization. *Fermentation* **2022**, *8*, 366. [CrossRef]
108. Obeng, E.M.; Budiman, C.; Ongkudon, C.M. Identifying additives for cellulase enhancement—A systematic approach. *Biocatal. Agric. Biotechnol.* **2017**, *11*, 67–74. [CrossRef]
109. Cai, C.; Qiu, X.; Zeng, M.; Lin, M.; Lin, X.; Lou, H.; Zhan, X.; Pang, Y.; Huang, J.; Xie, L. Using polyvinylpyrrolidone to enhance the enzymatic hydrolysis of lignocelluloses by reducing the cellulase non-productive adsorption on lignin. *Bioresour. Technol.* **2017**, *227*, 74–81. [CrossRef]
110. Rocha-Martín, J.; Martinez-Bernal, C.; Pérez-Cobas, Y.; Reyes-Sosa, F.M.; García, B.D. Additives enhancing enzymatic hydrolysis of lignocellulosic biomass. *Bioresour. Technol.* **2017**, *244*, 48–56. [CrossRef]
111. Rai, M.; Ingle, A.P.; Pandit, R.; Paralikar, P.; Biswas, J.K.; Da Silva, S.S. Emerging role of nanobiocatalysts in hydrolysis of lignocellulosic biomass leading to sustainable bioethanol production. *Catal. Rev.* **2019**, *61*, 1–26. [CrossRef]

112. Grewal, J.; Ahmad, R.; Khare, S. Development of cellulase-nanoconjugates with enhanced ionic liquid and thermal stability for in situ lignocellulose saccharification. *Bioresour. Technol.* **2017**, *242*, 236–243. [CrossRef]
113. Cheng, G.; Xing, J.; Pi, Z.; Liu, S.; Liu, Z.; Song, F. α-Glucosidase immobilization on functionalized Fe_3O_4 magnetic nanoparticles for screening of enzyme inhibitors. *Chin. Chem. Lett.* **2019**, *30*, 656–659. [CrossRef]
114. Hossain, N.; Mahlia, T.M.I.; Saidur, R. Latest development in microalgae-biofuel production with nano-additives. *Biotechnol. Biofuels* **2019**, *12*, 125. [CrossRef]
115. Karnaouri, A.; Muraleedharan, M.N.; Dimarogona, M.; Topakas, E.; Rova, U.; Sandgren, M.; Christakopoulos, P. Recombinant expression of thermostable processive MtEG5 endoglucanase and its synergism with MtLPMO from Myceliophthora thermophila during the hydrolysis of lignocellulosic substrates. *Biotechnol. Biofuels* **2017**, *10*, 126. [CrossRef]
116. Vijayalakshmi, S.; Govindarajan, M.; Al-Mulahim, N.; Ahmed, Z.; Mahboob, S. Cellulase immobilized magnetic nanoparticles for green energy production from *Allamanda schottii* L.: Sustainability research in waste recycling. *Saudi J. Biol. Sci.* **2021**, *28*, 901–910. [CrossRef]
117. Hwangbo, M.; Tran, J.L.; Chu, K.-H. Effective one-step saccharification of lignocellulosic biomass using magnetite-biocatalysts containing saccharifying enzymes. *Sci. Total Environ.* **2019**, *647*, 806–813. [CrossRef]
118. Yan, J. *Handbook of Clean Energy Systems*; 6 Volume Set; John Wiley & Sons: Hoboken, NJ, USA, 2015; ISBN 978-1-118-38858-7.
119. Sharma, S.; Sharma, P.; Sharma, V.; Bajaj, B.K. Polyhydroxybutyrate as an Eco-Friendly Alternative of Synthetic Plastics. In *Environmental and Agricultural Microbiology*; John Wiley & Sons: Hoboken, NJ, USA, 2021; pp. 101–149; ISBN 978-1-119-52589-9.
120. Azhar, S.H.M.; Abdulla, R.; Jambo, S.A.; Marbawi, H.; Gansau, J.A.; Faik, A.A.M.; Rodrigues, K.F. Yeasts in sustainable bioethanol production: A review. *Biochem. Biophys. Rep.* **2017**, *10*, 52–61. [CrossRef]
121. Ramachandra, T.; Hebbale, D. Bioethanol from macroalgae: Prospects and challenges. *Renew. Sustain. Energy Rev.* **2020**, *117*, 109479. [CrossRef]
122. Hossain, S.; Theodoropoulos, C.; Yousuf, A. Techno-economic evaluation of heat integrated second generation bioethanol and furfural coproduction. *Biochem. Eng. J.* **2019**, *144*, 89–103. [CrossRef]
123. Ayodele, B.V.; Alsaffar, M.A.; Mustapa, S.I. An overview of integration opportunities for sustainable bioethanol production from first- and second-generation sugar-based feedstocks. *J. Clean. Prod.* **2020**, *245*, 118857. [CrossRef]
124. Jin, Y.; Shi, Z.; Xu, G.; Yang, H.; Yang, J. A stepwise pretreatment of sugarcane bagasse by alkaline and hydroxymethyl reagent for bioethanol production. *Ind. Crop. Prod.* **2020**, *145*, 112136. [CrossRef]
125. Wang, H.; Peng, X.; Zhang, H.; Yang, S.; Li, H. Microorganisms-promoted biodiesel production from biomass: A review. *Energy Convers. Manag. X* **2021**, *12*, 100137. [CrossRef]
126. Yusuf, N.; Kamarudin, S.; Yaakub, Z. Overview on the current trends in biodiesel production. *Energy Convers. Manag.* **2011**, *52*, 2741–2751. [CrossRef]
127. Wang, H.; Rehman, K.U.; Liu, X.; Yang, Q.; Zheng, L.; Li, W.; Cai, M.; Li, Q.; Zhang, J.; Yu, Z. Insect biorefinery: A green approach for conversion of crop residues into biodiesel and protein. *Biotechnol. Biofuels* **2017**, *10*, 304. [CrossRef]
128. Bateni, H.; Karimi, K. Biodiesel production from castor plant integrating ethanol production via a biorefinery approach. *Chem. Eng. Res. Des.* **2016**, *107*, 4–12. [CrossRef]
129. Preethi; Banu, J.R.; Kavitha, S.; Kannah, R.Y.; Varjani, S.; Gunasekaran, M. Mild hydrogen peroxide interceded bacterial disintegration of waste activated sludge for efficient biomethane production. *Sci. Total Environ.* **2022**, *817*, 152873. [CrossRef]
130. Okolie, J.A.; Mukherjee, A.; Nanda, S.; Dalai, A.K.; Kozinski, J.A. Next-generation biofuels and platform biochemicals from lignocellulosic biomass. *Int. J. Energy Res.* **2021**, *45*, 14145–14169. [CrossRef]
131. Kohli, K.; Prajapati, R.; Sharma, B.K. Bio-Based Chemicals from Renewable Biomass for Integrated Biorefineries. *Energies* **2019**, *12*, 233. [CrossRef]
132. Gandini, A.; Belgacem, M.N. Recent Contributions to the Preparation of Polymers Derived from Renewable Resources. *J. Polym. Environ.* **2002**, *10*, 105–114. [CrossRef]
133. Ruby, M.-P.; Schüth, F. Synthesis of N-alkyl-4-vinylpyridinium-based cross-linked polymers and their catalytic performance for the conversion of fructose into 5-hydroxymethylfurfural. *Green Chem.* **2016**, *18*, 3422–3429. [CrossRef]
134. Zhao, J.; Zhou, C.; He, C.; Dai, Y.; Jia, X.; Yang, Y. Efficient dehydration of fructose to 5-hydroxymethylfurfural over sulfonated carbon sphere solid acid catalysts. *Catal. Today* **2016**, *264*, 123–130. [CrossRef]
135. Bhatia, S.K.; Jagtap, S.S.; Bedekar, A.A.; Bhatia, R.K.; Rajendran, K.; Pugazhendhi, A.; Rao, C.V.; Atabani, A.; Kumar, G.; Yang, Y.-H. Renewable biohydrogen production from lignocellulosic biomass using fermentation and integration of systems with other energy generation technologies. *Sci. Total. Environ.* **2021**, *765*, 144429. [CrossRef]
136. Mechery, J.; Thomas, D.M.; Kumar, C.S.P.; Joseph, L.; Sylas, V.P. Biohydrogen production from acidic and alkaline hydrolysates of paddy straw using locally isolated facultative bacteria through dark fermentation. *Biomass-Convers. Biorefin.* **2021**, *11*, 1263–1272. [CrossRef]
137. Cieciura-Włoch, W.; Borowski, S.; Otlewska, A. Biohydrogen production from fruit and vegetable waste, sugar beet pulp and corn silage via dark fermentation. *Renew. Energy* **2020**, *153*, 1226–1237. [CrossRef]
138. Irmak, S.; Meryemoglu, B.; Sandip, A.; Subbiah, J.; Mitchell, R.B.; Sarath, G. Microwave pretreatment effects on switchgrass and miscanthus solubilization in subcritical water and hydrolysate utilization for hydrogen production. *Biomass Bioenergy* **2018**, *108*, 48–54. [CrossRef]

139. Prabha, S.P.; Nagappan, S.; Rathna, R.; Viveka, R.; Nakkeeran, E. 21—Blue Biotechnology: A Vision for Future Marine Biorefineries. In *Refining Biomass Residues for Sustainable Energy and Bioproducts*; Kumar, R.P., Gnansounou, E., Raman, J.K., Baskar, G., Eds.; Academic Press: Cambridge, MA, USA, 2020; pp. 463–480; ISBN 978-0-12-818996-2.
140. Chang, W.-R.; Hwang, J.-J.; Wu, W. Environmental impact and sustainability study on biofuels for transportation applications. *Renew. Sustain. Energy Rev.* **2017**, *67*, 277–288. [CrossRef]
141. Dehghanimadvar, M.; Aslani, A.; Ahmadi, M.H.; Ghomi, N.S.K. Current status and future forecasting of biofuels technology development. *Int. J. Energy Res.* **2019**, *43*, 1142–1160. [CrossRef]

Disclaimer/Publisher's Note: The statements, opinions and data contained in all publications are solely those of the individual author(s) and contributor(s) and not of MDPI and/or the editor(s). MDPI and/or the editor(s) disclaim responsibility for any injury to people or property resulting from any ideas, methods, instructions or products referred to in the content.

environments

MDPI

Review

Process Evaluation of Scandium Production and Its Environmental Impact

Aratrika Ghosh [1], Soniya Dhiman [1], Anirudh Gupta [1] and Rohan Jain [2,*]

[1] Department of Biochemical Engineering and Biotechnology, Indian Institute of Technology-Delhi, New Delhi 110016, India
[2] Helmholtz-Zentrum Dresden-Rossendorf, Helmholtz Institute Freiberg for Resource Technology, 01328 Dresden, Germany
* Correspondence: rohanjain.iitd@gmail.com; Tel.: +49-351-260-2725

Abstract: With the advancement of technology and a global shift towards clean energy, the need for rare earth metals is increasing. Scandium, a rare earth metal, has been extensively used over the decades in solid oxide fuel cells and aluminum–scandium alloys that have a vast, evolving market in aerospace, automobiles and 3D printing. However, the market struggles to maintain the supply chain due to expensive production processes and the absence of uniform global distribution of primary sources. Therefore, identification of alternative sources and technological advancements for scandium recovery are needed. To this end, an effort has been made to provide a review of the advances in different technologies applied in scandium recovery from diverse sources. Emphasis has been given to the improvements and upgrades to technologies in terms of environmental impact and recovery efficacy. An attempt has been made to discuss and deliver a clear representation of the challenges associated with every source for scandium recovery and the major developments in solving them. The environmental impact of scandium recovery and recycling has also been discussed.

Keywords: hydrometallurgy; leaching; adsorption; solvent extraction; crystallization; life cycle assessment

Citation: Ghosh, A.; Dhiman, S.; Gupta, A.; Jain, R. Process Evaluation of Scandium Production and Its Environmental Impact. *Environments* **2023**, *10*, 8. https://doi.org/10.3390/environments10010008

Academic Editors: Manuel Duarte Pinheiro and Claude Fortin

Received: 10 October 2022
Revised: 19 December 2022
Accepted: 20 December 2022
Published: 28 December 2022

Copyright: © 2022 by the authors. Licensee MDPI, Basel, Switzerland. This article is an open access article distributed under the terms and conditions of the Creative Commons Attribution (CC BY) license (https://creativecommons.org/licenses/by/4.0/).

1. Introduction

The release of carbon from the waste materials generated by the mining of minerals significantly influences the environment and the climate, which have a great impact on human health and biodiversity [1]. However, the role of mining is also important for the recovery of critical metals like gallium, indium, scandium and other rare earths that are used in high-tech and low carbon emission technologies [2]. Furthermore, the mining industries are also important from an economical point of view for various states and provinces where mining activities are mostly concentrated. Usually, the wastes generated during mining activities have been discarded as such in the form of slag and tailings dams, even though these contain valuable minerals. In addition, the failure of the tailings dams has led to unmitigated disasters in Brazil, Hungary and Italy [3]. Therefore, mining waste recycling may stimulate innovative local industries, reduce waste production and natural resources intake, prevent environmental damage and create financial assets. The assessment of environmental benefits after mining waste reprocessing and final disposal of waste is important. It is also necessary to employ cost and benefits methods to assess the expenditure of waste reprocessing and the monetary value of recovered metals. For this, a detailed understanding of the metal extraction process is important. In this review, scandium has been discussed as it is considered an expensive as well as rare metal due to its difficult extraction and poor distribution [4]. It is generated as an ore-processing by-product and is generally present in the waste liquors, tailings, slags and residues. However, since the concentration of scandium is very low in comparison to contaminating metals, its recovery becomes challenging, expensive and environmentally hazardous. Additionally, a

low recycling rate, irreplaceable application in green technologies, limited mining regions and high economic importance makes it therefore important to focus on high efficiency recovery. It is also referred to as a critical metal by Brazil, the USA and the European Union [5,6].

Scandium is one of the most highly abundant metals in the earth's crust, yet, it is not readily available for mining and extraction due to its dispersed nature. Scandium as an ore with a concentration greater than 40% has been reported only in Norway [7]. Other countries with main scandium resources are China, Russia, the United States of America, Madagascar, Australia and Kazakhstan [8–10]. Scandium predominantly occurs in traces along with other minerals in ores of cobalt, iron, nickel, tin, etc. [11,12]. The major application of scandium is as an alloy with metals like aluminum, magnesium, zirconium, etc. These alloys find extensive use in sports, military [9] aircraft industries [13] and solid oxide fuel cells (SOFCs), respectively [14]. At present, the worldwide market for scandium has a demand of 98 t/annum of scandium for aircraft and vehicles, which will increase to 3000 t/annum of scandium by 2032 [15]. Owing to this steep increase in demand, scandium has been classified as a critical metal [16].

With such a predicted rise in the demand of scandium in the upcoming decade, the production rate does not seem to increase accordingly. The low production and demand of scandium is a chicken and egg problem. The high price and limited market availability seem to discourage industries from using this raw material. Hence, the number of buyers is low. Due to the small market, metal producers are deterred from investing in the recovery of scandium, despite its high price. Presently, the amount of scandium produced is clearly insufficient to address the increasing demand across the world. Therefore, new supply strategies for scandium are highly desirable. Paradoxically, although scandium is abundant in the earth's crust, it is not an ore-forming metal. Therefore, it rarely occurs in concentrations above 100 ppm as a primary source, making its extraction economically unattractive [15]. Hence, new sources and recovery processes are required to break this cycle.

Few review articles have been published on scandium separation and recovery from different sources [12,17–20]. Wang and Cheng [12] reviewed the separation and purification of scandium by synergistic solvent extraction and solvent extraction with chelating extractants, focusing on their recovery performance as well as their extraction mechanisms. In addition, ion exchange and liquid membrane extraction for scandium recovery were also discussed. Zou et al. [17] reviewed the extraction chemistry of scandium in different extraction systems in detail. Wang et al. [18] reviewed scandium recovery through metallurgical pathway from various resources, including scandium ores, residues, tailings and waste liquors, focusing on the selection of processes to recover scandium as a minor element and incorporating the scandium recovery process into the main flowsheet for the production of the main metal. Junior et al. [19] also reviewed scandium extraction from different sources. However, the primary focus was on eco-friendly processing and clean technologies. Pyrzynska et al. [20] discussed some recent progress made in the research on scandium separation, purification and pre-concentration from different sources such as ores, electronic waste (e-waste), water, sediment, soil and plants both in industrial as well as laboratory systems. However, consolidated information on the advances in the recovery of scandium from various sources, especially from mining tailings/e-waste is not discussed properly. Moreover, the diversity in the treatment process and the associated prospects and consequence of these methodologies with respect to their environmental impact and metallurgical gain have not been discussed properly. Different metallurgical operations have been used to recover scandium from secondary sources. One such choice is pyrometallurgy, which is a conventional method to recover different metals from different type of wastes. However, high energy consumption and generation of toxic substances are the disadvantages associated with pyrometallurgy [21]. In recent times, the principal technologies being used to recover scandium from secondary sources are based on hydrometallurgical processes. Hydrometallurgical processes are suitable alternatives for the

treatment of industrial materials waste because of their cost effectiveness, reduced formation of poisonous gases and dust, operational selectivity, simple control of the procedure and effectiveness [22,23]. In comparison to pyrometallurgy, hydrometallurgical processes utilize low temperatures and are more predictable and controllable, which make them more environmentally friendly. Therefore, the main objective of the present review is to give a clear portrait of the growth in hydrometallurgical processes regarding scandium recovery from various sources especially mining tailings/e-waste. It will provide a deep insight into the wide-ranging technologies that are available, from leaching to the use of polymer inclusion membranes for the recovery of the metals, along with their advantages and disadvantages. Further, to support the idea, discussions on several cases of scandium recovery carried out across the world for the last decade have also been included.

2. Scandium Sources

Scandium seldom occurs in concentrated quantities and is usually found distributed as traces in rocks containing ferromagnesium reserves [18]. Worldwide, there is about 2 million tons of scandium, with China accounting for 27.5% of the total reserves [24]. However, most of the reserves cannot be exploited due to technical, economic and environmental challenges [19]. Therefore, the extraction of scandium in pure form is complicated as well as expensive [24]. Across the globe, scandium occurs in more than 800 variants of minerals in low concentrations and a highly complexed state. The scandium minerals containing considerable quantities of the metal (i.e., more than 20 wt%) are thortveitite ($Sc_2Si_2O_7$), pretulite ($ScPO_4$) and kolbeckite ($ScPO_4 \cdot 2H_2O$) [25].

2.1. Scandium Abundance

Major scandium ore deposits have been found in the USA, Norway, Australia, China, Russia, Madagascar, Kazakhstan and Ukraine [8,11]. Any resources with scandium concentration between 20–50 mg/kg can be considered as ore for exploitation [26]. In USA and Kazakhstan, scandium sources are mainly ores of aluminum uranium, zirconium and tantalum. In Australia, it occurs in ores of nickel laterite. In China, Russia and Ukraine, scandium is found in ores of tungsten, iron and tin, while in Madagascar and Norway, it occurs in pegmatite rocks. Globally, the principal source of scandium is niobium-rare earth element-iron (Nb–REE–Fe), the largest REE resource and second largest resource of scandium in the world. It is located in Inner Mongolia, China and accounts for approximately 90% of global scandium production. In Bayan Obo, scandium is regenerated as a by-product of mining of the other REEs and iron [27]. The scandium content of the Bayan Obo deposit ranges between 26–110 ppm in various ores and it reaches 163 ppm of scandium in the REE ore tailings [28]. Scandium in the Bayan Obo deposit is mainly hosted by Aegirine. Numerous lateritic deposits in eastern Australia (New South Wales and Queensland) that have sumptuous scandium content and are being considered for viable mining [29]. A mining lease has been awarded for the Nyngan deposit in New South Wales, Australia. The laterites in these deposits are generated due to intense weather conditioning of ultramafic and mafic rocks. These rocks have concentrated scandium in the range of 100–400 ppm by the adsorption of geothite or incorporation into the hematite structure [29]. The Zhovti body deposit in Russia is graded at 105 ppm scandium and contains aegirine as its main scandium bearing mineral (Table 1) [25]. The most important and largest source of scandium in Russia is the Kovdor baddeleyite–magnetite–apatite deposit. It contains a scandium reserve of 420 tons and the grade of the ore is 800 ppm of scandium [30]. The other major source of scandium in Russia is Tomtor, one of the world's largest carbonatites contributors, which has elevated concentrations of the REEs, including scandium up to 570 ppm (Table 1) [31–33]. High scandium content (45%) is found in thortveitite-rich pegmatites in Madagascar and Norway. It is also reported that in the Iveland-Evje district of Norway, scandium-bearing pegmatites contain approximately 1000 ppm scandium [25]. Table 1 shows some of other primary sources of scandium.

Table 1. Concentration of scandium in different mineral ores other than bauxite ores.

S. No.	Mineral Ore	Scandium Content	References
1.	Aegirine (Russia)	105 ppm	[25]
2.	Pegmatites	1000 ppm	[25]
3.	Aegirine (Bayan Obo)	26–110 ppm	[28]
4.	Lateritic deposits	100–400 ppm	[29]
5.	Baddeleyite–magnetite–apatite	800 ppm	[30]
6.	Araxa (SE Brazil) complex REE (Nb–P) ore	219–322 ppm (Sc_2O_3)	[32,33]
7.	Tomtor deposit	570 ppm (Sc_2O_3)	[32,33]
8.	REE–monazite	15 ppm	[34]
9.	REE–allanite	24 ppm	[35]

2.2. Scandium from Secondary Sources (Mining Process and End-of-Life Products)

Scandium was classified as a critical metal owing to its steep increase in demand [16]. An economically profitable option is to recover scandium from waste streams of scandium-associated ore processing units. Scandium is found in a large extent in aluminum ores. Bauxite is the most common aluminum ore, which has a high content of scandium. The Bayer process associated with aluminum extraction results in enrichment of the scandium concentration in the bauxite residue [36]. The concentration of rare earth elements in bauxite varies from their region of origin. Table 2 gives the scandium concentration in red mud from studies done in recent years for its recovery. A review by Zang et al. gives a detailed discussion about the sources, concentration and scandium recovery from red mud [10]. In red mud, the approximate concentration of rare earths varies in the range of 500–1700 ppm, with scandium concentrations ranging between 130–390 ppm [37]. If all the scandium present in red mud could be recovered, then 6600–20,400 t/annum would be available [15]. Several rare earth metals are present in bauxite residue. However, the maximum concentration in terms of presence belongs to scandium which is around 95%compared to rest rare earth metals present in the waste [38]. However, the presence of other metals like iron, aluminum, etc., in large concentrations hinders the hydrometallurgical processes making it difficult to recover such high concentrations.

Table 2. List of countries reported to be generating bauxite ore in recent years and the scandium content of the ore.

S. No.	Country	Scandium Content	Reference
1.	Jamaica	550 ppm	[15]
2.	Canada	31,100 ppm	[39]
3.	Greece	20 ppm	[40]
4.	China	20–38 ppm	[41]
5.	Russia	70–120 ppm	[42]
6.	Germany	57 ppm	[42]
7.	Hungary	94 ppm	[42]

One important source of scandium is coal/coal combustion byproducts (CCPs) [43–49]. CCPs accumulate at an annual rate of 115 million tons in the United States alone and contain an average scandium concentration of 36–70 ppm along with up to 1000 ppm rare earth metals (REEs). Technoeconomic analyses suggest that scandium extraction from these waste residues will be critical for industrially viable recovery of REEs since scandium comprises more than 90% of the total REE value at current prices [46]. Scandium at low concentrations is also found with transition and rare earth elements like molybdenum, tungsten, titanium, tantalum, yttrium, zirconium, etc. [50]. The rare earth minerals such as bastnasite and monazite contain scandium in the range of 20–50 ppm [51]. Scandium is also found in ores of uranium as uraninite in Russia, Kazakhstan, Australia, Namibia

and Canada [52]. It is also recovered from titanium ore like magnetovana–ilmenite located in Panzhihua, China at a concentration as high as 0.04% [53]. A report by the United States Geological Survey, (Mineral commodity summaries, 2019) stated that approximately 5,400,000 metric tons of ilmenite ($FeTiO_3$) and 750,000 metric tons of rutile (TiO_2) are mined across the globe annually [54]. Apart from that, major titanium ores are found in India, Norway, Australia, Canada and South Africa [16], accounting for a potential global yield of scandium (Sc_2O_3) in the range of 96–194 tons. A noticeable amount of scandium is also found in tungsten [55], nickel and cobalt ores. Nickel laterite ores from Cuba, the Dominican Republic and New Caledonia [56] have high concentration of scandium, up to 100 ppm, and are a probable source for exploitation. Apart from the sources mentioned above, there are many new potential sources that have been identified, such as electronics and electrical waste, municipality waste, coal fly ash, phosphor-gypsum and phosphate rocks and many more that have been identified to contain recoverable amounts of scandium [19]. The main problem with the exploitation of these sources is the irregularity in the metal's concentration. For example, use of e-waste as a scandium source needs collection and segregation of the waste, which is an additional challenge. Moreover, the exploitation of the phosphorus reserves as a scandium source is restricted due to their insufficiency [53].

3. Scandium Applications

The two main applications of scandium are in solid oxide fuel cells and aluminum–scandium alloys. An enhanced oxygen ion conductivity can be attained in solid oxide fuel cells through scandium doping with zirconia in place of yttrium [19]. Aluminum–scandium alloys are among the most promising candidates for light weight alloys [57]. The advantages of a minor addition, generally 0.2–0.6 wt% of scandium in aluminum alloys, are improved strength, thermal resistance, weldability and corrosion resistance. The main application of aluminum–scandium alloys is in the aerospace and automotive industries and for sports equipment (bikes, baseball bats, etc.) which rely on high performance materials. Scandium, along with aluminum and magnesium as an alloy is used in 3D printing which finds application in the aerospace and automobile industries. Sc_2O_3 is used in Erbium-doped yttrium–aluminum–garnet (Er:YSG) crystals for optics in laser applications [37].

Due to its specific mechanical and chemical properties, the applications of scandium are increasing, which has heightened the market demand for scandium. However, it is difficult to extract scandium because it is sparsely distributed in trace amounts in natural minerals, and the resources of scandium mineral deposits usually exist in complicated forms. There is an urgent need to separate and recover scandium from secondary resources.

4. Possible Flow Sheets for Scandium Recovery

A cascade of different operations is generally required to obtain and enhance the purity of any metal recovered from its ore or from byproducts of other metal extraction processes. The principal steps from the mining to the extraction of its purest form include liberation, separation/upgrading and purification. The most commonly used processes for metal processing for minor elements in hydrometallurgy include leaching, solvent extraction, ion-exchange, precipitation and electrochemical refining. The choices of the processes are based on the type of ore being handled. However, different options were developed in addition to the classical approach [58]. In the classical approach, scandium was recovered from uranium ores in Russia. The process began with low-concentration sulfuric acid leaching, followed by solvent extraction with 0.1 M dodecyl phosphoric acid solvent in kerosene to extract uranium. This led to the build-up of concentrated scandium, titanium and thorium in the organic phase leading to solvent poisoning. Stripping of the organic solvent with HF acid led to the precipitation of a scandium–thorium fluoride cake. The cake was then double-digested with NaOH for conversion to scandium hydroxide. The crude scandium hydroxide was digested again with hydrochloric acid to remove impurities like thorium, titanium, uranium, etc. Once the precipitate was removed, the filtrate was further

treated with controlled oxalic acid to recover scandium oxalate precipitate. The scandium oxalate cake was then calcined below 800 °C to generate scandium oxide. To enhance the purity of the oxide obtained, it was further dissolved in hydrochloric acid and stripped with ammonia. The scandium oxide formed was again calcined at 700 °C to generate scandium oxide with a purity of 99.5%. This process applies reagents, which are corrosive as well as poisonous resulting in the generation and release of toxic byproducts. Hence, it is clearly understandable that this process contributes to the environmental burden as it utilizes large amounts of hazardous chemicals and generates toxic products. However, since no life cycle assessment (LCA) has been done on the recovery of scandium following the classical approach from uranium ores, a direct relationship with indicators cannot be concluded. Recently, a study done by Wang et al. [27] discussed the environmental impact of scandium production from the Bayan Obo Mines. Figure 1 shows the processes followed in the recovery of Sc_2O_3 from the Byan Obo Mine's REEs tailings. The process is studied from ore mining to the final scandium products. It includes primary, secondary and tertiary separation of iron, other REEs, scandium and niobium. Once other major impurities are separated, scandium is further concentrated and purified by processes like pressure filtration, pressure acid leaching, extraction, back extraction, calcination, precipitation and many more. The environmental impact for the production of 1 kg of Sc_2O_3 was analyzed with the help of the Tools for Reduction and Assessment of Chemicals and Other Environmental Impacts (TRACI 2.1) which include ten potential environmental indicators some of which are Ecotoxicity, Human Toxicity Cancer, Human Toxicity Non-Cancer, Global Warming Air (GWA) and many more. From the assessment, it was seen that the process has a major environmental burden in form of GWA, with extraction and separation being the major contributors. However, in the present case where scandium contributes only 0.01% of the ore, the removal of the other REEs and iron takes up a large amount of energy as well as material. Hence, along with identification of new potential sources of scandium, advancement of technology that can reduce this burden is very important. As time advanced, new methodologies were developed and proposed to overcome the environmental problems along with the ability to recover the maximum scandium available in the source. The following sections will discuss all the possible alternatives that have been identified for scandium recovery.

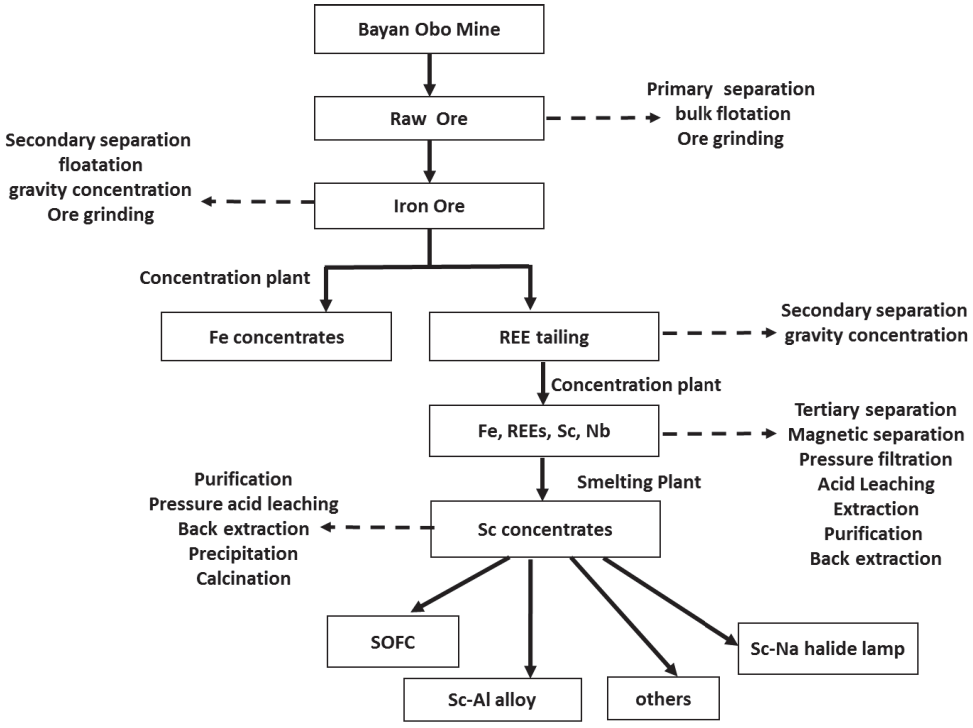


Figure 1. Sc_2O_3 from Byan Obo Mine's REEs tailings.

5. Separation Processes for Scandium Recovery

As scandium occurs in concentrations around 0.002–0.005% in ores of other metals, the recovery processes become complex as well as expensive. The major processes employed for recovery of scandium are hydrometallurgical in nature, such as extraction, adsorption filtration, ion-exchange, solvent extraction, etc. The flow of these processes is dependent upon the initial source and most of the process begins with leaching followed by a series of different hydrometallurgical processes. Thus, scandium's rare availability coupled with the complex recovery processes adds to its cost of production making it highly expensive. According to the US Geological Survey report [49], the price of 99.99% pure Sc_2O_3 is USD 2200 per kg and the global supply and consumption of scandium oxide was estimated to be about 15–25 tons per year [59]. In spite of the increasing cost, scandium demand is increasing for modern technologies in automotive, optical, electronics and related industries [9], as discussed above. Thus, different processes for the recovery and purification of scandium are in urgent need.

5.1. Chemical Leaching

Chemical leaching is one of the oldest and most important operations in metallurgical industries for the extraction of metals from their ores. It is a process through which the metals trapped in ore and industrial process waste are recovered using strong mineral acids. The performance of different leaching systems from different secondary sources reported in the literature for scandium leaching is reviewed and tabulated in Table 3. Li et al. [60], Wei et al. [61] and Xiao et al. [24] studied the recovery of scandium using hydrochloride acid (HCl) as the leaching agent. They further compared their studies with other mineral acids and concluded that the scandium leaching rate was either high or similar to the other leaching agents. Ochsenkuehn-Petropoulou et al. [62] and Rivera et al. [63] used H_2SO_4 as the leaching agent for the scandium leaching from bauxite residue, but it showed poor leaching efficiency among all the tested systems. Furthermore, Bonomi et al. [64] studied scandium recovery using ionic liquid at 200 °C. The biggest hurdle faced in the direct leaching of bauxite residue is the development of silica gel. Alkan et al. [65] provided a solution by preventing the synthesis of silica gel using hydrogen peroxide (H_2O_2). However, it affected the recovery as it reduced the leaching efficiency. Thus, as observed, the use of H_2O_2 can avoid silicon leaching and consequent silica gel formation.

Table 3. A brief summary of different systems of scandium leaching from secondary sources.

S. No.	Real Sample	Leaching System	Leaching Conditions	Leaching Rate of Scandium (%)	Reference
1.	Scandium Rough Concentrate	HCl	s/l = 1/1.5, 60 °C, 90 min	95.1	[24]
2.	Red Mud	HCl	75 °C, 2 h	99.97	[60]
3.	Red Mud	HCl	s/l = 1/10, 80 °C, 3 h	83.9	[61]
4.	Bauxite Residue	H_2SO_4	s/l = 1/5, 90 °C, 60 min.	50	[62]
5.	Bauxite Residue	H_2SO_4	s/l = 1/20, 25 °C, 24 h	40	[63]
6.	Bauxite Residue	1-ethyl-3methyl imidazolium hydrogen sulphate	s/l = 5% *w*/*v*, 200 °C, 12 h	80	[64]
7.	Bauxite Residue	H_2SO_4 + H_2O_2	s/l = 1/10, 90 °C, 30 min	68	[65]
8.	Red Mud	HCl + H_2O: Red mud: EDTA	40 mL HCl, 10 g red mud, 2 g EDTA, 70 °C, 4 h	79.6	[66]
9.	Bauxite Residue	CO_2 + H_2SO_4	s/l = 1/3, 30 °C, 6 h	50	[67]
10.	Bauxite Residue	H_2SO_4	s/l = 1/50, 80 °C, 60 min	60	[68]
11.	Fe-Ti Residue	H_2SO_4	s/l = 1/7, 95 °C, 5 h	85–95	[69]
12.	REE Silicate	H_2SO_4	s/l = 1/30, 200 °C, 15 h	-	[70]
13.	Blast Furnace Slag	H_2SO_4 + H_2O	400 rpm, 200 °C, 10 min	83	[71]
14.	Bayan Obo Tailings	H_2SO_4	s/l = 1/4, 245 °C	96	[72]
15.	Nb Ore Concentrate	HCl	s/l = 2.2, 100 °C	97	[73]

5.2. Bioleaching

Bioleaching, also known as microbial leaching or biomining, is a process where metals are solubilized from insoluble solid matter either by direct metabolism by the microbes or by the metabolism products of the microbes [74]. This procedure helps in recovering valuable metals from low-grade ores, industrial process wastes, mine tailings, etc., in a more effective and environment friendly way. This phenomenon typically occurs as a result of the microbe generating organic or inorganic acids in their metabolic pathway [75].

Bioleaching can be done either by using heterotrophic or autotrophic microorganisms. The autotrophic process follows bio-oxidation/reduction cycles in the presence of inorganic acids, while heterotrophic leaching is carried out by the produced organic metabolites that complexes with the metal leading to the formation of soluble chelates. Heterotrophic microorganisms have successfully leached scandium from primarily bauxite and fly ash residues (Table 4). Most of the microbes studied for the leaching of scandium produced mainly oxalic acid. The high production of oxalic acid is promoted by the high pH (6–10) of the system [76]. Apart from oxalic acid, other organic acids produced by the microbes are acetic acid, succinic acid, gluconic acid, malic acid, citric acid and lactic acid. In all the bioleaching studies mentioned here, the system follows low pulp density and one-step bioleaching. The stimulating effect of interactions between strains and scandium are long-lasting in one-step processes. Moreover, increasing the pulp density causes loss of microbial metabolic activities, inhibiting growth and resulting in poor leaching of the metal [77]. However, exceptionally high leaching efficiency (94%) has been seen when leaching has been done using *Gluconobacter oxydans* from red mud [78]. Only two studies have been reported that showed leaching of scandium from red mud through gluconic acid produced by *Gluconobacter oxydans* [79,80]. However, no such detailed discussion on the mechanism has been reported. Therefore, further detailed studies with gluconic acid on other scandium sources can be carried out in the future.

Table 4. A brief summary of different systems of scandium leaching from secondary sources.

S. No	Sample	Leaching System	Leaching Conditions	Leaching Agents	Leaching Rate of Scandium (%)	Mechanism	Reference
1.	Red Mud Indian and German	chemoorganotrophic microorganisms, *Gluconobacter oxydans* (DSMZ 46616)	10% pulp density, 37 °C, was observed after 18–20 d, 120 rpm	gluconic acid	83% and 94%, respectively	-	[80]
2.	Red Mud	*Penicillium tricolor* (RM-10)	10 days, 2% pulp density, one-step bioleaching	citric, oxalic, and gluconic acids	70%	Detoxification	[79]
3.	Residual Fly Ash	*C. bombicola, C. curvatus, P. chrysosporium*	Fly ash leached with supernatant 28 °C, 6 h, 50 rpm, 1% pulp density	-	63, 48.5 and 52.1, respectively	-	[81]
4.	Ash–Slag Waste	acidophilic chemolithotrophic microbial communities	45 °C, 10 days, 10% pulp density, pH 2.0 by adding sulfuric acid	sulfuric acid	52%	-	[82]
5.	Red Mud	chemoheterotrophic bacteria, *Acetobacter sp.*	30 °C, 120 rpm, 2% pulp density, one-step	succinic acid acetic acid, malic acid, oxalic acid, lactic acid	52%	Acidolysis, complexolysis	[83]
6.	Red Mud	fungal strain *Aspergillus niger* isolated from pistachio husk and grape skin	30 °C, 150 rpm, 20 days, 3% pulp density	citric and oxalic acids	29% and 38%, respectively	Detoxification and complexation by acidic metabolites	[84]
7.	Bauxite Residue	*Acetobacter tropicalis*	one-step bioleaching process at 1% s/l, 30 °C, 120 rpm, 20 days	acetic, oxalic, and citric acids	42%	Detoxification and complexation	[85]

Compared to conventional leaching methods, bioleaching has higher selectivity towards scandium in the presence of impurities. Moreover, it is a greener and better option for the extraction of metal from solid materials as it has operational flexibility, low cost, no toxic by-product generation, less energy consumption and is environmentally friendly [79]. The most significant disadvantage that has been observed is the low leaching efficiency

and high leaching time compared to conventional mineral acid leaching. Bioleaching is a significantly less exploited process for extraction of REEs. It has a huge scope in exploring scandium recovery from other sources, such as waste printing circuit boards, which contains neodymium, dysprosium, lanthanum, scandium and yttrium along with zinc, nickel, copper and gold. Bacterial or fungal bioleaching of scandium as well as rare earth elements from waste printing circuit boards, has not been addressed properly [78].

6. Recovery Processes

6.1. Liquid/Liquid Extraction

Liquid/liquid extraction, also known as solvent extraction, is a traditional method used extensively in the chemical industry for the separation of compounds based on their relative solubility in two different immiscible liquids [41]. For scandium recovery from various processing liquid wastes and leachates, solvent extraction is widely used because it generally offers the advantages of good processing capacity, operational ease at larger scales and lower operating costs. Different types of extractants, such as acidic, basic, neutral, chelating, as well as synergetic extraction systems have been explored for the extraction and purification of scandium [86]. The extraction studies that have been reported in the literature is reviewed and summarized in Table 5. These studies suggest that acidic organophosphorus extractants such as di-(2-ethylhexyl)phosphoric acid (DEHPA) and bis(2,4,4-trimethylpentyl)phosphonic acid (Cyanex 272), were the most applied extractants for the separation of scandium from various other metal ions. Due to its high charge density, scandium generally shows a higher extractability than the other rare earths. Upon application of Cyanex 272 and 923 (mixture of four tri-alkylphosphine oxides) in sulfuric acid media, the recovery of scandium was >98%, whereas selective separation of scandium from thorium and zirconium was achieved using Cyanex 572 (organo-phosphorus containing phosphinic and phosphonic acids) in HCl media. Selective separation of scandium from Fe was reported using betainium bis(trifluoromethanesulfonyl)imide ([Hbet][TF_2N]) in aqueous medium by Onghena et al. [87]. The percentage extraction of scandium was 99% using D2EHPA + tributyl phosphate (TBP), while 90% scandium was stripped when D2EHPA + primary amine (N1923) was applied as the extractant. The extraction percentage was greater than 99% using 2-ethylhexyl phosphonic acid mono-2ethylhexyl ester (P507) + TBP and trialkylphosphine oxide (TRPO) as extractants in different media. It is evident from the given data that sulfuric acid media was widely used for the recovery of scandium. The extraction percentage is greater than 90% using most of the reported extractants, which suggests that application of these extractants for the recovery of scandium is feasible. The comparative data also indicate that in order to obtain highly pure (>99%) scandium oxide, P507 + TBP and TRPO can be applied as extractants.

Table 5. Summary sheet on the extraction of scandium using different extractants.

S. No.	Starting Metals (mg/L)	Extractant	Aqueous Medium	Extraction Mechanism	Extracted Metal Ions	Comments	Reference
1.	Sc (9.9), Th (8.9), Ti (30.7), Zr (1.3), Fe (13,091.4), Mn (9530.9), REs (40.5), Al (506.5), Ca (5591.9), Mg (221.1)	Cyanex 572	HCl	$M^{+3}_{(aq)} + 3HL_{(org)} = ML_{3(org)} + 3H^{+}$	Sc, Th, Zr	Selective separation of Sc from Th and Zr; HCl as stripping agent	[55]
2.	Sc (1.8 mol/kg)	[Hbet][TF_2N]	-	$M^{+3} + 3[Hbet][TF_2N]_{(org)} = [M(bet)_3(TF_2N]_{3(org)} + 3H^{+}$	Sc, Fe	Selective separation of Sc from Fe using scrubbing; HCl as stripping agent	[88]
3.	Sc (139)	Cyanex 272+ Cyanex 923	H_2SO_4	$Sc^{+3} + (HL)_{2(org)} + B_{(org)} = Sc(HL_2)B(SO_4)_{org} + H^{+}$	Sc	98.79% Sc is recovered using oxalic acid as stripping agent	[89]
4.	Sc (9), Fe (22), Al (203), Si (28), Na (5837), Ca (416)	P204 P507 Versatic 10	H_2SO_4	$M^{+3} + 3(HA)_{2(org)} = MA_3.3HA_{(org)} + 3H^{+}$	Sc, Fe	P204 is a better extractant than P204 and Versatic acid 10; 97% recovery of Sc	[90]
5.	Sc (23.6)	P507 + isooctanol	H_2SO_4	$Sc^{+3} + 3(HA)_{2(org)} = Sc(HA_2)_{3(org)} + 3H^{+}$	Sc, Zr, Ti	$SF_{(Sc/Zr)} = 34$, $SF_{(Sc/Ti)} = 494$; 99% Sc is recovered using H_2SO_4 as stripping agent	[91]
6.	Sc (4.33), Na (23,800), Fe (107), La (14.4), Ti (0.08), Ca (400Al (2510), Y (15.3), Ce (30.3), Nd (3.06), Dy (1.74)	[Hbet][TF_2N]	H_2O	$M^{+3} + 3[Hbet][TF_2N]_{(org)} = [M(bet)_3(TF_2N]_{3(org)} + 3H^{+}$	Sc, Fe	Separation of Sc from Fe is achieved by reducing Fe; ascorbic acid as reducing agent; H_2SO_4 as stripping agent	[88]
7.	Sc (5.53), Ca (611), Fe (1653), Ti (311), V (49.1), Cr (9.36), Zr (5.91), Ga (2.00)	D2EHPA + TBP	H_2SO_4	-	Sc	D2EHPA is selective extractant for Sc; %E = 99%; TBP used as phase modifier; Sc is recovered as $Sc(OH)_3$ using NaOH as stripping agent	[92]
8.	Sc (365), Ti (579), Fe (6), Zr (53.9)	TRPO	$H_2SO_4 + H_2O_2$	$Sc^{+3}_{(aq)} + HSO_4^{-}{}_{(aq)} + SO_4^{2-}{}_{(aq)} = HSc(SO_4)_{2(aq)}$ $HSc(SO_4)_{2(aq)} + 2TRPO_{(org)} = HSc(SO_4)_2.2TRPO_{(org)}$	Sc	H_2O_2 is added to prevent the extraction of Ti; 99.9% stripping Sc using oxalic acid; 95% Sc_2O_3 is recovered with 99.34% purity	[93]
9.	Sc (17), Ti (3875), Fe (5562), Al (8431), Ca (29), Na (4824), Mg (1521)	P507 + TBP	$H_2SO_4 + CaF_2$	-	Sc	99% pure Sc_2O_3 is recovered after stripping, precipitation and calcinations; phase modifier is required	[94]
10.	Sc (23), Ti (2400), Fe (28,360), Mn (2400), Al (1030), Ca (1500), Mg (1900)	D2EHPA + N1923	H_2SO_4	$Sc^{+3} + (HL)_{2(org)} + [(RNH_3)_2(SO_4)]_{2(org)} + SO_4^{2-} = Sc(HL_2)[(RNH_3)_2(SO_4)]_2(SO_4)_{(org)} + H^{+}$	Sc, Ti	90% Sc is stripped using HNO_3; 80% Sc_2O_3 with 90% purity is obtained after precipitation and calcination	[95]

6.2. Adsorption

Adsorption is a surface phenomenon where the transfer of molecules from the bulk fluid occurs on the solid particle. The transfer can be physical or chemical in nature; however, it is usually reversible in nature. The reverse of adsorption is desorption in which the molecule is released back, regenerating the adsorbent without altering the chemistry of the adsorbent. Table 6 discusses different kinds of adsorbents that have been used for the recovery of scandium such as ion exchange resins, solvent impregnated resins, bio-sorbents and many more. Carbon-based adsorbents like wood dust biochar, coconut shell activated carbon nanotubes and pristine were able to adsorb scandium selectively over rare earth elements like cerium and neodymium in the acidic media. Although wood dust biochar has shown low adsorption capacity compared to those available commercially, it is cheap and developed from agricultural waste giving it a sustainability and economic advantage. Sol-gel-processed silica doped with bifunctional ionic liquid trioctylmethylammonium 1-phenyl-3-methyl-4-benzoylpyrazol-5-onate [96] and Fe_3O_4@SiO_2 nanoparticles functionalized with the coupling agent (3-aminopropyl) triethoxysilane (APTES) and ethylenediamine tetraacetic acid (EDTA) as a ligand were also used as adsorbent with high selectivity towards scandium compared to other rare earth elements [97]. The latter is a magnetic adsorbent with an adsorption capacity as high as 95% as well as being easy to handle. However, nothing has been reported regarding the elution of the metal from the adsorbent which is important for the recovery of scandium. A recent study showed that zirconium phosphate (ZrP), when used as an adsorbent, showed high selectivity towards scandium compared to iron (III) with a separation factor of approximately 23. Around 99.9% pure scandium was recovered, although the elution after two cycles could reach only 60% [98]. Adsorption overcomes most of the drawbacks of solvent extraction, such as loss of solvent, generation of chemical sludge, multiple stage operation, emulsification, etc. However, it has its own drawbacks, such as slow processing, time consuming, low specificity towards selective ions and low efficiency desorption. In this review, other kinds of adsorbents used and their related problems, advantages and disadvantages will be discussed.

6.3. Ion Exchange

Ion exchange is a chemical treatment process where metal ions from the solvent are exchanged with ions on the resins. In this process, the ions in a solution are replaced by ions attached to a solid phase. Thus, the ions present in solutions are replaced by different ions originally present in the resin. These ions are of different types but of the same polarity. Ion exchange has been applied for recovery of scandium from as early as 1957, where it was recovered from a mixture of scandium, vanadium and titanium with the help of Dowex 1. The adsorbed scandium was recovered through desorption with 0.1 M oxalic acid and 0.1 M HCl [99]. Though the ion exchange technique is not new, it has undergone massive changes over time, just being based on the principal of reversible adsorption of ions at the solid/liquid interface. The developments were made in resin utilization and activity enhancement for maximum extraction. To date, various kind of resins has been employed for the recovery of scandium from different type of real industrially processed feeds like zirconium tailing waste, uranium leachate, copper leachate, coal ash leachate, red mud leachate, etc. which has scandium along with other REEs, and high concentration of impurities like thorium, iron, aluminum, etc. that strongly interfere with the recovery process. As most feed sources containing scandium are acidic in nature, cationic resins are the primary choice for recovery [100–105]. However, anionic resins are also been reported for the recovery of scandium [106,107]. From Table 6, most of the resins lack high selectivity towards scandium. Hence with scandium, other REEs as well as impurities, are adsorbed. While eluting, along with scandium, some impurities like aluminum [105], REEs [108], thorium [108] and iron [109] are desorbed as well. Eluting methods have been further developed and modified where selective elution of scandium in the presence of other REEs from the resin was achieved to some extent [107,108].

The biggest hurdle faced in the retrieval of scandium from leaching solution is the separation and segregation of scandium from other metals especially like iron due to their chemical resemblances. To overcome this issue, functionalized resin materials have been used [109–112]. Ethyleneglycol tetraacetic acid (EGTA)-functionalized chitosan–silica particles and 732 resins were able to selectively adsorb scandium over iron [110]. 732 resins were used in a two-step adsorption system where the resin had an affinity for scandium, iron and aluminum. In the first stage, eluent containing Fe^{3+} is reduced in the presence of ascorbic acid and then scandium is complexed with EDTA. Since the resin had an affinity for iron (Fe^{2+}) and aluminum (Al^{3+}), they are adsorbed in the second stage adsorption, with only Sc–EDTA left in the eluent. The EGTA functionalized chitosan–silica possessed a much higher affinity for scandium over iron (by a factor of 10^5) which is then selectively eluted at pH 0.5 with nitric acid. Thus, ion exchange resins can be considered as a workable separation technique for the reclamation of metals from dilute solutions. However, they may involve many operational challenges, such as damaged resin, fouling and high costs [12]. They are re-usable, durable, less complex, have low maintenance costs, and are easy to operate with adjustable selectivity [113,114]. However, elution is an important parameter as recovery of the metal is the primary goal, which is often compromised. Therefore, more attention is needed towards developing a complete, optimized process of adsorption and desorption.

6.4. Immobilized Extractants

This is a new technique consisting of the immobilization of liquid extractants on different substrates. It involves the exchange of ions with chelating agents or solvents impregnated on resins. It is a simple and effective tool to selectively separate metal ions from aqueous solutions and effluents. Chelating resins and solvent impregnated resins can show an explicit affinity for certain metals due to the functional group(s) assimilated to the support matrix that possesses the advantages of both extraction and adsorption [115]. For the solvent to work effectively, proper sorption of the extractant by the polymeric support is very important. This is generally achieved through hydrophobic interactions and, sometimes, partly through polar or electrostatic forces. Using solvent-impregnated resin, scandium can be recovered with high selectivity from low concentration solutions containing high amounts of impurities [115–117]. When treating feeds with scandium and other REEs, solvent-impregnated resin effectively adsorbed scandium, which was successfully eluted to recover scandium metal [118]. When treating feeds from bauxite- and laterite-processed ores with high concentrations of iron and aluminum, which heavily interferes with selective scandium adsorption, solvent-impregnated resins have shown selectivity in the order scandium > iron > aluminum [116,119]. However, the elution of scandium was difficult as most of the studies have either not reported about elution [115,119,120] or claimed it to be challenging and problematic [115]. However, in a study done with XAD-7HP resin impregnated with extractants 2-ethylhexyl phosphonic acid mono-2-ethylhexyl ester (PC-88A) and neodecanoic acid (Versatic 10), scandium could be selectively recovered in presence of impurities such as iron, aluminum, zinc, etc. without undergoing any scrubbing or reduction of iron ions. Scandium could also be substantially eluted from the system with 2 M sulfuric acid [117]. Solvent-impregnated resin is an alternative separation method that is environmentally friendly, faster and relatively easy to handle, having tunable selectivity towards any ion compared to ion exchange and solvent extraction methods alone. However, the disadvantages of the process are the loss of impregnated solvent over the course of time due to its solubility in the aqueous phase and the challenging elution process of the metal ion for successful recovery.

6.5. Biosorption

Biosorption is the process by which biological agents such as bacteria, fungi, etc. act as absorbents (bio-sorbents) to accumulate heavy metal in their cells either via metabolic pathways or physico-chemical methods. Amino, carboxyl, hydroxyl, sulfhydryl and phosphate groups of polysaccharides, lipids and glycoproteins present on the microbial surface serve as the binding site for metals [121]. Biosorbents can be altered chemically or genetically to improve adsorption. In chemical modification, binding sites are either enhanced or they are impregnated on matrixes which enhance adsorption capacity and the selectivity of the adsorbent towards the metal ion [122–125]. The biosorbents shown in Table 6 are capable of selectively adsorbing scandium from low concentration solutions the in presence of low concentration of impurities. When the concentration of impurities increases, the sorbent fails to selectively separate scandium from feed sources, like acid mine drainage or leachate of red mud [123–125]. However, a study by G.I. Karavaiko claimed to selectively recover scandium from diluted red mud leachate using biomass *S. cerevisiae* as the biosorbent [126]. To avoid co-precipitation of scandium along with iron, aluminum and titanium, pH 0.6 was maintained in the system. The biosorbent showed exceptional selectivity towards scandium and after four cycles of adsorption and desorption, 98.9% of scandium was extracted [126]. The process of biosorption has many advantages, such as easy operations, no chemical sludge is produced and it is environmentally friendly. The biosorbents discussed were able to successfully recover scandium from diluted streams with low impurity. However, further work needs to be done on enhancing its selectivity from feeds with high amounts of contaminating metals with similar chemical properties as scandium.

Table 6. Summary of different kinds of adsorbent used for recovery of scandium.

S. No.	Sample	Adsorbent	Resin	Extractant/ Microbe	Adsorption Conditions	Desorption	Removal Percentage (%)	Isotherm Kinetics	Mechanism	Reference
1	HNO_3 leachate of Greek bauxite residue	EGTA-functionalized chitosan–silica	-	-	pH 1.25, Adsorbent dose 25.0 mg, 10.0 mL, initial conc. 0.50 mM, time 4 h	HNO_3 at pH 0.50	80%	Langmuir	ion exchange	[40]
2	Sc, Y, La, Ce, Lu, Nd, Sm, Eu, Tb, Dy, Ho, Er, Gd Tm, Yb and Pr	Sol-gel processed silica doped with a novel bifunctional ionic liquid, trioctyl-methylammonium 1-phenyl-3-methyl-4-benzoylpyrazol-5-onate	-	-	0.05 M HNO_3, V/m = 200 mL/g, 10 min	2 M HNO_3	-	Langmuir pseudo-second-order	chemisorption	[96]
3	Model aqueous phase of scandium	Fe_3O_4@SiO_2 coupling agent APTES as a and ligand (EDTA)	-	-	initial conc. 50 mg/L, pH 5, 50 mg adsorbent, 5 h, 25 °C	-	95%	Langmuir pseudo-second order kinetic	exchange or sharing of electrons	[97]
4	Sc, Fe, Al	-	TP 260 & TP 209	-	50 mg resin, 50 mL 1 M Na_2SO_4 solution, pH 2 initial conc. 50 mg-Sc/L, 70 °C, 36 h	-	-	Langmuir isotherm	intraparticle diffusion	[98]
5	Sc, V, Ti	-	Dowex 1	-	0.1 M oxalic acid	0.1 M oxalic acid and 0.1 M HCl	-	-	-	[99]
6	Th, Zr, Fe, Ti, Al and Ca	-	Diaion SK 1, a styrene-base strong acid type resin	-	1 mL per min, 10 g of dry resin.	1 M NH_4SCN and 0.5 M HCl	100%	-	-	[100]
7	Yt, La, Ce, Sm, Er, and Yb	-	AG 50W-X8 resin	-	20 g resin, flow rate of 3.0 mL/min	2 N sulfuric acid	100%	-	-	[101]
8	Sc, Yb, Eu, Ce, Sr, Na, and C	-	cation-exchange resin Dowex 50	-	95% $(CH_2)_4O$, 5%, 6 M HCl, 0.1 M TOPO, 1 g resin, flow rate: 0.5 mL/min	-	-	-	-	[102]
9	Raffinate copper leach solution	-	Purolite C100Na	-	0.1 g of washed and dried resin, pH-1.5, 25 °C, 24 h	1.7 M/L Na_2CO_3	-	Langmuir isotherm	-	[105]
10	REE mixture	-	Dowex 1X4 and Amberlite CG-400,	-	-	10% 7 M HNO_3 (90% methanol) mixture was prepared in 10 mL	scandium was not adsorbed to an appreciable extent	-	-	[106]
11	Zr-raffinate with REE	-	Anion-exchange resin Dowex 1X8, and cation exchange resins, Dowex 50X8	-	0.1 M HNO_3	anion-exchanger in 2.5% 7 M HNO_3–CH_3OH mixture cation-exchanger 5% 1.2 M HCl-$(CH_3)_2CO$ mixture, 91%	-	-	-	[107]

Table 6. *Cont.*

S. No.	Sample	Adsorbent	Resin	Extractant/ Microbe	Adsorption Conditions	Desorption	Removal Percentage (%)	Isotherm Kinetics	Mechanism	Reference
12	Uranium leachate	-	Tulsion CH 93	-	0.1 g sample of air-dried resin 50 mL of solution, shaken, 24 h, 20–23 °C	180 g/L Na_2CO_3, Sc and Th were 94.1 and 98.9%, respectively $(NH_4)_2SO_4$ (50 g/L) a mixture of 30% $(NH_4)_2CO_3$ + 70% NH_4HCO_3 (ACBM)	-	-	-	[108]
13	Red mud	-	AFI-21 and AFI-22	-	sulfuric acid media pH 0.9–4.9	NaOH, 20–30 g/L	50%	-	-	[109]
14	Sc, Ti, Fe(III), Ca, Al, Zr, Si	-	732-type acid cation exchange resin	-	pH 2.5, 200 r/ min, 0.55 g EDTA and 0.16 g ascorbic acid, pH 2.5, 180 min, 25 °C	-	84.2%	-	-	[110]
15	Al, Ti, Fe, Y, La, Ce	-	porous silica-polymer based TRPO/SiO_2-P	-	pH 2 H_2SO_4 s/L: 1.0 g/50 mL, initial conc. 10 mM, 2 h, room temperature	0.01 M EDTA	100	Langmuir adsorption isotherm	electron sharing	[111]
16	Sc, Fe, Al	-	TP 272	Cyanex 272	50 mg resin, 50 mL 1 M Na_2SO_4 solution at pH 2.5 with initial concentration of 50 mg-Sc/L, 22 °C, 12 h	-	-	Langmuir isotherm pseudo-second-order model	intraparticle diffusion	[113]
17	Coal, fly ash leachate	-	VP OC 1026, TP 272	D2EHPA, Cyanex 272	S/L ratio of 1/100 (wt./vol.) 40 °C 150 rpm, pH 2.33	2 M NH_4F, 40 °C 6 M H_2SO_4, 18 h	91% 85%	-	adsorbed via proton exchange with the phosphate groups	[114]
18	La, Dy, Ce, Pr, Nd, Eu, Sm, Gd, Tb, Ho, Er, Yb, Lu, Y, Tm, and Sc	-	Amberchrom CG-71c nonionic macroporous sorbent	P,N-containing podands	5 M $HClO_4$, ratio of the aq. sol. vol. to the sorbent weight: 100:1	-	-	-	complexation by enhanced protonation	[115]
19	Al^{3+}, $Fe^{3+,}$ Zr^{4+}, Mn^{2+}, Co^{2+}, Cu^{2+}, Ni^{2+}, and Zn^{2+}	-	XAD-7HP resin	extractants PC-88A and Versatic 10	50 mg resin, 5 mL aqueous solution, and 1 h shaking at room temperature	2 M sulfuric acid	-	Langmuir isotherm and second-order kinetics	-	[115]
20	Sc, Al, Fe	-	polymer support fabric (PP-g-PGMA)	phenylphosphinic acid (PPI)	1 ppm Sc, pH 2, 24 h at room temperature	-	98%	Langmuir	solvation mechanism of adsorption between Sc and PPI	[116]
21	REE	-	DIAION HP2MG (methacrylate resin)	Cyanex 272 1-octanol as modifier	20 mL of REE 1 mM solution, 20 mg of SIRs, constant shaking, 24 min, 298 K	5 M HCl	-	Langmuir	-	[118]

Table 6. *Cont.*

S. No.	Sample	Adsorbent	Resin	Extractant/ Microbe	Adsorption Conditions	Desorption	Removal Percentage (%)	Isotherm Kinetics	Mechanism	Reference
22	Sc, Tm, Yb and Lu	-	Modified Merrifield Resins	Cyanex 923,	5 mL of Sc solution, 200 mg of impregnated resins, constant stirring, 30 min, 25 °C	-	-	-	extraction of neutral complex and cation exchange	[119]
23	Sc solution	-	TVEX	TBP, di-isooctyl methyl phosphonate (DIOMP) and phosphine oxide with different alkyl groups (POR)	organic to aquas-phase ratio of 1:20, 25 °C, 24 h, >4 M HCl	-			TVEX-DIOMP as [ScCl $(DIOMP)_2$ $(H_2O)_3]^{2-}$ complx from 4 M HCl	[120]
24	Coal byproduct	-	microbe-encapsulated silica gel (MESG) biosorbent	cell loading of 1.0 g/mL, pH 3.0, 1 bed vol. 2 mL feedstock sol.	pH-6, 0.050 M sodium citrate	-	-	-	-	[122]
25	Red mud	-	Quaternized Algal/ Polyethyleneimine beads (Q-APEI) with dry algal biomass	pH > 4 SD: 0.6 g/L; 20 °C;40 rpm; 30 h	0.5 M HCl/$CaCl_2$ solutions 88.1%	-	-	Langmuir	complexation of the Sc with amine groups	[123]
26	Red mud	-	*Laminaria digitata* algal biomass/ polyethyleneimine beads, A_LPEI	pH 1–5, 1 mmol/L. SD: 2 g/L; T: 22 °C, 48 h; 170 rpm	acidic $CaCl_3$, 99%	-	-	Langmuir equation	ion exchange and chelation on protonated amine groups, sulfonic groups and carboxylate groups	[124]
27	AMD and seawater	-	*Posidonia oceanica* with 1-(2-pyridylazo)-2-naphthol (PAN) grafted on algal biomass (2-algae-P)	Adsorbent dosage 1 g/L. pH 5 (AMD), pH 6 (Seawater), REE = ~2 ppm, 45 °C, 1 h	-	-	-	Langmuir and pseudo-second order kinetics	binding by coordination mechanism with the ligand of PAN	[125]
28	Red mud	-	-	biomass of *Saccharomyces cerevisiae* and *Aspergillus terreus*	pH 0.6 fungi (0.2 g/L, dry wt) and yeasts (0.5 g/L, dry wt), 20 mL aliquots, 220 rpm, 20–25 °C, 1 h	with 20 mL of 10% *w*/*v* Na_2CO_3, 99.5%	*S. cerevisiae* 98.8%	Langmuir equation	-	[126]
29	Sc, Ce, La and Al (monazite processing liquor)	-	glycol amic acid embedded resin	-	24 h, pH 1, 0.1 g resin in 100 mL	2.0 M HCl solution at 80 °C,	45%	-	-	[127]
30	Sc and Nu	Biochar of wood dust	-	-	absorbent conc. 1–10 g/L, 24 h, 25 °C, 350 rpm	-	52% and 78%, respectively	-	-	[128]

Table 6. *Cont.*

S. No.	Sample	Adsorbent	Resin	Extractant/ Microbe	Adsorption Conditions	Desorption	Removal Percentage (%)	Isotherm Kinetics	Mechanism	Reference
31	Bauxite residue leachate	α-ZrP (α-zirconium phosphate)	-	-	0.05 g of ion exchanger, 20 mL feed solution, pH-1.5, 300 rpm, 18 h, at room temp in HCl media	2 M/L HCl, two-step elution	99.9%	Langmuir pseudo-second-order kinetics	chemical reaction at the surface	[129]
32	Tomtor Deposit leachate	-	Purolite D5041(Phosphorus) and Purolite C115 (carboxyl)	-	volume ratio ion exchanger: solution = 1:300 (for phosphorus) and 1:150 (carboxyl), contact time of 24 h	$(NH_4)HS$ (100 g/L) 2 h, 70–80 °C, 78.9% (phosphorus) 1 M HNO_3 solution was able to remove REEs	99.8–99.9%	-	-	[130]
33	Red mud	-	AFI-21 ampholyte	-	-	Na_2CO_3 conc of 150 g/Ldm^3 scandium desorption of 96%	76%	-	-	[130]
34	REEs(III)	macro-porous silica based polymer (SiO_2-P) based di(2-ethylhexyl) phosphonate adsorbent (HDEHP/ SiO_2-P)	-	-	m/V = 0.1 g/ 5 mL, 120 rpm, 30 min, H_2SO_4 5 M	-	-	Langmuir	ion exchange	[131]
35	Sc, Pd, Pt & Au	carboxymethylchitin (CMCht) hydrogel	-	-	pH 3.9, at initial conc. 100 ppb, adsorbent weight 50 mg, 2 h	-	35%	-	-	[132]

7. Purification Processes

7.1. Nanofiltration

Nanofiltration is a pressure-driven filtration-membrane process. Based on separation by size, nanofiltration is the upper end of reverse osmosis and lower end of ultra-filtration. The general pore size of the membrane varies between 1–10 nanometers. The transport across the membrane occurs due to both fluxes as well as trans-membrane pressure differences. The separation happens by diffusion of the molecules of the solvent through the mass of the membrane, controlled primarily by high trans-membrane pressure. It is a process by which part of the feed passes through semi-permeable membrane. For scandium retrieval, a pre-enrichment of scandium is needed to obtain higher concentrations for the subsequent selective extraction [133]. Here, nanofiltration can offer two vital advantages. First, it offers selectivity and secondly, it may reduce the volume to be extracted downstream, reducing the environmental impact caused by solvent extraction steps [134]. However, a major limitation of nanofiltration is that in high ionic strength solutions, adequate fluxes can only be accomplished via high operational pressures, which surges operational costs. Furthermore, there are limited numbers of commercial membranes that can withstand such highly acidic conditions. Remmen et al. [54] prepared layer-by-layer modified nanofiltration membranes that were optimized with respect to their selectivity towards scandium as well as acid resistance. The synthetic solutions consisted of scandium, iron and HCl. In this solution, under optimized conditions, the membrane retained a maximum of up to 64% scandium, efficiently eliminating iron (the major impurity). In real titanium dioxide pigment wastewater, the proposed membrane showed higher retention of scandium 60% compared to available commercial acid resistant membranes that showed only 50%.

7.2. Polymer Inclusion Membranes

Polymer inclusion membranes (PIMs) are membranes made up of a liquid extractant trapped in a polymer-based matrix that is typically prepared with polyvinyl chloride (PVC) or cellulose triacetate (CTA). As a separation technology, PIMs are used as the phase transfer medium, extraction, and pre-concentration unit for several cations and anions. In the past decades, PIMs have been extensively used for hydrometallurgical applications such as extraction and metal recovery because of their high selectivity, stability, durability, etc. [135]. A CTA-based PIM was developed with dioctyl phthalate (DOP) as a plasticizer with binary carrier PC-88A and Versatic 10 (decanoic acid). Scandium was selectively separated from a nitrate solution containing other rare earth metal ions. However, poor elution was an issue, which was addressed by using Versatic 10 along with PC-88A as carrier, thus enhancing the extraction of scandium [136]. A comparative study was done between using the PIM containing the amic acid extractants N-[N,N-di(2-ethylhexyl) aminocarbonylmethyl]glycine (D2EHAG) or N-[N,N-di(2-ethylhexyl)aminocarbonylmethyl]phenylalanine (D2EHAF) as carriers and the commercial carriers 2-thenoyltrifluoroacetone (HTTA) or 2-ethylhexylphosphoric acid mono-2-ethylhexyl ester (PC-88A). It was found that the PIM with the amic acid extractants (D2EHAG) or (D2EHAF) as carriers were more efficient in extracting and stripping scandium from a feed solution containing rare earth metals [137] and base metal ion solution containing iron (III) [138]. It was found that PIM with the amic acid extractant D2EHAF was able to successfully separate scandium in both cases. Thus, the PIM containing D2EHAF was able to quantitatively and selectively transport scandium from 0.1 M sulfate feed solution at pH 3, containing base metal (Fe, Al, Ca, Co, Ni, Mn, Cr and Mg) ions to a solution containing 0.5 M H_2SO_4 [138]. However, studies with industrial leach liquor containing scandium have yet to be done.

7.3. Precipitation and Crystallization

Precipitation is a separation process where soluble metal ions are separated using other salts by double displacement reactions where the targeted metal ion separates as an insoluble solid. The theoretical mechanism is that the dissolved metal ions are precipitated by

chemical reagents (precipitants), resulting in the creation of metal hydroxides, carbonates, sulfides, oxalates and phosphates that can be simply separated by filtration, sedimentation or centrifugation. It is mostly used for removal of heavy metals from industrial effluents. Table 7 reports the studies on the recovery of scandium through precipitation and crystallization. The most practiced method of scandium recovery by precipitation is by addition of oxalic acid resulting in scandium oxalate. Calcination of scandium oxalate at around 700 °C produces scandium oxide of 99.5% purity. Apart from oxalic acid, fluorides [65,139] and phosphates have been used for scandium precipitation [140]. However, the main problem is the presence of high concentration of iron (III) which co-precipitates along with scandium. Therefore, for maximum recovery of scandium in pure form, multiple stages of neutralization and precipitation have to be followed to eliminate the major impurities with minimal scandium loss [58,60,141]. Few studies have been reported regarding crystallization of scandium from red mud leachate. Two methods have been used: cooling crystallization and anti-solvent crystallization. The former has a low recovery while the later has a high recovery, but crystal size is very small (< 2 μm), which interferes with separation and filtration. Therefore, better crystallization and filtration techniques must be developed for this process. A uniform distribution of iron in the crystals as an impurity has also been found due to its similarity with scandium with highest purity of 98.3% [142,143]. Thus, the leach liquor feeds that have scandium in the form of $(NH_4)_3ScF_6$ with a low presence of impurities can be converted to crystals of high purity. However, the use of fluoride is of environmental concern. Therefore, further studies in this area are required.

Table 7. Summary of precipitation and crystallization methods.

S. No	Sample	Process	Agent	Condition	Recovery Percentage	Reference
1	Uranium leachate	Multiple precipitation	HF Oxalic acid	-	10% (99.5% purity)	[58]
2	Scandium and titanium	Neutralization precipitation	$Ca(OH)_2$	pH-2, 3.3 g/L titanium oxide	96.75	[60]
3	Red mud leachate	Dual-stage successive precipitation	Dibasic phosphate	-	$ScPO_4$	[65]
4	Synthetic scandium solution	-	sodium fluoride, ammonium hexafluoroscandate at molar ratios of F to Sc within 1–14	-	ScF_3, Na_3ScF_6, and $Na(NH_4)_2ScF_6$	[139]
5	H_2SO_4 leachate of bauxite	Triple-stage successive precipitation	NH_4OH NH_4OH $(NH_4)_2HPO_4$	pH-3.3–3.4 pH-3.6–3.7 pH-2.5–2.6	65% $ScPO_4$	[140]
6	Strip liquor containing 0.2 wt% Sc and minute impurities	Cooling crystallization Anti-solvent crystallization	- Ethanol	1 °C Ethanol-to-strip liquor volumetric ratio of 0.8	$(NH_4)_3ScF_6$ < 50% 98%	[142]
7	Ammonium scandium hexafluoride from solvent extraction strip liquors	Anti-solvent crystallization	Ethanol	Solvent to anti-solvent volumetric ratio of 1:1 ethanol conc of 8.6 mol/L	98% purities greater than 98.3%	[143]
8	Nickle leachate	Neutralization and sulfide precipitation	-	pH > 4	-	[144]
9	Tungstenic slag	Extraction precipitation	H_2SO_4	-	94% $ScCl_3$	[145]
10	Tungsten slag		Oxalic acid	-	85.2%	[146]

8. Recent Scandium Case Studies

After discussing the unit operations for scandium recovery, we will discuss some recent case studies on scandium recovery (Table 8). There are a number of projects dealing with scandium recovery: the SCALE project, EU; the Nyngan project in New South Wales, Australia; the polymetallic Elk Creek project in Nebraska; the polymetallic Owendale Project in New South Wales; the polymetallic Sunrise Project in New South Wales; the polymetallic SCONI project, Queensland; the Taganito high-pressure acid-leach nickel operation, Japan; byproduct of alumina refining in the Ural Mountains, Russia; and development of scandium recovery as a byproduct of uranium production, in Dalur, Kurgan region, Russia.

Table 8. Status of projects on scandium recovery.

S. No.	Country	Name of Project	Primary Resource	Status
1.	Australia	Nyngan scandium project	Typical tertiary laterite composed of limonites and saprolites	The feasibility study concludes that the project has the potential to produce an average of 37,690 kg of scandium oxide per year, at grades of 98.0–99.9%
2.	Nebraska, US	EIK Creek Niobium project	Carbonatite rocks	The mine is expected to produce 168,861 t of niobium in the form of ferroniobium, 3410 t of scandium oxide and 415,841 t of titanium dioxide over its operating life of 36 years
3.	New South Wales, Australia	Owendale scandium project	Platina resources	Stage one will produce 20 tons per annum (tpa) of scandium oxide during the initial five years of operation, while stage two will double the annual production capacity to 40 t with the processing plant upgrade

9. Environmental Risk Assessment

Extraction of REEs from their primary sources has led to severe environmental hazards. Presently, scandium is mainly recovered as a byproduct from the processing of other metals such as titanium dioxide, REEs and aluminum [12]. This makes the retrieval of scandium technically challenging [12] and environmentally hazardous [91]. The Mountain Pass mine in California, which controlled the global REE market for decades, was closed down in 2002 because of the pollution and environmental hazard it generated [146–148]. Similarly, the REE sources in China have now raised serious health and environmental concerns, such as emission of hazardous gases like H_2S, HF and H_2SO_4 [149]. It also causes heavy metal leakage to land groundwater as well as exposure to radioactive metals around the mining sites [150]. Moreover, prolonged mining leaves fine dust particles suspended in the air, long time inhalation of which gives rise to pneumoconiosis (black lung) [151]. The City of Baotou, located near the Bayan Obo mine, had many pollution issues caused by mining and nearby processing of REEs. The Chinese government has therefore closed many facilities as well as limited production based on the environmental damage [152].

LCA is a source-to-grave and, sometimes, especially with recycling units, source-to-source investigation techniques to evaluate environmental impacts accompanying all the stages of a product's life from raw materials to its distribution or recycling. It can assist decision makers to implement the means needed to improve the sustainability performance of the unit [152]. In short, LCA provides a complete outlook of the environmental effects caused over the entire life cycle of the product. It starts from raw material extraction and attainment, followed by manufacturing, transportation, supply, maintenance, reuse and recycling, and disposal and waste management [153]. Major features of LCA are that it avoids shifting environmental consequences from one geographical area, source and stage to another. The four main stages of LCA are shown below in Figure 2 that depicts the stages followed for life cycle assessment of any product. The first stage of LCA analysis defines what part of the product's life cycle will be used for analysis, thus defining the boundary for the assessment. The second stage provides information about the mass and energy flow across the set boundary in relation to raw materials consumed in these processes. In this stage, details about the environmental impact in terms of energy consumption, emission and interactions are also given. It serves as an inventory for impact assessment in the next stage. In the third stage, the inventory formed in the previous stage is analyzed in detail. Results in terms of indicators such as Human toxicity non-cancer (HTNC), Global Warming Air (GWA), Eutrophication, Toxicity and others are studied in detail for all impact categories. Every impact category is assessed in detail by weighing and normalizing in the third stage. Once the assessment is over, interpretation of the assessment is done in the fourth and final stage of LCA. It involves critically reviewing the data, understanding the sensitivity of the assessment and representation of the results. Thus, with LCA, a map can be drawn between the environment burdens such as pollutants and waste generated after each stage and the consumption of energy and raw material

for those stages individually. This will help in assessing the effect of the input and output parameters associated with the particular product and the accompanying pathway for the long-term sustainability of energy sources, human health, climate, biodiversity and many more. Thus, LCA helps in identifying the most suitable pathway for a particular product with the lowest environment burden. It generates a scope to identify the steps and their alternative approaches to reduce the negative impacts on the environment. The critical and specific nature of REEs, including scandium, demands an LCA to provide proper guidance for industries to adopt more eco-friendly approaches for downstream of the REEs. Many LCA studies have been done for accessing the environmental effects of REEs [152,154–156]. However, the environmental effects of scandium have been specifically studied only by Wang et al. [27]. From their study, it was concluded that HTNC and GWA are the top two significant challenges of Sc_2O_3 production. Steam and oxalic acid are the top two inputs with the greatest impacts on HTNC and GWA caused indirectly during production stage. Thus, reduction in the consumption of the above two inputs could reduce the overall impact associated with scandium mining. Moreover, use of alternative reagents with lower environmental impact or reduction of the dosage could be done to reduce the impact, were some of the suggestions provided. As scandium is predominantly recovered from bauxite residues, LCA can provide a better outlook towards its environmental effect. A recent LCA study was done by Joyce and Björklund [27] to understand the environmental effect of recovering valuable metals from bauxite residue with the primary goal of "Zero-Waste Valorization". Few observations were made by the authors, one of them was that the merging of technologies proved to be beneficial. For instance, combination of valorization with pretreatment can lead to environmental benefits. Moreover, modification and utilization of pathway residues for other purpose like construction would also decrease environmental impacts. Another important parameter pointed out was the incorporation of recycle and re-use of pathway reagents [156]. Thus, the key of LCA analysis is the acknowledgement that simple parameters of the pathway that may seem environmentally harmless in isolation can have major environmental impact indirectly when used in the processing stages. Therefore, this analysis gives us a close understanding of the process, different parameters and their effects on the environment.

However, since LCA analysis cannot be transferred to other sources or geographical locations, it is very important to assess the environmental effect of other primary and secondary sources as well. Moreover, process pathways associated with recycling and reuse must be assessed to understand the effect on the ecology. The recycling source pathways have many added advantages over virgin primary sources such as elimination of a number of processes, which has been seen to significantly contribute to the environmental impacts like ore mining, leaching etc. It also avoids undesirable byproducts which are fundamental to mining from primary sources [157]. Despite all the benefits associated with recycling as a source, it has not been explored properly for LCA to understand the environmental impacts. As the burden of mining has caused enough environmental damage to date, it is important to at least develop a Life Cycle Thinking (LCT) approach, with the initial source being recycling of valuable and critical metals. It will provide better understanding of the pathways and even give scope for the development of processes with a focus on environmental benefits. This will help decision and policy makers to make the appropriate decisions. It will further help to shift the burden of mining of major metal ores to valuable and critical metals, improve the associated global economic market of these metals, reduce the accompanying environmental effects, and provide a scope for more technological advancements in that arena.

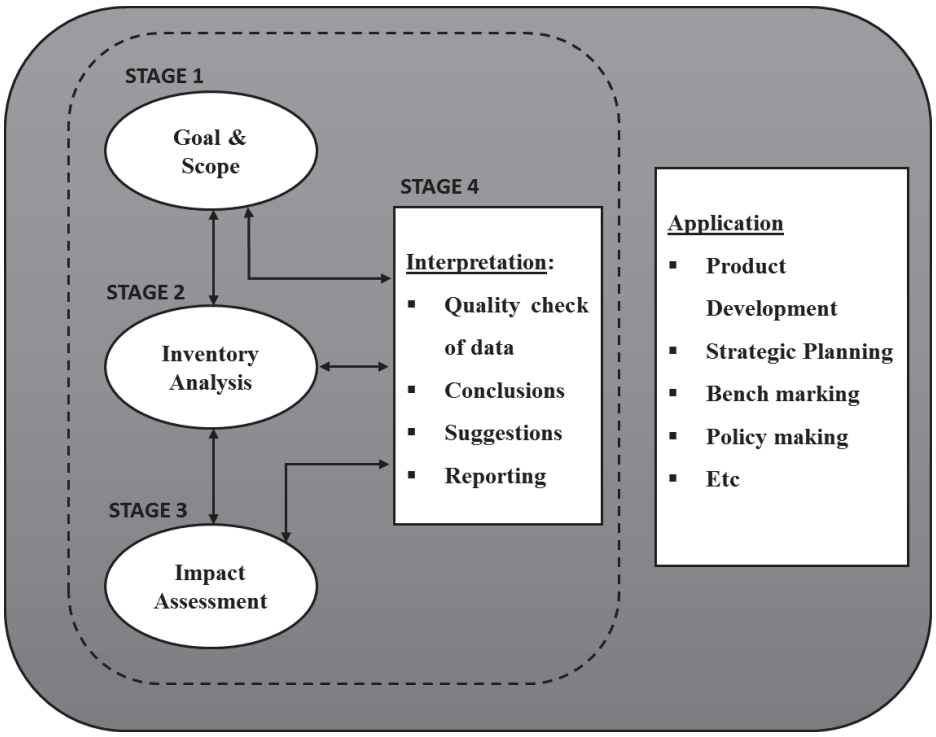


Figure 2. The stages of LCA analysis.

10. Conclusions

New technologies involving the use of scandium is emerging with time. Over the decades, the two main applications of scandium were in solid oxide fuel cells and aluminum–scandium alloys. However, due to its unique physico-chemical properties, scandium has sufficiently heightened its market demand with new applications in future aircraft and automotive manufacturing. Globally, scandium is found across many nations in the ores of other metals such as aluminum, uranium, tantalum and others. However, the largest contributor of scandium is the reserve of Nb–REE–Fe in Bayan Obo, Inner Mongolia, China, where it is generated from the REEs tailings as depicted in Figure 1. In addition, scandium is largely recovered from aluminum ore (bauxite) processing waste as a secondary source. However, due to the presence of other metals with similar geochemistry as scandium, efficient recovery of the metal becomes quite challenging. Many other sources have been identified but have not been explored, like electrical and municipal waste. Hence, exploration of urban mining as a viable source for scandium recovery is needed. Commercial recovery of scandium takes place following a number of different types of hydrometallurgical processes. These hydrometallurgical processes add to the environmental burden in the form of high energy consumption, utilization of toxic chemicals, production of secondary toxic waste, etc. Hence, this review outlines the technological advances over the decades across various hydrometallurgical separation processes stating their pros and cons as well as advantages of one process over another. An attempt has been made to identify some suitable advances based on their reduction in environmental damage and high scandium recovery efficiency. Since there are few discussions of the environmental impact of the technical advances in literature, it is hard to analyze and state their overall impact on the environment when applied for commercial recovery. As reported and discussed, there has been very limited studies on the environmental impact of commercial scandium recovery but they clearly shows that, the beneficiation and hydrometallurgy steps in the process contributes major burdens on the environment primarily because of low concentrations of scandium and the presence of high concentrations and numbers of impurities. Hence, it is important to identify and explore alternate sources as well as alternate hydrometallurgical processes that can lead to the reduction of the burden and impact on the

environment. Moreover, there is a huge gap and lack of attention towards the analysis of the environmental impact of scandium production from different available sources following different pathways. This could help in getting a clearer comparison and understanding of the relationship between the processes and the environmental burdens generated by them so that further studies could be done to reduce the environmental burden.

11. Understanding and Future Direction

The review presented here has been prepared with a goal of giving readers an understanding of the roots of the environmental burden caused by scandium production. There are few studies that discuss the environmental impact of scandium recovery from different sources. The authors have tried to summarize that information that is available. It is very well understood that scandium is associated with REEs and other metals when it is recovered from primary, secondary or tertiary sources; and, since the percentage of scandium is very low compared to other metals, its recovery has become expensive, challenging and environmentally hazardous. Thus, the removal of other metals along with efficient recovery of scandium is most important parameter that can help in reduction of environmental burden. There have been many technological advances. The authors have outlined the advancements made over years in different areas of technology with a focus on the enhancement of recovery efficiency of scandium. Each process discussed has been outlined with the associated benefits and limitations for the readers to understand and take up research in the unexplored areas that can benefit both the economy and the environment. For example, few studies have been done on the recovery of scandium from electronic waste. This source can be explored, as it will promote recycling as well as reduce the mining burden to some extent. Moreover, more exploration of bioleaching, biosorption, solid extractants and other methods with the aim of high selectivity for scandium needs to be done. Additionally, the unavailability of many studies on the life cycle assessment of scandium from different types of sources, very well reflects the lack of environmental awareness linked with scandium recovery. Therefore, more research needs to be done in this area to truly understand the role of the source and the processing pathway followed for scandium recovery. Thus, we will have a better idea of the direction to work in to achieve the goal of eco-friendly processes and sustainability.

Author Contributions: All authors contributed to the study conception and design. Material preparation and data collection were performed by A.G. (Aratrika Ghosh), S.D., A.G. (Anirudh Gupta) and R.J. The first draft of the manuscript was written by A.G. (Aratrika Ghosh), S.D. and A.G. (Anirudh Gupta) and all authors commented on previous versions of the manuscript. All authors have read and agreed to the published version of the manuscript.

Funding: The authors declare the support of the IGSTC project "BioCuInGe" with sanction No.: IGSTC/CALL2016/BIO-CULNGE/132017.

Informed Consent Statement: Not applicable.

Data Availability Statement: All data are true and valid and are available.

Acknowledgments: The authors would like to thank the IIT Delhi and HZDR administration for providing the necessary facilities to carry out the present study.

Conflicts of Interest: The authors declare no conflict of interest.

References

1. Sonter, L.J.; Ali, S.H.; Waston, J.E.M. Mining and biodiversity:key issues and research needs in conservation science. *Proc. Biol. Sci.* **2018**, *285*, 1892.
2. Agboola, O.; Babatunde, D.E.; Fayomi, O.S.I.; Sadiku, E.R.; Popoola, P.; Moropeng, L.; Yahaya, A.; Mamudu, O.A. A review on the impactof mining operation: Monitoring, assessment and management. *Results Eng.* **2020**, *8*, 100181. [CrossRef]
3. Falagan, C.; Grail, B.M.; Johnson, D.B. New approaches for extracting and recovering metals from mine tailings. *Miner. Eng.* **2017**, *106*, 71–78. [CrossRef]

4. Baba, Y.; Fukami, A.; Kubota, F.; Kamiya, N.; Goto, M. Selective extraction of scandium from yttrium and lanthanides with amic acid-type extractant containing alkylamide and glycine moieties. *RSC Adv.* **2017**, *4*, 50726–50730. [CrossRef]
5. European Commission. *2017 List of Critical Raw Materials for the EU, Brusseles*; European Commission: Brusseles, Belgium, 2017.
6. Sykes, J.P.; Wright, J.P.; Trench, A.; Miller, P. An assessment of the potential for transformational market growth amongst the critical metals. *Trans. Institutions Min. Metall. Sect. B Appl. Earth Sci.* **2016**, *125*, 21–56. [CrossRef]
7. Baptiste, P.E.J. Extraction of Scandium from Its Ores. U.S. Patent 2874039, 17 February 1959.
8. Munnoch, S.; Worstall, T. *Scandium*; Report of Minor metals Trade Association; MMTA: Kent, UK, 2016.
9. Hedrick, J.B. *Scandium*; Mineral Commodity Summaries 2010a; U.S. Geological Survey: Reston, VA, USA, 2010.
10. Zhang, N.; Li, X.K.; Liu, X.M. Recovery of scandium from bauxite residue—Red mud: A review. *Rare Met.* **2016**, *35*, 887–900. [CrossRef]
11. Hedrick, J.B. *Rare Earth*; Minerals Yearbook 2010b; U.S. Geological Survey: Reston, VA, USA, 2010.
12. Wang, W.; Cheng, C.Y. Separation and purification of scandium by solvent extraction and related technologies: A review. *J. Chem. Technol. Biotechnol.* **2011**, *86*, 1237–1246. [CrossRef]
13. Shalomeev, V.A.; Lysenko, N.A.; Tsivirko, E.I.; Lukinov, V.V.; Klochikhin, V.V. Structure and properties of magnesium alloys with scandium. *Met. Sci. Heat Treat.* **2008**, *50*, 34–37. [CrossRef]
14. Ciacchi, F.T.; Badwal, S.P.S.; Drennan, J. The system Y_2O_3–Sc_2O_3–ZrO_2: Phase characterisation by XRD, TEM and optical microscopy. *J. Eur. Ceram. Soc.* **1991**, *7*, 185–195. [CrossRef]
15. Narayanan, R.P.; Ma, L.C.; Kazantzis, N.K.; Emmert, M.H. Cost Analysis as a Tool for the Development of Sc Recovery Processes from Bauxite Residue (Red Mud). *ACS Sustain. Chem. Eng.* **2018**, *6*, 5333–5341. [CrossRef]
16. Gambogi, J. *USGS Minerals Information: Scandium*; U.S. Geological Survey: Reston, VA, USA, 2017; pp. 146–147.
17. Zou, D.; Deng, Y.; Chen, J.; Li, D. A review on solvent extraction of scandium. *J. Rare Earths* **2021**, *40*, 1499–1508. [CrossRef]
18. Wang, W.; Pranolo, Y.; Cheng, C.Y. Metallurgical processes for scandium recovery from various resources: A review. *Hydrometallurgy* **2011**, *108*, 100–108. [CrossRef]
19. Junior, A.B.B.; Espinosa, D.C.R.; Vaughan, J.; Tenorio, J.A.S. Recovery of scandium from various sources: A critical review of the state of the art and future prospects. *Miner. Eng.* **2021**, *172*, 107148. [CrossRef]
20. Pyrzyńska, K.; Kilian, K.; Pęgier, M. Separation and purification of scandium: From industry to medicine. *Sep. Purif. Rev.* **2019**, *48*, 65–77. [CrossRef]
21. Tunsu, C.; Petranikova, M.; Ekberg, C.; Retegan, T. A hydrometallurgical process for the recovery of rare earth elements from fluorescent lamp waste fractions. *Sep. Purif. Technol.* **2016**, *161*, 172–186. [CrossRef]
22. Cui, J.; Zhang, L. Metallurgical recovery of metals from electronic waste: A review. *J. Hazard. Mater.* **2008**, *158*, 228–256. [CrossRef]
23. Kumar, V.; Sahu, S.K.; Pandey, B.D. Prospects for solvent extraction processes in the Indian context for the recovery of base metals. A review. *Hydrometallurgy* **2010**, *103*, 45–53. [CrossRef]
24. Xiao, J.; Zou, K.; Zhong, N.; Gao, D. Selective separation of iron and scandium from Bayer Sc-bearing red mud. *J. Rare Earths* **2022**. [CrossRef]
25. Jones, A.E.W.; Vasyukoy, O.V. The economic geology of scandium, the runt of the rare earth element litter. *Econ. Geo.* **2018**, *113*, 973–988. [CrossRef]
26. Shaoquan, X.; Suqing, L. Review of the extractive metallurgy of scandium in China (1978–1991). *Hydrometallurgy* **1996**, *42*, 337–343. [CrossRef]
27. Wang, L.; Wang, P.; Chen, W.Q.; Wang, Q.Q.; Lu, H.S. Environmental impacts of scandium oxide production from rare earths tailings of Bayan Obo Mine. *J. Clean. Prod.* **2020**, *270*, 122464. [CrossRef]
28. Shimazaki, H.; Yang, Z.; Miyawaki, R.; Shigeoka, M. Scandium-Bearing minerals in the Bayan Obo Nb-REE-Fe deposit, inner Mongolia. *China. Resour. Geol.* **2007**, *58*, 80–86. [CrossRef]
29. Chassé, M.; Griffin, W.L.; O'Reilly, S.Y.; Calas, G. Scandium speciation in a world-class lateritic deposit. *Geochem. Perspect. Lett.* **2017**, *3*, 105–114. [CrossRef]
30. Kalashnikov, A.O.; Yakovenchuk, V.N.; Pakhomovsky, Y.A.; Bazai, A.V.; Sokharev, V.A.; Konopleva, N.G.; Mikhailova, J.A.; Goryainov, P.M.; Ivanyuk, G.Y. Scandium of the Kovdor baddeleyite–apatite–magnetite deposit (Murmansk Region, Russia): Mineralogy, spatial distribution, and potential resource. *Ore Geol. Rev.* **2016**, *72*, 532–537. [CrossRef]
31. Lapin, A.V.; Tolstov, A.V.; Kulikova, I.M. Distribution of REE, Y, Sc, and Th in the Unique Complex Rare-Metal Ores of the Tomtor Deposit. *Geochem. Int.* **2016**, *54*, 1067–1078. [CrossRef]
32. Kuzmin, V.I.; Flett, D.S.; Kuzmina, V.N.; Zhizhaev, A.M.; Gudkova, N.V.; Kuzmin, D.V.; Mulagaleeva, M.A.; Tolstov, A.V.; Logutenko, O.A. The composition, chemical properties, and processing of the unique niobium–rare earth ores of the Tomtor deposit. *Chem. Pap.* **2019**, *73*, 1437–1446. [CrossRef]
33. Neumann, R.; Medeiros, E.B. Comprehensive mineralogical and technological characterisation of the Araxá (SE Brazil) complex REE (Nb-P) ore, and the fate of its processing. *Int. J. Miner. Process.* **2015**, *144*, 1–10. [CrossRef]
34. Geneyton, A.; Filippov, L.O.; Heinig, T.; Buaron, N.; Menad, N.E. Towards the efficient flotation of monazite from silicate-rich tailings with fatty acids collectors using a lanthanum salt as a selective phosphate activator. *Miner. Eng.* **2021**, *160*, 106704. [CrossRef]
35. Kursun, I.; Terzi, M.; Ozdemir, O. Determination of surface chemistry and flotation properties of rare earth mineral allanite. *Miner. Eng.* **2019**, *132*, 113–120. [CrossRef]

36. Wang, Y.; Zhang, T.; Lyu, G.; Guo, F.; Zhang, W.; Zhang, Y. Recovery of alkali and alumina from bauxite residue (red mud) and complete reuse of the treated residue. *J. Clean. Prod.* **2018**, *188*, 456–465. [CrossRef]
37. Binnemans, K.; Pontikes, Y.; Jones, P.T.; Gerven, T.V.; Blanpain, B. Recovery of rare earths from industrial waste residues: A concise review. In Proceedings of the 3rd International Slag Valorisation Symposium Leuven, Leuven, Belgium, 19–20 March 2013; pp. 191–205.
38. Rivera, R.M.; Ulenaers, B.; Ounoughene, G.; Binnemans, K.; Gervena, T.V. Extraction of rare earths from bauxite residue (red mud) by dry digestion followed by water leaching. *Miner. Eng.* **2018**, *119*, 82–92. [CrossRef]
39. Anawati, J.; Azimi, G. Recovery of scandium from Canadian bauxite residue utilizing acid baking followed by water leaching. *Waste Manag.* **2019**, *95*, 549–559. [CrossRef] [PubMed]
40. Roosen, J.; Roosendael, S.V.; Borra, C.R.; Gerven, T.V.; Mullens, S.; Binnemans, K. Recovery of scandium from leachates of Greek bauxite residue by adsorption on functionalized chitosan–silica hybrid materials. *Green Chem.* **2016**, *18*, 2005–2013. [CrossRef]
41. Li, G.; Ye, Q.; Deng, B.; Luo, J.; Rao, M.; Peng, Z.; Jiang, T. Extraction of Scandium from Scandium-rich Material Derived from Bauxite Ore Residues. *Hydrometallurgy* **2018**, *176*, 62–68. [CrossRef]
42. Gentzmann, M.C.; Schraut, K.; Vogel, C.; Gabler, H.E.; Huthwelkerf, T.; Adam, C. Investigation of scandium in bauxite residues of different origin. *Appl. Geochem.* **2021**, *126*, 104898. [CrossRef]
43. Taggart, R.K.; Hower, J.C.; Dwyer, G.S.; Hsu-Kim, H. Trends in the rare earth element content of US-based coal combustion fly ashes. *Environ. Sci. Technol.* **2016**, *50*, 5919–5926. [CrossRef]
44. Zhang, W.; Honaker, R. Characterization and recovery of rare earth elements and other critical metals (Co, Cr, Li, Mn, Sr, and V) from the calcination products of a coal refuse sample. *Fuel* **2020**, *267*, 117236. [CrossRef]
45. Hussain, R.; Luo, K. Geochemical evaluation of enrichment of rare-earth and critical elements in coal wastes from Jurassic and Permo-Carboniferous coals in Ordos Basin, China. *Nat. Resour. Res.* **2020**, *29*, 1731–1754. [CrossRef]
46. Lefticariu, L.; Klitzing, K.L.; Kolker, A. Rare Earth Elements and Yttrium (REY) in coal mine drainage from the Illinois Basin, USA. *Int. J. Coal Geol.* **2020**, *217*, 103327. [CrossRef]
47. Honaker, R.Q.; Groppo, J.; Yoon, R.H.; Luttrell, G.H.; Noble, A.; Herbst, J. Process evaluation and flowsheet development for the recovery of rare earth elements from coal and associated byproducts. *Miner. Metall. Process.* **2017**, *34*, 107–115. [CrossRef]
48. Honaker, R.Q.; Zhang, W.; Werner, J. Acid leaching of rare earth elements from coal and coal ash: Implications for using fluidized bed combustion to assist in the recovery of critical materials. *Energy Fuels* **2019**, *33*, 5971–5980. [CrossRef]
49. Kermer, R.; Hedrich, S.; Bellenberg, S.; Brett, B.; Schrader, D.; Schoenherr, P. Lignite ash: Waste material or potential resource-Investigation of metal recovery and utilization options. *Hydrometallurgy* **2017**, *168*, 141–152. [CrossRef]
50. McGill, I. Rare Earth Elements. In *Ullmann's Encyclopedia of Industrial Chemistry*; Wiley-VCH Verlag GmbH & Co. KgaA: Weineim, Germany, 2000.
51. Liu, Y.; Naidu, R. Hidden values in bauxite residue (Red Mud): Recovery of metals. *Waste Manag.* **2014**, *34*, 2662–2673. [CrossRef] [PubMed]
52. Anon, World uranium mining. In *Report of World Nuclear Association*; World Nuclear Association: London, UK, 2010.
53. Deschamps, Y. *Scandium*; Report of BRGM (In French). BRGM: Orleans, France.
54. Remmen, K.; Schafer, R.; Hedwig, S.; Wintgens, T.; Wessling, M.; Lenz, M. Layer-by-layer membrane modification allows scandium recovery by nanofiltration. *Environ. Sci. Water Res. Technol.* **2019**, *5*, 1683–1688. [CrossRef]
55. Nie, H.; Wang, Y.; Wang, Y.; Zhao, Z.; Dong, Y.; Sun, X. Recovery of scandium from leaching solutions of tungsten residue using solvent extraction with Cyanex 572. *Hydrometallurgy* **2018**, *175*, 117–123. [CrossRef]
56. Aiglsperger, T.; Proenza, J.A.; Lewis, J.F.; Labrador, M.; Svojtka, M.; Rojas-Puron, A.; Ďurišová, J. Critical metals (REE, Sc, PGE) in Ni laterites from Cuba and the Dominican Republic. *Ore Geol. Rev.* **2016**, *73*, 127–147. [CrossRef]
57. Royset, J.; Ryum, N. Scandium in aluminium alloys. *Int. Mater. Rev.* **2005**, *50*, 19–44. [CrossRef]
58. Lash, L.D.; Ross, J.R. Scandium recovery from uranium solutions. *JOM* **1961**, *13*, 555–558. [CrossRef]
59. *US Geological Survey Report 2022*; US Geological Survey: Reston, VA, USA, 2022.
60. Lei, Q.; He, D.; Zhou, K.; Zhang, X.; Peng, C.; Chen, W. Separation and recovery of scandium and titanium from red mud leaching liquor through a neutralization precipitation-acid leaching approach. *J. Rare Earths* **2020**, *39*, 1126–1132. [CrossRef]
61. Wei, D.; Hui, X.J.; Yang, P.; Yue, S.S.; Tao, C.; Kai, Z.; Zhen, W. Extraction of Scandium and Iron from Red Mud. *Miner. Process. Extr. Metall. Rev.* **2022**, *43*, 61–68. [CrossRef]
62. Ochsenkuhn-Petropulu, M.T.; Hatzilyberis, K.S.; Mendrinos, L.N.; Salmas, C.E. Pilot-Plant Investigation of the Leaching Process for the Recovery of Scandium from Red Mud. *Ind. Eng. Chem. Res.* **2002**, *41*, 5794–5801. [CrossRef]
63. Rivera, R.M.; Xakalashe, B.; Ounoughene, G.; Binnemans, K.; Friedrich, B.; Van Gerven, T. Selective rare earth element extraction using high-pressure acid leaching of slags arising from the smelting of bauxite residue. *Hydrometallurgy* **2019**, *184*, 162–174. [CrossRef]
64. Bonomi, C.; Alexandri, A.; Vind, J.; Panagiotopoulou, A.; Tsakiridis, P.; Panias, P. Scandium and titanium recovery from bauxite residue by direct leaching with a brønsted acidic ionic liquid. *Metals* **2018**, *8*, 834. [CrossRef]
65. Alkan, G.; Yagmurlu, B.; Cakmakoglu, S.; Hertel, T.; Kaya, Ş.; Gronen, L.; Friedrich, B. Novel approach for enhanced scandium and titanium leaching efficiency from bauxite residue with suppressed silica gel formation. *Sci. Rep.* **2018**, *8*, 5676. [CrossRef] [PubMed]

66. Zhou, K.; Teng, C.; Zhang, X.; Peng, C.; Chen, W. Enhanced Selective Leaching of Scandium from Red Mud. *Hydrometallurgy* **2018**, *182*, 57–63. [CrossRef]
67. Rychkow, V.; Botalov, M.; Kirrillov, E.; Smyshlyaev, V. Intensification of carbonate scandium leaching from red mud (bauxite residue). *Hydrometallurgy* **2021**, *199*, 105524. [CrossRef]
68. Hatzilyberis, K.; Lymperopoulou, T.; Tsakanika, L.; Ochsenkuhn, K. Process design aspects for scandium-selective leaching of bauxite residue with sulphuric acid. *Minerals* **2018**, *8*, 79. [CrossRef]
69. Stepanova, S.I.; Boyarintseva, A.V.; Giganova, V.G. Use of Machining to Increase the Recovery of Scandium from Refractory Silicate Raw Material. *Theor. Found. Chem. Eng.* **2018**, *52*, 898–902. [CrossRef]
70. Zhang, X.; Zhou, K.; Wu, Y.; Chen, W. Separation and recovery of iron and scandium from acid leaching solution of red mud using D201 resin. *J. Rare Earths* **2020**, *38*, 1322–1329. [CrossRef]
71. Kim, A.; Azimi, G. Recovery of scandium and neodymium from blast furnace slag using acid baking–water leaching. *RSC Adv.* **2020**, *10*, 31936. [CrossRef]
72. Zhang, B.; Xue, X.; Yang, H. A novel process for recovery of scandium, rare earth and niobium from Bayan Obo tailings: NaCl-Ca$(OH)_2$-coal roasting and acid leaching. *Miner. Eng.* **2022**, *178*, 107401. [CrossRef]
73. Li, S.C.; Kim, S.C.; Kang, C.S. Recovery of scandium from KOH sub-molten salt leaching cake of fergusonite. *Miner. Eng.* **2019**, *137*, 200–206. [CrossRef]
74. Rulkens, W.H.; Grotenhuis, J.T.C.; Tichy, R. Methods for cleaning contaminated soils and sediments. In *Heavy Metals*; Springer: Berlin/Heidelberg, Germany, 1995; pp. 165–191.
75. Krebs, W.; Brombacher, C.; Bosshard, P.P.; Bachofen, R.; Brandl, H. Microbial recovery of metals from solids. *FEMS Microbiol. Rev.* **1997**, *20*, 605–617. [CrossRef]
76. Bosshard, P.P.; Bachofen, R.; Brandl, H. Metal leaching of fly ash from municipal waste incineration by Aspergillus niger. *Environ. Sci. Technol.* **1996**, *30*, 3066–3070. [CrossRef]
77. Aquino, L.; Morgana, M.; Carboni, M.A.; Staiano, M.; Antisari, M.V. Effect of some rare earth elements on the growth and lanthanide accumulation in different Trichoderma strains. *Soil Biol. Biochem.* **2009**, *41*, 2406–2413. [CrossRef]
78. Gonzalez-Baez, A.; Pantoja Munoz, L.; Garelick, H.; Purchase, D. Characterisation of rare earth elements in waste printed circuit boards (WPCBs) and their bioleaching potential. In Proceedings of the 16th International Conference on Environmental Science and Technology, Rhodes, Greece, 4–7 September 2019; pp. 4–7.
79. Qu, Y.; Lian, B. Bioleaching of rare earth and radioactive elements from red mud using Penicillium tricolor RM-10. *Bioresour. Technol.* **2013**, *136*, 16–23. [CrossRef]
80. Hedrich, S.; Schippers, A. Distribution of scandium in red mud and extraction using Gluconobacter oxydans. *Hydrometallurgy* **2021**, *202*, 105621.
81. Park, S.; Liang, Y. Bioleaching of trace elements and rare earth elements from coal fly ash. *Int. J. Coal Sci. Technol.* **2019**, *6*, 74–83. [CrossRef]
82. Muravyov, M.I.; Bulaev, A.G.; Melamud, V.S.; Kondrateva, T.F. Leaching of rare earth elements from coal ashes using acidophilic chemolithotrophic microbial communities. *Microbiology* **2015**, *84*, 194–201. [CrossRef]
83. Qu, Y.; Li, H.; Wang, X.; Tian, W.; Shi, B.; Yao, M.; Zhang, Y. Bioleaching of Major, Rare Earth, and Radioactive Elements from Red Mud by using Indigenous Chemoheterotrophic Bacterium *Acetobacter* sp. *Minerals* **2019**, *9*, 67. [CrossRef]
84. Pedram, H.; Hosseini, M.R.; Bahrami, A. Utilization of A. niger strains isolated from pistachio husk and grape skin in the bioleaching of valuable elements from red mud. *Hydrometallurgy* **2020**, *198*, 105495. [CrossRef]
85. Kiskira, K.; Lymperopoulou, T.; Tsakanika, L.A.; Pavlopoulos, C.; Papadopoulou, K.; Ochsenkühn, K.M.; Ochsenkühn-Petropoulou, M. Study of microbial cultures for the bioleaching of scandium from alumina industry by-products. *Metals* **2021**, *11*, 951. [CrossRef]
86. Salman, A.D.; Juzsakova, T.; Mohsen, S.; Abdullah, T.A.; Le, P.C.; Sebestyen, V.; Sluser, B.; Cretescu, I. Scandium Recovery Methods from Mining, Metallurgical Extractive Industries, and Industrial Wastes. *Materials* **2022**, *15*, 2376. [CrossRef] [PubMed]
87. Liu, C.; Chen, L.; Chen, J.; Zou, D.; Deng, Y.; Li, D. Application of P507 and isooctanol extraction system in recovery of scandium from simulated red mud leach solution. *J. Rare Earths* **2019**, *37*, 1002–1008. [CrossRef]
88. Onghena, B.; Borra, C.R.; Gerven, T.; Binnemans, K. Recovery of scandium from sulfation-roasted leachates of bauxite residue by solvent extraction with the ionic liquid betainium bis (trifluoromethylsulfonyl) imide. *Sep. Purif. Technol.* **2017**, *176*, 208–219. [CrossRef]
89. Hu, J.; Zou, D.; Chen, J.; Li, D. A novel synergistic extraction system for the recovery of scandium (III) by Cyanex 272 and Cyanex 923 in sulfuric acid medium. *Sep. Purif. Technol.* **2020**, *233*, 115977. [CrossRef]
90. Liu, Z.; Li, H.; Jing, Q.; Zhang, M. Recovery of Scandium from Leachate of Sulfation-Roasted Bayer Red Mud by Liquid–Liquid Extraction. *JOM* **2017**, *69*, 2373–2377. [CrossRef]
91. Onghena, B.; Binnemans, K. Recovery of scandium(III) from aqueous solutions by solvent extraction with the functionalized ionic liquid betainium bis(trifluoromethylsulfonyl)imide. *Ind. Eng. Chem. Res.* **2015**, *54*, 1887–1898. [CrossRef]
92. Wang, W.; Pranolo, Y.; Cheng, C.Y. Recovery of scandium from synthetic red mud leach solutions by solvent extraction with D2EHPA. *Sep. Purif. Technol.* **2013**, *108*, 96–102. [CrossRef]
93. Zhou, J.; Yu, Q.; Huang, Y.; Meng, J.; Chen, Y.; Ning, S.; Wang, X.; Liang, J. Recovery of scandium from white waste acid generated from the titanium sulphate process using solvent extraction with TRPO. *Hydrometallurgy* **2020**, *195*, 105398. [CrossRef]

94. Zhu, X.; Li, W.; Xing, B.; Zhang, Y. Extraction of scandium from red mud by acid leaching with CaF2 andsolvent extraction with P507. *J. Rare Earths* **2020**, *38*, 1003–1008. [CrossRef]
95. Zou, D.; Li, H.; Chen, J.; Li, D. Recovery of scandium from spent sulfuric acid solution in titanium dioxide production using synergistic solvent extraction with D2EHPA and primary amine N1923. *Hydrometallurgy* **2020**, *197*, 105463. [CrossRef]
96. Turanov, A.N.; Karandashev, V.K.; Sukhinina, N.S.; Masalov, V.M.; Emelchenko, G.A. Adsorption of lanthanides and scandium ions by silica sol-gel material doped with novel bifunctional ionic liquid, trioctylmethylammonium 1-phenyl-3-methyl-4-benzoyl-5-onate. *J. Environ. Chem. Eng.* **2016**, *4*, 3788–3796. [CrossRef]
97. Salman, A.D.; Juzsakova, T.; Ákos, R.; Ibrahim, R.I.; Al-Mayyahi, M.A.; Mohsen, S.; Domokos, E. Synthesis and surface modification of magnetic Fe_3O_4@ SiO_2 core-shell nanoparticles and its application in uptake of scandium (III) ions from aqueous media. *Environ. Sci. Pollut. Res. Int.* **2021**, *28*, 28428–28443. [CrossRef] [PubMed]
98. Avdibegović, D.; Zhang, W.; Xu, J.; Regadío, M.; Koivula, R.; Binnemans, K. Selective ion-exchange separation of scandium (III) over iron (III) by crystalline α-zirconium phosphate platelets under acidic conditions. *Sep. Purif. Technol.* **2019**, *215*, 81–90. [CrossRef]
99. Walter, R.I. Anion exchange studies of Sc (III) and V (IV). Separation of scandium, titanium and vanadium. *J. Inorg. Nucl. Chem.* **1958**, *6*, 58–62. [CrossRef]
100. Hamaguchi, H.; Kuroda, R.; Aoki, K.; Sugisita, R.; Onuma, N. Cation-exchange separation of scandium. *Talanta* **1963**, *10*, 153–162. [CrossRef]
101. Strelow, F.W.E.; Bothma, C.J.C. Separation of Scandium from Yttrium, Lanthanum, and the Rare Earths by Cation Exchange Chromatography. *Anal. Chem.* **1964**, *36*, 1217–1220. [CrossRef]
102. Orlandini, K.A.; Korkisch, J. Cation-Exchange Separation of Scandium from the Rare-Earth Elements. *Sep. Sci. Technol.* **1968**, *3*, 255–263. [CrossRef]
103. Molchanova, T.V.; Akimova, I.D.; Tatarnikov, A.V. Ion-Exchange Methods of Scandium Recovery from the Ores of the Tomtor Deposit. In *Russian Metallurgy (Metally)*; Springer: Berlin/Heidelberg, Germany, 2019; pp. 674–679.
104. Zhu, X.; Li, W.; Tang, S.; Zeng, M.; Bai, P.; Chen, L. Selective recovery of vanadium and scandium by ion exchange with D201 and solvent extraction using P507 from hydrochloric acid leaching solution of red mud. *Chemosphere* **2017**, *175*, 365–372. [CrossRef]
105. Hajmohammadi, H.; Jafari, A.H.; Nasab, M.E. Scandium recovery from raffinate copper leach solution as potential new source with ion exchange method. *Trans. Nonferrous Metal. Soc. China* **2020**, *30*, 3103–3113. [CrossRef]
106. Faris, J.P.; Warton, J.W. Anion Exchange Resin Separation of the Rare Earths, Yttrium, and Scandium in Nitric Acid-Methanol Mixtures. *Anal. Chem.* **1962**, *34*, 1077–1080. [CrossRef]
107. Swain, K.K.; Kayasth, S. High purity scandium and ion-exchangers: Application in neutron activation analysis. *J. Radioanal. Nucl. Chem.* **2004**, *260*, 595–599. [CrossRef]
108. Smirnov, A.L.; Titova, S.M.; Rychkov, V.N.; Bunkov, G.M.; Semenishchev, V.S.; Kirillov, E.V.; Svirsky, I.A. Study of scandium and thorium sorption from uranium leach liquors. *J. Radioanal. Nucl. Chem.* **2017**, *312*, 277–283. [CrossRef]
109. Smirnov, D.I.; Molchanova, T.V. The investigation of sulphuric acid sorption recovery of scandium and uranium from the red mud of alumina production. *Hydrometallurgy* **1997**, *45*, 249–259. [CrossRef]
110. Zhou, G.; Li, Q.; Sun, P.; Guan, W.; Zhang, G.; Cao, Z.; Zeng, L. Removal of impurities from scandium chloride solution using 732-type resin. *J. Rare Earths* **2018**, *36*, 311–316. [CrossRef]
111. Yu, Q.; Ning, S.; Zhang, W.; Wang, X.; Wei, Y. Recovery of scandium from sulfuric acid solution with a macro porous TRPO/SiO_2-P adsorbent. *Hydrometallurgy* **2018**, *181*, 74–81. [CrossRef]
112. Thapa, R. Recovery of Scandium and Uranium with Bisphosphonate Modified Mesoporous Silicon. Ph.D. Thesis, Itä-Suomen yliopisto, Kuopio, Finland, 2021.
113. Bao, S.; Hawker, W.; Vaughan, J. Scandium loading on chelating and solvent impregnated resin from sulfate solution. *Solvent Extr. Ion Exch.* **2018**, *36*, 100–113. [CrossRef]
114. Mostajeran, M.; Bondy, J.M.; Reynier, N.; Cameron, R. Mining value from waste: Scandium and rare earth elements selective recovery from coal fly ash leach solutions. *Miner. Eng.* **2021**, *173*, 107091. [CrossRef]
115. Turanov, A.N.; Karandashev, V.K.; Bondarenko, N.A. Extraction of rare-earth, yttrium, and scandium perchlorates by podands bearing diphenylphosphorylacetamide terminal groups. *Russ. J. Inorg. Chem.* **2008**, *53*, 1801–1808. [CrossRef]
116. Madrid, J.F.; Barba, B.J.D.; Pomicpic, J.C.; Cabalar, P.J.E. Immobilization of an organophosphorus compound on polypropylene-g-poly (glycidyl methacrylate) polymer support and its application in scandium recovery. *J. Appl. Polym. Sci.* **2022**, *139*, 51597. [CrossRef]
117. Sharaf, M.; Yoshida, W.; Kubota, F.; Goto, M. A novel binary-extractant-impregnated resin for selective recovery of scandium. *J. Chem. Eng. Jpn.* **2019**, *52*, 49–55. [CrossRef]
118. Moon, J.Y. Separation and Recovery of Rare Metals by Solvent Impregnated Resin. *Solvent Extr. Res. Dev. Jpn.* **2020**, *27*, 91–97. [CrossRef]
119. Zhu, L.; Liu, Y.; Chen, J.; Liu, W. Extraction of scandium (III) using ionic liquids functionalized solvent impregnated resins. *J. Appl. Polym. Sci.* **2011**, *120*, 3284–3290. [CrossRef]
120. Korovin, V.; Shestak, Y. Scandium extraction from hydrochloric acid media by Levextrel-type resins containing di-isooctyl methyl phosphonate. *Hydrometallurgy* **2009**, *95*, 346–349. [CrossRef]

121. Giese, E.C. Biosorption as green technology for the recovery and separation of rare earth elements. *World J. Microbiol. Biotechnol.* **2020**, *36*, 52. [CrossRef]
122. Dong, Z.; Mattocks, J.A.; Deblonde, G.J.P.; Hu, D.; Jiao, Y.; Cotruvo, J.A., Jr.; Park, D.M. Bridging hydrometallurgy and biochemistry: A protein-based process for recovery and separation of rare earth elements. *ACS Cent. Sci.* **2021**, *7*, 1798–1808. [CrossRef]
123. Hamza, M.F.; Wei, Y.; Guibal, E. Quaternization of algal/PEI beads (a new sorbent): Characterization and application to scandium sorption from aqueous solutions. *J. Chem. Eng.* **2020**, *383*, 123210. [CrossRef]
124. Hamza, M.F.; Salih, K.A.; Adel, A.H.; Zayed, Y.E.; Wei, Y.; Liang, J.; Guibal, E. Sulfonic-functionalized algal/PEI beads for scandium, cerium and holmium sorption from aqueous solutions (synthetic and industrial samples). *J. Chem. Eng.* **2021**, *403*, 126399. [CrossRef]
125. Ramasamy, D.L.; Porada, S.; Sillanpää, M. Marine algae: A promising resource for the selective recovery of scandium and rare earth elements from aqueous systems. *J. Chem. Eng.* **2019**, *371*, 759–768. [CrossRef]
126. Karavaiko, G.I.; Kareva, A.S.; Avakian, Z.A.; Zakharova, V.I.; Korenevsky, A.A. Biosorption of scandium and yttrium from solutions. *Biotechnol. Lett.* **1996**, *18*, 1291–1296. [CrossRef]
127. Van Nguyen, N.; Iizuka, A.; Shibata, E.; Nakamura, T. Study of adsorption behavior of a new synthesized resin containing glycol amic acid group for separation of scandium from aqueous solutions. *Hydrometallurgy* **2016**, *165*, 51–56. [CrossRef]
128. Komnitsas, K.; Zaharaki, D.; Bartzas, G.; Alevizos, G. Adsorption of scandium and neodymium on biochar derived after low-temperature pyrolysis of sawdust. *Minerals* **2017**, *7*, 200. [CrossRef]
129. Avdibegović, D.; Regadío, M.; Binnemans, K. Recovery of scandium (III) from diluted aqueous solutions by a supported ionic liquid phase (SILP). *RSC Adv.* **2017**, *7*, 49664–49674. [CrossRef]
130. Molchanova, T.V.; Akimova, I.D.; Smirnov, K.M.; Krylova, O.K.; Zharova, E.V. Hydrometallurgical methods of recovery of scandium from the wastes of various technologies. *Russ. Metall.* **2017**, *3*, 170–174. [CrossRef]
131. Zhang, W.; Yu, S.; Zhang, S.; Zhou, J.; Ning, S.; Wang, X.; Wei, Y. Separation of scandium from the other rare earth elements with a novel macro-porous silica-polymer based adsorbent HDEHP/SiO_2-P. *Hydrometallurgy* **2019**, *185*, 117–124. [CrossRef]
132. Wasikiewicz, J.M.; Nagasawa, N.; Tamada, M.; Mitomo, H.; Yoshii, F. Adsorption of metal ions by carboxymethylchitin and carboxymethylchitosan hydrogels. *Nucl. Instrum. Methods Phys. Res. Sect. B Beam Interact. Mater. At.* **2005**, *236*, 617–623. [CrossRef]
133. Qiu, H.; Wang, M.; Xie, Y.; Song, J.; Huang, T.; Li, X.M.; He, T. From trace to pure: Recovery of scandium from the waste acid of titanium pigment production by solvent extraction. *Process Saf. Environ. Prot.* **2019**, *121*, 118–124. [CrossRef]
134. Zimmermann, Y.S.; Niewersch, C.; Lenz, M.; Kul, Z.Z.; Corvini, P.F.X.; Schaffer, A.; Wintgens, T. Recycling of indium from CIGS photovoltaic cells: Potential of combining acid-resistant nanofiltration with liquid–liquid extraction. *Environ. Sci. Technol.* **2014**, *48*, 13412–134128. [CrossRef]
135. Keskin, B.; Gokoglu, B.Z.; Koyuncu, I. Polymer inclusion membrane applications for transport of metal ions: A critical review. *Chemosphere* **2021**, *279*, 130604. [CrossRef]
136. Sharaf, M.; Yoshida, W.; Kubota, F.; Kolev, S.D.; Goto, M. A polymer inclusion membrane composed of the binary carrier PC-88A and Versatic 10 for the selective separation and recovery of Sc. *RSC Adv.* **2018**, *8*, 8631–8637. [CrossRef] [PubMed]
137. Yoshida, W.; Baba, Y.; Kubota, Y.; Kolev, S.D.; Goto, M. Selective transport of scandium(III) across polymer inclusion membranes with improved stability which contain an amic acid carrier. *J. Membr. Sci.* **2019**, *572*, 291–299. [CrossRef]
138. Yoshida, W.; Kubota, F.; Baba, Y.; Kolev, S.D.; Goto, M. Separation and recovery of Scandium from sulfate media by solvent extraction and polymer inclusion membranes with Amic acid extractants. *ACS Omega* **2019**, *4*, 21122–21130. [CrossRef] [PubMed]
139. Sokolova, Y.V.; Cherepanin, R.N. Preparation and examination of the properties of complex scandium fluorides. *Russ. J. Appl. Chem.* **2011**, *84*, 1319. [CrossRef]
140. Yagmurlu, B.; Dittrich, D.; Friedrich, B. Effect of Aqueous Media on the Recovery of Scandium by Selective Precipitation. *Metals* **2018**, *8*, 314. [CrossRef]
141. Yagmurlu, B.; Dittrich, C.; Friedrich, B. Precipitation Trends of Scandium in Synthetic Red Mud Solutions with Different Precipitation Agents. *J. Sustain. Metall.* **2017**, *3*, 90–98. [CrossRef]
142. Peters, E.M.; Kaya, S.; Ditrrich, C.; Forsberg, K. Recovery of scandium by crystallization techniques. *J. Sustain. Metall.* **2019**, *5*, 49–56. [CrossRef]
143. Peters, E.M.; Svard, M.; Forsberg, K. Phase equilibria of ammonium scandium fluoride phases in aqueous alcohol mixtures for metal recovery by anti-solvent crystallization. *Sep. Purif. Technol.* **2022**, *252*, 117449. [CrossRef]
144. Akira, K.; Kosuke, M.; Hiromasa, Y. Processes for Recovering Scandium from Nickel-Containing Oxide Ore. European Patent EP0775753, 1999.
145. Zhong, X. Technology of extracting scandium oxide by primary amine. *Chin. J. Rare Met.* **2002**, *26*, 527–529.
146. Bourzac, K. Can the US rare earth industry rebound. *Technol. Rev.* **2010**, *29*, 139–166.
147. Zaitsev, A.N.; Wall, F.; Chakhmouradian, A.R. Rare-earth elements minerals in carbonites of the Kola Alkaline province (northern Fennoscandia). In Proceedings of the 1st European Rare Earth Resources Conference, Milos, Greece, 4–7 September 2014; pp. 343–347.
148. Shujing, Z.H. On problems in rare earth exports of China and countermeasures. *Int. Bus. Manag.* **2013**, *6*, 21–25.

149. Sonich-Mullin, C.; Reisman, D.; Weber, R. *Rare Earth Elements: A Review of Production, Processing, Recycling, and Associated Environmental Issues*; United States Environmental Protection Agency: Washington, DC, USA, 2012.
150. Liang, T.; Li, K.; Wang, L. State of rare earth elements in different environmental components in mining areas of China. *Environ. Monit. Assess.* **2014**, *186*, 1499–1513. [CrossRef] [PubMed]
151. Hirano, S.; Suzuki, K.T. Exposure, metabolism, and toxicity of rare earths and related compounds. *Environ. Health Perspect.* **1996**, *104*, 85–95. [PubMed]
152. Navarro, J.; Zhao, F. Life-cycle assessment of the production of rare-earth elements for energy applications: A review. *Front. Energy Res.* **2014**, *2*, 45. [CrossRef]
153. Lizin, S.; Van Passel, S.; De Schepper, E.; Maes, W.; Lutsen, L.; Manca, J.; Vanderzande, D. Life cycle analyses of organic photovoltaics: A review. *Energy Environ. Sci.* **2013**, *6*, 3136–3149. [CrossRef]
154. Vahidi, E.; Zhao, F. Environmental life cycle assessment on the separation of rare earth oxides through solvent extraction. *J. Environ. Manag.* **2017**, *203*, 255–263. [CrossRef] [PubMed]
155. Kossakowska, K.; Grzesik, K. The significance of energy consumption in environmental impact of rare earth elements recovery from tailings and mining waste. In *E3S Web of Conferences*; EDP Sciences: Les Ulis, France, 2019; Volume 108, p. 02011.
156. Joyce, P.J.; Björklund, A. Using life cycle thinking to assess the sustainability benefits of complex valorization pathways for bauxite residue. *J. Sustain. Metall.* **2019**, *5*, 69–84. [CrossRef]
157. Jin, H.; Afiuny, P.; McIntyre, T.; Yih, Y.; Sutherland, J.W. Comparative life cycle assessment of NdFeB magnets: Virgin production versus magnet-to-magnet recycling. *Procedia CIRP* **2016**, *48*, 45–50. [CrossRef]

Disclaimer/Publisher's Note: The statements, opinions and data contained in all publications are solely those of the individual author(s) and contributor(s) and not of MDPI and/or the editor(s). MDPI and/or the editor(s) disclaim responsibility for any injury to people or property resulting from any ideas, methods, instructions or products referred to in the content.

applied sciences

MDPI

Review

Biomass and Cellulose Dissolution—The Important Issue in Renewable Materials Treatment

Marta Przypis [1,2], Agata Wawoczny [1,2] and Danuta Gillner [1,2,*]

[1] Department of Organic Chemistry, Bioorganic Chemistry and Biotechnology, Faculty of Chemistry, Silesian University of Technology, 44-100 Gliwice, Poland
[2] Biotechnology Centre, Silesian University of Technology, 44-100 Gliwice, Poland
* Correspondence: danuta.gillner@polsl.pl; Tel.: +48-32-237-26-19

Abstract: Sustainable development strategies, as well as the shift toward a circular bioeconomy, has led to high interest in the development and implementation of technologies that efficiently utilize biomass as a raw material. Switching from fossil-based to bio-based resources requires the consideration of many new challenges and problems. One of the crucial issues is the solubility of lignocellulose or at least its ingredients. According to the trends and legislation, the selected chemicals and methods of dissolution/treatment should also be environmentally friendly. The pretreatment processes prepare biomass for further transformations (e.g., chemical, thermal including pyrolysis, or biological) to valuable products such as biofuels, bio-oils, Fine Chemicals, solvents, plastics, and many others. This review discusses the latest findings on the dissolution of biomass and its ingredients. The application of novel, green solvents such as ionic liquids or deep eutectic solvents is discussed in detail. The impact of the composition and structure of these solvents on the biomass/cellulose dissolution process, as well as the mechanism of cellulose–ionic liquid interaction, is presented. Some novel achievements in the usage of inorganic salts and specific metal complexes are also overviewed.

Keywords: lignocellulose; dissolution; inorganic salts; ionic liquids; deep eutectic solvents; delignification

Citation: Przypis, M.; Wawoczny, A.; Gillner, D. Biomass and Cellulose Dissolution—The Important Issue in Renewable Materials Treatment. *Appl. Sci.* **2023**, *13*, 1055. https://doi.org/10.3390/app13021055

Academic Editors: Mohammad Mahmudur Rahman, Dibyendu Sarkar, Rupali Datta and Prafulla Kumar Sahoo

Received: 12 December 2022
Revised: 10 January 2023
Accepted: 11 January 2023
Published: 12 January 2023

Copyright: © 2023 by the authors. Licensee MDPI, Basel, Switzerland. This article is an open access article distributed under the terms and conditions of the Creative Commons Attribution (CC BY) license (https://creativecommons.org/licenses/by/4.0/).

1. Introduction

The depletion of fossil resources, as well as extreme environmental pollution, resulted in several strategies and regulations on the use of renewable raw materials and the development of greener, environmentally friendly technologies.

The trends are also reflected in world politics. For example, starting in 2020, the development of the energy sector in the European Union is focused on renewable energy sources (RES), such as solar energy (photovoltaics), wind energy (wind farms), hydropower (hydropower plants), or biomass [1].

The problem with limited fossil resources and the negative environmental impact of fuels based on crude oil derivatives is very serious, so the strategy of many countries is to replace vehicles running on diesel or gasoline with electric ones. However, sustainable development does not only apply to energy. It is also necessary to increase the use of renewable raw materials in the chemical industry, ensuring biodiversity and environmental protection. Lignocellulosic biomass plays a crucial role in renewable materials and can be used in the production of so-called biochemicals. According to the report "Biomass production, supply, uses and flows in the European Union", prepared for the European Commission, annual biomass production in Europe is estimated at 1466 Mt of dry matter (agriculture 956 Mt and forestry 510 Mt) [2].

It is estimated that almost 50% of the world's biomass is lignocellulosic biomass, which is not used as food and has a higher energy value than the world's demand. For this reason, lignocellulosic biomass is the subject of many studies, aimed at developing efficient methods of its processing. The first goal of biorefineries is to selectively separate the major constituents of biomass (cellulose, hemicellulose, and lignin) and transform them

into valuable bioproducts. This includes the production of *Fine Chemicals* and solvents (e.g., lactic acid, furfural, levulinic acid, 5-hydroxymethylfurfural), biofuels (e.g., bioethanol), or energy (Figure 1).

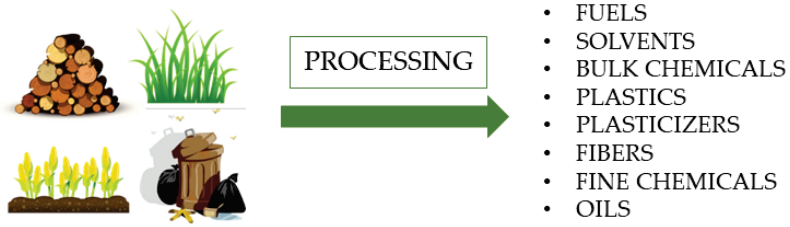


Figure 1. Possible methods of biomass processing in chemical industry.

The interest in biomass treatment is growing each year, which is reflected in the number of publications, e.g., in ScienceDirect (Figure 2).

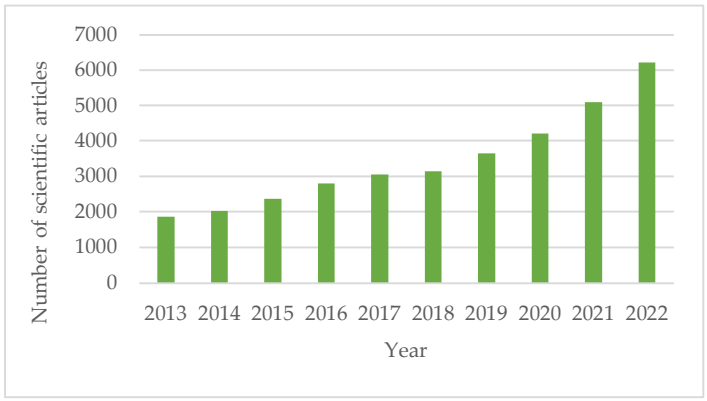


Figure 2. Number of publications for "lignocellulosic biomass" term (according to ScienceDirect).

Biomass pretreatment is an important part of its further conversion and can be classified as physical, physicochemical, chemical, and biological. In many cases, the combination of several methods is used. Selection of the appropriate pretreatment method depends on many factors, e.g., the type of biomass, further conversion methods, or desired products. The goal of this step is to obtain more homogeneous raw materials and overcome all handling difficulties. After pretreatment. the biomass is more susceptible to further transformations (chemical, enzymatic, chemoenzymatic, or thermal) into desired products. When the production of biofuels is considered, many thermal methods have been investigated (e.g., torrefaction, gasification, pyrolysis, and hydrothermal methods). One of the most promising methods is the pyrolysis of biomass (biomass degradation under elevated temperature, in the absence of oxygen), where biofuels, bio-oil, biogas, and biochar can be produced [3].

The dissolution of lignocellulose and/or extraction of its constituents is an important issue, prior to any further transformations to value-added chemicals. In this paper, we discuss novel, environmentally friendly methods and solvents for effective biomass and biomass constituent dissolution. Ionic liquids and deep eutectic solvents are discussed in detail.

2. General Characteristics of Lignocellulosic Biomass

The three main components of lignocellulosic biomass are cellulose (35–83% of dry mass), hemicelluloses (0–30%), and lignin (0–43%) [4–6]. It also contains small amounts of other molecules such as proteins, pectins, waxes, and minerals. The type and content of these ingredients depend on the type of plant, e.g., grain husks (rice, wheat) and corn cobs

are rich in silicon dioxide, while carbonates and phosphates can be commonly found in wood (e.g., willow) [7–9].

The content of cellulose, hemicelluloses, and lignin depends on the type of plant, as well as its part, age, and cultivating conditions. Generally, wooden species tend to have a higher amount of lignin compared to green and softer plants such as grass. In Table 1, the content of cellulose, hemicelluloses, and lignin in several examples of different plants is presented.

Table 1. Content of cellulose, hemicelluloses, and lignin in different types of lignocellulosic biomass.

Type of Biomass	Content [%]			References
	Cellulose	Hemicelluloses	Lignin	
Grass	28.8–38.0	18.4–30.0	4.0–17.5	[10,11]
Sawmill wood chips	35.0–50.0	15.0–39.0	20.0–34.0	[6,12]
Walnut shells	25.6	22.7	29.9–52.3	[6,13]
Hazelnut shells	25.9	29.9	42.5	[14]
Walnut tree wood	40.8–49.8	33.4	21.8–29.1	[15]
Olive tree wood	31.5–31.9	11.3–15.5	32.5	[16]
Softwood	35.0–45.2	25.0–31.3	21.7–30.0	[14,17]
Hardwood	45.0–50.0	20.0–25.0	20.0–28.0	[14,17]
Poplar	42.7	21.7	26.9	[18]
Willow	44.3	22.6	25.1	[18]
Pine sawmill chips	44.0	26.0	26.0	[19]
Pine bark	19.0–21.9	18.3–25.0	38.0–40.7	[18,20]
Spruce bark	29.7	13.9	45.1	[18]
Olive tree leaves	5.7–8.5	3.8–5.4	39.6	[16]
Wheat straw	28.8–40.0	20.0–39.1	15.0–20.5	[14,17,18]
Switchgrass millet	30.0–50.0	10.0–40.0	5.0–20.0	[17]

Cellulose is a structural component of cell walls and occurs as microfibrils. A higher number of tightly packed cellulose chains increases the mechanical strength, as can be observed in hard biomass (e.g., wood) [21–23]. Physical resistance is also improved by hemicelluloses, which are responsible for binding cellulose fibers to lignin [24,25]. The major chemical, enzymatic, and mechanical resistance of plant cells is provided by lignin, which is present in the external part of lignocellulose [26,27]. The general structure of lignocellulosic biomass is presented in Figure 3.

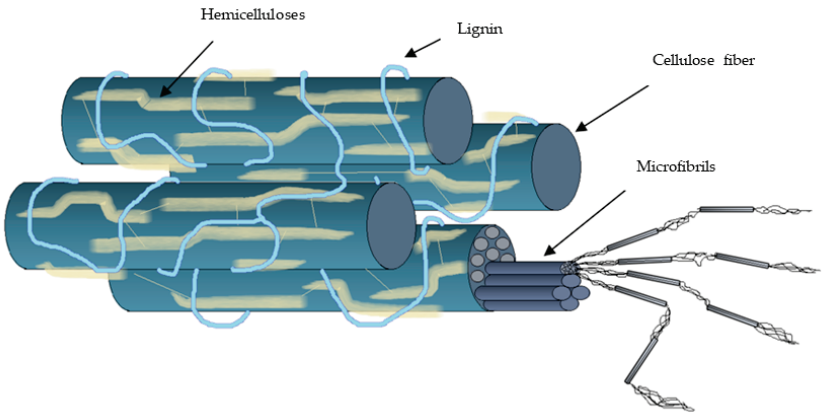


Figure 3. General structure of lignocellulose.

2.1. Cellulose

Cellulose is a homopolymer consisting of D-glucose monomers, linked by β-1,4-glycosidic bonds (Figure 4).

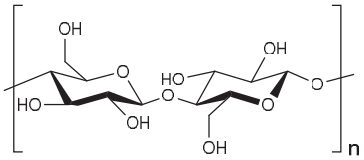


Figure 4. General chemical structure of cellulose.

A high number of hydroxyl groups on the surface of cellulose enables the formation of hydrogen-bond networks and van der Waals linkages. They stabilize the cellulose molecule and significantly improve its dissolution resistance (Figure 5) [28]. The amphiphilic character of cellulose, derived from the axial hydroxyl groups and ring surface CH groups, dictates the selection of the appropriate solvent [29,30]. The study has shown that the use of organic co-solvents (e.g., ethanol, acetone, γ-valerolactone, and tetrahydrofuran) in water can significantly reduce the number of hydrogen bonds formed between the cellulose chains and solvent [31].

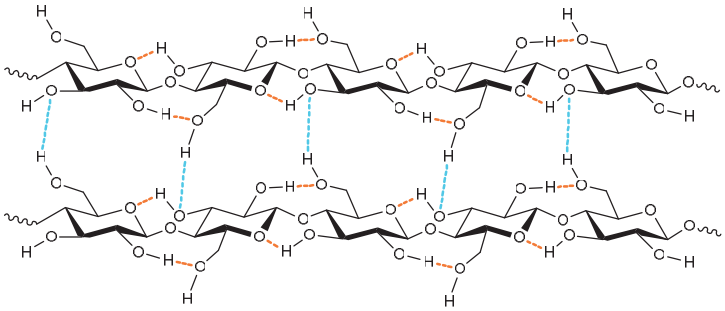


Figure 5. Hydrogen bonds present in cellulose structure.

Cellulose consists of crystalline and amorphous domains. The content of highly ordered, tightly packed crystalline regions in cellulose depends primarily on the type of plant, e.g., wood biomass has many regions with high crystallinity (up to 65% crystalline regions), which makes it insoluble in water and much more chemically and mechanically resistant [22,32]. Loosely arranged molecular chains are called amorphous regions [33]. In order to increase the reactivity, solubility, and susceptibility to the transformation of natural cellulose, the crystalline structure has to be destroyed to obtain an amorphous, or at least amorphized, biopolymer [34].

2.2. Hemicelluloses

Hemicelluloses are heteropolymers, consisting primarily of six-carbon sugars such as mannose, glucose, fucose, and galactose and five-carbon sugars such as arabinose and xylose. Therefore, several types of hemicelluloses are distinguished due to the dominant saccharide in the polymer structure, such as xylans, mannans, galactans, glucans, glucomannans, and arabinogalactans [35,36]. The sample chemical structure of xylan hemicellulose is presented in Figure 6.

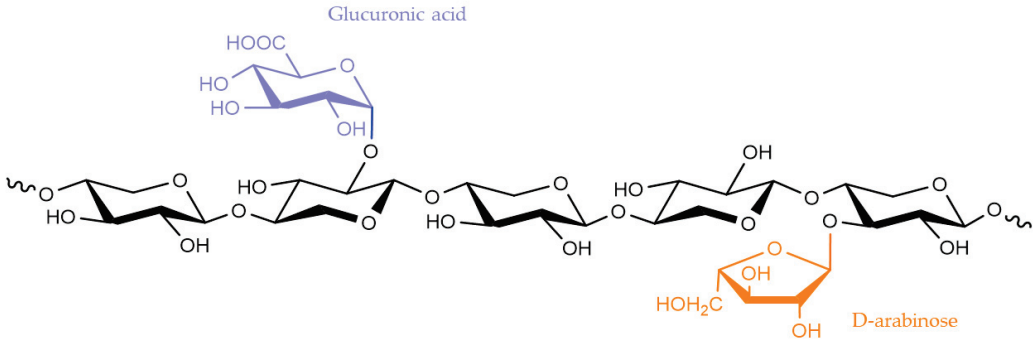


Figure 6. Chemical structure of xylan hemicellulose.

The chemical composition mainly depends on the type and part of the plant. Generally, hardwood contains a higher amount of xylan than softwood [37]. For example, in sapwood of broad-leaved trees, the main component in hemicellulose is xylose (approximately 80%), but in the leaves from the same species, the content of galactose and arabinose is higher (15% and 25%) [38].

2.3. Lignin

Lignin is an amorphous heteropolymer with both aliphatic and aromatic fragments. The main precursors are monolignols: *p*-coumaryl, coniferyl, and sinapyl alcohols (Figure 7) [39]. Depending on the source, different contents of particular precursors can be found in the lignin structure, e.g., softwood lignin contains mainly coniferyl alcohol, while in hardwood, coniferyl alcohol and sinapyl alcohol predominate. Grass lignin also contains *p*-coumaryl alcohol. The monomers are linked by ether bonds C-O-C and C-C bonds. In biomass, lignin forms a matrix with polysaccharides, which increases the physical strength of tissue and makes it more resistant to chemical and enzymatic transformations [26,32,40,41].

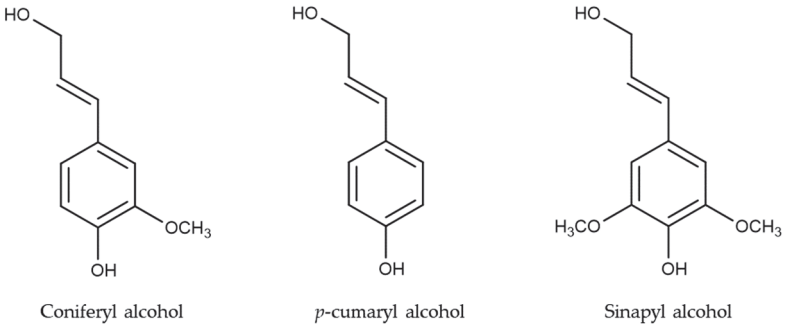


Figure 7. The main precursors of lignin.

Natural lignin is insoluble in water and organic solvents. A major part of it is also insoluble in acid solutions (Klason's lignin) and shows better solubility in alkaline solutions [42]. The lignin solubility can be changed via processing or chemical modification, e.g., in the Kraft process, the majority of hydroxyl groups are sulfonated, which makes it more susceptible to solubilization, even in organic solvents such as DMSO [43,44]. Because of this, delignification is one of the main methods of lignocellulose pretreatment. This process allows one to loosen the rigid structure of biomass and make the cellulose and hemicelluloses more accessible for chemicals and enzymes [45,46].

3. Dissolution of Biomass and Its Components

Biomass pretreatment and/or fractionation is a key step of the lignocellulose transformation into valuable products. Thanks to the diverse properties of cellulose, lignin, and hemicellulose, it is possible to fractionate the lignocellulose. There are several classic

methods, applying strong acids (e.g., H_2SO_4) or bases (e.g., NaOH), but such media are harmful, corrosive, and have a high negative impact on the environment. Additionally, after the treatment of biomass with alkaline or strong acid solutions, extra water washing steps are required to neutralize the mixture and remove the impurities before further transformations. It results in the need for the disposal of a large amount of wastewater. Because of that, new methods are constantly being developed, with the application of green solvents such as ionic liquids or deep eutectic solvents. The choice of the most suitable solvent depends on the type of biomass/biomass fraction, as well as on further conversion methods and the desired final product. Moreover, the characteristics of a solvent should be taken into consideration, such as toxicity, corrosivity, and thermal stability. In this chapter, all the major groups of solvents used in the dissolution of biomass and its components, especially cellulose and lignin, are discussed. Since classic alkaline and acidic solutions have been discussed in many papers, they will only be mentioned, and major attention will be paid to other, novel systems.

3.1. Alkaline Solutions

Cellulose is prone to swelling in alkaline solutions, such as sodium hydroxide or lithium hydroxide, but because of its amphiphilic character, it is not suitable to dissolve it completely [47]. Additionally, in the presence of NaOH, cellulose tends to form aggregates. In order to avoid this, the addition of chemicals preventing aggregation, e.g., urea, thiourea, and polyethylene glycol (PEG), is employed [48]. However, even in the presence of these agents, alkaline solutions are not very efficient at dissolving cellulose, e.g., in a NaOH/PEG mixture (a concentration of NaOH of 9%), only 13% of the biopolymer was dissolved [30,49,50].

Although cellulose dissolution in alkaline solutions is not effective, these solvents are capable of dissolving lignin. For instance, in an 18% NaOH solution, 66.6% (wt.%) of lignin from eucalyptus chips could be dissolved [51]. Hydroxyl groups, present in an alkaline solvent, can interact with lignin phenolic monomers, which results in polymer fragmentation to smaller molecules. Moreover, in alkaline conditions, linkages between lignin and polysaccharides can break [51,52]. However, because of the major disadvantages of alkaline solutions, which make them less attractive from an ecological point of view, they are not considered future solvents for biomass processing.

3.2. Acid Solutions

Acid solutions are commonly known for their ability to dissolve cellulose. Diluted acids can be applied for cellulose swelling, but in order to dissolve cellulose completely, more concentrated acids are needed. The treatment of lignocellulosic biomass with diluted acid solutions (lower than 5%) under a moderate temperature and pressure causes the degradation of hemicellulose to monomers. It is a possible way to separate hemicellulose from other components [53]. Sulfuric and hydrochloric acids are the most frequently used agents for cellulose dissolution. Concentrated sulfuric acid (approximately 70%) can break hydrogen bonds in cellulose. Additionally, it has to be taken into account that the esterification of hydroxyl groups in cellulose can occur, which results in replacing hydroxyl groups with sulfate. These processes lead to cellulose depolymerization [54]. Since Klason's lignin is insoluble in sulfuric acid, this method can be used in its separation from plant biomass [55]. Acidic biomass treatment also causes the further transformation of sugars into furfural and 5-hydroxymethylfurfural. Additionally, in the presence of strong acids, polymeric, insoluble polymers called humins are produced, which can significantly decrease the yield of valuable products produced in biomass transformations (e.g., glucose, fructose, levulinic acid, etc.) [56,57].

Organic acids, e.g., trifluoroacetic acid, dichloroacetic acid, and formic acid, can also be applied in biomass processing. This leads to the dissolution of cellulose via tderivatization of hydroxyl groups to acyl groups [58].

3.3. Inorganic Molten Salt Hydrates

Inorganic molten salt hydrates such as $Ca(SCN)_2 \cdot 3H_2O$ can dissolve cellulose at 120–140 °C within 40 min, without any additional pretreatment. Other salts or their mixtures can act differently: From dissolving this polysaccharide (e.g., $ZnCl_2 \cdot 3\text{-}4H_2O$, $LiClO_4 \cdot 3H_2O$, $Mg(ClO_4)_2/H_2O$; or $FeCl_3 \cdot 6H_2O$, $LiClO_4 \cdot 3H_2O$,$MgCl_2 \cdot 6H_2O$) or swelling it (e.g., $LiCl \cdot 2\text{-}5H_2O$, $LiClO_4 \cdot 3H_2O$, $Mg(ClO_4)_2/H_2O$; or $LiNO_3 \cdot 3H_2O$, $LiClO_4 \cdot 3H_2O$, $NaClO_4/H_2O$), and even decomposing it ($Mg(ClO_4)_2 \cdot 6H_2O$, $ZnCl_2/MgCl_2/H_2O$; or $MgCl_2 \cdot 6H_2O$) [48,59]. The ability to dissolve this polymer depends on the level of hydration, e.g., by increasing water content in lithium perchlorate to $LiClO_4 \cdot 4H_2O$, cellulose solubility decreases [60]. Iron salts can also be effectively applied in biomass pretreatment, especially upon dissolving hemicelluloses. $FeCl_3$ and $FeSO_4$ can dissolve this fraction at a level above 90%. In this process, cellulose is intact, so it could be used as a method for the separation of these fractions [61,62]. Biomass pretreatment with inorganic salts can also prepare the material for enhanced enzymatic transformations, without delignification. Zhang et al. used $AlCl_3$ with intense mechanical milling of sugarcane bagasse. It resulted in a significant reduction of biomass crystallinity and more efficient further biological hydrolysis of cellulose [63]. Nevertheless, applying inorganic salts has many disadvantages—they are expensive, unstable, toxic, and difficult to regenerate after processing [64].

3.4. Metal Complexes

Metal complexes containing a transition metal and an amine or ammonium component are good solvents of cellulose. One of the important examples is Schweizer's reagent ($[Cu(NH_3)_4(H_2O)_2](OH)_2$), which was originally used in the production of artificial silk. Today, many alternatives exhibiting good solution properties are known, e.g., $[Cu(NH_2(CH_2)_2NH_2)_2](OH)_2$ (Cuoxen), $[Ni(NH_2CH_2CH_2)_3N](OH)_2$ (Nitren), $[Pd(NH_2(CH_2)_2NH_2)](OH)_2$ (Pden), and $[Cd(NH_2(CH_2)_2NH_2)_3](OH)_2$ (Cadoxen). The last one was very efficient in dissolving cellulose with high DP. The mechanism involves deprotonation and coordinative binding of hydroxyl groups in the C2 and C3 positions of the anhydroglucose units [59,65,66].

3.5. Inorganic Salts in Organic Solvents

Cellulose can be effectively dissolved in an *N*,*N*-dimethylacetamide solution of lithium chloride (LiCl/DMAc) [67–69]. It is possible to dissolve up to 16% of the polymer present in various biomass sources, e.g., wheat straw, wood waste, and sugar cane bagasse, at 85 °C [70]. There are two proposed mechanisms of this process, both based on hydrogen bonding occurring between glucose monomers and chlorine anions, which results in the formation of the $Li^+(DMAc)_x$ cation complex. The first mechanism (Morgenstern) suggests direct linkages between lithium cation and hydroxy group oxygen atoms. The second one (McCormick) states that this type of hydrogen bond does not occur. Instead, the cellulose structure is charged negatively because of interactions with the chlorine ion. It results in cellulose fibers spreading apart and polymer solvation. Figure 8 presents both of these simplified mechanisms [67,70,71].

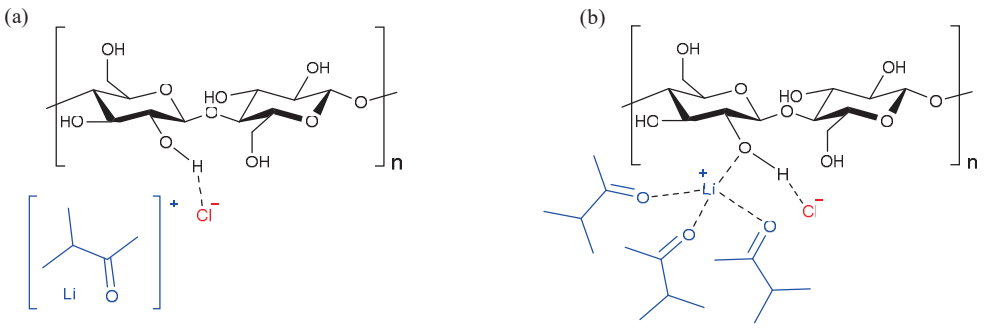


Figure 8. Proposed mechanisms of cellulose dissolving in LiCl/DMAc solution: (**a**) McCormick mechanism, (**b**) Morgenstern mechanism.

The combination of LiCl with DMAc is unique because only this certain mixture is able to dissolve cellulose effectively. By changing lithium to another metal or replacing DMAc (e.g., with DMF), the efficiency of the solvation effect decreases. Despite many advantages of LiCl/DMAc (the limitation of side effects, no need for applying additional chemicals), it was not introduced into the industrial scale due to the long processing time, high price, toxicity, corrosivity, and vapor pressure of solvent [70].

Another mixture that could be applied to dissolve cellulose is DMSO with tetrabutylammonium fluoride (TBAF). Similar to the previous example, changing fluoride to other anions causes a decrease in the effectiveness of such a mixture [72]. Fluoride is a very strong hydrogen bond acceptor. It has the ability to efficiently reduce the interaction between cellulose chains by competing with the hydroxyl and acetal oxygen atoms of cellulose. The other anions (Cl^-, Br^-) are not strong enough [73,74]. Additionally, TBA^+ cations prevent cellulose aggregation, which additionally enhances the process [75]. The main problem with TBAF application is its high hygroscopicity. The presence of a small amount of water causes an increase in viscosity and gelation [73]. Additionally, water is able to remove the fluoride anions from the cellulose chains, which results in the reformation of hydrogen bonds between cellulose chains. Anhydrous TBAF is unstable and expensive. The commercially available trihydrate $TBAF{\cdot}3H_2O$ is an alternative to be used in cellulose treatment [48,76].

3.6. Ionic Liquids

There are many problems and limitations related to the application of the abovementioned organic and inorganic solvents in biomass treatment, such as toxicity, corrosivity, high vapor pressure, and negative impact on the environment. It leads to intense activity in academic and industrial investigations to find more ecological alternatives. Ionic liquids are one such alternative, composed of organic cations and organic or inorganic anions. Because of the wide range of components, which can be used in ionic liquids, it is possible to alter their properties to the specific process. Many advantages of ionic liquids, such as a melting point below 100 °C, miscibility with many chemicals, low vapor pressure, chemical and thermal stability, non-flammability, and low toxicity, make them an ecological, green alternative to classic solvents [77]. Ionic liquids can be applied to many various chemical processes, and one of them is biomass transformations. In Figure 9, the most frequently applied ionic liquids are presented [78].

3.6.1. Ionic Liquids in Biomass Dissolution

Ionic liquids (ILs) can be applied in biomass pretreatment before further transformations into valuable products, as well as in transformation processes [79]. Plant biomass is a difficult material to dissolve due to its complex structure and differences in material composition and hardness. Soft biomass, e.g., grass, is easier to process than wood biomass [80]. Moreover, the level of biomass fragmentation is crucial—smaller particles have a larger contact surface with the solvent, which increases the efficiency of dissolution [81]. In addition to biomass properties and type, the viscosity of solvent has a major impact on process effectiveness. Lower viscosity facilitates mass transfer, which enhances the dissolution process. Rahim et al. (2021) examined ILs with ether-functionalized methylimidazolium cations (e.g., [MOE-mim]Cl 1-(2-methoxyethyl)-3-methylimidazolium chloride), with significantly lower viscosity, than the widely used [bmim]Cl. In [MOE-mim]Cl, the bamboo dissolution level was 96.45%, and in [bmim]Cl, it was 78.35%. Additionally, due to the extra oxygen atom present in the methoxy group, functionalized IL can create more hydrogen bonds with biomass fractions, which additionally enhances its dissolution [82]. Furthermore, the type of anions in IL matters in biomass processing. Solvents with higher basicity of hydrogen bonds, such as [emim][CH_3COO], are more effective for biomass dissolving [83]. Examples of biomass solubility in different ionic liquids are presented in Table 2.

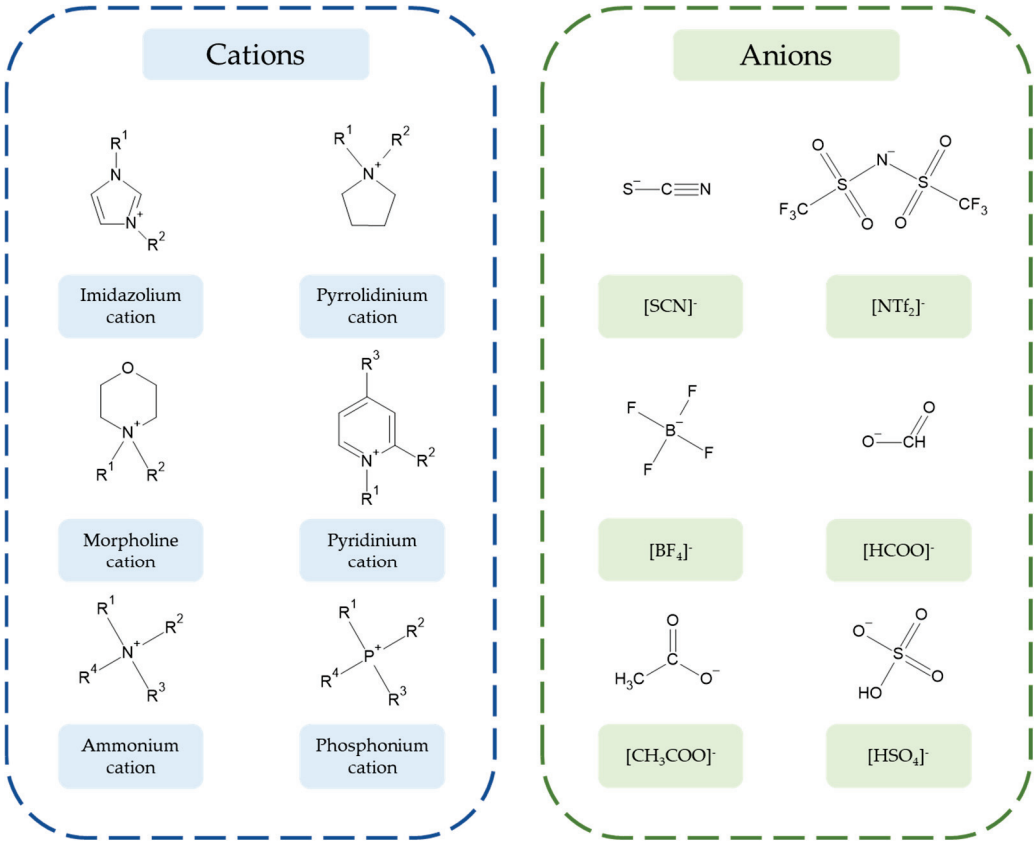


Figure 9. Ionic liquids cations and anions, which are the most frequently applied in biomass transformations (R—hydrogen atom or alkyl group).

Table 2. Biomass solubility in ionic liquids.

Biomass Type	Ionic Liquid	Temperature [°C]	Solubility [wt.%]	References
Hybrid poplar	[emim][CH_3COO] [emim][HCOO] [amim][CH_3COO] [amim][HCOO]	80	5.3 5.3 7.0 7.4	[84]
Miscanthus	[emim][CH_3COO] [emim][CH_3SO_3] [emim][HSO_4]	100	1.7 4.0 9.6	[85]
Peanut shells	[bmim]Cl [emim][CH_3COO]	120	2.3 5.8	[86]
Chestnut shells	[bmim]Cl [emim][CH_3COO]	120	4.7 7.0	
Miscanthus	[bmim][CH_3COO] [bmim]Cl [emim]Cl	130	4.0 3.0 4.0	[87]

The mechanism of biomass dissolution is based on the breakage of hydrogen bonds between lignocellulosic components. At the same time, the solvent's anion creates new hydrogen bonds with hydroxyl groups, especially cellulose. The possible role of the cation in polymer dissolution is connected to its size and hydrophobic character [88,89]. The biomass component, which is primarily dissolving ILs, is cellulose. Because of that, the effectiveness of biomass dissolution is dependent on the level of cellulose dissolution [80]. Uto et al. (2018) proposed a three-step mechanism of cellulose dissolution—first, IL's anion

penetrates through cellulose chains, which promotes hydrogen bond cleavage. At the same time, the cation increases the distance between these chains due to its size. Finally, cellulose chains are scattered [90]. The general idea of the cellulose dissolution mechanism is presented in Figure 10.

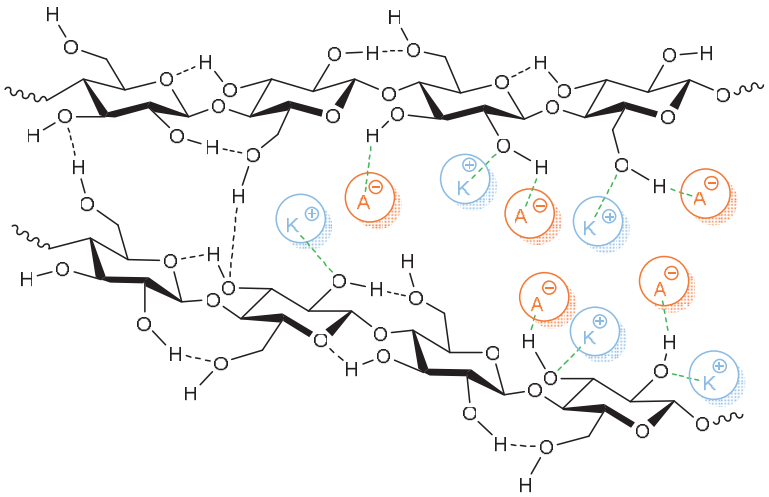


Figure 10. The mechanism of cellulose dissolution in ionic liquid.

The ability of ionic liquids to dissolve whole biomass results from the fact that some of the solvents can dissolve lignin, rather than only cellulose, e.g., imidazolium and ammonium ionic liquids with Cl^-, Tf_2N^-, and CH_3COO^- anions [24]. In *Eichhronia crassipes* (water hyacinth) dissolution using ionic liquids, the most effective solvent was the mixture of [bmim][CH_3COO] and water (water content of 40% v/v, and the level of biomass dissolution was approximately 85% of dry biomass). During this process, lignin was also dissolved [91]. Another popular ionic liquid [emim][CH_3COO] was applied in the production of composite fibers from hybrid poplar, where 6.5 wt. % of biomass could be dissolved [92]. The acetate anion has moderate basicity of hydrogen bonds (β), which enhances binding with lignin [85,91]. The addition of water to IL can increase lignin's dissolution level due to the formation of a higher number of hydrogen bonds [93,94]. The interactions between IL and hemicelluloses are also based on hydrogen bonds. Xylose, as a representative component of the hemicellulose monomer, can create fewer linkages with the solvent compared to glucose, due to the lower number of hydroxyl groups. Because of that, the hemicellulose solubility in IL is not as effective and might be a limiting factor in whole biomass dissolution [84].

3.6.2. Cellulose Dissolution in Ionic Liquids

The first patents on cellulose dissolution in melted ammonium and pyridinium salts were published in 1933–1934, but the application of 1-butyl-3-methylimidazolium chloride ([bmim]Cl) in 2002 began the intensive development in the field of ionic liquid applications.

The ability of ionic liquids to dissolve cellulose depends not only on the polymer characteristics, e.g., the degree of polymerization, crystallinity, type of plant, and process conditions (temperature, time, and presence of additional solvents), but also on ionic liquids properties [95–98]. Table 3 presents examples of cellulose solubility in ionic liquids.

Table 3. Cellulose solubility in ionic liquids.

Cellulose Type	Ionic liquid	Temperature [°C]	Solubility [wt. %]	References
MCC	[bmim][HCOO] [bmim][CH_3COO] [bmim][CH_3CH_2COO] [bmim][$CH_3(CH_2)_2COO$]	70	12.5 15.5 17.5 14.0	[99]
MCC	[emim][CH_3COO] [emim]DEP	90	27.0 15.0	[100]
MCC	[DBUH][HCOO] [DBUH][CH_3COO] [DBUH][CH_3CH_2COO]	90	18.9 14.8 12.6	[101]
MCC	[N_{2226}][CH_3COO]	80 90	15.0 22.0	[102]
Commercial Cellulose	[emim][CH_3COO] [emim][DEP] [DBUH][CH_3COO] [DBUH]][Prop] [DBNH][CH_3COO] [DBNH][Hex]	80	35.2 23.0 22.5 4.3 22.0 16.1	[103]
MCC	[amim][CH_3CH_2COO] [amim][C_6H_5COO]	30	19.0 <5.0	[104]
MCC	[DBUH][Lev] [DBNH][Lev]	100	15.0 20.0	[105]
MCC	[$emtr_{124}$][CH_3COO] [$emtr_{123}$]Br [emim][CH_3COO]	80	30.0 4.0 21.1	[106]
MCC	[amim][MP]	80	22.0	[107]
Commercial cellulose	[hmim][$CH_3CH(OH)COO$]	80	5.0	[108]
MCC	[ammorp][CH_3COO]	80	17.0	[109]

MCC—microcrystalline cellulose, DEP—diethylphosphate anion, DBUH—1,8-diazabicyclo [5.4.0]-undec-7-enium cation, DBNH—1,5-diazabicyclo [4.3.0]-undec-5-enium cation, N_{2226}—triethylhexylammonium cation, Prop—propanoate anion, Hex—hexanoate anion, $emtr_{124}$—1-ethyl-3-methyl-1,2,4-triazolium cation, $emtr_{123}$—1-ethyl-3-methyl-1,2,4-triazolium cation, MP—methyl phosphonate anion, hmim—2-methylimidazolium cation, ammorp—*N*-allyl-*N*-methylmorpholinium cation.

3.6.3. The Impact of Anion in Ionic Liquid on Cellulose Dissolution Effectiveness

The anion in ionic liquid has a major impact on cellulose dissolution. Generally, anions that are strong hydrogen bond acceptors, e.g., chloride, acetate, formate, and sulphate, are considered the most effective [100,110]. In order to estimate the anion effect on cellulose dissolution, Kamlet–Taft parameters describing the three independent polarity parameters (the hydrogen-bond-donating ability (α), the hydrogen-bond-accepting ability (β), and the polarizability/dipolarity (π*)) of a solvent are used. The most important seems to be the β parameter, related to the hydrogen bond basicity of the anion. The higher the β value of the anion, the better the dissolution properties of ionic liquid [111,112]. For example, 1-allyl-3-methylimidazolium formate [amim][$HCOO]^-$ is more effective than 1-allyl-3-methylimidazolium chloride ([amim]Cl) because of the higher basicity of hydrogen bonding of the $[HCOO]^-$ anion [96]. It has been also shown that replacing a hydrogen atom in the $[CH_3COO]^-$ anion with an electron-withdrawing group (e.g., $[HOCH_2COO]^-$, $[H_2NCH_2COO]^-$) decreases the solubility of cellulose [104].

3.6.4. The Impact of Ionic Liquid Cation on Cellulose Dissolution Effectiveness

The general order of cations in ionic liquids, which are most effective for cellulose dissolution, is imidazolium ILs > pyridinium ILs > ammonium ILs, which makes imidazolium-based solvents the most frequently studied in biomass dissolution processes [113]. In the imida-

zolium cation structure, alkyl substituents are common, e.g., 1-ethyl-3-methylimidazolium [emim]$^+$, 1-butyl-3-methylimidazolium [bmim]$^+$, 1-hexyl-3-methylimidazolium [hmim]$^+$, 1-octyl-3-methylimidazolium [omim]$^+$, and 1-allyl-3-methylimidazolium [amim]$^+$. With the increase in the alkyl chain length, the effectiveness of cellulose dissolution decreases. For instance, the solubility of cellulose at 100 °C in ionic liquids [*alkyl*mim]Cl decreased from 14 wt.% for [emim]Cl and 10 wt.% for [bmim]Cl to 5 wt.% for [hmim]Cl and nearly 0% for [omim]Cl [114,115]. It was also revealed that smaller cations in ILs enhance the solubility of cellulose. For example, 14.5 wt.% cellulose can be dissolved in 1-allyl-3-methylimidazolium chloride [amim]Cl at 80 °C [116]. This process is additionally supported by the entropic effect, which is a result of possible hydrogen bonds, due to the presence of a double bond in the cation structure [97]. The double bond is also responsible for the lower viscosity of the solvent, which has a beneficial impact on the process efficiency [117]. It could be concluded that cellulose-dissolving effectiveness increases if the imidazolium cation contains electron-donating substituents.

3.6.5. The Impact of the Addition of Other Chemicals and Process Conditions on Cellulose Dissolution Effectiveness in Ionic Liquids

Ionic liquids, despite the many advantages mentioned in this paper, have some drawbacks as solvents. Many ILs are viscous liquids, and their production costs are also quite high. In order to solve the viscosity problem, many researchers have added other solvents to the process. Organic polar aprotic solvents, e.g., DMSO or DMF, can significantly reduce the viscosity of ionic liquids, which results in better mass transport and increased polymer dissolution efficiency, without cellulose modifications [95,118,119]. Other solvents, such as acetonitrile or ethylene glycol, have a similar effect—they can reduce the viscosity of IL, e.g., [emim][CH_3COO] and [bmim][CH_3COO], by up to 50% [120]. In order to increase the efficiency of cellulose dissolution, inorganic additives can also be used. By adding 1% lithium salts (chloride, bromide, perchlorate, and nitrate) to ionic liquid [bmim][CH_3COO], the solubility increases from 15.5 wt.% (in IL) to 18–20 wt.% (IL+salt), at 70 °C [121]. It was also shown that the addition of water as a co-solvent decreases cellulose solubility in IL. It leads to the aggregation of cellulose. Water can be applied as an antisolvent in the precipitation and regeneration of dissolved polymers [122–125].

One of the most crucial factors in cellulose dissolution in ILs is temperature. An increase in temperature causes more efficient hydrogen bond breakage in cellulose, which relates to the better dissolution of this polymer. The solubility can additionally be enhanced by using a microwave-assisted process [114]. However, it must be noted that high temperatures cause the intensification of side reactions, such as polymer degradation or the formation of humins [126].

3.7. Deep Eutectic Solvents (DESs) in Biomass Processing

According to the latest publications, a new type of ionic liquid, namely, deep eutectic solvents (DESs), is being widely explored. They consist of hydrogen bond acceptors (HBA) and hydrogen bond donors (HBD), which are often natural compounds (Figure 11). Some properties of DESs are even better than classic ionic liquids, e.g., lower toxicity, lower production costs, biodegradability, and stability [127,128].

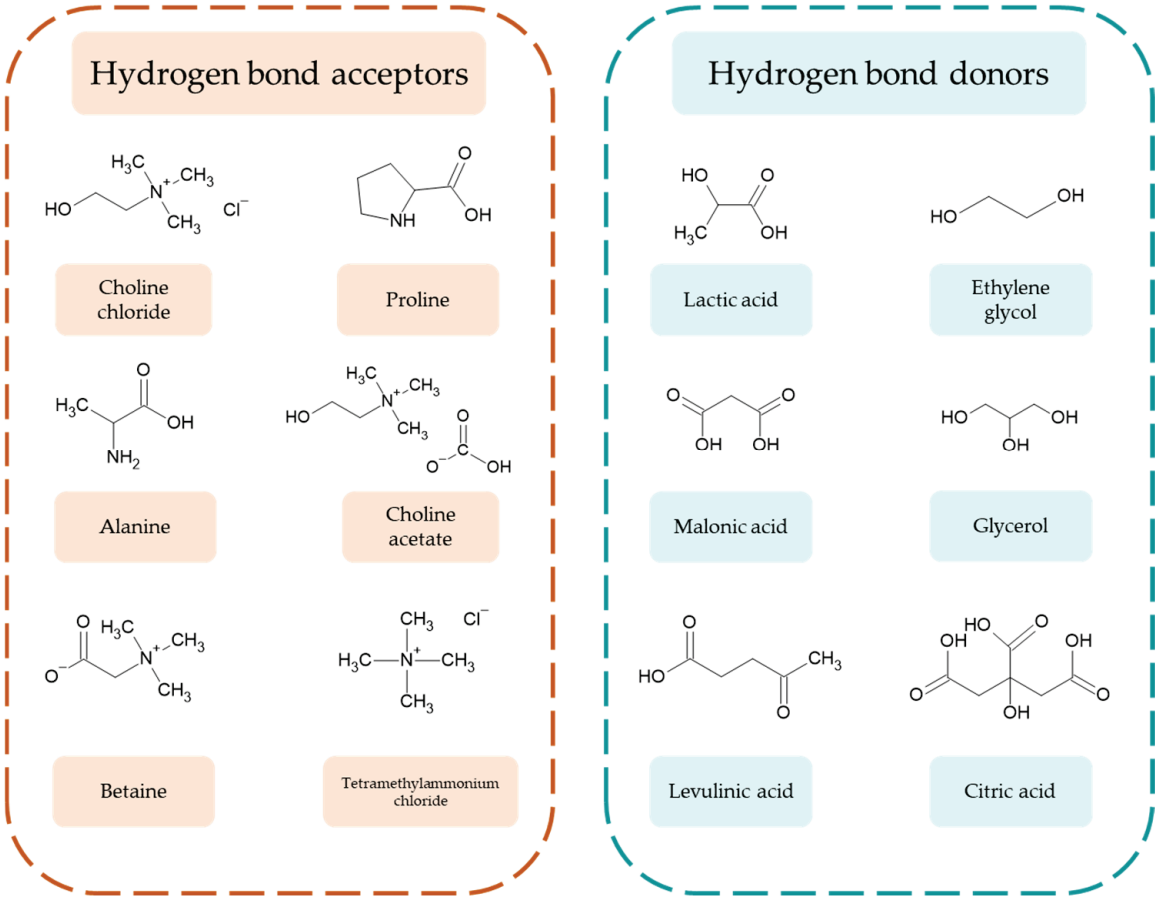


Figure 11. Hydrogen bond acceptors and donors most frequently applied in DESs, used in biomass processing [129–131].

3.7.1. Delignification of Biomass with DESs

The big advantage of DESs in biomass treatment is their higher activity in lignin dissolution compared to ionic liquids or alkaline solutions [132,133]. The main goal of biomass delignification is to increase the access of catalysts/enzymes to cellulose in further transformations into valuable chemicals. It was shown that efficient delignification can occur at elevated temperatures (above 100 °C). Lower temperatures are not sufficient for the breakage of the ether bonds in lignin. Poor mass transfer at lower temperatures is also a problem [45,134]. However, it must be noted that higher temperatures (above 160 °C) may, in turn, decrease the delignification level, because of phenolic side-product formations and their polymerization [135]. The effective delignification depends mostly on the properties of DESs. Generally, DESs based on acids are more effective (e.g., oxalic acid, lactic acid) than those based on polyols. It can be explained by the mechanism of lignin dissolution—ether bonds tend to break easier under acidic conditions [136,137]. Despite the large number of recent reports on biomass processing in DESs, the selection of the most effective solvent and process parameters still needs to be examined due to biomass variety and differences in its structure and chemical composition. Several examples of biomass processing with DESs are presented in Table 4.

Table 4. Delignification of plant biomass with DESs.

Biomass Type	DES (HBA:HBD Molar Ratio)	Temperature [°C]	Dissolution Technique	Time [h]	Delignification Level [%]	References
Rice straw	ChCl:Lac (1:5) Bet:Lac (1:5)	60	Stirring and heating	12	60.0 53.0	[138]
Miscanthus	ChCl:Fa (1:2)	60 130	Microwave	1	4.8 82.0	[135]
Birchwood	ChCl:Ox (1:1)	60 130	Microwave	1	43.0 85.0	
Bamboo stem	ChCl:U (1:2) ChCl:Ox (1:2)	120	Stirring and heating	10	19.4 25.4	[139]
Wheat straw Corn stalk Rapeseed stem	ChCl:Lac (1:5)	100	Stirring and heating	16	8.5 9.5 11.8	[140]
Sorghum straw	ChCl:Lac	150	Stirring and heating	0.5	49.0	[141]
Bamboo residues	ChCl:Lac (1:4)	110 130	Stirring and heating	1.5	42.3 83.6	[142]
	ChCl:Lac (1:8)	110 130			41.2 84.1	
Masson pine	ChCl:Lac (1:10)	110 140	Stirring and heating	6	58.1 87.5	[143]
Bagasse	ChCl:Ox (1:1) ChCl:Et (1:2)	100	Stirring and heating	4	47.9 8.6	[144]

(HBA—hydrogen bond acceptor, HBD—hydrogen bond donor, ChCl—choline chloride, Bet—betaine, Lac—lactic acid, Fa—formic acid, Ox—oxalic acid, U—urea, Et—ethylene glycol).

3.7.2. Hemicelluloses Dissolution in DESs

Some deep eutectic solvents can also be useful in the dissolution of hemicelluloses. Because of bonds connecting lignin and hemicelluloses, lignin removal is often followed by hemicelluloses extraction. By applying a solvent with a basic hydrogen bond acceptor and cholinium lysine with urea as the hydrogen bond donor, it was possible to extract approximately 62% of hemicelluloses from poplar wood [145]. Similar results (the removal of 63.3% hemicelluloses) were achieved in the process with DES consisting of choline chloride and monoethanolamine [146].

3.7.3. Cellulose Dissolution in DESs

Cellulose is the most difficult biomass fraction to dissolve in DESs. Recent reports show that it is still problematic to dissolve cellulose in DESs [147]. The amount of dissolved polymer depends on the source—microcrystalline cellulose is more soluble in DESs compared with that isolated from plant waste. For instance, the solubility of microcrystalline cellulose in ChCl:Lys 1:2 (*n*/*n*) (choline chloride:lysine) was approximately 8% of the initial amount, while in the case of cellulose isolated from wheat straw, it was only 6% (24 h, 90 °C). It is worth mentioning that these yields were obtained by applying ultrasound assistance in order to increase the solubility [148,149]. The poor solubility of cellulose and significantly better solubility of lignin in DESs allows one to separate biomass fractions, which is one of the main goals of plant waste pretreatment before further transformation into valuable chemicals.

4. Conclusions

The effective dissolution of biomass or its fractions is still a challenge in lignocellulosic waste processing. The wide variety of plant materials and differences in chemical compo-

sition makes the selection of an appropriate solvent even more difficult. The key step in making the process more efficient is to understand the mechanisms of biomass dissolution, which is generally based on the breakage of hydrogen bonds existing in lignocellulose and the creation of new ones between solvent and biomass components. Nowadays, the rules of the sustainable development strategy and green chemistry should be followed in the selection of appropriate solvents. Classic acidic and alkaline solutions, known for their ability to dissolve biomass fractions, should be replaced by more ecological solvents. Ionic liquids and deep eutectic solvents are promising groups of solvents. Ionic liquids are especially effective in cellulose dissolving. This ability mostly depends on the solvent's anion—the higher the hydrogen bond basicity of the anion, the better the biomass dissolution properties. Moreover, in many works, a substituted imidazolium cation is presented as the best one. However, the length of alkyl chains in cation substituents has a significant impact on the effectiveness of the process. Shorter chains are more suitable for dissolving cellulose (e.g., $[emim]^+$). If the process is devoted to lignin dissolution, it is recommended to use deep eutectic solvents, especially those with an acidic hydrogen bond donor. They are more effective than alkaline solutions. Because of the different abilities of ILs and DESs to dissolve lignocellulosic components, it is possible to use them in the separation of biomass polymers. Additionally, these solvents are considered green chemicals, which makes them a promising alternative to acidic and alkaline solutions. Except for the tunability of DESs and ILs, the primary advantage is their low toxicity and vapor pressure, high chemical and thermal stability, and miscibility with many chemicals. However, the novel systems also have some disadvantages. One of them is the high viscosity of many DESs, which significantly influences mass transfer. This problem can be overcome by using co-solvents or increasing the temperature (usually over 100 °C). Furthermore, the costs of some ILs and DESs might be considered a drawback.

Author Contributions: Conceptualization, M.P., A.W. and D.G.; draft preparation, M.P., A.W., and D.G.; writing—review and editing, M.P., A.W., and D.G.; supervision, D.G. All authors have read and agreed to the published version of the manuscript.

Funding: This research received no external funding.

Institutional Review Board Statement: Not applicable.

Informed Consent Statement: Not applicable.

Data Availability Statement: Not applicable.

Conflicts of Interest: The authors declare no conflict of interest.

References

1. Quintana-Rojo, C.; Callejas-Albiñana, F.E.; Tarancón, M.Á.; Martínez-Rodríguez, I. Econometric studies on the development of renewable energy sources to support the European Union 2020–2030 climate and energy framework: A critical appraisal. *Sustainability* **2020**, *12*, 4828. [CrossRef]
2. Camia, A. *Biomass Production, Supply, Uses and Flows in the European Union*; JRC: Brussels, Belgium, 2018.
3. Ramos, A.; Monteiro, E.; Rouboa, A. Biomass pre-treatment techniques for the production of biofuels using thermal conversion methods—A review. *Energy Convers. Manag.* **2022**, *270*, 116271. [CrossRef]
4. Ponnusamy, V.K.; Nguyen, D.D.; Dharmaraja, J.; Shobana, S.; Banu, J.R.; Saratale, R.G.; Chang, S.W.; Kumar, G. A review on lignin structure, pretreatments, fermentation reactions and biorefinery potential. *Bioresour. Technol.* **2019**, *271*, 462–472. [CrossRef] [PubMed]
5. Burhenne, L.; Messmer, J.; Aicher, T.; Laborie, M.P. The effect of the biomass components lignin, cellulose and hemicellulose on TGA and fixed bed pyrolysis. *J. Anal. Appl. Pyrolysis* **2013**, *101*, 177–184. [CrossRef]
6. Jahirul, M.I.; Rasul, M.G.; Chowdhury, A.A.; Ashwath, N. Biofuels production through biomass pyrolysis—A technological review. *Energies* **2012**, *5*, 4952–5001. [CrossRef]
7. Saddawi, A.; Jones, J.M.; Williams, A.; Le Coeur, C. Commodity fuels from biomass through pretreatment and torrefaction: Effects of mineral content on torrefied fuel characteristics and quality. *Energy Fuels* **2012**, *26*, 6466–6474. [CrossRef]
8. Prabha, S.; Durgalakshmi, D.; Rajendran, S.; Lichtfouse, E. Plant-derived silica nanoparticles and composites for biosensors, bioimaging, drug delivery and supercapacitors: A review. *Environ. Chem. Lett.* **2021**, *19*, 1667–1691. [CrossRef]

9. Schmitt, V.E.M.; Kaltschmitt, M. Effect of straw proportion and Ca- and Al-containing additives on ash composition and sintering of wood-straw pellets. *Fuel* **2013**, *109*, 551–558. [CrossRef]
10. Juneja, A.; Kumar, D.; Williams, J.D.; Wysocki, D.J.; Murthy, G.S. Potential for ethanol production from conservation reserve program lands in Oregon. *J. Renew. Sustain. Energy* **2011**, *3*, 063102. [CrossRef]
11. Surendra, K.C.; Richard, O.; Zaleski, H.M.; Hashimoto, A.G.; Khanal, S.K. High yielding tropical energy crops for bioenergy production: Effects of plant components, harvest years and locations on biomass composition. *Bioresour. Technol.* **2018**, *251*, 218–229. [CrossRef]
12. Ruan, R.; Zhang, Y.; Chen, P.; Liu, S.; Fan, L.; Zhou, N.; Ding, K.; Peng, P.; Addy, M.; Cheng, Y.; et al. Biofuels: Introduction. In *Biomass, Biofuels, Biochemicals: Biofuels: Alternative Feedstocks and Conversion Processes for the Production of Liquid and Gaseous Biofuels*; Elsevier: Amsterdam, The Netherlands, 2019; pp. 3–43.
13. Queirós, C.S.G.P.; Cardoso, S.; Lourenço, A.; Ferreira, J.; Miranda, I.; Lourenço, M.J.V.; Pereira, H. Characterization of walnut, almond, and pine nut shells regarding chemical composition and extract composition. *Biomass Convers. Biorefinery* **2020**, *10*, 175–188. [CrossRef]
14. Demirbaş, A. Calculation of higher heating values of biomass fuels. *Fuel* **1997**, *76*, 431–434. [CrossRef]
15. Španić, N.; Jambreković, V.; Klarić, M. Basic chemical composition of wood as a parameter in raw material selection for biocomposite production. *Cellul. Chem. Technol.* **2018**, *52*, 163–169.
16. Garcia-Maraver, A.; Salvachúa, D.; Martínez, M.J.; Diaz, L.F.; Zamorano, M. Analysis of the relation between the cellulose, hemicellulose and lignin content and the thermal behavior of residual biomass from olive trees. *Waste Manag.* **2013**, *33*, 2245–2249. [CrossRef]
17. McKendry, P. Energy Production from Biomass (Part 1): Overview of Biomass. *Bioresour. Technol.* **2002**, *83*, 37–46. [CrossRef] [PubMed]
18. Díez, D.; Urueña, A.; Piñero, R.; Barrio, A.; Tamminen, T. Determination of hemicellulose, cellulose, and lignin content in different types of biomasses by thermogravimetric analysis and pseudocomponent kinetic model (TGA-PKM Method). *Processes* **2020**, *8*, 1048. [CrossRef]
19. Rusanen, A.; Lappalainen, K.; Kärkkäinen, J.; Tuuttila, T.; Mikola, M.; Lassi, U. Selective hemicellulose hydrolysis of scots pine sawdust. *Biomass Convers. Biorefinery* **2019**, *9*, 283–291. [CrossRef]
20. Raitanen, J.E.; Järvenpää, E.; Korpinen, R.; Mäkinen, S.; Hellström, J.; Kilpeläinen, P.; Liimatainen, J.; Ora, A.; Tupasela, T.; Jyske, T. Tannins of conifer bark as Nordic piquancy—Sustainable preservative and aroma? *Molecules* **2020**, *25*, 567. [CrossRef]
21. Rongpipi, S.; Ye, D.; Gomez, E.D.; Gomez, E.W. Progress and opportunities in the characterization of cellulose—An important regulator of cell wall growth and mechanics. *Front. Plant Sci.* **2019**, *9*, 1894. [CrossRef]
22. Michelin, M.; Gomes, D.G.; Romaní, A.; Polizeli, M.d.L.T.M.; Teixeira, J.A. Nanocellulose production: Exploring the enzymatic route and residues of pulp and paper industry. *Molecules* **2020**, *25*, 3411. [CrossRef]
23. Owonubi, S.J.; Agwuncha, S.C.; Malima, N.M.; Shombe, G.B.; Makhatha, E.M.; Revaprasadu, N. Non-woody biomass as sources of nanocellulose particles: A review of extraction procedures. *Front. Energy Res.* **2021**, *9*, 608825. [CrossRef]
24. Lucenius, J.; Valle-Delgado, J.J.; Parikka, K.; Österberg, M. Understanding hemicellulose-cellulose interactions in cellulose nanofibril-based composites. *J. Colloid Interface Sci.* **2019**, *555*, 104–114. [CrossRef] [PubMed]
25. Hasanov, I.; Raud, M.; Kikas, T. The Role of ionic liquids in the lignin separation from lignocellulosic biomass. *Energies* **2020**, *13*, 4864. [CrossRef]
26. Liu, Q.; Luo, L.; Zheng, L. Lignins: Biosynthesis and biological functions in plants. *Int. J. Mol. Sci.* **2018**, *19*, 335. [CrossRef] [PubMed]
27. Polo, C.C.; Pereira, L.; Mazzafera, P.; Flores-Borges, D.N.A.; Mayer, J.L.S.; Guizar-Sicairos, M.; Holler, M.; Barsi-Andreeta, M.; Westfahl, H.; Meneau, F. Correlations between lignin content and structural robustness in plants revealed by X-ray ptychography. *Sci. Rep.* **2020**, *10*, 6023. [CrossRef]
28. Abushammala, H.; Mao, J. A review on the partial and complete dissolution and fractionation of wood and lignocelluloses using imidazolium ionic liquids. *Polymers* **2020**, *12*, 195. [CrossRef]
29. Sun, S.; Sun, S.; Cao, X.; Sun, R. The role of pretreatment in improving the enzymatic hydrolysis of lignocellulosic materials. *Bioresour. Technol.* **2016**, *199*, 49–58. [CrossRef]
30. Lindman, B.; Medronho, B.; Alves, L.; Costa, C.; Edlund, H.; Norgren, M. The relevance of structural features of cellulose and its interactions to dissolution, regeneration, gelation and plasticization phenomena. *Phys. Chem. Chem. Phys.* **2017**, *19*, 23704–23718. [CrossRef]
31. Thoresen, P.P.; Matsakas, L.; Rova, U.; Christakopoulos, P. Recent advances in organosolv fractionation: Towards biomass fractionation technology of the future. *Bioresour. Technol.* **2020**, *306*, 123189. [CrossRef]
32. Tursi, A. A review on biomass: Importance, chemistry, classification, and conversion. *Biofuel Res. J.* **2019**, *6*, 962–979. [CrossRef]
33. Credou, J.; Berthelot, T. Cellulose: From biocompatible to bioactive material. *J. Mater. Chem. B* **2014**, *2*, 4767–4788. [CrossRef] [PubMed]
34. Ioelovich, M. Preparation, characterization and application of amorphized cellulose—A review. *Polymers* **2021**, *13*, 4313. [CrossRef] [PubMed]
35. Bajpai, P. Wood and fiber fundamentals. In *Biermann's Handbook of Pulp and Paper*; Elsevier: Amsterdam, The Netherlands, 2018; pp. 19–74.

36. Jones, D.; Ormondroyd, G.O.; Curling, S.F.; Popescu, C.M.; Popescu, M.C. Chemical compositions of natural fibres. In *Cereal Straw as a Resource for Sustainable Biomaterials and Biofuels: Chemistry, Extractives, Lignins, Hemicelluloses and Cellulose*; Elsevier: Amsterdam, The Netherlands, 2010; pp. 23–58.
37. Kobetičová, K.; Nábělková, J. Effect of wood hemicellulose composition on binding interactions with caffeine. *Buildings* **2021**, *11*, 515. [CrossRef]
38. Schädel, C.; Blöchl, A.; Richter, A.; Hoch, G. Quantification and monosaccharide composition of hemicelluloses from different plant functional types. *Plant Phys. Biochem.* **2010**, *48*, 1–8. [CrossRef]
39. Patel, J.P.; Parsania, P.H. Characterization, testing, and reinforcing materials of biodegradable composites. In *Biodegradable and Biocompatible Polymer Composites: Processing, Properties and Applications*; Elsevier: Amsterdam, The Netherlands, 2017; pp. 55–79.
40. Lu, Y.; Lu, Y.C.; Hu, H.Q.; Xie, F.J.; Wei, X.Y.; Fan, X. Structural characterization of lignin and its degradation products with spectroscopic methods. *J. Spectrosc.* **2017**, *2017*, 1–15. [CrossRef]
41. Ajao, O.; Jeaidi, J.; Benali, M.; Restrepo, A.M.; El Mehdi, N.; Boumghar, Y. Quantification and variability analysis of lignin optical properties for colour-dependent industrial applications. *Molecules* **2018**, *23*, 377. [CrossRef]
42. Melro, E.; Alves, L.; Antunes, F.E.; Medronho, B. A brief overview on lignin dissolution. *J. Mol. Liq.* **2018**, *265*, 578–584. [CrossRef]
43. Dastpak, A.; Lourençon, T.V.; Balakshin, M.; Farhan Hashmi, S.; Lundström, M.; Wilson, B.P. Solubility study of lignin in industrial organic solvents and investigation of electrochemical properties of spray-coated solutions. *Ind. Crops Prod.* **2020**, *148*, 112310. [CrossRef]
44. Lange, H.; Decina, S.; Crestini, C. Oxidative upgrade of lignin—Recent routes reviewed. In *European Polymer Journal*; Elsevier: Amsterdam, The Netherlands, 2013; Volume 49, pp. 1151–1173.
45. da Costa Lopes, A.M.; Gomes, J.R.B.; Coutinho, J.A.P.; Silvestre, A.J.D. Novel insights into biomass delignification with acidic deep eutectic solvents: A mechanistic study of β-O-4 ether bond cleavage and the role of the halide counterion in the catalytic performance. *Green Chem.* **2020**, *22*, 2474–2487. [CrossRef]
46. Kang, X.; Kirui, A.; Dickwella Widanage, M.C.; Mentink-Vigier, F.; Cosgrove, D.J.; Wang, T. Lignin-polysaccharide interactions in plant secondary cell walls revealed by solid-state NMR. *Nat. Commun.* **2019**, *10*, 1–9. [CrossRef]
47. Mahdi, Y.S.; Mohammed, A.H.; Mohammed, A.K. Cellulose fibers dissolution in alkaline solution. *Al-Khwarizmi Eng. J.* **2019**, *14*, 107–115. [CrossRef]
48. Medronho, B.; Lindman, B. Brief overview on cellulose dissolution/regeneration interactions and mechanisms. *Adv. Colloid Interface Sci.* **2015**, *222*, 502–508. [CrossRef] [PubMed]
49. Wang, S.; Sun, P.; Liu, M.; Lu, A.; Zhang, L. Weak interactions and their impact on cellulose dissolution in an alkali/urea aqueous system. *Phys. Chem. Chem. Phys.* **2017**, *19*, 17909–17917. [CrossRef] [PubMed]
50. Sirviö, J.A.; Heiskanen, J.P. Room-temperature dissolution and chemical modification of cellulose in aqueous tetraethylammonium hydroxide–carbamide solutions. *Cellulose* **2020**, *27*, 1933–1950. [CrossRef]
51. Yang, J.; Sun, M.; Jiao, L.; Dai, H. Molecular weight distribution and dissolution behavior of lignin in alkaline solutions. *Polymers* **2021**, *13*, 4166. [CrossRef]
52. Lin, L.; Yan, R.; Jiang, W.; Shen, F.; Zhang, X.; Zhang, Y.; Deng, S.; Li, Z. Enhanced enzymatic hydrolysis of palm pressed fiber based on the three main components: Cellulose, hemicellulose, and lignin. *Appl. Biochem. Biotechnol.* **2014**, *173*, 409–420. [CrossRef]
53. Mussatto, S.I. Biomass pretreatment with acids. In *Biomass Fractionation Technologies for a Lignocellulosic Feedstock Based Biorefinery*; Elsevier: Amsterdam, The Netherlands, 2016; pp. 169–185.
54. Ioelovich, M. Study of cellulose interaction with concentrated solutions of sulfuric acid. *ISRN Chem. Eng.* **2012**, *2012*, 1–7. [CrossRef]
55. Fagerstedt, K.V.; Saranpää, P.; Tapanila, T.; Immanen, J.; Serra, J.A.A.; Nieminen, K. Determining the composition of lignins in different tissues of silver birch. *Plants* **2015**, *4*, 183–195. [CrossRef]
56. Pfab, E.; Filiciotto, L.; Luque, R. The dark side of biomass valorization: A laboratory experiment to understand humin formation, catalysis, and green chemistry. *J. Chem. Educ.* **2019**, *96*, 3030–3037. [CrossRef]
57. van Zandvoort, I.; Wang, Y.; Rasrendra, C.B.; van Eck, E.R.H.; Bruijnincx, P.C.A.; Heeres, H.J.; Weckhuysen, B.M. Formation, molecular structure, and morphology of humins in biomass conversion: Influence of feedstock and processing conditions. *ChemSusChem* **2013**, *6*, 1745–1758. [CrossRef]
58. Olsson, C.; Westm, G. Direct dissolution of cellulose: Background, means and applications. In *Cellulose—Fundamental Aspects*; InTech: Singapore, 2013.
59. Liebert, T. Cellulose solvents—Remarkable history, bright future. In *Cellulose Solvents: For Analysis, Shaping and Chemical Modification*; American Chemical Society: New York, NY, USA, 2010; pp. 3–54.
60. Leipner, H.; Fischer, S.; Brendler, E.; Voigt, W. Structural changes of cellulose dissolved in molten salt hydrates. *Macromol. Chem. Phys.* **2000**, *201*, 2041–2049. [CrossRef]
61. Loow, Y.L.; Wu, T.Y.; Tan, K.A.; Lim, Y.S.; Siow, L.F.; Jahim, J.M.; Mohammad, A.W.; Teoh, W.H. Recent advances in the application of inorganic salt pretreatment for transforming lignocellulosic biomass into reducing sugars. *J. Agric. Food Chem.* **2015**, *63*, 8349–8363. [CrossRef] [PubMed]
62. Du, H.; Deng, F.; Kommalapati, R.R.; Amarasekara, A.S. Iron based catalysts in biomass processing. *Renew. Sustain. Energy Rev.* **2020**, *134*, 110292.

63. Zhang, Y.; Huang, M.; Su, J.; Hu, H.; Yang, M.; Huang, Z.; Chen, D.; Wu, J.; Feng, Z. Overcoming biomass recalcitrance by synergistic pretreatment of mechanical activation and metal salt for enhancing enzymatic conversion of lignocellulose. *Biotechnol. Biofuels* **2019**, *12*, 1–15. [CrossRef] [PubMed]
64. Fischer, S.; Thümmler, K. Molten inorganic salts as reaction medium for cellulose. In *ACS Symposium Series*; American Chemical Society: New York, NY, USA, 2010; Volume 1033, pp. 91–101.
65. Saalwächter, K.; Burchard, W. Cellulose in new metal-complexing solvents. 2. Semidilute behavior in Cd-tren. *Macromolecules* **2001**, *34*, 5587–5598. [CrossRef]
66. Sen, S.; Martin, J.D.; Argyropoulos, D.S. Review of cellulose non-derivatizing solvent interactions with emphasis on activity in inorganic molten salt hydrates. *ACS Sustain. Chem. Eng.* **2013**, *1*, 858–870. [CrossRef]
67. McCormick, C.L.; Callais, P.A.; Hutchinson, B.H. Solution studies of cellulose in lithium chloride and N,N-dimethylacetamide. *Macromolecules* **1985**, *18*, 2394–2401. [CrossRef]
68. Ali, N.; Hamouda, H.I.; Su, H.; Li, F.L.; Lu, M. Combinations of alkaline hydrogen peroxide and lithium chloride/N,N-dimethylacetamide pretreatments of corn stalk for improved biomethanation. *Environ. Res.* **2020**, *186*, 109563. [CrossRef]
69. Li, H.; Xiong, L.; Chen, X.; Luo, M.; Chen, X.; Wang, C.; Huang, C.; Chen, X. Enhanced enzymatic hydrolysis of wheat straw via a combination of alkaline hydrogen peroxide and lithium chloride/N,N-dimethylacetamide pretreatment. *Ind. Crops Prod.* **2019**, *137*, 332–338. [CrossRef]
70. Sayyed, A.J.; Deshmukh, N.A.; Pinjari, D.V. A critical review of manufacturing processes used in regenerated cellulosic fibres: Viscose, cellulose acetate, cuprammonium, LiCl/DMAc, ionic liquids, and NMMO based lyocell. *Cellulose* **2019**, *26*, 2913–2940. [CrossRef]
71. Zhang, C.; Liu, R.; Xiang, J.; Kang, H.; Liu, Z.; Huang, Y. Dissolution mechanism of cellulose in N,N-dimethylacetamide/lithium chloride: Revisiting through molecular interactions. *J. Phys. Chem. B* **2014**, *118*, 9507–9514. [CrossRef] [PubMed]
72. Heinze, T.; Dicke, R.; Koschella, A.; Kull, A.H.; Klohr, E.A.; Koch, W. Effective preparation of cellulose derivatives in a new simple cellulose solvent. *Macromol. Chem. Phys.* **2000**, *201*, 627–631. [CrossRef]
73. Östlund, Å.; Lundberg, D.; Nordstierna, L.; Holmberg, K.; Nydén, M. Dissolution and gelation of cellulose in TBAF/DMSO solutions: The roles of fluoride ions and water. *Biomacromolecules* **2009**, *10*, 2401–2407. [CrossRef]
74. Nguyen, M.N.; Kragl, U.; Michalik, D.; Ludwig, R.; Hollmann, D. The effect of additives on the viscosity and dissolution of cellulose in tetrabutylphosphonium hydroxide. *ChemSusChem* **2019**, *12*, 3458–3462. [CrossRef] [PubMed]
75. Kostag, M.; Jedvert, K.; Achtel, C.; Heinze, T.; El Seoud, O.A. Recent advances in solvents for the dissolution, shaping and derivatization of cellulose: Quaternary ammonium electrolytes and their solutions in water and molecular solvents. *Molecules* **2018**, *23*, 511. [CrossRef] [PubMed]
76. Onwukamike, K.N.; Grelier, S.; Grau, E.; Cramail, H.; Meier, M.A.R. Critical review on sustainable homogeneous cellulose modification: Why renewability is not enough. *ACS Sustain. Chem. Eng.* **2019**, *7*, 1826–1840. [CrossRef]
77. Ghandi, K. A review of ionic liquids, their limits and applications. *Green Sustain. Chem.* **2014**, *4*, 44–53. [CrossRef]
78. Morais, E.S.; da Costa Lopes, A.M.; Freire, M.G.; Freire, C.S.R.; Coutinho, J.A.P.; Silvestre, A.J.D. Use of ionic liquids and deep eutectic solvents in polysaccharides dissolution and extraction processes towards sustainable biomass valorization. *Molecules* **2020**, *25*, 3652. [CrossRef]
79. Halder, P.; Kundu, S.; Patel, S.; Setiawan, A.; Atkin, R.; Parthasarthy, R.; Paz-Ferreiro, J.; Surapaneni, A.; Shah, K. Progress on the pre-treatment of lignocellulosic biomass employing ionic liquids. *Renew. Sustain. Energy Rev.* **2019**, *105*, 268–292. [CrossRef]
80. Fort, D.A.; Remsing, R.C.; Swatloski, R.P.; Moyna, P.; Moyna, G.; Rogers, R.D. Can ionic liquids dissolve wood? Processing and analysis of lignocellulosic materials with 1-n-butyl-3-methylimidazolium chloride. *Green Chem.* **2007**, *9*, 63–69. [CrossRef]
81. Badgujar, K.C.; Bhanage, B.M. Factors governing dissolution process of lignocellulosic biomass in ionic liquid: Current status, overview and challenges. *Bioresour. Technol.* **2015**, *178*, 2–18. [CrossRef] [PubMed]
82. Rahim, A.H.A.; Yunus, N.M.; Hamzah, W.S.W.; Sarwono, A.; Muhammad, N. Low-viscosity ether-functionalized ionic liquids as solvents for the enhancement of lignocellulosic biomass dissolution. *Processes* **2021**, *9*, 261. [CrossRef]
83. Xia, Z.; Li, J.; Zhang, J.; Zhang, X.; Zheng, X.; Zhang, J. Processing and valorization of cellulose, lignin and lignocellulose using ionic liquids. *J. Bioresour. Bioprod.* **2020**, *5*, 79–95. [CrossRef]
84. Moyer, P.; Smith, M.D.; Abdoulmoumine, N.; Chmely, S.C.; Smith, J.C.; Petridis, L.; Labbé, N. Relationship between lignocellulosic biomass dissolution and physicochemical properties of ionic liquids composed of 3-methylimidazolium cations and carboxylate anions. *Phys. Chem. Chem. Phys.* **2018**, *20*, 2508–2516. [CrossRef]
85. Dash, M.; Mohanty, K. Effect of different ionic liquids and anti-solvents on dissolution and regeneration of miscanthus towards bioethanol. *Biomass Bioenergy* **2019**, *124*, 33–42. [CrossRef]
86. Carneiro, A.P.; Rodríguez, O.; Macedo, E.A. Dissolution and fractionation of nut shells in ionic liquids. *Bioresour. Technol.* **2017**, *227*, 188–196. [CrossRef]
87. Padmanabhan, S.; Kim, M.; Blanch, H.W.; Prausnitz, J.M. Solubility and rate of dissolution for miscanthus in hydrophilic ionic liquids. *Fluid Phase Equilibria* **2011**, *309*, 89–96. [CrossRef]
88. Zhou, L.; Pan, F.; Liu, Y.; Kang, Z.; Zeng, S.; Nie, Y. Study on the regularity of cellulose degradation in ionic liquids. *J. Mol. Liq.* **2020**, *308*, 113153. [CrossRef]

89. Remsing, R.C.; Swatloski, R.P.; Rogers, R.D.; Moyna, G. Mechanism of cellulose dissolution in the ionic liquid 1-n-butyl-3-methylimidazolium chloride: A 13C and 35/37Cl NMR relaxation study on model systems. *Chem. Comm.* **2006**, *12*, 1271–1273. [CrossRef]
90. Uto, T.; Yamamoto, K.; Kadokawa, J.I. Cellulose crystal dissolution in imidazolium-based ionic liquids: A theoretical study. *J. Phys. Chem. B* **2018**, *122*, 258–266. [CrossRef]
91. Gogoi, G.; Hazarika, S. Dissolution of lignocellulosic biomass in ionic liquid-water media: Interpretation from solubility parameter concept. *Korean J. Chem. Eng.* **2019**, *36*, 1626–1636. [CrossRef]
92. Nguyen, N.A.; Kim, K.; Bowland, C.C.; Keum, J.K.; Kearney, L.T.; André, N.; Labbé, N.; Naskar, A.K. A fundamental understanding of whole biomass dissolution in ionic liquid for regeneration of fiber by solution-spinning. *Green Chem.* **2019**, *21*, 4354–4367. [CrossRef]
93. Ge, M.; Fang, T.; Zhou, G.; Li, C.; Li, Y.; Liu, X. Insight into the dual effect of water on lignin dissolution in ionic liquids. *Int. J. Biol. Macromol.* **2022**, *205*, 178–184. [CrossRef] [PubMed]
94. Manna, B.; Datta, S.; Ghosh, A. Understanding the dissolution of softwood lignin in ionic liquid and water mixed solvents. *Int. J. Biol. Macromol.* **2021**, *182*, 402–412. [CrossRef]
95. Bahadur, I.; Phadagi, R. Ionic liquids as environmental benign solvents for cellulose chemistry: A review. In *Solvents, Ionic Liquids and Solvent Effects*; IntechOpen: London, UK, 2020.
96. Wang, H.; Gurau, G.; Rogers, R.D. Ionic liquid processing of cellulose. *Chem. Soc. Rev.* **2012**, *41*, 1519–1537. [CrossRef]
97. Zakrzewska, M.E.; Bogel-Yukasik, E.; Bogel-Yukasik, R. Solubility of carbohydrates in ionic liquids. *Energy Fuels* **2010**, *24*, 737–745. [CrossRef]
98. Verma, C.; Mishra, A.; Chauhan, S.; Verma, P.; Srivastava, V.; Quraishi, M.A.; Ebenso, E.E. Dissolution of cellulose in ionic liquids and their mixed cosolvents: A review. *Sustain. Chem. Pharm.* **2019**, *13*, 100162. [CrossRef]
99. Xu, A.; Zhang, Y.; Lu, W.; Yao, K.; Xu, H. Effect of alkyl chain length in anion on dissolution of cellulose in 1-butyl-3-methylimidazolium carboxylate ionic liquids. *J. Mol. Liq.* **2014**, *197*, 211–214. [CrossRef]
100. Liu, Y.-R.; Thomsen, K.; Nie, Y.; Zhang, S.-J.; Meyer, A.S. Predictive screening of ionic liquids for dissolving cellulose and experimental verification. *Green Chem.* **2016**, *18*, 6246–6254. [CrossRef]
101. Li, X.; Li, H.; Ling, Z.; Xu, D.; You, T.; Wu, Y.Y.; Xu, F. Room-temperature superbase-derived ionic liquids with facile synthesis and low viscosity: Powerful solvents for cellulose dissolution by destroying the cellulose aggregate structure. *Macromolecules* **2020**, *53*, 3284–3295. [CrossRef]
102. Meng, X.; Devemy, J.; Verney, V.; Gautier, A.; Husson, P.; Andanson, J.M. Improving cellulose dissolution in ionic liquids by tuning the size of the ions: Impact of the length of the alkyl chains in tetraalkylammonium carboxylate. *ChemSusChem* **2017**, *10*, 1749–1760. [CrossRef]
103. Kuzmina, O.; Bhardwaj, J.; Vincent, S.R.; Wanasekara, N.D.; Kalossaka, L.M.; Griffith, J.; Potthast, A.; Rahatekar, S.; Eichhorn, S.J.; Welton, T. Superbase ionic liquids for effective cellulose processing from dissolution to carbonisation. *Green Chem.* **2017**, *19*, 5949–5957. [CrossRef]
104. Zhang, Y.; Xu, A.; Lu, B.; Li, Z.; Wang, J. Dissolution of cellulose in 1-allyl-3-methylimizodalium carboxylates at room temperature: A structure-property relationship study. *Carbohydr. Polym.* **2015**, *117*, 666–672. [CrossRef] [PubMed]
105. Becherini, S.; Mezzetta, A.; Chiappe, C.; Guazzelli, L. Levulinate amidinium protic ionic liquids (PILs) as suitable media for the dissolution and levulination of cellulose. *New J. Chem.* **2019**, *43*, 4554–4561. [CrossRef]
106. Brehm, M.; Pulst, M.; Kressler, J.; Sebastiani, D. Triazolium-based ionic liquids: A novel class of cellulose solvents. *J. Phys. Chem. B* **2019**, *123*, 3994–4003. [CrossRef]
107. Xu, K.; Xiao, Y.; Cao, Y.; Peng, S.; Fan, M.; Wang, K. Dissolution of cellulose in 1-allyl-3-methylimidazolium methyl phosphonate ionic liquid and its composite system with Na_2PHO_3. *Carbohydr. Polym.* **2019**, *209*, 382–388. [CrossRef] [PubMed]
108. Meenatchi, B.; Renuga, V.; Manikandan, A. Cellulose dissolution and regeneration using various imidazolium based protic ionic liquids. *J. Mol. Liq.* **2017**, *238*, 582–588. [CrossRef]
109. Raut, D.G.; Sundman, O.; Su, W.; Virtanen, P.; Sugano, Y.; Kordas, K.; Mikkola, J.P. A Morpholinium ionic liquid for cellulose dissolution. *Carbohydr. Polym.* **2015**, *130*, 18–25. [CrossRef]
110. Kostag, M.; Gericke, M.; Heinze, T.; El Seoud, O.A. Twenty-five years of cellulose chemistry: Innovations in the dissolution of the biopolymer and its transformation into esters and ethers. *Cellulose* **2019**, *26*, 139–184. [CrossRef]
111. Islam, T.; Islam Sarker, M.Z.; Uddin, A.H.; Bin Yunus, K.; Prasad, R.; Mia, M.A.R.; Ferdosh, S. Kamlet Taft parameters: A tool to alternate the usage of hazardous solvent in pharmaceutical and chemical manufacturing/synthesis—A gateway towards green technology. *Anal. Chem. Lett.* **2020**, *10*, 550–561. [CrossRef]
112. Weiß, N.; Schmidt, C.H.; Thielemann, G.; Heid, E.; Schröder, C.; Spange, S. The physical significance of the Kamlet-Taft: $\pi*$ parameter of ionic liquids. *Phys. Chem. Chem. Phys.* **2021**, *23*, 1616–1626. [CrossRef] [PubMed]
113. Li, Y.; Wang, J.; Liu, X.; Zhang, S. Towards a molecular understanding of cellulose dissolution in ionic liquids: Anion/cation effect, synergistic mechanism and physicochemical aspects. *Chem. Sci.* **2018**, *9*, 4027–4043. [CrossRef] [PubMed]
114. Swatloski, R.P.; Spear, S.K.; Holbrey, J.D.; Rogers, R.D. Dissolution of cellulose with ionic liquids. *J. Am. Chem. Soc.* **2002**, *124*, 4974–4975. [CrossRef] [PubMed]
115. Vitz, J.; Erdmenger, T.; Haensch, C.; Schubert, U.S. Extended dissolution studies of cellulose in imidazolium based ionic liquids. *Green Chem.* **2009**, *11*, 417–442. [CrossRef]

116. Zhang, H.; Wu, J.; Zhang, J.; He, J. 1-Allyl-3-methylimidazolium chloride room temperature ionic liquid: A new and powerful nonderivatizing solvent for cellulose. *Macromolecules* **2005**, *38*, 8272–8277. [CrossRef]
117. Pinkert, A.; Marsh, K.N.; Pang, S.; Staiger, M.P. Ionic liquids and their interaction with cellulose. *Chem. Rev.* **2009**, *109*, 6712–6728. [CrossRef]
118. Kasprzak, D.; Krystkowiak, E.; Stępniak, I.; Galiński, M. Dissolution of cellulose in novel carboxylate-based ionic liquids and dimethyl sulfoxide mixed solvents. *Eur. Polym. J.* **2019**, *113*, 89–97. [CrossRef]
119. Phadagi, R.; Singh, S.; Hashemi, H.; Kaya, S.; Venkatesu, P.; Ramjugernath, D.; Ebenso, E.E.; Bahadur, I. Understanding the role of dimethylformamide as co-solvents in the dissolution of cellulose in ionic liquids: Experimental and theoretical approach. *J. Mol. Liq.* **2021**, *328*, 115392. [CrossRef]
120. Fendt, S.; Padmanabhan, S.; Blanch, H.W.; Prausnitz, J.M. Viscosities of acetate or chloride-based ionic liquids and some of their mixtures with water or other common solvents. *J. Chem. Eng. Data* **2011**, *56*, 31–34. [CrossRef]
121. Xu, A.; Wang, J.; Wang, H. Effects of anionic structure and lithium salts addition on the dissolution of cellulose in 1-butyl-3-methylimidazolium-based ionic liquid solvent systems. *Green Chem.* **2010**, *12*, 268–275. [CrossRef]
122. Ding, Z.D.; Chi, Z.; Gu, W.X.; Gu, S.M.; Liu, J.H.; Wang, H.J. Theoretical and experimental investigation on dissolution and regeneration of cellulose in ionic liquid. *Carbohydr. Polym.* **2012**, *89*, 7–16. [CrossRef] [PubMed]
123. Li, B.; Asikkala, J.; Filpponen, I.; Argyropoulos, D.S. Factors affecting wood dissolution and regeneration of ionic liquids. *Ind. Eng. Chem. Res.* **2010**, *49*, 2477–2484. [CrossRef]
124. Manna, B.; Ghosh, A. Dissolution of cellulose in ionic liquid and water mixtures as revealed by molecular dynamics simulations. *J. Biomol. Struct. Dyn.* **2019**, *37*, 3987–4005. [CrossRef] [PubMed]
125. Fu, L.; Ju, Z.; Yu, M.; Luo, H.; Zhang, C.; Zhang, X.; Cheng, H.; Zheng, M.; Jin, L.; Ge, C. Cellulose regeneration in imidazolium-based ionic liquids and antisolvent mixtures: A density functional theory study. *ACS Omega* **2022**, *7*, 42170–42180. [CrossRef] [PubMed]
126. Feng, L.; Chen, Z.L. Research progress on dissolution and functional modification of cellulose in ionic liquids. *J. Mol. Liq.* **2008**, *142*, 1–5. [CrossRef]
127. Płotka-Wasylka, J.; de la Guardia, M.; Andruch, V.; Vilková, M. Deep eutectic solvents vs ionic liquids: Similarities and differences. *Microchem. J.* **2020**, *159*, 105539. [CrossRef]
128. Chen, Y.; Mu, T. Revisiting greenness of ionic liquids and deep eutectic solvents. *Green Chem. Eng.* **2021**, *2*, 174–186. [CrossRef]
129. Hansen, B.B.; Spittle, S.; Chen, B.; Poe, D.; Zhang, Y.; Klein, J.M.; Horton, A.; Adhikari, L.; Zelovich, T.; Doherty, B.W.; et al. Deep eutectic solvents: A review of fundamentals and applications. *Chem. Rev.* **2021**, *121*, 1232–1285. [CrossRef]
130. el Achkar, T.; Greige-Gerges, H.; Fourmentin, S. Basics and properties of deep eutectic solvents: A review. *Environ. Chem. Lett.* **2021**, *19*, 3397–3408. [CrossRef]
131. Gomes, G.R.; Mattioli, R.R.; Pastre, J.C. Amino acid-based deep eutectic solvents in biomass processing—Recent advances. *J. Braz. Chem. Soc.* **2022**, *33*, 815–823. [CrossRef]
132. Ji, H.; Lv, P. Mechanistic insights into the lignin dissolution behaviors of a recyclable acid hydrotrope, deep eutectic solvent (DES), and ionic liquid (IL). *Green Chem.* **2020**, *22*, 1378–1387. [CrossRef]
133. Cassoni, A.C.; Mota, I.; Costa, P.; Vasconcelos, M.W.; Pintado, M. Effect of alkaline and deep eutectic solvents pretreatments on the recovery of lignin with antioxidant activity from grape stalks. *Int. J. Biol. Macromol.* **2022**, *220*, 406–414. [CrossRef] [PubMed]
134. Chen, Y.; Shen, K.; He, Z.; Wu, T.; Huang, C.; Liang, L.; Fang, G. Deep eutectic solvent recycling to prepare high purity dissolving pulp. *Cellulose* **2021**, *28*, 11503–11517. [CrossRef]
135. Kohli, K.; Katuwal, S.; Biswas, A.; Sharma, B.K. Effective delignification of lignocellulosic biomass by microwave assisted deep eutectic solvents. *Bioresour. Technol.* **2020**, *303*, 122897. [CrossRef] [PubMed]
136. Soares, B.; da Costa Lopes, A.M.; Silvestre, A.J.D.; Rodrigues Pinto, P.C.; Freire, C.S.R.; Coutinho, J.A.P. Wood delignification with aqueous solutions of deep eutectic solvents. *Ind. Crops Prod.* **2021**, *160*, 113128. [CrossRef]
137. Xu, H.; Kong, Y.; Peng, J.; Wang, W.; Li, B. Mechanism of deep eutectic solvent delignification: Insights from molecular dynamics simulations. *ACS Sustain. Chem. Eng.* **2021**, *9*, 7101–7111. [CrossRef]
138. Kumar, A.K.; Parikh, B.S.; Pravakar, M. Natural deep eutectic solvent mediated pretreatment of rice straw: Bioanalytical characterization of lignin extract and enzymatic hydrolysis of pretreated biomass residue. *Environ. Sci. Pollut. Res.* **2016**, *23*, 9265–9275. [CrossRef] [PubMed]
139. Ramesh, R.; Nair, A.; Jayavel, A.; Sathiasivan, K.; Rajesh, M.; Ramaswamy, S.; Tamilarasan, K. Choline chloride-based deep eutectic solvents for efficient delignification of *Bambusa bambos* in bio-refinery applications. *Chem. Pap.* **2020**, *74*, 4533–4545. [CrossRef]
140. Suopajärvi, T.; Ricci, P.; Karvonen, V.; Ottolina, G.; Liimatainen, H. Acidic and alkaline deep eutectic solvents in delignification and nanofibrillation of corn stalk, wheat straw, and rapeseed stem residues. *Ind. Crops Prod.* **2020**, *145*, 111956. [CrossRef]
141. Wu, M.; Gong, L.; Ma, C.; He, Y.C. Enhanced enzymatic saccharification of sorghum straw by effective delignification via combined pretreatment with alkali extraction and deep eutectic solvent soaking. *Bioresour. Technol.* **2021**, *340*, 125695. [CrossRef]
142. Lin, W.; Xing, S.; Jin, Y.; Lu, X.; Huang, C.; Yong, Q. Insight into understanding the performance of deep eutectic solvent pretreatment on improving enzymatic digestibility of bamboo residues. *Bioresour. Technol.* **2020**, *306*, 123163. [CrossRef] [PubMed]
143. Yang, L.; Zheng, T.; Huang, C.; Yao, J. Using deep eutectic solvent pretreatment for enhanced enzymatic saccharification and lignin utilization of Masson pine. *Renew. Energy* **2022**, *195*, 681–687. [CrossRef]

144. Li, C.; Huang, C.; Zhao, Y.; Zheng, C.; Su, H.; Zhang, L.; Luo, W.; Zhao, H.; Wang, S.; Huang, L.J. Effect of choline-based deep eutectic solvent pretreatment on the structure of cellulose and lignin in bagasse. *Processes* **2021**, *9*, 384. [CrossRef]
145. Wang, Y.; Zhang, W.J.; Yang, J.Y.; Li, M.F.; Peng, F.; Bian, J. Efficient fractionation of woody biomass hemicelluloses using cholinium amino acids-based deep eutectic solvents and their aqueous mixtures. *Bioresour. Technol.* **2022**, *354*, 127139. [CrossRef]
146. Yang, J.; Wang, Y.; Zhang, W.; Li, M.; Peng, F.; Bian, J. Alkaline deep eutectic solvents as novel and effective pretreatment media for hemicellulose dissociation and enzymatic hydrolysis enhancement. *Int. J. Biol. Macromol.* **2021**, *193*, 1610–1616. [CrossRef]
147. Zhang, H.; Lang, J.; Lan, P.; Yang, H.; Lu, J.; Wang, Z. Study on the dissolution mechanism of cellulose by ChCl-based deep eutectic solvents. *Materials* **2020**, *13*, 278. [CrossRef] [PubMed]
148. Wang, J.; Wang, Y.; Ma, Z.; Yan, L. Dissolution of highly molecular weight cellulose isolated from wheat straw in deep eutectic solvent of choline/L-lysine hydrochloride. *Green Energy Environ.* **2020**, *5*, 232–239. [CrossRef]
149. Chen, Y.L.; Zhang, X.; You, T.T.; Xu, F. Deep eutectic solvents (DESs) for cellulose dissolution: A mini-review. *Cellulose* **2019**, *26*, 205–213. [CrossRef]

Disclaimer/Publisher's Note: The statements, opinions and data contained in all publications are solely those of the individual author(s) and contributor(s) and not of MDPI and/or the editor(s). MDPI and/or the editor(s) disclaim responsibility for any injury to people or property resulting from any ideas, methods, instructions or products referred to in the content.

applied sciences

MDPI

Article

A Machine-Learning-Based Approach to Predict Deforestation Related to Oil Palm: Conceptual Framework and Experimental Evaluation

Tarek Sboui [1,2,*], Salwa Saidi [1,3] and Ahmed Lakti [1]

[1] Department of Geology, Faculty of Science of Tunis, University of Tunis Al-Manar, Tunis 1068, Tunisia
[2] GREEN-TEAM Laboratory, INAT, Tunis 1082, Tunisia
[3] Water, Energy and Environment Laboratory (LR3E), ENIS.Bpw 1172, Sfax 3038, Tunisia
* Correspondence: tarek.sboui@fst.utm.tn

Featured Application: This work applies machine learning to enhance the prediction of deforestation related to oil palm. This research can be used for decision makers trying to foresee and manage deforestation caused by palm oil production. Providing information about deforestation prediction can help users to make appropriate decisions about where and when they can establish new plantations to ensure a sustainable oil palm production.

Abstract: Deforestation is recognized as an issue that has negative effects on the ecosystem. Predicting deforestation and defining the causes of deforestation is an important process that could help monitor and prevent deforestation. Deforestation prediction has been boosted by recent advances in geospatial technologies and applications, especially remote sensing technologies and machine learning techniques. This paper highlights the issue of predicting deforestation related to oil palm, which has not been focused on in existing research studies. The paper proposes an approach that aims to enhance the prediction of deforestation related to oil palm plantations and palm oil production. The proposed approach is based on a conceptual framework and an assessment of a set of criteria related to such deforestation. The criteria are assessed and validated based on a sensitivity analysis. The framework is based on machine learning and image processing techniques. It consists of three main steps, which are data preparation, model training, and validation. The framework is implemented in a case study in the Aceh province of Indonesia to show the feasibility of our proposed approach in predicting deforestation related to oil palm. The implementation of the proposed approach shows an acceptable accuracy for predicting deforestation.

Keywords: machine learning; deforestation prediction; accuracy; criteria assessment; image processing

Citation: Sboui, T.; Saidi, S.; Lakti, A. A Machine-Learning-Based Approach to Predict Deforestation Related to Oil Palm: Conceptual Framework and Experimental Evaluation. *Appl. Sci.* **2023**, *13*, 1772. https://doi.org/10.3390/app13031772

Academic Editors: Dibyendu Sarkar, Rupali Datta, Prafulla Kumar Sahoo and Mohammad Mahmudur Rahman

Received: 5 November 2022
Revised: 25 November 2022
Accepted: 25 November 2022
Published: 30 January 2023

Copyright: © 2023 by the authors. Licensee MDPI, Basel, Switzerland. This article is an open access article distributed under the terms and conditions of the Creative Commons Attribution (CC BY) license (https://creativecommons.org/licenses/by/4.0/).

1. Introduction

Deforestation is the loss of tree cover over a given time period, usually as a result of forests being cleared for other land uses, such as farming or ranching [1]. Over the past years, there has been a large amount of deforestation, which has affected the ecosystem. Deforestation is recognized as an issue that has negative effects in the ecosystem. There are many cases where people deforested areas without following rules and regulations [2]. Between 2015 and 2020, the rate of deforestation was estimated to be 10 million hectares per year [3]. Deforestation is caused by human and natural factors. Natural factors include forest fires and forest tree diseases. On the other hand, human activities are among the main causes of global deforestation. In fact, deforestation usually occurs when forests are cleared for human use, such as creating new houses and establishing new plantations. According to the Food and Agriculture Organization (FAO), the expansion of agricultural areas has caused nearly 80% of global deforestation. The remaining causes of deforestation

are diverse, including the construction of infrastructures, such as roads or dams, and mining activities and urbanization [4].

Due to the accelerated deforestation in the last decades, and considering the importance of forest and its impact on the global environment, deforestation needs to be analyzed and compensated in order to reduce its negative effects on the ecosystem and to promote sustainable development [5].

One of the aspects of deforestation is the production process of palm oil, which is an edible vegetable oil that comes from the fruit of oil palm trees [6]. Palm oil production can lead to the clearing of new land to create more space for plantations or to establish new plantations. One major issue is that palm oil production is not easy to oversee, as large areas are cultivated by smallholders. Nongovernmental institutions, such as the Roundtable on Sustainable Palm Oil (RSPO), are trying to tackle these problems and aim to ensure a sustainable palm oil production [7].

In addition, we have witnessed a growing availability of multisource forest data due to new remote sensing methods and techniques [8]. Several studies have demonstrated the usefulness of remote sensing images as an information source for forest management [9,10].

Forest satellite images have been processed using machine learning (ML) techniques [11–13]. Machine learning is a form of artificial intelligence, in which a computer is algorithmically trained to perform a task, such as event prediction or image classification [14,15]. The advantages of machine learning include flexibility and scalability compared with traditional statistical techniques, which makes it deployable for many tasks, such as phenomena stratification/clustering, classification, and predictions. Another advantage of machine learning algorithms is the ability to analyze diverse data types (e.g., geospatial data and descriptive data) and incorporate them into predictions [16]. Recent works show that machine learning techniques have proved to be an effective solution to detect deforestation [17–19].

While several works have shown promising results in detecting deforestation related to oil palm, there has been no research study that focuses on the prediction aspect of deforestation related to oil palm (i.e., oil palm plantations and palm oil production).

Additionally, with regard to the application of machine learning in preventing deforestation, existing works have not assessed the criteria considered in model training. Consequently, there is still uncertainty about the effect of each criterion in the deforestation prediction.

This research study focuses on the prediction aspect of deforestation related to oil palm. It aims to reduce uncertainty about the effect of each criterion by evaluating the influence of each criterion in the prediction of oil palm deforestation.

The main contribution of our approach relies on focusing on the prediction of deforestation related to oil palm. We developed a deforestation prediction model that can serve as useful information for decision makers trying to map and monitor deforestation caused by oil palm plantations and palm oil production.

Another contribution of our work is the evaluation of the effect of each criterion in predicting deforestation related to oil palm. Such evaluation would enhance the performance of model training by focusing on a small set of criteria (i.e., the most important criteria). Multicriteria evaluation is based on a sensitivity analysis that relies on changing only one criterion at a time while keeping the others constant.

The novelty of this study relies on the combination of different aspects: the prediction, the sensitivity analysis, and the use of machine learning in order to enhance the accuracy of the model results.

In the next section, we review some proposed approaches to detect deforestation based on machine learning. In Section 3, we present our proposed approach to enhance the prediction of deforestation related to oil palm. Our approach consists of a set of criteria for detecting deforestation and a framework based on machine learning that aims to detect deforestation. Sensitivity analysis is used to validate weights of criteria. In Section 4, we present a prototype developed to implement our approach. In Section 5, we conclude the study and present some perspectives for future study.

2. Related Works

The feasibility of machine learning approaches has been demonstrated in applications, such as earth observation [20], detecting changes on the earth's surface [21], and fire management [22].

Several studies have used machine learning for forest management and deforestation [23]. Studies have focused on various applications, including estimation of forest biophysical properties based on decoders and encoders [24,25], plant pattern identification and classification [26–32], semantic segmentation [33], and assessment of the sustainability of forest management [9,10,34]. Additionally, machine learning studies have been carried out on the interpretation and extraction of forest features [35–38].

With regard to deforestation, which is the general scope of this paper, machine learning approaches can be classified into two categories: approaches detecting the location of areas at risk of deforestation and approaches analyzing the variables that drive deforestation [39]. Chang et al. [40] proposed a machine learning model to enhance the estimates of forest land cover type and forest structural metrics. It is a multitask model that performs both classification and regression concurrently, thereby consolidating several independent tasks and models into one stream. Maeda et al. [41] applied a machine learning model to detect land use changes in the Amazon. Based on change interpretation, they could identify areas with high risk of being burned and improve current fire scar mapping by enabling the distinction between fires in primary forests and fires in previously burned areas. Kehl et al. [42] proposed a study to detect daily deforestation in the Amazon rainforest. They developed an approach to train machine learning models on satellite images, and conducted a spectrum temporal analysis of the deforestation area. The approach aided in understanding the dynamics of the deforestation in the Amazon rainforest. Rosa et al. proposed a spatially explicit model of deforestation in order to predict the potential magnitude and spatial pattern of Amazon deforestation. The model was validated and identified spatial areas of deforestation that accumulates over time [43]. Ye et al. developed a spatially explicit model for detecting Australia's forest cover change using long short-term memory (LSTM) deep learning neural networks. The model was applied to a multidimensional spatiotemporal dataset. The results showed that the model is reliable for projecting forest cover and agricultural production [44].

With regard to palm oil, some studies have focused on the detection of oil palm plantations based on satellite imagery. Li et al. used the texture of trees to train machine learning models in order to distinguish oil palm from high-resolution remote sensing images of Malaysian forests. The implementation results showed that most of the oil palm trees were correctly detected [45,46].

Cheng et al. used a support vector machine (SVM) classifier and a Mahalanobis distance (MD) classifier to undertake supervised classifications of oil palm plantations. They used Landsat, PALSAR, and combined Landsat and PALSAR data for two locations in peninsular Malaysia. Results indicate that accuracies from combined Landsat and PALSAR are better than accuracies from Landsat or PALSAR alone for both study areas using both classifiers [47]. Xu et al. [48] proposed a method to improve the accuracy of detecting and classifying oil palm types (e.g., mature or young). They used the random forest algorithm based on improved grid search optimization (IGSO-RF) in order to establish a classification model and detect oil palm plantations. The results showed that the proposed method improved the detection accuracy of oil palm plantation.

While the aforementioned machine-learning-based works showed promising results in detecting deforestation and in identifying the extent of oil palm areas, some challenges still need to be addressed, including the inadequate samples of imagery and the limitation of the number of parameters considered in the training model. Additionally, existing works have not focused on predicting deforestation caused by palm oil production and oil palm plantation.

In this work, we focus on predicting deforestation related to oil palm. We aim to enhance the accuracy of the prediction based on machine learning. For that, we propose

an approach that enriches the existing commonly used parameters for machine learning. Additionally, we perform sensitivity analysis to assess the effect of each parameter affecting oil palm deforestation.

The particularity of our approach lies in the prediction of deforestation related to palm oil. The developed prediction can serve as a useful document for decision makers trying to foresee and manage palm oil deforestation. Another particularity of our work is the validation of the machine training via sensitivity analysis by changing only one parameter at a time while the others remain constant. This can reveal the importance of each criterion and its effect on the deforestation related to oil palm. The sensitivity method has been used in various works [49–52].

The proposed approach is based on a conceptual framework and the assessment of a set of criteria related to deforestation. The conceptual framework consists of a set of processes that aims to predict oil palm deforestation.

3. Conceptual Framework for Predicting Oil Palm Deforestation

This section proposes a conceptual framework to predict deforestation related to palm oil. The framework involves several processes that should be implemented to detect deforestation: data preparation, creating daily alerts, identifying and assessing criteria, and model training and validation. The processes are shown in Figure 1 below.

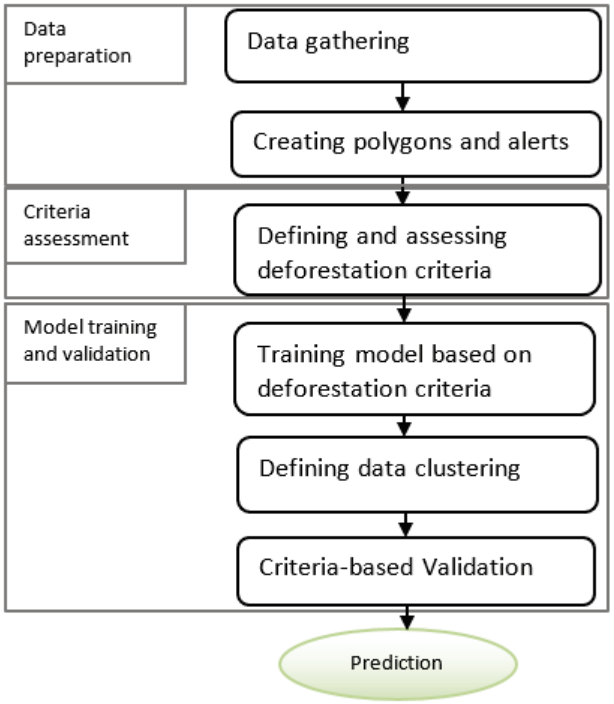


Figure 1. Proposed conceptual framework for deforestation prediction.

3.1. Data Preparation

We start by preparing data, which is one of the most time-consuming phases in the process of detecting deforestation. Data preparation includes remote sensing image gathering, creating alerts such as polygons, and attaching alerts to polygons.

Creating Daily Polygons and Alerts

In order to identify global deforestation areas, we transform satellite images into daily events that are represented by polygons on the map. Each polygon contains the date of the deforestation detection. Then, we cluster the daily polygons (i.e., patches) based on time and distance. Two or more polygons are merged together if they have the same deforestation day and they are directly adjacent. The clusters are defined based on

thresholds of time and distance. The thresholds are determined based on heuristics learned through past experience of deforestation. We create and attach an alert to each cluster. The creation of an alert on the map aims to make users aware of the deforestation area related to palm oil.

3.2. Identifying and Assessing Criteria

In order to interpret deforestation related to oil palm, we defined a set of criteria: distance to oil palm, (min, max, mean), distance to mills (nearest mills' distance), distance to roads, distance to water, distance to oil palm concessions, related alerts, number of patches, distance between patches (mean distance between patches inside the alert), and alert duration, as shown in Figure 2.

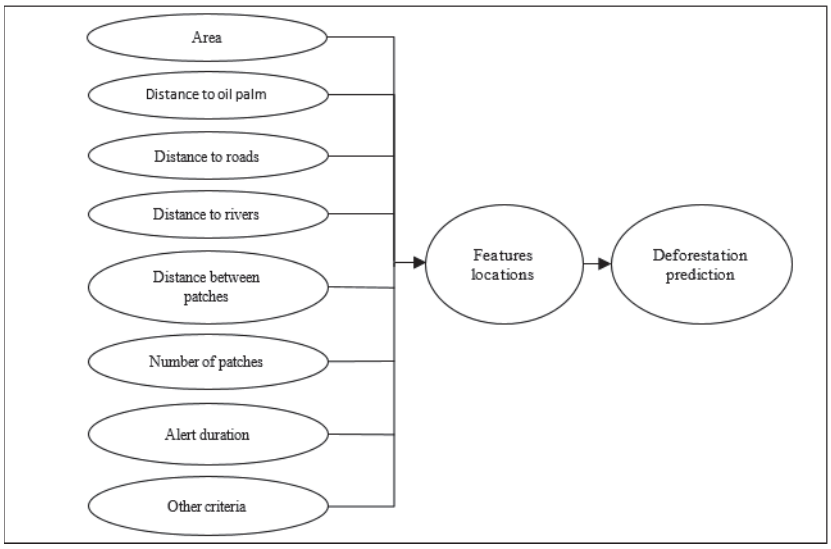


Figure 2. Defined criteria for predicting deforestation related to oil palm.

As for the perimeter, area, slope, and elevation criteria, they have been used in several studies. We will not discuss them in detail as they are widely covered in previous studies [53,54]. Figure 2 shows a set of criteria used to interpret deforestation related to oil palm.

1. Area: This criterion helps us to determine if a given deforestation area is related or not to oil palm, as it is likely for farmers to cut a minimum of 0.5 hectare to establish new oil palm plantations.
2. Distance to oil palm: We defined this criterion to determine how far oil palm plantations are from the deforestation events. The general idea is that it is more likely for farmers to use the deforested patches for plantations that are close to their already-existing plantations.
3. Distance to mills and roads: This criterion is used to determine how far the deforestation event is from the nearest mill or road. In fact, it is likely for farmers to make roads inside their plantations to help them collect oil palm easier and faster as such palm needs to arrive fresh in the mill (generally before 24 h from harvesting).
4. Distance to water: This criterion indicates that it is likely for farmers to use the deforested patches close to water for planting oil palm trees. This is the case especially for smallholders as oil palm requires a lot of water for irrigation, especially in the dry season [55]. In addition, making water pipelines for irrigation is very expensive.
5. Number of patches: The number of deforestation patches inside a given area should be assessed in order to control palm oil deforestation. This number should not exceed a certain limit.

6. Distance between patches: This criterion indicates that it is more likely for deforested patches close to each other in a given area to turn into oil palm plantations.
7. Alert duration: This criterion calculates the duration of the alert in days between the start date and the end date of the detection.

Criteria are characterized by rates that reflect their spatial variability and weights expressing their influence on deforestation.

We should notice that this restricted set of criteria assessments does not aim to be complete. A restricted set could allow us to predict deforestation related to palm oil. Future implementations should include other criteria, such as plantations for other crops, logging, and urbanization.

3.3. Training and Validation

Training and validation data aim to predict new data. We train the model to predict whether or not recent deforestation is caused by oil palm plantations.

We used sensitivity analysis via multiple iterations with different subdatasets to identify the best possible combinations of criteria with their corresponding thresholds.

The following section describes the implementation of the aforementioned processes of the conceptual framework, and presents the implementation results.

4. Implementation and Results

In order to show how our proposed framework works, we gathered images from the Sentinel satellites of the European Space Agency (ESA) and the Landsat satellites from NASA. Then, we transformed these images into useful information that can be used to predict deforestation. This transformation includes atmospheric correction and cloud masking.

4.1. Study Area

The area that was chosen for implementing our proposed framework is the state of Aceh, located in the north of Sumatra (Indonesia). The study area is depicted in Figure 3, which shows the state of Aceh, which is known for severe deforestation and a high oil palm plantation density and a lot of oil palm concessions. Indonesia was known to have the highest deforestation rate in the world.

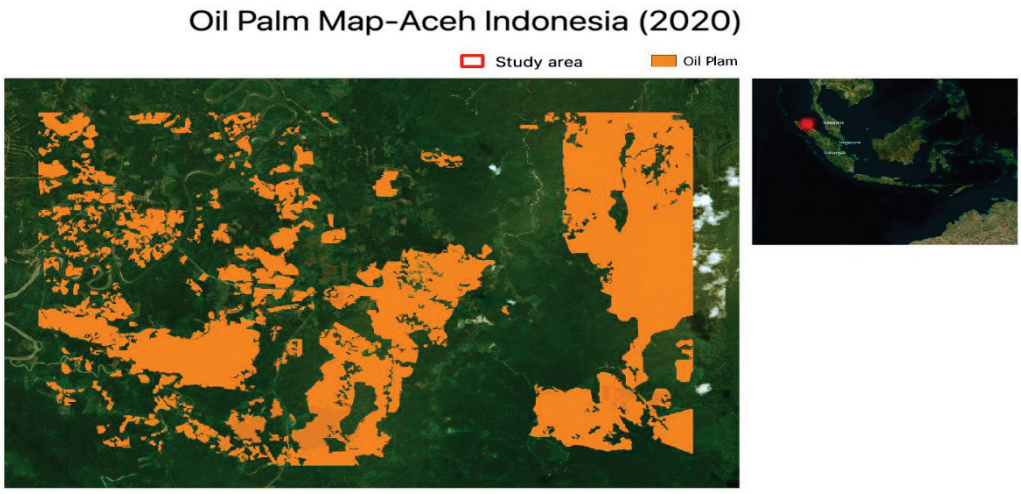


Figure 3. Study area: the state of Aceh in Indonesia.

We gathered data related to deforestation events between 1988 and 2020, a land cover map, Sentinel-1 Google Earth and Bing aerial imagery, maps of yearly distances to oil palm plantations from 1988 to 2020, a list of oil palm concessions, and a list of roads.

We used the well-known normalized difference vegetation index (NDVI) to define deforested areas. The NDVI is an indicator of vegetation health, because degradation of

ecosystem vegetation, or a decrease in green, would be reflected in a decrease in NDVI value. The decrease in NDVI values may indicate a degradation of vegetation cover (i.e., deforestation) [56].

We obtained a raster map where each pixel depicts the day and year of deforestation. The darker pixels represent more recent deforestation events, while the brighter pixels depict less recent deforestation events. The resulting raster map can be seen in Figure 4.



Figure 4. Deforestation of North Sumatra, Indonesia, 1988–2021.

The map above shows the deforestation dates pixel by pixel, which were then grouped together if they are directly adjacent or they have the same day of deforestation.

We then created a deforestation and water map by extracting oil palm and water pixels from the land cover map. Water and oil palm features can be seen in Figure 5. We implemented the extraction process using numpy and rasterio Python libraries. Python libraries are very useful for carrying out image processing to extract or enhance information useful for mapping purposes.

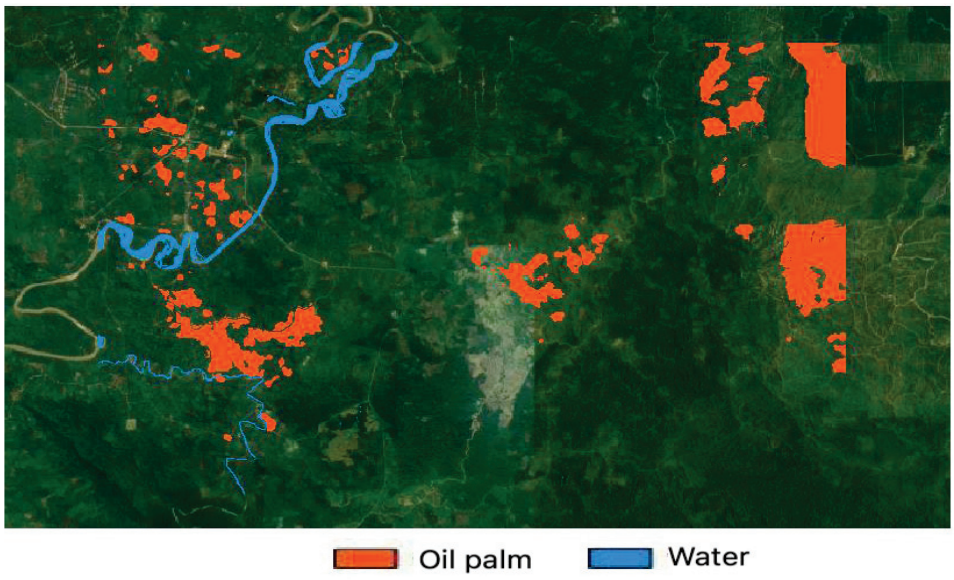


Figure 5. Map of oil palm and water grabbed from the classification map.

4.2. Creation of Daily Polygons and Alerts

We create daily polygons, which consist of transforming the deforestation map from raster into vector (polygons). Figure 6 shows the obtained polygons that represent defor-

estation. This transformation allows us to define each deforestation patch as a polygon instead of pixels. The reason for the vectorization (transforming raster to vector) is to use the area that each deforestation patch occupies as an independent feature that can be easily described by a set of attributes. Based on polygon features, we can clearly define the boundary of the deforestation patch. To create daily polygons, we developed a Python using rasterio, shapely, and geopandas libraries.

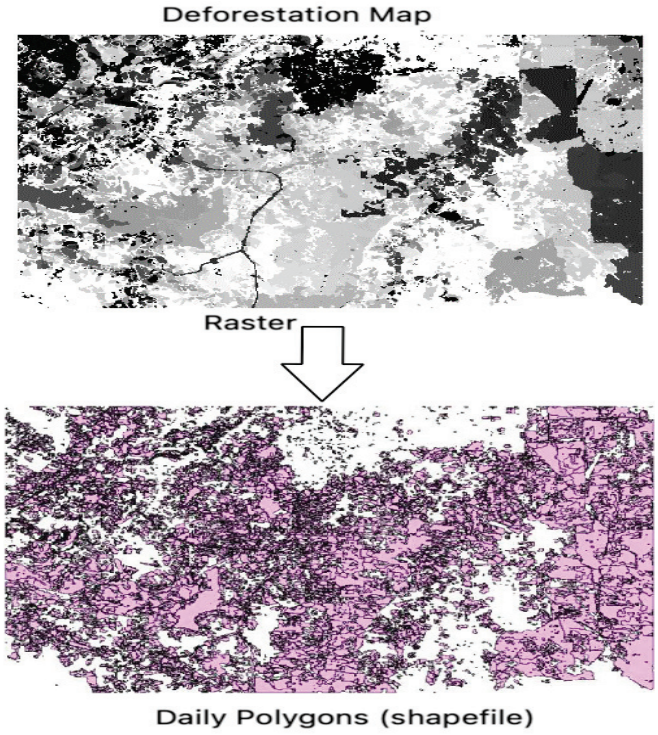


Figure 6. Creating daily polygons.

We then create alerts by clustering daily polygons based on time and distance. Alerts are basically multipolygons; polygons are grouped together if they are within 45 days and the distances between patches are not more than 250 m. We set the threshold as 45 days for the time and 250 m for the distance based on heuristic analysis. Alerts and polygons are shown in Figure 7. The highlighted polygon on the left image depicts a daily polygon detected on 7 July 2010, while the highlighted multipolygon on the right side depicts an alert (multipolygon) from 7 to 25 July 2010.

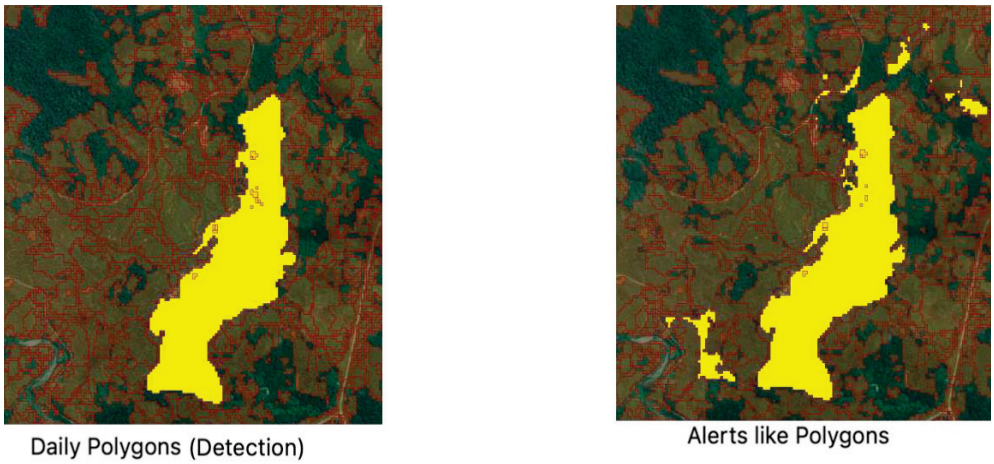


Figure 7. Daily Polygons (**left**) and Alerts (**right**).

4.3. Implementation of Criteria Assessment

We developed a Python program that calculates areas and yearly distances criteria (distance to oil palm, distance to roads, and distance to water) based on the information extracted from a deforestation oil palm map. We used Python as it is an excellent language for implementing data analysis [26,57,58].

The area and perimeter are calculated using the area and length methods of the geopandas library. With regard to distance between patches, it is calculated based on their mean distance inside the same alert.

In order to assess the distance criteria, we defined a set of assessment methods, which are:

- all;
- only_mean;
- only_max;
- only_min.

We calculated the yearly distances for each year between 1988 and 2020.

Table 1 represents assessment methods used to evaluate the distance criteria.

Table 1. Assessment methods for the evaluation of distance criteria.

Distance to Oil Palm	**Distance to River**	**Distance to Road**
distance_op_mean	distance_rivers_mean	distance_road_mean
distance_op_min	distance_rivers_min	distance_road_min
distance_op_max	distance_rivers_max	distance_road_max
Distance to Vector		
distance_concession		
distance_between_patches		

The model will be trained based on all these assessment methods; then the best method will be selected, the one that leads to the best prediction accuracy.

4.4. Training and Validation

4.4.1. Model Training

The model is trained using the random forest model, which has been very successful as a general-purpose classification and regression method. We chose the random forest algorithm as it can handle vast amounts of data, is less prone to overfitting, and can be analyzed with less time complexity [59].

For the model to be effectively trained, we need to define thresholds for image classification and feature detection [60,61]. In our case study, the land cover threshold has been defined based on heuristic experiences. In this study case, the threshold is defined for both the oil palm area and the distance between patches. For the area, if the alert contains 30% oil palm and contains at least 1 ha oil palm, then it could be considered deforestation related to oil palm, or else it will be considered deforestation related to other drivers. With regard to the distance between patches, only patches within distance mean superior or equal to 300 m will be clustered together. Figure 8 shows an example of an alert represented on the raster map.

4.4.2. Enhancing Accuracy

In order to enhance the optimum structure of the model and its accuracy, we perform hyperparameter tuning. Performing hyperparameter tuning can minimize loss function and give good results in the classification. For instance, Soomro et al. defined hyperparameters for three machine learning models (ANN, SVM, and KNN) to enhance the result of predicting the performance of the stratified thermal energy storage tank [62].



Figure 8. Alert inside the oil palm plantation.

We used hyperparameter tuning to identify the best-fitting parameters among the ones given to the model. Therefore, to determine the best-fitting parameter, we define parameters and their corresponding ranges. Our model tuning is based on 35 samplings of hyperparameter values. Table 2 shows the range of the parameters given to the model.

Table 2. Parameters and ranges used in hyperparameter tuning.

Parameter	Range	Explanation
max_depth	10–100, None	Maximum depth in each decision tree
n_estimators	10–1000	Number of trees
min_samples_split	10^{-5}–5×10^{-1}	Minimum samples in each node before the node is split (fraction)
min_samples_leaf	10^{-5}–5×10^{-1}	Minimum number of data points in a leaf node (fraction)
max_features	auto, sqrt	Maximum number of features considered when splitting a node
bootstrap	true, false	Random set of data for each tree

This tuning was performed with the 'mean' dataset. The highest accurate model is performed with a threshold for oil palm $\geq$30% and palm oil area $\geq$1 ha.

4.4.3. Sensitivity Analysis

In order to select parameters and define an order of importance for these parameters, we study the impact of each parameter on the accuracy of the model. For that, we fix all parameters except one; then we train multiple models with different values of that parameter. The higher is the magnitude of change in input parameter sensitivity, the higher is the importance of the parameter. Sensitivity analysis is a popular feature selection approach employed to identify the important features in a dataset. In sensitivity analysis, each input parameter is selected one at a time, and the response of the machine learning model is examined to determine the parameter's importance rank. Similar methods have been used to determine the optimum weights of parameters for the training model [52,63,64].

Figure 9 shows the model accuracy obtained when changing only one parameter at a time while keeping the others constant.

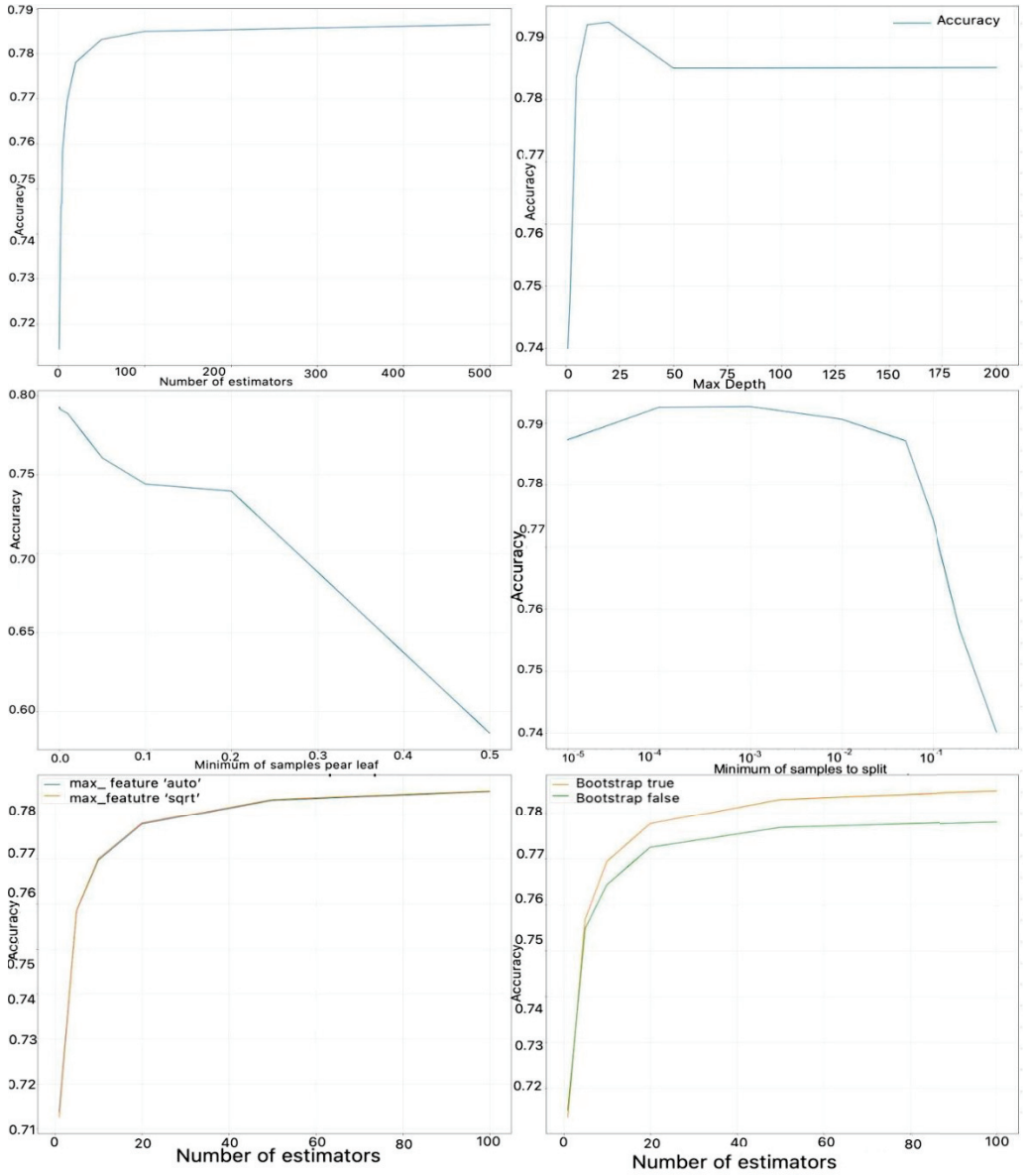


Figure 9. Changing one parameter while keeping the others fixed.

We also deal with the change of the clustering period and its impacts on the precision of the model. Therefore, to check whether the clustering period changes the precision of the model or not, three different dates with the same criterion were made as tests to check: 14, 45, and 140 days.

The graph represented in Figure 10 shows that the worst accuracy was in clustering patches within 45 days. The clustering within 140 days is quite good, but the best one is clustering within 14 days, where the less clustering period, the less avoiding multidrivers.

The best model was achieved based on the 'all' assessment method (see Section 4.3) with an accuracy of 82% in total area. This was performed with the following parameters:

- max_depth = 10;
- n_estimators = 100;
- min_samples_split = 10^{-4};
- min_samples_leaf = 10^{-5};
- max_features = 'auto';
- bootstrap = true;
- clustered within 14 days.

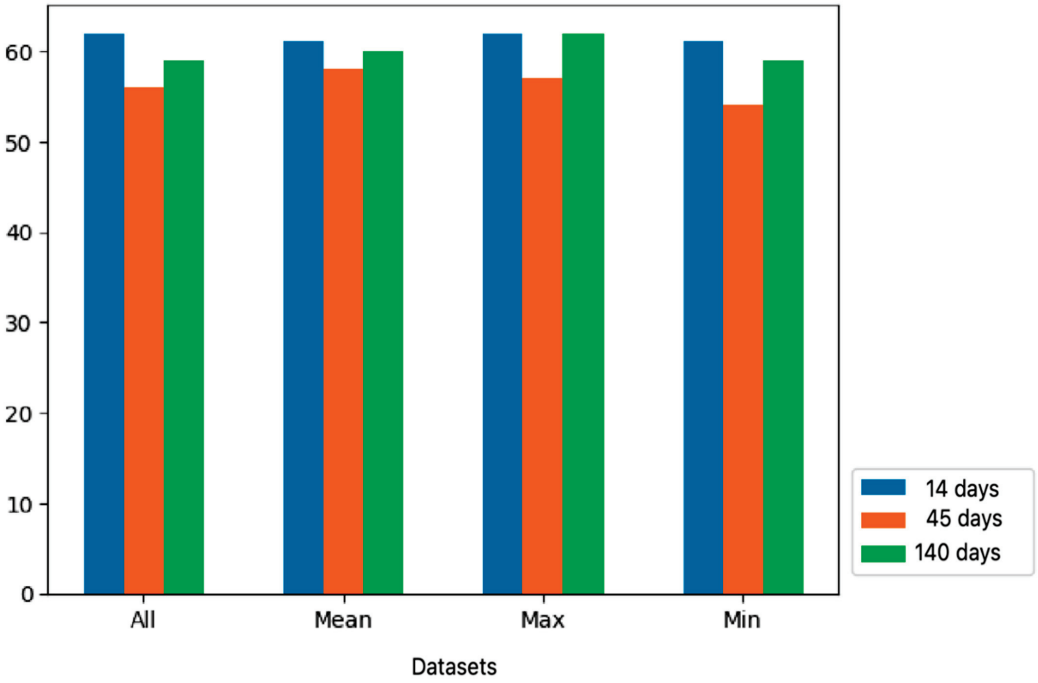


Figure 10. Accuracy vs. clustering thresholds.

When you consider the percentage and the area of the palm, the entire dataset reveals a lot of correlation between its criteria and the threshold of 0. The second-best dataset is with a threshold value of 30% and this for percentage and palm area >=1 ha.

Table 3 show the results of our training model for deforestation prediction.

Table 3. Results of our training model for deforestation prediction.

	Precision	Recall	F1 Score
1 (other)	0.97	0.98	0.97
0 (oil palm)	0.72	0.66	0.69
accuracy			0.95
macro avg	0.84	0.82	0.83
weighted avg	0.95	0.95	0.95

We measure the performance of our prediction model based on the F1 score (aka F-measure), which is a popular metric for evaluating the performance of a classification model. The F1 score calculation results in a set of different average scores (macro and weighted) in the classification report.

The model showed an accuracy of 0.82 of deforestation. It also indicates an F1 score of 0.69, a precision of 0.72, a recall of 0.66 for deforestation related to oil palm, an F1 score of 0.97, a precision of 0.97, and a recall of 0.98 for deforestation related to other drivers.

Results of these tests of the sensitivity analysis and the changing of the clustering period show that the importance of a criterion is the following:

1. Area (20.2%);
2. Largest_area (19.7%);
3. Perimeter (15.7%);
4. Distance_op_min (12.5%);
5. Distance_rivers_mean (7.89%);
6. Distance_road_max (7.74%);
7. Distances_patches (5.58%);
8. Distance_concession (4.59%).

Evaluating at the average feature values and the impact on the probability of predicting the polygon as oil palm plantations or not resulted in Figure 11. The blue lines depict when the model was correct in its decision, while the red lines depict when the model was wrong in its prediction. The biggest area's alert is more likely to be used for oil palm, and of course, the perimeter is proportional to the area. That is why they both have the same orientation.

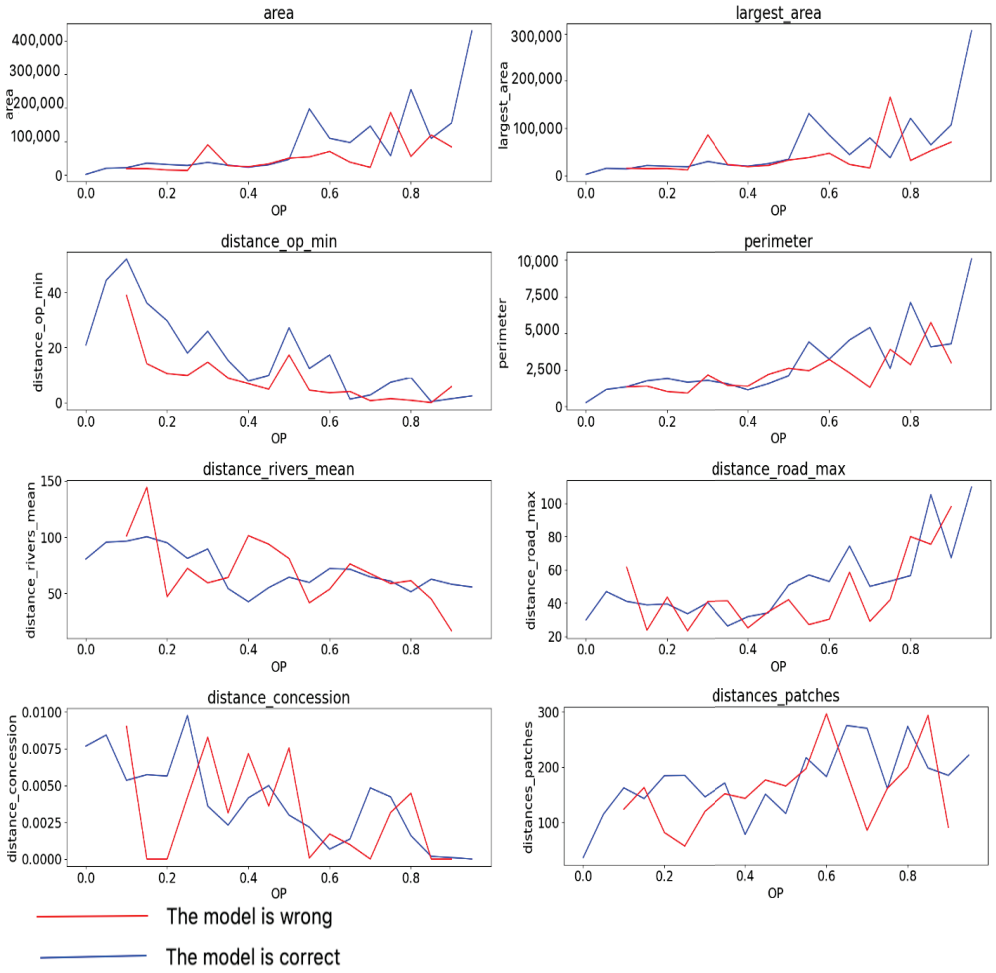


Figure 11. Average values of features versus the probability of being labeled as oil palm.

This can also be seen in the largest area metric, where the higher the value is, the more likely it will be used for oil palm plantations.

The closer the polygon is to already-existing plantations, the more likely it is used for oil palm. This can also be seen in the distance to the water. However, inversely for distance to roads, it is expected for patches that are in a way far from the principal roads (i.e., countryside) to be used for oil palm. Additionally, for sure it is predictable for alerts that are close or inside concessions to be used for oil palm.

Figure 11 depicts the average values of features versus the probability of being labeled as oil palm. The blue color indicates that the prediction of the model was correct, and the red color indicates that the prediction of the model was wrong, as shown in Figure 11.

5. Conclusions

The work presented in this paper focuses on predicting deforestation related to oil palm, an issue that has not been explored in existing research studies. The work proposes an approach that aims to enhance the prediction accuracy of deforestation related to oil palm. The approach consists of a framework for model training and a set of criteria: area,

distance to oil palm, distance to mills, distance to roads, distance to water, distance to oil palm concessions, related alerts, number of patches, and distance between patches.

The model is implemented using data about forest and oil palm plantations in the Aceh province of Indonesia, which faces one of the highest deforestations in the world.

The model implementation showed an acceptable accuracy of 0.82. It also indicates an F1 score of 0.69, a precision of 0.72, and a recall of 0.66 for deforestation related to oil palm and an F1 score of 0.97, a precision of 0.97, and a recall of 0.98 for deforestation related to other drivers.

The most important criterion is the area; then comes the proximity to oil palm plantations, the distance to water, and the distance to roads. The distance to water criterion is also significant and could help to make a distinction between oil palm and other crops.

We should note that this set of criteria assessments does not aim to be complete, but rather to allow us to predict deforestation related to palm oil. Future implementations should include other criteria, such as plantations for other crops, logging, and urbanization.

The proposed approach can support decision makers to define strategies concerning deforestation related to palm oil and the implementation of a sustainable forest. Providing information about deforestation prediction can help authorities to make appropriate decisions about where and when they can establish new plantations to ensure a sustainable oil palm. Additionally, based on the deforestation prediction, the companies of palm oil production can quickly determine which parts of their supply chain are not in line with their principles with regard to the sustainability of forests.

Although the model shows an acceptable accuracy for predicting deforestation related to oil palm, there are still some limitations.

- First, relatively large clustering periods (e.g., 14, 45, or 140 days) may affect the performance of the model as it may lead to considering several criteria at the same time.
- Second, larger datasets are needed to accurately train the model and more clearly distinguish oil palm from other plantations.

Further research using larger datasets will result in better prediction of deforestation related to oil palm. In addition, for future work, it is highly recommended to reduce the clustering period in order to avoid considering several criteria at the same time.

Author Contributions: Conceptualization, T.S.; methodology, T.S. and S.S.; software, A.L. and T.S.; validation, T.S., S.S. and A.L.; formal analysis, T.S. and S.S.; investigation, T.S. and A.L.; resources, T.S. and A.L.; data curation, A.L.; writing—original draft preparation, T.S., S.S. and A.L.; writing—review and editing, T.S. and S.S.; visualization, A.L., T.S. and S.S.; supervision, T.S.; project administration, T.S. and S.S.; funding acquisition, n/a. All authors have read and agreed to the published version of the manuscript.

Funding: This research received no external funding.

Institutional Review Board Statement: Not applicable.

Informed Consent Statement: Not applicable.

Acknowledgments: Many thanks to the stuff of Satelligence who helped with of this work. Big thanks to Rens Masselink, Loes Masselink, Michel Wolters, Berto Booijink, Vincent Schut, and Rob Verhoeven.

Conflicts of Interest: The authors declare no conflict of interest.

References

1. Gorte, R.W.; Sheikh, P.A. Deforestation and climate change. *Congr. Res. Serv.* **2010**, *7*, 57001.
2. Chitra, N.T.; Anusha, R.; Kumar, S.H.; Chandana, D.S.; Harika, C.; Kumar, V.U. Satellite Imagery for Deforestation Prediction using Deep Learning. In Proceedings of the 5th International Conference on Intelligent Computing and Control Systems (ICICCS), Madurai, India, 6–8 May 2021; pp. 522–525. [CrossRef]
3. FAO; UNEP. The State of the World's Forests 2020. In *Forests, Biodiversity and People*; FAO: Rome, Italy, 2020. [CrossRef]

4. Girase, S.D. Deforestation: Main Cause For Global Warming in Current Scenario. *EPRA Int. J. Clim. Resour. Econ. Rev. (CRER)* **2022**, *10*, 1–4.
5. Nicholson, S.E. Evolution and current state of our understanding of the role played in the climate system by land surface processes in semi-arid regions. *Glob. Planet. Chang.* **2015**, *133*, 201–222. [CrossRef]
6. Epling, H. The Palm Oil Industry—Destructive or Sustainable? Defining Sustainable Palm Oil. Bachelor's Thesis, The College of Wooster, Wooster, OH, USA, 2020.
7. Roundtable on Palm Oil. History & Milestones RSPO. Available online: https://www.rspo.org/about (accessed on 12 October 2022).
8. Kangas, A.; Astrup, R.; Breidenbach, J.; Fridman, J.; Gobakken, T.; Korhonen, K.T. Remote sensing and forest inventories in Nordic countries–roadmap for the future. *Scand. J. For. Res.* **2018**, *33*, 397–412. [CrossRef]
9. Franklin, S.E. *Remote Sensing for Sustainable Forest Management*; Lewis Publishers: Boca Raton, FL, USA, 2001; p. 407.
10. Kattenborn, T.; Leitloff, J.; Schiefer, F.; Hinz, S. Review on Convolutional Neural Networks (CNN) in vegetation remote sensing. *ISPRS J. Photogramm. Remote Sens.* **2021**, *173*, 24–49. [CrossRef]
11. Hallgren, W.; Beaumont, L.; Bowness, A.; Chambers, L.; Graham, E.; Holewa, H.; Laffan, S.; Mackey, B.; Nix, H.; Price, J.; et al. The Biodiversity and Climate Change Virtual Laboratory: Where ecology meets big data. *Environ. Model. Softw.* **2016**, *76*, 182–186. [CrossRef]
12. Jakeman, A.J.; Letcher, R.A.; Norton, J.P. Ten iterative steps in development and evaluation of environmental models. *Environ. Model. Softw.* **2006**, *5*, 602–614. [CrossRef]
13. Kelly, R.A.; Jakeman, A.J.; Barreteau, O.; Borsuk, M.E.; ElSawah, S.; Hamilton, S.H.; Henriksen, H.J.; Kuikka, S.; Maier, H.R.; Rizzoli, A.E.; et al. Selecting among five common modelling approaches for integrated environmental assessment and management. *Environ. Model. Softw.* **2013**, *47*, 159–181. [CrossRef]
14. Ciresan, D.C.; Meier, U.; Schmidhuber, J. Multi-column Deep Neural Networks for Image Classification. In Proceedings of the CVPR, Providence, RI, USA, 16–21 June 2012; pp. 3642–3649.
15. Hastie, T.; Tibshirani, R.; Friedman, J. *The Elements of Statistical Learning: Data Mining, Inference, and Prediction*; Springer: New York, NY, USA, 2009.
16. Ngiam, K.Y.; Khor, I.W. Big data and machine learning algorithms for health-care delivery. *Lancet Oncol.* **2019**, *20*, 262–273. [CrossRef]
17. Dominguez, D.; del Villar, L.D.; Pantoja, O.; González-Rodríguez, M. Forecasting Amazon Rain-Forest Deforestation Using a Hybrid Machine Learning Model. *Sustainability* **2022**, *14*, 691. [CrossRef]
18. Muller, M.; Vincent, S.; Kumar, O.P.; Vincent, S. Prediction of land-change using machine learning for the deforestation in Paraguay. *Bull. Electr. Eng. Inform.* **2020**, *9*, 1774–1782. [CrossRef]
19. Wittich, D.; Rottensteiner, F.; Voelsen, M.; Heipke, C.; Müller, S. Deep learning for the detection of early signs for forest damage based on satellite imagery. *ISPRS Ann.* **2022**, *2*, 307–315. [CrossRef]
20. Salcedo-Sanz, S.; Ghamisi, P.; Piles, M.; Werner, M.; Cuadra, L.; Moreno-Martínez, A.; IzquierdoVerdiguier, E.; Muñoz-Marí, J.; Mosavi, A.; Camps-Valls, G. Machine learning information fusion in Earth observation: A comprehensive review of methods, applications and data sources. *Inf. Fusion* **2020**, *63*, 256–272. [CrossRef]
21. Shi, W.; Zhang, M.; Zhang, R.; Chen, S.; Zhan, Z. Change detection based on artificial intelligence: State-of-the-art and challenges. *Remote Sens.* **2020**, *12*, 1688. [CrossRef]
22. Jain, P.; Coogan, S.C.P.; Subramanian, S.G.; Crowley, M.; Taylor, S.; Flannigan, M.D. A review of machine learning applications in wildfire science and management. *Environ. Rev.* **2020**, *28*, 478–505. [CrossRef]
23. Hamedianfar, A.; Mohamedou, C.; Kangas, A.; Vauhkonen, J. Deep learning for forest inventory and planning: A critical review on 410 the remote sensing approaches so far and prospects for further applications. *Forestry* **2022**, *95*, 451–465. [CrossRef]
24. García-Gutiérrez, J.; González-Ferreiro, E.; Mateos-García, D.; Riquelme-Santos, J.C. A preliminary study of the suitability of deep learning to improve LiDAR-derived biomass estimation. *Lect. Notes Comput. Sci.* **2016**, *9648*, 588–596.
25. Shao, Z.; Zhang, L.; Wang, L. Stacked sparse autoencoder modeling using the synergy of airborne LiDAR and satellite optical and SAR data to map Forest above-ground biomass. *IEEE J. Sel. Top. Appl. Earth Obs. Remote Sens.* **2017**, *10*, 5569–5582. [CrossRef]
26. Carpentier, M.; Giguere, P.; Gaudreault, J. Tree species identification from Bark Images using Convolutional Neural Networks. In Proceedings of the 2018 IEEE/RSJ International Conference on Intelligent Robots and Systems (IROS), Madrid, Spain, 1–5 October 2018. [CrossRef]
27. Ercanlı, I. Innovative deep learning artificial intelligence applications for predicting relationships between individual tree height and diameter at breast height. *For. Ecosyst.* **2020**, *7*, 12. [CrossRef]
28. Fricker, G.A.; Ventura, J.D.; Wolf, J.A.; North, M.P.; Davis, F.W.; Franklin, J. A convolutional neural network classifier identifies tree species in mixed-conifer forest from hyperspectral imagery. *Remote Sens.* **2019**, *11*, 2326. [CrossRef]
29. Guan, H.; Yu, Y.; Ji, Z.; Li, J.; Zhang, Q. Deep learning-based tree classification using mobile LiDAR data. *Remote Sens. Lett.* **2015**, *6*, 864–873. [CrossRef]
30. Mizoguchi, T.; Ishii, A.; Nakamura, H.; Inoue, T.; Takamatsu, H. Lidar-based individual tree species classification using convolutional neural network. In Proceedings of the SPIE Conference on Videometrics, Range Imaging, and Applications XIV, Munich, Germany, 25–29 June 2017; Volume 10332, pp. 193–199.

31. Zortea, M.; Nery, M.; Ruga, B.; Carvalho, L.B.; Bastos, A.C. Oil-palm tree detection in aerial images combining deep learning classifiers. In Proceedings of the IGARSS 2018—2018 IEEE International Geoscience and Remote Sensing Symposium, Valencia, Spain, 22–27 July 2018; pp. 657–660.
32. Zou, X.; Cheng, M.; Wang, C.; Xia, Y.; Li, J. Tree classification in complex forest point clouds based on deep learning. *IEEE Geosci. Remote Sens.* **2017**, *14*, 2360–2364. [CrossRef]
33. Chen, S.W.; Nardari, G.V.; Lee, E.S.; Qu, C.; Liu, X.; Romero, R.A.F.; Kumar, V. SLOAM: Semantic lidar odometry and mapping for Forest inventory. *IEEE Robot. Autom.* **2020**, *5*, 612–619. [CrossRef]
34. Zhu, X.; Tuia, D.; Mou, L.; Xia, G.-S.; Zhang, L.; Xu, F. Deep learning in remote sensing: A comprehensive review and list of resources. *IEEE Geosci. Remote Sens. Mag.* **2017**, *5*, 8–36. [CrossRef]
35. Ayrey, E.; Hayes, D.J. The use of three-dimensional convolutional neural networks to interpret LiDAR for forest inventory. *Remote Sens.* **2018**, *10*, 649. [CrossRef]
36. Contreras, J.; Denzler, J.; Sickert, S. Automatically estimating forestall characteristics in 3D point clouds using deep learning. In Proceedings of the iDiv Annual Conference, Leipzig, Germany, 29–30 August 2019; Available online: https://elib.dlr.de/133241/ (accessed on 5 November 2022).
37. Shah, S.A.A.; Manzoor, M.A.; Bais, A. Canopy height estimation at Landsat resolution using convolutional neural networks. *Mach. Learn. Knowl. Extr.* **2020**, *2*, 23–36. [CrossRef]
38. Su, C.; Wu, X.; Tang, X.; Hu, J. Growth height prediction for the trees under overhead lines based on deep learning algorithm. In Proceedings of the 2018 International Conference on Power System Technology (POWERCON), Guangzhou, China, 6–8 November 2018; pp. 3693–3699.
39. Mayfield, H.; Smith, C.; Gallagher, M.; Hockings, M. Use of freely available datasets and machine learning methods in predicting deforestation. *Environ. Model. Softw.* **2017**, *87*, 17–28. [CrossRef]
40. Chang, T.; Rasmussen, B.P.; Dickson, B.G.; Zachmann, L.J. Chimera: A multi-task recurrent convolutional neural network for forest classification and structural estimation. *Remote Sens.* **2019**, *11*, 768. [CrossRef]
41. Maeda, E.E.; Arcoverde, G.F.; Pellikka, P.K.; Shimabukuro, Y.E. Fire risk assessment in the Brazilian Amazon using Modis imagery and change vector analysis. *Appl. Geogr.* **2011**, *31*, 76–84. [CrossRef]
42. Kehl, T.N.; Todt, V.; Veronez, M.; Cazella, S. *Real Time Deforestation Detection Using ANN and Satellite Images: The Amazon Rainforest Study Case*; Springer: Berlin/Heidelberg, Germany, 2015.
43. Rosa, I.M.; Purves, D.; Souza, C., Jr.; Ewers, R.M. Predictive modelling of contagious deforestation in the Brazilian Amazon. *PLoS ONE* **2013**, *8*, e77231. [CrossRef] [PubMed]
44. Ye, L.; Gao, L.; Marcos-Martinez, R.; Mallants, D.; Bryan, B.A. Projecting Australia's forest cover dynamics and exploring influential factors using deep learning. *Environ. Model. Softw.* **2019**, *119*, 407–417. [CrossRef]
45. Li, W.; Fu, H.; Yu, L.; Cracknell, A. Deep learning based oil palm tree detection and counting for high-resolution remote sensing images. *Remote Sens.* **2017**, *9*, 22. [CrossRef]
46. Li, W.; Dong, R.; Fu, H.; Yu, L. Large-scale oil palm tree detection from high-resolution satellite images using two-stage convolutional neural networks. *Remote Sens.* **2019**, *11*, 11. [CrossRef]
47. Cheng, Y.; Yu, L.; Cracknell, A.P.; Gong, P. Oil palm mapping using Landsat and PALSAR: A case study in Malaysia. *Int. J. Remote Sens.* **2018**, *37*, 5431–5442. [CrossRef]
48. Xu, K.; Qian, J.; Hu, Z.; Duan, Z.; Chen, C.; Liu, J.; Sun, J.; Wei, S.; Xing, X. A new machine learning approach in detecting the oil palm plantations using remote sensing data. *Remote Sens.* **2021**, *13*, 236. [CrossRef]
49. Ankenbrand, M.J.; Shainberg, L.; Hock, M. Sensitivity analysis for interpretation of machine learning based segmentation models in cardiac MRI. *BMC Med. Imaging* **2021**, *21*, 27. [CrossRef] [PubMed]
50. Napolitano, P.; Fabbri, A.G. Single-parameter sensitivity analysis for aquifer vulnerability assessment using DRASTIC and SINTACS. In *Application of Geographic Information Systems in Hydrology and Water Resources Management*; Kovar, K., Nachtnebel, H.P., Eds.; IAHS Press: Wallingford, UK, 1996; Volume 235, pp. 559–566.
51. Saidi, S.; Bouri, S.; Ben Dhia, H. Sensitivity analysis in groundwater vulnerability assessment based on GIS in the Mahdia-Ksour Essaf aquifer, Tunisia: A validation study. *Hydrol. Sci. J.* **2011**, *56*, 288–304. [CrossRef]
52. Deb, P.; Pal, S.K. Interaction behavior and load sharing pattern of piled raft using nonlinear regression and LM algorithm-based artificial neural network. *Front. Struct. Civ. Eng.* **2021**, *15*, 1181–1198. [CrossRef]
53. Keshtkar, H.; Voigt, W.; Alizadeh, E. Land-cover classification and analysis of change using machine-learning classifiers and multi-temporal remote sensing imagery. *Arab. J. Geosci.* **2017**, *10*, 154. [CrossRef]
54. Park, S.; Kim, J. Landslide susceptibility mapping based on random forest and boosted regression tree models, and a comparison of their performance. *Appl. Sci.* **2019**, *9*, 942. [CrossRef]
55. Xue, J.; Su, B. Significant remote sensing vegetation indices: A review of developments and applications. *J. Sens.* **2017**, *2017*, 1353691. [CrossRef]
56. Meneses-Tovar, C.L. NDVI as indicator of degradation. *Unasylva* **2011**, *62*, 39–46.
57. Canty, M.J. *Image Analysis, Classification and Change Detection in Remote Sensing: With Algorithms for ENVI/IDL and Python*; CRC Press: Boca Raton, FL, USA, 2014.

58. Clewley, D.; Bunting, P.; Shepherd, J.; Gillingham, S.; Flood, N.; Dymond, J.; Lucas, R.; Armston, J.; Moghaddam, M. A python-based open source system for geographic object-based image analysis (GEOBIA) utilizing raster attribute tables. *Remote Sens.* **2014**, *6*, 6111–6135. [CrossRef]
59. Huang, Z.; Liu, Z. A Complex Terrain Simulation Approach Using Ensemble Learning of Random Forest Regression. *J. Indian Soc. Remote Sens.* **2022**, *50*, 2011–2023. [CrossRef]
60. Martinson, E.; Furlong, B.; Gillies, A. Training Rare Object Detection in Satellite Imagery with Synthetic GAN Images. In Proceedings of the IEEE/CVF Conference on Computer Vision and Pattern Recognition Workshops (CVPRW), Nashville, TN, USA, 19–25 June 2021; pp. 2763–2770.
61. Waldner, F.; Diakogiannis, F.I. Deep Learning on Edge: Extracting Field Boundaries from Satellite Images with a Convolutional Neural Network. *Remote Sens. Environ.* **2020**, *245*, 111741. [CrossRef]
62. Soomro, A.A.; Mokhtar, A.A.; Salilew, W.M.; Abdul Karim, Z.A.; Abbasi, A.; Lashari, N.; Jameel, S.M. Machine Learning Approach to Predict the Performance of a Stratified Thermal Energy Storage Tank at a District Cooling Plant Using Sensor Data. *Sensors* **2022**, *22*, 7687. [CrossRef]
63. Naik, D.L.; Kiran, R. A novel sensitivity-based method for feature selection. *J. Big Data* **2021**, *8*, 128. [CrossRef]
64. Rabiei, M.; Choobbasti, A.J. Innovative piled raft foundations design using artificial neural network. *Front. Struct. Civ. Eng.* **2020**, *14*, 138–146. [CrossRef]

Disclaimer/Publisher's Note: The statements, opinions and data contained in all publications are solely those of the individual author(s) and contributor(s) and not of MDPI and/or the editor(s). MDPI and/or the editor(s) disclaim responsibility for any injury to people or property resulting from any ideas, methods, instructions or products referred to in the content.

water

MDPI

Article

Experimental Evaluation of Tubular Flocculator Implemented in the Field for Drinking Water Supply: Application in the Developing World

Fernando García-Ávila [1,2,*], Angel Méndez-Heredia [1], Alex Trelles-Agurto [1], Esteban Sánchez-Cordero [3,4], Emigdio Antonio Alfaro-Paredes [5], Freddy Criollo-Illescas [1], María D. Tonon-Ordoñez [1] and Gina Heredia-Cabrera [6]

1 Carrera de Ingeniería Ambiental, Facultad de Ciencias Químicas, Universidad de Cuenca, Cuenca 010203, Ecuador
2 Grupo de Evaluación de Riesgos Ambientales en Sistemas de Producción y Servicios (RISKEN), Departamento de Química Aplicada y Sistemas de Producción, Cuenca 010203, Ecuador
3 Facultad de Ingeniería, Universidad de Cuenca, Cuenca 010203, Ecuador
4 Departamento de Ingeniería Civil, Universidad de Cuenca, Cuenca 010203, Ecuador
5 Professional School of Systems Engineering, Universidad César Vallejo, Lima 15314, Peru
6 Carrera de Medicina, Universidad Católica de Cuenca, Campus Azogues, Azogues 030102, Ecuador
* Correspondence: garcia10f@hotmail.com or fernando.garcia@ucuenca.edu.ec

Abstract: The purpose of this study was to evaluate the efficiency of a large-scale Horizontal Tubular Flocculator (HTF) as an easy-to-implement technology for potable water provision compared to the efficiency of a traditional baffle flocculator. The HTF was built with a 4-inch diameter PVC pipe and coupled to a sedimentation and filtration process. Experimental tests were performed using lengths of 68.4 m and 97.6 m for the HTF. These lengths were combined with raw water flow rates of 0.25, 0.5, 0.75, 1, and 2 L/s and five turbidity ranges <10 NTU, 10–20 NTU, 21–50 NTU, 51–100 NTU, >100 NTU, giving a total of 100 tests for one year. Jar tests were performed to determine the optimal dose of aluminum sulfate used as a coagulant. Hydraulic characteristics such as time of retention (TR) and velocity gradient (G) were evaluated; likewise, plug flow, dead volume, and short-circuit ratios were determined by tracer tests using the Wolf–Resnick model. The average results determined a removal of 98.8% of turbidity and 99.93% of color. The TR varied between 4.62 and 36.97 min and G varied between 6.15 and 109.62 s^{-1}. The results showed that HTF can be useful as a flocculation unit in a purification system.

Keywords: drinking water; enhanced flocculation; tubular flocculator; turbidity removal; rural communities

Citation: García-Ávila, F.; Méndez-Heredia, A.; Trelles-Agurto, A.; Sánchez-Cordero, E.; Alfaro-Paredes, E.A.; Criollo-Illescas, F.; Tonon-Ordoñez, M.D.; Heredia-Cabrera, G. Experimental Evaluation of Tubular Flocculator Implemented in the Field for Drinking Water Supply: Application in the Developing World. *Water* **2023**, *15*, 833. https://doi.org/10.3390/w15050833

Academic Editors: Dibyendu Sarkar, Rupali Datta, Prafulla Kumar Sahoo and Mohammad Mahmudur Rahman

Received: 12 January 2023
Revised: 3 February 2023
Accepted: 7 February 2023
Published: 21 February 2023

Copyright: © 2023 by the authors. Licensee MDPI, Basel, Switzerland. This article is an open access article distributed under the terms and conditions of the Creative Commons Attribution (CC BY) license (https://creativecommons.org/licenses/by/4.0/).

1. Introduction

The sustainable development goals were adopted by the United Nations Organization in 2015, recognizing that the sixth goal proposed was "to guarantee the availability and sustainable management of water and sanitation for all" [1]. This sixth goal reaffirmed that good quality drinking water and sanitation are essential for human development [2,3]. This right is not fulfilled on many occasions, especially in most rural communities, where they lack drinking water service, and the few communities that do have this service consume drinking water after poor treatment, which makes it difficult to use due to its unappetizing color, smell, and taste; in addition, this water puts health at risk due to the pathogens that can be found in the water [4].

The quality of raw water in places close to the catchment of water used for drinking water in rural areas has been affected by climate change [5], population growth, and the increase in anthropogenic activities, making the existing treatment systems in those sites inefficient due to the higher level of contaminants that must be removed [6]. To remove

this higher level of contaminants, it is necessary to implement conventional processes, and sometimes advanced treatments are needed [7,8]. A conventional treatment plant made up of coagulation, flocculation, sedimentation, filtration, and disinfection requires the construction of civil works [9], requiring financial resources for its implementation, which is unattainable due to the costs involved in the majority of developing communities [10,11].

However, considering that the flow in rural areas is small, the construction of conventional hydraulic baffle flocculators becomes complicated due to the small dimensions of the channel width, as well as certain conditions that the flocculator baffles must meet, causing relatively high investments of money for these communities, which, on many occasions, do not have such economic resources [12]. Mechanical flocculators are not recommended for treatment plants with small flows due to the use of electromechanical equipment and electrical energy consumption [13]. In this sense, it is necessary to investigate simple, effective, and low-cost solutions for the construction and operation of drinking water treatment plants for small flows that can be easily implemented in developing communities.

For the reasons stated in previous paragraphs, this study examined other appropriate technological options for flocculation that offer less dependence on proprietary infrastructure for water treatment in rural areas, presenting tubular flocculation as an alternative that is easy to implement within a water treatment process in a rural community.

Tubular flocculators are hydraulic flocculators that use the energy of water flow and have been used to treat wastewater, previously mixed with chemical products, promoting coagulation and flocculation [14,15]. In this respect, Boily and Butler [16] implemented a wastewater treatment system in a cheese-producing company with a horizontal flow tubular flocculator with a pipe length of 80 m with eleven 180° turns and a Reynolds number slightly above 4000, which is desirable for adequate mixing, although not too high in order to avoid breaking the formed flocs. This flocculator was connected to a sedimentation tank to remove the flocculent particles. This study determined that elevation should be taken into account along with the length of the pipe as the most critical parameters with respect to head loss within the system. This coagulation and flocculation system used aluminum sulphate as a coagulating agent.

Kurbiel et al. [17] studied the treatment of electroplating wastewater, which used a propeller mixer followed by a tubular flocculator. Two 20 m long tubular flocculators with different diameters were tested. These flocculators were made of transparent polyvinyl chloride (PVC), which allowed continuous monitoring of the experiment. Wastewater was treated with cyanide, chromium, nickel, and low concentrations of copper. The results of the experiments carried out on a pilot scale clearly indicated the good performance of the system. The reduction in turbidity and suspended solids achieved during the experiment were in the ranges of 90% to 99% and 88% to 98%, confirming the high efficiency of the system in treating electroplating wastewater. Some of the advantages of the mentioned system are less surface area and the ability to be operated without mechanical equipment; in addition, the total retention time in the flocculator can be 12 min, maintaining the total removal efficiency.

Pennock [18] developed a turbulent regime tubular flocculator with a total tube length of 56.35 m and an internal diameter of 0.93 cm and analyzed the changes in the flow direction of 180° and time of retention of 6.82 min in a laboratory-scale study. The coagulant used in this research was poly-aluminum chloride (PACl). After the suspension had flocculated, the water was passed to a settler and the turbidity of the settled effluent was used as a measure of flocculation performance. The turbidity of the water that entered the system of 150 NTU (nephelometric turbidity unit) was reduced to values that varied between 0.5 and 7 NTU at the outlet of the settler.

Oliveira and Teixeira [19] investigated the performance of the helical tubular flocculator for turbidity removal. This study used helically coiled tubes (HCT) as a coagulation–flocculation reactor coupled with a conventional decanter. Turbidity removal was analyzed to evaluate the proposed clarification system, while the hydraulic and geometric parameters in the HCT were varied. Removal efficiencies between 80% and 86.2% were obtained,

presenting better results than flocculators with baffles, which are commonly applied for purification in developing countries.

However, despite the advantages that this type of flocculators has presented in numerous industrial processes, in recent decades, no information has been presented about the application of tubular flocculators for drinking water and wastewater [20]. In previous studies, tubular flocculators have been evaluated when applied to wastewater, and other studies have been carried out at the laboratory and batch levels. There is a gap in the evaluation of tubular flocculators for drinking water at the field scale with continuous flow. Therefore, one of the objectives of the present study was to bridge the gap between laboratory tubular flocculation research and field research, contributing new knowledge in this research area and demonstrating that tubular flocculation is an alternative solution for small and medium-sized communities.

This study was carried out in a treatment plant, using raw water with turbidity that varied between 10 and 249.60 NTU with flows between 0.25 and 2 L/s, which can supply approximately 1000 people in rural areas. The velocity gradient, retention time, raw water quality, water flow, and tube length were analyzed as factors that influence the efficiency of drinking water treatment.

The results of this study made it possible to calculate the efficiency and feasibility of implementing this low-cost technology in developing communities. In addition, the results could be widely known among consultants and local government authorities, in order to be replicated in other parts of the world. The implementation of a horizontal flow tubular flocculator (HTF) made of straight PVC tubes will replace conventional concrete baffle flocculators (deflectors), avoiding the construction of civil works and reducing investment costs and physical space. Therefore, the main purpose of this study was to evaluate a tubular flocculator made of PVC in the field and its ease of implementation in treatment plants in rural communities, as well as to offer a framework for the sustainable development of the rural water supply.

2. Materials and Methods

2.1. The Description of the Location of the Study

The pilot treatment system that includes the HTF was implemented in the ¨Bayas¨ Drinking Water Treatment Plant (DWTP) using the same raw water that enters the DWTP and comparing the results of the Pilot Treatment System (PTS) with the DWTP. This DWTP belongs to a Drinking Water Board managed by people chosen from the members of the community and it is located in a rural area of the city of Azogues, Ecuador, at 2797 m above sea level, at coordinates 740,741 m E, 9,699,971 m S of zone 17 M. The temperature of the place of the execution of this research varied between 12 and 16 °C, which did not represent a high variation and, due to that reason, an analysis of the relation of the temperature with the coagulation was not realized.

The treatment plant of this community is of the conventional type with gravity operation, which includes the processes of coagulation, flocculation, sedimentation, rapid filtration, and disinfection [21]. This treatment plant uses aluminum sulphate as a coagulant, which is added at the foot of a rectangular weir used as a rapid mixer. The formation of flocs is carried out in a horizontal hydraulic flocculator and a vertical flocculator, of which the design flow is 10 L/s for each flocculator, treating a total of 20 L/s.

2.2. Design and Construction of the Pilot Treatment System

2.2.1. Rapid Mixer

The rapid mixing chamber (RMC) is the unit where the coagulant is dosed. For the experimental tests, the same RMC of the DWTP "Bayas" was used, that is, the flow rate necessary for the experimental tests in the PTS was derived from the already coagulated water (Figure 1). Therefore, it was not necessary to build an RMC for the PTS. The RMC operates through a rectangular weir, whose free flow of water allows the formation of a hydraulic jump to mix the aluminum sulphate with the raw water [22]. A channel provided

with holes was implemented to homogeneously distribute the coagulant and initiate the destabilization of the particles in the RMC. This RMC has a velocity gradient of 1700 s^{-1}, a retention time of 0.55 s, and a Froude number of 5.86, which allows it to maintain a hydraulic jump established for achieving adequate coagulation.

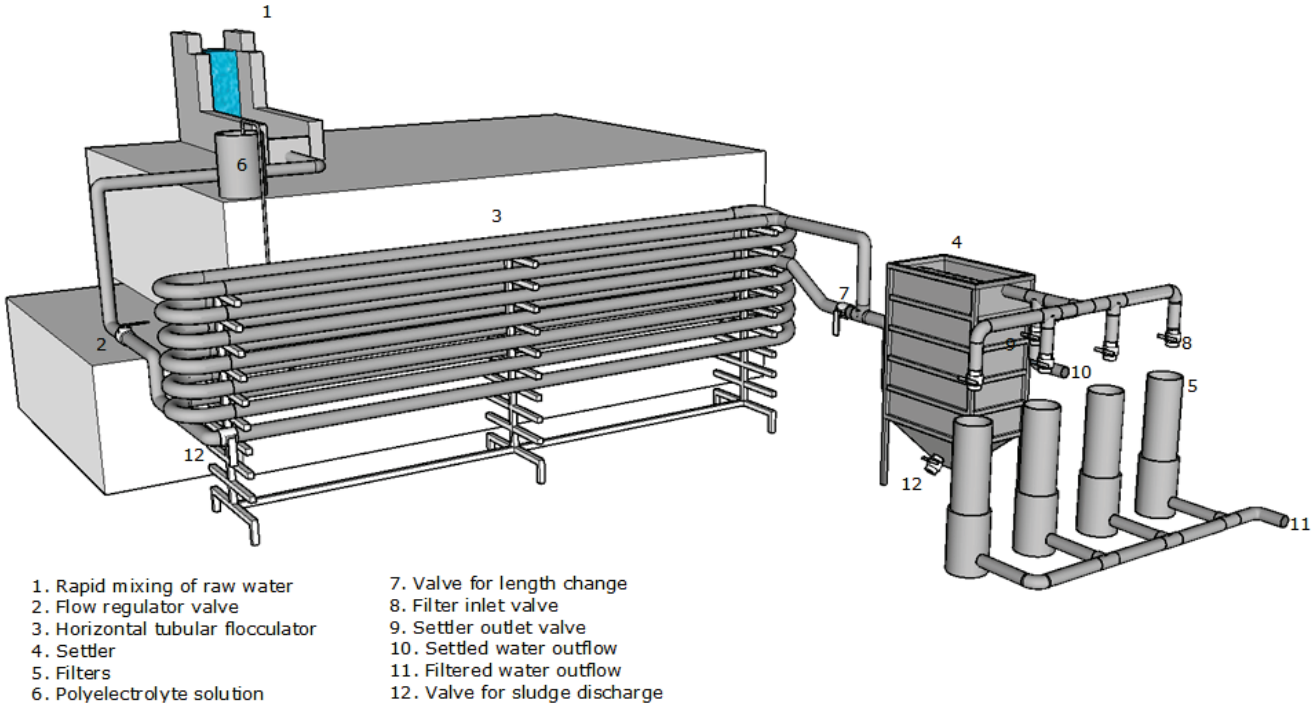


Figure 1. Pilot System that Includes HTF for the Potable Water Treatment.

2.2.2. Horizontal Flow Tubular Flocculator

Due to the fact that a methodology for the design of tubular flocculators was not found, the existing methodology for the design of hydraulic flocculators with horizontal flow deflectors of Haarhoff [12] and Romero [23] was used for a design flow rate of 1 L/s. These authors indicated that the most important parameters in the design of a horizontal flocculator with deflectors (HFD) are the following: The total length of the flocculator, the area of the channel, the velocity of the fluid, the flocculation time, and the velocity gradient. To start the design of the HTF, the flow rate (1 L/s), the speed, and the retention time were defined. Haarhoff [12] and Romero [23] recommended that the adequate retention period for an HFD must be in the range of 10 to 60 min, so a time of 12.5 min was chosen for the HTF design of this study. Romero [23] indicated that the speed in an HFD varies between 0.10 and 0.60 m/s, choosing a speed of 0.13 m/s. These values were chosen because this type of flocculator has the advantage of low retention times [17,18,24].

After having calculated the length and area of the HFD channel, these dimensions were correlated with the dimensions of PVC pipes. Thus, the calculated length of the HFD was divided by 6 to find the number of PVC pipes needed to build the HTF, due to the fact that a commercial PVC pipe is 6 m long. The channel width calculated for an HFD was conditioned to the area of a commercial PVC pipe. The configuration of the HTF was made with sections of straight pipe arranged horizontally, with each section made up of 6 m tubes, and an elbow of 180° was implemented at the end of each tube. Another straight tube was added to this elbow and was built in this way until the calculated number of tubes was completed. Figure 1 presents a schematic of the HTF.

PVC pipes of 110 mm in diameter were used; additionally, accessories were necessary such as 90° and 180° elbows, tees, and valves, thus forming a round-trip circuit. All this infrastructure was mounted on a metal shelf that served as support. Additionally, it should be indicated that pipes and fittings with elastomeric sealing of PVC were used in order to

be able to assemble and disassemble when convenient. A bypass was installed to evaluate the influence of the path length on the HTF efficiency, in such a way that the system could be operated only with a shorter length of L1 = 68.4 m and only with a longer length of L2 = 97.6 m.

2.2.3. High-Rate Settler

A high-rate settler was necessary to retain the flocculent particles formed in the HTF. The sedimentation tank was provided with honeycomb-shaped sedimentation modules made of ABS. These modules have cells inclined at 60°, with a cell gap of 5 cm, so that the water rises through the cells with laminar flow. For the design of the settler, the methodology set forth by Romero [23] and Arboleda [25] was used. The following criteria were taken into account: (a) A flow rate of 1 L/s, (b) surface load of 120 m^3/m^2d, and (c) Reynolds Number of 71. Finally, a settler 0.6 m in width, 1.20 m in length, and 1.80 m in depth was obtained. Figure 1 shows the location of the high-rate settler, which was made of galvanized brass.

2.2.4. Rapid Sand Filters

A system of four rapid filters that operated with a filtration rate of 5 $m^3/m^2/h$ was implemented to retain the particles that were not retained in the settler, and these filters were interconnected at the outlet with each other by means of valves located in the back. Individual valves located at the top of the filters were provided to evacuate the backwash water. For the design of the filters, the methodology used by Romero [23] and Arboleda [25] was used. A filter bed made up of gravel and sand was used. For the design, a filtration rate of 120 $m^3/m^2/day$ and a sand depth of 0.6 m were used. The following characteristics were chosen for the sand: (a) Effective size TE = 0.55 mm, (b) a uniformity coefficient CU = 1.60, and (c) a porosity = 0.42. With the collaboration of the "Bayas" Water Board, the filters could be implemented using PVC pipes 300 mm in diameter. Each one of the four filters was built operating with a flow rate of 0.098 L/s and producing a flow of 0.39 L/s jointly. The other 0.61 L/s was sent to the DWTP filters. Figure 1 shows the location of the rapid sand filters after the settler.

2.3. Hydraulic Evaluation of the Pilot Horizontal Tubular Flocculator

2.3.1. Calculation of the Theoretical Retention Time

Equation (1) was used to calculate the theoretical retention time (TRT or t_o) in the HTF, in which V is the volume of the flocculator and Q is the flow rate of water entering the system. The volume of the HTF was determined from the length (L) and the radius (r) of the pipe ($V = \pi r^2 L$). The TRT was calculated for the five flows used (0.25, 0.5, 0.75, 1.0, and 2.0 L/s) and for the two lengths tested (L1 = 68.4 m and L2 = 97.6 m).

$$t_o = \frac{V}{Q} \quad (1)$$

2.3.2. Determination of Mean Retention Time

The tracer technique was used through the application of instantaneous doses, using a saline substance of NaCl in solution with water to determine the mean retention time (MRT) (tm). The tracer was added at the entrance of the HTF. The measurement of total dissolved solids (TDS) was performed at the end of the HTF (before the water enters the settler). The samples were taken every minute from the addition of the tracer at the moment that a sudden change in the TDS was detected. The sampling time was reduced to 30 s. The data obtained from the tracer test permitted us to make graphs of the time vs. concentration of TDS, and the MRT was obtained from this curve. For TDS measurements, a digital dissolved solids meter was used. The methodology applied by Mastrocicco et al. [26] was followed for the application of the tracer technique. This method allowed the identification of the

hydrodynamic characteristics of HTF, for which the mean retention time was determined using Equation (2) [27].

$$t_m = \frac{\sum_{i=0}^{n} t_i \ (C_i - C_o)}{\sum_{i=0}^{n} (C_i - C_o)} \quad (2)$$

where t_m is the mean retention time, C_o is the initial concentration of the tracer substance, and C_i is the concentration in an instant t_i.

2.3.3. Hydraulic Characteristics of the HTF

Water does not flow homogeneously in a flocculator. Different types of flows can occur, such as piston flow in which the particles move perpendicularly following a certain order [28]. On the other hand, mixed flow can occur, in which the composition of the mass is the same throughout the effluent [28,29]. Likewise, there could be dead spaces, which are spaces where the fluid remains static [30]. The short circuits constituted the mass of water that comes out at t = 0. The efficiency of the system increases while the piston flow increases [30,31]. The simplified Wolf–Resnick model was applied to identify the hydrodynamic characteristics of the HTF. This method provided information to determine the percentage values of piston flow (PF), mixed flow (MF), and dead zones; when there are no dead spaces, it is considered that the sum of the PF and MF ratio is equal to the unit for any reactor (Equation (3)).

$$p + (1 - p) = 1 \quad (3)$$

where p is the piston flow; (1 − p) = non-piston flow = mixed flow

When there are dead spaces, if m is the fraction of the volume considered dead space, the fraction that does not have dead spaces will be equal to 1 − m and, for that we have Equation (4) [31].

$$p \times (1 - m) + (1 - p)\ (1 - m) + m = 1 \quad (4)$$

In most of the reactors used in treatment plants, there is a volume of water that leaves before the TRT and another after the TRT. The fraction of the volume that comes out first is called F. Wolf and Resnick [30] indicated that the function F(t) is represented by Equation (5) for real systems. The initial postulate of Wolf and Resnick was that if piston flow (p) and mixed flow (M) accompanied by dead zones (m) were present in a reactor, then Equation (5) would describe this design model.

$$F(t) = 1 - e^{-\frac{1}{(1-p)\times(1-m)}\left(\frac{t}{t_o} - p\ (1-m)\right)} \quad (5)$$

Taking logarithms on both sides and rearranging them gives Equation (6)

$$\log[1 - F(t)] = \frac{-\log(e)}{(1-p)(1-m)}\left[\frac{t}{t_o} p(1-m)\right] \quad (6)$$

This equation corresponds to a straight line whose slope is given by Equation (7).

$$\tan\ \alpha = \frac{\log(e)}{(1-p)(1-m)} \quad (7)$$

Upon multiplying and dividing p and substituting the value of log e = 0.435, Equation (8) is obtained.

$$\tan\ \alpha = \frac{0.435p}{p(1-p)(1-m)} \quad (8)$$

Considering θ = p (1 − m) in the equation and calculating p (piston flow), Equation (9) is obtained.

$$p = \frac{\theta\ \tan\ \alpha}{0.435 + \theta\ \tan\ \alpha} \quad (9)$$

The values of the unknowns θ and tan α are obtained by plotting the curve on a semilogarithmic scale [1−F(t)] on the ordinates and as a function of dimensionless time

(t/to) on the abscissas, resulting in a line that forms an angle with the horizontal, as is described in Figure 2. The values of the remaining fraction are in logarithmic form, while those of dimensionless time t/to are in arithmetic form. A tangent line is drawn at the point where the line begins to turn vertically. α is the angle between the tangent line and the horizontal and θ is the intercept of the line with the abscissa axis, obtaining Equation (9) and θ = p (1 − m) [28,31].

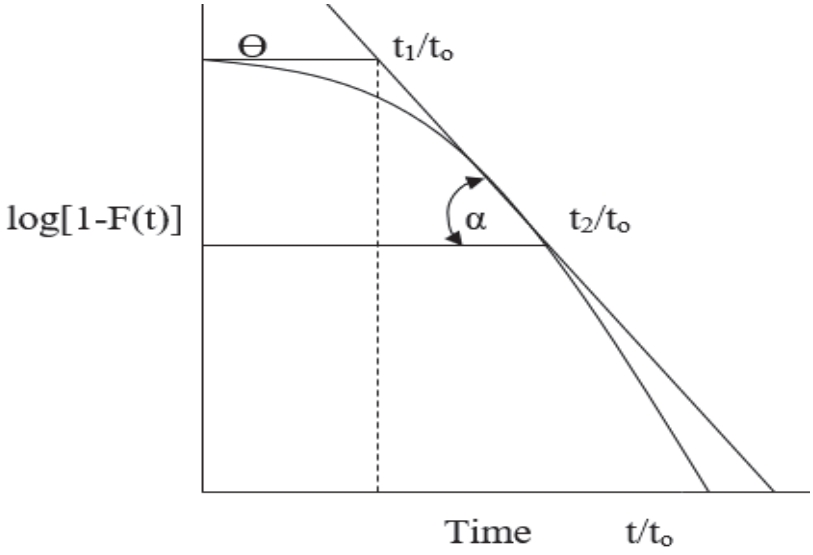


Figure 2. Curve of 1 − F(t) plotted to calculate α and θ.

The volume of dead spaces (m) will be equal to Equation (10)

$$m = 1 - \frac{\theta}{p} \tag{10}$$

and the mixed flow (M) will be equal to Equation (11).

$$M = 1 - p \tag{11}$$

The statistical program STATGRAPHICS 16.1 was used to graph the semi-logarithmic curve given by the function 1-F(t) and t/to, obtaining the equation of the straight line adjusted to the points, which permitted us to determine the values of piston flow, mixed flow, and dead zones based on Equations (9)–(11).

2.3.4. Calculation of the Velocity Gradient

According to Oliveira and Teixeira [19], the velocity gradient (G) can be calculated using Equation (12). For the calculation of G, the theoretical retention period was considered. Water properties such as density and dynamic viscosity were taken into account, considering the average water temperature measured during the experimental part.

$$G = \sqrt{\frac{\rho * g * h_f}{\mu * t}} \tag{12}$$

where G is the mean velocity gradient (s^{-1}), h_f is the head loss (m), ρ is the water density (kg/m^3), g is the gravity (m/s^2), μ is the dynamic viscosity of water (kg/m s), and t is the retention time (s).

Meng et al. [32] mentioned that the Darcy–Weisbach equation allows the calculation of head losses through pipes (Equation (13)). The hf was determined for HTF lengths of 68.4 m and 97.6 m.

$$h_f = f * \frac{L}{D} * \frac{v^2}{2g} \tag{13}$$

where f is the friction factor (dimensionless), L is the pipe length (m), D is the pipe diameter (m), and v is the average speed (m/s).

Anaya et al. [33] proposed the Chen expression for the calculation of the friction factor (f) established in Equation (14). The roughness of the 3.0×10^{-7}m PVC pipe was taken into account [34].

$$f = \frac{1}{\left(-2\log\left\{\frac{\varepsilon}{3.7065D} - \frac{5.0452}{Re}\log\left[\frac{1}{2.8257}\left(\frac{\varepsilon}{D}\right)^{1.1098} + \frac{5.8506}{Re^{0.8981}}\right]\right\}\right)^2} \tag{14}$$

where ε is the pipe roughness (m) and Re is the Reynolds number, which was calculated using Equation (15).

$$Re = \frac{\rho * D * v}{\mu} \tag{15}$$

The load loss for the accessories of the system was also taken into account. Flores et al. [35] pointed out the expression that allows one to determine h_f in Equation (16), taking into account the coefficient of kinetic load (K), which varies depending on the type of accessory.

$$hf_a = K\frac{v^2}{2g} \tag{16}$$

where hf_a is the load loss due to accessories (m) and K is the coefficient of kinetic load (dimensionless).

2.4. Experimental Analysis for Evaluating the Horizontal Tubular Flocculator

2.4.1. Pilot System Operation

For each experimental trial, in the first instance, a sample of the raw water that entered the DWTP Bayas was taken. Subsequently, the raw water sample was taken to the laboratory to determine the optimal dose of coagulant by means of the jar test.

The flow rate of the coagulant solution that had to be added to the bottom of the rectangular weir to generate the coagulation must be determined considering the raw water flow rate, optimal coagulant dose, and concentration of the coagulant solution (2%). It should be noted that rapid mixing was common for both the pilot system and the DWTP Bayas. A PVC pipe was implemented in the rapid mixer, which transported the coagulated water to the HTF. Polyelectrolyte was added to one-fifth of the length of the HTF. After the water flocculated in the HTF, the water entered the high-rate settler, and finally, the settled water moved to the rapid filters.

2.4.2. Determination of Optimal Dose of Coagulant

As mentioned above, the dose of coagulant applied to the experimental treatment system was determined by jar tests [35]. The agitation time that was applied in the jar tests was taken from the results of the tracer tests (the time was taken for a length of 97.6 m and a design flow rate of 1 L/s). Meanwhile, the velocity gradient applied in the jar test was obtained from Equation (12). The jar tests were carried out using a Phipps and Bird six-blade programmable blender (The equipment was lent by the drinking water company of the city of Azogues, EMAPAL). The dose of coagulant (aluminum sulphate) was determined for each one of the different turbidities of the raw water that was obtained during the year of experimental tests [36].

For each jar test, a known amount of coagulant was dosed after 30 s of the start of the test in order for the coagulant solution to be well distributed. This rapid mixing at 300 rpm

took 1 min to destabilize the colloidal particles. The next period was the slow mixture that took 13 min. This time was determined by the tracer test. It was maintained at 50 rpm for adequate flocculation.

2.4.3. Experimental Tests varying Lengths of the HTF, Flow Rates, and Turbidities of Raw Water

As mentioned above, two lengths of the HTF (68.4 and 97.6 m) were used for the purpose of evaluating the relationship between length and efficiency. The HTF and the high-rate settler of the pilot plant were designed for a flow rate of 1 L/s; however, different flow rates were used to compare system performance under different operating conditions. The water was fed through a PVC pipe from the DWTP rapid mix channel to the HTF.

A regulating valve located in the HTF inlet pipe allowed the calibration of different flows that entered the system. Five different flows were tested (0.25, 0.5, 0.75, 1, and 2 L/s). The flows were measured by volumetric appraisal after the regulating valve. Likewise, different turbidities of the raw water were tested with the purpose of covering both the summer and winter seasons. According to the turbidity of the raw water obtained, the experimental tests were grouped into five groups, turbidities < 10 NTU, 10–20 NTU, 21–50 NTU, 51–100 NTU, and >100 NTU. In short, we experimented with combining 2 lengths, 5 flow rates, and 5 turbidity ranges, performing 50 tests. Each test was performed in duplicate in order to obtain reliable data on the removal of the analyzed parameters. A total of 100 experimental tests were performed between January and December 2020.

2.4.4. Sampling and Parameter Analysis

Turbidity and color were established as the main parameters for determining the efficiency of HTF. A HACH model 2100 Q turbidimeter was used for measuring turbidity, a HACH model DR/890 colorimeter for color, and a HANNA pH meter for pH and temperature; the equipments belongs to the "Bayas" DWTP. The water samples were taken at three points: (1) In the rectangular weir of the “Bayas” DWTP, that is, raw water (before the dosage of coagulant); (2) at the outlet of the module pilot settler (settled water); and (3) at the outlet of the pilot sand filters (filtered water). The sampling sites can be seen in Figure 3. Two water samples were taken simultaneously in the DWTP system, two at the outlet of the DWTP module settler, and three at the outlet of the DWTP modules and the outlet of the DWTP sand filters. These two additional samples made it possible to compare the efficiency of turbidity and color removal between the pilot system that includes the HTF and the conventional DWTP that has a horizontal hydraulic screen flocculator.

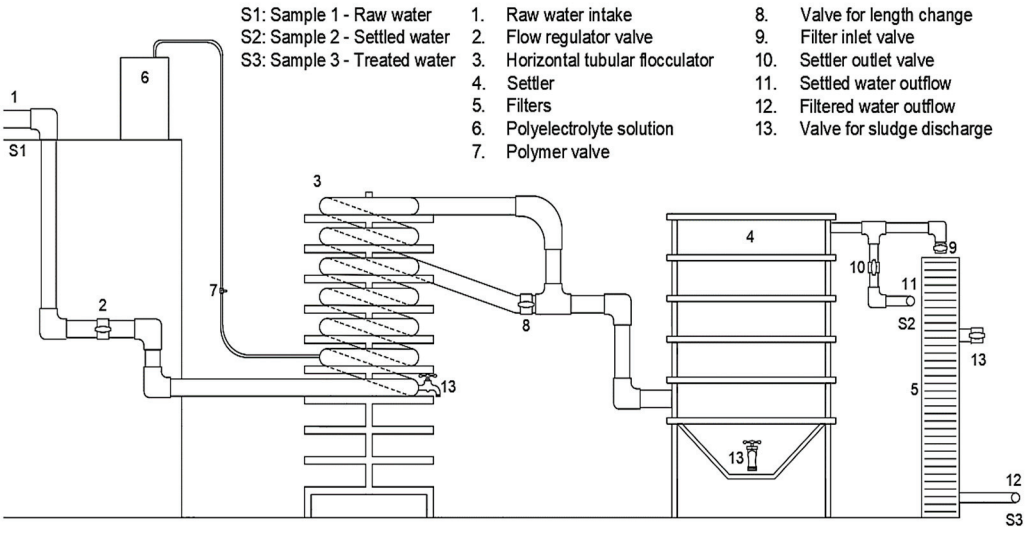


Figure 3. Location of sampling points: (a) S1 Raw water, (b) S2 settled water, and (c) S3 filtered water.

2.4.5. Removal Efficiency

Equation (17) proposed by Oliveira and Teixeira [24] allowed us to determine the percentage of turbidity and color removal from the systems. The removal efficiency (RE) of turbidity and color was calculated in each experimental test carried out, obtaining average removal values at the settler outlet and the filter outlet, both from the pilot system and the Bayas DWTP.

$$E\ (\%) = \left[1 - \left(\frac{Remanent\ Parameter}{Initial\ Parameter}\right)\right]100 \quad (17)$$

Using the values of the turbidity and color removal efficiency, a box plot was made, using the length of 68.4 m and 97.6 m of the HTF. Likewise, a box plot was made with the removal values obtained from the DWTP. These box plots permitted us to analyze the turbidity and color removal efficiency of the Bayas DWTP settler vs. the pilot settler, as well as the turbidity and color removal efficiency of the Bayas DWTP filter vs. pilot filter. The R Studio program was used for the described analysis.

2.5. Statistical Analysis

To determine if there is a significant difference between the results of the efficiency obtained when using the HTF with a length of 68.4 m and 97.6 m, the Wilcoxon statistical test was used. This non-parametric test was used because the data did not present a normal distribution [37]. A significance level (α) of 0.05 was used. The null hypothesis Ho was considered true unless there was evidence to reject this hypothesis, and this happens when $p < 0.05$ because it represents a statistically significant difference [38]. For this study, Ho was considered: "The efficiency of turbidity removal at the outlet of the settler and pilot filter does not change as the length of the HTF increases". Meanwhile, we considered the alternative hypothesis Ha: "The turbidity removal efficiency at the outlet of the settler and pilot filter changes with the increase of the HTF length". Using the Infostat program, the *p*-value was determined to reject or confirm Ho. Likewise, it was determined if there is a significant difference between the results of the efficiency of turbidity and color removal considering the different flows and turbidity of the raw water. We also determined whether there was a significant difference between the turbidity and color removal efficiency, applying the HTF of the pilot system with respect to the turbidity and color removal efficiency by applying the HFD of the Bayas DWTP.

Finally, the Stepwise regression method was used to build multiple linear regression models. With this method, partial correlation coefficients were gradually added to the model starting with the highest and most significant variable. This process continued until there were no significant relationships [39]. A Stepwise regression model was performed in a multiple linear regression analysis to estimate the efficiency of the HTF.

2.6. Construction Cost Comparison

The construction cost of a drinking water treatment plant varies according to each place or city, the proposed design, and the specific evaluation of costs for each component of the project [40]. The construction cost of a concrete HFD was compared to the construction cost of the HTF used in this study. To determine the construction cost of the conventional flocculator, Equation (18) proposed by Deb and Richards [41] was used. In order to determine the construction costs of the HTF, the costs of each of the materials used in the implementation of this flocculator were added.

$$CC = 1553\ (Q_M)^{0.45} \quad (18)$$

CC is the construction cost in USD and Q_M is the maximum daily flow in mgd.

3. Results

3.1. This Evaluation of the Theoretical Retention Time in the Tubular Flocculator

For the different flow rates tested, the theoretical retention time (TRT) or "to" was calculated (0.25, 0.5, 0.75, 1, and 2 L/s). TRT was used in the text paragraphs and "to" was used in formulas. In the first instance, it was calculated for a length of 68.4 m and then for a length of 97.6 m from the HTF. The calculated TRTs are presented in Table 1. The time difference that exists between both lengths for the same flow rate can be identified. For all flows except for the flow of 2 L/s, the calculated theoretical times would be in compliance with the minimum time required for the flocculation process, which is 10 min. It shows that this implemented pilot system would meet the TRT conditions for flows equal to or less than 1 L/s.

Table 1. Theoretical and mean retention time of HTF.

HTF Length (m)	Flow Rate (L/s)	Theoretical Retention Time (min)	Mean Retention Time (min)
68.4	0.25	36.97	32.20
	0.50	18.48	19.10
	0.75	12.32	14.33
	1.0	9.24	7.25
	2.0	4.62	4.42
97.6	0.25	52.67	52.05
	0.50	26.33	22.43
	0.75	17.56	16.11
	1.0	13.17	12.30
	2.0	6.58	5.22

3.2. Evaluation of Mean Retention Time

Once the tracer test was applied, the mean retention times (MRT) were calculated. These values can be seen in Table 1. As the operational flow decreases, the retention time in the reactor increases. For the same flow rate and length, the different theoretical retention times (TRT) and mean retention times (MRT) do not differ much. For the MRT analysis, the minimum retention time for flocculation was taken into account according to Garland et al. [42], which is between 10 and 30 min. For the length of 68.4 m, only the flows of 0.5 and 0.75 fulfilled the condition of the minimum retention time of 10 min. For the length of 68.4 m with a flow rate of 1.0 and 2.0 L/s, the minimum time of 10 min for both the MRT and the TRT is not met. For the two lengths of the HTF and the same flow rate of 2 L/s, both the MRT and TRT are less than the retention time recommended for conventional flocculators by the different authors cited by Romero [23], due to the fact that the flocculator worked with a double flow rate compared to the design flow rate in this case.

By increasing the length to 97.6 m, the minimum retention time for flocculation is met for all flows except 2 L/s. For the design flow rate (1 L/s) and the length of 97.6 m, the TRT (13.17 min) was close to the MRT (12.3 min), which, in turn, was close to the retention time used for the flocculator design (12.5 min).

Figure 4 shows the concentration curve of the tracer vs. time curve obtained in the hydrodynamic study. From this curve, the MRTs were obtained in a comparative way. The TRT was calculated by Equation (1). The results obtained are presented in Table 1. A slight decreasing "tail" can be observed after reaching the maximum concentration in Figure 4, but with a fast trend and little symmetry in the curve (more Gaussian and less exponential), which allowed the verification that the real average residence time in the system was similar to the calculated theoretical time.

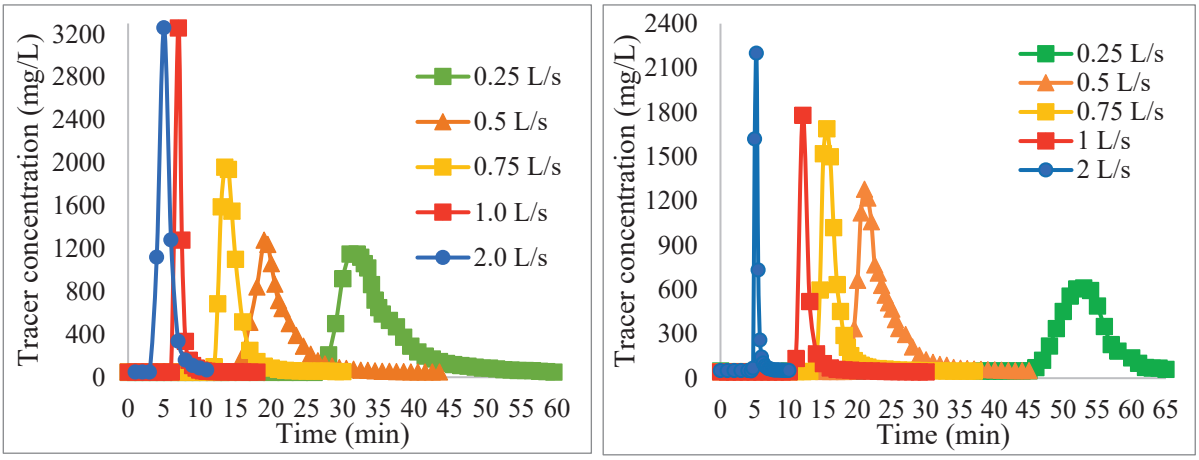


Figure 4. Tracer distribution curves in the HTF effluent.

3.3. Evaluation of the Hydraulic Behavior of the HTF by Means of the Wolf Resnick Simplified Method

Table 2 shows the percentages of piston flow, mixed flow, and dead spaces calculated for the different flows. It can be identified that the piston flow percentages are in the range of 88.5% to 94.11%. The presence of mixed flow could be attributed primarily to the 13 existing 180° turns in the system, by which the fluid goes through a mixing or turbulence process and therefore increases the percentage of mixing in the system. The piston flow values obtained by Ispilco [43] in a conventional horizontal flocculation system using the Wolf–Resnick model was 89.4% with a mixed flow of 10.6% and no dead zones, while Aguirre [44] evaluated a baffle flocculator and obtained a piston flow of 93% and mixed flow of 7%.

Table 2. Application Results of the Wolf–Resnick Model in the Tubular Flocculator.

Length (m)	Flow Rate (L/s)	Equation	R^2	%p	%M	m
HTF 68.4	0.25	log [1 − F(t)] = 8.75064 − 8.42073 (t/to)	98.33	89.74	10.26	−0.15
	0.5	log [1 − F(t)] = 10.1537 − 6.50166 (t/to)	99.00	91.03	8.97	−0.71
	0.75	log [1 − F(t)] = 11.7424 − 7.43647 (t/to)	96.08	92.15	7.85	−0.71
	1.0	log [1 − F(t)] = 12.9807 − 12.9278 (t/to)	97.45	92.85	7.15	−0.08
	2.0	log [1 − F(t)] = 7.7437 − 4.73155 (t/to)	98.86	88.56	11.44	−0.84
HTF 97.6	0.25	log [1 − F(t)] = 9.54051 − 6.08172 (t/to)	97.59	90.51	9.49	−0.73
	0.5	log [1 − F(t)] = 10.366 − 8.02142 (t/to)	98.52	91.20	8.80	−0.41
	0.75	log [1 − F(t)] = 10.8456 − 8.32531 (t/to)	95.66	91.56	8.44	−0.42
	1.0	log [1 − F(t)] = 9.05445 − 6.2873 (t/to)	92.85	90.05	9.95	−0.59
	2.0	log [1 − F(t)] = 16.1483 − 13.0555 (t/to)	92.77	94.11	5.89	−0.03

Note: p = piston flow, M = mixed flow, m = dead zones.

Analyzing the values presented in Table 2, the only value that is below the percentages found in other studies was for the flow rate of 2 L/s with a length of 68.4 m, corresponding to a piston flow of 88.5%; however, the difference is not significant. Rojas and García [45]

mentioned that the efficiency of the flocculator increases when the piston flow is closer to 100%. The percentage of dead spaces was negative, which indicates that there were no dead spaces in the system. It can be attributed to the configuration of the system, due to the fact that the piston flow does not allow the existence of these zones, having an advantage over flocculators in conventional horizontal hydraulics, in which, due to the use of rectangular screens, short circuits could occur in the system. Therefore, in the HTF, as there is a predominance of piston flow, the mean retention times were similar to the theoretical retention times, for the range of flows analyzed.

3.4. Velocity Gradient Evaluation

The results indicated a direct relationship between the hydraulic gradient (G) and the operational flow. Similarly, the G calculated with both the MRT and the TRT increased with the increase in the length of the HTF for the same flow rate; however, this increase in the gradient was not significant (Table 3).

Table 3. Theoretical velocity gradient and real velocity gradient of the HTF.

Length (m)	Flow Rate (l/s)	Theoretical Hydraulic Gradient (s^{-1})	Real Hydraulic Gradient (s^{-1})
HTF 68.4	0.25	6.15	6.59
	0.5	16.22	16.54
	0.75	29.27	27.14
	1	41.13	46.44
	2	109.62	112.09
HTF 97.6	0.25	6.21	6.24
	0.5	16.97	18.39
	0.75	29.50	30.80
	1	41.35	42.78
	2	110.13	123.67

For the flows of 0.25, 0.5, 0.75, and 1 L/s in the two lengths, the values of G were found in the ranges recommended by the various authors for conventional flocculators (Table 4). However, for the flow rate of 2 L/s in the two lengths of the HTF, the value of G calculated exceeds 100 s^{-1}, which is the maximum value recommended for conventional flocculators [23]. However, if the range suggested by Mohammed and Shakir [46] for G is taken into account, which is 10 and 75 s^{-1}, only flows of 0.5, 0.75, and 1 L/s meet the range established by these authors. After the analysis of the values of the theoretical gradients with respect to the real gradients, it can be seen that the theoretical gradients are slightly less than the real gradients at each flow rate. This situation occurs because the mathematical models indicate ideal values due to the fact that these models do not take into account the real physical and geometric conditions of a certain unit.

3.5. Evaluation of the Dose of Coagulant

3.5.1. Dosage Curve Obtained by Jar Test

Jar tests were carried out for ensuring the correct dosage of coagulant for the different turbidities of the raw water. Their results allowed the elaboration of the dosage curve in Figure 5. The applied agitation time in the jar tests was 12.3 min, taken from the results of the tracer tests (Table 1) for the design flow rate (1 L/s). Meanwhile, the velocity gradient applied in the jar test was 41 s^{-1}, obtained by applying Equation (12) for the aforementioned retention time.

Table 4. Recommended retention time ranges for conventional hydraulic flocculators.

Author	Velocity Gradient (s^{-1})	Retention Time (min)
Smethurst	20–100	10–60
Arboleda	10–100	15–20
Insfopal (horizontal flow)	-	15–60
Hardenbergh and Rodie	-	20–50
Fair and Geyer	-	10–90
AWWA	5–100	10–60

Note: Source: Romero (1999).

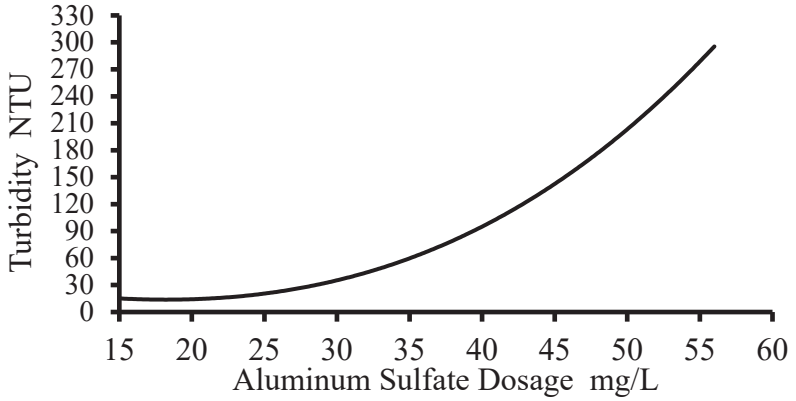


Figure 5. Coagulant dosage curve.

Once the raw water entered the rapid mixing unit, the dose of coagulant corresponding to the turbidity of the raw water (Figure 5) was applied to carry out the coagulation process. Once the water was coagulated, the corresponding flow was conducted for each one of the tests in the HTF. Applying Figure 5, the correct dosage was guaranteed for the different turbidities used.

3.5.2. Applied Doses in Field Trials

It should be emphasized that Figure 5 served as applying a starting dose, due to the fact that a visual follow-up of the floc formation that entered the settler was continuously made and the turbidities at the settler outlet were also monitored and, if necessary, the dose was adjusted until the obtention of minimum turbidity in the effluent of the settler.

The raw water turbidities (RWT) and alum doses that were used in the different flows of the HTF68.4 m in length are expressed in Figure 6a. For the 68.4 m length, the maximum recorded raw water turbidity (RWT) was 240.18 NTU with a corresponding dose of aluminum sulphate of 52.1 mg/L, applied at an operational flow rate of 0.50 L/s. The minimum RWT recorded during the tests at this length was 8.82 NTU with a dose of 19.4 mg/L of alum applied at a flow rate of 2 L/s.

Figure 6b shows the different RWTs and alum doses for the 97.4 m length of the HTF. For this length of 97.4 m, the maximum RWT recorded was 249.6 NTU, with an alum dose of 55.6 mg/L applied at a flow rate of 1 L/s, while the minimum RWT recorded was 7.93 NTU with an alum dose of 17.7 mg/L for a flow rate of 0.25 L/s. For the RWT and applied alum dose dataset, it was determined that there is no normal distribution by means of the modified Shapiro–Wilk normality test, due to the fact that $p < 0.05$ in both data series. As there was no normal distribution in these datasets, the correlation of two variables was performed using Spearman's correlation coefficient. Spearman's value for the RWT data series and alum dose in the HTF was 0.97, displaying a very strong correlation.

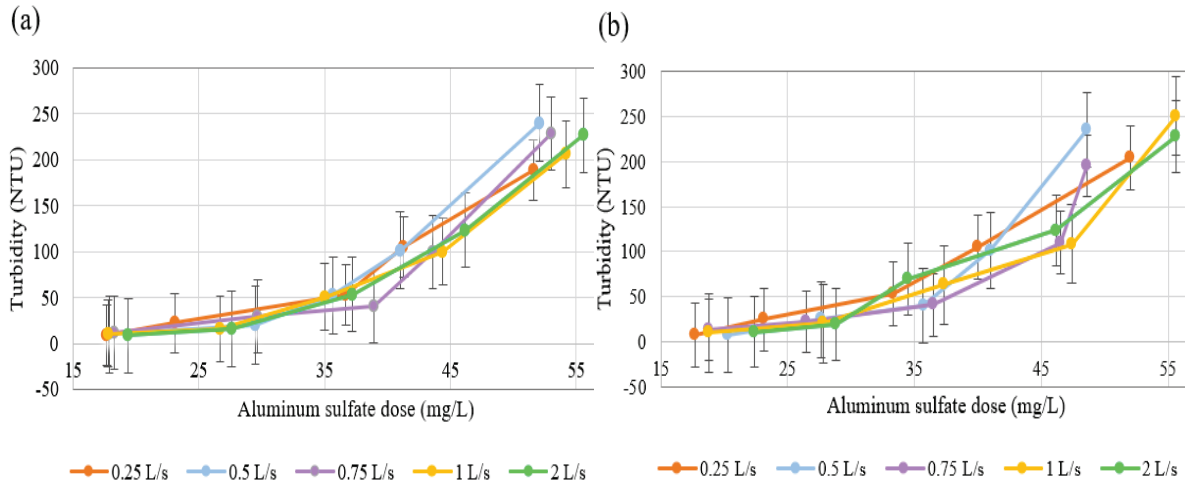


Figure 6. Dose of coagulant applied for (**a**) length of 68.4 m and (**b**) length of 97.6 m.

3.6. Turbidity and Color Removal Efficiency

3.6.1. Impact of HTF on Turbidity and Color Removal Efficiency after Settler

Figure 7 shows the turbidity removal efficiency measured in the pilot settler and once the water had been flocculated in the HTF using the length of 68.4 and 97.6 m (Figure 7a,b, respectively). Figure 7c also shows the turbidity removal efficiency in the DWTP settler and once the water had passed through the conventional baffle flocculator. It was performed to compare the efficiency between these systems. It can be seen that when the flow rate increased to 2 L/s in the pilot system, there is a lower turbidity removal efficiency (RE), although this trend is significantly reduced, especially for flows of 0.75, 1, and 2 L/s with the increase in the length of the HTF to 97.6 m. Meanwhile, the RE in the DWTP Bayas was constant. It should be emphasized that the characteristics of the raw water were the same for both the pilot system and the DWTP Bayas. The minimum RE in the HTF was presented for a flow of 2 L/s and a length of the HTF of 68.4 m, precisely due to the flow overload to the system, by doubling the design flow. The turbidity RE was 86.9% when the 68.4 m HTF was used; meanwhile, the RE was 83.89% when a length of 97.6 m was used.

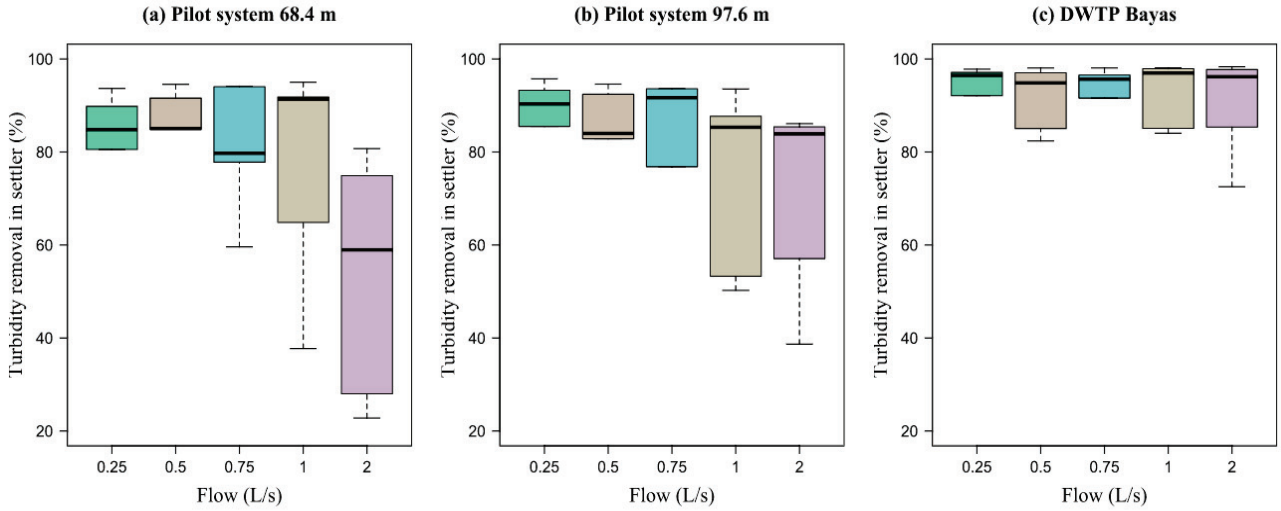


Figure 7. Efficiency of turbidity removal in the settler: (**a**) With HTF of 68.4 m; (**b**) with HTF of 97.6 m, and (**c**) in the filter of the DWTP "Bayas". The bluish-green boxes correspond to a flow of 0.25 L/s, the brown boxes correspond to a flow of 0.5 L/s, the turquoise boxes correspond to a flow of 0.75 L/s, the beige boxes correspond to a flow rate of 1.0 L/s, purple boxes correspond to a flow rate of 2.0 L/s.

Figure 8 shows the color RE for both lengths of the HTF, as well as for the settler of the DWTP Bayas. As in the case of turbidity removal, the color RE at the outlet of the settler using the length of 68.4 m in the HTF was greater than when 97.6 m was used for flows of 0.25, 0.5, 0.75, and 1 L/s (Figure 8a,b). Meanwhile, for the flow rate of 2 L/s, the RE was higher when 97.6 m was used. For the case of DWTP, the color RE was constant (Figure 8b).

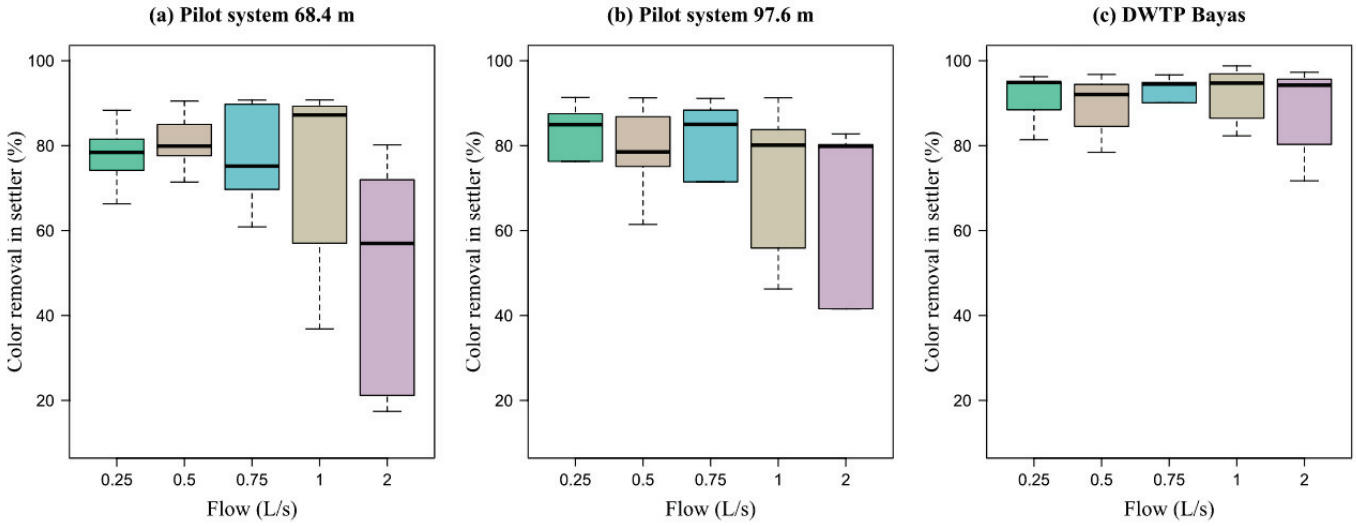


Figure 8. Color removal efficiency in the settler: (**a**) With HTF of 68.4 m, (**b**) with HTF of 97.6 m, and (**c**) in the filter of the DWTP "Bayas". The bluish-green boxes correspond to a flow of 0.25 L/s, the brown boxes correspond to a flow of 0.5 L/s, the turquoise boxes correspond to a flow of 0.75 L/s, the beige boxes correspond to a flow rate of 1.0 L/s, purple boxes correspond to a flow rate of 2.0 L/s.

At flow rates of 0.25, 0.5, 0.75, and 1 L/s, the color RE was similar using the two HTF lengths. However, for the 2 L/s flow rate, the RE was higher when a length of 97.6 m was used, with 79.87% efficiency, relative to the RE of 58.96% when a length of 68.4 m was used. Therefore, for flows higher than the design, a length of the HTF greater than 68.4 m will be required in order to increase the RE of color in the settler.

3.6.2. Impact of HTF on Turbidity and Color Removal Efficiency after the Filter

Figure 9 shows how the turbidity RE at the filter outlet of the pilot system presents a similar behavior when the two lengths of the HTF were used for each tested flow rate. This RE can be compared with the efficiency of the conventional DWTP filter, due to the fact that REs greater than 99% have been achieved at all flow rates. For flow rates of 0.25, 0.5, 0.75, and 1 L/s and using the two lengths of the HTF, the average turbidity RE is greater than 98.7% in the pilot filtration unit. However, for the flow rate of 2 L/s, the average RE in the two lengths of the pilot system was 97.88%, a relatively high efficiency considering that the retention time in both lengths of the HTF does not reach 10 min as suggested by the previously cited authors for adequate flocculation. However, an inadequate formation of flocs due to the short retention time when flow rates higher than the design flow rate are used in the HTF can cause a lower removal efficiency in the settler, as well as rapid saturation or clogging in the sand filters, meaning that the maintenance of this unit needs to be realized in short intervals of time.

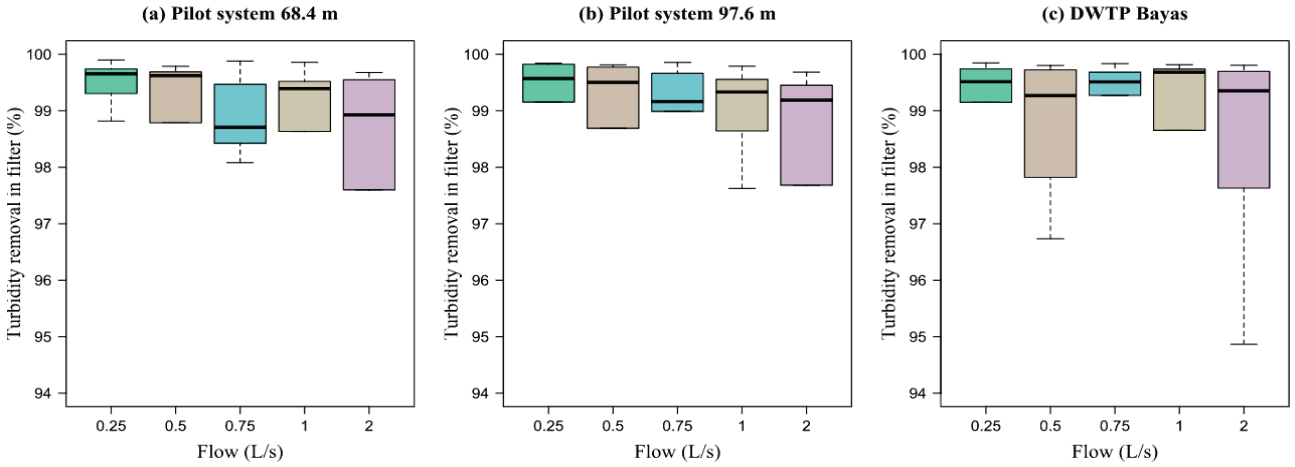


Figure 9. Turbidity removal efficiency in the filter: (**a**) With HTF of 68.4 m, (**b**) with HTF of 97.6 m, and (**c**) in the filter of the DWTP "Bayas". The bluish-green boxes correspond to a flow of 0.25 L/s, the brown boxes correspond to a flow of 0.5 L/s, the turquoise boxes correspond to a flow of 0.75 L/s, the beige boxes correspond to a flow rate of 1.0 L/s, purple boxes correspond to a flow rate of 2.0 L/s.

Figure 10 shows the color RE at the filter outlet after the water has passed through the HTF, as well as the RE of the filter after having passed the water through the DWTP baffle flocculator. The color RE at the filter outlet in the pilot system was similar for all flow rates, reaching 100% removal. High values were obtained at the output of the DWTP filter, with the RE of this parameter also reaching 100%. The average color removal at the filter outlet in the pilot system was 99.64% for the 68.4 m length and 99.56% for the 97.6 m length. Therefore, as in the case of turbidity, the color also meets the standards necessary for the supply of drinking water using a purification system that includes an HTF.

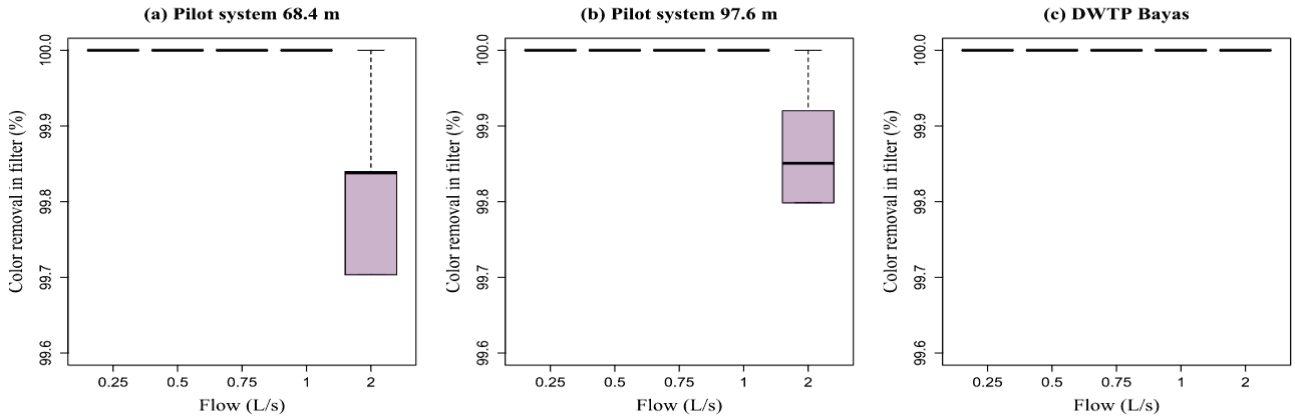


Figure 10. Color removal efficiency in the filter: (**a**) With HTF of 68.4 m, (**b**) with HTF of 97.6 m, and (**c**) in the filter of the DWTP "Bayas".

3.7. Comparison of Turbidity and Color Removal between the Pilot System and the Conventional Plant

3.7.1. Statistical Summary of the Efficiency of the HTF + Settler System

Table 5 shows the maximum values, minimum values, arithmetic mean (mean), and median (Me) of the turbidity and color removal obtained in the pilot settler after the water has passed through the HTF using the two lengths, as well as the removal of turbidity and color obtained in the DWTP settler.

Table 5. Statistical Parameters of the Turbidity and Color Removal Efficiency after HTF + Settler in the Studied Systems.

System	Turbidity (%)					Color (%)				
	Mean	Me	SD	Min	Max	Mean	Me	SD	Min	Max
HTF 68.4 m	75.45	80.73	20.89	22.79	95.00	71.53	77.62	20.45	17.42	90.77
HTF 97.6 m	77.41	85.42	19.37	38.68	95.73	73.39	80.11	18.06	38.46	91.35
DWTP Bayas	91.80	96.19	7.56	72.53	98.33	90.14	96.19	7.67	71.72	98.78

The Bayas DWTP had the highest average turbidity RE at the settler outlet with 91.80%; meanwhile, the average RE of the pilot system with the HTF of 97.6 m and 68.4 m in length was 77.41% and 75.45%, respectively (to see Table 5). However, excluding the 2 L/s flow rate, the turbidity RE increased to 81.04% for the 68.4 m length of the reactor. Similarly, for the length of 97.6 m, the RE increased to 79.20%.

Oliveira and Teixeira [19] used a tubular helical flocculator (THF) for turbidity removal with different lengths between 1.89 m and 36.84 m. The average RE of turbidity in the THF and decanter was higher than 80%, with a maximum removal of 86.2%. In this study, the best removal results occurred with the lowest velocity gradients. Therefore, the turbidity removals in the settler + THF were slightly lower than those obtained in the settler + HTF system. However, the maximum turbidity RE values (95.73%) using HTF were higher than the maximum value (86.2%) using THF.

The maximum RE value of turbidity in the DWTP was 98.33% for a CT $\geq$ 200 NTU (Figure 11). In the HTF, for the length of 97.6 m, the maximum value of RE was 95.73% for an RWT $\geq$ 200 NTU. In the length of 68.4 m, the maximum value of RE was 95% with RWT $\geq$ 200 NTU. In the 68.4 m system, the minimum RE was 22.79% with RWT $\approx$ 10 NTU. The minimum RE for the length of 97.6 m was 38.68%, with RWT $\approx$10 NTU. For the DWTP Bayas, the minimum RE was 72.53% when the tests were carried out with RWT $\approx$ 10 NTU.

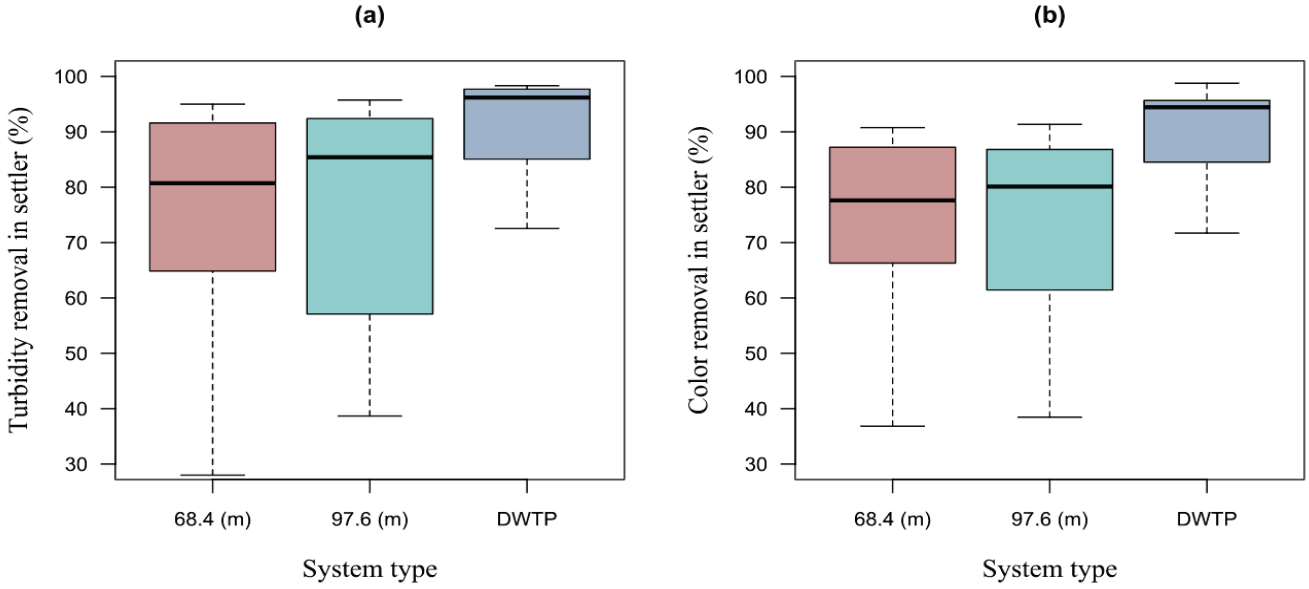


Figure 11. Average, maximum, and minimum values of RE in the pilot settler with HTF of 68.4 m, with HTF of 97.6 m, and in the settler of the DWTP Bayas: (**a**) Turbidity and (**b**) color. The pink boxes correspond to the PTS with a 68.4m long tubular flocculator, the turquoise boxes correspond to the PTS with a 97.6m long tubular flocculator and the Light Steel Blue boxes correspond to the "Bayas" DWTP.

Therefore, the RE of color was similar in the pilot settler after the use of the HTF of 68.4 m and 97.6 m, with average values of 71.53% and 73.39%, respectively (see the right

panel of Figure 11). For the DWTP, the color RE was higher than the pilot system with an average value of 90.14%.

Considering national and World Health Organization (WHO) regulations for water for human consumption require a maximum for turbidity and color of 5 NTU and 15 UC_Pt-Co, respectively, according to Table 6, it can be seen that the water obtained at the outlet of the settler does not meet these requirements. Meanwhile, the water obtained at the filtration outlet complies with the regulations for all flow rates tested for turbidity and color, indicating that in order to obtain water that complies with the regulations, it is necessary to implement a sedimentation and filtration system after the HTF.

Table 6. Turbidity values in NTU and color in UC Pt-Co obtained at the outlet of the settler and the filter.

Flow (L/s)	Settler Outlet				Filter Outlet			
	HTF 68.4 m		HTF 97.6 m		HTF 68.4 m		HTF 97.6 m	
	Turbidity	Color	Turbidity	Color	Turbidity	Color	Turbidity	Color
0.25	7.78	73.40	5.87	60.00	0.21	0	0.24	0
0.50	7.11	67.00	6.99	65.00	0.32	0	0.29	0
0.75	7.88	72.90	7.39	70.40	0.41	0	0.35	0
1.0	7.08	68.00	11.00	91.00	0.34	0	0.39	0
2.0	23.05	148.35	15.39	119.6	0.56	1	0.63	1

In the case of the raw water pH, 91% of the measurements were in the range of 7.4 to 7.9 and 9% of the measurements were between 7.2 and 7.4. The pH measurement at the outlet of the experimental pilot system in 79% of the data was between 7.2 and 7.5; meanwhile, in 19% of the data, it was between 6.9 and 7.2, and in 2% of the data, it was between 6.8 and 6.9. In all cases, the pH of the treated water was within the range recommended by national regulations, which is from 6.5 to 8 for human consumption.

Regarding the average concentration of aluminum in the raw water, it was between 0.011 and 0.026 mg/L, obtaining an average concentration of 0.013 and 0.031 mg/L in the treated water. According to the previous results, the concentrations of residual aluminum were much lower than the limit allowed in the national regulations and the WHO (0.2 mg/L).

3.7.2. Statistical Summary of the Efficiency of the HTF + Settler + Filter System

Table 7 shows the maximum values, minimum values, arithmetic mean (Mean), and median (Me) of the turbidity and color removal obtained in the pilot filter after the water had passed through the settler and HTF using the two lengths, as well as the removal of turbidity and color obtained in the DWTP Bayas filter. The turbidity removal in both the pilot system using HTF with the two lengths and in the DWTP Bayas do not differ, being similar in their average values, with values of 98.80, 98.74, and 98.78%, respectively.

Table 7. Statistical Parameters of the Turbidity and Color Removal Efficiency after HTF + Settler + Filter in the Studied Systems.

System	Turbidity (%)					Colour (%)				
	Mean	Me	SD	Min	Max	Mean	Me	SD	Min	Max
HTF 68.4 m	98.80	99.39	1.43	93.65	99.90	99.93	100	0.24	98.82	100
HTF 97.6 m	98.74	99.33	1.52	93.40	99.86	99.91	100	0.35	98.23	100
DWTP	98.78	99.51	1.41	94.87	99.85	100	100	0	100	100

In the pilot system with the HTF length of 64.8 m and 97.6 m, the maximum values of RE of color were 100% and minimum values were 98.82 and 98.23%, respectively. There was an overall RE of 100% for this parameter in the DWTP, showing that there is no difference in color removal both in the pilot system and in the conventional DWTP.

The RE of turbidity and color obtained in the filter of the pilot system after the settler and HTF using both lengths is shown in Figure 12. Likewise, the RE of turbidity and color obtained in the DWTP Bayas filter can be observed. There are no differences in the average values with respect to the DWTP values. The maximum value of turbidity RE at the filter outlet using the HTF with a length of 64.8 m had a value of 99.9%, for a flow rate of 0.25 L/s and RWT $\approx$ 100 NTU. For the system with an HTF of 97.6 m, the highest RE was 99.86% with a flow rate of 0.75 L/s and RWT $\geq$ 200 NTU. Finally, the maximum value of RE in the DWTP was 99.85% when the test was performed with raw water turbidity (RWT) $\approx$ 100 NTU. The minimum turbidity RE value using the HTF length of 97.6 m was 92.53% with a flow rate of 2 L/s and RWT $\approx$10 NTU. For the same flow rate and RWT mentioned above, the minimum RE was given in the length of the HTF of 64.8 m, with a value of 93.65%. Finally, the minimum RE of turbidity in the DWTP was 94.87% when the test was performed with RWT $\approx$10 NTU.

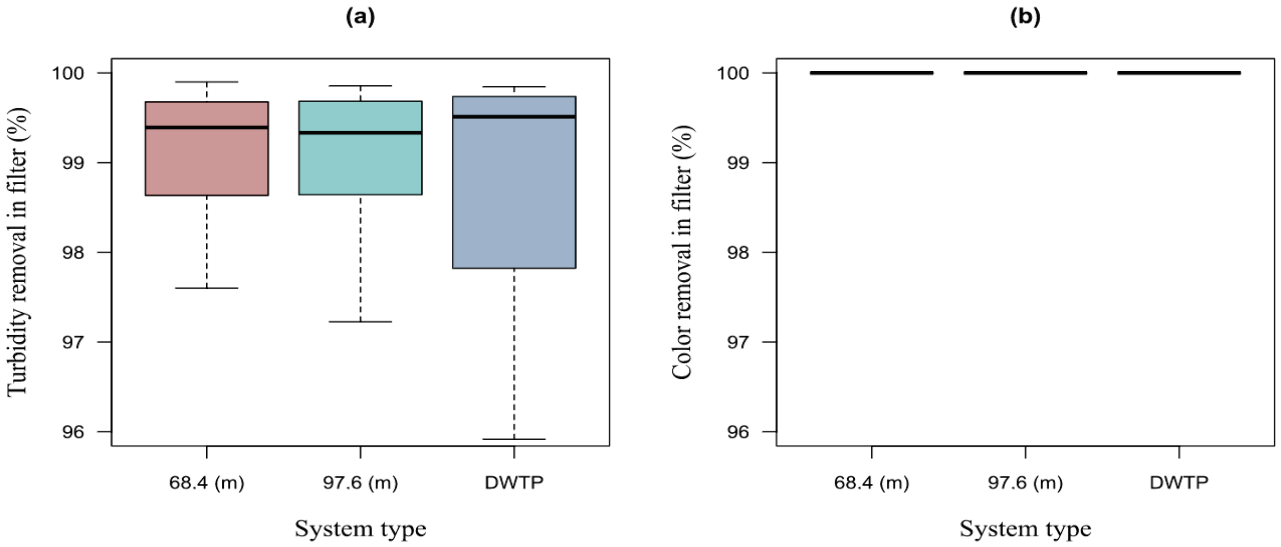


Figure 12. Average, maximum, and minimum values of the RE in the pilot filter with HTF of 68.4 m, with HTF of 97.6 m, and in the DWTP Bayas filter: (**a**) Turbidity and (**b**) color. The pink boxes correspond to the PTS with a 68.4m long tubular flocculator, the turquoise boxes correspond to the PTS with a 97.6m long tubular flocculator and the Light Steel Blue boxes correspond to the "Bayas" DWTP.

The color RE was similar in the pilot filter after having used the settler and HTF of 68.4 m and 97.6 m, with average values of 99.93 and 99.91%, respectively (see the right panel in Figure 12). For the DWTP, the average color RE had an average value of 100%, showing that there is no difference in color removal both in the pilot system and in the conventional DWTP.

3.8. Comparison of Means with Wilcoxon Test

It was found that there is no normal distribution in the turbidity removal efficiency data measured at the settler outlet, nor at the filtration outlet; for this reason, the Wilcoxon test was applied to determine if there is a significant difference between the removal efficiency when using the HTF with 68.4 m and the HTF with 97.6 m. The results obtained determined that the *p*-value was >0.05. This value allowed us to validate the null hypothesis, which establishes that there is no significant difference in the RE when using the two established lengths of the HTF. Table 8 shows the *p*-values calculated using the Wilcoxon test. The

comparison of the RE of the pilot settler using the 68.4 m HTF vs. the RE of the DWTP Bayas settler, as well as the RE of the settler of the pilot system using the 97.6 m HTF vs. the RE of the settler of the DWTP Bayas, showed that the *p*-value was <0.05 (see Table 8). The foregoing finding allowed us to reject the null hypothesis, establishing that there is a significant difference in the RE of the settler with the use of an HTF compared to a conventional system with a horizontal hydraulic screen flocculator.

Table 8. *p*-value of Turbidity Removal Efficiency with HTF of 68.4 and 97.6 m.

Observation 1	Observation 2	*p*-Value	Interpretation
Turbidity RE in settler using 68.4 m HTF	Turbidity RE in settler using 97.6 m HTF	0.55	No Significant Difference
Turbidity RE in filter using 68.4 m HTF	Turbidity RE in filter using 97.6 m HTF	0.74	No Significant Difference
Turbidity RE in settler using 68.4 m HTF	Turbidity RE in the DWTP Bayas settler	<0.0001	Significant Difference
Turbidity RE in filter using 68.4 m HTF	Turbidity RE in the DWTP Bayas filter	0.39	No Significant Difference
Turbidity RE in settler using 97.6 m HTF	Turbidity RE in the DWTP Bayas settler	0.0002	Significant Difference
Turbidity RE in filter using 97.6 m HTF	Turbidity RE in the DWTP Bayas filter	0.31	No Significant Difference

When comparing the RE of the pilot filter using the 68.4 m HTF vs. the RE of the DWTP Bayas filter, as well as the RE of the pilot system filter with a length of 97.6 m vs. the RE of the DWTP Bayas, the *p*-value was >0.05 (to see Table 8). These results confirm the null hypothesis that there is no significant difference in the RE of a system made up of HTF + settler + filter compared to a conventional system made up of HFD + settler + filter. These results indicate that it is advisable to use a tubular flocculator followed by a sedimentation and filtration process.

3.9. Turbidity Removal Estimation Model

A model was defined to estimate the removal efficiency in the pilot system using HTF + settler + filter, for which it was necessary to define the variables that influence the efficiency of the HTF. Six variables were analyzed: (a) Reynolds number, (b) retention time, (c) hydraulic gradient, (d) operating flow rate, (e) raw water turbidity, and (f) HTF length.

Through the correlation matrix (Table 9), it was possible to identify the variables that have a significant correlation in the model. It was identified that the turbidity of the raw water is the factor that has the most influence on the efficiency of the HTF. It can be seen that there is a relationship between MRT, Reynolds, and flow with the hydraulic gradient because the aforementioned variables are involved in its calculation.

Table 9. Correlation matrix of influential factors in the HTF system.

Variable	Efficiency	Reynolds	MRT	Gradient	Flow Rate	Turbidity	Length
Efficiency	1						
Reynolds	−0.39	1					
MRT	0.24	−0.76	1				
Gradient	−0.39	1	−0.71	1			
Flow Rate	−0.39	1	−0.76	1	1		
Turbidity	0.62	0.04	−0.03	0.04	0.04	1	
Length	0.05	2.12×10^{-16}	0.22	0.002	-2.97×10^{-15}	0.02	1

After a statistical analysis of collinearity, it was found that there is no collinearity of efficiency with the variables of Length, Gradient, and Turbidity of the raw water. For this reason, an adjusted model was applied using the Stepwise multiple linear regression statistical model [38,41]. In the Stepwise regression, two significant factors that influence the efficiency of the HTF were identified: Raw water turbidity with a positive coefficient and velocity gradient with a negative coefficient (see Table 10). The inclusion of the explanatory variable "raw water turbidity" with positive coefficients in the Stepwise regression model confirmed the considerable impact on the HTF efficiency, due to the fact that the HTF efficiency increases with the increase in raw water turbidity. Furthermore, considering that the velocity gradient has a relatively high incidence of flocculation, its inclusion with a negative coefficient indicated the important role of water agitation in the efficiency of the flocculation process.

Table 10. Statistical values obtained from regression analysis for turbidity removal efficiency models.

Model	R	R^2	Adjusted R^2	Se	Durbin-Watson
1	0.701	0.491	0.47	12.62	1.618
2	0.815	0.664	0.65	0.067	1.711

Tests carried out at different speed gradients show a tendency for the efficiency of THF to increase with the decrease in the speed gradient in flocculation. For a given raw water turbidity, the efficiency decreases slightly with the velocity gradient used in this study from 6 to 120 s^{-1}. For a given gradient, the efficiency increases with the turbidity of the raw water used in this study from 10 to 246 NTU. The velocity gradient associated with raw water turbidity constitutes an optimum value for a given efficiency.

The results of the multiple linear regression are presented in Table 10, where R is the correlation coefficient $R \in [-1, 1]$, R^2 is the square of the correlation coefficient or determination coefficient ($R^2 \in [0, 1]$), Adjusted R^2 is the R^2 adjusted by the number of variables of the model (Adjusted $R^2 \in [0, 1]$), and Se is the standard error of the estimation. Durbin–Watson values should be greater than 1.5 and less than 2.5 to indicate that the multiple linear regression data are free of first-order linear autocorrelation. For efficiency, the Durbin–Watson values were 1.618 and 1.711 in the linear model and in the model applying logarithms, respectively. In both models, the Durbin–Watson values are within the accepted range.

The non-standardized coefficient B for the Turbidity variable was 0.146 (see Table 11). This value indicates that if the turbidity variable increased by one unit, efficiency increased by 0.146. Furthermore, if the turbidity variable is reduced by one unit, efficiency decreased by 0.146. This interpretation is valid if the effect of the other variable remains constant.

Table 11. Standardized and non-standardized regression function coefficients for HTF efficiency.

Modelo		Non-Standardized Coefficients		Standardized Coefficients	t	Sig.
		B	Dev. Error	Beta		
1	(Constant)	72.077	3.234		22.284	<0.001
	Turbidity	0.146	0.024	0.664	6.196	<0.001
	Gradient	−0.159	0.053	−0.319	−2.981	0.005
2	(Constant)	1.670	0.048		35.061	<0.001
	LogGradient	−0.079	0.024	−0.283	−3.258	0.002
	LogTurbidity	0.190	0.021	0.794	9.136	<0.001

The non-standardized coefficient B for the Gradient variable was −0.159. This value indicates that if the Gradient variable is increased by one unit, efficiency is reduced by

0.159. Moreover, if the Gradient variable is reduced by one unit, efficiency increases by 0.159. This interpretation is valid if the effect of the other variable remains constant.

With the models obtained, it was determined that the variables influencing the efficiency were the hydraulic gradient and the turbidity of the raw water, due to the fact that they met the necessary statistical conditions [47]. Table 12 presents the first model according to the Stepwise methodology, which was not properly adjusted considering that it had an adjusted R^2 of 0.47. The second model was a closer representation due to the fact that it had an adjusted R^2 of 0.65, as a result of the application of logarithms in the model according to Al-Zubaidi et al. [48]. Vaneli and Teixeira [49] found turbidity removal estimation models for helical flocculators whose R^2 was 0.5.

Table 12. Stepwise Multiple Linear Regression Models to Estimate Treatment Efficiency Using an HTF.

Obtained Model	Adjusted R^2
$Efic = 72.077 - 0.159\ G + 0.146\ T$	0.47
$Efic = 10^{[1.67 - 0.079\ \log(G) + 0.19\ \log(T)]}$	0.65

3.10. Control Test

Two control tests were finally carried out to evaluate the efficiency of the tubular flocculator. The first test was not for using the HTF; that is, the coagulated water was sent directly to the settler and later to the filter. The second test consisted of feeding raw water without coagulant to the HTF, for its subsequent circulation to the settler and filter.

These tests were performed in triplicate using the design flow rate (1 L/s) with an average raw water turbidity value of 43.4 NTU and an average color value of 451 UC_Pt-Co. The results are presented in Table 13, obtaining average turbidity and color removal values of 49.3% and 51.1%, respectively, in the first test. These RE values were lower compared to the RE when the full pilot system was used. It shows the importance of the inclusion of the HTF before the settler and filter.

Table 13. Turbidity and color removal in control tests.

Pilot System	Turbidity Removal (%)	Color Removal (%)
Settler + filter (Coagulated water without HTF)	49.3	51.1
HTF_68.4m + Settler + filter (No coagulant)	16.38	12.91
HTF_97.6m + Settler + filter (No coagulant)	20.12	16.73

Meanwhile, in the second test, RE of turbidity and color were obtained at the outlet of the HTF_68.4m + Settler + filter of 16.38% for turbidity and 12.91% for color, while in the HTF_97.6m + Settler + filter system, the RE was 20.12% and 16.73% for turbidity and color, respectively. These RE values are lower in contrast to the RE when a coagulant (aluminum sulphate) was used. It evidences the importance of the use of a coagulant for eliminating turbidity and color in raw water using an HTF.

3.11. Comparison of Costs

Applying Equation (18), the construction cost of a conventional baffle flocculator with concrete was calculated; the construction cost was calculated for each of the five experimentally tested. Table 14 shows the costs incurred in the case of building a conventional baffle flocculator. Considering that the design flow of the HTF was 1 L/s, it was deduced that the construction cost of a conventional baffled flocculator of 1 L/s would be 11547.14 USD, approximately.

Table 14. Construction cost of a conventional flocculator.

Flow Rate (L/s)	Flow Rate (mgd)	Construction Cost (USD)
0.25	0.0057	6187.96
0.5	0.0114	8453.00
0.75	0.0171	10,145.00
1.0	0.0228	11,547.14
2.0	0.0456	15,773.86

Table 15 details the necessary materials for the construction of the HTF, as well as their respective prices. A total cost of 2074.75 USD was determined. PVC with elastomeric sealing (U/Z) materials increase costs, so costs could be further reduced if bondable PVC material is used. PVC with elastomeric sealing (U/Z) materials allow the system to be disassembled if necessary. The construction cost of the HTF is lower due to the avoidance of the necessary labor in civil works, as well as the replacement of the concrete in the conventional DWTP units with PVC pipe for the HTF.

Table 15. Summary of Materials and Used Prices.

N°	Item	Unit Price	Quantity	Final Price
1	PVC pipe 110 mm × 1.00 mpa × 6 m U/Z	28.75	15	431.25
2	PVC elbow 110 mm × 90 U/Z	16	26	416.00
3	Tee PVC 110 mm U/Z	51	1	51.00
4	PVC bell flange mm U/Z	23	2	46.00
5	Repair joint 110 mm U/Z	11	4	44.00
6	Elbow 110 mm E/C	11	6	66.00
7	Wafer valve of 110 mm (ductile iron)	128.5	1	128.50
9	PVC ball valve 110 mm	52	1	52.00
10	Pipe rack (iron)	840	1	840.00
	Total			2074.75

Note: U/Z = elastomeric sealing.

It was possible to determine that there is no significant difference in the efficiency of turbidity and color removal between a system composed of an HTF + settler + filter and a system composed of an HFD + settler + filter. The average efficiency of the pilot system of 98.77% for turbidity and 99.92% for color was determined, while the average efficiency of the DWTP Bayas was 98.78% for turbidity and 100% for color. However, the efficiency at the outlet of the pilot settler did represent a significant difference when compared to the efficiency of the DWTP settler, with the average removal efficiency in the settler of the pilot system of 76.43% for turbidity and 72.46% for color, while the efficiency at the outlet of the DWTP settler was 91.80% for turbidity and 90.14% for color. It is important to mention that some design parameters differed between the conventional system and the pilot system [50].

Table 16 shows the specifications of the pilot system and the conventional DWTP. The retention time in the hydraulic baffle flocculator (HBF) was 21 min, while in the HTF it was 12.5 min. It can be seen that the retention time of HBF was superior to HTF in 8.5 min. Although the retention time in the pilot system was lower than the retention time of the DWTP, the efficiencies were similar. The retention time in the DWTP Bayas settler was 25 min, while it was 12 min for the design flow (1 L/s) in the pilot settler. There was also a longer retention time in the settler of the DWTP, almost double with respect to the retention time of the used pilot system settler. The retention time is directly dependent on the depth

of the settler to lower depth, and the shorter detention period necessary to collect said particle; for this reason, the removal efficiency of the flocculent particles will depend on the depth of the tank. The sedimentation rate in the DWTP Bayas settler was 94 m^3/m^2d, while it was 120 m^3/m^2d in the pilot settler. Considering that the efficiency decreases as the sedimentation load increases, the aforementioned could have influenced the existence of a lower turbidity and color removal efficiency in the pilot settler. The filtration rate was the same in both the DWTP Bayas filters and the pilot filters.

Table 16. Specifications of the pilot system and the conventional DWTP.

Component	Retention Time (min)	Surface Load (m^3/m^2d)
Pilot Horizontal Tubular Flocculator (HTF)	12.5	
Conventional horizontal screen flocculator	21.0	
Conventional DWTP High Rate Settler Bayas	25.0	94
High rate pilot settler	12.0	120
Conventional DWTP Sand Filter Bayas		120
Pilot sand filter		120

As can be seen in Table 16, the conventional DWTP has some parameters that offer better efficiency compared to the pilot system under study. Despite this, the pilot system composed of HTF + settler + filter had efficiencies similar to the obtained efficiencies of the HBF + settler + filter system.

In the operation of the HTF with raw water turbidity less than 20 NTU and working with the design flow rate (1 L/s), residual turbidity in the filter less than 0.75 NTU was obtained, which is below the Ecuadorian norm of 5 NTU, obtaining a removal efficiency of over 96%, which is very acceptable. With flow rates less than the design flow rate, that is, 0.25, 0.5, and 0.75 L/s, and with raw water turbidity conditions less than 20 NTU, residual turbidity in the filter less than 0.5 NTU was obtained, below what is indicated as standard, obtaining a removal efficiency over 98%, which is also very acceptable. With a flow greater than the design flow, that is, 2 L/s, and with raw water turbidity conditions less than 20 NTU, residual turbidity in the filter less than 1 NTU was obtained reaching a removal efficiency of 95%, which is below the norm but slightly lower quality than the design flow conditions, which is equally acceptable.

In the case of tests with turbidity greater than 100 NTU, working with the different flow rates, there was a resulting turbidity up to 0.53 NTU, which represents a removal efficiency greater than 99%. Up to 75 NTU, the relationship between the increase in the dose of coagulant and the increase in turbidity was linear. The increase was exponential after 75 NTU, indicating that as turbidity increased, small increments of the coagulant dose had to be added.

Once the particles are destabilized in the coagulation, the collision between them occurs efficiently in the HTF, allowing the growth of microflocs, until they form larger flocs [35]. This good formation of flocs in the HTF occurs after subjecting the microflocs to slow agitation with average gradients of 42 s^{-1} for the design flow rate, allowing the union of these in larger aggregates or flocs, with sufficient cohesion and density to submit them to the next stage of sedimentation. The aforementioned gradients prevented the breakage and disintegration of the already-formed flocs. For a flow rate of 2 L/s, the gradient was 123 s^{-1}; however, the efficiency was acceptable, with the only limitation being that the filtration run decreased to 8 h.

For the different flows used, the theoretical retention time was practically equal to real time, which indicates that the unit has been designed well. This type of flocculator does not require electrical energy for its operation, which is why the production cost is very

low. It was shown that piston flow predominates in this type of unit, which is why a good adjustment of the retention time is achieved.

It is known that by varying the plant's operating flow rate, the retention times and velocity gradients in the reactors are modified. The HTF is somewhat flexible to these variations. Thus, when the flow rate decreased, the velocity gradient was reduced, therefore, the retention time increased; furthermore, when the flow rate increased, the effect was reversed. Depending on how much the operating flow is increased, velocity gradients so high that they can break the floc can be generated. In this study, the design flow rate was doubled, obtaining a maximum gradient of 126 s^{-1}, which is somewhat higher than the maximum (100 s^{-1}) recommended by the literature.

Table 17 presents a comparison between the present study and other studies carried out in terms of the efficiency obtained and some characteristics of the HTFs used. It can be seen that in the present study, much greater lengths and diameters of pipe were tested than those used in the studies by Tse et al. [14] and Oliveira and Teixeira [51], which is why this pilot system was able to treat many higher flows (3.6 m^3/h) than those used in the aforementioned studies. In the studies by Kurbiel et al. [17], two diameters of 71.4 and 86.4 mm were used, which are slightly smaller than the one used in the present study, and for this reason, Kurbiel et al. [17] used flow rates of 3.5 and 4 m^3/h. The gradients in the studies in Table 17 were between 10 and 100 s^{-1}, which is recommended for tubular flocculators, with the exception of the study carried out by Oliveira and Teixeira (2018). The retention times used in the studies realized by Kurbiel et al. [17] and Oliveira and Teixeira (2018) were relatively low compared to the time used in the present study.

All the studies in Table 17 have shorter retention times in this type of tubular flocculators than those used in baffle flocculators. The times in the tubular flocculators varied from 56.2 to 738 s; meanwhile, in the screen flocculators, the times vary between 600 and 1800 s (Romero, 1999). The tubular flocculators used by Kurbiel et al. (1989) had more similar characteristics to this study, where the values of the pipe diameter, velocity gradient, and flow rate were similar, with the length of the pipe being the aspect that did present a difference between said study and this study. This difference in length made the retention time in this study much longer than the time used by Kurbiel et al. (1989); however, it was possible to show that there was a higher removal efficiency in this study.

Table 17. Characteristics of the HTF used in other studies.

Author	Flocculator Length (m)	Pipe Diameter (mm)	Gradient G (s^{-1})	Flow Rate (m^3/h)	Time (s)	Initial Turbidity (NTU)	Efficiency(%)
(Tse et al., 2011) [14]	28	9.5	40	0.13	650	50 ± 5	94
(Kurbiel et al., 1989) [17]	20	71.4	52.7	3.5	82.3		68.8
(Kurbiel et al., 1989) [17]	20	86.4	33.2	4	105		54.3
(Oliveira and Teixeira, 2018) [51]	11.37	1.58	160	0.12	56.2	50	82.3
This study	68.4	110	46	3.6	435	206.1	91.37
This study	97.6	110	42	3.6	738	249.6	85.32

Compared to a mechanical flocculator where the speed remains constant and the residence time increases or decreases according to the flow rate variation, the HTF is somewhat flexible to these variations in operation. If the velocity gradient range is properly selected, this property can be exploited in the design of plants that integrate an HTF, in which small daily flow variations can be expected.

Among the advantages of this type of flocculators, it can be mentioned that the cleaning of these units is easy, performing a backwash. It is a very simple unit to build and operate [52]. It is very efficient when it is complemented with a high-rate settler and a rapid filter. When it is well designed, the theoretical and real retention times are practically the same, eliminating the possibility of dead spaces and short circuits. The operation of the HTF is completely hydraulic, so the operation is very reliable and economical as it does not require electricity. It is a very suitable solution for medium to large plants. Due to its great depth, it requires small areas, and very compact designs are achieved.

Among the restrictions of this type of flocculators, it can be mentioned that it is only a recommended solution for small plants. Therefore, the use of HTF followed by a sedimentation-filtration and disinfection treatment is recommended, especially for small populations, due to its easy implementation and low cost, making it an option for rural communities with low resources. The results of the study allowed a contribution to the fulfilment of the sixth objective of the 2030 Agenda for Sustainable Development, which mentions "To guarantee the availability and sustainable management of water and sanitation for all". The accomplishment of this objective is a great challenge considering that there are limitations in the treatment and distribution of drinking water, particularly in developing communities. An efficient, proven, easy-to-implement, and low-cost water purification system has been presented.

The growing need for adequate water treatment systems for rural and small populations led to the design and implementation of a tubular hydraulic flocculator, which allowed field research to be carried out. This tubular hydraulic flocculator presented high turbidity removal efficiency and low detection time compared to other flocculators commonly used in drinking water plants. This study evaluated a compact purification system made up of an HTF, high-rate settling, and rapid sand filters, with the aim of proposing a prediction model for turbidity removal efficiency. This pilot system has the capacity to treat 86,400 L/day (considering the design flow rate of 1 L/s), which makes it possible to provide drinking water to a rural community with a population of approximately 720 people, considering an allocation of 120 L/person/day.

In this study, other inlet configuration options were not evaluated, such as the introduction of raw water through the top of the flocculator or the effect that the variation of the diameter along the pipe could have on the efficiency of turbidity removal. Length 1 with a 3-inch pipe and length 2 with a 4-inch pipe could be tested at the beginning of flocculation in such a way that there would be a higher velocity gradient at the beginning and a lower gradient at the end as occurs in baffle flocculators, which could improve floc formation [49,53]. During the flocculation process, the size of the floc increases gradually. Considering that large flocs break easily, the value of G should be gradually reduced from the beginning of flocculation to the end of flocculation.

3.12. Pilot Treatment System

Figure 13 shows images of the implementation of the pilot treatment system.



Figure 13. Implementation of the Pilot Treatment System. The upper left figure shows the HTF implementation; in the upper right, the implementation of the settler is presented. The complete experimental system is presented in the lower left and right figures, as follows: (a) HTF, (b) high-rate settler, and (c) rapid sand filters.

4. Conclusions

In this study on the evaluation of tubular hydraulic flocculators for purifying small flows, it was determined that the calculations used for the design of a horizontal baffle flocculator are useful for identifying the length and diameter parameters when building the pilot HTF. Experimental trials have been carried out in the field through the implementation of a pilot system for calculating the efficiency of a tubular flocculator, which allowed us to consider the variation in the turbidity conditions of the natural raw water used in a purification plant in a rural community. A large-scale experimental investigation of a hydraulic tubular flocculator was carried out to evaluate the hydraulic conditions corresponding to the different conditions tested.

The removal efficiency values do not differ significantly with the use of an HTF of 68.4 and 97.6 m in length; therefore, using a shorter length is possible, which confirms that this type of flocculator has a low retention time. In addition, the system is flexible to fluctuations in the operating flow due to the fact that it has adapted to decreases of up to 75% and increases of up to 100% with respect to the design flow.

The design of the HTF was satisfactory, working under normal operating conditions (design flow rate = 1 L/s) and even with high turbidity. The purpose of the study was obtained due to the fact that the quality of the water in the effluent of the filtration process was below the maximum permissible limits that are set in international standards and the recommendations of the World Health Organization.

It should be noted that better removal efficiency results were obtained (99.65%) in the tests with the minimum flow rate of 0.25 L/s compared with the results of the maximum flow rate of 2 L/s (98.93%). However, it is recommended that efforts must be made to work with flows close to the design flow during the operation stage of these systems, to avoid damage to the quality of the water in the effluent. It should also be noted that there was no significant difference in turbidity and color removal between the pilot system that included the HTF and the conventional plant that included an HBF. In addition, this type of technology would be convenient for developing countries due to the fact that it eliminates the costs of electricity and equipment maintenance, its operation is simpler, and it does not require specialized labor during its implementation.

Using multiple linear regression analysis, it was possible to obtain two turbidity removal efficiency prediction models: One using the Stepwise methodology and the other using logarithms with coefficients of determination of 0.49 and 0.66, respectively. Finally, the results of this work showed that for obtaining greater efficiency in drinking water using a flow rate of 1 L/s, the HTF pipe should have a diameter of 110 mm, a length of 68 m, a speed of 0.13 m/s, a retention time of 12.5 min, and a velocity gradient of 42 s^{-1}. A specific methodology for the design of tubular hydraulic flocculators has to be investigated, considering that the present study used the design methodology of hydraulic screen flocculators to establish the size of the pilot HTF.

Author Contributions: Conceptualization, F.G.-Á. and E.A.A.-P.; methodology, F.G.-Á.; software, A.M.-H.; validation, A.T.-A., F.C.-I., and A.M.-H.; formal analysis, F.G.-Á. and M.D.T.-O.; investigation, A.T.-A.; data curation, F.G.-Á.; writing—original draft preparation, F.G.-Á.; writing—review and editing, E.A.A.-P. and G.H.-C.; funding acquisition, E.S.-C. All authors have read and agreed to the published version of the manuscript.

Funding: This research received no external funding.

Data Availability Statement: All data generated or analyzed during this study are within the submitted manuscript.

Acknowledgments: The authors thank the Vicerrectorado de Investigación de la Universidad de Cuenca for the support provided to the project "Transferencia de nuevas tecnologías sostenibles de bajo costo para tratamiento de agua potable en comunidades en desarrollo" (Transfer of new low-cost sustainable technologies for drinking water treatment in developing communities).

Conflicts of Interest: The authors declare no conflict of interest.

References

1. Villeneuve, C.; Tremblay, D.; Riffon, O.; Lanmafankpotin, G.Y.; Bouchard, S. A Systemic Tool and Process for Sustainability Assessment. *Sustainability* **2017**, *9*, 1909. [CrossRef]
2. Mraz, A.L.; Tumwebaze, I.K.; McLoughlin, S.R.; McCarthy, M.E.; Verbyla, M.E.; Hofstra, N.; Rose, J.B.; Murphy, H.M. Why pathogens matter for meeting the united nations' sustainable development goal 6 on safely managed water and sanitation. *Water Res.* **2020**, *189*, 116591. [CrossRef] [PubMed]
3. Castro-Jiménez, C.C.; Grueso-Domínguez, M.C.; Correa-Ochoa, M.A.; Saldarriaga-Molina, J.C.; García, E.F. A Coagulation Process Combined with a Multi-Stage Filtration System for Drinking Water Treatment: An Alternative for Small Communities. *Water* **2022**, *14*, 3256. [CrossRef]
4. Machado, A.V.M.; dos Santos, J.A.N.; Alves, L.M.C.; Quindeler, N.D.S. Contributions of Organizational Levels in Community Management Models of Water Supply in Rural Communities: Cases from Brazil and Ecuador. *Water* **2019**, *11*, 537. [CrossRef]
5. García-Ávila, F.; Avilés-Añazco, A.; Sánchez-Cordero, E.; Valdiviezo-Gonzáles, L.; Ordoñez, M.D.T. The challenge of improving the efficiency of drinking water treatment systems in rural areas facing changes in the raw water quality. *South Afr. J. Chem. Eng.* **2021**, *37*, 141–149. [CrossRef]
6. Ahmed, T.; Zounemat-Kermani, M.; Scholz, M. Climate Change, Water Quality and Water-Related Challenges: A Review with Focus on Pakistan. *Int. J. Environ. Res. Public Health* **2020**, *17*, 8518. [CrossRef]
7. Park, C.M.; Chu, K.H.; Her, N.; Jang, M.; Baalousha, M.; Heo, J.; Yoon, Y. Occurrence and Removal of Engineered Nanoparticles in Drinking Water Treatment and Wastewater Treatment Processes. *Sep. Purif. Rev.* **2016**, *46*, 255–272. [CrossRef]
8. Mustereț, C.P.; Morosanu, I.; Ciobanu, R.; Plavan, O.; Gherghel, A.; Al-Refai, M.; Roman, I.; Teodosiu, C. Assessment of Coagulation–Flocculation Process Efficiency for the Natural Organic Matter Removal in Drinking Water Treatment. *Water* **2021**, *13*, 3073. [CrossRef]

9. Na Nagara, V.; Sarkar, D.; Elzinga, E.J.; Datta, R. Removal of heavy metals from stormwater runoff using granulated drinking water treatment residuals. *Environ. Technol. Innov.* **2022**, *28*, 102636. [CrossRef]
10. Arman, N.Z.; Salmiati, S.; Aris, A.; Salim, M.R.; Nazifa, T.H.; Muhamad, M.S.; Marpongahtun, M. A Review on Emerging Pollutants in the Water Environment: Existences, Health Effects and Treatment Processes. *Water* **2021**, *13*, 3258. [CrossRef]
11. Gonzales, L.G.V.; Ávila, F.F.G.; Torres, R.J.C.; Olivera, C.A.C.; Paredes, E.A.A. Scientometric study of drinking water treatments technologies: Present and future challenges. *Cogent Eng.* **2021**, *8*, 38. [CrossRef]
12. Haarhoff, J. Design of around-the-end hydraulic flocculators. *J. Water Supply: Res. Technol.* **1998**, *47*, 142–152. [CrossRef]
13. Ghawi, A.H. Optimal design parameters for hydraulic vertical flocculation in the package surface water treatment plant. *Przegląd Nauk. Inżynieria i Kształtowanie Środowiska* **2018**, *27*, 438–451. [CrossRef]
14. Tse, I.C.; Swetland, K.; Weber-Shirk, M.L.; Lion, L.W. Fluid shear influences on the performance of hydraulic flocculation systems. *Water Res.* **2011**, *45*, 5412–5418. [CrossRef]
15. Sun, Y.; Zhou, S.; Chiang, P.-C.; Shah, K.J. Evaluation and optimization of enhanced coagulation process: Water and energy nexus. *Water-Energy Nexus* **2019**, *2*, 25–36. [CrossRef]
16. Boily, K.; Butler, C. *Coagulation-Flocculation System for the Treatment of Cheese Production Wastewater*; McGill University: Montreal, QC, Canada, 2014.
17. Kurbiel, J.; Spulak, A.; Schade, H. Application of pipe flocculator and cross-flow tilted plate settler for effective separation of precipitate from electroplating wastewater. *Water Sci. Technol.* **1989**, *21*, 539–546. [CrossRef]
18. Pennock, W. *Development of the Turbulent Tube Flocculator*; Cornell University: Ithaca, NY, USA, 2016.
19. Oliveira, D.S.; Teixeira, E.C. Experimental evaluation of helically coiled tube flocculators for turbidity removal in drinking water treatment units. *Water SA* **2017**, *43*, 378. [CrossRef]
20. Carissimi, E.; Rubio, J. The flocs generator reactor-FGR: A new basis for flocculation and solid–liquid separation. *Int. J. Miner. Process.* **2005**, *75*, 237–247. [CrossRef]
21. García-Ávila, F.; Valdiviezo-Gonzales, L.; Iglesias-Abad, S.; Gutiérrez-Ortega, H.; Cadme-Galabay, M.; Donoso-Moscoso, S.; Arévalo, C.Z. Opportunities for improvement in a potabilization plant based on cleaner production: Experimental and theoretical investigations. *Results Eng.* **2021**, *11*, 100274. [CrossRef]
22. Sánchez, L.D.; Marin, L.M.; Visscher, J.T.; Rietveld, L.C. Low-cost multi-stage filtration enhanced by coagulation-flocculation in upflow gravel filtration. *Drink. Water Eng. Sci.* **2012**, *5*, 73–85. [CrossRef]
23. Romero, J. *Water Purification*, 3rd ed.; Mexico, D.F., Ed.; Alfaomega: Kryoneri, Attica, 1999.
24. Oliveira, D.S.; Teixeira, E.C. Hydrodynamic characterization and flocculation process in helically coiled tube flocculators: An evaluation through streamlines. *Int. J. Environ. Sci. Technol.* **2017**, *14*, 2561–2574. [CrossRef]
25. Arboleda, J. Teoría y Práctica de la Purificación del Agua [Theory and Practice of the Water Purification]. Bogotá, Colombia, s.e. 2000. pp. 1–390. Available online: https://docer.com.ar/doc/v8xcse. (accessed on 3 November 2022).
26. Mastrocicco, M.; Prommer, H.; Pasti, L.; Palpacelli, S.; Colombani, N. Evaluation of saline tracer performance during electrical conductivity groundwater monitoring. *J. Contam. Hydrol.* **2011**, *123*, 157–166. [CrossRef] [PubMed]
27. Maran, S. A stochastic approach to the evaluation of residence times. *Water Resour. Res.* **2002**, *38*, 1–8. [CrossRef]
28. Pérez, J.M. Analysis of Flows and Factors that Determine Retention Periods. 2005. Available online: https://xdoc.mx/preview/analisis-de-flujos-y-factores-que-determinan-los-periodos-5ddae47319f3d. (accessed on 1 November 2022).
29. Moruzzi, R.B.; de Oliveira, S.C. Mathematical modeling and analysis of the flocculation process in chambers in series. *Bioprocess Biosyst. Eng.* **2012**, *36*, 357–363. [CrossRef]
30. Wolf, D.; Resnick, W. Residence Time Distribution in Real Systems. *Ind. Eng. Chem. Fundam.* **1963**, *2*, 287–293. [CrossRef]
31. Alcocer, D.J.R.; Vallejos, G.G.; Champagne, P. Assessment of the plug flow and dead volume ratios in a sub-surface horizontal-flow packed-bed reactor as a representative model of a sub-surface horizontal constructed wetland. *Ecol. Eng.* **2012**, *40*, 18–26. [CrossRef]
32. Meng, F.; Van Wie, B.J.; Thiessen, D.B.; Richards, R.F. Design and fabrication of very-low-cost engineering experiments via 3-D printing and vacuum forming. *Int. J. Mech. Eng. Educ.* **2018**, *47*, 246–274. [CrossRef]
33. Anaya-Durand, A.I.; Cauich-Segovia, G.I.; Funabazama-Bárcenas, O.; Gracia-Medrano-Bravo, V.A. Evaluación de ecuaciones de factor de fricción explícito para tuberías. *Educ. Química* **2014**, *25*, 128–134. [CrossRef]
34. Mott, R.L. *Fluid Mechanics*, 6th ed.; Pearson Education: Mexico City, Mexico, 2006.
35. Flores, J.H.N.; Neto, O.R.; Faria, L.C.; Timm, L.C. ESTIMATION OF THE KINETIC HEAD COEFFICIENT (k) BASED ON THE GEOMETRIC CHARACTERISTICS OF EMITTER PIPES. *Eng. Agríc.* **2017**, *37*, 1091–1102. [CrossRef]
36. Benalia, A.; Derbal, K.; Khalfaoui, A.; Bouchareb, R.; Panico, A.; Gisonni, C.; Crispino, G.; Pirozzi, F.; Pizzi, A. Use of *Aloe vera* as an Organic Coagulant for Improving Drinking Water Quality. *Water* **2021**, *13*, 2024. [CrossRef]
37. Ahumada, L.K.; Sanchez, I.D. Application of the Wilcoxon Test to correlate the results of the Saber 11 and Saber T&T Test. *IOP Conf. Series: Mater. Sci. Eng.* **2019**, *519*, 012034. [CrossRef]
38. Turner, D.P.; Deng, H.; Houle, T.T. Statistical Hypothesis Testing: Overview and Application. *Headache* **2020**, *60*, 302–308. [CrossRef] [PubMed]
39. Jia, R.; Fang, S.; Tu, W.; Sun, Z. Driven Factors Analysis of China's Irrigation Water Use Efficiency by Stepwise Regression and Principal Component Analysis. *Discret. Dyn. Nat. Soc.* **2016**, *2016*, 8957530. [CrossRef]
40. Sethi, V.; Clark, R. Cost estimation models for drinking water treatment unit processes. *Indian J. Eng. Mater. Sci.* **1998**, *5*, 223–235.

41. Deb, A.K.; Richards, W.G. Evaluating the economics of alternative technology for small water systems. *J. AWWA* **1983**, *75*, 177–183. [CrossRef]
42. Garland, C.; Weber-Shirk, M.; Lion, L.W. Revisiting Hydraulic Flocculator Design for Use in Water Treatment Systems with Fluidized Floc Beds. *Environ. Eng. Sci.* **2017**, *34*, 122–129. [CrossRef]
43. Ispilco, P. Efficiency of the Raw Water Treatment Plant for the City of San Marcos, 2017. (Cajamarca, Peru). 2018. Available online: https://repositorio.unc.edu.pe/handle/20.500.14074/2585. (accessed on 3 November 2022).
44. Aguirre, D. Evaluation of the Flocculator in the "La Esperanza" Drinking Water Treatment Plant that Supplies the Cantons of Machala, Pasaje, and Guabo, El Oro province. Bachelor's Thesis, Universidad Técnica de Machala, Machala, Ecuador, 2015. Available online: http://repositorio.utmachala.edu.ec/bitstream/48000/2928/1/EVALUACI%c3%93N%20PTAP%20LA%20ESPERANZA..pdf. (accessed on 13 November 2022).
45. Rojas, A.; García, A. Analysis of the residence time distribution curve in a leaching system. *Tecnol. Química* **2010**, *30*, 61–68.
46. Mohammed, T.J.; Shakir, E. Effect of settling time, velocity gradient, and camp number on turbidity removal for oilfield produced water. *Egypt. J. Pet.* **2018**, *27*, 31–36. [CrossRef]
47. Smith, G. Step away from stepwise. *J. Big Data* **2018**, *5*, 32. [CrossRef]
48. Al-Zubaidi, H.A.M.; Naje, A.S.; Al-Ridah, Z.A.; Chabuck, A.; Ali, I.M. A Statistical Technique for Modelling Dissolved Oxygen in Salt Lakes. *Cogent Eng.* **2021**, *8*, 1875533. [CrossRef]
49. Vaneli, B.P.; Teixeira, E.C. Aperfeiçoamento de modelo de estimativa da eficiência de remoção de turbidez da água em floculadores tubulares helicoidais. *Eng. Sanit. e Ambient.* **2019**, *24*, 773–783. [CrossRef]
50. Mcconnachie, G.; Liu, J. Design of baffled hydraulic channels for turbulence-induced flocculation. *Water Res.* **2000**, *34*, 1886–1896. [CrossRef]
51. Oliveira, D.S.; Teixeira, E.C. Swirl number in helically coiled tube flocculators: Theoretical, experimental, and CFD modeling analysis. *Int. J. Environ. Sci. Technol.* **2018**, *16*, 3735–3744. [CrossRef]
52. García-Ávila, F.; Tenesaca-Pintado, D.; Novoa-Zamora, F.; Alfaro-Paredes, E.A.; Avilés-Añazco, A.; Guanuchi-Quito, A.; Tonon-Ordoñez, M.D.; Zhindón-Arévalo, C. Vertical tubular flocculator: Alternative technology for the improvement of drinking water treatment processes in rural areas. *J. Environ. Manag.* **2023**, *331*, 117342. [CrossRef]
53. Haarhoff, J.; Van Der Walt, J.J. Towards optimal design parameters for around-the-end hydraulic flocculators. *J. Water Supply Res. Technol.* **2001**, *50*, 149–160. [CrossRef]

Disclaimer/Publisher's Note: The statements, opinions and data contained in all publications are solely those of the individual author(s) and contributor(s) and not of MDPI and/or the editor(s). MDPI and/or the editor(s) disclaim responsibility for any injury to people or property resulting from any ideas, methods, instructions or products referred to in the content.

water

MDPI

Article

Comparative Study of Two Organic Wastes as Adsorbents in the Treatment of Water Rich in Nitrogen Compounds

Thais Fernandes Neulls [1], Paulo Leonardo Santos Gouveia [1], Carlos Drielson da Silva Pereira [2], Camilla Stephane Dias Souza [3], Fernanda Nayr Sena Chaves [3], Isabela Nascimento Souza [4], Rudys Rodolfo de Jesus Tavarez [5], Amanda Silva dos Santos Aliança [6], Maria Cláudia Gonçalves [1], Wolia Costa Gomes [1], Darlan Ferreira da Silva [1], Maria Raimunda Chagas Silva [1], Fabrício Brito Silva [1], Álvaro Silva Lima [4], Edelvio de Barros Gomes [7] and Rita de Cássia M. de Miranda [8,*]

1 Postgraduate Department, Program of Master in Environment, University of CEUMA, São Luís 65075-120, Brazil
2 Postgraduate Department, Program of Master in Microbial Biology, University of CEUMA, São Luís 65075-120, Brazil
3 Health Department, Biomedicine Course, University of CEUMA, São Luís 65075-120, Brazil
4 Post Graduate in Process Engineering, Institute of Technology and Research, Tiradentes University, Aracaju 49032-490, Brazil
5 Postgraduate Department, Program of Master in Odontology, University of CEUMA, São Luís 65075-120, Brazil
6 Postgraduate Departament, Program of Master in Health Service Program Management, University of CEUMA, São Luís 65075-120, Brazil
7 Federal Institute of Sergipe, Campus Glória, Aracaju 49680-000, Brazil
8 Postgraduate Department, Program of Master in Environment and Program Microbial Biology, University of CEUMA, São Luís 65075-120, Brazil
* Correspondence: rita.miranda@ceuma.br; Tel.: +55-98-99213-5500

Citation: Neulls, T.F.; Gouveia, P.L.S.; da Silva Pereira, C.D.; Souza, C.S.D.; Chaves, F.N.S.; Souza, I.N.; Tavarez, R.R.d.J.; Aliança, A.S.d.S.; Gonçalves, M.C.; Gomes, W.C.; et al. Comparative Study of Two Organic Wastes as Adsorbents in the Treatment of Water Rich in Nitrogen Compounds. *Water* **2023**, *15*, 876. https://doi.org/10.3390/w15050876

Academic Editors: Dibyendu Sarkar, Rupali Datta, Prafulla Kumar Sahoo and Mohammad Mahmudur Rahman

Received: 30 December 2022
Revised: 2 February 2023
Accepted: 7 February 2023
Published: 24 February 2023

Copyright: © 2023 by the authors. Licensee MDPI, Basel, Switzerland. This article is an open access article distributed under the terms and conditions of the Creative Commons Attribution (CC BY) license (https://creativecommons.org/licenses/by/4.0/).

Abstract: Background: The objective of this work was to propose the treatment of the wastewater from Laguna da Jansen using adsorptive processes of residues of pineapple crown and shrimp chitosan. Methods: Residual substrates were distributed in 11 Erlenmeyers, and 250 mL of residual pond water were added; the solution was incubated under agitation at the times and amounts established by the Experimental Design (DCCR). After this period, analyses of pH, electrical conductivity, turbidity, nitrate, and nitrite, morphological analyses by SEM, and structural analyses by FTIR and XRD were performed. Results: The FTIR and SEM results showed that the biomass presented active chemical groups and a morphology rich in pores. The experimental design showed that the substrate content was the variable that influenced the lagoon effluent treatments for both tested biomasses; however, when observing the specific values of the response variables, the vegetable adsorbent was more efficient with the conditions of 15g of substrate and 30 days of process. Conclusion: Plant biomass is more efficient in the treatment of effluents rich in organic materials. It can be used in treatment plants as an alternative for the removal of toxic compounds present in wastewater and effluents.

Keywords: adsorption biomass; pineapple crown; chitosan; treatment

1. Introduction

Problems related to the burning of fossil fuels, automotive vehicle use, habitat destruction, natural landscapes, inconsistencies between energy resource limitations, adoption of urban transport models, and growing housing demands originate from human activities [1,2], which reflect a lack of adequate sanitation [3].

The importance of sanitation to the quality of life of a population is evident. However, water and effluent treatments do not cover the entire Brazilian population. In 2016, only 51.9% of the Brazilian population had a sewage system; only 44.9% of the sewage produced in the country received treatment. The remaining waste was inappropriately disposed of in

rivers, lakes, and lagoons [4]. Nutrient transport from terrestrial sources to surface water bodies is a natural phenomenon; however, increases in the human population and the expansion of urban areas without urban planning promote increases in the discharge loads of solid waste and sewage, accelerating the natural eutrophication process of these environments [5]. Globally, several countries have documented high levels of eutrophication in coastal lagoons due to anthropogenic activity, causing effects that can lead to toxic algal blooms, a decrease in or an absence of oxygen, fish mortality, reductions in biodiversity, and the loss of fish stocks, which can harm inhabitants on the margins of these ecosystems [5].

In this scenario of pollution generated by the urban environment, the Ecological Park of Lagoa da Jansen is an example initially implemented as an ecological and tourist reserve; however, since its formation, this park has suffered from severe environmental degradation, due to pollution generated on-site (i.e., degradation of both esthetic and landscape aspects, resulting in an imbalance in the local ecosystem) [6]. The park was built in a mangrove region and now constitutes a body of water reduced to a lagoon with marine characteristics, due to the interaction with the sea through a drainage channel [6]. The lagoon is characterized by nutrient concentrations (such as phosphate, nitrite, and sulfide) above the limits established by CONAMA Resolution No. 357 on 17 March 2005, which characterizes it as a eutrophic environment. Most material found in the lagoon is allochthonous, reaffirming its state of contamination resulting from human activity [6].

Eutrophication produces cloudy water in an ecosystem, yielding an unpleasant odor that often causes organism mortality. These processes negatively affect tourism and fishing activities, harming the local economy while also affecting public health, owing to the possible release of toxins harmful to human health, such as cyanobacteria and red, green, and brown algae, as well as the consumption of contaminated seafood that can generate severe human intoxication [7]. Therefore, we must recognize the vulnerability of aquatic systems and formulate remediation strategies. The selection of an appropriate treatment depends on economic, social, and geographic factors, as well as the physical, chemical, and microbiological quality of the water that requires treatment. Alternative treatments that are low-cost and effective are, therefore, the priority [7].

As a low-cost process for different types of effluents, adsorption using biomass as an adsorbent has generated significant interest [8]. Plant and animal biomasses have been used to decontaminate water via organic substances and have advantages over mineral coal due to their low costs [9]. Adsorption is a term generally used to describe the physical and chemical phenomena that occur when there are differences between the concentrations present in the fluid phase and the compounds that have a porous, solid form [10]. We examined pineapple crown, popularly known as pineapple, as the plant biomass and chitosan extracted from shrimp as the animal biomass.

Brazil is the second-largest producer of pineapple [*Ananas comosus* var. comosus (L.) Merril], accounting for 15% of global production, equivalent to 1,617,684 thousand tons and a planted area of 60,016 ha in 2019 [11]. Maranhão ranks fourth in terms of pineapple production and area in northeastern Brazil, with 1218 ha representing 5.4% of the area, which accounts for 37.2% of the cultivated area of Brazil [11]. Several by-products can be obtained from the pineapple-processing residue and discarded biological material during the pineapple production chain. Reducing the environmental damage caused by inadequate waste management can add value to these materials and yield new products of biotechnological interest [12]. Chitosan was obtained from shrimp waste; its national production, in greater quantities in the northeast region, was approximately 69,385 thousand tons in 2015 [11]. Shrimp fishing is a primary activity in marine, estuarine, or freshwater ecosystems. Large amounts of solid waste are generated during shrimp processing, particularly during the shelling process, which corresponds to approximately 40% of the total industrialized mass [13]. This residue is often discarded in the sea and in rivers, causing environmental problems. Considering this residue consists of chitin [14], significant interest centers on its reuse to develop products with high added values.

Despite these possibilities, Jansen Lagoon has suffered from significant environmental degradation, mainly due to the dumping of untreated domestic sewage. The release of untreated sewage into the lagoon intensifies the eutrophication process, which seriously affects the structure of the ecosystem, generating imbalances and potentially causing toxic algal blooms. The objective of this study was to compare two biomasses used as substrates for the treatment of water from Laguna da Jansen via an adsorptive process.

2. Materials and Methods

2.1. Study Area

The absorbate used in this study was water from Laguna da Jansen, located in São Luis, Maranhão between latitudes 2°30′ and 8°38″ S and longitudes 44°18′ and 35°26′ W. The ecosystem is characterized as a lagoon because it has a direct connection with the sea, which yields brackish water. Figure 1 shows the locations of the sample collection at five different points. These points were selected because they were near sewage spill pipes.

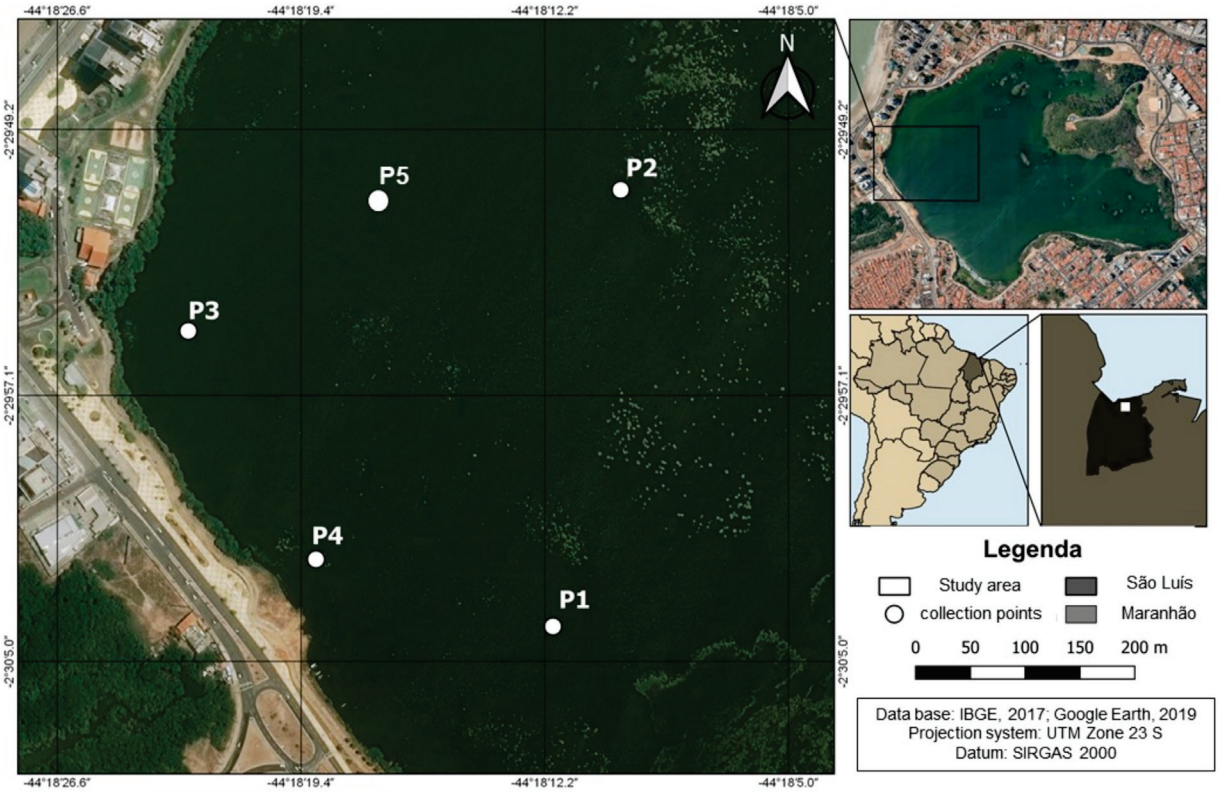


Figure 1. Location map of Laguna da Jansen indicating the collection points of water requiring treatment.

Five liters of the absorbate was then collected in gallons. After collection, the samples were transported to the Environmental Science Laboratory (LACAM) at Ceuma University (UNI-CEUMA) to prepare a composite sample.

2.2. Physicochemical Characterization of Lagoon Water (Adsorbate)

Physical and chemical analyses of the lagoon water were performed, including nitrate, nitrite, electrical conductivity, hydrogen potential (pH), and turbidity. A benchtop photometer was used to measure the nitrate and nitrite concentrations. The electrical conductivity was measured using a bench meter. To measure the pH, instrumental measurements were performed using a portable digital pH meter. The turbidity analyses were performed using a bench turbidimeter. All readings were performed in quintuplicate, and the analytical procedures were based on standard methods for water and wastewater. AWWA APHA WEF [15].

2.3. Preparation of Adsorptive Material

2.3.1. Pineapple Crown

To prepare the adsorptives, 12 pineapple (*Ananas comosus*) crowns were detached from the leaves, washed, cut, and dried in an oven at 80 °C for 12 h. After drying, they were ground in an industrial processor (ULTRA) and sieved (ABRONZINOX) to obtain a granulometry of 0.32 to 0.6 mesh, resulting in a total substrate of 189.6 g [16].

2.3.2. Chitin and Chitosan Preparation

Chitin was obtained in stages according to the methodology recommended by Moura et al. [17]: pretreatment, demineralization, deproteinization, deodorization, and drying. Therefore, 5 kg of shrimp shells were used for laboratory and pilot tests. Chitosan was produced by chitin deacetylation, followed by reaction with 45% NaOH solution (42.3%) under stirring and heating. The reactor was maintained at 130 °C for 2 h. At the end of the reaction, excess reagent was removed [18]. Chitosan was obtained after deacetylation and was then purified, precipitated, and neutralized [18].

2.4. Characterization of Adsorbent Support

2.4.1. Morphological Characterization

Photomicrographs of the treated biomass samples were obtained using scanning electron microscopy (SEM; JEOL model JSM5310, Tokio, Japan), based on the secondary detection of electrodes after depositing the sample on a gold substrate. The particle sizes and surface visualizations were obtained at magnifications of up to 5000×. The analyses were performed at the Federal Institute of Bahia (IFBA).

2.4.2. Structural Characterization

The amorphous and crystalline regions of the samples were characterized by energy-dispersive X-ray diffraction spectroscopy (XRD; Shimadzu Corp., model XRD-6000), with a CuK radiation source radiamo-delo XRD-6000 fraction from Eram caramA. Scans were completed over a range of 2 values from 10 to 90, with a scan speed of 0.05° min^{-1} [14] at the Instituto Federal da Bahia (IFBA). Characterization, in terms of identifying and/or determining the structural characteristics, mainly with regard to the functional groups and bonds present in the samples, was carried out using Fourier-transform infrared spectroscopy (FTIR) (Nicolet 6700-FTIR) [19]. These analyses were conducted at the Institute of Technology and Research (ITP).

2.5. Treatment Conditions

To obtain the treatment conditions, the methodology of the fractional factorial experimental design matrix was used, which consisted of two levels (−1, +1), two axial points (−1.41, +1.41), and three central points for 11 experiments, where time and amount of substrate content were the independent variables (Table 1). The pH, conductivity, and turbidity parameters, in addition to the contents of nitrogen compounds, ammonia, nitrate, and nitrite, were dependent variables and analyzed according to APHA (American Public Health Association) (APHA, 2012) [15]. The experimental matrix, as well as the analysis of the results, were processed with the Statistic software, Version 8.0.

Eleven Erlenmeyer flasks (250 mL) were used; 200 mL of the sample was added to each Elernmeyer flask. The samples were placed in a rotating incubator at 70 °C and incubated according to the times stipulated in the matrix. To avoid loss, the containers were covered during the entire process.

Subsequently, all samples were filtered. The solid portion was dried in an oven at 80 °C for approximately 5 h and morphology analyzed in SEM. In the liquid phase, 1 mL of the sample was removed and diluted in 100 mL of distilled water to determine the pollutant concentrations. All measurements were performed in triplicate.

Table 1. Experimental matrix containing coded and real values of the independent variables of the experimental design Central Compost Rotational (CCR).

Runs	Independent Paramenters			
	Codes Values		Reals Values	
	Substrate (g)	Time (d)	Substrate (g)	Time (d)
1	−1	−1	8	4
2	+1	−1	22	4
3	−1	+1	8	26
4	+1	+1	22	26
5	−1.41	0	5	15
6	+1.41	0	25	15
7	0	−1.41	15	0
8	0	+1.41	15	30
9	0	0	15	15
10	0	0	15	15
11	0	0	15	15

2.6. Toxicity Assessment

The acute toxicities of the liquid, solid, and treated wastes were evaluated using an in vivo model (*Tenebrio molitor* larva), which allowed for a comparison with the immune system and may provide some indication of the toxicity in this area. Ten microliters of the phosphate buffer solution (PBS) control buffer and lagoon water samples were inoculated with 10 larvae and properly packed into the identified plates. The larvae were maintained at 30 °C for 10 d; dead or non-stimulation-responding larvae were quantified at 24 h intervals.

2.7. Statistical Analysis

For physicochemical analyses, the results were expressed as the mean ± standard deviation (SD) using Microsoft Excel Professional Plus 2019. Significant variables in the form process were evaluated using the ANOVA methodology, considering a confidence level of 95% ($p < 0.05$) in the Grand Prism 8 software.

The data generated in the toxicity test using the *T. molitor* larvae were analyzed using the GraphPad Prism version 5.0 software, with a significance level of $p < 0.05$. The survival curve was plotted based on the Kaplan–Meier analysis; the results were analyzed using the log-rank test.

3. Results

3.1. Physicochemical Characterization of Crude Adsorbate

Samples were collected from Laguna da Jansen. The analyses were carried out to characterize the liquid residue in terms of the nitrogen compound contents, conductivity, turbidity, and pH. Table 2 presents the pH as approximately neutral, the only parameter that conformed to the values stipulated by the CONAMA/2005 legislation [20]. The turbidity parameter was 153NU, fourfold higher than that in the legislation, similar to the nitrogen compounds, where ammonia was 13.57mg/NL^{-1}, nitrate was 4.95 mg/L, and nitrite was 0.23 mg/L.

The Ministry of Health, in its Consolidation Ordinance No. 5, does not stipulate values for the electrical conductivity, nor do these values appear in the CONAMA resolution 357/2005 [20,21]; however, for natural water, conductivity values range from 10 to 100 μS/cm. In environments polluted by domestic sewage, these values can reach 1000 μS/cm [20].

Table 2. Physicochemical characterization of the crude adsorbate used for the treatment of water from Laguna da Jansen.

Physicochemical Parameters	Unit	CONAMA 357/2005	Gross Adsorbate
pH		6.5–8.5	6.65 ± 0.89
Conductivity	(μS/cm)	***	845.5 ± 2.61
Turbidity	(UNT)	40	153 ± 2.24 **
Ammonia	(mg/NL^{-1})	5	13.57 ± 1.86
Nitrate	(mg/L)	0.4	4.95 ± 0.15 **
Nitrite	(mg/L)	0.07	0.23 ± 0.00 **

** $p < 0.01$. *** no reference value.

When performing statistical data analysis and comparisons with the values provided in the CONAMA/357 resolution [20], we observed a significant statistical difference in the turbidity, nitrate, and nitrite parameters ($p < 0.01$). This demonstrates the value above that is determined as acceptable by law.

3.2. Characterization of Adsorptive Supports

Figure 2 shows the morphological and structural characterizations of the residues used as adsorptive supports. In the FTIR characterization, typical adsorptive spectra were observed (Figure 2A). In the spectrum, we observed a broad band in the range of 3400–3500 cm^{-1}, characterizing O-H bond stretching of the phenolic groups or carboxylic acids [22]. The band at 1634 cm^{-1} was attributed to the C=O vibrations of carboxylates originating from organic matter [23]. The region between 2850 and 3000 cm^{-1} was attributed to C-H bonds in alkanes, between 1620 and 1680 cm^{-1} to C=C bonds in alkenes, and between 1000 and 1400 cm^{-1} to C-F bonds in alkyl halide.

The diffractogram in Figure 2C shows that the adsorptive material had crystalline and amorphous regions. In the SEM images (Figure 2E) at 5000× magnification, "pits" or a surface area could be observed, where the material attracted to the surface of the adsorptive was lodged.

Typical chitin and chitosan spectra were observed based on the FTIR analyses (Figure 2B). Differences between these materials were observed in the region from 3000 to 3600 cm^{-1}, in which the OH and NH elongation bands overlapped. In the chitin spectrum, two bands were observed at 3200 and 3450 cm^{-1}, which could be attributed to NH bonds and hydrogen in the amide groups, respectively. These bands were absent in the chitosan spectrum. The region from 1500–1700 cm^{-1} presented angular deformation bands of C=O (1650 cm^{-1}) and N-H (1550 cm^{-1}). In the chitin spectrum, the intensities of these bands were essentially identical, whereas the intensity of the C=O band significantly decreased in chitosan, indicative of chitin deacetylation.

The diffractogram (Figure 2D) shows that chitosan had a structure with crystalline and amorphous regions. Crystalline regions were observed at angles of 20°, 32°, 45°, and 78°. "Pits" were observed in the microphotographs of chitosan (Figure 2F) at 5000× magnification, i.e., small holes where materials attracted to the chitosan surface were lodged. Based on these characteristics, chitosan can be used as an adsorptive, owing to its structure and morphology [24].

Each of these methods (photographic and diffractometric) have advantages and disadvantages. The photographic technique instantaneously records the entire diffraction pattern and is excellent for initially locating diffraction maxima; however, it does not excel at producing quantitative data, owing to problems with the photometric reading of the data. In contrast, the diffraction counter directly provides quantitative results; however, there may be loss of diffraction points, which provides adequate conditions for obtaining the diffractogram [25].

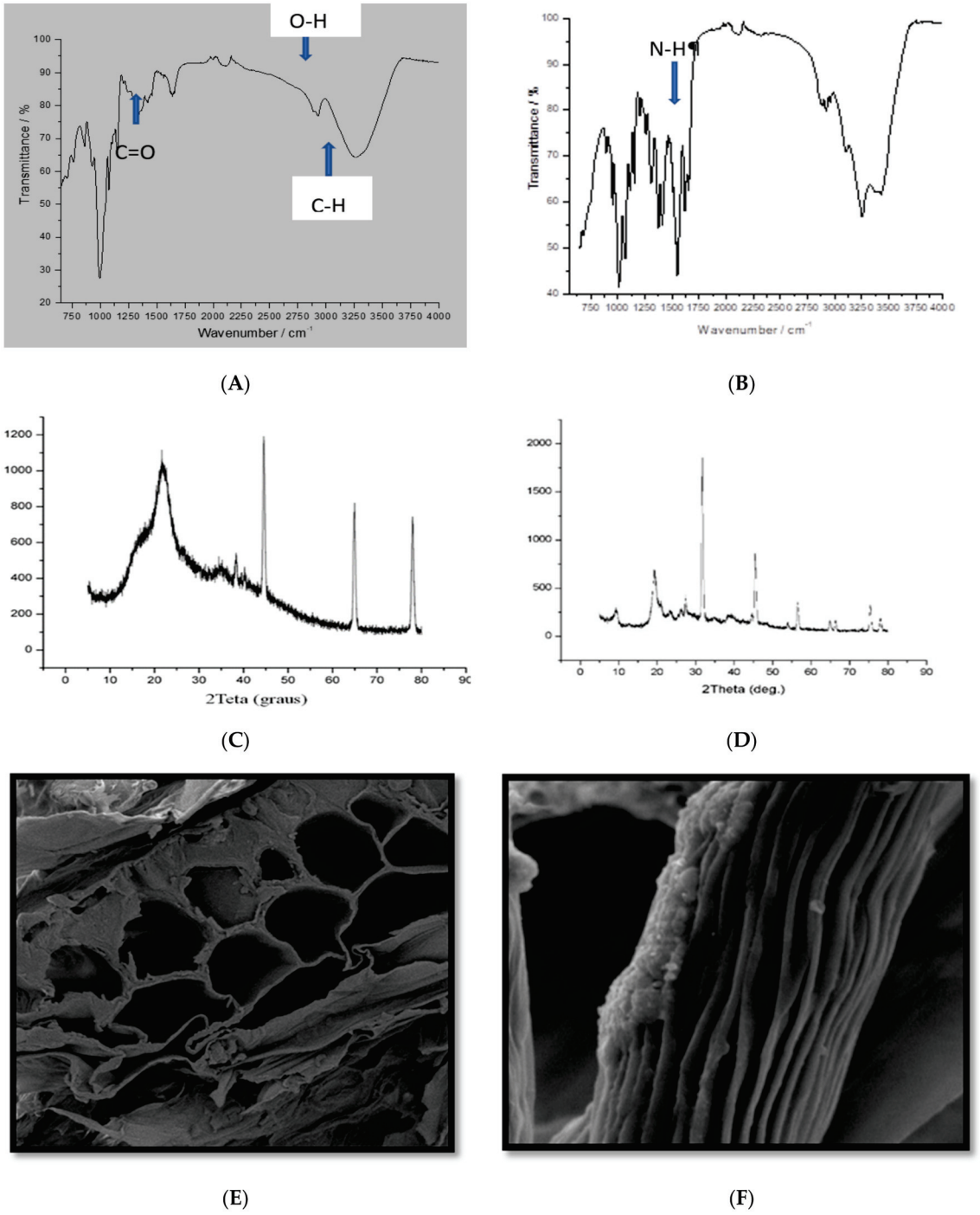


Figure 2. Characterization of the (**A**) pineapple crown and (**B**) chitosan in terms of the Fourier-transform infrared spectroscopy (FTIR) analyses. X-ray diffraction analyses of the (**C**) pineapple crown and (**D**) chitosan. Scanning electron microscopy (SEM) analyses of the (**E**) pineapple crown and (**F**) chitosan (500×).

3.3. Lagoon Water Treatment Conditions

Optimal water treatment conditions were established using the factorial planning methodology with the response surface graph in the Statistic software (version 8.0) (Figure 3A–F).

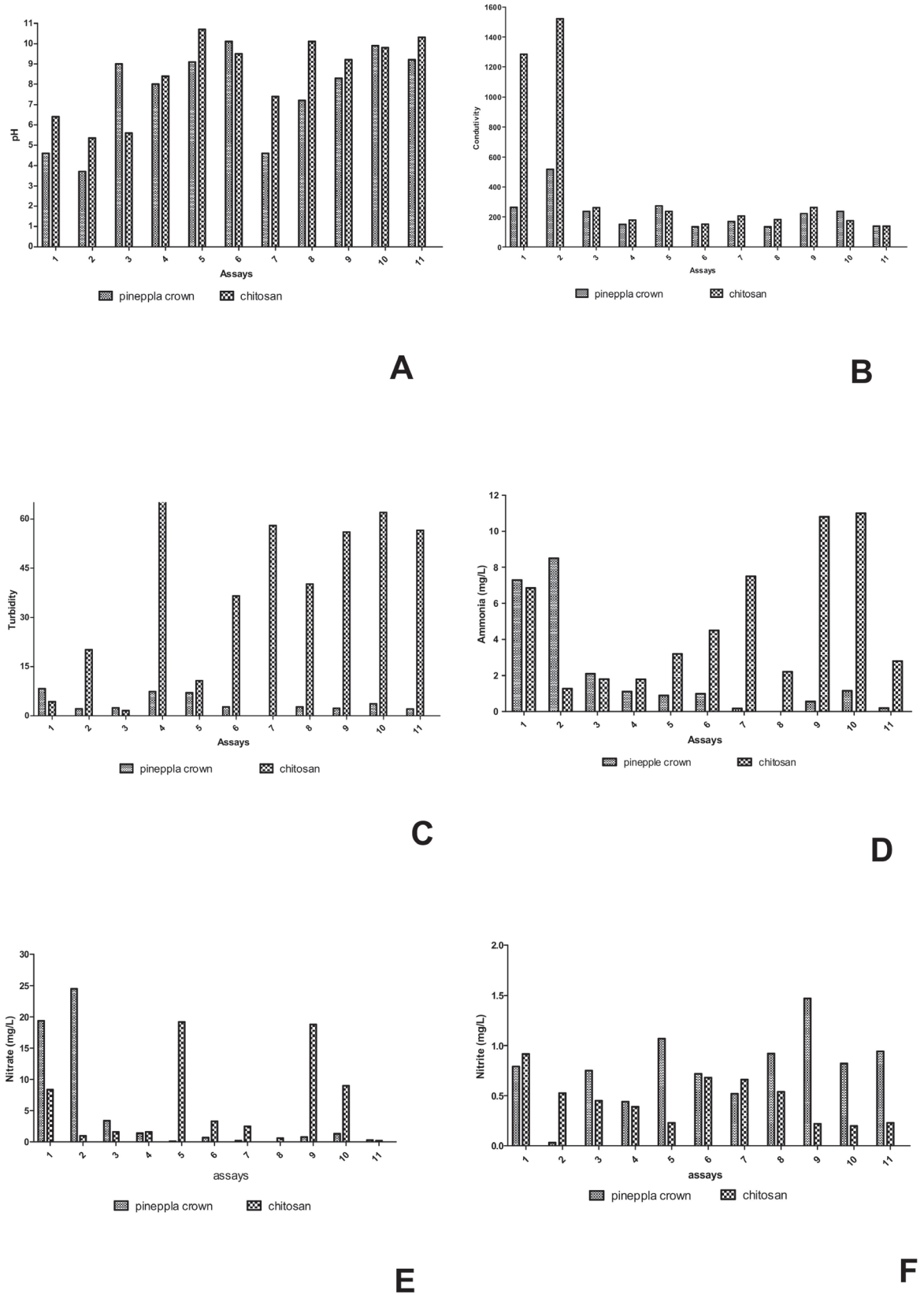


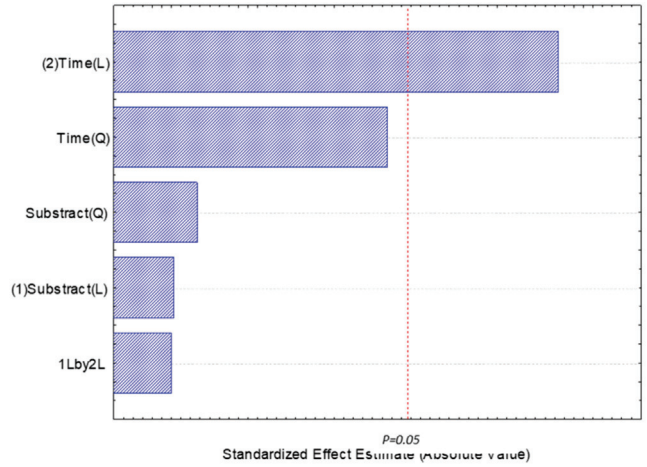
Figure 3. pH (**A**), conductivity (**B**), turbidity (**C**), ammonia (**D**), nitrate (**E**), and nitrite (**F**) values obtained in the tests using the conditions established in the rotational composite central experimental design (DCCR).

After the experiment, we observed that the lowest values in relation to the parameters tested in the adsorbate occurred at 15 g of adsorption during the period of 30 days of Experiment 8 when the pineapple crown was used as the adsorbent, based on the central rotational composite experimental design (DCCR).

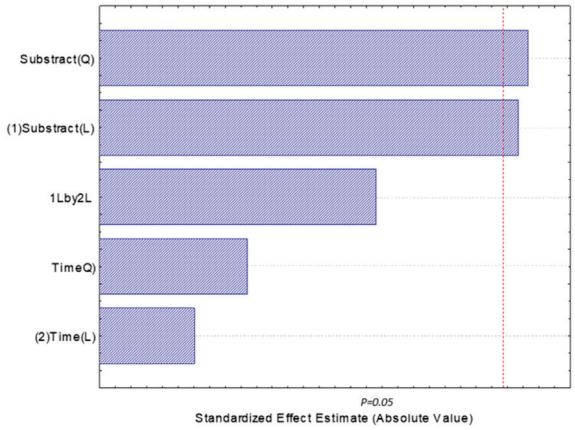
The pH, conductivity, and turbidity values in the absorbate were 6.65, 845.5 µS/cm, and 153NU. After the treatment of wastewater using the adsorptive pineapple crown, a decrease in pH value to 7.2 was observed, which remained around neutral, as well as an increase in conductivity to 135 µS/cm and a decrease in turbidity to 3.70NU.

The ammonia, nitrate, and nitrite contents in the crude absorbate were 13.57 mg/NL^{-1}, 4.95 mg/L, and 0.23 mg/L, respectively. After the treatment using the pineapple crown as the adsorbent, according to the conditions previously established, a decrease in nitrogen compounds was observed, with 00 mg/L of ammonia, 00 mg/L of nitrate, and 0.92 mg/L of nitrite. L was similar to the values provided in the CONAMA 357/2005 legislation. Although lower nitrite values were observed in the absorbate treated with chitosan, it was also observed that nitrite and ammonia values were found, which suggested that total conversion by the bacterial group did not occur.

After analyzing the variables, according to Pareto's graphs, we observed that when the substrate was pineapple crown, the time variable was the influencing variable in its linear form (Figure 4A). In contrast, when chitosan was used, the influencing variable was the substrate in linear and quadratic forms (Figure 4B).



(**A**)



(**B**)

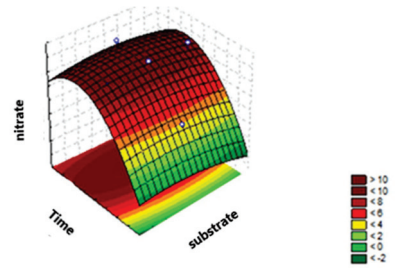
Figure 4. Pareto chart representing the variables that influenced the lagoon water treatment process using residues of (**A**) pineapple crown and (**B**) chitosan as the absorbates.

To generate the response surface from the Pareto graph, the predicted model of the pH variable was generated as follows:

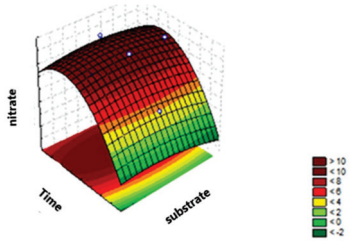
$$\text{Nitrate} = 9.30 + 4.47\ x^2 \text{ and} \quad (1)$$

$$\text{Nitrite} = 57.16 + 31.90\ x^1 - 38.81\ x^2 \quad (2)$$

Based on the predicted model, we generated a surface response graph to determine the trends of the adsorbent values and the time for adsorbate treatment (Figure 5).



(**A**)



(**B**)

Figure 5. Response surface indicating the trend of the optimal values when treating the lagoon water with adsorbents of (**A**) vegetable and (**B**) animal origins.

When the adsorptive had a vegetable origin (pineapple crown), we observed a region with a higher concentration in relation to the nitrate parameter (i.e., the dark red areas in Figure 5A) and a lower concentration region (i.e., the red areas in Figure 5A). These regions showed a trend toward optimal time and substrate values for the nitrate variable. From this perspective, after the experimental period, we observed that 15 g of the adsorbent in the 30 d period, as established in Experiment 8 of the DCCR, presented the lowest nitrate values, compared with the other tested conditions.

When the evaluated applicator was of animal origin, the influence of the time and substrate on the nitrite variable was evident in the experimental planning. Figure 5B shows the trend of the nitrite response variable. There was a region with a higher concentration in relation to the nitrite parameter (i.e., dark red areas in Figure 5B) and a lower concentration region (i.e., light red areas in Figure 5A). Thus, we could verify the existence of an optimal region for low nitrite values, i.e., a ring-shaped band in the light-red color near 0. The optimal nitrite variable values in the experimental design were 8 g of adsorptive and 26 d of treatment.

We noted that the nitrate and nitrite contents found in water constituted a preponderant factor for analyzing the physicochemical properties of water. For example, the higher the contents of these substances, the lower the water quality [26,27].

The response surface methodology consists of a collection of statistical and mathematical techniques useful for developing, improving, and optimizing treatment processes. It also has important applications in planning, developing, and formulating new products, as well as in improving existing projects and products [28,29]. In this work, the methodology was used to optimize the treatment process of water rich in nitrogen compounds, reducing treatment cost and time.

The microphotograph of the post-treatment substrate showed wear of the pits of both biomasses. However, the plant biomass was a little more preserved. It was possible to observe dirt particles adsorbed on the surface of both biomasses, showing their ability to adsorb particulates.

3.4. Toxicity Assessment

When evaluating the survival percentage (Figure 6), we observed that the value for larvae in pure water was 20%. When the water was treated with a vegetable adsorbent, there was a survival percentage of 70% for the larvae of *T. molitor*. In the treatment with an animal adsorbent (chitosan), the survival percentage decreased to 40%.

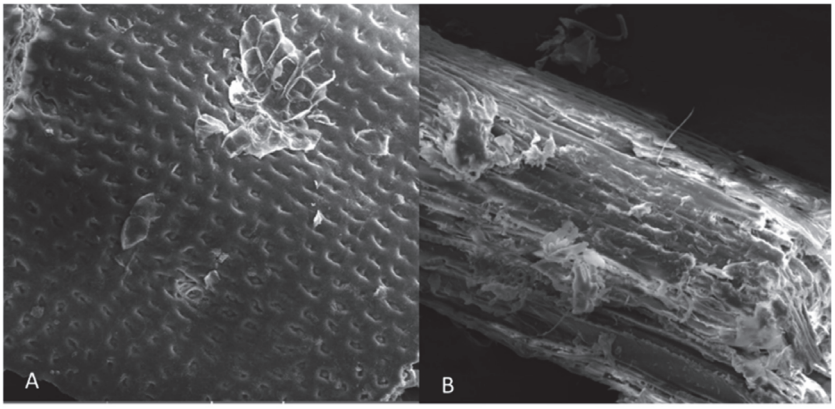


Figure 6. Microphotography of the plant adsorptive from the pineapple crown (**A**) and chitosan (**B**) after the treatment of polluted pond water with nitrogenous compounds. 500× magnification.

In Figure 7 it can be observed the difference in the survival percentages was confirmed based on statistical analyses using the log-rank test, where a statistically significant difference was observed in the survival percentage of larvae subjected to untreated water and water treated with an adsorbent of animal origin, compared with the control group (p = 0.026 and 0.035, respectively).

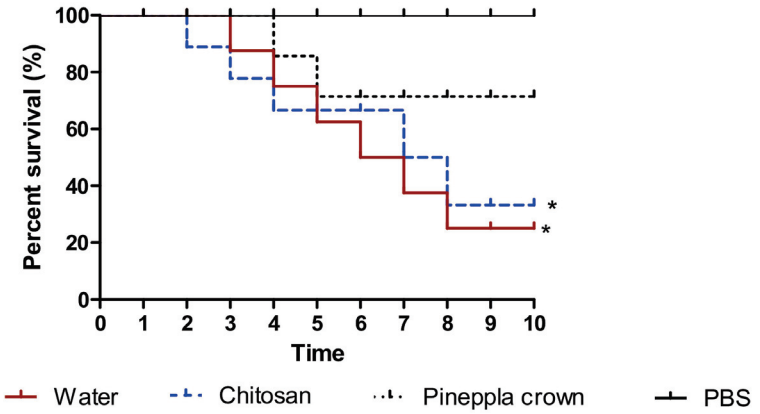


Figure 7. Toxicity evaluation of the treatments using different adsorptives in *Tenebrio molitor* larvae under conditions established by the experimental design. * Significant statistical difference in relation to the control.

4. Discussion

The characterization of the lagoon water showed that, despite approximately neutral pH values, i.e., within the parameter values provided by the CONAMA 357 legislation, the turbidity, nitrate, and nitrite parameters were high when compared to those of the established values. According to da Silva et al. [30], changes in water quality parameters indicate a need for treatment, especially in urban waterbodies or those used by inhabitants for recreation. Some studies have demonstrated that urban lakes suffer from human interference, such as sewage discharge, boat traffic, and waste disposal. These activities interfere with the water quality, increasing the levels of organic compounds, such as nitrogen and phosphorus, which facilitate eutrophication processes [30,31]. All changes in water quality parameters indicate the need for treatment.

The characterization of the adsorptive support is important because it allows us to understand the nature of the morphology and the chemical compounds that form the adsorptive matrix. The biomasses used in this study showed adequate characteristics for optimal adsorptive support, with a low cost and ease of acquisition.

Several characterization methodologies can be used to identify the crystallinity, which is important for understanding the behavior of organic materials of a cellulosic nature, such as pineapple crowns and chitosan, as they have different crystalline and amorphous regions, as identified in the XRD-generated diffractogram. These regions demonstrate that the biomasses present have a potentially adsorptive area, owing to their purity, as reflected in the crystalline areas. Therefore, plant biomass (pineapple crown) was more suitable because it has more crystalline regions than that of chitosan, which has a semi-crystalline nature. Some studies have attributed this characteristic to strong interactions between the hydrogen bonds, which chemically compose the cellulose [16,32,33].

An adsorptive is commercially attractive when it has certain characteristics, such as an extensive internal surface area, which must be accessible through pores that are sufficiently large to allow the adsorption of the particles of interest [10]. The morphology of the pineapple crown, as identified by SEM, presented a surface with many openings, concavities, and exposed pores, known as "pits", which provided a greater area for adsorbate deposition, thus ensuring a higher adsorption rate. These spaces were attributed to the fiber configuration of the carbohydrate cellulose. Meurer and Silva [33] and Miranda et al. [16] reported similar results; they analyzed the morphology of different materials of lignocellulosic origin. In contrast, the chitosan morphology presented a spiral shape, with limited openings and concavities, which yielded a surface area more limited by the absence of the "pits".

The FTIR spectra of the pineapple crown showed a large number of peaks, indicating a highly complex material. Machado et al. [34] used activated carbon for the adsorption of phenol and bisphenol A. Miranda et al. [16] characterized the adsorptive in terms of its chemical characteristics, identifying substances such as cellulose, hemicellulose, lignin, extractives, and ash. Vaz Junior [35] stated that such compounds are characteristic of lignified plant biomass. The spectrum of chitosan revealed polysaccharides (carbohydrates); when these materials experience hydrolysis (contact with water), they transform into natural polymers.

The characterization carried out after the treatment proposed in the experimental design showed that, in terms of the chemical analyses, the adsorptive method was efficient in improving the quality of most parameters in the adsorbate.

We observed the influence of a pH value of 7.0 on the reduction of nitrogenous compounds; in neutrality, the residue surface was characterized by enhanced interactions with cations. This is a common behavior for lignocellulosic materials, such as pineapple crowns, whose surface agglomerates have not been charred. The decrease in conductivity and turbidity values also influence bacterial activity, as they favor cation exchange and allow the incidence of sunlight, favoring the activity of chlorophyll organisms and thus keeping dissolved O_2 available for the metabolic activity of aerobic bacteria. Albina et al. [36] reported that absorptivity, as it contains substances of basic character, such as glucose and lignin, increases the pH, as observed during treatment. This is a factor that influences

bacterial activity, as it favors growth and metabolic activity, which consequently reduces nitrate to nitrite. Nitrogen compounds, such as nitrate, nitrite, and ammonia, are the main forms of nitrogen associated with water contamination [36].

The accumulation of these compounds favors eutrophication processes; thus, previous studies have already reported increasing levels of pollution, which can even compromise human health. High levels of nitrite in the blood induce the formation of metal hemoglobin, causing several neurological dysfunctions [37,38]. Although both treatments showed a decrease in the values obtained for the nitrogen compounds, we found that when the adsorptive substrate was pineapple crown, the reduction was more significant than that when using chitosan. (The basic pH favors the growth of denitrifying bacteria.) This group of bacteria participates in the conversion of nitrite to nitrate, followed by the formation of free nitrogen [38].

According to Peng et al. [39], the adsorption technique has been used for a long time, predominantly with mineral adsorptive (activated carbon); however, more recent studies have demonstrated the efficiency of natural substrates or bio-sorbents, as they are renewable, available in large quantities, and cheaper when compared to other materials, making the process economically viable [40]. In this context, several researchers have investigated the removal of various pollutants using natural materials, such as chicken feathers [41], banana skins [42], potato skins [43], pumpkin skins [44], orange peels [42], leaf dust of jackfruit [45], *Moringa oleifera* seed powder [46], brown macroalgae [47], and shell [48], as low-cost bio-sorbents.

The effectiveness of biomass suggests that it is useful as a substrate in continuous batch water treatment in fixed-bed reactors. Some studies have demonstrated the possibility of staggering water treatment using natural biomass through continuous batch fixed-bed reactors [49–51].

Evaluations of the water quality based on the *T. molitor* larvae can reveal the toxicity of the lagoon water (resulting from nitrogen compound contents), as well as the treatment efficiency. Based on the toxicity tests, the increase in the larvae survival percentage may have been directly related to a higher nitrogen compound content, considering that the plant-derived adsorbent was more efficient in reducing the content of these compounds than that of the animal adsorbent. Toxicity is a highly important parameter in water quality evaluations because, based on evaluations of living organisms, we can observe whether the accumulation of xenobiotic compounds in water influences the biology of the organism [52].

5. Conclusions

Based on our results, both adsorptives were efficient in the adsorptive treatment; however, the vegetal biomass, pineapple crown, was more efficient in the removal of organic contaminants in waterbodies compared with that of the animal biomass and chitosan. An alternative is its use in treatment plants for the removal of toxic compounds in water and effluents. The use of these biomass types represents a technique for reducing the accumulation of waste in dumps and sanitary landfills. It is an economical and viable alternative because no biomass treatments are required; they are a by-product of the consumption of the original material and have no commercial or domestic value, which reflects the final value of this process.

Author Contributions: T.F.N.—methodology; P.L.S.G.—methodology; C.D.d.S.P.—methodology; C.S.D.S.—methodology; F.N.S.C.—methodology; I.N.S.—methodology; R.R.d.J.T.—statistical analysis; A.S.d.S.A.—conceptualization and methodology; M.C.G.—review paper; W.C.G.—conceptualization and methodology; D.F.d.S.—software; M.R.C.S.—conceptualization and methodology; F.B.S.—methodology; Á.S.L.—conceptualization and methodology; E.d.B.G.—conceptualization and methodology; R.d.C.M.d.M.—conceptualization, writing, and original draft preparation. All authors have read and agreed to the published version of the manuscript.

Funding: This research was funded by the Fundação de Amparo a Pesquisa do Maranhão (FAPEMA). Process number UNIVERSAL-00810/19.

Data Availability Statement: All research data are presented in the article.

Acknowledgments: The authors thank Ceuma University for providing infrastructure and logistical support.

Conflicts of Interest: The authors declare no conflict of interest.

References

1. Haughton, G.E.; Hunter, C. Sustainable Development and Geographical Equity. In Proceedings of the Annual Conference of the Association of American Geographers, Chicago, IL, USA, 24–28 February 1994.
2. Harphan, T.; Vaughan, P.; Lusty, L. *In the Shadow of the City: Community Health and the Urban Poor*; Oxford University Press: Oxford, UK, 1998.
3. Tucci, C.E. *Urbanização e Recursos Hídricos*; Análise Estratégica; Instituto de Pesquisas Hidráulicas da Universidade Federal do Rio Grande do Sul: Águas do Brasil, São Paulo, Brazil, 2007.
4. SNIS; Sistema Nacional de Informações Sobre Saneamento [SNS]; Secretaria Nacional de Saneamento. Informações e Indicadores Municipais Consolidados. 2016. Available online: http://app4.cidades.gov.br/serieHistorica/# (accessed on 13 August 2019).
5. Silva, V.E.C.; Franco, D.; Fonseca, A.L.; Fontes, M.L.; Donnangelo, A.R. Space-time evolution 59 of the trophic state of a subtropical lagoon: 60 Lagoa da Conceição, Florianópolis Island of 61 Santa Catarina, Brazil. *Scielo Anal.-62 Rev. Bras. De Recur. Hídricos* **2017**, *22*, 1–6317.
6. Rojas, M.O.I.; Costa Neto, J.d.J.; Barbiere, R.; Siqueira, L.F.S. Avaliação físico-química da água da Laguna da Jansen. *Acta Tecnol.* **2013**, *8*, 19–24. [CrossRef]
7. Silva, K.; Guimarães, T.; Wasserman, J.C. Distribuição espacial da concentração de nutrientes em sedimentos na Laguna hipersalina de Araruama—RJ, Brasil. *Geochim. Bras.* **2019**, *33*, 16–27. [CrossRef]
8. McLannes, A.S.; Quigg, A. Near-annual fish kills in small embayments: Casual vs. causal factors. *J. Coast. Res.* **2010**, *26*, 957–966. [CrossRef]
9. Souza, R.S.; Lima, L.M.R.; Silva, V.L.M.M. Adsorção de óleo diesel em sistema de leito diferencial com biomassa bagaço de cana-de-açúcar. *Rev. Eletrônica Mater. E Process.* **2011**, *6*, 123–126.
10. Machado, C.R.; Saggioro, E.M.; Silva, Y.G.L.; Pereira, L.P.d.S.; Campos, J.C. Avaliação da adsorção de fenol e bisfenol A em carvões ativados comerciais de diferentes matrizes carbonáceas. *Rev. Ambient. Água Taubaté* **2015**, *10*, 915–927.
11. IBGE. Levantamento Sistemático da Produção Agrícola (LSPA). 2010. Available online: https://biblioteca.ibge.gov.br/index.php/biblioteca-catalogo?view=detalhes&id=76 (accessed on 12 September 2021).
12. Baidhe, E.; Kigozi, J.; Mukisa, I.; Muyanja, C.; Namubiru, L.; Kitarikawe, B. Unearthing the potential of solid waste generated along the pineapple drying process line in Uganda: A review. *Environ. Chall.* **2020**, *2*, 100012. [CrossRef]
13. IBGE. *Culturas Temporárias e Permanentes*; Instituto Brasileiro de Geografia e Estatística: Rio de Janeiro, Brazil, 2015.
14. Gildberg, A.; Stenberg, E. A new process for advanced utilization of shrimp waste. *Process Biochem.* **2001**, *36*, 809–812. [CrossRef]
15. APHA (American Public Health Association); AWWA (American Water Works Association); WPCF (Water Pollution Control Federation). *Standard Methods for the Examination of Water and Wastewater*, 21st ed.; American Public Health Association: Washington, WA, USA, 2012.
16. Miranda, R.C.M.; Neta, J.L.V.; Ferreira, L.F.R.; Gomes, W.A.; do Nascimento, C.S.; Gomes, E.B.; Mattedi, S.; Soares, C.M.F. Pineapple crown delignification using low-cost ionic liquid based on ethanolamine and organic acids. *Carbohydr. Polym.* **2018**, *206*, 302–308. [CrossRef]
17. Moura, C.; Muszinski, P.; Schmidt, C.; Almeida, J.; de Pinto, L.A.A. Quitina Quitosana produzidas a partir de resíduos de camarão e siri: Avaliação do processo em escala piloto. *Rev. Ciências Exatas Eng.* **2006**, *16*, 37–45.
18. Soares, N.M. Obtenção e purificação da quitosana a partir de resíduos de camarão em escala piloto. In Proceedings of the Encontro de Iniciação Científica Latino-Americano, São José dos Campos, Brazil, 15–18 October 2002.
19. UFRGS. Espectroscopia No Infravermelho Com Transformada de Fourier (FTIR). 2019. Available online: http://www.ufrgs.br/lapol/ftir.htm (accessed on 16 September 2019).
20. Brasil, C.D.M. *Resolução CONAMA n. 357, de 17 de março de 2005*; Diário Oficial da União: Brasília, Brazil, 2005; pp. 58–63.
21. Silverstein, R.M.; Bassler, G.C. *Identificação Espectrométrica de Compostos Orgânicos*, 5th ed.; LTC: Guanabara, Brazil, 2006.
22. Pimentel, P.M.; Silva, C.N., Jr.; Melo, D.M.A.; Maldonado, G.; Henrique, D.M. Caracterização e uso de xisto para adsorção de chumbo (II) em solução. *Cerâmica* **2006**, *52*, 194–199. [CrossRef]
23. Vedula, S.S.; Yadav, G.D. Wastewater treatment containing methylene blue dye as pollutant using adsorption by chitosan lignin membrane: Development of membrane, characterization and kinetics of adsorption. *J. Indian Chem. Soc.* **2021**, *99*, 100263. [CrossRef]
24. Ahmed, H.B.; Helal, M.H.; Abdo, M.H.; Fekry, M.M.; Abdelhamid, A.E. Disarmament of micropollutants from wastewater using nylon waste/chitosan blended with algal biomass as recoverable membrane. *Polym. Test.* **2021**, *104*, 107381. [CrossRef]
25. Zhang, J.; Wang, Y.; Zhang, L.; Zhang, R.; Liu, G.; Cheng, G. Understanding changes in cellulose crystalline structure of lignocellulosic biomass during ionic liquid pretreatment by XRD. *Bioresour. Technol.* **2014**, *151*, 402–405. [CrossRef] [PubMed]
26. Piratoba, A.R.A.; Ribeiro, H.M.C.; Morales, G.P.; Gonçalves, W.G. Caracterização de parâmetros de qualidade da água na área portuária de Barbacena, PR. *Rev. Ambiente Água* **2017**, *12*, 435–456. [CrossRef]

27. Wilson, P.L. *Water Quality Nots: Water Clarity (Turbidity, Suspended Solids, and Color)*; University of Florida: Gainesville, FL, USA, 2010.
28. Kou, S.; Peters, L.; Mucalo, M. Chitosan: A review of molecular structure, bioactivities and interactions with the human body and micro-organisms. *Carbohydr. Polym.* **2022**, *282*, 119132. [CrossRef]
29. Musarurwa, H.; Tavengwa, N.T. Advances in the application of chitosan-based metal organic frameworks as adsorbents for environmental remediation. *Carbohydr. Polym.* **2022**, *283*, 119153. [CrossRef]
30. Cavalcanti, K.G.S.; da Silva, D.F.; Lima, N.S.; Miranda, R.C.M.; Neto, W.R.N.; Silva, M.R.C. Quantitative vulnerability assessment of Corda river water basin: Impacts of seasonality on water quality in the State of Maranhao. *Ciência E Nat.* **2020**, *42*, e2. [CrossRef]
31. Cavalcante, G.H.; Vieira, F.; Abouleish, M.; Atabay, S.; Campos, E.; Bento, R. Environmental aspects of semi-closed lagoons in the Sharjah coastline during spring/neap tides, southern Arabian/Persian Gulf coast. *Reg. Stud. Mar. Sci.* **2021**, *46*, 101896. [CrossRef]
32. Couson, D.O.; Richardson, J.F. *Chemical Engineering. Particle Technology and Separation Process*; Butteworth-Heinemann: New York, NY, USA, 2002; Volume 2.
33. Meurer, M.C.; Silva, F.V. Uso de Erva-mate Como Biossorvente de Contaminantes no Tratamento da Água. *Rev. Tecnol. Tendências* **2018**, *1*, 35–60. [CrossRef]
34. Sun, L.; Li, C.; Xue, Z.; Simmons, B.A.; Singh, S. Unveiling high-resolution, tissue specific dynamic changes in corn stover during ionic liquid pretreatment. *RSC Adv.* **2012**, *3*, 2017–2027. [CrossRef]
35. Vaz Junior, S. Towards a Renewable Brazilian Chemistry from Vegetal Biomass. *Rev. Virtual Química* **2017**, *9*, 238–247. [CrossRef]
36. Albina, P.; Durban, N.; Bertron, A.; Albrecht, A.; Robinet, J.-C.; Erable, B. Nitrate and nitrite bacterial reduction at alkaline pH and high nitrate concentrations, comparison of acetate versus dihydrogen as electron donors. *J. Environ. Manag.* **2020**, *280*, 111859. [CrossRef]
37. Másmela-Mendoza, J.E.; Lizarazo-Forero, L.M.; Aranguren Riaño, N.J. Bacterias nitrificantes cultivables de la zona limnética del lago de Tota, Boyacá. *Rev. UDCA Actual. Divulg. Científica* **2019**, *22*, 1–10.
38. Costa, D.D.; Kempka, A.P.; Skoronski, E. A contaminação de mananciais de abastecimento pelo nitrato: O panorama do problema no Brasil, suas consequências e as soluções potenciais. *REDE Rev. Eletrôn. Prodema* **2017**, *10*, 49–61. [CrossRef]
39. Peng, X.; Hu, X.; Fu, D.; Lam, F.L. Adsorption removal of acid black 1 from aqueous solution using ordered mesoporous carbon. *Appl. Surf. Sci.* **2014**, *294*, 71–80. [CrossRef]
40. Ojha, A.K.; Bulasara, V.K. Adsorption characteristics of jackfruit leaf powder for the removal of Amido black 10B dye. *Environ. Prog. Sustain. Energy* **2014**, *34*, 461–470. [CrossRef]
41. Mittal, A.; Thakur, V.; Gajbe, V. Adsorptive removal of toxic azo dye Amido Black 10B by hen feather. *Environ. Sci. Pollut. Res.* **2012**, *20*, 260–269. [CrossRef]
42. Annadurai, G.; Juang, R.-S.; Lee, D.-J. Use of cellulose-based wastes for adsorption of dyes from aqueous solutions. *J. Hazard. Mater.* **2002**, *92*, 263–274. [CrossRef]
43. Hoseinzadeh, E.; Samarghandi, M.-R.; McKay, G.; Rahimi, N.; Jafari, J. Removal of acid dyes from aqueous solution using potato peel waste biomass: A kinetic and equilibrium study. *Desalination Water Treat.* **2013**, *52*, 4999–5006. [CrossRef]
44. Çelekli, A.; Küçükgüner, B.; Bozkurt, H. Diazo dye sorption by Ni-modified pumpkin husk. *Desalinat. Water Treat.* **2016**, *57*, 25242–25255. [CrossRef]
45. Dalhatou, S.; Laminsi, S.; Pétrier, C.; Baup, S. Competition in sonochemical degradation of Naphthol Blue Black: Presence of an organic (nonylphenol) and a mineral (bicarbonate ions) matrix. *J. Environ. Chem. Eng.* **2018**, *7*, 102819. [CrossRef]
46. Shirani, Z.; Santhosh, C.; Iqbal, J.; Bhatnagar, A. Waste Moringa oleifera seed pods as green sorbent for efficient removal of toxic aquatic pollutants. *J. Environ. Manag.* **2018**, *227*, 95–106. [CrossRef] [PubMed]
47. Daneshvar, E.; Kousha, M.; Jokar, M.; Koutahzadeh, N.; Guibal, E. Acidic dye biosorption onto marine brown macroalgae: Isotherms, kinetic and thermodynamic studies. *Chem. Eng. J.* **2012**, *204*, 225–234. [CrossRef]
48. Wang, W.; Huang, G.; An, C.; Xin, X.; Zhang, Y.; Liu, X. Transport behaviors of anionic azo dyes at interface between surfactant-modified flax shives and aqueous solution: Synchrotron infrared and adsorption studies. *Appl. Surf. Sci.* **2017**, *405*, 119. [CrossRef]
49. Ahmad, A.; Khan, N.; Giri, B.S.; Chowdhary, P.; Chaturvedi, P. Removal of methylene blue dye using rice husk, cow dung and sludge biochar: Characterization, application, and kinetic studies. *Bioresour. Technol.* **2020**, *306*, 123202. [CrossRef] [PubMed]
50. Yao, X.; Ji, L.; Guo, J.; Ge, S.; Lu, W.; Cai, L.; Wang, Y.; Song, W.; Zhang, H. Magnetic activated bioc nanocomposites derived from wakame and its application in methylene blue adsorption. *Bioresourc. Technol.* **2020**, *302*, 122842. [CrossRef]
51. Oveisi, M.; Asli, M.A.; Mahmoodi, N.M. MIL-Ti metal-organic frameworks (MOFs) nanomaterials as superior adsorbents: Synthesis and ultrasound-aided dye adsorption from multicomponent wastewater systems. *J. Hazard. Mater.* **2018**, *347*, 123–140. [CrossRef]
52. Methneni, N.; GonzÃlez, J.A.M.; Van Loco, J.; Anthonissen, R.; de Maele, J.V.; Verschaeve, L.; Fernandez-Serrano, M.; Mansour, H.B. Ecotoxicity profile of heavily contaminated surface water of two rivers in Tunisia. Environ. *Toxicol. Pharmacol.* **2021**, *82*, 103550. [CrossRef]

Disclaimer/Publisher's Note: The statements, opinions and data contained in all publications are solely those of the individual author(s) and contributor(s) and not of MDPI and/or the editor(s). MDPI and/or the editor(s) disclaim responsibility for any injury to people or property resulting from any ideas, methods, instructions or products referred to in the content.

water

MDPI

Review

A Review on the Stability, Sustainability, Storage and Rejuvenation of Aerobic Granular Sludge for Wastewater Treatment

K. S. Shameem and P. C. Sabumon *

School of Civil Engineering, Vellore Institute of Technology, Chennai Campus, Chennai 600127, India
* Correspondence: pcsabumon@vit.ac.in; Tel.: +91-44-3993-1048; Fax: +91-44-3993-2555

Abstract: Aerobic granular sludge (AGS) is a recent innovative technology and is considered a forthcoming biological process for sustainable wastewater treatment. AGS is composed of the dense microbial consortium of aerobic, anaerobic, and facultative types of bacteria. The mechanism of AGS formation and its stability for long-term operation is still a subject of current research. On the other hand, AGS makes the treatment process sustainable in a cost-effective way. However, in order for AGS to be applied in a broader range of applications, there are several challenges to overcome, such as slow-speed granulation and the disintegration of AGS after granulation. Many factors play a role in the stability of granules. The storage of granules and the later use of them for granulation startup is a feasible method for reducing the time for granulation and maintaining stability. This review focuses on the granulation process and characteristics of AGS, granulation time and the stability of AGS under different conditions, the comparison of different storage methods of granules, and their recovery and rejuvenation. From this review, it is evident that additional research is required to assess the effectiveness of regenerated AGS after prolonged storage to promote AGS technology for commercial applications.

Keywords: aerobic granulation; stability; granule storage; recovery; reactivation; sustainability

Citation: Shameem, K.S.; Sabumon, P.C. A Review on the Stability, Sustainability, Storage and Rejuvenation of Aerobic Granular Sludge for Wastewater Treatment. *Water* **2023**, *15*, 950. https://doi.org/10.3390/w15050950

Academic Editors: Dibyendu Sarkar, Rupali Datta, Prafulla Kumar Sahoo and Mohammad Mahmudur Rahman

Received: 26 January 2023
Revised: 20 February 2023
Accepted: 23 February 2023
Published: 1 March 2023



Copyright: © 2023 by the authors. Licensee MDPI, Basel, Switzerland. This article is an open access article distributed under the terms and conditions of the Creative Commons Attribution (CC BY) license (https://creativecommons.org/licenses/by/4.0/).

1. Introduction

As a novel microbial community, aerobic granular sludge (AGS) is capable of eliminating nitrogen, carbon, and phosphorus, as well as other pollutants simultaneously [1,2]. AGS is regarded as being one of the most effective wastewater treatment technologies because of its high biomass retention, lower energy usage and footprint, and good settling [2–5]. AGS technology has been implemented in the full-scale treatment of municipal and industrial wastewater [5].

The discovery of granular sludge in anaerobic blanket systems was first reported in the 1980s [6]. Afterward, in the 1990s, carrier-less AGS was developed in sequential batch reactors (SBRs). Wastewater treatment technologies such as "Nereda" are substituted globally, for example, there are many mainstream full-scale systems using AGS technology for treating urban and industrial wastewater [5,6]. Doubtlessly, the AGS technology has a lot of advantages when compared with the conventional activated sludge process (ASP) [5,6]. Conventional ASP takes a longer time to treat wastewater and it requires a large land area to build the plant [6]. On the other hand, AGS technology requires less hydraulic retention time compared to ASP, resulting in a very compact reactor with a 75% reduced size. Moreover, other proven benefits include reduced wastewater treatment costs and energy requirements [7]. Because of these advantages, the scientific and engineering communities have become increasingly interested in AGS technology [5,8]. For example, scientists employ AGS technology for the full-scale treatment of highly toxic and refractory substances in wastewater, such as nitrogen, particulates, phenol, heavy metals, pharmaceutical compounds including antibiotics, and so on.

Sequencing batch reactors (SBRs) are a widely used wastewater treatment process worldwide and AGS is commonly grown in SBRs during wastewater treatment [7]. When compared to other wastewater treatment methods, only a single tank with a lesser area is needed for SBRs. SBRs have a defined cycle of operation that lasts for 3–6 h [7,9]. Each cycle of operation is further broken down into a filling period, a mixing or aeration period, a settling period, and an effluent drawing or decanting period [7]. Among the main features of SBRs are its operation cycle and time periods, which play a direct role in the formation of granules [7,10].

In full-scale reactors, the challenge of forming granular sludge from flocculent sludge is emphasized and also more time is required to start the granulation process [11]. The inoculation of reactors using granules that were formed in enduring treatment plants is one of the most intriguing options for reducing start-up time and expanding the applicability of AGS technology [11]. However, transporting AGS in wet form from one location to another may be time-consuming and expensive. As a result, questions concerning appropriate biomass storage methods and its reactivation become pertinent. Because of the variable circumstances over which granular sludge is dependent when being stored, the granule reactivation period after storage becomes unpredictable [11]. In this regard, difficulties must be overcome during granular storage on various substrates in order to retain microbial activity, structural stability, and integrity [11]. Several other characteristics must be properly explored before adopting the strategy of using stored and pre-formed AGS as an alternative for the start-up of the AGS in another reactor. Furthermore, the comparison and feasibility of various storage systems need to be understood thoroughly. Currently, there is no literature comparing different storage mechanisms and their reactivation times except for one study which is related to the review of storage and re-activation of AGS [12]. However, this study lacks a detailed analysis and comparison of different storage methods, the performance after reactivation, and its effectiveness as well as rejuvenation. In this context, the present review focuses on the granulation process and characteristics of AGS, granulation time, and stability of AGS under different conditions which include operational conditions, substrates used, types of inoculum sludge, and physical and chemical parameters leading to AGS disintegration. Additionally, the comparison of different storage methods of granules, their recovery, rejuvenation, and sustainability aspects of AGS are discussed. The work reviewed helps to advance the AGS technology by promoting more research in the storage and re-use of granules for sustainable wastewater treatment.

2. Aerobic Granulation Process

Aerobic granulation is the result of the interaction between the sludge particles and the microorganisms present in the sludge and this interaction will result in small and compact spherical-shaped aerobic granules [13]. In the matrix of extracellular polymeric substances, the microbial cells are self-immobilized. The granulation is favored by the environmental conditions, operations, and feeding, short settling time, larger height-to-diameter ratios, and stronger hydrodynamic shear forces in the SBR [14]. Granule formation is a gradual process that begins with seed sludge, mainly in the form of flocs, and progresses to microbial aggregates by the action of hydrodynamic forces, thermodynamic forces, gravity, diffusion of particles, Van der Waals forces, ion-exchange inter-particulate binding, and cell membrane fusion in later stage and then to granular sludge by synthesizing more and more EPS (Extracellular Polymeric Substances). This promotes the granulation process, and finally, mature granules are formed. This is illustrated in Figure 1. AGS can be cultured using inoculum in lab-scale reactors using wastewater prepared synthetically and also on a pilot scale with real wastewater [14]. The AGS developed in laboratory-scale SBR is more stable than that of pilot-scale reactors [15]. These granules are made of different layers which are described in Figure 2. The outermost zone of this granule is the aerobic layer since it is exposed to the outer environment. This layer consists of aerobic types of microorganisms. The middle or the second zone is the anoxic layer, and the innermost layer

is the anaerobic layer, which consists of anaerobic microbes due to the scarcity of oxygen in depth.

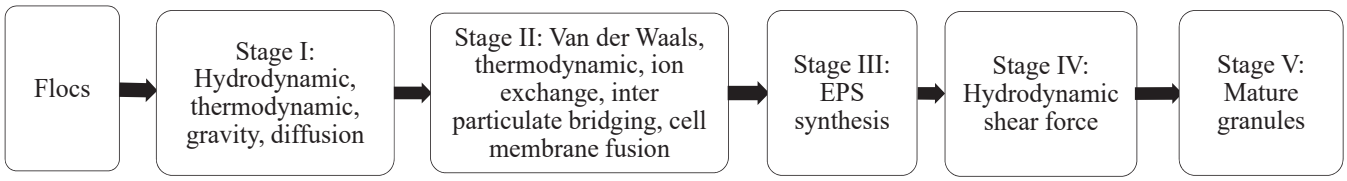


Figure 1. Stages of granulation.

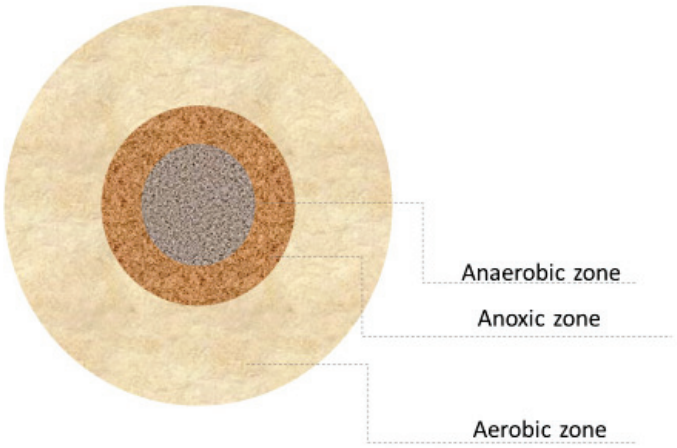


Figure 2. Schematic diagram of different layers of AGS.

The simultaneous removal of phosphorus, nitrates, nitrites, and ammonia can be accomplished within one reactor itself when large-size AGS is used. This is because, within a single granule, electron donors and acceptors diffuse, creating different redox conditions [15]. This aids in the growth of several microbial guilds within the same granule. High phosphorus removal is possible due to aerobic and anaerobic environments of granular structure as well as the SBR operation mode. Enhanced biological phosphorus removal (EBPR) and phosphorus precipitation within the granular matrix are the main two pathways for phosphorus removal in AGS systems [16]. In EBPR, polyphosphate accumulating organisms in the AGS will release phosphorus to the liquid in the anaerobic phase, then utilize phosphorus from the liquid in the aerobic phase, storing it as intra-cellular polyphosphates within their cells and using it for energy production. Assimilation, simultaneous nitrification and denitrification, and anaerobic ammonium oxidation (anammox) are some of the nitrogen removal processes used in AGS. All of these processes work well to remove nitrogen from the wastewater; it has been reported that AGS-based treatment can remove as much as 78.4% of total nitrogen and 99.7% of NH_4^+-N [17]. Microbes responsible for nitrification predominate in the aerobic zone, whereas heterotrophic microbes found in the anoxic zone are primarily involved in denitrification. Assimilation is another way of removing nitrogen in addition to nitrification and denitrification. Nitrogen will be assimilated by the generation of new biomass at the time of the granular development phase.

In an aerobic granule, soluble proteins such as enzymes cannot be secreted into the main liquid due to the EPS matrix that accumulates surrounding the cells. The polysaccharide complex, which forms the core of the EPS matrix, may capture the proteins that are released by the cells [17]. Because of this, the proteins secreted into the bulk liquid may be reduced by the EPS matrix and the granular structure of the AGS. Thus, if the activated sludge process is substituted by the AGS technique, superior effluent quality with reduced organic-N might be anticipated. In a significant study, it is clearly articulated that, the DO of the bulk solution was limited due to the sCOD and NH_4^+-N depletion during the initial

period of the aeration phase, creating an anaerobic core within the aerobic granules that promoted denitrification [18]. Afterwards, DO levels increased until attaining a saturation point, resulting in increased oxygen transfer within the granules. Moreover, the COD to N ratio was about 3 at that point, which was insufficient for the complete denitrification process. Enhancing denitrification must be one of the main purposes of AGS technology in order to guarantee low nitrate levels in the effluent. It can be attained by increasing the COD/N ratio and maintaining low DO and redox conditions. Volatile fatty acids (VAFs) in wastewater are easily accessible carbon sources for microorganisms. More complex carbon sources are typically converted to VFAs before they are used by microbes. VFAs act as electron (e^-) donors during denitrification, with nitrate serving as the terminal e^- acceptor [17]. The concentration of VFAs in municipal wastewater can range from 22 to 91.6 mg-COD/L [19]. This quantity is typically insufficient for effective nutrient removal in SBR operation. So, the addition of VFAs to wastewater is recommended for improved biological nutrient removal (BNR) processes and it is possible by recirculating sludge hydrolyzed effluent from the sludge treatment section during the anoxic phase of SBR operation.

3. Characteristics of AGS

The stability of granules may depend on one or more attributes of the granules. Better knowledge and understanding of the characterization and formation of granules would help in knowing more about the stability of granules. The characteristics of aerobic granules can be broadly classified by their physical, chemical, and biological attributes and are described below.

3.1. Physical Characteristics

The physical as well as chemical constraints in the reactor contribute to the strength of the granulation system. The physical characteristics of AGS which depend upon the stability of AGS include settling properties, specific gravity, density, and physical strength. The settling ability is one of the main important factors that seem to be related to solid–liquid separation and biomass retention capacity [20]. The settling velocity of the AGS ranged from 20–80 m/h and sometimes more than 100 m/h, which was more than that of flocs with a range of 7–10 m/h [21]. This high settling velocity indirectly promotes granule stability by enabling desirable biomass retention in the reactor. Physical strength is the next important parameter that determines the capability and the structural trait to withstand high shear force and abrasion. A denser biofilm develops as shear stress increases and these shear forces regulate granule outgrowth and become more significant as the microbial population grows faster. Hence, it is vital to maintain a proper balance between shear and growth in order to encourage the formation of dense, stable granules. The reactor type and its operating parameters determine the granule's exposure to outer shear forces. The strength of the granules is a function of the interaction of certain forces that act in the reactor, the concentration of EPS, and wastewater. The granular physical strength has been measured and compared using a number of methods, including measurement in a stirred flask, mixing in a stirred type of tank reactor with a conventional system layout, and in a bubble column that can withstand high shear force and abrasion. Smaller-sized particles are likely to be denser than large-sized particles. So, these smaller-sized particles tend to have more stability than large-sized ones [22,23]. The physical strength of bacterial granules varies from that of fungi granules. Bacterial granules are stronger than fungi due to the loose macro structure of fungi which may be broken easily [21].

The operation and design of AGS depend heavily on granular density. In veritably, the two types of criteria collectively affect granule density [24]. The buoyant granule density, also known as the wet granule density, is the first parameter to consider [24]. It is the granular mass including all components present in it (other microbial cells, water, precipitates, EPS, etc.) per unit of volume of the sample. The granule biomass density, also known as dry granule density, is the second factor referred to as granule density and is defined as the mass of total dry solids per granule volume [24]. The buoyant density or wet

density of granules has been reported to be between 1005 and 1070 kg/m^3 [24]. A granule's wet density is related to the fluid dynamics of the AGS reactor. A force balance can be used to estimate a granule's settling velocity based on its size and density, and thus, wet density is a critical characteristic for hydro-dynamic design and for the stability of granules in the reactor [24]. The dry density has been reported to be in the 50–100 gVSS/L range [24,25]. The dry density affects the diffusion of the substrate into granules because, with more cells and EPS, the diffusing molecules are more severely constrained [24]. The pycnometer method, settling velocity method, the Percoll density gradient method, and the dextran-blue method are the different methods for measuring granular density. Among these, the pycnometer is the most reliable method and is efficient with less standard deviation and easy to use. Density directly relates to specific gravity. AGS formed in SBRs had a range of specific gravity of 1.004–1.1 kg/m^3, which was much more than that of flocculent sludge (1.002–1.006 kg/m^3) [17]. Density and specific gravity can be increased by adding some carrier materials or precipitating materials. For instance, calcium-rich granules tend to have more compressive strength and specific gravity than less calcium-containing granules [26]. Overall, the granules should have higher physical strength, settling properties, density, and specific gravity in terms of stability. The granules that are denser and have higher specific gravity tend to have higher settling properties making the granules stable. The majority of research related to physical strength is mainly focused on granular settling velocity and other settling characteristics. Limited works in literature are available based on the density of granules, which directly affects the settling characteristics of granules. The aspects of granular shear stress, hydrodynamic shear force, compression property, and viscosity need to be further explored in the physical attributes of AGS.

3.2. Chemical Characteristics

Aerobic granules are primarily composed of six major elements: C, H, O, N, P, and S [27]. Granule samples are dried until constant weight at 105 °C and then pulverized to analyze the elemental compositions. Then, elemental components of granules can be determined using a CHNS/O analyzer, and multi-elemental analysis can be performed using an inductively coupled plasma (ICP) emission spectrometer. In addition to that, numerous analytical methods, including X-ray diffraction, chemical extractions, scanning electron microscopy, and energy dispersive X-ray analysis (SEM-EDX), can be used to examine AGS to identify chemical deposition and precipitation, such as calcium precipitation inside the granules. The chemical characteristics include hydrophobicity, pH, and EPS. Surface hydrophobicity has a dominant function in the granulation process. The hydrophobicity of AGS is double when compared to that of bio-flocs [28]. Based on thermodynamic theory, the rise in the cell hydrophobicity could lead to a depletion of the surplus Gibbs energy in the cell and thus promote cell-to-cell self-agglomeration. Numerous analytical techniques, including contact angle measurement, bacterial adhesion to hydrocarbons, phenanthrene adsorption, and angle measurements, can be used to determine the cell hydrophobicity of AGS [29,30].

The physical and chemical properties of sludge are affected by pH, which is also a key factor in the development of biological processes. pH also controls bacterial metabolism, alters the nature and contents of EPS, and influences the pollutant removal capabilities and structural stability of sludge granules. Despite being able to maintain their structure and settleability in acidic to neutral pH environments (pH from 5.5 to 7), AGS had a negative irreversible effect on their stability in alkaline environments [31]. Likewise, strong acid (pH less than 3) may hydrolyze EPS, causing the AGS to become unstable and disintegrate. The stability of granules under different pH levels is explained in Section 4.6.

EPS of various types play distinct roles in the formation of AGS which include loosely bound EPS (LB-EPS) and tightly bound EPS (TB-EPS). The influence of LB-EPS on sludge changed to repulsion from attraction during the AGS process. On the other hand, TB-EPS might facilitate hydrophobicity and zeta potential and exhibit effectiveness in the granulation process, by sludge cell adhesion and this TB-EPS is one of the main contributors

to granule formation [32]. According to the experimentation of Liu et al., when the mature granules developed, EPS concentration sustained at about 240 mg/g MLVSS, which was greater than the seed sludge (212 mg/g MLVSS), and then grew noticeably higher than 333 mg/g MLVSS [33]. The increased EPS and Sludge Volume Index (SVI) values were negatively correlated; however, the granule formation and higher EPS content were strongly positively correlated. AGS's morphology and structure are significantly influenced by EPS. On the basis of published research, the function of each matrix of EPS elements in granular stabilization has not been explained so far. The method of extraction may be one of the reasons. The compact nature of aerobic granules made it difficult to extract EPS from them.

3.3. Microbial Characteristics

Light microscopy, scanning electron microscopy (SEM), fluorescence in situ hybridization (FISH), and confocal laser scanning microscopy (CLSM) are employed to observe microscopically the microbial structure of aerobic granules. The content of culture media and granular structure play a key role in determining microbial diversity. There has been a report of dead cells and anaerobiosis in the center of AGS. When anaerobic microorganisms are present in the aerobic granules, organic acids and gases are produced [34]. Aerobic granules could eventually disintegrate as a result of these end products of anaerobic metabolism. A polysaccharide network surrounds the non-cellular protein core of the mature granule. At the outer regimes, cells are accumulated. A CLSM image depicts granulation as (i) cell-to-cell aggregation, (ii) the cell grows and grows to a size that hinders substrate transfer, resulting in lysis of the cell, and (iii) shear force compacts the granular structure, leaving a non-cellular polysaccharide (PS) and protein (PN) core [34]. Granules have a smooth outer surface that minimizes damage from collisions between granules, and the PN-PS core provides mechanical and physical strength to the granules. For minimizing substrate transport resistance, functional strains are mainly distributed at the rim regime [34,35].

The specific oxygen utilization rate (SOUR) is the measurement of microbial activity. It is reported that aerobic granules have 34–168 mg O_2/g VSS/h of SOUR values. The SOUR is associated with increased superficial velocity, which is typically a result of liquid shear. Bio flocculation and the stability of its microbial flocs are directly dependent upon the surface charge of the cell. As the PN to PS ratio increases, the surface negative charge of the microbe is decreased, thereby lowering microbial electrostatic repulsion and enhancing granule formation [21].

The microbial communities in flocs and granules have been the subject of numerous research, but generally speaking, they are more comparable with granules and flocs in the same reactor than between similar fractions in separate reactors [36]. However, in the future it is possible that when the AGS technology matures to handle complex wastewaters, microbial diversity may be expected between granules and flocs.

4. Granulation Time and Stability

Granulation time and stability depends upon a number of factors which includes substrate composition, temperature, pH, organic loading rate (OLR), seed inoculum, etc. Granulation achieved quickly might not produce stable granules. Similarly, long-term enabled granulation may not always lead to stability. Recently, researchers have been trying to create granules with higher decontamination efficiency that are stable in a short period of time. The recent application of AGS and its granulation time and stability are described in Table 1. It shows that the addition of a positively charged carrier enhances the stability by binding with the negatively charged microbial surface. However, the addition of bio carriers was not improving the stability of granules and, in contrast, the granules became unstable. With the addition of polyaniline (PANI), which is a conducting polymer, the biomass retention has been improved and it also enhances the AGS pores which helped to induce polysaccharides to improve the granular stability. An investigation revealed that 2–3 mm-sized granules are more stable when compared to others by ultrasonic crushing [37]. For example, the rate of granulation of 0.0–1 mm granules significantly reduced from

92.31% to around 48.48–65.85% after ultrasonic crushing. In addition, granulation rates of 1–3 mm granules exhibited a general upward trend, peaking at 2–3 mm. However, after the ultrasonic crushing of granules, 3 mm or larger reduced slightly. The findings showed that the granules smaller than 1 mm performed poorly when it came to resisting ultrasonic crushing, whereas granules between 2–3 mm performed best in this category. Under high DO, rapid granulation is possible but has lower stability, and on the other hand, low DO requires a long start-up period but has greater stability.

Table 1. Recent application of AGS technology and its granulation time and stability.

Seed Sludge Source	Operational Conditions	Stability Factor	Operational Period	Effect on Stability	References
Low strength wastewater	3 reactors; Control, CCM—cell culture micro-carriers, and GAC-granular activated carbon	Slow growing organismsm and positively charged carriers	operated for 120 days	Mature granulation was attained in all reactors in less than 80 days. The particle sizes in control = 904.08 µm, CCM = 915.71 µm, and GAC = 1091.20 µm.	[2]
Domestic wastewater	2 SBRs with bio-carriers	Bio-carrier	Operated for 25 days	Granulation was achieved within 20 days; However, it was not stable after 20 days.	[38]
Flocculent sludge from domestic wastewater treatment plant	Automated 3L SBR with 5 different phases	DO/fasting/ feeding cycle	Operated for 250 days	Granulation was observed at the end of Phase II (day 75). At the beginning of phase V, the bigger granules (1.3–8 mm) formed in the previous phase disintegrated. During phase V, stable spherical granules (1.5 to 2.5 mm) were developed. The DO (1–2 mg/L) and feeding strategy aided in the control of granule size and stability.	[39]
Sewage sludge	Operated in 2L with 12-h cycle and 2 cycles per day	polyaniline (PANI) addition	Operated for 33 days	The PANI injected during the start-up phase improved biomass retention, hastening the granulation process. Additionally, the PANI enhanced the AGS's pores and channels, which favored the granules' enduring stability. Additionally, PANI induced the release of polysaccharides from the cells, aiding in the maintenance of AGS stability.	[40]
Sewage sludge	Pilot scale SBR of volume 120.5 L, (diameter 29.2 cm, and height 180 cm)	Granular size	40 days	After ultra-sonic crushing, 2 to 3 mm seemed to have the highest rate of granulation, the lowest SOUR was found in 2 to 3 mm granules, easier to maintain stability because their particle sizes increased at the slowest rate.	[37]
Brewery wastewater	3 SBRs with 4L capacity (height = 100 cm)	Extended famine conditions	operated for 120 days with 2 different cycles of 60 days (6h cycle and 12 cycle)	Granules redeveloped with more structural stability in 12 h cycle than during the 6 h cycle period, indicating that a prolonged starving phase increased proteinaceous synthesis of EPS. Overall, prolonged famine environments favored granule stability, probably due to the bacteria with the ability to store energy molecules thrive under such settings.	[41]
Secondary sedimentation tank of STP	2 SBR of 1.4 L working volume	magnetic Fe_3O_4@polyaniline effect (Fe_3O_4@PANI)	40 days	Fe_3O_4 @ PANI prompted the granules for EPS secretion and better protein-to-polysaccharide ratio, improving AGS stability.	[42]
Anaerobic granular sludge (AnGS) and crude sewage from aeration tank	2 L SBR	DO	60 days	After 60 days of operation—90% AnGS turned from black color to brown color. The granules continued to be compact, and the average sizes were constant.	[43]

A study revealed that the granular formation from anaerobic granular sludge (AnGS) as seed biomass will produce more stable granules [43]. That study claims that converting already formed AnGS into AGS with domestic wastewater rather than floccular seed sludge is one of the possible methods to cultivate AGS that reduces the long cultivation time of AGS technology, and the removal efficiency of more than 80% reveals that the granules can survive and adapt to the fluctuating concentration of the real wastewater which makes it more stable. It is observed that granule morphology changes and bacterial community changes at the phylum level during the granule development. Moreover, by comparing with the bacterial community in aerobic granules cultivated from flocculent activated sludge, some bacteria (affiliated with Comamonadaceae, Xanthomonadaceae, Rhodocyclaceae, Moraxellaceae, and Nitrosomonadaceae) playing significant roles in maintaining the structures and functions of aerobic granules. In contrast, many studies have reported that during continuous operation, aerobic granules break down. Some of the reasons for this disintegration and loss of stability are the growth of filamentous bacteria, anaerobic core hydrolyzation, functional loss of strain, and of EPS [34]. The organic loading rate (OLR) has a significant influence on the formation, stability, and structure of aerobic granules [44]. The stability and formation of AGS are discussed in detail in the next sections and Figure 3 shows the influencing factors on AGS stability.

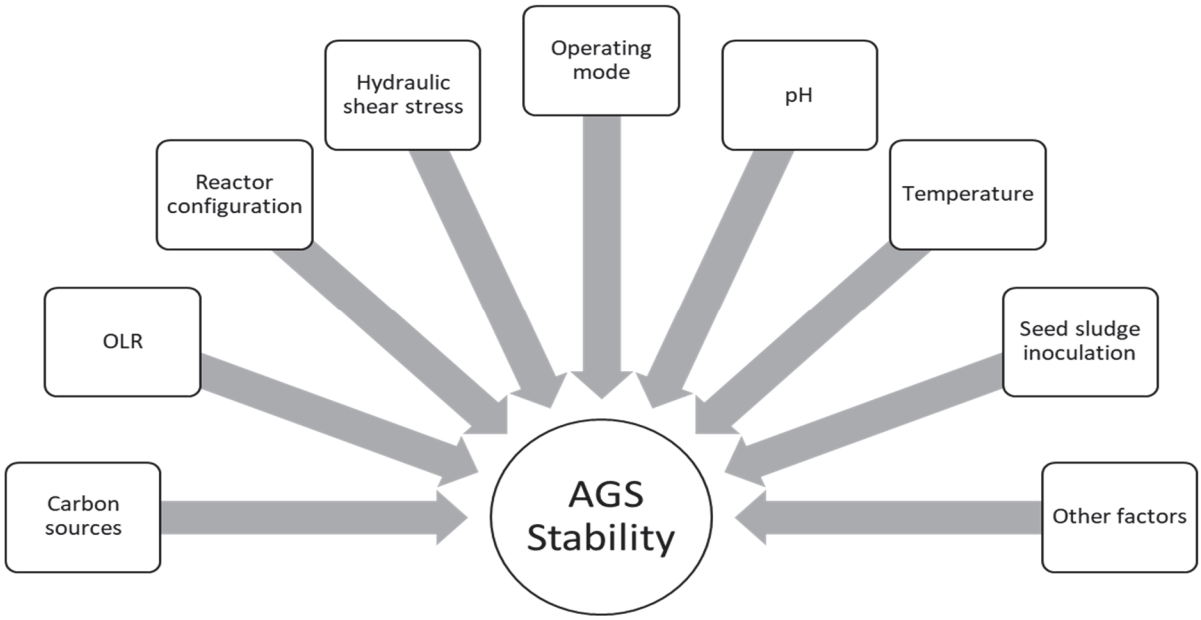


Figure 3. Influencing factors on AGS stability.

4.1. Stability under Different Carbon Sources

There are some research works that emphasize the purpose of substrate in granular formation, its maturation period, and stability. Glucose-based substrate, acetate ethanol-based substrate, and ethanol-based substrate were used for the AGS formation. Aerobic granulation was accomplished in acetate 14 days after the start-up, but ethanol and glucose exhibited granulation 40 and 60 days after, respectively [45]. Though the granulation was achieved within 14 days for acetate, the stability of granules was achieved only after two months of operation and also disintegration occurred at day 72. The disintegration probably occurred due to the formation of large diameter (>3 mm) granules, particularly closer to the reactor's bottom, and due to the thick layers formed on the biofilm made it difficult for these granules to diffuse oxygen and carbon [45]. Since there is not enough oxygen input and the carbon input is low, the anaerobic layer becomes large, thereby the most important bacterial metabolic processes in the region close to the innermost layer will be endogenous respiration and fermentation [45]. In other investigations, when acetate was used as

the carbon source, granule disintegration was noticed with long-term operation [45,46]. With that in mind, some investigations have found that the average size of the granules ought to be less than 2–3 mm, and granules developed on acetate as the substrate had the best sedimentation properties; nevertheless, when glucose is present, the AGS showed maximum resistance [45]. EPS are biopolymers made from polysaccharides (PS), proteins (PN), and other contents that act like "biological adhesives" for the development and stabilization of granules. In the EPS of stable aerobic granules, protein (PN) is the chemical that is most prevalent in EPS. Consequently, it is vital to determine the ratio between PN and PS. The only granules with a higher protein content than polysaccharides were those produced in the presence of glucose, and as a result, the impact of the carbon source on the EPS content of the AGS was amply confirmed [45]. In contrast, other experiments using glucose as a carbon source support the notion that glucose does not promote the formation of EPS [47].

The change in granule diameter (%) and stability coefficient (S) before and after the shear test are used to illustrate the resistance of aerobic granules. 'S' can therefore be used as a predictor of the stability of aerobic granules because it is connected to the stability of aerobic granules under shear stress. The detailed procedure to determine 'S' is illustrated in Nor-Anuar et al. [48] and the AGS strength increases with a decrease in the 'S' value. In other words, the more stable the aerobic granules, 'S' is an acceptable and logical way to show the AGS strength against the shear stress, even though it is not a precise tool for measuring the precise shear strength parameters in the biological process [48]. Aerobic granules are more stable for the smaller S values (percent). The acetone-fed granules had less S% when compared with glucose-fed granules. This indicates that acetone-fed granules are more stable. The microbial diversity within granules will increase the pollutant-removing capability of that AGS system. By comparing with different carbon sources, acetate encouraged the most species which gave rise to the most richness of microbes in the granules produced [45,49]. The creation and properties of the granules were influenced by the carbon source. In general, acetate facilitated the quick granule formation that produced the highest performance, and larger diameters. Though ethanol produced granules that were more stable, and it performed worse than those that were developed on acetate [45]. The substrate that required more time to granulate was glucose, and additionally, the least diverse and effective microbiotas were found in the granules grown on glucose [45]. These investigations have demonstrated the higher stability of ethanol-fed granules, but their removal and performance efficiency fell short of that of glucose-fed and acetate-fed granules. Although the microbial diversity and treatment performance were higher for the glucose-fed granules, the acetate-fed ones are more stable. Implementing them in the treatment of real wastewater is pretty challenging because the composition of the real wastewater is highly variable, despite the stability being highly dependent on these substrates feeding circumstances. Furthermore, all of these experiments used synthetic feeding in laboratory-scale reactors. In order to treat real wastewater, several investigations need to be performed in pilot-scale and full-scale reactors to assess the granular formation and its stability.

4.2. Stability under Different Organic Loading Rates

One of the most important factors influencing biological wastewater treatment systems is the OLR. Low OLR values (less than 2 kg COD/m^3 d), medium OLR values (2–4 kg COD/m^3 d), and higher OLR values (over 4 kg COD/m^3 d) are the three categories used to classify OLR levels [50]. It has been shown that AGS can occur both at extremely low OLRs (0.6 kg COD/m^3 d) and higher OLRs (24 kg COD/m^3 d) [50]. The duration of AGS formation and the nature of the granules that result are the variables. At low OLR, AGS development takes a couple of weeks, whereas at high OLR, it just takes a few hours or even day and it would be preferable for AGS to develop at a low OLR when sufficient time is available for granulation so that small sized and stable AGS are produced [50]. The fundamental issue is maintaining the stability of AGS when OLR is high because by raising

the OLR, granular size is increased, which eventually creates an anaerobic environment inside the granular core because of the restrictions on oxygen diffusion [50]. As a result, stability lowers which leads to the disintegration of granules. To sustain granule integrity, previous researchers had looked into switching between low and high OLRs. In order to enhance granule stability, a study on the combination of high OLR and feeding anaerobic is recommended. It is possible to further make use of the newly discovered technique for AG stability by OLR stressing (higher OLR for granular formation) and then reducing the OLR when a steady state condition is reached [51]. Overall, high OLR is preferred for speedy and quick granulation, while for stability and performance, an OLR of low to medium is ideal.

4.3. Operating Mode of Reactor

According to the available studies, SBR is typically utilized for aerobic granulation, owing to its fill-and-draw operation and stage of aerobic deprivation. This is because, the SBR's fill-and-draw mode makes aerobic granulation easier due to quick settling of sludge and SBR has two distinct periods of adequate substrate activity and substrate starvation, with aerobic starvation accounting for as much as 75% of the overall cycle. Extracellular polymeric substances are extensively consumed by microbes at the time of aerobic starvation, which lowers the sludge's surface-negative charge and increases its hydrophobicity, causing the sludge to develop dense and stable AGS [52]. Granulation in a continuous flow reactor is inherently unstable. Many researchers emphasized the importance of additional studies for granule stability in continuous flow reactors for prolonged time periods, which is highly desired [53,54]. Another reactor is an aerobic granular sludge membrane bioreactor (AGMBR), a hybrid system that involves aerobic granules as the biomass for treating, and the treated water is obtained through a membrane filter. Several literature studies are available on Membrane Bio Reactor (MBR)-based AGS systems [55]. For more than a decade, there has been a huge interest in the AGS-MBR with the outcome of the combining of AGS and MBR technologies to reduce membrane fouling. However, the key difficulty identified is in maintaining the structural stability of granular sludge, and another significant concern is the granule breaking affecting a rise in irreversible (i.e., pore-blocking) membrane fouling [56]. It is still necessary to find a solution for this issue in order to use AGS in real applications. In light of the performances under various favorable operational conditions, methods for producing more stable granules were proposed [57]. A recent literature study identified four major elements as the primary keys for developing stable AGS-MBR systems. The first one is to form granules directly in the AGS-MBR setup rather than seeding granules from SBR; the second one is to ensure the presence of anaerobic and aerobic conditions in continuous reactors; the third one is to ensure that the mean dimensions of the granules are far from the critical values (0.2 mm); and the fourth one is to regulate AGS scouring [56]. Compared to all reactors in these studies, the AGS in SBR is more stable and reliable. However, there are significant issues that need to be resolved, such as how to accomplish granule formation and ensure structural stability of AGS at the time of continuous operation of the reactor.

4.4. Aspect Ratio of Reactor (H/D)

In most literature studies, higher height to diameter (H/D) is preferable for stable granules. For example, SBRs with high H/D ratios took less time to reach stable granules than SBRs with low H/D ratios, even at the same operating volume [58]. Conventional wisdom holds that a height to diameter ratio of 15 to 30 is optimal for accelerating the maturation of granules with a thick surface [52]. In contrast, research has shown that granules with a dense layered structure can also develop in SBR even if the aspect ratio is relatively low [59]. This investigation has shown that when AGS properties are suitable, the aspect ratio of an SBR is not necessarily a requirement for maintaining the stability of AGS.

4.5. Hydraulic Shear Stress

In aerobic sludge granulation, hydraulic shear acts as a significant selection pressure [60]. AGS' structural stability is further enhanced by the hydrophobicity of its surface under hydraulic shear stress [52]. Higher hydraulic shear stress with superficial gas velocity (SGV) > 2.4 cm/s induced microbial aggregation in the granular sludge and encouraged its structural stability [60]. However, as a result of excessive hydraulic shear stresses, particles become more abrasive, which weakens their mechanical strength and incurs significant operational costs [61]. Moreover, particle structural stability and hydraulic shear stress depend on substrate concentration when it comes to sludge granulation [62]. They found that even at low SGV (0.41 m/s), wastewater with low COD concentrations (300 mg/L) produced stable granular sludge, but at 600 mg/L and higher COD concentrations, AGS could not be produced. The microbiological aggregation was enhanced, and the structural integrity of the granular sludge was favored by the higher hydraulic shear stress at SGV over 2.4 cm/s [60]. According to the hydraulic shear analysis, the SBR (airlift) with a lower aspect ratio, the overall shear rate was higher with the same SGV, whereas the total shear rate in the AGS system with a higher aspect ratio reached (0.56–2.31) $\times$ 10^5/s. This showed that higher hydraulic shear stress encourages the structural integrity and development of AGS and could be provided by the reactor. Only a few literature studies are available on this aspect. Further study needs to be carried out based on this hydrodynamic shear stress to assess the structural integrity of AGS.

4.6. pH

Granulation is mostly stable in neutral pH. According to research findings, at pH 9, the AGS disintegrated, and the system converted to a mainly flocculent nature, leading to a considerable decrease in bioparticle dimension. The results revealed that the AGS are not stable at increased pH after a 9-day pH spike [63]. On the other hand, pH 6 shocks did not cause granular sludge breakage, and the size distribution remained constant after 9 days of operation at low pH [63]. On the contrary, acidic pH controls the epistasis of the filamentous aerobic granules and significantly alters the microbial community within the granule [64]. These filamentous microbes will affect granular stability. The stability of AGS will be impacted by these filamentous microbes. The most efficient strategy to prevent filamentous outgrowth and preserve granule stability is to keep the suspension in either a neutral or low-alkaline environment. There is no substantive study available regarding the metagenomic analysis of AGS under high or low pH. This could be tested on two systems, one of which would operate with a low pH influent and the other would operate with a standard pH. This would support the notion that the microbial ecology in a granular system is influenced by influent pH. In terms of stability, AGS is more stable in acidic to neutral pH ranges (6 to 7.3). This can be accomplished by utilizing an integrated alkali-acid pumping system in the operation of reactors.

4.7. Temperature

Temperature is an important factor that affects micro-organisms and their activities. The type of microbes for contaminant removal that thrive in the sludge depends on the temperature of the sludge. For instance, the ideal temperature for nitrification by Ammonium Oxidizing Bacteria (AOB) is 31 °C. On the other hand, Phosphate Accumulating Organisms (PAOs) will survive in lower temperatures. To survive, 20 to 25 °C is the ideal temperature for the majority of bacteria. The kind and growth rate of the microorganisms involved have a significant impact on AG morphology, which is related to the temperature. Temperature changes may also have an impact on AG stability. AGS will experience particle disintegration and biomass loss due to filamentous bacteria multiplying excessively at too low of a temperature, especially temperatures less than 10 °C. Whereas, the granulation system will become unstable at too higher a temperature (greater than 35 °C) due to enzyme inactivation and protein denaturation [65]. Some researchers have effectively cultivated low-temperature (<7 °C) adapted granules with excellent removal efficiency and

are highly stable so that they can expand the application of AGS in sub-freezing places [66]. Although AGS has good sedimentation capabilities at higher temperatures (30–50 °C), the effectiveness of pollutant removal declined [67]. These studies revealed that the AGS is more stable in temperatures ranging from 20 °C to 30 °C and reported the best pollutant removal performance in this range.

4.8. Seed Sludge Inoculation

The development of AGS was not greatly affected by the seed sludge inoculation concentration, and optimal MLSS value ranged between 1 to 20 g/L with an SVI of 7 to 220 mL/g [59]. Some bacteria in sludge are capable of strong EPS secretion, which increases the likelihood that stable AGS will form. Municipal seed sludge had a greater diversity of microbes whereas the sludge inoculation from industrial wastewater contains microbes that are resistant and adaptable to toxicity [68]. It is because industrial wastewater contains the only microbes that thrive in extreme toxicity for their survival, and they secrete more EPS which will develop stable AGS [68]. In a study, AGS was produced from saline water successfully in 52 days and effectively turned into AGS as well as retaining the structural integrity of granules [69]. It was found that the addition of stored granular sludge greatly reduces total granulation time when compared to the sludge that is flocculent, and AGS with excellent settling properties and stable structure may be created within 22 days [70]. Some researchers are focused on the addition of AGS directly into the system instead of flocculent sludge. Adding the entire granular sludge resulted in significantly reduced bulking of sludge, as well as obtaining stable AGS [71]. Overall, it is observed that industrial seed sludge is superior for stability whereas municipal seed sludge is superior for quick granulation and microbial diversity.

4.9. Other Factors Affecting AGS Stability

Other factors include microbial community structure, microbial quorum sensing effect, and physiochemical properties of sludge such as PN/PS ratio and particle size. The contaminant removal effectiveness and mechanical stability of AGS are significantly impacted by microbial diversity and structure. The structure of microbial communities is controlled by organic matter, pH, temperature, and stage of granulation, which are challenging to control, and cause AGS to exhibit substantial variances [72]. The structural stability of AGS will be increased by the right number of filamentous bacteria, which will aid in granulation by tying the particles to the skeleton of AGS. However, a lot of filamentous bacteria will ruin the AGS structure, which will decrease the stability. Apart from this, the stability depends on other factors which have not yet been discovered. There is scope for more studies to be carried out to find what the other factors affecting AGS stability.

5. Storage and Recovery of Granules

It is difficult to determine the exact mechanism of action behind the storage of aerobic granules, which is influenced by substrate, temperature, and storage time [73]. Most of the methods adopted for storage in the studies are mainly drying methods [69–71]. It has been shown that dehydrated aerobic granules, if sufficiently recovered, offer a promising long-term storage option [74–76]. In addition, the freezing and thawing method was also adopted [77]. Some studies also showed the saline storage of aerobic granules [78].

The foundation for the practicality and commercialization of AGS was to retain the stability of granules stored for a long time and to accomplish rapid recovery of physical features and microbiological activity of stored granules [74]. With prolonged storage, endogenous respiration, protein hydrolysis, and internal cell hydrolysis are thought to gradually degrade granule physical properties and bioactivity, which seems to be controlled by the substrate used, temperature, and duration of storage [75]. Biomass that was held for a lesser period of time was more resistant to breaking and had a more consistent color shift. The sections below give a brief account of storage methods for AGS.

5.1. Freezing Method

The majority of microbial activity will come to a halt under frozen conditions, so long-term granule storage is possible [79]. The development of granular storage at a lower temperature (20 °C) and its recovery for wastewater treatment was first reported in the year 2007 [80]. In another study, the performance of recovered granules was determined by storing the AGS at −25 °C, 4 °C, and room temperature, and recovered later [73]. According to studies it was observed that freezing temperatures (−20 to −80 °C) seemed to have no negative consequences on recovering granule's nitrification ability [81]. Nevertheless, wet conditions gradually destabilize the stored granules, partly because proteins are hydrolyzed at the cores of the granules, which weakens their integrity [82–84].

The first research that completely dehydrated and restored granules with their structural integrity was reported in the year 2018 [77]. Another study looked at the influence of varied airflow temperatures and acetone dehydration on aerobic granule drying and found that, based on their structure and reactivity, most dried granules might be retrieved to some extent [76]. A total of six different protocols were used in the study which include two air-drying methods, one freeze-drying method, ethanol/acetone dehydration methods, and one direct approach using a microwave oven [75]. They were then recovered for wastewater treatment. The measured properties are presented, and granule stability is connected with the operational stresses in the rejuvenated AGS rather than settleability, hydrophobicity, or extracellular polymeric material composition [75]. As a result of dehydration by air in the absence of moisture, minimal damage is caused to functional strains such as *Brevundimonas* and *Comamonas*, and marked deterioration is caused to structural breaker strains such as *Acinetobacter* of *Moraxellaceae*, resulting in granules that are stable and tough during rehydration. After dehydration, there is high volumetric shrinkage and color change. However, comparing this to the freeze-drying method, the shrinkage is quite low, and also the minimum color change with compact granules [75].

Comparisons of the actual granules, dehydrated ones, and the five-day recovered ones are illustrated in Table 2 [75]. Granules A, B, and E were mostly recovered after 5 days of recultivation, whereas D and F had deteriorated considerably, and C had rejuvenated partially and degraded partially [75]. Protocol A is dehydrated for 24 h at room temperature using adsorbent sheets [75]. The acetone protocol B involves successive immersion in different percentages of acetone (50, 80, and 100%), the ethanol protocol C, and freeze-dry technique D, which involves dehydrating for 7 h at 50 °C and then vacuum freezing for around 20 h [75]. A mean settling velocity of 12.2 m/h was determined for the original granules while settling velocity ranged from 10.8 to 17.4 m/h for the dehydrated ones. When granules were recovered after 5 days, if they were stable, they had a small increase in settling velocity. Due to the same sizes of the recovered granules, during dehydration and recovery, granule density should be raised [75]. Drying by air at 25 °C or 50 °C and dehydration protocols were used in this study to recover stable granules having a high potential for pollutant degradation [75]. Those strains having functions that remain after dehydration are enriched with recovered granules [75]. Those functional strains that remain are enhanced after dewatering with granules that are recovered and the durability and shape of granules were greatly influenced by the storage temperature [11]. COD, ammonia, and phosphorus were eliminated 13–90%, 8–27%, and 23%, respectively, using wet medium and freeze storage procedures [9]. In another work, the granular biomass was kept at 4 °C and the sample of granules was stored for 40 days to see how the storage time affected the physical and biochemical characteristics of the biomass, while the other sample was retained for 180 days [11]. In general, granules were unaffected by storage substrates, with granules at 4 °C storage exhibiting efficient recovery and granules held at ambient temperatures exhibiting the poorest restoration ability [73].

Table 2. Comparisons of the actual granules, dehydrated ones, and the five-day recovered ones according to Lv et al. [75].

Samples	Settling Velocity (m/h)		Strength-Index		Protein (mg/g)		Polysaccharides (mg/g)	
	Before Recovery	On Day 5 Recovered	Actual or Dried	On Day 5 Recovered	Before Recovery	On Day 5 Recovered	Before Recovery	On Day 5 Recovered
Before recovery	12.20	N/A	0.0460	N/A	103	N/A	111	N/A
A	17.40	13.90	0.0230	0.015	57.4	34.7	76	104.6
B	14	22.9	0.0410	0.0028	63.8	36.2	74.3	41.7
C	15.1	19.3	0.065	0.002	28.1	23.5	173	38.1
D	10.8	GD	0.024	GD	90.4	4.5	59.6	133
E	14.4	18.9	0.025	0.0220	49.3	10	82.7	113
F	14.4	GD	0.060	GD	29.7	27.6	37.1	57.9

Note: GD—Granules deteriorated.

5.2. Drying Method

Dried sludge significantly reduces volume and weight, so the drying process facilitates the storage and transportation of granules, significantly reducing the cost of handling and shipping [9]. Moreover, unlike the freezing of dried granules, this does not require storage below freezing temperatures, saving energy costs [9,85]. It has been proposed to dry granules to facilitate storage and handling and to enhance the efficiency of bioreactor treatment by adding them as inoculums for quick start-up [86]. The drying procedure is the most practical of the several approaches recommended for preserving granules. Since it is in a dry state, it can be stored for a longer time. On re-activation, granules can be recovered in a short time with minimal loss [9]. However, previous studies have not fully developed a drying process for the dried granules to be successfully reactivated.

The original granules were yellow with an average size of 4 to 6 mm in diameter. After drying, these aerobic granules had reduced their size by half about 2.1 to 3 mm in diameter, and weight also gets reduced to 25 to 30 mg/granule [9,76,87]. The color of the granule had turned to dark brown after drying but the integrity of the granules remained. As a result of the present drying methods, granules would lose >80% of their volume and >85% of their weight [87]. However, the granules could be re-cultivated in their original state in 5 to 12 days without losing structural integrity. For this to happen, the granule matrix must be extremely resilient, capable of withstanding 80 percent volume shrinkage in drying and volume recovery in re-cultivation without breaking down; the strains must thrive in drier conditions [87]. Interestingly, the researcher has produced aerobic granules with high protein to polysaccharide ratios using seven different drying protocols: drying at 37, 60, 4 °C, in the sun, the dark, a moving air stream, or with concentrated acetone solutions and 80% volume shrinkage was experienced by all dried granules without any structural breakage [76]. Despite three recovery batches, all dried granules were restored to the majority of their original size and organic matter degradation potential, notwithstanding the loss of some volatile suspended particles [87]. In Table 3, after the first recovery, the COD removal rate of original granules was far higher than acetone-dried granules, but acetone-dried granules performed better compared to other drying methods [76]. The dark-dried, sun-dried, and air-steamed dried granules had almost the same COD removal rates [76]. The COD removal rates subsequently increased for the second recovery stage and complete COD removal was achieved within 38 h. After the third recovery, the COD removal rate for acetone-drying or dark-drying granules was even higher than that of the original granules [76]. So, some species may grow more quickly if their competitors are removed during the drying process. Nevertheless, the fact that drying can improve performance should not be taken as a blanket statement in this regard.

Table 3. COD removal capabilities of dried granules.

Stage of Recovery	COD Removal Capability	Reference
1st stage	original >> acetone-dried > 4 °C dried > 37 °C dried > 60 °C dried > dark-dried = sun-dried = air stream-dried	[76]
2nd stage	original > 37 °C dried = 4 °C dried > sun-dried = 60 °C dried > dark-dried > air stream-dried > acetone-dried	
3rd stage	dark-dried > acetone > original > sun-dried > 37 °C dried > air stream-dried > 37 °C dried = 4 °C dried	

5.3. Wet Storage Method

The wet storage method is another option for storing aerobic granules. The aerobic granular sludge is kept hydrated in this method by being kept in a moist medium. This was reported clearly that the aerobic granules are stored in tap water at room temperature (20–22 °C) for 6 months and 12 months and the COD removal efficiencies were restored to 80% of actual performance after three days of reactivation [88]. The COD elimination effectiveness increased to 90–99% after 7 days of operation, and the capacity to remove organic carbon was nearly entirely restored [88]. An ideal granule reactivation technique was proposed based on the amount of time it took to recover various operating tactics [88]. The best conditions for reactivating granules were found to be an OLR of 0.8 kg COD/m^3/day, a 2.6 cm/s superficial up flow air velocity, and 15–20 mg/L ammonia concentration [88]. Aerobic granules were dark brown in color after 12 months of storage and stayed elliptical or spherical with a slight size decrease, presumably due to endogenous respiration and internal cell hydrolysis of aerobic granules during long-term storage [88]. Even though, if the granules settled poorly, with 7 days of operation with SVI of 123.79 mL/g and a low settle velocity of 17.12 m/h, it is possible to resettle the granules into brown-yellow in color similar to fresh granules. Based on MLSS variation, granules gradually revived and increased steadily. Another researcher pointed out that the collected AGS in glucose solution of 400 mg/L and distilled at a temperature of 25 °C, 4 °C, and properly maintained temperature (from 20 to 26 °C) for the duration of 8 months and the findings clearly indicate that storage substrate had only a negligible impact on granules whereas temperature for storage had a significant impact on their shape and physical characteristics. The process of granular reactivation involved stabilizing their physical, chemical, and microbial characteristics. Granules held at 4 °C in glucose solution at room temperature in distilled water were ellipsoidal or spherical in shape, brown-yellow in color, thick, and transparent. When held at a temperature of 25 °C with glucose solution or water, granules were dark in color, flaky and irregular with minute holes in structure, and shape.

The process of freezing and thawing that happened when being stored causes the granules to partially break down [73]. Granules kept at 20 to 26 °C remained elliptical or spherical, with very little cell debris and granular size loss, and showed no symptoms of disintegration [73]. Granules changed color from yellow-brown to dark brown with time [73] and after reactivation, granules held at 25 °C had a great ability to settle and the PN/PS ratio remained almost unaltered, demonstrating that storage at 25 °C is better for maintaining the internal microstructure. The aerobic granules were kept in liquid media for storage at 4 °C using five storage protocols and these storage protocols are listed in Table 4.

Table 4. Storage protocols according to Wan et al. [89].

Type of Media	Composition of Media	Physical Characteristics after Storage	Bioactivity after Reactivation
DI water (SW)	500 mL DI water	Mild shrinkage, smooth surface	SOUR-28 mgO_{2}/g MLSS/h
Acetone (SA)	AGS bathed in acetone solution (50–100%) for 2 h and kept in 500 mL acetone solution (100%)	No structural change, rough surface with cell agglomerations	SOUR-22.3, mgO_{2}/g MLSS/h
Saline water (SS)	500 mL NaCl solution (3% w/w)	No structural change, rough surface with cell agglomerations	SOUR-26 mgO_{2}/g MLSS/h
Acetone/isoamyl acetate solution (SAA)	AGS bathed in acetone solution (50–100%) for 2 h and kept in 500 mL acetone-isoamyl acetate solution	Severe shrinkage, rough surface with cell agglomerations	SOUR-16.6 mgO_{2}/g MLSS/h
Formaldehyde solution (SF)	500 mL formaldehyde solution (10%)	No structural change, rough surface	SOUR-13.5 mg O_{2}/g MLSS/h

Note: DI-Deionized water.

Visual assessment of the SF, SS, and SA granules after almost a year of storage indicated no structural changes; slight shrinking of the SW granules, and extreme shrinking of the SAA granules. Isoamyl acetate miscibility after application may contribute to volume shrinkage. The SI (original granules) and SW granule displayed smooth surface, whilst some granules have rough surfaces with agglomerations of cells and this aggregation of cells can be induced by high osmotic pressure or toxic substrates and SOUR for these recovered AGS were SI > SS > SA > SAA > SW > SF [89]. All of these granules were still more active than those kept in glucose or acetate solution [90]. Apart from formaldehyde, the other stored AGS were effectively revived with appropriate performance and strength in just 24 h.

6. Reactivation Time of Stored Granules

Many factors influenced the storage and reactivation time of AGS, which include the storage temperature, granular morphology, storage substrate, and granular environment. There was a great deal of influence of storage temperature on granule morphological and external properties, while the substrate used for storing had a limited influence. The reactivation of AGS was actually a restoration of physical properties, the structure of granules, and microbial properties. Consequently, granules stored at 4 °C were better suited to maintain structural integrity and at −25 °C were better suited to maintain microstructure and PN/PS ratio after reactivation, which confirmed the effectiveness of storage at −25 °C in maintaining microstructure [73]. Stored AGS can be successfully employed as bio-seed for reactor fast start-up 10 days after prolonged storage, regardless of storage temperature or substrate [73].

Dried granules had a lesser reactivation period. Other storage methods indicated in the literature were not as effective as dried granules in restoring their original treatment performance. The drying methods showed higher removal rates than methods using a wet medium or freezing storage after 1d reactivation [73,88,91]. Surprisingly the recommended drying procedures could result in the effective rejuvenation of AGS in the reactor as the COD removal efficiency was 97% and no ammonia and phosphorus were detected [9]. Removal performance is stabilized or reaches the original performance after 4–16 d using a wet

medium and 1–5 d using a freezing medium, respectively [75,88,91,92]. The drying method, however, takes 1–2 d [9,76,92]. COD, ammonia, and phosphorus removal rates were 13–90%, 8–27%, and 23% for wet storage and freeze storage systems, respectively [77,91–93]. Dry storage methods, on the other hand, achieved impressive removal of 97% COD, and phosphorus and ammonia removal were nearly 100% [9]. In another work, it is reported that after 1 d of re-activation, the PO_4-P removal efficiency of 90%, and the performance increased and became constant till the completion of the study. On the contrary, in another study, the removal efficiency of PO_4-P after 1 d of reactivation was around 20%, and it took around 7 d to completely restore PO_4-P removal after granules have been stored in a wet media at room temperature for 12 months [88].

The wet medium and frozen granules which were stored at room temperature, 20 °C and 25 °C up to 6 to 12 months in tap water and glucose solution had a reactivation time of 5 d with NH_4^+-N removal rate of 5–10% after 1d reactivation and it had a recovery time of 8 to 27 d for effective ammonia removal [73]. The wet medium stored granules at 20 to 26 °C had a higher reactivation time and the organics and nutrient removal rate is lower than that of frozen ones [88]. In the drying methods, in Table 4, the stepwise acetone drying method and chemical dehydration and drying method had higher efficiency than the air-dried method. By comparing the storage methods in Table 3, the drying method after chemical dehydration showed better performance but it is stored for only 1 d. In the storage methods mentioned in Table 4, none of the methods showed the storage period exceeds 8 months. Long-term storage and the maximum duration that is possible for storing the dried granules need to be further studied.

7. Impact of Additives for the Establishment of Fast and Stable Granulation

Additives such as calcium ions, magnesium ions, sodium ions, ferric ions, polyaluminium chloride, magnetite nanoparticle, xanthan gum, powdered ceramsite, and calcium alginate gel beads enhanced the settleability of granules and decreased granulation period while having no effect on treatment efficiency [94]. The efficiency of treatment fluctuates, particularly in prolonged operations (more than 100 days). It is important to indicate that additives generally have no discernible impact on the removal of phosphorus, ammonia, and COD. Their major focus was on rapid granulation and repairing of disintegrated granules. The addition of nanoscale zero-valent iron (nZVI) enhanced the secretion of EPS and improved the growth rate of certain species of bacteria, including *Xanthomonadales* and *Rhizobiales*, while reducing the rate of growth of others, including *Clostridiales*, affirming that the effect of nZVI on bacterial growth was genera reliant. AGS was formed successfully in the reactors in less than 50 days, and the presence of nZVI enhanced the settling rate and size and of the granules to a certain level [95]. In a study, it was found that the addition of Fe^0 coated with $Mg(OH)_2$ promoted bacterial growth, improved methane concentration, and stabilized the pH in the bioreactors [96]. This can be applied to the aerobic granular sludge to obtain its benefit.

8. Ensuring Sustainability through the Usage of AGS

The usage of AGS is a proven method for wastewater treatment across the globe. It is easy to cultivate AGS cost-effectively and in an environmentally friendly way. Moreover, like any other treatment method, AGS does not require any media replacement, cleaning, or regeneration. In addition to this, no chemical is required for its working as well as cleaning. There is a huge scope for the usage of AGS in developing countries and underdeveloped economies around the world. This will foster the sustainable development goals of the United Nations (SPG 3—Good health and well-being, SPG 6—clean water and sanitation, SPG 11—sustainable cities and communities, SPG 15—life on land, SPG 13—climate action) [97]. As countries are currently facing economic slowdown and lacking resources, this cost-effective process using AGS may enable countries to deal with wastewater treatment effectively.

Several recent articles have highlighted the fact that AGS has a high potential for resource recovery. This includes alginate-like exopolysaccharides (ALE), tryptophan, polyhydroxyalkanoates (PHAs), phosphorus, etc., and can be extracted by different methods [98]. ALE is extracted from the extracellular matrix, and it has the capability to form a gel in the presence of uranic acid residue and calcium ions. ALE is used as a surface coating to enhance the waterproofing resistance of paper, bio-adsorbent for dye as well as in civil construction and agriculture. Tryptophan is found in EPS. The nine essential amino acids for humans include L-tryptophan. Due to its antioxidant activities, it is utilized for preserving food and as a supplement in the feed of animals. Furthermore, it has applications for pharmaceutical and agricultural purposes. Phosphorus is taken out from the wastewater in AGS systems by PAOs or accumulates in the matrix of EPS. This extracted phosphorus can be used as soil fertilizers. The PHAs are found in intracellular intrusions. PHAs are a class of biopolymers with characteristics similar to plastics that can be utilized to make paints, packaging, insecticides, strong fibers, and sanitary products, as well as having uses in biomedicine [98].

Furthermore, the storage and reuse of AGS reduce the duration of the wastewater treatment cycle. The total cost and efforts for wastewater treatment are drastically reduced through the storage and reuse of AGS. The cost of maintaining and reusing AGS is relatively low compared to other available treatment methods such as the activated sludge process, chemical precipitation, adsorption, ion exchange, etc. Some of these methods are costly, unsustainable, and cause environmental degradation and health hazards. On the other hand, the usage of AGS makes the treatment process easier, cost-effective, environmentally friendly, sustainable, and futuristic.

9. Research Gaps and Future Prospects

In wastewater treatment plants, it has been expected that AGS will replace the current activated sludge system. However, the granulation procedure excludes the sludge with less density and only keeps sludge that has good settling properties. This means not really being able to change overall activated sludge to AGS. Then, as a result, developing techniques to speed up the process of turning entire sludge into granules remains difficult and requires substantial study. The majority of aerobic granulation processes use SBR systems, which are the best kind of reactors. However, since the majority of treatment plants use a continuous type of reactors, implementing sequencing batch reactors in a full-scale is quite challenging to deal with larger wastewater volume.

It may take several months for AGS to form. However, more research is needed to assess the granular stability and the process of disintegration brought on by unknown variables. There is a scope for developing a basic understanding of microbial interactions and granulation. Even though efforts made to improve the AGS process's use globally, some elements of this system remain obscure. The actual use of this system and the fulfillment of its advantages are being hampered by a lack of knowledge of the underlying principles regulating the formation of biofilm, the prolonged granulation phase, and disintegration of granules when operating it for long term. Moreover, the significance of EPS and its molecular mechanism in the formation and stability of granular biofilms is unknown. In addition to that, uncertainty exists regarding the effects of various operation modes and composition of wastewater on microbial environment and EPS.

Applications of AGS in the remediation of hazardous wastes, along with heavy metal and emerging toxins adsorption are not explored much. This decontamination aspect at a higher level should be looked forward for treating more and more complex wastewater. Most of the AGS studies are based on sequencing batch reactors and stability of AGS was explored in SBR only. Till now there is no study related to the stability of AGS in continuous flow reactors. So, there is an opportunity to create a novel SGS-based continuous flow reactor design.

There is a lot of scope for developing a realistic model for the storage of AGS, pilot-scale and full-scale applications for granule storage, its recovery, and rejuvenation. Only

laboratory-scale granule storage has so far been investigated. Studies should be conducted for further investigations to evaluate the effectiveness of decontamination, removal of nutrients and organics, and granule attributes such as stability, integrity, settling, and size of recovered granules during prolonged storage. Research should be conducted to determine the viability of commercializing stored granules for enhancing the use of AGS for wastewater treatment.

10. Conclusions and Perspectives

Even after 25 years since the discovery of AGS, the basic mechanism of granulation is still a matter of current research. Several hypotheses have been drawn by many researchers, but it is still a subject of current research. The formation of AGS is caused by the agglomeration of several microbial guilds which form together and perform the removal of COD, nutrients, etc. It is still necessary to improve fundamental aspects of AGS in bioreactors, such as the stability of AGS and to achieve long-term and steady operation, regardless of existing knowledge in granulation. In this review, the granulation process, nutrient removal pathway and characteristics, the stability of granules, and long-term storage of granules were comprehensively summarized. It is crucial that the physical size and structure of granules be determined by the composition and operational circumstances of the feed wastewater in order for AGS systems to perform well. In fact, it is important to note that substrate type, method of influent addition; hydraulic shear forces, organic loading rate, operational hydraulic and sludge retention times, and settling time have an impact, on AGS stability. Multiple pathways contribute to the AGS disintegration, including the outgrowth of filamentous organisms, EPS hydrolysis at the substrate-depleted core, an increased growth rate of heterotrophic micro-organisms, variations in microbial distribution patterns, and heavy metal ion toxicity. This in turn decreases the density of AGS and consequently decays into small particles with very low settleability, which are easily removed from the reactor. A major focus of contemporary research in this area is to develop operational strategies for maintaining long-term stability based on a better understanding of the microstructural characteristics that ensure AG's integrity. However, the current research developments are insufficient to meet the needs of large-scale industries and inadequate for the cost-effective and efficient usage of AGS. Further investigation is required to determine granule stability and disintegration processes caused by unknown factors to support the large-scale cost-effective usage of AGS.

The storage of AGS could provide a potential remedy to the prolonged initial time frame needed to grow granular sludge and for maintaining the stability of granules. There are different storage methods for AGS out of which dehydration and drying methods are quite efficient. Due to intra-granular protein hydrolysis during storage in a wet media, the granule lost structural integrity. Granule storage at sub-freezing temperatures, however, was impractical. In comparison with wet granules, dried granules were easier to store and handle. In recent studies, most of the researchers stored granules by drying it. Dehydration and drying are preferred over other storage methods because of their effectiveness in rejuvenating and removing contaminants. Researchers need to undertake further investigations to assess the capability of AGS for recovery, after prolonged storage in terms of removal and decontamination efficiency as well as granule characteristics such as stability, integrity, settleability, and size. A new concept of commercializing stored granules for sustainable wastewater treatment at a large scale can be presented, if all these aspects are explored. Moreover, AGS has a greater potential for resource recovery such as phosphorus, ALE, PHA, and tryptophan. The storage of granules and recovering them for later use eliminates sludge disposal and its consequences. All of these factors contribute to the AGS being a more sustainable method of treatment.

Author Contributions: K.S.S. is involved in writing the original draft, data compilation, and improvement after each review by the senior author. P.C.S. is involved in conceptualization, data curation and writing (review & editing), project administration, and fund acquisition. All authors have read and agreed to the published version of the manuscript.

Funding: This research was funded by the Department of Science and Technology (DST), Government of India with grant number DST/TM/WIC/WTI/2K17/82(G4).

Institutional Review Board Statement: Not applicable.

Informed Consent Statement: Not applicable.

Data Availability Statement: Not deposited in any repository.

Acknowledgments: Authors thank VIT management in supporting the APC for publication in a distinguished open access journal.

Conflicts of Interest: The authors declare no conflict of interest.

References

1. Nancharaiah, Y.V.; Sarvajith, M.; Mohan, T.V.K. Aerobic granular sludge: The future of wastewater treatment. *Curr. Sci.* **2019**, *117*, 395–404. [CrossRef]
2. Liang, D.; Guo, W.; Li, D.; Ding, F.; Li, P.; Zheng, Z.; Li, J. Enhanced aerobic granulatio{n for treating low-strength wastewater in an anaerobic-aerobic-anoxic sequencing batch reactor by selecting slow-growing organisms and adding carriers. *Environ. Res.* **2022**, *205*, 112547. [CrossRef] [PubMed]
3. Sarvajith, M.; Nancharaiah, Y. Enhancing biological nitrogen and phosphorus removal performance in aerobic granular sludge sequencing batch reactors by activated carbon particles. *J. Environ. Manag.* **2021**, *303*, 114134. [CrossRef] [PubMed]
4. Wang, L.; Yu, X.; Xiong, W.; Li, P.; Wang, S.; Fan, A.; Su, H. Enhancing robustness of aerobic granule sludge under low C/N ratios with addition of kitchen wastewater. *J. Environ. Manag.* **2020**, *265*, 110503. [CrossRef]
5. Liang, D.; Li, J.; Zheng, Z.; Zhang, J.; Wu, Y.; Li, D.; Li, P.; Zhang, K. Rapid start-up of the aerobic granular reactor under low temperature and the nutriment removal performance of granules with different particle sizes. *Water* **2021**, *13*, 3590. [CrossRef]
6. Rosa-Masegosa, A.; Muñoz-Palazon, B.; Gonzalez-Martinez, A.; Fenice, M.; Gorrasi, S.; Gonzalez-Lopez, J. New advances in aerobic granular sludge technology using continuous flow reactors: Engineering and microbiological aspects. *Water* **2021**, *13*, 1792. [CrossRef]
7. Sarma, S.J.; Tay, J.H. Aerobic granulation for future wastewater treatment technology: Challenges ahead. Environ. *Sci. Water Res. Technol.* **2017**, *4*, 9–15. [CrossRef]
8. Muñoz-Palazon, B.; Rodriguez-Sanchez, A.; Hurtado-Martinez, M.; Gonzalez-Lopez, J.; Pfetzing, P.; Gonzalez-Martinez, A. Performance and microbial community structure of aerobic granular bioreactors at different operational temperature. *J. Water Process Eng.* **2020**, *33*, 101110. [CrossRef]
9. Ogura, S.; Hamza, R.A.; Tay, J.H. Dried aerobic granules for fast startup of aerobic granular sludge reactors: Reactivation and performance. *J. Water Process Eng.* **2020**, *36*, 101298. [CrossRef]
10. Leal, C.; del Río, A.V.; Mesquita, D.P.; Amaral, A.L.; Ferreira, E.C. Prediction of sludge settleability, density and suspended solids of aerobic granular sludge in the presence of pharmaceutically active compounds by quantitative image analysis and chemometric tools. *J. Environ. Chem. Eng.* **2022**, *10*, 107136. [CrossRef]
11. Duarte, K.; Castellanos, R.; Costa, R.; Mahler, C.; Bassin, J. Start-up of an aerobic granular sludge system from stored granules: Evaluating the impact of storage period on biomass activity and stability and the effect of temperature on nitrification and phosphorus removal rates. *J. Environ. Manag.* **2021**, *296*, 113200. [CrossRef] [PubMed]
12. Wan, C.; Fu, L.; Li, Z.; Liu, X.; Lin, L.; Wu, C. Formation, application, and storage-reactivation of aerobic granular sludge: A review. *J Environ Manag.* **2022**, *323*, 116302. [CrossRef] [PubMed]
13. Tomar, S.K.; Chakraborty, S. Chakraborty, Comparison of rapid granulation developed from the same industrial sludge with two different substrates. *Int. Biodeterior. Biodegrad.* **2019**, *142*, 218–226. [CrossRef]
14. Wilén, B.; Liébana, R.; Persson, F.; Modin, O.; Hermansson, M. The mechanisms of granulation of activated sludge in wastewater treatment, its optimization, and impact on effluent quality. *Appl. Microbiol. Biotechnol.* **2018**, *102*, 5005–5020. [CrossRef] [PubMed]
15. Szabó, E.; Liébana, R.; Hermansson, M.; Modin, O.; Persson, F.; Wilén, B. Comparison of the bacterial community composition in the granular and the suspended phase of sequencing batch reactors. *AMB Express* **2017**, *7*, 1–12. [CrossRef]
16. Iorhemen, O.; Ukaigwe, S.; Dang, H.; Liu, Y. Phosphorus Removal from Aerobic Granular Sludge: Proliferation of Polyphosphate-Accumulating Organisms (PAOs) under Different Feeding Strategies. *Processes* **2022**, *10*, 1399. [CrossRef]
17. Sarma, S.; Tay, J.-H. Carbon, nitrogen and phosphorus removal mechanisms of aerobic granules. *Crit. Rev. Biotechnol.* **2018**, *38*, 1077–1088. [CrossRef]
18. Wagner, J.; Guimarães, L.; Akaboci, T.; Costa, R. Aerobic granular sludge technology and nitrogen removal for domestic wastewater treatment. *Water Sci. Technol.* **2015**, *71*, 1040–1046. [CrossRef]
19. Barajas, M.; Escalas, A.; Mujeriego, R. Fermentation of a low VFA wastewater in an activated primary tank. *Water SA* **2002**, *28*, 89–98. [CrossRef]
20. Su, K.-Z.; Yu, H.-Q. Formation and Characterization of Aerobic Granules in a Sequencing Batch Reactor Treating Soybean-Processing Wastewater. *Environ. Sci. Technol.* **2005**, *39*, 2818–2827. [CrossRef]

21. Gao, D.; Liu, L.; Liang, H.; Wu, W. Aerobic granular sludge: Characterization, mechanism of granulation and application to wastewater treatment. *Crit. Rev. Biotechnol.* **2011**, *31*, 137–152. [CrossRef]
22. Setianingsih, N.; Yuliasni, R. Development of Aerobic Microbial Granules to Enhance the Performance of Activated Sludge Technology for Wastewater Treatment Application. *IOP Conf. Series Earth Environ. Sci.* **2020**, *477*, 012001. [CrossRef]
23. Toh, S.K.; Tay, J.H.; Moy, B.Y.P.; Ivanov, V.; Tay, S.T.L. Size-effect on the physical characteristics of the aerobic granule in a SBR. *Appl. Microbiol. Biotechnol.* **2003**, *60*, 687–695. [CrossRef] [PubMed]
24. Berg, L.V.D.; Pronk, M.; van Loosdrecht, M.C.; de Kreuk, M.K. Density measurements of aerobic granular sludge. *Environ. Technol.* **2022**, 1–11. [CrossRef]
25. Cassidy, D.; Belia, E. Nitrogen and phosphorus removal from an abattoir wastewater in a SBR with aerobic granular sludge. *Water Res.* **2005**, *39*, 4817–4823. [CrossRef] [PubMed]
26. Ren, T.; Liu, L.; Sheng, G.; Liu, X.; Yu, H.; Zhang, M.; Zhu, J. Calcium spatial distribution in aerobic granules and its effects on granule structure, strength and bioactivity. *Water Res.* **2008**, *42*, 3343–3352. [CrossRef] [PubMed]
27. Yang, S.; Tay, J.; Liu, Y. Respirometric activities of heterotrophic and nitrifying populations in aerobic granules developed at different substrate N/COD ratios. *Curr. Microbiol.* **2004**, *49*, 42–46. [CrossRef]
28. Liu, Y.; Yang, S.-F.; Tay, J.-H.; Liu, Q.-S.; Qin, L.; Li, Y. Cell hydrophobicity is a triggering force of biogranulation. *Enzyme. Microb. Technol.* **2004**, *34*, 371–379. [CrossRef]
29. Li, Y.; Liu, Y.; Xu, H. Is sludge retention time a decisive factor for aerobic granulation in SBR? *Bioresour. Technol.* **2008**, *99*, 7672–7677. [CrossRef]
30. Tay, S.T.-L.; Moy, B.Y.-P.; Jiang, H.-L.; Tay, J.-H. Rapid cultivation of stable aerobic phenol-degrading granules using acetate-fed granules as microbial seed. *J. Biotechnol.* **2005**, *115*, 387–395. [CrossRef]
31. Jiang, Y.; Yang, K.; Shang, Y.; Zhang, H.; Wei, L.; Wang, H. Response and recovery of aerobic granular sludge to pH shock for simultaneous removal of aniline and nitrogen. *Chemosphere* **2019**, *221*, 366–374. [CrossRef] [PubMed]
32. Wang, Y.; Wang, J.; Liu, Z.; Huang, X.; Fang, F.; Guo, J.; Yan, P. Effect of EPS and its forms of aerobic granular sludge on sludge aggregation performance during granulation process based on XDLVO theory. *Sci. Total Environ.* **2021**, *795*, 148682. [CrossRef] [PubMed]
33. Liu, X.; Pei, Q.; Han, H.; Yin, H.; Chen, M.; Guo, C.; Li, J.; Qiu, H. Functional analysis of extracellular polymeric substances (EPS) during the granulation of aerobic sludge: Relationship among EPS, granulation and nutrients removal. *Environ. Res.* **2022**, *208*, 112692. [CrossRef] [PubMed]
34. Lee, D.-J.; Chen, Y.-Y.; Show, K.-Y.; Whiteley, C.G.; Tay, J.-H. Advances in aerobic granule formation and granule stability in the course of storage and reactor operation. *Biotechnol. Adv.* **2010**, *28*, 919–934. [CrossRef]
35. Ni, B.-J. *Formation, Characterization and Mathematical Modeling of the Aerobic Granular Sludge*; Springer: New York, NY, USA, 2013; Volume 131. [CrossRef]
36. Adler, A.; Holliger, C. Multistability and Reversibility of Aerobic Granular Sludge Microbial Communities Upon Changes From Simple to Complex Synthetic Wastewater and Back. *Front. Microbiol.* **2020**, *11*, 2757. [CrossRef]
37. Long, B.; Xuan, X.; Yang, C.; Zhang, L.; Cheng, Y.; Wang, J. Stability of aerobic granular sludge in a pilot scale sequencing batch reactor enhanced by granular particle size control. *Chemosphere* **2019**, *225*, 460–469. [CrossRef]
38. Lin, H.; Sun, S.; Lin, Z.; Chen, M.; Fang, L.; Ma, R.; Lin, J.; Luo, J. Bio-carrier–enhanced aerobic granulation: Effects on the extracellular polymeric substances production and microorganism community. *Chemosphere* **2021**, *280*, 130756. [CrossRef]
39. Desireddy, S.; Sabumon, P. Development of aerobic granulation system for simultaneous removal of C, N, and P in sequencing batch airlift reactor. *J. Environ. Chem. Eng.* **2021**, *9*, 106100. [CrossRef]
40. Ouyang, L.; Huang, W.; Huang, M.; Qiu, B. Polyaniline improves granulation and stability of aerobic granular sludge. *Adv. Compos. Hybrid Mater.* **2022**, *5*, 1126–1136. [CrossRef]
41. Corsino, S.; di Biase, A.; Devlin, T.; Munz, G.; Torregrossa, M.; Oleszkiewicz, J. Effect of extended famine conditions on aerobic granular sludge stability in the treatment of brewery wastewater. *Bioresour. Technol.* **2017**, *226*, 150–157. [CrossRef]
42. Ouyang, L.; Qiu, B. Positive effects of magnetic Fe3O4@polyaniline on aerobic granular sludge: Aerobic granulation, granule stability and pollutants removal performance. *Bioresour. Technol.* **2023**, *368*, 128296. [CrossRef]
43. Zahra, S.; Purba, L.; Abdullah, N.; Tanavarotai, K.; Anuar, A.N.; Aris, A.; Lei, Z.; Hakim, M.; Halim, A. Rapid method of aerobic granular sludge bioreactor start-up for domestic wastewater treatment. *Open Access IOP Conf. Ser. Earth Environ. Sci.* **2022**, *1091*, 012049. [CrossRef]
44. Liu, Y.; Tay, J. The essential role of hydrodynamic shear force in the formation of biofilm and granular sludge. *Water Res.* **2002**, *36*, 1653–1665. [CrossRef]
45. Rollemberg, S.L.D.S.; de Oliveira, L.Q.; Barros, A.R.M.; Melo, V.M.M.; Firmino, P.I.M.; dos Santos, A.B. Effects of carbon source on the formation, stability, bioactivity and biodiversity of the aerobic granule sludge. *Bioresour. Technol.* **2019**, *278*, 195–204. [CrossRef]
46. Verawaty, M.; Tait, S.; Pijuan, M.; Yuan, Z.; Bond, P. Breakage and growth towards a stable aerobic granule size during the treatment of wastewater. *Water Res.* **2013**, *47*, 5338–5349. [CrossRef]
47. Liu, Y.; Liu, Z.; Wang, F.; Chen, Y.; Kuschk, P.; Wang, X. Regulation of aerobic granular sludge reformulation after granular sludge broken: Effect of poly aluminum chloride (PAC). *Bioresour. Technol.* **2014**, *158*, 201–208. [CrossRef]

48. Nor-Anuar, A.; Ujang, Z.; van Loosdrecht, M.; De Kreuk, M.K.; Olsson, G. Strength characteristics of aerobic granular sludge. *Water Sci. Technol.* **2012**, *65*, 309–316. [CrossRef]
49. Pronk, M.; Abbas, B.; Al-zuhairy, S.; Kraan, R.; Kleerebezem, R.; van Loosdrecht, M. Effect and behaviour of different substrates in relation to the formation of aerobic granular sludge. *Appl. Microbiol. Biotechnol.* **2015**, *99*, 5257–5268. [CrossRef]
50. Iorhemen, O.; Liu, Y. Effect of feeding strategy and organic loading rate on the formation and stability of aerobic granular sludge. *J. Water Process Eng.* **2021**, *39*, 101709. [CrossRef]
51. Liu, Y.-Q.; Tay, J.-H. Fast formation of aerobic granules by combining strong hydraulic selection pressure with overstressed organic loading rate. *Water Res.* **2015**, *80*, 256–266. [CrossRef] [PubMed]
52. Hou, Y.; Gan, C.; Chen, R.; Chen, Y.; Yuan, S.; Chen, Y. Structural Characteristics of Aerobic Granular Sludge and Factors That Influence Its Stability: A Mini Review. *Water* **2021**, *13*, 2726. [CrossRef]
53. Zhou, D.; Liu, M.; Gao, L.; Shao, C.; Yu, J. Calcium accumulation characterization in the aerobic granules cultivated in a continuous-flow airlift bioreactor. *Biotechnol. Lett.* **2013**, *35*, 871–877. [CrossRef] [PubMed]
54. Zhou, D.; Liu, M.; Wang, J.; Dong, S.; Cui, N.; Gao, L. Granulation of activated sludge in a continuous flow airlift reactor by strong drag force. *Biotechnol. Bioprocess Eng.* **2013**, *18*, 289–299. [CrossRef]
55. Liébana, R.; Modin, O.; Persson, F.; Wilén, B. Integration of aerobic granular sludge and membrane bioreactors for wastewater treatment. *Crit. Rev. Biotechnol.* **2018**, *38*, 801–816. [CrossRef] [PubMed]
56. Campo, R.; Lubello, C.; Lotti, T.; Di Bella, G. Aerobic Granular Sludge–Membrane BioReactor (AGS–MBR) as a Novel Configuration for Wastewater Treatment and Fouling Mitigation: A Mini-Review. *Membranes* **2021**, *11*, 261. [CrossRef]
57. Xu, D.; Li, J.; Qu, X.; Ma, H. Advances in continuous flow aerobic granular sludge: A review. *Process. Saf. Environ. Prot.* **2022**, *163*, 27–35. [CrossRef]
58. Awang, N.A.; Shaaban, G. The impact of reactor height/diameter (H/D) ratio on aerobic granular sludge (AGS) formation in sewage. *J. Teknol.* **2015**, *77*, 95–103. [CrossRef]
59. Hamiruddin, N.A.; Awang, N.A. The Relationship Between the Biokinetic Parameters of an Aerobic Granular Sludge System and the Applied Operating Conditions. *Civ. Environ. Eng. Rep.* **2021**, *31*, 161–171. [CrossRef]
60. Zhu, L.; Zhou, J.; Yu, H.; Xu, X. Optimization of hydraulic shear parameters and reactor configuration in the aerobic granular sludge process. *Environ. Technol.* **2015**, *36*, 1605–1611. [CrossRef]
61. Zhou, J.-H.; Zhang, Z.-M.; Zhao, H.; Yu, H.-T.; Alvarez, P.J.; Xu, X.-Y.; Zhu, L. Optimizing granules size distribution for aerobic granular sludge stability: Effect of a novel funnel-shaped internals on hydraulic shear stress. *Bioresour. Technol.* **2016**, *216*, 562–570. [CrossRef]
62. TDevlin, T.; di Biase, A.; Kowalski, M.; Oleszkiewicz, J. Granulation of activated sludge under low hydrodynamic shear and different wastewater characteristics. *Bioresour. Technol.* **2017**, *224*, 229–235. [CrossRef] [PubMed]
63. Lashkarizadeh, M.; Munz, G.; Oleszkiewicz, J.A. Impacts of variable pH on stability and nutrient removal efficiency of aerobic granular sludge. *Water Sci. Technol.* **2016**, *73*, 60–68. [CrossRef] [PubMed]
64. Wan, C.; Yang, X.; Lee, D.; Zhang, Q.; Li, J.; Liu, X. Formation of filamentous aerobic granules: Role of pH and mechanism. *Appl. Microbiol. Biotechnol.* **2014**, *98*, 8389–8397. [CrossRef]
65. Muñoz-Palazon, B.; Rodriguez-Sanchez, A.; Hurtado-Martinez, M.; Santana, F.; Gonzalez-Lopez, J.; Mack, L.; Gonzalez-Martinez, A. Polar Arctic Circle biomass enhances performance and stability of aerobic granular sludge systems operated under different temperatures. *Bioresour. Technol.* **2020**, *300*, 122650. [CrossRef]
66. Gonzalez-Martinez, A.; Muñoz-Palazon, B.; Rodriguez-Sanchez, A.; Maza-Márquez, P.; Mikola, A.; Gonzalez-Lopez, J.; Vahala, R. Start-up and operation of an aerobic granular sludge system under low working temperature inoculated with cold-adapted activated sludge from Finland. *Bioresour. Technol.* **2017**, *239*, 180–189. [CrossRef] [PubMed]
67. Ab Halim, M.H.; Anuar, A.N.; Jamal, N.S.A.; Azmi, S.I.; Ujang, Z.; Bob, M.M. Influence of high temperature on the performance of aerobic granular sludge in biological treatment of wastewater. *J. Environ. Manag.* **2016**, *184*, 271–280. [CrossRef]
68. Jin, Y.; Xiong, W.; Zhou, N.; Xiao, G.; Wang, S.; Su, H. Role of initial bacterial community in the aerobic sludge granulation and performance. *J. Environ. Manag.* **2022**, *309*, 114706. [CrossRef]
69. Meng, F.; Huang, W.; Liu, D.; Zhao, Y.; Huang, W.; Lei, Z.; Zhang, Z. Application of aerobic granules-continuous flow reactor for saline wastewater treatment: Granular stability, lipid production and symbiotic relationship between bacteria and algae. *Bioresour Technol.* **2020**, *295*, 122291. [CrossRef]
70. Wang, X.; Chen, Z.; Kang, J.; Zhao, X.; Shen, J.; Yang, L. The key role of inoculated sludge in fast start-up of sequencing batch reactor for the domestication of aerobic granular sludge. *J. Environ. Sci.* **2019**, *78*, 127–136. [CrossRef]
71. Zou, J.; Pan, J.; Wu, S.; Qian, M.; He, Z.; Wang, B.; Li, J. Rapid control of activated sludge bulking and simultaneous acceleration of aerobic granulation by adding intact aerobic granular sludge. *Sci. Total Environ.* **2019**, *674*, 105–113. [CrossRef]
72. Yuan, Q.; Gong, H.; Xi, H.; Xu, H.; Jin, Z.; Ali, N.; Wang, K. Strategies to improve aerobic granular sludge stability and nitrogen removal based on feeding mode and substrate. *J. Environ. Sci.* **2019**, *84*, 144–154. [CrossRef] [PubMed]
73. Gao, D.; Yuan, X.; Liang, H. Reactivation performance of aerobic granules under different storage strategies. *Water Res.* **2012**, *46*, 3315–3322. [CrossRef] [PubMed]
74. Lv, Y.; Wan, C.; Lee, D.-J.; Liu, X.; Zhang, Y.; Tay, J.-H. Dehydrated and recovered aerobic granules: Identifying acetone-dehydration resistant strains. *Bioresour. Technol. Rep.* **2019**, *5*, 99–103. [CrossRef]

75. Lv, Y.; Wan, C.; Lee, D.-J.; Liu, X.; Zhang, Y.; Tay, J.-H. Recovery of dehydrated aerobic granules: A comparison. *Bioresour. Technol.* **2018**, *267*, 769–773. [CrossRef]
76. Hu, J.; Zhang, Q.; Chen, Y.-Y.; Lee, D.-J. Drying and recovery of aerobic granules. *Bioresour. Technol.* **2016**, *218*, 397–401. [CrossRef]
77. Lv, Y.; Wan, C.; Liu, X.; Zhang, Y.; Lee, D.-J.; Tay, J.-H. Tay, Freezing of aerobic granules for storage and subsequent recovery. *J. Taiwan Inst. Chem. Eng.* **2013**, *44*, 770–773. [CrossRef]
78. Wan, C.; Lee, D.-J.; Yang, X.; Wang, Y.; Lin, L. Saline storage of aerobic granules and subsequent reactivation. *Bioresour. Technol.* **2014**, *172*, 418–422. [CrossRef]
79. Chen, Y.; Zhu, J.-Y.; Qin, Y.; Zhang, Z.-M.; Yuan, S.-C. Reactivation of hypersaline aerobic granular sludge after Low-temperature storage. *Tecnol. Cienc. Agua* **2017**, *8*, 61–70. [CrossRef]
80. Adav, S.S.; Lee, D.-J.; Tay, J.H. Activity and structure of stored aerobic granules. *Environ Technol.* **2007**, *28*, 1227–1235. [CrossRef]
81. Yan, L.; Guo, Y.; Zhang, X.; Yu, L.; Bao, X.; Hao, G.; Chen, Z.; Ren, Y. Influence of storage strategies on the reactivation characteristics of shortcut nitrification aerobic granular sludge. *Chem. Biochem. Eng. Q.* **2017**, *31*, 115–121. [CrossRef]
82. Zhang, Q.; Hu, J.; Lee, D.-J. Aerobic granular processes: Current research trends. *Bioresour. Technol.* **2016**, *210*, 74–80. [CrossRef] [PubMed]
83. Chen, K.; Zhao, Z.; Yang, X.; Lei, Z.; Zhang, Z.; Zhang, S. Desorption trials and granular stability of chromium loaded aerobic granular sludge from synthetic domestic wastewater treatment. *Bioresour. Technol. Rep.* **2018**, *1*, 9–15. [CrossRef]
84. Adav, S.S.; Lee, D.-J.; Lai, J.-Y. Proteolytic activity in stored aerobic granular sludge and structural integrity. *Bioresour. Technol.* **2009**, *100*, 68–73. [CrossRef] [PubMed]
85. Hung, W.; Feng, W.; Tsai, I.; Lee, D.; Hong, S. Uni-directional freezing of waste activated sludges: Vertical freezing versus radial freezing. *Water Res.* **1997**, *31*, 2219–2228. [CrossRef]
86. Show, K.-Y.; Lee, D.-J.; Tay, J.-H. Aerobic granulation: Advances and challenges. *Appl. Biochem. Biotechnol.* **2012**, *167*, 1622–1640. [CrossRef] [PubMed]
87. Lv, Y.; Wan, C.; Liu, X.; Zhang, Y.; Lee, D.-J.; Tay, J.-H. Tay, Drying and re-cultivation of aerobic granules. *Bioresour. Technol.* **2013**, *129*, 700–703. [CrossRef] [PubMed]
88. Yuan, X.; Gao, D.; Liang, H. Reactivation characteristics of stored aerobic granular sludge using different operational strategies. *Appl. Microbiol. Biotechnol.* **2012**, *94*, 1365–1374. [CrossRef]
89. Wan, C.; Zhang, Q.; Lee, D.-J.; Wang, Y.; Li, J. Long-term storage of aerobic granules in liquid media: Viable but non-culturable status. *Bioresour. Technol.* **2014**, *166*, 464–470. [CrossRef]
90. Tay, J.H.; Liu, Q.S.; Liu, Y. Characteristics of Aerobic Granules Grown on Glucose and Acetate in Sequential Aerobic Sludge Blanket Reactors. *Environ. Technol.* **2002**, *23*, 931–936. [CrossRef]
91. Zeng, P.; Zhuang, W.-Q.; Tay, S.T.-L.; Tay, J.-H. The influence of storage on the morphology and physiology of phthalic acid-degrading aerobic granules. *Chemosphere* **2007**, *69*, 1751–1757. [CrossRef]
92. Wang, X.-H.; Zhang, H.; Yang, F.; Wang, Y.; Gao, M. Long-term storage and subsequent reactivation of aerobic granules. *Bioresour. Technol.* **2008**, *99*, 8304–8309. [CrossRef] [PubMed]
93. Zhu, J.; Wilderer, P.A. Effect of extended idle conditions on structure and activity of granular activated sludge. *Water Res.* **2003**, *37*, 2013–2018. [CrossRef] [PubMed]
94. Da Costa, N.P.A.V.; Libardi, N.; Schambeck, C.M.; Filho, P.B.; da Costa, R.H.R. Impact of additive application on the establishment of fast and stable aerobic granulation. *Appl. Microbiol. Biotechnol.* **2020**, *104*, 5697–5709. [CrossRef] [PubMed]
95. Eljamal, R.; Kahraman, I.; Eljamal, O.; Thompson, I.P.; Maamoun, I.; Yilmaz, G. Impact of nZVI on the formation of aerobic granules, bacterial growth and nutrient removal using aerobic sequencing batch reactor. *Environ. Technol. Innov.* **2020**, *19*, 100911. [CrossRef]
96. Eljamal, R.; Maamoun, I.; Bensaida, K.; Yilmaz, G.; Sugihara, Y.; Eljamal, O. A novel method to improve methane generation from waste sludge using iron nanoparticles coated with magnesium hydroxide. *Renew. Sustain. Energy Rev.* **2022**, *158*, 112192. [CrossRef]
97. The 17 GOALS | Sustainable Development. Available online: https://sdgs.un.org/goals (accessed on 30 November 2022).
98. Carvalho, C.D.A.D.; dos Santos, A.F.; Ferreira, T.J.T.; Lira, V.N.S.A.; Barros, A.R.M.; dos Santos, A.B. Resource recovery in aerobic granular sludge systems: Is it feasible or still a long way to go? *Chemosphere* **2021**, *274*, 129881. [CrossRef]

Disclaimer/Publisher's Note: The statements, opinions and data contained in all publications are solely those of the individual author(s) and contributor(s) and not of MDPI and/or the editor(s). MDPI and/or the editor(s) disclaim responsibility for any injury to people or property resulting from any ideas, methods, instructions or products referred to in the content.

environments

MDPI

Review

Pathways for the Valorization of Animal and Human Waste to Biofuels, Sustainable Materials, and Value-Added Chemicals

Jude A. Okolie [1,*], Toheeb Jimoh [2], Olugbenga Akande [3], Patrick U. Okoye [4], Chukwuma C. Ogbaga [5,6], Adekunle A. Adeleke [7], Peter P. Ikubanni [8], Fatih Güleç [9,10] and Andrew Nosakhare Amenaghawon [11]

1 Engineering Pathways, Gallogly College of Engineering, University of Oklahoma, Norman, OK 73019, USA
2 Department of Chemical Engineering, University of Ilorin, Ilorin 240003, Nigeria
3 Department of Advanced Convergence, Handong Global University, 558 Handong-ro, Heunghae-eup, Buk-gu, Pohang 37554, Republic of Korea
4 Instituto de Energías Renovables (IER-UNAM), Privada Xochicalco s/n Col. Centro, Temixco 62580, México
5 Department of Biological Sciences, Nile University of Nigeria, Airport Road Bypass, Abuja 900001, Nigeria
6 Department of Microbiology and Biotechnology, Nile University of Nigeria, Airport Road Bypass, Abuja 900001, Nigeria
7 Department of Mechanical Engineering, Nile University of Nigeria, Abuja 900001, Nigeria
8 Mechanical Engineering Department, Landmark University, Omu Aran 251103, Nigeria
9 Low Carbon Energy and Resources Technologies Research Group, Faculty of Engineering, University of Nottingham, Nottingham NG7 2TU, UK
10 Advanced Materials Research Group, Faculty of Engineering, University of Nottingham, Nottingham NG7 2RD, UK
11 Bioresources Valorization Laboratory, Department of Chemical Engineering, Faculty of Engineering, University of Benin, Benin City 300213, Nigeria
* Correspondence: jude.okolie@ou.edu

Abstract: Human and animal waste, including waste products originating from human or animal digestive systems, such as urine, feces, and animal manure, have constituted a nuisance to the environment. Inappropriate disposal and poor sanitation of human and animal waste often cause negative impacts on human health through contamination of the terrestrial environment, soil, and water bodies. Therefore, it is necessary to convert these wastes into useful resources to mitigate their adverse environmental effect. The present study provides an overview and research progress of different thermochemical and biological conversion pathways for the transformation of human- and animal-derived waste into valuable resources. The physicochemical properties of human and animal waste are meticulously discussed, as well as nutrient recovery strategies. In addition, a bibliometric analysis is provided to identify the trends in research and knowledge gaps. The results reveal that the USA, China, and England are the dominant countries in the research areas related to resource recovery from human or animal waste. In addition, researchers from the University of Illinois, the University of California Davis, the Chinese Academy of Sciences, and Zhejiang University are front runners in research related to these areas. Future research could be extended to the development of technologies for on-site recovery of resources, exploring integrated resource recovery pathways, and exploring different safe waste processing methods.

Keywords: thermochemical conversion; biological conversion; human excreta; waste-to-energy; livestock manure

Citation: Okolie, J.A.; Jimoh, T.; Akande, O.; Okoye, P.U.; Ogbaga, C.C.; Adeleke, A.A.; Ikubanni, P.P.; Güleç, F.; Amenaghawon, A.N. Pathways for the Valorization of Animal and Human Waste to Biofuels, Sustainable Materials, and Value-Added Chemicals. *Environments* **2023**, *10*, 46. https://doi.org/10.3390/environments10030046

Academic Editors: Dino Musmarra and Simeone Chianese

Received: 19 January 2023
Revised: 19 February 2023
Accepted: 24 February 2023
Published: 6 March 2023

Copyright: © 2023 by the authors. Licensee MDPI, Basel, Switzerland. This article is an open access article distributed under the terms and conditions of the Creative Commons Attribution (CC BY) license (https://creativecommons.org/licenses/by/4.0/).

1. Introduction

Human and animal waste management is a growing concern globally. Human and animal waste, in this context, refers to waste products originating from human or animal digestive systems, including urine and feces. In contrast, animal manure comprises feces, urine, and other excrement produced by animals, as well as animal manure derived from animal feces. The lack of sewerage in densely populated areas, especially in underdeveloped

countries, often leads to the indiscriminate and unhealthy disposal of solid waste, including feces and urine [1]. The World Health Organization (WHO) projected that more than 20% of 7.8 billion individuals in the world do not have access to well-managed sanitation and are often practicing open defecation [2]. Approximately three-fifths of globally generated fecal wastes are not subjected to any treatment process and are often disposed of in small or large water bodies [3]. As a result, the water bodies become unsafe for drinking and pose severe contamination risks to the aquatic ecosystem. Approximately 500,000 deaths of children under 5 years old are recorded yearly from diarrhea, due to drinking water contaminated by human and animal wastes [4]. There is no doubt that human and animal waste constitute serious environmental nuisances.

Poor sanitation and fecal sludge management can affect human health and contaminate soil and water bodies. Moreover, human feces and animal waste contain an array of pathogens that can cause waterborne diseases if released into the environment without adequate treatment. Additionally, the progressing production rate of human- and animal-derived waste is another issue that requires attention. The increasing world population, as well as industrialization and urbanization, have contributed to the increasing demand for dairy and animal products, thereby increasing the amount of animal waste produced annually. For example, China's livestock industry generated approximately 4 billion tons of manure, which is six times that of the past 40 years, followed by the United States, with approximately 1.4 billion tons [2]. Animal manure has always been used as a soil conditioner and as a nutrient to enhance crop growth [5]. However, when manure decomposes, it releases methane gas (CH_4), which is a contributor to global warming and a major greenhouse gas (GHG).

Improved sanitation could help reduce the adverse effect of human waste and provide a decent barrier between humans and harmful pathogens [6]. However, factors such as sustainability concerns related to the emissions of GHG from domestic wastewater treatment facilities and the rapidly increasing population of individuals without sanitation have hindered the development of sanitation technologies. Therefore, it is imperative to consider alternative waste valorization routes to complement the development of advanced sanitation facilities worldwide.

Human and animal waste can be converted into valuable resources through several process steps and conversion pathways. The two key conversion pathways are thermochemical and biological processes [7]. Thermochemical processes include gasification, pyrolysis, and liquefaction. Such processes proceed with the aid of thermal and chemical energy at high temperatures. In contrast, biological processes, such as anaerobic digestion (AD) and fermentation, employ microorganisms for the degradation of organic waste [8]. Thermochemical or biological valorization of human and animal waste could help promote sustainable development goals (SDGs) 6 (clean water and sanitation) and 7 (affordable and clean energy).

Human and animal waste are complex and heterogeneous, and most of the waste also contains high moisture contents. Compositing human and animal waste has been an effective traditional method of eliminating pathogenic bacteria and balancing the carbon-to-nitrogen ratio [9]. AD is also another effective method for human and animal waste valorization [9]. Several studies have reported that human or animal waste could be an effective source of energy or nutrients [10–13]. Hunter and Deshusses [3] developed nitrification and denitrification filters to post-treat human waste-derived digestate, so that they can efficiently recover nutrients that may be used as fertilizer [3]. Oa [14] studied the recovery of resources from animal waste. They proposed an integrated system for the recovery of nutrients. The integrated system comprises incineration processes, anaerobic digestion or microbial fuel cells, mechanical vapor compression distillation for recovering nitrogen, and struvite precipitation for recovering phosphorus [14].

Some authors have also published excellent reviews related to the valorization of human and animal waste, as summarized in Table 1. However, the available information on resource recovery from human or animal waste is scattered in the literature considering the

environmental relevance of the topic. Moreover, most of the available studies either focus on one type of waste (human or animal waste) or one resource recovery pathway (biological or thermochemical routes). Although, there have been some pioneering studies on the use of human urine as fertilizer [15]. To the best of the authors' knowledge, comprehensive studies that consider both human and animal waste, including animal manure, as well as all possible resource recovery methods, are scarce in the literature. Furthermore, a bibliometric analysis of research studies related to the valorization of human and animal waste has not been documented in the literature. Thus, this study comprehensively reviewed different pathways for the recovery of resources from human and animal waste. It also discusses and compares the physical and chemical properties of human and livestock urine and feces. Human and livestock urine and feces, as a source of fertilizer, were also discussed in this paper. An overview of the key contents of this study is summarized in Table 1.

Table 1. Summary of review articles related to resource recovery from human and animal waste.

Review Title	The Main Issue Addressed	References
A review of sanitation technologies to achieve multiple sustainable development goals that promote resource recovery	• Reviewed different sanitation technologies to safely recover resources from human waste. • Presented various nitrogen and phosphorus recovery pathways.	Orner and Mihelcic [6]
Resource recovery processes from animal waste as best available technology	• Discussed the available nutrient recovery technology from animal waste. • Proposed an integrated cost-effective system for the recovery of nutrients from animal waste.	Lee and Oa. [14]
Sustainable Valorization of Animal Manures via Thermochemical Conversion Technologies: An Inclusive Review on Recent Trends	• Discussed various sustainable pathways for the conversion of animal manure to useful resources. • Discussed the properties of animal manure, modelling, and optimization of thermochemical conversion of animal manure as well as the life cycle assessment.	Rout et al. [16]
Energy production from biogas: A conceptual review for use in Nigeria	• Reviewed global methods of biogas production from animal manure. • Discussed the ecological and economic benefits of producing biogas from animal manure in Nigeria.	Olugasa et al. [17]

Table 1. *Cont.*

Review Title	The Main Issue Addressed	References
Sustainable Animal Manure Management Strategies and Practices	• Discussed various sustainable and unsustainable animal manure handling practices. • Reviewed the risks associated with irresponsible handling of animal manure.	Malomo et al. [18]
Human excreta management: human excreta as an important base of sustainable agriculture	• Discussed research progress related to resource recovery from human feces. • Compared the environmental impacts of toilet flushing with the benefits and necessity of composting human feces.	Zseni. [19]
A technical review on resource recovery from human and animal waste	• Provides a comparative evaluation of the physical and chemical properties of various human and animal waste. • Comprehensively reviewed different thermochemical and biological processes for the valorization of human and animal waste. • Outlines the current status and progress of nutrient recovery technologies from human and animal waste. • Discussed the bibliometric research trends related to resource recovery from human and animal waste.	This study

2. Physical and Chemical Properties of Human and Livestock Urine and Feces

Figure 1 shows the different classifications of human and animal waste considered in this study. Human waste, such as feces and urine, are meticulously reviewed. The combination of human feces and urine is known as excreta. In contrast, animal manure from livestock, domestic animals, poultry, and horses are also discussed.

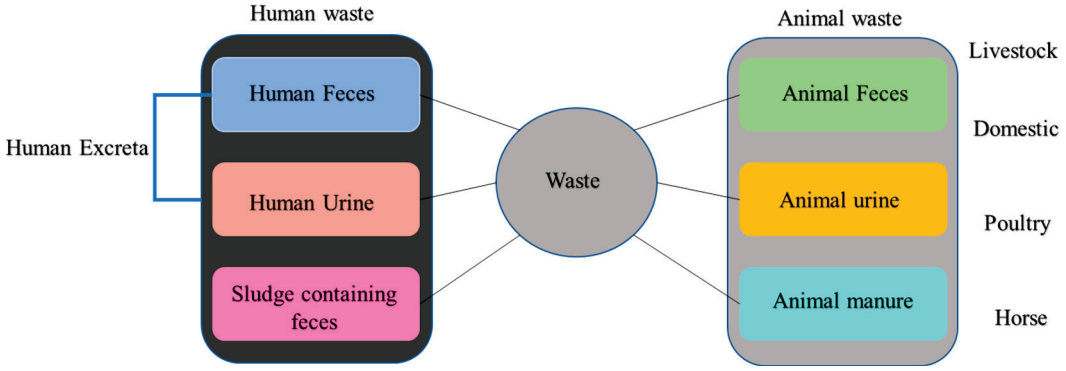


Figure 1. Classification of human and animal waste considered in this study. Note that, while there are several waste classifications, the one presented herein is based on the authors' experience and the scope of the present study.

Manures are valuable organic matter derived from solid animal waste, including cow dung, and biogas plant slurries. They can be used as a nutrient source to enhance crop growth and as a soil conditioner. Animal waste is a combination of waste feeds, feces, urine, and bedding materials. It consists of macronutrients such as nitrogen (N), phosphorus (P), and potassium (K) and micronutrients such as iron (Fe), sodium (Na), cobalt (Co), manganese (Mn), sulphur (S), and magnesium (Mg). The physicochemical properties of manure are one of the most important factors in evaluating the most promising valorization pathways [16,18]. Animal manure can also be classified based on its moisture content into liquid manure (up to 95% moisture content), semisolid and slurry manure (between 75% and 95% moisture content), and solid manure (less than 75% moisture content) [19]. The average composition and nutrient content of human excreta (urine and feces) and animal manure are comprehensively compared and summarized in Table 2.

Table 2. Composition and nutrient content of animal manure and human excreta [20–22].

Category	Moisture Content (%)	Weight (kg)	N (kg)	K (kg)	P (kg)	Volatile Solids (kg)	Total Solids (kg)	Biological Oxygen Demand, (BOD) (kg)
Poultry manures								
Broilers	74	40.00	0.44	0.25	0.13	7.72	9.99	2.41
Duck	74	46.31	0.45	0.23	0.16	7.26	12.26	2.04
Layers	75	25.88	0.50	0.18	0.15	5.00	6.81	1.51
Swine manure								
Boar	90	8.63	0.06	0.04	0.03	0.77	0.86	0.30
Gestating sow	90	11.34	0.07	0.05	0.03	1.04	1.14	0.38
Lactating sow	90	26.79	0.20	0.13	0.06	2.45	2.68	0.91
Beef manure								
Finishing cattle	92	29.51	0.16–0.23	0.11	0.02–0.03	1.95	2.36	0.45
Beef cow in confinement	88	47.22	0.16	0.11	0.04	5.00	5.90	1.14
Growing calf in confinement	88	34.96	0.20	0.13	0.04	3.50	4.18	0.77
Human								
Human feces	72	0.225	0.01	0.004	0.01	-	-	5.48
Human urine	95	0.12	0.02	0.005	0.005	-	-	1.83

The data in Table 2 show that the composition of animal manure varies among animals. However, they are all rich in N, P, and K contents, making them valuable fertilizer resources. They also contain high moisture content between 70 and 92%. Compared to animal manure, human excreta have a higher biological oxygen demand (BOD). BOD is an indication of

the amount of oxygen that is required by microorganisms to break down organic matter in water. Given that organic matter in the water can have a detrimental effect on aquatic life, it is a crucial indicator of the quality of the water. High BOD levels can be a sign of excess nutrients, such as nitrogen and phosphorus, which can cause eutrophication or excessive growth of plants and algae. Aquatic life may be harmed or killed if the substance's oxygen levels fall as a result. High BOD levels may also be a sign of the existence of pathogenic (disease-causing) organisms that could be dangerous to people.

The proximate and ultimate analysis of human feces and animal manure is presented in Table 3. The manures are rich in carbon content and volatile matter. Chicken manure has a relatively high volatile matter content (65.6 wt.%), compared to human feces (50.2 wt.%). In contrast, the carbon content of human feces is higher (43.5 wt.%).

The fixed carbon content provides an overview of the amount of char formation during the thermochemical conversion process. It is the solid combustible residue that remains after the volatile matter is driven off. A relatively high fixed carbon indicates an improved char production during the thermochemical conversion process. However, the fixed carbon content of animal manure is less than 26%. Lower ash content is also favorable for thermochemical processes. Therefore, the low fixed carbon of human and animal waste makes them promising thermochemical process precursors. However, severe agglomeration and erosion problems could occur, as the ash content significantly exceeded the 6% threshold.

Both human and animal waste are also characterized by low S content and high O content (Table 3). The energy content of human and animal waste is defined by the higher heating value (HHV). The HHV of animal manure ranges between 13.2 and 22.5 MJ/kg. This value is within the range of the HHV value of a typical lignocellulosic biomass (15–21 MJ/kg) [21]. The higher HHV and lower S content confirm that human and animal waste are promising fuel sources. The H/C and O/C ratios of animal manures are higher than those of coal and biochar, as indicated in the van Krevelen diagram in Figure 2 [22]. The position of the animal manures in the van Krevelen plot is similar to the position of plant biomass. Pig manure had a significantly lower O/C ratio, while beef manure had a low H/C ratio. Low O/C and H/C ratios may indicate that a compound is more reduced, meaning that it contains more hydrogen and less oxygen, relative to carbon. Compounds with low O/C and H/C ratios may be more stable and have lower reactivity, compared to compounds with high O/C and H/C ratios.

Table 3. Proximate and ultimate analysis of human and livestock wastes, expressed on a dry basis.

Waste Types	Proximate Analysis			Ultimate Analysis				Higher Heating Value	References
	Volatile Matter (wt.%)	Fixed Carbon (wt.%)	Ash Content (wt.%)	C (wt.%)	S (wt.%)	O (wt.%)	H (wt.%)	HHV (MJ/kg)	
Chicken manure	65.6	12.9	21.7	35.6	1.5	35.5	4.6	13.2	Hussein et al. [23]
Human feces	50.2	25.1	14.8	43.5	0.7	30.1	6.4	19.3	Yacob et al. [24]
Horse manure	70.4	11	10.5	46.1	0.2	53.1	5.4	22.5	Nitsche et al. [25] Chong et al. [26]
Pig manure	-	-	22.3	40.4	0.4	50.6	6.3	13.7	Wu et al. [27]
Cattle manure	-	-	7.2	35.4	-	57.5	4.7	15.2	Islam et al. [28]

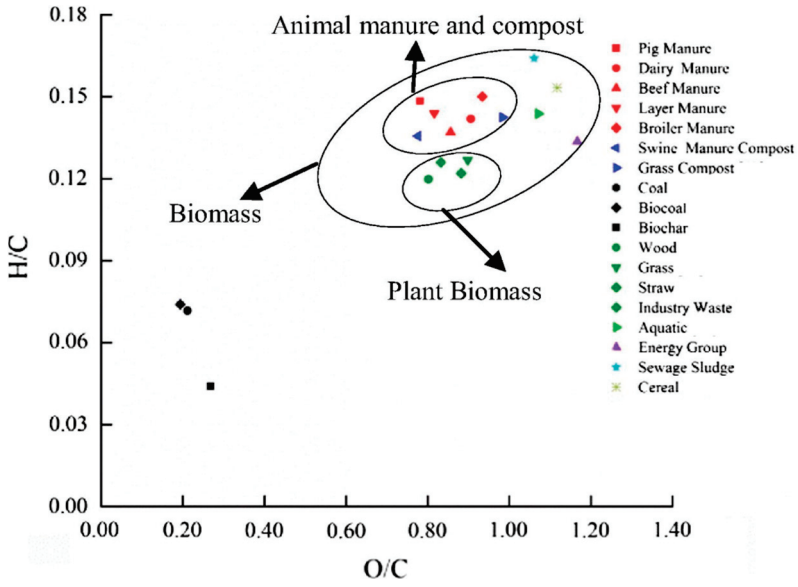


Figure 2. Van Krevelen diagram representing the heating values of the different types of animal manures, compared with solid fuels. Adapted from Shen et al. 2 [22] with permission from Elsevier.

The physicochemical characterization of different animal manures for energy production has been the focus of some research studies. Shen et al. [22] revealed that different types of animal manure presented a wide variation in their composition. Their study on the composition analysis of different Chinese animal manures showed a significant difference in composition among the various types of animal manures.

The physicochemical properties of human excreta depend on gender, age, protein, the quantity of fiber, calories taken in, geographical location, diet, and sociocultural factors. Human excreta is mostly composed of water. Feces water content is a factor of health status, the quantity of water taken in, and the duration the feces spends in the intestine before it is excreted [20,29]. Fresh human feces contain 75–80% moisture content, while the rest are solids (ash, undigested fats, food remnants, and proteins). The pH of feces is approximately 5–7 [30], and urine contains approximately 90% water, with the rest being inorganic salts, organic compounds, organic ammonium salts, and urea [31].

An individual excretes approximately 50 kg of feces and 500 kg of urine each year with the following composition: 1.2 kg K, 0.6 kg P, and 5.7 kg N, but only 60–65% of total P, 50–80% of total K, and 90% of total N are excreted in the urine [32]. The average urine per capita per year is 500 L. North America and Europe produce feces of 130–520 g person^{-1} d^{-1} and 100–200 person^{-1} d^{-1}, respectively. Urine has lower K/N and P/N ratios than synthetic fertilizers [32].

Generally, animal manure also contains heavy metals, such as Pb, Cu, Zn, Fe, and Sr, in large quantities. A recent study showed that lactating dromedary manure samples contain 2189 mg kg^{-1} Fe, 183 mg kg^{-1} Mn, 293 mg kg^{-1} Sr, and 87 mg kg^{-1} Zn heavy metals [32]. The presence of heavy metals in animal manure could constitute environmental challenges.

3. Thermochemical Conversion of Human and Animal Waste

The thermochemical conversion processes discussed in this section include pyrolysis, gasification, and liquefaction. These processes are used in the conversion of human and animal waste into various valuable chemicals and biofuels.

3.1. Pyrolysis

Pyrolysis refers to the thermal decomposition of biogenic waste in an oxygen-free environment to produce bio-oil, gases, and biochar, depending on the reaction conditions. Operating conditions such as the pressure, temperature, physicochemical properties of

the feed materials, residence time, and heating rate influence the product yields and composition during pyrolysis.

Pyrolysis can be classified into slow pyrolysis, flash pyrolysis, and fast pyrolysis, based on the operating conditions utilized in the process [8]. The operating conditions and key products of different types of pyrolysis are summarized in Figure 3. Slow pyrolysis requires a lower temperature and longer residence time to complete the process with biochar as the major product. Slow pyrolysis yields higher biochar yields (15–40 wt.%) and lower bio-oil (25–35 wt.%) and gas yields (10–25 wt.%). In contrast, fast pyrolysis occurs under a very high temperature, high heating rate, and relatively short residence time. This results in bio-oil formation as the key product during slow and flash pyrolysis. Flash pyrolysis is an extremely rapid thermal decomposition pyrolysis that occurs at a relatively high heating rate and short residence time and temperatures between 800 and 1000 °C. The rapid heating and cooling rates in flash pyrolysis allow for the production of high-quality pyrolysis products with minimal degradation or secondary reactions. The major products are gases and bio-oil with minimal biochar formation. Generally, flash pyrolysis produces approximately 60–75 wt.% bio-oil, 10–25 wt.% biochar, and 10–30 wt.% gases [33].

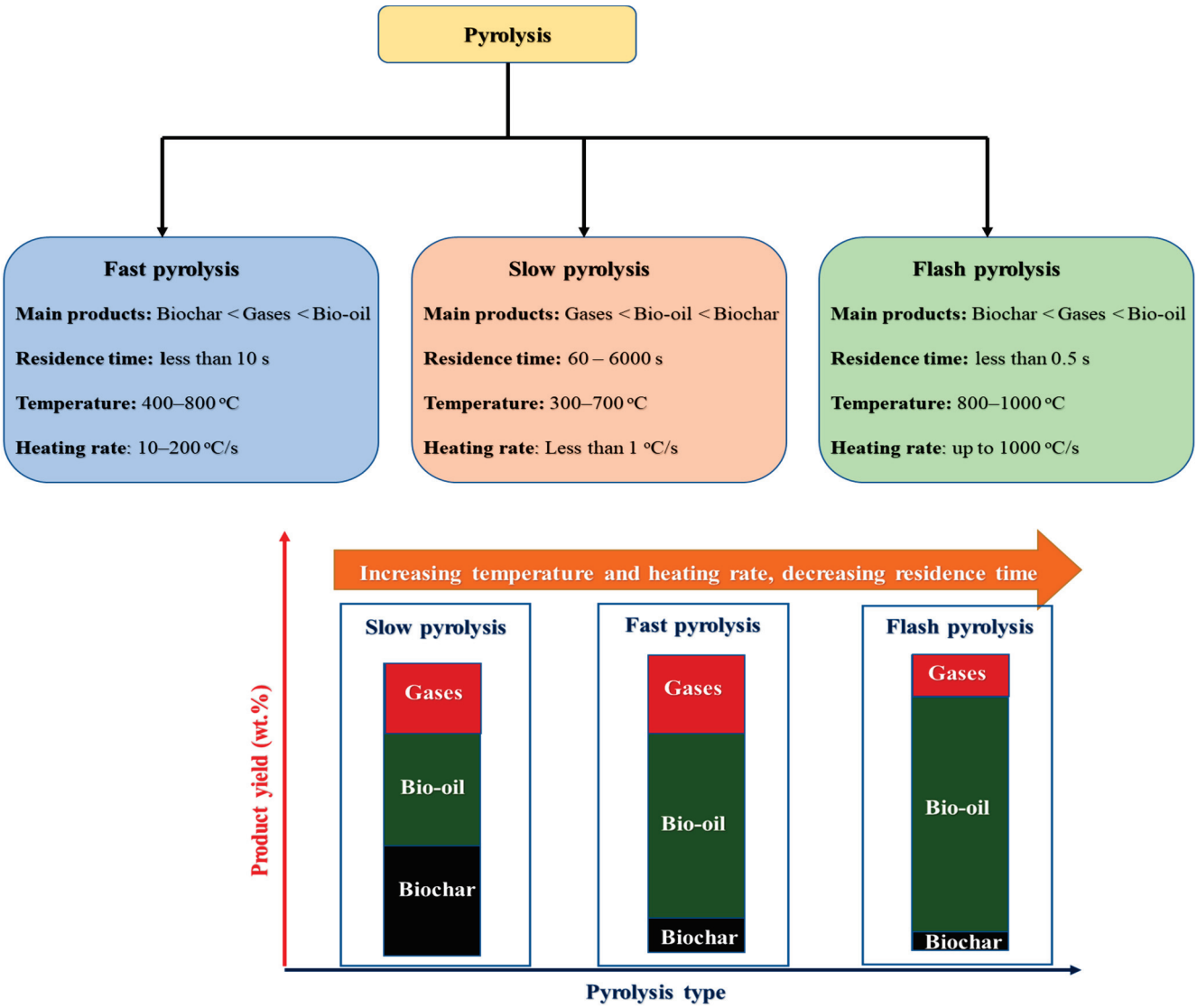


Figure 3. Overview of different types of pyrolysis. Data were obtained from Okolie et al. [8].

Several studies have reported the pyrolysis of human and animal waste for biochar and bio-oil production [34–37]. Most of the studies either focus on process optimization or evaluation of the influence of reaction conditions on biochar production [38], a study of the reaction mechanism, or the development of new catalysts [39]. Cantrell et al. [38] reported the effect of pyrolysis temperature on the physicochemical properties of biochar derived from five different animal manure precursors (poultry litter, swine-separated solids, turkey litter, dairy manure, and paved feedlot manure). The study revealed that the biochar obtained from dairy manure had the highest energy density, carbon, and volatile matter, coupled with the lowest contents of N, S, and ash. Moreover, the biochar produced from poultry litter had the highest electrical conductivity. Their results showed that the properties of animal manure precursors and reaction temperatures play a significant role in the physicochemical properties of the produced biochar. Recently, some researchers have explored the application of pyrolysis technology for the intermediate conversion of partially wet sanitary fecal sludge generated on train toilets [36]. The novel twin auger pyrolysis reactor produced about 50% bio-oil yield, 40% syngas yield, and 10% biochar yield at 500 °C.

Krounbi et al. [1] performed a comparative study to determine the soil amendment quality by torrefaction, composting, and pyrolysis of human wastes (feces and urine). The physicochemical properties of pyrolysis-treated human waste were largely influenced by temperature. Additionally, pyrolysis-treated human waste at 600 °C had five times the available potassium (7400 mg K/kg) and four times phosphorus (3120 mg P/kg), when compared to thermophilic composting. Yacob et al. [24] performed human feces pyrolysis at low, intermediate, and high temperatures, with a heating rate of 10 °C/min. They reported that slow pyrolysis (at low temperatures) gave a 20.9% yield of non-condensable gases. Carbon dioxide (CO_2) and methane (CH_4) were dominant during mild pyrolysis (at intermediate temperature). Moreover, fast pyrolysis (>600 °C) gave a 45% yield of hydrogen. Mong et al. [40] developed a microwave pyrolysis technology for the conversion of horse manure into biofuels and biochemicals. The reactor produced gaseous products with 67% syngas and 37% biochar yield.

Few studies have also explored the soil amendment potential of human and animal waste-derived biochar. Liu et al. [41] showed that pyrolysis-derived biochar from dry human waste could be used as a promising additive for enhancing soil fertility. Zhou et al. [42] reported a comparative study on the characteristics of biochar from the slow pyrolysis of chicken manure, pig manure, and cattle manure. Regarding carbon content, chicken manure had the highest carbon content (41 wt. %), followed by cattle manure (35–38 wt. %) and then pig manure. Pig manure had the highest ash content, followed by cattle manure (46–47 wt. %) and chicken manure (21 wt. %). The produced biochar is perceived as a promising soil additive.

Catalysts have been employed during the pyrolysis of human and animal waste for several reasons. First, the use of catalysts ensures that the reaction proceeds at lower temperatures, thereby significantly lowering the energy demand. Additionally, catalysts help improve the quality of the product and yield, especially for fast and flash pyrolysis [43]. Catalyst deactivation, due to coke or char formation, is still a major challenge. Overall, pyrolysis catalysts could be homogeneous or heterogeneous. Homogeneous catalysts exist in a single phase (usually a liquid solution), while heterogeneous catalysts are solid and have the advantages of ease of regeneration and reuse. Commonly used heterogeneous catalysts for waste pyrolysis include metals supported on carbon and basic oxides, zeolites, and solid acid catalysts. Studies related to catalytic and noncatalytic human and animal waste pyrolysis are summarized in Table 4.

Table 4. Summary of past studies on the pyrolysis of human and livestock wastes.

Type of Pyrolysis and Key Products	Main Findings	Reference
Feedstock: Animal manure Type: Slow pyrolysis Non-catalytic Main product: Biochar	• Biochar properties depend on the type of feedstock and reaction temperature. • The biochar produced from the poultry litter had the highest electroconductivity, while the one from dairy animals had the highest energy density, carbon, and volatile matter content.	Cantrell et al. [38]
Feedstock: Human waste Type: Slow pyrolysis Non-catalytic Main product: Biochar	• The pyrolyzed human wastes gave five times potassium and quadrupled phosphorus than the composted wastes. • Composted human wastes had higher nitrogen contents than pyrolyzed human wastes.	Krounbi et al. [1]
Feedstock: Human Faces Type: Slow pyrolysis Non-catalytic Main product: Biochar	• The slow pyrolysis) gave a 20.9% yield of non-condensable gases, while the fast pyrolysis (>600 °C) gave a 45% hydrogen yield. • Kinetic analysis with a model-free method (iso-conversion), as well as a DAEM (distributed activated energy model), produced similar activation energy values, ranging from 141 kJ/mol to 409 kJ/mol.	Yacob et al. [24]
Feedstock: Dry toilet substrates comprising of urine, feces, and wood chips Type: Slow pyrolysis Non-catalytic Main product: Biochar	• The result showed that biochar is a suitable additive for soil remediation. • It is recommended that urine separation should be considered when producing biochar from human excreta. • Heavy metal concentration in biochar is within European regulation standards.	Blueler et al. [44]
Feedstock: Chicken manure Physical activation with CO_2 to activated carbon. Type: Slow pyrolysis Catalyst: Homogeneous NaOH Main product: Biochar	• Untreated char contains higher carbon and inorganic contents, as well as heavy metals. • Physical activation and chemical treatment improved the physicochemical properties of char for energy applications.	Koutcheiko [45]
Feedstock: Goat manure Type: Fast pyrolysis Non-catalytic Main product: Bio-oil	• The pyrolysis produced 26.1 wt.% yield of bio-oils at 500 °C. • The result also revealed that the bio-oil had a 52% carbon content, compared to the raw goat manure's 42%. • Bio-oil chemical composition involves organic compounds for instance, benzenes, alcohols, alkanes, alkenes, ketones, phenols, and polyaromatic hydrocarbons (PAHs).	Erdogdu et al. [46]

Table 4. *Cont.*

Type of Pyrolysis and Key Products	Main Findings	Reference
Feedstock: Equine manure Type: Fast pyrolysis Catalyst: HZSM-5 catalyst Main product: Bio-oil	• Bio-oil chemical composition includes compounds such as acetic acid, acetol, and levoglucosan. • The use of catalysts helped improve the overall quality of bio-oil for subsequent catalytic upgrading.	Elkasabi et al. [47]
Feedstock: Poultry litter Type: Fast pyrolysis Non-catalytic Main product: Biochar and gases	• Pyrolytic gases accounted for 15–22 wt.% of the product. • The carbon content in biochar increased from 47 to 48.5 wt.%, with an increase in the pyrolysis temperature.	Pandey et al. [48]
Feedstock: Horse manure Type: Microwave-assisted pyrolysis Catalyst: Activated carbon Main product: Biochar and gases	• Produced gaseous product contains up to 73.1 vol% of syngas components. • Produced biochar has a heating value of 35.5 MJ/kg, with a high surface-to-pore volume ratio. • Bio-oil yield is relatively low when compared to biochar and gaseous products. This was attributed to the presence of extractives in the horse manure that partly inhibits bio-oil production.	Mong et al. [49]
Feedstock: Hen manure Type: CO_2-assisted catalytic pyrolysis Catalyst: Transition metal Main product: Biochar, bio-oil and gases	• The main bio-oil components include phenolic and nitrogenous compounds. • CO_2 assisted in the thermal cracking of volatile matters produced from hen manure pyrolysis into syngas.	Lee et al. [50]

In addition to catalytic studies, some authors have also explored the mechanism of animal manure pyrolysis. He et al. [51] developed a detailed mechanistic reaction pathway for the pyrolysis of cattle manure (Figure 4). The pathway indicates that major products, such as aldehydes, ketones, acids, hydrocarbons, phenolic compounds, and nitrogenous compounds, in bio-oil are formed in the temperature range of 180–350 °C. Alkenes are formed at higher temperatures above 500 °C. Moreover, the cracking of cellulose and CC chains led to the formation of acetaldehyde at 180 °C. Increasing temperature inhibits acetaldehyde formation, while promoting the generation of ketones and acids.

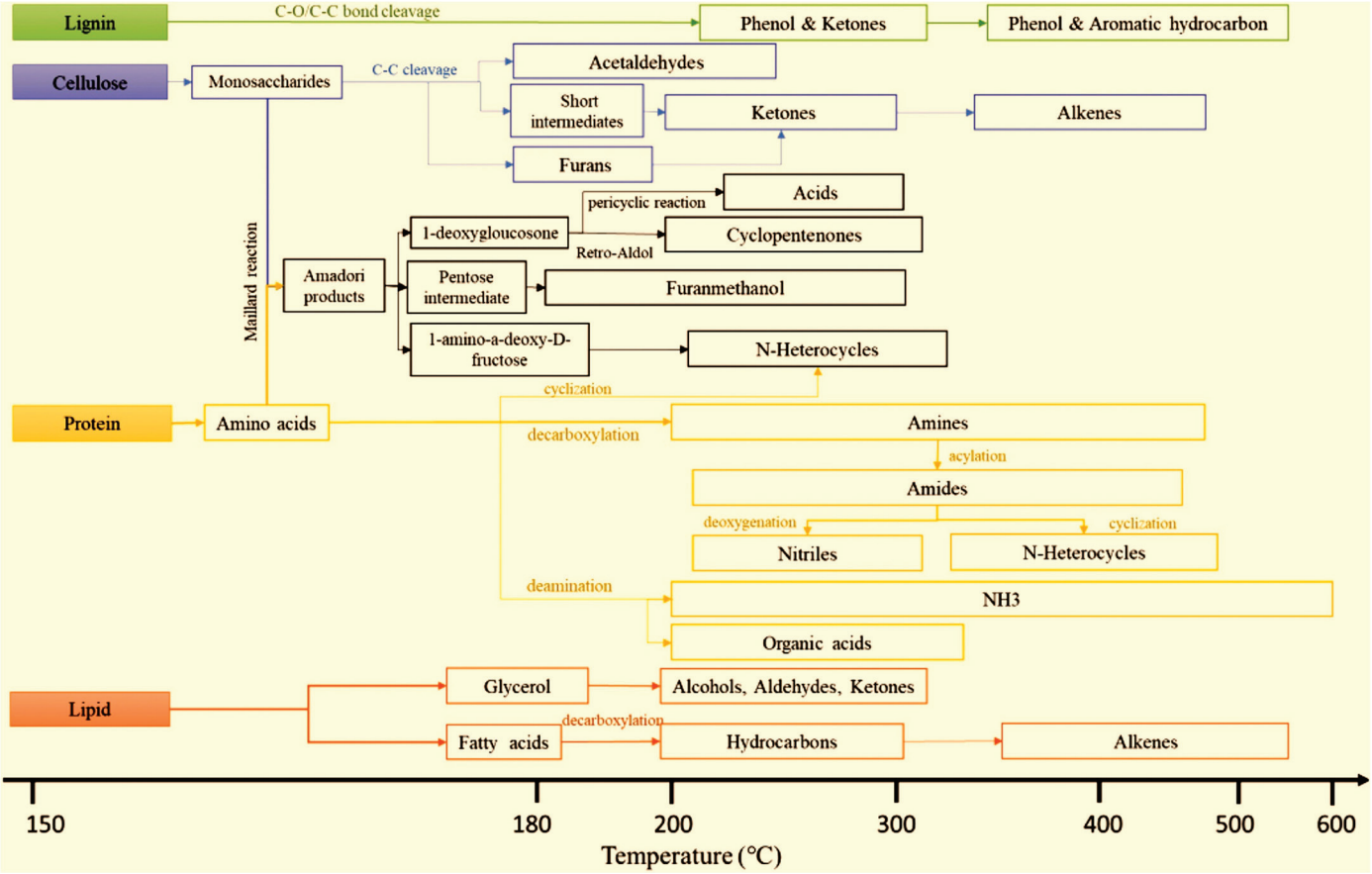


Figure 4. Mechanistic reaction pathways for the pyrolysis of animal manure to bio-oils. Adapted from He et al. [51].

3.2. Gasification

Gasification is another thermochemical conversion pathway that can convert human and animal waste into solid, liquid, and gaseous products (syngas). Gasification is often referred to as a biomass-to-gas conversion process because its target is hydrogen-rich gas comprising mostly H_2 and CO. Substantial quantities of hydrocarbons, such as CH_4, as well as CO_2 and H_2O, and often N_2, are also present in the gaseous product from gasification [7]. Synthetic gas (syngas) is defined as a gas with H_2 and CO as the main components, and it is a product of gasification. Syngas has myriad applications as a precursor for the production of higher alcohols, green fuels, and chemicals via syngas fermentation of Fischer–Tropsch (FT) synthesis.

Gasification can be grouped as conventional or hydrothermal gasification, based on the temperature, pressure, and gasifying agents. It should be mentioned that both gasification processes have identical products, but their composition and yield are often different. Figure 5 outlines the differences between conventional and hydrothermal gasification processes.

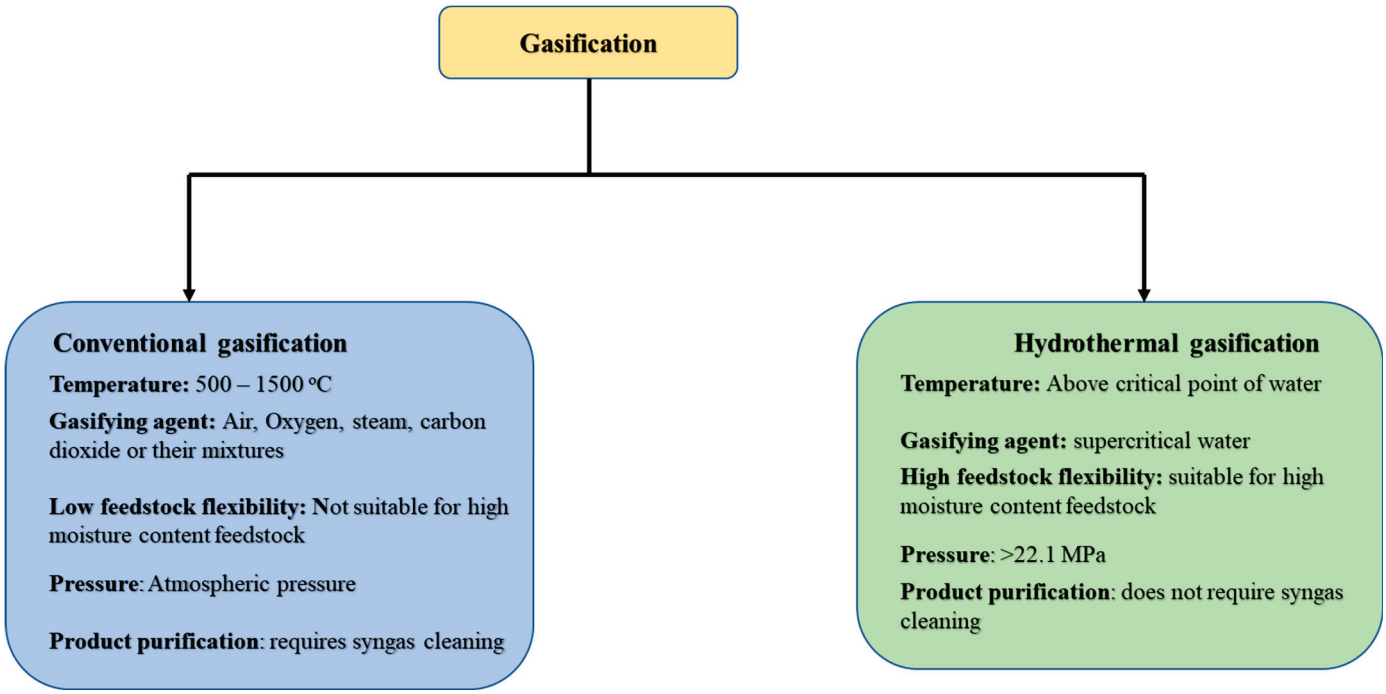


Figure 5. An overview of the difference between conventional and hydrothermal gasification.

Studies on the gasification of human and animal waste are related to the parametric evaluation of the impact of process conditions on gaseous yield, process optimization [52], energy and exergy analysis [53], kinetics studies [54], and techno-economic and life cycle assessment [55,56]. Some researchers have also focused on developing innovative heterogeneous catalysts for improving product yield and selectivity or co-gasification with other waste materials [57].

Liu et al. [57] studied the synergistic effect of a gasifying mixture of petroleum coke and chicken manure. They reported that chicken manure addition during the gasification of petroleum coke helped increase the hydrogen content in the produced syngas. The authors also explored the catalytic effect of chicken manure ash on gasification efficiency. Chicken manure ash increased the gasification efficiency by five times. They suggested that this must have been due to the ash's high potassium and calcium content. Onabanjo et al. [53] explored the possibility of producing hydrogen from human feces through conventional gasification. Aspen Plus thermodynamic equilibrium modelling was used to estimate the quantity of energy that could be produced from human feces. They reported that a 3–6 wt.% ash content in fresh human feces makes it a viable raw material for gasification. The product gas obtained from human feces at an optimal equivalence ratio (ER) of 0.31 was characterized by 24 MJ/kg and 17 MJ/kg lower heating and exergy values, respectively [53].

Hussein et al. [23] studied the effects of gasifying agents (air, steam, carbon dioxide, and nitrogen) and temperatures ranging from 600 to 1000 °C on the pyrolysis and gasification of chicken manure. It was reported that a higher temperature will produce a higher syngas yield. Regarding the gasifying media, in terms of increasing order, the air medium produced the lowest yield, followed by nitrogen, steam, and carbon dioxide. They revealed that the reaction time is inversely proportional to the energy yield. The feasibility of a two-step gasification route for producing hydrogen gas from cattle manure was examined by studying the temperature impact on not only biochar characteristics, but also product distribution. The biochar from the joint pyrolysis-carbonization was found to have a low volatile percentage composition and high carbon composition at 500 °C. This result suggests that hydrogen can be produced from the two-step gasification process [23].

Hydrothermal gasification is a suitable valorization pathway for animal manure, due to the high moisture content of the materials [58,59]. Nanda et al. [59] explored the feasibility

of hydrogen production from horse manure via alkali catalyst-enhanced hydrothermal gasification. The impact of temperature (400–600 °C), two biomass-to-water ratios (BTW) of 1:5 and 1:10, and reaction time (15–45 min) at a pressure range of 23–25 MPa on hydrogen yield was comprehensively explored. The maximum hydrogen yield was obtained at a high temperature of 600 °C and a 1:10 biomass-to-water ratio for 45 min with a 2 wt.% Na_2CO_3 catalyst. Another study showed that cattle manure could be used as a promising feedstock for hydrothermal gasification with Ni heterogeneous catalysts supported by hydrochar prepared from cattle feed [60]. Liu et al. [61] proposed a mechanism for the transformation of nitrogenous compounds during the hydrothermal gasification of chicken manure (Figure 6). Two main mechanisms were inherent: ionic and free radical degradation, with both mechanisms dependent on temperature. The ionic mechanism occurs at low temperature subcritical or near critical conditions, while the free radical degradation is inherent at high temperatures >400 °C. Some intermediate products, such as amino acids, are also produced via the Maillard reaction. Three main reactions are involved in free radical degradation: steam reforming, pyrolysis, and Maillard reaction. An elevation in temperature led to the migration of nitrogenous compounds in the raw materials to the aqueous liquid, while the Maillard reaction conditions are created by the hydrolysis of proteins and amino acids in the initial phases. As the temperature increases beyond 400 °C, some nitrogen-containing compounds are converted into condensable gases via stream reforming and pyrolysis (Figure 5).

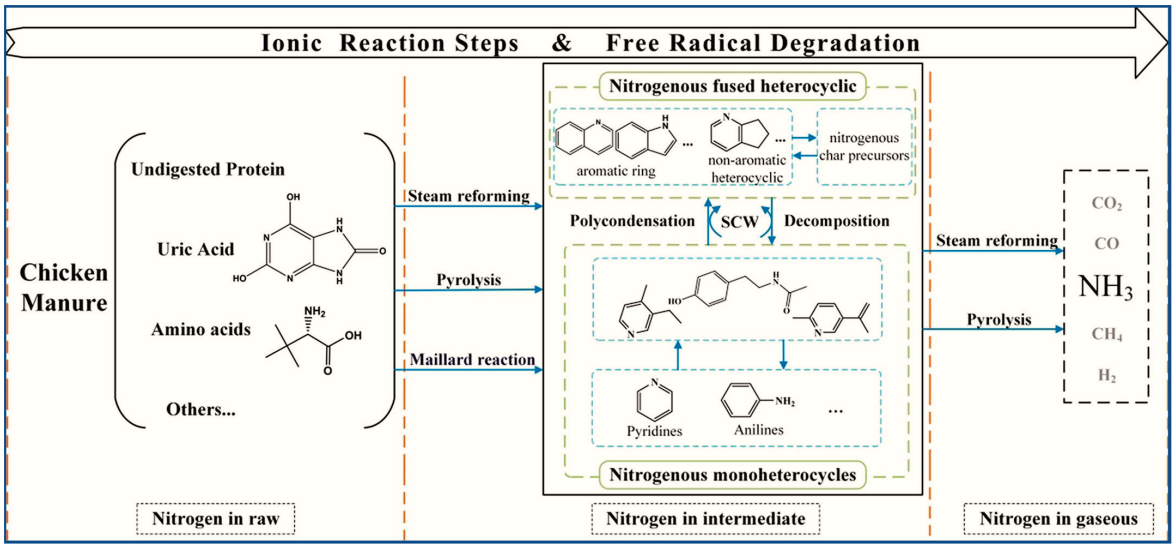


Figure 6. An overview of the reaction mechanism for nitrogen recovery during the hydrothermal gasification of chicken manure. Adapted from Liu et al. [61].

A summary of the studies related to heterogeneous catalyzed gasification of human and animal waste, kinetics studies, and process integration studies is presented in Table 5. Detailed information on the gasification of different biogenic waste can also be found elsewhere [7,62].

Hydrothermal gasification is still a challenging technology, due to the high temperature and pressure requirement. The mechanism of hydrothermal gasification of human and animal waste is still unclear. Although some researchers have documented the reaction mechanism of liquid feedstock decomposition, such as glycerol in supercritical water [63]. Problems such as corrosion issues, reactor material durability, waste heat utilization, safety, and risk are associated with extreme reaction conditions. Catalysts are often used to reduce the reaction temperature during hydrothermal gasification. However, the harsh environment facilitates the decline in the surface area of metallic catalysts and some structural changes causing significant deactivation, a phenomenon known as catalyst sintering [7].

Table 5. Summary of the studies related to heterogeneous catalyzed gasification of human and animal waste, kinetics studies, and process integration studies.

Type of Gasification and Key Products	Key Findings	References
Gasification type: Conventional fluidized bed gasification Feedstock: Poultry litter Study focus: Parametric studies and process optimization To investigate the effect of adding limestone ($CaCO_3$), different gasifying agents and temperatures on product gas yield, and cold gas efficiency during gasification	• Highest temperature of 800 °C resulted in a product gas with a lower heating value of 4.5 MJ/Nm^3 and cold gas of 89% efficiency. • Gas composition at optimum process conditions include: H2: 10.78%, CO: 9.38%, CH_4: 2.61, and CO_2: 13.13 • Owing to the high quantity of potassium and phosphorus in poultry ash, the limestone drastically reduced the bed's agglomeration.	Pandey et al. [64]
Gasification type: Conventional gasification Feedstock: Chicken manure Study focus: Co-gasification and catalytic studies. Study the synergistic effect of gasifying petroleum coke and chicken manure, while the chicken manure is a catalyst	• Chicken manure is a promising precursor for hydrogen production via co-gasification with pet coke in the presence of chicken manure-derived ash as a catalyst. • The high potassium and calcium content in chicken manure ash made it efficient as a catalyst, as it yielded fivefold of CO than what the petroleum coke alone would have yielded.	Liu et al. [61]
Gasification type: Conventional gasification Feedstock: Human faces Study focus: Thermodynamic and energy analysis with Aspen Plus simulation. Explored the viability of human feces as a raw material for gasification. Estimation of the quantity of energy that could be produced from human feces	• They reported that human feces comprise 3–6 wt. % ash and 70–82 wt. % moisture, making it a suitable precursor for gasification. • The product gas from human feces is optimum at an equivalence ratio of 0.31, and it is characterized by 24 MJ/kg and 17 MJ/kg lower heating and exergy values, respectively	Onabanjo et al. [53]
Gasification type: Conventional gasification Feedstock: Chicken manure Study focus: Parametric studies The effect of gasifying media (air, steam, carbon dioxide, and nitrogen) and temperatures ranging from 600 °C to 1000 °C on the pyrolysis and gasification of chicken manure	• Higher temperatures favor improved product gas yield. • It was revealed that reaction time is inversely proportional to the energy yield. • Air gasification is the most preferred among all other gasifying agents.	Hussein et al. [23]
Gasification type: Conventional gasification Feedstock: Cattle manure Study focus: Parametric studies The viability of a two-step gasification route for producing hydrogen gas was examined by studying the temperature impact on biochar characteristics and product distribution	• Approximately 1.61 m^3/kg of syngas, 0.93 m^3/kg of hydrogen, and 57.58% of hydrogen concentration was obtained at an optimum temperature of 850 °C. • The biochar produced from the two-step gasification process has a low volatile percentage composition and high carbon content.	Xin et al. [58]

Table 5. *Cont.*

Type of Gasification and Key Products	Key Findings	References
Gasification type: Hydrothermal gasification Feedstock: Horse manure Catalyst: Homogeneous alkali catalyst including NaOH, Na_2CO_3, and K_2CO_3 Study focus: Parametric studies Explored the effect of reaction temperature (400–600 °C), biomass-to-water ratio (1:5 and 1:10), and reaction time (15–45 min) at a pressure range of 23–25 MPa on product yield during horse manure gasification in supercritical water	• Higher temperature favored hydrogen yield and selectivity. • Na_2CO_3 performed better than other homogeneous catalyst in improving hydrogen yield. • At optimum conditions (600 °C and 1:10 biomass-to-water ratio for 45 min), a maximum hydrogen yield of 5.31 mmol/g was reported.	Nanda et al. [59]
Gasification type: Conventional gasification Feedstock: Pig manure compost Heterogeneous catalyst: Ni/Al_2O_3, Ni-loaded brown coal char Study focus: Catalytic effect of supported Ni catalyst during gasification and parametric studies.	• Ni-loaded brown coal char is a promising gasification catalyst, even at lower temperatures. • The catalysts developed promising resistance to coke formation, compared to the commercial Ni/Al_2O_3. • Temperature and steam/biomass–carbon ratio is an important consideration in improving gas yield.	Xiao et al. [65]
Gasification type: Hydrothermal gasification Feedstock: Chicken manure Catalyst: K_2CO_3 Study focus: Parametric studies, kinetics, and reaction mechanism evaluation	• Complete gasification efficiency was attained with the use of 10 wt.% and K_2CO_3 at 700 °C. • The migration pathways of nitrogenous intermediates show that the Maillard reaction plays a significant role. Two reaction mechanisms for the removal of nitrogen in chicken manure gasification are ionic and free radical degradation.	Liu et al. [57]

3.3. Liquefaction

Liquefaction is a biomass-to-liquid (BTL) conversion pathway, similar to pyrolysis, but different in terms of operating temperature (200–450 °C), pressure (5–25 MPa), and the presence of a solvent, usually water or alcohols. It is mostly used for the conversion of wet biomass (wastes) into crude oil, also referred to as biocrude oil [66]. The yield and quality of biocrude oil are dependent on the raw material composition, residence time, catalyst, temperature, pressure, and solvent [67].

Hydrothermal liquefaction (HTL) is different from other hydrothermal processes, such as supercritical water gasification and hydrothermal carbonization (HTC), in terms of the desired products and operating conditions. Figure 7 describes different phase diagrams for hydrothermal processes, as well as the operating conditions ranges. Hydrothermal gasification is favorable at high-temperature supercritical conditions (>400 °C) and the desired product is high-quality syngas [67]. In contrast, HTC is focused on the formation of solid fuels with improved physicochemical properties for subsequent energy and environmental applications.

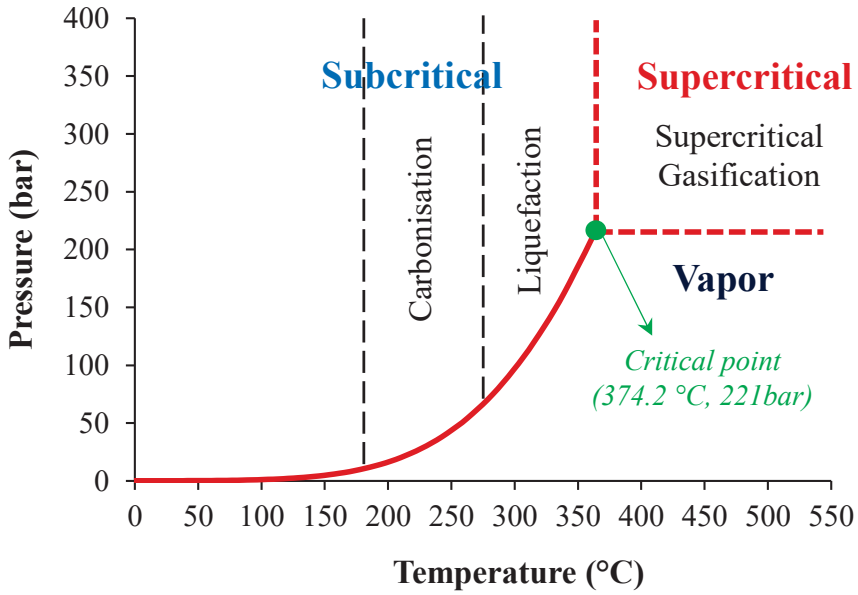


Figure 7. Hydrothermal processing condition in water phase diagram. Adapted from [67].

The biocrude oil obtained from liquefaction has a lower oxygen content, is more viscous, and has an elevated HHV, compared to pyrolysis oils [47]. Hydrothermal liquefaction (HTL) offers the advantages of feedstock flexibility and does not require precursor drying. Studies on the liquefaction of human waste focus on developing pathways for nitrogen transformation [68], process optimization, or the development of novel heterogeneous catalysts for improving oil yield and quality [68]. Lu et al. [69] investigated the effects of temperature (260 °C, 300 °C, 340 °C), retention time (10 min, 30 min, 50 min), and total solid content (5%, 15%, 25%) on biocrude yield and nutrient recovery during the HTL of human feces. They revealed that approximately half of the carbon content in human feces was converted to biocrude oil, while 72% of nitrogen was found in the aqueous phase. They also reported that human feces contained metals such as calcium, aluminum, magnesium, zinc, iron, sodium, and potassium. The results showed that human feces are a potential source of energy and nutrient recovery. The authors proposed possible reaction pathways for the conversion of human feces via HTL (Figure 8).

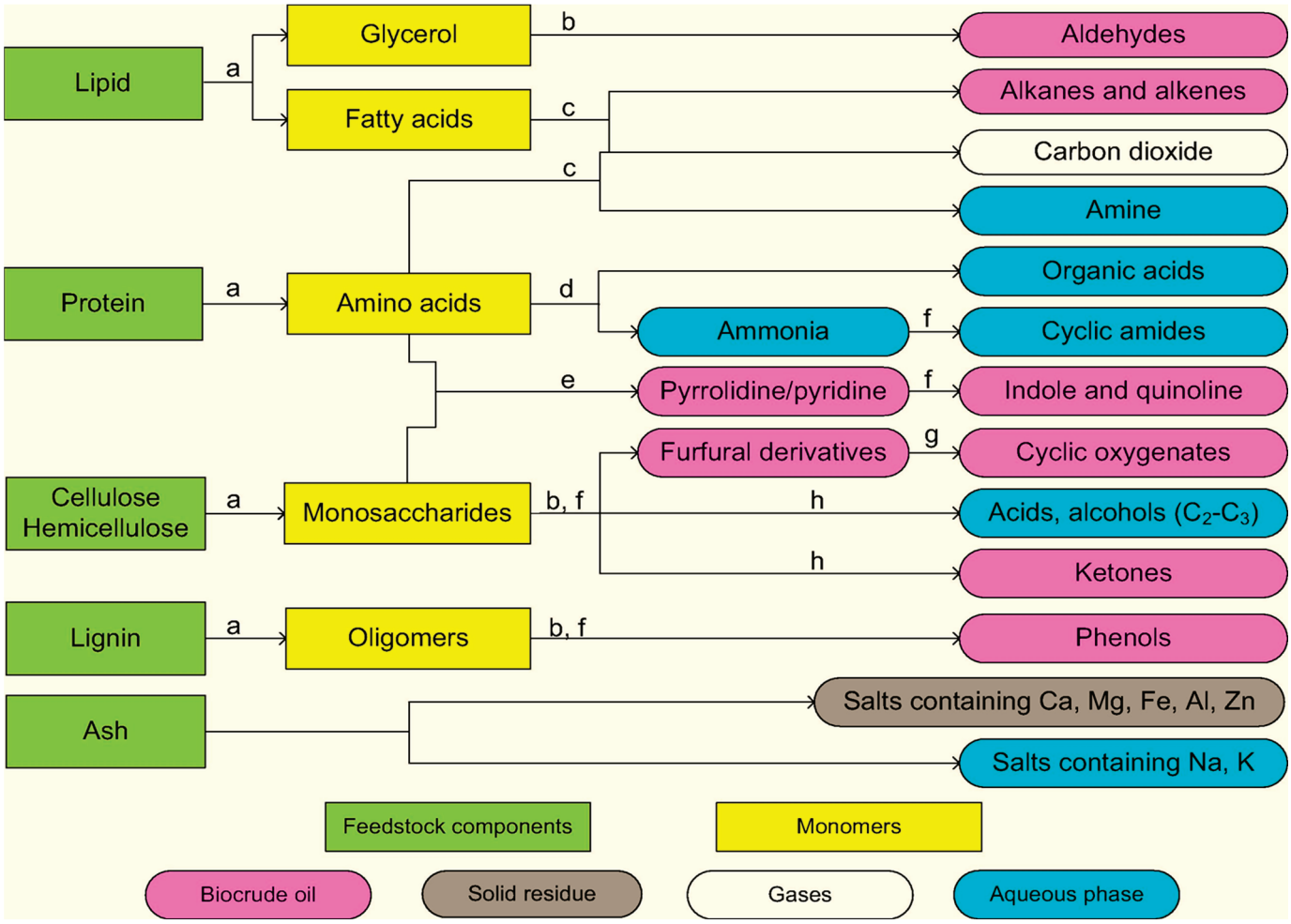


Figure 8. Proposed reaction pathways involved in the hydrothermal conversion of waste materials, such as human feces to biocrude and value-added chemicals. Adapted from Lu et al. [69]. ((**a**) hydrolysis; (**b**) dehydration; (**c**) decarboxylation; (**d**) deamination; (**e**) Maillard reaction; (**f**) cyclization; (**g**) polymerization; (**h**) decomposition).

The pathways in Figure 8 include intermediate reactions, such as (a) hydrolysis; (b) dehydration; (c) decarboxylation; (d) deamination; (e) Maillard reaction; (f) cyclization; (g) polymerization; and (h) decomposition [69]. The hydrocarbons found in the biocrude oil during HTL were produced through the decarboxylation of the fatty acids. It should be mentioned that the fatty acids are from the hydrolysis of lipids in human waste. The ketones and aldehyde functional groups were produced from polysaccharides through a series of intermediate reactions, including hydrolysis, dehydration, and decomposition reactions [69]. In contrast, nitrogenous compounds such as pyridine, pyrrolidine indole, and quinolone are derived from monosaccharides and amino acids through the cyclization and Maillard reactions.

Conti et al. [70] explored the possibility of recovering nutrients and energy production from the biodegradation of animal manure, sewage sludge, and fish sludge, with or without K_2CO_3 (catalyst) under subcritical (350 °C) and supercritical conditions (450 °C). They reported that all the wastes gave a high yield of biocrude, with fish sludge and sewage sludge giving yields of 50% and 45%, respectively. Moreover, animal manure was able to produce a quality biocrude in the presence of the catalyst and under supercritical conditions. Inorganics, such as calcium, phosphorus, and magnesium, were obtained from the solid phase, as approximately 55–80% and 50–60% of carbon were recovered from fish and swine sludge, respectively.

Li et al. [71] compared the HTL of dairy manure, broiler manure, laying hen manure, swine manure, and beef manure. They revealed that swine manure had the highest biocrude oil yield (30.85%) at 340 °C, while the other manure yields ranged from 15% to 25%. The heavy metals from these manures (copper, zinc, lead, cadmium) are heavily distributed in the solid residue after hydrothermal liquefaction. The influence of temperature, solvent filling rate, and solid–liquid rate on the constituents, features, and yield of bio-oil derived from pig manure was examined by some researchers [27]. The highest yield of the bio-oil was found to be 35.56%, while its heating value ranged from 34.39 to 37.03 MJ/kg. The bio-oil was composed of ketones, nitrogen compounds, organic acids, long-chain hydrocarbons, ethanol, and esters. The yield of the bio-oils had an inverse relationship with the solid–liquid rates, while it increased and decreased with solvent filling rates and temperature, respectively [27]. A summary of previous studies related to the liquefaction of human and animal waste is presented in Table 6.

Table 6. Summary of past studies on the gasification of human and livestock wastes.

Aim of Study	Key Findings	Authors
To examine the effects of temperature, holding time, and catalyst on the product distribution of a Ni-Tm/TiO_2-catalyzed liquefaction of human feces.	• They reported that the catalyst increases the product yield by 35% and gives energy recovery of 87%. • A temperature of 330 °C and a holding time of 30 min gave the highest yield of biocrude (53.16%).	Wang et al. [72]
The feasibility of using hydrothermal liquefaction to produce energy (biocrude oil), recover nutrients and metals from human feces at specific retention times, temperatures, and total solid contents.	• More than four-fifths of the waste was liquefied, which gives a yield of 34% and HHV of 40 MJ/kg. • The results reported showed that human feces is a potential source of energy and nutrient recovery. • Metals such as calcium, aluminum, magnesium, zinc, iron, sodium, and potassium are key components of human feces.	Lu et al. [69]
Nutrient recovery and energy production from the decomposition of animal manure, sewage sludge, and fish sludge, with or without K_2CO_3 (catalyst), under subcritical (350 °C) and supercritical conditions (450 °C).	• The animal manure produced a quality biocrude in the presence of a catalyst and under supercritical conditions. • All the wastes produced a high yield of biocrude, as fish sludge and sewage sludge produced yields of 50% and 45%, respectively.	Conti et al. [70]
Studied the influence of temperatures, solvent filling rates, and solid–liquid rates on the composition and yield of bio-oil derived from pig manure are examined.	• The highest bio-oil yield was found to be 35.56%, while its higher heating value ranged from 34.39 to 37.03 MJ/kg. • The major bio-oil components include ketones, nitrogen compounds, organic acids, long-chain hydrocarbons, ethanol, and esters.	Wu et al. [27]
To compare the hydrothermal liquefaction of dairy manure, broiler manure, dairy manure, laying hen manure, swine manure, and beef manure.	• The swine manure had the highest biocrude oil yield (30.85%) at 340 °C, while the other manure yield ranged from 15% to 25%. • The solids recovered from these manures (copper, zinc, lead, cadmium) are heavily distributed in the solid residue from hydrothermal liquefaction.	Li et al. [71]

Table 6. *Cont.*

Aim of Study	Key Findings	Authors
Explored the possibilities of converting camel manure into bio-oil and upgrading to drop in fuel via hydrothermal liquefaction.	• Optimum bio-oil yield of 37.9% was obtained during the liquefaction of camel manure. • The bio-oil was upgraded to a drop-in fuel with similar properties to gasoline. The fuel has a minimum selling price of 0.87 USD/kg. • The produced gasoline led to a 7% reduction in emissions, compared to the conventional gasoline production process.	Alherbawi et al. [73]
Studied the synergistic effect during the co-liquefaction of corn cob and cattle manure.	• Co-liquefaction helped to improve the quality of bio-oil and yield, compared to a single liquefaction of each feedstock. • Developed a detailed reaction network mechanism for hydrothermal co-liquefaction of cattle manure and corn cob. Key intermediate products, such as acids, amines, and CO_2 and 3, can influence the reaction environment pH value and then affect the subsequent intermediate reactions.	He et al. [74]

3.4. Hydrothermal Carbonization

Hydrothermal carbonization (HTC) is a thermochemical process for the pre-treatment of high moisture content biomass to make it viable for energy production. HTC uses relatively low temperatures and is suitable for any kind of biomass feedstock [75]. HTC can convert human and animal waste into solid hydrochar, which has better physicochemical characteristics than raw feedstocks [76] and produces liquid products that contain organic and inorganic value-added chemicals. The HTC hydrochar exhibits lower O/C and H/C ratios, compared to dry torrefaction, and turns into more lignin or coal-type materials [77]. HTC hydrochar can be used in a wide range of processes, such as soil amendment [78], CO_2 capture [78], nanoparticles (for making composites) [79], energy production [80], and water purification [81], due to their unique physicochemical properties [82].

HTC could be adopted for the sustainable and environmentally benign treatment of human and animal waste for several environmental and energy applications. Some researchers have explored the conversion of human feces to hydrochar via HTC [83]. The effect of temperature (180, 210, and 240 °C) and reaction times (30, 60, and 120 min) during the HTC of human excreta reveals that hydrochar yield decreased with elevating HTC temperature [83]. In addition, the calorific value of the produced hydrochar rose from 24.7 to 27.6 MJ/kg with a rise in temperature. Afolabi et al. [84] showed that an hydrochar, with improved HHV ranging from 19.79–25.01 MJ/kg, was produced during the microwave HTC of raw human fecal sludges with increasing temperature ranges of 160–200 °C. Some researchers also assessed the energy efficiency during the HTC of human fecal wastes [85]. The energy balance results obtained during the HTC of fecal waste conducted at 200 °C, with a reaction time of 30 min, reveals that feces with 25% solids requires 63–65% of the overall reactor input energy for efficient heating. On the contrary, feces with lower solids (15% solid) would need lower energy (about 62–64%) [85]. Another study showed that HTC could be used as an effective technology for the mitigation of SARS-CoV-2 in sewage sludge [86].

HTC can also be used to upgrade the properties of livestock manure for subsequent fuel applications. Jang et al. [87] reported that the HTC of livestock manure reduced the amount of C–O and C–H functional groups and elevated the number of aromatic C–H functional groups. Additionally, HTC increased the fixed carbon content and energy density of livestock manure, while the H/C and O/C ratios decreased. HTC could also be used

aa nutrient recovery strategy from animal waste. Qaramaleki et al. [88] showed that cow manure is a promising source of phosphorus and nitrogen via HTC. However, the extent of phosphate extraction is dependent on the reaction temperature, acid addition, and acid concentration. Increasing HTC temperature and the addition of either citric acid or HCl led to an improved phosphate recovery in the aqueous phase. HTC could also be used for the valorization of anaerobic digestate to promote the circular economy and optimize material utilization [89].

4. Biological Conversion of Human and Animal Waste

As mentioned earlier, the biological conversion process is a waste-to-energy process that uses microorganisms to convert biogenic materials into energy or other value-added products. Anaerobic digestion (AD) and fermentation are the two main biological processes used for the valorization of human and animal waste. Both processes involve microorganisms breaking down organic matter in the absence of oxygen. Detailed information about the advantages and limitations of each process, as well as the reaction pathways, can be found elsewhere [8]. Most of the studies related to resource recovery from human and animal waste via biological conversion pathways mostly focus on anaerobic digestion. In contrast, fermentation uses microorganisms to convert sugars into carbon dioxide and ethanol.

4.1. Anaerobic Digestion

AD is a biological process that converts wastes into biogas and digestate under anaerobic conditions. These wastes include animal manure, human waste, sewage sludge, food waste, and lignocellulosic materials. Its products, which include digestate and biogas, have proven to be useful. The former can be used as a fertilizer because it contains nutrients such as nitrogen, potassium, and phosphorus. In contrast, the former can be used to generate electricity and heat, thus reducing the overreliance on fossil fuels.

AD of biogenic waste proceeds in four different stages: hydrolysis, acidogenesis, acetogenesis, and methanogenesis [90]. In hydrolysis, compounds with high molecular mass (polymers) are deconstructed into lower molecular weight compounds (monomers). This stage is of paramount importance because it is where microorganisms in the digestion medium have access to the material's energy potential [90,91]. Acidogenic bacteria further decompose the remaining compounds into volatile fatty acids (VFAs), carbon dioxide, ammonia, and other byproducts in the acidogenesis stage. The next stage (acetogenesis) involves acetogens digesting the monomers formed in the acidogenesis stage to form acetic acid, hydrogen, and carbon dioxide. Methanogens then convert the previously formed products into methane, carbon dioxide, and water, which constitute biogas.

AD of human and animal waste for biogas production has been the focus of some research studies, as shown in Table 7. Although, AD could also be adopted for the treatment of sludge. A survey of the available literature shows that mono-feedstock digestion is more common. The use of a single feedstock has been reported to be problematic because of several challenges, such as poor biogas yield, limited year-round feedstock availability, and digester instability [92]. To some extent, these challenges can be overcome through different methods, such as pH adjustment [93], manipulation of the digestion time [94], intermittent feeding [95], multistage AD processes [96], the introduction of external microorganisms, and co-digestion [97]. Among these options, co-digestion of more than one feedstock has been reported to be very successful in overcoming the challenges associated with mono-feedstock digestion. Co-digestion results in higher biogas yields, improved digester stability, and, in particular, the combination of multiple feedstocks, with their unique properties providing a more balanced nutrient composition, a diversified microbial community, and a better buffering capacity against the accumulation of VFAs [98]. For example, Ihoeghian et al. [12] investigated the co-digestion of cattle rumen content and food waste. They found that both materials had desirable characteristics necessary for biogas production. Their findings showed that co-digestion enhanced the carbon-to-nitrogen ratio with an attendant-positive

impact on biogas yield and pH of the AD medium. A 50:50 ratio of cattle rumen content and food waste was found to be optimum for biogas production, with a maximum cumulative biogas yield of 320.52 mL gVS-1. The profile of pH, total ammonia nitrogen, and volatile fatty acids were improved via co-digestion.

Ma et al. [99] employed the meta-analysis approach to compare methane yield between mono-digestion and co-digestion of animal manure with other feedstocks. A higher methane yield was obtained from the co-digestion (animal manure mixed with other feedstock (249 Lkg^{-1} was recorded), compared to mono-digestion (171 Lkg^{-1}). The superior methane yield was attributed to the high volatile solid concentration and the carbon-to-nitrogen ratio of the manure. In another study, an equal proportion of rice straw and human feces (50:50) was the optimal ratio that produced the highest biogas yield (61% yield, volume of 6391 mL) during the anaerobic co-digestion of rice straw and human feces. In other studies, Kaur and Kommalapati [100] reported a biogas yield of 262 $mlgVS^{-1}$ for the 20:80 co-digestion of goat manure and cotton gin trash, while a value of 250 $mlgVS^{-1}$ was reported by Alfa et al. [101] for the 25:75 co-digestion of cow dung and horse dung. Hazmah et al. [102] showed that co-digestion of pineapple waste with cow dung improved the process stability, in terms of the C/N ratio, total ammonia nitrogen, VS removal, and pH. Arifan and Sumardiono [103] studied the effectiveness of co-digestion of chicken manure, cow manure, and liquid tofu waste for producing biogas. They then revealed that the best proportion that gave the highest biogas yield was 15% chicken manure, 70% cow manure, and 15% liquid tofu waste, totaling 3252 mL of biogas. Moreover, they also reported a huge decrease in BOD and COD at 95% and 98%, respectively.

The AD process is a complex series of biochemical reactions that involve the conversion of various biomolecules by a diverse microbial community [104]. Direct interspecies electron transfer (DIET) between the microorganisms that facilitate the biodegradation of complex biodegradable compounds and methanogens has been reported to be responsible for facilitating the syntrophic conversion process during the methanogenesis stage of AD [105]. The interruption of this syntrophic process is often the cause of digester instability, which results from the lowering of the pH, as a consequence of the accumulation of VFAs [106]. Research efforts have been directed toward mitigating this situation, with a particular focus on the introduction (into the digester) of conductive materials that can also serve as immobilizing media for microbes [107]. Examples of materials that have been assessed in this regard include polyethylene [108], glass [109], polyvinyl alcohol [110], activated carbon [111], oxides of iron [112], and biochar [113]. The porous nature of these materials provides the necessary surface area for microbial immobilization, which has an overall effect of shortening the AD start-up phase and enhancing feedstock digestibility, especially when the feedstock is a recalcitrant lignocellulosic material.

Table 7. Summary of past studies on anaerobic digestion and fermentation of human and livestock wastes.

Authors	Aim of Study	Key Findings
Ihoeghian et al. [12]	Conversion pathway: Anaerobic digestion Investigated and established the best co-digestion ratio for cattle rumen content and food waste for synergistic biogas production.	A 50:50 ratio of cattle rumen content and food waste was recommended for biogas production Co-digestion of cattle rumen content and food waste enhanced biogas production
Ma et al. [99]	Conversion pathway: Anaerobic digestion Adopted the meta-analysis approach to compare the methane yield between mono-digestion and co-digestion of animal manure with other feedstock.	Higher methane yield was obtained from the co-digestion (animal manure mixed with other feedstock) when compared to mono-digestion.
Adjama et al. [114]	Conversion pathway: Anaerobic digestion To investigate the proportions of anaerobic co-digestion of rice straws and human feces that will give the optimal biogas yield.	An equal ratio of rice straws and human feces produced the highest biogas yield (61% percentage yield).
Arifan et al. [103]	Conversion pathway: Anaerobic digestion To study the effectiveness of co-digestion of chicken manure, cow manure, and liquid tofu waste for producing biogas.	The best combination of feed materials that produced the optimum yield are as follow: 15% chicken manure, 70% cow manure, and 15% liquid tofu waste.
Eduok et al. [115]	Conversion pathway: Anaerobic digestion To compare the effectiveness of water, human urine, and sodium bicarbonate (Na_2CO_3) as a buffering agent for the codigestion of poultry feces and lignocellulosic biomass for the generation of biogas.	The urine-buffered reactors produced the highest yield up to five times greater than those buffered with sodium bicarbonate and water.
Silwadi et al. [116]	Conversion pathway: Anaerobic digestion To compare the biogas yield and composition resulting from mono-digestion (cow, chicken, and camel) and co-digestion (mixtures of cow, chicken, and camel).	The co-digestion gave a higher yield than the mono-digestion. Biogas yield increased 5 (co-digestion with chicken manure), 12 (co-digestion with cow manure), and 28 (co-digestion with camel manure) times when compared to mono-digestion.
Pan et al. [117]	Conversion pathway: Anaerobic digestion Investigated the role of wood-based biochar during AD of chicken manure.	25% reduction in TAN accumulation. 69% increase in biogas production compared to the control.
Kizito et al. [118]	Conversion pathway: Anaerobic digestion Investigated the role of biochar on the removal of TAN during AD of piggery waste	60% reduction in TAN accumulation which enhanced AD stability.
Recebli et al. [119]	Conversion pathway: Fermentation To compare the daily biogas production rate from poultry manure and bovine animal manure.	Approximately 0.83 m^3 and 6.33 m^3 of biogas are produced daily from poultry manure and bovine animal manure, respectively. The lower heating value of the produced methane and biogas is 34,000 KJ/m^3 and 21,000 kJ/m^3 respectively.
Zlateva et al. [120]	Conversion pathway: Fermentation To determine the quantity of biogas and energy produced from the anaerobic fermentation of cow manure, chicken manure, and pig manure.	It was revealed that approximately 556,000 kWh per annum of energy is produced. At the same time, 55,660 methane is released per annum, with pig manure, cow manure, and chicken manure contributing to the release of 7493 Nm^3CH4/a, 234,111 Nm^3CH_4/a, and 24,756 Nm^3CH_4/a, respectively.

Table 7. *Cont.*

Authors	Aim of Study	Key Findings
Andreev et al. [121]	Conversion pathway: Fermentation To subject human urine to lactic acid fermentation to reduce its odor and enhance its fertilizing ability.	The pH of the treated urine ranges from 3.8–4.7 compared to the untreated which is 6.1. The ammonia composition decreases by 20–30% compared to the untreated, whose ammonia composition increases by 30% owing to hydrolysis.
Andreev et al. [122]	Conversion pathway: Fermentation To subject human excreta to lactic acid fermentation to reduce the loss of nutrients and the number of pathogens present in them.	Human excreta is a promising source of nutrients via lactic acid fermentation. The nutrient loss is lowered in the presence of lactic acid with 7–10 days fermentation.
Adjama et al. [114]	Conversion pathway: Fermentation To investigate anaerobic fermentation chicken manure and straw mixtures in a batch reactor at a temperature of 37 °C for ten weeks	The straw ratio of 3% gave the highest methane yield of 292.87 $mLgVS^{-1}$ which is 17% greater than pure chicken manure.
Dong-Jun Lee et al. [123]	Conversion pathway: Fermentation Evaluate the impact of two different pretreatment methods (NaOH and H_2SO_4) on the bioethanol yield during horse manure fermentation.	Alkaline/enzyme-hydrolysates showed higher bioethanol productivity (0.075 g $L^{-1}h^{-1}$) than those of acid/enzyme-hydrolysates (0.050 g $L^{-1}h^{-1}$). Fermentation of hydrolysates produced less inhibitory compounds due to the alkaline pretreatment.

Anaerobic co-digestion of lignocellulosic materials with animal manure is also a promising strategy to maintain its stability and keep the pH between 6.8 and 7.2 [115]. Human urine has been shown to be a promising waste material with a similar composition to buffer materials used during anaerobic digestion [115]. Eduok et al. [115] compared the performance of water, human urine, and sodium bicarbonate (Na_2CO_3) as buffering agents for the co-digestion of poultry feces and lignocellulosic biomass for the generation of biogas. The urine-buffered reactors were found to have a mean volume of 37 ± 8 mL gVS^{-1} to 101 ± 18 mL gVS^{-1}. These values are 1 to 5 times greater than those of reactors buffered with sodium bicarbonate and water. The positive effect of urine as a buffering agent for biogas production is reflected in its volatile fatty acid concentration, which was reported to fall between 396 and 1400 mg L^{-1}, in contrast to that of water (386 and 3109 mg L^{-1}). Another study showed that human urine could be used as a co-feedstock to improve the gas yield during anaerobic co-digestion with cassava liquid waste [124,125]. Twizerimana et al. [126] further confirmed that source-separated human urine could help stabilize the anaerobic digestion of cotton yarn waste and improve the gas yield. Significant fluctuations in pH during AD are not desirable, as they can negatively impact microbial activity. This is important, as reduced fluctuations will encourage a better performance from the microbes, as their performance is highly pH-dependent [127].

Some studies have explored the role of biochar in process stability during AD. Biochar's ability to confer stability to an AD system has been linked to its buffering ability, which is a consequence of its alkaline nature. Pan et al. [117] reported that wood-based biochar reduced the TAN concentration by 25%, in comparison with the control, which resulted in enhanced biogas production, while Kizito et al. [118] reported a 60% TAN reduction for the digestion of biochar-amended piggery waste, with a consequent increase in biogas production.

4.2. Fermentation

Fermentation is a biological process that deals with the decomposition of wastes (manures) into biogas and digestate at temperatures appropriate for mesophilic or thermophilic bacteria [128]. The fermentation process could either be dry or wet fermentation based on the moisture content of the feed material. For the former, the feed material usually has over 85% water content, while for the latter, the feed material usually has approximately 60% water content. The fermentation process is influenced by the pH of the medium, temperature, raw materials composition, sludge stirring, and humidity [128,129].

During the fermentation of manure, the feed is collected and transferred to a fermentation tank. The collected manure will then be blended with the reactor's agitator, so that they become homogenized for the microorganisms to decompose the manure into methane (CH_4), carbon dioxide (CO_2), and organic fertilizer in an anaerobic environment. The fermentation process normally lasts up to 23 days, either for thermophilic-type (33–34 °C) or mesophilic-type (53–55 °C) conditions [120].

Several studies have documented the fermentation of human and animal waste for biofuel production, as shown in Table 7. Recebli et al. [119] conducted a comparative study to determine the daily biogas production rate from poultry and bovine animal manure. They separately filled 375 kg of poultry manure blend and 350 kg of bovine animal manure into 0.5 m^3 of the fermentation reactor. Their results revealed that approximately 0.83 m^3 and 6.33 m^3 of biogas were produced daily from poultry manure and bovine animal manure, respectively. Zhang et al. [130] showed that the co-fermentation of waste-activated sludge and animal manure promotes glucocorticoid degradation. Their study revealed that chicken manure is a better co-fermentation precursor than dairy manure.

Fertilizers made from human excreta can cause eutrophication in aquatic bodies if there is runoff. Andreev et al. [121] explored the lactic acid fermentation of human urine to reduce its odor and enhance its fertilizing ability. To do this, they fermented the urine with bacterial inoculum in a closed jar for approximately 36 days. The pH of the treated urine ranged from 3.8–4.7 to the untreated 6.1, and the ammonia composition decreased by 20–30%, compared to the untreated, whose ammonia composition increased by 30%, owing

to hydrolysis. The results showed that the treated urine has a reduced odor intensity and can be a good fertilizer because it lowers the volatilization of ammonia.

Bioethanol is an environmentally benign fuel that provides comparable efficiency at a lower cost, when compared with gasoline. AD intermediates, including the fermentable sugars obtained from hydrolysis and acetogenesis, can be used as useful feedstocks for bioethanol production via fermentation. The process is characterized by faster reaction kinetics and lower CO_2 production. Some researchers have demonstrated that lignocellulosic feedstock, including animal manure, can be converted to bioethanol and green chemicals via enzyme hydrolysis and fermentation or through simultaneous saccharification and fermentation processes [123,131]. Figure 9 shows the sequential steps involved in the simultaneous saccharification and fermentation process. Doreswamy et al. [132] adopted the conventional anaerobic fermentation method for the production of bioethanol from piggery excreta. The authors reported approximately 89.59% high-purity bioethanol production and a theoretical yield of 0.765–1.02 gm/200 mL. Yan et al. [133] reported that the use of *Saccharomyces cerevisiae* for simultaneous saccharification and fermentation could produce bioethanol from pretreated and anaerobically digested cow dung, with yields of 0.19 and 0.13 g/g-raw biomass.

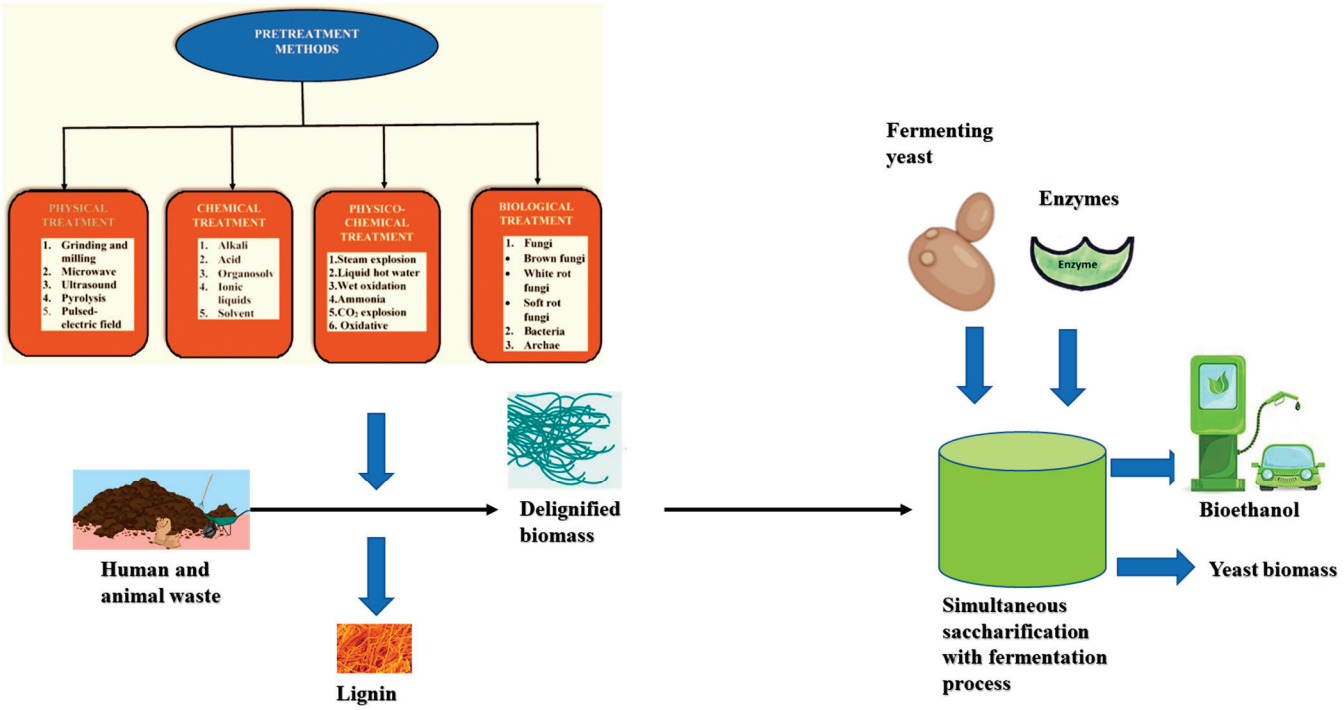


Figure 9. An overview of the sequential steps involved in the simultaneous saccharification with the fermentation process.

5. Nutrient and Fertilizer Recovery from Human and Animal Waste

Fertilizer is known for its beneficial impact on agricultural practices, with the common impact being enhancing soil fertility. Hence, its use has increased tremendously over the past years. This is reflected in its global demand, which rose from 186.6 Mt in 2016 to 194.4 Mt in 2018, and this value is projected to increase every year [134]. The fertilizer could be synthetic (chemical fertilizer) or organic fertilizer (animal manure manure-based fertilizers and human waste-based fertilizers).

Chemical fertilizers are inorganic fertilizers that enhance plant growth when added to the soil. They are also known as synthetic fertilizers. They usually have an equal distribution of the three important nutrients (nitrogen, potassium, and phosphorus) needed for plant growth [135]. They include urea, ammonium chloride, ammonium nitrate, and ammonium sulphate. However, this fertilizer is known for its unstable and soaring price and

environmental degradation (polluting water bodies, acidifying soil, and global warming contributor), a result of its increased and continuous usage [136]. Hence, there is a need to switch to a cost-effective fertilizer type that is also environmentally friendly.

Organic fertilizers, on the other hand, which are bio-based, are the perfect alternative to chemical fertilizers because they also increase the productivity and yield of crops, improve the quality of soil, and enhance sustainability, while being friendly to the environment. They are rich in carbon and essential nutrients needed for plant growth. They cause minimal or no degradation, compared to synthetic fertilizers [137]. They are usually animal manure or human wastes (urine and feces).

Over the years, human feces have demonstrated excellent fertilization prospects by releasing organic matter and plant nutrients that help improve the structure of the soil and prevent erosion. Unprocessed human feces could be harmful to the soil, as they contain pathogens that reduce soil fertility [138]. Composting can be employed to eliminate all pathogens in human feces, so that they can be used to produce fertilizers. Human feces contain nutrients (potassium, nitrogen, sulphur phosphorus, magnesium, and calcium) for plant growth. Comparatively, human feces are richer in potassium, phosphorus, and organic matter than human urine [19]. Moya et al. [139] conducted a comparative study on the effect of artificial fertilizers and human-based fertilizers on the growth of French beans in Nairobi. They then reported that human feces-based fertilizers gave a 30% yield increase, compared to artificial fertilizers.

Human urine also contains potassium, phosphorus, sulphur, and nitrogen. Plants easily absorb these nutrients because they are in ionic forms [140]. Pathy et al. [141] reported that NPK biofertilizers can be obtained from human urine. Akpan-idiok et al. [142] compared the effect of human urine-based fertilizers and inorganic fertilizers on the *Abelmoschus esculentus* crop. It was reported that human urine-based fertilizers gave a higher yield of the crop than inorganic fertilizers.

The characteristics of urine are affected by the quantity of water taken in, the organism's body size and feeding habits, the source of the urine, and the well-being of the microorganisms that excrete the urine. Urine is made up of organic compounds (primarily creatine, uric acid, and creatinine) and inorganic compounds (primarily nitrogen, potassium, and phosphorus) [29]. The percentage concentration of the critical elements in urine mainly determines the various components of urine. Ions such as Na^+, Mg^{2+}, Cl^-, and Cu^{2+} are also constituents of urine. They enhance the growth of plants. The pH of stored urine is different from that of fresh urine because of the former hydrolyses ammonia and bicarbonate in a germ-free environment. The products (ammonia and bicarbonate) are released into the environment, while the residual bicarbonate increases the pH of the stored urine. Urine is reported to typically contain 1 g and 9.1 g of phosphorus and nitrogen per litre, respectively. The high composition of nutrients in unadulterated urine enables the development of more efficient energy recovery techniques and practical nutrient recovery concepts [29]. The developed nutrient recovery concept will help mitigate the environmental degradation that nutrients (potassium, phosphorus, and nitrogen) are likely to cause.

5.1. Overview of Nutrient Recovery Technologies

Nutrient recovery technologies are adopted for the recovery of nutrients from human and animal waste. Primary macronutrients, such as phosphorous, nitrogen, and potassium, as well as secondary macronutrients, including sulphur, magnesium, and calcium, are relevant nutrients that are in demand in several industries, such as the food, pharmaceutical, and fertilizer industries. Some of these technologies, including struvite precipitation, ammonia stripping, evaporation, and selective adsorption of nutrients, are briefly discussed as follows. For detailed information and a technical background of each recovery method, the readers are referred to the excellent review by Veneeckhaute et al. [143]. Patel et al. [144] also provided a comparative review of different nutrient recovery technologies from human urine.

5.1.1. Selective Adsorption

This technique employs an adsorbent to obtain nutrients from urine that are suitable for soil conditioning and amendment. It is mainly used to recover nitrogen with a zeolite adsorbent, which is composed of alumina and silica [145]. It can also be used to recover phosphorus if combined with struvite precipitation. A magnesium oxide (MgO) concentration of 0.5 mg/L and a supernatant phosphorus concentration of 10 gm^{-3} are reported to give the highest recovery of nitrogen. In contrast, 0.015 mg/L of zeolite with 1000 gNm^{-3} of supernatant nitrogen concentration gave the highest recovery of nitrogen. The nitrogen obtained from this technique can be used as a soil conditioner because it has proven helpful in enhancing the water retention and nutrients of soils with low nutrients [69].

5.1.2. Struvite Precipitation

This technology can be used for the simultaneous recovery of phosphorus and nitrogen. It is also employed in the treatment of wastewater. Struvite is an equimolar ratio of the anion (phosphate) and cations (ammonium ions and magnesium). Struvite precipitation for nutrient recovery can be made more effective by adding magnesium to urine. The precipitate produced can then be washed and filtered after it has been dried. Ahmed et al. [146] revealed that 12.5% of phosphorus and 5.7% of nitrogen constitute dry and pure struvite. The higher phosphorus concentration could be traced to the drying and precipitation processes. With this method, it is possible to recover nitrogen in the form of ammonium and phosphorus.

5.1.3. Ammonia Stripping

Ammonia stripping is used to recover ammonia from urine. During this process, ammonia is transferred between the liquid and gaseous phases. The recovery of ammonia is triggered by the pH, which can be increased by adding sodium hydroxide (NaOH) and calcium oxide (CaO) [146]. Papurello et al. [147] reported a 97% ammonia recovery from their study, where ammonia was stripped in a batch reactor with air, followed by its absorption in sulfuric acid. The product of this reaction, ammonia sulfate solution, can be used as a fertilizer. Stripping stored urine at 0.4 bar and 40 °C, followed by adsorbing the resulting gas at 5 bar and 20 °C, resulted in 10% ammonia recovery.

5.1.4. Evaporation

This technique is a volume reduction method because it helps reduce the water content in urine, thereby increasing the concentration of other nutrients. This technology is usually faced with problems such as energy and ammonia loss. The former can be prevented by recovering the energy, while the latter can be addressed by employing an acidification process [146]. Table 8 provides a summary of different nutrient recovery technologies and their efficiencies.

Table 8. Summary of nutrient recovery technologies from human and livestock urine.

Recovery Technology	Nutrients Recovered	Source	Efficiency (%)	References
Air stripping	Ammonium	Human urine	90	Wei et al. [148]
Struvite precipitation	Phosphorus	Human urine	94	Masrura et al. [149]
Membrane separation	Ammonium, phosphate	Human urine	Above 90	Zhang et al. [150]
Bio-electrochemical systems	Ammonia	Human urine	60	Martin et al. [137]
Wet extraction	Phosphorus	Pig manure	92–97	Azuara et al. [151]
Chemical precipitation	Phosphate	Dairy manure	82	Zhang et al. [152]

6. Bibliometric Research Trends on Resource Recovery from Human and Animal Waste

A bibliometric analysis is presented in this article to investigate the development of resource recovery from human and animal waste and identify the trends in publishing, dominant contributing authors, institutions, countries, potential publishing sources, and the most cited publications in this research area. Through bibliometric analysis, gaps in research were identified and presented in the next section. A summary of the methodology used in developing the bibliometric analysis is presented in Figure 10. The Web of Science (WoS) Core Collection database was used to compile the data used in the bibliometric analysis. The database was selected because of its large spectrum of data, compared to other databases. All research articles and proceeding papers related to resource recovery from human and animal waste for the last fifteen years were selected, with keywords such as animal manure, human feces, and urine (Figure 10). All relevant data were imported into the VOS viewer to create network maps for co-authorships, countries, and institutions. In addition, maps were developed for journal participation and keywords co-occurrence.

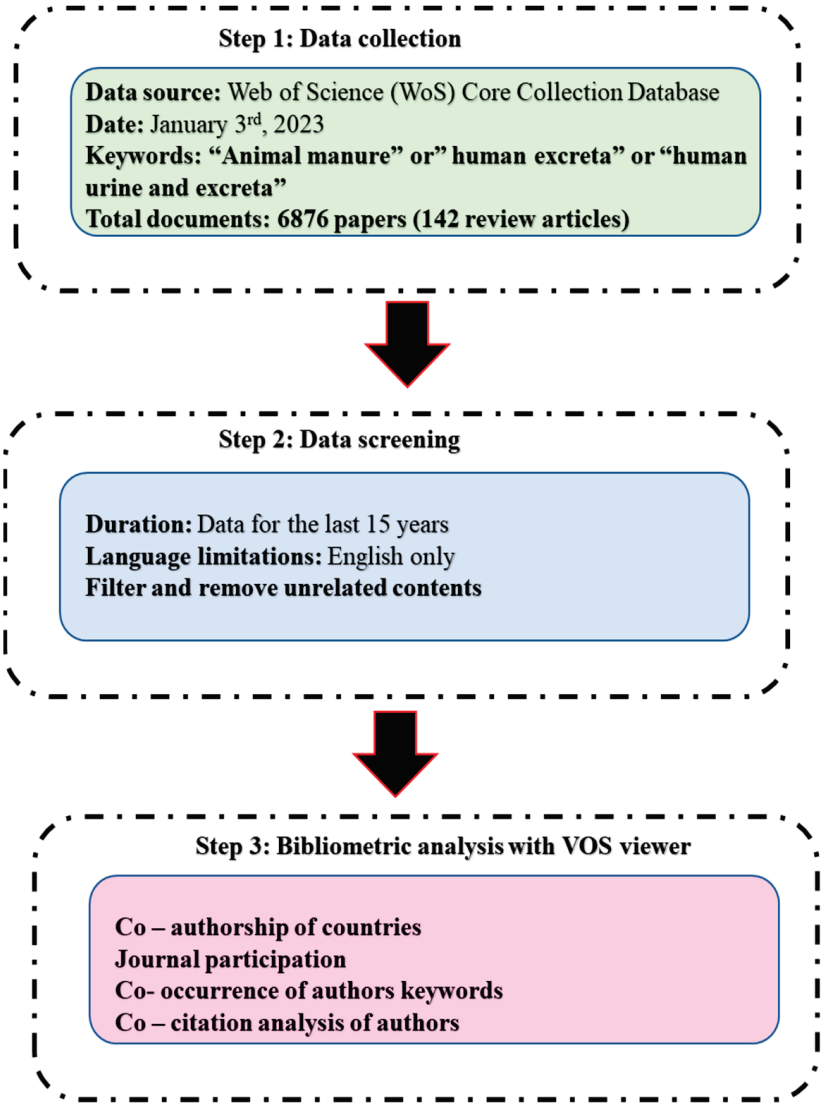


Figure 10. Flow chart of the bibliometric analysis methodology.

Figure 11 shows the network visualization maps of journals with a minimum of five citations per source between 2007 and 2022. It should be mentioned that the size of the circle on a map was determined by the number of citations. Therefore, journals with relatively

large circles are highly cited. The journals were grouped into six distinct clusters, based on the circle colors. The journals with the highest number of citations in each cluster include scientific reports journal under nature portfolio, PLoS ONE, applied and environmental microbiology, nutrients, science of the total environment, and xenobiotica. The strong participation in journals such as scientific reports, science of total environments, and PLoS ONE is expected, since most of them are focused on resource recovery from hazardous waste materials, including human and animal waste. Some of them also explore different environmental remediation techniques.

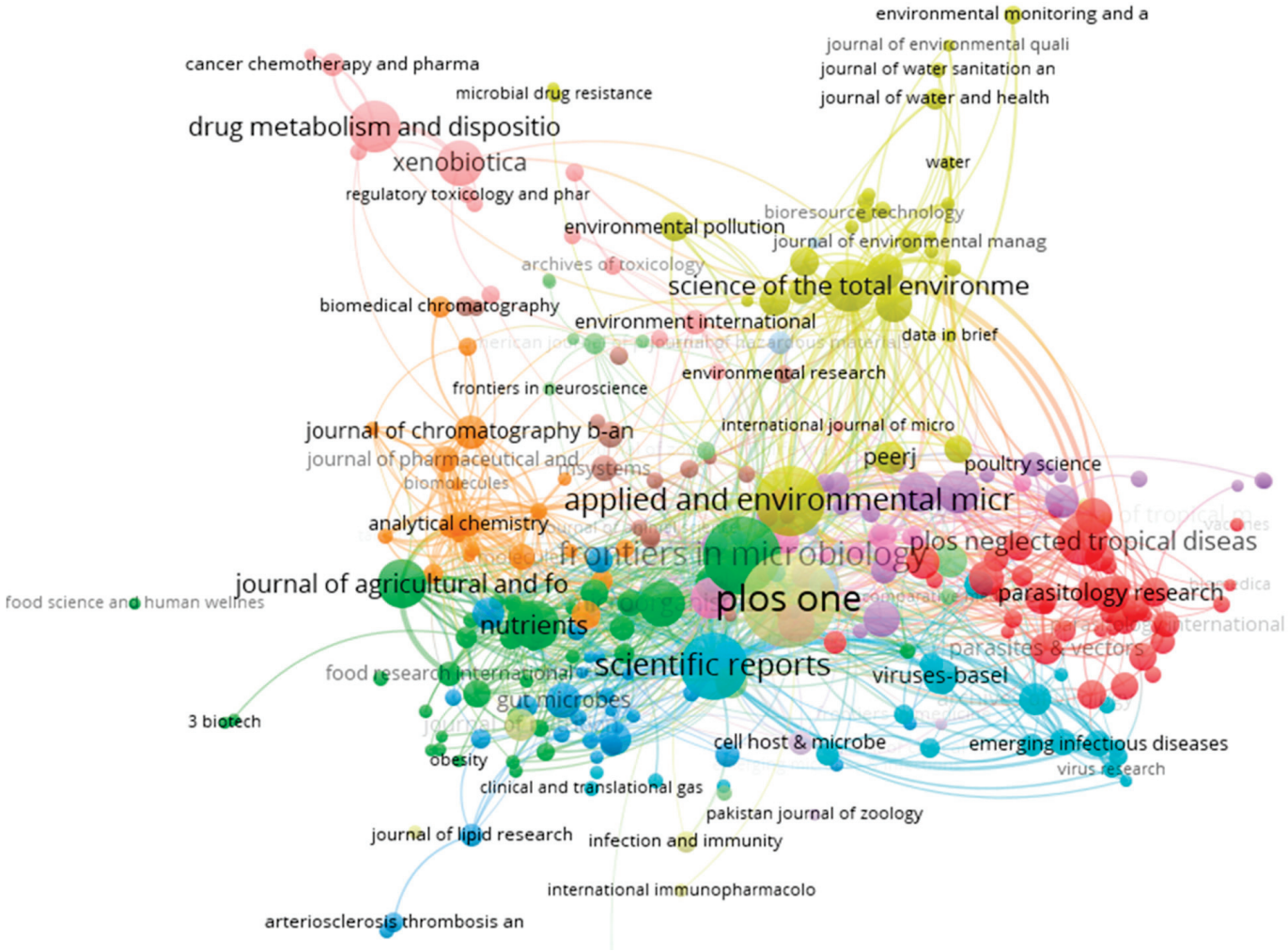


Figure 11. Network visualization map of journals with a minimum of 5 publications related to resource recovery from human and animal waste (2007–2022).

Figure 12 presents the co-authorship map of countries collaborating in resource recovery from human and animal waste. The map outlines how countries relate to each other in the research area. The size of the circle represents the collaboration intensity of each country. In this case, the USA, China, and England are the leading countries, in terms of collaboration intensity. This could be attributed to the significant amount of investment in new technologies from these countries. Moreover, the line thickness indicates the link strength between two items, while the distance between two countries indicates the similarity between them.

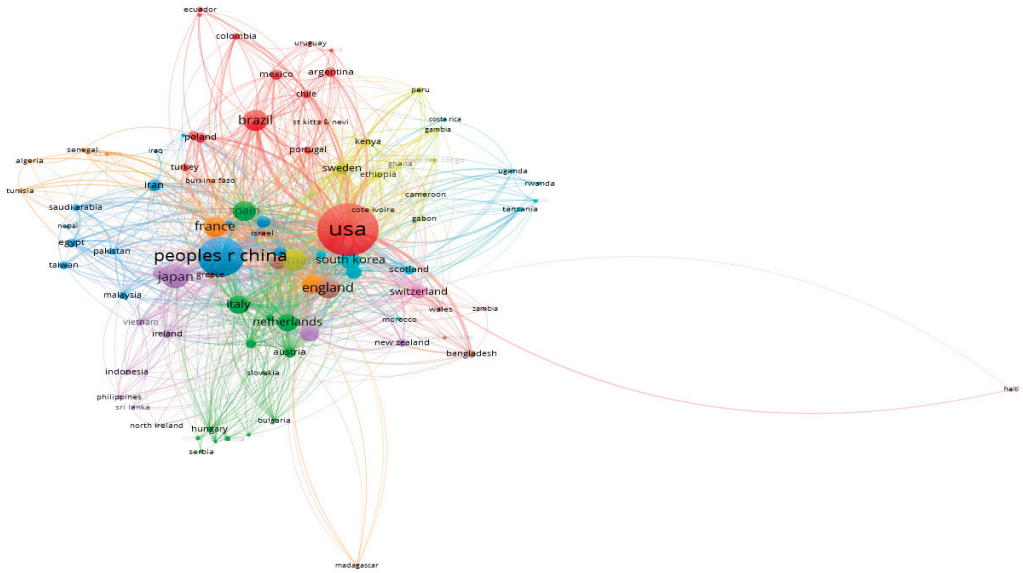


Figure 12. Co-authorship map of countries collaborating in resource recovery from human and animal waste.

The line thickness and distance analysis in Figure 12 shows that there is a significant research collaboration between the USA and other closer countries in the cluster. The institution participation map presented in Figure 13 also confirms that most of the institutions reported to be actively involved in resource recovery from human and animal waste research are found in China and the USA. The University of Illinois, University of California Davis, the Chinese Academy of Sciences, Zhejiang University, and the University of Reading had the highest number of publications, compared to the rest of the map.

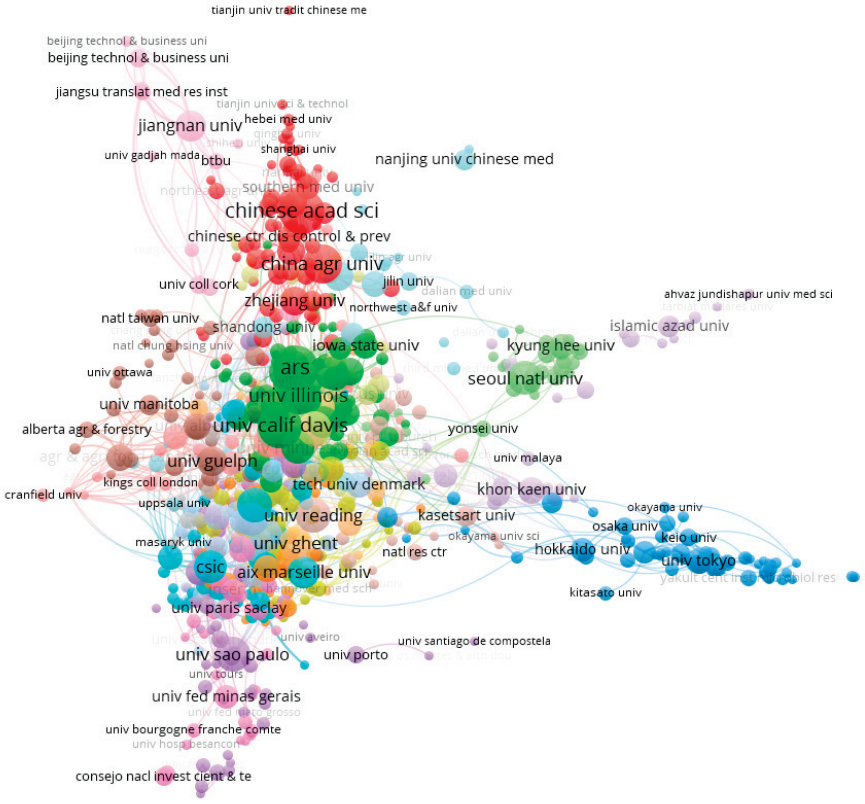


Figure 13. Network visualization map showing organizations' contributions.

7. Conclusions and Future Research Directions

Over the years, human and animal wastes have caused pollution (groundwater, soil, air, and land pollution), which has resulted in environmental degradation. This has resulted in researchers looking for a means to reuse, recycle, or recover byproducts from waste. Biological processes (fermentation and anaerobic digestion) and thermochemical methods (pyrolysis, gasification, and liquefaction) are promising valorization pathways. The present study provides an overview and the research progress in the valorization of human and animal waste via thermochemical and biological conversion pathways. While both pathways are promising routes for the conversion of waste into biofuels and value-added materials, they face several limitations. Thermochemical processes are expensive and require extremely high temperatures. In contrast, biological processes often produce low biofuel yields and require extended processing times. Therefore, an integrated biorefinery combining the two processes is suggested for the effective valorization of human and animal waste.

A bibliometric analysis was also presented in this study. The analysis confirmed that the USA, China, and England are the most productive countries in this research area. The University of Illinois, University of California Davis, the Chinese Academy of Sciences, Zhejiang University, and the University of Reading had the highest number of publications. Based on the results presented herein, the following future research gaps are observed.

- Developing effective and safe methods for processing human and animal waste is needed. There is a need for safe and effective methods for processing hazardous waste to optimize nutrients and resource recovery.
- It is imperative to examine the most effective ways to use the recovered resources. Once resources have been recovered from human or animal waste, there is a need to determine the most effective ways to use them, such as for agricultural purposes or as a source of energy, while considering the environmental impacts of different utilization methods.
- Understanding the potential impacts of using recovered resources: It is important to understand any potential negative impacts of using recovered resources on the environment on a large scale. Usually, a cradle-to-grave lifecycle assessment should be performed.
- Developing technologies for the on-site recovery of resources: There is a need for technologies that can be used to recover resources from feces on-site, such as at a wastewater treatment plant or in a portable system. Offsite or district waste processing facilities with improved heat optimization and materials recovery could also be a viable alternative.

Author Contributions: Conceptualization, T.J, A.N.A. and J.A.O.; methodology, C.C.O., T.J., A.N.A., J.A.O., P.U.O., P.P.I., F.G., O.A, A.A.A. and J.A.O.; investigation, C.C.O., T.J., A.N.A., J.A.O., P.U.O., P.P.I., F.G., O.A., A.A.A. and J.A.O.; software and data processing; J.A.O. and P.U.O.; writing original draft, C.C.O., T.J., A.N.A., J.A.O., P.U.O., P.P.I., F.G., O.A, A.A.A. and J.A.O.; writing review draft, C.C.O., P.U.O., F.G. and J.A.O. project administration, J.A.O. All authors have read and agreed to the published version of the manuscript.

Funding: This research received no external funding.

Data Availability Statement: All data are contained within the article.

Conflicts of Interest: The authors declare no conflict of interest.

References

1. Krounbi, L.; Enders, A.; van Es, H.; Woolf, D.; von Herzen, B.; Lehmann, J. Biological and thermochemical conversion of human solid waste to soil amendments. *Waste Manag.* **2019**, *89*, 366–378. [CrossRef] [PubMed]
2. WHO. Population Practising Open Defecation (%). Available online: https://www.who.int/data/gho/indicator-metadata-registry/imr-details/4823 (accessed on 20 January 2023).

3. Hunter, B.; Deshusses, M.A. Resources recovery from high-strength human waste anaerobic digestate using simple nitrification and denitrification filters. *Sci. Total. Environ.* **2019**, *712*, 135509. [CrossRef] [PubMed]
4. Hart, C.A.; Umar, L.W. Diarrhoeal Disease. *Trop. Dr.* **2000**, *30*, 170–172. [CrossRef] [PubMed]
5. Szogi, A.A.; Vanotti, M.; Ro, K. Methods for Treatment of Animal Manures to Reduce Nutrient Pollution Prior to Soil Application. *Curr. Pollut. Rep.* **2015**, *1*, 47–56. [CrossRef]
6. Orner, K.D.; Mihelcic, J.R. A review of sanitation technologies to achieve multiple sustainable development goals that promote resource recovery. *Environ. Sci. Water Res. Technol.* **2018**, *4*, 16–32. [CrossRef]
7. Okolie, J.A.; Nanda, S.; Dalai, A.K.; Berruti, F.; Kozinski, J.A. A review on subcritical and supercritical water gasification of biogenic, polymeric and petroleum wastes to hydrogen-rich synthesis gas. *Renew. Sustain. Energy Rev.* **2020**, *119*, 109546. [CrossRef]
8. Okolie, J.A.; Epelle, E.I.; Tabat, M.E.; Orivri, U.; Amenaghawon, A.N.; Okoye, P.U.; Gunes, B. Waste biomass valorization for the production of biofuels and value-added products: A comprehensive review of thermochemical, biological and integrated processes. *Process. Saf. Environ. Prot.* **2022**, *159*, 323–344. [CrossRef]
9. Lu, J.; Zhang, J.; Zhu, Z.; Zhang, Y.; Zhao, Y.; Li, R.; Watson, J.; Li, B.; Liu, Z. Simultaneous production of biocrude oil and recovery of nutrients and metals from human feces via hydrothermal liquefaction. *Energy Convers. Manag.* **2017**, *134*, 340–346. [CrossRef]
10. Min, K.J.; Park, K.Y. Economic feasibility of phosphorus recovery through struvite from liquid anaerobic digestate of animal waste. *Environ. Sci. Pollut. Res.* **2021**, *28*, 40703–40714. [CrossRef]
11. Onwosi, C.O.; Igbokwe, V.C.; Ezugworie, F.N. Decentralized Anaerobic Digestion Technology for Improved Management of Human Excreta in Nigeria. In *Anaerobic Biodigesters for Human Waste Treatment*; Springer: Cham, Switzerland, 2022; pp. 137–163. [CrossRef]
12. Ihoeghian, N.A.; Amenaghawon, A.N.; Ajieh, M.U.; Oshoma, C.E.; Ogofure, A.; Erhunmwunse, N.O.; Edosa, V.I.; Tongo, I.; Obuekwe, I.S.; Isagba, E.S.; et al. Anaerobic co-digestion of cattle rumen content and food waste for biogas production: Establishment of co-digestion ratios and kinetic studies. *Bioresour. Technol. Rep.* **2022**, *18*, 101033. [CrossRef]
13. Liu, H.; Li, X.; Zhang, Z.; Nghiem, L.D.; Wang, Q. Urine pretreatment significantly promotes methane production in anaerobic waste activated sludge digestion. *Sci. Total. Environ.* **2022**, *853*, 158684. [CrossRef] [PubMed]
14. Lee, Y.; Oa, S.-W. Resource-recovery processes from animal waste as best available technology. *J. Mater. Cycles Waste Manag.* **2015**, *18*, 201–207. [CrossRef]
15. Kirchmann, H.; Pettersson, S. Human urine—Chemical composition and fertilizer use efficiency. *Nutr. Cycl. Agroecosyst.* **1994**, *40*, 149–154. [CrossRef]
16. Rout, P.R.; Pandey, D.S.; Haynes-Parry, M.; Briggs, C.; Manuel, H.L.C.; Umapathi, R.; Mukherjee, S.; Panigrahi, S.; Goel, M. Sustainable Valorisation of Animal Manures via Thermochemical Conversion Technologies: An Inclusive Review on Recent Trends. *Waste Biomass-Valorization* **2022**, *14*, 553–582. [CrossRef]
17. Olugasa, T.T.; Odesola, I.; Oyewola, M. Energy production from biogas: A conceptual review for use in Nigeria. *Renew. Sustain. Energy Rev.* **2014**, *32*, 770–776. [CrossRef]
18. Malomo, G.A.; Madugu, A.S.; Bolu, S.A. Sustainable Animal Manure Management Strategies and Practices. In *Agricultural Waste and Residues*; IntechOpen: London, UK, 2018. [CrossRef]
19. Zseni, A. *Human Excreta Management: Human Excreta as an Important Base of Sustainable Agriculture. Proceedings of the 4th MAC 2015, Prague, Czech Republic, 20–21 February 2015*; MAC Prague consulting Ltd.: Prague, Czech Republic, 2015.
20. Tsai, W.-T.; Huang, C.-N.; Chen, H.-R.; Cheng, H.-Y. Pyrolytic Conversion of Horse Manure into Biochar and Its Thermochemical and Physical Properties. *Waste Biomass Valorization* **2015**, *6*, 975–981. [CrossRef]
21. Afolabi, I.C.; Epelle, E.I.; Gunes, B.; Güleç, F.; Okolie, J.A. Data-Driven Machine Learning Approach for Predicting the Higher Heating Value of Different Biomass Classes. *Clean Technol.* **2022**, *4*, 1227–1241. [CrossRef]
22. Shen, X.; Huang, G.; Yang, Z.; Han, L. Compositional characteristics and energy potential of Chinese animal manure by type and as a whole. *Appl. Energy* **2015**, *160*, 108–119. [CrossRef]
23. Hussein, M.; Burra, K.; Amano, R.; Gupta, A. Temperature and gasifying media effects on chicken manure pyrolysis and gasification. *Fuel* **2017**, *202*, 36–45. [CrossRef]
24. Yacob, T.W.; Fisher, R.; Linden, K.G.; Weimer, A.W. Pyrolysis of human feces: Gas yield analysis and kinetic modeling. *Waste Manag.* **2018**, *79*, 214–222. [CrossRef]
25. Nitsche, M.; Hensgen, F.; Wachendorf, M. Energy Generation from Horse Husbandry Residues by Anaerobic Digestion, Combustion, and an Integrated Approach. *Sustainability* **2017**, *9*, 358. [CrossRef]
26. Chong, C.T.; Mong, G.R.; Ng, J.-H.; Chong, W.W.F.; Ani, F.N.; Lam, S.S.; Ong, H.C. Pyrolysis characteristics and kinetic studies of horse manure using thermogravimetric analysis. *Energy Convers. Manag.* **2019**, *180*, 1260–1267. [CrossRef]
27. Wu, Q.; Wang, H.; Zheng, X.; Liu, F.; Wang, A.; Zou, D.; Yuan, J.; Xiao, Z. Thermochemical liquefaction of pig manure: Factors influencing on oil. *Fuel* **2020**, *264*, 116884. [CrossRef]
28. Islam, M.N.; Park, J.-H. A short review on hydrothermal liquefaction of livestock manure and a chance for Korea to advance swine manure to bio-oil technology. *J. Mater. Cycles Waste Manag.* **2016**, *20*, 1–9. [CrossRef]
29. Rose, C.; Parker, A.; Jefferson, B.; Cartmell, E. The Characterization of Feces and Urine: A Review of the Literature to Inform Advanced Treatment Technology. *Crit. Rev. Environ. Sci. Technol.* **2015**, *45*, 1827–1879. [CrossRef]

30. Salana, S.; Banerji, T.; Kumar, A.; Singh, E.; Kumar, S. Resource Recovery-Oriented Sanitation and Sustainable Human Excreta Management. In *Sustainable Resource Management: Technologies for Recovery and Reuse of Energy and Waste Materials*; Wiley VCH: Weinheim, Germany, 2021; pp. 109–136. [CrossRef]
31. Biswas, J.K.; Rana, S.; Meers, E. Bioregenerative Nutrient Recovery from Human Urine: Closing the Loop in Turning Waste into Wealth. In *Biorefinery of Inorganics: Recovering Mineral Nutrients from Biomass and Organic Waste*; John Wiley & Sons Ltd.: Hoboken, NJ, USA, 2020.
32. Simha, P.; Ganesapillai, M. Ecological Sanitation and nutrient recovery from human urine: How far have we come? A review. *Sustain. Environ. Res.* **2017**, *27*, 107–116. [CrossRef]
33. Jha, S.; Nanda, S.; Acharya, B.; Dalai, A.K. A Review of Thermochemical Conversion of Waste Biomass to Biofuels. *Energies* **2022**, *15*, 6352. [CrossRef]
34. Rowles, L.S.; Morgan, V.L.; Li, Y.; Zhang, X.; Watabe, S.; Stephen, T.; Lohman, H.A.C.; DeSouza, D.; Hallowell, J.; Cusick, R.D.; et al. Financial Viability and Environmental Sustainability of Fecal Sludge Treatment with Pyrolysis Omni Processors. *ACS Environ. AU* **2022**, *2*, 455–466. [CrossRef]
35. Selim, O.M.; Amano, R.S. Co-Pyrolysis of Chicken and Cow Manure. *J. Energy Resour. Technol.* **2021**, *143*, 011301. [CrossRef]
36. Beik, F.; Williams, L.; Brown, T.; Wagland, S. Development and prototype testing of a novel small-scale pyrolysis system for the treatment of sanitary sludge. *Energy Convers. Manag.* **2023**, *277*, 116627. [CrossRef]
37. Wang, Q.; Ren, X.; Sun, Y.; Zhao, J.; Awasthi, M.K.; Liu, T.; Li, R.; Zhang, Z. Improvement of the composition and humification of different animal manures by black soldier fly bioconversion. *J. Clean. Prod.* **2021**, *278*, 123397. [CrossRef]
38. Cantrell, K.B.; Hunt, P.G.; Uchimiya, M.; Novak, J.M.; Ro, K.S. Impact of pyrolysis temperature and manure source on physicochemical characteristics of biochar. *Bioresour. Technol.* **2012**, *107*, 419–428. [CrossRef]
39. Lee, D.-J.; Jung, S.; Jeong, K.-H.; Lee, S.-H.; Park, Y.-K.; Kwon, E.E. Catalytic pyrolysis of cow manure over a Ni/SiO2 catalyst using CO2 as a reaction medium. *Energy* **2020**, *195*, 117077. [CrossRef]
40. Mong, G.R.; Chong, C.T.; Ng, J.-H.; Chong, W.W.F.; Ong, H.C.; Tran, M.-V. Multivariate optimisation study and life cycle assessment of microwave-induced pyrolysis of horse manure for waste valorisation and management. *Energy* **2021**, *216*, 119194. [CrossRef]
41. Liu, X.; Li, Z.; Zhang, Y.; Feng, R.; Mahmood, I.B. Characterization of human manure-derived biochar and energy-balance analysis of slow pyrolysis process. *Waste Manag.* **2014**, *34*, 1619–1626. [CrossRef] [PubMed]
42. Zhou, S.; Liang, H.; Han, L.; Huang, G.; Yang, Z. The influence of manure feedstock, slow pyrolysis, and hydrothermal temperature on manure thermochemical and combustion properties. *Waste Manag.* **2019**, *88*, 85–95. [CrossRef]
43. Al-Salem, S.M.; Antelava, A.; Constantinou, A.; Manos, G.; Dutta, A. A review on thermal and catalytic pyrolysis of plastic solid waste (PSW). *J. Environ. Manag.* **2017**, *197*, 177–198. [CrossRef]
44. Bleuler, M.; Gold, M.; Strande, L.; Schönborn, A. Pyrolysis of Dry Toilet Substrate as a Means of Nutrient Recycling in Agricultural Systems: Potential Risks and Benefits. *Waste Biomass-Valorization* **2021**, *12*, 4171–4183. [CrossRef]
45. Koutcheiko, S.; Monreal, C.; Kodama, H.; McCracken, T.; Kotlyar, L. Preparation and characterization of activated carbon derived from the thermo-chemical conversion of chicken manure. *Bioresour. Technol.* **2007**, *98*, 2459–2464. [CrossRef] [PubMed]
46. Erdogdu, A.E.; Polat, R.; Ozbay, G. Pyrolysis of goat manure to produce bio-oil. *Eng. Sci. Technol. Int. J.* **2018**, *22*, 452–457. [CrossRef]
47. Elkasabi, Y.; Mullen, C.A.; Pighinelli, A.L.; Boateng, A.A. Hydrodeoxygenation of fast-pyrolysis bio-oils from various feedstocks using carbon-supported catalysts. *Fuel Process. Technol.* **2014**, *123*, 11–18. [CrossRef]
48. Pandey, D.S.; Katsaros, G.; Lindfors, C.; Leahy, J.J.; Tassou, S.A. Fast Pyrolysis of Poultry Litter in a Bubbling Fluidised Bed Reactor: Energy and Nutrient Recovery. *Sustainability* **2019**, *11*, 2533. [CrossRef]
49. Mong, G.R.; Chong, C.T.; Ng, J.-H.; Chong, W.W.F.; Lam, S.S.; Ong, H.C.; Ani, F.N. Microwave pyrolysis for valorisation of horse manure biowaste. *Energy Convers. Manag.* **2020**, *220*, 113074. [CrossRef]
50. Lee, D.-J.; Jung, S.; Jang, Y.; Jo, G.; Park, S.H.; Jeon, Y.J.; Park, Y.-K.; Kwon, E.E. Offering a new option to valorize hen manure by CO2-assisted catalytic pyrolysis over biochar and metal catalysts. *J. CO2 Util.* **2020**, *42*, 101344. [CrossRef]
51. He, S.; Cao, C.; Wang, J.; Yang, J.; Cheng, Z.; Yan, B.; Pan, Y.; Chen, G. Pyrolysis study on cattle manure: From conventional analytical method to online study of pyrolysis photoionization time-of-flight mass spectrometry. *J. Anal. Appl. Pyrolysis* **2020**, *151*, 104916. [CrossRef]
52. Ren, C.; Guo, S.; Wang, Y.; Liu, S.; Du, M.; Chen, Y.; Guo, L. Thermodynamic analysis and optimization of auto-thermal supercritical water gasification polygeneration system of pig manure. *Chem. Eng. J.* **2022**, *427*, 131938. [CrossRef]
53. Onabanjo, T.; Patchigolla, K.; Wagland, S.; Fidalgo, B.; Kolios, A.; McAdam, E.; Parker, A.; Williams, L.; Tyrrel, S.; Cartmell, E. Energy recovery from human faeces via gasification: A thermodynamic equilibrium modelling approach. *Energy Convers. Manag.* **2016**, *118*, 364–376. [CrossRef]
54. Parthasarathy, P.; Fernandez, A.; Al-Ansari, T.; Mackey, H.R.; Rodriguez, R.; McKay, G. Thermal degradation characteristics and gasification kinetics of camel manure using thermogravimetric analysis. *J. Environ. Manag.* **2021**, *287*, 112345. [CrossRef]
55. Sobamowo, G.M.; Ojolo, S.J. Techno-Economic Analysis of Biomass Energy Utilization through Gasification Technology for Sustainable Energy Production and Economic Development in Nigeria. *J. Energy* **2018**, *2018*, 4860252. [CrossRef]
56. Jia, J.; Shu, L.; Zang, G.; Xu, L.; Abudula, A.; Ge, K. Energy analysis and techno-economic assessment of a co-gasification of woody biomass and animal manure, solid oxide fuel cells and micro gas turbine hybrid system. *Energy* **2018**, *149*, 750–761. [CrossRef]

57. Liu, M.; Li, F.; Liu, H.; Wang, C.-H. Synergistic effect on co-gasification of chicken manure and petroleum coke: An investigation of sustainable waste management. *Chem. Eng. J.* **2020**, *417*, 128008. [CrossRef]
58. Xin, Y.; Cao, H.; Yuan, Q.; Wang, D. Two-step gasification of cattle manure for hydrogen-rich gas production: Effect of biochar preparation temperature and gasification temperature. *Waste Manag.* **2017**, *68*, 618–625. [CrossRef]
59. Nanda, S.; Dalai, A.K.; Gökalp, I.; Kozinski, J.A. Valorization of horse manure through catalytic supercritical water gasification. *Waste Manag.* **2016**, *52*, 147–158. [CrossRef] [PubMed]
60. Tavasoli, A.; Aslan, M.; Salimi, M.; Balou, S.; Pirbazari, S.; Hashemi, H.; Kohansal, K. Influence of the blend nickel/porous hydrothermal carbon and cattle manure hydrochar catalyst on the hydrothermal gasification of cattle manure for H2 production. *Energy Convers. Manag.* **2018**, *173*, 15–28. [CrossRef]
61. Liu, S.; Cao, W.; Wang, Y.; Wei, W.; Li, L.; Jin, H.; Guo, L. Characteristics and mechanisms of nitrogen transformation during chicken manure gasification in supercritical water. *Waste Manag.* **2022**, *153*, 240–248. [CrossRef]
62. De Blasio, C. Notions of Biomass Gasification. In *Fundamentals of Biofuels Engineering and Technology*; Springer: Cham, Switzerland, 2019; pp. 307–334. [CrossRef]
63. Salierno, G.; Marinelli, F.; Likozar, B.; Ghavami, N.; De Blasio, C. Supercritical Water Gasification of glycerol: Continuous reactor kinetics and transport phenomena modeling. *Int. J. Heat Mass Transf.* **2022**, *183*, 122200. [CrossRef]
64. Pandey, D.S.; Kwapinska, M.; Gómez-Barea, A.; Horvat, A.; Fryda, L.E.; Rabou, L.P.L.M.; Leahy, J.J.; Kwapinski, W. Poultry Litter Gasification in a Fluidized Bed Reactor: Effects of Gasifying Agent and Limestone Addition. *Energy Fuels* **2016**, *30*, 3085–3096. [CrossRef]
65. Xiao, X.; Cao, J.; Meng, X.; Le, D.D.; Li, L.; Ogawa, Y.; Sato, K.; Takarada, T. Synthesis gas production from catalytic gasification of waste biomass using nickel-loaded brown coal char. *Fuel* **2013**, *103*, 135–140. [CrossRef]
66. Perera, S.M.; Wickramasinghe, C.; Samarasiri, B.; Narayana, M. Modeling of thermochemical conversion of waste biomass—A comprehensive review. *Biofuel Res. J.* **2021**, *8*, 1481–1528. [CrossRef]
67. Güleç, F.; Riesco, L.M.G.; Williams, O.; Kostas, E.T.; Samson, A.; Lester, E. Hydrothermal conversion of different lignocellulosic biomass feedstocks—Effect of the process conditions on hydrochar structures. *Fuel* **2021**, *302*, 121166. [CrossRef]
68. Castello, D.; Pedersen, T.H.; Rosendahl, L.A. Continuous Hydrothermal Liquefaction of Biomass: A Critical Review. *Energies* **2018**, *11*, 3165. [CrossRef]
69. Lu, J.; Li, H.; Zhang, Y.; Liu, Z. Nitrogen Migration and Transformation during Hydrothermal Liquefaction of Livestock Manures. *ACS Sustain. Chem. Eng.* **2018**, *6*, 13570–13578. [CrossRef]
70. Conti, F.; Toor, S.S.; Pedersen, T.H.; Seehar, T.H.; Nielsen, A.H.; Rosendahl, L.A. Valorization of animal and human wastes through hydrothermal liquefaction for biocrude production and simultaneous recovery of nutrients. *Energy Convers. Manag.* **2020**, *216*, 112925. [CrossRef]
71. Li, H.; Lu, J.; Zhang, Y.; Liu, Z. Hydrothermal liquefaction of typical livestock manures in China: Biocrude oil production and migration of heavy metals. *J. Anal. Appl. Pyrolysis* **2018**, *135*, 133–140. [CrossRef]
72. Wang, W.; Yang, L.; Yin, Z.; Kong, S.; Han, W.; Zhang, J. Catalytic liquefaction of human feces over Ni-Tm/TiO2 catalyst and the influence of operating conditions on products. *Energy Convers. Manag.* **2018**, *157*, 239–245. [CrossRef]
73. Alherbawi, M.; Parthasarathy, P.; Al-Ansari, T.; Mackey, H.R.; McKay, G. Potential of drop-in biofuel production from camel manure by hydrothermal liquefaction and biocrude upgrading: A Qatar case study. *Energy* **2021**, *232*, 121027. [CrossRef]
74. He, S.; Wang, J.; Cheng, Z.; Dong, H.; Yan, B.; Chen, G. Synergetic effect and primary reaction network of corn cob and cattle manure in single and mixed hydrothermal liquefaction. *J. Anal. Appl. Pyrolysis* **2021**, *155*, 105076. [CrossRef]
75. Wei, L.; Sevilla, M.; Fuertes, A.B.; Mokaya, R.; Yushin, G. Hydrothermal Carbonization of Abundant Renewable Natural Organic Chemicals for High-Performance Supercapacitor Electrodes. *Adv. Energy Mater.* **2011**, *1*, 356–361. [CrossRef]
76. Álvarez-Murillo, A.; Sabio, E.; Ledesma, B.; Román, S.; González-García, C. Generation of biofuel from hydrothermal carbonization of cellulose. Kinetics modelling. *Energy* **2016**, *94*, 600–608. [CrossRef]
77. Kambo, H.S.; Dutta, A. Strength, storage, and combustion characteristics of densified lignocellulosic biomass produced via torrefaction and hydrothermal carbonization. *Appl. Energy* **2014**, *135*, 182–191. [CrossRef]
78. Guangzhi, Y.; Jinyu, Y.; Yuhua, Y.; Zhihong, T.; DengGuang, Y.; Junhe, Y. Preparation and CO_2 adsorption properties of porous carbon from camphor leaves by hydrothermal carbonization and sequential potassium hydroxide activation. *RSC Adv.* **2017**, *7*, 4152–4160. [CrossRef]
79. Liu, Z.; Zhang, F.; Hoekman, S.K.; Liu, T.; Gai, C.; Peng, N. Homogeneously Dispersed Zerovalent Iron Nanoparticles Sup-ported on Hydrochar-Derived Porous Carbon: Simple, in situ Synthesis and Use for Dechlorination of PCBs. *ACS Sustain. Chem. Eng.* **2016**, *4*, 3261–3267. [CrossRef]
80. Fan, F.; Xing, X.; Shi, S.; Zhang, X.; Zhang, X.; Li, Y.; Xing, Y. Combustion Characteristic and Kinetics Analysis of Hydrochars. *Trans. Chin. Soc. Agric. Eng.* **2016**, *32*, 219–224. [CrossRef]
81. Hao, W.; Björkman, E.; Lilliestråle, M.; Hedin, N. Activated Carbons for Water Treatment Prepared by Phosphoric Acid Ac-tivation of Hydrothermally Treated Beer Waste. *Ind. Eng. Chem. Res.* **2014**, *53*, 15389–15397. [CrossRef]
82. Titirici, M.-M.; Antonietti, M.; Baccile, N. Hydrothermal carbon from biomass: A comparison of the local structure from poly- to monosaccharides and pentoses/hexoses. *Green Chem.* **2008**, *10*, 1204–1212. [CrossRef]
83. Spitzer, R.Y.; Mau, V.; Gross, A. Using hydrothermal carbonization for sustainable treatment and reuse of human excreta. *J. Clean. Prod.* **2018**, *205*, 955–963. [CrossRef]

84. Afolabi, O.O.D.; Sohail, M.; Thomas, C.P.L. Microwave Hydrothermal Carbonization of Human Biowastes. *Waste Biomass-Valorization* **2015**, *6*, 147–157. [CrossRef]
85. Danso-Boateng, E.; Holdich, R.; Martin, S.; Shama, G.; Wheatley, A. Process energetics for the hydrothermal carbonisation of human faecal wastes. *Energy Convers. Manag.* **2015**, *105*, 1115–1124. [CrossRef]
86. Czerwińska, K.; Śliz, M.; Wilk, M. Hydrothermal carbonization process: Fundamentals, main parameter characteristics and possible applications including an effective method of SARS-CoV-2 mitigation in sewage sludge. A review. *Renew. Sustain. Energy Rev.* **2022**, *154*, 111873. [CrossRef]
87. Jang, E.-S.; Ryu, D.-Y.; Kim, D. Hydrothermal carbonization improves the quality of biochar derived from livestock manure by removing inorganic matter. *Chemosphere* **2022**, *305*, 135391. [CrossRef] [PubMed]
88. Qaramaleki, S.V.; Villamil, J.A.; Mohedano, A.F.; Coronella, C.J. Factors Affecting Solubilization of Phosphorus and Nitrogen through Hydrothermal Carbonization of Animal Manure. *ACS Sustain. Chem. Eng.* **2020**, *8*, 12462–12470. [CrossRef]
89. Ghavami, N.; Özdenkçi, K.; Chianese, S.; Musmarra, D.; De Blasio, C. Process simulation of hydrothermal carbonization of digestate from energetic perspectives in Aspen Plus. *Energy Convers. Manag.* **2022**, *270*, 116215. [CrossRef]
90. Neshat, S.A.; Mohammadi, M.; Najafpour, G.D.; Lahijani, P. Anaerobic co-digestion of animal manures and lignocellulosic residues as a potent approach for sustainable biogas production. *Renew. Sustain. Energy Rev.* **2017**, *79*, 308–322. [CrossRef]
91. Lee, S.Y.; Sankaran, R.; Chew, K.W.; Tan, C.H.; Krishnamoorthy, R. BMC Energy Waste to Bioenergy: A Review on the Recent Conversion Technologies. *BMC Energy* **2019**, *1*, 4. [CrossRef]
92. Karki, R.; Chuenchart, W.; Surendra, K.; Shrestha, S.; Raskin, L.; Sung, S.; Hashimoto, A.; Khanal, S.K. Anaerobic co-digestion: Current status and perspectives. *Bioresour. Technol.* **2021**, *330*, 125001. [CrossRef]
93. Dalke, R.; Demro, D.; Khalid, Y.; Wu, H.; Urgun-Demirtas, M. Current status of anaerobic digestion of food waste in the United States. *Renew. Sustain. Energy Rev.* **2021**, *151*, 111554. [CrossRef]
94. Ilo, O.; Simatele, M.; Nkomo, S.; Mkhize, N.; Prabhu, N. Methodological Approaches to Optimising Anaerobic Digestion of Water Hyacinth for Energy Efficiency in South Africa. *Sustainability* **2021**, *13*, 6746. [CrossRef]
95. Ripoll, V.; Agabo-García, C.; Solera, R.; Perez, M. Anaerobic digestion of slaughterhouse waste in batch and anaerobic sequential batch reactors. *Biomass Convers. Biorefinery* **2022**, 1–12. [CrossRef]
96. Rajendran, K.; Mahapatra, D.; Venkatraman, A.V.; Muthuswamy, S.; Pugazhendhi, A. Advancing anaerobic digestion through two-stage processes: Current developments and future trends. *Renew. Sustain. Energy Rev.* **2020**, *123*, 109746. [CrossRef]
97. Donkor, K.O.; Gottumukkala, L.D.; Lin, R.; Murphy, J.D. A perspective on the combination of alkali pre-treatment with bioaugmentation to improve biogas production from lignocellulose biomass. *Bioresour. Technol.* **2022**, *351*, 126950. [CrossRef]
98. Awosusi, A.; Sethunya, V.; Matambo, T. Synergistic effect of anaerobic co-digestion of South African food waste with cow manure: Role of low density-polyethylene in process modulation. *Mater. Today Proc.* **2021**, *38*, 793–803. [CrossRef]
99. Ma, G.; Ndegwa, P.; Harrison, J.H.; Chen, Y. Methane yields during anaerobic co-digestion of animal manure with other feedstocks: A meta-analysis. *Sci. Total. Environ.* **2020**, *728*, 138224. [CrossRef] [PubMed]
100. Kaur, H.; Kommalapati, R.R. Optimizing anaerobic co-digestion of goat manure and cotton gin trash using biochemical methane potential (BMP) test and mathematical modeling. *SN Appl. Sci.* **2021**, *3*, 724. [CrossRef]
101. Alfa, M.I.; Owamah, H.I.; Onokwai, A.O.; Gopikumar, S.; Oyebisi, S.O.; Kumar, S.S.; Bajar, S.; Samuel, O.D.; Ilabor, S.C. Evaluation of biogas yield and kinetics from the anaerobic co-digestion of cow dung and horse dung: A strategy for sustainable management of livestock manure. *Energy, Ecol. Environ.* **2020**, *6*, 425–434. [CrossRef]
102. Hamzah, A.F.A.; Hamzah, M.H.; Man, H.C.; Jamali, N.S.; Siajam, S.I.; Show, P.L. Biogas Production Through Mono- and Co-digestion of Pineapple Waste and Cow Dung at Different Substrate Ratios. *BioEnergy Res.* **2022**, 1–12. [CrossRef]
103. Arifan, F.; Abdullah, A.; Sumardiono, S. Effectiveness Analysis of Anaerobic Digestion Method in Making Biogas from Animal Manure and Tofu Liquid Waste. *J. Ilmu Teknol. Has. Ternak* **2021**, *16*, 84–94. [CrossRef]
104. Ren, Y.; Yu, M.; Wu, C.; Wang, Q.; Gao, M.; Huang, Q.; Liu, Y. A comprehensive review on food waste anaerobic digestion: Research updates and tendencies. *Bioresour. Technol.* **2018**, *247*, 1069–1076. [CrossRef]
105. Xu, H.; Chang, J.; Wang, H.; Liu, Y.; Zhang, X.; Liang, P.; Huang, X. Enhancing direct interspecies electron transfer in syntrophic-methanogenic associations with (semi)conductive iron oxides: Effects and mechanisms. *Sci. Total. Environ.* **2019**, *695*, 133876. [CrossRef]
106. Lv, N.; Zhao, L.; Wang, R.; Ning, J.; Pan, X.; Li, C.; Cai, G.; Zhu, G. Novel strategy for relieving acid accumulation by enriching syntrophic associations of syntrophic fatty acid-oxidation bacteria and H2/formate-scavenging methanogens in anaerobic digestion. *Bioresour. Technol.* **2020**, *313*, 123702. [CrossRef]
107. Wang, P.; Peng, H.; Adhikari, S.; Higgins, B.; Roy, P.; Dai, W.; Shi, X. Enhancement of biogas production from wastewater sludge via anaerobic digestion assisted with biochar amendment. *Bioresour. Technol.* **2020**, *309*, 123368. [CrossRef]
108. Zhang, L.; Tsui, T.-H.; Loh, K.-C.; Dai, Y.; Tong, Y.W. Effects of plastics on reactor performance and microbial communities during acidogenic fermentation of food waste for production of volatile fatty acids. *Bioresour. Technol.* **2021**, *337*, 125481. [CrossRef]
109. Arif, S.; Liaquat, R.; Adil, M. Applications of materials as additives in anaerobic digestion technology. *Renew. Sustain. Energy Rev.* **2018**, *97*, 354–366. [CrossRef]
110. Sitthi, S.; Hatamoto, M.; Watari, T.; Yamaguchi, T. Enhancing anaerobic syntrophic propionate degradation using modified polyvinyl alcohol gel beads. *Heliyon* **2020**, *6*, e05665. [CrossRef] [PubMed]

111. Zhao, J.; Li, Y.; Euverink, G.J.W. Effect of bioaugmentation combined with activated charcoal on the mitigation of volatile fatty acids inhibition during anaerobic digestion. *Chem. Eng. J.* **2022**, *428*, 131015. [CrossRef]
112. Lu, X.; Wang, H.; Ma, F.; Zhao, G.; Wang, S. Improved process performance of the acidification phase in a two-stage anaerobic digestion of complex organic waste: Effects of an iron oxide-zeolite additive. *Bioresour. Technol.* **2018**, *262*, 169–176. [CrossRef] [PubMed]
113. Zhang, J.; Cui, Y.; Zhang, T.; Hu, Q.; Tong, Y.W.; He, Y.; Dai, Y.; Wang, C.-H.; Peng, Y. Food waste treating by biochar-assisted high-solid anaerobic digestion coupled with steam gasification: Enhanced bioenergy generation and porous biochar production. *Bioresour. Technol.* **2021**, *331*, 125051. [CrossRef]
114. Adjama, I.; Derkyi, N.S.A.; Uba, F.; Akolgo, G.A.; Opuko, R. Anaerobic Co-Digestion of Human Feces with Rice Straw for Biogas Production: A Case Study in Sunyani. *Model. Simul. Eng.* **2022**, *2022*, 608045. [CrossRef]
115. Eduok, S.; John, O.; Ita, B.; Inyang, E.; Coulon, F. Enhanced Biogas Production From Anaerobic Co-digestion of Lignocellulosic Biomass and Poultry Feces Using Source Separated Human Urine as Buffering Agent. *Front. Environ. Sci.* **2018**, *6*, 67. [CrossRef]
116. Silwadi, M.; Mousa, H.; Al-Hajji, B.Y.; Al-Wahaibi, S.S.; Al-Harrasi, Z.Z. Enhancing biogas production by anaerobic digestion of animal manure. *Int. J. Green Energy* **2022**, *20*, 1–8. [CrossRef]
117. Pan, J.; Ma, J.; Liu, X.; Zhai, L.; Ouyang, X.; Liu, H. Effects of different types of biochar on the anaerobic digestion of chicken manure. *Bioresour. Technol.* **2019**, *275*, 258–265. [CrossRef] [PubMed]
118. Kizito, S.; Wu, S.; Kirui, W.K.; Lei, M.; Lu, Q.; Bah, H.; Dong, R. Evaluation of slow pyrolyzed wood and rice husks biochar for adsorption of ammonium nitrogen from piggery manure anaerobic digestate slurry. *Sci. Total. Environ.* **2015**, *505*, 102–112. [CrossRef] [PubMed]
119. Recebli, Z.; Selimli, S.; Ozkaymak, M.; Gonc, O. Biogas Production from Animal Manure. *J. Eng. Sci. Technol.* **2015**, *10*, 722–729.
120. Zlateva, P.; Terziev, A.; Yordanov, K. Study of regime parameters of the fermenter in the production of biogas from animal liquid waste materials. *E3S Web Conf.* **2021**, *286*, 02010. [CrossRef]
121. Andreev, N.; Ronteltap, M.; Boincean, B.; Wernli, M.; Zubcov, E.; Bagrin, N.; Borodin, N.; Lens, P. Lactic acid fermentation of human urine to improve its fertilizing value and reduce odour emissions. *J. Environ. Manag.* **2017**, *198*, 63–69. [CrossRef] [PubMed]
122. Andreev, N.; Ronteltap, M.; Boincean, B.; Lens, P.N.L. Lactic acid fermentation of human excreta for agricultural application. *J. Environ. Manag.* **2018**, *206*, 890–900. [CrossRef] [PubMed]
123. Lee, D.-J.; Yim, J.H.; Jung, S.; Jang, M.-S.; Jeong, G.-T.; Jeong, K.-H.; Kim, J.K.; Tsang, Y.F.; Jeon, Y.J.; Kwon, E.E. Valorization of animal manure: A case study of bioethanol production from horse manure. *Chem. Eng. J.* **2021**, *403*, 126345. [CrossRef]
124. Jimenez, J.; Bott, C.; Love, N.; Bratby, J. Source Separation of Urine as an Alternative Solution to Nutrient Management in Biological Nutrient Removal Treatment Plants. *Water Environ. Res.* **2015**, *87*, 2120–2129. [CrossRef]
125. Koffi Konan, F.; Kouame, M.K.; Author, C.; Koffi Félix, K.; Nazo Edith, K.-K.; Théophile, G.; Kotchi Yves, B.; Kouamé Martin, K.; Yao Francis, K.; Kablan, T. Improving Anaerobic Biodigestion of Manioc Wastewater with Human Urine as Co-Substrate. *Int. J. Innov. Appl. Stud.* **2013**, *2*, 335–343.
126. Twizerimana, M.; Marimi, M.; Bura, X.; Nganyi, E.O. Biogas Production from Co-digestion of Cotton Yarn Waste and Human Urine. *J. Energy Res. Rev.* **2020**, *6*, 20–29. [CrossRef]
127. Giwa, A.S.; Xu, H.; Chang, F.; Wu, J.; Li, Y.; Ali, N.; Ding, S.; Wang, K. Effect of biochar on reactor performance and methane generation during the anaerobic digestion of food waste treatment at long-run operations. *J. Environ. Chem. Eng.* **2019**, *7*, 103067. [CrossRef]
128. Wienchol, P.; Szlęk, A.; Ditaranto, M. Waste-to-energy technology integrated with carbon capture—Challenges and opportunities. *Energy* **2020**, *198*, 117352. [CrossRef]
129. Liu, X.Y.; Wang, J.J.; Nie, J.M.; Wu, N.; Yang, F.; Yang, R.J. Biogas production of Chicken Manure by Two-stage fermentation process. *E3S Web Conf.* **2018**, *38*, 01048. [CrossRef]
130. Zhang, A.; He, J.; Shen, Y.; Xu, X.; Liu, Y.; Li, Y.; Wu, S.; Xue, G.; Li, X.; Makinia, J. Enhanced degradation of glucocorticoids, a potential COVID-19 remedy, by co-fermentation of waste activated sludge and animal manure: The role of manure type and degradation mechanism. *Environ. Res.* **2021**, *201*, 111488. [CrossRef]
131. Svetlitchnyi, A.V.; Kensch, O.; A Falkenhan, D.; Korseska, S.G.; Lippert, N.; Prinz, M.; Sassi, J.; Schickor, A.; Curvers, S. Single-step ethanol production from lignocellulose using novel extremely thermophilic bacteria. *Biotechnol. Biofuels* **2013**, *6*, 31. [CrossRef] [PubMed]
132. Doreswamy, R.; Deb, R.; De, S. Potential use of piggery excreta as a viable source of bioethanol production. *J. Clean. Prod.* **2021**, *316*, 128246. [CrossRef]
133. Yan, Q.; Liu, X.; Wang, Y.; Li, H.; Li, Z.; Zhou, L.; Qu, Y.; Li, Z.; Bao, X. Cow manure as a lignocellulosic substrate for fungal cellulase expression and bioethanol production. *AMB Express* **2018**, *8*, 190. [CrossRef] [PubMed]
134. Dadrasnia, A.; Muñoz, I.D.B.; Yáñez, E.H.; Lamkaddam, I.U.; Mora, M.; Ponsá, S.; Ahmed, M.; Argelaguet, L.L.; Williams, P.M.; Oatley-Radcliffe, D.L. Sustainable nutrient recovery from animal manure: A review of current best practice technology and the potential for freeze concentration. *J. Clean. Prod.* **2021**, *315*, 128106. [CrossRef]
135. Ruiz, D.; Miguel, G.S.; Corona, B.; Gaitero, A.; Domínguez, A. Environmental and economic analysis of power generation in a thermophilic biogas plant. *Sci. Total. Environ.* **2018**, *633*, 1418–1428. [CrossRef] [PubMed]

136. Almeida, R.F.; Queiroz, I.D.S.; Mikhael, J.E.R.; Oliveira, R.C.; Borges, E.N. Enriched animal manure as a source of phosphorus in sustainable agriculture. *Int. J. Recycl. Org. Waste Agric.* **2019**, *8*, 203–210. [CrossRef]
137. Martin, T.M.P.; Esculier, F.; Levavasseur, F.; Houot, S. Human urine-based fertilizers: A review. *Crit. Rev. Environ. Sci. Technol.* **2020**, *52*, 890–936. [CrossRef]
138. Sugihara, R. Reuse of Human Excreta in Developing Countries: Agricultural Fertilization Optimization. *Consilience* **2020**, *22*, 58–64. [CrossRef]
139. Moya, B.; Parker, A.; Sakrabani, R. Challenges to the use of fertilisers derived from human excreta: The case of vegetable exports from Kenya to Europe and influence of certification systems. *Food Policy* **2019**, *85*, 72–78. [CrossRef]
140. Ajiboye, T.O.; Ogunbiyi, O.D.; Omotola, E.O.; Adeyemi, W.J.; Agboola, O.O.; Onwudiwe, D.C. Urine: Useless or useful "waste"? *Results Eng.* **2022**, *16*, 100522. [CrossRef]
141. Pathy, A.; Ray, J.; Paramasivan, B. Challenges and opportunities of nutrient recovery from human urine using biochar for fertilizer applications. *J. Clean. Prod.* **2021**, *304*, 127019. [CrossRef]
142. Akpan-Idiok, A.U.; Udo, I.A.; Braide, E.I. The use of human urine as an organic fertilizer in the production of okra (Abelmoschus esculentus) in South Eastern Nigeria. *Resour. Conserv. Recycl.* **2012**, *62*, 14–20. [CrossRef]
143. Vaneeckhaute, C.; Lebuf, V.; Michels, E.; Belia, E.; Vanrolleghem, P.A.; Tack, F.M.G.; Meers, E. Nutrient Recovery from Digestate: Systematic Technology Review and Product Classification. *Waste Biomass Valorization* **2017**, *8*, 21–40. [CrossRef]
144. Patel, A.; Mungray, A.A.; Mungray, A.K. Technologies for the recovery of nutrients, water and energy from human urine: A review. *Chemosphere* **2020**, *259*, 127372. [CrossRef]
145. Harder, R.; Wielemaker, R.; Larsen, T.A.; Zeeman, G.; Öberg, G. Recycling nutrients contained in human excreta to agriculture: Pathways, processes, and products. *Crit. Rev. Environ. Sci. Technol.* **2019**, *49*, 695–743. [CrossRef]
146. Ahmed, N.; Shim, S.; Won, S.; Ra, C. Struvite recovered from various types of wastewaters: Characteristics, soil leaching behaviour, and plant growth. *Land Degrad. Dev.* **2018**, *29*, 2864–2879. [CrossRef]
147. Papurello, D.; Boschetti, A.; Silvestri, S.; Khomenko, I.; Biasioli, F. Real-time monitoring of removal of trace compounds with PTR-MS: Biochar experimental investigation. *Renew. Energy* **2018**, *125*, 344–355. [CrossRef]
148. Wei, S.P.; van Rossum, F.; van de Pol, G.J.; Winkler, M.-K.H. Recovery of phosphorus and nitrogen from human urine by struvite precipitation, air stripping and acid scrubbing: A pilot study. *Chemosphere* **2018**, *212*, 1030–1037. [CrossRef] [PubMed]
149. Masrura, S.U.; Dissanayake, P.; Sun, Y.; Ok, Y.S.; Tsang, D.C.W.; Khan, E. Sustainable use of biochar for resource recovery and pharmaceutical removal from human urine: A critical review. *Crit. Rev. Environ. Sci. Technol.* **2020**, *51*, 3016–3048. [CrossRef]
150. Zhang, J.; She, Q.; Chang, V.W.C.; Tang, C.Y.; Webster, R.D. Mining Nutrients (N, K, P) from Urban Source-Separated Urine by Forward Osmosis Dewatering. *Environ. Sci. Technol.* **2014**, *48*, 3386–3394. [CrossRef] [PubMed]
151. Azuara, M.; Kersten, S.R.; Kootstra, A.M.J. Recycling phosphorus by fast pyrolysis of pig manure: Concentration and extraction of phosphorus combined with formation of value-added pyrolysis products. *Biomass-Bioenergy* **2012**, *49*, 171–180. [CrossRef]
152. Zhang, T.; Bowers, K.E.; Harrison, J.H.; Chen, S. Releasing Phosphorus from Calcium for Struvite Fertilizer Production from Anaerobically Digested Dairy Effluent. *Water Environ. Res.* **2010**, *82*, 34–42. [CrossRef]

Disclaimer/Publisher's Note: The statements, opinions and data contained in all publications are solely those of the individual author(s) and contributor(s) and not of MDPI and/or the editor(s). MDPI and/or the editor(s) disclaim responsibility for any injury to people or property resulting from any ideas, methods, instructions or products referred to in the content.

toxics

MDPI

Review

A Comprehensive Review of the Current Progress of Chromium Removal Methods from Aqueous Solution

Md. Monjurul Islam [1], Anika Amir Mohana [1], Md. Aminur Rahman [2,3,*], Mahbubur Rahman [4], Ravi Naidu [2,5] and Mohammad Mahmudur Rahman [2,5,6]

[1] Applied Chemistry and Chemical Engineering, Faculty of Engineering and Technology, Islamic University, Kushtia 7003, Bangladesh
[2] Global Centre for Environmental Remediation (GCER), College of Engineering, Science and Environment, The University of Newcastle, Callaghan, NSW 2308, Australia
[3] Zonal Laboratory, Department of Public Health Engineering (DPHE), Jashore 7400, Bangladesh
[4] Chittagong University of Engineering and Technology, Faculty of Civil Engineering, Chattogram 4349, Bangladesh
[5] CRC for Contamination Assessment and Remediation of the Environment, The University of Newcastle, Callaghan, NSW 2308, Australia
[6] Department of General Educational Development, Faculty of Science & Information Technology, Daffodil International University, Dhaka 1207, Bangladesh
* Correspondence: md.aminur.rahman@uon.edu.au

Abstract: Chromium (Cr) exists in aqueous solution as trivalent (Cr^{3+}) and hexavalent (Cr^{6+}) forms. Cr^{3+} is an essential trace element while Cr^{6+} is a dangerous and carcinogenic element, which is of great concern globally due to its extensive applications in various industrial processes such as textiles, manufacturing of inks, dyes, paints, and pigments, electroplating, stainless steel, leather, tanning, and wood preservation, among others. Cr^{3+} in wastewater can be transformed into Cr^{6+} when it enters the environment. Therefore, research on Cr remediation from water has attracted much attention recently. A number of methods such as adsorption, electrochemical treatment, physico-chemical methods, biological removal, and membrane filtration have been devised for efficient Cr removal from water. This review comprehensively demonstrated the Cr removal technologies in the literature to date. The advantages and disadvantages of Cr removal methods were also described. Future research directions are suggested and provide the application of adsorbents for Cr removal from waters.

Keywords: chromium; adsorption; remediation; wastewater

Citation: Islam, M.M.; Mohana, A.A.; Rahman, M.A.; Rahman, M.; Naidu, R.; Rahman, M.M. A Comprehensive Review of the Current Progress of Chromium Removal Methods from Aqueous Solution. *Toxics* **2023**, *11*, 252. https://doi.org/10.3390/toxics11030252

Academic Editor: Roberto Rosal

Received: 4 February 2023
Revised: 1 March 2023
Accepted: 3 March 2023
Published: 8 March 2023



Copyright: © 2023 by the authors. Licensee MDPI, Basel, Switzerland. This article is an open access article distributed under the terms and conditions of the Creative Commons Attribution (CC BY) license (https://creativecommons.org/licenses/by/4.0/).

1. Introduction

Chromium (Cr) is classified as a Group 1 element that is carcinogenic to living organisms, is a great risk to the environment, and is ranked fifth of the potentially worst toxic elements [1]. The superfund-controlled contaminated sites in the United States declared Cr as one of the top 20 toxic substances [2]. Most water sources contain only the hexavalent (Cr^{6+}) and trivalent (Cr^{3+}) forms of Cr in stable states [3]. Compounds of Cr^{3+} are adsorbed and form precipitates with very low solubility, which hinders its leaching into groundwater. Comparatively, Cr^{6+} exhibits high stability and strong oxidation [4,5]. Thus, due to its non-biodegradability behavior, Cr^{6+} has the potential to be hidden and persist in the long-term [6,7]. Cr is mainly used for the production of Cr-based alloys (around 60%) while the rest is consumed for electroplating, furnace blocks, and other refractory items [8,9]. The Cr metal contains a body-centered cubic crystal system which makes Cr an appropriate component that can improve compounds and increment consumption resistivity, color change, metallic luster, and additionally hardness [10]. The life circle of Cr in the environment is depicted in Figure 1.

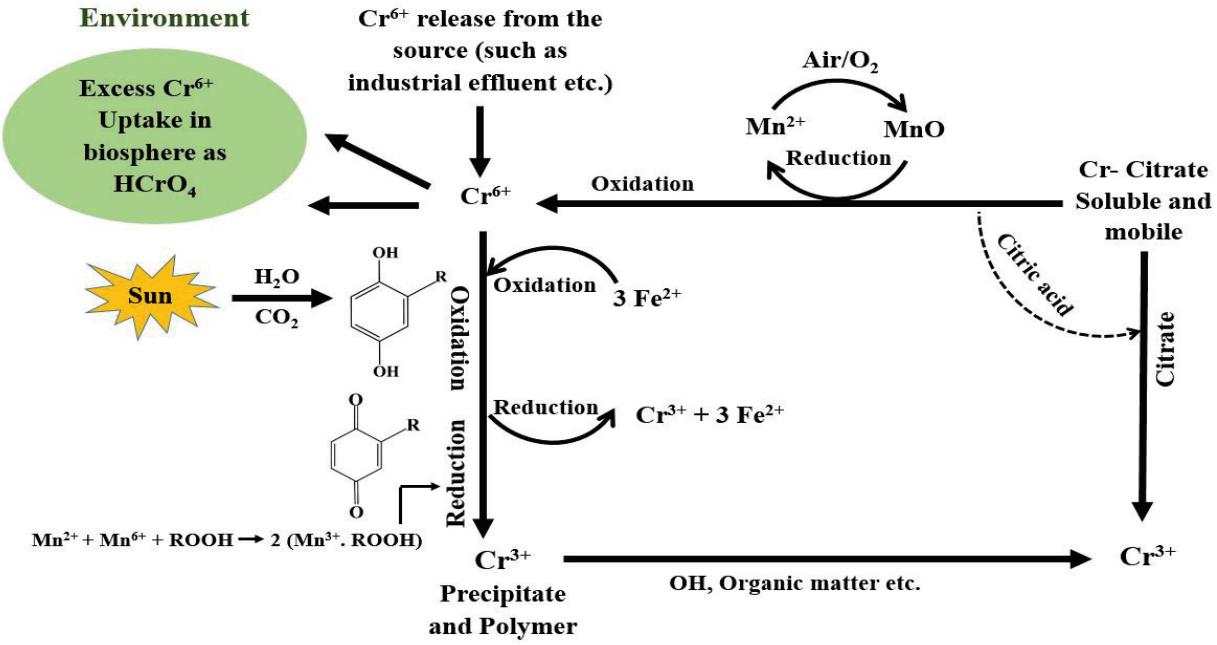


Figure 1. Chromium cycle in the environment.

The conveyance of compounds containing Cr^{3+} and Cr^{6+} relies upon redox potential, pH, presence of oxidizing or reducing compounds, the kinetics of the redox reactions, formation of Cr^{3+} complexes or insoluble Cr^{3+} salts, and total Cr concentration [11]. In general, Cr^{6+} salts are more soluble than those of Cr^{3+}, making Cr^{6+} moderately portable [12].

The major forms of Cr^{6+} in an aqueous solution are $Cr_2O_7^{2-}$, CrO_4^{2-}, H_2CrO_4, and $HCrO_4^-$ [13]. The pH of the solution, the overall concentration of Cr, the presence of oxidizing and reducing chemicals, the redox potential, and the kinetics of redox processes all affect how this distribution is distributed. Whereas $HCrO_4^-$ predominates in the pH range of one to six, CrO_4^{2-} is the only ion present if the solution's pH is higher than 7 (Figure 2). When the pH is below 3.9, Cr^{3+} exists as water-soluble Cr^{3+} cations, and as the pH rises to 5, the amount of Cr^{3+} steadily declines (Figure 2). Hydrolysis produces $Cr(OH)^{2+}$ when pH is greater than 5. Water-insoluble $Cr(OH)_3$ precipitate forms when the pH is greater than 6. Compounds containing Cr^{3+} are easily absorbed by soil colloids and create deposits with a very low solubility, which prevents them from penetrating the groundwater or being taken up by plants. The chromate and dichromate forms of Cr^{6+} (CrO_4^{2-}, $HCrO_4^-$, and $Cr_2O_7^{2-}$), on the other hand, have strong oxidative and high solubility properties [14].

The solubility of Cr^{3+} is minimum in natural water at pH 7.5–8.5. Cr^{6+} exists in solution as monomeric species/ions: $H_2CrO_4^0$, $HCrO_4^-$ (hydrogen chromate), and CrO_4^{2-} (chromate); or as the dimeric ion $Cr_2O_7^{2-}$ (dichromate, exists in emphatically acidic solution) [11]. At pH 1–10 and low concentration, Cr exists as either monovalent $HCrO_4^-$ or divalent chromate CrO_4^{2-} in groundwater. The monovalent structure prevails in acidic water while the divalent structure prevails at neutral pH or above. The monomeric species of Cr^{6+} with a concentration of more than 1 mg/L is responsible for the yellow color of water [11]. As indicated by the World Health Organization (WHO) drinking water guidelines, the greatest permissible cutoff for Cr is 0.05 mg/L [15].

Normally, Cr concentrations in groundwater are very low (below 2 mg/L), in spite of the fact that concentrations as high as 120 mg/L have been revealed (WHO 2006). It enters into various environmental systems (air, water, soil, etc.), through some natural processes (mining of ores) and anthropogenic activities such as refining and mining of ores, pesticides, batteries, paper industries, tanneries, fertilizer applications, and solid wastes disposal including sewage sludge, wastewater irrigation, and vehicular exhaust [4,16–20]. Figure 3 shows how toxic Cr emerges from various sources in our environment.

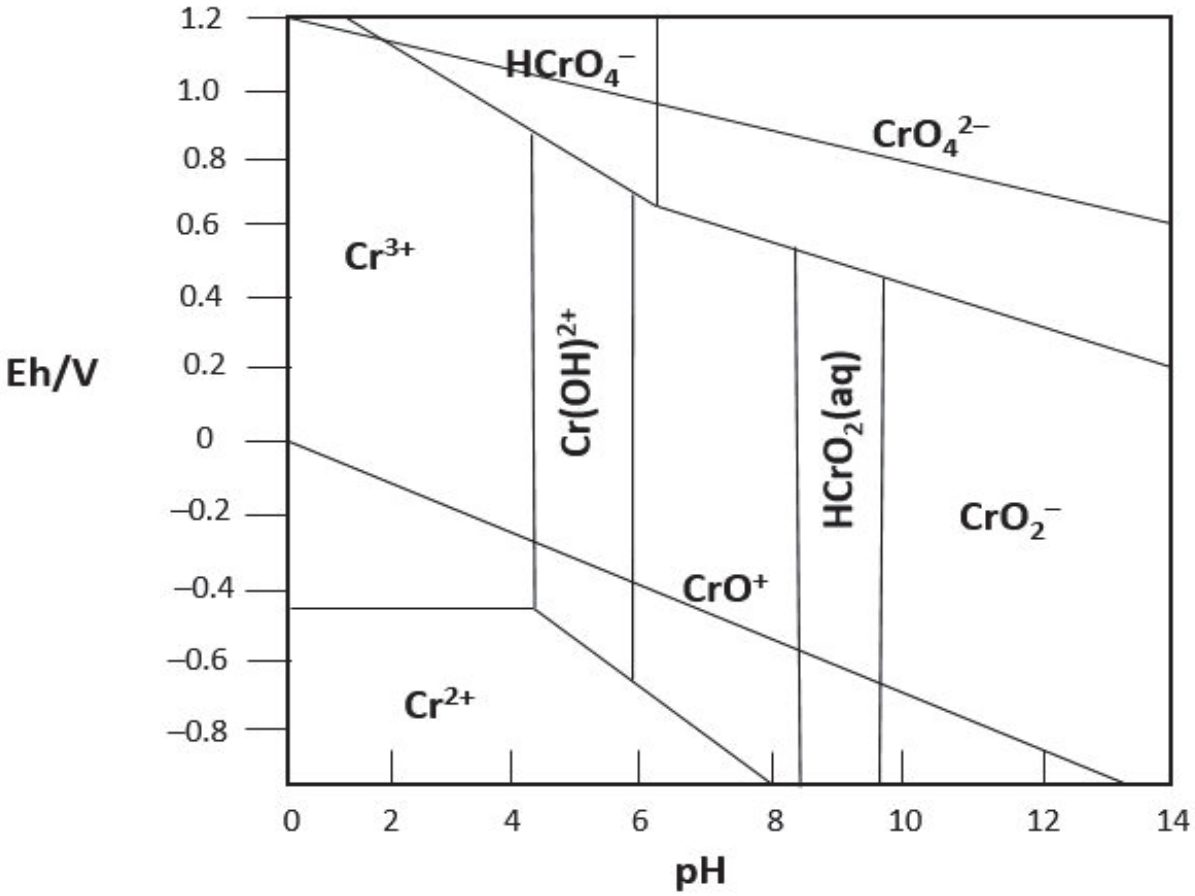


Figure 2. Pourbaix diagram for Cr chemical species in aqueous solution (Chen et al. 2021) [13].

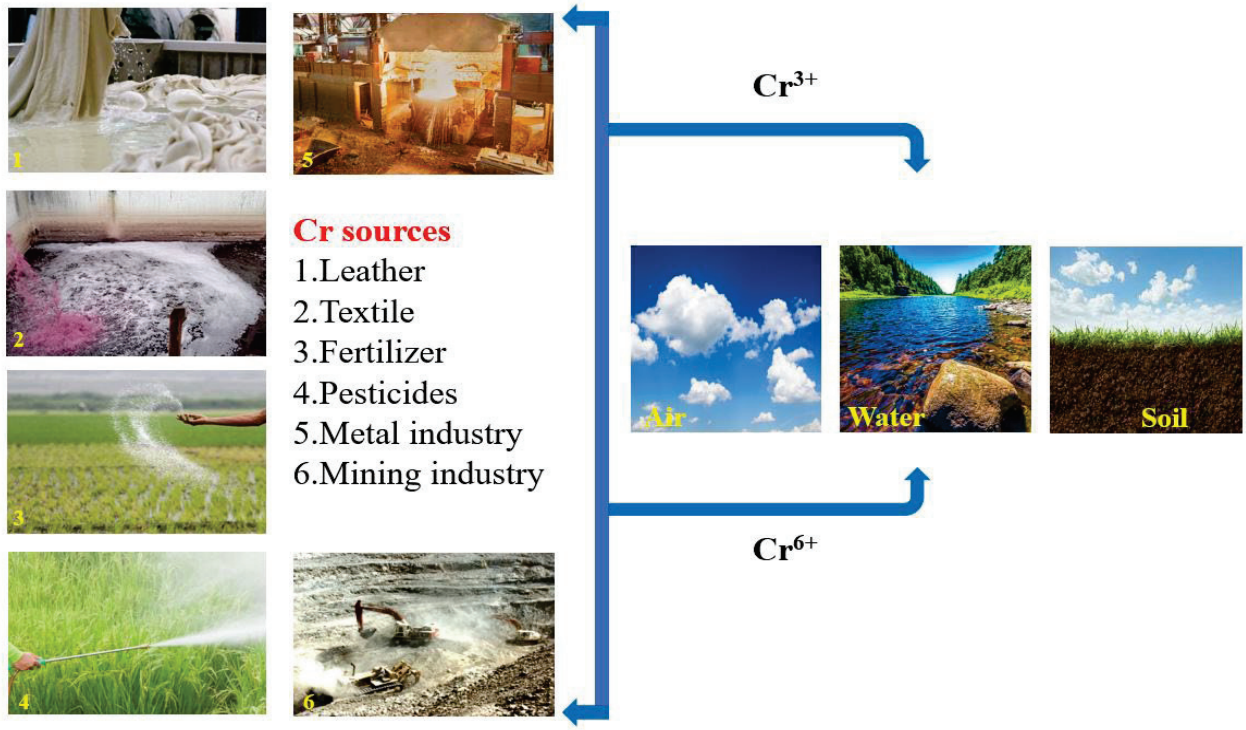


Figure 3. Exposure of chromium.

Adsorption of Cr^{6+} is normally restricted and diminishes with expanding pH [9,21]. Fe^{2+}, certain organic compounds with sulfhydryl groups, and sulfides can reduce Cr^{6+} effectively. Interestingly, Cr^{3+} is oxidized quickly by an enormous excess of MnO_2 and gradually by oxygen under conditions such as natural waters. It can therefore be asserted that both the concentration of Cr^{6+} and absolute Cr define the quality of water. Indeed, even at Cr^{6+} levels estimated in the parts per billion (ppb), it appears to be poisonous [22]. Cr^{6+} can enter or infiltrate the cell divider and apply its poisonous impact in the cell itself, serving as a wellspring of different malignant growth sicknesses or diseases [23–25]. At transient exposure levels above the most extreme contaminant level, Cr^{6+} causes skin and stomach disturbance or ulceration.

Long-haul introduction at levels above the greatest contaminant can cause dermatitis, harm to the liver, kidney dissemination, nerve tissue harm, and death as a result of huge dosages [26,27]. Cr^{6+} is substantially more toxic than Cr^{3+} for both intense and interminable exposures [15,28]. Acute ingestion of large amounts of Cr^{6+} causes gastrointestinal problems, including stomach torment, vomiting, and hemorrhage, while ceaseless exposure to Cr^{6+} brings about perforations and ulcerations of the septum, which have dangerous consequences for the respiratory tract. Epidemiological and animal studies recommend that Cr^{6+} mixtures, especially those that are water-insoluble, are responsible for different types of DNA harm and carcinogenicity [29,30]. Consequently, urgent and efficient Cr clean-up technology is essential.

Considering the above Cr toxicity in the environment, a number of different methods have been used for several years to remove Cr from different wastewaters, such as adsorption, electrochemical treatments, physico-chemical processes, biological removal (phytoremediation), membrane filtration, and chelation. Several articles have discussed the removal technologies of Cr. Notably, Aigbe and Osibote (2020) discussed hexavalent chromium removal from aqueous solutions utilizing the sorption technique with nanomaterials [31]. Another review paper published by Ukhurebor et al. (2021) discussed the effects and remediation of hexavalent Cr from soil [25]. Sharma et al. (2008) focused their review entirely on various technologies that remove Cr from water [11]. These authors discussed five different technologies that had been used till 2008 for removing Cr from wastewater [32]. Another review article published by Narayani and Shetty (2013) discussed the use of chromium-resistant bacteria for the removal of hexavalent Cr [33]. However, there is a significant paucity of research on the overall Cr removal techniques (both Cr^{3+} and Cr^{6+}) in recent years. The present review paper comprehensively examines various techniques employed for the removal of Cr, expatiating upon a multitude of experimental parameters. Notably, a meticulous comparison of the advantages and disadvantages inherent to each technique is provided. Additionally, this review presents an insightful discussion concerning the novel research directions and promising future prospects, thus contributing significantly to the advancement of knowledge in this field.

2. Cr Removal Methods

There are various methods available in the literature for the removal of Cr from wastewater, which are mostly suitable for eliminating high concentrations of the substance. Traditional removal methods usually focus on removing and reusing Cr [32]. Conventional methods that have been employed in Cr removal include chemical reduction, precipitation, flotation, solvent extraction, membrane separation (ultrafiltration, reverse osmosis, nanofiltration, microfiltration, hybrid membrane systems, ion exchange membranes, surfactant-based membranes, and liquid membranes), electrochemical treatment (electrodialysis, electrolysis, electrocoagulation) and ion exchange [25]. Of these, flocculation and membrane separation are very popular for industrial applications. Currently, the most important technology for Cr removal from wastewater is chemical precipitation. However, biosorption and metal oxide adsorption are cost-effective and promote recyclability [31]. The advantages and disadvantages of these methods are shown in Table 1.

Table 1. Advantages and disadvantages of Cr removal methods.

Name of the Technique	Name of Methods	Advantages	Disadvantages	References
Adsorption/Sorption	Adsorption	1. Both anionic and cationic Cr species can be absorbed 2. Removal of Cr is comparatively higher than precipitation process 3. Efficient to remove both Cr^{3+} and Cr^{6+} 4. Minimum sludge production. 5. Recycle of adsorbent	1. Adjustment of pH is difficult 2. Limited capacity 3. Requires proper disposal system to reduce environmental pollution	[34,35]
Electro-chemical treatment	Electrocoagulation	1. Requires minimal capital 2. Requires low pretreatment 3. Both Cr^{3+} and Cr^{6+} can be removed efficiently 4. Cr can be recovered for further use 5. Minimum reaction time 6. Fe electrode is more efficient for Cr^{6+} removal	1. Multi-stage process required 2. Difficulties may arrive due to the presence of complex metal and anion 3. Difficulties in the removal of micro flocks 4. Huge amount of sludge is produced 5. Polishing treatment may be required for colloidal flocks removal	[36–38]
	Electro-floatation	1. Does not require additional chemical 2. Easy to control 3. Electrode can give total coverage	1. Big bubbles can hinder the process	[39]
	Electro chemical reduction	1. Minimum time requires for both reaction and retention 2. Single step process 3. Minimum metal residue concentration	1. Excess precipitation of iron hydroxide increases sludge quantity	[36,40]
Physico-chemical treatment	Ion exchange method	1. Easy to operate 2. Highly Effective and reliable 3. Efficient for small and large installation 4. Varieties of resins are available	1. Regular regeneration 2. Concentrate disposal 3. Resin fouling 4. Other ions can interfere with removal efficiency	[41–45]
	Reduction process	1. Single step process 2. Low concentration of metal residue 3. Reductants can be dehydrated readily	1. Costly and unsuitable for drinking water treatment	
Biological removal		1. Eco friendly 2. Simple operation	1. Time-consuming process	[6]
Membrane filtration	Reverse osmosis	1. One of the best available technology for Cr removal 2. 60–100% removal is possible 3. Wide range pollutants can be removed effectively and simultaneously	1. High investment and operational cost 2. Membrane fouling 3. Disposal of brine	[38,46]
	Nano filter	1. Has bulk surface area	1. Requires pre-treatment	

2.1. Adsorption

Nowadays adsorption is considered to be a suitable and economical technique for the removal of Cr from wastewater. In this process, Cr ion adheres to the surface of the adsorbent that has high surface area due to its porosity. Surface charge of the adsorbent plays an important role in adsorption mechanism. Modification of surface charge by changing the functional group can enhance the capacity of adsorbent. Among various modification methods, nitrogenation, oxidation, and sulfuration are the most employed techniques to

enhance the specific surface area, pore structure, adsorption capacity, thermal stability, and mechanical strength [47]. However, they depend mainly on adsorbent materials, which sometimes are very expensive. Subsequently, the cost of adsorbent should be considered in choosing the most suitable adsorbents [48]. In light of the fact that adsorption is sometimes reversible, adsorbents can be recovered by reasonable desorption. In comparison with conventional methods, adsorption has various advantages such as minimal cost, availability, ease of operation, and efficiency, especially from economic and environmental points of view [49–51]. There are various suitable adsorbents available including natural adsorbents, composites, bio-sorbents, metal oxides, etc., for the removal of Cr.

2.1.1. Natural Adsorbents

Various materials such as natural materials, agricultural wastes, etc., can be deployed as low-cost adsorbents. It is found to be much more encouraging to use these adsorbents for the removal of heavy metals [52]. These low-cost adsorbents can be collected from natural and anthropogenic sources. Different kinds of natural adsorbents are being used in recent times such as pulp [53], clay [54,55], clinoptilolite [56], zeolite [57], leaf [58], activated carbon [59], charcoal [60], green walnut shell [61], etc. (Table 2).

Some research found that clay minerals are economical as adsorbents for removing industrial pollutants. Zhao et al. (2015) used pristine Akadama clay (AC) activated by HCl [55]. The experiments were conducted using the batch process. The optimum pH ranged between 2 and 3–9 after the activation of the clay (HCl–AC). The pseudo-second-order model serves to explain the kinetics of the obtained experimental data. Around 98.9% of Cr^{6+} was removed from tannery wastewater using the mentioned adsorbent, which can easily compete with other adsorbents. In their work, Bentchikou et al. (2017) investigated the removal of Cr from aqueous solution, using natural Algerian brown clay, in batch mode, at different temperatures [54]. Kinetic experiments showed that the pseudo-second-order model can explain the adsorption process.

The results showed that natural brown clay is effective in removing about 90% of Cr^{6+} at 20 °C and contact time was 60 min. At that same period of time, Zanin et al. (2017) reported natural clinoptilolite zeolite as an adsorbent could remove Cr^{3+} in wastewater from the graphic industry [56]. These authors found that up to 85% Cr removal is possible at 25 °C and pH 4.0. Elsewhere, Adam et al. (2018) used both natural zeolite and clinoptilolite, in the form of hollow fiber ceramic membrane (HFCM) to remove Cr^{6+} from aqueous solution [57]. The performance of the HFCM in adsorption/filtration was 44% of Cr^{6+} removal at the initial concentration of 40 mg/L and pH 4.

Table 2. Types of adsorbents and their maximum Cr removal capacities. [Superscripts a, b, and c indicating removal amount in percentages, mg/L, and μmol g^{-1}, respectively. L = Langmuir, F = Freundlich, T = Toth, R–P = Redlich–Peterson, S = Sips, E = Elovich, D–R = Dubinin–Radushkevich, D = Dahlquist, S = Scatchard, Tm = Temkin].

Type of Adsorbent	Adsorbent	pH	Removal Quantity (mg/g)	Isotherm	References
Agricultural Wastes	Bagasse sugarcane	2.0	13.4	L, F	[62]
	Bran rice	2.0	285.7	L, F	[63]
	Wheat bran	2.1	35	L	[64,65]
	Olive cake	2.0	35.44	L, F	[66]
	Sawdust Acacia arabica (pretreated)	6.0	111.6	L, F	[67]
	Shell Almond	4.0	22.20	L, F	[68]
	Lignin from paper Industry	3.0	13.48	L	[69]
	Soya cake	<1.0	0.28	L, F	[70]
	Coir Coconut	2.0	6.3	L, F, R–P, T, etc.	[71]

Table 2. *Cont.*

Type of Adsorbent	Adsorbent	pH	Removal Quantity (mg/g)	Isotherm	References
	Husk and hull Bengal gram husk	2.0	91.64	L, F	[72]
	Acrylonitrile grafted banana peels	3.0	96 [a]	L, F	[73]
	Rice husk	5.0	38.4	-	[74]
	Rye husk	3.0	80 [a]	L	[75]
	Chitosan-coated banana and areca fiber	4.5	75 [a]	-	[76]
	Rice husk	6	92.99 [a]	L	[77]
	Saw dust	2	100 [a]	F	[78]
	SCM-CC	2	99.92 [a]	F	[79]
	Green walnut shell	3.6	95 [a]	-	[61]
Plants	Sugarcane bagasse	1.9	23	L, D, S	[80]
	Sunflower stem waste (pretreated)	2.0	5.37–4.81	L, F, D-R	[81]
	London plane leaves	3.0	68.03	L	[82]
	Modified Pine sawdust	2.0	30.49	L, F	[83]
	Hazelnut shell	3.5	8.28	L, F	[84]
	Almond shell	2.0	10.61	L, F	[66]
	Rubber wood sawdust (Polyacrylamide grafted)	3.0	22.6	F	[85]
	Tradescantia pallida leaf	2.0	94 [a]	L	[86]
	Caryota urens seeds	2.0	52.63	L	[87]
	Aminated rice straw-grafted-poly (vinyl alcohol) (A-RS/PVA)	2.0	140.39	E, F	[88]
	Paddy straw	2.0	21.50	L, D, S	[89]
	Rubber leaf	1.5	96 [a]	-	[58]
Algae	*Scenedesmus* sp.	6.0	98.63 [a]	-	[90]
	Scenedesmus quadri-cauda (Chlorophyta)	6.0	98.3 [a]	L, F	[91]
	Sargassum myriocystum	5.2	66.66	L, T	[92]
	Cladophora glomerata	2.0	66.6	L, F	[93]
	Oedogonium hatei	2.0	35.2	L	[94]
	Sargassum sp	2.0	39.61	L	[95]
	Nostoc calcicola HH-12	3.0–4.0	12.23	L	[96]
	Chroococcus sp. *HH-11*	3.0–4.0	21.36	L	[96]
	Sargassum seaweed (marine algae)	3.5	60 [b]	L, F	[97]
	Scenedesmus incrassalulus (green micro algae)	-	52.7 [a]	-	[98]
	Spyrogyra species (green filamentous algae)	2.0	90 [a]	L	[99]
Fungi	*Penicillium janthinellum*	1.0	58.6 [a]	F, D-R	[100]
	Aspergillus niger	2.0	11.79	Tm, F	[101]
	Aspergillus niger	3.0	95.7 [a]	-	[102]
	Aspergillus ustus	2.0	6466.7 [c]	L, F	[103]
	Fusarium verticillioides	2.0	6400.0 [c]	L, F	[103]
	Pencillium funiculosum	2.0	3800.0 [c]	L, F	[103]
	Aspergillus niger	3.0	96.3 [a]	-	[104]
	Agaricus bisporus	1.0	8.0	F	[105]

Table 2. *Cont.*

Type of Adsorbent	Adsorbent	pH	Removal Quantity (mg/g)	Isotherm	References
Bacteria	*Aspergillus niger*	2.0	17.92	F	[106]
	Aspergillus sydoni	2.0	9.07	L	[106]
	Marine *Aspergillus niger*	1.0	117.33	L	[107]
	Basidiomycete, BDT-14	6.5	83.33	L	[108]
	Aspergillus sp. (filamentous)	2.0	10.0–27.5	L, F	[109]
	Fusarium sp. (filamentous)	5.0	18.2–71.0	-	[110]
	Spirulina sp.	5.0	90.91	F	[111]
	Eshcherichia coli and *Staphylococcus epidermidis*	3.0–6.0	16.9	L, F	[112]
	Rhodococcus opacus	5	82	F	[113]
	Rhodococcus rhodochrous	5	62	F	[113]
	Staphylococcus sp. and *Pseudomonas* sp.	5		L, F	[114]
	Azotobacter beijreinckii	-	26 [a]	-	[115]
	Bacillus subtilis	-	48 [a]	-	[115]
	Bacillus licheniformis	2.5	60.5	L	[116]
	Bacillus subtilis	2.0	14.54	L	[117]
	Staphylococcus xylosus	1.0	143	L, F	[118]
	Pseudomonas sp.	4.0	95	L, F	[118]
	Rhodococcus opacus	6.0	72.9	L	[119]
	Streptomyces rimosus	4.8	83	L	[120]
	Bacillus circulans biofilm	7.0	48 [a]	-	[121]
	Bacillus circulan	2.5	34.5	-	[122]
	Bacillus megaterium	2.5	32	-	[122]
	Bacillus coaglans	2.5	23.8	-	[123]
	Microbacterium liquuefaciens MP30	-	90 [a]	-	[124]
Activated Carbon	*Aegle marmelos* fruit shell	2.0	82.3 [a]	-	[59]
	Animal bone charcoal	2	92 [a]	-	[60]
	Cellulose-clay composite	4	2.37	-	[125]
	CHA/MFC	-	2.208 [d]	-	[126]
	CNC/clay composite	4	100 [a]	-	[127]
	Cellulose/chitosan composite	4	56 [a]	-	[128]
	Clay-alumina ceramic membrane	-	91.44 [a]	-	[129]
	MWCNTs-CTAB	5	98 [a]	L	[130]
	MWCNTs-M-SLS	5	99 [a]	L	[130]
	Chi@Fe_3O_4	-	142.32	-	[131]
	Chi@Fe_3O_4GO	-	100.51	-	[131]
	FeNi@HPC	4	30 [b]	-	[132]
Miscellaneous	Shale waste rock	3–6	90–91 [a]	L, F	[133]
	Iron/biochar beads (FMIB)	4	87.7 [a]	L	[134]
	Zn and Al modified pristine hydrochar	2–4	65 [a] (Zn-HC) 50 [a] (Al-HC)	L	[135]
	CDGF	3	99.8 [a]	-	[136]
	m-phenylenediamine-modified magnetic chitosan	<4	227.27	-	[137]
	TWNP	3.0	59.88 (64 [a])	L	[53]
	HFCM	4.0	40 [a]	-	[57]
	Brown clay	4.0	90 [a]	-	[54]
	Clinoptilolite	4.0	85 [a]	-	[56]

Dehghani et al. (2016) used treated waste newspaper pulp (TWNP) to remove Cr^{6+} from aqueous solution using batch experiments [53]. The adsorption parameters were: initial Cr^{6+} concentration (5, 20, 50 mg/L), contact time (60 min), adsorbent dose (3.0 g/L), and solution pH (3.0). The adsorption of Cr^{6+} was pH dependent and the experimental data fitted well to the Langmuir isotherm (R^2 = 0.98; maximum adsorption capacity 59.88 mg/g) and pseudo-second-order kinetics model. The rate constant k_2 varied from 0.0019 to 0.0068 at an initial Cr^{6+} concentration ranging from 5 to 20 mg/L. The percentage of Cr^{6+} removed was 59.88 mg/g (64% at pH 3). Nag et al. (2016) prepared both batch and continuous column mode experiments for rubber leaf and the pseudo-second-order model firmly described the kinetic process with a correlation coefficient of 0.99 [58].

Cr^{6+} (100%) was spontaneously removed according to an endothermic process at pH 1.5. Yasmeen et al. (2016) prepared synthesized adsorbent from shrimp shells and waste cotton rags which proved to be a viable adsorbent for removing Cr^{6+} ions from tannery effluent. Here the optimum pH for the maximum adsorption was pH 5.0, 93% with a composite concentration (2 g/L) and the effective rate was 240 min [138]. It emerged that Langmuir isotherm was well fitted with R^2 value of 0.997. Wan et al. (2018) tested m-phenylenediamine-modified magnetic chitosan for the concurrent reduction-absorption of Cr^{6+} and 227.27 mg/g Cr could be removed at pH < 4 [137]. Wang et al. (2019) used a β-cyclodextrin (b-CD) functionalized three-dimensional structured graphene foam for the removal of Cr^{6+} and achieved 99.8% efficiency at pH 3 [136].

Activated carbon can be another feasible solution for Cr removal from water. Agarwal and Gupta (2015) used animal bone charcoal (ABC) as an adsorbent to remove Cr^{6+} from effluent water at pH 2 with an initial concentration of 100 mg/L at constant temperature [60]. After shaking for 120 min at 140 rpm, 92% was removed. In their research, Zafarani et al. (2015) investigated the adsorption capacity of green walnut shell (GWS) for the removal of Cr^{6+} remaining in aqueous medium using batch experiments [61]. The ideal operational conditions for Cr^{6+} removal was: 10 mg/L, pH = 3.6, t = 5 min, and GWS doses = 6 g/L. The corresponding Cr^{6+} removal efficiency was 95%. In a similar study, Gottipati and Mishra (2016) developed microporous activated carbon (MAC) from an economically feasible plant precursor, i.e., *Aegle marmelos* fruit shell using $ZnCl_2$ activation and 82.3% removal of Cr^{6+} became possible at pH 2.0 [59].

Li et al. (2020) investigated the removal of Cr from aqueous solution using Zn- and Al-modified pristine hydrochar. Kinetic experiments showed that the pseudo-second-order model could explain the adsorption process and fit the Langmuir model [135]. The results showed that this modified hydrochar is effective in removing Cr^{6+} at pH 2–4. Qiao et al. (2020) prepared floatable magnetic iron/biochar beads (FMIB) using *Enteromorpha prolifera*, where the optimum ratio was 2:1, for the removal of Cr species [134]. After three cycles, the FMIB bed successfully removed 21.5% and 40.5% of Cr^{6+} and Cr^{3+}, respectively. Furthermore, the experiments show that it has the potential to remove 87.7% of the total Cr from leather processing wastewater. The best level of pH for this process was 4. The contact times for Cr^{3+} and Cr^{6+} were 120–480 min and 900 min, respectively. This result demonstrated the kinetics could be described using the pseudo-second-order model and the isotherm model fitted the Langmuir model well. Recently, Jabłońska (2020) used shale waste rocks to remove Cr^{3+} and Cr^{6+} from aqueous solution [133]. The maximum sorption (90–91%) took place at pH 3–6 for Cr^{3+} and pH 4–5 for Cr^{6+}. The sorption process was well described by the Langmuir–Freundlich isotherm model. Though natural adsorbents are good for the adsorption of Cr, they are blended to form a composite to improve efficiency.

2.1.2. Bio-Sorbents

Each type of biological species has an attraction for metals, yet microbial organisms such as bacteria and fungi are prudently used to execute most of the biosorption experiments [139,140]. Many researchers in removing Cr used bio-materials instead of available physico-chemical advances as a dynamic alternative. Several reviews have been published

on the usage of various kinds of bio-sorbents, which are famous for their Cr binding capacities, for example, agricultural wastes, bacteria, fungi, algae, etc. [139–145].

Bacteria

To remove Cr^{3+} and Cr^{6+} from wastewater, several types of bacteria have been studied, for example: *Spirulina* sp. [111], *Escherichia coli* [112], *Staphylococcus epidermidis* [112], *Rhodococcus opacus* [113], *Rhodococcus rhodochrou* [113], *Staphylococcus* sp. [114], *Pseudomonas* sp. [114], *Azotobacter beijreinckii* [115], and *Bacillus subtilis* [115].

The experiment carried out by Rezaei (2016) using dried *Spirulina* sp. biomass showed that at 40 °C and pH 5, the biomass confirmed the highest Cr^{6+} adsorption capacity when the initial concentration was 10 mg/L [111]. The Freundlich model fitted experimental data better than the Langmuir model as both models were used to analyze them and maximum biosorption capacity was found to be 90.91 mg/g. In their paper, Quiton et al. (2018) reported *E. coli* and *Staphylococcus epidermidis* biofilms supported on kaolin for the removal of Cr^{6+} from aqueous solution [112] (Table 2). Optimum pH for the biosorption of Cr^{6+} was 3.0–6.0. When the initial concentration of Cr was 200 mg/L, the highest biosorption capacity was 16.9 mg/g. The biosorption of Cr^{6+} by *E. coli* biofilm supported on kaolin fits the Langmuir isotherm well, whereas the Freundlich isotherm best describes the Cr^{6+} biosorption onto *S. epidermidis* biofilm.

On the other hand, Dobrowolski et al. (2017) chose two different kinds of species of bacteria, namely *Rhodococcus opacus* and *Rhodococcus rhodochrous* and carried out the experiment with pH 5 at 25 °C in batch process for the removal of Cr^{6+} from aqueous solution [113]. The equilibrium data of the biosorption was well described by the Freundlich isotherm model rather than the Langmuir model. The maximum removals of Cr^{6+} were 82 and 62 mg/g for biopolymer from *Rhodococcus rhodochrous* and *Rhodococcus opacus*, respectively, which are very low. Thus, these bio-sorbents are not suitable for Cr^{6+} removal. Emran et al. (2019) also used two different kinds of species—*Staphylococcus* sp. and *Pseudomonas* sp.—for the biosorption of Cr^{6+} and determined the optimum pH, contact time, and biomass concentration [114]. The equilibrium time was 24 h when the desired pH was 5 at 50 °C. The equilibrium data were well described by both the Langmuir and Freundlich isotherms. Meanwhile, Chug et al. (2016) used both *Azotobacter beijreinckii* and *Bacillus subtilis* bacteria for developing Extracellular Polymeric Substances to remove Cr^{6+} [115]. *A. beijreinckii* and *B. subtilis* bacteria could remove 26% and 48% of Cr^{6+}, respectively, from aqueous solution after 24 h incubation. This occurred when the initial concentration of Cr was 10 mg/L. After 24 h, the removal percentage is independent of incubation period (Table 2).

Fungi

One of the best-known low-cost adsorbents for removing Cr from wastewater is fungi biomass. To date, *Aspergillus niger* was found to be the most efficient fungi [102,104]. Saravanan et al. (2016) [102] and Mondal et al. (2017) [101] used blended *Aspergillus niger.* Saravanan et al. (2016) [102] used these fungi with custard apple seeds for experiments that were carried out in the batch process (Table 2). Authors found that the optimum initial concentration was 100 mg/L and bio-sorbent loading was 10 g/L when the pH was 3.0 at 36 °C. The largest amount of Cr^{6+} removed from the wastewater, at the stated conditions, was 95.7%. Mondal et al. (2017) used the batch process for their experiment [101], and these authors found that the optimum values were: initial concentration = 33.33 mg/L, pH = 4.6, adsorbent dose = 1.0 g/L and contact time = 48.45 min. At initial pH of 2.0, the maximum adsorption capacity for *A. niger* was 11.79 mg/g. The biosorption process followed the pseudo-second-order kinetic model, and the equilibrium data were well described by both Temkin and Freundlich isotherms. The activation energy of the adsorption was estimated as 2.9×10^{-3} kJ/mol.

Chen et al. (2019) examined the consumption of marine-derived fungus *Penicillium janthinellum* (P1) for the removal of aqueous Cr^{6+} in batch experiments [100]. Their results

showed that maximum Cr^{6+} biosorption capacity for living fungus P1 pellets was about 87% at the optimum condition of beginning concentration of Cr^{6+} = 250 mg/L, beginning pH = 1, temperature = 30 °C, bio-sorbent dosage = 30 g/L and contact time = 8 h. Similarly, maximum Cr^{6+} biosorption capacity for non-living fungus P1 pellets amounted to approximately 58.6% at the desired conditions of: initial concentration of Cr^{6+} = 100 mg/L; initial pH = 1; temperature = 30 °C; bio-sorbent dose = 3 g/L; and contact time = 12 h. After analyzing the data, it emerged that the biosorption process was well described by the Freundlich, Dubinin–Radushkevich (D–R) isotherms followed by the pseudo-second-order kinetic model.

In comparison, Mahmoud et al. (2015) produced three highly effective bio-sorbents, i.e., (1) NSi-Asp, (2) NSi-Fus, and (3) NSi-Pen from three fungal strains, named (1) *Aspergillus ustus* (Asp), (2) *Fusarium verticillioides* (Fus), and (3) *Pencillium funiculosum* (Pen),. This was completed by immobilizing them on nanosilica (NSi) surface [103]. The highest biosorption capacities for Cr^{3+} were 2466, 2666, and 1866 μmol/g by using NSi-Asp, NSi-Fus, and NSi-Pen, respectively, at pH 7.0 whereas for Cr^{6+} the values were 6466, 6400, and 3800 μmol/g at pH 2.0. Both Langmuir and Freundlich isotherms were used to describe the data of sorption equilibria, which was obtained at about 15 min. Sivakumar (2016) carried out a comparative investigation of the efficiencies of *Aspergillus foetidus*, *Aspergillus fumigatus*, *Aspergillus heteromorphus*, *Aspergillus viridinutans*, *Aspergillus flavus*, *Aspergillus nidulans*, and *Aspergillus niger* for the removal of Cr^{6+} from tannery wastewater [104]. The outcome was that the sequence for the highest removal of Cr^{6+} with initial concentration of 18.125 mg/L (dilution ratio 4) was: *A. niger* > *A. flavus* > *A. fumigatus* > *A. nidulans* > *A. heteromorphus* > *A. foetidus* > *A. viridinutans* at pH 3 when the fungi biomass was 4 g. Furthermore, *Aspergillus niger* proved to be the most efficient Cr^{6+} remover (96.3%) in comparison with other fungi species when the concentration of Cr^{6+} was kept at 18.12 mg/L.

Algae

Several algae species have been used as bio-sorbents for the recovery of Cr from industrial effluents. These include *Scenedesmus* sp. [90], *Scenedesmus quadri-cauda* [91], *Sargassum myriocystum* [92], *Cladophora glomerata* [93], etc. Jayakumar et al. (2015) [92] used *Sargassum myriocystum* as a bio-sorbent. The ideal conditions of the process were: sorbent dosage = 2.017 g/L, contact time = 108 min, pH = 5.2, agitation speed = 120 rpm. The sorption process was well fitted to the Langmuir and Toth isotherm models (R^2 = 0.993 and 0.992), followed by both pseudo-second-order and Elovich and power function kinetic models, with the highest sorption capacity of 66.66 mg/g. A Chlorophyta named *Scenedesmus quadri-cauda* served as an effective bio-sorbent by Shokri Khoubestani et al. (2015) in order to remove both Cr^{3+} and Cr^{6+} using batch experiments. A total of 98.3% (at pH 6) and 47.6% (at pH 1) of Cr^{3+} and Cr^{6+} were, respectively, removed by this process having an equilibrium time of 120 min [91]. The Langmuir model described the biosorption process of Cr^{3+}, while conversely, Freundlich isotherm model was used for Cr^{6+}. Both processes followed the pseudo-second-order kinetic model. The maximum biosorption capacities were 58.47 and 46.51 mg/g for Cr^{3+} and Cr^{6+}, respectively, according to the Langmuir model (Table 2).

Al-Homaidan et al. (2018) treated *Cladophora glomerata* with acid for the preparation of the bio-sorbent utilized for the removal of heavy metals [93]. The maximum removal of Cr was 66.6% at pH 2.0 when 1.0 g dried algal cells/100 mL aqueous solution containing an initial concentration of 20 mg/L Cr was employed (Table 2). The wastewater and bio-sorbent were kept in contact for 60 min at 45 °C. Although both Langmuir and Freundlich isotherm models can be used to describe the equilibrium data, the Freundlich model fits well. Losada et al. (2018) investigated the removal of Cr^{6+} from tannery wastewater using *Scenedesmus sp* [90]. The initial concentration of Cr was 352.2 mg/L. The result strongly suggested that the greatest Cr removal occurred with 98.63% (4.82 mg/L) effectiveness, acting as a removal agent at pH of 6.0, constant aeration, temperature of 28 °C, and time lasting 48 h. Gupta et al. (2008) conducted sorption and desorption studies of Cr^{6+}

from wastewater using nonviable cyanobacterium *Nostoc muscorum* biomass [146]. The maximum Cr^{6+} biosorption capacity for *N. muscorum* has been found to be 22.92 mg/g at a dose of 1.0 g/L with initial Cr^{6+} concentration of 100 mg/L and optimum pH of 3.0. It was found that of all the desorbents tested, EDTA and HNO_3 were the most effective, whereas desorption with deionized water was essentially negligible [146].

Plants

Cr biosorption was examined through the usage of various plants, including *Tradescantia pallida* [86] and *Caryota urens* [87]. Sinha et al. (2015) used *Tradescanti pallida* leaf as a bio-sorbent to remove 94% of Cr^{6+} with a sorption capacity of 64.672 mg/g by batch experiments at pH 2 [86]. Pseudo-second-order kinetic model was used to explain the kinetics of Cr^{6+} while the Langmuir model described the isotherm data better than the Freundlich model. In another study, Suganya et al. (2016) used *Caryota urens* seeds as part of an investigation into the effects of various parameters, such as initial concentration, pH, bio-sorbent dosage, and contact time, on the biosorption of Cr^{6+} (Table 2) [87]. The biosorption process can be described using both Langmuir and Freundlich isotherm models, whereas the kinetic data followed the pseudo-second-order kinetic model. According to the Langmuir isotherm model, the best biosorption capacity was 52.63 mg/g at an optimum pH of 2 when the temperature remained at 303 K. Lin et al. (2018) used aminated rice straw-grafted-poly (vinyl alcohol) (A-RS/PVA) for the removal of Cr^{6+} [88]. From batch adsorption experiments, it can be said that the adsorption data can be described well using both Elovich and Freundlich isotherm models. At initial pH 2.0 and 60 °C the adsorption capacity of A-RS/PVA (140.39 mg/g) was much larger than that of original rice straw (34.9 mg/g).

Agricultural Wastes

Agricultural waste is one of the feasible and popular materials for the removal of Cr from wastewater. Ali et al. (2016) used acrylonitrile-grafted banana peels (GBPs) for the removal of Cr^{6+} from wastewater [73]. During the process, grafted banana peels (GBPs) successfully adsorbed 96% of Cr^{6+}, when the optimum conditions were pH 3, adsorbent dose 4 g/L, concentration 400 mg/L, and contact time of 120 min (Table 2). Both Freundlich and Langmuir isotherm models were used to describe the adsorption data followed by the pseudo-second-order kinetic model, and it proved to be an exothermic spontaneous process. In their work, Yari et al. (2016) removed hexavalent Cr using rice husk [74]. With biomass dose of 5 g/L, the maximum adsorption capacity was 38.4 mg/g at optimum conditions of pH 5.0 and contact time of 75 min at 30 °C (Table 2). The best correlation was provided by the second-order kinetic model, as was demonstrated by the Langmuir isotherm model. A similar study by Pourfadakari et al. (2017) examined the removal of Cr^{6+} from aqueous solution using nanosized cellulose fibers obtained from rice husk [77] (Table 2). The experiment showed that the adsorption efficiency reached 92.99% at pH = 6, contact time = 100 min, adsorbent dose = 1.5 g/L, and 30 mg/L initial Cr concentration. Additionally, the Langmuir isotherm with (R^2 = 0.998 at 303 °K) and pseudo-first-order kinetic model (R^2 = 0.993) were the best models for describing the Cr^{6+} adsorption reactions. In another study, Altun et al. (2016) investigated the biosorption process of Cr^{6+} using rye husk (RH) under various conditions [75]. About 68% of 5.0 mM Cr was removed within 140 min when 0.5 g RH was taken at pH 3 (Table 2). Application of the Langmuir isotherm model yielded maximum biosorption capacity of 0.43 mmol/g at pH 3, where the first-order reversible and pseudo-second-order kinetics models were used to evaluate the data.

Ahmed et al. (2019) used sodium chlorite-modified coir coconut (SCM-CC) for the removal of Cr^{6+} [79]. A total of 99.92% of Cr removal was removed at pH 2 (Table 2). Freundlich isotherm had a better fit than the Langmuir isotherm and the kinetic data were described using Ho's pseudo-second-order kinetics. Begum et al. (2020) utilized chitosan-coated banana and areca fiber for the removal of Cr^{6+} from wastewater [76]

(Table 2). The maximum removal obtained after 150 min at pH 4.5 was 75%. A report on the modification of sawdust for the removal of Cr^{6+} from wastewater was given by Chakraborty et al. (2021) [78]. The maximum removal of Cr^{6+} was found to be 100% at pH 2.0, initial Cr^{6+} concentration of 10 mg/L, and adsorbent dose of 4 g/L. Equilibrium isotherms for the removal of Cr^{6+} were analyzed by the Langmuir, Freundlich, and Temkin isotherm models, and the experimental data were well explained by the Freundlich variant. The maximum adsorption capacity was 8.84 mg/g and the obtained data fitted best to the pseudo-second-order kinetic model.

Shakya and Agarwal (2019) prepared biochar using waste pineapple peel biomass with slow pyrolysis at 350, 450, 550, and 650 °C to explore the effect of temperature treatment on characteristic properties of biochar [147]. Biochar prepared at 350 °C was found to have the highest adsorption capacity of 41.67 mg/g. Complete Cr^{6+} removal was achieved at 10 mg/L Cr^{6+} concentration with all biochars. In a recent study, Saravanan et al. (2021) utilized raw and pyrolysis-assisted dragon fruit peel along with fungal biomass (*Fusarium subglutinans*), a mixed adsorbent, for removing Cr^{6+} from polluted water [148]. Batch adsorption tests reveal that optimum conditions for the effective removal of Cr^{6+} ions onto mixed biomasses (pH = 4.0; biomass dosage = 6.0 g/L for *Fusarium subglutinans*—RDFP, 3.5 g/L for *Fusarium subglutinans*—PADFP; temperature = 30 °C; Cr^{6+} ion concentration = 25 mg/L; equilibrium time = 60 min). The adsorption equilibrium data and contact time data were best fitted to the Langmuir and pseudo-first-order models, respectively. Tytłak et al. (2015) investigated the removal of hexavalent chromium using two potential biochars produced by the thermal decomposition of wheat straw (BCS) and wicker (BCW) [149]. The optimal adsorption capacities were obtained at pH 2 and were 24.6 and 23.6 mg/g for BCS and BCW, respectively. The desorption studies of Cr^{6+} ions in relation to HCl and HNO_3 concentrations were performed to check the reversibility of biochar. The least amount of desorption was seen for BCW (51%) and the most for BCS (79%), when nitric acid was used as a desorptive agent. For hydrochloric acid, a distinct impact was seen, with BCS desorption being the lowest (39%) and BCW desorption being the highest (47%). This work demonstrated that Cr^{6+} ions do not completely desorb from the surface of biochar, even when concentrated hydrochloric or nitric acid was applied [149].

A comparison between three kinds of adsorbents was performed by Imran et al. (2020) [150]. These authors used novel biochar derived from *Chenopodium quinoa* crop residues (QBC), QBC activated with magnetite nanoparticles (QBC/MNPs), and strong acid HNO_3 (QBC/Acid) to evaluate their batch and column scale potential to remove Cr (VI) from polluted water. The impact of different process parameters including dose of the adsorbent (1–4 g/L), contact time (0–180 min), initial concentration of Cr (25–200 mg/L) as well as solution pH (2–8) was evaluated on the Cr^{6+} removal from contaminated water. Results revealed that QBC/MNPs proved more effective (73.35–93.62%) for Cr^{6+} removal with 77.35 mg/g adsorption capacity as compared with QBC/Acid (55.85–79.8%) and QBC (48.85–75.28%) when Cr concentration changed from 200 to 25 mg/L.

Composites

Composites are used to remove Cr due to easy handling, low cost, high efficiency, improved process ability, surface area, stability, and tunable properties. Different kinds of composites are used for this purpose. Zhou et al. (2016) fabricated a hydrophobic magnetic adsorbent based on polypyrrole coating on acid-dissolved fly ash (MSFA/PPy, which can float on the water body's surface and easily collected by a magnetic field after adsorption [151]. The biosorption process best fitted the Langmuir isotherm model followed by the pseudo-second-order kinetic model, reaching the highest adsorption of Cr^{6+} which was 66.93−119.33 mg/g at experimental conditions. Islam et al. (2017) prepared bio-composite from cellulose and Bijoypur clay (Kaolinite) exhibited enhanced properties compared to their original counterparts [125]. The best result was found for the composite containing 20% clay and 80% crystalline cellulose at pH 4 and 27 °C which was 2.37 mg/g. Hokkanen et al. (2016) synthesized hydroxyapatite micro-fibrillated cellulose (CHA/MFC)

composite for removing Cr^{6+} from wastewater through the batch process, where the maximum adsorption capacity obtained was 2.208 mmol/g at 25 °C [126]. Similarly, Islam et al. (2021) were able to remove 100% of Cr from industrial wastewater using Banana rachis CNC/clay composite in both cases for 40–60% and 30–70% CNC-clay ratio [127]. Rahaman et al. (2021) implemented a biodegradable composite of modified cellulose and chitosan applied to Cr and removed 56% efficiently at pH 4 when the metal concentration and adsorbent dosage were, respectively, 60 mg/L and 1.0 g/L [128] (Table 3).

Table 3. Cr removal capacities of available adsorbents in the literature. (The superscripts a and b represent the results in percentages (%) and mg/L).

Adsorbents	pH	Removing Capacities (mg/g)	References
Iron (nanoparticles)	7	-	[152]
Maghemite (10 nm)	2.5	-	[153]
Akaganeite (3−6 nm)	5.5	80	[154]
$MnFe_2O_4$ (10 nm)	2	31.5	[155]
Carbon nanotube-supported ceria (6 nm)	3.0–7.4	30.2	[153]
δ-FeOOH coated maghemite γ-Fe_2O_3 (15 nm)	2.5	25.8	[156]
Activated charcoal cloth	1	5 mmol/g	[157]
Coconut shell	2–6	75.0–107.1	[158]
Wood	2–6	71.6–87.6	[158]
Dust coal	2–6	60.5–101.9	[158]
Sawdust and waste tires (0.38 mm)	2	30–43	[159]
Cactus	2	8.5–34.5	[66]
Wool	2	8.5–34.5	[66]
Charcoal	2	8.5–34.5	[66]
Pine needles	2	8.5–34.5	[66]
Hazelnut Shell	2.5–3.5	17.7	[160]
Single-walled Carbon Nanotubes (SWCNT)	2.5	2.35	[161]
Multi-walled Carbon Nanotubes (MWCNT)	2.5	1.26	[161]
Unfunctionalized MWCNT	6	98 [a]	[162]
Oxidized MWCNT	2.05	4.26	[163]
MWCNTs/nano iron oxide	5–6	-	[164]
Modified MWCNT	7		[165]
Activated carbon-coated CNT	4	9.0	[166]
Waste eggshell	6–12	90 [a]	[167]
Chitosan-coated acid-treated seed shells	4.5–5.0	60–85	[168]
Green algae (*Ulva lactuca*)	1	10.61	[169]
Activated carbon from green algae (*Ulva lactuca*)	1	112.36	[169]
Biofilm of *E. coli* supported on NaY zeolite	4.6–5.1	>85.5 [a]	[170]
Pseudomonas aeruuginosa immobilized MWCNT	8.5–9.5	6.23	[171]
Saccharomyces carlsbergensis immobilized on amberlite	8	95 [a]	[172]
Wallnut shell	3.5	8.01	[84]
Hazelnut shell	3.5	8.28	[84]
Almond shell	3.2	3.40	[84]
Ficus carica biosorbent	1.0–3.0	19.68	[173]
Straw from *Triticum aestivum*	5	21	[174]
Wheat Bran from *Triticum aestivum*	>4	35	[64]
Wheat Bran from *Triticum aestivum*	1	40.8	[175]
Wheat Bran from *Triticum aestivum*	2	310.58	[176]
Wheat Bran from *Triticum aestivum*	2	0.942	[177]
Wheat Bran from *Triticum aestivum*	5	93	[178]

Table 3. *Cont.*

Adsorbents	pH	Removing Capacities (mg/g)	References
Coconut coir	1–5	26.6–27	[71]
Sawdust	3	1.48	[179]
Rice husks	3	0.63	[179]
Coirpith	3	0.16	[179]
Vermiculite	3	0.26	[179]
Spirogyra condensata	5	14	[96]
Rhizoclonium hieroglyphicum	4	11.81	[96]
Chlorella vulgaris	1–5	2.98	[180]
Clodophara crispata	1–2	6.20	[180]
Zoogloea ramigera	1–2	3.40	[180]
Rhizopus arrhizus	1–2	8.40	[180]
Saccharomyces cerevisiae	1–2	4.30	[180]
Chitosan-ceramic alumina composite	4	153.85	[181]
Surfactant-modified coconut coir pith	2	76.3	[182]
Cross-linked xanthated chitosan beds (CMBC)	3	256.4	[183]
Cross-linked xanthated chitosan flakes (CMCF)	3	625	[183]
Eggshells	3.54	81.47 [a]	[184]
Carrot residue	4	45.09	[185]
Fungal biomass	2	119.2	[186]
Chitosan-coated fly ash	5	33.27	[187]
Grape waste	4	1.91 mol/kg	[188]
Dundiella algae	2	45.5	[189]
Pine Needles powder	3	40	[190]
Laminaria japonica	1	96.31	[175]
P. yezoensis Ueda	1	95.81	[175]
Rice bran	1	95.35	[175]
PAN-CNTs-TiO_2-NH_2 composite	2	80 [a]	[191]
Hydrophobic magnetic adsorbent based on polypyrrole coating on acid-dissolved fly ash (MSFA/PPy)	-	66.93−119.33	[151]
MWCNTs-COOH	2	143–164	[192]
LDHs@MoS_2	5	76.3	[193]
Shrimp shell and waste cotton rags	5	93 [a]	[138]
PANI-NC	6	92.59	[194]
FeNi@HPC	4	30 [b]	[132]
Cellulose and chitosan composite	4	60 [b]	[128]
Red mud and rice straw	6	97.74 [a]	[195]
Carbonized chitosan into triethylenetetramine-modified sodium alginate (CTS/CS-50)	1	144.49	[196]
nZVI/ZIF-8	5	>99 [a]	[197]

Mohamed et al. (2017) used the electrospinning method to fabricate polyacrylonitrile (PAN) and carbon nanotube (CNTs)/titanium dioxide nanoparticles (TiO_2) containing amine groups (TiO_2-NH_2) composite nanofibers for the removal of Cr^{6+} from wastewater [191]. The maximum adsorption capacity of PAN-CNT/TiO_2-NH_2 for Cr^{6+} was 714.27 mg/g at 293 K at pH 2, and instead of the pseudo-second-order model the process can be better described using the nonlinear pseudo-first-order model. After 5 usage cycles, up to 80% adsorption capacity can be achieved. For the removal of Cr^{6+} anionic species, Huang et al. (2018) used a simple polymer cross-linking method for adsorption in aqueous solutions. Carboxylated multi-walled carbon nanotubes were modified with chitosan to increase adsorption of Cr^{6+} in acidic aqueous solutions (pH = 2), where the maximum adsorption capacities were 143–164 mg/g within only 30 min [192] (Table 3).

On the other hand, Wang et al. (2017) went through a simple hydrothermal method for the preparation of molybdenum disulfide coated Mg/Al layered double hydroxide composites (LDHs@MoS_2) for adsorption [193]. At pH 5.0, 76.3 mg/g Cr^{6+} was removed relying on ionic strength and pH. Choudhury et al. (2018) fabricated a clay-alumina ceramic composite membrane comprising hydroxyethyl cellulose and CuO nanoparticles for removing Cr^{6+} from contaminated water [129]. Here the maximum percentage of adsorption for Cr^{6+}, obtained at 2 bar trans-membrane pressure, was 91.44%. In a more recent report, Dokmaji et al. (2020) modified multiwall carbon nanotubes (MWCNTs) chemically for the removal of both Cr^{3+} and Cr^{6+} from wastewater [130]. Cationic surfactant cetyl trimethyl ammonium bromide (CTAB) was used to modify which resulted in a product named MWCNTs-CTAB. At optimum conditions, it can remove almost 98% of Cr. On the other hand, when MWCNTs are modified using an anionic surfactant, such as sodium lauryl sulfate (SLS) after magnetization with magnetite (M), produces MWCNTs-M-SLS, which can remove 99% of Cr. The isotherm of both components fitted the Langmuir model properly where the adsorption capacities for Cr^{3+} and Cr^{6+} were 66.2 and 27.8 mg/g, respectively. The optimum parameters were: pH = 5, contact time = 60 min (for Cr^{3+}) and 30 min (for Cr^{6+}), initial concentration = 150 mg/L (for Cr^{3+}), and 300 ppm (for Cr^{6+}).

Kumar et al. (2020) introduced polyaniline-impregnated nanocellulose (PANINC) composites for the removal of Cr^{6+} from wastewater [194]. Their experiment showed that this composite can remove 92.59 mg/g (96.5%) of Cr^{6+} (Table 3). The optimum contact time and pH were 60 min and 6, respectively, where the initial concentration was observed to be 100 mg/L for the maximum removal of Cr^{6+}. The isotherm model fitted the Langmuir model better than the Freundlich model. Wang et al. (2022) used integrated micro-electrolysis composites (IMC) through a facile one-pot method with red mud and rice straw [195]. The maximum adsorption efficiency reached was 97.74% at pH 6. Wu et al. (2022) prepared a polysaccharide-derived composite by embedding carbonized chitosan into triethylenetetramine-modified sodium alginate (CTS/CS-50) [196]. The synthesized composite has exhibited a maximum adsorption capacity of 144.49 mg/g for Cr^{6+} at pH 1.

Stoica-Guzun et al. (2016) used three factorial Box–Behnken Design (BBD) to determine the capacity of bacterial cellulose composites (BC-Fe_3O_4) for the adsorption of Cr^{6+} under various conditions [198]. Cr^{6+} can be removed efficiently when the initial pH is 4 with a minimum release of iron. Subedi et al. (2019) used magnetic chitosan (Chi@Fe_3O_4) and graphene oxide-modified magnetic chitosan (Chi@Fe_3O_4GO) nanocomposite for the removal of Cr^{6+} from water [131]. The maximum adsorption capacities were 142.32 and 100.51 mg/g for Chi@Fe_3O_4 and Chi@Fe_3O_4GO, respectively. In one study, straw-derived hierarchically porous carbon-supported FeNi bimetallic nanoparticles (FeNi@HPC) were prepared for effective removal of Cr^{6+} from water [132]. Higher temperatures favored the removal of Cr^{6+} and FeNi@HPC manifested the lowest activation energy when compared to Fe@HPC and FeNi NPs. The best conditions for the activity of FeNi@HPC were assessed, and the highest removal efficiency equivalent to 30 mg/L of Cr^{6+} was achieved at pH= 4.0 in 360 min with a dosage of 0.5 g/L.

Metal–Organic Framework

Metal–Organic framework (MOF), a porous material, has attracted the attention of researchers because of its tunable structures, porosity, flexibility, and functionality that provide the chances to utilize these materials for multiple functionalities such as catalysis, adsorption, etc. [199]. Generally, two kinds of primary building units are contained by these MOFs, one is the organic linker and the other one is metal core. The organic portion acts as a linker such as terephthalic acid, trimesic acid, fumaric acid, etc. On the other hand, transition metals (Fe, Zn, Cu), p-block elements (In, Ga), lanthanide, and actinide series (La, U, Th) are used for the building of the metal core [200]. A number of researchers have mentioned the utilization of MOFs for the successful removal of different heavy metals from wastewater including Cr. nFe_3O_4@MIL-88A(Fe)/APTMS nanocomposite was synthesized using microwave for the removal of Cr^{6+}. This MOF was able to remove

7.99 mg/g Cr^{6+} from wastewater when pH was <4 at contact time of 30 min [201]. A water-stable MOF named BUC-17 was synthesized using solvothermal process and was able to adsorb 68.2 mg/g of Cr^{6+} when the adsorbent dosage was 150 mg/L maintained at pH 4 after 500 min [202]. Another study was reported by Han et al. [203] where they synthesized La-Zr bimetallic MOFs containing the molar ratio at 1:1 ($1LaUN_{12}$) for the efficient removal of Cr^{6+} from wastewater. Maximum adsorption of Cr^{6+} was 222.5 mg/g at pH 2. Moreover, above 40% of Cr^{6+} was also reduced to less toxic Cr^{3+} by amino groups and immobilized over the surface of $1LaUN_{12}$ [203]. Although MOFs have promising properties and are good at removing Cr, they have poor chemical stability. In order to implement MOFs into industrial wastewater applications, further research is required to optimize their structures and scale them up. Further, different functionalization methods must be proposed and applied to enhance MOF stability and sorption kinetics.

Mesoporous Silica

Because of its exceptional surface features, which include thermal/chemical stability, high specific area, low casting, low density, and a range of pore volume and distribution, porous silica has been used for a long time as inorganic catalysts and supporting materials [204]. Porous silica's morphology, pore size distribution, and structural characteristics can be easily modified as compared to those of other porous materials, such as carbonaceous and zeolite, to allow for greater flexibility in meeting the demands of various applications [205]. On the other hand, the pore size of porous silica has demonstrated the impact of pore structure on products and is connected to selectivity and catalytic activity. Because of its spongy architecture and high thermal/chemical stability, researchers have spent the last two decades concentrating on the meso-class of porous silica with nanoparticle size [205–207]. The flexibility and great selectivity of the internal and exterior surface of mesoporous silicates, which are their best qualities, can generally be altered with a variety of inorganic/organic functional groups [208–210]. Tetraethyl orthosilicate (TEOS), an alkoxysilane precursor, is typically hydrolyzed to create mesoporous silicas, which then condense and polymerize in the presence of a suitable catalyst and template to produce a network of siloxanes (-Si-O-Si- links) (surfactant) [210]. Mesoporous silicas are widely employed with surface modification for the adsorption of heavy metals because they have outstanding characteristics [211].

By grafting N-(3-trimethoxysilylpropyl) diethylenetriamine (DAEAPTS) onto SBA-15, Kim et al. (2018) produced two forms (powdered and granular) of mesoporous silica for the removal of Cr^{6+} [212]. Batch experiments revealed that the Cr^{6+} sorption was favorable at acidic pH conditions with the greatest sorption at pH 3 reaching the equilibrium within 10 min and the maximum sorption obtained was 330.88 mg/g [212]. The chromisorption of chromium also followed a pseudo second-order kinetics in mesoporous silica magnetic nanoparticles modified with 3-aminopropyl-triethoxyxilane. The Langmuir adsorption isotherm was able to fit the adsorption data with high accuracy, and the highest adsorption capacity was 185.2 mg/g [213]. For the purpose of chromium adsorption, mesoporous silica surfaces functionalized with monoamino [3-aminopropyl trimethoxysilane] (APTMS) and triamino [N-(3-trimethoxysilyl propyl) diethylenetriamine] (DETA) were employed. It was discovered that APTMS-MCM-41 displayed greater adsorption capacity than DETA-MCM-41. The maximum adsorption reported was 111.1 mg/g at pH 3 [214]. Hexavalent chromium is completely removed by a composite of microporous silica and hierarchical hollow multi-shells. The material demonstrated an adsorption capacity of 257.57 mg/g at 20 °C at an optimal pH of 4 with a loading of 5 mg because of its large surface area and extremely small 1.22 nm pore size [215,216].

Zeolites

Zeolites are aluminosilicate minerals with micropores that have various cavity structures made of a three-dimensional framework and a negatively charged lattice. Na^+, K^+, Ca^{2+}, Mg^{2+}, and other cations that can readily exchange with other cations in the solu-

tions balance the negative charge. Zeolites are appealing adsorbents for the removal of heavy metal ions from aqueous systems due to their high specific surface areas, strong ion-exchange capacity, and comparatively inexpensive cost [217]. The use of synthetic zeolites for heavy metal sequestration in wastewater treatment has been found to have the greatest applicability, followed by modified zeolites. Due to the fact that natural zeolites' mineralogical composition varies widely between regions and even within a single mineral deposit, natural variants, despite being extremely desirable from an economic standpoint, show the lowest metal sorption for the majority of heavy metals [218]. In addition, numerous additional minerals that behave as pollutants due to their low metal sorption capacity are frequently found in the ore along with other varieties of zeolite. Quartz, albite, biotite, illite, montmorillonite, feldspar, calcite, halite, and heulandite are among the contaminating minerals that are frequently found [219,220]. Adsorbents with remarkable uniformity in their characteristics, such as pore size distribution, hydrophobicity/hydrophilicity, and the presence of a single compensatory cation, are synthetic zeolites, which are typically composed of a single phase. These factors taken together ensure that they have a higher cation exchange capacity than natural zeolites [221].

The removal of Cr^{6+} was possible after modification of clinoptilolite using hexadecyl pyridinium bromide which was not achievable in case of natural or synthetic zeolites [222]. Neolaka et al. (2022) utilized activated natural zeolite-magnetic composite (ANZ–Fe_3O_4) adsorbent material for the removal of Cr^{6+} from synthetic wastewater [223]. The outcome showed that the best adsorption took place at a pH of 2, with an adsorbent mass of 0.20 g, for 50 min at a temperature of 298 K [223]. For the purpose of removing Cr^{6+} from wastewater, synthetic zeolite spheres filled with nanoscale Fe-Al bimetallic oxide were produced. With an initial Cr^{6+} concentration of 20 mg/L (pH = 3), the results showed that nano Fe-Al bimetallic oxide was an efficient material for removing Cr^{6+}, with a maximum removal efficiency of 84.9% [224]. Clinoptilolite, a natural zeolite, was used to create hollow fiber ceramic membranes (HFCM) to study the adsorptive removal of hexavalent chromium, Cr^{6+}, from an aqueous solution. At a pH of 4 and a Cr^{6+} concentration of 40 mg/L, the HFCM performed in adsorption/filtration with a 44% removal of Cr^{6+} efficiency [57].

Due to simple operation, broad applicability, high removal rate, and affordable reusability, adsorption has become the most promising and widely investigated technology for removing chromium from wastewater. However, the present methods of surface modification require intense heat and pressure, powerful acids and bases, or vigorous oxidation and reduction reactions. The carbon-based adsorbents are expensive due to this labor-intensive preparation process, which limits their widespread use in industrial applications. On the other hand, chitosan-based adsorbents exhibit limited reusability without adjustments. Strong bonds (between the metal ions and the adsorbent surface) may be responsible for this behavior, as well as low thermal/chemical stability, low mechanical strength, incomplete desorption, a decline in the efficiency of the adsorbate–adsorbent interaction, and a lack of adsorption sites. The dosage of biosorbent has a significant impact on the removal effectiveness because it provides more active biosorption sites. At higher temperatures, bond rupturing, Gibb's free energy reduction, and decreased solution viscosity may all contribute to an increase in the biosorbent capacity. These factors boost the biosorbent active sites and raise the collision frequency (mobility and kinetic energy) between them and metal ions, which results in a higher affinity [225]. At higher temperatures, the bonding force between the biosorbent and the contaminants might weaken, which would result in less biosorbent being absorbed. It was revealed that as the mixed agitation rate increases, the elimination efficiency rises [226]. In case of MOF though it has good capability to remove Cr efficiently, sometimes it contains micropores that are inaccessible for the target material and most of them are highly unstable in water. MOFs have been fabricated using Mn, Fe, and Cu, although the majority of them have poor chemical stability. In order to scale up these materials and fine-tune the MOFs' structure for use in industrial wastewater applications, more study is still required. Moreover, various functionalization techniques should be suggested and used to improve the sorption kinetics and stability of

MOFs. So, it is still a challenge for researchers to develop an adsorbent with the qualities such as low-cost materials, high uptake, and efficient regeneration processes.

2.2. Electrochemical Treatment

Electrochemical treatments of wastewater have not received much consideration in view of the need for enormous capital cost and power supply, which is also expensive [173,227]. However, in accordance with stringent ecological guidelines for wastewater exposure, electrochemical technologies have become very significant worldwide in the last two decades [228]. Electrochemical Cr^{6+} decrease strategies can be utilized, contingent upon the pH of the fluid arrangement, the power of the current density, and the electrode material utilized [229]. In an electrochemical system, oxidation reaction occurred in the anode (positive side) and the reduction process occurs at cathode (negative side), where the electrons transfer. These two chemical reactions are called redox (reduction–oxidation), leading to Cr removal from wastewater. Selection of the anode and cathode mainly decides the type of the electrochemical method and influences the removal efficiency towards specific metal ions [230].

A number of simultaneous procedures could occur on the outer layer of the electrode or in the given solution [231]. In this review, some significant electrochemical treatment technologies for the removal of Cr including electrocoagulation (EC), electro flotation (EF), electrochemical reduction (ER), and electrically driven ion transport are described.

2.2.1. Electrocoagulation

Electrocoagulation (EC) is a straightforward and gainful innovation utilized in wastewater treatment industries [232]. However, it was never deemed to be a dependable technique because of its poor efficient reactor structure and issues of electrode dependability [227]. As of late, EC is known as a little-scale wastewater treatment strategy with improved specialized techniques. Removal of Cr by EC is tabulated in Table 4.

Table 4. Removal of Cr by electrocoagulation (EC).

Types of Electrode	pH	Removal (%)	Current Density	References
Fe-S 304	6.9	97	50 A m^{-2}	[233]
Al-S 304	5	15	50 A m^{-2}	[233]
Fe-Al	3	100	10 mA cm^{-2}	[234]
Fe-Fe	9.56	100	4 mA cm^{-2}	[235]
Mild S	5.91	99	1000 mA	[236]
Al-Fe	4	99	-	[237]
Al alloy-galvanized Fe	7	98.2	0.2 A dm^{-2}	[238]
Fe-Fe, Al-Al, Al, Pt, Ti, Pt/Ti/Fe,		<0.5 mg/L	1 Am^{-2}	[239]
Fe-Al	7–9	>90	2 mA cm^{-2}	[240]
Fe-Fe	4	100	50 mA cm^{-2}	[241]
Fe-Al	2	100	0.73 mA cm^{-2}	[242]
Al-Al/Cu/Mg alloy	5.3	99	400 Am^{-2}	[243]
Al-Al	3.5–4.0	90–99.8	11.57 Am^{-2}	[244]

Iron Electrodes

A number of parameters, for example, pH, applied electrical current, and application time can affect the efficiency of Cr^{6+} removal using iron electrodes and a high efficiency (>90%) can be obtained at optimum conditions. There are two stages involved in the electrocoagulation system. Firstly, Cr^{6+} reduces to Cr^{3+} either directly at the cathode or by Fe^{2+} ions obtained from the oxidation of iron anode, and secondly, co-precipitation of the Fe^{3+}/Cr^{3+} hydroxides is formed subsequently. The reduction of Cr^{6+} to Cr^{3+} by Fe^{2+} ions is favored at low pH, while conversely, the precipitation of Fe^{3+}/Cr^{3+} hydroxides occurred at high pH (>3) because metal hydroxide species (both chromic and iron hydroxides) are

soluble at low pH [245]. Kim et al. (2020) examined the removal of Cr from wastewater using iron electrode. They found that the optimum pH of this process was 7–9 while the mass of sludge formed and the amount of energy consumed were 0.68–2.5 kg/m^3 and 0.37–2.78 kW h/m^3, respectively [246]. The process fitted both the first-order and second-order kinetic models. Lu et al. (2016) successfully removed Cr^{6+} from aqueous solution using iron electrode via the EC process. The optimum conditions were: pH = 2; current density = 0.73 mA/cm^2; electrolysis time = 50 min [242]. Verma et al. (2013) were able to remove 100% Cr for both Cr^{3+} and Cr^{6+} and hexavalent Cr, for an electrolysis time lasting 45 min at 4 pH with current density of 50 mA cm^{-2} [241].

Aluminum Electrodes

Al $(OH)_3$ acts both like an adsorbent and trap to separate heavy metals [247]. An investigation directed by Mansoorian et al. (2014) demonstrated that larger amounts of metal ions can be removed by the electrocoagulation process using adsorbents such as hydroxide iron and steel flocs [240]. Mahmad et al. (2016) utilized aluminum electrodes for the removal of total Cr and 72.65% of total Cr was removed at pH 3 and the voltage was 2.5 V [248]. Elabbas et al. (2016) removed 99% Cr using Al electrode when the current density was 400 A/m^2 [243]. The pH was 5.3 and it took 360 min for the process to be completed. Recently, Lu et al. (2022) investigated the EC technique with Fe and Al anode for the elimination of Cr^{6+} from wastewater at initial pH of 3.5–4.0 [244]. The study showed that the EC with Al-Al-Al-Al combination (anode–cathode-anode–cathode) exhibited the highest removal efficiency among different electrode combination modes, whereas the EC with Fe-Fe-Fe-Fe combination exhibited the poorest removal efficiency. At the initial pH of 3–6, Al EC displayed desirable removal efficiency for Cr^{6+} (84.2–96.4%), and total Cr (83.1–94.9%). At the conductivity of 899–2300 μS/cm, excellent pollutant removal efficiency was maintained (90.2–99.8%).

2.2.2. Electro-Floatation

Today, heavy metal contaminants can be removed using the electro-flotation (EF) process [249–251]. since different strategies for treating wastewater for the most part do not work productively for extremely weakened arrangements (fixations underneath 50 m/gm^3) [252]. EF became highly regarded in light of its flexibility, straightforwardness in plan and activity, ecological sensitivity, low operational expenses, and little and reduced units [253]. To overcome the impediments of the procedures referred to previously, a few examinations consolidated EC and EF, and it prompted higher expulsion effectiveness in contrast to utilizing only one. This joint strategy is an increasingly advocated and successful approach to expel toxins [254]. The blending of EC and EF is called electrocoagulation-floatation (ECF) and the strategy leads to better expulsion rates. Various analyses were undertaken to explore the impacts of the working conditions on the expulsion of substantial metals. However, the completion of this process for the removal of Cr is rare. Zouboulis et al. (2003) removed Cr using a process where 95% of Cr was removed successfully [255].

2.2.3. Electrochemical Reduction

As the sacrificial anodes are consumed during the electrocoagulation process, they should be replaced occasionally. There are alternative options for the electrochemical removal of Cr^{6+} using non-sacrificial cathodes, which are: (i) Cr^{6+} is directly or indirectly reduced to Cr^{3+}, and (ii) using the adsorption or precipitation process [256]. The electrode materials and reactor arrangement study the removal of Cr^{6+} to a greater extent. It is noted that lead dioxide (PbO_2) coatings and noble metal oxides (dimensionally stable anodes, DSA) coatings on titanium (Ti) are generally used as the non-sacrificial anode electrode for commercial purposes due to the oxidative and destructive properties of Cr^{6+} [257]. The productivity and procedure cost execution at regular cathode materials, for example, Fe and Cu, is not that fulfilled [258]. Subsequently, significant endeavors have been conducted

to generate better cathode materials and increasingly proficient expulsion procedures for electrochemical Cr^{6+} reduction.

Carbon-Based Electrode

Wang and Na (2014) detailed the Cr^{6+} evacuation utilizing carbon nanotube (CNT), and it exhibited legitimately developed on stainless steel mesh (SSM) [259]. At first, the reduction of Cr^{6+} was completed by utilizing negatively polarized electrode surface area and then the same electrode attracted the adsorbed Cr^{3+} cations, namely Cr^{3+} and $Cr(OH)^{2+}$ by an electrostatic force. In this way, the anode can be recovered by turning around the polarization to discharge Cr^{3+}. The electrochemical Cr^{6+} reduction performance is determined by various parameters in the corresponding regions [260].

Gold Electrodes

A number of experiments have been conducted by Jin and Yan (2015) for the electrochemical reduction of Cr^{6+}-consuming gold-based electrodes. These authors confirmed that it, however, shows greater activity in alkaline solution [261]. As a result, for the electrochemical reduction of trace amount of Cr^{6+}, Jin et al. (2014) used gold nanoparticle-enriched TiO_2 nanotube clusters [262]. The electrodes were arranged with metal–semiconductor heterojunction infrastructure and large outer area in an exceptional way, which boosted its activity 23 times greater than that of polycrystalline gold electrodes. It resulted in a potential lignin-treated adsorption–discharge method, which enhanced the electrochemical evacuation of Cr^{6+}. Two levels of pH were used: 2 and 11. The former pH was maintained for the adsorption and initial concentration of Cr^{6+}, while the latter was used for the discharge and electrochemical decrease. Insoluble $Cr(OH)_3$ can be obtained from discharged Cr^6 which was then effectively isolated.

Conducting Polymers

To commercially reduce Cr^{6+} efficiently from wastewater, an unconstrained electron donor, conducting polymer, was successfully tested in 1993 [263]. In order to provide a bulk surface area, conducting polymer films are accumulated on substrates followed by submerging in Cr^{6+} solution. The application of polypyrrole (PPy) films onto an aluminum substrate, the electro-polymerization adherent, for the reduction of Cr^{6+} was narrated by Conroy and Breslin (2004) [264]. If the subsequent electrodes are reduced to a negative potential without Cr^{6+}, the consumed catalyst can be regained. The polypyrrole (PPy)-modified electrode is much more effective for the same purpose because it is more effective than stainless steel (SS) [265]. Under stirring conditions, 92% of Cr^{6+} was removed (PPy electrode), 18% (SS electrode) in the potentiostatic (PS) process, 100% (ppy electrode), and 36% (SS electrode) in the potentiodynamic (PD) process, respectively. The PPy stability under PD was not as effective as PS conditions. Because of quick reaction and greater stability, polyaniline (PANI) is considered to be a reasonable material according to Ruotola et al. (2003) [266]. Almost 100% Cr^{6+} can be reduced PANI film and no significant degradation occurs in polyaniline due to the cathodic protection technique. The reaction rates of Cr^{6+} reduction observed at reticulated vitreous carbon (RVC) and PANI electrode were much higher than that of the uncovered RVC electrodes when they were compared [267,268]. Graphene–polyaniline (GR-PANI) electrodes were blended through a combination of electrochemical polymerization and chemical system by Gao et al. (2011) [269]. The GR-PANI showed enormous sensitivity and an outstanding electrocatalytic action in reducing Cr^{6+} due to its bulk surface area and unfastened structure.

2.2.4. Electrically-Driven Ion Transport

To reduce energy consumption and waste production, the membrane technology integrated and optimized with the electrochemical strategy has been developed to treat Cr^{6+} from wastewater. Without affecting the physical condition or consuming chemical substances, synchronous concentration and separation are achieved and the elementary is the

recommended position of a membrane procedure. This process is specifically implemented for the removal of Cr^{6+} electrochemically [270].

Electrodialysis and Electro-Electrodialysis

Electrodialysis is used in wastewater treatment, desalination, and electrolyte detachment. When an electrodialysis system is used for the treatment of wastewater, an anionic layer hinders the movement of the other metallic ion pollutants while allowing Cr^{6+} to move towards the anode through an anionic layer [271]. Due to the increasing ion transport at lower pH, efficient removal of Cr^{6+} at a lower concentration is possible [272]. Chen et al. (2009) utilized monovalent-specific electrodialysis layer in order to build up an electrodialysis system to remove Cr^{6+} when the electroplating wastewater was at low pH [273]. When the current density and stream rate were high along with greater membrane area, chromate recovery was enhanced.

Electro-Deionization

Ion exchange resin, a solid conductive ion medium has been introduced into the dilute compartment to overcome drawbacks. That is how a highly efficient ion separation and energetically proficient technology has been developed by joining two different methods, ED and ion exchange process. The synergistic arrangement of these two technologies is called electro-deionization (EDI) or continuous electro-deionization (CEDI). In this method, ion exchange resins are used as a conductor between the ion exchange films. Moreover, by splitting water into H^+ and OH^- ion exchange resins can be recovered to their proton and hydroxide forms. A strong potential large-scale reticular anion exchange resin (Amberlite® IRA900) with a high limit with respect to Cr^{6+} transport (116 mg Cr^{6+} per gram of resin) was introduced by Alvarado et al. (2009) [274]. Consuming this anionic resin and Amberlite® 200C, about 98.5% removal of Cr^{6+} became possible under 0.07 kWh/m^3 energy consumption in a continuous electro-deionization process. A fraction of the developed H^+ and OH^- ions recombine before recovering the resins at monopolar film and by using EDI with bipolar layers, additional improvement can be obtained in treatment proficiency [275]. Though ED or EDI-based partitions need more refinement they are currently an efficient technique for clean evacuation of Cr^{6+} [275,276].

Due to electrode passivation and significant electrical energy consumption, the electrochemical process is a highly expensive technological procedure. To improve the effectiveness of the wastewater treatment, more consideration should be given to the reactor design and operating conditions in case of ER. The issue of energy consumption needs to be resolved in order to commercialize this kind of treatment for use in industrial applications. Electrode passivation and relatively high energy consumption are EC limitations, along with the difficulty of large-scale applications at lower energy consumption [277,278]. Several effective methods, including aggressive ion-addition, alternating current operation, polarity reversal operation, ultrasonication, mechanical cleaning of electrodes, chemical cleaning of electrodes, and hydrodynamic scouring, have been suggested to reduce the passivation of the electrode. Each option, however, has disadvantages, including the development of hazardous byproducts, high costs for extra infrastructure and treatment, and increased sludge production [279]. As a result, the EC process is still not entirely applications mature.

2.3. Physico-Chemical Processes

Physico-chemical treatment of wastewater focuses primarily on the separation of colloidal particles. This is achieved by adding chemicals that modify the contaminants' physical state. This process may consecutively be performed in a single unit or in separate units. This process includes the ion exchange method, chemical reduction, photocatalytic reduction, etc.

2.3.1. Ion Exchange Method

Scholars have studied ion exchange methods extensively and they have been viewed as a suitable process for the removal of Cr at low concentrations [43,44,280]. The ion exchange method is a reversible chemical reaction used to replace undesirable metal ions with harmless and environmentally friendly ones. Cr is removed by attaching it to an immobile solid particle as a replacement for the solid particle cation. The material of solid ion-exchange particles could be either natural, e.g., inorganic zeolites, or synthetically produced, e.g., organic resins [230]. Cr^{3+} and Cr^{6+} can effectively be removed using a two-step ion exchanger, i.e., cation and anion resins, respectively. Strong basic anion exchangers containing an exchangeable counter ion of Cl_2 are commonly used for the removal of Cr^{6+} [44]. There are a number of ion exchange resins such as strong anionic resins (e.g., Amberlite IR and IRA-900, DOWEX 1), weak anionic resins (e.g., Amberlite IR 67RF and IRA-94, DOWEX MA43, and MAC3) and cation exchange resins (e.g., Amberlite IR-120, IRN77, and SKN1) [43,44]. Effluent water passes through Amberlite IR-120 and Amberlite IRA-402, which removes Cr^{6+} [37].

Generally, weak base anion exchange resins are used to remove chromates from water under acidic pH values. The resins keep a stoichiometric ratio with sodium hydroxide when regenerated. On the other hand, strong base anion exchange resins can only be used when it is necessary to remove trace amounts of chromate from tap water. Using concentrated NaCl (5–8%) these resins can be regenerated which can subsequently be improved by adding NaOH to the solution to transform the resin from $HCrO_4^-$ to CrO_4^{2-}. However, the need for continuous regeneration and concentrate disposal, dynamic fouling of the resins, and the effect of other ions present in the water are the disadvantages of the discussed method.

Using an ion exchange process, Tiravanti et al. (1997) conducted the pretreatment of tannery wastewater for the removal and recovery of Cr^{3+} [281]. They found that, compared to the traditional treatment, the process requires minimal costs for sludge treatment and disposal since sludge production fell by 80% and showed a significant reduction of chemical compounds. El-Moselhy and Hakami (2015) utilized carminic acid-modified anion exchanger (IRA 900) for the removal of Cr^{6+} [282]. Maximum adsorption occurred when the pH was between 4.0 and 4.5 and the adsorption isotherm fitted the Langmuir model best. The adsorption capacity was 19.27 mg Cr^{6+}/g of the adsorbent. Zang et al. (2018) conducted an experiment for the removal of Cr^{6+} using Poly-epichlorohydrin-dimethylamine (EPIDMA) modified weak base anion exchange resin D301 [283]. The maximum adsorption capacity was 194 mg/g at 25 °C and at pH 2. The kinetic data were best fitted by the pseudo-second-order kinetic model while the batch equilibrium data followed the Langmuir isotherm model well.

2.3.2. Reduction Process

Reduction reactions chemically convert hazardous pollutants into less toxic compounds that are less mobile or inert. In this process, Cr^{6+} adopts an electron and converts it into Cr^{3+}. According to the process of electron generation, the reduction process can be classified into chemical and photocatalytic reduction. These are explained in more detail below.

Chemical Reduction

In the case of chemical reduction process, the electron is generated from a chemical reaction. A reducing compound is used to reduce Cr^{6+} to Cr^{3+}, for example, sulfur compounds, iron salts, etc.

1. Sulfur Compounds

The formation of Cr^{3+} hydroxide precipitation from Cr^{6+} is the widely accepted typical procedure for treating chromate-containing rinse water. Commonly, industries use acidic solutions of sulfur dioxide gas or sodium bisulfite as a reducing agent. In order to neutralize

the acidity, NaOH solution or $Ca(OH)_2$ slurry is used to treat the effluent and precipitate the Cr. It has been advised to use NaOH when the sludge formation needs to be minimized as much as possible [284]. The formation of a large amount of residual sludge, which creates difficulties in managing, transporting, final disposal issues, and associated cost, is one of the major problems of these techniques. When the initial concentration of Cr^{3+} was 100 mg/L, the percentage removed reached 99.37% to 99.6% at pH 7–11 [273].

2. Iron Salts

Iron can reduce Cr^{6+} generally under acidic conditions. Hexavalent Cr is reduced to trivalent state using $FeCl_2$ and $FeSO_4$ at low pH, given that Fe (II) and (III) appears as free ions, for subsequent precipitation [285].

$$6Fe^{2+}\ (aq) + Cr_2O_7{}^{-2}\ (aq) + 14H^+\ (aq) \rightarrow 6Fe^{3+}\ (aq) + 2Cr^{3+}\ (aq) + 7H_2O$$

$$Cr^{3+}\ (aq) + OH^-\ (aq) \rightarrow Cr(OH)_3(s)$$

Fe (II) requires highly acidic conditions to remain in the solution, despite the fact it remains a free ion up to a pH of 4.7. Better reduction rate can be achieved at low pH due to charge distribution and spatial configuration changes. One study shows that the reduction kinetics of Cr^{6+} remain slow at pH 3.7 but stay stable for months and even years. To enhance the reduction reaction the pH must be less than 3 [285].

Using $FeSO_4$ or Na_2SO_3 as a reducing agent, Cr^{6+} is chemically reduced to its trivalent state followed by the formation of precipitation with alkali. This process has some problems. For example, using $FeSO_4$ will produce solid $Fe(OH)_3$ as waste which should be disposed of immediately. On the other hand, toxic SO_2 is produced, causing air pollution when Na_2SO_3 is consumed. Moreover, none of them is suitable for treating dilute Cr^{6+} solution [285].

Photocatalytic Reduction

1. Organic Matter for Cr^{6+} Reduction

Under predominant acidic conditions, some dissolved organic matter (DOM) shows very slow but appreciable Cr^{6+} reduction kinetics. Metal reductants such as zerovalent iron, aqueous Fe (II), Fe (II) hydroxides, adsorbed Fe (II), and Fe (II)-chelates, perform better in comparison with organic reductants [286]. The rate of Cr^{6+} reduction can be enhanced due to the complexation of Fe (II) and DOM when Fe (III) is released as a humic acid solution. It is hypothesized that there is some unknown reductant present in humic acid, which is mainly responsible for the reduction of Fe (III) to Fe (II). It is very clear that Fe (II), which is oxidized during the reduction of Cr^{6+}, can be recycled. As a result, $Fe(OH)_2$ is a stronger reductant than Fe (II)–DOM complexes and is formed by redox-active fulvic acid moieties depending on pH during this process [286]. Humic acid (HA), when coupled with Fe nanoparticles occupies the reactive sites of the surface and curtails the reduction of Cr^{6+}, creating both synergistic and antagonistic outcomes.

Conversely, the reduction of Cr^{6+} can be enhanced due to the presence of quinone compounds in HA which acts like an electron shuttle. Agglomeration can be prevented and inhibitory effects can be counteracted by using HA; thus, the nanoparticles are stabilized [287]. The remediation rate of the Cr^{6+}-Fe (0) complex can be increased and protection can be provided on the surface of iron by adding benign naturally occurring organic molecules including α-hydroxyl carbonyl, α-hydroxyl carboxylate, α-carbonyl carboxylate, phenolate, carboxylates and/or thiol groups, siderophore, ascorbic acid, or chelating agents such as ethylenediaminetetraacetic acid derivates and acetylacetone [288]. Wu et al. (2022) prepared a polysaccharide-derived composite by embedding carbonized chitosan into triethylenetetramine-modified sodium alginate (CTS/CS-50). The amount of Cr(VI) removed could reach 98% within 80 min under UV light irradiation [196].

2. Fe (III) Photocatalytic Reduction of Cr^{6+} by Organic Acids

Research has focused on Cr^{6+} reduction by organic acids using the photocatalytic impact of Fe (III). The key stage of this reduction reaction is the formation of Fe (III)-organic acid complex which is significantly feasible when applied to organic acids containing an α-OH group [289].

3. TiO_2 Photocatalytic Reduction of Cr^{6+} by Organic Acids

At pH 3, the photocatalytic reduction capability of TiO_2 has been studied for the removal of Cr^{6+} due to its properties of oxidizing organic compounds and reducing the metal ions simultaneously. Li et al. (2016) conducted an experiment to remove Cr^{6+} using a TiO_2-graphene hydrogel with a three-dimensional (3D) network structure facilitated by the photocatalytic reduction process. A total of 100% Cr^{6+} was removed from the solution containing 5 mg/L within 30 min under UV irradiation [290]. Naimi-Joubani et al. (2015) removed Cr^{6+} using illuminated ZnO/TiO_2 composite [291]. The efficiency in removing Cr^{6+} was 99.99% when the $UV/ZnO/TiO_2$ process was used. The photocatalyst dosage was kept at 4 g/L at pH 3 and the process suited the Langmuir–Hinshelwood (L–H) model well. De Bittencourt et al. (2020) used bio-photocatalysts which were successfully prepared by direct coating of the raw and protonated (immersion into 0.2 M HNO_3) brown algae *Laminaria hyperborea* with $FeCl_3$, $AlCl_3$, and TiO_2 solutions [292]. The results showed that the material previously protonated and coated with iron presented the best Cr^{6+} removal results, reaching an efficiency of 100% after 90 min.

4. Photocatalytic Reduction of Cr^{6+} by Ag/Ag_3PO_4/Reduced Graphene Oxide Microspheres

The photocatalytic process is considered a simple process for the removal of Cr that uses light and semiconductors. Three key steps are taken in this process: charged carrier photogeneration, charged carrier separation and diffusion to the photocatalyst surface, and redox reaction on the photocatalyst surface [293]. Despite having many positive advantages such as in-site generation of reactive radicals, no chemicals used, and no sludge production; this technology has some drawbacks. It is still on a laboratory scale, low throughput, dependent on pH, and inefficient when different metals are present [294]. Liu et al. (2020) conducted an experiment for the removal of Cr^{6+} from wastewater using Ag/Ag_3PO_4/reduced graphene oxide microspheres [295]. With controlled ratios, Ag/Ag_3PO_4 components were well distributed on reduced graphene oxide (rGO) sheets using polydopamine as a good reductant and effective linker. More than 90% of Cr^{6+} removal became possible under a continuous photocatalytic system for more than 30 h.

Moreover, Li et al. (2017) achieved rapid Cr^{6+} reduction using Mn_3O_4@ZnO under simulated sunlight irradiation at 95.3% in 110 min [296]. Du et al. (2019) used a metal–organic framework (MOF) and UiO-66-NH_2(Zr/Hf) membrane as photocatalysts to reduce Cr^{6+} ions. They successfully removed more than 94% of it after 20 cycles [297]. Qi et al. (2020) prepared a number of composites using ZnS-Ga_2S_3, a flower-like hierarchical heterojunction, which has photo-catalytical properties [298]. Among the composites, ZnS-Ga_2S_3-3(ZnS/Ga_2S_3 molar ratio 3:1) proved to be the best. The adsorption capacity of ZnS-Ga_2S_3-3 was 54.42 mg/g, and its total removal efficiency was 99.10% for 100 mg/L Cr^{6+} solution after 160 min. The Langmuir, pseudo-second-order, and first-order models well described the adsorption isotherm, adsorption kinetics, and photo-reduction kinetics of ZnS-Ga_2S_3, respectively. Zhou et al. (2022) prepared nZVI/ZIF-8 MOF nanocomposites for the effective removal of Cr^{6+} [197]. More than 99% was removed from wastewater using nZVI/ZIF-8 nanocomposites at pH 5. Photocatalytic degradation and reduction of available used catalysts in the literature is described in Table 5.

Photocatalytic reduction technology has significant limitations despite the fact that it produces reactive radicals on-site, without the need for chemicals or the creation of sludge. It is still laboratory-scale, has a low throughput, is pH-dependent, and is ineffective when there are different metals present [294]. In the case of the ion exchange technique, further study is needed on the stability and reusability.

Table 5. Photocatalytic degradation and reduction of available used catalysts in the literature.

Electron Donor	Type/Source of Catalyst	Reduction (%)	Contact Time	Radiation	References
Tartaric, citric, malic, and n-butyric acids	Diluted and Fe(III) adsorbed onto clay	100	7–80 min	Visible Light	[289]
Tartaric and citric acids	Soils	100	4 h	Mimic Solar	[299]
Alginate	γ-Fe_2O_3 nanoparticles	≈100	50 min	Sunlight	[300]
Salicylic acid	$CuFe_2O_4$ nanoparticles	60	2.8 h	-	[301]
	TiO_2 powder	95	2 h	visible light	[302]
-	TiO_2 nanoparticles modified with $C_{60}(CHCOOH)_2$	97	1.5 h	UV radiation	[303]
-	$La_2Ti_2O_7$ and salts (NaCl, KCl, $CaCl_2$, $MgCl_2$, Na_2SO_4)	98	3 h	UV light	[304]
Salicylic acid	TiO_2 powder	-	300–900 min	UV 253.7 nm	[305]
Methanol, formic acid, acetic acid, triethanolamine, EDTA	TiO_2	100	-	550 nm, visible light	[306]
Salicylic acid	$CuAl_2O_4/TiO_2$	95	3 h	visible light, 1.7–2.5 eV	[307]
Citric acid	WO dopped TiO_2 nanotube	-	-	UV light	[308]
Other photocatalysts Added electron donor	NiO nanoparticles	90	75 min	Laser Radiation	[309]
Added electron donor	ZnO nanoparticles	95	60 min	Laser Radiation	[310]
	Ag/Ag_3PO_4/reduced graphene oxide microspheres	90	30 h	Visible light	[295]
	Mn_3O_4@ZnO	95.3	110 min	Sunlight	[296]
	UiO-66-NH_2(Zr/Hf)	94	120 min	Visible light	[297]
	ZnS-Ga_2S_3-3	99.1	160 min	Solar light	[298]

2.4. Biological Removal

Biological removal of Cr^{6+} refers to microbial removal. The process consists of three stages: firstly, Cr is bound to the cell surface; secondly, Cr is translocated into the cell; and thirdly, Cr^{6+} is reduced to Cr^{3+} [311].

2.4.1. Aerobic Cr^{6+} Reducing Bacteria

Cr^{6+} is first reduced to the short-lived intermediates Cr^{5+} and/or Cr^{4+} and then finally reduced to the thermodynamically stable end-product Cr^{3+} when bacterial reduction of Cr^{6+} takes place in the presence of oxygen. Cr^{6+} is regenerated when Cr^{6+} goes through a one-electron redox cycle by transferring the electron to oxygen. The process generates a reactive oxygen species (ROS) that easily combines with DNA–protein complexes. However, it is quite unclear if the reduction reactions are spontaneous or enzyme-mediated [312].

Cr^{6+} can be reduced using aerobic heterotrophic cells, non-growing cells, growing cells with chromate reductase activity, and growing cells that have lost chromate reductase activity. When *Bacillus* sp. and *Staphylococcus capitis* are employed, the influence of proteins and electron donors such as glucose, fructose, sucrose, and bagasse extract enhanced the reduction rate of Cr^{6+} [313]. Among them, glucose is the best electron donor [314]. Cr^{6+} can be reduced by *Brevibacterium casei* with an azo dye Acid Orange 7 (AO7) and this is a new mechanism. AO7 was used as an e^- donor by the reduction enzyme(s) of *B. casei* under nutrient-limiting conditions. The oxidized AO7 produces complex with

the resultant Cr^{3+} to form a purple-colored intermediate [315]. Yu et al. (2016) tested *Pseudomonas brassicacearum* LZ-4 for the removal of Cr^{6+} from wastewater and showed that this immobilized strain could remove 80% of 10 mg/L Cr^{6+} [316]. A total of 93% Cr^{6+} (10 mg/L) was successfully removed by An et al. (2020) using *Pseudomonas aeruginosa* strain G12 in wastewater [317].

2.4.2. Anaerobic Cr^{6+} Reducing Bacteria

The reducing activities for Cr^{6+} differ from aerobes in the case of anaerobes where the process is associated with their electron transfer systems. These catalyze both the electron shuttle and respiratory chain [312]. Cr^{6+} can be reduced using micro-organisms under anaerobic conditions with glucose as described below [311]:

$$CrO_4{}^{2-}\,(aq) + 8H^+\,(aq) + 3e^- \rightarrow Cr^{3+}\,(aq) + 4H_2O$$

$$Cr^{3+}\,(aq) + 4H_2O \rightarrow Cr(OH)_3(s) + 3H^+\,(aq) + H_2O$$

$$C_6H_{12}O_6 + 8CrO_4{}^{2-}\,(aq) + 14H_2O \rightarrow 8Cr(OH)_3(s) + 10OH^-\,(aq) + 6HCO^-\,(aq)$$

The anaerobic reduction potential of *Pannonibacter phragmitetus* is better than the aerobic variant under alkaline conditions, showing a potential application for Cr^{6+} detoxification [318]. *P. phragmitetus* cells coated with polyethylenimine-functionalized magnetic nanoparticles can reduce Cr^{6+} efficiently and be easily separated from reaction mixtures by magnetic force. The results of the magnetically immobilized cells prove that the magnetic cell separation technology can be efficient when applied to Cr^{6+} removal from alkaline wastewater [319].

The rapid anaerobic removal and reduction of chromate by the rest of *E. coli* cells were significantly enhanced by: firstly, the quinone redox mediators lawsone, menadione, anthraquinone-2-sulfonate, and anthraquinone-2,6-disulfonate; and secondly, the addition of glucose as an electron donor [320]. Cr^{6+} was adsorbed by chitosan beads and bio-reduced by *E. coli* cells which made possible the bio-regeneration of the chitosan beads after *E. coli* biofilm had grown significantly [321]. Moreover, chromate reduction was enhanced by these cells in the presence of quinone redox mediators [322]. Biogenic iron (II) and sulfides generated by IRB (iron-reducing bacteria) and SRB (sulfate-reducing bacteria) show 100 times faster reduction than CRB alone. H_2S, a Cr^{6+} reductant, is produced from SRB and conducts the process through three stages [323]: (i) sulfate reduction, (ii) chromate reduction by sulfides, and (iii) precipitation of Cr^{6+} by sulfide:

$$SO_4{}^{2-}\,(aq) + 2CH_2O + H^+\,(aq) \rightarrow HS^-\,(aq) + 2H_2O + 2CO_2(g)$$

$$8CrO_4{}^{2-}\,(aq) + 3HS^-\,(aq) + 17H_2O \rightarrow 8Cr(OH)_3(s) + 3SO_4{}^{2-}\,(aq) + 13OH^-\,(aq)$$

$$Cr^{6+}\,(aq) + 3HS^-\,(aq) \rightarrow CrS_3(s) + 3H^+\,(aq)$$

Fe (II), produced from Fe (III) using IRB, reduces the hexavalent Cr into trivalent [323].

$$C_6H_{12}O_6 + 24Fe^{3+} + 12H_2O \rightarrow 6HCO_3{}^- + 24Fe^{2+} + 3OH^-$$

$$3/4C_3H_5O_3{}^- + 3Fe(OH)_3(s) \rightarrow 3/4C_2H_3O_2{}^- + 3Fe^{2+} + 3/4HCO_3{}^- + 2H_2O + 1/4OH^-$$

$$3Fe^{2+} + HCrO_4{}^- + 8H_2O \rightarrow 3Fe(OH)_3(s) + Cr(OH)_3(s) + 5H^+$$

An air bubbling-cathode in an air–cathode dual-chamber microbial fuel cell (MFC) can reduce Cr^{6+} efficiently. When Cr^{6+} is reduced in situ at a carbon-felt cathode, the electrogenerated H_2O_2 at the cathode driven by iron-reducing bacteria can be strongly associated with the reduction of Cr^{6+} [323]. Enzymatic anaerobic Cr^{6+} reduction involves members of the cytochrome family (e.g., cytochrome b and c) [324].

2.4.3. Cr^{6+} Reducing Fungi

The species of fungi which can be reduced to Cr^{6+} to Cr^{3+} can be identified by a number of processes such as isolation, characterization, and examination of their Cr-reducing capability under various conditions. Two chromate-resistant filamentous fungi, *Aspergillus* sp. N_2 and *Penicillium* sp. N_3 were used to test their reduction efficiency in 50 mg/L Cr^{6+} solution at almost neutral pH. *Aspergillus* sp. N_2 and *Penicillium* sp. N_3 exhibited 75% and 35% reductions, respectively. The enzymatic reduction and sorption to mycelia were the mechanisms of this method [325]. Gola et al. (2016) investigated the efficiency of *Beauveria bassiana* in the removal of Cr^{6+} [326]. The study found that maximum Cr removal was possible at neutral pH when the temperature was kept at 30 °C at 150 rpm and 120 h. Chakraborty et al. (2018) used *Aspergillus* sp., isolated from soil of the Sunderban mangrove forest, West Bengal, for the efficient removal of Cr^{6+} (98.96%) at pH 4 [327]. Chatterjee et al. (2020) successfully fabricated superparamagnetic iron oxide nanoparticles (IONPs) (Fe_3O_4) of 20–40 nm size using manglicolous (mangrove) fungus *Aspergillus niger* BSC-1 for the removal of Cr^{6+} from aqueous solution [328]. Maximum removal of Cr^{6+} occurred at 40 °C, pH 3, and with a 2.5 g/L dose of IONPs. The biological removal of Cr^{6+} is listed together in Table 6.

Table 6. Biological removal of Cr^{6+} in different literature (the superscript "a" denotes in mg/g).

Species	Initial Conc. of Cr^{6+}	pH	Temperature (°C)	Period (Hours)	Reduction (%)	References
Pseudomonas brassicacearum LZ-4	10 [a]	7.5	37	-	80	[316]
Brevibacterium casei	5 [b]	7	35	-	83.4 ± 0.6	[315]
Bacillus sp. JDM-2-1	100 [a]	7	37	96	85	[313]
Staphylococcus capitis	100 [a]	7	37	96	81	[313]
Pseudomonas aeruginosa strain G12	10 [a]	7	30	72	93	[317]
Pannonibacter phragmitetus	1000 [a]	9	37	24	100	[318]
Pannonibacter phragmitetus LSSE-09 coated with polyethylenimine-functionalized magnetic nanoparticles	350 [a]	9	37	0.33	100	[319]
Resting *Escherichia coli* cells	150 [a]	7	-	4	97.5	[322]
Bacillus subtilis	50 [a]	9	30	65	100	[324]
Beauveria bassiana	30 [a]	7	30	12	61.1	[326]
Aspergillus sp.	50 [a]	4	27	-	98.96	[327]
Iron oxide nanoparticles fabricated *Aspergillus niger* BSC-1	10 [a]	3	40	2	99.75	[328]

2.5. Membrane Filtration Process

Technological advancements in membrane development have led to an increase in the use of membranes over the years for the removal of Cr from wastewater. There are several factors that can affect membrane separation, including material, membrane pore size, and composition [329]. Various other technologies were also used with membrane technology, including ion exchange, adsorption, and electrochemistry. Among the membrane filtration processes, reverse osmosis is considered to be one of the best available technologies for Cr removal [21,330]. A few publications have favored the nanofiltration process for removing Cr^{6+} [330]. The performance of membranes for the treatment of Cr^{6+} is illustrated in Table 7.

Table 7. The performances of membranes for the treatment of Cr^{6+} (the superscript "a" denotes in mg/g).

Initial Concentration (mg/L)	Application/Membrane Type	Pressure (bar)	pH	Removal %	References
0.4	Nanofilter	14	7.1	95	[331]
0.4	Nanofilter	5	7.1	85	[331]
0.1	Nanofilter	5	7.1	52.7	[331]
0.05	Reverse osmosis	100	N. A.	98.3	[332]
0.05	Reverse osmosis	500	N. A.	100	[332]
0.05	Reverse osmosis	3.5	3	99.01	[332]
0.05	Reverse osmosis	3.5	9	>99.9	[332]
10,000	Reverse osmosis	200 psi	6–7	100	[32]
SCMC-GA-NF	Nanofilter	3	4	79.85	[333]
Nano Uio-66-NH2	Nanofilter	-	6.5	32.36 [a]	[334]
FeNPs-CaAlg	Hydrogel		5.41	99.5	[335]
Aminated-Fe_3O_4 chitosan/polyvinyl alcohol-PES	Nanofilter	-	3	509.7 [a]	[336]
SAMPI	-	-	3		[337]
PAH-TFC	-	-	3	99.5	[338]
PPy-B	-	-	2	586.9 [a]	[339]

Sulfated carboxymethyl cellulose nanofilter membrane by cross-linking of glutaraldehyde (GA) supported on polysulfone membrane (SCMC-GA-NF) was undertaken by Gasemloo et al. (2019) [333]. The maximum Cr^{6+} removal efficiency of 79.85% was obtained at pH = 4, pressure = 3 bar, and SO_3/Pyridine:CMC ratio (1:1) in filter. Wu et al. (2018) prepared an efficient adsorbent, nano Uio-66-NH_2 metal–organic frameworks (MOFs) [334]. The maximum adsorption capacity was 32.36 mg/g at pH 6.5. The process fitted the pseudo-second-order kinetics model and Langmuir isotherm model best. Liu et al. (2019) utilized green tea extract for the biosynthesis of iron nanoparticles (FeNPs)-calcium alginate (CaAlg) hydrogel membrane [335]. The FeNPs-CaAlg hydrogel membrane (0.6 g) can remove as high as 99.5% of 1 mg/L (50 mL) Cr^{6+} at room temperature (23 °C) and original pH (5.41) within 10 min.

Koushkbaghi et al. (2018) prepared dual-layer mixed matrix membranes (MMMs) by incorporating aminated Fe_3O_4 nanoparticles into the chitosan/polyvinyl alcohol nanofibers polyethersulfone (PES) membrane for the removal of Cr^{6+} [336]. The maximum adsorption capacity of Cr^{6+} was found to be 509.7 mg/g at optimum pH of 3 in a binary system. Zhijiang et al. (2017) [337] used surface amidoxime-modified polyindole (SAMPI) nanofiber membrane for the removal of Cr^{6+}. Maximum adsorption occurred at pH 3 while the other parameters were: temperature 25 °C, initial Cr^{6+} concentration 400 mg/L, and contact time 24 h. The isotherm fitted the Langmuir isotherm model best. Jo et al. (2022) prepared IP-assembled poly(acryloyl hydrazide)-branched star polymer (PAH-TFC) for the removal of hexavalent chromium from wastewater. It exhibited significantly higher Cr^{6+} rejection compared to other representative commercial RO membranes (Cr^{6+} rejection of ∼55% at pH 3) with similar water permeance [338].

Because of its poor removal capacity, the use of MF in Cr removal has not received adequate attention. Nonetheless, it has been utilized by altering the feed solution's membrane or chemical pre-treatment.

2.6. Chelation

Chelation is another method employed for removing Cr. Malek et al. (2009) described a novel strategy that allows chromium-containing leather wastes to be decontaminated [340]. These researchers used two different procedures to remove Cr from wastewater.

Organic salts and acids such as potassium oxalate, potassium tartrate, and acetic and citric acids were tested for their efficiency to separate the chromium from the leather waste.

This ability was determined by the amount of chromium extracted with each organic chelate, and the best yield was about 95%. In their first experiment, they noticed that the effect of organic salts on chromium extraction yield was more important than that of organic acids. Of the different chelates tested, tartrate generated the best results, with approximately 69.7% of chromium extraction yield [340].

Generally, after treatment in a basic medium, the residual chromium content obtained in each case steadily falls to the 0.24–1.1% range. According to the results of both procedures, it is concluded that alkaline medium is the best way and potassium tartrate is the most efficient medium for chromium extraction. In their recent study, Shukla et al. (2022) [341] statistically designed lab-scale soil washing experiments using two chelating agents, i.e., ethylene diamine tetra acetic acid (EDTA) and *N*-acetyl-L-cysteine (NAC). The effects of pH, contact time, and dosage of wash solution on chromium (Cr^{+6}) removal efficiency (RE) were investigated and optimized using response surface methodology (RSM). The projected Cr^{+6} RE under these optimum conditions (pH—5.5, contact time—216 h, dosage of EDTA—4128 mg/kg, and dosage of NAC—300 mg/kg) was 14.3% and 65.7%, for EDTA and NAC, respectively. The results of this investigation indicate that washing soil with NAC could be a better alternative to EDTA for removing Cr^{+6} from the soil [341].

The membrane was able to adsorb 99.5% Cr^{6+} at pH 3. A flexible polypyrrole (PPy) membrane with bayberry-like vesicle structures (PPy-B) was prepared by Li et al. (2022) who resorted to template-assisted interfacial polymerization [339]. The PPy-B membrane exhibited an enhanced adsorption capacity of Cr^{6+} (586.90 mg/g) when pH 2 was maintained. The membrane was capable of adsorbing 99.5% Cr^{6+} at pH 3. A flexible PPy membrane with bayberry-like vesicle structures (PPy-B) was prepared by Li et al., (2022) via template-assisted interfacial polymerization [339]. PPy-B membrane exhibited an enhanced adsorption capacity of Cr^{6+} (586.90 mg/g) when pH 2 was maintained.

3. Conclusions

Among all the heavy metals, Cr is one of the potentially toxic substances. Because of its toxicity and carcinogenicity, Cr has become an important problem to research; its presence in water and the devised removal technologies have been well documented. In this review, we discussed various Cr removal technologies, for instance, adsorption, electrochemical treatment, physico-chemical process, and biological removal of both Cr^{3+} and Cr^{6+} from water. Cr^{6+} removal was evaluated when different conditions were taken into account, such as pH, initial Cr concentration, temperature, ratios, etc. It would not be a wise decision to restrict the effluent treatment methods to laboratory conditions and synthesized samples alone. Based on the advantages and disadvantages of different methods, the most viable treatment technique should be chosen depending on the initial Cr concentration, operational cost, and wastewater characteristics. However, further research is required on more efficient, cost-effective, and progressively recyclable methods that will produce less noxious byproducts during adsorption. Finally, more research in the future and especially on the systematic application of Cr remediation in the environment is urgently required.

Funding: This research received no external funding.

Institutional Review Board Statement: Not applicable.

Informed Consent Statement: Not applicable.

Data Availability Statement: The data of this study will be shared upon reasonable request to the corresponding author.

Conflicts of Interest: The authors declare no conflict of interest.

References

1. Zhitkovich, A. Chromium in drinking water: Sources, metabolism, and cancer risks. *Chem. Res. Toxicol.* **2011**, *24*, 1617–1629. [CrossRef]
2. Chrysochoou, M.; Johnston, C.P.; Dahal, G. A comparative evaluation of hexavalent chromium treatment in contaminated soil by calcium polysulfide and green-tea nanoscale zero-valent iron. *J. Hazard. Mater.* **2012**, *201*, 33–42. [CrossRef]
3. Wittbrodt, P.R.; Palmer, C.D. Effect of temperature, ionic strength, background electrolytes, and Fe (III) on the reduction of hexavalent chromium by soil humic substances. *Environ. Sci. Technol.* **1996**, *30*, 2470–2477. [CrossRef]
4. Ashraf, A.; Bibi, I.; Niazi, N.K.; Ok, Y.S.; Murtaza, G.; Shahid, M.; Kunhikrishnan, A.; Li, D.; Mahmood, T. Chromium (VI) sorption efficiency of acid-activated banana peel over organo-montmorillonite in aqueous solutions. *Int. J. Phytoremediation* **2017**, *19*, 605–613. [CrossRef]
5. Xia, S.; Song, Z.; Jeyakumar, P.; Shaheen, S.M.; Rinklebe, J.; Ok, Y.S.; Bolan, N.; Wang, H. A critical review on bioremediation technologies for Cr (VI)-contaminated soils and wastewater. *Crit. Rev. Environ. Sci. Technol.* **2019**, *49*, 1027–1078. [CrossRef]
6. Jobby, R.; Jha, P.; Yadav, A.K.; Desai, N. Biosorption and biotransformation of hexavalent chromium [Cr (VI)]: A comprehensive review. *Chemosphere* **2018**, *207*, 255–266. [CrossRef]
7. Antoniadis, V.; Zanni, A.A.; Levizou, E.; Shaheen, S.M.; Dimirkou, A.; Bolan, N.; Rinklebe, J. Modulation of hexavalent chromium toxicity on Origanum vulgare in an acidic soil amended with peat, lime, and zeolite. *Chemosphere* **2018**, *195*, 291–300. [CrossRef]
8. Brown, T.; LeMay, H.; Wilson, R. *Chemistry: The Central Science (No. QD 31.2. B76 1988)*; Prentice Hall: Hoboken, NJ, USA, 1988.
9. Janus, J.; Krajnc, E. *Integrated Criteria Document Chromium: Effects*; National Institute of Public Health and Environmental Protection Bilthoven: Bilthoven, The Netherlands, 1990.
10. Wallwork, G. The oxidation of alloys. *Rep. Prog. Phys.* **1976**, *39*, 401. [CrossRef]
11. Sharma, S.K.; Petrusevski, B.; Amy, G. Chromium removal from water: A review. *J. Water Supply Res. Technol.—AQUA* **2008**, *57*, 541–553. [CrossRef]
12. Rakhunde, R.; Deshpande, L.; Juneja, H. Chemical speciation of chromium in water: A review. *Crit. Rev. Environ. Sci. Technol.* **2012**, *42*, 776–810. [CrossRef]
13. Chen, J.; Tian, Y. Hexavalent chromium reducing bacteria: Mechanism of reduction and characteristics. *Environ. Sci. Pollut. Res.* **2021**, *28*, 20981–20997. [CrossRef] [PubMed]
14. Zhang, R.; Tian, Y. Characteristics of natural biopolymers and their derivative as sorbents for chromium adsorption: A review. *J. Leather Sci. Eng.* **2020**, *2*, 24. [CrossRef]
15. Owlad, M.; Aroua, M.K.; Daud, W.A.W.; Baroutian, S. Removal of hexavalent chromium-contaminated water and wastewater: A review. *Water Air Soil Pollut.* **2009**, *200*, 59–77. [CrossRef]
16. Niazi, N.K.; Bishop, T.F.; Singh, B. Evaluation of spatial variability of soil arsenic adjacent to a disused cattle-dip site, using model-based geostatistics. *Environ. Sci. Technol.* **2011**, *45*, 10463–10470. [CrossRef] [PubMed]
17. Niazi, N.K.; Singh, B.; Minasny, B. Mid-infrared spectroscopy and partial least-squares regression to estimate soil arsenic at a highly variable arsenic-contaminated site. *Int. J. Environ. Sci. Technol.* **2015**, *12*, 1965–1974. [CrossRef]
18. Shahid, M.; Khalid, S.; Abbas, G.; Shahid, N.; Nadeem, M.; Sabir, M.; Aslam, M.; Dumat, C. Heavy metal stress and crop productivity. In *Crop Production and Global Environmental Issues*; Springer: Berlin/Heidelberg, Germany, 2015; pp. 1–25.
19. Vimercati, L.; Gatti, M.F.; Gagliardi, T.; Cuccaro, F.; De Maria, L.; Caputi, A.; Quarato, M.; Baldassarre, A. Environmental exposure to arsenic and chromium in an industrial area. *Environ. Sci. Pollut. Res.* **2017**, *24*, 11528–11535. [CrossRef]
20. Hasan, S.M.; Akber, M.; Bahar, M.; Islam, M.; Akbor, M.; Siddique, M.; Bakar, A. Chromium contamination from tanning industries and Phytoremediation potential of native plants: A study of savar tannery industrial estate in Dhaka, Bangladesh. *Bull. Environ. Contam. Toxicol.* **2021**, *106*, 1024–1032. [CrossRef]
21. Faust, S.; Ali, O. *Chemistry of Water Treatment*; Ann Arbor Press: Chelsea, MI, USA, 1998.
22. Pradhan, D.; Sukla, L.B.; Sawyer, M.; Rahman, P.K. Recent bioreduction of hexavalent chromium in wastewater treatment: A review. *J. Ind. Eng. Chem.* **2017**, *55*, 1–20. [CrossRef]
23. Barnowski, C.; Jakubowski, N.; Stuewer, D.; Broekaert, J.A. Speciation of chromium by direct coupling of ion exchange chromatography with inductively coupled plasma mass spectrometry. *J. Anal. At. Spectrom.* **1997**, *12*, 1155–1161. [CrossRef]
24. Gil, R.; Cerutti, S.; Gásquez, J.; Olsina, R.; Martinez, L. Preconcentration and speciation of chromium in drinking water samples by coupling of on-line sorption on activated carbon to ETAAS determination. *Talanta* **2006**, *68*, 1065–1070. [CrossRef]
25. Ukhurebor, K.E.; Aigbe, U.O.; Onyancha, R.B.; Nwankwo, W.; Osibote, O.A.; Paumo, H.K.; Ama, O.M.; Adetunji, C.O.; Siloko, I.U. Effect of hexavalent chromium on the environment and removal techniques: A review. *J. Environ. Manag.* **2021**, *280*, 111809. [CrossRef] [PubMed]
26. Katz, S.A.; Salem, H. *The Biological and Environmental Chemistry of Chromium*; VCH Publishers: Hoboken, NJ, USA, 1994.
27. Kotaś, J.; Stasicka, Z. Chromium occurrence in the environment and methods of its speciation. *Environ. Pollut.* **2000**, *107*, 263–283. [CrossRef] [PubMed]
28. Saha, R.; Nandi, R.; Saha, B. Sources and toxicity of hexavalent chromium. *J. Coord. Chem.* **2011**, *64*, 1782–1806. [CrossRef]
29. Tian, Z.; Yang, B.; Cui, G.; Zhang, L.; Guo, Y.; Yan, S. Synthesis of poly (m-phenylenediamine)/iron oxide/acid oxidized multi-wall carbon nanotubes for removal of hexavalent chromium. *RSC Adv.* **2015**, *5*, 2266–2275. [CrossRef]
30. Malkoc, E.; Nuhoglu, Y.; Dundar, M. Adsorption of chromium (VI) on pomace—An olive oil industry waste: Batch and column studies. *J. Hazard. Mater.* **2006**, *138*, 142–151. [CrossRef]

31. Aigbe, U.O.; Osibote, O.A. A review of hexavalent chromium removal from aqueous solutions by sorption technique using nanomaterials. *J. Environ. Chem. Eng.* **2020**, *8*, 104503. [CrossRef]
32. Mohammadi, H.; Gholami, M.; Rahimi, M. Application and optimization in chromium-contaminated wastewater treatment of the reverse osmosis technology. *Desalination Water Treat.* **2009**, *9*, 229–233. [CrossRef]
33. Narayani, M.; Shetty, K.V. Chromium-resistant bacteria and their environmental condition for hexavalent chromium removal: A review. *Crit. Rev. Environ. Sci. Technol.* **2013**, *43*, 955–1009. [CrossRef]
34. Kumar, A.S.K.; Jiang, S.-J.; Tseng, W.-L. Effective adsorption of chromium (VI)/Cr (III) from aqueous solution using ionic liquid functionalized multiwalled carbon nanotubes as a super sorbent. *J. Mater. Chem. A* **2015**, *3*, 7044–7057. [CrossRef]
35. Duan, C.; Ma, T.; Wang, J.; Zhou, Y. Removal of heavy metals from aqueous solution using carbon-based adsorbents: A review. *J. Water Process Eng.* **2020**, *37*, 101339. [CrossRef]
36. Hashem, A.; Akasha, R.; Ghith, A.; Hussein, D. Adsorbent based on agricultural wastes for heavy metal and dye removal: A review. *Energy Educ. Sci. Technol.* **2007**, *19*, e86.
37. Rahman, M.A.; Lamb, D.; Rahman, M.M.; Bahar, M.M.; Sanderson, P.; Abbasi, S.; Bari, A.F.; Naidu, R. Removal of arsenate from contaminated waters by novel zirconium and zirconium-iron modified biochar. *J. Hazard. Mater.* **2021**, *409*, 124488. [CrossRef] [PubMed]
38. Allen, S.J.; Gan, Q.; Matthews, R.; Johnson, P.A. Kinetic modeling of the adsorption of basic dyes by kudzu. *J. Colloid Interface Sci.* **2005**, *286*, 101–109. [CrossRef] [PubMed]
39. Siti, N.; Mohd, H.; Md, L.K.; Shamsul, I. Adsorption process of heavy metals by low-cost adsorbent: A review. *World Appl. Sci. J.* **2013**, *28*, 1518–1530.
40. Dehghani, M.H.; Sanaei, D.; Ali, I.; Bhatnagar, A. Removal of chromium (VI) from aqueous solution using treated waste newspaper as a low-cost adsorbent: Kinetic modeling and isotherm studies. *J. Mol. Liq.* **2016**, *215*, 671–679. [CrossRef]
41. Bentchikou, L.; Mechelouf, F.-Z.; NEGGAZ, F.; Mellah, A. Removal of hexavalent chromium from water by using natural brown clay. *J. Turk. Chem. Soc. Sect. B Chem. Eng.* **2017**, *1*, 43–52.
42. Zhao, Y.; Qi, W.; Chen, G.; Ji, M.; Zhang, Z. Behavior of Cr (VI) removal from wastewater by adsorption onto HCl activated Akadama clay. *J. Taiwan Inst. Chem. Eng.* **2015**, *50*, 190–197. [CrossRef]
43. Zanin, E.; Scapinello, J.; de Oliveira, M.; Rambo, C.L.; Franscescon, F.; Freitas, L.; de Mello, J.M.M.; Fiori, M.A.; Oliveira, J.V.; Dal Magro, J. Adsorption of heavy metals from wastewater graphic industry using clinoptilolite zeolite as adsorbent. *Process Saf. Environ. Prot.* **2017**, *105*, 194–200. [CrossRef]
44. Adam, M.R.; Salleh, N.M.; Othman, M.H.D.; Matsuura, T.; Ali, M.H.; Puteh, M.H.; Ismail, A.; Rahman, M.A.; Jaafar, J. The adsorptive removal of chromium (VI) in aqueous solution by novel natural zeolite based hollow fibre ceramic membrane. *J. Environ. Manag.* **2018**, *224*, 252–262. [CrossRef] [PubMed]
45. Nag, S.; Mondal, A.; Mishra, U.; Bar, N.; Das, S.K. Removal of chromium (VI) from aqueous solutions using rubber leaf powder: Batch and column studies. *Desalination Water Treat.* **2016**, *57*, 16927–16942. [CrossRef]
46. Gottipati, R.; Mishra, S. Preparation of microporous activated carbon from Aegle Marmelos fruit shell and its application in removal of chromium (VI) from aqueous phase. *J. Ind. Eng. Chem.* **2016**, *36*, 355–363. [CrossRef]
47. Agarwal, A.; Gupta, P.K. Adsorption study of Cr (II) from aqueous solution using animal bone charcoal as low cost adsorbent. *Int. J. Eng. Technol. Manag. Appl. Sci.* **2015**, *3*, 151–163.
48. Zafarani, H.R.; Bahrololoom, M.E.; Noubactep, C.; Tashkhourian, J. Green walnut shell as a new material for removal of Cr (VI) ions from aqueous solutions. *Desalination Water Treat.* **2015**, *55*, 431–439. [CrossRef]
49. Das, N.; Konar, J.; Mohanta, M.; Srivastava, S. Adsorption of Cr (VI) and Se (IV) from their aqueous solutions onto Zr^{4+}-substituted ZnAl/MgAl-layered double hydroxides: Effect of Zr^{4+} substitution in the layer. *J. Colloid Interface Sci.* **2004**, *270*, 1–8. [CrossRef] [PubMed]
50. Bailey, R.; Bennett, T.; Benjamin, M. Sorption onto and recovery of Cr (VI) using iron-oxide-coated sand. *Water Sci. Technol.* **1992**, *26*, 1239–1244. [CrossRef]
51. Nriagu, J.O.; Nieboer, E. *Chromium in the Natural and Human Environments*; John Wiley & Sons: Hoboken, NJ, USA, 1988; Volume 20.
52. Beszedits, S. Chromium removal from industrial wastewaters. *Chromium Nat. Hum. Environ.* **1988**, *20*, 231.
53. USBR. *Hexavalent Chromium Treatment Technologies*; U.S. Department of the Interior Bureau of Reclamation Research and Development Office: Denver, CO, USA, 2018.
54. Sillanpää, M.; Shestakova, M. *Electrochemical Water Treatment Methods: Fundamentals, Methods and Full Scale Applications*; Butterworth-Heinemann: Oxford, UK, 2017.
55. Mukhopadhyay, B.; Sundquist, J.; Schmitz, R.J. Removal of Cr (VI) from Cr-contaminated groundwater through electrochemical addition of Fe (II). *J. Environ. Manag.* **2007**, *82*, 66–76. [CrossRef]
56. Sengupta, A.K.; Clifford, D. Important process variables in chromate ion exchange. *Environ. Sci. Technol.* **1986**, *20*, 149–155. [CrossRef]
57. Sengupta, A.K.; Clifford, D.; Subramonian, S. Chromate ion-exchange process at alkaline pH. *Water Res.* **1986**, *20*, 1177–1184. [CrossRef]
58. Rengaraj, S.; Yeon, K.-H.; Moon, S.-H. Removal of chromium from water and wastewater by ion exchange resins. *J. Hazard. Mater.* **2001**, *87*, 273–287. [CrossRef]

59. Galán, B.; Castañeda, D.; Ortiz, I. Removal and recovery of Cr (VI) from polluted ground waters: A comparative study of ion-exchange technologies. *Water Res.* **2005**, *39*, 4317–4324. [CrossRef] [PubMed]
60. Gode, F.; Pehlivan, E. A comparative study of two chelating ion-exchange resins for the removal of chromium (III) from aqueous solution. *J. Hazard. Mater.* **2003**, *100*, 231–243. [CrossRef] [PubMed]
61. Faust, S.D.; Aly, O.M. *Chemistry of Water Treatment*, 2nd ed.; CRC Press: Boca Raton, FL, USA, 2018.
62. Yasmeen, S.; Kabiraz, M.K.; Saha, B.; Qadir, M.; Gafur, M.; Masum, S. Chromium (VI) ions removal from tannery effluent using chitosan-microcrystalline cellulose composite as adsorbent. *Int. Res. J. Pure Appl. Chem.* **2016**, *10*, 1–14. [CrossRef]
63. Wan, Z.; Li, M.; Zhang, Q.; Fan, Z.; Verpoort, F. Concurrent reduction-adsorption of chromium using m-phenylenediamine-modified magnetic chitosan: Kinetics, isotherm, and mechanism. *Environ. Sci. Pollut. Res.* **2018**, *25*, 17830–17841. [CrossRef]
64. Wang, Z.; Lin, F.; Huang, L.; Chang, Z.; Yang, B.; Liu, S.; Zheng, M.; Lu, Y.; Chen, J. Cyclodextrin functionalized 3D-graphene for the removal of Cr (VI) with the easy and rapid separation strategy. *Environ. Pollut.* **2019**, *254*, 112854. [CrossRef] [PubMed]
65. Sharma, D.; Forster, C. A preliminary examination into the adsorption of hexavalent chromium using low-cost adsorbents. *Bioresour. Technol.* **1994**, *47*, 257–264. [CrossRef]
66. Singh, K.; Rastogi, R.; Hasan, S. Removal of Cr (VI) from wastewater using rice bran. *J. Colloid Interface Sci.* **2005**, *290*, 61–68. [CrossRef]
67. Dupont, L.; Guillon, E. Removal of hexavalent chromium with a lignocellulosic substrate extracted from wheat bran. *Environ. Sci. Technol.* **2003**, *37*, 4235–4241. [CrossRef]
68. Dupont, L.; Bouanda, J.; Ghanbaja, J.; Dumonceau, J.; Aplincourt, M. Use of analytical microscopy to analyze the speciation of copper and chromium ions onto a low-cost biomaterial. *J. Colloid Interface Sci.* **2004**, *279*, 418–424. [CrossRef]
69. Dakiky, M.; Khamis, M.; Manassra, A.; Mer'Eb, M. Selective adsorption of chromium (VI) in industrial wastewater using low-cost abundantly available adsorbents. *Adv. Environ. Res.* **2002**, *6*, 533–540. [CrossRef]
70. Meena, A.K.; Kadirvelu, K.; Mishra, G.; Rajagopal, C.; Nagar, P. Adsorptive removal of heavy metals from aqueous solution by treated sawdust (*Acacia arabica*). *J. Hazard. Mater.* **2008**, *150*, 604–611. [CrossRef] [PubMed]
71. Agarwal, G.; Bhuptawat, H.K.; Chaudhari, S. Biosorption of aqueous chromium (VI) by *Tamarindus indica* seeds. *Bioresour. Technol.* **2006**, *97*, 949–956. [CrossRef] [PubMed]
72. Celik, A.; Dost, K.; Sezer, H. An investigation of chromium(VI) ion removal from wastewaters by adsorption on residual lignin. *Fresenius Environ. Bull.* **2004**, *13*, 124–127.
73. Daneshvar, N.; Salari, D.; Aber, S. Chromium adsorption and Cr (VI) reduction to trivalent chromium in aqueous solutions by soya cake. *J. Hazard. Mater.* **2002**, *94*, 49–61. [CrossRef] [PubMed]
74. Gonzalez, M.H.; Araújo, G.C.; Pelizaro, C.B.; Menezes, E.A.; Lemos, S.G.; De Sousa, G.B.; Nogueira, A.R.A. Coconut coir as biosorbent for Cr (VI) removal from laboratory wastewater. *J. Hazard. Mater.* **2008**, *159*, 252–256. [CrossRef]
75. Ahalya, N.; Kanamadi, R.; Ramachandra, T. Biosorption of chromium (VI) from aqueous solutions by the husk of Bengal gram (*Cicer arientinum*). *Electron. J. Biotechnol.* **2005**, *8*, 258–264. [CrossRef]
76. Ali, A.; Saeed, K.; Mabood, F. Removal of chromium (VI) from aqueous medium using chemically modified banana peels as efficient low-cost adsorbent. *Alex. Eng. J.* **2016**, *55*, 2933–2942. [CrossRef]
77. Yari, A.R.; Kord Mostafapour, F.; Mahdavi, Y.; Joghataei, A. Agricultural Waste as Adsorbent for Removal of Chromium (VI) from aqueous solution. *Arch. Hyg. Sci.* **2016**, *5*, 310–318.
78. Altun, T.; Parlayıcı, Ş.; Pehlivan, E. Hexavalent chromium removal using agricultural waste "rye husk". *Desalination Water Treat.* **2016**, *57*, 17748–17756. [CrossRef]
79. Begum, H.A.; Haque, A.M.; Islam, M.D.; Hasan, M.M.; Ahmed, S.; Razzak, M.; Khan, R.A. Analysis of the adsorption of toxic chromium (VI) by untreated and chitosan treated banana and areca fiber. *J. Text. Sci. Technol.* **2020**, *6*, 81. [CrossRef]
80. Pourfadakari, S.; Jorfi, S.; Ahmadi, M.; Takdastan, A. Experimental data on adsorption of Cr (VI) from aqueous solution using nanosized cellulose fibers obtained from rice husk. *Data Brief* **2017**, *15*, 887–895. [CrossRef] [PubMed]
81. Chakraborty, R.; Verma, R.; Asthana, A.; Vidya, S.S.; Singh, A.K. Adsorption of hazardous chromium (VI) ions from aqueous solutions using modified sawdust: Kinetics, isotherm and thermodynamic modelling. *Int. J. Environ. Anal. Chem.* **2021**, *101*, 911–928. [CrossRef]
82. Ahmed, N.; Islam, M.; Hossain, M.; Rahman, A.; Sultana, A. Modified coconut coir to remove hexavalent chromium from aqueous solution. *Bangladesh J. Sci. Ind. Res.* **2019**, *54*, 89–98. [CrossRef]
83. Krishnani, K.; Meng, X.; Dupont, L. Metal ions binding onto lignocellulosic biosorbent. *J. Environ. Sci. Health Part A* **2009**, *44*, 688–699. [CrossRef]
84. Jain, M.; Garg, V.; Kadirvelu, K. Chromium (VI) removal from aqueous system using *Helianthus annuus* (sunflower) stem waste. *J. Hazard. Mater.* **2009**, *162*, 365–372. [CrossRef]
85. Aoyama, M. Removal of Cr (VI) from aqueous solution by London plane leaves. *J. Chem. Technol. Biotechnol. Int. Res. Process Environ. Clean Technol.* **2003**, *78*, 601–604. [CrossRef]
86. Uysal, M.; Ar, I. Removal of Cr (VI) from industrial wastewaters by adsorption: Part I: Determination of optimum conditions. *J. Hazard. Mater.* **2007**, *149*, 482–491. [CrossRef]
87. Pehlivan, E.; Altun, T. Biosorption of chromium (VI) ion from aqueous solutions using walnut, hazelnut and almond shell. *J. Hazard. Mater.* **2008**, *155*, 378–384. [CrossRef]

88. Raji, C.; Anirudhan, T. Batch Cr (VI) removal by polyacrylamide-grafted sawdust: Kinetics and thermodynamics. *Water Res.* **1998**, *32*, 3772–3780. [CrossRef]
89. Sinha, V.; Pakshirajan, K.; Chaturvedi, R. Evaluation of Cr (VI) exposed and unexposed plant parts of *Tradescantia pallida* (Rose) DR Hunt. for Cr removal from wastewater by biosorption. *Int. J. Phytoremediation* **2015**, *17*, 1204–1211. [CrossRef]
90. Suganya, E.; Rangabhashiyam, S.; Lity, A.; Selvaraju, N. Removal of hexavalent chromium from aqueous solution by a novel biosorbent *Caryota urens* seeds: Equilibrium and kinetic studies. *Desalination Water Treat.* **2016**, *57*, 23940–23950. [CrossRef]
91. Lin, C.; Luo, W.; Luo, T.; Zhou, Q.; Li, H.; Jing, L. A study on adsorption of Cr (VI) by modified rice straw: Characteristics, performances and mechanism. *J. Clean. Prod.* **2018**, *196*, 626–634. [CrossRef]
92. Krishnani, K.K.; Meng, X.; Christodoulatos, C.; Boddu, V.M. Biosorption mechanism of nine different heavy metals onto biomatrix from rice husk. *J. Hazard. Mater.* **2008**, *153*, 1222–1234. [CrossRef] [PubMed]
93. Losada, V.A.R.; Bonilla, E.P.; Pinilla, L.A.C.; Serrezuela, R.R. Removal of chromium in wastewater from tanneries applying bioremediation with algae, orange peels and citrus pectin. *Contemp. Eng. Sci.* **2018**, *11*, 433–449. [CrossRef]
94. Shokri Khoubestani, R.; Mirghaffari, N.; Farhadian, O. Removal of three and hexavalent chromium from aqueous solutions using a microalgae biomass-derived biosorbent. *Environ. Prog. Sustain. Energy* **2015**, *34*, 949–956. [CrossRef]
95. Jayakumar, R.; Rajasimman, M.; Karthikeyan, C. Sorption and desorption of hexavalent chromium using a novel brown marine algae *Sargassum myriocystum*. *Korean J. Chem. Eng.* **2015**, *32*, 2031–2046. [CrossRef]
96. Al-Homaidan, A.A.; Al-Qahtani, H.S.; Al-Ghanayem, A.A.; Ameen, F.; Ibraheem, I.B. Potential use of green algae as a biosorbent for hexavalent chromium removal from aqueous solutions. *Saudi J. Biol. Sci.* **2018**, *25*, 1733–1738. [CrossRef]
97. Uluozlu, O.D.; Sari, A.; Tuzen, M.; Soylak, M. Biosorption of Pb (II) and Cr (III) from aqueous solution by lichen (*Parmelina tiliaceae*) biomass. *Bioresour. Technol.* **2008**, *99*, 2972–2980. [CrossRef]
98. Bernardo, G.-R.R.; Rene, R.-M.J. Chromium (III) uptake by agro-waste biosorbents: Chemical characterization, sorption–desorption studies, and mechanism. *J. Hazard. Mater.* **2009**, *170*, 845–854. [CrossRef]
99. Onyancha, D.; Mavura, W.; Ngila, J.C.; Ongoma, P.; Chacha, J. Studies of chromium removal from tannery wastewaters by algae biosorbents, *Spirogyra condensata* and *Rhizoclonium hieroglyphicum*. *J. Hazard. Mater.* **2008**, *158*, 605–614. [CrossRef]
100. Barkhordar, B.; Ghias, A.M. Comparison of Langmuir and Freundlich equilibriums in Cr, Cu and Ni adsorption by Sargassum. 2004, 1, 58–64. *Iran. J. Environ. Health Sci.* **2004**, *1*, 58–64.
101. Pena-Castro, J.; Martınez-Jerónimo, F.; Esparza-Garcıa, F.; Canizares-Villanueva, R. Heavy metals removal by the microalga *Scenedesmus incrassatulus* in continuous cultures. *Bioresour. Technol.* **2004**, *94*, 219–222. [CrossRef] [PubMed]
102. Gupta, V.; Shrivastava, A.; Jain, N. Biosorption of chromium (VI) from aqueous solutions by green algae *Spirogyra* species. *Water Res.* **2001**, *35*, 4079–4085. [CrossRef]
103. Chen, H.; Lu, Y.; Yin, P.; Li, X.; Shan, Y. Exploring the mechanisms of biosorption of Cr (Vi) by marine-derived *Penicillium janthinellum* P1. *Int. J. Agric. Biol.* **2019**, *22*, 913–920.
104. Mondal, N.K.; Samanta, A.; Dutta, S.; Chattoraj, S. Optimization of Cr (VI) biosorption onto *Aspergillus niger* using 3-level Box-Behnken design: Equilibrium, kinetic, thermodynamic and regeneration studies. *J. Genet. Eng. Biotechnol.* **2017**, *15*, 151–160. [CrossRef] [PubMed]
105. Saravanan, A.; Senthil Kumar, P.; Preetha, B. Optimization of process parameters for the removal of chromium (VI) and nickel (II) from aqueous solutions by mixed biosorbents (custard apple seeds and *Aspergillus niger*) using response surface methodology. *Desalination Water Treat.* **2016**, *57*, 14530–14543. [CrossRef]
106. Mahmoud, M.E.; Yakout, A.A.; Abdel-Aal, H.; Osman, M.M. Speciation and selective biosorption of Cr (III) and Cr (VI) using nanosilica immobilized-fungi biosorbents. *J. Environ. Eng.* **2015**, *141*, 04014079. [CrossRef]
107. Sivakumar, D. Biosorption of hexavalent chromium in a tannery industry wastewater using fungi species. *Glob. J. Environ. Sci. Manag.* **2016**, *2*, 105–124.
108. Ertugay, N.; Bayhan, Y. Biosorption of Cr (VI) from aqueous solutions by biomass of *Agaricus bisporus*. *J. Hazard. Mater.* **2008**, *154*, 432–439. [CrossRef]
109. Preetha, B.; Viruthagiri, T. Batch and continuous biosorption of chromium (VI) by *Rhizopus arrhizus*. *Sep. Purif. Technol.* **2007**, *57*, 126–133. [CrossRef]
110. Elangovan, R.; Philip, L.; Chandraraj, K. Biosorption of chromium species by aquatic weeds: Kinetics and mechanism studies. *J. Hazard. Mater.* **2008**, *152*, 100–112. [CrossRef] [PubMed]
111. Gupta, V.; Rastogi, A. Biosorption of hexavalent chromium by raw and acid-treated green alga *Oedogonium hatei* from aqueous solutions. *J. Hazard. Mater.* **2009**, *163*, 396–402. [CrossRef] [PubMed]
112. Sen, M.; Dastidar, M.G. Adsorption-desorption studies on Cr (VI) using non-living fungal biomass. *Asian J. Chem.* **2010**, *22*, 2331.
113. Sen, M.; Dastidar, M.G.; Roychoudhury, P.K. Biological removal of Cr (VI) using Fusarium solani in batch and continuous modes of operation. *Enzym. Microb. Technol.* **2007**, *41*, 51–56. [CrossRef]
114. Rezaei, H. Biosorption of chromium by using *Spirulina* sp. *Arab. J. Chem.* **2016**, *9*, 846–853. [CrossRef]
115. Quiton, K.G.; Doma, B., Jr.; Futalan, C.M.; Wan, M.-W. Removal of chromium (VI) and zinc (II) from aqueous solution using kaolin-supported bacterial biofilms of Gram-negative *E. coli* and Gram-positive *Staphylococcus epidermidis*. *Sustain. Environ. Res.* **2018**, *28*, 206–213. [CrossRef]

116. Dobrowolski, R.; Szcześ, A.; Czemierska, M.; Jarosz-Wikołazka, A. Studies of cadmium (II), lead (II), nickel (II), cobalt (II) and chromium (VI) sorption on extracellular polymeric substances produced by *Rhodococcus opacus* and *Rhodococcus rhodochrous*. *Bioresour. Technol.* **2017**, *225*, 113–120. [CrossRef]
117. Emran, F.K.; Walli, H.A.; Shinjar, F.J.; Abdulameer, M.A. Chromium Bioremoval by *Staphylococcus* sp. and *Pseudomonas* sp. Isolated from Industrial Waste Water in Baghdad, Iraq. *J. Phys. Conf. Ser.* **2019**, *1294*, 072014. [CrossRef]
118. Chug, R.; Gour, V.S.; Mathur, S.; Kothari, S. Optimization of extracellular polymeric substances production using *Azotobacter beijreinckii* and *Bacillus subtilis* and its application in chromium (VI) removal. *Bioresour. Technol.* **2016**, *214*, 604–608. [CrossRef]
119. Zhou, M.; Liu, Y.; Zeng, G.; Li, X.; Xu, W.; Fan, T. Kinetic and equilibrium studies of Cr (VI) biosorption by dead *Bacillus licheniformis* biomass. *World J. Microbiol. Biotechnol.* **2007**, *23*, 43–48. [CrossRef]
120. Sivaprakash, A.; Aravindhan, R.; Rao, J.R.; Nair, B.U. Kinetics and equilibrium studies on the biosorption of hexavalent chromium from aqueous solutions using *Bacillus subtilis* biomass. *Appl. Ecol. Environ. Res.* **2009**, *7*, 45–57. [CrossRef]
121. Ziagova, M.; Dimitriadis, G.; Aslanidou, D.; Papaioannou, X.; Tzannetaki, E.L.; Liakopoulou-Kyriakides, M. Comparative study of Cd (II) and Cr (VI) biosorption on *Staphylococcus xylosus* and *Pseudomonas* sp. in single and binary mixtures. *Bioresour. Technol.* **2007**, *98*, 2859–2865. [CrossRef] [PubMed]
122. Bueno, B.; Torem, M.; Molina, F.; De Mesquita, L. Biosorption of lead (II), chromium (III) and copper (II) by *R. opacus*: Equilibrium and kinetic studies. *Miner. Eng.* **2008**, *21*, 65–75. [CrossRef]
123. Sahmoune, M.; Louhab, K.; Boukhiar, A. Biosorption of Cr (III) from aqueous solutions using bacterium biomass *Streptomyces rimosus*. *Int. J. Environ. Res.* **2009**, *3*, 229–238.
124. Khanafari, A.; Eshgh, D.S.; Mashinchian, A. Removal of lead and chromium from aqueous solution by *Bacillus circulans* biofilm. *Iran. J. Environ. Health. Sci. Eng.* **2008**, *5*, 195–200.
125. Srinath, T.; Verma, T.; Ramteke, P.; Garg, S. Chromium (VI) biosorption and bioaccumulation by chromate resistant bacteria. *Chemosphere* **2002**, *48*, 427–435. [CrossRef]
126. Srinath, T.; Garg, S.; Ramteke, P. Chromium (VI) accumulation by *Bacillus circulans*: Effect of growth conditions. *Indian J. Microbiol.* **2002**, *42*, 141–146.
127. Pattanapipitpaisal, P.; Brown, N.; Macaskie, L. Chromate reduction by *Microbacterium liquefaciens* immobilised in polyvinyl alcohol. *Biotechnol. Lett.* **2001**, *23*, 61–65. [CrossRef]
128. Islam, M.M.; Khan, M.N.; Biswas, S.; Choudhury, T.R.; Haque, P.; Rashid, T.U.; Rahman, M.M. Preparation and characterization of bijoypur clay-crystalline cellulose composite for application as an adsorbent. *Adv. Mater. Sci* **2017**, *2*, 1–7. [CrossRef]
129. Hokkanen, S.; Bhatnagar, A.; Repo, E.; Lou, S.; Sillanpää, M. Calcium hydroxyapatite microfibrillated cellulose composite as a potential adsorbent for the removal of Cr (VI) from aqueous solution. *Chem. Eng. J.* **2016**, *283*, 445–452. [CrossRef]
130. Islam, M.M.; Islam, M.S.; Maniruzzaman, M.; Haque, M.M.-U.; Mohana, A.A. Banana rachis CNC/Clay composite filter for dye and heavy metals adsorption from industrial wastewater. *Eng. Sci. Technol.* **2021**, *2*, 140–152. [CrossRef]
131. Rahaman, M.H.; Islam, M.A.; Islam, M.M.; Rahman, M.A.; Alam, S.N. Biodegradable composite adsorbent of modified cellulose and chitosan to remove heavy metal ions from aqueous solution. *Curr. Res. Green Sustain. Chem.* **2021**, *4*, 100119. [CrossRef]
132. Choudhury, P.R.; Majumdar, S.; Sahoo, G.C.; Saha, S.; Mondal, P. High pressure ultrafiltration CuO/hydroxyethyl cellulose composite ceramic membrane for separation of Cr (VI) and Pb (II) from contaminated water. *Chem. Eng. J.* **2018**, *336*, 570–578. [CrossRef]
133. Dokmaji, T.; Ibrahim, T.; Khamis, M.; Abouleish, M.; Alam, I. Chemically modified nanoparticles usage for removal of chromium from sewer water. *Environ. Nanotechnol. Monit. Manag.* **2020**, *14*, 100319. [CrossRef]
134. Subedi, N.; Lähde, A.; Abu-Danso, E.; Iqbal, J.; Bhatnagar, A. A comparative study of magnetic chitosan (Chi@ Fe_3O_4) and graphene oxide modified magnetic chitosan (Chi@ Fe_3O_4GO) nanocomposites for efficient removal of Cr (VI) from water. *Int. J. Biol. Macromol.* **2019**, *137*, 948–959. [CrossRef] [PubMed]
135. Wang, H.; Zhuang, M.; Shan, L.; Wu, J.; Quan, G.; Cui, L.; Zhang, Y.; Yan, J. Bimetallic FeNi nanoparticles immobilized by biomass-derived hierarchically porous carbon for efficient removal of Cr (VI) from aqueous solution. *J. Hazard. Mater.* **2022**, *423*, 127098. [CrossRef]
136. Jabłońska, B. Removing of Cr (III) and Cr (VI) compounds from aqueous solutions by shale waste rocks. *Desalination Water Treat.* **2020**, *186*, 234–246. [CrossRef]
137. Qiao, K.; Tian, W.; Bai, J.; Zhao, J.; Du, Z.; Song, T.; Chu, M.; Wang, L.; Xie, W. Synthesis of floatable magnetic iron/biochar beads for the removal of chromium from aqueous solutions. *Environ. Technol. Innov.* **2020**, *19*, 100907. [CrossRef]
138. Li, F.; Zimmerman, A.R.; Hu, X.; Gao, B. Removal of aqueous Cr (VI) by Zn-and Al-modified hydrochar. *Chemosphere* **2020**, *260*, 127610. [CrossRef]
139. Gadd, G.M. Biosorption: Critical review of scientific rationale, environmental importance and significance for pollution treatment. *J. Chem. Technol. Biotechnol. Int. Res. Process Environ. Clean Technol.* **2009**, *84*, 13–28. [CrossRef]
140. Volesky, B. Biosorption and me. *Water Res.* **2007**, *41*, 4017–4029. [CrossRef] [PubMed]
141. Arief, V.O.; Trilestari, K.; Sunarso, J.; Indraswati, N.; Ismadji, S. Recent progress on biosorption of heavy metals from liquids using low cost biosorbents: Characterization, biosorption parameters and mechanism studies. *CLEAN–Soil Air Water* **2008**, *36*, 937–962. [CrossRef]
142. Vijayaraghavan, K.; Yun, Y.-S. Bacterial biosorbents and biosorption. *Biotechnol. Adv.* **2008**, *26*, 266–291. [CrossRef] [PubMed]

143. Lesmana, S.O.; Febriana, N.; Soetaredjo, F.E.; Sunarso, J.; Ismadji, S. Studies on potential applications of biomass for the separation of heavy metals from water and wastewater. *Biochem. Eng. J.* **2009**, *44*, 19–41. [CrossRef]
144. Demirbas, A. Heavy metal adsorption onto agro-based waste materials: A review. *J. Hazard. Mater.* **2008**, *157*, 220–229. [CrossRef]
145. Sud, D.; Mahajan, G.; Kaur, M. Agricultural waste material as potential adsorbent for sequestering heavy metal ions from aqueous solutions—A review. *Bioresour. Technol.* **2008**, *99*, 6017–6027. [CrossRef]
146. Gupta, V.; Rastogi, A. Sorption and desorption studies of chromium (VI) from nonviable cyanobacterium *Nostoc muscorum* biomass. *J. Hazard. Mater.* **2008**, *154*, 347–354. [CrossRef]
147. Shakya, A.; Agarwal, T. Removal of Cr (VI) from water using pineapple peel derived biochars: Adsorption potential and re-usability assessment. *J. Mol. Liq.* **2019**, *293*, 111497. [CrossRef]
148. Saravanan, A.; Kumar, P.S.; Varjani, S.; Karishma, S.; Jeevanantham, S.; Yaashikaa, P. Effective removal of Cr (VI) ions from synthetic solution using mixed biomasses: Kinetic, equilibrium and thermodynamic study. *J. Water Process Eng.* **2021**, *40*, 101905. [CrossRef]
149. Tytłak, A.; Oleszczuk, P.; Dobrowolski, R. Sorption and desorption of Cr (VI) ions from water by biochars in different environmental conditions. *Environ. Sci. Pollut. Res.* **2015**, *22*, 5985–5994. [CrossRef]
150. Imran, M.; Khan, Z.U.H.; Iqbal, M.M.; Iqbal, J.; Shah, N.S.; Munawar, S.; Ali, S.; Murtaza, B.; Naeem, M.A.; Rizwan, M. Effect of biochar modified with magnetite nanoparticles and HNO_3 for efficient removal of Cr (VI) from contaminated water: A batch and column scale study. *Environ. Pollut.* **2020**, *261*, 114231. [CrossRef] [PubMed]
151. Zhou, Q.; Yan, C.; Luo, W. Polypyrrole coated secondary fly ash–iron composites: Novel floatable magnetic adsorbents for the removal of chromium (VI) from wastewater. *Mater. Des.* **2016**, *92*, 701–709. [CrossRef]
152. Mohamed, A.; Nasser, W.; Osman, T.; Toprak, M.; Muhammed, M.; Uheida, A. Removal of chromium (VI) from aqueous solutions using surface modified composite nanofibers. *J. Colloid Interface Sci.* **2017**, *505*, 682–691. [CrossRef] [PubMed]
153. Huang, Y.; Lee, X.; Macazo, F.C.; Grattieri, M.; Cai, R.; Minteer, S.D. Fast and efficient removal of chromium (VI) anionic species by a reusable chitosan-modified multi-walled carbon nanotube composite. *Chem. Eng. J.* **2018**, *339*, 259–267. [CrossRef]
154. Wang, J.; Wang, P.; Wang, H.; Dong, J.; Chen, W.; Wang, X.; Wang, S.; Hayat, T.; Alsaedi, A.; Wang, X. Preparation of molybdenum disulfide coated Mg/Al layered double hydroxide composites for efficient removal of chromium (VI). *ACS Sustain. Chem. Eng.* **2017**, *5*, 7165–7174. [CrossRef]
155. Kumar, N.; Kardam, A.; Jain, V.; Nagpal, S. A rapid, reusable polyaniline-impregnated nanocellulose composite-based system for enhanced removal of chromium and cleaning of waste water. *Sep. Sci. Technol.* **2020**, *55*, 1436–1448. [CrossRef]
156. Wang, H.; Cui, T.; Chen, D.; Luo, Q.; Xu, J.; Sun, R.; Zi, W.; Xu, R.; Liu, Y.; Zhang, Y. Hexavalent chromium elimination from wastewater by integrated micro-electrolysis composites synthesized from red mud and rice straw via a facile one-pot method. *Sci. Rep.* **2022**, *12*, 14242. [CrossRef]
157. Wu, S.; Li, M.; Xin, L.; Long, H.; Gao, X. Efficient removal of Cr (VI) by triethylenetetramine modified sodium alginate/carbonized chitosan composite via adsorption and photocatalytic reduction. *J. Mol. Liq.* **2022**, *366*, 120160. [CrossRef]
158. Stoica-Guzun, A.; Stroescu, M.; Jinga, S.I.; Mihalache, N.; Botez, A.; Matei, C.; Berger, D.; Damian, C.M.; Ionita, V. Box-Behnken experimental design for chromium (VI) ions removal by bacterial cellulose-magnetite composites. *Int. J. Biol. Macromol.* **2016**, *91*, 1062–1072. [CrossRef]
159. Khan, N.A.; Hasan, Z.; Jhung, S.H. Adsorptive removal of hazardous materials using metal-organic frameworks (MOFs): A review. *J. Hazard. Mater.* **2013**, *244*, 444–456. [CrossRef]
160. Sun, Y.; Zhou, H.-C. Recent progress in the synthesis of metal–organic frameworks. *Sci. Technol. Adv. Mater.* **2015**, *16*, 054202. [CrossRef]
161. Mahmoud, M.E.; Amira, M.F.; Seleim, S.M.; Mohamed, A.K. Amino-decorated magnetic metal-organic framework as a potential novel platform for selective removal of chromium (Vl), cadmium (II) and lead (II). *J. Hazard. Mater.* **2020**, *381*, 120979. [CrossRef] [PubMed]
162. Guo, J.; Li, J.-J.; Wang, C.-C. Adsorptive removal of Cr (VI) from simulated wastewater in MOF BUC-17 ultrafine powder. *J. Environ. Chem. Eng.* **2019**, *7*, 102909. [CrossRef]
163. Han, C.; Xie, J.; Min, X. Efficient adsorption H3AsO4 and Cr (VI) from strongly acidic solutions by La-Zr bimetallic MOFs: Crystallinity role and mechanism. *J. Environ. Chem. Eng.* **2022**, *10*, 108982. [CrossRef]
164. Meier, M.; Ungerer, J.; Klinge, M.; Nirschl, H. Formation of porous silica nanoparticles at higher reaction kinetics. *Powder Technol.* **2018**, *339*, 801–808. [CrossRef]
165. Zhang, X.; Liu, X.; Peng, J.; Zhao, Y.; Yang, Q. Highly efficient solid catalysts for asymmetric hydrogenation fabricated via facile adsorption of Rh–MonoPhos on porous silicas. *Catal. Sci. Technol.* **2014**, *4*, 1012–1016. [CrossRef]
166. Prieto, G.; Shakeri, M.; De Jong, K.P.; De Jongh, P.E. Quantitative relationship between support porosity and the stability of pore-confined metal nanoparticles studied on $CuZnO/SiO_2$ methanol synthesis catalysts. *ACS Nano* **2014**, *8*, 2522–2531. [CrossRef]
167. Buntara, T.; Melián-Cabrera, I.; Tan, Q.; Fierro, J.L.; Neurock, M.; De Vries, J.G.; Heeres, H.J. Catalyst studies on the ring opening of tetrahydrofuran–dimethanol to 1,2,6-hexanetriol. *Catal. Today* **2013**, *210*, 106–116. [CrossRef]
168. Fechete, I.; Donnio, B.; Ersen, O.; Dintzer, T.; Djeddi, A.; Garin, F. Single crystals of mesoporous tungstenosilicate W-MCM-48 molecular sieves for the conversion of methylcyclopentane (MCP). *Appl. Surf. Sci.* **2011**, *257*, 2791–2800. [CrossRef]
169. Staub, H.L.N.; Del Rosal, I.; Maron, L.; Kleitz, F.; Fontaine, F.D.R.-G. On the interaction of phosphines with high surface area mesoporous silica. *J. Phys. Chem. C* **2012**, *116*, 25919–25927. [CrossRef]

170. Shi, Y.-T.; Cheng, H.-Y.; Geng, Y.; Nan, H.-M.; Chen, W.; Cai, Q.; Chen, B.-H.; Sun, X.-D.; Yao, Y.-W. The size-controllable synthesis of nanometer-sized mesoporous silica in extremely dilute surfactant solution. *Mater. Chem. Phys.* **2010**, *120*, 193–198. [CrossRef]
171. Li, C.M.; Wang, X.P.; Jiao, Z.H.; Zhang, Y.S.; Yin, X.B.; Cui, X.M.; Wei, Y.Z. Functionalized porous silica-based nano/micro particles for environmental remediation of hazard ions. *Nanomaterials* **2019**, *9*, 247. [CrossRef] [PubMed]
172. Kim, J.-H.; Kang, J.-K.; Lee, S.-C.; Kim, S.-B. Synthesis of powdered and granular N-(3-trimethoxysilylpropyl) diethylenetriamine-grafted mesoporous silica SBA-15 for Cr (VI) removal from industrial wastewater. *J. Taiwan Inst. Chem. Eng.* **2018**, *87*, 140–149. [CrossRef]
173. Shariati, S.; Khabazipour, M.; Safa, F. Synthesis and application of amine functionalized silica mesoporous magnetite nanoparticles for removal of chromium (VI) from aqueous solutions. *J. Porous Mater.* **2017**, *24*, 129–139. [CrossRef]
174. Idris, S.A.; Alotaibi, K.; Peshkur, T.A.; Anderson, P.; Gibson, L.T. Preconcentration and selective extraction of chromium species in water samples using amino modified *mesoporous silica*. *J. Colloid Interface Sci.* **2012**, *386*, 344–349. [CrossRef] [PubMed]
175. Soltani, R.; Marjani, A.; Hosseini, M.; Shirazian, S. Synthesis and characterization of novel N-methylimidazolium-functionalized KCC-1: A highly efficient anion exchanger of hexavalent chromium. *Chemosphere* **2020**, *239*, 124735. [CrossRef] [PubMed]
176. Soltani, R.; Marjani, A.; Soltani, R.; Shirazian, S. Hierarchical multi-shell hollow micro–meso–macroporous silica for Cr (VI) adsorption. *Sci. Rep.* **2020**, *10*, 9788. [CrossRef] [PubMed]
177. Atkovska, K.; Lisichkov, K.; Ruseska, G.; Dimitrov, A.T.; Grozdanov, A. Removal of heavy metal ions from wastewater using conventional and nanosorbents: A review. *J. Chem. Technol. Metall.* **2018**, *53*, 202–219.
178. Marantos, I.; Christidis, G.; Ulmanu, M. Zeolite formation and deposits. In *Handbook of Natural Zeolites*; Bentham Science Publishers: Sharjah, United Arab Emirates, 2012.
179. Alvarez-Ayuso, E.; Garcıa-Sánchez, A.; Querol, X. Purification of metal electroplating waste waters using zeolites. *Water Res.* **2003**, *37*, 4855–4862. [CrossRef]
180. Dal Bosco, S.M.; Jimenez, R.S.; Carvalho, W.A. Removal of toxic metals from wastewater by Brazilian natural scolecite. *J. Colloid Interface Sci.* **2005**, *281*, 424–431. [CrossRef]
181. de Magalhães, L.F.; da Silva, G.R.; Peres, A.E.C. Zeolite application in wastewater treatment. *Adsorpt. Sci. Technol.* **2022**, *2022*, 4544104. [CrossRef]
182. Zeng, Y.; Woo, H.; Lee, G.; Park, J. Adsorption of Cr (VI) on hexadecylpyridinium bromide (HDPB) modified natural zeolites. *Microporous Mesoporous Mater.* **2010**, *130*, 83–91. [CrossRef]
183. Neolaka, Y.A.; Lawa, Y.; Naat, J.; Riwu, A.A.; Mango, A.W.; Darmokoesoemo, H.; Widyaningrum, B.A.; Iqbal, M.; Kusuma, H.S. Efficiency of activated natural zeolite-based magnetic composite (ANZ-Fe_3O_4) as a novel adsorbent for removal of Cr (VI) from wastewater. *J. Mater. Res. Technol.* **2022**, *18*, 2896–2909. [CrossRef]
184. Kong, F.; Zhang, Y.; Wang, H.; Tang, J.; Li, Y.; Wang, S. Removal of Cr (VI) from wastewater by artificial zeolite spheres loaded with nano Fe–Al bimetallic oxide in constructed wetland. *Chemosphere* **2020**, *257*, 127224. [CrossRef]
185. Pacheco, S.; Tapia, J.; Medina, M.; Rodriguez, R. Cadmium ions adsorption in simulated wastewater using structured alumina–silica nanoparticles. *J. Non-Cryst. Solids* **2006**, *352*, 5475–5481. [CrossRef]
186. Di, Z.-C.; Ding, J.; Peng, X.-J.; Li, Y.-H.; Luan, Z.-K.; Liang, J. Chromium adsorption by aligned carbon nanotubes supported ceria nanoparticles. *Chemosphere* **2006**, *62*, 861–865. [CrossRef]
187. Skubal, L.; Meshkov, N.; Rajh, T.; Thurnauer, M. Cadmium removal from water using thiolactic acid-modified titanium dioxide nanoparticles. *J. Photochem. Photobiol. A Chem.* **2002**, *148*, 393–397. [CrossRef]
188. Hu, J.; Lo, I.M.; Chen, G. Fast removal and recovery of Cr (VI) using surface-modified jacobsite ($MnFe_2O_4$) nanoparticles. *Langmuir* **2005**, *21*, 11173–11179. [CrossRef]
189. Hu, J.; Lo, I.M.; Chen, G. Performance and mechanism of chromate (VI) adsorption by δ-FeOOH-coated maghemite (γ-Fe_2O_3) nanoparticles. *Sep. Purif. Technol.* **2007**, *58*, 76–82. [CrossRef]
190. Jayson, G.; Sangster, J.; Thompson, G.; Wilkinson, M. Adsorption of chromium from aqueous solution onto activated charcoal cloth. *Carbon* **1993**, *31*, 487–492. [CrossRef]
191. Selomulya, C.; Meeyoo, V.; Amal, R. Mechanisms of Cr (VI) removal from water by various types of activated carbons. *J. Chem. Technol. Biotechnol. Int. Res. Process Environ. Clean Technol.* **1999**, *74*, 111–122. [CrossRef]
192. Hamadi, N.K.; Chen, X.D.; Farid, M.M.; Lu, M.G. Adsorption kinetics for the removal of chromium (VI) from aqueous solution by adsorbents derived from used tyres and sawdust. *Chem. Eng. J.* **2001**, *84*, 95–105. [CrossRef]
193. Cimino, G.; Passerini, A.; Toscano, G. Removal of toxic cations and Cr (VI) from aqueous solution by hazelnut shell. *Water Res.* **2000**, *34*, 2955–2962. [CrossRef]
194. Dehghani, M.H.; Taher, M.M.; Bajpai, A.K.; Heibati, B.; Tyagi, I.; Asif, M.; Agarwal, S.; Gupta, V.K. Removal of noxious Cr (VI) ions using single-walled carbon nanotubes and multi-walled carbon nanotubes. *Chem. Eng. J.* **2015**, *279*, 344–352. [CrossRef]
195. Pillay, K.; Cukrowska, E.; Coville, N. Multi-walled carbon nanotubes as adsorbents for the removal of parts per billion levels of hexavalent chromium from aqueous solution. *J. Hazard. Mater.* **2009**, *166*, 1067–1075. [CrossRef] [PubMed]
196. Hu, J.; Chen, C.; Zhu, X.; Wang, X. Removal of chromium from aqueous solution by using oxidized multiwalled carbon nanotubes. *J. Hazard. Mater.* **2009**, *162*, 1542–1550. [CrossRef] [PubMed]
197. Gupta, V.; Agarwal, S.; Saleh, T.A. Chromium removal by combining the magnetic properties of iron oxide with adsorption properties of carbon nanotubes. *Water Res.* **2011**, *45*, 2207–2212. [CrossRef]

198. Atieh, M.A.; Bakather, O.Y.; Tawabini, B.S.; Bukhari, A.A.; Khaled, M.; Alharthi, M.; Fettouhi, M.; Abuilaiwi, F.A. Removal of chromium (III) from water by using modified and nonmodified carbon nanotubes. *J. Nanomater.* **2010**, *2010*, 232378. [CrossRef]
199. Atieh, M.A. Removal of chromium (VI) from polluted water using carbon nanotubes supported with activated carbon. *Procedia Environ. Sci.* **2011**, *4*, 281–293. [CrossRef]
200. Park, H.J.; Jeong, S.W.; Yang, J.K.; Kim, B.G.; Lee, S.M. Removal of heavy metals using waste eggshell. *J. Environ. Sci.* **2007**, *19*, 1436–1441. [CrossRef]
201. Amuda, O.; Adelowo, F.; Ologunde, M. Kinetics and equilibrium studies of adsorption of chromium (VI) ion from industrial wastewater using *Chrysophyllum albidum* (*Sapotaceae*) seed shells. *Colloids Surf. B Biointerfaces* **2009**, *68*, 184–192. [CrossRef] [PubMed]
202. El-Sikaily, A.; El Nemr, A.; Khaled, A.; Abdelwehab, O. Removal of toxic chromium from wastewater using green alga *Ulva lactuca* and its activated carbon. *J. Hazard. Mater.* **2007**, *148*, 216–228. [CrossRef] [PubMed]
203. Quintelas, C.; Rocha, Z.; Silva, B.; Fonseca, B.; Figueiredo, H.; Tavares, T. Biosorptive performance of an *Escherichia coli* biofilm supported on zeolite NaY for the removal of Cr (VI), Cd (II), Fe (III) and Ni (II). *Chem. Eng. J.* **2009**, *152*, 110–115. [CrossRef]
204. Tuzen, M.; Saygi, K.O.; Usta, C.; Soylak, M. *Pseudomonas aeruginosa* immobilized multiwalled carbon nanotubes as biosorbent for heavy metal ions. *Bioresour. Technol.* **2008**, *99*, 1563–1570. [CrossRef]
205. Baytak, S.; Türker, A.R. Determination of iron (III), cobalt (II) and chromium (III) in various water samples by flame atomic absorption spectrometry after preconcentration by means of *Saccharomyces carlsbergensis* immobilized on amberlite XAD-4. *Microchim. Acta* **2005**, *149*, 109–116. [CrossRef]
206. Gupta, V.; Pathania, D.; Agarwal, S.; Sharma, S. Removal of Cr (VI) onto *Ficus carica* biosorbent from water. *Environ. Sci. Pollut. Res.* **2013**, *20*, 2632–2644. [CrossRef]
207. Chojnacka, K. Biosorption of Cr (III) Ions by Wheat Straw and Grass: A Systematic Characterization of New Biosorbents. *Pol. J. Environ. Stud.* **2006**, *15*, 845–852.
208. Wang, X.S.; Li, Z.Z.; Sun, C. Removal of Cr (VI) from aqueous solutions by low-cost biosorbents: Marine macroalgae and agricultural by-products. *J. Hazard. Mater.* **2008**, *153*, 1176–1184. [CrossRef]
209. Singh, K.; Hasan, S.; Talat, M.; Singh, V.; Gangwar, S. Removal of Cr (VI) from aqueous solutions using wheat bran. *Chem. Eng. J.* **2009**, *151*, 113–121. [CrossRef]
210. Nameni, M.; Alavi Moghadam, M.; Arami, M. Adsorption of hexavalent chromium from aqueous solutions by wheat bran. *Int. J. Environ. Sci. Technol.* **2008**, *5*, 161–168. [CrossRef]
211. Farajzadeh, M.A.; Monji, A.B. Adsorption characteristics of wheat bran towards heavy metal cations. *Sep. Purif. Technol.* **2004**, *38*, 197–207. [CrossRef]
212. Sumathi, K.; Mahimairaja, S.; Naidu, R. Use of low-cost biological wastes and vermiculite for removal of chromium from tannery effluent. *Bioresour. Technol.* **2005**, *96*, 309–316. [CrossRef] [PubMed]
213. Nourbakhsh, M.; Sag, Y.; Özer, D.; Aksu, Z.; Kutsal, T.; Caglar, A. A comparative study of various biosorbents for removal of chromium (VI) ions from industrial waste waters. *Process Biochem.* **1994**, *29*, 1–5. [CrossRef]
214. Boddu, V.M.; Abburi, K.; Talbott, J.L.; Smith, E.D. Removal of hexavalent chromium from wastewater using a new composite chitosan biosorbent. *Environ. Sci. Technol.* **2003**, *37*, 4449–4456. [CrossRef] [PubMed]
215. Namasivayam, C.; Sureshkumar, M. Removal of chromium (VI) from water and wastewater using surfactant modified coconut coir pith as a biosorbent. *Bioresour. Technol.* **2008**, *99*, 2218–2225. [CrossRef]
216. Sankararamakrishnan, N.; Dixit, A.; Iyengar, L.; Sanghi, R. Removal of hexavalent chromium using a novel cross linked xanthated chitosan. *Bioresour. Technol.* **2006**, *97*, 2377–2382. [CrossRef]
217. Daraei, H.; Mittal, A.; Mittal, J.; Kamali, H. Optimization of Cr (VI) removal onto biosorbent eggshell membrane: Experimental & theoretical approaches. *Desalination Water Treat.* **2014**, *52*, 1307–1315.
218. Nasernejad, B.; Zadeh, T.E.; Pour, B.B.; Bygi, M.E.; Zamani, A. Camparison for biosorption modeling of heavy metals (Cr (III), Cu (II), Zn (II)) adsorption from wastewater by carrot residues. *Process Biochem.* **2005**, *40*, 1319–1322. [CrossRef]
219. Bai, R.S.; Abraham, T.E. Studies on chromium (VI) adsorption–desorption using immobilized fungal biomass. *Bioresour. Technol.* **2003**, *87*, 17–26.
220. Wen, Y.; Tang, Z.; Chen, Y.; Gu, Y. Adsorption of Cr (VI) from aqueous solutions using chitosan-coated fly ash composite as biosorbent. *Chem. Eng. J.* **2011**, *175*, 110–116. [CrossRef]
221. Chand, R.; Narimura, K.; Kawakita, H.; Ohto, K.; Watari, T.; Inoue, K. Grape waste as a biosorbent for removing Cr (VI) from aqueous solution. *J. Hazard. Mater.* **2009**, *163*, 245–250. [CrossRef] [PubMed]
222. Dönmez, G.; Aksu, Z. Removal of chromium (VI) from saline wastewaters by *Dunaliella species*. *Process Biochem.* **2002**, *38*, 751–762. [CrossRef]
223. Hadjmohammadi, M.R.; Salary, M.; Biparva, P. Removal of Cr (VI) from aqueous solution using pine needles powder as a biosorbent. *J. Appl. Sci. Environ. Sanit.* **2011**, *6*, 1–13.
224. Zhou, L.; Yi, Y.; Fang, Z. Nanoscale zero-valent iron immobilized by ZIF-8 metal-organic frameworks for enhanced removal of hexavalent chromium. *Chemosphere* **2022**, *306*, 135456. [CrossRef]
225. Maksoud, M.A.; Elgarahy, A.M.; Farrell, C.; Ala'a, H.; Rooney, D.W.; Osman, A.I. Insight on water remediation application using magnetic nanomaterials and biosorbents. *Coord. Chem. Rev.* **2020**, *403*, 213096. [CrossRef]

226. Gupta, V.K.; Ali, I.; Saleh, T.A.; Siddiqui, M.; Agarwal, S. Chromium removal from water by activated carbon developed from waste rubber tires. *Environ. Sci. Pollut. Res.* **2013**, *20*, 1261–1268. [CrossRef]
227. Holt, P.K.; Barton, G.W.; Mitchell, C.A. The future for electrocoagulation as a localised water treatment technology. *Chemosphere* **2005**, *59*, 355–367. [CrossRef]
228. Wang, L.K.; Hung, Y.-T.; Shammas, N.K. *Advanced Physicochemical Treatment Technologies*; Springer: Berlin/Heidelberg, Germany, 2007; Volume 5.
229. Jin, W.; Du, H.; Zheng, S.; Zhang, Y. Electrochemical processes for the environmental remediation of toxic Cr (VI): A review. *Electrochim. Acta* **2016**, *191*, 1044–1055. [CrossRef]
230. Qasem, N.A.; Mohammed, R.H.; Lawal, D.U. Removal of heavy metal ions from wastewater: A comprehensive and critical review. *npj Clean Water* **2021**, *4*, 36. [CrossRef]
231. Barrera-Díaz, C.E.; Lugo-Lugo, V.; Bilyeu, B. A review of chemical, electrochemical and biological methods for aqueous Cr (VI) reduction. *J. Hazard. Mater.* **2012**, *223–224*, 1–12. [CrossRef]
232. Emamjomeh, M.M.; Sivakumar, M. Review of pollutants removed by electrocoagulation and electrocoagulation/flotation processes. *J. Environ. Manag.* **2009**, *90*, 1663–1679. [CrossRef]
233. Arroyo, M.; Pérez-Herranz, V.; Montanes, M.; García-Antón, J.; Guinon, J. Effect of pH and chloride concentration on the removal of hexavalent chromium in a batch electrocoagulation reactor. *J. Hazard. Mater.* **2009**, *169*, 1127–1133. [CrossRef] [PubMed]
234. Kim, T.; Kim, T.-K.; Zoh, K.-D. Removal mechanism of heavy metal (Cu, Ni, Zn, and Cr) in the presence of cyanide during electrocoagulation using Fe and Al electrodes. *J. Water Process Eng.* **2020**, *33*, 101109. [CrossRef]
235. Lu, J.; Wang, Z.-R.; Liu, Y.-L.; Tang, Q. Removal of Cr ions from aqueous solution using batch electrocoagulation: Cr removal mechanism and utilization rate of in situ generated metal ions. *Process Saf. Environ. Prot.* **2016**, *104*, 436–443. [CrossRef]
236. Verma, S.K.; Khandegar, V.; Saroha, A.K. Removal of chromium from electroplating industry effluent using electrocoagulation. *J. Hazard. Toxic Radioact. Waste* **2013**, *17*, 146–152. [CrossRef]
237. Aber, S.; Amani-Ghadim, A.; Mirzajani, V. Removal of Cr (VI) from polluted solutions by electrocoagulation: Modeling of experimental results using artificial neural network. *J. Hazard. Mater.* **2009**, *171*, 484–490. [CrossRef]
238. Akbal, F.; Camcı, S. Copper, chromium and nickel removal from metal plating wastewater by electrocoagulation. *Desalination* **2011**, *269*, 214–222. [CrossRef]
239. Al-Shannag, M.; Al-Qodah, Z.; Bani-Melhem, K.; Qtaishat, M.R.; Alkasrawi, M. Heavy metal ions removal from metal plating wastewater using electrocoagulation: Kinetic study and process performance. *Chem. Eng. J.* **2015**, *260*, 749–756. [CrossRef]
240. Golder, A.K.; Samanta, A.N.; Ray, S. Trivalent chromium removal by electrocoagulation and characterization of the process sludge. *J. Chem. Technol. Biotechnol. Int. Res. Process Environ. Clean Technol.* **2007**, *82*, 496–503. [CrossRef]
241. Heidmann, I.; Calmano, W. Removal of Ni, Cu and Cr from a galvanic wastewater in an electrocoagulation system with Fe-and Al-electrodes. *Sep. Purif. Technol.* **2010**, *71*, 308–314. [CrossRef]
242. Vasudevan, S.; Lakshmi, J.; Sozhan, G. Studies on the Al–Zn–In-alloy as anode material for the removal of chromium from drinking water in electrocoagulation process. *Desalination* **2011**, *275*, 260–268. [CrossRef]
243. Mouedhen, G.; Feki, M.; De Petris-Wery, M.; Ayedi, H. Electrochemical removal of Cr (VI) from aqueous media using iron and aluminum as electrode materials: Towards a better understanding of the involved phenomena. *J. Hazard. Mater.* **2009**, *168*, 983–991. [CrossRef] [PubMed]
244. Mansoorian, H.J.; Mahvi, A.H.; Jafari, A.J. Removal of lead and zinc from battery industry wastewater using electrocoagulation process: Influence of direct and alternating current by using iron and stainless steel rod electrodes. *Sep. Purif. Technol.* **2014**, *135*, 165–175. [CrossRef]
245. Elabbas, S.; Ouazzani, N.; Mandi, L.; Berrekhis, F.; Perdicakis, M.; Pontvianne, S.; Pons, M.-N.; Lapicque, F.; Leclerc, J.-P. Treatment of highly concentrated tannery wastewater using electrocoagulation: Influence of the quality of aluminium used for the electrode. *J. Hazard. Mater.* **2016**, *319*, 69–77. [CrossRef]
246. Lu, J.; Fan, R.; Wu, H.; Zhang, W.; Li, J.; Zhang, X.; Sun, H.; Liu, D. Simultaneous removal of Cr (VI) and Cu (II) from acid wastewater by electrocoagulation using sacrificial metal anodes. *J. Mol. Liq.* **2022**, *359*, 119276. [CrossRef]
247. Hanay, Ö.; Hasar, H. Effect of anions on removing Cu^{2+}, Mn^{2+} and Zn^{2+} in electrocoagulation process using aluminum electrodes. *J. Hazard. Mater.* **2011**, *189*, 572–576. [CrossRef]
248. Mahmad, M.K.N.; Rozainy, M.M.R.; Abustan, I.; Baharun, N. Electrocoagulation process by using aluminium and stainless steel electrodes to treat total chromium, colour and turbidity. *Procedia Chem.* **2016**, *19*, 681–686. [CrossRef]
249. Merzouk, B.; Gourich, B.; Sekki, A.; Madani, K.; Chibane, M. Removal turbidity and separation of heavy metals using electrocoagulation–electroflotation technique: A case study. *J. Hazard. Mater.* **2009**, *164*, 215–222. [CrossRef]
250. Oussedik, S.M.; Khelifa, A. Reduction of copper ions concentration in wastewaters of galvanoplastic industry by electroflotation. *Desalination* **2001**, *139*, 383. [CrossRef]
251. Gao, P.; Chen, X.; Shen, F.; Chen, G. Removal of chromium (VI) from wastewater by combined electrocoagulation–electroflotation without a filter. *Sep. Purif. Technol.* **2005**, *43*, 117–123. [CrossRef]
252. da Mota, I.d.O.; de Castro, J.A.; de Góes Casqueira, R.; de Oliveira Junior, A.G. Study of electroflotation method for treatment of wastewater from washing soil contaminated by heavy metals. *J. Mater. Res. Technol.* **2015**, *4*, 109–113. [CrossRef]
253. Zodi, S.; Potier, O.; Lapicque, F.; Leclerc, J.-P. Treatment of the textile wastewaters by electrocoagulation: Effect of operating parameters on the sludge settling characteristics. *Sep. Purif. Technol.* **2009**, *69*, 29–36. [CrossRef]

254. Khandegar, V.; Saroha, A.K. Electrocoagulation for the treatment of textile industry effluent—A review. *J. Environ. Manag.* **2013**, *128*, 949–963. [CrossRef] [PubMed]
255. Zouboulis, A.; Matis, K.; Lazaridis, N.; Golyshin, P. The use of biosurfactants in flotation: Application for the removal of metal ions. *Miner. Eng.* **2003**, *16*, 1231–1236. [CrossRef]
256. Frenzel, I.; Holdik, H.; Barmashenko, V.; Stamatialis, D.F.; Wessling, M. Electrochemical reduction of dilute chromate solutions on carbon felt electrodes. *J. Appl. Electrochem.* **2006**, *36*, 323–332. [CrossRef]
257. Rodriguez-Valadez, F.; Ortiz-Éxiga, C.; Ibanez, J.G.; Alatorre-Ordaz, A.; Gutierrez-Granados, S. Electroreduction of Cr (VI) to Cr (III) on reticulated vitreous carbon electrodes in a parallel-plate reactor with recirculation. *Environ. Sci. Technol.* **2005**, *39*, 1875–1879. [CrossRef]
258. Almaguer-Busso, G.; Velasco-Martínez, G.; Carreño-Aguilera, G.; Gutiérrez-Granados, S.; Torres-Reyes, E.; Alatorre-Ordaz, A. A comparative study of global hexavalent chromium removal by chemical and electrochemical processes. *Electrochem. Commun.* **2009**, *11*, 1097–1100. [CrossRef]
259. Wang, H.; Na, C. Binder-free carbon nanotube electrode for electrochemical removal of chromium. *ACS Appl. Mater. Interfaces* **2014**, *6*, 20309–20316. [CrossRef]
260. Walsh, F.C. *A First Course in Electrochemical Engineering*; Electrochemical Consultancy: Romsey, UK, 1993.
261. Jin, W.; Yan, K. Recent advances in electrochemical detection of toxic Cr (VI). *RSC Adv.* **2015**, *5*, 37440–37450. [CrossRef]
262. Jin, W.; Zhang, Z.; Wu, G.; Tolba, R.; Chen, A. Integrated lignin-mediated adsorption-release process and electrochemical reduction for the removal of trace Cr (VI). *RSC Adv.* **2014**, *4*, 27843–27849. [CrossRef]
263. Wei, C.; German, S.; Basak, S.; Rajeshwar, K. Reduction of hexavalent chromium in aqueous solutions by polypyrrole. *J. Electrochem. Soc.* **1993**, *140*, L60–L62. [CrossRef]
264. Conroy, K.G.; Breslin, C.B. Reduction of hexavalent chromium at a polypyrrole-coated aluminium electrode: Synergistic interactions. *J. Appl. Electrochem.* **2004**, *34*, 191–195. [CrossRef]
265. Tian, Y.; Huang, L.; Zhou, X.; Wu, C. Electroreduction of hexavalent chromium using a polypyrrole-modified electrode under potentiostatic and potentiodynamic conditions. *J. Hazard. Mater.* **2012**, *225*, 15–20. [CrossRef] [PubMed]
266. Ruotolo, L.; Gubulin, J. Reduction of hexavalent chromium using polyaniline films. Effect of film thickness, potential and flow velocity on the reaction rate and polymer stability. *J. Appl. Electrochem.* **2003**, *33*, 1217–1222. [CrossRef]
267. Ruotolo, L.; Liao, A. Reaction rate and electrochemical stability of conducting polymer films used for the reduction of hexavalent chromium. *J. Appl. Electrochem.* **2004**, *34*, 1259–1263. [CrossRef]
268. Ruotolo, L.; Santos-Júnior, D.; Gubulin, J. Electrochemical treatment of effluents containing Cr (VI). Influence of pH and current on the kinetic. *Water Res.* **2006**, *40*, 1555–1560. [CrossRef]
269. Gao, M.; Zhang, G.; Zhang, G.; Wang, X.; Wang, S.; Yang, Y. The resistance to over-oxidation for polyaniline initiated by the resulting quinone-like molecules. *Polym. Degrad. Stab.* **2011**, *96*, 1799–1804. [CrossRef]
270. Kulikov, S.; Kulikova, O.; Scharkova, O.; Maximovskaya, R.; Kozhevnikov, I. Use of electromembrane technology for waste water treatment and modern acidic catalyst synthesis. *Desalination* **1996**, *104*, 107–111. [CrossRef]
271. Martí-Calatayud, M.C.; García-Gabaldón, M.; Pérez-Herranz, V. Study of the effects of the applied current regime and the concentration of chromic acid on the transport of Ni^{2+} ions through Nafion 117 membranes. *J. Membr. Sci.* **2012**, *392*, 137–149. [CrossRef]
272. Nataraj, S.; Hosamani, K.; Aminabhavi, T. Potential application of an electrodialysis pilot plant containing ion-exchange membranes in chromium removal. *Desalination* **2007**, *217*, 181–190. [CrossRef]
273. Chen, Q.; Luo, Z.; Hills, C.; Xue, G.; Tyrer, M. Precipitation of heavy metals from wastewater using simulated flue gas: Sequent additions of fly ash, lime and carbon dioxide. *Water Res.* **2009**, *43*, 2605–2614. [CrossRef] [PubMed]
274. Alvarado, L.; Ramírez, A.; Rodríguez-Torres, I. Cr (VI) removal by continuous electrodeionization: Study of its basic technologies. *Desalination* **2009**, *249*, 423–428. [CrossRef]
275. Xu, T.; Huang, C. Electrodialysis-based separation technologies: A critical review. *AIChE J.* **2008**, *54*, 3147–3159. [CrossRef]
276. Schlichter, B.; Mavrov, V.; Erwe, T.; Chmiel, H. Regeneration of bonding agents loaded with heavy metals by electrodialysis with bipolar membranes. *J. Membr. Sci.* **2004**, *232*, 99–105. [CrossRef]
277. Liu, L.; Chen, H.; Yang, X.; Tan, W.; Liu, C.; Dang, Z.; Qiu, G. High-efficiency As (III) oxidation and electrocoagulation removal using hematite with a charge-discharge technique. *Sci. Total Environ.* **2020**, *703*, 135678. [CrossRef]
278. Zaied, B.; Rashid, M.; Nasrullah, M.; Zularisam, A.; Pant, D.; Singh, L. A comprehensive review on contaminants removal from pharmaceutical wastewater by electrocoagulation process. *Sci. Total Environ.* **2020**, *726*, 138095. [CrossRef]
279. Ingelsson, M.; Yasri, N.; Roberts, E.P. Electrode passivation, faradaic efficiency, and performance enhancement strategies in electrocoagulation—A review. *Water Res.* **2020**, *187*, 116433. [CrossRef]
280. Korngold, E.; Belayev, N.; Aronov, L. Removal of chromates from drinking water by anion exchangers. *Sep. Purif. Technol.* **2003**, *33*, 179–187. [CrossRef]
281. Tiravanti, G.; Petruzzelli, D.; Passino, R. Pretreatment of tannery wastewaters by an ion exchange process for Cr (III) removal and recovery. *Water Sci. Technol.* **1997**, *36*, 197–207. [CrossRef]
282. El-Moselhy, M.M.; Hakami, O.M. Selective removal of chromate using hybrid anion exchanger. *Desalination Water Treat.* **2015**, *56*, 2917–2924. [CrossRef]

283. Zang, Y.; Yue, Q.; Kan, Y.; Zhang, L.; Gao, B. Research on adsorption of Cr (VI) by Poly-epichlorohydrin-dimethylamine (EPIDMA) modified weakly basic anion exchange resin D301. *Ecotoxicol. Environ. Saf.* **2018**, *161*, 467–473. [CrossRef] [PubMed]
284. Canning, W.; Co., L. *The Canning Handbook: Surface Finishing Technology, Integrated Design*; Springer: Berlin/Heidelberg, Germany, 1982.
285. Jardine, P.; Fendorf, S.; Mayes, M.; Larsen, I.; Brooks, S.; Bailey, W. Fate and transport of hexavalent chromium in undisturbed heterogeneous soil. *Environ. Sci. Technol.* **1999**, *33*, 2939–2944. [CrossRef]
286. Agrawal, S.G.; Fimmen, R.L.; Chin, Y.-P. Reduction of Cr (VI) to Cr (III) by Fe (II) in the presence of fulvic acids and in lacustrine pore water. *Chem. Geol.* **2009**, *262*, 328–335. [CrossRef]
287. Wang, Q.; Cissoko, N.; Zhou, M.; Xu, X. Effects and mechanism of humic acid on chromium (VI) removal by zero-valent iron (Fe0) nanoparticles. *Phys. Chem. Earth Parts A/B/C* **2011**, *36*, 442–446. [CrossRef]
288. Rivero-Huguet, M.; Marshall, W.D. Influence of various organic molecules on the reduction of hexavalent chromium mediated by zero-valent iron. *Chemosphere* **2009**, *76*, 1240–1248. [CrossRef]
289. Sun, J.; Mao, J.-D.; Gong, H.; Lan, Y. Fe (III) photocatalytic reduction of Cr (VI) by low-molecular-weight organic acids with α-OH. *J. Hazard. Mater.* **2009**, *168*, 1569–1574. [CrossRef]
290. Li, Y.; Cui, W.; Liu, L.; Zong, R.; Yao, W.; Liang, Y.; Zhu, Y. Removal of Cr (VI) by 3D TiO2-graphene hydrogel via adsorption enriched with photocatalytic reduction. *Appl. Catal. B Environ.* **2016**, *199*, 412–423. [CrossRef]
291. Naimi-Joubani, M.; Shirzad-Siboni, M.; Yang, J.-K.; Gholami, M.; Farzadkia, M. Photocatalytic reduction of hexavalent chromium with illuminated ZnO/TiO_2 composite. *J. Ind. Eng. Chem.* **2015**, *22*, 317–323. [CrossRef]
292. de Bittencourt, M.A.; Novack, A.M.; Scherer Filho, J.A.; Mazur, L.P.; Marinho, B.A.; da Silva, A.; de Souza, A.A.U.; de Souza, S.M.G.U. Application of $FeCl_3$ and TiO_2-coated algae as innovative biophotocatalysts for Cr (VI) removal from aqueous solution: A process intensification strategy. *J. Clean. Prod.* **2020**, *268*, 122164. [CrossRef]
293. Barakat, M. New trends in removing heavy metals from industrial wastewater. *Arab. J. Chem.* **2011**, *4*, 361–377. [CrossRef]
294. Crini, G.; Lichtfouse, E. Advantages and disadvantages of techniques used for wastewater treatment. *Environ. Chem. Lett.* **2019**, *17*, 145–155. [CrossRef]
295. Liu, Y.; Yang, D.; Xu, T.; Shi, Y.; Song, L.; Yu, Z.-Z. Continuous photocatalytic removal of chromium (VI) with structurally stable and porous Ag/Ag_3PO_4/reduced graphene oxide microspheres. *Chem. Eng. J.* **2020**, *379*, 122200. [CrossRef]
296. Li, N.; Tian, Y.; Zhao, J.; Zhang, J.; Zhang, J.; Zuo, W.; Ding, Y. Efficient removal of chromium from water by Mn_3O_4@ ZnO/Mn_3O_4 composite under simulated sunlight irradiation: Synergy of photocatalytic reduction and adsorption. *Appl. Catal. B Environ.* **2017**, *214*, 126–136. [CrossRef]
297. Du, X.-D.; Yi, X.-H.; Wang, P.; Zheng, W.; Deng, J.; Wang, C.-C. Robust photocatalytic reduction of Cr (VI) on UiO-66-NH2 (Zr/Hf) metal-organic framework membrane under sunlight irradiation. *Chem. Eng. J.* **2019**, *356*, 393–399. [CrossRef]
298. Qi, Y.; Fan, Y.; Liu, T.; Zheng, X. Flower-like hierarchical ZnS-Ga_2S_3 heterojunction for the adsorption-photo-reduction of Cr (VI). *Chemosphere* **2020**, *261*, 127824. [CrossRef]
299. Tian, X.; Gao, X.; Yang, F.; Lan, Y.; Mao, J.-D.; Zhou, L. uCatalytic role of soils in the transformation of Cr (VI) to Cr (III) in the presence of organic acids containing α-OH groups. *Geoderma* **2010**, *159*, 270–275. [CrossRef]
300. Idris, A.; Hassan, N.; Ismail, N.S.M.; Misran, E.; Yusof, N.M.; Ngomsik, A.-F.; Bee, A. Photocatalytic magnetic separable beads for chromium (VI) reduction. *Water Res.* **2010**, *44*, 1683–1688. [CrossRef]
301. Nasrallah, N.; Kebir, M.; Koudri, Z.; Trari, M. Photocatalytic reduction of Cr (VI) on the novel hetero-system $CuFe_2O_4$/CdS. *J. Hazard. Mater.* **2011**, *185*, 1398–1404. [CrossRef]
302. Wang, J.; Lv, Y.; Zhang, Z.; Deng, Y.; Zhang, L.; Liu, B.; Xu, R.; Zhang, X. Sonocatalytic degradation of azo fuchsine in the presence of the Co-doped and Cr-doped mixed crystal TiO_2 powders and comparison of their sonocatalytic activities. *J. Hazard. Mater.* **2009**, *170*, 398–404. [CrossRef]
303. Mu, R.; Xu, Z.; Li, L.; Shao, Y.; Wan, H.; Zheng, S. On the photocatalytic properties of elongated TiO_2 nanoparticles for phenol degradation and Cr (VI) reduction. *J. Hazard. Mater.* **2010**, *176*, 495–502. [CrossRef]
304. Yang, Q.-L.; Kang, S.-Z.; Chen, H.; Bu, W.; Mu, J. $La_2Ti_2O_7$: An efficient and stable photocatalyst for the photoreduction of Cr (VI) ions in water. *Desalination* **2011**, *266*, 149–153. [CrossRef]
305. Wang, N.; Zhu, L.; Deng, K.; She, Y.; Yu, Y.; Tang, H. Visible light photocatalytic reduction of Cr (VI) on TiO_2 in situ modified with small molecular weight organic acids. *Appl. Catal. B Environ.* **2010**, *95*, 400–407. [CrossRef]
306. Kim, G.; Choi, W. Charge-transfer surface complex of EDTA-TiO_2 and its effect on photocatalysis under visible light. *Appl. Catal. B Environ.* **2010**, *100*, 77–83. [CrossRef]
307. Gherbi, R.; Nasrallah, N.; Amrane, A.; Maachi, R.; Trari, M. Photocatalytic reduction of Cr (VI) on the new hetero-system $CuAl_2O_4$/TiO_2. *J. Hazard. Mater.* **2011**, *186*, 1124–1130. [CrossRef]
308. Yang, L.; Xiao, Y.; Liu, S.; Li, Y.; Cai, Q.; Luo, S.; Zeng, G. Photocatalytic reduction of Cr (VI) on WO_3 doped long TiO_2 nanotube arrays in the presence of citric acid. *Appl. Catal. B Environ.* **2010**, *94*, 142–149. [CrossRef]
309. Qamar, M.; Gondal, M.; Yamani, Z. Synthesis of nanostructured NiO and its application in laser-induced photocatalytic reduction of Cr (VI) from water. *J. Mol. Catal. A Chem.* **2011**, *341*, 83–88. [CrossRef]
310. Qamar, M.; Gondal, M.; Yamani, Z. Laser-induced efficient reduction of Cr (VI) catalyzed by ZnO nanoparticles. *J. Hazard. Mater.* **2011**, *187*, 258–263. [CrossRef]

311. Singh, R.; Kumar, A.; Kirrolia, A.; Kumar, R.; Yadav, N.; Bishnoi, N.R.; Lohchab, R.K. Removal of sulphate, COD and Cr (VI) in simulated and real wastewater by sulphate reducing bacteria enrichment in small bioreactor and FTIR study. *Bioresour. Technol.* **2011**, *102*, 677–682. [CrossRef]
312. Cheung, K.; Gu, J.-D. Mechanism of hexavalent chromium detoxification by microorganisms and bioremediation application potential: A review. *Int. Biodeterior. Biodegrad.* **2007**, *59*, 8–15. [CrossRef]
313. Zahoor, A.; Rehman, A. Isolation of Cr (VI) reducing bacteria from industrial effluents and their potential use in bioremediation of chromium containing wastewater. *J. Environ. Sci.* **2009**, *21*, 814–820. [CrossRef]
314. Kathiravan, M.N.; Karthick, R.; Muthukumar, K. Ex situ bioremediation of Cr (VI) contaminated soil by *Bacillus* sp.: Batch and continuous studies. *Chem. Eng. J.* **2011**, *169*, 107–115. [CrossRef]
315. Ng, T.W.; Cai, Q.; Wong, C.-K.; Chow, A.T.; Wong, P.-K. Simultaneous chromate reduction and azo dye decolourization by *Brevibacterium casei*: Azo dye as electron donor for chromate reduction. *J. Hazard. Mater.* **2010**, *182*, 792–800. [CrossRef]
316. Yu, X.; Jiang, Y.; Huang, H.; Shi, J.; Wu, K.; Zhang, P.; Lv, J.; Li, H.; He, H.; Liu, P. Simultaneous aerobic denitrification and Cr (VI) reduction by Pseudomonas brassicacearum LZ-4 in wastewater. *Bioresour. Technol.* **2016**, *221*, 121–129. [CrossRef] [PubMed]
317. An, Q.; Deng, S.; Xu, J.; Nan, H.; Li, Z.; Song, J.-L. Simultaneous reduction of nitrate and Cr (VI) by *Pseudomonas aeruginosa* strain G12 in wastewater. *Ecotoxicol. Environ. Saf.* **2020**, *191*, 110001. [CrossRef] [PubMed]
318. Xu, L.; Luo, M.; Li, W.; Wei, X.; Xie, K.; Liu, L.; Jiang, C.; Liu, H. Reduction of hexavalent chromium by *Pannonibacter phragmitetus* LSSE-09 stimulated with external electron donors under alkaline conditions. *J. Hazard. Mater.* **2011**, *185*, 1169–1176. [CrossRef]
319. Xu, L.; Yang, L.; Luo, M.; Liang, X.; Wei, X.; Zhao, J.; Liu, H. Reduction of hexavalent chromium by *Pannonibacter phragmitetus* LSSE-09 coated with polyethylenimine-functionalized magnetic nanoparticles under alkaline conditions. *J. Hazard. Mater.* **2011**, *189*, 787–793. [CrossRef]
320. Liu, L.; Yuan, Y.; Li, F.-B.; Feng, C.-H. In-situ Cr (VI) reduction with electrogenerated hydrogen peroxide driven by iron-reducing bacteria. *Bioresour. Technol.* **2011**, *102*, 2468–2473. [CrossRef]
321. Lin, Y.-H.; Wu, C.-L.; Li, H.-L.; Hsu, C.-H. Verification of model for adsorption and reduction of chromium (VI) by *Escherichia coli* 33456 using chitosan bead as a supporting medium. *Appl. Math. Model.* **2011**, *35*, 2736–2751. [CrossRef]
322. Liu, G.; Yang, H.; Wang, J.; Jin, R.; Zhou, J.; Lv, H. Enhanced chromate reduction by resting *Escherichia coli* cells in the presence of quinone redox mediators. *Bioresour. Technol.* **2010**, *101*, 8127–8131. [CrossRef]
323. Somasundaram, V.; Philip, L.; Bhallamudi, S.M. Laboratory scale column studies on transport and biotransformation of Cr (VI) through porous media in presence of CRB, SRB and IRB. *Chem. Eng. J.* **2011**, *171*, 572–581. [CrossRef]
324. Mangaiyarkarasi, M.M.; Vincent, S.; Janarthanan, S.; Rao, T.S.; Tata, B. Bioreduction of Cr (VI) by alkaliphilic *Bacillus subtilis* and interaction of the membrane groups. *Saudi J. Biol. Sci.* **2011**, *18*, 157–167. [CrossRef] [PubMed]
325. Fukuda, T.; Ishino, Y.; Ogawa, A.; Tsutsumi, K.; Morita, H. Cr (VI) reduction from contaminated soils by *Aspergillus* sp. N_2 and *Penicillium* sp. N_3 isolated from chromium deposits. *J. Gen. Appl. Microbiol.* **2008**, *54*, 295–303. [CrossRef] [PubMed]
326. Gola, D.; Dey, P.; Bhattacharya, A.; Mishra, A.; Malik, A.; Namburath, M.; Ahammad, S.Z. Multiple heavy metal removal using an entomopathogenic fungi Beauveria bassiana. *Bioresour. Technol.* **2016**, *218*, 388–396. [CrossRef] [PubMed]
327. Chakraborty, V.; Sengupta, S.; Chaudhuri, P.; Das, P. Assessment on removal efficiency of chromium by the isolated manglicolous fungi from Indian Sundarban mangrove forest: Removal and optimization using response surface methodology. *Environ. Technol. Innov.* **2018**, *10*, 335–344. [CrossRef]
328. Chatterjee, S.; Mahanty, S.; Das, P.; Chaudhuri, P.; Das, S. Biofabrication of iron oxide nanoparticles using manglicolous fungus *Aspergillus niger* BSC-1 and removal of Cr (VI) from aqueous solution. *Chem. Eng. J.* **2020**, *385*, 123790. [CrossRef]
329. Peng, H.; Guo, J. Removal of chromium from wastewater by membrane filtration, chemical precipitation, ion exchange, adsorption electrocoagulation, electrochemical reduction, electrodialysis, electrodeionization, photocatalysis and nanotechnology: A review. *Environ. Chem. Lett.* **2020**, *18*, 2055–2068. [CrossRef]
330. Hafiane, A.; Lemordant, D.; Dhahbi, M. Removal of hexavalent chromium by nanofiltration. *Desalination* **2000**, *130*, 305–312. [CrossRef]
331. Gasemloo, S.; Khosravi, M.; Sohrabi, M.R.; Dastmalchi, S.; Gharbani, P. Response surface methodology (RSM) modeling to improve removal of Cr (VI) ions from tannery wastewater using sulfated carboxymethyl cellulose nanofilter. *J. Clean. Prod.* **2019**, *208*, 736–742. [CrossRef]
332. Wu, S.; Ge, Y.; Wang, Y.; Chen, X.; Li, F.; Xuan, H.; Li, X. Adsorption of Cr (VI) on nano Uio-66-NH_2 MOF_s in water. *Environ. Technol.* **2018**, *39*, 1937–1948. [CrossRef]
333. Liu, H.; Sun, Y.; Yu, T.; Zhang, J.; Zhang, X.; Zhang, H.; Zhao, K.; Wei, J. Plant-mediated biosynthesis of iron nanoparticles-calcium alginate hydrogel membrane and its eminent performance in removal of Cr (VI). *Chem. Eng. J.* **2019**, *378*, 122120. [CrossRef]
334. Koushkbaghi, S.; Zakialamdari, A.; Pishnamazi, M.; Ramandi, H.F.; Aliabadi, M.; Irani, M. Aminated-Fe3O4 nanoparticles filled chitosan/PVA/PES dual layers nanofibrous membrane for the removal of Cr (VI) and Pb (II) ions from aqueous solutions in adsorption and membrane processes. *Chem. Eng. J.* **2018**, *337*, 169–182. [CrossRef]
335. Zhijiang, C.; Xianyou, S.; Qing, Z.; Yuanpei, L. Amidoxime surface modification of polyindole nanofiber membrane for effective removal of Cr (VI) from aqueous solution. *J. Mater. Sci.* **2017**, *52*, 5417–5434. [CrossRef]
336. Jo, J.H.; Shin, S.S.; Jeon, S.; Park, S.-J.; Park, H.; Park, Y.-I.; Lee, J.-H. Star polymer-assembled adsorptive membranes for effective Cr (VI) removal. *Chem. Eng. J.* **2022**, *449*, 137883. [CrossRef]

337. Okhovat, A.; Mousavi, S.M. Modeling of arsenic, chromium and cadmium removal by nanofiltration process using genetic programming. *Appl. Soft Comput.* **2012**, *12*, 793–799. [CrossRef]
338. Ozaki, H.; Sharma, K.; Saktaywin, W. Performance of an ultra-low-pressure reverse osmosis membrane (ULPROM) for separating heavy metal: Effects of interference parameters. *Desalination* **2002**, *144*, 287–294. [CrossRef]
339. Li, Y.; Lan, L.; Zhou, F.; Peng, J.; Guo, L.; Wang, F.; Zhang, Z.; Wang, L.; Mao, J. Flexible and easy-handling pristine polypyrrole membranes with bayberry-like vesicle structure for enhanced Cr (VI) removal from aqueous solution. *J. Hazard. Mater.* **2022**, *439*, 129598. [CrossRef]
340. Malek, A.; Hachemi, M.; Didier, V. New approach of depollution of solid chromium leather waste by the use of organic chelates: Economical and environmental impacts. *J. Hazard. Mater.* **2009**, *170*, 156–162. [CrossRef]
341. Shukla, M.; Baksi, B.; Mohanty, S.P.; Mahanty, B.; Mansi, A.; Rene, E.R.; Behera, S.K. Remediation of chromium contaminated soil by soil washing using EDTA and N-acetyl-L-cysteine as the chelating agents. *Prog. Org. Coat.* **2022**, *165*, 106704. [CrossRef]

Disclaimer/Publisher's Note: The statements, opinions and data contained in all publications are solely those of the individual author(s) and contributor(s) and not of MDPI and/or the editor(s). MDPI and/or the editor(s) disclaim responsibility for any injury to people or property resulting from any ideas, methods, instructions or products referred to in the content.

energies

MDPI

Essay

Study on Atomization and Dust Reduction Mechanisms of AEO-9-Charged Solution

Liying Sun, Shaocheng Ge *, Xi Chen and Shuo Liu

College of Safety and Emergency Management Engineering, Taiyuan University of Technology, Taiyuan 030024, China
* Correspondence: geshaocheng@163.com; Tel.: +86-134-5315-6217

Abstract: To effectively improve the dust reduction rate of fine dust and prevent the occurrence of secondary dust, surfactant-charged water mist dust reduction technology is proposed. First, the water mist induction-charged atomization mechanism was perfected by an induction-charged spray experiment and the optimal atomization-charged voltage was determined to be 10 kV. Second, by surface tension and spray experiments on AEO-9-charged solutions, the lower the surface tension and viscosity of the solution, the better the atomization effect; the best atomization solution was 10 kV and 0.02% AEO-9. Finally, according to an electrostatic adsorption experiment, it was identified that there was an electrostatic interaction between coal dust and charged droplets. The contact angle experiment showed that the contact angle of the AEO-9 droplets decreased by 68.44% compared with water after 3 s of contact with coal dust. The wetting effect of bituminous coal was significantly improved by adding AEO-9 to water. A molecular simulation was used to study the molecular interaction mechanism among the H_2O, AEO-9, and bituminous coal molecules. The simulation results showed that AEO-9 was more active than water, it easily interacted with bituminous coal, and the hydrophilic group covered the surface of the bituminous coal molecules, which increased the electrostatic interaction between the water molecules and bituminous coal surface molecules. After adding AEO-9 to H_2O, the intermolecular interaction energy of the H_2O/AEO-9/bituminous coal system was enhanced more than that of the H_2O/bituminous coal system. This study provides the basis for the application of surfactant-charged water mist dust reduction technology.

Keywords: AEO-9-charged solution; spray droplet size; charged and atomization mechanism; molecular simulation; dust reduction mechanism

Citation: Sun, L.; Ge, S.; Chen, X.; Liu, S. Study on Atomization and Dust Reduction Mechanisms of AEO-9-Charged Solution. *Energies* **2023**, *16*, 2800. https://doi.org/10.3390/en16062800

Academic Editors: Mohammad Mahmudur Rahman, Dibyendu Sarkar, Rupali Datta and Prafulla Kumar Sahoo

Received: 25 February 2023
Revised: 13 March 2023
Accepted: 15 March 2023
Published: 17 March 2023

Copyright: © 2023 by the authors. Licensee MDPI, Basel, Switzerland. This article is an open access article distributed under the terms and conditions of the Creative Commons Attribution (CC BY) license (https://creativecommons.org/licenses/by/4.0/).

1. Introduction

China is the largest coal producer in the world. Coal plays a major role in the country's energy consumption structure, but the dust pollution caused by the process of coal mining is a serious concern [1–3]. Currently, there is a high incidence rate of pneumoconiosis in China due to the presence of fine dust (PM2.5) as the main source of pollution. Fine dust adsorbs toxic and harmful gases into the human body, which can cause pneumoconiosis [4–6].

Charged and surfactant sprays are the two main components used to reduce dust [7–10] by decreasing the surface tension of water and increasing the activity of water molecules [11,12]. However, there are many limitations involved in this technique. In the charged spray dust reduction technique, the collision landing of the charged water mist and coal dust results in the disappearance of the charge of the water mist. Upon air drying the system, the settled fine dust rises with the wind and causes secondary dust pollution. The surfactant spray dust reduction increases the interaction between the coal dust and water mist, but there is no electrostatic attraction between them, resulting in a low collision efficiency. Surfactant-charged water dust reduction technology can maintain an effective collision rate and prevent secondary dust.

In the field of charged spray dust reduction, Teng et al. studied the influence of charging voltage, dust air velocity, and dust concentration on the dust reduction effect

through experiments [8]. D'Addio et al. studied the adsorption of 100~450 nm ultrafine particles by employing free-falling charged droplets. The results showed that the collection efficiency of the charged droplets on ultrafine particles was very significant [13]. Carotenuto et al. analyzed the influence of contact time between mist droplets and dust particles, water consumption, relative velocity of water/gas, and droplet size on the droplet-charged dust reduction effect and developed a mathematical model for charged spray dust reduction [14]. In the field of surfactant spray dust reduction, Yan et al. performed chemical modifications on sodium alginate and selected an environment-friendly and economical surfactant with high water retention, appropriate viscosity, and good wettability [15]. Sun et al. used starch, methyl methacrylate, acrylamide, and a surfactant as raw materials to prepare a dust suppressant with good wind resistance and hardness [16]. Chang et al. studied the dust reduction efficiency of different surfactant solutions through a wind tunnel test [17]. Although there have been remarkable advancements in the field of charged spray and surfactant spray dust reduction techniques, the performance and mechanisms of dust reduction of the combination of the two technologies remain to be further studied.

In this study, a highly efficient and environment-friendly fatty alcohol polyoxyethylene ether (AEO-9) was selected as the surfactant. By comparing the droplet size and the growth rate at different distances and charged voltages in a water mist induction-charged spray experiment, the mechanism of water mist induction-charged atomization was improved and the optimal charging voltage was determined. The surface tension values of the AEO-9 solution at different concentrations were also measured by a contact angle measuring instrument. Based on the surface tension values, three concentrations of AEO-9 solution were selected for the spray experiment and compared with the spray droplet size to determine the optimal AEO-9 concentration. The optimal charged voltage and concentration were then selected to compare the droplet size and the growth rate of the charged water mist, AEO-9 water mist, and AEO-9-charged water mist at different distances, and the atomization mechanism of the AEO-9-charged water mist was proposed. Finally, the dust reduction mechanism was revealed through an electrostatic adsorption experiment of the coal dust and charged droplets, a contact angle experiment of the AEO-9 solution at different concentrations, and a molecular simulation of the orbital information, electrostatic potential, and intermolecular interaction energy in different systems.

2. Experiment and Simulation

2.1. Experiment Details

2.1.1. Materials and Instruments

In this study, the purity of AEO-9 was $\geq$99%, produced from Shandong Yousuo Chemical Technology Co., Ltd., Qingdao, Shandong, China. The experimental coal sample was obtained from Lingshi County, Jinzhong, China. The coal samples were obtained by crushing and sieving; the particle size of the coal dust was $\leq$74 μm. The prepared coal dust was placed in a desiccator for storage.

The instruments and models used for the experiment are shown in Table 1.

Table 1. Experimental instruments and models.

Equipment Name	Model
Ball mill	GMJ–2
Vibrating screen	BZS−−300 mm
Vacuum drying oven	101–00AS
Air compressor	1500–2
High–voltage electrostatic DC generator (−)	TD2202N50–2000–A03
Blender	ZH18T
Laser particle size analyzer	HELOS (H4116) and UNIVERSAL
Magnetic stirrer	SN–MS–H
Contact angle measuring instrument	SDC–350
Tableting machine	YP–15

2.1.2. Measurement of the Droplet Size of the Spray

To measure the fog droplet size, a fog droplet measurement platform was built, as shown in Figure 1.

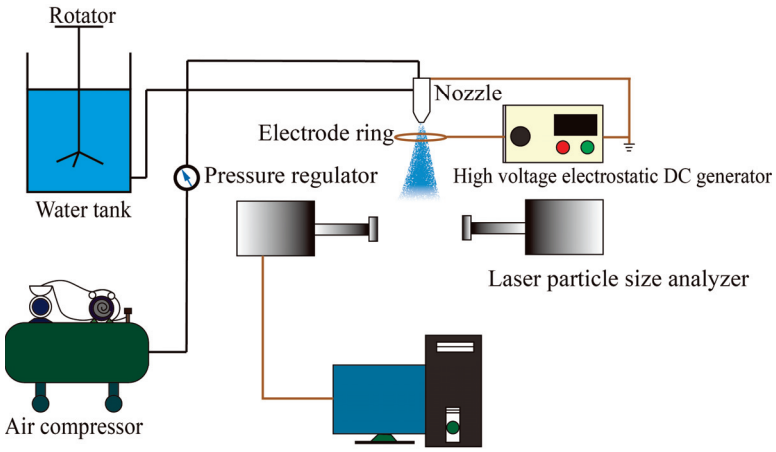


Figure 1. Schematic diagram of the experimental device.

It mainly included a water tank, rotator, air compressor, pressure regulator, siphon air atomization nozzle (grounded), electrode ring, high-voltage electrostatic DC generator (−), and laser particle size analyzer. The relevant parameters were set to 0.005%, 0.02%, and 0.04% mass concentration of the AEO-9 solution; 0.4 MPa atomization air pressure; 1 mm nozzle aperture (grounded); 50 mm electrode ring diameter; 5 kV, 10 kV, and 15 kV charged voltages; and 0.01 μm measurement accuracy of the laser particle size analyzer [18], which was characterized by the volume mean droplet (VMD) size. The measurement process was as follows: the AEO-9 solution was continuously stirred using a mixer, the air compressor was turned on, the water mist was ejected, the electrode ring was located in front of the nozzle and connected to a negative high-voltage electrostatic DC generator (grounded) to charge the water mist, and finally the water mist droplet sizes at 5 cm, 30 cm, 60 cm, 90 cm, and 120 cm away from the nozzle were measured by the laser particle size analyzer.

2.1.3. Measurement of the Surface Tension and Contact Angle

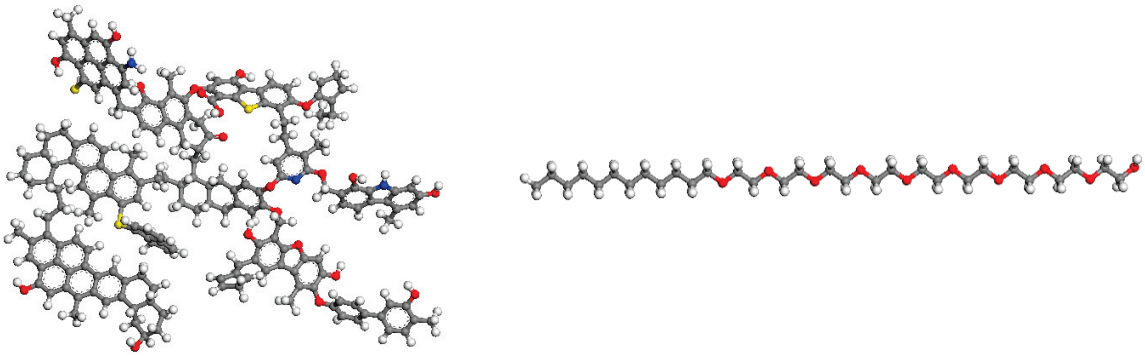
The AEO-9 solutions with mass concentrations of 0.005%, 0.007%, 0.01%, 0.02%, 0.03%, 0.04%, and 0.05% were taken, and their surface tension was determined using the contact angle measuring instrument. The measurement accuracy was 0.001 mN/m. We turned on the automatic liquid supply and surface tension measurement function, and the surface tension value of the solution was measured when the droplets broke up instantaneously. In addition, the surface tension and contact angle of the 0.02% AEO-9 and water solution were measured, and the measurement accuracy was 0.001°. First, the coal sheet was prepared in a tableting machine under a coal dust mass of 50 mg, pressure of 20 MPa, and time of 1 min. We then placed the prepared coal sheet on the workbench, adjusted the workbench and injector, and started the drip. When the droplets were about to fall, we opened the continuous shooting function to capture the instantaneous contact between the droplets and the coal sheet. The automatic fitting method was used to measure the contact angle of the coal dust.

2.1.4. Electrostatic Adsorption Experiment for Coal Dust and Charged Droplet

The experiment was performed using a contact angle measuring instrument and a negative high-voltage electrostatic DC generator. The negative high-voltage electrostatic DC generator was connected to the metal part of the syringe and grounded. The charged voltage was set to 3 kV. About 50 mg of coal dust was placed directly below the charged droplets. The distance between the charged droplets and coal dust was varied to observe the motion state.

2.2. Simulation Details

In this paper, a classical Wiser bituminous coal model [19,20] was used. The molecular structures of the bituminous coal and AEO-9 are presented in Figure 2.

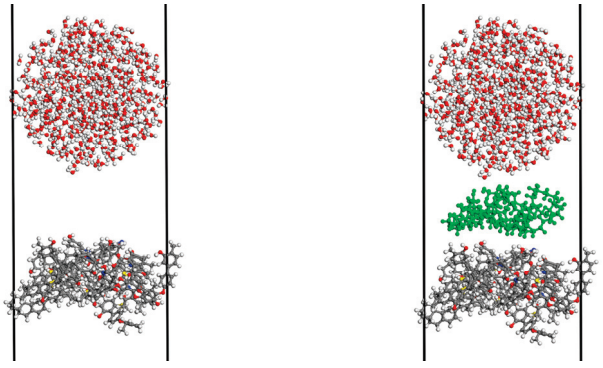


(**a**) $C_{191}H_{169}N_3O_{21}S_3$ (**b**) $C_{30}H_{62}O_{10}$

Figure 2. Molecular models: (**a**) bituminous coal; (**b**) AEO-9. The red, grey, white, yellow, and blue balls represent O, C, H, S, and N, respectively.

The HOMO orbital information, LOMO orbital information, and molecular surface electrostatic potential were obtained through a quantum mechanical simulation. The relevant parameters were set as follows: the module was Doml3, the task was geometry optimization, the quality was fine, the maximum iterations were 500, the functional was GGA, the employed method was BLYP, and the basis set was DNP.

The AC module was used to construct H_2O sphere, AEO-9, and bituminous coal molecule crystal models [21,22]. The water molecular density was set to 0.98 and the spherical diameter was set to 30 Å. The number of AEO-9 and bituminous coal molecules were 2 and 3, respectively. The build layer tool was then used to build the water/bituminous coal and water/AEO-9/bituminous coal models. The size of the models was 30 Å × 30 Å × 150 Å, as shown in Figure 3. First, the geometry optimization of the water/bituminous coal and the water/AEO-9/bituminous coal system was performed by the Forcite module, and the bond length, bond angle, and molecular configuration of the molecules in the systems were optimized. The relevant parameters were set as follows: the quality was ultrafine, maximum iterations were 50,000, the forcefield was compass II, the electrostatic summation method was Ewald, and the van der Waals summation method was Ewald. After optimization, a molecular dynamic simulation was performed under the relevant parameters mentioned as follows: the canonical ensemble (NVT) was selected, the thermostat was set as Nose, and the total simulation time was 1000 ps (the temperature and energy tended to be stable, and the systems had reached an equilibrium) [23].



(**a**) (**b**)

Figure 3. Different system models: (**a**) H_2O/bituminous coal; (**b**) H_2O/AEO-9/bituminous coal.

Although the molecular simulation conditions differed from the experimental conditions, the setting of the above two system parameters was the same. Therefore, by comparing the interaction energy of the two systems, the wetting properties and mechanism of the AEO-9 solution on bituminous coal could be qualitatively determined.

3. Results and Discussion

3.1. Water Mist Induction-Charged Atomization Mechanism

Figure 4 presents the water mist droplet size at different distances and charged voltages. At 0 kV and a 5 cm distance, the water mist droplet size was larger than it was at 5 kV and 10 kV. In the range of 30–120 cm, the droplet size of the water mist under 0 kV was less than that of the charged water mist. Based on former research [24] and the above results, the mechanism of the water mist-induced charged atomization was perfected, as shown in Figure 5. An electrode ring was placed directly below the nozzle, and an electric field was formed between the nozzle and the electrode ring [25]. According to the principle of induced charging, when the water mist was sprayed from the nozzle, a thick electric double layer was formed at the contact between the water and the nozzle. Under the action of the electrostatic field, the water mist carried positive charges, and the negative charges of the electric double layer were introduced into the earth from the nozzle. The water mist contained the same charges; thus, they repelled each other, leading to the breakup of the droplets. When the positive water mist passed through the negative electrode ring, there was a higher voltage difference between the electrode ring and the droplets. When the distance between the droplets and the electrode ring was small, the air was broken down and part of the droplets carried negative charges. After the water mist left the electrode ring, a large number of positive and negative charges remained within the system. With the increase in the distance, the droplets reunited under the action of static electricity and hydrogen bonding. The larger the growth rate of the spray droplets' size, the better the spray charging effect.

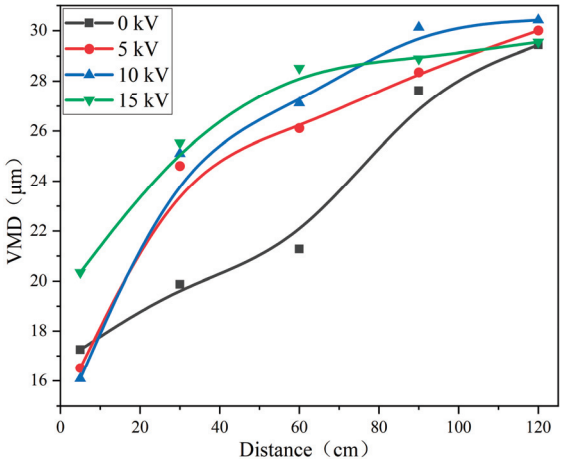


Figure 4. The water mist droplet size at different distances and charged voltages.

Figure 6 shows the growth rate of the spray droplets' size at different distances and charging voltages; the optimum charge voltage was 10 kV. With the increase in the induction-charged voltage, an optimal value was observed for the charged effect of the droplets because a corona discharge occurred after the voltage reached a certain value. The corona discharge was opposite to the charge of the induced charged spray droplets [18] and attracted each other. Therefore, the VMD was the largest at a distance of 5 cm and 15 kV.

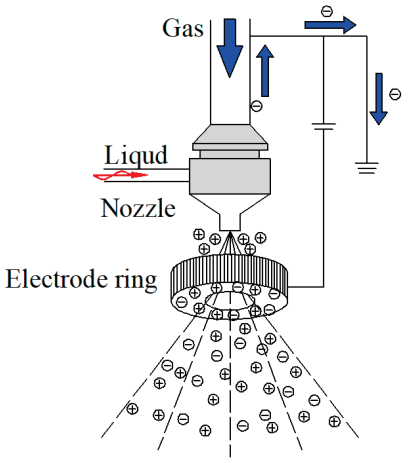


Figure 5. The water mist-induced charged atomization mechanism.

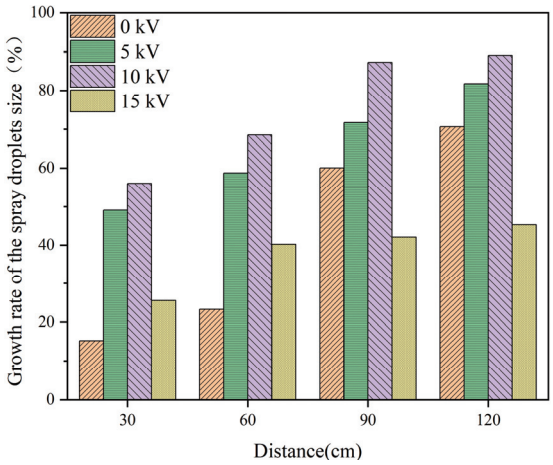


Figure 6. The growth rate of the spray droplets at different distances and charging voltages.

3.2. Atomization Mechanism of the AEO-9-Charged Solution

3.2.1. The Atomization Effect of the AEO-9 Solution

Figure 7 shows the surface tension of different concentrations of the AEO-9 solution. With the increase in concentration, the surface tension initially decreased and tended to stabilize when the concentration reached 0.02%, reaching a critical micelle concentration. Therefore, three concentrations—namely, 0.005%, 0.02%, and 0.04%—were selected for the spray experiments.

Figure 8 shows the spray droplet size of the AEO-9 solution with different concentrations and distances. The spray droplet size of 0.02% AEO-9 solution was the smallest. Although the surface tensions of 0.005% and 0.04% AEO-9 solutions were less than that of water, the viscosity was larger than that of water, which plays a major role, so the atomization effect of the water solution was better. Based on the above results, surface tension and viscosity together determined the atomization effect of the AEO-9 solution. In this study, the optimal atomization concentration of the AEO-9 solution was found to be 0.02%.

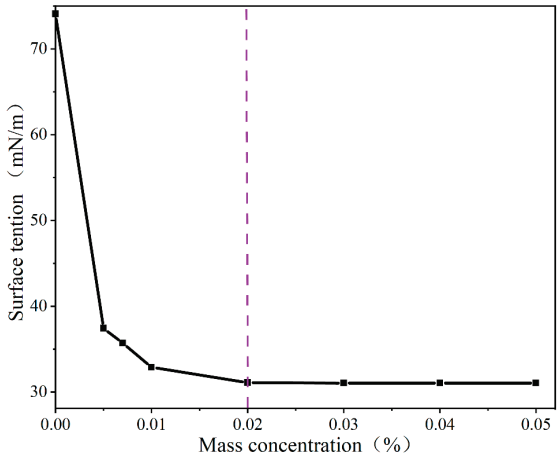


Figure 7. The surface tension of the AEO-9 solution at different concentrations.

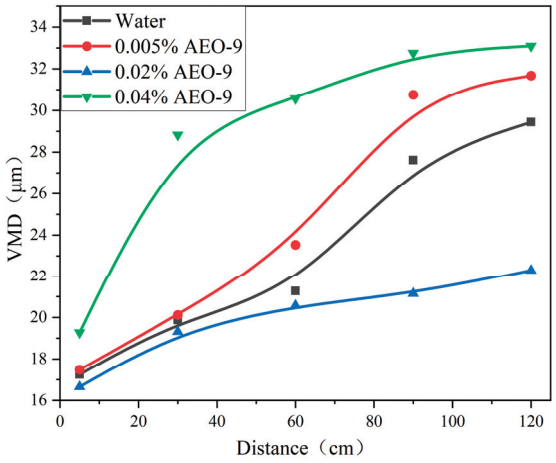


Figure 8. The spray droplet size of the AEO-9 solution at different concentrations.

3.2.2. Atomization Effect of the AEO-9-Charged Solution

Figure 9 shows the spray droplet size of 10 kV water, 0.02% AEO-9, and 10 kV and AEO-9 solutions. At 5 cm, the order of the spray droplet sizes of different solutions were 10 kV water < 10 kV and 0.02% AEO-9 < 0.02% AEO-9 because of the low viscosity and surface tension of 10 kV water (according to Figure 10). Figure 10 shows the surface tensions and shapes of 0.02% AEO-9 and water droplets at different charged voltages. With a further increase in the charged voltage, the surface tension of the droplets gradually decreased, resulting in the breakage of droplets. When the charged voltage was 10 kV, the AEO-9-charged droplets and water-charged droplets could not maintain their spherical shape and dripped continuously from the syringe. As the viscosity of water was relatively low, the droplet size was smaller. For 10 kV and 0.02% AEO-9 and 0.02% AEO-9 solutions, the viscosity was the same, but the surface tension of the former was lower (according to Figure 10), so the droplet size of 10 kV and 0.02% AEO-9 was slightly smaller.

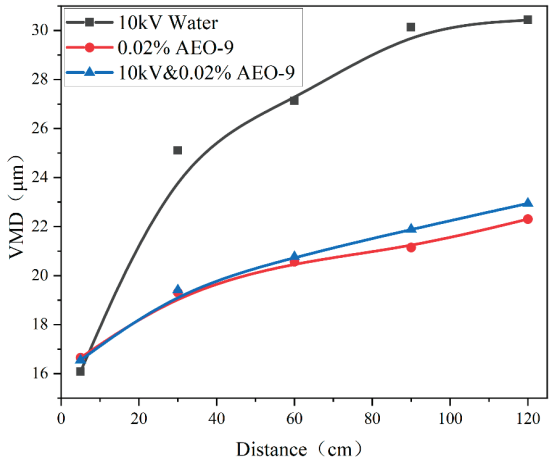
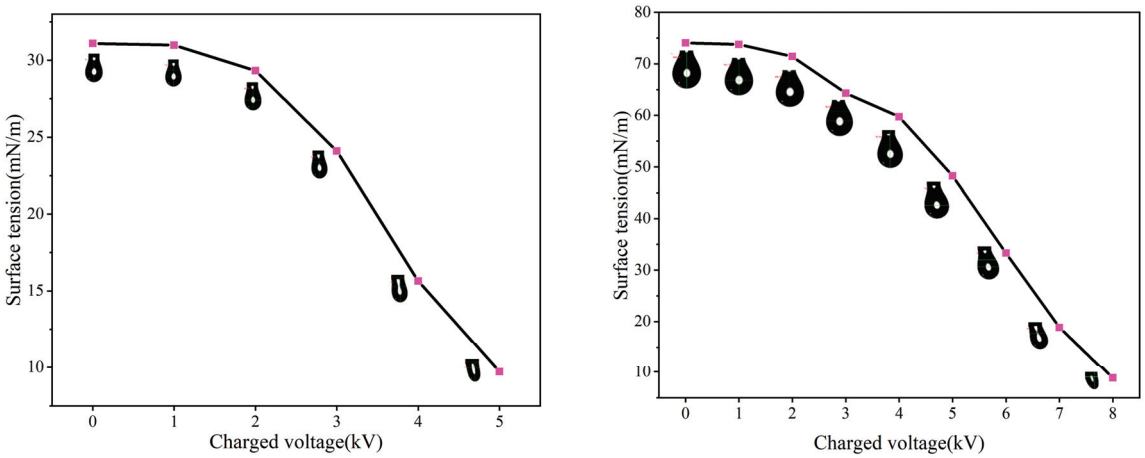


Figure 9. The water mist droplet size of 10 kV water, 0.02% AEO-9, and 10 kV and AEO-9.



(**a**) (**b**)

Figure 10. The surface tensions and shapes of droplets under different charged voltages: (**a**) 0.02% AEO-9-charged; (**b**) water-charged.

The droplets' reunion with the increase in distance and the growth rate of the spray droplet size is shown in Figure 11. Along 30–120 cm, the order of the droplets' reunion rate was 0.02% AEO-9 < 10 kV and 0.02% AEO-9 < 10 kV water. According to the water mist-induced charged principle as described in Section 3.1, more positive and negative charges accumulated in the spray with a higher spray droplet growth rate, and the better the charged effect. At 0–120 cm, considering the charged and atomization effect of the different solutions, the optimal solution was found to be 10 kV and 0.02% AEO-9.

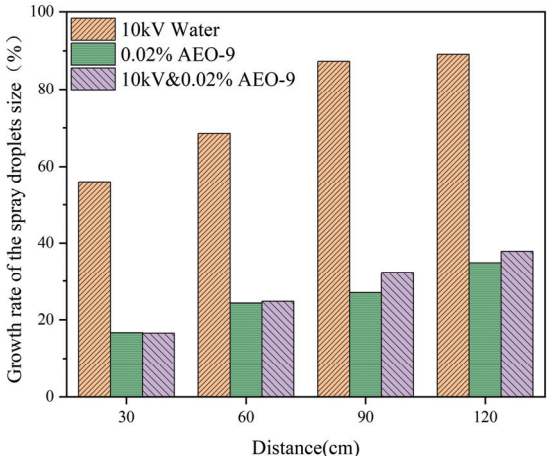


Figure 11. The droplet size growth rate of 10 kV water, 0.02% AEO-9, and 10 kV and 0.02% AEO-9.

3.3. Dust Reduction Mechanism of the AEO-9-Charged Solution

3.3.1. Electrostatic Adsorption Process

The schematic diagram of the interaction between 0.02% AEO-9-charged droplets and coal dust particles is given in Figure 12. As the distance between the coal dust particles and AEO-9-charged droplets decreased, the AEO-9-charged droplets gradually stretched and the electrostatic interaction between them was enhanced. This was mainly because the AEO-9-charged droplets induced positive and negative charges. As the distance between the droplets and coal dust particles decreased, the surface of the coal dust particles induced opposite charges under the action of mirroring force, increasing the electrostatic interaction between the two. The smaller the distance, the stronger the electrostatic interaction between the two. In summary, the AEO-9 solution was charged, increasing the dynamic collision probability between the coal dust particles and spray droplets.

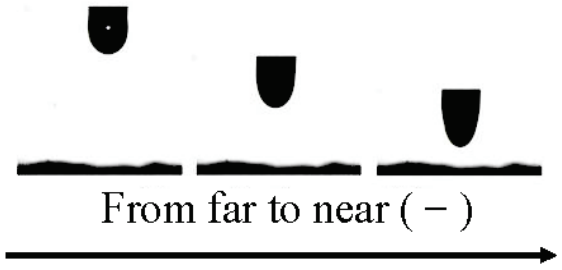


Figure 12. The interaction between the 0.02% AEO-9-charged droplets and coal dust particles.

3.3.2. Process and Contact Angle of Droplet-Wetting Coal Dust

After the combination of coal dust and charged droplets, the wettability of the droplets to coal dust determines the dust reduction efficiency. The contact angle is an important index to evaluate the wettability of a solution. The wettability is enhanced with a decrease in the contact angle [26,27]. Figure 13 is the wetting process and contact angle of water and 0.02% AEO-9 droplets to coal dust (time interval of 1 s). As the time changed, the droplets were slowly immersed in coal dust and the contact angle gradually decreased. After adding AEO-9 into the water, the contact angle decreased and the wettability increased.

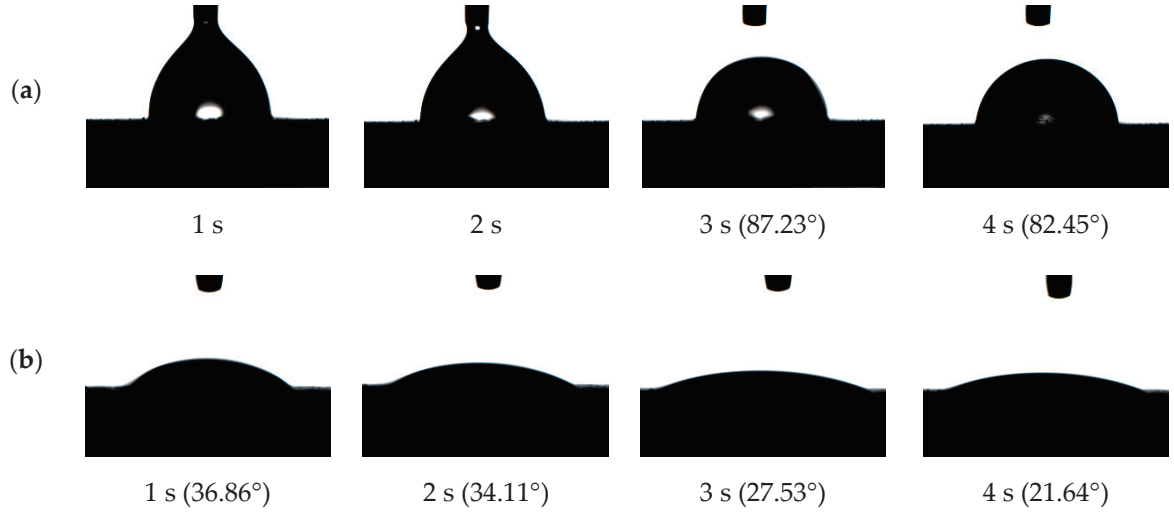


Figure 13. The wetting process and contact angle of the different solutions to coal dust: (**a**) water; (**b**) 0.02% AEO-9.

3.3.3. Front Orbital Analysis

The activities of the H_2O and AEO-9 molecules were determined by obtaining the energy values of the HOMO and LOMO orbitals. The HOMO occupies the highest energy and generally promotes the loss of electrons. As the energy of the HOMO level increases, the ability to lose electrons is enhanced. The LUMO occupies the lowest energy and usually accepts electrons. With the decrease in the energy of the LUMO level, there is an enhancement in the electron-accepting nature. The molecular activity becomes stronger with the decrease in the energy difference between the HOMO and LUMO levels [28,29]. Table 2 shows the HOMO and LOMO orbital energy information of the H_2O and AEO-9 molecules. AEO-9 showed a higher electron loss and electron acceptance capacity than H_2O. The difference between the two values of AEO-9 was less than H_2O. Therefore, the activity of AEO-9 was higher than that of H_2O, which effectively combined the bituminous coal molecules.

Table 2. HOMO and LOMO orbital energy values of H_2O and AEO-9 molecules.

Molecules	HOMO (Hartree/e)	LOMO (Hartree/e)	ΔE (Hartree/e)
H_2O	0.0313	−0.2458	0.2771
AEO-9	0.0173	−0.2049	0.2222

3.3.4. Electrostatic Potential Analysis

The electrostatic potential of molecules reflects the electrostatic interaction among them [23,30]. Figure 14 displays the electrostatic potential of the H_2O, AEO-9, and bituminous coal molecules. Table 3 shows the electrostatic potential values of the different molecules. The maximum positive potential of the bituminous coal was greater than that of H_2O, and the maximum negative potential was less than that of H_2O. The electrostatic attraction of H atoms connected with the O, N, and S atoms in the bituminous coal to the O atom in H_2O was greater than that of H atoms in H_2O, and the electrostatic attraction of O, N, S, and the benzene ring to the H atoms in H_2O was less than that of the O atom in H_2O. However, the proportion of H atoms connected to the O, N, and S atoms of the bituminous coal molecules was small, and the electrostatic effect between H_2O was stronger, leading to poor wettability of the water with the bituminous coal molecules.

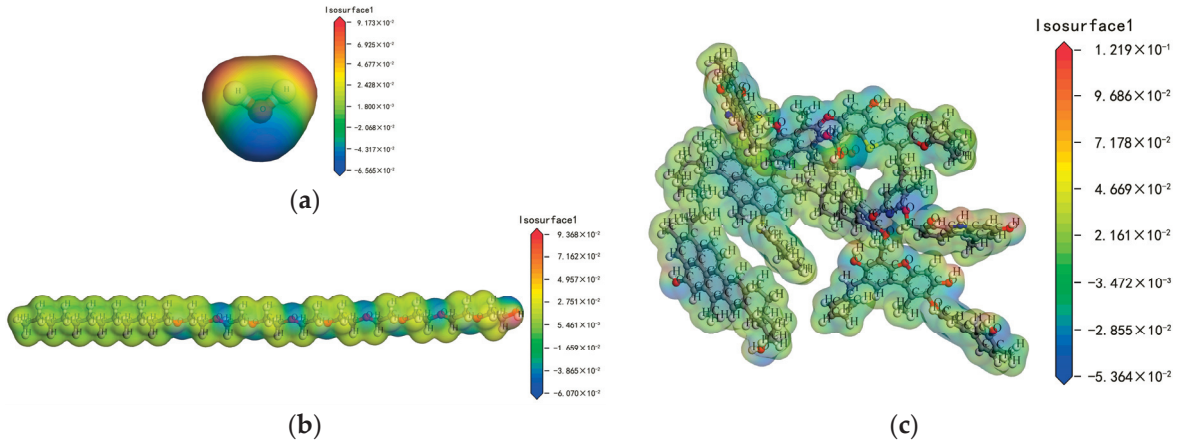


Figure 14. The electrostatic potential of different molecules: (**a**) H_2O; (**b**) AEO-9; (**c**) bituminous coal.

Table 3. The molecular electrostatic potential values of H2O, AEO-9, and bituminous coal.

Molecules	Maximum Positive Potential (Hartree/e)	Location	Maximum Negative Potential (Hartree/e)	Location
H_2O	0.09173	Near H	−0.06565	Near O
AEO-9	0.09368	Near hydroxyl H	−0.0607	Near ether group and hydroxyl O
Bituminous coal	0.1219	Near H connected with O, N, and S	−0.05364	Near O, N, S, and the benzene ring

The addition of AEO-9 in water connected with the H_2O and bituminous coal molecules, changing the hydrophobicity of the bituminous coal. The maximum positive potential of AEO-9 was greater than that of H_2O, and the maximum negative potential was less than that of H_2O. The electrostatic attraction of the hydroxyl H atom in AEO-9 to the O atom in H_2O was greater than that of the H atoms in H_2O. The electrostatic attractions of the O atom in the ether and hydroxyl groups to the H atoms in H_2O were less than that of the O atom in H_2O. However, the number of H atoms in H_2O was greater than that of the O atom, so a part of the H_2O attracted the O atoms in the ether and hydroxyl groups of AEO-9, which caused the number of hydrogen bonds between the H_2O molecules to be reduced from 825 to 801. Therefore, the hydrogen bond interaction between the water molecules was weakened and the activity of the water molecules was enhanced. The corresponding electrostatic potential of the hydrophobic group in AEO-9 was near 5.461×10^{-3} Hartree/e. Under an electrostatic interaction, the hydrophobic groups were attached to the O, N, S, and benzene rings of the bituminous coal molecules.

3.3.5. Intermolecular Interaction Energy Analysis

The interaction energy characterizes the intermolecular interaction of the simulated system. The higher the interaction energy, the better the wettability of the coal dust [31,32]. In this paper, the potential energy was chosen to characterize the interaction energy of the simulation system, which was mainly composed of electrostatic and van der Waals energies. Table 4 displays the interaction energy of the different simulation systems. Upon the addition of AEO-9 to water, the electrostatic energy and van der Waals energy were increased between the water and bituminous coal molecules, and the wettability of the bituminous coal was improved.

Table 4. The interaction energy of different simulation systems.

System	Potential Energy (kcal/mol)	Electrostatic Energy (kcal/mol)	van der Waals Energy (kcal/mol)
H_2O/bituminous coal	−378.284	−286.405	−87.553
H_2O/AEO-9/bituminous coal	−499.718	−309.297	−186.757

4. Conclusions

The water mist induction charging mechanism was under the action of the electric field between the nozzle and the electrode ring. The water mist carried a large amount of positive charge, and the negative charges of the electric double layer flowed into the earth from the nozzle. When the water mist with a positive charge passed through the electrode ring with a negative charge, there was a high-voltage difference between the electrode ring and the water mist. The distance between the water mist and the electrode ring was small; under the action of the voltage difference, the air decomposed and part of the water mist had a negative charge. When the water mist left the electrode ring, the water mist contained a large number of positive and negative charges.

The droplet size of the AEO-9-charged solution decreased with the decrease in surface tension and viscosity of the solution. The optimal atomized solution was 10 kV and 0.02% AEO-9. As the spray distance increased, the AEO-9-charged droplets reunited under the action of electrostatic and hydrogen bonds, thus increasing the size of the droplets.

Compared with the water solution, the AEO-9-charged solution increased the electrostatic adsorption between the coal dust particles and droplets. It reduced the contact angle of the AEO-9 solution on the surface of the coal dust and increased the wettability of the coal dust.

The mechanism of the AEO-9 solution in improving the wettability of coal dust was revealed at a micro-level by a molecular simulation: the electron loss and electron-accepting ability of the AEO-9 molecule was higher than the H_2O molecule, which was effectively combined with the bituminous coal molecule. Under an electrostatic interaction between the H_2O and AEO-9 molecules, the number of hydrogen bonds between the H_2O molecules was reduced, resulting in the hydrogen bond interaction between the water molecules being weakened and the activity of the water molecules being enhanced. After AEO-9 was added to water, the electrostatic energy and van der Waals energy among the molecules in the system were enhanced, which improved the wetting ability of water on bituminous coal.

Author Contributions: Conceptualization, L.S., S.G. and S.L.; Methodology, L.S., S.G. and S.L.; Software, L.S. and S.L.; Validation, S.G. and X.C.; Formal Analysis, L.S.; Investigation, L.S.; Resources, L.S.; Data Curation, S.L.; Writing—Original Draft Preparation, L.S.; Writing—Review and Editing, S.G.; Visualization, L.S.; Supervision, S.G.; Project Administration, X.C.; Funding Acquisition, S.G. All authors have read and agreed to the published version of the manuscript.

Funding: This work was supported by the Transformation of Scientific and Technological Achievements Programs of Higher Education Institutions in Shanxi (grant number 2020CG022), the Youth Science Fund of the National Natural Science Foundation of China (grant number 51704145), and the Study on the Mechanism of Permeability and Wetting Improvement Induced By Sonic Blasting Fluctuating Activated Water Injection For Dust Suppression (grant number 52174195).

Data Availability Statement: The data from this study are available from the corresponding author upon request.

Conflicts of Interest: The authors declare no conflict of interest.

References

1. Jing, D.; Jia, X.; Ge, S.; Zhang, T.; Ma, M. Numerical simulation and experimental study of vortex blowing suction dust control in a coal yard with multiple dust production points. *Powder Technol.* **2021**, *388*, 554–565. [CrossRef]
2. Jing, D.; An, R.; Chen, J.; Ge, S.; Sun, L. Study on the Atomization and Dust-Reduction Performance of a New Type of External Pneumatic Vortex Fog Curtain Dust Removal Device in Fully Mechanized Excavation Face. *Adv. Mater. Sci. Eng.* **2020**, *2020*, 8356456. [CrossRef]
3. Yang, L.; Ge, S.; Huang, Z.; Jing, D.; Chen, X. The influence of surfactant on the wettability of coal dust and dust reduction efficiency. *Arab. J. Geosci.* **2021**, *14*, 1336. [CrossRef]
4. Li, B.; Yang, J.; Dong, H.; Li, M.; Cai, D.; Yang, Z.; Zhang, C.; Wang, H.; Hu, J.; Bergmann, S.; et al. PM2.5 constituents and mortality from a spectrum of causes in Guangzhou, China. *Ecotoxicol. Environ. Saf.* **2021**, *222*, 112498. [CrossRef]
5. Li, Y.; Li, C.; Liu, J.; Meng, C.; Xu, C.; Liu, Z.; Wang, Q.; Liu, Y.; Han, J.; Xu, D. An association between PM(2.5) and pediatric respiratory outpatient visits in four Chinese cities. *Chemosphere* **2021**, *280*, 130843. [CrossRef]
6. Nirmalkar, J.; Haswani, D.; Singh, A.; Kumar, S.; Raman, R.S. Concentrations, transport characteristics, and health risks of PM(2.5)-bound trace elements over a national park in central India. *J. Environ. Manag.* **2021**, *293*, 112904. [CrossRef]
7. Shi, G.; Qi, J.; Wang, Y.; Liu, S. Experimental study on the prevention of coal mine dust with biological dust suppressant. *Powder Technol.* **2021**, *391*, 162–172. [CrossRef]
8. Teng, C.; Li, J. Experimental Study on Particle Removal of a Wet Electrostatic Precipitator with Atomization of Charged Water Drops. *Energy Fuels* **2020**, *34*, 7257–7268. [CrossRef]
9. Tessum, M.W.; Raynor, P.C. Effects of Spray Surfactant and Particle Charge on Respirable Coal Dust Capture. *Saf. Health Work.* **2017**, *8*, 296–305. [CrossRef]
10. Zhou, L.; Yang, S.; Hu, B.; Yuan, Z.; Wu, H.; Yang, L. Evaluating of the performance of a composite wetting dust suppressant on lignite dust. *Powder Technol.* **2018**, *339*, 882–893. [CrossRef]
11. Zillgitt, M.; Schmidt, E. Determination of Operating Parameters for the Use of an Electrostatically Charged Water Spray Mist. *Chem. Eng. Technol.* **2021**, *44*, 1178–1184. [CrossRef]
12. Yao, Q.; Xu, C.; Zhang, Y.; Zhou, G.; Zhang, S.; Wang, D. Micromechanism of coal dust wettability and its effect on the selection and development of dust suppressants. *Process. Saf. Environ. Prot.* **2017**, *111*, 726–732. [CrossRef]
13. D'Addio, L.; Carotenuto, C.; Balachandran, W.; Lancia, A.; Di Natale, F. Experimental analysis on the capture of submicron particles (PM0.5) by wet electrostatic scrubbing. *Chem. Eng. Sci.* **2014**, *106*, 222–230. [CrossRef]
14. Carotenuto, C.; Di Natale, F.; Lancia, A. Wet electrostatic scrubbers for the abatement of submicronic particulate. *Chem. Eng. J.* **2010**, *165*, 35–45. [CrossRef]
15. Yan, J.; Nie, W.; Zhang, H.; Xiu, Z.; Bao, Q.; Wang, H.; Jin, H.; Zhou, W. Synthesis and performance measurement of a modified polymer dust suppressant. *Adv. Powder Technol.* **2020**, *31*, 792–803. [CrossRef]
16. Sun, J.; Zhou, G.; Gao, D.; Wei, Z.; Wang, N. Preparation and performance characterization of a composite dust suppressant for preventing secondary dust in underground mine roadways. *Chem. Eng. Res. Des.* **2020**, *156*, 195–208. [CrossRef]
17. Chang, P.; Zhao, Z.; Xu, G.; Ghosh, A.; Huang, J.; Yang, T. Evaluation of the coal dust suppression efficiency of different surfactants: A factorial experiment. *Colloids Surf. A Physicochem. Eng. Asp.* **2020**, *595*, 124686. [CrossRef]
18. Marchewicz, A.; Sobczyk, A.; Krupa, A.; Jaworek, A. Induction charging of water spray produced by pressure atomizer. *Int. J. Heat Mass Transf.* **2019**, *135*, 631–648. [CrossRef]
19. Bertero, M.; Sedran, U. Conversion of pine sawdust bio-oil (raw and thermally processed) over equilibrium FCC catalysts. *Bioresour. Technol.* **2013**, *135*, 644–651. [CrossRef]
20. Li, B.; Liu, S.; Fan, M.; Zhang, L. The effect of ethylene oxide groups in dodecyl ethoxyl ethers on low rank coal flotation: An experimental study and simulation. *Powder Technol.* **2018**, *344*, 684–692. [CrossRef]
21. You, X.; He, M.; Zhu, X.; Wei, H.; Cao, X.; Wang, P.; Li, L. Influence of surfactant for improving dewatering of brown coal: A comparative experimental and MD simulation study. *Sep. Purif. Technol.* **2019**, *210*, 473–478. [CrossRef]
22. Xu, C.; Wang, H.; Wang, D.; Zhu, X.; Zhu, Y.; Bai, X.; Yang, Q. Improvement of Foaming Ability of Surfactant Solutions by Water-Soluble Polymers: Experiment and Molecular Dynamics Simulation. *Polymers* **2020**, *12*, 571. [CrossRef] [PubMed]
23. Niu, W.; Nie, W.; Yuan, M.; Bao, Q.; Zhou, W.; Yan, J.; Yu, F.; Liu, C.; Sun, N.; Xue, Q. Study of the microscopic mechanism of lauryl glucoside wetting coal dust: Environmental pollution prevention and control. *J. Hazard. Mater.* **2021**, *412*, 125223. [CrossRef] [PubMed]
24. Wang, J.; Zhang, S.; Zuo, Z. Experimental Study of Influence Rules on Spray Charged Characteristics in the Induction Charging Process. *High Volt. Eng.* **2017**, *43*, 514–519.
25. Xu, Y.-L.; Wang, L.-Y.; Yu, M.-G.; Wan, S.-J.; Song, Z.-P.; Wang, S.-K. Study on the characteristics of gas explosion affected by induction charged water mist in confined space. *J. Loss Prev. Process. Ind.* **2016**, *40*, 227–233. [CrossRef]
26. Yuan, M.; Nie, W.; Zhou, W.; Yan, J.; Bao, Q.; Guo, C.; Tong, P.; Zhang, H.; Guo, L. Determining the effect of the non-ionic surfactant AEO9 on lignite adsorption and wetting via molecular dynamics (MD) simulation and experiment comparisons. *Fuel* **2020**, *278*, 118339. [CrossRef]
27. Li, W.; Wang, H.; Li, X.; Liang, Y.; Wang, Y.; Zhang, H. Effect of mixed cationic/anionic surfactants on the low-rank coal wettability by an experimental and molecular dynamics simulation. *Fuel* **2020**, *289*, 119886. [CrossRef]

28. Martínez-Magadán, J.-M.; Oviedo-Roa, R.; García, P.; Martínez-Palou, R. DFT study of the interaction between ethanethiol and Fe-containing ionic liquids for desulfuration of natural gasoline. *Fuel Process Technol.* **2012**, *97*, 24–29. [CrossRef]
29. Israelachvili, J.N.; Adams, G.E. Direct measurement of long range forces between two mica surfaces in aqueous KNO_3 solutions. *Nature* **1976**, *262*, 774–776. [CrossRef]
30. Li, Y.; Zhou, G.; Li, J.; Gu, B.-L.; Duan, W. Alkali-Metal-Doped B_{80} as High-Capacity Hydrogen Storage Media. *J. Phys. Chem. C* **2008**, *112*, 19268–19271. [CrossRef]
31. Zhang, Z.; Wang, C.; Yan, K. Adsorption of collectors on model surface of Wiser bituminous coal: A molecular dynamics simulation study. *Miner. Eng.* **2015**, *79*, 31–39. [CrossRef]
32. Guo, J.; Zhang, L.; Liu, S.; Li, B. Effects of hydrophilic groups of nonionic surfactants on the wettability of lignite surface: Molecular dynamics simulation and experimental study. *Fuel* **2018**, *231*, 449–457. [CrossRef]

Disclaimer/Publisher's Note: The statements, opinions and data contained in all publications are solely those of the individual author(s) and contributor(s) and not of MDPI and/or the editor(s). MDPI and/or the editor(s) disclaim responsibility for any injury to people or property resulting from any ideas, methods, instructions or products referred to in the content.

toxics

MDPI

Article

Can Green-Technology Innovation Reduce Atmospheric Environmental Pollution?

Jingkun Zhou [1], Yunkai Zhou [2,*] and Xu Bai [3]

[1] School of Business, Ludong University, 186 Hongqizhong Road, Yantai 264025, China
[2] Adam Smith Business School, University of Glasgow, Glasgow G12 8QQ, UK
[3] School of Public Administration, Hebei University of Economics and Business, Shijiazhuang 050061, China; baixu092069@163.com
* Correspondence: zhouyunkai88@gmail.com

Abstract: Rapid economic growth leads to such problems as resource scarcity and environmental degradation. Local governments successively take measures such as technological innovation to solve atmospheric environmental pollution; however, technological innovation fails to fundamentally alleviate atmospheric environmental pollution. Therefore, local governments come to realize the importance of green-technology innovation, which means an inevitable choice for various countries in the world to seek long-term development and win competitive advantage. Under such circumstances, this paper chooses the panel data of 30 provinces and regions in China from 2005 to 2018, takes environmental regulation as the threshold variable, and empirically analyzes the relationship between green-technology innovation and atmospheric environmental pollution by constructing a Spatial Measurement Model and Panel Regression Model. As evinced, green-technology innovation has a significant inhibitory effect and a spatial spillover effect on atmospheric environmental pollution. When environmental regulation reaches a level of intensity, green-technology innovation can effectively curb atmospheric environmental pollution. Accordingly, relevant parties should strengthen green-technology innovation, coordinate the development of the governance system of green-technology innovation, establish a joint prevention and control mechanism, increase the investment in green technology research and development, and augment the role of green-technology innovation.

Keywords: green-technology innovation; atmospheric environmental pollution; spatial spillover effect; threshold characteristic

Citation: Zhou, J.; Zhou, Y.; Bai, X. Can Green-Technology Innovation Reduce Atmospheric Environmental Pollution? *Toxics* **2023**, *11*, 403. https://doi.org/10.3390/toxics11050403

Academic Editor: Dibyendu Sarkar

Received: 15 March 2023
Revised: 12 April 2023
Accepted: 15 April 2023
Published: 24 April 2023

Copyright: © 2023 by the authors. Licensee MDPI, Basel, Switzerland. This article is an open access article distributed under the terms and conditions of the Creative Commons Attribution (CC BY) license (https://creativecommons.org/licenses/by/4.0/).

1. Introduction

According to data from Bulletin of China's Ecological Environment in 2021 released by the Ministry of Ecology and Environment, among 337 prefecture-level and above cities in China, 121 cities suffer excessive pollution in terms of ambient air quality, accounting for 35.7%, down by 3.5% over 2020 [1]. Nevertheless, the problem of atmospheric environmental pollution needs to be deeply investigated. Therefore, reducing atmospheric environmental pollution with green-technology innovations [2] and then promoting the high-quality development of China's green economy signal the top priorities for future development. Simultaneously, can green-technology innovation effectively mitigate atmospheric environmental pollution? Does green-technology innovation form a spatial spillover effect with atmospheric environmental pollution? For one region, will green-technology innovation affect the environment of neighboring regions? This paper will examine or solve these questions.

1.1. Green-Technology

Since Brawn and Wield first introduced the concept of "green technology" in 1994 [3], the importance of innovation in this field has been increasingly recognized in response to the growing severity of environmental problems [4,5]. Green technology refers to the application

of innovative and sustainable solutions to address environmental challenges and promote sustainable development. It encompasses a wide range of fields, including renewable energy, green building materials, energy-efficient transportation, and waste reduction.

In 2019, China's National Development and Reform Commission and Ministry of Science and Technology issued the Guiding Opinions on Building a Market-oriented Green Technology Innovation System, which defined green technology innovation as an emerging technological innovation that reduces consumption, minimizes pollution, improves ecology, promotes the construction of an ecological civilization, and realizes harmonious coexistence between human beings and nature. This encompasses fields such as energy conservation and environmental protection, clean production, clean energy, ecological protection and restoration, urban and rural green infrastructure, and ecological agriculture, as well as technology in product design, production, consumption, and recycling. (https://www.ndrc.gov.cn/xxgk/zcfb/tz/201904/t20190419_962441.html (accessed on 10 March 2023)).

Currently, numerous nations across the globe are utilizing green technology to tackle environmental obstacles and advance sustainable development. For instance, many countries are embracing renewable energy sources such as solar and wind power to decrease dependence on fossil fuels and contain greenhouse gas emissions. Additionally, certain cities worldwide are employing eco-friendly building materials and designs to curtail energy consumption and foster a salubrious living environment. Green technology boasts several benefits. Firstly, it can notably diminish carbon emissions, enhance air and water quality, and assuage climate change. Secondly, green technology can stimulate sustainable development and buttress economic growth. Thirdly, it can assist countries and communities to curtail their reliance on fossil fuels, thereby economizing costs and heightening energy security. Nevertheless, green technology also encompasses some drawbacks. Firstly, elevated initial investment costs may pose a significant hindrance to its widespread adoption. Secondly, green technology typically necessitates significant technological advancements, which can be daunting. Finally, certain green technologies (such as biofuels) may yield inadvertent negative impacts on the environment and society. In conclusion, green technology holds the potential to combat diverse environmental challenges and advance sustainable development. Nonetheless, its benefits and drawbacks must be astutely evaluated, and its implementation must be ensured to be sustainable and salutary in the long run.

1.2. The Relationship between Green-Technology Innovation and Atmospheric Environmental Pollution

As illustrated in Figure 1, the relationship between green technology innovation and air pollution can be described as follows: green technology innovation can improve the quality of the atmosphere by reducing the number of air pollutants emitted, decreasing the level of air pollution, and increasing the carrying capacity of the atmosphere. However, the relationship between green technology innovation and air pollution has caused controversy in the academic community, with scholars holding differing opinions on the matter. One view is that green technology innovation can improve the state of atmospheric pollution. Carrion-Flores and Innes (2010) assert that green technology innovation can improve environmental outcomes and to some extent help curb atmospheric pollution [6]. Oyebanji and Kirikkaleli (2023) found that the adoption of green technology and green electricity significantly reduces environmental pollution, including atmospheric pollution. Specifically, they discovered that in countries with high levels of green technology and green electricity, levels of air pollutants such as nitrogen oxides (NO_x) and sulfur dioxide (SO_2) are lower [7]. Zhou Jieqi (2014) observed that green-technology innovation has a significant impact on the reduction of carbon emissions [8]. Nie Puyan (2015) researched the heterogeneity of the impact of market concentration and technological innovation on the intensity of industrial carbon emission, revealing that technological innovation can facilitate energy progress and reduce environmental pollution [9]. Lu Xuehuan et al. (2020) concluded that green-technology innovation effectively curbs fog-haze pollution [10]. The other view is that green-technology innovation cannot help to reduce atmospheric environmental pollution.

Li Fen et al. (2017) suggested that technological innovation aggravates environmental pollution. Technological innovation improves production efficiency; however, it consumes a lot of resources and causes environmental pollution [11]. Chen Yang et al. (2019) disclosed that in some cities in the northeast and northwest regions, the level of technological innovation serves industrial development and fails to reduce environmental pollution [12]. Schmidt (2019) argued that the total amount of environmental pollution generally increases, and technological innovation will not necessarily decrease environmental pollution [13].

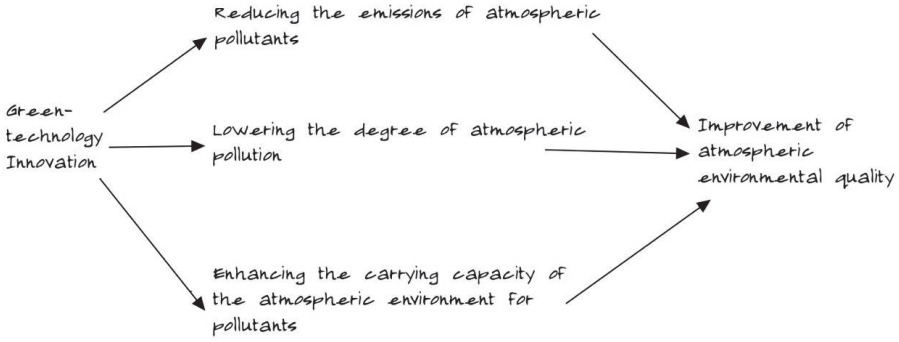


Figure 1. Schematic diagram illustrating the relationship between green technology innovation and air pollution.

1.3. The Spatial Spillover Effect of Green-Technology Innovation on Atmospheric Environmental Pollution

The spatial spillover of atmospheric environmental pollution signifies that environmental pollution affects one region as well as the atmospheric environment of its neighboring regions. Green-technology innovation can inhibit atmospheric environment pollution in one region and its neighboring regions. In this regard, scholars have carried out relevant research. Liu Xiaohong (2019) examined the effect of green innovation on fog-haze pollution under a spatial correlation, demonstrating that the direct effect, indirect effect, and total effect of green innovation prove significantly negative. This means the rise of the green-innovation level can effectively curb fog-haze pollution in local and neighboring regions, with an obvious spatial spillover effect [14]. Lu Na et al. (2019) constructed a dynamic Spatial Durbin Model to empirically test the spatial spillover effect of groundbreaking low-carbon technological innovation on carbon emission, upholding that groundbreaking low-carbon technological innovation has a significant inhibitory effect on carbon emission and insignificant effect on carbon emission in neighboring regions [15]. Ren Yayun et al. (2020) believe that urban innovation in China can curb fog-haze, with a significant spatial spillover effect [16]. According to Wang et al. (2022), the increase in intergovernmental competition and fiscal decentralization may lead to more green technology innovation, which in turn reduces air pollution in innovative regions and their surrounding areas [17]. Lu Xuehuan et al. (2020) noticed that green-technology innovation can effectively reduce fog-haze pollution, with a positive spatial spillover effect [10].

1.4. The Threshold Effect of Green-Technology Innovation on Atmospheric Environmental Pollution

Presently, scholars have scrutinized the threshold effect of green-technology innovation on atmospheric environmental pollution. Specifically, this paper mainly takes the intensity of environmental regulation as the threshold variable and discusses the threshold effect of green-technology innovation on atmospheric environmental pollution. Lan and Munro (2014) showed that as the intensity of environmental regulation increases, the market demand for environmental-protection technology expands. Therefore, enterprises will invest more human and material resources in the research and development of environmental-protection technology to improve environmental quality [18]. Huang Tianhang et al. (2020) confirmed that technological innovation under environmental regulation plays a positive role in reducing environmental pollution [19]. Lu Xuehuan et al. (2020) noted that when the level of regional environmental regulation proves relatively high,

green-technology innovation has a significant inhibitory effect on fog-haze pollution [10]. Wu Lichao et al. (2020) asserted that as the level of environmental regulation rises, green-technology innovation produces a more significant effect on improving environmental quality [20].

Currently, scholars highlight the research on the relationship between technological innovation and atmospheric environmental pollution yet ignore the research on green-technology innovation. Moreover, the existing research centers on provincial regions rather than municipal regions (as research conducted at the level of prefecture-level cities is more specific and closer to actual circumstances). The literature mostly focuses on the regulation of the relationship between technological innovation and atmospheric environmental pollution, and attaches less attention to the regulation of green-technology innovation and atmospheric environmental pollution with the environment as a mediator. Given the inadequacies in the existing research, this paper investigates the problems of green-technology innovation and atmospheric environmental pollution, constructs the Panel Threshold Model and Spatial Durbin Model that represents the relationship between green-technology innovation and atmospheric environmental pollution, and clarifies the atmospheric pollution reduction effects of green-technology innovation. Additionally, based on regional differences in the selection of data samples, this paper first explores the distribution characteristics of the samples of green-technology innovation, and proceeds to deeply analyze the heterogeneous impact or effect of green-technology innovation on atmospheric environmental pollution in different regions.

2. Research Hypotheses and Design

2.1. Research Hypotheses

Many factors need to be considered in the research on whether green-technology innovation reduces atmospheric environmental pollution, including environmental regulation, economic development, industrial transfer and agglomeration, and governmental regulation. The difference in the level of regional economic development also affects the introduction of green-technology innovation, after which the spillover effect of green-technology innovation extends to neighboring regions and forms an external factor. Therefore, this paper focuses on the relationship between green-technology innovation and atmospheric environmental pollution, the spatial spillover effect, and threshold characteristic, which possesses practical significance.

Hypothesis 1: *The innovation of green technology is advantageous in mitigating atmospheric pollution.*

In economic development, atmospheric environmental pollution presents the biggest problem, and green-technology innovation forms an important measure to reduce atmospheric environmental pollution. In technological development, enterprises often sacrifice the ecological environment in the pursuit of economic benefits, which not only impairs tectological balance, but also undermines environmental bearing capacity. Under such a background, green-technology innovation hedges against the impact on environmental bearing capacity. According to Ullah et al. (2021), the effects of technological innovation on environmental quality are asymmetric, with the positive impacts exceeding the negative ones. Specifically, by enhancing energy efficiency, reducing waste, and promoting sustainable development, technological innovation can significantly reduce environmental pollution [21]. The influencing factors of environmental pollution basically comprise scale effect, structure effect, and technology effect. Among them, the technological effect plays the most important role in improving environmental quality. More advanced technology means less pollution (Grossman and Krueger, 1991) [22]. The effect of production technology manifests itself in the facts that technological progress will improve the production efficiency and resource utilization of enterprises, and that the saving of resources will reduce the damage to the environment, thus weakening environmental pollution. The effect

of treatment technology lies in the fact that the improvement of production equipment and pollution-treatment equipment can reduce the emission of pollutants. Naturally, less emission of pollutants helps to reduce the emission of exhaust gas in the air, which alleviates atmospheric environmental pollution. The effect of structural optimization testifies to the fact that technological progress promotes the optimization and upgrading of industrial structure, eliminates the secondary industry, and actively develops the modern service industry and high-tech industry. This boosts the upgrading of industrial structure, reshapes the production model of industry, and definitely improves environmental quality. Simultaneously, green-technology innovation lowers the cost of environmental protection and fosters the growth of the green economy (David Popp, 2012) [23]. Gradually, the problem of environmental pollution becomes one of the most prominent problems and arouses the attention of various parties of green-technology innovation. Therefore, they tend to use scientific and technological means to solve the problem of environmental pollution. In the development of technological innovation, the integration of the idea of sustainable and ecology-oriented scientific and technological innovation helps to mitigate environmental pollution (Liu Guomai et al., 2020) [24].

Grounded in the above analysis, this paper proposes research Hypothesis 1: green-technology innovation can reduce atmospheric environmental pollution.

Hypothesis 2: *The spatial spillover effect of green-technology innovation on atmospheric environmental pollution.*

Green-technology innovation functions as an effective means to realize the construction of ecological civilization. For some regions, the improvement of green-technology innovation reduces atmospheric environmental pollution in both these regions and neighboring regions, forming inter-regional interactions and spatial spillover effects (a spatial spillover is an essential form of spatial interaction, which manifests itself in the diffusion of socioeconomic factors in space). The reason lies in the fact that local industries play a learner role in the development and operation, and continuously learn and practice advanced approaches in green-technology innovation in neighboring regions. The knowledge in technological innovation has viscosity, both spatially and geographically (knowledge stickiness refers to the adhesive effect on knowledge caused by various factors, including the nature of knowledge (causal ambiguity and unverifiability), the source of knowledge (lack of incentives and unreliability), the recipient of knowledge (lack of absorption and retention abilities), and the knowledge transfer environment (lack of organizational environment and fragile internal connections)), with geographical distance proportional to the cost of knowledge dissemination (Wu Yuming, 2006) [25], thus enhancing regional capacity in green-technology innovation. Moreover, when the level of green-technology innovation in neighboring regions improves, the resource-utilization rate will increase, and the pollutant-emission rate will decrease accordingly. To put it another way, the reduction of atmospheric environmental pollution in neighboring regions indirectly eases local atmospheric environmental pollution (Lu Xuehuan et al., 2020) [10]. Evidently, as the level of green-technology innovation in neighboring regions improves, governments take more effective measures to control atmospheric environmental pollution, tighten the intensity of environmental regulation, and release corresponding policies on the control of atmospheric environmental pollution. If relevant policies in neighboring regions are well-implemented, local governments will naturally learn the policies on environmental regulation from neighboring regions, which has an indirect impact on the local treatment of atmospheric environmental pollution. For instance, in 2015, the Chinese National Development and Reform Commission issued a policy on the construction of demonstration cities and counties for a circular economy (http://www.gov.cn/xinwen/2015-09/24/content_2938128.htm (accessed on 10 March 2023)). Noteworthily, strengthening green-technology innovation in neighboring regions probably raises higher requirements for local policies, which urges local governments to participate in the strategic competition of environmental-protection policies,

having a negative impact on local treatment of atmospheric environmental pollution (Li Zihao, 2016) [26].

Grounded in the above analysis, this paper proposes research Hypothesis 2: the rise of the level of local green-technology innovation helps to reduce atmospheric environmental pollution in neighboring regions, with a significant spatial spillover effect.

Hypothesis 3: *The threshold characteristic of green-technology innovation on atmospheric environmental pollution.*

As governments and citizens pay more attention to environmental protection, the role of environmental regulation becomes increasingly prominent, which promotes the development of green-technology innovation, enables the market to meet the requirements of environmental regulation, and reduces environmental pollution (Li Fengqi, 2021) [27]. The innovation compensation effect of environmental regulation propels enterprises to carry out green-technology innovation, and the intensification of environmental regulation increases the expenditure of enterprises. In a way, this enhances the capacity of green-technology innovation (Lin Chunyan et al., 2019) [28]. When the intensity of environmental regulation remains low, the marginal cost of corporate environmental pollution proves less than the marginal profit, with the lack of driving force for the progress of green technology. When the intensity of environmental regulation rises, environmental regulation occasions the phenomenon of "the survival of the fittest" among enterprises (Jin Pei, 2009) [29]. To offset more production costs caused by greater intensity of environmental regulation, some enterprises take the initiative in green-technology innovation, thus strengthening the capacity of green-technology innovation (Jiang Fuxin et al., 2013) [30]. This enables enterprises to launch clean production and reduce atmospheric environmental pollution. Simultaneously, market-incentivized environmental regulation, which hinges on such means as pollution-fee income and environmental tax, increases the costs of enterprises with economic incentives and compels enterprises to promote pollution treatment and technological innovation. The model embodies "Polluter Pays Principle" and indirectly achieves the purpose of improving environmental quality (Fan Dan et al., 2020) [31]. Environmental regulation has a significant effect on reducing the atmospheric environmental pollution. Admittedly, under the impact of economic growth, environmental regulation probably produces the reverse effect. Yet, the impact of environmental regulation on the reduction of the emission of atmospheric environmental pollution gradually changes. With economic development, citizens raise their living standards and enhance their awareness of environmental protection, from which the impact of environmental regulation arises. Certainly, the reinforcement of the intensity of environmental regulation does not mean the automatic improvement of atmospheric environmental pollution. What matters is to establish and improve the overall system of environmental regulation.

Grounded in the above analysis, this paper proposes research Hypothesis 3: when environmental regulation reaches a higher level, the effect of green-technology innovation on reducing atmospheric environmental pollution proves more significant.

2.2. Research Design

2.2.1. Model Construction

(1) Model Construction I:

Xiang Kun et al. (2015) constructed a Non-Spatial Interaction Model and a Spatial Durbin Model to test the economic drivers of fog-haze pollution based on six-year interval data (1985, 1990, 1995, 2000, 2005, 2010). As evidenced, the increase in coal consumption will worsen fog-haze pollution in one region and its neighboring regions, while the increase in power consumption can alleviate local fog-haze pollution and aggravate fog-haze pollution in neighboring regions [32]. Shao Shuai et al. (2016) conducted empirical identification and discussed corresponding haze-control policies on key factors that affect fog-haze pollution via the Dynamic Spatial Panel Model and System Generalized Method of Moments. As

the results suggest, there is a significant spatial spillover effect of fog-haze pollution in provinces in China [33]. Based on the panel data of 285 prefecture-level and above cities in China, Cheng Zhonghua et al. (2019) constructed a Dynamic Spatial Panel Model to empirically analyze the impact of industrial-structure adjustment and technological progress on the reduction of fog-haze emission [34]. Based on the research of existing literature, this paper uses the Spatial Panel Regression Model to analyze the spatial spillover effect of green-technology innovation on atmospheric environmental pollution.

1. The Spatial Autoregression Model is expressed as follows:

$$lnsmog1_{it} = \rho \sum_{j=1}^{N} W_{it}\, lnsmog1_{it} + \beta_1 lner1_{it} + \beta_2 lnden_{it} + \beta_3 lnuba_{it} + \beta_4 lney_{it} + \beta_5 lnin_{it} + \mu_i + \lambda_i + \varepsilon_{it} \quad (1)$$

In particular, ρ stands for the spatial lag (autoregression) coefficient. W_{it} stands for the i-row and j-column elements of the normalized non-negative spatial weight matrix W in the N $*$ N dimension. The subscripts i and t stand for the year t of the ith province, respectively. μ_i and λ_i stand for space (individual) effect and time effect, respectively.

2. The Spatial Durbin Model is expressed as follows:

$$\begin{aligned} lnsmog_{it} = \; & \rho \sum_{j=1}^{N} W_{it}\, lnsmog_{it} + \beta_1 lnden_{it} + \beta_2 lnuba_{it} + \beta_3 lney_{it} + \beta_4 lnin_{it} \\ & + \beta_5 \sum_{j=1}^{N} W_{it}\, lnden_{it} + \beta_6 \sum_{j=1}^{N} W_{it}\, lnuba_{it} + \beta_7 \sum_{j=1}^{N} W_{it}\, lney_{it} \\ & + \beta_8 \sum_{j=1}^{N} W_{it} lnin_{it} + \mu_i + \lambda_i + \varepsilon_{it} \end{aligned} \quad (2)$$

In particular, ρ stands for the spatial regression coefficient. W_{it} stands for the i-row and j-column elements of the normalized non-negative spatial weight matrix W in the N $*$ N dimension. The subscripts i and t stand for the year t of the ith province, respectively. μ_i and λ_i stand for space (individual) effect and time effect, respectively.

(2) Model Construction II:

Guan Aiping et al. (2014) constructed a Non-Dynamic Panel Threshold Regression Model in their research on the impact of industrial transfer on technological innovation, to empirically test the technological spillover effect of inter-regional industrial transfer on developing western regions, as well as the impact of the absorptive capacity index on the technological spillover effect from the angles of economic development level, human capital, and technological gap of the transfer-in regions. As concluded, the inter-regional industrial transfer has a positive technological spillover effect on developing western regions [35]. Qin Bingtao et al. (2019) used the Threshold Panel Regression Model to analyze the relationship between the transfer of high-pollution industries and environmental pollution by taking the relative intensity of environmental regulation as the threshold variable. As the results show, there is a progressive-increase nonlinear relationship between the transfer of high-pollution industries and environmental pollution. As the intensity of relative environmental regulation jumps from a low threshold to a high threshold, the problem of environmental pollution caused by the transfer of high-pollution industries intensifies [36]. By combing the existing literature, this paper uses Hansen's Threshold Regression Model to analyze the data and determine the threshold value. This paper explores the relationship between green-technology innovation and atmospheric environmental pollution, and takes environmental regulation as the threshold value to clarify the impact of green-technology innovation on atmospheric environmental pollution. The threshold model is expressed as follows:

$$\begin{aligned} lnsmog_{it} = \; & \beta_0 + \beta_1 \mathrm{er}(lner_{it} < \gamma) + \beta_2 lner_{it}(lner_{it} \geq \gamma) + \beta_3 lngt_{it} + \beta_4 lnden_{it} + \beta_5 lnuba_{it} + \beta_6 lney_{it} + \beta_7 lnin_{it} \\ & + \varepsilon_{it} \end{aligned} \quad (3)$$

In particular, β stands for the constant term. *lnsmog* stands for the natural logarithm of atmospheric environmental pollution. *ln er* stands for environmental regulation. ε_{it} stands

for the disturbance term. As delineated in Table 1, Control variables include population density, built-up area, economic development level, and industrial structure, respectively.

Table 1. Variable Description.

Name	Name Description
smog	Atmospheric Environmental Pollution
gt	Green-Technology Innovation
er	Environmental Regulation
den	Population Density
uba	Built-up Area
ey	Economic Development Level
in	Industrial Structure

2.2.2. Variable Description

(1) Explanatory Variable

This paper chooses green-technology innovation as the explanatory variable, expressed by the number of green-patent authorizations. The World Intellectual Property Organization classified green patents in the IPC Green Inventory released in 2010 (Wang Zhenyu et al., 2020) [37]. The China National Intellectual Property Administration defines the idea of the green patent as "patents for inventions, utility models and registered designs under the theme of green technologies conducive to resource conservation, energy-efficiency improvement and pollution prevention and control". Green technology plays an important part in ecological civilization and serves as a major factor to coordinate ecology and economy and lead green development (Wang Banban et al., 2019) [38]. This paper chooses green-patent authorization rather than green-patent application, because the former better represents the innovation achieved in one region.

(2) Explained Variable

Following the construction method of Zhu Pingfang et al. (2011) [39] on atmospheric environmental pollution comprehensive index, this paper uses the comprehensive index (industrial sulfur dioxide/GDP + industrial smoke or powder dust/GDP + PM2.5/GDP)/3 to represent atmospheric environmental pollution and takes atmospheric environmental pollution as the explained variable.

(3) Threshold Variable

This paper takes environmental regulation as the threshold variable. Atmospheric environmental pollution mostly comes from the emission of gaseous pollutants in the production of industrial enterprises, so governmental control of gaseous pollutants can effectively measure regional environmental regulation. Following the practice of Shen Kunrong et al. (2017), this paper expresses environmental regulation with the removal amount of industrial sulfur dioxide in various regions [40].

(4) Control Variable

1. Population density. The increase in population density probably promotes energy consumption and causes more pollution. The increase in population basically tallies with the growing trend of the emissions of sulfur dioxide and carbon. Notably, the impact of population density on environmental pollution depends on the dominant role of the scale effect and agglomeration effect (Liang Rui et al., 2020) [41].
2. Built-up area. The built-up area refers to the area within an urban administrative area that has actually been developed and constructed in a large area, with municipal public facilities and public facilities basically available. The expansion of urban built-up areas has an impact on urban traffic, and the traffic demand increases with the expansion of the radius of the built-up area, thus emitting massive automobile exhaust and damaging the atmospheric environment (Hu Xuan, 2015) [42].

3. Economic development level. This paper uses per capita GDP to measure the level of regional economic development. The level of regional economic development determines the consumption of natural resources to a large extent, and economic growth improves people's living standards and consumption levels, which enhances their awareness of environmental protection and advances the reduction of environmental pollution.
4. Industrial structure. This paper measures the proportion of the added value of the secondary industry in the local GDP in various regions or cities. The industrialization process spawns a significant increase in fossil-energy consumption and construction dust. The expansion of secondary-industry capacity undoubtedly constitutes an important source of fog-haze pollution (Lu Xuehuan et al., 2020) [10].

2.2.3. Data Source and Variable Description & Statistics

Given the availability of data, this paper chooses 286 prefecture-level cities in China from 2005 to 2018 as the research object. Specifically, the data on fog-haze pollution of regions or cities come from the data of the annual mean of global PM2.5 concentration based on satellite monitoring published by the Socioeconomic Data and Applications Center of Columbia University(https://beta.sedac.ciesin.columbia.edu/, accessed on 10 March 2023). The emissions of industrial sulfur dioxide and industrial smoke (powder) dust as well as the removal of industrial sulfur dioxide in regions or cities come from the China Urban Statistical Yearbook and provincial statistical yearbooks, which are manually sorted by the author of this paper. The amount of green-patent authorization comes from the China National Intellectual Property Administration, which is manually sorted by the author of this paper. The data on indicators such as population density, built-up area, level of economic development, and industrial structure are sourced from the China Statistical Yearbook. Also Variable Description & Statistics is explicated in Table 2.

Table 2. Variable Description and Statistics.

Variable	Sample Size	Mean Value	Standard Deviation	The Minimum Value	The Maximum Value
smog	3990	−21.08713	2.28609	−27.25011	0.00000
gt	3990	2.92953	4.67108	−23.02585	9.49830
er	3990	10.32545	2.18277	−11.51293	16.72783
den	3990	7.94237	0.80561	3.29584	9.92010
uba	3990	4.36596	0.87574	1.87947	7.97903
ey	3990	10.31334	0.77566	4.59512	15.67520
in	3990	3.84681	0.24964	2.19723	4.51053

3. Empirical Analysis

3.1. The Empirical Analysis of Spatial Spillover Effect

Based on the data of 30 provinces, autonomous regions, and municipalities directly under the Central Government in China from 2005 to 2018, this paper constructs a Spatial Autoregression Model and Spatial Durbin Model to analyze the relationship between green-technology innovation and atmospheric environmental pollution, drawing the conclusion that green-technology innovation forms a significant spatial correlation with atmospheric environmental pollution. In other words, the level of atmospheric environmental pollution in one region is affected by the level (or emission) of atmospheric environmental pollution in neighboring regions.

The results of the Spatial Autoregression Model roughly accord with that of the Spatial Durbin Model; therefore, this paper mainly analyzes the results of the Spatial Durbin Model. As shown in Tables 3–6, the main regression coefficient of the Spatial Durbin Model determines whether the direct effect proves significant, positive, or negative, so this paper combines the main regression coefficient with the cause of the direct effect. The main regression coefficient and direct effect of green-technology innovation both prove significantly negative, which demonstrates that green-technology innovation can effectively

address the emission of environmental pollution. The spatial spillover of green-technology innovation proves significantly negative. One possible reason is that the development of local green-technology innovation significantly improves the production efficiency of enterprises and attracts enterprises from neighboring regions to agglomerate in the region, which reduces the emission of environmental pollutants in neighboring regions. Additionally, green-technology innovation can fundamentally reduce the emission of pollutants, upgrade the equipment and technology of industrial production, and then help to reduce the emission of pollutants in neighboring regions. The main regression coefficient and the direct effect of population density prove positive yet insignificant, which demonstrates that the pressure from the increase of local population density on atmospheric environmental pollution in one region and its neighboring regions proves insignificant, with no direct relationship. That is because the increase in population density slightly increases regional energy consumption and actualizes governmental treatment policies, with an insignificant impact on atmospheric environmental pollution. The main regression coefficient and the direct effect of the built-up area prove significantly negative, because the increase of local built-up area facilitates the transfer of pollution industries from neighboring regions, reduces the number of pollution industries in neighboring regions, and improves atmospheric environmental pollution in these regions. Additionally, owing to the expansion of the built-up area, the local energy-conservation industry multiplies, and the emission of pollutants from the energy-conservation industry decreases, which mitigates local atmospheric environmental pollution. The main regression coefficient and the direct effect of economic development level prove significantly negative, which demonstrates that China starts to change the production model of economic growth at the expense of the environment. The rise of the economic development level spurs enterprises to replace pollution-generation equipment with pollution-reduction equipment. A higher level of economic development means better control of pollution emissions and more reduction of environmental pollution. The main regression coefficient and the direct effect of industrial structure prove significantly positive, which demonstrates that the growth of the secondary industry aggravates atmospheric environmental pollution in neighboring regions. The flow of human and capital resources among various industries has a significant spatial correlation, and atmospheric environmental pollution per se has a spatial correlation, so the expansion of the secondary industry augments the pressure on one region and its neighboring regions in the treatment of atmospheric environmental pollution.

Table 3. Main regression coefficients for spatial effects (Main).

	Lny	
Main		Wx
Lnx	−0.013 ***	0.001
	(−2.622)	(0.439)
lnm1	0.007	−0.007
	(0.199)	(−0.586)
lnm2	−0.540 ***	−0.096 ***
	(−6.907)	(−2.943)
lnm3	−1.401 ***	0.096 ***
	(−19.672)	(4.873)
lnm4	0.737 ***	−0.207 ***
	(4.587)	(−4.398)
Spatial		
rho	0.098 ***	
	(31.649)	
Variance		
sigma2_e	1.061 ***	
	(43.870)	
N	3990	
R2	0.030	

t statistics in parentheses. *** $p < 0.01$.

Table 4. Spatial autocorrelation direct effects (LR_Direct).

LR_Direct	Lnpy
Lnx	−0.013 **
	(−2.304)
lnm1	0.001
	(0.029)
lnm2	−0.636 ***
	(−7.808)
lnm3	−1.433 ***
	(−20.773)
lnm4	0.647 ***
	(4.248)

t statistics in parentheses. ** $p < 0.05$, *** $p < 0.01$.

Table 5. The indirect spatial autocorrelation effects (LR_Indirect).

LR_Indirect	Lnpy
Lnx	−0.001
	(−0.062)
lnm1	−0.071
	(−0.528)
lnm2	−1.615 ***
	(−4.654)
lnm3	−0.442 **
	(−2.509)
lnm4	−1.436 ***
	(−3.164)

t statistics in parentheses. ** $p < 0.05$, *** $p < 0.01$.

Table 6. The total spatial autocorrelation effect (LR_Total).

LR_Total	Lnpy
Lnx	−0.014
	(−0.526)
lnm1	−0.070
	(−0.468)
lnm2	−2.250 ***
	(−5.787)
lnm3	−1.875 ***
	(−9.438)
lnm4	−0.789 *
	(−1.651)
N	3990
R2	0.030

t statistics in parentheses. * $p < 0.1$, *** $p < 0.01$.

The regression coefficient of the indirect effect of green-technology innovation on atmospheric environmental pollution proves negative yet insignificant. This demonstrates that the introduction of green-technology innovation helps to alleviate atmospheric environmental pollution in neighboring regions, with unsatisfactory effect. With less attention to green-technology innovation, many enterprises uphold the logic of "Treatment after Pollution" and pursue short-term profits. As a result, atmospheric environmental pollution becomes more serious, and green-technology innovation alone can hardly slow down the pollution. Simultaneously, green-technology progress requires high costs. Local enterprises hope to "hitch a ride" and heavily rely on enterprises in neighboring regions. Therefore, green-technology progress in neighboring regions has a weak effect on the mitigation of atmospheric environmental pollution in one region. The indirect effect of the built-up area on atmospheric environmental pollution proves significantly negative, which demonstrates

that the increase of the built-up area can reduce atmospheric environmental pollution in neighboring regions. After the expansion of the built-up area, motors and other vehicles that emit exhaust gas scatter and no longer produce massive exhaust gas, which reduces atmospheric environmental pollution in neighboring regions. Moreover, the expansion of built-up areas usually involves adding a large amount of non-building areas or green spaces, so the expansion of built-up areas will also increase the coverage of green areas, and neighboring regions learn to optimize the construction of green areas, which accelerates the treatment of environmental pollution in neighboring regions. The indirect effect of economic development level on atmospheric environmental pollution proves significantly negative, which demonstrates that the rise of economic development level makes people's lives better. With their demands in daily life satisfied, people start to focus on their health. Since atmospheric environmental pollution means a major threat to their health, they hope relevant measures shall be taken to reduce it. Meanwhile, the rise of the economic development level materializes the increase of investment in the environmental treatment and the reinforcement of governmental policies on environmental regulation. Under such circumstances, neighboring regions will gain advanced experience, which helps to reduce atmospheric environmental pollution in neighboring regions. The indirect effect of industrial structure on atmospheric environmental pollution proves significantly negative because the change of industrial structure (with spatial effect) entails changes of talents, technologies, and resources. The spillover effect of talents, technologies, and resources urges enterprises in neighboring regions to learn and accept relevant development models, which will reduce the capital cost of industrial-structure adjustment in neighboring regions and increase the corresponding capital cost of pollution treatment. Likewise, the improvement of environmental quality depends on the upgrading and optimization of urban industrial structures. The reasonable transformation of industrial structures can effectively improve the atmospheric environment and mitigate environmental pollution in neighboring regions.

The empirical analysis of the Spatial Autoregression Model and Spatial Durbin Model verifies Hypothesis 1 (i.e., green-technology innovation can reduce atmospheric environmental pollution) and Hypothesis 2 (i.e., the rise of local green-technology innovation helps to reduce atmospheric environmental pollution in neighboring regions and produces a significant spatial spillover effect).

3.2. Threshold Characteristic

The single threshold value of environmental regulation reaches 11.6373, and the double threshold value of environmental regulation reaches 11.7913 and 10.2717. When the F value of the double threshold reaches 28.02 and 24.5, it proves significant at the level of 5%, with a double threshold effect.

As shown in Table 7, environmental regulation has the characteristic of double threshold. When environmental regulation reaches lower than 10.2717, the regression coefficient of environmental regulation on atmospheric environmental pollution proves positive yet insignificant. This demonstrates that environmental regulation has a weak impact on the relationship between green-technology innovation and atmospheric environmental pollution at the initial stage of implementation. One reason is that at the early stage, policies on environmental regulation are neither well-designed nor thoroughly implemented. Coupled with other factors, the intensity of environmental regulation remains low and has an insignificant regulatory effect on atmospheric environmental pollution. The level of green-technology innovation also improves slightly. When environmental regulation reaches higher than 10.2717 yet lower than 11.7913, the regression coefficient of environmental regulation on atmospheric environmental pollution proves negative and insignificant. This is because with the improvement of environmental regulation, China attaches more importance to green-technology innovation and atmospheric environmental pollution and invests financial funds for the upgrading of green-technology equipment, the change of pollution-emission means, and the improvement of production technology. Under such a

background, enterprises emit less pollution and reduce atmospheric environmental pollution. At the transitional stage, however, green-technology innovation has a limited inhibitory effect on atmospheric environmental pollution. When environmental regulation reaches higher than 11.7913, the regression coefficient of environmental regulation on atmospheric environmental pollution proves significant and reaches −0.078. This demonstrates that with the rise of environmental regulation, green-technology innovation has a greater inhibitory effect on atmospheric environmental pollution. The fact that China pays attention to environmental regulation quickens the maturity of green-technology innovation. The inhibitory effect of green-technology innovation on environmental pollution mainly exists in the effect of production technology, the effect of treatment technology, and the effect of structural optimization. Specifically, the effect of production technology stems from the progress of production technology, which improves the utilization rate of resources and energy in industrial production, tremendously saves or effectively utilizes resources, and reduces pollutant emissions accordingly. The effect of treatment technology comes from the progress of green technology, including the use of clean energy and pollution-treatment equipment in production as well as a green and environment-friendly production process, which decreases the emission of pollutants. The effect of structural optimization refers to the fact that the progress of green technology promotes the structural optimization and upgrading of industrial enterprises and achieves the reduction of pollutant emissions in terms of overall industrial scale and structure. Besides, green-technology innovation advances, with a significant impact on the reduction of pollutant emissions. Therefore, enterprises should invest more capital or attach more attention to green technology, choose large-scale areas for the development of green-technology innovation, and make better use of green technology to produce a learning effect, so that green technology extends to more fields and plays a better role in curbing pollutant emissions.

Table 7. The Regression Results of Threshold Characteristic.

	Lnsmog	**Lnsmog**
lngt	−0.018 ***	−0.018 ***
	(−3.149)	(−3.144)
lnden	−0.055	−0.064
	(−1.329)	(−1.556)
lnuba	−0.762 ***	−0.755 ***
	(−8.120)	(−8.062)
lney	−2.177 ***	−2.127 ***
	(−37.271)	(−35.913)
lnin	0.691 ***	0.686 ***
	(4.170)	(4.144)
0._cat#c.lner	−0.044 **	0.005
	(−2.386)	(0.244)
1._cat#c.lner	−0.078 ***	−0.028
	(−4.370)	(−1.492)
2._cat#c.lner		−0.061 ***
		(−3.359)
_cons	3.096 ***	2.348 ***
	(3.865)	(2.876)
N	3990	3990
R2	0.581	0.583
adj. R2	0.548	0.550

t statistics in parentheses. ** $p < 0.05$, *** $p < 0.01$.

Therefore, the above analysis verifies Hypothesis 3: when environmental regulation reaches a higher level, the effect of green-technology innovation on reducing atmospheric environmental pollution becomes more significant.

4. Robustness Test: A Case Study of the Yangtze River Delta

Following the practice of Liu Chenyue et al. (2017) [43], this paper replaces the explained variable of atmospheric environmental pollution and uses annual fog-haze pollution (pm) in various cities to measure the atmospheric environmental pollution and conduct a robustness test.

The single threshold value of environmental regulation reaches 11.0739, and the double threshold value of environmental regulation reaches 11.4563 and 10.6199.

As shown in Table 8, after replacing the explained variable, green-technology innovation in one region and neighboring regions still significantly improves the treatment of atmospheric environmental pollution, and the spatial spillover effect generally agrees with the above research hypotheses. Simultaneously, green-technology innovation has a significant double threshold effect on fog-haze pollution in terms of environmental regulation. Environmental regulation plays an effective role in curbing fog-haze pollution vis green-technology innovation. Therefore, the major results in this paper prove to be robust and reliable.

Table 8. Robustness Test.

	The Threshold Characteristic of Panel Threshold Model		**Spatial Durbin Model**		
			Total Effect	**Direct Effect**	**Indirect Effect**
	lnpm	lnpm	lnpm	lnpm	lnpm
lngt	−0.010 ***	−0.009 ***	−0.007 ***	−0.006 *	0.010
	(−3.244)	(−2.973)	(−2.726)	(−1.945)	(0.943)
lnden	0.035 ***	0.035 ***	0.016 *	0.015 *	−0.007
	(3.247)	(3.314)	(1.905)	(1.706)	(−0.210)
lnuba	−0.055 ***	−0.057 ***	−0.030 ***	−0.056 ***	−0.320 ***
	(−3.741)	(−3.941)	(−2.613)	(−4.280)	(−5.199)
lney	−0.079 ***	−0.087 ***	−0.040 ***	−0.039 ***	0.011
	(−6.201)	(−6.790)	(−2.854)	(−2.835)	(0.274)
lnin	0.421 ***	0.446 ***	0.213 ***	0.183 ***	−0.361 ***
	(10.718)	(11.335)	(5.673)	(4.653)	(−3.206)
0._cat#c.lner	−0.009 **	−0.017 ***			
	(−2.088)	(−3.577)			
1._cat#c.lner	−0.003	−0.011 ***			
	(−0.719)	(−2.607)			
2._cat#c.lner		−0.006			
		(−1.342)			
_cons	3.021 ***	3.069 ***	2.713 ***		
	(14.836)	(15.131)	(13.638)		
Spatial rho			0.141 ***	0.129 ***	
			(33.144)	(25.782)	
Spatial rho			0.009 ***	0.011 ***	
			(25.660)	(23.830)	
				−2.699 ***	
				(−24.212)	
N	1386	1386	1386	1386	
R2	0.297	0.309	0.000	0.001	
adj. R2	0.240	0.251			

t statistics in parentheses. * $p < 0.1$, ** $p < 0.05$, *** $p < 0.01$.

5. Heterogeneity Analysis

Case Studies of the Beijing-Tianjin-Hebei Region, the Yangtze River Delta, the Pearl River Delta, the Chengdu-Chongqing Region and Northeastern Region

This paper completes the heterogeneity test of the Beijing-Tianjin-Hebei Region, the Yangtze River Delta, the Pearl River Delta, the Chengdu-Chongqing Region, and the Northeastern Region with the Spatial Measurement Model.

As shown in Table 9, in the Yangtze River Delta, the Pearl River Delta and Beijing-Tianjin-Hebei Region, the main regression coefficient and the direct effect of green-technology innovation prove significantly negative; yet, in the Pearl River Delta and Beijing-Tianjin-Hebei Region, the indirect effect of green-technology innovation proves insignificant. In the Northeastern Region, the main regression coefficient and the direct effect of green-technology innovation prove positive and insignificant, and the indirect effect of green-technology innovation proves negative and insignificant. In the Chengdu-Chongqing Region, the main regression coefficient of green-technology innovation proves negative and insignificant, and the direct effect and indirect effect of green-technology innovation prove negative and significant.

Table 9. The heterogeneity analysis of the Spatial Durbin Model.

	The Yangtze River Delta	**The Pearl River Delta**	**Beijing-Tianjin-Hebei Region**	**Northeastern Region**	**Chengdu-Chongqing Region**
	lnsmog	lnsmog	lnsmog	lnsmog	lnsmog
Total Effect					
lngt	−0.068 ***	−0.568 ***	−0.772 ***	0.012	−0.008
	(−3.861)	(−2.831)	(−7.309)	(0.498)	(−0.697)
lnden	−0.101	0.052	0.190	0.076	−0.095
	(−1.061)	(0.276)	(1.306)	(0.732)	(−1.080)
lnuba	−0.076	0.361	0.823 ***	0.054	−1.539 ***
	(−0.969)	(1.126)	(5.418)	(0.251)	(−7.443)
lney	−1.309 ***	−1.029 ***	−1.100 ***	−2.959 ***	−0.134
	(−9.805)	(−3.309)	(−4.309)	(−11.116)	(−1.560)
lnin	3.329 ***	2.456 ***	0.768	2.909 ***	−1.767 ***
	(11.988)	(3.979)	(1.614)	(6.792)	(−4.726)
_cons	−19.079 ***	−19.766 ***	−14.956 ***	−1.901	−4.829 ***
	(−12.436)	(−5.416)	(−4.543)	(−0.846)	(−3.001)
N	574	126	182	490	266
R2	0.676	0.744	0.764	0.441	0.382
Direct Effect					
lngt	−0.138 ***	−0.638 ***	−0.820 ***	0.012	−0.045 ***
	(−5.924)	(−3.201)	(−5.889)	(0.459)	(−2.643)
lnden	0.005	0.051	0.170	0.076	−0.080
	(0.043)	(0.245)	(0.857)	(0.767)	(−0.924)
lnuba	0.054	0.394	1.002 ***	0.126	−1.559 ***
	(0.549)	(0.966)	(5.013)	(0.570)	(−6.459)
lney	−1.252 ***	−0.949 ***	−1.048 ***	−2.979 ***	−0.117
	(−9.204)	(−3.049)	(−3.475)	(−12.015)	(−1.087)
lnin	3.613 ***	2.951 ***	1.129 *	2.881 ***	−1.575 ***
	(12.081)	(3.699)	(1.659)	(7.053)	(−3.955)
Indirect Effect					
lngt	−0.959 ***	−0.586	−0.489	−0.026	−0.404 ***
	(−6.143)	(−1.523)	(−0.839)	(−0.445)	(−4.182)
lnden	1.490 **	0.048	−0.123	0.092	0.210
	(2.383)	(0.092)	(−0.157)	(0.455)	(0.725)
lnuba	1.659 ***	0.078	1.551	1.048	−0.450
	(2.628)	(0.049)	(1.605)	(1.390)	(−0.438)
lney	0.856 *	0.715	0.665	−0.230	0.227
	(1.728)	(1.207)	(0.549)	(−0.601)	(0.420)
lnin	3.766 ***	3.506	3.079	−0.564	2.165
	(2.924)	(1.565)	(1.021)	(−0.927)	(1.476)

t statistics in parentheses. * $p < 0.1$, ** $p < 0.05$, *** $p < 0.01$.

In the Yangtze River Delta, the Pearl River Delta, and the Beijing-Tianjin-Hebei Region, the main regression coefficient and the direct effect of green-technology innovation prove significantly negative. This is mainly because the Yangtze River Delta, which covers Shanghai, Jiangsu, Zhejiang, and Anhui, boasts advanced economic development, with a high level of economic openness. The development level of a green economy in the Yangtze River Delta is higher than that in the Beijing-Tianjin-Hebei Region and Northeastern Region. Shanghai and Zhejiang have taken the lead in green-technology innovation in China. The industrial structure of Shanghai is dominated by the tertiary industry, which emits fewer industrial pollutants. Compared with Jiangsu, Zhejiang, and Anhui, Shanghai invests the

most capital for the treatment of environmental pollution. Therefore, Shanghai plays a decisive role in promoting the level of green-technology innovation in the Yangtze River Delta. Noticeably, in 2018, to accelerate the construction of a complete local legal system for environmental protection, Shanghai revised local laws and regulations such as The Regulations for the Prevention & Control of Atmospheric Pollution in Shanghai, which mitigates atmospheric environmental pollution to a certain extent. Zhejiang rapidly improves the level of Internet information, and Hangzhou becomes a major base for new media culture in China. Zhejiang and Jiangsu vigorously develop the secondary industry and introduce many industrial products; however, the spatial spillover effect of green-technology innovation can effectively reduce atmospheric environmental pollution. Meanwhile, in the Yangtze River Delta, residents embody a high educational level, and the investment to scientific research proves sufficient, which raises the regional technological level and promotes the development of green-technology innovation. Green-technology innovation in the Yangtze River Delta produces a spatial spillover effect, which effectively drives the development of relatively backward cities in the region, improves the level of green-technology innovation in the region and its neighboring regions, and reduces the impact on atmospheric environmental pollution. Vis-à-vis the Yangtze River Delta, the Pearl River Delta sees faster economic development and enjoys better air quality than the Yangtze River Delta and Beijing-Tianjin-Hebei Region. The development of high-tech enterprises in Shenzhen, Guangzhou, Dongguan, and other cities significantly heightens regional green productivity, and achieves remarkable results in the transformation and upgrading of the manufacturing industry. Scientific and technological innovation serves as a major driving force for high-quality economic growth. Moreover, there are many coastal cities in the Pearl River Delta, where air quality is better than the interior region. The amount of wind and rainfall is also an important factor that reduces local atmospheric environmental pollution. However, there are numerous high-tech enterprises and high-end manufacturing industries as well as traditional manufacturing industries in the Pearl River Delta, which restricts the spillover effect of green-technology innovation. Developing cities may not actively learn from developed cities in green-technology innovation, and green-technology innovation plays an insignificant role in reducing the atmospheric environmental pollution in neighboring regions. Covering Beijing, Tianjin, and Hebei, the Beijing-Tianjin-Hebei Region suffers the most serious atmospheric environmental pollution in China. The Beijing-Tianjin-Hebei Region mainly adopts the development model of an extensive industry that features high energy consumption, high pollution, and high input. Compared with the Yangtze River Delta and the Pearl River Delta, the Beijing-Tianjin-Hebei Region has fewer high-tech industries, especially in Hebei. As a circum-capital urban cluster, the industrial structure and economic development of Beijing, Tianjin, and Hebei are subject to governmental policies. In the 21st century, the development of Beijing and Tianjin relies on support from neighboring cities. With the best geographical location, Hebei undertakes the industrial transfer from Beijing and Tianjin. Furthermore, Hebei possesses abundant mineral resources and supports the development of Beijing and Tianjin, which exacerbates atmospheric environmental pollution in Hebei. Simultaneously, extensive industries near Beijing are successively shut down, and the emission of pollutants decreases accordingly. This happens later in Tianjin and Hebei, so atmospheric environmental pollution in Hebei remains serious. Located in the Circum-Bohai Sea Economic Zone, the Beijing-Tianjin-Hebei Region has high-level openness and introduces more green technologies. Enterprises in Beijing, Tianjin, and Hebei exchange ideas on green technology, which makes green technology mature and alleviates local atmospheric environmental pollution. Yet, neighboring regions of the Beijing-Tianjin-Hebei Region attach less attention to green-technology innovation. The Yangtze River Delta and the Pearl River Delta see rapid economic development and great progress in green-technology innovation. In contrast, in the Beijing-Tianjin-Hebei Region, green-technology innovation remains at a low level, which limits the learning effect in neighboring regions. In other words, green-technology innovation plays a minor role in attenuating atmospheric environmental pollution in neighboring regions. As a

result, the coefficient of green-technology innovation in the Beijing-Tianjin-Hebei Region proves insignificant.

Different from the Yangtze River Delta, the Pearl River Delta, and Beijing-Tianjin-Hebei Region, the Northeastern Region and Chengdu-Chongqing Region see an insignificant spatial effect. Firstly, in the Northeastern Region, the main regression coefficient and the direct effect prove positive and insignificant, and the indirect effect proves negative and insignificant. This is because in economic development, the Northeastern Region lags far behind the Yangtze River Delta, the Pearl River Delta, the Beijing-Tianjin-Hebei Region, and the Chengdu-Chongqing Region. The Northeastern Region includes Heilongjiang, Jilin, and Liaoning provinces as well as three cities and one league of Inner Mongolia. With a low level of green-technology innovation, the Northeastern Region is beset with a high proportion of brain drain, high-level talents, and technological backbone in particular. Owing to the unsatisfactory policy environment in the Northeastern Region, the adequacy rates of talent and technology remain low. The Northeastern Region functions as the "granary" of China. In agriculture, it focuses on traditional farming and stockbreeding that make low demands on green-technology innovation. In the Northeastern Region, the economy develops slowly, green-technology innovation remains at a low level, and many high-level talents leave. Simultaneously, there is a great quantity of industrial enterprises. Therefore, in the Northeastern Region, green-technology innovation plays a minor role in reducing the emission of pollutants from industrial enterprises and mitigating atmospheric environmental pollution. The main regression coefficient and the direct effect prove positive and insignificant. In spite of this, the learning effect of green-technology innovation allows neighboring regions to introduce green-technology innovation, which reaches a low level yet has an inhibitory impact on neighboring regions. In contrast, in the Chengdu-Chongqing Region, the main regression coefficient of green-technology innovation proves negative yet insignificant, and the direct effect and indirect effect of green-technology innovation prove significantly negative. This is because the Chengdu-Chongqing Region forges the most developed economy in western China and forms a major urban belt in China. In terms of the overall level of green-technology innovation, the Chengdu-Chongqing Region rivals the Beijing-Tianjin-Hebei Region. However, the level of scientific and technological innovation in various cities in the Chengdu-Chongqing Region is significantly polarized. In Chengdu and Chongqing, there are more scientific research institutes, high-tech enterprises, and R and D investment to scientific and technological innovation than in other cities in the region, with a significantly higher level of scientific and technological innovation. The low level of scientific and technological innovation in other cities has an adverse effect on the overall level in the region. Most cities in the Chengdu-Chongqing Region stand in the Sichuan Basin, with unique geographical conditions. Atmospheric pollution arises from complex causes or seasonal factors, which makes it hard to improve the atmospheric environment. Moreover, in the Chengdu-Chongqing Region, atmospheric environmental pollution embodies high spatial correlation. Chongqing enjoys better air quality. Therefore, in the region, the main regression coefficients of green-technology innovation and atmospheric environmental pollution prove insignificant. Conspicuously, the level of green-technology innovation constantly increases, and the funds for green-technology innovation continuously enlarge. With more attention given to green-technology innovation, the scale effect of green-technology innovation alleviates atmospheric environmental pollution in the Chengdu-Chongqing Region. Simultaneously, neighboring regions continue to learn from green-technology innovation in the Chengdu-Chongqing Region, which weakens atmospheric environment pollution in the neighboring regions.

As the above analysis suggests, there are obvious differences in the level of green-technology innovation, the investment to R and D, the level of economic development, geographical location, and air quality among the Yangtze River Delta, the Pearl River Delta, the Beijing-Tianjin-Hebei Region, the Northeastern Region, and the Chengdu-Chongqing Region. Therefore, the degree of atmospheric environmental pollution in these regions

varies, with significant heterogenicity in the impact of green-technology innovation on atmospheric environmental pollution.

6. Conclusions and Policy-Related Suggestions

6.1. Research Conclusions

Based on the panel data of 30 provinces, autonomous regions, and municipalities directly under the Central Government in China from 2005 to 2018, this paper constructs a Spatial Autoregression Model and Spatial Durbin Model to analyze the relationship between green-technology innovation and atmospheric environmental pollution. This paper concludes at three levels. Firstly, green-technology innovation has a significant inhibitory effect on atmospheric environmental pollution, which mainly exists in the effect of production technology, the effect of treatment technology, and the effect of structural optimization. Secondly, green-technology innovation has a significant spatial spillover effect on atmospheric environmental pollution. When local industries give play to the learning effect and continue to learn and practice advanced approaches in green-technology innovation in neighboring regions, local capability in green-technology innovation will remarkably rise. Thirdly, when the intensity of environmental regulation reaches its value, green-technology innovation can effectively inhibit atmospheric environmental pollution. When environmental regulation reaches lower than the threshold, the effect of environmental regulation on atmospheric environmental pollution proves insignificant.

6.2. Policy-Related Suggestions

6.2.1. Fostering Green Technology Innovation for Environmental Sustainability and Economic Growth

Enhancing green technology innovation can help reduce atmospheric pollution. To strengthen green-technology innovation for the treatment of the atmospheric environment, local governments need to increase the investment to the research and development of green-technology innovation, expedite the research and development of green technology, promote the application of green-technology innovation in production, and reduce the use cost of green-technology innovation. Moreover, high-quality talents play an indispensable role in the development of green-technology innovation. Local governments can formulate favorable policies on talent-introduction and settlement, consider how to attract and introduce high-quality talents, and enhance the green acuity of high-quality talents, so as to disseminate the idea of green development among the public. As clear property rights mobilize enterprises to participate in green-technology innovation, local governments should highlight the protection of green intellectual property systems, establish strict supervision mechanisms, and protect the achievements of green-technology innovation. Additionally, local governments should quicken the research and development of environmental-protection technologies and institutions, integrate green technology into corporate development and people's daily life, and accelerate the realization of green and coordinated development of the economy and environment.

6.2.2. Leveraging High-Level Green-Tech Innovation Regions for Coordinated Development and Knowledge Exchange

Augmenting the supporting role of regions with a high level of green-technology innovation and fostering the coordinated development of neighboring regions are important goals. The improvement of the level of green-technology innovation necessitates the implementation of the development strategy of "one leads two". To firstly strengthen the policy support for regions with high-level green-technology innovation and then drive the coordinated development of neighboring regions enlarges the coverage of green-technology innovation. Specifically, governments should strengthen the exchanges on the knowledge of green-technology innovation. Governments of regions with high-level green-technology innovation can reinforce the publicity of green-technology innovation to give play to the learning effect of green-technology innovation, so that neighboring regions learn the gist of

green technology. Additionally, enterprises should deepen technological cooperation and exchanges in green-technology innovation. Enterprises in regions with high-level green-technology innovation can promote the research and development of clean technologies for energy conservation and emission reduction and pollution prevention, so as to gain profits and arouse the research and development interest of enterprises in neighboring regions. Governments should also establish a joint prevention and control mechanism for atmospheric environmental pollution, and work together with neighboring regions to design, formulate, and implement the plans for the treatment of atmospheric environmental pollution, develop the treatment system of green-technology innovation, and share the achievements of green-technology innovation, so as to produce the spillover effect of treatment policies and results.

6.2.3. Enhancing Environmental Regulation to Encourage Green-Tech Innovation in Heavily Polluted Regions

We highlight the importance of boosting up the intensity of environmental regulation in heavily polluted regions and making full use of the inhibitory effect of green-technology innovation. Governments should promote the development of green-technology innovation with the policies on environmental regulation. In line with the degree of regional pollution, local governments can adopt different policies on environmental regulation and prevent atmospheric environmental pollution with appropriate methods, so as to formulate policies suitable for various regions and effectively avoid a one-size-fits-all approach. To give full play to the role of different environmental-regulation tools in green-technology innovation, governments should vigorously support market-oriented incentive policies, which play a significant role in boosting green-technology innovation and produce an external effect via environmental tax, emission trading licenses, and other means. In terms of mandatory regulatory tools such as command and control that are difficult to practice, governments can make reasonable planning to achieve ideal treatment. Lastly, regions with more serious environmental pollution must tighten the policies on environmental regulation. Local governments ought to focus on the intensity of the policies on environmental regulation in heavily polluted regions, actively design the policies on environmental regulation to promote the development of green-technology innovation, and provide relevant subsidies to enterprises in the use of green technology to encourage enterprises to expand the application of green technology.

Author Contributions: Writing—original draft, J.Z., Y.Z. and X.B.; Writing—review & editing, Y.Z. and X.B. Data Curation, J.Z. All authors have read and agreed to the published version of the manuscript.

Funding: This research was funded by The National Social Science Fund of China (20BGL193).

Data Availability Statement: The data on fog-haze pollution of regions or cities come from the data of the annual mean of global PM2.5 concentration based on satellite monitoring published by the Socioeconomic Data and Applications Center of Columbia University (https://beta.sedac.ciesin.columbia.edu/ assessed on 10 March 2023). The emissions of industrial sulfur dioxide and industrial smoke (powder) dust as well as the removal of industrial sulfur dioxide in regions or cities come from the China Urban Statistical Yearbook and provincial statistical yearbooks, which are manually sorted by the author of this paper. The amount of green-patent authorization comes from the China National Intellectual Property Administration, which is manually sorted by the author of this paper. The data on indicators such as population density, built-up area, level of economic development, and industrial structure are sourced from the China Statistical Yearbook.

Conflicts of Interest: The authors declare no conflict of interest.

References

1. Ministry of Ecology and Environment of the People's Republic of China. *Bulletin of China's Ecological Environment in 2021*; Ministry of Ecology and Environment of the People's Republic of China: Beijing, China, May 2002.
2. Acemoglu, D.; Aghion, P.; Bursztyn, L.; Hemous, D. The Environment and Directed Technical Change. *Am. Econ. Rev.* **2012**, *102*, 131–166. [CrossRef] [PubMed]
3. Braun, E.; Wield, D. Regulation as a means for the social control of technology. *Technol. Anal. Strateg. Manag.* **1994**, *6*, 59–272. [CrossRef]
4. Chen, H.; Zheng, Q. Development Status and Prospects of Global Green Technology Innovation. *Econ. Res. Ref.* **2018**, *51*, 70–79.
5. Wang, L.Z.; Chen, M.Y.; Niu, L. Construction and dynamic evolution of enterprise green innovation path. *China Soft Sci.* **2021**, *3*, 141–154.
6. Carrion-Flores, C.E.; Innes, R. Environmental innovation and environmental performance. *J. Environ. Econ. Manag.* **2010**, *59*, 27–42. [CrossRef]
7. Oyebanji, M.O.; Kirikkaleli, D. Green technology, green electricity, and environmental sustainability in Western European countries. *Environ. Sci. Pollut. Res.* **2023**, *30*, 38525–38534. [CrossRef]
8. Zhou, J.; Wang, T. The Impact of Independent Technological Innovation on China's Carbon Emission: An Empirical Study Based on Inter-Provincial Panel Data. *Sci. Technol. Prog. Policy* **2014**, *31*, 29–35.
9. Nie, P.; Luo, Y.; Tan, X. The Heterogeneity of the Impact of Market Concentration and Technological Innovation on the Intensity of Industrial Carbon Emission. *Ind. Econ. Rev.* **2015**, *6*, 25–37.
10. Lu, X.; Bai, T. How Green-Technology Innovation Effectively Reduces Fog-Haze Pollution? *China Soft Sci.* **2020**, *6*, 174–182.
11. Li, F.; Sun, X.; Zhang, L. Industrial Agglomeration, Technological Innovation and Environmental Pollution. *Technol. Econ.* **2017**, *36*, 1–7.
12. Chen, Y.; Lu, J.; Yu, P. Can Technological Innovation Reduce Environmental Pollution: Empirical Evidences from 285 Cities in China. *J. Xi'an Jiaotong Univ. (Soc. Sci.)* **2019**, *39*, 78.
13. Schmidt, T.S.; Sewerin, S. Measuring the Temporal Dynamics of Policy Mixes: An Empirical Analysis of Renewable Energy Policy Mixes' Balance and Design Features in Nine Countries. *Res. Policy* **2019**, *48*, 103557. [CrossRef]
14. Liu, X. Research on the Effect of Green Innovation on Fog-Haze Pollution Under Spatial Correlation. *East China Econ. Manag.* **2019**, *33*, 48–57.
15. Lu, N.; Wang, W.; Wang, M.; Cai, Z.; Hua, L. Groundbreaking Low-Carbon Technological Innovation and Carbon Emission: Direct Impact and Spatial Spillover. *China Popul. Resour. Environ.* **2019**, *29*, 30–39.
16. Ren, Y.; Zhang, G. Can Urban Innovation Eliminate Fog-Haze? *China Popul. Resour. Environ.* **2020**, *30*, 111–120.
17. Wang, D.; Zhang, Z.; Shi, R. Fiscal Decentralization, Green Technology Innovation, and Regional Air Pollution in China: An Investigation from the Perspective of Intergovernmental Competition. *Int. J. Environ. Res. Public Health* **2022**, *19*, 8456. [CrossRef]
18. Lan, J.; Munro, A. Environmental Regulatory Stringency and the Market for Abatement Goods and Services in China. *Grips Discuss. Pap.* **2014**, *14*, 105–123. [CrossRef]
19. Huang, T.; Zhao, X.; Chen, K. Technological Innovation, Environmental Pollution and Regulatory Policy: A Perspective of the Transformation and Innovation Policies. *Sci. Sci. Manag. S. T.* **2020**, *41*, 58.
20. Wu, L.; Han, H. Environmental Regulation, Green-Technology Innovation and Regional Environmental Quality. *Urban Environ. Stud.* **2020**, *2*, 38–65.
21. Ullah, S.; Ozturk, I.; Majeed, M.T.; Ahmad, W. Do technological innovations have symmetric or asymmetric effects on environmental quality? Evidence from Pakistan. *J. Clean. Prod.* **2021**, *316*, 128239. [CrossRef]
22. Grossman, G.M.; Krueger, A.B. *Environmental Impacts of a North American Free Trade Agreement*; NBER Working Paper (No. 3914); NBER: Cambridge, MA, USA, 1991.
23. Popp, D. *The Role of Technological Change in Green Growth: General Information*; NBER Working Paper (No. w18506); NBER: Cambridge, MA, USA, 2012.
24. Liu, G.; Yu, L. Research on the Environmental Tendency of Technological Innovation. *Mod. Econ. Res.* **2020**, *4*, 101–108.
25. Wu, Y. Research on the Application of Spatial Measurement Model in Provincial R & D and Innovation. *J. Quant. Tech. Econ.* **2006**, *5*, 74–85.
26. Li, Z. Research on Regional Difference, Sources of Foreign Capital and the Effect of FDI Environmental Regulation. *China Soft Sci.* **2016**, *8*, 89–101.
27. Li, F.; Gong, J. Can Green-Technology Progress Alleviate Fog-Haze Pollution? *J. Xiangtan Univ. (Philos. Soc. Sci.)* **2021**, *45*, 82–92.
28. Lin, C.; Gong, X.; Kong, F. Environmental Regulation and Green-Technology Progress: Promoting or Inhibiting? Based on the Perspective of Spatial Effect. *Macroeconomics* **2019**, *45*, 131–141.
29. Jin, B. Theoretical Research on the Relationship Between Resource and Environmental Regulation and Industrial Competitiveness. *China Ind. Econ.* **2009**, *3*, 5–17.
30. Jiang, F.; Wang, Z.; Bai, J. The Dual Effect of Environmental Regulation on Technological Innovation: An Empirical Study Based on Dynamic Panel Data of Manufacturing Industry in Jiangsu. *China Ind. Econ.* **2013**, *7*, 44–55.
31. Fan, D.; Sun, X. Environmental Regulation, Green-Technology Innovation and Green Economic Growth. *China Popul. Resour. Environ.* **2020**, *30*, 105–115.

32. Xiang, K.; Song, D. A Spatial Empirical Study on PM2.5 Pollution in Various Provinces in China. *China Popul. Resour. Environ.* **2015**, *25*, 153–159.
33. Shao, S.; Li, X.; Cao, J.; Li, Y. The Choice of Economic Policies in the Treatment of Fog-Haze Pollution in China: Based on the Perspective of Spatial Spillover Effect. *Econ. Res. J.* **2016**, *9*, 73–88.
34. Cheng, Z.; Liu, J.; Li, L. Research on the Effect of Industrial-Structure Adjustment and Technological Progress on the Reduction of Fog-Haze Emission. *China Soft Sci.* **2019**, *1*, 146–154.
35. Guan, A.; Li, N. Research on the Threshold Effect of Technological Spillover and Absorptive Capacity of Inter-Regional Industrial Transfer in China: An Empirical Analysis Based on Inter-Provincial Panel Data in Western Region. *Soft Sci.* **2014**, *2*, 32–36.
36. Qin, B.; Ge, L. The Transfer of High-Pollution Industries and Overall Environmental Pollution in China: An Empirical Study Based on the Threshold Model of Inter-Regional Relative Environmental Regulation. *China Environ. Sci.* **2019**, *39*, 3572–3584.
37. Wang, Z.; Cao, Y.; Lin, S. The Impact Characteristic and Heterogeneity of Environmental Regulation on Green-Technology Innovation of Enterprises: Based on Green-Patent Data of Listed Companies in China. *Stud. Sci. Sci.* **2021**, *39*, 909–919, 929.
38. Wang, B.; Zhao, C. Green-Technology Innovation in China: Patent Statistics and Influencing Factors. *J. Ind. Technol. Econ.* **2019**, *38*, 53–66.
39. Zhu, P.; Zhang, Z.; Jiang, G. FDI and Environmental Regulation: An Empirical Study Based on the Perspective of Local Decentralization. *Econ. Res. J.* **2011**, *46*, 133–145.
40. Shen, K.; Jin, G.; Fang, X. Does Environmental Regulation Cause the Transfer of Pollution to Neighboring Regions? *Econ. Res. J.* **2017**, *5*, 44–59.
41. Liang, R.; Gao, M.; Wu, X. A Further Test of the Relationship Between Environmental Regulation and the Reduction of Atmospheric Pollution: An Analysis Based on the Threshold Effect of Economic Growth. *Ecol. Econ.* **2020**, *36*, 182–187.
42. Hu, X. Solving Fog-Haze Calls for the Optimization of Urban Planning. *China Environ. News* **2015**, *2*.
43. Liu, C.; Xu, Y. How Urbanization Affects the Treatment of Fog-Haze Pollution: An Empirical Study Based on Intermediary Effect. *Econ. Manag.* **2017**, *8*, 6–23.

Disclaimer/Publisher's Note: The statements, opinions and data contained in all publications are solely those of the individual author(s) and contributor(s) and not of MDPI and/or the editor(s). MDPI and/or the editor(s) disclaim responsibility for any injury to people or property resulting from any ideas, methods, instructions or products referred to in the content.

energies

MDPI

Review

Review on Separation Processes of End-of-Life Silicon Photovoltaic Modules

Jongwon Ko [1,†], Kyunghwan Kim [1,†], Ji Woo Sohn [1], Hongjun Jang [2], Hae-Seok Lee [2], Donghwan Kim [1] and Yoonmook Kang [2,*]

[1] Department of Materials and Engineering, Korea University, Seoul 02841, Republic of Korea
[2] Graduate School of Energy and Environment (KU-KIST Green School), Korea University, Seoul 02841, Republic of Korea
* Correspondence: ddang@korea.ac.kr; Tel.: +82-2-3290-3713
† These authors contributed equally to this work.

Abstract: Solar energy has gained prominence because of the increasing global attention received by renewable energies. This shift can be attributed to advancements and innovations in solar cell technology, which include developments of various photovoltaic materials, such as thin film and tandem solar cells, in addition to silicon-based solar cells. The latter is the most widely commercialized type of solar cell because of its exceptional durability, long-term stability, and high photoconversion efficiency; consequently, the demand for Si solar cells has been consistently increasing. PV modules are designed for an operation lifespan of 25–30 years, which has led to a gradual increase in the number of end-of-life PV modules. The appropriate management of both end-of-life and prematurely failed PV modules is critical for the recovery and separation of valuable and hazardous materials. Effective methods for end-of-life PV waste management are necessary to minimize their environmental impact and facilitate transition to a more sustainable and circular economy. This paper offers a comprehensive overview of the separation processes for silicon PV modules and summarizes the attempts to design easily recyclable modules for sustainable solar module development. Based on the studies summarized in this paper, suggestions are provided for future research.

Keywords: renewable energy; photovoltaic (PV) module; recycling; silicon solar cell; separation; recovery; environment; waste

Citation: Ko, J.; Kim, K.; Sohn, J.W.; Jang, H.; Lee, H.-S.; Kim, D.; Kang, Y. Review on Separation Processes of End-of-Life Silicon Photovoltaic Modules. *Energies* **2023**, *16*, 4327. https://doi.org/10.3390/en16114327

Academic Editors: Mohammad Mahmudur Rahman, Dibyendu Sarkar, Rupali Datta and Prafulla Kumar Sahoo

Received: 21 April 2023
Revised: 23 May 2023
Accepted: 23 May 2023
Published: 25 May 2023

Copyright: © 2023 by the authors. Licensee MDPI, Basel, Switzerland. This article is an open access article distributed under the terms and conditions of the Creative Commons Attribution (CC BY) license (https://creativecommons.org/licenses/by/4.0/).

1. Introduction

With the world focusing on minimizing carbon emissions and achieving net-zero targets, renewable energy sources have gradually gained increasing importance [1]. Among renewable energy sources, solar energy has gained considerable prominence [2], and in 2022, solar photovoltaic (PV) technology accounted for two-thirds of all renewable electricity technologies because of its potential to provide a limitless supply of clean, green energy without emitting harmful pollutants into the environment [3,4]. Solar power is considered a key component in our transition to a more sustainable future, which has led to an exponential increase in the number of PV module installations [5]. According to the International Energy Agency Photovoltaic Power Systems Program (IEA-PVPS) report, the global installed PV capacity reached 1185 GW in 2022, representing a remarkable increase of at least 240 GW from 2021 [3].

Therefore, the significance of recycling and reusing cannot be overstated. PV modules have an estimated lifespan of 25–30 years, and at the end of their life, they can pose a significant environmental challenge if not disposed properly [5–7]. PV modules contain materials such as silicon, glass, aluminum, copper, lead, and other materials that can be hazardous if released into the environment [8–11]. According to a report from the International Renewable Energy Agency (IRENA) and IEA-PVPS, the cumulative number of end-of-life PV modules in 2050 is estimated to be 60 and 78 million tons in the regular

and early loss scenarios, respectively [12]. In 2016, the expected installation capacity of PV modules for 2025 was 954 GW [12]; however, a report published in 2023 showed that the installation capacity for 2022 reached 1185 GW, which was significantly higher than the previous predictions [3]. Therefore, there is a high probability that the cumulative amount of waste from photovoltaic modules will increase.

Effective recycling and reuse strategies are necessary to address this growing challenge. Such strategies are beneficial to both the environment and the economy [13]. Appropriately recycling and reusing PV modules can help minimize raw material requirements and lower the carbon footprint associated with the production of new modules [14]. In addition, recycling and reusing PV modules creates new economic opportunities by creating jobs in the recycling industry and reducing the cost of producing new PV modules [15,16]. Moreover, by implementing effective recycling and reuse strategies, we can ensure that the valuable materials used in PV modules are recovered and utilized instead of being lost to the environment [17,18]. This can help conserve resources and reduce the environmental impact of PV module production and disposal [19,20].

In recent years, researchers and industries have developed innovative recycling and reuse methods for PV modules; these methods aim to improve recycling efficiency and reduce the cost of recycling and reusing PV modules [21]. Currently, there are several approaches to recycling PV modules, e.g., mechanical, thermal, and chemical processes [17,18,22–47].

This study examined the current progress in the research on recycling and reusing PV modules. To this end, PV module separation methods were categorized into mechanical, thermal, and chemical treatments based on the separation of materials, and the distinctive features and research directions of each method were analyzed:

(1) The PV modules were broken down into their individual components through mechanical operations, such as crushing, shredding, and grinding. These processes use heavy-duty machinery for crushing the modules and separating the materials based on their size, shape, and density. These broken-down components are subsequently sorted and processed for recycling or reuse [22–33];
(2) Thermal processes utilize high-temperature processes, such as combustion, pyrolysis, and electro-thermal heating, to recover valuable materials from the PV modules. However, these processes require specialized equipment and expertise to ensure the safe and effective recovery of materials [17,18,22,29,34–41];
(3) Chemical processes use solvents or acids to dissolve and separate different materials in the PV modules, and the separated components are then processed for recycling or reuse. These processes require careful management and disposal of the chemicals used, as well as proper treatment of the wastewater generated during the process [42–48].

2. Structure of a Silicon Photovoltaic Module

Figure 1 shows a typical silicon PV module that consists of glass, an encapsulant, silicon solar cell, a backsheet, a frame, and a junction box. In the past, 60-cell modules were commonly produced; however, 72-cell modules and 144-cell modules have only recently been manufactured using half-cut technology. In addition, modules with glass or transparent backsheets have been commercialized for producing bifacial solar modules. Table 1 lists the amounts of materials contained in the silicon PV module.

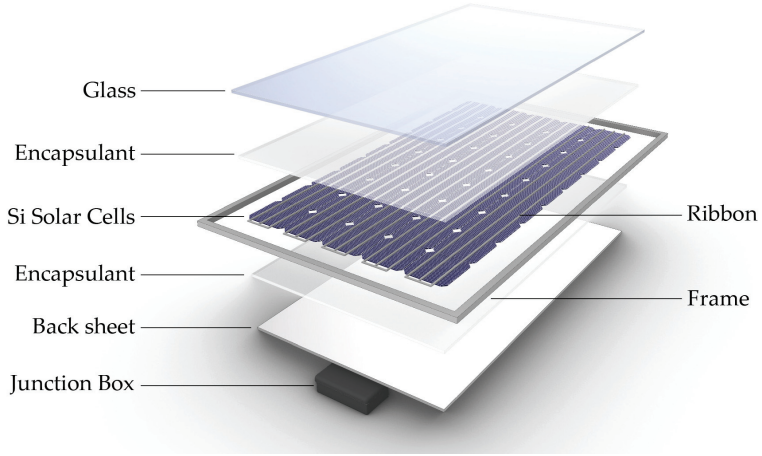


Figure 1. Structure of a silicon photovoltaic module.

Table 1. Material composition of Si photovoltaic module (60-cell with glass cover, backsheet) (Reproduced with permission [49]. Copyright 2017 Elsevier).

Material	kg/m^2	wt%
Ag	8.89×10^{-3}	5.76×10^{-2}
Al	2.54	16.5
Cu	1.13×10^{-1}	7.32×10^{-1}
Mg	8.02×10^{-2}	5.20×10^{-1}
Ni	1.63×10^{-4}	1.06×10^{-3}
Pb	7.20×10^{-4}	4.66×10^{-3}
Si	1.22×10^{-1}	7.90×10^{-1}
Sn	9.02×10^{-6}	5.84×10^{-5}
Steel	1.47	9.52
Ti	8.01×10^{-7}	5.19×10^{-6}
Zn	1.20×10^{-6}	7.77×10^{-6}
EVA	1.00	6.48
Glass	10.1	65.4
Total	15.4	100

A low-iron glass with a thickness of approximately 3 mm is commonly used as the front glass to ensure high transparency and to protect PV modules from external damage. Recently, the use of 2.5 mm thick or less than 2 mm thick glass has increased [50]. In bifacial PV modules, glass is used as a backsheet alternative, allowing the generation of solar energy from both sides [51]. Antireflection coatings are applied to glass to form textured surfaces for reducing light reflection and increasing light absorption. This not only enhances the efficiency of the modules but also improves their aesthetics. With the anti-reflection coatings, the transparency of the glass improves to approximately 94.5%, which is approximately 3% higher than that of the uncoated glass. The use of antireflection coatings and textured surfaces has become standard practice in PV module manufacturing, and it has led to a higher energy output and a more attractive appearance [50]. Anti-soiling, anti-glare, color coating, and structuring treatments are applied based on the environment in which the module is used [52].

An encapsulant combines the components of a module and plays an essential role in ensuring its long-term stability. Ethylene-vinyl acetate (EVA) is commonly used for this purpose. However, during the operation of a solar module in the field, potential-induced degradation (PID) can occur when EVA is used. Acetic acid, which can be generated from EVA, can potentially corrode glass-cell interfaces and metal components; this can pose challenges for the recycling processes. To mitigate this issue, polyolefins are sometimes used as substitutes for EVA, and their use has been gradually increasing [50,53,54].

Si solar cells are typically based on n- or p-type Si wafers. These solar cells are electrically connected using ribbons containing lead [55]; however, there is an increasing trend toward the use of lead-free materials for ribbons in module production for reducing the amount of lead used. In addition, the use of electrically conductive adhesives (ECA) to connect the busbar of solar cells without using a ribbon is expected to increase gradually [50].

The backsheet in PV modules ensures the electrical safety inside the module and protects the internal electrical wires and junction box from moisture, dust, debris, and other external factors [56]. The backsheet is composed of a three-layer structure made of EVA or polyvinylidene fluoride (PVF) sandwiched between two layers of polyethylene terephthalate (PET) film [57]. White backsheets are commonly used in PV modules; however, black backsheets are also used depending on the usage environment and purpose of the module [58]. Transparent backsheets or glass are used in bifacial PV modules [53]. The aluminum frame protects the edges of the module from external impacts and facilitates the installation of the solar module. In general, silver is used; however, other colors can also be used depending on the situation [59]. The junction box connects the electricity generated from the solar cells of the module to the external environment through cables. In addition, bypass diodes in the junction box prevent hotspots from occurring when the module is not illuminated uniformly, such as in the presence of shadows [60].

3. Photovoltaic Module Recycling Processes

Mechanical, thermal, and chemical processes are used to separate and recycle the components of a PV module. The mechanical processes for recycling end-of-life silicon PV modules typically involve crushing and sorting. The modules are broken down into small pieces in the crushing process, and useful materials, such as glass, cells, and aluminum, are separated and processed for reuse in the sorting process. It is difficult to separate the components of a module using only mechanical methods, and therefore, thermal and chemical methods are often employed afterward. This approach is relatively simple and can rapidly process a large number of modules. Furthermore, this approach offers environmental benefits because it reduces the waste generated during the crushing and sorting processes. The components of the module are crushed, and therefore, they cannot be recovered without being broken. In addition, the fine particulate matter generated during crushing can contribute to environmental pollution [22–33].

Thermal processes are used to remove encapsulants after the mechanical process; they can also be used to recover the glass and silicon solar cells of a module without breaking them. However, thermal methods require considerable energy and produce significant amounts of harmful gases and byproducts during treatment. If the frame, junction box, and cable are removed from the module and the module is immediately subjected to thermal treatment, harmful gases, such as HF, may be generated because the backsheet contains fluorine. Thus, the backsheet is often removed before thermal treatment, and the process is subsequently performed [17,18,22,29,34–41].

Chemical processes such as the thermal method that has been described can also be utilized to remove the encapsulant after the mechanical method. Chemical methods can be used to recover intact module components; however, the reaction time required increases with an increase in the area of the module. Research is currently underway to solve this problem [42–48]. Another disadvantage of this process is the burden of additional environmental pollution generated by the treatment of used chemicals.

The three processes were compared in terms of processing speed, environmental impact, possibility of mass processing, and state of component recovery. The results indicate that the mechanical process is the fastest among all methods and realized a lower environmental impact than that of the other two. In addition, the thermal process offers the advantage of being able to handle large quantities of modules, and is the most effective method of recovering components in intact conditions after processing.

3.1. Mechanical Process

Granata et al. conducted research on the classification and crushing of PV modules using two methods. The first method involved the use of a two-blade rotor followed by thermal treatment; the second method involved the use of a two-blade rotor followed by hammer crushing. In the first method, roughly 70% of the resulting particles had a diameter greater than 8 mm and were joined together with EVA when crushed. Thermal treatment was carried out at 650 °C to eliminate EVA. Approximately 85% of the particles with diameters greater than 1 mm were recovered directly as glass, whereas only 10% were recovered with diameters below 1 mm. Silicon was mixed with glass for particles with diameter ranging between 0.08 and 1 mm; an additional process was necessary to recover them. In the second method, in which hammer crushing was used, the size distribution of the particles was similar to that of the first method. However, EVA was still present in particles with diameters greater than 5 mm. Si was successfully recovered from particles with diameters smaller than 0.08 mm. Compared to the first method, slightly more glass was recovered from the second method using hammer crushing [23].

Pagnanelli et al. increased the glass recovery rate through three consecutive crushing processes using a two-blade rotor. The resulting particles were sieved into five sub-fractions: 8, 5, 1 mm, 0.4 mm, and 0.08 mm. During the first crushing process, 70% of particles larger than 8 mm and approximately 20% of particles ranging from 1 mm to 5 mm were sieved. During the second crushing process, 50% of the particles that were larger than 8 mm, 20% of particles ranging from 1 to 5 mm, and 10% of particles ranging from 0.4 to 1 mm were sieved. After the last third crushing process, 40% of particles larger than 8 mm, 25% of particles ranging from 1 to 5 mm, 17% of particles ranging from 0.4 to 1 mm, and 10% of particles ranging from 0.08 to 0.4 mm were sieved out. Approximately 12 $\pm$ 6% of the total glass was recovered from the 0.4 to 1 mm particles. The three consecutive crushing processes had two benefits: (1) After crushing, only a coarse fraction required thermal treatment, reducing the amount of waste that needed to be treated in subsequent processes. Approximately 85% of the waste required thermal treatment after one crushing process, and after three crushing processes, only 62% required thermal treatment; (2) The glass recovery rate increased. After one crushing process, less than 10% of the total glass was recovered; however, after three crushing processes, approximately 17% was recovered. Next, particles larger than 1 mm, which accounted for about 65% of the total number of particles, were heated in a furnace at a heating rate of 10 °C/min up to 650 °C for 1 h. After thermal treatment, the weight loss was approximately 15%, which was almost identical to the general EVA content, indicating that EVA was removed completely from the particles. After sieving the particles, approximately 50% of particles ranging from 1 to 5 mm, 20% of particles ranging from 0.4 to 1 mm, and 10% of particles ranging from 0.08 to 0.4 mm were sieved. Approximately 66 $\pm$ 8% and 12 $\pm$ 6% of the total glass weight was recovered from particles ranging from 1 to 5 mm and 0.4 to 1 mm, respectively. A glass recovery rate of over 91% was achieved after three crushing processes and thermal treatments; this recovery rate is higher than that achieved in a previous study (85%). Three consecutive crushing processes, combined with a thermal treatment, can lead to higher glass recovery rates, and this can help reduce waste and promote sustainability [24].

La Mia Energia Scarl developed an on-site recycling method for PV modules using portable equipment. Initially, they cut the PV modules into 100 $\times$ 100 mm pieces using a cutting machine. These cut pieces were then processed using a hammer mill and sieved consecutively through 6 mm and 2 mm meshes. The resulting fragments were sorted into three categories based on size, and each category was recovered separately. The first category (ranging from 0.5 to 2 mm) contained plastic and copper. A rotating magnetic field was used to induce currents to recover copper, other metals, and plastics. The second category (ranging from 0.5 to 0.315 mm) contained relatively small silicon fragments mixed with glass. The third category (below 0.315 mm) contained relatively large amounts of silicon fragments mixed with glass. By using a rotating magnetic field, valuable materials,

such as copper and silicon, could be efficiently recovered from PV modules onsite using portable equipment [25].

Yingli Solar utilized cryogenic methods to separate the PV modules. The modules were crushed and the resulting mixture was abraded at cryogenic temperatures. The mixture consisted of EVA, silicon, silver, and aluminum, which were separated using the electrostatic separation method. However, the separated Si has low purity and cannot be reprocessed into new wafers; thus, further research is required to address this issue [26].

NPC incorporated, Japan developed a method that uses a heated blade (hot knife) to separate the EVA between the glass and the cells. The heated blade (hot knife) is a 1 m long steel blade heated to 180–300 °C. This method can be used to recover intact glass and it only requires approximately 40–60 s per module. However, during the separation process, cells can break, and additional processing is required to separate them [27,28].

The Mitsubishi Materials Corporation developed a glass-scraping method that can process one module per minute. Toho Kasei scraped the backsheet instead of the glass and recovered the materials through additional chemical processes. In the Full Recovery End-of-Life Photovoltaic (FRELP) project in Europe, modules were heated to 90–120 °C using an IR heater; the glass was recovered using roller mills and high-frequency vibrating knives [29].

Li et al. proposed a mechanical treatment to remove and recycle the EVA layer from the PV module. Their approach employed a 1064 nm optical-fiber pulsed laser to irradiate the back EVA layer, followed by mechanical peeling. Initially, the backsheet of the module was removed, and then, the laser was applied through the back EVA layer to the interface between the cell and the back EVA. The metal electrode at the back of the cell absorbed the laser energy, leading to a rise in temperature at the cell/EVA interface, weakening the adhesion of EVA to the cell. The experiment demonstrated that an increase in the laser output density (P) and pulse repetition rate (PRR) enhanced the debonding effect. However, excessive P or PRR values can lead to significant damage to the cell and to the back of the EVA layer because of the significant rise in temperature at the cell/EVA interface. The thermal decomposition and charring of the EVA layer were also observed. Through experiments, Li et al. achieved a perfect debonding effect by controlling the laser using an optimized combination of P and PRR (P 2.1 MW/cm^2 and PRR 50 kHz). Consequently, the back EVA layer was easily removed mechanically, and both the removed EVA and cells were recyclable and not damaged by laser treatment. This innovative approach for removing and recycling the EVA layer using laser-based mechanical treatment has a significant potential toward improving the sustainability and cost-effectiveness of the PV module industry [30].

Song et al. applied high-voltage fragmentation (HVF) as a mechanical treatment for decamping PV panels. Based on their experimental results, they claimed that HVF resulted in significantly less material wastage and improved crushing effects. When HVF is applied to PV panels, discharge channels are formed at the interfaces of the different layers because of the varying dynamic fracture strengths of the dielectrics that constitute the panel materials. These channels then expand radially and eventually exceed the tensile strength of the materials, fragmenting the constituent components of the layers. Based on this principle, HVF was used to investigate the distribution of Cu, Al, Pb, Ag, and Sn at various particle sizes and to explore the energy consumption and mechanism of the HVF for the PV panel crushing effects. During the experiment, an upper electrode in the form of a 5.7 mm diameter column was used along with a grounding electrode equipped with a 1 mm hole. The experiment demonstrated that the average particle size of the crushed PV panels decreased with an increase in the pulse number and voltage amplitude. The optimal conditions for HVF in terms of energy savings were determined to be 192.99 J/g following 300 pulses at 160 kV. The PV panels were crushed into particles with an average size of 4.1 mm. The experimental results showed that, with the exception of Al, a relatively low proportion of metals was found in particles ranging from 1 to 5 mm. Over 95% of Cu and 96% of Ag were detected in particles smaller than 1 mm, whereas 85% of Al was detected in particles ranging from 0.25 to 2 mm. In particles smaller than 0.5 mm, 85% of Pb and 87%

of Sn were detected; this method is environmentally friendly because it does not generate additional pollution, unlike the thermal and chemical treatment methods. The crushed particles are concentrated in specific size fractions convenient for metal recovery, and their energy consumption is relatively low, which makes them an economically attractive method. However, HVF has the disadvantage of requiring strict conditions such as the pulse rise time of less than 500 ns, a high-voltage volume of 100 kV or more, and a repetition pulse frequency [31].

Nevala et al. proposed a mechanical treatment method that employs electrohydraulic fragmentation (EHF), which is a type of high-voltage pulse crushing, to achieve a higher separation efficiency. The EHF process crushes various materials that constitute the PV modules using mechanical shock waves generated in a fluid medium. EHF generates short, powerful shockwave pulses through an electrohydraulic mechanism between electrodes in a fluid, fracturing weak points in the interface between different materials. In the experiments, shockwave impulses of 600 J were used at rates of 300 and 500 pulses/s. The resulting crushed particles were collected and heated in a muffle furnace at 60 °C for 24 h before being sieved into six categories: smaller than 0.25 mm, from 0.25 to 0.5 mm, from 0.5 to 1 mm, from 1 to 2 mm, from 2 to 4 mm, and larger than 4 mm. The results of the EHF experiments demonstrated that compositions of 99% Cu, 60% Ag, and 80% Pb, Sn, and Al could be obtained in crushed particles larger than 4 mm when using a rate of 300 pulses per second. However, the rate of 500 pulses per second resulted in a lower metal content in the crushed particles that were larger than 4 mm, with compositions of 98% Cu, 40% Ag, and 60% Pb, Sn, and Al. Furthermore, after EHF, 99% high-purity Si could be extracted from particles larger than 0.5 mm and smaller than 2 mm. This method offers the advantage of facilitating subsequent processing and extraction compared to conventional crushing methods; furthermore, it can produce significantly higher-purity Si. EHF is a promising mechanical treatment method that can increase separation efficiency during the decomposition of PV modules. The utilization of shock waves generated in a fluid medium using an electrohydraulic mechanism highlights the superiority of this method over conventional crushing methods. EHF provides a high separation efficiency for various metals and it produces high-purity Si, which is beneficial for subsequent processing and extraction [32].

Akimoto et al. developed a high-voltage pulse crushing technique that combines sieving and dense-medium separation for mechanical treatment to separate the materials in the PV panels. The experiments involved two stages: primary and secondary crushing. In the primary crushing stage, a high-voltage pulse crushing technique using an impact wave transmitted to the Al electrode and Si substrate was employed for separating the glass and backsheet layers. Experiments with discharge voltages of 90, 110, 130, and 180 kV and 10 or 20 pulses confirmed that the glass and backsheet layers could be separated without damaging the cell at 110 kV and 20 pulses. In the secondary crushing stage, high-voltage pulse crushing was applied to the glass layer to separate the EVA and glass and to the backsheet layer to separate the bus bar. Experiments with discharge voltages of 90, 130, and 180 kV and 50, 100, 150, 200, and 250 pulses showed that EVA and glass could be separated without destruction at 90 kV with 250 pulses. The crushed particles obtained from the secondary crushing stage were sieved, which resulted in a small amount of glass, including Si powder in the size range of 45–850 μm. The glass containing the Si powder was refined by dense-medium separation at a specific gravity of 2.4. Metals such as Cu, Sn, and Pb were recovered in the range of 1.0–8.0 mm, while Ag was recovered in sizes below 20 μm, as well as in the ranges 2.0–4.0 mm and 4.0–8.0 mm. These results demonstrated the effectiveness of the high-voltage pulse crushing technique for separating the various materials in the PV panels [33].

Table 2 provides a concise overview of the mechanical processes.

Table 2. Mechanical processes used for the separation of module components in the referenced studies.

Process	Tested Module Size	Recovered Materials	Remarks	Ref.
Two-blade rotors crushing with thermal treatment or hammer crushing	N/A	Glass fractions	- Only mechanical methods were used to recover glass fractions. - The same method was applied to a-Si and CdTe solar modules.	[23]
Two-blade rotors triple crushing	40 cm × 40 cm	Glass fractions	- Thermal treatment for d > 1 mm fractions. - The same method was applied to a-Si and CdTe solar modules.	[24]
Oscillating hammers milling and mill impact hammer set	10 cm × 10 cm	Copper, metals, plastic (EVA/backsheet), silicon	- Photovoltaic mobile recycling device. - Separate materials by induced currents generated by a rotating magnetic field for 0.5 mm < d < 2 mm particles.	[25]
Cryogenic abrading	N/A	EVA, backsheet particles, silicon powder, silver, aluminum, glass	- Recover materials as particles. - Dismantle and smash module before abrading. - Separate materials by electrostatic separation. - Recovered silicon cannot be used for recycling to reprocess new wafers because of its low purity.	[22, 26]
Heated blade (hot knife)	Maximum: 1090 mm × 2100 mm Minimum: 800 mm × 800 mm	Glass (intact)	- High-speed process (about 40–60 s per module). - Additional separation process is required for the remaining separated parts.	[27, 28]
Optical-fiber pulsed laser	156 mm × 156 mm	EVA, silicon solar cell (intact)	- Proposed to recycle EVA and significantly minimize CO_2 emissions. - The solar cell (intact) expands the potential for recycling in future processes.	[30]
High-voltage fragmentation (HVF)	3 cm × 3 cm	-	- Greater potential for recycling metals through particle size reduction in particles than conventional crushing methods. - Presents minimal material waste and superior crushing performance. - Suggests the possibility of recovering glass, Si powder, Ag, Cu, Sn, and Pb.	[31]
Electro-hydraulic fragmentation (EHF)	12 cm × 8 cm	-	- Concentration of metals in either the largest fraction >4 mm or <0.5 mm. - Suggests the possibility of recovering glass, Si powder, Ag, Cu, Sn, and Pb.	[32]
High-voltage pulse crushing	50 mm × 50 mm	-	- Suggests the possibility of recovering glass, Si powder, Ag, Cu, Sn, and Pb.	[33]

3.2. Thermal Process

Lee et al. developed a method for recovering intact Si wafers via thermal treatment. To achieve this, the modules were pre-treated using three methods: glass cracking, EVA patterning, or a combination of both. The pre-treated modules were subjected to heat treatment at 200, 250, and 300 °C, and the results were examined. EL imaging confirmed breakage in the cells, and the thermogravimetric analysis (TGA) showed thermal decomposition in the range of 25–550 °C. The expansion behavior of EVA was confirmed through the expansion mode of thermal mechanical analysis (TMA). During the experiment, the cells underwent significant changes when exposed to different temperatures. Exposure to a temperature of 300 °C resulted in the cells breaking and becoming carbonized, appearing black with numerous bubbles present. However, the cells did not break when exposed to a temperature of 250 °C; however, they underwent carbonization, resulting in a brown coloration. TGA was used to confirm the stages of EVA decomposition; the TGA results showed that EVA decomposition occurs in two stages, with the first stage occurring in the temperature range of 240–300 °C. This stage was influenced by the round cracks that occurred in the cells. The round cracks were formed at temperatures above 240 °C because of the acetic acid generated during this process (the acetic acid is subsequently removed at temperatures near 370 °C). The second stage of decomposition occurs in the temperature range of 420–450 °C, and it is attributed to combustion reactions. Finally, EVA was completely combusted at 520 °C. The pressure generated by trapped gases ultimately leads to cell breakage. The expansion behavior of the laminated EVA was confirmed using TMA, which revealed that EVA expands up to 79 °C as it transitions from its crystalline state to the amorphous state. Then, it contracts up to 130 °C because of the cross-linking reactions that cure EVA. Acetic acid is generated and subsequently removed, and EVA undergoes further expansion and contraction within the temperature range of 130–270 °C during carbonization, with the EVA contracting up to a temperature of 370 °C because of the evaporation of acetic acid. EVA was combusted at temperatures above 420 °C. Various methods were applied to recover intact Si wafers from modules, and the results were examined. Finally, intact Si wafers were recovered from modules in which both glass cracking and EVA patterning were applied. When only glass cracking was applied, round cracks appeared because of the acetic acid generated during the process. When only EVA patterning was applied, cracks occurred following the crystal orientation because of the expansion and contraction of the EVA material [34].

Park et al. introduced a jig to prevent damage to the cells. The PV modules were subjected to tests with and without the use of a specifically designed jig, which featured 5 mm wide grooves spaced at 5 mm intervals to facilitate the release of gas generated during the annealing process. The annealing temperature and ramp-up rate were analyzed. Two sample groups were established. The first group had a fixed annealing temperature of 480 °C tested at five different ramp-up rates, 5, 10, 15, 20, and 30 °C/min. The second group had a fixed ramp-up rate of 15 °C/min tested with four different annealing temperatures, 350, 400, 450, and 480 °C. In the first group, the cells remained undamaged and could be recovered when the jig was used in conjunction with a ramp-up rate of 15 °C/min. Conversely, cells without jigs were damaged under all conditions. In the second group, the cells remained undamaged and could be recovered when using the jig with an annealing temperature of 480 °C; however, cells without the jig were found to be damaged under all conditions. The complete separation of the EVA and backsheet was not observed at temperatures below 450 °C. During the annealing process, gas accumulates in the EVA layer between the cells and the backsheet and between the cells and the glass. Among these, the gas that accumulates between the cells and the glass has a more significant impact on cell damage because the backsheet is relatively more effective at releasing gas than glass. The accumulation of gas leads to stress in the cells, and cell damage occurs when this stress reaches a critical level. The jig used in this study prevented excessive stress on the cells; the gas generated during annealing was released through the grooves in the jig, resulting

in the recovery of undamaged cells. These findings emphasize the importance of using a specially designed jig for preventing cell damage during the annealing of PV modules [35].

Wang et al. developed a two-step heating profile to recover intact glass and prevent cracks caused by the expansion of the backsheet and EVA. In the first step, the module was heated to 330 °C for 30 min to separate the backsheet from the EVA. Although the EVA did not separate because of the decomposition of the backsheet temperature range of 260 °C to 300 °C, the backsheet was removed successfully. In the second step, the module was heated to 400 °C for 120 min to burn off the EVA and backsheet. The two-step process prevented the deformation of the backsheet and EVA, and this in turn prevented glass cracks and allowed the recovery of intact glass [36].

Frisson et al. investigated two pyrolysis methods using a conveyor belt furnace and a fluidized bed reactor. In a conveyor belt furnace, pyrolysis was conducted at 450 °C in both air and nitrogen atmospheres. The air atmosphere resulted in an exothermic reaction on the silicon surface, causing the cells to break; however, this exothermic reaction was avoided in a nitrogen atmosphere, and a recovery yield of over 80% was achieved. In the fluidized bed reactor, pyrolysis was conducted at 450 °C for 45 min using very fine sand as the bed material. The sand particles were fluidized at a velocity of 1 cm/s for a particle diameter of 100 μm, and modules were placed in a netting envelope. A recovery yield of over 80% was obtained, and almost 100% of the glass was recovered from the modules [37].

Doni and Dughiero utilized an electrothermal heating method instead of a conventional furnace for separating the components of the PV modules. They employed an RF power generator and positioned nonmagnetic flat electrodes above and below the module to generate a uniform transverse RF electric field. The lower electrode was grounded, and the upper electrode was connected to apply the RF voltage. They found that glass fragments separated easily from the EVA, and the remaining parts from which the glass had been removed could be recovered for other recycled materials through post-treatment processes. The recovered glass could be recycled directly [38].

The Kitakyushu Foundation for the Advancement of Industry, Science, and Technology (FAIS) utilized a milling machine to remove the backsheet, preheated the module at 350 °C, and then combusted it up to 500 °C before cooling it down to 250 °C. The heat generated by the combustion of the EVA in the furnace was reused. The Chinese Research Academy of Environmental Sciences (CRAES) and the Institute of Electrical Engineering, Chinese Academy of Science (IEE CAS) utilized a tube furnace for performing a two-step thermal process at 250–300 °C and 500–550 °C with the environment inside the tube alternating between oxygen and nitrogen [29].

Fiandra et al. proposed an advanced thermal treatment method for the minimizing hazardous gas emissions that occur during the degradation of the backsheet in PV waste. In this method, a PV waste sample was inserted into a quartz sample holder and placed in a tube furnace, where it was heated at a rate of 450 °C/h to 200 °C in the absence of gas flow. The sample was held at 200 °C for 30 min, and then cooled to room temperature. This combustion process was designed to remove the polymer layer from the backsheet, which could be easily removed manually from the initial PV sample. Afterward, air was supplied to the reactor at a flow rate of 24 L/h, and EVA was removed by heating at a rate of 450 °C/h to 500 °C for 1 h. This method proved effective in removing hydrofluoric acid and fluorinated organic compounds generated during the decomposition of the backsheet [52]. In a follow-up study, Fiandra et al. aimed to reduce the emission of pollutants and decrease the mass and energy consumption of PV waste sent for thermal treatment using a milling machine to remove the backsheet layer. To prevent the cracking of the silicon wafer, the module was pretreated with glass cracking and EVA patterning before thermal treatment. The backsheet layer was removed using a vacuum-suctioned and panel-fixed machine with an 18 mm tip diameter at 18,000 rpm and a cooling system that used air. The rest of the backsheet was removed by chipping the backsheet–EVA interface. The experimental results showed that the mechanical removal of the backsheet from the PV module removed HF, COF_2, and fluorinated organic compounds, which are hazardous to human health and the

environment. In addition, the trend of carbon in gaseous products, such as CO, CO_2, and volatile organic compounds (VOCs), generated during EVA thermal treatment at variable temperatures was investigated. The carbon combustion efficiency was the highest at 500 °C and 600 °C. The results showed a reduction in VOCs under oxidation conditions because carbonaceous byproducts were oxidized to CO_2 under these conditions. Therefore, EVA thermal treatment at 500 °C under N_2 flow was conducted to reduce energy consumption and VOC emissions. This approach successfully reduced the VOC emissions generated during the EVA thermal treatment [40].

Riech et al. conducted experiments to realize the complete combustion of EVA through thermal treatment that uses a combination of time (50–60 min) and temperature (400–650 °C). The results showed that the complete combustion of EVA was achieved in a sample treated at 550 °C for 60 min. There were no significant differences in the results when the treatment time or temperature were increased, except for an increase in energy consumption. In the next experiment, they investigated the time and temperature required for the complete combustion of EVA based on energy consumption. The results showed that EVA could be completely combusted with the lowest energy consumption when treated at 650 °C for 30 min [41].

Table 3 provides a concise overview of the thermal processes.

3.3. Chemical Process

Doi et al. investigated the effects of 12 different solvents, including lacquer thinner, acetone, toluene, petroleum benzene, ethanol, isopropanol, methyl ethyl ketone, methyl isobutyl ketone, tetrahydrofuran, ethylene glycol, trichloroethylene, and glycerin, on the separation of modules by observing the changes in EVA. The EVA was categorized based on crosslinking, and the solvents were tested at room temperature and at 80 °C. Trichloroethylene was found to cause the most significant change in EVA under all conditions; it was, therefore, selected as the solvent for the experiment. A one-cell module with a glass/EVA/cell/EVA/aluminum foil structure was created to confirm the separation of the module. However, when the module was initially immersed in trichloroethylene at room temperature, the cells were damaged after a few days due to EVA swelling. To address this issue, glass was added to the back of the module for mechanical pressure, and the experiment was conducted at room temperature and at 80 °C. An intact solar cell was recovered under the condition of 80 °C with the addition of one glass to the back, which took approximately 7–10 days. In addition, the same experiment was conducted using o-dichlorobenzene as the solvent, and an intact solar cell was recovered without additional glass at 120 °C after one week [42].

Kang et al. conducted experiments to confirm the dissolution of EVA in 10 different solvents: 2-propanol, 4-methyl-2-pentanone, petroleum benzene, tetrahydrofuran, trichloroethylene, toluene, o-dichlorobenzene, glycerin, acetone, and ethyl alcohol. They confirmed that tetrahydrofuran, o-dichlorobenzene, and toluene can be used for this purpose. Toluene was selected because of its low cost and high stability; it took approximately two days for the glass to separate from the module at 90 °C. The EVA laminated on the module comprised crosslinked and non-crosslinked parts. EVA dissolved in the non-crosslinked part when organic solvents were applied. The solvents swell the cross-linked part of EVA, which weakens its binding force and leads to its dissolution and swelling [43].

Table 3. Thermal processes used for the separation of module components in the referenced studies.

Process	Tested Module Size	Recovered Materials		Remarks	Ref.
Combustion (550 °C, 5 °C/min, 2 h)	1-cell module	Glass (damaged), silicon solar cell (intact)	-	Pretreatment (glass cracking, EVA patterning).	[34]
			-	Recovered unbroken silicon solar cell is chemically etched and then remanufactured into new solar cell.	
Combustion (480 °C, 15 °C/min, 1 h)	1-cell module	Glass (intact), silicon solar cell (intact)	-	Using designed and employed fixture.	[35]
			-	Recovered unbroken silicon solar cell is chemically etched and then remanufactured into new solar cell.	
Combustion (1st—330 °C, 30 min, 2nd—400 °C, 2 h)	60-cell module	Glass (intact), silicon solar cell (broken)	-	Recovered silicon solar cell is chemically etched.	[18]
	1-cell module				[36]
Pyrolysis (Conveyer belt furnace, fluidized bed reactor, 450 °C)	8-cell module 36-cell module	Glass (intact), silicon solar cell (intact)	-	Recovered unbroken silicon solar cell is chemically etched and then remanufactured into new solar cell.	[37]
			-	Producing a new module using recycled results in lower energy consumption compared to manufacturing a module with new wafers.	
Electrothermal heating (RF heating 400 W)	1-cell module	Glass (broken)	-	Further treatments are required to separate the sandwich structure (EVA/cell/backsheet).	[38]
Pyrolysis (550 °C, 15 min)	N/A (EoL silicon PV modules made by Hyundai)	Glass (broken), silicon solar cells (broken)	-	Pretreatment (shred the module in small pieces approximately 40 mm × 40 mm in size).	[17]
			-	The recovered silicon solar cells were further treated with chemicals (HNO_3, H_2SO_4) to recover metals.	
Combustion (500 °C, 1 h)	10 cm × 10 cm	Glass (broken), silicon (broken), ribbon	-	Remove HF and fluorinated organic compounds generated during the decomposition of the backsheet.	[39]
Combustion (500 °C, 1 h)	10 cm × 10 cm	Glass (broken), silicon (broken), ribbon	-	Under an N_2 flow, VOCs are reduced because the carbonaceous byproducts under the oxidative conditions are converted into CO_2.	[40]
Combustion (650 °C, 30 min)	10 cm × 10 cm	Silicon (broken)	-	After thermal treatment, a chemical etching process is conducted to recover silicon.	[41]

Kim et al. conducted experiments on four different solvents (toluene, trichloroethylene, o-dichlorobenzene, and benzene) to investigate their ability to dissolve EVA at various concentrations and temperatures with the addition of ultrasonic treatment. Ethyl alcohol was used to adjust the alcohol concentration. They confirmed that solubility was greater at 3 M than at 1 M and that solubility increased with the increasing temperature. Under the conditions of 3 M toluene, 70 °C, 60 min, and 450 W ultrasonic treatment, EVA was dissolved completely; however, the cells were damaged because of EVA swelling. Increasing the ultrasonic intensity at higher temperatures resulted in a more effective dissolution. However, in toluene, there was little difference in the degree of dissolution when only the ultrasonic intensity was changed under the same conditions. This suggests that toluene was more influenced by the concentration. Under 3 M o-dichlorobenzene, 70 °C, 60 min, and 900 W conditions, EVA was dissolved completely without damaging the solar cell. However, other solvents can cause cell damage. Finally, under 3 M o-dichlorobenzene, 70 °C, 30 min, and 900 W conditions, EVA was dissolved completely without damaging the cell, and the cell was recovered [44].

Azeumo et al. conducted experiments to determine the optimal conditions for dissolving EVA using water, toluene, xylene, 2,4-trimethylpentane, n-heptane, and *N*,*N*-dimethylformamide. The variables used were solvent residence time, temperature, and ultrasonic treatment. The effect of preheating the module at 200 °C before immersing it in the solution was also investigated. After preheating, the module was immersed in each solvent at its boiling point and subjected to an ultrasonic treatment for 2 h. The results indicated that water, 2,4-trimethylpentane, n-heptane, and *N*,*N*-dimethylformamide did not dissolve EVA. However, xylene and toluene dissolved more than 90% of the EVA. Toluene was then used under various conditions, and it was found that EVA dissolved by more than 95% with ultrasonic treatment at 60 °C for 50 min, while it detached completely without ultrasonic treatment at 110 °C for 30 min. Preheating the module did not significantly affect the results [45].

Tembo et al. used hexane as a solvent for the chemical treatment to dissolve EVA and recover PV cells. The initial results showed a separation rate of 66% for the hexane-based system after 24 h at 25 °C. Using temperature as a variable, the highest separation rate of 79.7% was observed at 70 °C, slightly above the boiling point of hexane at 66 °C. Hexane at 70 °C showed greater separation rates compared to those at 80 °C and 90 °C. The separation rates were measured at different hexane concentrations, including 1, 2, 5 M, and pure hexane. Pure hexane exhibits the highest recovery rate. The effect of ultrasonic treatment at various concentrations at 70 °C was also investigated. The sample was treated with ultrasonic waves for 15 min and then dissolved in pure hexane at 70 °C. The experiment showed that the sample treated with ultrasonic waves for 15 min and chemically treated with pure hexane at 70 °C had the highest separation rate of 92.4% [46].

Xu et al. devised a solvothermal swelling with thermal decomposition (SSTD) method that allowed the recovery of intact solar cells during heat treatment. However, during the thermal decomposition process, gases were produced from the ethylene vinyl acetate (EVA) located between the glass and the cell; these gases were trapped by the glass, ultimately causing damage to the cell. To address this issue, channels were created to discharge the gas generated horizontally during pretreatment. The pretreatment conditions were optimized by testing various temperatures, processing times, and solution conditions. Ultimately, a mixture of 0.2 M toluene and 0.2 M ethanol was used for the pre-treatment, exposing the module to organic vapors at 190 °C for 2 h, followed by thermal treatment in a 500 °C furnace to remove the residual EVA and backsheet and obtain intact solar cells. The recovery rate of the intact solar cells was 86.11% for a commercial 36-cell PV module. The recovered cells were obtained in wafer form via chemical etching, and their durability was confirmed to be comparable to that of the new wafers [47].

Table 4 provides a concise overview of the chemical processes.

Table 4. Chemical processes used for the separation of module components in the referenced studies.

Process	Tested Module Size	Recovered Materials	Remarks	Ref.
Trichloroethylene (80 °C, 10 days)	1-cell module 125 mm × 125 mm	Silicon solar cell (intact)	- Suppressing EVA swelling by applying mechanical pressure. - Cross-linking treatment at 155 °C for 15 min is required before chemical treatment.	[42]
O-dichlorobenzene (120 °C, 7 days)	1-cell module 125 mm × 125 mm	Silicon solar cell (intact)	- Suppressing EVA swelling by applying mechanical pressure. - Cross-linking treatment at 155 °C for 15 min is required before chemical treatment.	[42]
Toluene (90 °C, 2 days) with thermal treatment (600 °C, 1 h)	60-cell module (975 mm × 1455 mm)	Silicon powder	- Recovering pure silicon using chemical etching after thermal treatment. - Recovery of silicon with 99.99% (4N) purity.	[43]
Toluene (70 °C, 60 min, 3 M, 450 W ultrasonic)	55 mm × 25 mm	Silicon (broken)	- Cracks occur due to the swelling of EVA.	[44]
O-dichlorobenzene (70 °C, 30 min, 3 M, 900 W ultrasonic)	55 mm × 25 mm	Silicon (intact)	- No cracks caused by complete EVA dissolution within 30 min.	[44]
Toluene (110 °C, 30 min)	13 cm × 13 cm	Glass, silicon	- Module disassembly and crushing for aluminum frame removal via mechanical treatment. - 95% of EVA is dissolved under ultrasonic conditions at 60 °C for 50 min.	[45]
Hexane (70 °C, 24 h, pure, ultrasonic)	17 cm × 17 cm	Silicon solar cell (intact)	- Achieved a separation efficiency of 92.4% using hexane.	[46]
Solvothermal swelling (190 °C, 2 h, 0.2 M toluene, 0.2 M ethanol, 1.2–1.4 MPa) with thermal treatment (500 °C, 30 min)	1-cell module (50 mm × 50 mm, cell size: 39 mm × 19 mm × 220 μm, mc-Si) 36-cell module (230 mm × 240 mm, Cell size: 52 mm × 19 mm × 220 μm, mc-Si)	Glass (intact), silicon solar cell (intact)	- Organic solvents are used before heat treatment to prevent solar cell breakage during subsequent processes. - Confirmed that the recovered solar cells are intact.	[47]

4. Silicon Photovoltaic Module Designs for Recycling

PV modules require a long-term stability of approximately 30 years, and manufacturers produce modules by increasing their durability to achieve this. However, these efforts have resulted in difficulties in separating the PV module components. The cost of recycling PV modules is higher than that of landfill [13]. Therefore, there is an urgent need to develop methods that can effectively recycle PV modules both economically and environmentally. It is important to not only find ways to recycle end-of-life PV modules but also to consider their recyclability during the manufacturing process. Thus far, several attempts have been made to design modules while considering their recyclability [61–64].

4.1. Nonadhesive Sheet

Doi et al. proposed a "double encapsulation module (DEM)" structure in which nonadhesive sheets were placed between the EVA and the solar cells in the standard module structure. The layers were cut on the backsheet using an ultrasonic cutter, and 91% of the solar cells were recovered intact. In addition, long-term stability tests (JIS C 8917-Appendix 2, 11 [65]) were conducted on the modules with the new structure; the results demonstrated their good durability [61].

However, this design's weakness is the reduced power consumption, which can be attributed to the addition of a nonadhesive sheet. To address this issue, Li et al. proposed a "DEM with optical coupler (DEMOC)" structure that adds an optical coupler (OC) between the front nonadhesive sheet and the solar cells [62]. Although the power was not directly compared because of the differences in module design, it was predicted that the power would improve based on the changes in I_{sc} before and after encapsulation for each module structure. This structure improved reflectance compared to that of the DEM module, and it showed characteristics similar to those of the standard module. It became relatively difficult to separate the solar cells because the OC was applied. First, the backsheet was cut, and then the interface between the nonadhesive sheet and OC was separated from the nonadhesive sheet/OC/solar cell structure using a thin wire. The separated OC/solar cell structure was further separated to recover the solar cells; 50% of the solar cells were recovered successfully.

4.2. Module Structure without Encapsulant

Apollon Solar developed a module called the "New Industrial Solar Cell Encapsulation (NICE)" module; it does not have an encapsulant and the edges are sealed using polyisobutylene (PIB). Furthermore, PIB is used as an adhesive to attach solar cells and ribbons. The module uses glass or metal foil on the back and has an edge-sealing integrated external connector. It passes the damp heat and thermocycle tests in IEC 61215 [66]. To separate the components of this module, a PIB/silicone edge seal was cut using thermocutters or standard cutters combined with a hot air gun [64,67–69].

Fraunhofer ISE proposed a gas-filled edge sealing structure called the "TPedge" module [63,70–72]. Silicone and a thermoplastic spacer (TPS) were used for edge sealing, and air was filled between the front and back glass. The front glass was coated with anti-reflection coating (ARC) on both sides to minimize reflection losses. To attach the solar cells to the back glass, a UV-cured acrylate adhesive was used to provide additional mechanical stability. Compared to the standard modules, the TPedge module had a material cost that was approximately 15.3% lower but it has more production steps. The production time is shorter and it is less than 1 min [63]. The module underwent IEC 61215/61730 [73] testing and passed 400 thermal cycles, damp heat, a potential-induced degradation (PID) test, hot-spot endurance, and UV stability tests. In addition, it was subjected to mechanical load testing up to 5400 Pa, and it showed no degradation after the hail impact testing. Furthermore, after 14 months of outdoor exposure, there was little change in the power. However, the cell-to-module (CTM) loss was higher than that of the standard module because of the small CTM gain by coupling [71].

5. Conclusions

With an increase in the installation capacity of photovoltaic modules globally, effective recycling and reuse strategies for end-of-life modules are crucial in minimizing environmental impacts and reducing production costs. In recent years, significant progress has been made in developing innovative recycling methods for PV modules, including mechanical, thermal, and chemical processes. However, each process has advantages and limitations, and a combination of different processes may be necessary for effective and efficient recycling. Furthermore, the efficiency and cost-effectiveness of recycling PV modules can also be improved. It is essential to continue research and development in this field to ensure that the growing number of waste photovoltaic modules will not pose a significant environmental challenge in the future.

This review summarized the existing research on the separation processes of silicon PV modules for recycling and identified future research directions. A considerable amount of research on separation processes focused on recovering materials from modules that require remanufacturing for recycling purposes.

The energy required to produce Si wafers accounts for a significant portion of the energy used to produce PV modules [62,74]. In addition, recycling glass can reduce energy consumption by approximately 40% compared to the energy consumption that results from the production of new glass [75]. Therefore, more research studies are required to recover intact glass and solar cells from end-of-life PV modules. Various studies have focused on the recovery of intact Si solar cells by chemical etching to obtain Si wafers. If efficient methods for recovering solar cells in their intact state can be improved, various studies related to the recycling of Si solar cells can be effectively combined. This would lead to the development of recycling processes for end-of-life solar modules in terms of energy consumption and economy.

In addition to developing methods for recycling modules, efforts have been made to change module designs and materials to make them more recyclable. The validation of their long-term stability is necessary when the structure and materials change. However, if its durability is validated and it is cost-effective with mass-production capability, it can become a new standard for PV modules.

Author Contributions: J.K.: Conceptualization, formal analysis, investigation, data curation, writing—original draft preparation, writing—review and editing, and visualization. K.K.: Conceptualization, formal analysis, investigation, data curation, writing—original draft preparation, writing—review and editing, and visualization. J.W.S.: investigation and data curation. H.J.: Formal analysis and data curation. H.-S.L.: validation and supervision. D.K.: validation and supervision. Y.K.: Conceptualization, validation, supervision, project administration, writing—review, and editing. All authors have read and agreed to the published version of the manuscript.

Funding: This research was supported by BK21 FOUR Program through the National Research Foundation of Korea (NRF) funded by the Ministry of Education (4199990514635), and this work was also supported by the National Research Foundation of Korea (NRF) grant funded by the Korea government (MSIT). (No. 2022M3J7A1066428).

Data Availability Statement: Data sharing not applicable.

Conflicts of Interest: The authors declare no conflict of interest.

Nomenclature

PV	Photovoltaic
IEA-PVPS	International Energy Agency Photovoltaic Power Systems Program
IRENA	International Renewable Energy Agency
EVA	Ethylene Vinyl Acetate
PID	Potential-Induced Degradation
ECA	Electrically Conductive Adhesive
PVF	Polyvinyl Fluoride
PET	Polyethylene Terephthalate

FRELP	Full Recovery End-of-Life Photovoltaic
P	Laser Output Density
PRR	Pulse Repetition Rate
HVF	High-Voltage Fragmentation
EHF	Electro-Hydraulic Fragmentation
TGA	Thermogravimetric Analysis
TMA	Thermal Mechanical Analysis
RF	Radiofrequency
FAIS	Kitakyushu Foundation for the Advancement of Industry, Science and Technology
CRAES	The Chinese Research Academy of Environmental Sciences
IEE CAS	Institute of Electrical Engineering, Chinese Academy of Science
EoL	End of Life
VOC	Volatile Organic Compound
SSTD	Solvothermal Swelling with Thermal Decomposition
DEM	Double Encapsulation Module
DEMOC	Double Encapsulation Module with Optical Coupler
OC	Optical Coupler
NICE	New Industrial Solar Cell Encapsulation
PIB	Poly-isobutylene
TPS	Thermoplastic Spacer
ARC	Anti-Reflection Coating
CTM	Cell-to-Module

References

1. Chowdhury, M.S.; Rahman, K.S.; Chowdhury, T.; Nuthammachot, N.; Techato, K.; Akhtaruzzaman, M.; Tiong, S.K.; Sopian, K.; Amin, N. An overview of solar photovoltaic panels' end-of-life material recycling. *Energy Strategy Rev.* **2020**, *27*, 100431. [CrossRef]
2. Xu, Y.; Li, J.; Tan, Q.; Peters, A.L.; Yang, C. Global status of recycling waste solar panels: A review. *Waste Manag.* **2018**, *75*, 450–458. [CrossRef] [PubMed]
3. IEA-PVPS. Snapshot of Global PV Markets 2023. Available online: https://iea-pvps.org/snapshot-reports/snapshot-2023/ (accessed on 21 April 2023).
4. Fthenakis, V.M.; Kim, H.C.; Alsema, E. Emissions from photovoltaic life cycles. *Environ. Sci. Technol.* **2008**, *42*, 2168–2174. [CrossRef]
5. Venkatachary, S.K.; Samikannu, R.; Murugesan, S.; Dasari, N.R.; Subramaniyam, R.U. Economics and impact of recycling solar waste materials on the environment and health care. *Environ. Technol. Innov.* **2020**, *20*, 101130. [CrossRef]
6. Tao, M.; Fthenakis, V.; Ebin, B.; Steenari, B.-M.; Butler, E.; Sinha, P.; Corkish, R.; Wambach, K.; Simon, E.S. Major challenges and opportunities in silicon solar module recycling. *Prog. Photovolt. Res. Appl.* **2020**, *28*, 1077–1088. [CrossRef]
7. Aman, M.; Solangi, K.; Hossain, M.; Badarudin, A.; Jasmon, G.; Mokhlis, H.; Bakar, A.; Kazi, S. A review of Safety, Health and Environmental (SHE) issues of solar energy system. *Renew. Sustain. Energy Rev.* **2015**, *41*, 1190–1204. [CrossRef]
8. Latunussa, C.E.L.; Ardente, F.; Blengini, G.A.; Mancini, L. Life Cycle Assessment of an innovative recycling process for crystalline silicon photovoltaic panels. *Sol. Energy Mater. Sol. Cells* **2016**, *156*, 101–111. [CrossRef]
9. Duflou, J.R.; Peeters, J.R.; Altamirano, D.; Bracquene, E.; Dewulf, W. Demanufacturing photovoltaic panels: Comparison of end-of-life treatment strategies for improved resource recovery. *Cirp Ann.-Manuf. Technol.* **2018**, *67*, 29–32. [CrossRef]
10. Parida, B.; Iniyan, S.; Goic, R. A review of solar photovoltaic technologies. *Renew. Sustain. Energy Rev.* **2011**, *15*, 1625–1636. [CrossRef]
11. Goe, M.; Gaustad, G. Identifying critical materials for photovoltaics in the US: A multi-metric approach. *Appl. Energy* **2014**, *123*, 387–396. [CrossRef]
12. IRENA; IEA-PVPS. *End-of-Life Management: Solar Photovoltaic Panels*; Technical Report; IRENA: Masdar City, Abu Dhabi; IEA-PVPS: Bern, Switzerland, 2016. Available online: https://www.irena.org/publications/2016/Jun/End-of-life-management-Solar-Photovoltaic-Panels (accessed on 21 April 2023).
13. Deng, R.; Chang, N.L.; Ouyang, Z.; Chong, C.M. A techno-economic review of silicon photovoltaic module recycling. *Renew. Sustain. Energy. Rev.* **2019**, *109*, 532–550. [CrossRef]
14. Huang, B.; Zhao, J.; Chai, J.; Xue, B.; Zhao, F.; Wang, X. Environmental influence assessment of China's multi-crystalline silicon (multi-Si) photovoltaic modules considering recycling process. *Sol. Energy* **2017**, *143*, 132–141. [CrossRef]
15. Hernandez-Lopez, D.A.; Rasikh, T.; El Mekaoui, A.; Bassam, A.; Vega De Lille, M.; Ricalde, L.J.; Riech, I. Does recycling solar panels make this renewable resource sustainable? Evidence supported by environmental, economic, and social dimensions. *Sustain. Cities Soc.* **2022**, *77*, 103539. [CrossRef]

16. Cui, H.; Heath, G.; Remo, T.; Ravikumar, D.; Silverman, T.; Deceglie, M.; Kempe, M.; Engel-Cox, J. Technoeconomic Analysis of High-Value, Crystalline Silicon Photovoltaic Module Recycling Processes. *Sol. Energy Mater. Sol. Cells* **2022**, *238*, 111592. [CrossRef]
17. Theocharis, M.; Pavlopoulos, C.; Kousi, P.; Hatzikioseyian, A.; Zarkadas, I.; Tsakiridis, P.E.; Remoundaki, E.; Zoumboulakis, L.; Lyberatos, G. An Integrated Thermal and Hydrometallurgical Process for the Recovery of Silicon and Silver from End-of-Life Crystalline Si Photovoltaic Panels. *Waste Biomass-Valoriz.* **2022**, *13*, 4027–4041. [CrossRef]
18. Shin, J.; Park, J.; Park, N. A method to recycle silicon wafer from end-of-life photovoltaic module and solar panels by using recycled silicon wafers. *Sol. Energy Mater. Sol. Cells* **2017**, *162*, 1–6. [CrossRef]
19. Vellini, M.; Gambini, M.; Prattella, V. Environmental impacts of PV technology throughout the life cycle: Importance of the end-of-life management for Si-panels and CdTe-panels. *Energy* **2011**, *138*, 1099–1111. [CrossRef]
20. McDonald, N.; Pearce, J. Producer responsibility and recycling solar photovoltaic modules. *Energy Policy* **2010**, *38*, 7041–7047. [CrossRef]
21. Heath, G.A.; Silverman, T.J.; Kempe, M.; Deceglie, M.; Ravikumar, D.; Remo, T.; Cui, H.; Sinha, P.; Libby, C.; Shaw, S.; et al. Research and development priorities for silicon photovoltaic module recycling to support a circular economy. *Nat. Energy* **2020**, *5*, 502–510. [CrossRef]
22. Jia, Z.; Fang, L. Review of Solar Photovoltaic System Recycling Technologies and Regulations in China. In Proceedings of the 2016 International Conference on Power Engineering & Energy, Environment, Singapore, 18–19 January 2016.
23. Granata, G.; Pagnanelli, F.; Moscardini, E.; Havlik, T.; Toro, L. Recycling of photovoltaic panels by physical operation. *Sol. Energy Mater. Sol. Cells* **2014**, *123*, 239–248. [CrossRef]
24. Pagnanelli, F.; Moscardini, E.; Granata, G.; Atia, T.A.; Altimari, P.; Havlik, T.; Toto, L. Physical and chemical treatment of end of life panels: An integrated automatic approach viable for different photovoltaic technologies. *Waste Manag.* **2017**, *59*, 422–431. [CrossRef] [PubMed]
25. LA MIA ENERGIA Scarl. PV-MOREDE PhotoVoltaic Panels Mobile Recycling Device Deliverable D3.3 Second PV-Morede Device Manufactured. Available online: http://www.pvmorede.it/public/D%203.3%20SECOND%20PVMOREDE%20DEVICE%20MANUFACTURED.pdf (accessed on 21 April 2023).
26. Zhang, J.; Lv, F.; Ma, L.Y.; Yang, L.J. The status and trends of crystalline silicon PV module recycling treatment methods in Europe and China. *Adv. Mater. Res.* **2013**, *724–725*, 200–204. [CrossRef]
27. Japanese Companies Work on Ways to Recycle a Mountain of Solar Panels. Nikkei Asia. Available online: https://asia.nikkei.com/magazine/20161117-INCOMING/Tech-Science/Japanese-companies-work-on-ways-to-recycle-a-mountain-of-solar-panels (accessed on 21 April 2023).
28. Solar Panel Recycling Service. Available online: www.npcgroup.net/eng/solarpower/reuse-recycle/recycle-service (accessed on 21 April 2023).
29. IEA-PVPS. End-of-Life Management of Photovoltaic Panels: Trends in PV Module Recycling Technologies. Available online: https://iea-pvps.org/key-topics/end-of-life-management-of-photovoltaic-panels-trends-in-pv-module-recycling-technologies-by-task-12/ (accessed on 21 April 2023).
30. Li, X.; Liu, H.; You, J.; Diao, H.; Zhao, L.; Wang, W. Back EVA recycling from c-Si photovoltaic module without damaging solar cell via laser irradiation followed by peeling. *Waste Manag.* **2022**, *137*, 312–318. [CrossRef] [PubMed]
31. Song, B.-P.; Zhang, M.-Y.; Fan, Y.; Jiang, L.; Kang, J.; Gou, T.-T.; Zhang, C.-L.; Yang, N.; Zhang, G.-J.; Zhou, X. Recycling experimental investigation on end of life photovoltaic panels by application of high voltage fragmentation. *Waste Manag.* **2020**, *101*, 180–187. [CrossRef] [PubMed]
32. Nevala, S.-M.; Hamuyuni, J.; Junnila, T.; Sirviö, T.; Eisert, S.; Wilson, B.P.; Serna-Guerrero, R.; Lundström, M. Electro-hydraulic fragmentation vs conventional crushing of photovoltaic panels–Impact on recycling. *Waste Manag.* **2019**, *87*, 43–50. [CrossRef]
33. Akimoto, Y.; Iizuka, A.; Shibata, E. High-voltage pulse crushing and physical separation of polycrystalline silicon photovoltaic panels. *Miner. Eng.* **2018**, *125*, 1–9. [CrossRef]
34. Lee, J.K.; Lee, J.S.; Ahn, Y.S.; Kang, G.H.; Song, H.E.; Kang, M.G.; Kim, Y.H.; Cho, C.H. Simple pretreatment processes for successful reclamation and remanufacturing of crystalline silicon solar cells. *Prog. Photovolt. Res. Appl.* **2018**, *26*, 179–187. [CrossRef]
35. Park, J.; Kim, W.; Cho, N.; Lee, H.; Park, N. An eco-friendly method for reclaimed silicon wafers from a photovoltaic module: From separation to cell fabrication. *Green Chem.* **2016**, *18*, 1706–1714. [CrossRef]
36. Wang, T.-Y.; Hsiao, J.-C.; Du, C.-H. Recycling of materials from silicon base solar cell module. In Proceedings of the 2012 38th IEEE Photovoltaic Specialists Conference, Austin, TX, USA, 3–8 June 2012. [CrossRef]
37. Frisson, L.; Lieten, K.; Bruton, T.; Declercq, K.; Szlufcik, J.; De Moor, H.; Goris, M.; Benali, A.; Aceves, O. Recent improvements in industrial PV module recycling. In Proceedings of the 16th European Photovoltaic Solar Energy Conference, Glasgow, UK, 1–5 May 2000.
38. Doni, A.; Dughiero, F. Electrothermal heating process applied to c-Si PV recycling. In Proceedings of the 2012 38th IEEE Photovoltaic Specialists Conference, Austin, TX, USA, 3–8 June 2012. [CrossRef]
39. Fiandra, V.; Sannino, L.; Andreozzi, C.; Graditi, G. End-of-life of silicon PV panels: A sustainable materials recovery process. *Waste Manag.* **2019**, *84*, 91–101. [CrossRef]

40. Fiandra, V.; Sannino, L.; Andreozzi, C.; Corcelli, F.; Graditi, G. Silicon photovoltaic modules at end-of-life: Removal of polymeric layers and separation of materials. *Waste Manag.* **2019**, *87*, 97–107. [CrossRef]
41. Riech, I.; Castro-Montalvo, C.; Wittersheim, L.; Giácoman-Vallejos, G.; González-Sánchez, A.; Gamboa-Loira, C.; Acosta, M.; Méndez-Gamboa, J. Experimental Methodology for the Separation Materials in the Recycling Process of Silicon Photovoltaic Panels. *Materials* **2021**, *14*, 581. [CrossRef] [PubMed]
42. Doi, T.; Tsuda, I.; Unagida, H.; Murata, A.; Sakuta, K.; Kurokawa, K. Experimental study on PV module recycling with organic solvent method. *Sol. Energy Mater. Sol. Cells* **2001**, *67*, 397–403. [CrossRef]
43. Kang, S.; Yoo, S.; Lee, J.; Boo, B.; Ryu, H. Experimental investigations for recycling of silicon and glass from waste photovoltaic modules. *Renew. Energy* **2012**, *47*, 152–159. [CrossRef]
44. Kim, Y.; Lee, J. Dissolution of ethylene vinyl acetate in crystalline silicon PV modules using ultrasonic irradiation and organic solvent. *Sol. Energy Mater. Sol. Cells* **2012**, *98*, 317–322. [CrossRef]
45. Azeumo, M.F.; Germana, C.; Ippolito, N.M.; Franco, M.; Luigi, P.; Settimio, S. Photovoltaic module recycling, a physical and a chemical recovery process. *Sol. Energy Mater. Sol. Cells* **2019**, *193*, 314–319. [CrossRef]
46. Tembo, P.M.; Heninger, M.; Subramanian, V. An Investigation of the Recovery of Silicon Photovoltaic Cells by Application of an Organic Solvent Method. *ECS J. Solid State Sci. Technol.* **2021**, *10*, 025001. [CrossRef]
47. Xu, X.; Lai, D.; Wang, G.; Wang, Y. Nondestructive silicon wafer recovery by a novel method of solvothermal swelling coupled with thermal decomposition. *Chem. Eng. J.* **2021**, *418*, 129457. [CrossRef]
48. Klugmann-Radziemska, E.; Ostrowski, P. Chemical treatment of crystalline silicon solar cells as a method of recovering pure silicon from photovoltaic modules. *Renew. Energy* **2010**, *35*, 1751–1759. [CrossRef]
49. Domínguez, A.; Geyer, R. Photovoltaic waste assessment in Mexico. *Resour. Conserv. Recycl.* **2017**, *127*, 29–41. [CrossRef]
50. International Technology Roadmap for Photovoltaic (ITRPV) 2021 Results. Available online: https://www.vdma.org/international-technology-roadmap-photovoltaic (accessed on 21 April 2023).
51. Lorenzo, E. On the historical origins of bifacial PV modelling. *Sol. Energy* **2021**, *218*, 587–595. [CrossRef]
52. Tao, J.; Yu, S. Review on feasible recycling pathways and technologies of solar photovoltaic modules. *Sol. Energy Mater. Sol. Cells* **2015**, *141*, 108–124. [CrossRef]
53. Mahmood, F.I.; Kumar, A.; Afridi, M.; TamizhMani, G. Potential induced degradation in c-Si glass-glass modules after extended damp heat stress. *Sol. Energy* **2023**, *254*, 102–111. [CrossRef]
54. Zhang, J.; Cao, D.; Diaham, S.; Zhang, X.; Yin, X.; Wang, Q. Research on potential induced degradation (PID) of polymeric backsheet in PV modules after salt-mist exposure. *Sol. Energy* **2019**, *188*, 475–482. [CrossRef]
55. Song, D.; Xiong, J.; Hu, Z.; Li, G.; Wang, H.; An, H.; Yu, B.; Grenko, B.; Borden, K.; Sauer, K.; et al. Progress in n-type Si solar cell and module technology for high efficiency and low cost. In Proceedings of the 2012 38th IEEE Photovoltaic Specialists Conference, Austin, TX, USA, 3–8 June 2012.
56. Zhou, J.-C.; Zhang, Z.; Liu, H.-J.; Yi, Q. Temperature distribution and back sheet role of polycrystalline silicon photovoltaic modules. *Appl. Eng.* **2017**, *111*, 1296–1303. [CrossRef]
57. De Oliveira, M.C.C.; Cardoso, A.S.A.D.; Viana, M.M.; Lins, V.d.F.C. The causes and effects of degradation of encapsulant ethylene vinyl acetate copolymer (EVA) in crystalline silicon photovoltaic modules: A review. *Renew. Sustain. Energy Rev.* **2018**, *81*, 2299–2317. [CrossRef]
58. Hartley, J.Y.; Owen-Bellini, M.; Truman, T.; Maes, A.; Elce, E.; Ward, A.; Khraishi, T.; Roberts, S.A. Effects of Photovoltaic Module Materials and Design on Module Deformation Under Load. *IEEE J. Photovolt.* **2020**, *10*, 838–843. [CrossRef]
59. Keoleian, G.A.; Lewis, G.M. Application of Life-cycle Energy Analysis to Photovoltaic Module Design. *Prog. Photovolt. Res. Appl.* **1997**, *5*, 287–300. [CrossRef]
60. Dhere, N.G. Reliability of PV modules and balance-of-system components. In Proceedings of the Conference Record of the Thirty-First IEEE Photovoltaic Specialists Conference, Lake Buena Vista, FL, USA, 3–7 January 2005.
61. Doi, T.; Igari, S.; Tsuda, I. Development of a Recyclable PV-Module -Expansion to Multi-Cells Modules. In Proceedings of the Conference Record of the Thirty-First IEEE Photovoltaic Specialists Conference, Lake Buena Vista, FL, USA, 3–7 January 2005.
62. Li, H.Y.; Luo-Hoffmann, Y.; Ballif, C.; Perret-Aebi, L.E. Re-Use of c-Si Solar Cells from Failed PV Modules. In Proceedings of the 26th European Photovoltaic Solar Energy Conference and Exhibition, Hamburg, Germany, 5–9 September 2011.
63. Mittag, M.; Haedrich, I.; Neff, T.; Hoffmann, S.; Eitner, U.; Wirth, H. TPedge: Qualification of a Gas-Filled, Encapsulation-Free Glass-Glass Photovoltaic Module. In Proceedings of the 31st European Photovoltaic Solar Energy Conference and Exhibition, Hamburg, Germany, 14–18 September 2015.
64. Einhaus, R.; Bamberg, K.; Franclieu, R.; Lauvray, H. New industrial solar cell encapsulation (NICE) technology for PV module fabrication at drastically reduced costs. In Proceedings of the 19th European Photovoltaic Solar Energy Conference, Paris, France, 7–11 June 2004.
65. *JIS C 8917*; Environmental and Endurance Test Methods for Crystalline Solar PV Modules. Japanese Standards Association: Tokyo, Japan, 1998.
66. *IEC 61215*; Terrestrial Photovoltaic (PV) Modules—Design Qualification and Type Approval. International Electrotechnical Commission: Geneva, Switzerland, 2016.

67. Bellmann, M.P.; Roligheten, R.; Park, G.S.; Denafas, J.; Buchholz, F.; Einhaus, R.; Lombardi, I.; Ehlen, B.; Wambach, K.; Romero, P.; et al. Eco-Solar Factory: 40% Plus Eco-Efficiency Gains in the Photovoltaic Value Chain with Minimised Resource and Energy Consumption by Closed Loop Systems. In Proceedings of the 32nd European Photovoltaic Solar Energy Conference and Exhibition, Munich, Germany, 20–24 June 2016.
68. Saint-Sernin, E.; Einhaus, R.; Bamberg, K.; Panno, P. Industrialisation of Apollon Solar's NICE Module Technology. In Proceedings of the 23rd European Photovoltaic Solar Energy Conference and Exhibition, Valencia, Spain, 1–5 September 2008.
69. Einhaus, R.; Madon, F.; Degoulange, J.; Wambach, K.; Denafas, J.; Lorenzo, F.R.; Abalde, S.C.; García, T.D.; Bollar, A. Recycling and Reuse potential of NICE PV-Modules. In Proceedings of the 2018 IEEE 7th World Conference on Photovoltaic Energy Conversion (WCPEC) (A Joint Conference of 45th IEEE PVSC, 28th PVSEC & 34th EU PVSEC), Waikoloa, HI, USA, 10–15 June 2018.
70. Reliability of TPedge PV Modules Successfully Tested. Available online: https://www.ise.fraunhofer.de/en/press-media/press-releases/2017/reliability-of-tpedge-pv-modules-successfully-tested.html (accessed on 21 April 2023).
71. Mittag, M.; Eitner, U.; Neff, T. TPedge: Progress on Cost-Efficient and Durable Edge-Sealed PV Modules. In Proceedings of the 33rd European Photovoltaic Solar Energy Conference and Exhibition, Amsterdam, The Netherlands, 25–29 September 2017.
72. Mittag, M.; Neff, T.; Hoffmann, S.; Ebert, M.; Eitner, U.; Wirth, H. TPedge: Glass-glass photovoltaic module for BiPV-applications. In Proceedings of the Engineered Transparency/Glasstec, Düsseldorf, Germany, 21–22 October 2014.
73. *IEC 61730*; Photovoltaic (PV) Module Safety Qualification. International Electrotechnical Commission: Geneva, Switzerland, 2016.
74. Alsema, E.A.; De Wild-Scholten, M.J. The real environmental impacts of crystalline silicon PV modules: An analysis based on up-to-date manufacturers data. In Proceedings of the 20th European Photovoltaic Solar Energy Conference, Barcelona, Spain, 6–10 June 2005.
75. Strachala, D.; Hylský, J.; Vaněk, J.; Fafilek, G.; Jandová, K. Methods for recycling photovoltaic modules and their impact on environment and raw material extraction. *Acta Montan. Slovaca* **2017**, *22*, 257–269.

Disclaimer/Publisher's Note: The statements, opinions and data contained in all publications are solely those of the individual author(s) and contributor(s) and not of MDPI and/or the editor(s). MDPI and/or the editor(s) disclaim responsibility for any injury to people or property resulting from any ideas, methods, instructions or products referred to in the content.

water

MDPI

Review

Practices for Eutrophic Shallow Lake Water Remediation and Restoration: A Critical Literature Review

Antônio Cavalcante Pereira and Catherine N. Mulligan *

Department of Building, Civil and Environmental Engineering, Concordia University, Montreal, QC H3G 1M8, Canada; antoniocp.eng@gmail.com
* Correspondence: mulligan@civil.concordia.ca

Abstract: Lake water has been impaired with nutrients due to the synergic action of human-made activities and climate change. This situation is increasing eutrophication around the globe faster than before, causing water degradation, loss of its uses, and water-associated economic and health effects. Following the Sustainable Development Goal 6, more precisely its target 6.6, nations are already behind schedule in protecting and restoring water-related ecosystems (i.e., rivers and lakes). As concerns with eutrophication are escalating, eutrophic water remediation practices are the keys for restoring those lake waters. Diverse methodologies have been investigated focusing on the nutrient that limit primary productivity (i.e., phosphorus), but few have been applied to in-lake eutrophic water remediation. Thus, the objective of this paper is to provide an overview and critical comments on approaches and practices for facing eutrophic lake water remediation. Information on the successful cases and possible challenges/difficulties in the peer-reviewed literature are presented. This should be useful for supporting further remediation project selection by the stakeholders involved. In summary, for a successful and durable restoration project, external nutrient inputs need to be managed, followed by holistic and region-specific methods to attenuate internal legacy nutrients that are continually released into the water column from the sediment. When aligned well with stakeholder participation and continuous monitoring, these tools are the keys to long-lasting water restoration.

Keywords: eutrophication; total phosphorus; algae; cyanobacteria; lanthanum modified bentonite; dredging; lake water; remediation; surface water

Citation: Pereira, A.C.; Mulligan, C.N. Practices for Eutrophic Shallow Lake Water Remediation and Restoration: A Critical Literature Review. *Water* **2023**, *15*, 2270. https://doi.org/10.3390/w15122270

Academic Editors: Mohammad Mahmudur Rahman, Dibyendu Sarkar, Rupali Datta and Prafulla Kumar Sahoo

Received: 1 May 2023
Revised: 3 June 2023
Accepted: 14 June 2023
Published: 17 June 2023

Copyright: © 2023 by the authors. Licensee MDPI, Basel, Switzerland. This article is an open access article distributed under the terms and conditions of the Creative Commons Attribution (CC BY) license (https://creativecommons.org/licenses/by/4.0/).

1. Introduction

Water, an essential resource for humans and economic improvement (i.e., sustainable water), is suffering cumulative pressures from nutrient pollution. Increasing world population and anthropogenic actions [1–3], new climate change circumstances (i.e., changes in nutrient mixing and availability due to increased water temperature) and climate extremes [4–7] are exerting pressure on water resources. In addition, there is frequently a lack of enforcing environmental policies [8,9]. These influences lead to high levels of two macronutrients (i.e., phosphorus and nitrogen) by allochthonous sources (i.e., external sources) and/or autochthonous sources (i.e., internal sources). External sources are characterized by contaminated watershed runoff, direct discharge, and/or incompletely treated effluent release, and internal sources are represented by past catchment-derived emissions that have accumulated in the sediment, releases from sediment disturbances, and/or organic matter decomposition in the water.

With this significant nutrient increase in lakes, there are subsequent eutrophication occurrences [4,5]. In these, lake waters go through chemical and biological changes including decreased dissolved oxygen concentration [10], obnoxious smells and taste [11,12], and blue-green algae/cyanobacteria biota domination [13,14] with potential harmful toxin production (i.e., neurotoxins, hepatotoxins, and endotoxins) [15]. Studies suggest economic and health concerns due to eutrophication related to lake waterfront property value

decrease [16,17], recreational use loss [17,18] and increased costs with drinking water treatment as a preventive measure for any negative health effect [17–19].

In this framework, as the concern with eutrophication will be escalating in the following years by the variables suggested, eutrophic lake water remediation is the key for nations to restore those waters not only for the present generation but also for generations to come. This idea aligns well with Sustainable Development Goal 6 (SDG6) (i.e., clean water and sanitation) from the UN (United Nations) agenda, further detailed in the 6.6 target. This target for restoration of the water-related ecosystems was to be achieved by nations in 2020. Thus, following the mentioned concern, in-situ technological practices for water remediation/restoration are of high priority.

The focus is on the primary limiting nutrient, phosphorus (P), the essential component required to constrain primary productivity development [20]. Approaches and practices for reducing eutrophication circumstances, which already have been applied in situ, are based on distinct technologies directly or indirectly used for reducing the phosphorus concentration in the water column. Correspondingly, it is implied that control of the external loadings and the management of sediment legacy phosphorus due to particle settling [21,22] play an important role in successful and sustainable remediation. In this paper, in situ lake remediation procedures that are physical, chemical, biological, combined, and emerging will be discussed.

There are several distinct and well-established eutrophic in-lake water remediation practices in specialized literature. This article will review well-documented practices centered on whole lake restoration in addition to emerging methods. Physical techniques include sediment dredging and hypolimnetic water aeration. Chemical techniques are sediment capping with inert elements or phosphorus inactivation in water and bottom sediments by chemical addition. Comprising the application of pure oxygen into hypolimnetic water and capping with lanthanum-modified bentonite (LMB) and coagulants (aluminum and iron-based). The biological methods underlined are biomanipulation and macrophyte management.

Emerging methods, which support waterbody restoration and take advantage of the ecosystem's natural response to changes [23], will be presented. Those ecological engineering techniques involve primary productivity control by minimally invasive nutrient abstraction. The ones highlighted in this paper will be geotextile filtration and floating wetland use. Combined remediation practices with two or more of all mentioned methodologies will be also discussed as a holistic approach to water restoration.

Thus, the objective of this paper is to provide an overview and critical comments on in-lake/situ approaches and practices for mitigating eutrophication worldwide. Thus, by providing summarized information on the successful cases and challenges in the peer-reviewed literature, the aim is to facilitate other further remediation project selection by stakeholders involved (i.e., environmental managers, and society in general). For guiding this review, two research questions were developed as follows:

1. What in situ practices with plausible results have been applied to address eutrophication in lake waters?
2. What are the major challenges/disadvantages to these water restorations?

2. Human-Induced Eutrophication Processes

Eutrophication is described as a water enrichment process by excess plant nutrients, nitrogen, and phosphorus (P) which can lead to enhanced algae/cyanobacteria growth, periphyton, or macrophytes [24,25] in lake water systems. From an ecological standpoint, this is a natural process in which a waterbody goes through growth-promoting processes [26] over a long-time frame. However, due to the increased nutrient input coming point and diffuse external and internal sources, this timeframe has been reduced. Those nutrients are primarily associated with human activities as presented in Figure 1.

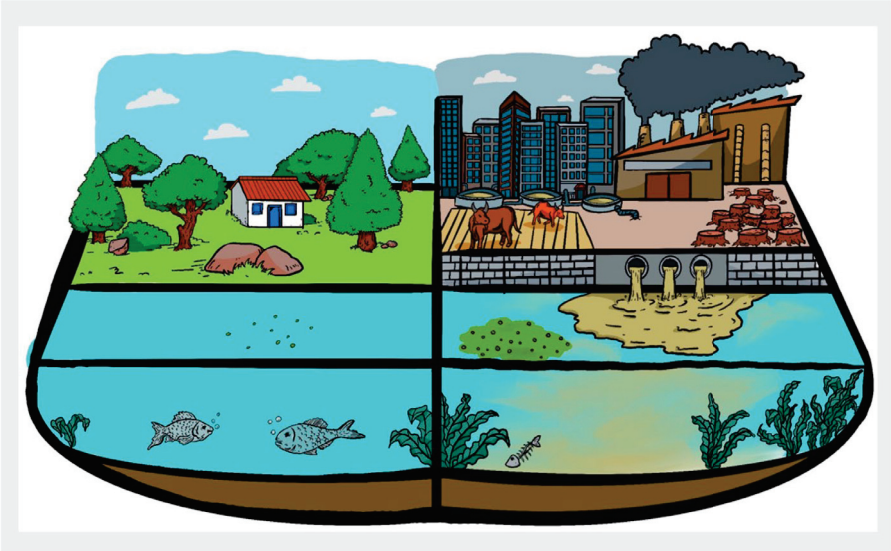


Figure 1. Visual representation of balanced/non-polluted (**left**) and nutrient-polluted (**right**) systems.

Anthropogenic actions synergically associated with the new climate change developments and population growth have been instigating nutrient stresses in aquatic environments. Point sources include direct contaminant discharge, as well as untreated sewage disposal. Diffuse sources originate from agriculture (i.e., fertilizer over(use)) and livestock (i.e., animal feces) as well as increased contaminated watershed runoff due to climate extremes. Internal sources are related to former external sources which have settled and accumulated in the sediment and organic matter degradation in the water column/sediment. As an example, when the excessive phytoplankton degrades and settles to the sediment surface, decomposition can lead to possible low oxygen concentrations in the lower water levels, which could cause releases of P from the same sediment [27]. Thus, the sediment acts as a sink and source of P, an important characteristic in the lacustrine ecosystem health and any possible remediation/restoration practice application.

Various issues are manifested as the total excessive phytoplankton growth effects, the main disturbance on a eutrophication occurrence, leading to imbalanced primary and secondary productivity and a faster succession/ageing rate [26]. Some of the distresses are related to benthic primary productivity (i.e., macrophytes and periphyton) shifting to pelagic primary production (i.e., phytoplankton) [28], causing phytoplankton biomass density to increase. Usually, this upsurge will trigger a change to a cyanobacteria-dominated phytoplankton community [29]. Consequently, with these possible excessive cyanobacteria developments, harmful toxin production [5,30] as well as possible water anoxia, obnoxious scum, and smells will occur. Thus, eutrophication development will not only bring recreational and drinking advisories due to possible harmful toxin production but will also have diverse economic and health effects associated with it.

2.1. Phosphorus Cycle and Water/Sediment Interactions

The phosphorus (P) cycle is formed by this element's interaction between terrestrial and aquatic ecosystems. As shown in Figure 2, the terrestrial phosphorus contribution could be associated with P rich rock/soils as well as fertilizer uses and livestock practices. Thus, by runoff, possible leaching due to chemical weathering reactions and/or physical erosion of soil/rocks can occur, transferring this component from the terrestrial ecosystem to the aquatic one. The mineral P form (i.e., inorganic) mostly present in rocks is apatite, which comprises hydroxyapatite, fluorapatite, and chlorapatite [31], which can then be found in aquatic ecosystems. On the other hand, hydrous ferric oxides such as goethite (FeOOH) and ferrihydrite ($Fe(OH)_3$) are the common form in well-drained soils and important sinks or sources of soluble phosphate in aquatic environments [32]. When related to anthropogenic

terrestrial P (i.e., fertilizer and livestock) this will be mostly organic and soluble in water which will runoff from the land.

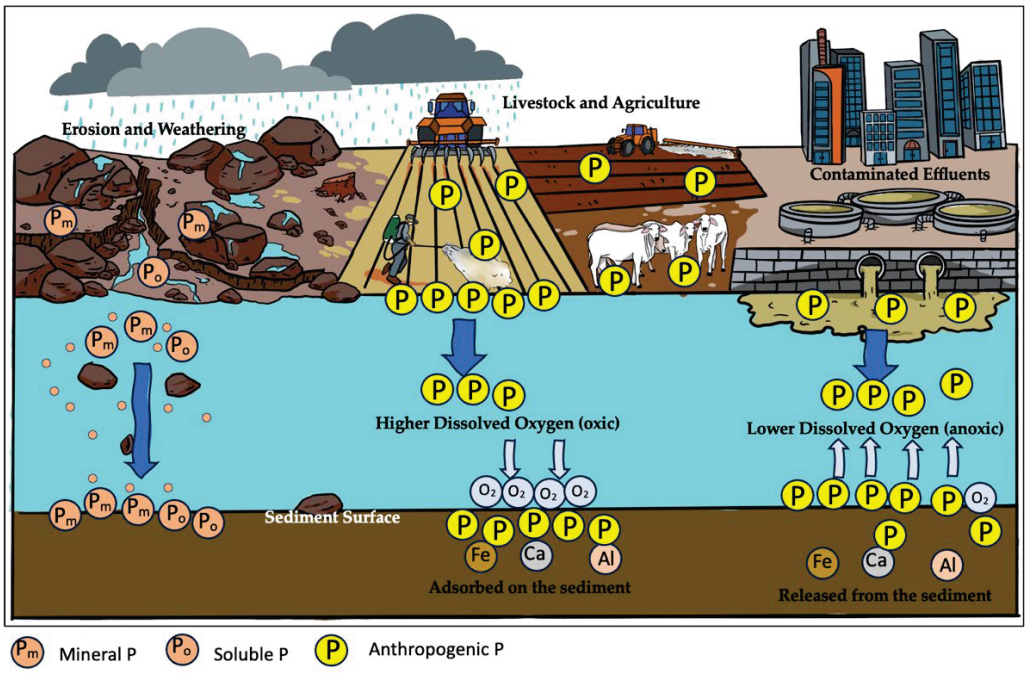


Figure 2. Phosphorus enrichment process in the environment and simplified cycle. Modified from [26].

Related to the aquatic ecosystem, sediments play a crucial role in controlling P availability in the water column in water environments by acting as an internal source and sink [20]. As shown in the phosphorus enrichment process (Figure 2), phosphorus (P) can enter waterbodies in two ways, continuously in runoff water and by diverse inlet streams [26]. This nutrient input nearly always exceeds the output, thus causing the settling of it and enrichment in the sediments [33]. When accumulated in the sediment, some interactions between sediments and overlying waters (i.e., based on dissolved oxygen concentration) will occur, which can determine the bioavailability of this element in the water column.

Different P forms in sediments have different bioavailability and are released by changes in lake environmental conditions to become a potential source contributing to lake eutrophication [34]. An example is related to dissolved oxygen concentration. If there is oxygen in the bottom water, P is strongly bound to metals in the sediment such as iron, aluminum, and calcium. These complexes are difficult to dissolve and make the P unavailable to phytoplankton and other plants and do not contribute to eutrophication [27]. In the absence of oxygen, for example, redox-dependent P species may still be released within the anoxic bulk sediment and diffuse into the water column. As an example, the sediment geochemical cycling of P is tightly coupled to the cycling and redox dynamics of Fe [35,36] shown in Figure 3.

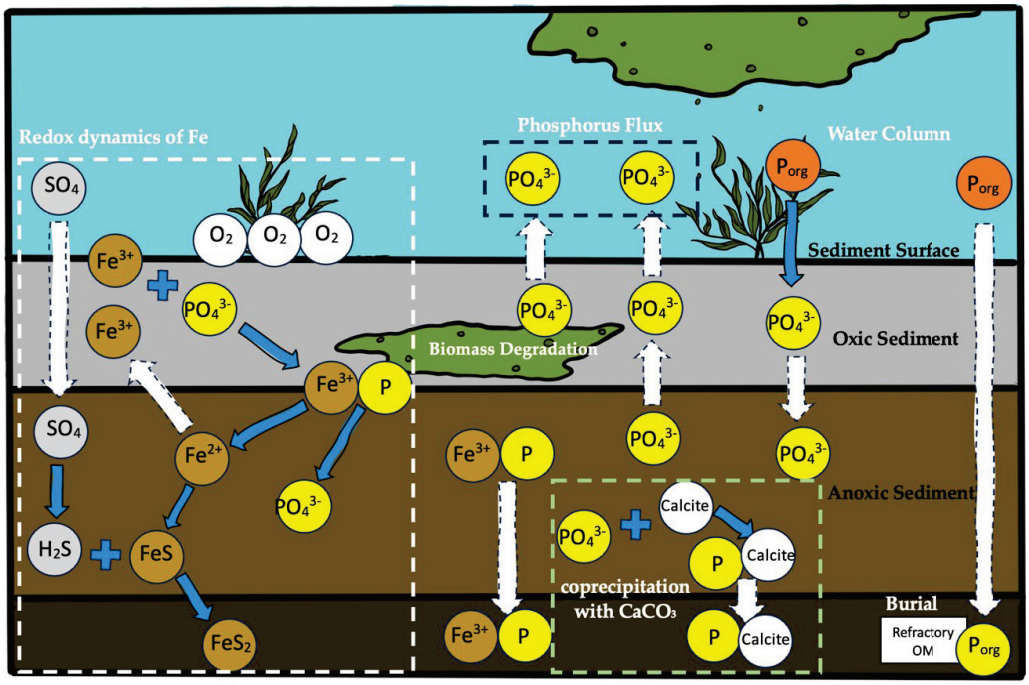


Figure 3. Simplified sediment Fe-P cycling and coprecipitation with $CaCO_3$ schematic. Modified from [36].

This iron-bound phosphorus accounts for a substantial fraction of total P in sediments (~30%) and is regarded as active P (i.e., readily released under anoxic conditions) [37]. In this diagram, since Fe III (hydr)oxide is redox sensitive and its surface is unevenly charged, P sorption on the Fe III (hydr)oxide surface becomes reliant on the redox potential and pH of the environment [38]. Under anoxic conditions in the pore or bottom water, the oxidized iron is reduced to a ferrous ion (Fe (II)) that subsequently diffuses into the water column and is re-oxidized to Fe (III). Sulphate also strongly interferes with iron-phosphorus chemistry and stimulates organic matter anaerobic decomposition. The main product of sulphate reduction under anoxic conditions is dissolved sulphide, which may react with dissolved reduced iron and particulate iron (hydr)oxides under the same condition. The results of this reaction between sulphide and iron under anoxic conditions are the highly insoluble iron sulphide (FeS_2) minerals while phosphate adsorbed to the iron (hydr)oxides or present as iron phosphates become mobilized [39]. Another example is related to the P form which cannot be affected by environmental changes, formed by the phosphate coprecipitation with $CaCO_3$ and considered the most important endogenous process in removing P from the water column [40]. This form is found at the stream bottom and might not easily be suspended [41].

2.2. External Measures: A Primary Step for Reducing Nutrient Loading

Ceasing, attenuating, and regulating external phosphorus nutrient loadings into eutrophic lakes should be the first and foremost action, in the order mentioned, taking into consideration in any lake remediation/restoration practices. These actions are considered the most prominent action for possible further in situ corrective measures. Without this step, even in the case of a possible in situ restoration within the lakes, minimal to no results will occur [42]. As lake catchments are characterized by large differences in hydrology, climate, geology, soils, land cover, and ecosystem type [43], diverse practices could be suggested.

Practices are mainly characterized by four possible actions: land-use modifications, wastewater (domestic/industrial) treatment, planned urban development around water-bodies and their possible water uses, and modification changes in agricultural/livestock management approaches. These strategies are the central focus for mitigating the external nutrient input in lacustrine ecosystems. In more detail, land use changes within forestry

practices can contribute for reducing any uncovered land which can erode due to watershed runoff to a water body. Additionally, increasing vegetation buffer zones on lakes will play a large part in acting as a filter for capturing nutrients. Wastewater tertiary treatment processes focused on nutrient removal should also be implemented in places where the effluents are discharged directly into water bodies.

It is worth mentioning that water management/protection is not a straightforward action and specific methodologies should be adapted depending on the region and by always prioritizing external nutrient remediation. This is strongly reliant on the contribution of diverse sectors and the stakeholders involved, and the practices must be adjusted on a case-by-case basis. Thus, the contribution of representative local stakeholders who are affected by the eutrophic water must be included, promoting inclusive and transformative change in valuing this water [44]. If an internal lake water restoration practice is applied without any external load control/attenuation, the eutrophic aquatic environment will not improve over the long term, mainly because the waterbody is going to have a continuous phosphorus input which is dated to be stored in the sediment, acting as a source of P for the waterbody. P migration from the sediment into the overlying water can be reported as a persistent phenomenon, thus delaying the water quality improvement for a considerable time even after the control of external sources [36]. Thus, for further improvement of any eutrophic waterbody, which suffers from external nutrient inputs, internal nutrient sources should be managed.

2.3. Lakes Trophic States Classification and World Eutrophic Waters Overview

Lakes are often classified by their "trophic status", which can be determined via measures of productivity or nutrient load [45]. In the most used classifications, water quality parameters are used to roughly assess waterbody primary productivity status. For example, these parameters can include the concentration of the limiting nutrient (phosphorus), chlorophyll-a (an indicator of phytoplankton biomass), and transparency (dependent on both algal biomass and sediment resuspension), expressed as Secchi depth [24]. Diverse indices are proposed such as the Carlson-type TSI (trophic state index), which assumes algal biomass to be the basis for trophic state classification. It is calculated by three hydro-ecological characteristics mentioned as follows: the chlorophyll-a concentrations, total phosphorus (TP) in water, and the Secchi depth (SD) [46]. For classification criterion, waters with low productivity are termed oligotrophic and waters with high productivity are eutrophic. The other trophic categories are mesotrophic, the one located between low- and high-productivity waters, and hypertrophic, the one higher than eutrophic water.

Eutrophication occurrences have not only been prevalent in economically developing nations but also in economically developed countries. Freshwater basins are becoming oversaturated with phosphorus [47], causing anthropogenic eutrophication to become a primary water quality issue worldwide [48,49]. Roughly 50% of the world's largest lakes (including Asia, Europe, and North and South America) are eutrophic because of high TP loadings [50]. Additionally, surveys have shown that 54% of lakes in Asia are eutrophic in Europe, 53% in North America, 48% in South America, 41% and in Africa, 28% [51]. Large eutrophic lakes such as Lake Erie (North America), Lake Winnipeg (Manitoba, Canada), Lake Taihu (China), Lakes Biwa and Kasimagaura (Japan), Lake Victoria (Africa) [52], Lake Jacarepaguá (Rio de Janeiro, Brazil), and others are a small worldwide snapshot of this issue. Other smaller and shallow waterbodies not well monitored and documented are also increasingly exhibiting eutrophication characteristics. Nutrient releases to waterbodies are the main factor. As little to no efforts have been made to reduce this contamination, the number of affected waterbodies will tend to increase even more. In both scenarios, in economically emergent and economically developed nations, the lack of enforcement of environmental policies is associated with increased eutrophication.

3. In Situ Practices for Eutrophic Water Restoration

Eutrophication restoration of lakes has been undertaken by simple algal killing and reduction in the endogenous nutrient concentration by multiple technologies in the lake ecosystem [53]. The in situ remediation techniques mainly involve phosphorus concentration management, either in the water column and sediment. This is because P is typically the most cost-efficient nutrient for abatement measures [43]. Presently, there is no international agreements for classifying in situ techniques for lake water remediation [54]. Thus, the following classification presented in Figure 4 will be used in this paper. In situ lake remediation techniques technologies are allocated into physical, chemical, biological, combined, and emerging methods.

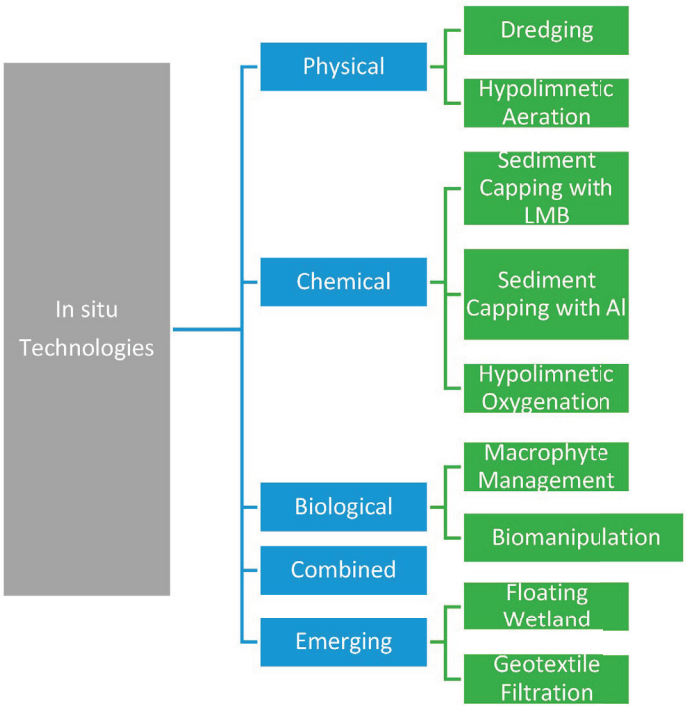


Figure 4. In situ lake remediation techniques classification.

Due to the water qualities heterogeneity in eutrophic waterbodies, the decision on the option(s) to be applied to a disturbed aquatic ecosystem will depend on the following: (1) water quality characteristics, (2) nutrient pollution source, (3) sediment phosphorus bioavailability, (4) lake nuisance concerns (i.e., macrophyte overgrowth, harmful primary productivity), (5) available capital, (6) possible stakeholders involved/affected, and the (7) method's sustainability. With this understanding, decision-support frameworks for these restorations have been created and are diverse [27,55,56]. They are indicated for facilitating not only the selection but also further requirements for a successful and durable restoration (i.e., monitoring and continuous external loading reduction).

A simplified decision support framework is presented in Figure 5, which shows the necessary steps to be taken in a possible eutrophic lake water remediation project. The first step to be taken is lake water/sediment characterization with the identification of external and internal sources. External load attenuation should always be followed by an in-lake remediation practice for accumulated nutrients in the lake sediment. In the remediation option management parameters such as chemical dose, waste disposal, monitoring, and others need to be defined. Thus, after the remediation procedure takes place, continuous monitoring needs to be performed to investigate not only the restoration outcomes, but also continuously verify if the water needs additional treatments.

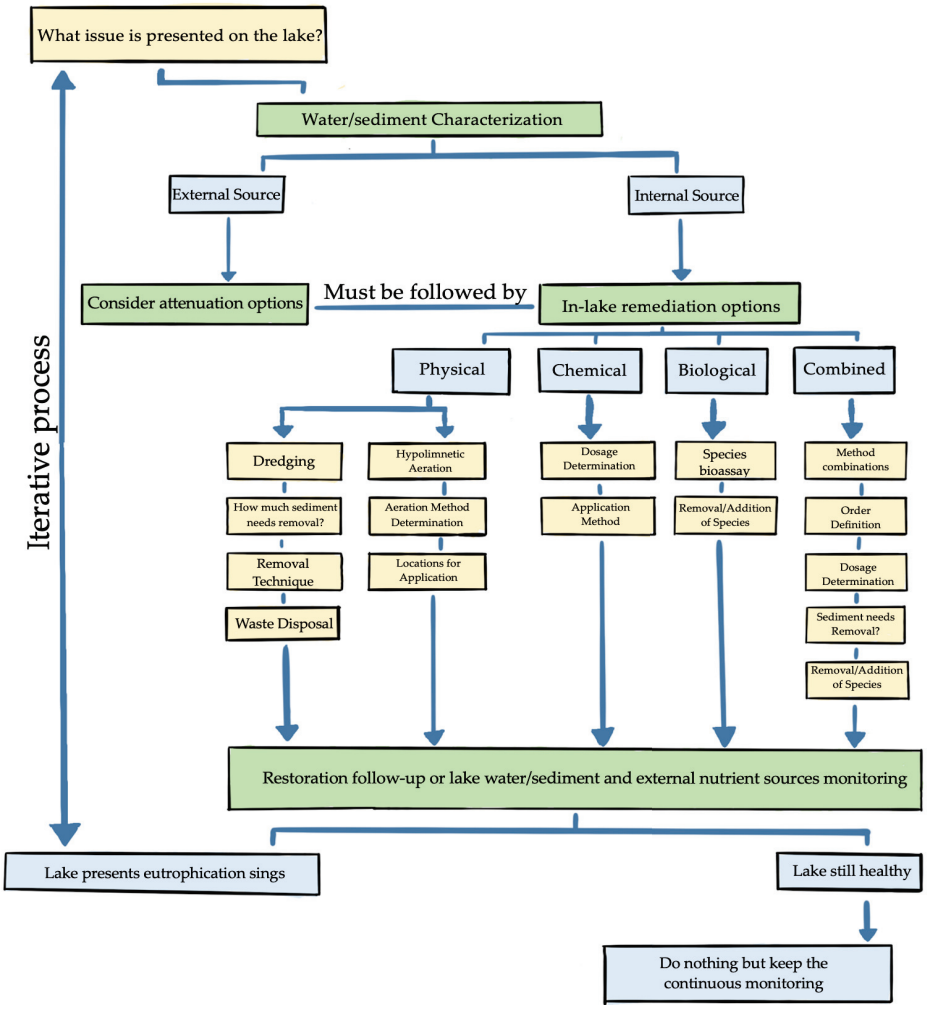


Figure 5. Simplified decision support framework for eutrophic water restoration selection.

In any case, the decision support frameworks as well as selected methodologies must always be tailored to the region's perspective regarding affected stakeholders' insights and needs. This paper has been completed to provide an overview of addressing eutrophication in lake waters. It is expected not only to emphasize major challenges/disadvantages but also the necessary parameters for effective and durable lake water restoration practice. Thus, a guided overview has been completed for providing and facilitating further remediation project investigations by stakeholders involved in various lakes.

3.1. Physical Remediation

3.1.1. Dredging

In this treatment category, phosphorus (P) rich sediment is removed from the lake as a restoration method. Sediment is excavated by mechanical means with specific equipment and brought to the surface and dewatered in geotextile bags prior to disposal. Generally, this sediment removal will reduce the internal P loading immediately and substantially. The positive effects on lake water quality included a decline in water column nutrients, reduction in phytoplankton, the disappearance of cyanobacterial blooms, and increased coverage of macrophytes [57]. Although there are benefits, several trade-offs have been presented by this remediation. The removal of lake water sediment can cause secondary pollution due to leaching metals/contaminants from the sediment into the water column. Additionally, an imperative concern is waste disposal, which needs to be evaluated. Some dredging projects have been analyzed and are presented in Table 1.

Table 1. In situ remediation studies of dredging.

Reference	Lake Name	Country	Mean Depth	Area Excavated/Excavated Depth	Treatment Year	TP Before/TP After
			[m]	[ha]/[m]	[Year]	[µg/L/µg/L]
[57]	Lake Mustijärv	Estonia	1.1	1/1.1	2016–2017	44/100
[58]	Dongqian Lake	China	2.2	1991/0.50	June 2009 to January 2013	142/100
[59]	Lake Wuli	China	2.5	560/0.30	June 2002 to November 2003	n.d *
[60]	Lake Yuehu	China	n.d *	61/1 m	June 2006, to October 2006	431 ± 236/254 ± 84
[61]	Lake Nanhu	China	1.2	n.d *	August 2017 to March 2018	3470/470

Note: * n.d—Not determined.

Generally, it was observed that dredging projects only have short-term positive effects on lake ecosystems even though there are changes in the sediment phosphorus content, as well as the water column, directly after the removal [57,58]. The projects reviewed have no external nutrient attenuation plan or action performed, which has affected the proposed remediation performance/durability. Additionally, no mention of dredged sediment disposal has been given, which should be a strong concern regarding the sustainability of those projects. For the results reviewed, dredging should be only recommended if combined with other ecological lake restoration techniques, which will be further discussed [59–61].

Related to this remediation practice's possible cost, a range from 20,000 to 75,000 USD per acre dredged could be presented. Contaminated sediment final disposal is not included, which will bring an additional significant amount depending directly on the disposal site distance from the water body [62]. Not only the value for the actual dredging process but also the risks associated with the technique application, workers' safety, equipment transportation to the site, vegetation, and bathymetric assessment should also be considered and included, if necessary.

3.1.2. Hypolimnetic Withdrawal

Hypolimnetic withdrawal is a practice based on the mixing of deep anoxic waters with shallow oxygenated epilimnion waters to prevent low dissolved oxygen water near the sediment surface, which could increase phosphorus bioavailability for a possible eutrophication occurrence. For this objective, several methods have been used such as air compression water mixers as well as new technologies of solar-driven aeration units (SolarBee®). In the specialized literature reviewed, there are variable results regarding the capacity of this water remediation. Some studies have been analyzed and are shown in Table 2.

Table 2. In situ remediation studies of hypolimnetic withdrawal.

Reference	Lake Name	Country	Mean Depth	Treatment Year	Aeration Type	TP Before/TP After
			[m]	[year]		[µg/L/µg/L]
[63]	Lake Durowskie	Poland	4.6	2009–2017	Pulverizing aerator	40/30
[64]	Fossil Creek Lake	United States	2	2009–n.d *	Submerged aeration	1150-90/76-40
[65]	Lake Długie	Poland	5.3	1987, 1999, 2000	Destratification	58/48
[66]	Greenfield Lake	United States	1.5	February 2005	Solar Bee Unit **	145 ± 425/ 96.1 ± 69.7

Note: * n.d—Not determined; ** Additional treatments have been done.

Frequently, the water aeration technique must counteract high organic levels in the sediment [63], and most times the oxygen demand for microorganisms is greater than the oxygen supply capacity of the aerator. Therefore, the oxygen deficit is going to be reduced each year as the mineralization of accumulated organic matter instigated by the oxygen presence reduces its demand. In other cases, even though phosphorus is immobilized in

the bottom sediments, high concentrations will remain in the water due to continuous external pollution, and the low sediment sorptive capacity (i.e., low concentrations of iron and manganese, which bind phosphorus) which prevents further association with phosphorus [65].

This sorption capacity is an important parameter to be evaluated if water aeration is a selected remediation method in the lake. Additionally, TP inputs to the water column vary from year to year depending on the ecosystem, a factor not considered by the present lake management efforts [66]. Nevertheless, hypolimnetic aeration seems to alleviate eutrophication symptoms, and thus it should be used in combination with other methods [63]. External nutrient sources are a recurring issue, and attenuation should be performed to enhance the potential of this remediation. Cost-wise, this practice will depend on the type of aerator chosen. An average monetary value evaluated in a recent study has shown 3800.00 USD per acre for the capital cost [67] and 700.00 USD per acre for operation and maintenance.

3.2. Chemical Remediation

3.2.1. Sediment Capping with LMB

The lanthanum-modified bentonite (LMB) use has been a highly implemented approach on the market and literature for eutrophic waterbody remediation. This method has been used when a higher internal nutrient source remains to sustain recurrent eutrophication occurrences in lakes. This method is based on modified clay addition in a slurry form or granules in the eutrophic water column which will sorb phosphorus present on it and settle it, creating a thin barrier that will retain and reduce phosphorus sediment bioavailability. The quantity of LMB necessary to inactivate phosphorus in aquatic systems is based on the supplier-recommended mass ratio (La/P) 100:1 (100 kg Phoslock®/1 kg phosphorus), which needs to be calculated based on the TP measured in the water column and potentially releasable phosphorus in the sediments (labile, reductant-soluble, metal oxide). Some LMB lake application studies have been reviewed in Table 3.

Table 3. Sediment capping studies with LMB application.

Reference	Lake Name	Country	Mean Depth	Treatment Year	Dosage Used	TP Before/TP After
			[m]	[Year]	[ton/ha]	[μg/L/μg/L]
[68]	Swan Lake	Canada	1.86	Spring 2013	4.6	247/99 (1st year) and then 60 (2sd year)
[69]	Laguna Niguel Lake	United States	3.66	29 April 2013 to 2 May 2013	4.13	(>80% decrease)
[70]	Lake Bromont	Canada	4.88	Fall 2017	3.77	23.63 ± 4.12/18.20 ± 3.19
[71]	Lake Bärensee	Germany	2.63	June 2007/May 2010/March 2013	1.9/0.5/0.5	80/35
[72]	Mere Mere *	United Kingdom	2.8	9 March 2013	5.1	76.6/49.8
[73]	Hatchmere **	United Kingdom	1.4	11 March 2013, to 13 March 2013	5.3	83.2/64.4

Notes: * 18 lakes study (most recently selected); ** 10 lakes study (most recently selected).

Dosage determination plays an important role in the definition and results obtained with this remediation application. An appropriate LMB application can bind soluble reactive phosphorus (SRP) in the water column and cap bioavailable forms of P in the sediments [71]. However, it is important to mention that humic substances can be a strong complexing agent for lanthanides, causing the clay to underperform in those scenarios [74]. Additionally, this compound could react with hydroxyl species under high pH conditions (>8.35) and decrease the potential binding efficiency [69].

In circumstances where external nutrient inputs have not been attenuated in the waterbodies before LMB application, it is understood that these are going to possibly accumulate on the sediment surfaces above the La barrier and are expected soon to trigger

eutrophication reoccurrences due to P release. In those scenarios, even though costs will increase, reapplications of the product are recommended as a feasible way to ensure long-term water quality when the applied dosage was or has become insufficient [68,73]. The monetary cost of this remediation practice will depend on the water body size which directly affects the amount of LMB required. As presented in [75], total costs ranging from 152.00 to 253.00 USD per pound of phosphorus mitigated should be expected depending on the water body size. Additionally, another example [76] showed provided the material cost of LMB was 3100.00 CAD/t or 2279.00 USD/t (metric ton) in 2015, and the application cost was 200 CAD/t or 147.00 USD/t for Elk Lake, Canada. The cited cost only includes a one-time application; if any reapplication is necessary, additional costs will incur.

3.2.2. Sediment Capping with Al

This method involves adding an aluminum solution to the lake water, which settles in the sediment and binds phosphorus to it, preventing its release into the water column. Surface complexation–sorption reactions are the primary binding mechanism for phosphate by Al hydroxides [71]. Additionally, for this compound, there is an optimal pH range (i.e., 6–8). In the case of acidic water pH, the form Al^{3+}, which is toxic to organisms, dominates in the solution [74]. Increasing concerns are still not well explained regarding the chronic toxicity of aluminum exposure to humans, which affects the selection for this treatment method. Some in situ lake aluminum applications are presented in Table 4.

Table 4. In situ remediation studies of sediment capping with Al.

Reference	Lake Name	Country	Mean Depth	Treated Area	Treatment Year	Dosage Used	TP Before/TP After
			[m]	[m^2]	[Year]	[g/m^2]	[μg/L/μg/L]
[77]	Lake Harriet	United States	8.7	littoral zone	May 2001	32	n.d
[78,79]	Lake Barleber	Germany	6.7	whole lake	1986 ****	36	SRP: 180/3
[80]	Lake Klasztorne Małe	Poland	8.1	2 m isobath for iron portion of the lake PAC	2021	73.2 (iron)/49.7 (PAC)	211 ± 131/31 ± 72
[81]	Trekanten *	Sweden	3.6	whole lake	2011	60 (PAC)	n.d
[82]	Starodworskie Lake	Poland	9.4 m	area below isobath 10 m	1994–1995	18.6	1700/700
[83]	Lake Vedsted **	Denmark	5.0	whole lake	2009	26.6	n.d
[84]	Nordborg ***	Denmark	5.0	whole lake	2006	44	231/26 (2007), 37 (2008)

Notes: n.d—Not determined; PAC: Poly-Aluminum-Chloride; SRP: Soluble Reactive Phosphorus * 7 lakes studied (most recently selected); ** 114 lakes treated with aluminum (most recent selected); *** 6 lakes treated with aluminum (most recent selected) **** results after 30 years of remediation presented.

Similar to LMB remediation, a high requirement is needed to adequately address the dosage. This should be performed to achieve an active barrier (i.e., capable of binding SRP in the water column and to cap bioavailable forms of P in the sediments) and for addressing possible external nutrient sources for which attenuation has not been performed. Additionally, this phosphorus inactivation method does not directly affect the content of organic phosphorus [78–80]. Any reduction in the phosphorus organic form is the result of reduced primary production in the water body. The cost of this remediation practice will depend on the amount of aluminum solution and its type required. A study has suggested [67] an average of 4812.00 USD per acre for capital costs and a range of 0 USD to 619 USD operation and maintenance costs if continuous monitoring is added to the practice application.

3.2.3. Hypolimnetic Oxygenation

This treatment/remediation option is based on the introduction of oxygen in deep anoxic water to prevent low dissolved oxygen concentrations. The main goal is to satisfy the sediment oxygen demand (SOD) and increase the redox potential at the water-sediment

interface, limiting the seasonal release of nutrients from the bottom sediments into the water column [85]. The common effect of hypolimnetic oxygenation has been to eliminate hypoxic conditions with strong suppression of sediment solubilization of TP, Fe, and Mn [86,87]. Some in situ hypolimnetic oxygenation practices applications are presented in Table 5.

Table 5. In situ remediation studies of hypolimnetic oxygenation.

Reference	Lake Name	Country	Mean Depth	Method Used	Treatment Year	Dosage Used	TP Before/TP After
			[m]		[Year]	[kg O_2/d]	[μg/L/μg/L]
[84]	Lake Vedsted *	Denmark	5.0	Bubble diffusers	1995/2003–2007	50	25/16
[86]	Lake Pleasant	United States	8	Bubble linear diffusers	2014–2018	1775	552/53
[87]	Lake Serraia	Italy	7	Octagonal diffusers 1 m above sediment	2006 and 2007	144	40/n.d **
[88]	Aha Reservoir	China	13	Bubble plume diffusers	2017	28.58	40/20

Note: * 6 lake studies (most recently selected) additional treatment with Al, ** n.d—Not determined.

As with hypolimnetic aeration, sediment with low sorptive capacity (low amount of binding phosphorus substances such as iron and manganese) will affect the phosphorus attenuation. If the lake has a high content of organic matter (OM) accumulated on the sediment, oxygen concentration demand will increase at the start of the procedure, playing an important role in this remediation. Additionally, when further OM oxidation in the superficial layer of the lake sediments takes place, reduction in the sediment oxygen demand throughout the application and improvement of the trophic state if accompanied by reduction in the external nutrient load [87] will be noted. If this methodology is required, it should be combined with other ecological lake restoration techniques. Capital, operational, and maintenance costs for the implementation of this method vary depending on many site-specific parameters such as oxygenation equipment chosen, type of oxygen generator employed, or transportation of pure oxygen tanks and practice maintenance. For a better perspective, a diffuser oxygenation system installation is between $0.5 M and $2.5 M ($40 to $800 per hectare meter), with annual operating costs between $30 K and $140 K ($5 to $36 per hectare meter) [89] with values in USD.

3.3. Biological Remediation

3.3.1. Macrophyte Management

Macrophyte management is characterized by plant biomass removal from the lake water as well as the repopulation of endogenous species. The first one can be performed with specific equipment, which can either remove the macrophyte or cut it down as much as possible, and the second is performed with small enclosed aquatic gardens which will be used to spread a certain macrophyte species on the waterbody. Both have been investigated for in-lake applications, and the results have been variable. Removing macrophyte biomass from lakes is often an effective treatment to control a nuisance macrophyte problem [90]. Harvesting these submerged macrophytes has four distinct effects on water quality: leaching of soluble compounds from macrophyte organs, sediment resuspension, reduction in macrophyte litter in the lake [91], and plant fragment dispersal. Macrophyte repopulation or phytoremediation, on the other hand, is a new approach which is still under investigation and is based on the large-scale cultivation of a macrophyte species (indigenous in the area), which can assimilate some of the nutrients in the water. Some in-lake studies have been highlighted in Table 6.

Table 6. In situ remediation studies of macrophyte management.

Reference	Lake Name	Country	Mean Depth	Method Used	Treatment Year	TP Before/TP After
			[m]		[Year]	[μg/L/μg/L]
[91]	Lake Biwa	Japan	3.5	Annual macrophyte harvesting	July to September (every year)	n.d *
[92]	Lake Caohai	China	2.5	Large-scale cultivation of water hyacinths	2011–2013	54/15
[93]	West Lake	China	2.27	Sediment covered by a layer of modified clay minerals (10 cm)	July 2013–2019	70 ± 30/20 ± 10

Note: * n.d—Not determined.

In this procedure, it is recommended for the macrophyte harvesting, a method to avoid sediment resuspension [91] to further reduce metal ion (i.e., Ca, Mg, Sr, and Fe) and nutrient dissolution in the water. In other words, instead of removing rooted plants, the technique recommended is to just cut the upper plant part. With the macrophyte repopulation, it is highlighted that P is assimilated from lake water and partially in the sediment. Thus, this method could be performed on sites with large algae concentrations, for declining assimilated nutrients and removing endogenous sources.

3.3.2. Biomanipulation

Biomanipulation or the aquatic food chain manipulation is a procedure to reduce phytoplankton biomass and is achieved by planktivorous fish removal and the introduction of piscivorous fish into a lake [92]. Removal could be performed with the use of nets and/or electric fishing. The main objectives of this technique are to decrease the high concentration of toxic phytoplankton in the water bodies as well as reduce sediment disturbance. Well-studied methodologies have presented variable results. In reviewed papers, improvement in water clarity is mainly due to reduced sediment disturbance by fish [94,95]. It is worth mentioning that a reduction in turbidity will possibly cause a reduction in nutrient concentration in the water column, but this will not remove it from the sediment. Because of that, some of the papers have combined biomanipulation with the transplantation of macrophytes (to create a more stable sediment surface) [94–96]. Some in situ biomanipulation practices are presented in Table 7.

Table 7. In situ remediation studies of biomanipulation.

Reference	Lake Name	Country	Mean Depth	Method Used	Treatment Year	TP Before/TP After
			[m]		[Year]	[μg/L/μg/L]
[94]	Meishan Dongpo Lake	China	2.5	Biomass screening/Removal of Fish/Macrophyte Addition	November 2015 to July 2016	379/lower than 50
[95]	Lake Eymir	Turkey	3.1	Multiple mesh-sized gill nets	August 1998–1999	324 ± 31/381 ± 21

Table 7. *Cont.*

Reference	Lake Name	Country	Mean Depth	Method Used	Treatment Year	TP Before/TP After
			[m]		[Year]	[μg/L/μg/L]
[96]	Lake Wuli	China	2.1	Gillnets and electric fishing/Richardson, and piscivorous fish addition with macrophytes	2010	n.d *
[97]	Huizhou West Lake	China	1.6	Plankti-benthivorous fish was followed by the planting of submerged macrophytes and stocking of piscivorous fish	-	126/lower than 50

Note: * n.d—Not determined.

As a possible disadvantage of biomanipulation, the water has a higher clarity after manipulation, and the sediments which thus retain more P. Aquatic species could disturb the sediment, causing further nutrient releases from the sediments. Usually, three specific activities will define the cost of biomanipulation: the fish removal, the stocking, and the fish population monitoring. For giving a perspective on costs for biomanipulation of the Twin Lakes in Golden Valley, Minnesota, amounts have been shared as follows: 8000 USD for the combination of netting and electrofishing fish removal, and 45,000 USD was used for stocking (i.e., which will directly be dependent on the species). This included a fish population yearly monitoring cost of 1000 USD per year [98].

3.4. Combined Remediation Techniques

In this type of practice, more than one remediation technique is used to achieve the desired objective of a healthy water body without signs of eutrophication. This is considered a rounded methodology, well established in the specialized literature for treating eutrophic aquatic ecosystems. An overview of possible combinations is summarized in Table 8.

Table 8. Combined in situ remediation studies.

Reference	Lake Name	Country	Mean Depth	Method Used	Treatment Year	Dosage Used	TP Before/TP After
			[m]		[year]		[μg/L/μg/L]
[99]	Lake De Kuil	Netherlands	4	Coagulation/Flocculation/LMB Capping	18 May to 22 May 2009	65.35 $FeCl_3$ g/m^2, 2.03 tLMB/ha superficially and 4.17 tLMB/ha	50/20
[100]	Lake Głębokie	Poland	2.4	Aeration/coagulation (iron sulphate III)/biomanipulation	2008–2012	A total of 7.90 g/m^2 divided in 8 applications	140/65
[101]	Swarzędzkie Lake	Poland	2.6	Aeration/coagulation (iron sulphate III) and magnesium chloride ($MgCl_2$)/biomanipulation	2012–2014	15 kg/ha ($FeSO_4$)	114.6/76
[102]	Lake Kleine Melanen	Netherlands	1.0	Biomanipulation/dredging/sand capping/LMB application and flocculant	2010–2012	4.14 t LMB/ha	300/110
[103]	Lake Rauwbraken	Netherlands	8	Coagulation and LMB capping	April 21st to 23rd 2008	(0.8 t LMB/ha + 77 g/m^2 PAC *) + 6.4 t LMB/ha	134/14
[104]	Lake Schmaler	Germany	14.7	$Ca(OH)_2$ injection and hypolimnetic aeration	1996–1998	300 t of $Ca(OH)_2$	n.d **

Note: * PAC: Poly-Aluminum-Chloride; ** n.d—Not determined.

The holistic approaches presented in the reviewed articles are well-known doses of coagulant and LMB to achieve the desired objective of a healthy lake free of eutrophication signs [99,102,103]. This practice is based on coagulant addition, and in some cases was followed by water column aeration. Then, LMB is supplemented to increase flocculation in the applied water body, thus causing particles to settle more easily and sorb phosphorus on them, thus capturing P as an active capping layer on the sediment surface. Investigation into the order of addition is needed to obtain the best attenuation scenario. Additionally, as presented after the particles settle, biomanipulation can take place during this treatment. As this procedure is well studied in the literature with positive results, this in-lake practice application could be a future preference for dealing with eutrophic waterbodies soon. These coagulation and flocculation practices reported monetary values as a total amount including all the steps required. For example, Lake De Kuil had a cost of €140,000 or 150,800 USD [99] and Lake Rauwbraken [105] was €50,000 or 53,854 USD.

Another option presented is the procedure of dredging followed by imposing a sand capping layer for the exposed dredged sediment [102], then addition of the P fixative modified clay and flocculant poly-aluminum chloride. Both methods have presented reliable results for eutrophication control. Some other examples such as the addition of $Ca(OH)_2$ and hypolimnetic aeration [104], which has induced calcium carbonate precipitation, combined with deep water aeration lower P flux in the sediment, but further investigation is needed.

3.5. Emerging Remediation Techniques including Geotextile Filtration and Floating Wetlands

Emerging remediation measures are based on minimally invasive lake restoration techniques which take the benefits of the natural response of lake water to changes made within it. This has been used for nutrient abstraction or algae suppression. When compared with implemented technologies, these methods are considered less invasive, easily deployed, cheaper, and more sustainable, characterizing them as an environmentally friendly remediation option. While the floating wetland (i.e., ecological floating beds) uses floating plant units, which can uptake nutrients from the water column and thus decrease the incidence of harmful algae blooms, the lake water filtration technique is based on using custom-made geotextiles, generally used in layers for strata separation, soil improvement, reinforcement, and drainage as filter layers for attenuating suspended solids and thus particulate phosphorus. A significant improvement in lake water has been found in investigations performed with geotextiles onsite and in situ [106–108]. However, additional investigations are still required for both methods for any further scale-up and whole lake applications.

3.6. Critical Overview of Practices for Eutrophic Shallow Lake Water Remediation

As previously mentioned, water management/protection is not a straightforward action and technologies must be adjusted on a case-by-case basis. The same understanding should be taken into internal nutrient remediation practices selection and further application. On those, there is no better remediation than the other, as well as no go-to manual for selection—just recommendations to be followed. This is mainly due to water/sediment quality heterogeneity in eutrophic waterbodies. With this thinking, frameworks for selection should always be applied with the perspective on issues presented on the eutrophic waterbody for its attenuation. It is well known that cost plays an important role in this procedure, but it should also be taken into consideration that if the remediation is not performed promptly, the eutrophic water body will not return to its original condition, and costs will tend to increase yearly (i.e., external nutrient attenuation is not performed) or will reach a point of no return.

Summarized information on in situ remediation practices is presented in Table 9. Apart from sediment dredging, all other procedures do not remove higher sediment phosphorus accumulated inside the aquatic ecosystem; thus, the other methods may not permanently reduce eutrophication occurrences. However, this should not be the first and foremost

recommended methodology for lake water remediation, mainly because of its associated byproducts generated (i.e., possible metal leaching and waste). This methodology needs to be further investigated and refined to precisely remove less sediment, causing less disturbance and secondary pollution.

Table 9. Overview of practices for eutrophic shallow lake water remediation.

Practice	Procedure	Advantage	Disadvantage/Challenge	Estimated Capital and/or Operating Costs
Dredging	Sediment is excavated mechanically and removed from the waterbody.	Reduction in the internal P loading immediately and substantially.	• Secondary pollution due to leaching metals/contaminants. • Imperative concern for waste disposal.	20,000 USD to 75,000 per acre dredged + Waste disposal cost.
Hypolimnetic Aeration	Mixing of deep anoxic waters with shallow oxygenated epilimnion waters.	Alleviation of eutrophication symptoms.	• Oxygen deficit at start will be high due to accumulated organic matter mineralization. • Does not deal with the issue and combination with other methods is required.	Average of 3800.00 USD per acre for the capital cost and 700.00 USD per acre for operation and maintenance.
LMB Capping	Modified clay addition in a slurry form or granules in the water column which will sorb phosphorus and settle creating a thin barrier.	Sequestration of phosphorus and retention in the sediment and reduced phosphorus sediment bioavailability.	• Dosage determination plays an important role in the results obtained. • Humic substances can complex with lanthanides. • Under high pH conditions (>8.35) the potential binding efficiency decreases. • Reapplication of the product could be required.	2279.00 USD/t for LMB and 147.00 USD/t for application in some cases.
Aluminium Capping	Involves adding an aluminum solution to the lake water which settles in the sediment and binds phosphorus, preventing its release into the water column.	Sequestration of phosphorus and retention in the sediment and reduced phosphorus sediment bioavailability.	• Dosage determination plays an important role in the results obtained. • Optimal pH range is needed (i.e., 6–8). • Acidic water pH, the form Al^{3+}, which is toxic to organisms. • Concerns are still not well explained regarding the chronic effects. • Method does not directly affect the content of organic phosphorus.	Average of 4812.00 USD per acre for capital costs and a range of 0 USD to 619.00 USD operation and maintenance costs in some cases.

Table 9. *Cont.*

Practice	Procedure	Advantage	Disadvantage/Challenge	Estimated Capital and/or Operating Costs
Hypolimnetic Oxygenation	Oxygen introduction in the deep anoxic water to prevent low dissolved oxygen concentrations.	Increased redox potential at the water–sediment interface, limited seasonal release of nutrients from the bottom sediments into the water column.	• Dosage determination plays an important role in the results obtained. • If high content of organic matter accumulated on the sediment, oxygen concentration demand will increase. • It should be combined with other ecological lake restoration techniques.	System installation: 40.00 to 800.00 USD per hectare meter) and operation and maintenance: 5.00 to 36.00 USD per hectare meter in some cases.
Macrophyte Management	Characterized by plant biomass from aquatic ecosystem removal by plunking or cutting it down. Or macrophyte repopulation with endogenous species.	Reduction in macrophyte litter in the lake.	• Leaching of soluble compounds from macrophyte organs • Sediment resuspension and dispersal of plant fragments. • No reduction in phosphorus in the sediment.	Will depend on the price of the equipment acquired/or endogenous plant species to be introduced.
Biomanipulation	Aquatic food chains manipulation achieved by planktivorous fish removal and introduction of piscivorous fish into a lake.	Decreased high concentration of toxic phytoplankton in the water bodies as well as reduced sediment disturbance.	• More P retention in the sediments could lead to further P release into the water.	Removal by netting and electrofishing (8000 USD), 45,000 USD to stock populations, with a yearly monitoring of 1000 USD in some cases.

Sediment capping practices, on the other hand, could be considered a direct and quick solution to decrease eutrophication occurrences, which in some cases is what the stakeholders involved want. The fast application of this active layer on the sediment would have representative direct results, but the higher sediment phosphorus remains. Resuspension or sediment disturbances would easily decrease its effectiveness. Additionally, some capping materials, aluminum and LMB, are well received in some countries and not in many others due to policy restrictions that could affect their selection and application. Additionally, material production of LMB or other specific materials are still focused on just specific world regions and monetary costs are still not practical for all nations.

As with the hypolimnetic oxygenation and aeration method, this technique will just limit the seasonal release of nutrients from the bottom sediments into the water column and is thus a temporary eutrophication alleviation practice. This means that with the interruption of the mentioned technologies, the waterbody could possibly return to its initial eutrophic condition. For macrophyte removal and repopulation, caution should be used. Phytoplankton biota domination or macrophyte dispersal could be worsened due to plant fragments depending on the macrophyte population. Thus, this should be avoided for all unnecessary scenarios (i.e., visual impairment) and if truly needed, the only removal method recommended is cutting the macrophytes to guarantee fewer negative effects on water body quality.

Treatment combinations should be the future practice for eutrophic shallow lake water remediation. Firstly, methods attempting to remov higher phosphorus content sediments

from the lake should be followed by methods dealing with the remaining phosphorus concentration in the water column. These practices need to be increased in the remediation market. It is worth commenting that further enhancement of these remediation techniques must include circular economy and waste management approaches for addressing material production as well proper waste reuse or disposal. Additionally, sustainability frameworks need to be developed for ensuring proper application. Environment government bodies must act now on either providing funding for research or allowing pilot studies on lakes by specialized personnel, which can further be expanded to full scale lake restoration.

4. Discussion and Future Perspectives

It is better to prevent than to treat the disease (i.e., eutrophication occurrence). When this premise cannot be applied, it is necessary first to remove/attenuate external nutrient sources followed by a holistic, region-specific, and sustainable remediation method for internal phosphorus load reduction to ensure healthy waters and assurance of all its possible uses for present and future generations. This is achieved by setting targets in close consultation with local authorities and the stakeholders to safeguard a pragmatic and realistic communication of the remediation process [71]. The affected society's involvement should be present not only prior to but also during and after the remediation measures, acting as a valuable promotion of restored water value and if required possible supervision.

Related to external nutrient sources, even though radical and rapid elimination, in many cases, is not possible, especially in the case of non-point sources [63], actions in this direction need to be promoted and documented. These could be achieved using proper land use planning or employing/increasing buffer strips (i.e., to prevent erosion and act as a filter to intercept contaminated watershed runoff). Environmental regulatory government bodies must also present and enforce stricter restrictions/policies for nutrient apport/emission on water bodies to stop the increase in eutrophication scenarios. By designing harsher nutrient removal and emission strategies/guidelines for external sources (i.e., untreated/incompletely treated effluents/sewage disposal) on lakes, the actual eutrophic waterbodies and the ones increasing nutrient concentration will have a time frame to be dealt with it. Past/present nutrient emitters should also be strongly financially accountable for any nutrient attenuation/monitoring of the affected water body.

In the case of internal nutrient remediation strategies selection, this decision must be only based on well-known decision frameworks sustained by prior monitoring results of lake water and sediment. This prior investigation should comprise phosphorus and organic matter content in the water column and sediment, as well as phosphorus bioavailability in the sediment with some other important parameters for best treatment selection, which are pH, DO, turbidity, and chlorophyll-a. The determination of whether internal P load is important relative to external P inputs needs to be understood by the quantification and their contribution to lake P concentration established [68]. In addition, scientifically reliable data on the efficacy of proactive approaches need to be provided to assist water resource managers in making informed decisions [69]. Technologies should be chosen according to their suitability for the site and not solely on an economic basis [23]. Thus, remediation corporation portfolios could and should be used, but compulsory caution on region-specific presented results needs to be included. Even though costs for the various practices are quite different, the final selection will depend on the probable recommendation of environmental government body and the responsible payers to that, which will take into consideration the cost/benefit perspective.

Monitoring actions should always be integrated into the lake restoration practices with a proper definition of follow-up steps and actions if there is a deviation from the expected remediation results. This could be completed by direct guidelines on reapplications, increasing mixing or chemical addition concentration (e.g., O_2 concentration), and rigorous actions to further attenuate the external source if this is the issue. The sustainability of remediation projects also needs to be further investigated and increased in some cases because generating a large quantity of waste without proper disposal (i.e., biomanipulation,

sediment dredging) or using non-renewable energy for applications (i.e., diverse chemical addition application, sediment dredging, biomanipulation) are not sustainable. Emergent remediation techniques should be further investigated, and if presented, reliable results used with well-established options for healthy lake water.

With the understanding that every person has the right to clean and safe water, eutrophication must be prevented/attenuated on a global scale promptly. Even though the essential awareness and financial aspect for remediation projects will not be presented equally around world nations, as was noticed throughout the cases presented in Tables 1–8, this lack is mainly occurring in economically developing nations. It is implicit that those nations also suffering from this matter receive all attention and assistance required. Additionally, to assure equitable access to essential knowledge and technologies development/application for water remediation restoration, international environmental organizations must further cooperate not only in the exchange of realities/experiences/perspectives but also for financial and technical support. Only with proper policies and programs for training and development and further investments can nations develop their practices and policies, and remediate their eutrophic waterbodies.

5. Conclusions

Concern with eutrophication in lakes is escalating and in-situ, holistic, and region-specific approaches are the only possible option for the restoration of eutrophic aquatic ecosystems for present and future generations. By the combination of attenuation and regulation of external phosphorus loads with diverse internal nutrient source control and proactive technologies, this is going to be accomplished. In this paper, the principal procedures being applied for in situ eutrophic water remediation has been emphasized in association with possible parameters and disadvantages/challenges encountered by various water restoration techniques. By reviewing these in-situ approaches around nations, a guided summary has been completed, providing concise information on the in-situ restoration cases and challenges in the peer-reviewed literature to facilitate further remediation project investigation, studies, and further selection by stakeholders involved (i.e., environmental managers, and society in general). Two additional steps are compulsory for successful and durable water remediation which are external nutrient attenuation and continuous monitoring. It is also imperative that the affected society participates prior to, during and after the eutrophic remediation measures as a possible way of valuing this water and for long-term and effective water management.

Author Contributions: Conceptualization, A.C.P.; investigation, A.C.P.; writing—original draft preparation, A.C.P.; writing—review and editing, C.N.M.; visualization, A.C.P.; supervision, C.N.M.; project administration, C.N.M.; funding acquisition, C.N.M. All authors have read and agreed to the published version of the manuscript.

Funding: This research was funded by NSERC ALLRP 549706-19 grant, Concordia University and Titan Environmental Containment.

Data Availability Statement: The data for this study are available from the authors upon reasonable request.

Acknowledgments: The authors are also grateful to the visual artist Alisson Clebson Nogueira Siqueira for assistance with the diagram and figures included in this paper.

Conflicts of Interest: The authors declare no conflict of interest.

References

1. Beaulieu, J.J.; DelSontro, T.; Downing, J.A. Eutrophication will increase methane emissions from lakes and impoundments during the 21st century. *Nat. Commun.* **2019**, *10*, 1375. [CrossRef] [PubMed]
2. Tong, Y.; Sun, J.; Uddin, M.; Kong, X.; Lin, Y.; Wang, M.; Zhang, H.; Xu, X.; Wu, Z. Perspectives and challenges of applying the water-food-energy nexus approach to lake eutrophication modelling. *Water Secur.* **2021**, *14*, 100095. [CrossRef]
3. Scherer, L.; Pfister, S. Global biodiversity loss by freshwater consumption and eutrophication from Swiss food consumption. *Environ. Sci. Technol.* **2016**, *50*, 7019–7028. [CrossRef] [PubMed]

4. Paerl, H.W.; Gardner, W.S.; Havens, K.E.; Joyner, A.R.; McCarthy, M.J.; Newell, S.E.; Qin, B.; Scott, J.T. Mitigating cyanobacterial harmful algal blooms in aquatic ecosystems impacted by climate change and anthropogenic nutrients. *Harmful Algae* **2016**, *54*, 213–222. [CrossRef]
5. Yindong, T.; Xiwen, X.; Miao, Q.; Jingjing, S.; Yiyan, Z.; Wei, Z.; Mengzhu, W.; Xuejun, W.; Yang, Z. Lake warming intensifies the seasonal pattern of internal nutrient cycling in the eutrophic lake and potential impacts on algal blooms. *Water Res.* **2021**, *188*, 116570. [CrossRef]
6. Woolway, R.I.; Kraemer, B.M.; Lenters, J.D.; Merchant, C.J.; O'Reilly, C.M.; Sharma, S. Global lake responses to climate change. *Nat. Rev. Earth Environ.* **2020**, *1*, 388–403. [CrossRef]
7. Woolway, R.I.; Merchant, C.J. Worldwide alteration of lake mixing regimes in response to climate change. *Nat. Geosci.* **2019**, *12*, 271–276. [CrossRef]
8. Häder, D.P.; Banaszak, A.T.; Villafañe, V.E.; Narvarte, M.A.; González, R.A.; Helbling, E.W. Anthropogenic pollution of aquatic ecosystems: Emerging problems with global implications. *Sci. Total Environ.* **2020**, *713*, 136586. [CrossRef]
9. Chowdhary, P.; Bharagava, R.N.; Mishra, S.; Khan, N. Role of industries in water scarcity and its adverse effects on environment and human health. In *Environmental Concerns and Sustainable Development: Volume 1: Air, Water and Energy Resources*; Springer: New York, NY, USA, 2020; pp. 235–256. [CrossRef]
10. Le Moal, M.; Gascuel-Odoux, C.; Ménesguen, A.; Souchon, Y.; Étrillard, C.; Levain, A.; Moatar, F.; Pannard, A.; Souchu, P.; Lefebvre, A.; et al. Eutrophication: A new wine in an old bottle? *Sci. Total Environ.* **2019**, *651*, 1–11. [CrossRef]
11. Li, H.; Gu, X.; Chen, H.; Mao, Z.; Shen, R.; Zeng, Q.; Ge, Y. Co-occurrence of multiple cyanotoxins and taste-and-odor compounds in the large eutrophic Lake Taihu, China: Dynamics, driving factors, and challenges for risk assessment. *Environ. Pollut.* **2022**, *294*, 118594. [CrossRef]
12. Smith, V.H.; Sieber-Denlinger, J.; de Noyelles, F., Jr.; Campbell, S.; Pan, S.; Randtke, S.J.; Blain, G.T.; Strasser, V.A. Managing taste and odor problems in a eutrophic drinking water reservoir. *Lake Reserv. Manag.* **2002**, *18*, 319–323. Available online: https://www.tandfonline.com/doi/abs/10.1080/07438140209353938 (accessed on 30 April 2023). [CrossRef]
13. Wang, Z.; Akbar, S.; Sun, Y.; Gu, L.; Zhang, L.; Lyu, K.; Huang, Y.; Yang, Z. Cyanobacterial dominance and succession: Factors, mechanisms, predictions, and management. *J. Environ. Manag.* **2021**, *297*, 113281. [CrossRef] [PubMed]
14. Brasil, J.; Attayde, J.L.; Vasconcelos, F.R.; Dantas, D.D.; Huszar, V.L. Drought-induced water-level reduction favors cyanobacteria blooms in tropical shallow lakes. *Hydrobiologia* **2016**, *770*, 145–164. [CrossRef]
15. Kaur, S.; Srivastava, A.; Ahluwalia, A.S.; Mishra, Y. *Cyanobacterial blooms and Cyanotoxins: Occurrence and Detection. Algae: Multifarious Applications for a Sustainable World*; Springer: New York, NY, USA, 2021; pp. 339–352. [CrossRef]
16. USEPA (US Environmental Protection Agency). A Compilation of Cost Data Associated with the Impacts and Control of Nutrient Pollution. 2015. Available online: https://www.epa.gov/sites/default/files/2015-04/documents/nutrient-economics-report-2015.pdf (accessed on 30 April 2023).
17. Dodds, W.K.; Bouska, W.W.; Eitzmann, J.L.; Pilger, T.J.; Pitts, K.L.; Riley, A.J.; Schloesser, J.T.; Thornbrugh, D.J. Eutrophication of US freshwaters: Analysis of potential economic damages. *Environ. Sci. Technol.* **2009**, *43*, 12–19. [CrossRef]
18. Pretty, J.N.; Mason, C.F.; Nedwell, D.B.; Hine, R.E. *A Preliminary Assessment of the Environmental Costs of the Eutrophication of Fresh Water in England and Wales*; University of Essex: Colchester, UK, 2002. Available online: https://buckinghamcanal.org.uk/wp-content/uploads/resources/EAEutrophReport.pdf (accessed on 30 April 2023).
19. Walker, W.W., Jr. Significance of eutrophication in water supply reservoirs. *J. Am. Water Work. Assoc.* **1983**, *75*, 38–42. [CrossRef]
20. Golterman, H.L. Chapter 17 Nutrient Budgets and Eutrophication. In *Physiological Limnology—An Approach to the Physiology of Lake Ecosystems*; Elsevier: Amsterdam, The Netherlands, 1975; pp. 357–402. [CrossRef]
21. Sharpley, A.; Jarvie, H.P.; Buda, A.; May, L.; Spears, B.; Kleinman, P. Phosphorus legacy: Overcoming the effects of past management practices to mitigate future water quality impairment. *J. Environ. Qual.* **2013**, *42*, 1308–1326. [CrossRef] [PubMed]
22. Song, K.; Adams, C.J.; Burgin, A.J. Relative importance of external and internal phosphorus loadings on affecting lake water quality in agricultural landscapes. *Ecol. Eng.* **2017**, *108*, 482–488. [CrossRef]
23. Dunalska, J.A. How the integrated engineering solutions can support the lakes restoration? *Ecohydrol. Hydrobiol.* **2021**, *21*, 36–45. [CrossRef]
24. Istvánovics, V. Eutrophication of Lakes and Reservoirs. In *Encyclopedia of Inland Waters*; Elsevier: San Diego, CA, USA, 2009; pp. 157–165. [CrossRef]
25. O'Hare, M.T.; Baattrup-Pedersen, A.; Baumgarte, I.; Freeman, A.; Gunn, I.D.; Lázár, A.N.; Sinclair, R.; Wade, A.J.; Bowes, M.J. Responses of aquatic plants to eutrophication in rivers: A revised conceptual model. *Front. Plant Sci.* **2018**, *9*, 451. [CrossRef]
26. Khan, F.A.; Ansari, A.A. Eutrophication: An ecological vision. *Bot. Rev.* **2005**, *71*, 449–482. [CrossRef]
27. Sellergren, M.; Li, J.; Drakare, S.; Thöns, S. Decision Support for Lake Restoration: A Case Study in Swedish Freshwater Bodies. *Water* **2023**, *15*, 668. [CrossRef]
28. McCormick, A.R.; Phillips, J.S.; Botsch, J.C.; Ives, A.R. Shifts in the partitioning of benthic and pelagic primary production within and across summers in Lake Mývatn, Iceland. *Inland Waters* **2021**, *11*, 13–28. [CrossRef]
29. Senar, O.E.; Creed, I.F.; Trick, C.G. Lake browning may fuel phytoplankton biomass and trigger shifts in phytoplankton communities in temperate lakes. *Aquat. Sci.* **2021**, *83*, 21. [CrossRef]

30. O'Keeffe, J. *Cyanobacteria and Drinking Water: Occurrence, Risks, Management and Knowledge Gaps for Public Health*; National Collaborating Centre for Environmental Health: Vancouver, BC, Canada, 2019. Available online: https://ncceh.ca/documents/evidence-review/cyanobacteria-and-drinking-water-occurrence-risks-management-and (accessed on 30 April 2023).
31. Mackey, K.R.M.; Paytan, A. Phosphorus Cycle. In *Encyclopedia of Microbiology*; Elsevier: Oxford, UK, 2009; pp. 322–334. [CrossRef]
32. Denver, J.M.; Cravotta, C.A.; Ator, S.W.; Lindsey, B.D. *Contributions of Phosphorus from Groundwater to Streams in the Piedmont, Blue Ridge, and Valley and Ridge Physiographic Provinces, Eastern United States*; US Department of the Interior, US Geological Survey: Denver, CO, USA, 2010; Volume 2010. Available online: https://pubs.usgs.gov/sir/2010/5176/support/sir2010-5176old2282011.pdf (accessed on 30 April 2023).
33. Slomp, C.P.; Mort, H.P.; Jilbert, T.; Reed, D.C.; Gustafsson, B.G.; Wolthers, M. Coupled dynamics of iron and phosphorus in sediments of an oligotrophic coastal basin and the impact of anaerobic oxidation of methane. *PLoS ONE* **2013**, *8*, e62386. [CrossRef] [PubMed]
34. Yu, W.; Yang, H.; Chen, J.; Liao, P.; Chen, Q.; Yang, Y.; Liu, Y. Organic Phosphorus Mineralization Dominates the Release of Internal Phosphorus in a Macrophyte-Dominated Eutrophication Lake. *Front. Environ. Sci.* **2022**, *747*, 812834. [CrossRef]
35. Zhou, Z.; Henkel, S.; Kasten, S.; Holtappels, M. The iron "redox battery" in sandy sediments: Its impact on organic matter remineralization and phosphorus cycling. *Sci. Total Environ.* **2023**, *865*, 161168. [CrossRef] [PubMed]
36. Kapsalis, V.C.; Kalavrouziotis, I.K. Eutrophication—A worldwide water quality issue. In *Chemical Lake Restoration: Technologies, Innovations and Economic Perspectives*; Springer: New York, NY, USA, 2021; pp. 1–21. [CrossRef]
37. Søndergaard, M.; Jensen, J.P.; Jeppesen, E. Role of sediment and internal loading of phosphorus in shallow lakes. *Hydrobiologia* **2003**, *506*, 135–145. [CrossRef]
38. Li, Y.; Yu, S.; Strong, J.; Wang, H. Are the biogeochemical cycles of carbon, nitrogen, sulfur, and phosphorus driven by the "Fe III–Fe II redox wheel" in dynamic redox environments? *J. Soils Sediments* **2012**, *12*, 683–693. [CrossRef]
39. Smolders, A.J.; Lucassen, E.C.; Bobbink, R.; Roelofs, J.G.; Lamers, L.P. How nitrate leaching from agricultural lands provokes phosphate eutrophication in groundwater fed wetlands: The sulphur bridge. *Biogeochemistry* **2010**, *98*, 1–7. [CrossRef]
40. Avilés, A.; Rodero, J.; Amores, V.; De Vicente, I.; Rodríguez, M.I.; Niell, F.X. Factors controlling phosphorus speciation in a Mediterranean basin (River Guadalfeo, Spain). *J. Hydrol.* **2006**, *331*, 396–408. [CrossRef]
41. House, W.A. Geochemical cycling of phosphorus in rivers. *Appl. Geochem.* **2003**, *18*, 739–748. [CrossRef]
42. Wetzel, R.G. 26—Inland waters: Understanding is essential for the future. In *Limnology*, 3rd ed.; Elsevier: Oxford, UK, 2001; pp. 825–841. [CrossRef]
43. Jilbert, T.; Couture, R.M.; Huser, B.J.; Salonen, K. Preface: Restoration of eutrophic lakes: Current practices and future challenges. *Hydrobiologia* **2020**, *847*, 4343–4357. [CrossRef]
44. UNESCO. The United Nations World Water Development Report 2021: Valuing Water. 2021. Available online: https://unesdoc.unesco.org/ark:/48223/pf0000375724 (accessed on 30 April 2023).
45. Schlesinger, W.H.; Bernhardt, E.S. Inland Waters—Chapter 8. *Biogeochemistry* **2020**, *132*, 293–360. [CrossRef]
46. Carlson, R.E. A trophic state index for lakes. *Limnol. Oceanogr.* **1977**, *22*, 361–369. [CrossRef]
47. Mekonnen, M.M.; Hoekstra, A.Y. Global anthropogenic phosphorus loads to freshwater and associated grey water 671 footprints and water pollution levels: A high-resolution global study. *Water Resour. Res.* **2018**, *54*, 345–358. [CrossRef]
48. Smith, V.H.; Schindler, D.W. Eutrophication science: Where do we go from here? *Trends Ecol. Evol.* **2009**, *24*, 201–207. [CrossRef]
49. Ho, J.C.; Michalak, A.M.; Pahlevan, N. Widespread global increase in intense lake phytoplankton blooms since the 1980s. *Nature* **2019**, *574*, 667–670. [CrossRef]
50. Kakade, A.; Salama, E.S.; Han, H.; Zheng, Y.; Kulshrestha, S.; Jalalah, M.; Harraz, F.A.; Alsareii, S.A.; Li, X. World eutrophic pollution of lake and river: Biotreatment potential and future perspectives. *Environ. Technol. Innov.* **2021**, *23*, 101604. [CrossRef]
51. International Lake Environment Committee, (I.L.E.C.); Lake Biwa Research Institute. *1988–1993 Survey of the State of the World's Lakes*; International Lake Environment Committee, Otsu and United Nations Environment Programme: Nairobi, Kenya, 2002; Volume I–IV.
52. Paerl, H.W.; Xu, H.; McCarthy, M.J.; Zhu, G.; Qin, B.; Li, Y.; Gardner, W.S. Controlling harmful cyanobacterial blooms in a hyper-eutrophic lake (Lake Taihu, China): The need for a dual nutrient (N & P) management strategy. *Water Res.* **2011**, *45*, 1973–1983. [CrossRef]
53. Zhang, Y.; Luo, P.; Zhao, S.; Kang, S.; Wang, P.; Zhou, M.; Lyu, J. Control and remediation methods for eutrophic lakes in the past 30 years. *Water Sci. Technol.* **2020**, *81*, 1099–1113. [CrossRef]
54. Wang, C.; Jiang, H.L. Chemicals used for in situ immobilization to reduce the internal phosphorus loading from lake sediments for eutrophication control. *Crit. Rev. Environ. Sci. Technol.* **2016**, *46*, 947–997. [CrossRef]
55. Rast, W.; Holland, M. Eutrophication of lakes and reservoirs: A framework for making management decisions. *Ambio* **1988**, *17*, 2–12. Available online: https://www.jstor.org/stable/4313411 (accessed on 30 April 2023).
56. Hickey, C.W.; Gibbs, M.M. Lake sediment phosphorus release management—Decision support and risk assessment framework. *N. Z. J. Mar. Freshw. Res.* **2009**, *43*, 819–856. [CrossRef]
57. Kiani, M.; Tammeorg, P.; Niemistö, J.; Simojoki, A.; Tammeorg, O. Internal phosphorus loading in a small shallow Lake: Response after sediment removal. *Sci. Total Environ.* **2020**, *725*, 138279. [CrossRef] [PubMed]

58. Jing, L.; Bai, S.; Li, Y.; Peng, Y.; Wu, C.; Liu, J.; Liu, G.; Xie, Z.; Yu, G. Dredging project caused short-term positive effects on lake ecosystem health: A five-year follow-up study at the integrated lake ecosystem level. *Sci. Total Environ.* **2019**, *686*, 753–763. [CrossRef] [PubMed]
59. Liu, C.; Zhong, J.; Wang, J.; Zhang, L.; Fan, C. Fifteen-year study of environmental dredging effect on variation of nitrogen and phosphorus exchange across the sediment-water interface of an urban lake. *Environ. Pollut.* **2016**, *219*, 639–648. [CrossRef]
60. Zhang, S.; Zhou, Q.; Xu, D.; Lin, J.; Cheng, S.; Wu, Z. Effects of sediment dredging on water quality and zooplankton community structure in a shallow of eutrophic lake. *J. Environ. Sci.* **2010**, *22*, 218–224. [CrossRef]
61. Wan, W.; Zhang, Y.; Cheng, G.; Li, X.; Qin, Y.; He, D. Dredging mitigates cyanobacterial bloom in eutrophic Lake Nanhu: Shifts in associations between the bacterioplankton community and sediment biogeochemistry. *Environ. Res.* **2020**, *188*, 109799. [CrossRef]
62. Natural Technique for Dredging a Pond or Lake—Clean-Flo. Available online: https://clean-flo.com/alternative-dredging-techniques-muck-removal (accessed on 28 May 2023).
63. Dondajewska, R.; Kowalczewska-Madura, K.; Gołdyn, R.; Kozak, A.; Messyasz, B.; Cerbin, S. Long-term water quality changes as a result of a sustainable restoration—A case study of dimictic Lake Durowskie. *Water* **2019**, *11*, 616. [CrossRef]
64. Zhang, X. Restoration of a Small, Shallow, Eutrophic Lake by Submerged Aeration and Comparison with a Similar Lake. Ph.D. Dissertation, Colorado State University, Fort Collins, CO, USA, 2013. Available online: https://www.proquest.com/docview/1416433047 (accessed on 30 April 2023).
65. Grochowska, J.; Brzozowska, R.; Parszuto, K. The influence of different recultivation techniques on primary production processes in a degraded urban lake. *Oceanol. Hydrobiol. Stud.* **2014**, *43*, 211–218. [CrossRef]
66. Mallin, M.A.; McIver, M.R.; Wambach, E.J.; Robuck, A.R. Algal blooms, circulators, waterfowl, and eutrophic Greenfield Lake, North Carolina. *Lake Reserv. Manag.* **2016**, *32*, 168–181. [CrossRef]
67. ITRC. *Review of Strategies for Preventing and Managing Harmful Cyanobacterial Blooms*; Interstate Technology and Regulatory Council: Washington, DC, USA, 2020; Available online: https://hcb-1.itrcweb.org/c-2-cost-compilation-for-several-mitigation-strategies/ (accessed on 28 May 2023).
68. Nürnberg, G.K.; LaZerte, B.D. Trophic state decrease after lanthanum-modified bentonite (Phoslock) application to a hypereutrophic polymictic urban lake frequented by Canada geese (Branta canadensis). *Lake Reserv. Manag.* **2016**, *32*, 74–88. [CrossRef]
69. Bishop, W.M.; McNabb, T.; Cormican, I.; Willis, B.E.; Hyde, S. Operational evaluation of Phoslock phosphorus locking technology in Laguna Niguel Lake, California. *Water Air Soil Pollut.* **2014**, *225*, 1–11. [CrossRef]
70. Neweshy, W.; Planas, D.; Tellier, E.; Demers, M.; Marsac, R.; Couture, R.M. Response of sediment phosphorus partitioning to lanthanum-modified clay amendment and porewater chemistry in a small eutrophic lake. *Environ. Sci. Process. Impacts* **2022**, *24*, 1494–1507. [CrossRef]
71. Epe, T.S.; Finsterle, K.; Yasseri, S. Nine years of phosphorus management with lanthanum modified bentonite (Phoslock) in a eutrophic, shallow swimming lake in Germany. *Lake Reserv. Manag.* **2017**, *33*, 119–129. [CrossRef]
72. Spears, B.M.; Mackay, E.B.; Yasseri, S.; Gunn, I.D.; Waters, K.E.; Andrews, C.; Cole, S.; De Ville, M.; Kelly, A.; Meis, S.; et al. A meta-analysis of water quality and aquatic macrophyte responses in 18 lakes treated with lanthanum modified bentonite (Phoslock®). *Water Res.* **2016**, *97*, 111–121. [CrossRef] [PubMed]
73. Dithmer, L.; Nielsen, U.G.; Lürling, M.; Spears, B.M.; Yasseri, S.; Lundberg, D.; Moore, A.; Jensen, N.D.; Reitzel, K. Responses in sediment phosphorus and lanthanum concentrations and composition across 10 lakes following applications of lanthanum modified bentonite. *Water Res.* **2016**, *97*, 101–110. [CrossRef]
74. Lürling, M.; Faassen, E.J. Controlling toxic cyanobacteria: Effects of dredging and phosphorus-binding clay on cyanobacteria and microcystins. *Water Res.* **2012**, *46*, 1447–1459. [CrossRef] [PubMed]
75. Tetra Tech. Assessment of Nutrient Management Technology Submission Phoslock®Phosphorus Locking Technology. 2022. Available online: https://h2.ohio.gov/wp-content/uploads/2022/09/H2Ohio-Technology-Assessment-Final-Report-Phoslock-Jan-2022.pdf (accessed on 30 April 2023).
76. Nürnberg, G.K. Attempted management of cyanobacteria by Phoslock (lanthanum-modified clay) in Canadian lakes: Water quality results and predictions. *Lake Reserv. Manag.* **2017**, *33*, 163–170. [CrossRef]
77. Huser, B.J. Aluminum application to restore water quality in eutrophic lakes: Maximizing binding efficiency between aluminum and phosphorus. *Lake Reserv. Manag.* **2017**, *33*, 143–151. [CrossRef]
78. Dadi, T.; Schultze, M.; Kong, X.; Seewald, M.; Rinke, K.; Friese, K. Sudden eutrophication of an aluminum sulphate treated lake due to abrupt increase of internal phosphorus loading after three decades of mesotrophy. *Water Res.* **2023**, *235*, 119824. [CrossRef] [PubMed]
79. Rönicke, H.; Frassl, M.A.; Rinke, K.; Tittel, J.; Beyer, M.; Kormann, B.; Gohr, F.; Schultze, M. Suppression of bloom-forming colonial cyanobacteria by phosphate precipitation: A 30 years case study in Lake Barleber (Germany). *Ecol. Eng.* **2021**, *162*, 106171. [CrossRef]
80. Kowalski, H.; Grochowska, J.K.; Łopata, M.; Augustyniak-Tunowska, R.; Tandyrak, R. A Unique Application Methodology for the Use of Phosphorus Inactivation Agents and Its Effect on Phosphorus Speciation in Lakes with Contrasting Mixing Regimes. *Water* **2022**, *15*, 67. [CrossRef]
81. Agstam-Norlin, O.; Lannergård, E.E.; Futter, M.N.; Huser, B.J. Optimization of aluminum treatment efficiency to control internal phosphorus loading in eutrophic lakes. *Water Res.* **2020**, *185*, 116150. [CrossRef] [PubMed]

82. Augustyniak, R.; Tandyrak, R.; Łopata, M.; Grochowska, J. Long Term Sediment Modification Effects after Applications of P Inactivation Method in Meromictic Lake (Starodworskie Lake, Olsztyn Lakeland, Poland). *Land* **2021**, *10*, 411. [CrossRef]
83. Huser, B.J.; Egemose, S.; Harper, H.; Hupfer, M.; Jensen, H.; Pilgrim, K.M.; Reitzel, K.; Rydin, E.; Futter, M. Longevity and effectiveness of aluminum addition to reduce sediment phosphorus release and restore lake water quality. *Water Res.* **2016**, *97*, 122–132. [CrossRef]
84. Jensen, H.S.; Reitzel, K.; Egemose, S. Evaluation of aluminum treatment efficiency on water quality and internal phosphorus cycling in six Danish lakes. *Hydrobiologia* **2015**, *751*, 189–199. [CrossRef]
85. Gantzer, P.A.; Bryant, L.D.; Little, J.C. Effect of hypolimnetic oxygenation on oxygen depletion rates in two water-supply reservoirs. *Water Res.* **2009**, *43*, 1700–1710. [CrossRef]
86. Austin, D.; Scharf, R.; Chen, C.F.; Bode, J. Hypolimnetic oxygenation and aeration in two Midwestern USA reservoirs. *Lake Reserv. Manag.* **2019**, *35*, 266–276. [CrossRef]
87. Toffolon, M.; Ragazzi, M.; Righetti, M.; Teodoru, C.R.; Tubino, M.; Defrancesco, C.; Pozzi, S. Effects of artificial hypolimnetic oxygenation in a shallow lake. Part 1: Phenomenological description and management. *J. Environ. Manag.* **2013**, *114*, 520–529. [CrossRef]
88. Lan, C.; Ji, Y.; Wang, J.; Yang, H. Water Quality Restoration of a Drinking Water Outlet Area in a Eutrophic Reservoir Using Hypolimnetic Oxygenation in Southwest China. *Pol. J. Environ. Stud.* **2021**, *30*, 1237–1246. [CrossRef] [PubMed]
89. Mobley, M.; Gantzer, P.; Benskin, P.; Hannoun, I.; McMahon, S.; Austin, D.; Scharf, R. Hypolimnetic oxygenation of water supply reservoirs using bubble plume diffusers. *Lake Reserv. Manag.* **2019**, *35*, 247–265. [CrossRef]
90. Cooke, G.D.; Welch, E.B.; Peterson, S.; Nichols, S.A. *Restoration and Management of Lakes and Reservoirs*; CRC Press: Boca Raton, FL, USA, 2016.
91. Ban, S.; Toda, T.; Koyama, M.; Ishikawa, K.; Kohzu, A.; Imai, A. Modern lake ecosystem management by sustainable harvesting and effective utilization of aquatic macrophytes. *Limnology* **2019**, *20*, 93–100. [CrossRef]
92. Zhang, Y.; Liu, H.; Yan, S.; Wen, X.; Qin, H.; Wang, Z.; Zhang, Z. Phosphorus removal from the hyper-eutrophic Lake Caohai (China) with large-scale water hyacinth cultivation. *Environ. Sci. Pollut. Res.* **2019**, *26*, 12975–12984. [CrossRef]
93. Bai, G.; Zhang, Y.; Yan, P.; Yan, W.; Kong, L.; Wang, L.; Wang, C.; Liu, Z.; Liu, B.; Ma, J.; et al. Spatial and seasonal variation of water parameters, sediment properties, and submerged macrophytes after ecological restoration in a long-term (6 years) study in Hangzhou west lake in China: Submerged macrophyte distribution influenced by environmental variables. *Water Res.* **2020**, *186*, 116379. [CrossRef]
94. Chen, Z.; Zhao, D.; Li, M.; Tu, W.; Liu, X. A field study on the effects of combined biomanipulation on the water quality of a eutrophic lake. *Environ. Pollut.* **2020**, *265*, 115091. [CrossRef]
95. Beklioglu, M.; Ince, O.; Tuzun, I. Restoration of the eutrophic Lake Eymir, Turkey, by biomanipulation after a major external nutrient control I. *Hydrobiologia* **2003**, *490*, 93–105. [CrossRef]
96. Yu, J.; Liu, Z.; Li, K.; Chen, F.; Guan, B.; Hu, Y.; Zhong, P.; Tang, Y.; Zhao, X.; He, H.; et al. Restoration of shallow lakes in subtropical and tropical China: Response of nutrients and water clarity to biomanipulation by fish removal and submerged plant transplantation. *Water* **2016**, *8*, 438. [CrossRef]
97. Liu, Z.; Hu, J.; Zhong, P.; Zhang, X.; Ning, J.; Larsen, S.E.; Chen, D.; Gao, Y.; He, H.; Jeppesen, E. Successful restoration of a tropical shallow eutrophic lake: Strong bottom-up but weak top-down effects recorded. *Water Res.* **2018**, *146*, 88–97. [CrossRef]
98. Chandler, K.L. *Feasibility Report for Water Quality Improvements in Twin Lake CIP Project TW-2*; Barr Engineering Company: Minneapolis, MN, USA, 2013.
99. Waajen, G.; van Oosterhout, F.; Douglas, G.; Lürling, M. Management of eutrophication in Lake De Kuil (The Netherlands) using combined flocculant–Lanthanum modified bentonite treatment. *Water Res.* **2016**, *97*, 83–95. [CrossRef]
100. Kozak, A.; Gołdyn, R.; Dondajewska, R.; Kowalczewska-Madura, K.; Holona, T. Changes in phytoplankton and water quality during sustainable restoration of an urban lake used for recreation and water supply. *Water* **2017**, *9*, 713. [CrossRef]
101. Kowalczewska-Madura, K.; Rosińska, J.; Dondajewska-Pielka, R.; Gołdyn, R.; Kaczmarek, L. The effects of limiting restoration treatments in a shallow urban lake. *Water* **2020**, *12*, 1383. [CrossRef]
102. Waajen, G.; Lürling, M.; van de Sande, R. The unfulfilled promise of urban Lake Kleine Melanen (The Netherlands): Diagnostics, experiment on reduction of sediment P-release and in-lake restoration. *Lake Reserv. Manag.* **2019**, *35*, 8–24. [CrossRef]
103. van Oosterhout, F.; Waajen, G.; Yasseri, S.; Marinho, M.M.; Noyma, N.P.; Mucci, M.; Douglas, G.; Lürling, M. Lanthanum in Water, Sediment, Macrophytes and chironomid larvae following application of Lanthanum modified bentonite to lake Rauwbraken (The Netherlands). *Sci. Total Environ.* **2020**, *706*, 135188. [CrossRef]
104. Dittrich, M.; Gabriel, O.; Rutzen, C.; Koschel, R. Lake restoration by hypolimnetic $Ca(OH)_2$ treatment: Impact on phosphorus sedimentation and release from sediment. *Sci. Total Environ.* **2011**, *409*, 1504–1515. [CrossRef]
105. van Oosterhout, F.; Yasseri, S.; Noyma, N.; Huszar, V.; Manzi Marinho, M.; Mucci, M.; Waajen, G.; Lürling, M. Assessing the long-term efficacy of internal loading management to control eutrophication in Lake Rauwbraken. *Inland Waters* **2021**, *12*, 61–77. [CrossRef]
106. Inoue, T.; Fukue, M.; Mulligan, C.N.; Uehara, K. In situ removal of contaminated suspended solids from a pond by filtration. *Ecol. Eng.* **2009**, *35*, 1249–1254. [CrossRef]

107. Veetil, D.P.; Arriagada, E.C.; Mulligan, C.N.; Bhat, S. Filtration for improving surface water quality of a eutrophic lake. *J. Environ. Manag.* **2021**, *279*, 111766. [CrossRef]
108. Pereira, A.C.; Mulligan, C.N.; Veetil, D.P.; Bhat, S. An In-Situ Geotextile Filtration Method for Suspended Solids Attenuation and Algae Suppression in a Canadian Eutrophic Lake. *Water* **2023**, *15*, 441. [CrossRef]

Disclaimer/Publisher's Note: The statements, opinions and data contained in all publications are solely those of the individual author(s) and contributor(s) and not of MDPI and/or the editor(s). MDPI and/or the editor(s) disclaim responsibility for any injury to people or property resulting from any ideas, methods, instructions or products referred to in the content.

environments

Article

Assessment of the Impact of a New Industrial Discharge on an Urban Wastewater Treatment Plant: Proposal for an Experimental Protocol

Maria Cristina Collivignarelli [1,2], Francesca Maria Caccamo [1,*], Stefano Bellazzi [1], Alessandro Abbà [3] and Giorgio Bertanza [3]

[1] Department of Civil Engineering and Architecture, University of Pavia, Via Ferrata 3, 27100 Pavia, Italy; mcristina.collivignarelli@unipv.it (M.C.C.); stefano.bellazzi01@universitadipavia.it (S.B.)
[2] Interdepartmental Centre for Water Research, University of Pavia, Via Ferrata 3, 27100 Pavia, Italy
[3] Department of Civil, Environmental, Architectural Engineering and Mathematics, University of Brescia, Via Branze 43, 25123 Brescia, Italy; alessandro.abba@unibs.it (A.A.); giorgio.bertanza@unibs.it (G.B.)
* Correspondence: francescamaria.caccamo01@universitadipavia.it

Abstract: Assessing the compatibility of industrial discharges with the biological process of a municipal wastewater treatment plant (WWTP) may represent a critical task. Indeed, either focusing only on chemical characterization or ecotoxicity tests designed to assess the impact on surface waters may lead to questionable or misleading conclusions. The feasibility of an industrial connection to the sewer should better take into account the features of the downstream WWTP, in particular by studying the potential effects on the biomass of that specific plant. With this aim, a multi-step experimental protocol applicable by water utilities has been proposed: (step 1) calculation of the flow rate/load ratio between industrial discharge (ID) and urban wastewater (WW); (step 2) analysis of the modified operating conditions of the biological stage; (step 3) experimental assessment of the impact of the ID on the WWTP biomass by means of respirometric tests. An application of this protocol is presented in this work as a case study, namely a new ID (average flowrate 200 m^3 d^{-1}) coming from an aqueous waste treatment plant (AWTP) to be connected to the public sewer. The integrated evaluation of results showed that no negative impacts could be expected on the downstream urban activated sludge WWTP (treating a flow rate of around 45,000 m^3 d^{-1}).

Keywords: aqueous waste; public sewer; respirometry; respirogram; multi-OUR

Citation: Collivignarelli, M.C.; Caccamo, F.M.; Bellazzi, S.; Abbà, A.; Bertanza, G. Assessment of the Impact of a New Industrial Discharge on an Urban Wastewater Treatment Plant: Proposal for an Experimental Protocol. *Environments* **2023**, *10*, 108. https://doi.org/10.3390/environments10070108

Academic Editors: Dibyendu Sarkar, Rupali Datta, Prafulla Kumar Sahoo and Mohammad Mahmudur Rahman

Received: 25 May 2023
Revised: 16 June 2023
Accepted: 20 June 2023
Published: 22 June 2023

Copyright: © 2023 by the authors. Licensee MDPI, Basel, Switzerland. This article is an open access article distributed under the terms and conditions of the Creative Commons Attribution (CC BY) license (https://creativecommons.org/licenses/by/4.0/).

1. Introduction

Both domestic wastewater (WW) from residential settlements and services, and industrial WW, deriving mainly from commercial activities and generated by production processes, are discharged into the public sewers to be treated by a wastewater treatment plant (WWTP) [1–3]. National regulations have imposed emission limits for WW discharge into sewers, as in Italy with the Legislative Decree No. 152 of 2006 (Third part, Annex 5, Ref. [4]). Considering the industrial WW, attention is therefore placed on the quantitative and qualitative characteristics of the industrial discharge (ID) which mixes with the other WW conveyed by the sewer. For example, according to the Italian legislation, the emission limits in sewer per product unit referred to specific production cycles are reported (Third part, Annex 5, Ref. [4]).

In addition to necessitating various limits to be respected by several parameters, the Italian law requires the same toxicity test to be applied for discharges both into surface water and into the sewer. The acute toxicity test is mandatory and must be performed on *Daphnia magna*, and, in addition, on *Ceriodaphnia dubia*, *Selenastrum capricornutum*, bioluminescent bacteria, or organisms such as *Artemia salina*, for saltwater discharges, or other organisms. For discharges into sewer, the sample is considered toxic when, after 24 h, the number of

immobile organisms is equal to or greater than 80% of the total. If more than one toxicity test is performed, the worst result should be considered (Third part, Annex 5, Ref. [4]).

The toxicity tests thus imposed appear appropriate for assessing the suitability of a final discharge into a surface water body. Conversely, for a more suitable and reliable evaluation of the compatibility of a discharge into the sewer, the experimental assessment using the biomass present in the downstream WWTP (such as respirometry tests) could be suggested. Furthermore, a non-negligible operational aspect is that the respirometric does not require complex and expensive equipment [5]. In this way, attention is paid to the urban WWTP and the biological treatment that must purify the WW that is discharged into the sewer.

The scientific literature reports that respirometry could be effectively applied, in biological treatments of real WWTP, for (i) daily management and/or operational control to evaluate a possible plant upgrade [6–8], (ii) performance diagnosis [2,9], (iii) detection of toxicity caused by influent WW [1,10–12] and (iv) WW characterisation/COD fractionation [2,3,13]. Arias-Navarro et al. [9] applied respirometric tests to a real WWTP serving an equivalent population of 730,000 and the results revealed that the WWTP was operated at low efficiency and under overload. With a similar aim, in the work of Vitanza et al. [14], an activated sludge model was calibrated using respirometric results obtained from three WWTPs. After the calibration, the simulation of the operation of one of the plants was performed and the goodness of the simulation demonstrated that the model was able to predict WWTP performance. Respirometry techniques were used by Aguilar et al. [12] to evaluate the toxic and inhibitory effect of several heavy metals on the activated sludge collected from a WWTP which also treated industrial WW. The results showed that toxicity caused by heavy metals studied follows the order: Hg $\gg$ Zn > Cr > Pb > Ni [12].

This work proposes an experimental protocol to be used to assess the compatibility of a new ID to be discharged in a sewer system served by an activated sludge WWTP. The study of the quantitative and qualitative characteristics of ID is proposed to examine and predict any possible impact on the WWTP. The focus is placed on the biological sector, through the control of compliance with the operating conditions and the measurement, through respirometry, of the influent WW biodegradability/toxicity towards autotrophic and heterotrophic biomass.

This study is aimed at responding to some needs of the WW treatment world, such as those expressed by Mainardis et al. [15]:

(i) the proposal and development of a technical-scientific experimental methodology, shared and universally applicable by all water utilities, also to guarantee homogeneous and unambiguous comparisons between different realities;
(ii) the promotion of greater integration and application of respirometry into WWTP management as a diagnostic tool, in particular for ecotoxicity assessments of new industrial sewerage connections.

As a case study, in this work, the application of the proposed procedure is presented for the assessment of the ID of an aqueous waste treatment plant (AWTP) to be discharged into a public sewer served by an activated sludge WWTP.

2. Materials and Methods

2.1. Case Study and ID Characteristics

The studied ID was produced in a new AWTP which encompassed both chemical-physical and thermophilic biological treatments. The aqueous waste treated came mainly from pharmaceutical and galvanic processes. The new ID of the AWTP had to be discharged, with an average flowrate of 200 $m^3\ d^{-1}$, through an authorized pipeline, into the public sewer. In Table 1, the main characteristics of ID are reported. According to the permission, the ID had to be stopped (i) in case of rain, with the aim to not overload the sewage system, (ii) in the case of maintenance to sewage sections of interest and (iii) under specific circumstances upon request by the urban WWTP manager.

Table 1. Qualitative characteristics of AWTP industrial effluent. n: number of data.

	Mean Value	Confidence Interval
pH (-)	10.1 [n: 12]	±0.24
COD (mg L^{-1})	2143 [n: 12]	±85
BOD_5 (mg L^{-1})	317 [n: 12]	±77
TN (mg L^{-1})	154 [n: 5]	±50
N-NO_3^- (mg L^{-1})	15.5 [n: 12]	±3.5
N-NH_4^+ (mg L^{-1})	15.4 [n: 12]	±3.5

The monitoring data of AWTP refer to the year 2019.

The public sewer, as usual, reached the urban WWTP, located downstream of the AWTP, as shown in Figure 1a. The urban WWTP treated an average WW flow rate of about 45,000 m^3 d^{-1} in a water-line typical of a conventional activated sludge (CAS) plant, consisting of primary sedimentation, pre-denitrification, oxidation and nitrification in a single compartment, and finally secondary sedimentation.

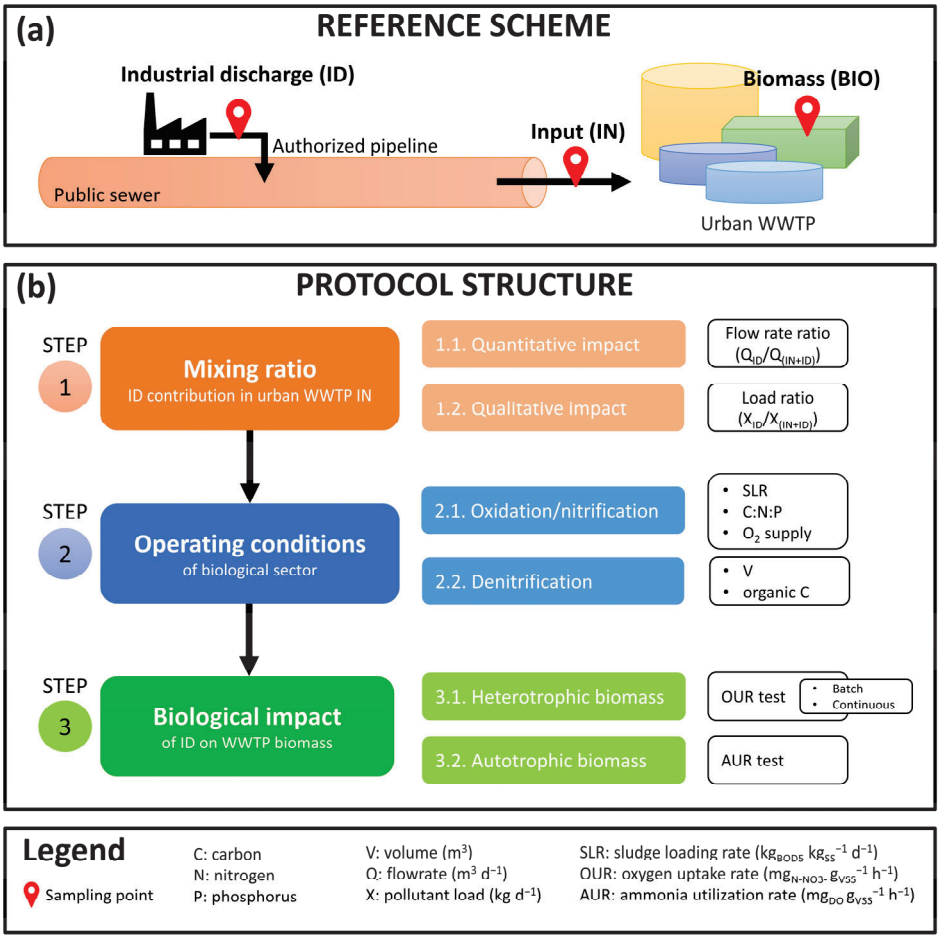


Figure 1. (**a**) Reference scheme of the case study and (**b**) structure of the experimental protocol. ID: industrial discharge; IN: WW entering the urban WWTP; BIO: autotrophic and heterotrophic biomass sampled in WWTP; WWTP: wastewater treatment plant.

2.2. Experimental Protocol Structure

The purpose of the experimental protocol is to evaluate the quantitative and qualitative impact of a new ID on a CAS WWTP. First, the sampling points must be carefully identified:

(i) ID: industrial water which must be discharged into the public sewer.
(ii) IN: WW entering the WWTP (without ID).
(iii) BIO: biomass in the oxidation-nitrification tank.

In the case of a WWTP equipped with primary sedimentation, the IN sample should coincide with the entrance to the biological compartment (primary sedimentation exit), for greater precision in the evaluation of the polluting loads (BOD_5, COD, etc.) that really impact on the biological activity. In this study, the IN sample was taken upstream of the primary sedimentation, considering slightly higher pollutant loads in favour of safety. The purification efficiency of primary sedimentation has therefore been neglected.

If the WWTP had separate oxidation and nitrification compartments, with dedicated biomass separation units, two biomass samples from both reactors would have been required. In this WWTP, a single biomass sample was taken due to the configuration of the process in a single tank.

A further possibility, without considering the sampling point ID, could be to study only the sampling point IN during two different conditions: (i) in the presence of ID and (ii) in the absence of ID. To make the first condition possible, it was necessary (i) to interface with the AWTP staff for the request to the competent authority for a temporary ID permit, (ii) to wait sufficient time to find the ID at the sampling point IN. The minimum time interval needed was calculated starting from the length of the sewer section between the ID and the WWTP.

Figure 1b shows the structure of the experimental protocol.

- Step 1 concerns the estimation of the weight of the ID on the WW to be treated in the WWTP. We assessed (i) the quantitative impact of the ID on the WWTP through the ratio between the ID flowrate Q_{ID} and the mixed WW flowrate $Q_{(IN+ID)}$ (or Q_{INNEW}), and (ii) the qualitative impact of the ID on the WWTP through the ratio between the mass load of selected pollutants in the ID (X_{ID}) and the mixed WW ($X_{(IN+ID)}$ or X_{INNEW}). The pollutants of concern should be identified as the most significant and critical for the WWTP.
- Step 2 includes a check of the operating conditions in which the oxidation/nitrification and denitrification reactors should work with the addition of the new ID into the sewer. First, it is necessary to check the volumes available, in order to verify any possible under-sizing caused by the ID. Subsequently, for the oxidation/nitrification stage, the following checks should be carried out: (i) the new sludge loading rate (SLR) has to guarantee the correct performance of the nitrification process; (ii) the new BOD:N:P ratio should not deviate too much from the optimal one for aerobic systems equal to 100:5:1 (BOD/N = 20, BOD/P = 100) [16–19]; (iii) the capacity of the present air supply system has to cover the increase in the oxygen demand for the oxidation processes. For denitrification, the availability of organic carbon with respect to the new load of $N\text{-}NO_3^-$ must be envisaged.
- Step 3 involves the study of the ID biological impact on the biomass grown in the urban WWTP and represents a crucial assessment. For a CAS system, the biological activities of heterotrophic and autotrophic biomass can be evaluated through oxygen uptake rate (OUR) and ammonia utilization rate (AUR) tests, respectively. In case potential criticalities arose from Step 1 and Step 2, a more in-depth analysis through the application of continuous respirometry is strictly recommended. In effect, thanks mainly to the longer duration of the test, it is possible to obtain more detailed information on the biological activity, compared to the more immediate and easier to apply batch OUR tests (described below in Section 2.5.2). Indeed, the authors advise to include continuous OUR tests, regardless of the result of point 1.

The step-by-step application of the assessment protocol to the case study is described in the following paragraphs.

2.3. Mixing Ratio Estimate (Step 1)

For the estimation of the future ID contribution on the WW entering the urban WWTP, (i) WWTP monitoring data of the year 2021 and (ii) an estimate of the ID flow rate provided by the AWTP company were considered. The ID quantitative contribution was calculated as follow:

$$\text{ID quantitative impact } (\%) = \frac{Q_{ID}\left(m^3 d^{-1}\right)}{Q_{(IN+ID)}\left(m^3 d^{-1}\right)} \quad (1)$$

where:

- Q_{ID} (m^3 d^{-1}): estimated ID flow rate.
- $Q_{(ID+IN)}$ (or Q_{INNEW}) (m^3 d^{-1}): sum of IN point flow rate, from WWTP monitoring data, and estimated ID flow rate. This represents the overall WW arriving from the sewer and treated by WWTP, if ID is authorised.

As regards the IN-flow rates, the monthly average values were considered.

To study the ID qualitative impact on the urban WWTP, the loads of the most critical polluting parameters for this case study were calculated, namely: chemical oxygen demand (COD), total nitrogen (TN), nitric nitrogen (N-NO_3^-) and ammoniacal nitrogen (N-NH_4^+). The authors recommend evaluating the polluting parameters to be taken into consideration on a case-by-case basis, including 5-day biological oxygen demand (BOD_5), total suspended solids, total phosphorus, and other specific pollutants of concern such as heavy metals, surfactants, persistent organic pollutants, etc. The loads were calculated starting from daily concentrations of COD, TN, N-NO_3^-, N-NH_4^+ (measured on 24-h composite samples), multiplied by the flow rates. The data of the flow rates and concentrations of the chemical parameters were provided by the management staff of the AWTP and the WWTP. For WWTP data, a public online database is also available from which to download the necessary information. The qualitative contribution of ID was defined by the following equation:

$$\text{ID qualitative impact } (\%) = \frac{X_{ID}\left(\text{kg } d^{-1}\right)}{X_{(IN+ID)}\left(\text{kg } d^{-1}\right)} \quad (2)$$

where:

- X_{ID} (kg d^{-1}): load of generic ID polluting parameter.
- $X_{(ID+IN)}$ (or X_{INNEW}) (kg d^{-1}): sum of IN pollutant load, from WWTP monitoring data, and ID pollutant load for the generic parameter. This represents the overall load of WW arriving from the sewer and treated by the WWTP, if ID is authorised.

2.4. Operating Conditions (Step 2)

For the oxidation/nitrification compartment, the following parameters, both for IN and IN_{NEW} (IN + ID) condition, were calculated:

$$\text{1. Sludge loading rate (SLR) } \left(kg_{BOD_5} kg_{SS}^{-1} d^{-1}\right) = \frac{X_{BOD_5,IN\ BIO}}{SS * V_{ox}} \quad (3)$$

where:

- $X_{BOD5,IN\ BIO}$ (kg d^{-1}): BOD_5 daily load entering the biological oxidation/nitrification compartment.
- SS (kg m^{-3}): total suspended solids concentration in the oxidation/nitrification tank (hp: equal in both IN and IN_{NEW} phases).
- V_{ox} (m^3): volume of the existing oxidation/nitrification tank.

$$\text{2. Oxygen supply } \left(kg_{02} d^{-1}\right) = k * \alpha * X_{BOD_5,IN\ BIO} + \beta * V_{ox} * SS + k * \gamma * X_{nit} \quad (4)$$

where:

- k (-): safety factor to consider for the oscillations of the influent load to the WWTP, assumed equal to 1.5.
- α (kg_{O2} $kg_{BOD5removed}$): amount of oxygen required to oxidize 1 kg of organic substance (BOD_5) in the oxidation tank, assumed equal to 0.5 [20].
- $X_{BOD5,IN\ BIO}$ (kg d^{-1}): BOD_5 average daily load entering the biological oxidation/nitrification compartment;
- β (kg_{O2} kg_{SS}^{-1} d^{-1}): amount of oxygen consumed in 1 day by 1 kg of biomass, assumed equal to 0.1 [20].
- V_{ox} (m^3): volume of the existing oxidation/nitrification tank.
- SS (kg m^{-3}): total suspended solids concentration in oxidation/nitrification tank (hp: equal in both IN and IN_{NEW} phases).
- γ (kg_{O2} kg_N): amount of oxygen required to nitrify 1 kg of ammonia nitrogen, assumed equal to 4.57 [20].
- X_{nit} (kg d^{-1}): nitrogen daily load which must be nitrified, determined by a balance on total Kjeldahl nitrogen (TKN) (Equation (5)):

$$X_{nit} = TKN_{IN} - TKN_{ass} - TKN_{out} \quad (5)$$

where:

- TKN_{IN} (kg d^{-1}): TKN of WW entering the WWTP (if possible, better entering the biological reactor).
- TKN_{ass} (kg d^{-1}): TKN assimilated by the biomass for vital functions, calculated as 5% of BOD_5 removed [21].
- TKN_{out} (kg d^{-1}): TKN limit load in the WWTP effluent and calculated from a concentration limit equal to 2 mg L^{-1}, assumed based on the emission limits of the Italian regulation (Table 2, Annex 5, Part III, Legislative Decree n° 152 of 2006 [4]).

For the pre-denitrification tank the following parameters were determined:

$$1.\ \text{Required denitrification tank volume } (V_{DEN})(m^3) = \frac{X_{den}}{v_{den,s} * VSS} \quad (6)$$

where:

- X_{den} (kg d^{-1}): nitrogen daily load which must be denitrified, determined by a balance on TN (Equation (7)):

$$X_{den} = TN_{IN} - TN_{ass} - TN_{out} \quad (7)$$

where:

- TN_{IN} (kg d^{-1}): TN of WW entering the WWTP.
- TN_{ass} (kg d^{-1}): TN assimilated by biomass for vital functions, calculated as 5% of BOD_5 removed in the oxidation tank [19].
- TN_{out} (kg d^{-1}): TN limit load in the WWTP effluent and calculated from a concentration limit equal to 8 mg L^{-1}, assumed based on the emission limits of the Italian regulation (Annex 5, Part III, Legislative Decree n° 152 of 2006 [4]).
- $v_{den,s}$ ($kg_{N\text{-}NO3^-}$ kg_{VSS}-1 d^{-1}): denitrification specific rate, determined with the following equation [22,23]:

$$v_{den,s}\left(\frac{kg_{N\text{-}NO_3^-}}{kg_{VSS}\ d}\right) = v_{den,s\ [20\ °C]} * \theta^{(T-20)} \quad (8)$$

where:

- T (°C): temperature of water in denitrification tank.

- $v_{den,s\ [20\ °C]}$ ($kg_{N\text{-}NO3}{}^{-}\ kg_{VSS}{}^{-1}\ d^{-1}$): denitrification rate at 20 °C (standard values: 2.9–3.0 $g_{N\text{-}NO3}{}^{-}\ kg_{VSS}{}^{-1}\ h^{-1}$ [24]), assumed equal to 0.07 $kg_{N\text{-}NO3}{}^{-}\ kg_{VSS}{}^{-1}\ d^{-1}$.
- θ (-): van't Hoff-Arrhenius coefficient, assumed equal to 1.10 [20].

- VSS (kg m^{-3}): volatile suspended solids concentration in denitrification tank (hp: equal in both IN and IN_{NEW} phases).

$$\text{2. Required organic carbon } (OC)\left(\text{kg d}^{-1}\right) = \frac{BOD_5}{N\text{-}NO_3^-}\ \text{ratio} * X_{DEN} \quad (9)$$

where:

- $BOD_5/N\text{-}NO_3{}^{-}$ ratio (-) necessary to ensure efficient denitrification, assumed equal to 5 [20].
- X_{den} (kg d^{-1}): nitrogen daily load which must be denitrified, determined with Equation (7).

2.5. OUR and AUR Tests (Step 3)

OUR and AUR tests, whose important applicability has been demonstrated in many previous studies [2,25–29], were inevitably included in the protocol structure to study the impact of different substrates on the autotrophic and heterotrophic mesophilic biomass of the urban WWTP. In particular, the aim was to evaluate the effect of the ID on the biological activity of the CAS system.

For all tests, the heterotrophic/autotrophic biomass was sampled directly from the urban WWTP (BIO-sampling point, Figure 1a) and was used shortly after sampling, and after 1 h of re-aeration. The substrates used were sampled only at the IN-sampling point (24-h composite samples), at the urban WWTP, but at two different times: (i) with the presence of ID in WW from the sewer (IN_{NEW}), and (ii) without ID into WW arriving from the sewage system (IN). This approach was possible thanks to collaboration agreements between the AWTP company and the personnel of the WWTP. If this approach was not possible, the authors would have maintained two sampling points IN and ID (as explained in Section 2.2) and recreated the IN_{NEW} substrate in the chemical laboratory by mixing IN and ID. The mixing ratio (quantitative contribution of ID) had been estimated in step 1 of the proposed protocol (Section 3.1). All tests were conducted at room temperature, maintaining continuous stirring of the mixture at about 300–400 rpm, with a magnetic stirrer.

2.5.1. Analytical Methods

COD was measured according to ISPRA 5135 method [30]. For ammoniacal nitrogen ($N\text{-}NH_4{}^{+}$) and TKN, the methods of APAT IRSA-CNR 4030 [31] and APAT IRSA-CNR 5030 [32] were used, respectively. $N\text{-}NO_3{}^{-}$ concentrations were studied according to UNI EN ISO 10304-1:2009 [33]. UNI 11658:2016 [34] was applied for TN. Volatile suspended solids (VSS) were determined following the APAT-IRSA-CNR 2090 method [35]. pH was measured using the probe WTW-IDS, Model SenTix® 940 (Xylem Analytics Germany Sales GmbH & Co, Mainz, Germany). Dissolved oxygen (DO) concentration was measured by WTW Multi-parameter portable meter MultiLine® Multi 3510 IDS thanks to WTW Optical IDS dissolved oxygen sensors FDO® 925 (Xylem Analytics Germany Sales GmbH & Co, Mainz, Germany) (called DO probe in the next sections). The measured DO concentration was transferred to a portable PC via USB connection and the MultiLab® Importer for data acquisition via Excel® software was used.

2.5.2. OUR Test

Respirometry deals with the measurement and interpretation of dissolved oxygen consumption by a biological system to degrade a substrate [36]. The application of respirometry to WWTP can provide information on the characterization of the influential WW biodegradability, therefore, on any inhibitory effect of WW on the WWTP biomass. Both endogenous and exogenous OUR were evaluated in this study. The endogenous OUR represents the oxygen consumed only for biomass respiration, while the exogenous OUR consists in the consumption of oxygen necessary for (i) the oxidation of the organic substance or

of the nitrogenous compounds present in the WW and (ii) the cellular respiration of the biomass [15,37].

Batch Test

The great advantage of OUR tests in batch mode is the immediate performance both for the modest instrumentation required (Figure 2) and for the immediacy of execution [2,38]. The experimental set-up was similar to that employed by Borzooei et al. [13] and Capodici et al. [39].

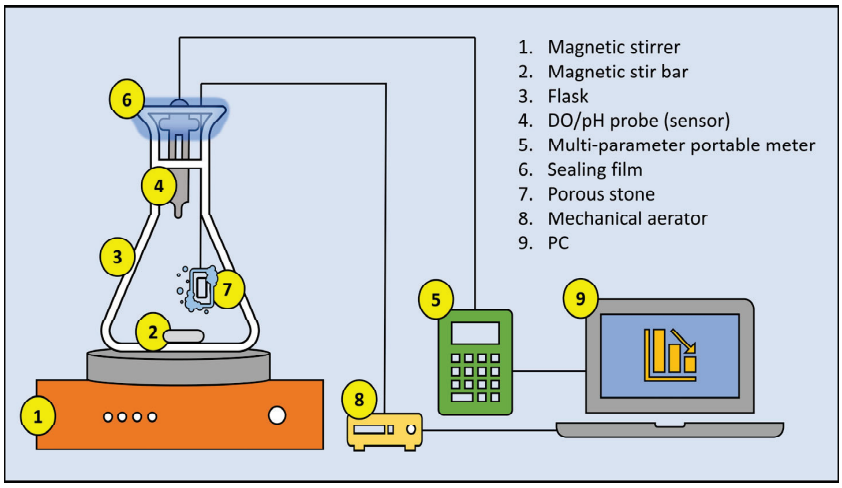


Figure 2. Laboratory respirometric apparatus.

Endogenous OUR tests were first conducted with 500 mL of heterotrophic biomass to study endogenous respiration alone. In exogenous OUR tests, 500 mL of oxidizing biomass was aerated up to a DO concentration of 7.5–8.0 mg L^{-1}, and then mixed with 500 mL of substrate. At this point the aeration was stopped and the laboratory scale batch reactor with a 1 L mixture was hermetically isolated to avoid oxygen exchange with the external environment. During the test, the DO concentration (mg L^{-1}) was measured every 5 s. Each batch OUR test, stopped when the dissolved oxidation concentration was below 2 mg L^{-1}, lasted approximately 10–20 min. Due to the limited duration, the batch OUR was allowed to evaluate "only" (i) the rapidly biodegradable fraction of organic substance and (ii) any acute, therefore immediate, toxic-inhibiting effect of the WW against the biomass.

At the end of the test, the OUR value ($mg_{DO}\ g_{VSS}{}^{-1}\ h^{-1}$) was calculated according to the following equation:

$$\text{OUR}\ (mg_{DO}\ g_{VSS}{}^{-1}h^{-1}) = \frac{\text{Slope of the DO utilization curve}\ (mg_{DO}\ L^{-1}h^{-1})}{\text{VSS concentration in batch reactor}\ (g_{VSS}L^{-1})} \quad (10)$$

Continuous Test

Continuous OUR tests were carried out with a laboratory scale reactor (2 L), containing 1 L of heterotrophic biomass and 200 mL of substrate. This option was set to maintain a low S/X ratio (biomass/substrate) in the range 0.01–0.2 $g_{COD}\ g_{VSS}{}^{-1}$, thus considering (i) biomass growth negligible and (ii) endogenous respiration remained approximately constant [40]. Similarly, Mainardis et al. [15] recommended a narrower range equal to 0.01–0.05 $g_{COD}\ g_{VSS}{}^{-1}$.

The reactor was isolated to avoid oxygen exchanges with the surrounding atmosphere and loss of volume by evaporation (Figure 2). The aeration was always kept in the 2–5 mg L^{-1} range thanks to the connection of the aeration system to an electric mechanism that guaranteed the connection-detachment of the aeration itself. The electrical mechanism was regulated by software installed on a PC and through the DO concentration measured by the DO probe. The latter was in turn connected to the laptop. Of extreme importance was the data acquisition system, which allowed the DO data, measured in the reactor, to be acquired on the PC. In some cases, these tests lasted up to 48 h.

At the end of the test, a succession of decreasing curves (DO consumption curves) was obtained, alternating phases of non-aeration and phases of aeration in the reactor. With the same process described for batch OUR, more final OUR values ($mg_{DO}\ g_{VSS}{}^{-1}\ h^{-1}$) were calculated. A curve, called respirogram, with the OUR trend over time was drawn [15].

Continuous tests can provide additional information compared to batch tests: (i) possible medium-long term toxic effects caused by the substrate towards the biomass, (ii) evaluation of the different fractions of COD present in the substrate (quickly and slowly biodegradable). Batch tests are quicker to perform, but continuous tests, lasting for several hours, have the great strength of monitoring toxicity over a period as long as the hydraulic retention time of the WWTP [38].

2.5.3. AUR Test

Thanks to the AUR test, it is possible to easily measure the activity of the nitrifying bacteria present in the biomass of CAS plants. The AUR test can be applied to: (i) measure the nitrification kinetics [41], and (ii) evaluate the degree of inhibition (via determination of any inhibitory effect on nitrifying bacteria by sewage containing potentially toxic substances) [42,43].

First, 500 mL of biomass, after aeration, was mixed with 500 mL of substrate to obtain a total volume of 1 L in a batch reactor (Figure 2). Continuous aeration up to DO saturation conditions were maintained in the mixture. The pH was maintained approximately equal to that (7.5–8.5) measured in the mesophilic biomass at the time of sampling in the oxidation tank. Tests were conducted for about 5–6 h and 25 mL of mixture was sampled every hour or half hour. The samples were filtered with 0.45-micron filter paper to separate the biomass. AUR value was determined considering the VSS concentration in the batch reactor and the positive slope of $N\text{-}NO_3{}^-$ production curve (negligible concentrations for $N\text{-}NO_2{}^-$) as reported in Equation (2):

$$\text{AUR}\left(mg_{N\text{-}NO_3^-}\ g_{VSS}{}^{-1}h^{-1}\right) = \frac{\text{Slope of } N\text{-}NO_3^-\text{ production curve}\left(mg_{N\text{-}NO_3^-}L^{-1}h^{-1}\right)}{\text{VSS concentration in batch reactor}\left(g_{VSS}L^{-1}\right)} \quad (11)$$

3. Results and Discussion

3.1. Step 1: Mixing Ratio

Table 2 shows flow rates and loads of polluting parameters in terms of (i) average annual values for WWTP input and (ii) available values (either assumed or measured) for ID. The quantitative contribution of ID was defined based on the flow rates. Assuming that the ID was authorized by the competent authority, ID represented 0.45% of all WW arriving at the WWTP ($Q_{INNEW} = Q_{IN} + Q_{ID}$), identifying a low mixing ratio of 1/250. At least from a quantitative point of view, it was possible to state that the ID considered did not represent a problem for the urban WWTP.

Table 2. Flow rates ($m^3\ d^{-1}$) and loads ($kg\ d^{-1}$) of the polluting parameters in ID, IN, IN_{NEW} and mixing ratio of ID in IN_{NEW}. n: number of data.

	ID	**IN**	**IN_{NEW} * (IN + ID)**	**Mixing Ratio (ID/IN_{NEW})**
Q ($m^3\ d^{-1}$)	200 ± 50 [set/estimated]	45.575 ± 2053 [n: 12]	45.775 [calculated]	0.45 ± 0.05% [n: 12]
COD ($kg\ d^{-1}$)	441 ± 43 [n: 12]	12.677 ± 2606 [n: 70]	13.118 [calculated]	3.7 ± 0.7% [n: 12]
TN ($kg\ d^{-1}$)	28.4 ± 9.3 [n: 5]	1044.6 ± 10 [n: 5]	1073 [calculated]	2.6 ± 0.9% [n: 5]
$N\text{-}NO_3{}^-$ ($kg\ d^{-1}$)	3.0 ± 0.8 [n: 12]	10.1 ± 3.4 [n: 70]	13 [calculated]	27.3 ± 8.5% [n: 12]
$N\text{-}NH_4{}^+$ ($kg\ d^{-1}$)	3.2 ± 0.9 [n: 12]	731.1 ± 94 [n: 70]	734 [calculated]	0.44 ± 0.12% [n: 12]

The monitoring data of AWTP and WWTP refer to the year 2019. * Calculated from the sum of IN and ID mean values.

The qualitative contribution was obtained from COD and different nitrogenous forms. ID had an almost negligible contribution in terms of TN, N-NH_4^+, and COD on the WW treated by WWTP, showing no critical issues. Instead, the load of nitrates brought by the industrial WW was significant, on average above 27%. An important load of N-NO_3^- could possibly represent a problem for the denitrification compartment, in terms of the insufficient volume available. The subsequent steps envisaged by the protocol had the aim, among others, of further investigating these aspects.

3.2. Step 2: Operating Conditions of the Biological Stage

Table 3 reports the comparison between geometric and process parameters during the two different conditions studied at the urban WWTP, first in the absence and then with the addition of the new ID in the incoming WW. For the oxidation/nitrification process, no significant changes were observed with the addition of the ID. The main operating conditions have remained unchanged; therefore, the nitrification process should not undergo critical issues, at least due to the aspects just investigated. Only the daily oxygen supply saw a slight increase of 0.8% compared to the starting situation without ID. This increase should not undermine the air supply systems in any way, nor create any problems to be addressed.

Table 3. Operating conditions at the urban WWTP, without ID (IN) and with ID (IN_{NEW}: IN + ID) into the WW to be treated. SLR: sludge loading rate, V_{OX}: oxidation/nitrification volume, V_{DEN}: denitrification volume, OC: organic carbon.

	IN	**IN_{NEW} (IN + ID)**
Oxidation/nitrification		
SLR (kg_{BOD5} kg_{SS}^{-1} d^{-1})	0.111	0.109
BOD:N:P	100:26:4	100:26:4
Oxygen supply (kg_{O2} d^{-1})	12′300	12′400
Denitrification		
V_{DEN} (m^3)	6700 (14 °C) 3785 (20 °C) (Real volume: 6000 m^3)	6990 (14 °C) 3950 (20 °C) (Real volume: 6000 m^3)
OC (kg d^{-1})	2500 ($BOD_{5,\ IN\ BIO}$: 4370 kg d^{-1})	2600 ($BOD_{5,\ IN\ BIO}$: 4440 kg d^{-1})

$BOD_{5,IN\ BIO}$ (kg d^{-1}): BOD_5 daily load entering the biological oxidation/nitrification compartment.

More marked variations resulted in denitrification, in particular in the tank volume. Even in the situation without ID, the denitrification volume was undersized for the autumn/winter water temperatures (<15 °C). This criticality has been expanded with the IN_{NEW} condition: at a water temperature of 14 °C, a volume deficit of about 1000 m^3 was estimated. Compared to the previous situation (IN), there was a need for an additional volume of 300 m^3. Despite the under-sizing of the denitrification tank, if the process did not previously present functioning issues, the authors excluded the occurrence of a denitrification crisis with the addition of ID.

As widely known, denitrification by heterotrophic bacteria requires organic carbon (OC) [44–46]. Demand for OC in the IN_{NEW} condition increased by about 4%. Despite this, the BOD_5 entering the biological compartment, therefore the pre-denitrification, has always been more than sufficient to guarantee complete denitrification.

3.3. Step 3: Biological Impact on Biomass

3.3.1. Heterotrophic Biomass

The effect of ID of AWTP on heterotrophic biomass of urban WWTP was first evaluated with respirometric tests. Figure 3 shows the results of batch OUR tests. First, to understand

the health status of biomass, endogenous OUR, before each exogenous test, was carried out. An average value of 3.8 mg_{DO} $g_{VSS}{}^{-1}$ h^{-1} showed a regular respiration of the WWTP mesophilic biomass, according to our previous research [47,48]. VSS in the BIO-sample (Figure 1) were about 1.8–2 g L^{-1}, as adopted in other experimental studies [40].

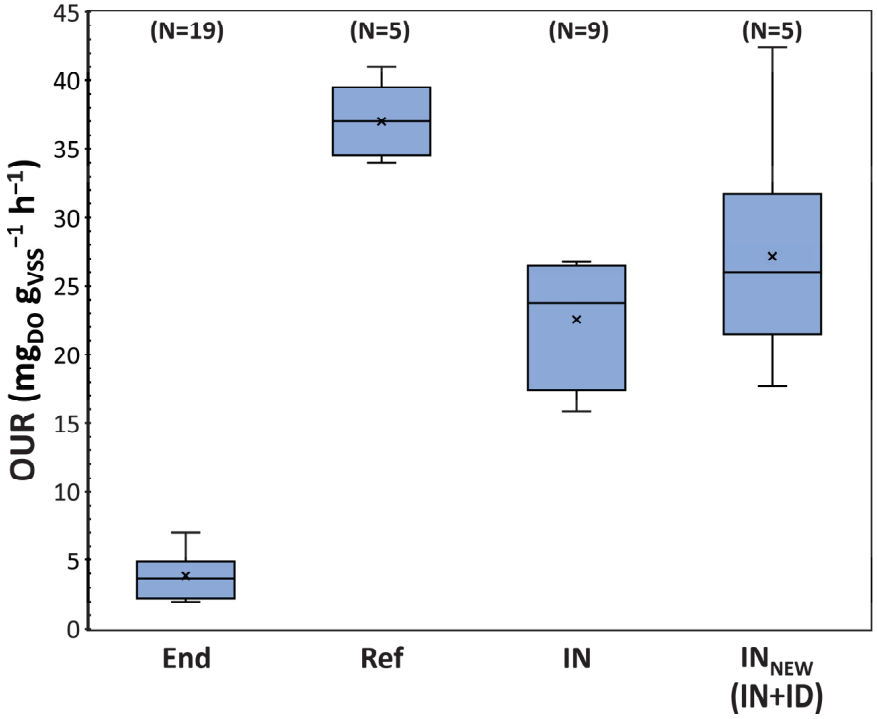


Figure 3. Results of the batch OUR tests carried out with the heterotrophic biomass sampled in the WWTP. End: Endogenous OUR. Ref: Reference value. Boxplots represent the distance between the first and third quartiles while whiskers are set as the most extreme (lower and upper) data point not exceeding 1.5 times the quartile range from the median. The cross represents the mean value. N: number of replicated tests.

A domestic WW without industrial aqueous waste was used as the reference substrate (COD: 300–400 mg L^{-1}, in line with domestic sewage COD reported in the literature [49]). The present WW, which includes different industrial discharges, showed lower biodegradability (23 mg_{DO} $g_{VSS}{}^{-1}$ h^{-1}) than domestic WW (37 mg_{DO} $g_{VSS}{}^{-1}$ h^{-1}), as expected. Contrarily, the studied ID improved the biodegradability of WW entering the urban WWTP (from 23 mg_{DO} $g_{VSS}{}^{-1}$ h^{-1} to 27 mg_{DO} $g_{VSS}{}^{-1}$ h^{-1}). In general, despite the reduction of OUR values, in respect to the reference, no acute inhibition effects were observed, especially from the ID under study. The reduction in biodegradability between the reference and the IN substrate was due to the integrated and synergistic effect of multiple industrial WWs discharged into the sewer. Nevertheless, in all cases, the mean OUR values were more than acceptable, above 20 mg_{DO} $g_{VSS}{}^{-1}$ h^{-1}.

Figure 4 reports the results of OUR tests, performed in parallel and continuous modes, with biomass sampled in the oxidation/nitrification tank of the WWTP (BIO-sampling point, Figure 1a). The addition of IN (Figure 4a) and IN_{NEW} (Figure 4b) substrate were tested under the same boundary experimental conditions. Respirograms in Figure 4 show, before the substrate dosage, the endogenous OUR (first point of the discretized respirogram). Time by time, the regular respiration of the biomass must be evaluated, otherwise the test should be invalidated. The values acquired around 2.5–3.5 mg_{DO} $g_{VSS}{}^{-1}$ h^{-1} (5–7 mg_{DO} L^{-1} h^{-1} with VSS in BIO-sample of about 1.8–2 g L^{-1}) indicated, as reported in other literature studies [50], a regular endogenous respiration for activated sludge in urban WWTP. After endogenous evaluation, the substrates (COD: 300–350 mg L^{-1}, low S/X ratio guaranteed: 0.03–0.04 g_{COD} $g_{VSS}{}^{-1}$) were dosed and their degradation over time was studied (exogenous

OUR—endogenous OUR). The peak values of exogenous OUR, reached after 0.35 h, were similar and equal to 27.2 and 27.0 $mg_{DO}\ g_{VSS}^{-1}\ h^{-1}$, respectively for IN and IN_{NEW}. These were comparable with the results of batch OUR and remained approximately constant from 0.35 h to 0.6–0.65 h for both IN and IN_{NEW}, indicating an immediate and continuous degradation of the easily biodegradable organic substance. After 0.6–0.65 h, exogenous OUR began to decrease, indicating a final phase of degradation of the residual and more slowly biodegradable organic matter. The experimental tests were considered completed once the exogenous OUR reached values close to the endogenous ones.

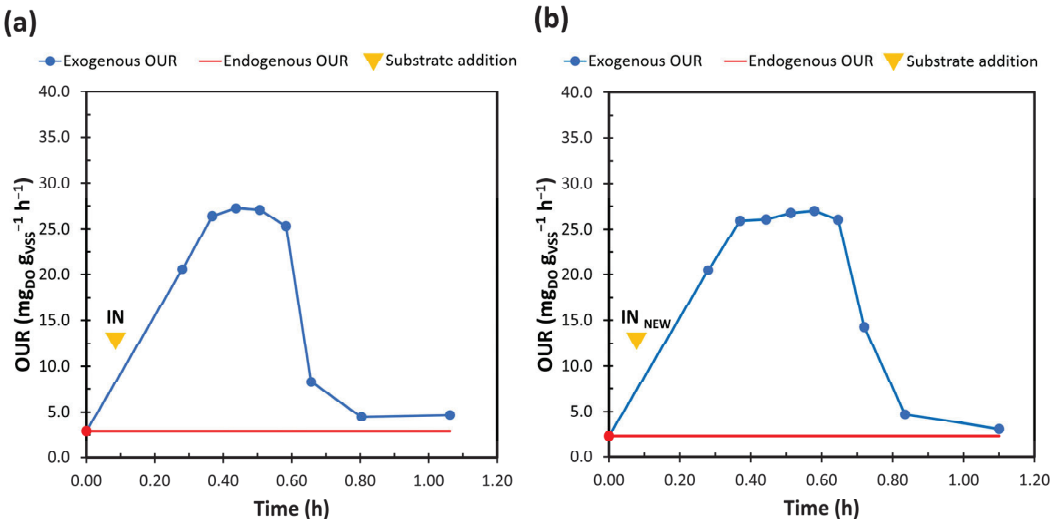


Figure 4. Continuous OUR tests performed in parallel with (**a**) IN and (**b**) IN_{NEW} (IN + ID) substrate.

In general, exogenous OUR always maintained values above the endogenous, thus indicating the absence of toxic-inhibitory effects towards the biomass. The areas of the exogenous respirograms were about 14.5 $mg_{DO}\ g_{VSS}^{-1}$ and 16.2 $mg_{DO}\ g_{VSS}^{-1}$ for IN and IN_{NEW}, respectively. However, the oxygen used by biomass only for the substrate degradation was 11.4 $mg_{DO}\ g_{VSS}^{-1}$ for IN and 13.6 $mg_{DO}\ g_{VSS}^{-1}$ for IN_{NEW}. Hence, a slightly higher oxygen consumption was observed for IN_{NEW} substrate degradation. This result was expected, as IN_{NEW} contained an aliquot of ID, which, although reduced, brought with it a series of "more difficult" and slower biodegradable molecules.

For the degradation of substrates, an oxygen consumption in the range of 21–27 mg_{DO} has been observed (area of the degradation "bell" equal to 11–14 $mg_{DO}\ g_{VSS}^{-1}$, multiplied by VSS concentration of about 1.8–2 $g\ L^{-1}$). Considering (i) COD dosed with substrates equal to 60–70 mg_{COD}, (ii) BOD_5/COD ratio of about 50% for both IN and IN_{NEW}, 30–35 mg_{BOD5} were dosed at the beginning of the tests. A BOD_5 removal of 70–80% was observed in just over 1 h. This result was conceptually correct, as BOD_5 is a measurement corresponding to a contact time of 5 days, and a complete degradation of the substrates in terms of biodegradable organic matter would not have been visible in 1 h. For a simpler and more immediate performance of the continuous test, an approximation was assumed: the tests were stopped at exogenous OUR values close to the endogenous.

3.3.2. Autotrophic Biomass

The impact of ID on the nitrification activity of case study biomass was also investigated (Figure 5). A sample of civil sewage, with domestic WW only, was used as the reference substrate. The WW entering the oxidation/nitrification reactor (IN) showed a visible acute inhibition effect (2.1 $mg_{N\text{-}NO3^-}\ g_{VSS}^{-1}\ h^{-1}$) compared to the reference substrate (2.9 $mg_{N\text{-}NO3^-}\ g_{VSS}^{-1}\ h^{-1}$). As for OUR tests, this could be due to various toxic-inhibiting substances for autotrophic biomass present in many industrial wastes that reach the sewage system. With the addition of the studied ID, a further reduction of the nitrifying kinetics was observed, down to 1.6 $mg_{N\text{-}NO3^-}\ g_{VSS}^{-1}\ h^{-1}$. This result could be linked to (i) new

inhibitory pollutants for the autotrophic biomass or (ii) excessive increase in loads of substances already present in WW entering the WWTP. In any case, the nitrifying biomass was put in contact with a new substrate (ID contained in IN_{NEW}) to which it had not yet acclimatised. After an initial period of instability and transition, thanks to a better acclimatization of the autotrophic biomass, better nitrification kinetics cannot be excluded. However, IN_{NEW}-AUR values did not seem to be excessively alarming, since some literature studies have shown a nitrification kinetic with WW (and properly enriched with $N\text{-}NH_4^+$), usually treated by the nitrifying biomass, equal to 1.8 $mg_{N\text{-}NOx}\ g_{VSS}{}^{-1}\ h^{-1}$ [26]. In any case, despite these results, the conditions for prohibiting the company from discharging into the public sewer did not seem to exist; however, further insights should not be excluded, for example a more in-depth AUR test campaign.

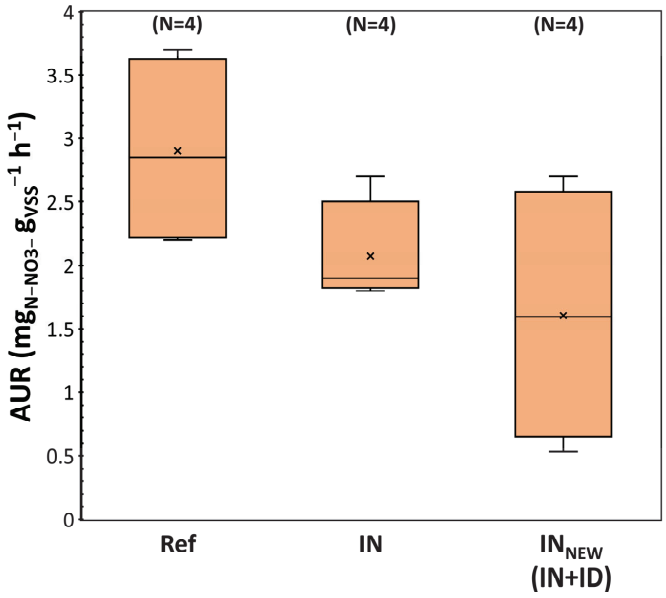


Figure 5. Results of the batch AUR tests with autotrophic biomass sampled in the case study-WWTP. Ref: Reference value. Boxplots represent the distance between the first and third quartiles while whiskers are set as the most extreme (lower and upper) data point not exceeding 1.5 times the quartile range from the median. The cross represents the mean value. N: number of replicated tests.

4. Future Outlooks

This study represented the first approach and first version of an experimental protocol to evaluate the impact of new industrial waste on the urban WWTP. The authors are aware and hope that further steps will be taken in future research, to make this protocol even more complete, reliable, and easily applicable by both the urban WWTP receiving the ID, and by the company responsible for the discharge into the sewer.

The proposed methodology is valid if the industrial WW is discharged with a constant flow rate/pollutant load throughout the day, further investigation is required if significant variations in flow rate and/or load are found. Most urban WWTPs are made up of traditional biological treatments which generally cannot tolerate significant variations in the influent sewage. With the occurrence of a negative impact on the WWTP, the company responsible for the discontinuous effluent could be suggested/requested to insert a homogenization tank before discharge into the sewer.

The adaptation of step 1 to the specific case is of fundamental importance. The choice of pollutants for the assessment of the ID qualitative impact on the WWTP (load ratio) is essential. The most critical pollutants in the ID (such as heavy metals, surfactants, persistent organic pollutants, aromatic and nitrogenous organic solvents, chlorinated solvents, etc.) can only be identified through a case-by-case analysis based on company production processes. The authors recommend not considering in practice only the parameters of this case study, as they refer to the specific situation. A further step could be envisaged, to study the impact of

some target pollutants, carried by ID, on the removal efficiencies of the urban WWTP. In this case, the WWTP effluent should also be monitored.

The integrated approach of this experimental protocol aims to make all the realities gravitating around the world of WW treatment more attentive. Greater awareness of companies translates into better management of industrial waste and better care and protection of the environment. Greater safeguarding of urban WWTPs guarantees efficient and optimized treatment, more controlled effluents, and therefore a reduced environmental impact.

5. Conclusions

The possibility to connect to the public sewer a new discharge coming from an AWTP, with an average flowrate of 200 m^3 d^{-1}, was studied in this work by adopting an integrated assessment protocol, based on operating data processing as well as experimental tests. The sewage is treated in an urban WWTP, with a conventional activated sludge process; the average incoming flow rate is 45,000 m^3 d^{-1}. In Italy, for getting the permission to discharge into sewers, an acute toxicity test is mandatory, but the prescribed method is the same used for assessing the toxicity of discharge into natural water bodies. This may lead to wrong evaluations. Contrarily, an effective and reliable evaluation of the compatibility of new discharge with the centralized WWTP should be carried out by considering the site-specific features of the plant and the biological prosses. In this work, the dimensional characteristics of the WWTP (flow rate/load mixing ratio, volumes), the operating conditions (SLR, C:N:P, OC, oxygen supply), and the response and activity of the biomass (both heterotrophic and autotrophic) have been pointed out as fundamental issues to consider. To meet this need, a multi-step experimental protocol for WW utilities has been proposed, where respirometry (OUR and AUR tests) plays a relevant role.

Author Contributions: Conceptualization, F.M.C. and M.C.C.; Methodology, F.M.C. and G.B.; Software, F.M.C. and S.B.; Validation, M.C.C., G.B. and A.A.; Formal Analysis, G.B.; Investigation, F.M.C.; Resources, M.C.C.; Data Curation, F.M.C.; Writing—Original Draft Preparation, F.M.C.; Writing—Review & Editing, F.M.C., G.B., S.B. and A.A.; Visualization, F.M.C.; Supervision, M.C.C.; Project Administration, M.C.C. All authors have read and agreed to the published version of the manuscript.

Funding: This research received no external funding.

Data Availability Statement: All data generated or analysed during this study are included in this published article.

Conflicts of Interest: The authors declare no conflict of interest.

Abbreviations

AUR	Ammonia utilization rate
AWTP	Aqueous waste treatment plant
BIO	Oxidation/nitrification biomass
CAS	Conventional activated sludge
COD	Chemical oxygen demand
DO	Dissolved oxygen
ID	Industrial discharge
IN	Input to the WWTP
N-NH_4^+	Ammoniacal nitrogen
N-NO_3^-	Nitric nitrogen
OC	Organic carbon
OUR	Oxygen uptake rate
TN	Total nitrogen
TKN	Total Kjeldahl nitrogen
SLR	Sludge loading rate
SS	Total suspended solids
VSS	Volatile suspended solids
WW	Wastewater
WWTP	Wastewater treatment plant

References

1. Ren, S. Assessing wastewater toxicity to activated sludge: Recent research and developments. *Environ. Int.* **2004**, *30*, 1151–1164. [CrossRef]
2. Hagman, M.; La, J.; Jansen, C. Oxygen uptake rate measurements for application at wastewater treatment plants. *Vatten* **2007**, *63*, 131–138.
3. Mhlanga, F.T.; Brouckaert, C.J. Characterisation of wastewater for modelling of wastewater treatment plants receiving industrial effluent. *Water SA* **2012**, *39*, 403–408. [CrossRef]
4. Government of Italy Legislative Decree 3 April 2006, n. 152. Environmental Regulations. Available online: https://www.gazzettaufficiale.it/dettaglio/codici/materiaAmbientale (accessed on 17 January 2023). (In Italian)
5. Rahman, M.S.; Mousumi, M.Z.; Sakib, M.A.A.; Chy, T.J.; Fahad, M.S.A.; Author, C. Development of a respirometry and cod based rapid experimental protocol for analyzing wastewater. In Proceedings of the 4th International Conference on Advances in Civil Engineering 2018 (ICACE 2018), CUET, Chittagong, Bangladesh, 19–21 December 2018; pp. 19–21.
6. Li, Z.H.; Zhu, Y.M.; Yang, C.J.; Zhang, T.Y.; Yu, H.Q. A simple respirogram-based approach for the management of effluent from an activated sludge system. *Bioresour. Technol.* **2018**, *261*, 412–419. [CrossRef] [PubMed]
7. Torretta, V.; Ragazzi, M.; Trulli, E.; De Feo, G.; Urbini, G.; Raboni, M.; Rada, E.C. Assessment of biological kinetics in a conventional municipal WWTP by means of the oxygen uptake rate method. *Sustainability* **2014**, *6*, 1833–1847. [CrossRef]
8. Collivignarelli, M.C.; Bertanza, G.; Abbà, A.; Torretta, V.; Katsoyiannis, I.A. Wastewater treatment by means of thermophilic aerobic membrane reactors: Respirometric tests and numerical models for the determination of stoichiometric/kinetic parameters. *Environ. Technol.* **2019**, *40*, 182–191. [CrossRef]
9. Arias-Navarro, M.; Villen-Guzman, M.; Perez-Recuerda, R.; Rodriguez-Maroto, J.M. The use of respirometry as a tool for the diagnosis of waste water treatment plants. A real case study in Southern Spain. *J. Water Process Eng.* **2019**, *29*, 100791. [CrossRef]
10. Vasiliadou, I.A.; Molina, R.; Martinez, F.; Melero, J.A.; Stathopoulou, P.M.; Tsiamis, G. Science of the Total Environment Toxicity assessment of pharmaceutical compounds on mixed culture from activated sludge using respirometric technique: The role of microbial community structure. *Sci. Total Environ.* **2018**, *630*, 809–819. [CrossRef]
11. Oviedo, M.D.C.; Sánchez, J.B.; Cruz, C.A.; Alonso, J.M.Q. A new approach to toxicity determination by respirometry. *Environ. Technol.* **2009**, *30*, 1601–1605. [CrossRef]
12. Aguilar, M.I.; Lloréns, M.; Fernández-Garrido, J.M.; Pérez-Marín, A.B.; Ortuño, J.F.; Meseguer, V.F. Heavy metals effect on the heterotrophic activity of activated sludge. *Int. J. Environ. Sci. Technol.* **2020**, *17*, 3111–3118. [CrossRef]
13. Borzooei, S.; Simonetti, M.; Scibilia, G.; Chiara, M. Journal of Environmental Chemical Engineering Critical evaluation of respirometric and physicochemical methods for characterization of municipal wastewater during wet-weather events. *J. Environ. Chem. Eng.* **2021**, *9*, 105238. [CrossRef]
14. Vitanza, R.; Colussi, I.; Cortesi, A.; Gallo, V. Implementing a respirometry-based model into BioWin software to simulate wastewater treatment plant operations. *J. Water Process Eng.* **2016**, *9*, 267–275. [CrossRef]
15. Mainardis, M.; Buttazzoni, M.; Cottes, M.; Moretti, A.; Goi, D. Science of the Total Environment Respirometry tests in wastewater treatment: Why and how? A critical review. *Sci. Total Environ.* **2021**, *793*, 148607. [CrossRef]
16. Bashaar, Y.A. Nutrients requirements in biological industrial wastewater treatment. *Afr. J. Biotechnol.* **2004**, *3*, 236–238. [CrossRef]
17. Permatasari, R.; Rinanti, A.; Ratnaningsih, R. Treating domestic effluent wastewater treatment by aerobic biofilter with bioballs medium. *IOP Conf. Ser. Earth Environ. Sci.* **2018**, *106*, 012048. [CrossRef]
18. Hamza, R.A.; Zaghloul, M.S.; Iorhemen, O.T.; Sheng, Z.; Tay, J.H. Optimization of organics to nutrients (COD:N:P) ratio for aerobic granular sludge treating high-strength organic wastewater. *Sci. Total Environ.* **2019**, *650*, 3168–3179. [CrossRef]
19. Metcalf & Eddy Inc.; Tchobanoglous, G.; David Stensel, H.; Tsuchihashi, R.; Burton, F.L. *Wastewater Engineering: Treatment and Resource Recovery*, 5th ed.; McGraw-Hill: London, UK, 2013; ISBN 9780073401188.
20. Masotti, L. *Depurazione delle Acque. Tecniche ed Impianti per il Trattamento delle Acque di Rifiuto*; Calderini: Milan, Italy, 2011. (In Italian)
21. Metcalf & Eddy Inc.; Tchobanoglous, G.; Burton, F.L.; Stensel, H.D. *Wastewater Engineering: Treatment and Reuse*, 4th ed.; McGraw-Hill: New York, NY, USA, 2003.
22. Raboni, M.; Torretta, V.; Viotti, P.; Urbini, G. Calculating specific denitrification rates in pre-denitrification by assessing the influence of dissolved oxygen, sludge loading and mixed-liquor recycle. *Environ. Technol.* **2014**, *35*, 2582–2588. [CrossRef]
23. Raboni, M.; Viotti, P.; Rada, E.C.; Conti, F.; Boni, M.R. The sensitivity of a specific denitrification rate under the dissolved oxygen pressure. *Int. J. Environ. Res. Public Health* **2020**, *17*, 9366. [CrossRef]
24. US EPA Process Design Manual for Nitrogen Control. Available online: https://nepis.epa.gov/Exe/ZyNET.exe/9100PUPQ.TXT?ZyActionD=ZyDocument&Client=EPA&Index=Prior+to+1976&Docs=&Query=&Time=&EndTime=&SearchMethod=1&TocRestrict=n&Toc=&TocEntry=&QField=&QFieldYear=&QFieldMonth=&QFieldDay=&IntQFieldOp=0&ExtQFieldOp=0&XmlQuery=& (accessed on 10 March 2023).
25. Collivignarelli, M.C.; Abbà, A.; Caccamo, F.M.; Miino, M.C.; Durante, A.; Bellazzi, S.; Baldi, M.; Bertanza, G. How to Produce an Alternative Carbon Source for Denitrification by Treating and Drastically Reducing Biological Sewage Sludge. *Membranes* **2021**, *11*, 977. [CrossRef]
26. Collivignarelli, M.C.; Carnevale Miino, M.; Caccamo, F.M.; Baldi, M.; Abbà, A. Performance of full-scale thermophilic membrane bioreactor and assessment of the effect of the aqueous residue on mesophilic biological activity. *Water* **2021**, *13*, 1754. [CrossRef]
27. Kristensen, G.H.; Jorgensen, P.E.; Henze, M. Characterization of functional microorganism groups and substrate in activated sludge and wastewater by AUR, NUR and OUR. *Water Sci. Technol.* **1992**, *25*, 43–57. [CrossRef]

28. Collivignarelli, M.C.; Pedrazzani, R.; Bellazzi, S.; Carnevale Miino, M.; Caccamo, F.M.; Baldi, M.; Abbà, A.; Bertanza, G. Numerical Analysis of a Full-Scale Thermophilic Biological System and Investigation of Nitrate and Ammonia Fates. *Appl. Sci.* **2022**, *12*, 6952. [CrossRef]
29. Surmacz-Gorska, J.; Gernaey, K.; Demuynck, C.; Vanrolleghem, P.; Verstraete, W. Nitrification monitoring in activated sludge by oxygen uptake rate (OUR) measurements. *Water Res.* **1996**, *30*, 1228–1236. [CrossRef]
30. ISPRA Measurement Procedure for the Determination of the Chemical Oxygen Demand (COD) by Cuvette Test: Method 5135. Available online: https://www.isprambiente.gov.it/it/pubblicazioni/manuali-e-linee-guida/procedura-di-misurazione-per-la-determinazione-della-richiesta-chimica-di-ossigeno-cod-mediante-test-in-cuvetta-metodo-5135 (accessed on 25 May 2023). (In Italian)
31. APAT-IRSA-CNR 4030 Analytical Methods for Water. Section 4000—Non-Metallic Inorganics. Ammonia Nitrogen. Non-Metallic Inorganic Constituents. METHOD A1—Spectrophotometric Determination of Indophenol. Available online: https://www.irsa.cnr.it/wp/wp-content/uploads/2022/04/Vol2_Sez_4000_InorganiciNonMetallici.pdf (accessed on 12 May 2023). (In Italian)
32. APAT-IRSA-CNR 5030 Analytical Methods for Water. Section 5000—Organic Constituents. Organic Nitrogen. Available online: https://www.irsa.cnr.it/wp/wp-content/uploads/2022/04/Vol2_Sez_5000_Organici.pdf (accessed on 25 May 2023). (In Italian)
33. UNI EN ISO 10304-1:2009 Water Quality—Determination of Dissolved Anions by Ion Liquid Chromatography—Part 1: Determination of Bromides, Chlorides, Fluorides, Nitrates, Nitrites, Phosphates and Sulphates. Available online: https://store.uni.com/uni-en-iso-10304-1-2009 (accessed on 25 May 2023). (In Italian)
34. UNI 11658:2016 Water Quality—Determination of Total Nitrogen in Wastewater, Natural and Intended for Human Consumption by Means of a Cuvette Test. Available online: https://store.uni.com/uni-11658-2016 (accessed on 25 May 2023). (In Italian)
35. APAT-IRSA-CNR 2090 Analytical Methods for Water. Section 2000—Physical, Chemical Parameters and Chemical-Physical. Solids (Total Dissolved; Total Suspended; Sedimentable; Fixed and Volatile at 600 °C). Available online: https://www.irsa.cnr.it/wp/wp-content/uploads/2022/04/Vol1_Sez_2000_Parametri-chimico-fisici.pdf (accessed on 12 May 2023). (In Italian)
36. Rahman, M.S.; Islam, M.A.; Habib, S.; Sarker, J. Measuring Biodegradability of Industrial Wastewater by A Low-Cost Differential Respirometer. *Res. J. Eng. Sci.* **2013**, *2*, 1–4.
37. Hoque, M.A.; Aravinthan, V.; Pradhan, N.M. Can we decode the messages of activated sludge through the respirograms? *Water Air Soil Pollut. Focus* **2009**, *9*, 449–459. [CrossRef]
38. Andreottola, G.; Foladori, P.; Ziglio, G.; Cantaloni, C.; Bruni, L.; Cadonna, M. Methods for Toxicity Testing of Xenobiotics in Wastewater Treatment Plants and in Receiving Water Bodies. In *Dangerous Pollutants (Xenobiotics) in Urban Water Cycle*; Springer: Dordrecht, The Netherlands, 2007; pp. 191–206.
39. Capodici, M.; Fabio, S.; Di, F.; Di, D.; Torregrossa, M. An innovative respirometric method to assess the autotrophic active fraction: Application to an alternate oxic–anoxic MBR pilot plant. *Chem. Eng. J.* **2016**, *300*, 367–375. [CrossRef]
40. Etienne, P.; Mathieu, S. Estimation of wastewater biodegradable COD fractions by combining respirometric experiments in various So/Xo ratios. *Water Res.* **2000**, *34*, 1233–1246.
41. Di Trapani, D.; Christensson, M.; Torregrossa, M.; Viviani, G.; Ødegaard, H. Performance of a hybrid activated sludge/biofilm process for wastewater treatment in a cold climate region: Influence of operating conditions. *Biochem. Eng. J.* **2013**, *77*, 214–219. [CrossRef]
42. Statiris, E.; Dimopoulos, T.; Petalas, N.; Noutsopoulos, C.; Mamais, D.; Malamis, S. Investigating the long and short-term effect of free ammonia and free nitrous acid levels on nitritation biomass of a sequencing batch reactor treating thermally pre-treated sludge reject water. *Bioresour. Technol.* **2022**, *362*, 127760. [CrossRef]
43. Inglezakis, V.J.; Malamis, S.; Omirkhan, A.; Nauruzbayeva, J.; Makhtayeva, Z.; Seidakhmetov, T.; Kudarova, A. Investigating the inhibitory effect of cyanide, phenol and 4-nitrophenol on the activated sludge process employed for the treatment of petroleum wastewater. *J. Environ. Manag.* **2017**, *203*, 825–830. [CrossRef]
44. Kujawa, K.; Klapwijk, B. A method to estimate denitrification potential for predenitrification systems using NUR batch test. *Water Res.* **1999**, *33*, 2291–2300. [CrossRef]
45. Peng, Y.Z.; Ma, Y.; Wang, S. ying Denitrification potential enhancement by addition of external carbon sources in a predenitrification process. *J. Environ. Sci.* **2007**, *19*, 284–289. [CrossRef]
46. Itokawa, H.; Hanaki, K.; Matsuo, T. Nitrous oxide production in high-loading biological nitrogen removal process under low cod/n ratio condition. *Water Res.* **2001**, *35*, 657–664. [CrossRef]
47. Collivignarelli, M.C.; Abbà, A.; Bertanza, G.; Baldi, M.; Setti, M.; Frattarola, A.; Carnevale Miino, M. Treatment of high strength wastewater by thermophilic aerobic membrane reactor and possible valorisation of nutrients and organic carbon in its residues. *J. Clean. Prod.* **2021**, *280*, 124404. [CrossRef]
48. Collivignarelli, M.C.; Carnevale Miino, M.; Arab, H.; Bestetti, M.; Franz, S. Efficiency and Energy Demand in Polishing Treatment of Wastewater Treatment Plants Effluents: Photoelectrocatalysis vs. Photocatalysis and Photolysis. *Water* **2021**, *13*, 821. [CrossRef]
49. Dulekgurgen, E.; Doğruel, S.; Karahan, Ö.; Orhon, D. Size distribution of wastewater COD fractions as an index for biodegradability. *Water Res.* **2006**, *40*, 273–282. [CrossRef]
50. Lagarde, F.; Tusseau-Vuillemin, M.H.; Lessard, P.; Héduit, A.; Dutrop, F.; Mouchel, J.M. Variability estimation of urban wastewater biodegradable fractions by respirometry. *Water Res.* **2005**, *39*, 4768–4778. [CrossRef]

Disclaimer/Publisher's Note: The statements, opinions and data contained in all publications are solely those of the individual author(s) and contributor(s) and not of MDPI and/or the editor(s). MDPI and/or the editor(s) disclaim responsibility for any injury to people or property resulting from any ideas, methods, instructions or products referred to in the content.

environments

MDPI

Article

Definition and Validation of Vineyard Management Zones Based on Soil Apparent Electrical Conductivity and Altimetric Survey

João Serrano [1,*], Vasco Mau [1], Rodrigo Rodrigues [1], Luís Paixão [2], Shakib Shahidian [1], José Marques da Silva [1,2], Luís L. Paniagua [3] and Francisco J. Moral [4]

[1] MED—Mediterranean Institute for Agriculture, Environment and Development and CHANGE—Global Change and Sustainability Institute, Universidade de Évora, Pólo da Mitra, Ap. 94, 7006-554 Évora, Portugal; m50209@alunos.uevora.pt (V.M.); rjtr@uevora.pt (R.R.); shakib9@gmail.com (S.S.); jmsilva@uevora.pt (J.M.d.S.)
[2] AgroInsider Lda., 7005-841 Évora, Portugal; lgpaixao@gmail.com
[3] Escuela de Ingenierías Agrarias, Universidad de Extremadura, Avenida Adolfo Suárez, S/N, 06007 Badajoz, Spain; llpsimon@unex.es
[4] Departamento de Expresión Gráfica, Escuela de Ingenierías Industriales, Universidad de Extremadura, Avenida de Elvas, S/N, 06006 Badajoz, Spain; fjmoral@unex.es
* Correspondence: jmrs@uevora.pt; Tel.: +351-266-760-800

Abstract: In the current context of increasing costs of production factors, it is essential to optimize the management of available resources, seeking to incorporate technologies that improve knowledge of the variables involved in the agronomic production process. The aim of this study is to define and validate management zones (MZ) in a 3.3 ha vineyard located near Évora, in the South of Portugal. A contact sensor ("Veris 2000 XA") was used to map soil apparent electrical conductivity (EC_a) and a precision altimetric survey of the field was carried out with a global navigation satellite system receiver (GNSS). The results of these surveys were submitted to geostatistical treatments that allowed the definition of three MZ (less, intermediate, and more productive potential). The validation of such MZ was carried out by laboratory analysis of soil samples (texture, pH, organic matter—OM, moisture content, phosphorous, potassium, exchange bases, and cation exchange capacity—CEC), measurements of soil compaction (cone index—CI) with an electronic cone penetrometer, and through indices (Normalized Difference Vegetation Index—NDVI, and Normalized Difference Water Index—NDWI) obtained by remote sensing (RS) using Sentinel-2 satellite images. All these parameters (soil parameters and RS indices) proved the validity of the MZ (of less, intermediate, and more productive potential) defined from the EC_a and altimetric survey. This validation attests to the interest of expeditious technological tools for monitoring EC_a as a fundamental step in implementing smart agronomic decision-making processes.

Keywords: precision viticulture; spatial variability; sensors; site-specific management

Citation: Serrano, J.; Mau, V.; Rodrigues, R.; Paixão, L.; Shahidian, S.; Marques da Silva, J.; Paniagua, L.L.; Moral, F.J. Definition and Validation of Vineyard Management Zones Based on Soil Apparent Electrical Conductivity and Altimetric Survey. *Environments* **2023**, *10*, 117. https://doi.org/10.3390/environments10070117

Academic Editors: Dibyendu Sarkar, Rupali Datta, Prafulla Kumar Sahoo and Mohammad Mahmudur Rahman

Received: 18 May 2023
Revised: 30 June 2023
Accepted: 30 June 2023
Published: 6 July 2023

Copyright: © 2023 by the authors. Licensee MDPI, Basel, Switzerland. This article is an open access article distributed under the terms and conditions of the Creative Commons Attribution (CC BY) license (https://creativecommons.org/licenses/by/4.0/).

1. Introduction

One of the main challenges for the agricultural sector, and in particular, viticulture, is to adapt to climate change while ensuring the quality of production and its sustainability [1]. Within this context, compounded by rising input costs, it is essential to optimize the management of available resources, by incorporating technologies that provide information on the variables involved in the agronomic production process. This perspective is within the framework of Precision Agriculture (PA), which has expanded in the last decade to practically all crops.

The main goal of Precision Viticulture (PV) is to assess the spatial variability of physiological needs of the vines belonging to different areas of the vineyard in order to implement the management techniques in a more site- and time-specific manner, reducing the use of

production factors and, consequently, the environmental impact and maximizing the yield and quality of production [2].

The spatial variability of grapevine (*Vitis vinifera* L.) within a single vineyard is a relevant issue for growers and winemakers [3], essential for making management decisions [4,5]. A very diverse set of management decisions are required in this crop, ranging from input management (irrigation, fertilizing, spraying) up to cultural practices (pruning, shoot and cluster thinning, canopy management, inter-row cover, or segmented harvesting) [3].

Within-field variability of vine development and, consequently, grape yield and composition, is the result of both spatial and temporal variation of many factors, including edaphic, biological, climatic, topographic, and anthropogenic [4]. Many studies have shown and quantified the existence of significant variability within the vineyards [6]. Knowing the spatial variability of soil characteristics allows a better understanding of the variability of the physiological response of the vines [2]. This variability can be surveyed using a regular sampling grid [6], however, given the cost and time required for this type of sampling and the necessity of many soil samples to achieve an effective spatial representation of any soil property, it cannot be considered a viable and practical process at farm level [7,8]. The use of sensors is becoming the norm for mapping the relevant soil properties, thus reducing the number of soil samples needed to describe field variability [9].

Some factors responsible for variability in a vineyard remain stable over time, such as topography and some soil properties; therefore, the knowledge of their spatial variability can provide a better understanding of this complex decision-making scenario [3] and the definition of management zones (MZ). These represent subfield areas with homogeneous characteristics, such as texture, topography, or nutrient levels [7], and may be used to adapt viticulture practices [5]. The ability to map the spatial variability in vine and soil characteristics allows grape growers to move from a random sampling approach to a smart sampling methodology based on sampling zones of uniform vine characteristics [10]. This can be considered the first step in the application of site-specific crop management [7]. Understanding the spatial variability of factors that influence crop yield is essential to the application of site-specific management [11].

This new possibility of considering perspective of spatial variability is a consequence of the technological means made available by PV to the farm manager [2,10]. These spatially enabled digital technologies provide the possibility of gathering georeferenced spatial datasets [2], information with high spatial resolution (small areas within the field) and great flexibility in the timing of data acquisition, and managing these areas differentially [4,10]. The importance of remote and proximal sensing as tools for smart viticulture application has been evidenced in several reviews published in the last two decades [10].

Variation in soil and topography is likely to have a large impact on vineyard variability [10]. The proximal monitoring of soil variability includes the use of a wide range of sensors [2]. The apparent soil electrical conductivity (EC_a) sensing technology, mounted on mobile platforms and coupled with GNSS receivers, are highly relevant when designing new vineyards and redeveloping existing vineyards [10], but also for the definition of MZ and site-specific management [7]. There are two types of sensors currently on the market to measure soil EC_a based on the method of measurement: contact or non-contact. The first type (e.g., Veris sensor) is invasive and uses electrodes, usually in the shape of coulters that make contact with the soil, generating electrical currents in the soil with an electrode and then measuring the potential difference thanks to a second receiver electrode, which measures the electrical resistivity (i.e., the inverse of conductivity). The second type (e.g., Dualem or EM38 sensors) is non-invasive and is composed of a transmitter and a receiver coil usually installed at opposite ends of a non-conductive bar. This sensor type works on the principle of electromagnetic induction: it generates a magnetic field that induces an electric current in the soil, which in turn creates a second magnetic field proportional to its conductivity, which is measured by the sensor [2,7]. The EC_a is usually related to various soil physical and chemical properties across a wide range of soils [12], such as texture

and depth, water retention capacity, organic matter content, salinity [2], cation exchange capacity (CEC), pH, exchangeable magnesium, and other soil nutrients [9].

Another electronic sensor that can help to characterize soil spatial variability and, consequently, its productive potential is the cone penetrometer [13,14]. This measures the cone index (CI, in kPa), which reflects soil compaction and is considered an important tool for the diagnosis of the most restrictive soil layers for root growth at depth [15]. For these reasons, it can be a very interesting parameter in terms of validating MZ.

Other new technologies have made it possible to characterize the crop vegetative vigor. In the last years, several works have shown the potential of remote sensing (RS) in crop monitoring, in particular the vineyard [9,10,16]. The significant impact of soil on vine nutrition and development has led researchers to associate the EC_a maps with vegetation indexes maps to assess the field spatial variability [9,17]. For example, the normalized difference vegetation index (NDVI) can be used to evaluate plant photosynthetic activity and, therefore, its canopy vigor, as well as crop yield and grape quality characteristics [8,10,16]. On the other hand, the normalized difference water index (NDWI) can be used to evaluate plant water stress and leaf water content during growth phases [16]. These vegetation indices have been successfully used by several teams to delineate areas with homogeneous vigor within vineyards for the purpose of site-specific management [3,9,17,18].

This study aims (i) to assess the soil spatial variability of a vineyard through EC_a survey with a contact sensor; (ii) to evaluate the temporal stability of EC_a measurements; (iii) to define MZ based on geostatistical treatment of EC_a and topographic survey; and (iv) to validate MZ by several approaches (soil laboratory analysis, CI and RS indices).

2. Materials and Methods

Figure 1 summarizes, schematically and chronologically, the methodology used in this study to monitor the spatial variability of a vineyard and define and validate MZ. The study was conducted between May 2022 and April 2023.

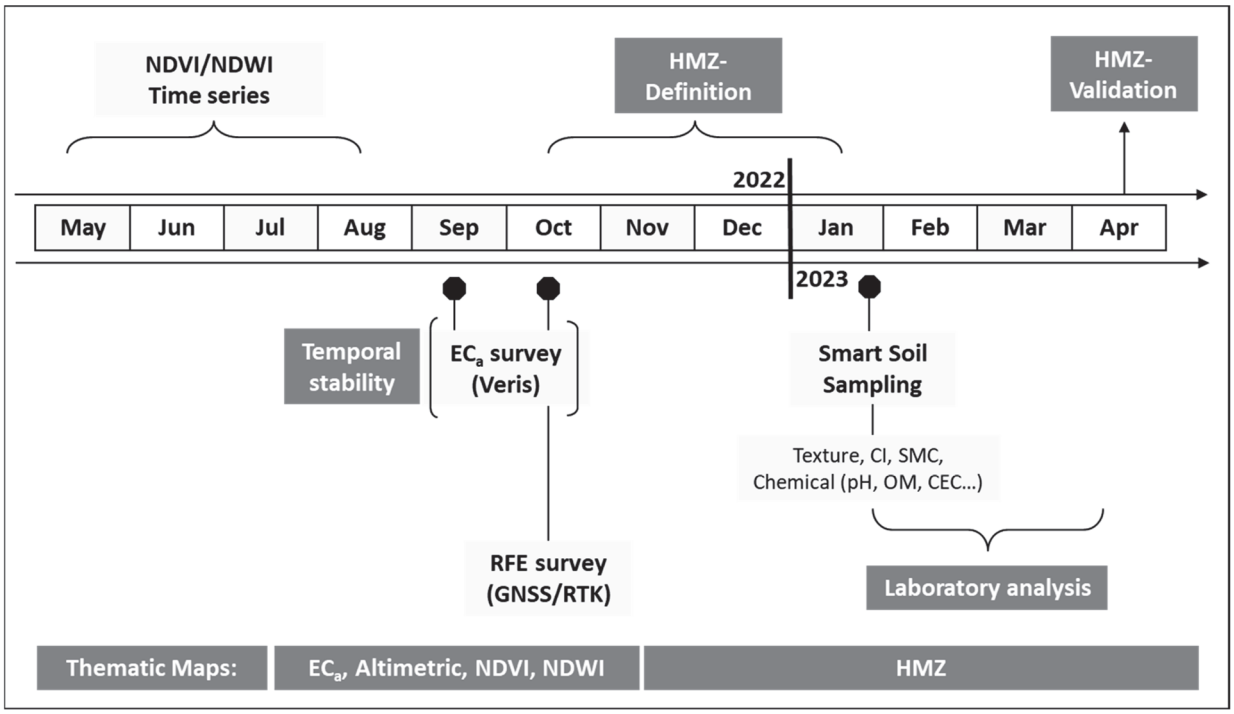


Figure 1. Schematic and chronological representation of methodology used in this study.

2.1. Study Area

The study field is a 3.3 ha vineyard, located at the "Mitra" farm of "University of Évora" (38.532° N; 8.015° W). The aerial image of the Mitra vineyard (Figure 2) shows two

areas: (i) white grapes (1.30 ha, about 85% of which is planted with three varieties: "Arinto", "Síria", and "AntãoVaz") and (ii) red grapes (2.0 ha, about 82% of which is planted with three varieties: "Aragonez", "Trincadeira", and "Castelão"). Despite this variability, the information available on the vineyard management history indicates uniform cultural operations (pruning, fertilization, irrigation, phytosanitary treatments, etc.).

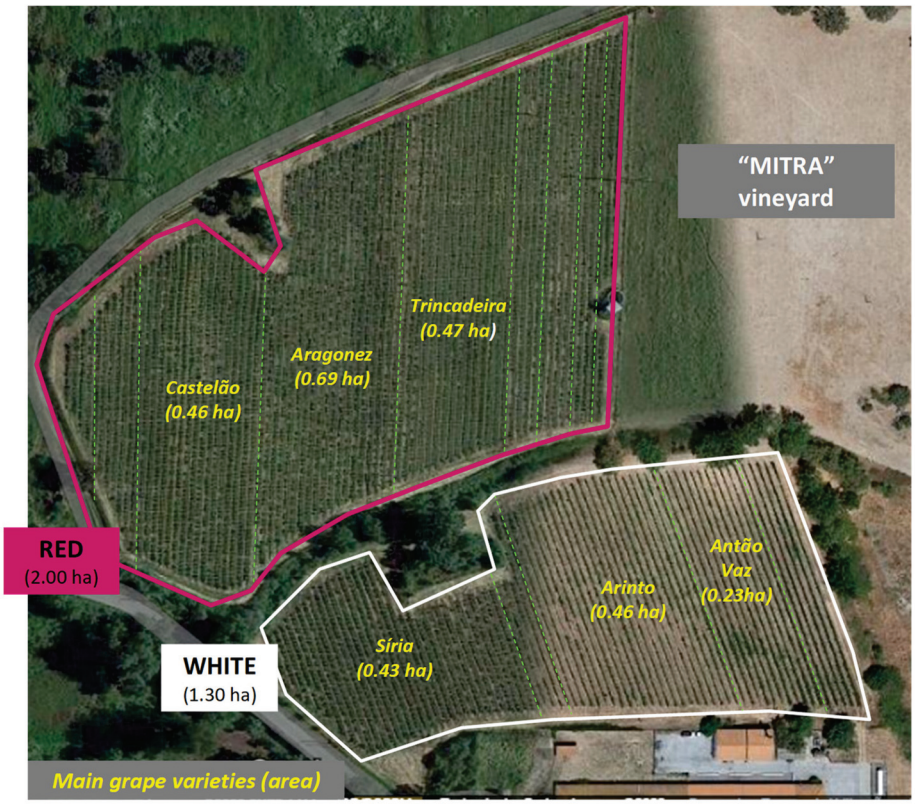


Figure 2. Aerial image of the Mitra vineyard. The main white and red grape varieties are indicated.

A precision altimetric survey of the field was carried out during October 2022 using a real-time kinematic (RTK) GPS instrument (Trimble RTK/PP-4700 GPS manufactured by TRIMBLE Navigation Limited, USA). The altimetric map (Figure 3) was generated using the triangulated irregular network interpolation tool, converted into a grid surface with a 1 m grid resolution using the Spatial Analyst Tools of ArcGIS (version 10.5, ESRI, Inc., Redlands, California, USA). The two sub-fields ("white", "W" and "red", R) show a gradual gradient (from South to North in the "W" area and from North to South in the "R" area), and slopes that converge to a flow line, which represents the lowest elevation of the study area.

The dominating soil type of the study area is Cambisol with a granite origin [19], characterized by little or no profile differentiation, slight or moderate weathering of parent material, and by absence of appreciable quantities of illuviated clay and organic matter. Acid Cambisols are not very fertile and are mainly dedicated to mixed agro-silvo-pastoral systems. Cambisols in undulating or hilly terrain (mainly colluvial) are planted to a variety of annual and perennial crops or are used as grazing land. The study area also includes hydromorphic soils and Luvisols. In the Mediterranean region, the often-eroded hills are used for extensive grazing or planted to tree crops [19].

The climate of this Mediterranean region is classified as Csa (Köppen–Geiger classification) [20] and is characterized by high inter-annual irregularity and low rainfall (<600 mm). The thermo-pluviometric diagram of the Évora meteorological station in the year under study (between May 2022 and April 2023; Figure 4) shows an accumulated precipitation of 526 mm, concentrated mainly (98%) in six months (September–January, and March), and the remaining six months with practically no precipitation (February and April–August).

In this period without precipitation, particularly between May and August, the average temperature is around 20–30 °C.

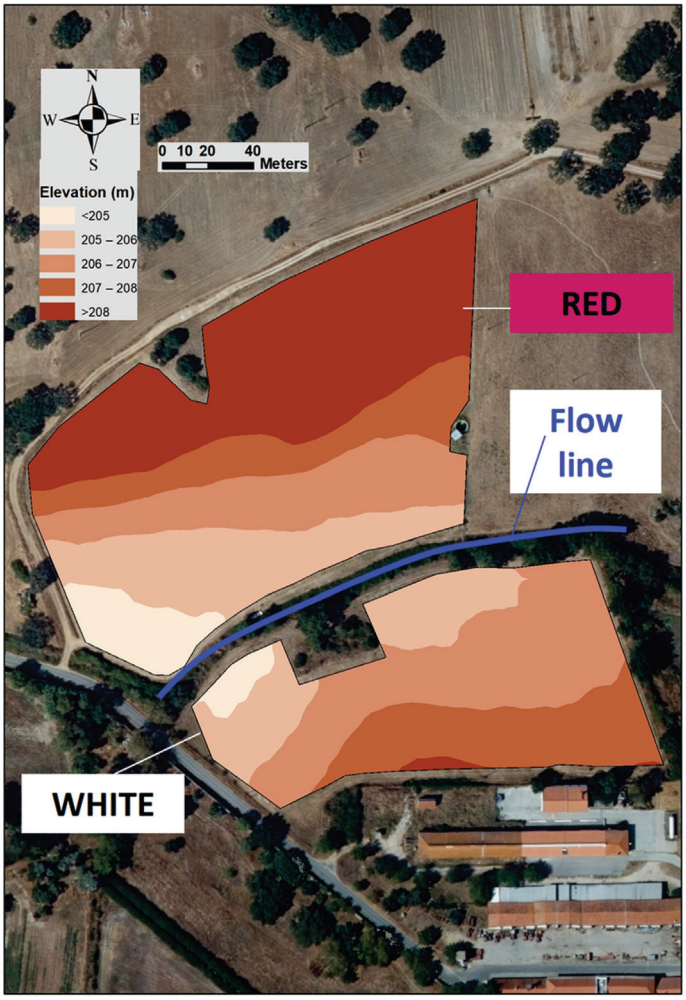


Figure 3. Altimetric map of the experimental field.

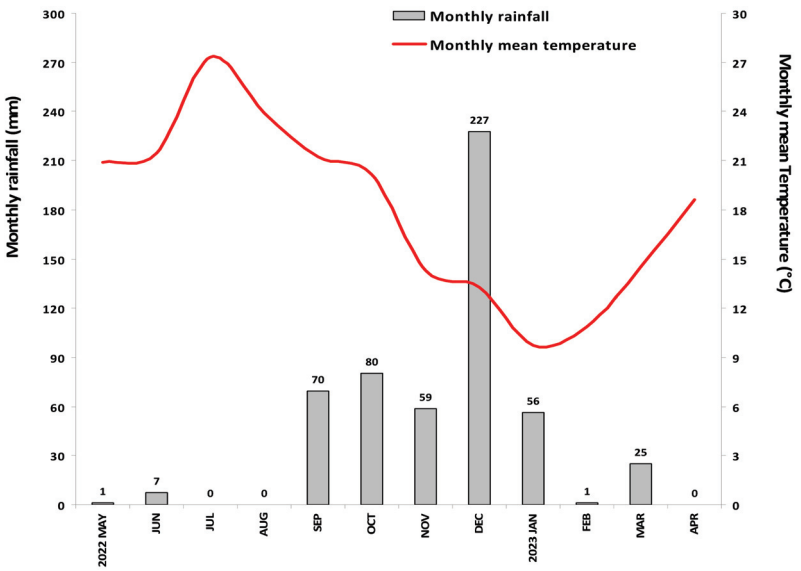


Figure 4. Thermo-pluviometric diagram of Mitra (Évora, Portugal) between May 2022 and April 2023.

2.2. Soil Apparent Electrical Conductivity (EC_a) Surveys and Processing

The Veris 2000 XA contact-type sensor (Veris Technologies, Salina, KS, USA; Figure 5) equipped with a GNSS antenna was used to measure the soil EC_a of the experimental field on 29 September 2022 (only white grapes area) and on 24 October 2022 (whole field). This sensor is mounted on a chassis supported on two wheels and is formed by two pairs of coulter-electrodes (adjustable rotating discs): one pair injects a current into the soil (outermost discs), while the other pair (innermost discs) measures the voltage drop. The adjustment of the discs generated one set of topsoil data (from 0 to 0.30 m depths). The sensor was pulled by a four-wheel drive vehicle in the vineyard rows at an average speed of 5 km·h^{-1} and was programmed to register the measurements each second.

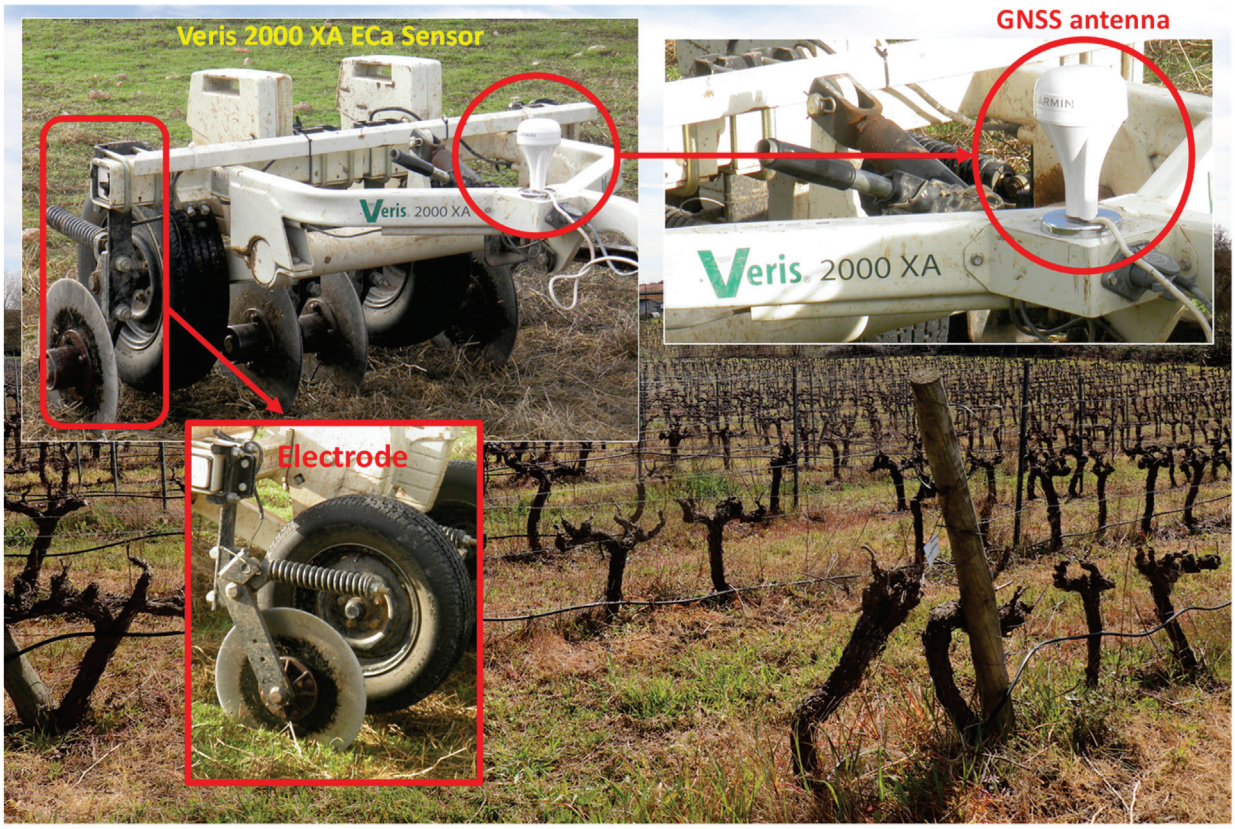


Figure 5. General view of the Mitra vineyard and detail of the soil apparent electrical conductivity sensor (Veris 2000 XA).

On both dates (29 September and 24 October 2022), twenty random soil samples (0–0.30 m depth) were collected in the white grapes area to calculate the mean soil moisture content (SMC).

Estimating EC_a at unsampled locations was conducted with the ordinary point kriging algorithm, integrating the spatial correlation structure described with the variograms. The kriged maps showing the spatial distribution of EC_a in the experimental field were obtained from the estimated values. Finally, the kriged maps of EC_a were produced with the ArcMap module of the ArcGIS.

2.3. Definition of Management Zones (MZ)

The results of EC_a and altimetric surveys were used as input for the geostatistical analyses that allowed the definition of management zones (MZ). These homogeneous subfields were delineated using a fuzzy cluster algorithm [21]. The MZ Analyst (MZA) software (Microsoft Corp., Redmond, WA, USA) was utilized in this study. Fridgen et al. [22] described the procedures for delineating and evaluating the number of MZ used in this software. The fuzzy c-means, an unsupervised continuous classification procedure, which

is implemented in the MZA program, was used to divide the fields into different cluster classes. The ISO Cluster approach in ArcGIS was used to perform the classification. This algorithm organizes the data in the input raster into a user-defined number of groups to produce signatures which are utilized to classify the data using the "Maximum Likelihood Classifier" (MLC) function. The fuzziness exponent was set at the conventional value of 1.3 and the "Mahalanobis" measure of similarity was selected since it is the most suitable for multivariate data classification [23]. From a practical perspective, three management zones with different productive potential (less, intermediate, and more potential) were considered in each vineyard area (white grapes, MZ: W−, W_{int}, and W+, respectively; and red grapes, MZ: R−, R_{int}, and R+, respectively). Both indices, the fuzziness performance index (FPI) and the normalized classification entropy (NCE) [22], confirmed that the number was adequate because their values were at minimum. FPI is a measure of the degree of membership sharing among classes: 0 indicates different classes with no membership sharing and 1 reflects a strong sharing of membership. NCE is an estimate of the amount of disorganization created by several classes: 0 indicates high organization and 1 represents a strong disorganization. When each index is at minimum, which indicates the least membership sharing (FPI) and greatest amount of organization (NCE) as a result of the clustering process, the optimum number of classes is achieved.

2.4. Validation of Management Zones (MZ)s

The validation of MZ was carried out by laboratory analysis of soil samples, measurements of soil compaction (CI) with an electronic cone penetrometer, and through indices (NDVI and NDWI) obtained by RS using Sentinel-2 satellite images.

2.4.1. Soil Sampling Collection and Reference Analysis

After the definition of the MZs (with less, intermediate, and more productive potential), in the validation process (Figure 1), soil parameters (moisture content—SMC, CI, texture, pH, organic matter—OM, P_2O_5, K_2O, degree of base saturation–DBS, sum of the exchange bases—SEB, and cation exchange capacity—CEC), and crop vegetation indices (NDVI and NDWI) at sampling locations were employed to check their differences.

Four sampling areas were randomly GNSS georeferenced in each MZ and in each field (white and red grapes areas). The soil georeferenced samples were collected on 25 January 2023 using a gouge auger and a hammer, at a depth range of 0–0.30 m. Each composite sample was the result of five sub-samples collected within a radius of 1 m, one taken from the center of the sampling area, and the other four taken according to diagram presented in Figure 6. In the laboratory, the soil samples were weighed, dried at 105 °C until constant weight, and then weighed again to establish the SMC. Afterwards, the samples were processed for particle-size distribution (texture: sand, silt, and clay content) using a sedimentographer (Sedigraph 5100, manufactured by Micromeritics). The fine components of the soil (fraction with diameter < 2 mm) were subjected to chemical analyses using the following standard reference laboratory methods [24]: pH (in 1:2.5, soil: water suspension) was determined using the potentiometric method; organic matter (OM) was measured by combustion and CO_2 measurement, using an infrared detection cell; phosphorous (P_2O_5) and potassium (K_2O) were extracted by Egner–Riehm method, P_2O_5 was measured using colorimetric method, and K_2O was measured with a flame photometer; degree of base saturation (DBS), sum of the exchange bases (SEB; calcium—Ca^{2+}, magnesium—Mg^{2+}, sodium—Na^{+} and potassium—K^{+}) and cation exchange capacity (CEC) were extracted with ammonium acetate.

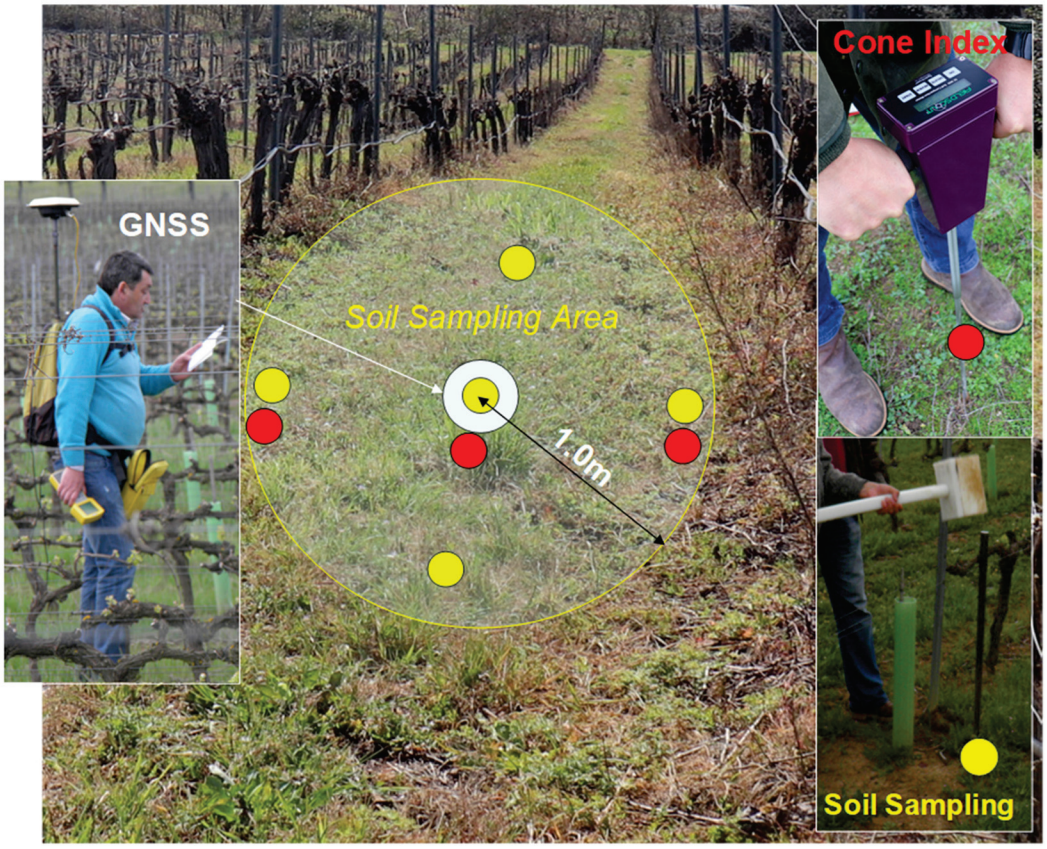


Figure 6. Soil sampling diagram: georeferentiation with global navigation satellite system (GNSS), soil sampling collection and cone index (CI) measurement.

2.4.2. Cone Index (CI) Measurements

Simultaneously with the collection of soil samples, and as part of the validation process (Figure 1), the soil resistance to penetration (Cone Index, CI, in kPa) was measured with a manual electronic cone penetrometer "FieldScout SC 900" (Spectrum Technologies, Aurora, IL, USA). In each sampling point, three CI measurements were carried out between 0–45 cm depth, one in the central point of the sampling area, and one in each side next to each row of plants (Figure 6). To minimize possible errors resulting from the uncertainty of maintaining a constant penetration rate during the determination, measurements were always carried out by the same experienced operator. Readings for all treatments were taken on the same day to avoid soil moisture variability, which can affect the resistance measurements [13,14].

After the field measurements, the following data processing was implemented: (i) a preliminary analysis was conducted to remove outliers from the data set; (ii) the mean CI value of measurements of each sampling area of each MZ was calculated for each depth of determination (range of 2.5 cm); (iii) the graphic representation of mean CI as a function of soil depth (0–45 cm) for each MZ was generated; (iv) the mean CI values of measurements of each sampling area of each MZ was calculated for the following depth ranges: 0–15 cm, 15–30, and 30–45 cm.

2.4.3. Multispectral Measurements by Remote Sensing

With the aim of monitoring the spatial variability of crop vegetative vigor, satellite images of the vegetative cycle of this vineyard in 2022 were retrieved (Figure 1). Sentinel-2 optical images (freely available from the European Space Agency, ESA), were used through the electronic platform "http://agromap.agroinsider360.com". For this work, Sentinel-2 band 4 (B4; 10 m spatial resolution; 665 nm), band 8 (B8; 10 m spatial resolution; 842 nm), band 8A (B8A; 20 m spatial resolution; 865 nm), and band 11 (B11; 20 m spatial resolution;

1610 nm), atmospherically corrected imagery, were extracted from the Copernicus data hub and used to calculate NDVI (Equation (1)) and NDWI (Equation (2)). Images were processed with open-source ORG/GDAL Python libraries. These data were obtained for NDVI pixels (10 m resolution) and NDWI pixels (20 m resolution). A preliminary processing was carried out on these records to remove outliers due to the presence of clouds.

$$\text{NDVI} = \frac{\text{B8} - \text{B4}}{\text{B8} + \text{B4}} \quad (1)$$

$$\text{NDWI} = \frac{\text{B8A} - \text{B11}}{\text{B8A} + \text{B11}} \quad (2)$$

In the period of the vineyard's greatest vegetative vigor (May–August) due to the favorable temperature and precipitation (Figure 4), four evaluation moments were considered, one at the end of each month (24 May, 28 June, 28 July, and 27 August), all from cloud-free satellite images. Figure 7 illustrates the vineyard in May 2022, where the contrast between the strong vigor of the canopy and the dry vegetation between the rows is visible.



Figure 7. The vineyard in May 2022: contrast between the strong vigor of the canopy and the dry vegetation between the rows.

In addition to the NDVI and NDWI maps for the referred dates, for the purposes of MZ validation, the average values of these indices in each MZ were calculated based in twenty sampling points used to soil collection.

2.5. Statistical Analysis of the Data

To assess the soil and crop spatial variability, descriptive statistical analysis (mean, standard variation, and range) was performed for the measured parameters.

The data of EC_a obtained by Veris sensor in September and in October were synchronized using the geographic co-ordinates of each point to evaluate the temporal stability of EC_a measurements. A combined data set was created in each date: each Veris data point obtained in September was combined with the nearest data point obtained in October based on GNSS co-ordinates. If a match in spatial co-ordinates was not found within a 2 m radius, that point was removed from the data set, a procedure like that used by Sudduth et al. [12]. A total of 1377 points were found to have common geographic co-ordinates in both surveys.

These sets of data were subjected to linear correlation analysis, carried out in the IBM SPSS statistical package (version 24, IBM Corp, Armonk, NY, USA) to obtain the Pearson correlation coefficients (r) using the method of minimum squares ($p < 0.05$).

With the aim of evaluating if three MZ were significantly different, with a 95% significance level ($p < 0.05$), since the normality in the data cannot be assumed, the Kruskal–Wallis nonparametric test and the Dunn post hoc test were used. Thus, the differences in the mean values of both soil properties and crop indices were considered.

3. Results

3.1. From Spatial Variability to the Definition of Management Zones (MZ)

The soil variability associated with the topography (Figure 3) and consequent solar exposure and microclimate, the variety of vine cultivars (Figure 2), and the seasonality of temperature and precipitation (Figure 4) are factors that induce spatial variability. The vine responds accordingly, highlighting different physiological expressions [2]. The NDVI (Figure 8) and NDWI (Figure 9) maps referring to the previous year's vegetative cycle (2022) show the evolution of the crop's vegetative vigor and demonstrate this spatial variability.

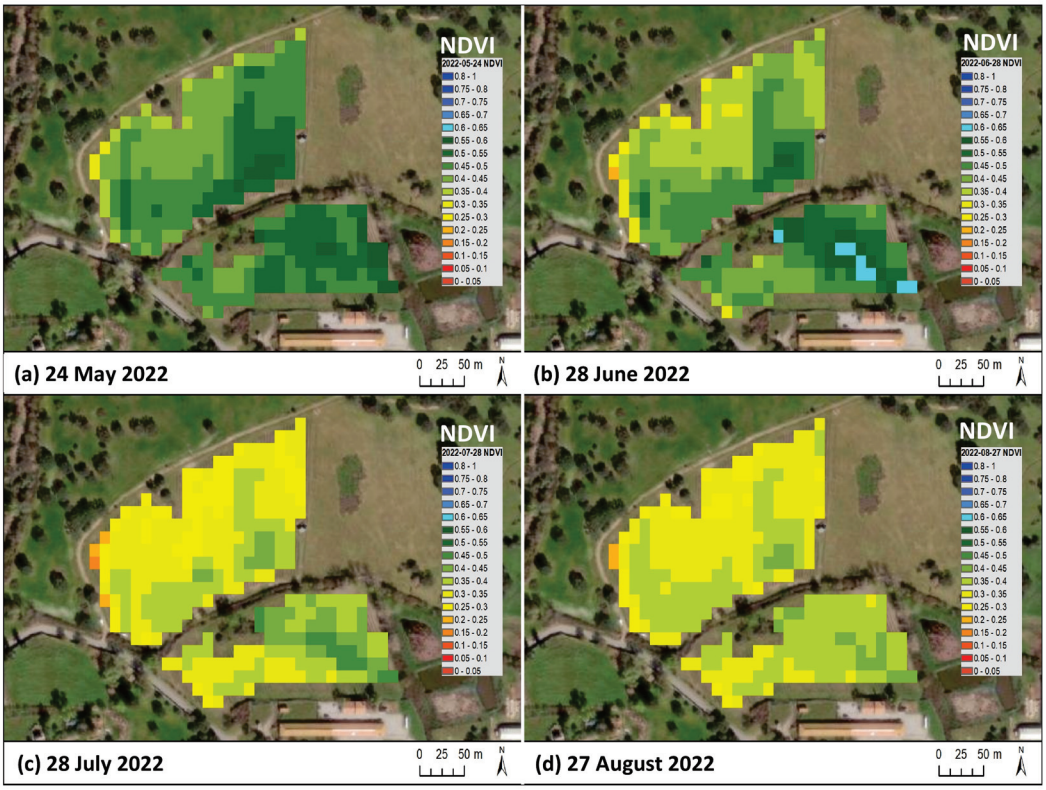


Figure 8. Normalized difference vegetation index (NDVI) maps over the vegetative cycle of 2022 (May, June, July, and August).

This study aims to assess whether the expeditious monitoring of EC_a allows capturing, in a temporally stable way, the soil spatial variability. The maps of Figure 10 show important EC_a spatial variability in the white grapes field. Nevertheless, both maps indicate a stable pattern of EC_a, with a decreasing gradient from east to west (Figure 10a,b) and, simultaneously, a lower expression of low EC_a (<1.5 $mS \cdot m^{-1}$) and a higher expression of high EC_a (>9.5 $mS \cdot m^{-1}$) in the September map (Figure 10a), relative to the October map (Figure 10b). This temporal stability of EC_a pattern is evidenced by the significant correlation between the measurements of September and the measurements of October (Figure 11; $R^2 = 0.7134$), after synchronization of the geographical coordinates of the two surveys ($n = 1377$).

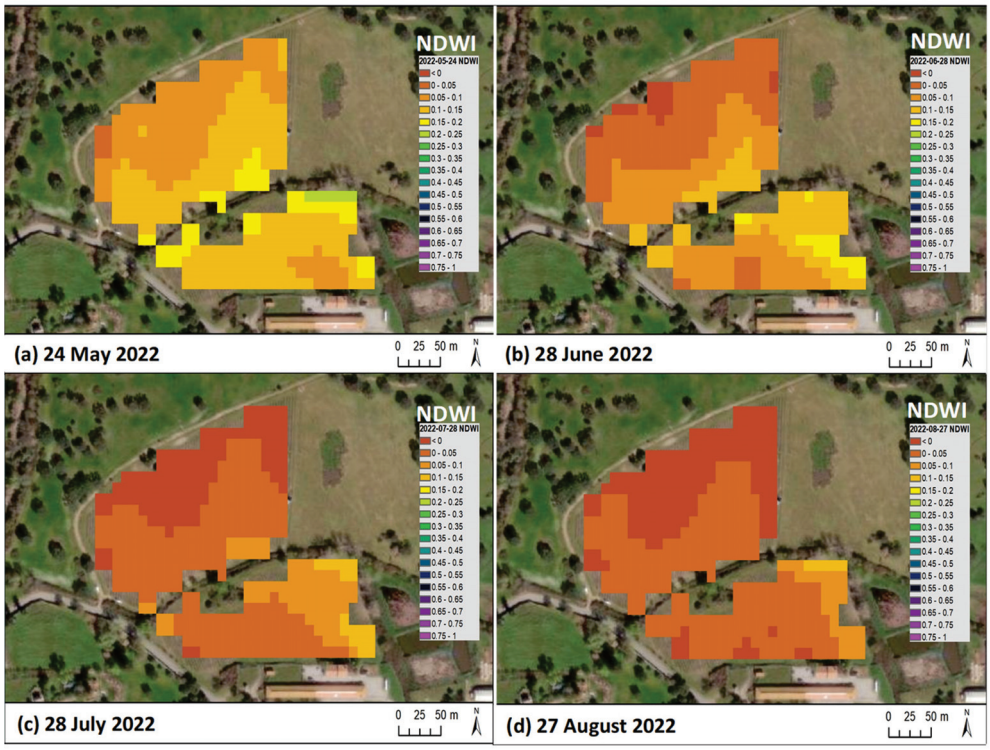


Figure 9. Normalized difference water index (NDWI) maps over the vegetative cycle of 2022 (May, June, July, and August).

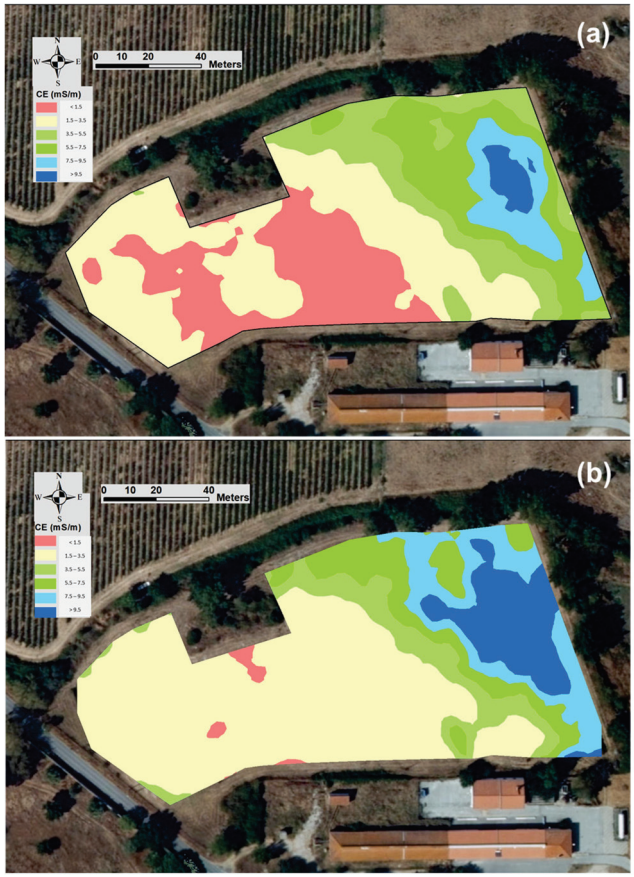


Figure 10. Average soil apparent electrical conductivity (EC_a) maps of white grapes field in September (**a**) and October (**b**) 2022.

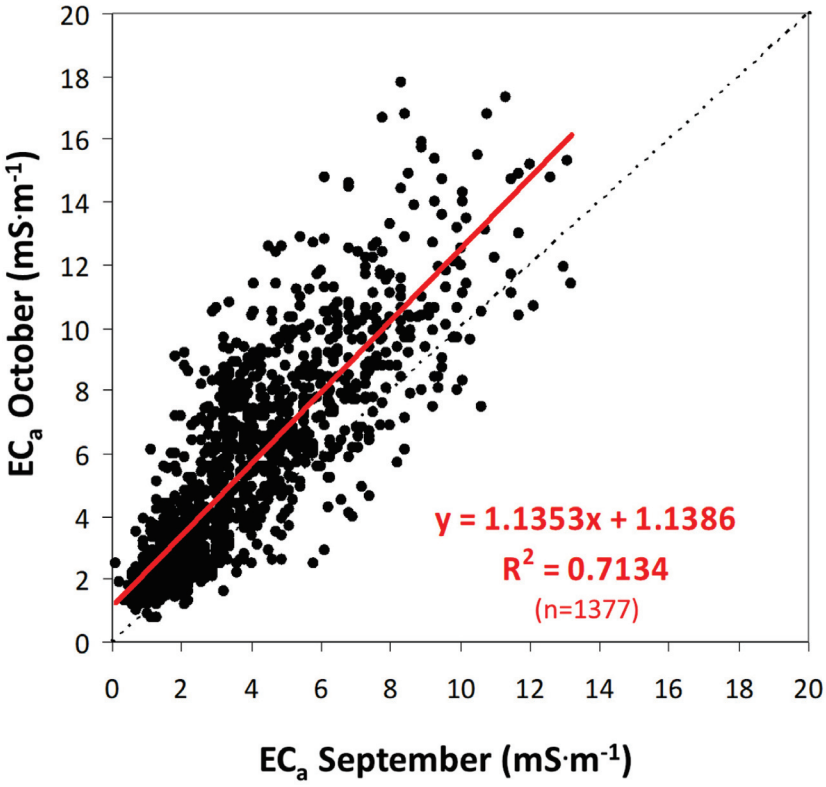


Figure 11. Soil apparent electrical conductivity (EC_a) of white grapes field: correlation between September and October measurements.

The EC_a spatial variability is common to the entire vineyard (Table 1), with a CV of around 65% in the white grapes field and 56% in the red grapes field. The SMC, however, shows less spatial variability, with a CV of around 29% in white grapes field and 8% in red grapes field (Table 1).

Table 1. Soil apparent electrical conductivity (EC_a) and soil moisture content (SMC) of vineyard in September and October 2022.

Parameter	Vineyard "W" (White Grapes)			Vineyard "R" (Red Grapes)		
Date	Mean ± SD	CV (%)	Range	Mean ± SD	CV (%)	Range
EC_a (mS·m^{-1})						
29 September	3.6 ± 2.4	67.6	0.1–13.2	–	–	–
24 October	5.3 ± 3.4	64.9	0.8–17.8	4.6 ± 2.6	55.8	0.3–17.1
SMC (%)						
29 September	14.6 ±4.1	28.1	10.3–19.5	–	–	–
24 October	17.7 ± 5.2	29.2	14.5–38.8	16.2 ± 1.3	8.1	14.0–18.7

SD—Standard deviation; CV—Coefficient of variation; EC_a—Soil apparent electrical conductivity; SMC—Soil moisture content.

The transformation of the EC_a (based on the October measurement) and altimetric maps into a MZ map by applying a geostatistical algorithm is presented in Figure 12. Three MZ were defined in white grapes field (less, intermediate, and more productive potential) and, based on the lower EC_a spatial variability and, especially on the SMC, only two MZ were defined in red grapes field (less and more productive potential).

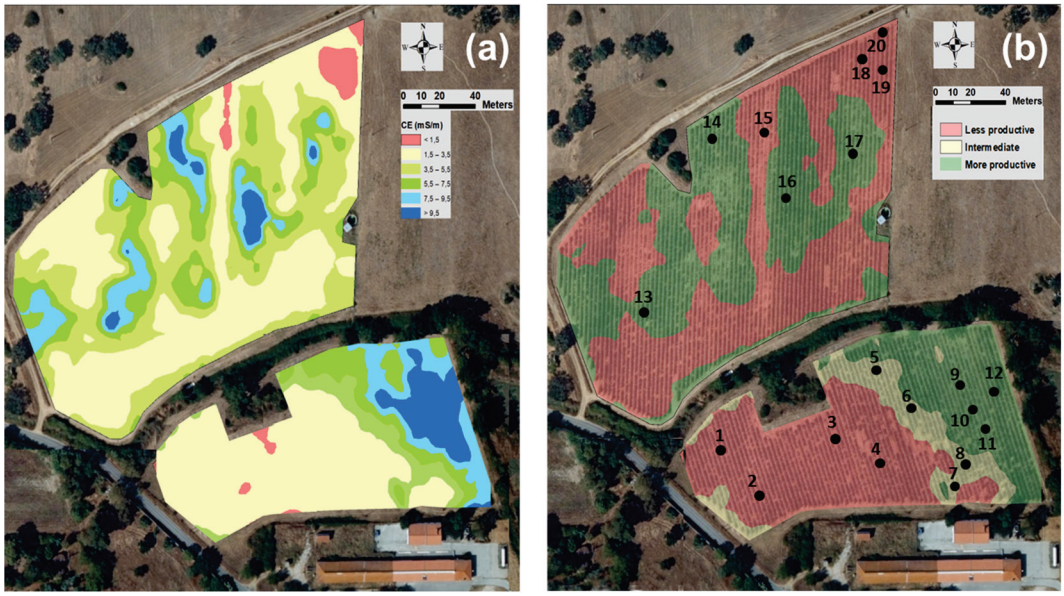


Figure 12. Soil apparent electrical conductivity (EC_a; (**a**)) and management zones (MZ; (**b**)) maps of white and red grapes fields (location of the twenty sampling points, twelve in white grapes area and eight in red grapes area).

3.2. Validation of Management Zones (MZ)

The results of soil sampling (Table 2) show that it is a coarse to medium textured soil (clay content of about 15%; textural classification between sandy loam and sandy clay loam) [19], with low OM content (especially in red grapes field, with 1%), pH close to neutral, with strong contrast between the two subfields in terms of phosphorus and potassium availability (extremely high in white grapes field and low in red grapes field). The spatial variability is very pronounced, with CV greater that 20–30% in practically all soil evaluated parameters, except for pH (CV of 7–9%) and sand content (CV of 11%).

Table 2. Characteristics of soil vineyard (0–0.30 m) in January 2023.

Soil Parameter	**Vineyard "W" (White Grapes)**			**Vineyard "R" (Red Grapes)**		
(25 January 2023)	**Mean ± SD**	**CV (%)**	**Range**	**Mean ± SD**	**CV (%)**	**Range**
Clay (%)	14.9 ± 4.8	32.2	10.4–23.9	14.6 ± 6.0	41.2	7.4–26.5
Silt (%)	13.6 ± 3.0	22.4	10.6–19.0	11.3 ± 2.4	20.9	7.8–15.4
Sand (%)	71.5 ± 7.6	10.7	58.4–78.7	74.0 ± 7.9	10.7	61.1–84.9
SMC (%)	17.6± 4.4	25.0	11.2–27.5	14.6 ± 3.7	25.2	7.2–18.5
OM (%)	1.7 ± 0.5	30.7	1.0–2.5	1.0 ± 0.2	23.6	0.7–1.5
pH	6.5 ± 0.5	7.0	5.8–7.1	6.1 ± 0.5	8.8	5.6–7.0
P_2O_5 ($mg.kg^{-1}$)	350.7 ± 209.1	59.6	101.4–722.6	28.9 ± 12.4	42.9	16.3–53.1
K_2O ($mg.kg^{-1}$)	118.7 ± 44.5	37.5	44.0–201.0	40.0 ± 24.7	61.8	10.0–78.2
DBS (%)	61.1 ± 33.6	55.0	13.5–121.9	61.4 ± 42.3	69.0	15.5–118.0
SEB ($cmol.kg^{-1}$)	8.2 ± 5.4	65.0	3.3–18.0	8.7 ± 7.1	81.1	2.0–19.7
CEC ($cmol.kg^{-1}$)	14.9 ± 5.9	39.5	8.2–28.0	18.2 ± 11.1	61.0	8.3–41.8

SD—Standard deviation; CV—Coefficient of variation; SMC—Soil moisture content; OM—Organic matter; P_2O_5—Assimilable phosphorous; K_2O—Assimilable potassium; DBS—Degree of base saturation; SEB—Sum of the exchange bases; CEC—Cation exchange capacity (CEC).

The validation of the MZ defined in each field (white and red grapes areas) based on the differences in the mean values of soil properties (Table 3) confirmed significantly higher values of clay, silt, SMC, OM, pH, DBS, SEB, and CEC and significantly lower values of sand in MZ with greater productive potential ("More").

Table 3. Validation of management zones (MZ): mean values of each soil property for MZ (less productive zone, "Less"; intermediate zone, "Inter."; and more productive zone, "More").

MZ	Clay (%)	Silt (%)	Sand (%)	SMC (%)	OM (%)	pH	P_2O_5 (mg·kg^{-1})	K_2O (mg·kg^{-1})	DBS (%)	SEB (cmol·kg^{-1})	CEC (cmol·kg^{-1})
"White"											
Less	12.2 a	11.3 a	76.5 a	14.7 a	1.2 a	6.0 a	204.7 a	113.8 a	34.0 a	3.7 a	14.2 a
Inter.	11.7 a	12.2 a	76.2 a	18.2 b	1.6 b	6.6 b	341.2 b	134.5 b	46.4 b	5.9 b	16.7 b
More	20.9 b	17.4 b	61.8 b	19.8 c	2.2 c	7.0 c	506.1 c	107.8 a	103.0 c	15.1 c	18.0 c
"Red"											
Less	10.8 a	9.6 a	79.6 a	12.1 a	0.9 a	5.7 a	38.0 a	47.8 a	23.2 a	2.5 a	15.1 a
More	18.5 b	13.1 b	68.5 b	17.0 b	1.2 b	6.6 b	19.9 b	33.0 b	99.5 b	15.0 b	21.3 b

MZ—Management zones; SMC—Soil moisture content; OM—Organic matter; P_2O_5_Assimilable phosphorous; K_2O—Assimilable potassium; DBS—Degree of base saturation; SEB—Sum of the exchange bases; CEC—Cation exchange capacity (CEC); Different letters indicate significant differences ($p < 0.05$) according to the Dunn test.

In terms of CI (Table 4; Figure 13; Figure 14), the results show a tendency for (i) higher values in the red grapes field than in the white grapes field; (ii) higher values in MZ with lower productive potential; (iii) higher values as depth increases; (iv) higher CV (25–70%) in the topsoil layer (0–15 cm). The graphical representation of the average CI in the topsoil layer (0–30 cm), in each MZ, as a function of mean SMC (Figure 15) confirms the inverse relationship between CI and SMC.

Table 4. Cone index (CI) of soil vineyard in three depths (0–15, 15–30, and 30–45 cm) in January 2023.

CI (kPa)	Vineyard "W" (White Grapes)		Vineyard "R" (Red Grapes)	
MZ—Depth (cm)	Mean ± SD	Range	Mean ± SD	Range
Less potential				
0–15	1278 ± 632	440–2091	1872 ± 511	1169–2467
15–30	2502 ± 184	2256–2673	2513 ± 183	2283–2730
30–45	2550 ± 308	2078–2928	3316 ± 340	2973–3967
Intermediate				
0–15	916 ± 639	172–1768	–	–
15–30	2072 ± 151	1941–2355	–	–
30–45	1698 ± 338	1265–2070	–	–
More potential				
0–15	902 ± 281	405–1143	1081 ± 274	677–1393
15–30	1139 ± 98	1030–1298	1802 ± 224	1587–2199
30–45	1122 ± 92	970–1220	2240 ± 302	1759–2557

SD—Standard deviation; CI—Cone index.

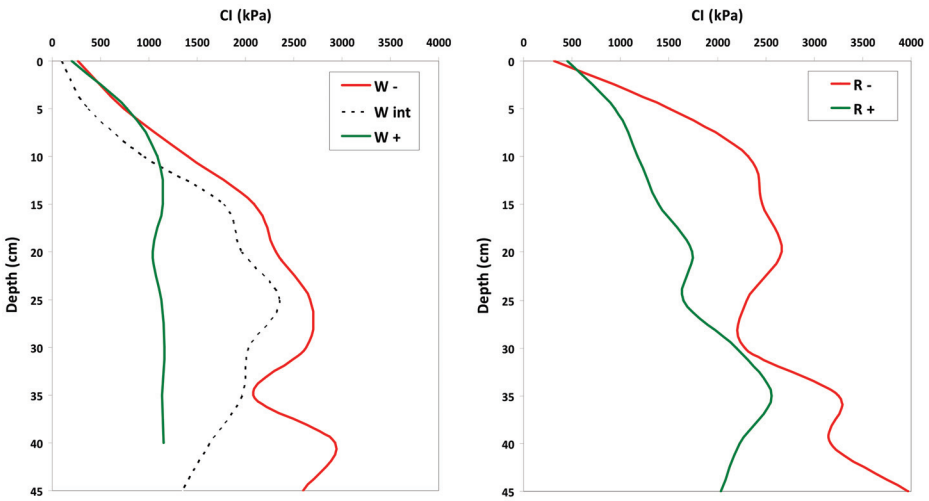


Figure 13. Average cone index (CI) profile as a function of soil depth (0–45 cm), for each MZ ("−", less, "int", intermediate, and "+", more productive potential) within each grape field ("W"—white; "R"—red).

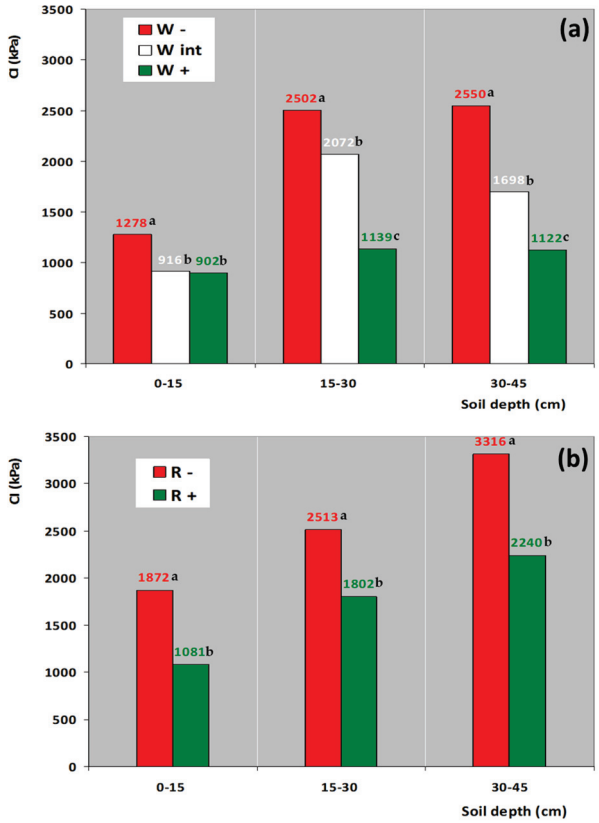


Figure 14. Average cone index (CI): mean values in each MZ ("−", less, "int", intermediate, and "+", more productive potential) and depth range (0–15, 15–30, and 30–45 cm), in white (**a**) and red grapes field (**b**). Different letters next to the mean values indicate significant differences ($p < 0.05$) according to the Dunn test.

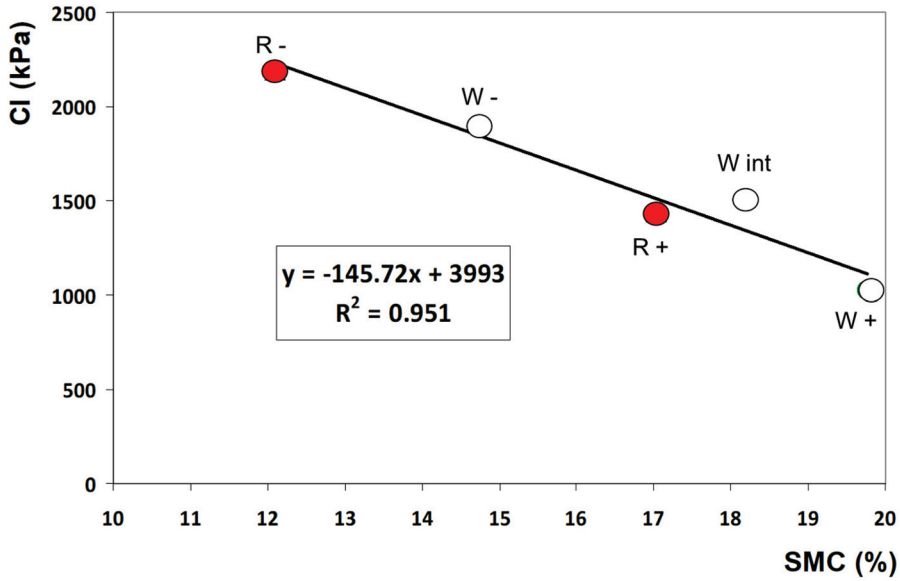


Figure 15. Average cone index (CI) in the 0–30 cm topsoil layer, in each MZ ("−", less, "int", intermediate, and "+", more productive potential) for each grape field (("W"—white; "R"—red), as a function of mean soil moisture content (SMC).

In terms of validating the MZ based on the vineyard vegetative vigor measured by RS indices, NDVI (Table 5; Figure 16) and NDWI (Table 6; Figure 17) in the vegetative cycle of 2022, the results show (i) a gradual decrease in NDVI and NDWI as the vegetative

cycle progresses; (ii) higher values in the white grapes field than in the red grapes field; (iii) higher values in MZ with more productive potential.

Table 5. Normalized difference vegetation index (NDVI) of vineyard (white and red grapes fields) in each MZ, on four dates in 2022 (24 May, 28 June, 28 July, and 27 August).

NDVI	Vineyard "W" (White Grapes)		Vineyard "R" (Red Grapes)	
MZ—Date (2022)	**Mean ± SD**	**Range**	**Mean ± SD**	**Range**
Less potential				
24 May	0.499 ± 0.030	0.469–0.538	0.446 ± 0.019	0.432–0.460
28 June	0.467 ± 0.022	0.447–0.498	0.378 ± 0.037	0.352–0.404
28 July	0.351 ± 0.015	0.343–0.374	0.306 ± 0.029	0.286–0.326
27 August	0.353 ± 0.003	0.350–0.357	0.320 ± 0.027	0.300–0.339
Intermediate				
24 May	0.539 ± 0.018	0.527–0.559	–	–
28 June	0.581 ± 0.047	0.527–0.613	–	–
28 July	0.452 ± 0.046	0.400–0.485	–	–
27 August	0.396 ± 0.010	0.384–0.402	–	–
More potential				
24 May	0.514 ± 0.022	0.488–0.526	0.483 ± 0.031	0.450–0.525
28 June	0.521 ± 0.004	0.519–0.526	0.426 ± 0.042	0.381–0.474
28 July	0.404 ± 0.003	0.400–0.405	0.331 ± 0.026	0.301–0.364
27 August	0.395 ± 0.010	0.384–0.401	0.338 ± 0.023	0.311–0.362

SD—Standard deviation; NDVI—Normalized difference vegetation index.

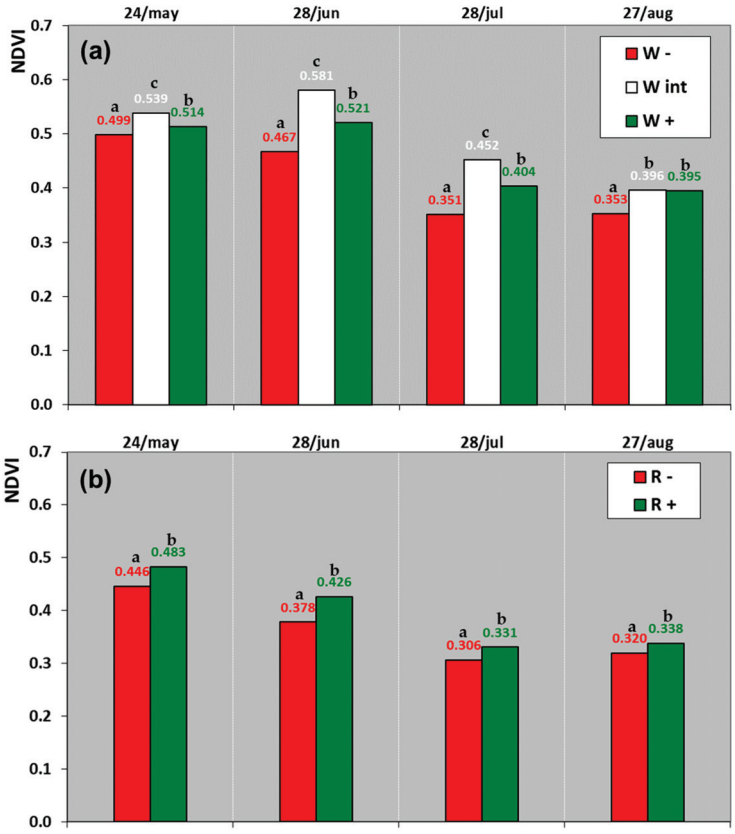


Figure 16. Average normalized difference vegetation index (NDVI) of vineyard: mean values in each MZ ("−", less, "int", intermediate, and "+", more productive potential) and date (24 May, 28 June, 28 July, and 27 August), in white (**a**) and red grapes field (**b**). Different letters next to the mean values indicate significant differences ($p < 0.05$) according to the Dunn test.

Table 6. Normalized difference water index (NDWI) of vineyard (white and red grapes fields) in each MZ, on four dates in 2022 (24 May, 28 June, 28 July, and 27 August).

NDWI	Vineyard "W" (White Grapes)		Vineyard "R" (Red Grapes)	
MZ—Date (2022)	**Mean ± SD**	**Range**	**Mean ± SD**	**Range**
Less potential				
24 May	0.126 ± 0.013	0.113–0.139	0.087 ± 0.013	0.078–0.097
28 June	0.061 ± 0.018	0.038–0.082	0.012 ± 0.003	0.010–0.014
28 July	0.016 ± 0.007	0.006–0.022	−0.010 ± 0.002	−0.012–(−0.009)
27 August	0.006 ± 0.005	0.000–0.013	−0.008 ± 0.006	−0.012–(−0.003)
Intermediate				
24 May	0.108 ± 0.015	0.095–0.126	–	–
28 June	0.117 ± 0.041	0.059–0.149	–	–
28 July	0.063 ± 0.031	0.022–0.097	–	–
27 August	0.029 ± 0.021	−0.002–0.041	–	–
More potential				
24 May	0.131 ± 0.008	0.121–0.137	0.101 ± 0.019	0.073–0.115
28 June	0.145 ± 0.014	0.137–0.165	0.041 ± 0.028	0.006–0.065
28 July	0.088 ± 0.001	0.087–0.089	0.005 ± 0.017	−0.017–0.020
27 August	0.054 ± 0.003	0.051–0.056	−0.003 ± 0.016	−0.020–0.011

SD—Standard deviation; NDWI—Normalized difference water index.

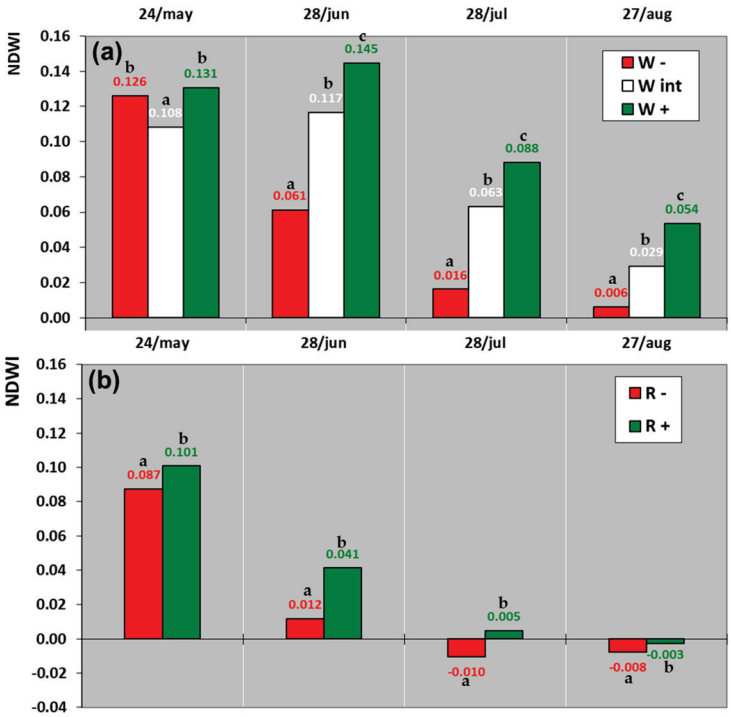


Figure 17. Average normalized difference water index (NDWI) of vineyard: mean values in each MZ ("−", less, "int", intermediate, and "+", more productive potential) and date (24 May, 28 June, 28 July, and 27 August), in white (**a**) and red grapes field (**b**). Different letters next to the mean values indicate significant differences ($p < 0.05$) according to the Dunn test.

4. Discussion

The interest in PV has been highlighted in several reviews published in recent years [2,10,25,26]. Research of PV have focused on four main areas: (i) evaluation of spatial variability; (ii) delimitation of MZ; (iii) development of variable rate technologies (VRT); and (iv) implementation of site-specific vineyard management [2]. This study focuses on the first two areas: to assess the soil spatial variability in a vineyard, and to define and validate MZ.

4.1. Spatial Variability

Spatial variability is the starting point that justifies the implementation of the PA concept [2]. The MZ represent the link between spatial variability and potential differentiated management [4,7].

Mobile soil EC_a measurements constitute one of the most efficient ways to quickly map soil spatial variability [7,17]. According to Ammoniaci et al. [2] and Rodriguez-Pérez et al. [27], EC_a could save time and resources during the planning and establishment of new vineyards and, also, during monitoring and management of established vineyards. The CV of EC_a obtained in this study (about 60%) classifies this parameter as having high spatial variability [5] and, therefore, is a potential indicator of the soil characteristics, which suggest the convenience of defining different MZ [7]. In this study, terrain elevation was also used in MZ delineation due to its impact on water flow and accumulation, as well as redistribution of soil mineral particles and OM, and, therefore, on crop growth and development [4,6]. Other works have sought to complement the EC_a information with other parameters, namely crop vegetative vigor. Esteves et al. [9], for example, associated the NDVI measurement, obtained from the Sentinel-2 satellite images, with EC_a to define three zones of differentiated vine management. Serrano et al. [28] also associated the EC_a with NDVI and NDWI to define three MZ, but in pasture management.

Although several factors may contribute to the variability of vineyard development (soil, topography, grape varieties, etc.) [3], the NDVI (Table 5) showed a relatively low CV (<10%) on all assessment dates, which may reflect, on the one hand, the uniform cultural operations carried out throughout the vineyard (e.g., pruning, shoot and grape thinning and, especially, canopy management) [18], but mainly the sampling procedure used in the MZ validation, based only on 20 sampling points and not on the whole vineyard area (contrary to what happened in the EC_a measurement, carried out practically continuously). In contrast, the NDVI and NDWI maps (Figure 8; Figure 9, respectively), represent the entire area of the vineyard and attest to the expression of the variability identified by the EC_a measurement.

In addition to spatial variability, another important characteristic that should be assessed in a PV process is the within-field temporal stability of spatial patterns [29]. Measuring EC_a is frequently conducted to reveal this spatial soil heterogeneity. Various studies have demonstrated the possibilities for significant changes in the measured quantities over time with relatively stable spatial structure representations [30]. One of the great advantages of EC_a measurement is its temporal stability, maintaining the spatial pattern over time, so it only needs to be measured once in the medium term [31]. In this study, the EC_a surveys of September and October led to similar EC_a maps (Figure 10), with a strong R^2 (0.7134; Figure 11). The positive effect of SMC (higher in October that in September, which reflects an accumulated precipitation of 75 mm in the week preceding the measurement in October, while in the week preceding the measurement in September the accumulated precipitation was only 18 mm) in EC_a is reported in several works [2,26]. This temporal stability allows decision making in post-processing, which avoids the technological complexity of real-time variable application systems.

4.2. Validation of Management Zones (MZ)

The EC_a can help to guide the sampling for the purpose of characterizing the spatial variability [11]. The validation of the defined MZ was carried out by smart sampling of (i) soil parameters (texture, SMC, pH, OM, phosphorous, potassium, DBS, SEB, CEC, and CI); and (ii) normalized indices (NDVI and NDWI) obtained by RS.

Areas with higher EC_a led to MZ with more productive potential, and vice-versa (Figure 12). The validation showed that the zones with more productive potential present a soil profile (0–30 cm depth) with higher clay, moisture, OM, pH, DBS, SEB, and CEC contents, and lower sand content and CI values (this last parameter in all the depth classes that were considered: 0–15, 15–30, and 30–45 cm), which is reflected in higher vine vegetative vigor (higher NDVI and NDWI). The relationship between EC_a and soil

texture has been documented in several studies [2,7,9,11,17,32], positively correlated with the finer texture component, clay, and negatively correlated with the coarser textures such as coarse and fine sands [7,17,25], even leading to the indication of specific reference values of EC_a for certain soil characteristics (rocky substrate, sand, clay, water, etc.) [2]. Mean EC_a of 3–6 $mS \cdot m^{-1}$ (Table 1) classify the soil of this vineyard as coarse-textured and dryland soils [14], typical of this region of South of Portugal. The relationship between EC_a and others soil physical and chemical properties, namely OM content [2], SMC [17,27,29], CEC, pH, exchangeable magnesium, and other soil nutrients [9], has been demonstrated across a wide range of soils [12]. In arid or semiarid regions, for example, moisture availability is the primary factor that controls land productivity; therefore, SMC should be considered as one of the most important factors to delimit management zones, which is very dependent on the topography of the field [33]. In this study, however, the main macronutrients phosphorus and potassium (P_2O_5 and K_2O, respectively) did not follow the trend defined by the MZ in white grapes area, with mean contents very high in intermediate MZ (Table 3). This result makes it difficult to transpose these MZ maps to fertilization prescription maps. Since these abnormally high values of P and K occur only in the white grapes area (Table 2), where the OM values are also much higher (mean of 1.7% versus 1.0% in red grapes area), the proximity of a pigsty (upstream of the white grape vineyard and of a water flow line) could be the origin of this unexpected pattern, which may have led the geostatistical algorithm to set an intermediate MZ in this field. In this case, the intermediate MZ can be an indicator of this external effect (drainage of effluents from intensive livestock production) on topsoil spatial variability. If fertilization was based on a composite sample of the entire vineyard area of 3.3 ha, as is common practice in traditional agriculture in the region, the average values of P and K would be adequate (more than 100 $mg \cdot kg^{-1}$) and therefore would not justify fertilization, however, spatial analysis shows, for example, that the red grapes area has low P and K values (around 30–40 $mg \cdot kg^{-1}$), which requires P and K fertilization.

The inverse correlation between EC_a and soil compaction (zones with more productive potential present systematically lower CI values) is in line with several other works [13,14,27,34,35], some of them even suggesting the potential of EC_a as a rapid alternative for assessing soil compaction [34,35].

Relatively to validation of MZ through of RS indices, the results of Ferrer et al. [3] suggest that NDVI could be a useful tool for defining and categorizing zones (high, medium, and low) within the vineyards in order to establish site-specific management practices according to the grapevine needs. Tardaguilla et al. [10], in a review paper about the use of smart technologies in viticulture, reinforces the relevance of vine vigor maps from previous years in designing site-specific management strategies for the upcoming year. Comparetti and Silva [16], on the other hand, demonstrated the usefulness of NDVI and NDWI obtained from the Sentinel-2 satellite images to identify the same three levels of vegetative vigor (high, medium, and low) and support decision making for vintage segmentation, which makes it possible process different quality grapes to produce different wines, differentiating the grapes on the basis of their potentiality and typicality, highlighting the "terroir effect" over the years [2]. Comparetti and Silva [16] also foresee the use of NDVI and NDWI in variable rate fertilizer application, however, point out the challenge to be overcome in PV in terms of establishing correlations between plant vegetative vigor, crop yield, wine quality, and soil parameters in order to produce spatially variable input application maps that can increase crop yields. The successful results documented by Hubbard et al. [17] in a vineyard, using pixel-by-pixel as well as block-by-block comparisons lay the groundwork for future research directions; for example, the significant correlation between soil texture, EC_a, and NDVI suggest that vegetation properties during the growing season could be estimated, and possibly predicted, through soil texture or EC_a information.

4.3. Study Limitations and Perspectives

Given that this is an exploratory study, carried out in a relatively restricted area of vineyard (3.3 ha), under specific soil and climatic conditions, further studies, in different soil types and different regions should be conducted.

An important note should be considered: several studies showed a direct correlation between NDVI and crop yield components, suggesting that the zones with the highest vigor are also the highest yielding. However, in the vineyard the issue is complex, with zones of low vigor (NDVI) tending to produce higher quality wine in some instances [36]. Since the main aim of modern oenology is to produce wines of recognized quality and typically, which can then be differentiated in the market, it is essential to consider that the potential quality of wine is established in the vineyard [5]. Therefore, it will be interesting in the next campaign to evaluate the impact of this topsoil spatial variability on productivity (yield maps) and, especially, on grape quality and, consequently, on wine quality, using a segmented harvest to clarify the practical impact and the agronomic significance of this MZ delineation.

It is also fundamental to develop algorithms to evaluate the agronomic significance of this classification (MZ) and establish more general methods of mapping and quantifying variable input prescriptions based in EC_a.

The closing of the PA cycle by agricultural machinery (namely fertilizer distributors or sprayers), based on prescription maps (built from MZ), or other means, provides a rigorous variable rate application [37]. Despite the existence of this technologies to improve and maximize efficiency of inputs and profitability of individual fields [38], the scattered and interlaced MZ delineation can be challenging for the farmer, and in some cases, it might be advisable to unify the MZ to larger working units in order to simplify the operationalization of the process.

5. Conclusions

The results of this study showed that the use of fast and easy tools for measuring and mapping EC_a and altimetry allows capturing, in a temporally stable way, the spatial variability of physical (texture, compaction, moisture) and chemical (pH, OM, degree of base saturation, exchange bases, and cation exchange capacity) topsoil (0–30 cm) characteristics, leading to the definition and validation of zones (MZ) of high and low productive potential. These MZ may be relevant when designing new vineyards or replanting existing vineyards, e.g., for the selection of the most adapted cultivars, or for field orientation (sun exposure, drainage, etc.) for a given "terroir". This approach can also be useful for a more-informed decision-making process for site-specific management of inputs and guide viticultural practices. The ability to map the soil spatial variability allows grape growers to move from a random soil sampling to an optimized methodology based on MZ (smart soil sampling).

It will be important to validate these results in other conditions, with different soil types or in different regions, extending the database and so, improve the process for prescribing spatially differentiated inputs.

Author Contributions: Conceptualization, J.S. and V.M.; methodology, J.S., V.M., R.R., L.P., S.S., J.M.d.S., L.L.P. and F.J.M.; software, J.S. and F.J.M.; validation, J.S.; formal analysis, J.S., L.L.P. and F.J.M.; investigation, J.S., V.M. and R.R.; data curation, J.S. and J.M.d.S.; writing—original draft preparation, J.S.; writing—review and editing, J.S., S.S. and F.J.M.; visualization, J.S. and S.S.; supervision, J.S.; project administration, J.S.; funding acquisition, J.S. All authors have read and agreed to the published version of the manuscript.

Funding: This work was funded by National Funds through FCT (Foundation for Science and Technology) under the Project UIDB/05183/2020.

Data Availability Statement: The data presented in this study are available on request from the corresponding author. The data are not publicly available because they are part of a dissertation project that is ongoing (not completed).

Conflicts of Interest: The authors declare no conflict of interest.

References

1. Casson, A.; Ortuani, B.; Giovenzana, V.; Brancadoro, L.; Corsi, S.; Gharsallah, O.; Guidetti, R.; Facchi, A. A multidisciplinary approach to assess environmental and economic impact of conventional and innovative vineyards management systems in Northern Italy. *Sci. Total Environ.* **2022**, *838*, 156181. [CrossRef]
2. Ammoniaci, M.; Kartsiotis, S.-P.; Perria, R.; Storchi, P. State of the art of monitoring technologies and data processing for Precision Viticulture. *Agriculture* **2021**, *11*, 201. [CrossRef]
3. Ferrer, M.; Echeverría, G.; Pereyra, G.; Gonzalez-Neves, G.; Pan, D.; Mirás-Avalos, J.M. Mapping vineyard vigor using airborne remote sensing: Relations with yield, berry composition and sanitary status under humid climate conditions. *Prec. Agric.* **2020**, *21*, 178–197. [CrossRef]
4. Córdoba, M.; Bruno, C.; Costa, J.; Balzarini, M. Subfield management class delineation using cluster analysis from spatial principal components of soil variables. *Comput. Electron. Agric.* **2013**, *97*, 6–14. [CrossRef]
5. Unamunzaga, O.; Besga, G.; Castellón, A.; Usón, M.A.; Chéry, P.; Gallejones, P.; Aizpurua, A. Spatial and vertical analysis of soil properties in a Mediterranean vineyard soil. *Soil Use Manag.* **2014**, *30*, 285–296. [CrossRef]
6. Verdugo-Vásquez, N.; Acevedo-Opazo, C.; Valdés-Gómez, H.; Pañitrur-De la Fuente, C.; Ingram, B.; García de Cortázar-Atauri, I.; Tisseyre, B. Identification of main factors affecting the within-field spatial variability of grapevine phenology and total soluble solids accumulation: Towards the vineyard zoning using auxiliary information. *Precis. Agric.* **2022**, *23*, 253–277. [CrossRef]
7. Moral, F.; Terrón, J.; Silva, J.M. Delineation of management zones using mobile measurements of soil apparent electrical conductivity and multivariate geostatistical techniques. *Soil Tillage Res.* **2010**, *106*, 335–343. [CrossRef]
8. Sams, B.; Bramley, R.G.V.; Sanchez, L.; Dokoozlian, N.; Ford, C.; Pagay, V. Remote sensing, yield, physical characteristics, and fruit composition variability in Cabernet Sauvignon vineyards. *Am. J. Enol. Vitic.* **2022**, *73*, 93–105. [CrossRef]
9. Esteves, C.; Fangueiro, D.; Braga, R.P.; Martins, M.; Botelho, M.; Ribeiro, H. Assessing the contribution of ECa and NDVI in the delineation of management zones in a vineyard. *Agronomy* **2022**, *12*, 1331. [CrossRef]
10. Tardaguila, J.; Stoll, M.; Gutiérrez, S.; Proffitt, T.; Diago, M.P. Smart applications and digital technologies in viticulture: A review. *Smart Agric. Technol.* **2021**, *1*, 100005. [CrossRef]
11. Bottega, E.L.; Marin, C.K.; Oliveira, Z.B.d.; Lamb, C.D.C.; Amado, T.J.C. Soil density characterization in management zones based on apparent soil electrical conductivity in two field systems: Rainfeed and center-pivot irrigation. *AgriEngineering* **2023**, *5*, 460–472. [CrossRef]
12. Sudduth, K.A.; Kitchen, N.R.; Bollero, G.A.; Bullock, D.G.; Wiebold, W.J. Comparison of electromagnetic induction and direct sensing of soil electrical conductivity. *Agron. J.* **2003**, *95*, 472–482. [CrossRef]
13. Serrano, J.; Marques, J.; Shahidian, S.; Carreira, E.; Marques da Silva, J.; Paixão, L.; Paniagua, L.L.; Moral, F.; Ferraz de Oliveira, I.; Sales-Baptista, E. Sensing and mapping the effects of cow trampling on the soil compaction of the montado Mediterranean ecosystem. *Sensors* **2023**, *23*, 888. [CrossRef] [PubMed]
14. Serrano, J.; Carreira, E.; Shahidian, S.; de Carvalho, M.; Marques da Silva, J.; Paniagua, L.L.; Moral, F.; Pereira, A. Impact of deferred versus continuous sheep grazing on soil compaction in the Mediterranean Montado ecosystem. *AgriEngineering* **2023**, *5*, 761–776. [CrossRef]
15. Pias, O.H.C.; Cherubin, M.R.; Basso, C.J.; Santi, A.L.; Molin, J.P.; Bayer, C. Soil penetration resistance mapping quality: Effect of the number of subsamples. *Acta Sci.* **2018**, *40*, e34989. [CrossRef]
16. Comparetti, A.; Marques da Silva, J.R. Use of Sentinel-2 satellite for spatially variable rate fertiliser management in a Sicilian vineyard. *Sustainability* **2022**, *14*, 1688. [CrossRef]
17. Hubbard, S.S.; Schmutz, M.; Balde, A.; Falco, N.; Peruzzo, L.; Dafon, B.; Léger, E.; Wu, Y. Estimation of soil classes and their relationship to grapevine vigor in a Bordeaux vineyard: Advancing the practical joint use of electromagnetic induction (EMI) and NDVI datasets for precision viticulture. *Precis. Agric.* **2021**, *22*, 1353–1376. [CrossRef]
18. Gatti, M.; Garavani, A.; Squeri, C.; Diti, I.; Monte, A.; Scotti, C.; Poni, S. Effects of intra-vineyard variability and soil heterogeneity on vine performance, dry matter and nutrient partitioning. *Precis. Agric.* **2022**, *23*, 150–177. [CrossRef]
19. FAO. *World Reference Base for Soil Resources*; Food and Agriculture Organization of the United Nations, World Soil Resources Reports N 103; FAO: Rome, Italy, 2006.
20. Peel, M.C.; Finlayson, B.L.; McMahon, T.A. Updated world map of the Köppen-Geiger climate classification. *Hydrol. Earth Syst. Sci.* **2007**, *11*, 1633–1644. [CrossRef]
21. Höppner, F.; Klawonn, F.; Kruse, R.; Runkler, T.A. *Fuzzy Cluster Analysis*; Wiley: Chichester, UK, 1999.
22. Fridgen, J.J.; Kitchen, N.R.; Sudduth, K.A.; Drummond, S.T.; Wiebold, W.J.; Fraisse, C.W. Management Zone Analyst (MZA): Software for subfield management zone delineation. *Agron. J.* **2004**, *96*, 100–108. [CrossRef]
23. Tagarakis, A.; Liakos, V.; Fountas, S.; Koundouras, S.; Gemtos, T.A. Management zones delineation using fuzzy clustering techniques in grapevines. *Precis. Agric.* **2013**, *14*, 18–39. [CrossRef]
24. AOAC. *Official Methods of Analysis of AOAC International*, 18th ed.; AOAC International: Arlington, VA, USA, 2005.
25. Barriguinha, A.; de Castro Neto, M.; Gil, A. Vineyard yield estimation, prediction, and forecasting: A systematic literature review. *Agronomy* **2021**, *11*, 1789. [CrossRef]
26. Cataldo, E.; Fucile, M.; Mattii, G.B. A review: Soil management, sustainable strategies and approaches to improve the quality of modern viticulture. *Agronomy* **2021**, *11*, 2359. [CrossRef]

27. Rodríguez-Pérez, J.R.; Plant, R.E.; Lambert, J.-J.; Smart, D.R. Using apparent soil electrical conductivity (ECa) to characterize vineyard soils of high clay content. *Precis. Agric.* **2011**, *12*, 775–794. [CrossRef]
28. Serrano, J.; Shahidian, S.; Da Silva, J.M.; Paixão, L.; Calado, J.; De Carvalho, M. Integration of soil electrical conductivity and indices obtained through satellite imagery for differential management of pasture fertilization. *AgriEngineering* **2019**, *1*, 567–585. [CrossRef]
29. Serrano, J.; Shahidian, S.; Marques da Silva, J. Apparent electrical conductivity in dry versus wet soil conditions in a shallow soil. *Precis. Agric.* **2013**, *14*, 99–114. [CrossRef]
30. Su, A.S.M.; Adamchuk, V.I. Temporal and operation-induced instability of apparent soil electrical conductivity measurements. *Front. Soil Sci.* **2023**, *3*, 1137731.
31. Serrano, J.; Shahidian, S.; Paixão, L.; Marques da Silva, J.; Moral, F. Management zones in pastures based on soil apparent electrical conductivity and altitude: NDVI, soil and biomass sampling validation. *Agronomy* **2022**, *12*, 778. [CrossRef]
32. Corwin, D.; Lesch, S. Apparent soil electrical conductivity measurements in agriculture. *Comput. Electron. Agric.* **2005**, *46*, 11–43. [CrossRef]
33. Farrel, M.; Leizica, E.; Gili, A.; Noellemeyer, E. Identification of management zones with different potential moisture availability for sustainable intensification of dryland agriculture. *Precis. Agric.* **2023**, *24*, 1116–1131. [CrossRef]
34. Krajco, J. Detection of Soil Compaction Using Soil Electrical Conductivity. Master's Thesis, Cranfield University, Silsoe, UK, 2007; pp. 3–92.
35. Pentos, K.; Pieczarka, K.; Serwata, K. The relationship between soil electrical parameters and compaction of sandy clay loam soil. *Agriculture* **2021**, *11*, 114. [CrossRef]
36. Kasimati, A.; Psiroukis, V.; Darra, N.; Kalogrias, A.; Kalivas, D.; Taylor, J.A.; Fountas, S. Investigation of the similarities between NDVI maps from different proximal and remote sensing platforms in explaining vineyard variability. *Precis. Agric.* **2023**, *24*, 1220–1240. [CrossRef]
37. Katz, L.; Ben-Gal, A.; Litaor, M.I.; Naor, A.; Peres, M.; Bahat, I.; Netzer, Y.; Peeters, A.; Alchanatis, V.; Cohen, Y. Spatiotemporal normalized ratio methodology to evaluate the impact of field-scale variable rate application. *Precis. Agric.* **2022**, *23*, 1125–1152. [CrossRef]
38. Fabiani, S.; Vanino, S.; Napoli, R.; Zajicek, A.; Duffkova, R.; Evangelou, E.; Nino, P. Assessment of the economic and environmental sustainability of Variable Rate Technology (VRT) application in different wheat intensive European agricultural areas. A Water energy food nexus approach. *Environ. Sci. Policy* **2020**, *114*, 366–376. [CrossRef]

Disclaimer/Publisher's Note: The statements, opinions and data contained in all publications are solely those of the individual author(s) and contributor(s) and not of MDPI and/or the editor(s). MDPI and/or the editor(s) disclaim responsibility for any injury to people or property resulting from any ideas, methods, instructions or products referred to in the content.

environments

MDPI

Review

Artificial Reefs around the World: A Review of the State of the Art and a Meta-Analysis of Its Effectiveness for the Restoration of Marine Ecosystems

Carolina Bracho-Villavicencio [1,2], Helena Matthews-Cascon [1] and Sergio Rossi [1,2,3,*]

[1] Graduate Program in Tropical Marine Sciences (PPGCMT), Institute of Marine Sciences (LABOMAR), Laboratory of Marine Invertebrates of Ceará (LIMCe), Biology Department, Science Center, Campus of Pici, Federal University of Ceará, Fortaleza 60440-900, Brazil; cbvillavi@gmail.com (C.B.-V.); helenamc@gmail.com (H.M.-C.)
[2] Underwater Gardens International, C/Paris 207, 08008 Barcelona, Spain
[3] Department of Biological and Environmental Sciences and Technologies (DiSTeBA), University of Salento, Via Monteroni s/n, 73100 Lecce, Italy
* Correspondence: sergio.rossi@unisalento.it

Abstract: Over the past decade, there has been increasing interest in marine restoration, requiring a consideration of various approaches for optimal success. Artificial reefs (ARs) have been employed for marine restoration and fisheries management, but their effectiveness in restoring ecosystems lacks well-defined ecological criteria and empirical evidence. A systematic review of the literature on ARs articles between 1990–2020, a meta-analysis of their effectiveness based on the similarity of species composition with reference natural reefs (NRs), as well as bias risk analyses were carried out. Research on ARs primarily focused production of marine communities (n = 168). There are important information gaps regarding socioeconomic aspects; design, materials, and disposal in the selected habitats; legal, management, and planning aspects considering long-term monitoring. Regarding effectiveness, few articles (n = 13) allowed comparisons between ARs and NRs, highlighting the need to apply proper reference sites in AR implementations. Meta-analysis showed that ARs are not similar to reference NRs (p = 0.03, common effect and p = 0.05 random effect models). However, a high index of heterogeneity (88%) suggests that this relation may be influenced by factors other than the reef type. Thus, further analysis can disguise variables conditioning this AR–NR similarity as a measure of restoration for degraded marine ecosystems.

Keywords: artificial reefs; active restoration; effectiveness; marine ecosystems; coastal management

Citation: Bracho-Villavicencio, C.; Matthews-Cascon, H.; Rossi, S. Artificial Reefs around the World: A Review of the State of the Art and a Meta-Analysis of Its Effectiveness for the Restoration of Marine Ecosystems. *Environments* **2023**, *10*, 121. https:// doi.org/10.3390/environments10070121

Academic Editors: Dibyendu Sarkar, Rupali Datta, Prafulla Kumar Sahoo and Mohammad Mahmudur Rahman

Received: 20 June 2023
Revised: 10 July 2023
Accepted: 11 July 2023
Published: 14 July 2023

Copyright: © 2023 by the authors. Licensee MDPI, Basel, Switzerland. This article is an open access article distributed under the terms and conditions of the Creative Commons Attribution (CC BY) license (https://creativecommons.org/licenses/by/4.0/).

1. Introduction

The loss of biodiversity, complexity, and long-living biomass of organisms has been evidenced in marine systems during the last two decades, but has been stressed at an alarming rate of change especially during the last three-four years [1]. The systematic destruction of complexity due to direct and indirect factors [2] brought entire nations and communities to take seriously the regenerative programs at large scale, such as the targets of the Restoration Decade promoted by the UN to enhance the recovery of biodiversity, blue carbon and associated biomass [3]. As we know, restoration programs are not new, but the upscaling and its feasibility on the long term has become a target that needs a good selection of methods, money, and political commitment [4].

Artificial reefs (ARs) are intentionally placed benthic structures intended to protect, enhance or restore components of marine ecosystems [5], while they can concentrate populations of living marine resources [6]. They have historically been implemented as a strategy to increase the production of species of recreational and commercial interest, receiving more attention since the 1980s [7]. However, ARs may be also considered an

active restoration tool for degraded marine ecosystems that have lost habitat heterogeneity, biomass, diversity, richness, and abundance of marine organisms due to various impacts such as mining, oil and gas extraction, trawling, overfishing and pressure for tourism [8,9]. In addition, there are incidental or accidental ARs such as anti-drag tools [10], ARs for coastal erosion protection [11], tourism pressure mitigation on corals [12], etc. Altogether, they can be complementary tools to speed up programs of marine ecosystem restoration [9].

Nevertheless, ARs were often based on structures that were not designed to meet the specific needs of the biota [9]. Therefore, several problems have been associated with AR deployments such as attraction and depletion of species stocks with socioeconomic conflicts [13,14], pollution, and toxicity [15], changes in species composition with the possible introduction and dispersion of exotic species [16], and changes in the hydrodynamics of the site [17].

In this sense, a great conflict about ARs is evident, there are great contrasts between the theory and its application [18], which gives a questionable position to the use of ARs as a restoration measure by some scientific groups [19]. However, it is known that, when implemented correctly, ARs represent a tool that assists in the active restoration of highly degraded reef ecosystems [20]. All this leads us to question ourselves about what causes a successful AR deployment to achieve the necessary restoration of marine ecosystems.

A restoration project aims to re-establish a functioning ecosystem that emulates the reference ecosystem at a comparable ecological age [21]. When a system is restored, it may be applying silviculture methods [22], but the idea is not to completely recover the ancient habitat (which is impossible), but to give enough complexity to the habitat to enhance the biodiversity and biomass lost; thus, restoration must have a very long-term vision [4]. It has to be highlighted, however, that many of the actual plans are not based on an ecosystem engineering approach [23]. A proper assessment of a restoration program should preferably include a BACI (before/after–control/impact) type analysis in which control sites and restored/degraded sites should be compared before and after an impact, in order to verify a change in the intervention site [8]. While it is often unpredictable to know if an impacted site has been monitored and has baseline data that allows for a before-and-after comparison, a comparison of control and impacted sites is more often available when evaluating the success of a restoration program.

Furthermore, studies that have hypothesized the success of ARs based on changes in abundance, biomass, diversity, and species richness [24] could disguise a failed restoration, as their metrics usually identify variations of these metrics but cannot reflect changes in the composition of species, ignoring relevant problems related to ARs such as changes in community structure and invasive species introduction [25]. Thus, we would know that a restoration project is successful if the reef's ecosystems intervened by ARs achieved a similar state of the reference "healthy" natural reefs (NRs) in terms of species composition, an approach recently applied through meta-analysis in terrestrial ecosystems, known as the species composition–ecosystem function relationship [26,27].

There are also important gaps regarding ARs characteristics and their implementation, which can be filled by reviewing results from published data and analyzing them for an integral evaluation of the social, economic, and environmental aspects [9,18,28].

Although there are some recent systematic reviews on ARs, they focus on the restoration of a limited geographic region [29], or they review qualitative measures of effectiveness based on self-reports and other characteristics of AR implementations [30]. Thus, there is no global statement on the application of ARs, or a measurement of effectivity can be biased, once it was not based on qualitative and verifiable results. The aim of the present study is to address a global measurement of AR restoration success in coastal and marine ecosystems, using quantitative contrasted data on species composition between ARs and their reference NRs. In addition, we have compiled a general historical description of the ARs over the past thirty years around the world.

2. Materials and Methods

2.1. Overview of ARs Deployments around the World

A systematic literature review (SLR) was carried out following the PRISMA Protocol [31] on indexed research articles from 1990 to 2020. The literature search was performed in Scopus® and Web of Science® (WOS) databases using the term "artificial reef" as keywords in the title of the article of any language on 1st March 2020.

We compiled 1265 documents (Figure S1), then studies were selected based on exclusion criteria adapted from [31] (Table 1). For the first exclusion criterion, books, theses, dissertations, technical reports, reviews, and opinion articles were excluded, as information in this type of literature is not granted by per-review validation. Second, duplicate indexed articles were excluded and considered as a single document. Third, articles were excluded if the full document was not available online or, after reading the abstract, if the article did not address the implementation of ARs as its main subject.

Table 1. Inclusion and exclusion criteria taken into account for the systematic literature review.

Inclusion Criteria	Exclusion Criteria
Indexed original articles	Non-indexed articles, reviews, perspective or opinion articles, scientific notes, books, book chapters, dissertations, thesis, conference abstracts, technical reports
Published articles between the years 1990–2020	Articles that were not published between the years 1990–2020
Articles that evaluated the implementation of ARs, which were available online and with DOI	Articles that did not assess the implementation of ARs or that were not available online or without DOI

Information was extracted from each reference including author's name and year of publication; study title; main theme of the study; newspaper name; financing information; country of publication; and the number of times it was cited. In addition, to describe general aspects of ARs around the world, the articles were classified by: (a) type of AR: primary purpose of structure was or was not an AR, such as accidentally sunk vessels, ports, oil platforms, jetties, wharves, breakwaters; (b) purpose of the AR: purpose of creation reported; (c) material used for AR construction; (d) shape of the AR, (e) type of study: observational or experimental; (f) type of ecosystem: marine, freshwater or estuarine ecosystems; (g) type of substrate: environment on which the AR was installed; (h) ecosystem degradation reported; (i) type of impact; (j) active restoration action taken, when reported: coral transplantation, larval resettlement, gardening, etc.; (k) depth of implantation; (l) area of AR system (km^2); (m) AR module area (m^2) and (l) module weight (kg); (n) distance from the coast (km); (o) exploratory variable evaluated; (p) time of AR implantation (years); (q) time of AR monitoring (months); (r) sampling method; (s) involvement of the community: civil, commercial, scientific and/or governmental entity; (t) within a protected area; (u) restricted fishing; (v) control sites: NRs, non-reef sites or the same site prior to implementation; (w) funding; and (x) country of implementation of the AR.

2.2. Restoration Effectiveness in ARs Deployments

Articles that were included for the description of global AR deployment were examined by applying additional exclusion criteria: Articles where AR sites were not compared with reference healthy NRs as appropriate control or reference sites, as well as articles that did not report data by species for ARs and NRs sites separately, and those that did not have an appropriate number of replicates of ARs and NRs sites, were excluded (Table 2).

Table 2. Inclusion and exclusion criteria taken into account for the meta-analysis.

Inclusion Criteria	Exclusion Criteria
Original articles that allow quantitative comparisons between ARs and more than two NRs or spatial replicas of NR sites	Articles that do not allow quantitative comparisons between ARs and more than two NRs or spatial replicas of NR sites
Articles with adequate reference NRs regarding the characteristics of the ARs implementation site	Articles without adequate reference NRs regarding the characteristics of the ARs implementation site
Articles that report data on complete species composition, by taxonomic groups or functional groups in absolute or relative abundance for each AR and NR separately	Articles that do not report data on integral species composition, by taxonomic groups or functional groups in absolute or relative abundance for each AR and NR separately

In addition, due to the low number of articles that fulfill our criteria, we ran a new SLR following the PRISMA protocol for SLR and a meta-analysis, and population, intervention, control, and outcome (PICO) strategy was performed. We applied the PICO strategy using the string search in the Scopus database on May 2023 as follows: (TITLE (reef) OR TITLE (reefs) AND TITLE (natural) AND TITLE (artificial) AND TITLE-ABS-KEY (species)). The search resulted in 53 articles (Figure S2), to which the same exclusion criteria were applied for screening (Table 2).

Metrics for species composition used to calculate the Bray–Curtis similarity index were absolute or relative density, absolute or relative abundance, and proportional frequency of occurrence, among others [32]. Afterward, species composition lists were transcribed for AR and NR sites from studies that met the conditions (Table 2). We used the Bray–Curtis index to compare reported species composition similarity between ARs and NRs, due to it having several numerical qualities that make it suitable for comparing species or functional groups composition across ecological communities [32].

The similarity indices were calculated by making all possible comparisons between all NRs sites within a study as a control. Comparisons between each AR site and NRs were also calculated for each study as intervened. The mean and standard deviation of the similarity indices were calculated for control (similarity between NRs) and for intervened sites (similarity between RNs and ARs). Meta-analysis and bias analysis as funnel plot and Egger's test were performed in order to ensure the robustness of the meta-analysis using the RStudio software with the "meta" package.

Effect measure values (mean differences) around zero were desired as a successful outcome of the restoration, that is, ARs species compositions achieved were to be similar to those of reference NRs. Negative values should mean that ARs did not achieve the same species composition of reference NRs. Positive values should mean that ARs hold more species than reference NRs, which is probably associated with invasive species presence [26,27].

3. Results

3.1. Research on ARs between 1990–2020

From 502 articles screened, 281 articles showed that there was interest in ARs worldwide during the period 1990–2020 around the world, with a particular spike in 1994 and two increases in the years of 1998 and 2002 (Figure S3). Among the pioneer countries, Japan shows up in the implementation of ARs, along with the United States and Italy. In general, the country that led the studies on ARs in the world between 1990–2020 was the United States (n = 78), followed by Australia (n = 23), Italy (n = 24), Israel (n = 18), and China (n = 17) (Figure 1). While the number of surveys is not an identical reflection of the number of AR installations in the world, it does represent the interest of countries in evaluating ARs.

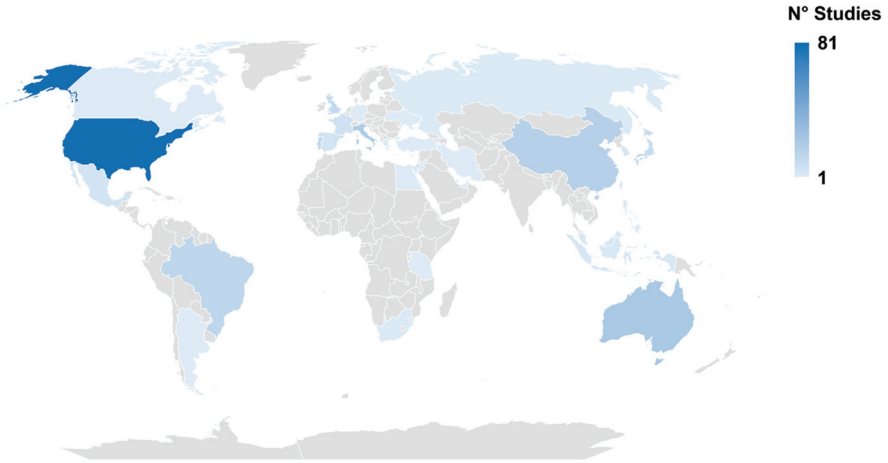


Figure 1. Distribution of AR surveys around the world included in the SLR between 1990–2020.

Most of the research (60%, n = 168) on ARs included in this review was focused on biomass production (Figure S4), including the association of biological and ecological aspects of species of commercial and food interest with ARs, such as changes in biomass, abundance, richness, species diversity, the effect of ARs on patterns of use, occupation, and the behavior of fish populations and communities, as well as topics related with aquaculture and the attraction–production dilemma. The production topic was followed by the topics of mitigation/restoration, including transplantation of corals and other invertebrates, larval resettlement of fish and corals, mitigation of habitat loss, by invasive species, by pollution of materials and mining; and effectivity/management with 12%, respectively (n = 33). Next, topics of monitoring and impacts represented 4.6% and 5%, respectively (n = 13 and 14, Figure S4). Additionally, the type of research that predominated was experimental, particularly during the period of 1990–2010, giving way in the last decade to observational research (Figure S5). The latter was often the report of continued long-term monitoring of implementations cited in previous years within the same period 1990–2020.

Research on ARs over the years 1990–2020 has focused on assessments of marine population and community structure. During the 1990s–2000s, 65% of the studies focused on production in terms of abundance, biomass, and richness of commercial species increases, while 10.6% of the studies evaluated impacts, 8.2% focused on themes of restoration and mitigation, and 7% of the articles evaluated effectiveness and management (Figure 2). In the following period 2001–2010, interest in production decreased to 60.8%, leading to more interest in studies of mitigation/restoration (12.4%) and effectivity and management (10.3%). During the 2001–2010 period, studies about impacts decreased to 4%, and a new topic related to the disposition and orientation of ARs was studied. More recently, 2011–2020 period, interest in production-focused studies dropped slightly (54.5%), while interest in effectiveness and management studies grew by 17.2%, as did efforts to restore and mitigation of marine ecosystems (14.1%). There has also been an increase in studies related to the development of monitoring methods; however, it is noteworthy a drop in studies in which ARs are related to environmental impacts, as well the low numbers of studies focused on socioeconomic aspects, abiotic changes, the development of new material technologies.

While production was the most popular topic, this was mainly evaluated using ichthyofauna as the explanatory variable (60%) (Figure 3). Studies of ichthyofauna (n = 101) were followed by studies that evaluated the fauna in general (n = 52), including studies that evaluated infauna, epifauna, and endofauna, as well as microfauna, meiofauna, and macrofauna (Figure 3). Twenty-one studies evaluated cnidarians, where corals were the main explanatory variable. Other variables less studied in association with ARs were changes of abiotic factors, socioeconomic aspects, aspects of the ARs, impact indicators such as microplastic and heavy metals, and biotic variables such as aquatic flora, crustaceans,

malacofauna, ascidians, plankton, bryozoans, echinoderms, and fungus (Figure 3). This highlights the need to diversify research and integrate key aspects in the assessment and management of ARs for restoration programs.

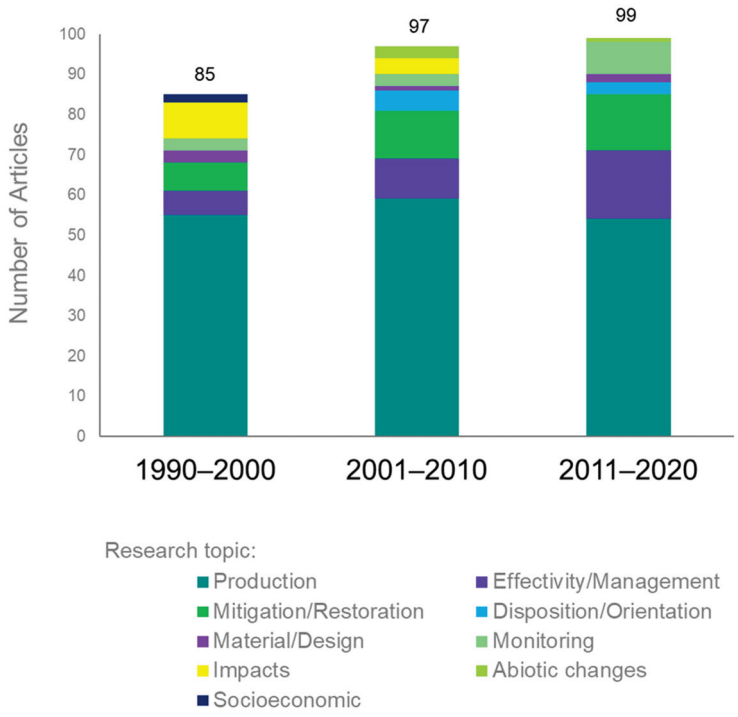


Figure 2. Main research topics found in studies of artificial reefs during the last three decades.

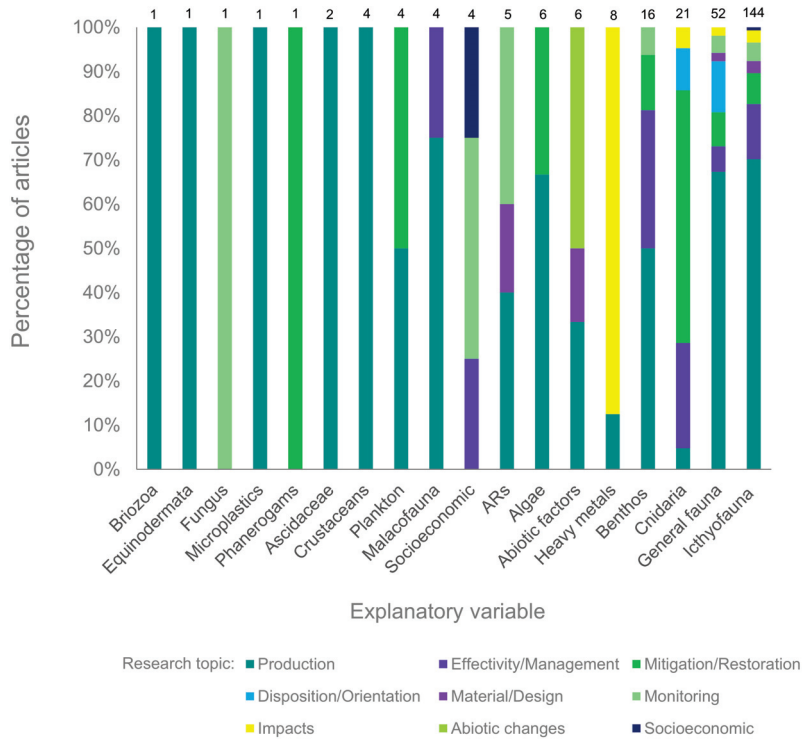


Figure 3. Exploratory variables used in studies regarding artificial reefs between 1990–2020.

On the other hand, if ARs will be installed as a restoration measure, it should be declared first which type of previous impact the ARs will restore in the deployment area. However, there is a high number of studies that did not report a previous impact in the

deployment area (84%, *n* = 236). Between the 16% of articles describing the impact of the site (*n* = 45), most were related to the fishing sector (17.8%), mentioning trawling, crops, overfishing, and the urban and economic development sector (17.8%). Heavy metals were reported as pollutants from the construction materials of ARs (13.3%), as well as articles evaluating the risk of trophic imbalance, including the introduction of invasive species (9%). Noteworthy is the low frequency of reports of other impacts, no less important for the conservation of reef ecosystems, such as climate change, oil spills, coral mining, plastic pollution, and accidental/incidental sinking of vessels (Figure 4).

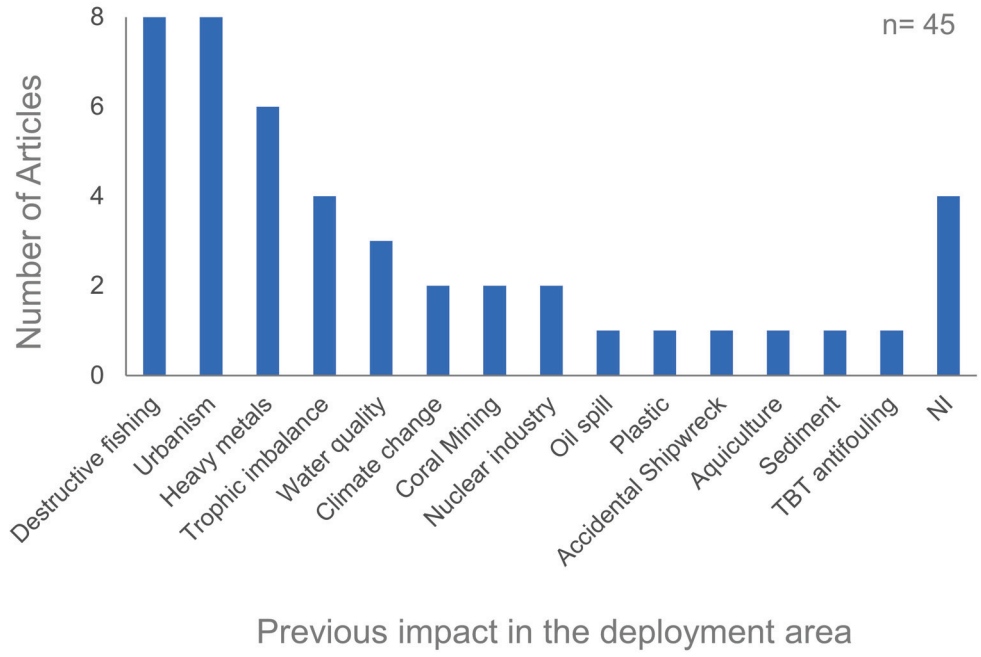


Figure 4. Reported impacts in studies related to ARs during the period of 1990–2020. NI = Studies that declared the site as impacted, but did not specify the impact type or cause of impact.

In addition, the time of deployment of ARs or "AR age", as well as the duration of the monitoring in the studies are important aspects as they can help to understand the evolution of the ecosystems where the ARs are implanted. Most studies had monitoring for up to 2 years, with an important number of articles where ARs were monitored between 1 and 12 months. Monitoring intervals of up to 4 years, 8 years, or more, were less frequent (Figure 5). In addition, 22 articles did not inform the monitoring time. Furthermore, most of the studies did not report the ARs age (*n* = 78). The age of the ARs varied between new structures of 1 month and old structures of more than 100 years, and the latter were mainly shipwrecks (Figure 5). There was a considerable number of ARs up to 42 years old; however, older ARs were less frequent in this review.

In addition, the preferred sampling method for monitoring ARs was the visual census (34.5%), followed by manual collection (17.4%), and photos or videos (8%, Figure S6). Methods with more advanced technologies were less frequent, but present from the late 1990s onwards, such as telemetry using ecosonar (*n* = 16, 5.7%) and remotely operated vehicles (ROV) or baited remote underwater video (BRUV) (*n* = 15, 5.3%). The collection through gillnet fishing was equally frequent with 14 articles. It is worth mentioning that few articles applied more than one sampling method, and there were 10 articles that omitted information about the data collection method (Figure S6).

Regarding monitoring of ARs, there was also a low consideration of control sites as a reference in the evaluation of ARs (23.5%), that is, almost 80% of the articles (*n* = 213) did not apply at least one control or reference site when monitoring the ARs progress (Figure 6). Of those articles that used control sites, 31 used non-reef ecosystems as reference sites, 26 articles applied RNs as reference sites, and 6 used NR and other non-reef ecosystems

as reference sites. Another way to assess a change in an ecosystem is to obtain a record prior to the intervention of AR as a control, which was the case of a few articles (n = 7). Most articles applied a single reference site (n = 34), and fewer articles used 2 (n = 13) or more than 3 reference sites (n = 21, Figure 6). In addition, only 16 articles reported to study ARs within protected areas, and 6 articles signaled the restriction of fishing in ARs, while 13 evaluated ARs with use for fishing and 268 did not inform the fishing status.

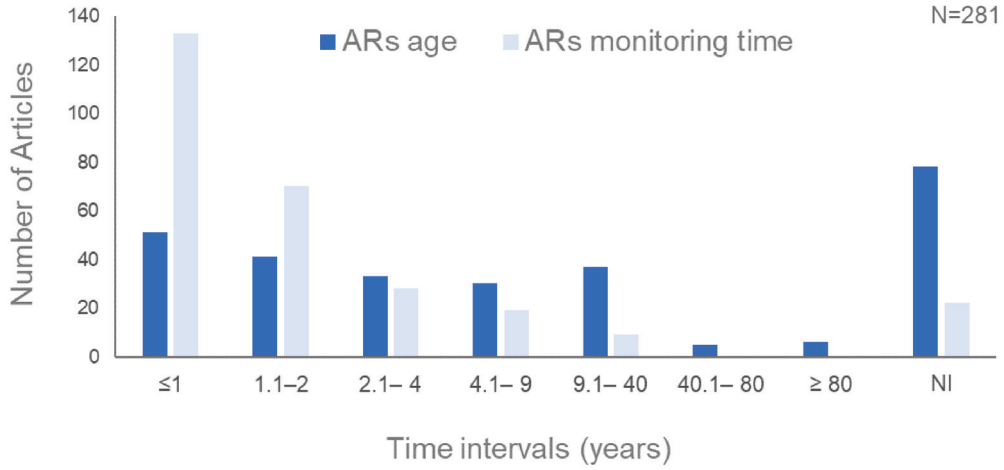


Figure 5. Time of deployment and monitoring of ARs in studies between 1990–2020.

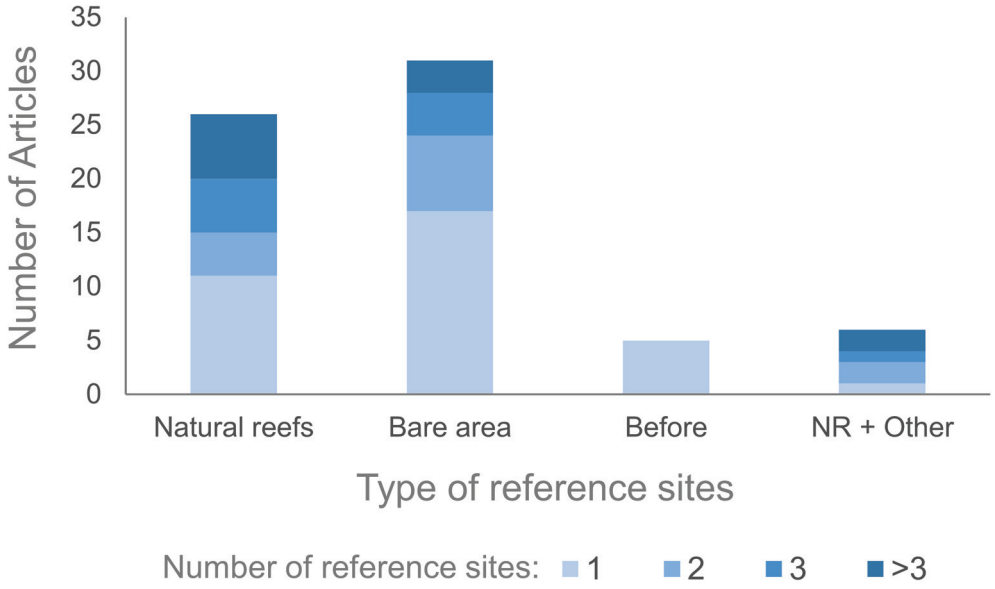


Figure 6. Types and number of reference sites taken into account in studies of ARs between 1990–2020.

Apart from the authors of the articles evaluated, other members of different communities were involved in the work effort for the development of most of the studies (74.3%) in which was recognized the participation of one or more personalities. In addition, there were few reports of implementations in which the civil community was involved (0.5%), with few exceptions of articles that assessed socioeconomic aspects through interviews with fishermen or administrators of ARs. On the other hand, in addition to the scientific community, commerce/industry and government agencies were among the most involved (9 and 3%, respectively). Other partnerships involving two or more societies represented 32.4% of studies, thus, demonstrating the need for interdisciplinary and logistical support in this type of enterprise (Figure S7).

Likewise, a large number of funded articles (79%), compared to research that did not report funding (21%), demonstrates the almost mandatory requirement for financial support

where one or more governmental, scientific, and commercial agencies have invested in research on ARs (Figure S8).

3.2. Characteristics of ARs in the World

Structures purposely built for the enhancement of marine ecosystems, here called ARs, were most cited (n = 209). The largest proportion of these types of ARs was constructed of concrete, rocks, metal, and concrete with metal, and a combination of various materials, although a considerable number did not specify the material used for the ARs studied (n = 17). Few articles reported the use of biogenic materials (n = 5), such as shells, corals, among others. Structures not intentionally constructed for marine ecosystems enhancement were metallic or wooden vessels sunk deliberately or accidentally, as well as ports, jetties, piers, oil platforms, cars, breakwaters, and dams, which were less frequently reported and whose materials were not always defined (n = 13, Figure 7).

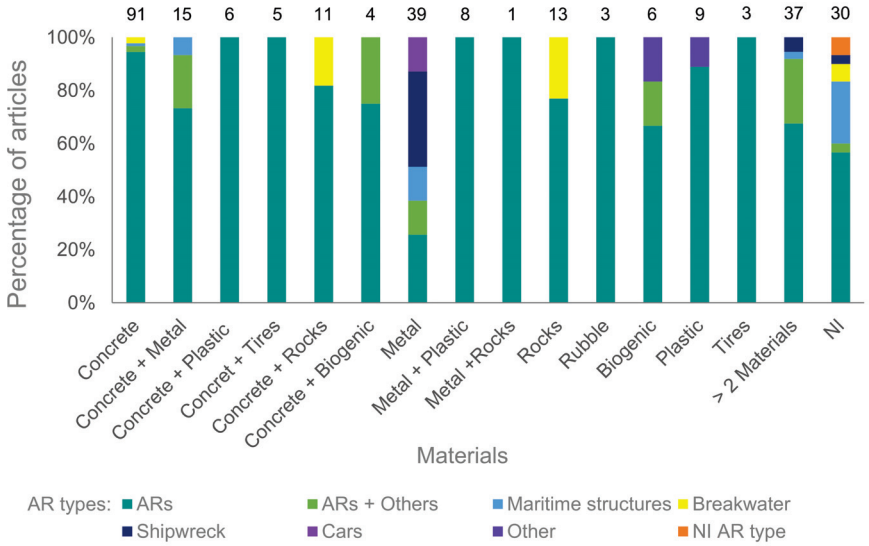


Figure 7. Types and materials of ARs used in studies during the period of 1990–2020.

Although many articles did not directly or indirectly report the purpose for which the AR was created, studies related to ecological or fishery research, evaluating the effect of ARs in promoting, increasing or changing the abundance, diversity or richness of species associated with structures, predominated (n = 168, Figure 8). These were classified as ARs for production purposes (60%), followed by ARs for restoration or conservation (7.5%), and by ARs for mitigation or compensation (5.3%, Figure 8).

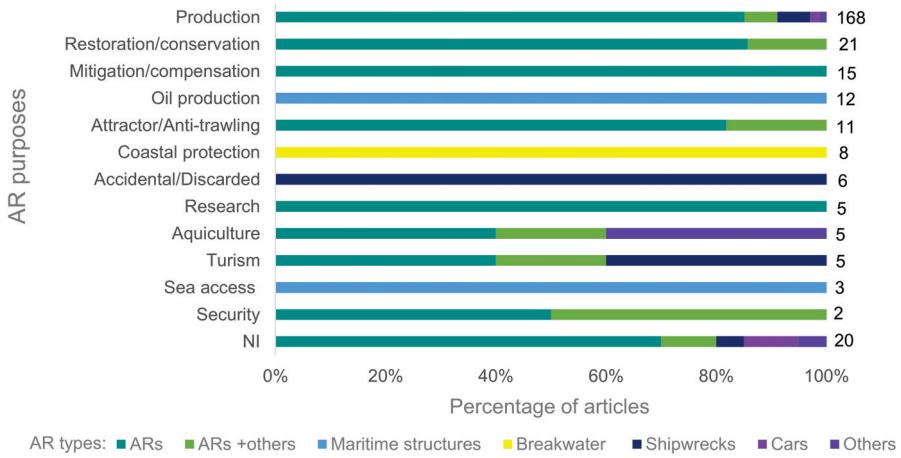


Figure 8. Purposes for which ARs were constructed during the period of 1990–2020.

There are some types of ARs that have not been initially created for it. For example, certain structures such as oil platforms, jetties, ports, piers, breakwaters, etc., despite their creation purpose, inevitably excerpt as incidental ARs, as they provide a new immerse surface that serves for marine fauna and flora to colonize. There were also other types of structures, such as vessels whose purpose of creation was transport, however purposely or accidentally sunken, in which the increase in biomass and diversity was sought for commercial, food, or recreational purposes. Thus, structures whose creation was accidental, or for coastal protection, maritime uses, cultivation of organisms, security, conservation, and scientific research, were less frequent (Figure 8).

Among the studies that had declared the ARs purpose of restoration and mitigation, some applied supplementary techniques for active restoration such as transplantation of coral, algae, and other taxa, larval and juvenile resettlement, among others (7.8%, n = 22, Figure 9).

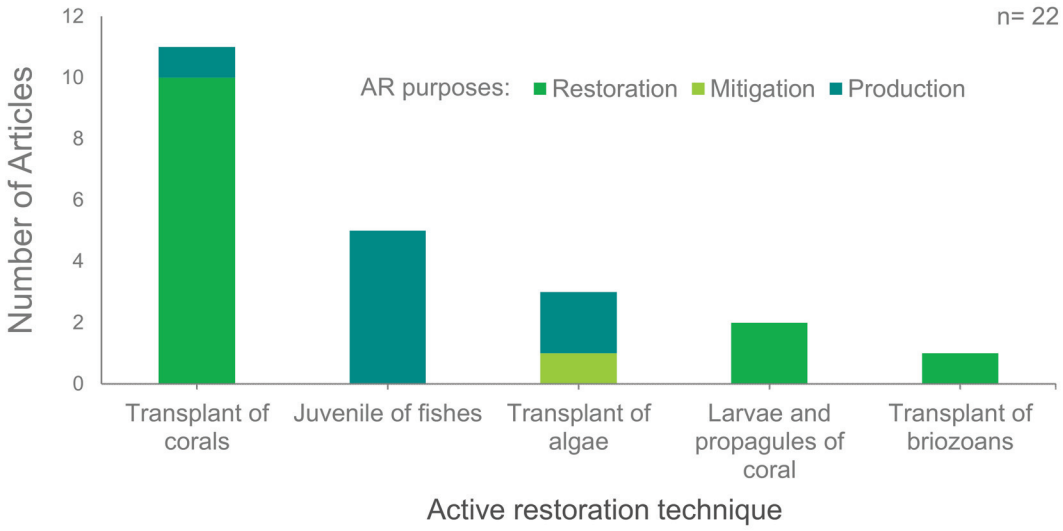


Figure 9. Active restore support actions during the period of 1990–2020.

The marine environment was almost exclusive in the use of ARs (n = 241); however, there were a few studies citing deployments in estuaries (n = 13) and rivers (n = 3), and 2 studies as laboratory experiments. The type of bottom, where the structures were installed, was predominantly sand (n = 62), muddy sand (n = 29), phanerogams (n = 13), reef (n = 11), or rocky (n = 10, Table S1).

Furthermore, most articles that reported distance from the coast (43%, n = 121) show that most structures were located no more than 5 km offshore (n = 77), followed by articles whose ARs were between 5 and 10 km (n = 19), by those between 11–50 km (n = 17), and those located more than 50 km offshore (n = 8). However, there were 160 articles in which this information was not provided. Likewise, the implementation depths also varied between the first 10 m (n = 79), as far as 20 m (n = 95), 30 m (n = 48), 40 m (n = 13), and deeper depths up to the 130 m (n = 7), and 39 articles did not report the depth where ARs were deployed.

In addition, the size of AR systems, as well as the size of each module, varied and depended on the purpose of their use. Large-scale AR systems were infrequent and usually consisted of various types of ARs including those built with primary and secondary purposes (systems with ARs of various materials, vessels, bridge debris, and cars) as disposal material and/or with a special purpose to promote the production of marine organisms. Medium-scale ARs were also used for production, usually built primarily for that. However, small-scale ARs were mostly used for restoration, mitigation, or scientific purposes.

Thus, most AR systems did not exceed the square kilometer, and most modules did not exceed the square meter. However, there were important gaps in this information as many studies did not report it (40%). On the other hand, the shapes of these ARs varied,

counting domes (Reefballs), pyramids, tetrahedrons, cubes, blocks, boxes, cones, cylinders, columns, walls, meshes, and panels or plates, with pyramidal and cubic configurations being the most popular between the studies reviewed (Table 3).

Table 3. Physical characteristics of ARs in studies during the period of 1990–2020.

AR Type	ARs	ARs + Other	Car	Maritime Structures	Shipwreck	Breakwater
Total area (km^2)						
0–1	58	8	1	4	1	1
1.1–5	9					1
5.1–10	3					
10.1–20	4					
20.1–50	2					
50.1–200	6			1		
200.1–500	2					
500.1–1000						
1000.1–5000	1		1			
5000.1–10,000						
10,000.1–20,000	1					
NI	123	12	3	10		7
Module area (m^2)						
0–1	34	1				
1.1–5	24	1				1
5.1–10	9	1		1		
10.1–30	8	1				
30.1–50	2		1			
50.1–100	4	1			1	
100.1–300	7	1				
300.1–500	2				1	
500.1–1000	1	1			2	
1000.1–5000	1				3	
5000.1–10,000	3					
> 10,000	3					
NI	111	13	4	14	10	8
Weight (kg)						
0–100	2					
101–500	5					
501–1000	3	1				
1001–5000	5					
5001–10,000	4					
10,001–50,000	5					
50,001–100,000	1					
100,001–500,000	1					
>500,000	4	1				
NI	176	18	5	15	17	9
Shape						
Conical/triangular/pyramidal	32	3				
Cubical/tetrahedron/block	47	1		1		3
Cylindrical/tubular	9			2		
Panel/plates	11	1				
Dome (Reefballs)	16	0				
Wall/mesh/column	4	0		1		1
Irregular	12	2	5	6	17	
ARs systems with several shapes	27	8				
NI	47	5		5		5

NI = Not informed.

3.3. Effectiveness of ARs Based on Similarity with RNs

Artificial reefs did not achieve the state of NRs, along the 13 studies that fulfilled the inclusion criteria. The species similarity values between ARs and NRs sites were significantly lower than similarity values between reference NRs sites (Figure 10).

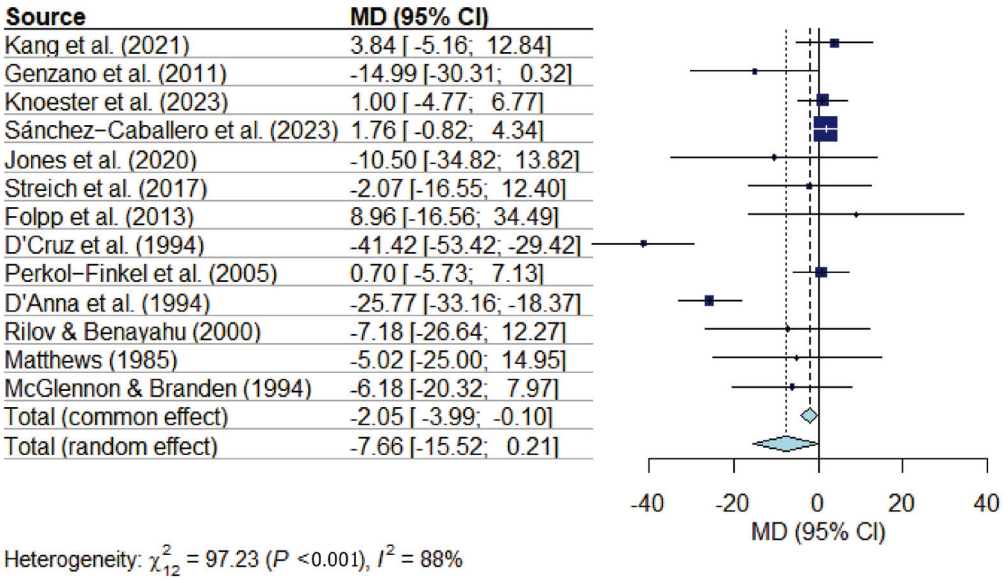


Figure 10. Forest plot of effect size (mean difference) for species similarity between ARs and NRs. Effect sizes and their 95% confidence intervals are provided for each study. Dark blue square sizes represent the weight of the effect size of each study, and the line width of squares corresponds to the 95% confidence interval limits for the effect size. Light blue diamond's represent the total effect size for species composition for the common effect model (smaller) and random effect model (bigger). Positive effect sizes indicate that species composition is higher on natural than artificial reefs, and a negative value means the opposite. Confidence intervals that overlap the zero line indicate that species composition is not significantly different on ARs vs. NRs. Kang et al. (2021) [33], Genzano et al. (2011) [34], Knoester et al. (2023) [35], Sánchez-Caballero et al. (2023) [36], Jones et al. (2020) [37], Streich et al. (2017) [38], Folpp et al. (2013) [39], D'Cruz et al. (1994) [40], Perkol-Finkel et al. (2005) [41], D'Anna et al. (1994) [42], Rilov & Benayahu (2000) [43], Matthews (1985) [44], McGlennon & Branden (1994) [45].

Despite the total effect measure almost reaching the null effect line (light blue diamonds, Figure 10), as few articles supported similar metrics describing species composition between artificial and natural reefs with a considerable weight ([35,36,41], both common and random effect models showed significant differences (total common effect $p = 0.03$, total random effect $p = 0.05$).

This result has proven to be robust enough as the funnel plot shows a consistency in values between articles (Figure S9). Furthermore, aside from detecting a significant heterogeneity ($p < 0.001$, $I^2 = 88\%$), the Egger test confirmed the robustness of the analysis ($p = 0.149$).

Characteristics of ARs in studies included for the meta-analysis also varied in features, as well as deployment characteristics and situations (Table 4).

Table 4. Conditions of AR deployments in studies included for the meta-analysis on restoration effectiveness.

Authors	AR Type	AR Purpose	Material	Shape	Size Module (m^2)	Depth (m)	Age (Months)	Variable
Knoester et al. (2023) [35]	AR	Restoration *	Concrete, glass, metal, plastic	Bottle, cage, cake	16	8	24	Benthos-ichthyofauna
Kang et al. (2021) [33]	AR	Production	Concrete	Cubic	16.7	21	588	Benthos, ichthyofauna MO
Folpp et al. (2013) [39]	AR	Production-tourism	Concrete	Dome (reef balls)	0.35	7	18	Ichthyofauna
D'Anna et al. (1994) [42]	AR	Production	Concrete	Pyramid of blocks	4	18	48	Ichthyofauna

Table 4. *Cont.*

Authors	AR Type	AR Purpose	Material	Shape	Size Module (m^2)	Depth (m)	Age (Months)	Variable
Matthews (1985) [44]	AR	Production	Concrete	Cylindrical	1.5	13.7		Ichthyofauna
McGlennon & Branden (1994) [45]	AR-sunken vessels	Production	Concrete and tires	Tetrahedron	3		72	Ichthyofauna
Sánchez–Caballero et al. (2023) [36]	Shipwreck	Production-restoration-tourism	Ni	Irregular	500	20	516	Benthos
Genzano et al. (2011) [34]	Shipwreck	Accidental	Ni	Irregular	Ni	23		Benthos and ichthyofauna
Perkol–Finkel et al. (2005) [41]	Shipwreck	Ni	Metal	Irregular	1170	15	1572	Coral
Jones et al. (2020) [37]	Vessel, caisson and debris	Ni	Ni	Irregular		130	132	Ichthyofauna
Rilov & Benayahu (2000) [43]	Jetty	Sea access	Metal	Cylindrical column	250	20	264	Ichthyofauna
Streich et al. (2017) [38]	Oil platform	Several	Ni	Irregular	3	58	Ni	Ichthyofauna
D'Cruz et al. (1994) [40]	Ni	Production	Ni	Ni	Ni	Ni		Ichthyofauna

* Coral transplantation implemented.

4. Discussion

4.1. Research on ARs in the World in the Last Thirty Years

Artificial reefs have received global attention, particularly with the purpose of increasing the hard surface to be colonized and the associated to the reef biomass of a marine ecosystem, regardless of their conservation status [18]. However, geographic regions, such as the equatorial and tropical zone, which have been most affected by the effects of climate change with coral bleaching [46], showed lower development of this kind of studies.

There was an explosion of ARs especially during the 1990s, where many formats, distributions and materials were tested [47]. The idea during these decades was that ARs may be promoters of hard bottom spaces, and that vagile fauna was especially attracted by such structures [48]. However, it was not clear at all if these structures were only attractors or if the vagile organisms could close part or the entire life cycle in the surrounding areas, and the sessile biomass, algae, and especially mega zoobenthos were not clear targets then [47,49].

Although recent advances have been made in studies of ARs, there are still gaps regarding more elaborate techniques, important to cover the full purpose of ARs [18]. It is necessary to develop studies that evaluate the socioeconomic sector, the reef design, materials and disposition, legislation, and planning aspects to consider the management and mitigation of impacts related to ARs, active restoration techniques with long-term monitoring of functional groups and to apply mathematical models that allow the evaluation of ecological, economic and social aspects for ecosystem restoration [9,18,48].

Recently the focus on artificial reefs has been driven to enhance the blue carbon and facilitate habitat restoration [50]. It is clear that ARs per se are not enough, as we need to design not only the morphology, texture, and material of the structures, but also their real functionality in terms of population connectivity, species growth enhancement, or complexity as a true marine forest [4,9].

Examples of proper AR assessments are infrequent compared to the level of reef development, because monitoring is often an afterthought in AR projects; thus, most reports are not very accurate in terms of evaluating these ARs [51]. Only 50% of ARs are successful, and the rest have no, little, or limited success [47]. Monitoring ARs to quantify the effects of their implementation is essential to assess their effectiveness, or to adjust them to achieve their objectives. Quantitative monitoring of biological, socioeconomic, and ecological aspects has already been shown to benefit other types of approaches such as aquaculture-based fisheries [48]. Such information is lacking in most of the analyzed studies.

To measure the success of ARs there must be an estimate that serves as a reference to prove the change caused by the AR in the habitat to restore. For example, control or reference sites are necessary taking into account the situation before and after the intervention. Thus, a BACI (before–after/control–impact) approach would be preferable for ecological monitoring to perceive ecological changes [8]. Furthermore, effective ARs should be similar to natural reference reefs in functional diversity and ecological processes (i.e., recruitment, species-habitat interactions, trophic interactions), which must also be researched through experimental approaches in order to advance these goals [52].

The lack of reference data highlights a need for consensus in the application of valid methods to demonstrate the effectiveness and evolution of ARs. Management of ARs must include adequate planning on the use and configuration of materials, site selection, and regulatory control of fisheries. Without long-term planning and management, ARs fail and represent yet another impact that contributes to the further degradation of marine environments [8,53]. In addition, sessile organisms, such as gorgonians, corals, algae, bryozoans, etc., which are easier to follow, were not considered in such monitoring programs, although they have an essential role as three-dimensional alive structures that enhance biodiversity and associated biomass [54].

Furthermore, in the attraction–production dilemma, bigger ARs concentrate biomass leading to an increase in the catchability of stocks. Therefore, trawling, overfishing, and crops were mostly identified as impacts associated with ARs. Local fishermen know this fact, and in many interventions, they were pro-positive (Bracho et al. submitted). Few articles reported the regulation of fisheries at ARs and there is a clear lack of information regarding the real impact on local fisheries. In this sense, fisheries must be regulated at different scales, including semi-industrial and industrial fisheries, particularly in relation to herbivorous species, whose presence directly impacts other trophic levels [49,55].

The implementation of ARs comes with a wide range of logistical, political, and social issues as it can incur high costs and is logistically challenging [55]. Joint decision-making, considering economic, cultural aspects, and preferences is essential for the success of these projects. Interdisciplinary programs can contribute to the simplification of logistics, permits, inspection, financing and administration, monitoring, education, and professional training, promoting an identity and sense of belonging to people around [8,56].

4.2. Structural Characteristics of Ars

Among the most important characteristics to be considered in the construction of Ars in tropical coral reef systems are related to the spatial orientation, complexity, and shape of the substrate [57]. Few studies considered testing depths [58], vertical or horizontal orientations [59], floating or fixed dispositions [60], or distances between NRs and ARs [61] on faunal colonization, aspects that could determine the first stages of settlement, colonization, and successional processes in the ARs. Controlling the above-mentioned aspects combined with a site selection for installation must mitigate the problem of species introduction. Non-native species are commonly associated with ports and oil platforms, as their dispersal mechanisms can be through the fouling attached to ships, ballast water, and fouling on oil platforms [62]. Therefore, the disposal of the ARs must avoid the sea currents that come from this type of installation, since they probably come loaded with larvae of foreign species, and the presence of the AR would facilitate this type of environmental impact.

Moreover, ARs can be made from waste materials to specific structures since, originally, almost any hard substrate that had been submerged in the sea could be called an AR [52]. Consequently, much of the accumulated knowledge about ARs has been empirically constructed, with materials that may not currently be considered the best option in environmental terms [9], such as tires, leftover material from civil construction, remains of vessels, entire ships, and oil platforms, decommissioned and sunk without proper maintenance, etc.

Some programs such as "rigs-to-reefs" gained value in some countries, due to the reef communities that were established over time when these accidental or incidental structures

were submerged, which originally were oil platforms, discarded ships, etc. Potential negative impacts of this program include physical damage to existing benthic habitats within the "fall zone", unwanted changes in marine food webs, facilitation of species invasions, and release of contaminants as platforms erode [63]. Thus, a great concern arises among scientists about an undiscriminating way of using ARs implementations. As well as us, some scientists emphasize the study and deepening of the knowledge of the ARs already installed and the development of technologies that allow for marine ecosystems to be restored, avoiding new impacts, before continuing to implement non-functional and even more impacting ARs [25,55].

Artificial reefs do not represent the only solution for damage to marine and coastal ecosystems. They are one of several management tools available, which, when properly managed, promote the improvement of habitats and biological productivity [20,53]. The use of concrete ARs in coral transplants [64] and plastic sheets in the resettlement of coral larvae [65], are a clear example of the use of these structures as active restoration tools. In places of great recreational activity, ARs appear as an alternative to diminishing human pressure in natural environments where visitation, sport fishing, and diving cause potential damage to RNs [9,66]. It is clear that the paradigm of these structures has to change to be much more efficient and in line with the real habitat needs in the zones where they may be implemented.

New studies are now bringing other potential textures, materials, and morphologies that emulate natural substrates [9], enhancing the settlement of vagile or sessile organisms depending on the silviculture paths that want to be promoted [67]. There were some attempts to improve materials for impact mitigation, testing different mixtures of materials for concrete, either in cost reduction [68,69], and mitigation of heavy metals when waste materials reused [70].

Some techniques manage to reproduce the specific material the properties of reef ecosystems from low voltage mineral deposition technology (LVMD) [71]. Although applying it at a large scale may be more difficult than other methods [23], the need for techniques to mitigate the effects of climate change, such as sea level rise coastal protection, increasing carbon sequestration capacity, etc. [9,50], are needs becoming more evident in today's world. ARs could act as facilitators of organisms that work as carbon immobilization species, as the sessile fauna that grows on their structures (sponges, corals, macroalgae, among others) sequester part of the CO_2 to build their hard three-dimensional organic or calcium carbonate ($CaCO_3$) structures, making them key ecosystems for mitigating the effects of climate change [9,54,72].

Some more specific conditions that ARs should fulfill include imitating the natural outcrop of rocky bottoms present in the target areas, having structural characteristics focused on the settlement of corals, gorgonians, and sponges, having cavities of different sizes and shapes to increase the presence of motile species (i.e., fish, mollusks and crustaceans), as well as being designed to capture CO_2, through the surface porosity of their own concrete structures, during the process known as carbonation [9].

Other approaches have been applied in the restoration of coral reef ecosystems, such as transplantation or repopulation by fragmenting corals or nubbins [73]; positive interactions between species [72]; floating reefs [60]; acoustic enrichment [74], integrated multitrophic aquaculture [75,76], among others.

All this suggests that the combination of active restoration methods including ARs can be the way to recover reef ecosystems that come to resemble conserved natural reefs, which can be called symbiotic artificial reefs (SAR). The implementation of artificial reefs to restore marine ecosystems can be well done, investing resources in studies specifically aimed at determining the appropriate characteristics of ARs for each location [77]. ARs should be considered strategically based on scientific assessments of specific location and resource needs to maximize the benefits of improving these habitats [20], with an emphasis on their use in the restoration of marine and coastal ecosystems [9].

4.3. Effectiveness of Artificial Reefs

Several authors have observed similarities between RNs and ARs in terms of abundance, biomass, and species richness, with some inconsistencies at geographical levels [20,78]. Nevertheless, as mentioned before, the species composition index would be preferable to avoid biased conclusions on effectivity. Assessments of the effect of installing ARs for restoration with veridically comparable and adequate reference sites are limited. Few studies have applied ARs for the restoration of highly degraded-declared ecosystems, while monitored by compared with NRs or equivalents (i.e., rocky ecosystems), in a good state of conservation, so that they serve as a comparison with the implementation site/restoration. However, most ARs deployments had little or limited ecological data available, which difficult for an integrated stock assessment [49].

Although there is a great lack of data availability, we tested that ARs harbor fewer species than NRs. On one hand, ARs did not resemble the reference NRs, that is, they did not achieve the restoration state, although studies included in the meta-analysis had a mean age of 30 years since deployment (n = 9), so it would be expected that ARs had reached a steady state at that point. On the other hand, ARs had fewer species than NRs of reference means less probability of the presence of invasive species, as they are globally related to AR structures [25,62], which represents a relevant problem in order to avoid trophic imbalance in already degraded ecosystems.

Among the studies that contributed in a greater measure to a null effect size or restoration state [35,36,41], two of them evaluated shipwrecks ARs of 500 and 1170 m^2 of area, at 20 and 15 m of depth in substrates with rock or reef with sand. They were also two of the older ARs with 43 and 131 years of deployment at the study execution time, and 10 and 1 month of monitoring, being the taxa analyzed benthos and coral species. Additionally, these studies reported impacts in the deployment area related with climate change effects and anthropogenic impacts, mostly related with trawling fishing and other destructive fishing methods, and with trophic imbalance. Furthermore, the study with more weight regarding replicates and sampling effort [79] compared ARs and NRs regarding coral species, thus species composition similarity is more achievable comparing species of a unique taxon than several (i.e., benthos).

However, in [35], ARs sites achieved restoration success in a shorter time, compared to their reference NRs (mean difference near the line of null effect, MD = 1, Figure 10). Using ARs intentionally made of concrete, with a combination of other materials such as glass, metal, and plastic, and applying an additional active restoration technique, such as coral transplantation [35], this study made a big difference in terms of the state of restoration of the ecosystem and the speed of it, comparing to those studies that did not apply it, since it achieved the reference NRs state at two years of monitoring [35]. Thus, the development of intentionally made ARs that achieve a restoration state comparable with natural reefs of reference in a few years is desirable for restoration program implementations, instead of accidental or incidental ARs that make it in several decades.

Furthermore, the restoration success of degraded ecosystems will have local needs related to the ecosystem itself, the impact type and cause of the impact, potential key species available to restore the degraded ecosystem, conflicts of use, etc., this is, ARs deployments must be site specific for each case. In addition, a high index of heterogeneity (88%) suggests that this relation may be influenced by factors other than the reef type. Thus, we suggest further analysis to investigate variables conditioning this AR–NR similarity as a measure of restoration for degraded marine ecosystems. Moreover, further studies must evaluate ecosystems' responses to ARs deployment from a restoration perspective, while concealing social and economic frameworks.

We call the attention of researchers in this area to carry out adequate experimental studies and allow the accessibility of data to evaluate and improve the efficiency of ARs in the restoration of degraded marine and coastal ecosystems. This is important as marine ecosystems harbor an immense diversity of habitats and life forms, as well as they are responsible for providing resources and environmental and economic services essential to

human survival, such as food and habitat supply, especially for coastal communities [80]. Efforts to conserve these ecosystems are insufficient measures that must be complemented with an understanding of ecological processes to carry out actions of restoration, given the extent and rapid rate of human impacts [9]. For example, ARs serve as corridors for marine organisms moving poleward and deep ward due to global warming effects in a possible tropicalization process across marine-coastal ecosystems while they can enhance local abundance and biomass of species at range edges [81].

Restoration of marine ecosystems, including active methods, is foolproof to promote the natural recruitment and survival of species of interest, the return of ecosystem structure and function, and the improvement of abiotic processes that shape the community, given the high degree of current degradation, especially in reef ecosystems as a result of climate change [21]. The application of new methods of ARs implementation in coastal and offshore areas may be as well the key to fostering habitat restoration, but it has to be made with an articulate, realistic, and upscaled plan that individuates strengths and weaknesses of such protocols, making an accurate study of local regeneration needs and limitations.

Supplementary Materials: The following supporting information can be downloaded at: https://www.mdpi.com/article/10.3390/environments10070121/s1, Figure S1: Flow diagram of the systematic literature review on artificial reefs; Figure S2: Flow diagram of the systematic literature review on artificial reefs effectivity; Figure S3: Number of studies on ARs during the period 1990–2020; Figure S4: Main research topics found in studies of artificial reefs by type of research; Figure S5: Number of experimental and observational surveys during the period 1990–2020; Figure S6: Sampling methods used in studies related to ARs during the period of 1990–2020; Figure S7: Society members involved in studies around Ars; Figure S8: Studies of ARs regarding their financing support; Figure S9: Funnel plot on meta-analysis of ARs effectiveness for marine ecosystem restoration. Table S1: Ecosystem type and substrate in which ARs were deployed.

Author Contributions: Conceptualization, S.R. and H.M.-C.; methodology, C.B.-V.; software, C.B.-V.; validation, S.R., H.M.-C. and C.B.-V.; formal analysis, C.B.-V.; investigation, S.R. and C.B.-V.; resources, S.R. and C.B.-V.; data curation, C.B.-V.; writing—original draft preparation, S.R. and C.B.-V.; writing—review and editing, S.R., H.M.-C. and C.B.-V.; visualization, S.R. and H.M.-C.; supervision, S.R. and H.M.-C.; project administration, S.R.; funding acquisition, S.R. All authors have read and agreed to the published version of the manuscript.

Funding: This research was funded by Coordenação de Aperfeiçoamento de Pessoal de Nível Superior (CAPES), grant number 88887.483420/2020-00 and 88887.758173/2022-00. This paper belongs to the project OCEAN CITIZEN ("Marine forest coastal restoration: an underwater gardening socio-ecological plan", Horizon Europe HORIZON-MISS-2021-OCEAN-02-01, Contract Number 101093910).

Data Availability Statement: Data available in a publicly accessible repository. The data presented in this study are openly available in FigShare at https://figshare.com/s/ec9082c17008aa437abc, accessed on 20 June 2023, doi:[10.6084/m9.figshare.23544834].

Acknowledgments: C.B.-V. thanks Coordenação de Aperfeiçoamento de Pessoal de Nível Superior (CAPES) for the scholarship funding, N° 88887.483420/2020-00 and 88887.758173/2022-00.

Conflicts of Interest: The authors declare no conflict of interest.

References

1. Worm, B.; Barbier, E.B.; Beaumont, N.; Duffy, J.E.; Folke, C.; Halpern, B.S.; Jackson, J.B.C.; Lotze, H.K.; Micheli, F.; Palumbi, S.R.; et al. Impacts of Biodiversity Loss on Ocean Ecosystem Services. Available online: https://www.science.org (accessed on 6 June 2023).
2. Rossi, S. The destruction of the 'animal forests' in the oceans: Towards an over-simplification of the benthic ecosystems. *Ocean Coast. Manag.* **2013**, *84*, 77–85. [CrossRef]
3. UNEP; FAO. Action Plan for the un Decade on Ecosystem Restoration, 2021–2030. Unated Nations Decade on Ecosystem Restoration 2021–2030, 2023. Available online: https://wedocs.unep.org/20.500.11822/42095 (accessed on 6 June 2023).
4. UNEP; CBD; COP. Report of the Eleventh Meeting of the Conference of the Parties to the Convention on Biological Diversity. Hyderabad, October 2012. Available online: https://www.cbd.int/doc/meetings/cop/cop-11/official/cop-11-35-en.pdf (accessed on 6 June 2023).

5. Seaman, W.; Lindberg, W. Artificial Reefs. In *Encyclopedia of Ocean Sciences*; Academic Press: Cambridge, MA, USA, 2009; pp. 226–233. [CrossRef]
6. London Convention and Protocol/UNEP. *London Convention and Protocol/UNEP Guidelines for the Placement of Artificial Reefs*; International Maritime Organization: London, UK, 2009; pp. 1–100.
7. West, J.E.; Buckley, R.M.; Doty, D.C. Ecology and habitat use of juvenile rockfishes (*Sebastes* spp.) associated with artificial reefs in Puget Sound, Washington. *Bull. Mar. Sci.* **1994**, *55*, 344–350.
8. Goergen, E.A.; Schopmeyer, S.; Moulding, A.L.; Moura, A.; Kramer, P.; Viehman, T.S. Coral reef restoration monitoring guide: Methods to evaluate restoration success from local to ecosystem scales. In *NOAA Technical Memorandum NOS NCCOS 279*; NOAA NOS NCCOS: Silver Spring, MD, USA, 2020; p. 145. [CrossRef]
9. Rossi, L.; Rizzo, S. Marine animal forests as Carbon immobilizers or why we should preserve these three-dimensional alive structures. In *Perspectives on the Marine Animal Forests*; Springer-Nature: Cham, Switzerland, 2020.
10. Hackradt, C.W.; Félix-Hackradt, F.C.; García-Charton, J.A. Influence of habitat structure on fish assemblage of an artificial reef in southern Brazil. *Mar. Environ. Res.* **2011**, *72*, 235–247. [CrossRef] [PubMed]
11. Clark, S.; Edwards, A.J. An evaluation of artificial reef structures as tools for marine habitat rehabilitation in the Maldives. *Aquat. Conserv.* **1999**, *9*, 5–21. [CrossRef]
12. Brock, R.E. Beyond Fisheries Enhancement: Artificlal Reefs and Ecotourism tool of resource managers for many years. This strategy usually involves the viewed as the development of productive habitat in an otherwise unproductive ness of artificial reefs in the impro. *Bull. Mar. Sci.* **1994**, *55*, 1181–1188.
13. GGrossman, D.; Jones, G.P.; Seaman, W.J. Do Artificial Reefs Increase Regional Fish Production? A Review of Existing Data. *Fisheries* **1997**, *22*, 17–23. [CrossRef]
14. Smith, J.A.; Lowry, M.B.; Champion, C.; Suthers, I.M. A designed artificial reef is among the most productive marine fish habitats: New metrics to address 'production versus attraction'. *Mar. Biol.* **2016**, *163*, 188. [CrossRef]
15. Zhang, D.; Cui, Y.; Zhou, H.; Jin, C.; Yu, X.; Xu, Y.; Li, Y.; Zhang, C. Microplastic pollution in water, sediment, and fish from artificial reefs around the Ma'an Archipelago, Shengsi, China. *Sci. Total Environ.* **2020**, *703*, 134768. [CrossRef]
16. Mangelli, T.S.; Creed, J.C. Comparative analysis of the invasive coral *Tubastraea* spp. (Cnidaria, Anthozoa) on natural and artificial substrates at Ilha Grande, Rio de Janeiro, Brazil. *Iheringia Ser. Zool.* **2012**, *102*, 122–130. [CrossRef]
17. Da Silva, G.V.; Hamilton, D.; Murray, T.; Strauss, D.; Shaeri, S.; Faivre, G.; Da Silva, A.P.; Tomlinson, R. Impacts of a Multi-Purpose Artificial Reef on Hydrodynamics, Waves and Long-Term Beach Morphology. *J. Coast. Res.* **2020**, *95*, 706–710. [CrossRef]
18. Lima, J.S.; Zalmon, I.R.; Love, M. Overview and trends of ecological and socioeconomic research on artificial reefs. *Mar. Environ. Res.* **2019**, *145*, 81–96. [CrossRef] [PubMed]
19. Tzvetkov, P.; Duzgunes, E.; Alexandrov, B.; Berov, D. *Research and Restoration of the Essential Filters of the Sea—REEFS Project Research Digest*; Bulgarian Biodiversity Foundation: Sofia, Bulgaria, 2015.
20. Paxton, A.B.; Shertzer, K.W.; Bacheler, N.M.; Kellison, G.T.; Riley, K.L.; Taylor, J.C. Meta-Analysis Reveals Artificial Reefs Can Be Effective Tools for Fish Community Enhancement but Are Not One-Size-Fits-All. *Front. Mar. Sci.* **2020**, *7*, 282. [CrossRef]
21. Gann, G.D.; McDonald, T.; Walder, B.; Aronson, J.; Nelson, C.R.; Jonson, J.; Hallett, J.G.; Eisenberg, C.; Guariguata, M.R.; Liu, J.; et al. International principles and standards for the practice of ecological restoration. Second edition. *Restor. Ecol.* **2019**, *27*, S1–S46. [CrossRef]
22. Hamel, S.; Gerung, G.S.; Reppie, E.; Budiman, J. Artificial Reef Habitat-Supported Integrated Aquaculture. *AACL Bioflux* **2021**, *14*, 2914–2928. Available online: https://www.bioflux.com.ro/docs/2021.2914-2928.pdf (accessed on 6 June 2023).
23. Rinkevich, B. Ecological engineering approaches in coral reef restoration. *ICES J. Mar. Sci.* **2020**, *78*, 410–420. [CrossRef]
24. Ambrose, R.F.; Anderson, T.W. Influence of an artificial reef on the surrounding infaunal community. *Mar. Biol.* **1990**, *107*, 41–52. [CrossRef]
25. Miranda, R.J.; Nunes, J.A.C.C.; Creed, J.C.; Barros, F.; Macieira, R.M.; Santos, R.G.; Lima, G.V.; Pontes, A.V.F.; Silva, L.G.F.C.; Cordeiro, R.T.; et al. Brazil policy invites marine invasive species. *Science* **2020**, *368*, 481. [CrossRef]
26. Crouzeilles, R.; Curran, M.; Ferreira, M.S.; Lindenmayer, D.B.; Grelle, C.E.V.; Benayas, J.M.R. A global meta-analysis on the ecological drivers of forest restoration success. *Nat. Commun.* **2016**, *7*, 11666. [CrossRef]
27. Carrick, P.J.; Forsythe, K.J. The species composition—Ecosystem function relationship: A global meta-analysis using data from intact and recovering ecosystems. *PLoS ONE* **2020**, *15*, e0236550. [CrossRef]
28. Seixas, L.B.; Barreto, N.R.; Dos Santos, L.N. Artificial Reefs for Marine And Freshwater Fish Management In Brazil: Researchers Profile and Academic Production over the 1990–2010 Period. *Oecologia Aust.* **2013**, *17*, 374–385. [CrossRef]
29. McLean, M.; Roseman, E.F.; Pritt, J.J.; Kennedy, G.; Manny, B.A. Artificial reefs and reef restoration in the Laurentian Great Lakes. *J. Great Lakes Res.* **2015**, *41*, 1–8. [CrossRef]
30. Vivier, B.; Dauvin, J.-C.; Navon, M.; Rusig, A.-M.; Mussio, I.; Orvain, F.; Boutouil, M.; Claquin, P. Marine artificial reefs, a meta-analysis of their design, objectives and effectiveness. *Glob. Ecol. Conserv.* **2021**, *27*, e01538. [CrossRef]
31. Moher, D.; Liberati, A.; Tetzlaff, J.; Altman, D.G. Guidelines and Guidance Preferred reporting items for systematic reviews and meta-analyses: The PRISMA statement. *PLoS Med.* **2009**, *6*, e1000097. [CrossRef] [PubMed]
32. Field, J.; Clarke, K.; Warwick, R. A Practical Strategy for Analysing Multispecies Distribution Patterns. *Mar. Ecol. Prog. Ser.* **1982**, *8*, 37–52. [CrossRef]

33. Kang, H.Y.; Lee, B.G.; Park, H.J.; Yun, S.G.; Kang, C.K. Trophic structures of artificial reef communities off the southern coast of the Korean peninsula as determined using stable isotope analyses. *Mar. Pollut. Bull.* **2021**, *169*, 112474. [CrossRef]
34. Genzano, G.; Giberto, D.; Bremec, C. Estudios del bentos de arrecifes naturales y artificiales de mar del Plata, Argentina, Atlántico sudoccidental. *Lat. Am. J. Aquat. Res.* **2011**, *39*, 553–566. [CrossRef]
35. Knoester, E.; Rienstra, J.; Schürmann, Q.; Wolma, A.; Murk, A.; Osinga, R. Community-managed coral reef restoration in southern Kenya initiates reef recovery using various artificial reef designs. *Front. Mar. Sci.* **2023**, *10*, 1152106. [CrossRef]
36. Sánchez-Caballero, C.; Borges-Souza, J.; Chavez-Hidalgo, A.; Abelson, A. Assessing benthic reef assemblages: A comparison between no-take artificial reefs and partially protected natural reefs. *Estuar. Coast. Shelf Sci.* **2023**, *287*, 108347. [CrossRef]
37. Jones, S.T.; Asher, J.M.; Boland, R.C.; Kanenaka, B.K.; Weng, K.C. Fish biodiversity patterns of a mesophotic-to-subphotic artificial reef complex and comparisons with natural substrates. *PLoS ONE* **2020**, *15*, e0231668. [CrossRef]
38. Streich, M.K.; Ajemian, M.J.; Wetz, J.J.; Stunz, G.W. A comparison of fish community structure at mesophotic artificial reefs and natural banks in the western gulf of Mexico. *Mar. Coast. Fish.* **2017**, *9*, 170–189. [CrossRef]
39. Folpp, H.; Lowry, M.; Gregson, M.; Suthers, I.M. Fish Assemblages on Estuarine Artificial Reefs: Natural Rocky-Reef Mimics or Discrete Assemblages? *PLoS ONE* **2013**, *8*, e63505. [CrossRef]
40. D'Cruz, T.; Creech, S.; Fernandez, J. Comparison of catch rates and species composition from artificial and natural reefs in Kerala, India. *Bull. Mar. Sci.* **1994**, *55*, 1029–1037.
41. Perkol-Finkel, S.; Shashar, N.; Barneah, O.; Ben-David-Zaslow, R.; Oren, U.; Reichart, T.; Yacobovich, T.; Yahel, G.; Yahel, R.; Benayahu, Y. Fouling reefal communities on artificial reefs: Does age matter? *Biofouling* **2005**, *21*, 127–140. [CrossRef] [PubMed]
42. D'Anna, G.; Badalamenti, F.; Gristina, M.; Pipitone, C. Influence of artificial reefs on coastal nekton assemblages of the Gulf of Castellammare (northwest Sicily). *Bull. Mar. Sci.* **1994**, *55*, 418–433.
43. Rilov, G.; Benayahu, Y. Fish assemblage on natural versus vertical artificial reefs: The rehabilitation perspective. *Mar. Biol.* **2000**, *136*, 931–942. [CrossRef]
44. Matthews, K.R. Species similarity and movement of fishes on natural and artificial reefs in Monterey Bay, California. *Mar. Pollut. Bull.* **1985**, *37*, 252–270.
45. McGlennon, D.; Branden, K.L. Comparison of catch and recreational anglers fishing on artificial reefs and natural seabed in Gulf St. Vincent, South Australia. *Bull. Mar. Sci.* **1994**, *55*, 51–523.
46. Harrison, H.B.; Álvarez-Noriega, M.; Baird, A.H.; Heron, S.F.; MacDonald, C.; Hughes, T.P. Back-to-back coral bleaching events on isolated atolls in the Coral Sea. *Coral Reefs* **2019**, *38*, 713–719. [CrossRef]
47. Baine, M. Artificial reefs: A review of their design, application, management and performance. *Ocean Coast. Manag.* **2001**, *44*, 241–259. [CrossRef]
48. Becker, A.; Taylor, M.D.; Folpp, H.; Lowry, M.B. Managing the development of artificial reef systems: The need for quantitative goals. *Fish Fish.* **2018**, *19*, 740–752. [CrossRef]
49. Roa-Ureta, R.H.; Santos, M.N.; Leitão, F. Modelling long-term fisheries data to resolve the attraction versus production dilemma of artificial reefs. *Ecol. Model.* **2019**, *407*, 108727. [CrossRef]
50. Rossi, S. How Carbon Immobilization from Restored Marine Forests May Help Climate Change Mitigation Plans? *Aquivos Ciências Mar* **2022**, *55*, 202–218. [CrossRef]
51. Seaman, W.J. Artificial Reef with Application to Natural Marine Habitats, Volume II. 2000. Available online: http://books.google.de/books?id=JyJMuPPdsMwC (accessed on 19 June 2023).
52. Miller, M.W. Using ecological processes to advance artificial reef goals. *ICES J. Mar. Sci.* **2002**, *59*, S27–S31. [CrossRef]
53. Pickering, H.; Whitmarsh, D.; Jensen, A. Artificial Reefs as a Tool to Aid Rehabilitation of Coastal Ecosystems: Investigating the Potential. *Mar. Pollut. Bull.* **1999**, *37*, 505–514. [CrossRef]
54. Rossi, C.; Bramanti, S.; Gori, L.; Orejas, A. *Marine Animal Forests*; Springer International Publishing: Cham, Switzerland, 2016. [CrossRef]
55. Rogers, A.; Harborne, A.R.; Brown, C.J.; Bozec, Y.-M.; Castro, C.; Chollett, I.; Hock, K.; Knowland, C.A.; Marshell, A.; Ortiz, J.C.; et al. Anticipative management for coral reef ecosystem services in the 21st century. *Glob. Chang. Biol.* **2015**, *21*, 504–514. [CrossRef]
56. Florisson, J.H.; Tweedley, J.R.; Walker, T.H.; Chaplin, J.A. Reef vision: A citizen science program for monitoring the fish faunas of artificial reefs. *Fish. Res.* **2018**, *206*, 296–308. [CrossRef]
57. Perkol-Finkel, S.; Shashar, N.; Benayahu, Y. Can artificial reefs mimic natural reef communities? The roles of structural features and age. *Mar. Environ. Res.* **2006**, *61*, 121–135. [CrossRef] [PubMed]
58. Rule, M.J.; Smith, S.D. Depth-associated patterns in the development of benthic assemblages on artificial substrata deployed on shallow, subtropical reefs. *J. Exp. Mar. Biol. Ecol.* **2007**, *345*, 38–51. [CrossRef]
59. Sammarco, P.; Lirette, A.; Tung, Y.; Boland, G.; Genazzio, M.; Sinclair, J. Coral communities on artificial reefs in the Gulf of Mexico: Standing vs. toppled oil platforms. *ICES J. Mar. Sci.* **2014**, *71*, 417–426. [CrossRef]
60. Perkol-Finkel, S.; Zilman, G.; Sella, I.; Miloh, T.; Benayahu, Y. Floating and fixed artificial habitats: Spatial and temporal patterns of benthic communities in a coral reef environment. *Estuar. Coast. Shelf Sci.* **2008**, *77*, 491–500. [CrossRef]
61. Zalmon, I.R.; de Sá, F.S.; Neto, E.J.D.; de Rezende, C.E.; Mota, P.M.; de Almeida, T.C.M. Impacts of artificial reef spatial configuration on infaunal community structure—Southeastern Brazil. *J. Exp. Mar. Biol. Ecol.* **2014**, *454*, 9–17. [CrossRef]

62. Creed, J.; Paula, A. Substratum Preference during Recruitment of Two Invasive Alien Corals onto Shallow-Subtidal Tropical Rocky Shores. *Mar. Ecol. Prog. Ser.* **2007**, *330*, 101–111. Available online: https://www.int-res.com/articles/meps2007/330/m330p101.pdf (accessed on 15 June 2023). [CrossRef]
63. Macreadie, P.I.; Fowler, A.M.; Booth, D.J. Rigs-to-reefs: Will the deep sea benefit from artificial habitat? *Front. Ecol. Environ.* **2011**, *9*, 455–461. [CrossRef] [PubMed]
64. Polak, O.; Shashar, N. Can a small artificial reef reduce diving pressure from a natural coral reef? Lessons learned from Eilat, Red Sea. *Ocean Coast. Manag.* **2012**, *55*, 94–100. [CrossRef]
65. Suzuki, G.; Kai, S.; Yamashita, H.; Suzuki, K.; Iehisa, Y.; Hayashibara, T. Narrower grid structure of artificial reef enhances initial survival of in situ settled coral. *Mar. Pollut. Bull.* **2011**, *62*, 2803–2812. [CrossRef]
66. Sutton, S.G.; Bushnell, S.L. Socio-economic aspects of artificial reefs: Considerations for the Great Barrier Reef Marine Park. *Ocean Coast. Manag.* **2007**, *50*, 829–846. [CrossRef]
67. Horoszowski-Fridman, Y.B.; Rinkevich, B. Restoration of the Animal Forests: Harnessing Silviculture Biodiversity Concepts for Coral Transplantation. *Mar. Anim. For.* **2016**, *36*, 1313–1335. [CrossRef]
68. Shu-Te, K.; Tsan-Chuan, H.; Kwang-Tsao, S. Experiences of Coal Ash Artificial Reefs in Taiwan. *Chem. Ecol.* **1995**, *10*, 233–247. [CrossRef]
69. Ponti, M.; Fava, F.; Perlini, R.A.; Giovanardi, O.; Abbiati, M. Benthic assemblages on artificial reefs in the northwestern Adriatic Sea: Does structure type and age matter? *Mar. Environ. Res.* **2015**, *104*, 10–19. [CrossRef] [PubMed]
70. Collins, K.J.; Jensen, A.C.; Lockwood, A.P.M.; Turnpenny, A.W.H. Evaluation of stabilized coal-fired power station waste for artificial reef construction. *Bull. Mar. Sci.* **1994**, *55*, 1251–1262.
71. Margheritini, L.; Møldrup, P.; Jensen, R.L.; Frandsen, K.M.; Antonov, Y.I.; Kawamoto, K.; de Jonge, L.W.; Vaccarella, R.; Bjørgård, T.L.; Simonsen, M.E. Innovative Material Can Mimic Coral and Boulder Reefs Properties. *Front. Mar. Sci.* **2021**, *8*, 652986. [CrossRef]
72. Shaver, E.C.; Silliman, B.R. Time to cash in on positive interactions for coral restoration. *Peer J.* **2017**, *5*, e3499. [CrossRef] [PubMed]
73. Oren, U.; Benayahu, Y. Transplantation of juvenile corals: A new approach for enhancing colonization of artificial reefs. *Mar. Biol.* **1997**, *127*, 499–505. [CrossRef]
74. Gordon, T.A.C.; Radford, A.N.; Davidson, I.K.; Barnes, K.; McCloskey, K.; Nedelec, S.L.; Meekan, M.G.; McCormick, M.I.; Simpson, S.D. Acoustic enrichment can enhance fish community development on degraded coral reef habitat. *Nat. Commun.* **2019**, *10*, 5414. [CrossRef]
75. Xu, Q.; Zhang, L.; Zhang, T.; Zhang, X.; Yang, H. Functional groupings and food web of an artificial reef used for sea cucumber aquaculture in northern China. *J. Sea Res.* **2017**, *119*, 1–7. [CrossRef]
76. Giangrande, A.; Gravina, M.F.; Rossi, S.; Longo, C.; Pierri, C. Aquaculture and Restoration: Perspectives from Mediterranean Sea Experiences. *Water* **2021**, *13*, 991. [CrossRef]
77. Seaman, W. Artificial habitats and the restoration of degraded marine ecosystems and fisheries. *Hydrobiologia* **2007**, *580*, 143–155. [CrossRef]
78. Hunter, W.R.; Sayer, M.D.J. The comparative effects of habitat complexity on faunal assemblages of northern temperate artificial and natural reefs. *ICES J. Mar. Sci.* **2009**, *66*, 691–698. [CrossRef]
79. Perkol-Finkel, S.; Benayahu, Y. Recruitment of benthic organisms onto a planned artificial reef: Shifts in community structure one decade post-deployment. *Mar. Environ. Res.* **2005**, *59*, 79–99. [CrossRef]
80. NAS: National Academies of Sciences, Engineering and Medicine. *A Research Review of Interventions to Increase the Persistence and Resilience of Coral Reefs*; The National Academies Press: Washington, DC, USA, 2019. [CrossRef]
81. Paxton, A.B.; Peterson, C.H.; Taylor, J.C.; Adler, A.M.; Pickering, E.A.; Silliman, B.R. Artificial reefs facilitate tropical fish at their range edge. *Commun. Biol.* **2019**, *2*, 168. [CrossRef]

Disclaimer/Publisher's Note: The statements, opinions and data contained in all publications are solely those of the individual author(s) and contributor(s) and not of MDPI and/or the editor(s). MDPI and/or the editor(s) disclaim responsibility for any injury to people or property resulting from any ideas, methods, instructions or products referred to in the content.

applied sciences

MDPI

Article

Effects of Wind Barrier Porosity and Inclination on Wind Speed Reduction

Sang-Hyun Lee [1], Hyun Kim [2], Hyunshik Moon [3,4], Hyun-Soo Kim [5], Sang-Sub Han [1] and Seonghun Jeong [3,4,*]

[1] Department of Forest Environmental Science, Jeonbuk National University, Jeonju 54896, Republic of Korea; leesh@jbnu.ac.kr (S.-H.L.); sshan@jbnu.ac.kr (S.-S.H.)
[2] Division of Environmental and Forest Science, Gyeongsang National University, Jinju 52725, Republic of Korea; kimhyun@gnu.ac.kr
[3] Department of Forest Environmental Resources, Gyeongsang National University, Jinju 52828, Republic of Korea; hsmoon@gnu.ac.kr
[4] Institute of Agriculture and Life Science, Gyeongsang National University, Jinju 52828, Republic of Korea
[5] Division of Warm Temperate and Subtropical Forest Research Center, National Institute of Forest Science, Jeju 63582, Republic of Korea; khsggam1@korea.kr
* Correspondence: nowwap@gmail.com; Tel.: +82-55-772-1858

Abstract: Wind barriers play a vital role in protecting saplings until maturity when planted as vegetative windbreak forests. Most previous studies have focused on the porosity of wind barriers, but no studies have simultaneously examined the effects of the porosity and inclination, despite the potential of the inclination to decrease wind speed. We tested three wind barrier cases in wind tunnel experiments: (1) Case A (porosity of 0% with inclinations (90°, 80°, and 70°)), (2) Case B (porosity of 25% with inclinations (90°, 80°, and 70°)), and (3) Case C (porosity of 50% with inclinations (90°, 80°, and 70°)). The vertical and horizontal wind velocities were measured at three vertical and seven horizontal points behind the barriers. The results demonstrated a statistically significant decrease in the correlation between the distance and mean wind velocity for all cases, with up to a six-fold wind protection effect. The wind barrier with 0% porosity and a 90° inclination provided the highest degree of wind protection. However, the wind protection range was limited downwind, and recirculation of wind flow could occur in the leeward direction, potentially damaging saplings. A wind barrier with 50% porosity and 70° inclination sufficiently decreased the wind velocity and prevented recirculation of wind flow, demonstrating that both porosity and inclination considerably impacted the wind protection effect by reducing wind velocity. Our findings offer novel insights into the influence of wind barriers with varying porosities and inclinations and can provide valuable guidance for constructing efficient windbreak forests.

Keywords: wind barrier; wind barrier inclination; wind barrier porosity; windbreak forest; wind tunnel experiment; wind velocity reduction

Citation: Lee, S.-H.; Kim, H.; Moon, H.; Kim, H.-S.; Han, S.-S.; Jeong, S. Effects of Wind Barrier Porosity and Inclination on Wind Speed Reduction. *Appl. Sci.* **2023**, *13*, 8310. https://doi.org/10.3390/app13148310

Academic Editors: Mohammad Mahmudur Rahman, Dibyendu Sarkar, Rupali Datta and Prafulla Kumar Sahoo

Received: 23 June 2023
Revised: 15 July 2023
Accepted: 17 July 2023
Published: 18 July 2023

Copyright: © 2023 by the authors. Licensee MDPI, Basel, Switzerland. This article is an open access article distributed under the terms and conditions of the Creative Commons Attribution (CC BY) license (https://creativecommons.org/licenses/by/4.0/).

1. Introduction

Wind can have a considerable influence on vegetation growth or death, depending on its strength and other environmental conditions [1–5]. Artificial wind barriers play an important role in the protection of vegetation, such as crops in paddy fields [6,7], fruit trees in orchards [7], shrubs in sandy deserts in semi-arid and arid regions [8], and vegetative windbreak forests in coastal areas [9,10]. The main approach to protecting vegetation is to reduce wind velocity, and accordingly, two types of wind fences, vegetative windbreaks and artificial wind barriers, are commonly constructed [8–11]. The growth of saplings in vegetative windbreak forests (vegetative windbreaks in coastal areas) is hindered by various negative environmental factors, such as stronger sea breezes with more salinity than land breezes, rapid wind shifts, higher humidity, and sand and dust on vegetation

(e.g., [10,12–14]). These factors can cause growth inhibition, mortality, and electrolyte imbalances [2,9,15–17]. Thus, wind barriers control wind velocity and reduce negative environmental factors in coastal areas. Wind barriers alter airflow [18,19]. The altered airflow reduces negative environmental factors like intense sea breezes [14], potentially decreasing salinity levels. They also modify microclimates [9,20], prevent sand and dust deposition on vegetation [8,12], promote soil productivity [21], and contribute to species-rich ecosystems [22]. Thus, wind barriers should be prioritized to support the growth of vegetation and construct vegetative windbreak forests in harsh conditions [8,9,13].

Numerous studies on the effectiveness of wind fences have been conducted. Heisler and Dewalle [18] conducted a comprehensive review of previous studies on the effect of wind fence structures and reported that the most effective wind fences depend on porosity, among other factors, such as type, shape, and height. Many studies have concluded that wind fences with lower porosity produce a greater reduction in wind velocity [23–32]. For instance, Perera [27] tested solid porous fences (porous range: 0% to 50%). The author also reported that the key factor was the porosity rather than the form of fence construction, and a porosity of 10% provided better sheltering efficiency among the porosities. Further, the reattachment could no longer be detected when the porosity was above 30%. Range Raine and Stevenson [29] reported that a porosity of 20% among porous fences of 0–50% was the best for shelter efficiency. Chen et al. [24] conducted a CFD numerical simulation to examine the shelter efficacy of a deflector-porous fence. They reported that a 30% porosity sand fence was the most effective at controlling dust emissions and concluded that the optimal porosity range could be between 30% and 50%. Yu et al. [32] reported that the lowest porosity of 36% among porous fences of 36%, 56%, 63%, and 75% had the strongest sheltering efficiency with the longest wind protection. In contrast, Wu et al. [8] reviewed recent studies that examined the shelter effect of porosity using field measurements, wind tunnel experiments, and numerical simulations and reported that the highest shelter effect was achieved at a porosity within the range of 20% to 40%. Consequently, the optimal design of wind barriers with varying porosities has been reported in different environmental conditions to date.

However, an inclination (i.e., the inclined angle of wind barriers), in addition to porosity, can change the wind velocity and affect the wind protection range of barriers. Kang [33] tested the wind flow angles (90°, 75°, 60°, and 45°) for vertical wind barriers using porous meshes (0%, 25%, 50%, and 75%) when the upstream wind direction toward the wind barriers changed. The author reported that the wind velocity distribution downstream generally differed among the wind flow angles. Naaim-Bouvet et al. [34] tested snow fences of different gradient slopes using a cold wind tunnel. The authors reported that the slope angle could substantially affect snowdrifts, but much depended on the porosity of the snow fence. These findings suggest that the effectiveness of wind barriers in providing wind protection may vary based on both porosity and inclination. However, to the best of our knowledge, no information is currently available on the simultaneous impact of wind barrier porosity and inclination on wind protection. Thus, quantitative research on this topic is required for the optimal design of windbreak systems.

Our study aimed to evaluate the effectiveness of wind barriers by examining both porosity and inclination using a wind barrier made of wood. To achieve this, we conducted wind tunnel experiments with three wind barrier cases: (1) Case A (porosity of 0% with three different inclinations (90°, 80°, and 70°)), (2) Case B (porosity of 25% with the same inclinations), and (3) Case C (porosity of 50% with the same inclinations). To analyze the reduction in wind speed, we measured the wind velocity on the windward and leeward sides of the wind barriers in relation to their distance. Our findings provide valuable insights for the design of windbreak systems, which can help protect saplings and improve windbreak forest management strategies.

2. Materials and Methods

2.1. Wind Experimental Design

A wind tunnel experiment was conducted at the Korea Construction Engineering and Transport Development Collaboratory Management Institute (KOCED) Wind Tunnel Center, Jeonbuk National University, Republic of Korea. The wind tunnel was a closed-circuit type. Of the dual test sections with low-speed and high-speed sections in the KOCED Wind Tunnel Center, our test was conducted in the low-speed section (test section size: 12 m wide, 2.5 m high, and 40 m long; wind velocity: 0.3 m s^{-1}~12.0 m s^{-1}). The turbulence intensity was less than 1.5%.

We designed a small-scale simulation model considering the blockage ratio (the ratio of the projected specimen area to the cross-sectional area of the wind tunnel) (Figure 1a) [35–38]. In general, the blockage ratio is corrected if >10% [35,36]. In this study, the blockage ratio was 6.7%, implying a negligible correction from the blockage ratio.

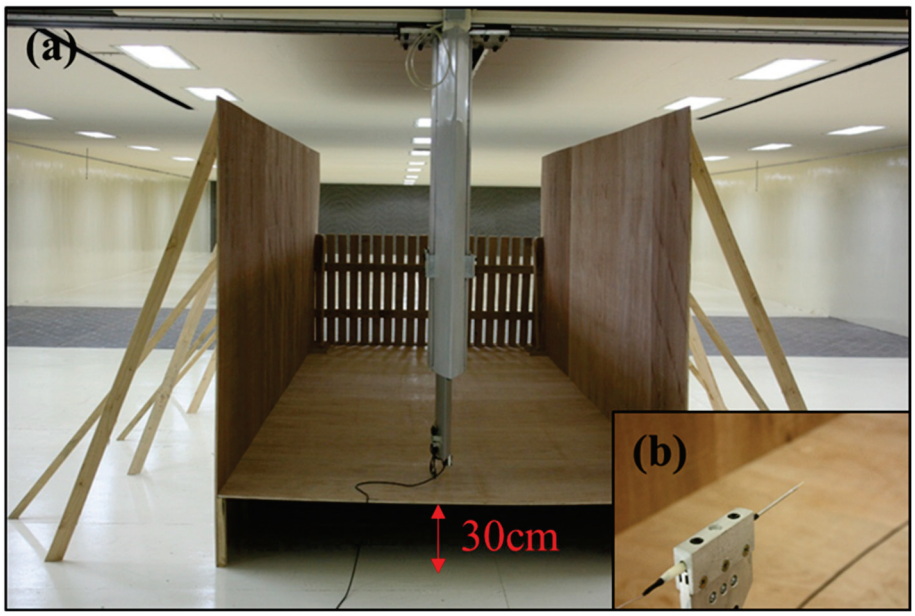


Figure 1. (**a**) Structure of a small-scale simulation model installed at a 30 cm height from the ground with a wind barrier and (**b**) a sensor for wind velocity.

Uniform wind flow was obtained above 30 cm from the ground (Figure 1a), which avoided the natural atmospheric boundary layer in the wind tunnel section. Owing to the insufficient width of the wind tunnel section, walls 2 m high and 7 m long were installed, which were sufficient to prevent the distortion of wind generated from each side of the two-dimensional test specimen (Figure 1a).

2.2. Wind Experimental Materials

Previous studies have reported that a decrease in wind velocity can be indicated in the wind protection porosity function (e.g., [23,28,30]). This suggests that the influence of porosity on decreasing wind velocity could be much larger than that of the shape and material of the wind fence. The porosity (%) at this point was computed as follows:

$$\Phi(\%) = \frac{A_e}{A_a} \times 100 \quad (1)$$

where Φ is the porosity, A_e is the projected area of the pores of the wind barrier, and A_a is the area of the perimeter of the wind barrier (i.e., height × width).

Different materials, such as metal, plastic, and wood, have been employed as wind barriers [36]. Among these windbreak materials, a wind barrier using a wood-based material is preferable because it is environment-friendly, light, simple, and inexpensive to

build. In this study, we tested both the porosity and inclinations to examine their potential for decreasing wind velocity using wood-based materials (Figure 2a). In previous studies, wind barrier porosity was typically designed within a range of 0% to 50%, taking material costs into account [8,18,27,29,32]. Lower porosity tends to be more expensive in practical applications [18], whereas higher porosity permits increased air penetration, resulting in less wind speed reduction [9]. Regarding wind barrier inclination, preliminary tests were conducted on inclinations ranging from 90° to 70° prior to the wind tunnel experiment owing to the challenges of field construction. Thus, using these wood-based materials, our study was designed for three cases: (1) Case A: porosity of 0% with three inclinations (90°, 80°, and 70°), (2) Case B: porosity of 25% with three inclinations (90°, 80°, and 70°), and (3) Case C: porosity of 50% with three inclinations (90°, 80°, and 70°) (Figure 2b).

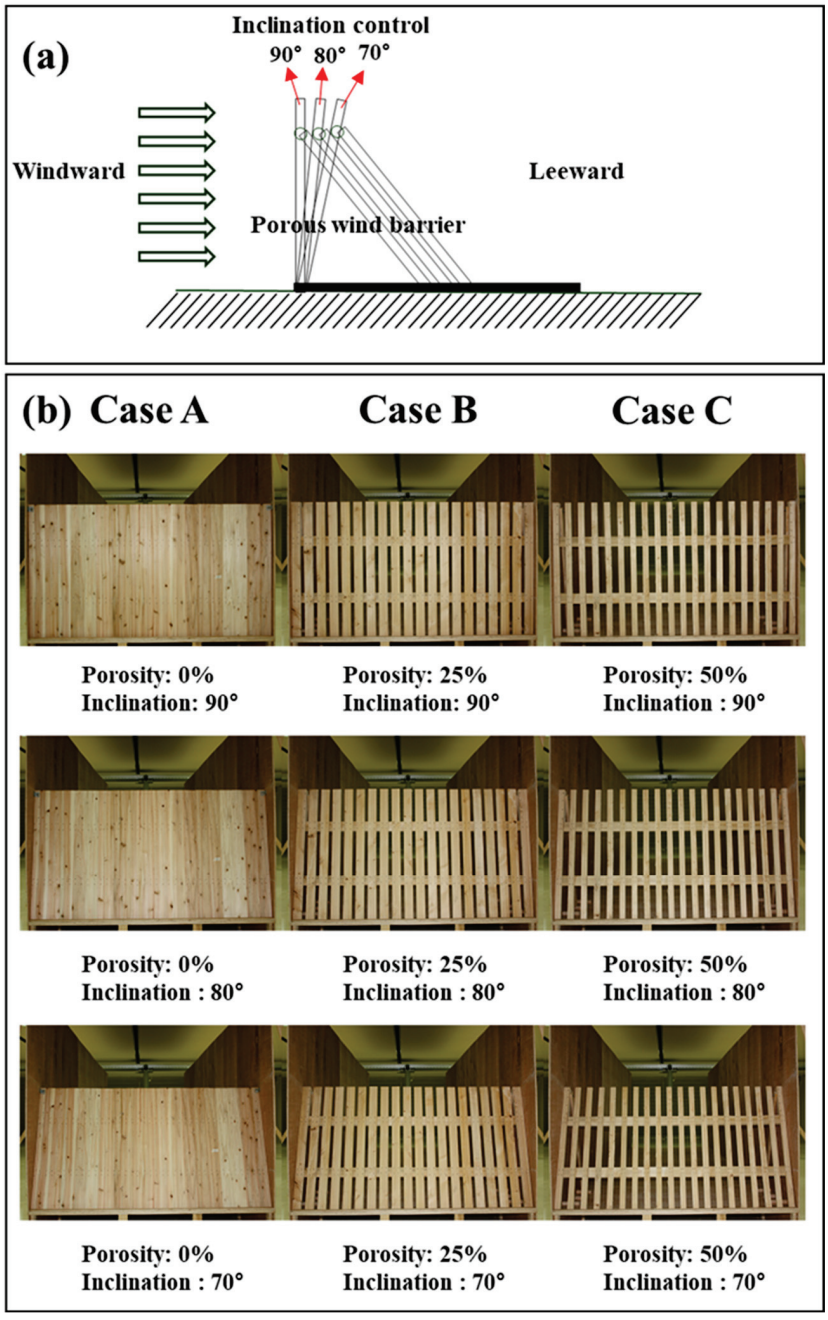


Figure 2. (**a**) Schematic diagram of porous and non-porous wind barriers at different inclinations and (**b**) three case studies (A, B, and C) with different porosities (0%, 25%, and 50%) and inclinations (90°, 80°, and 70°).

2.3. Measurements

The wind velocities at the windward and leeward sides of the wind barriers were measured using an I-type hot wire anemometer (Dantec I-type Probe 55P11, sampling rate: 16.67 data s^{-1}) and three-dimensional traverse equipment (Figure 1b). Wind velocity was measured at 3 points along the vertical (30, 60, and 90 cm) and 7 points along the horizontal (50 to 600 cm) points (i.e., 21 points in total leeward behind the wind barriers) (Figure 3). The wind velocity threshold required to move sand and dust in the coastal Saemangeum land of the Republic of Korea is assumed to be approximately 4.0 m s^{-1} at 0.5 elevation [9]. Thus, we used a wind velocity of 5.0 m s^{-1} at the windward side, which was approximately two-fold the 10-year monthly average wind speed for Gunsan city (approximately 2.2 m s^{-1}) of the land [39]. After operating the wind turbine for several minutes, the wind velocities on the windward and leeward sides stabilized.

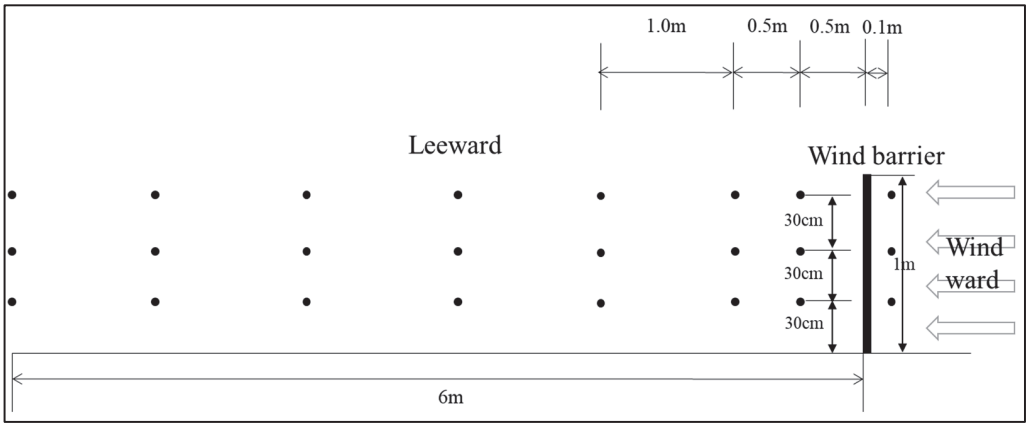


Figure 3. The 3 vertical measuring points in front of wind barriers and 3 vertical measuring points and 7 horizontal measuring points (i.e., 21 measuring points in total) behind wind barriers.

The wind velocity of the wind tunnel was initially set to 5.0 m s^{-1}. The wind velocities at each single measuring point on the windward (n = 3) and leeward (n = 21) sides were measured for 60 s (i.e., 1 min mean wind speed), and the average wind velocity of each measuring point was determined (Figure 3). We analyzed the change in the average wind velocity at the measured distances. Wind speed reduction is determined by the ratio of windward and leeward wind speeds.

$$U_R = \frac{U}{U_0} \times 100\ (\%) \tag{2}$$

where U_R is the ratio of windward and leeward wind speeds, U is the average leeward wind speed (m s^{-1}), and U_0 is the average windward wind speed (m s^{-1}).

Wind flow visualization was conducted to quantitatively determine the movement of the wind velocity provided in Section 3.

2.4. Statistical Analyses

The software SPSS ver. 21.0 (IBM SPSS, Armonk, NY, USA) was used for statistical analyses. One-way analysis of variance (ANOVA), which is a statistical method to compare the means of three or more groups to determine if there are significant differences between them [40], was used to identify the range of the reduction in wind velocity for Cases A, B, and C. Following the ANOVA test, Duncan analysis, employed to determine which specific groups or means are significantly different from each other [40], was performed to classify identical groups of the average wind velocity for each inclination of Cases A, B, and C. The significance level was established at a 0.05 probability level for all statistical analyses.

3. Results

3.1. Case A (Porosity of 0% with Inclinations of 90°, 80°, and 70°)

Table 1 shows variations in the decrease in average wind velocity at different distances for a wind barrier of 0% porosity at three different inclinations (90°, 80°, and 70°), and Figure 4 shows the visualization of the spatial distribution of the average wind velocity according to distance. For each inclination, the correlation between the distance and average wind speed decrease was statistically significant at $\alpha = 0.05$ (90°: F-value = 24.618, $p < 0.001$; 80°: F-value = 23.185, $p < 0.001$; 70°: F-value = 22.232, $p < 0.001$). The decrease in wind velocity for all inclinations was statistically significant up to six times (Table 1). The decrease in wind velocity differed slightly at each sample point according to the inclinations. The reduction ratio of the wind velocity for each inclination decreased as the distance increased, indicating a difference in the wind protection range (Table 1, Figure 4). The range of the reduction ratio also varied: 41–90% for 90°, 34–90% for 80°, and 37–90% for 70°. Among these different inclinations, the 90° vertical had a large decreasing effect for the greatest distance of 600 cm (Table 1).

Table 1. Case A—average wind velocity at 0% porosity and three different inclinations of wind barriers (90°, 80°, and 70°) for every measuring point.

Porosity (%)	Inclination (°)	Distance (cm)	Height (cm)	Velocity (m/s)	Wind Reduction Ratio (%)
0%	90°	−10 (C)	30, 60, 90	5.000 ± 0.000^{d}	0
		50	30, 60, 90	0.516 ± 0.120^{a}	90
		100	30, 60, 90	0.757 ± 0.756^{a}	85
		200	30, 60, 90	1.027 ± 0.989^{a}	79
		300	30, 60, 90	1.178 ± 0.365^{ab}	76
		400	30, 60, 90	1.412 ± 0.818^{ab}	72
		500	30, 60, 90	2.064 ± 1.340^{b}	59
		600	30, 60, 90	2.969 ± 1.400^{c}	41
	80°	−10 (C)	30, 60, 90	5.000 ± 0.000^{d}	0
		50	30, 60, 90	0.486 ± 0.230^{a}	90
		100	30, 60, 90	0.618 ± 0.614^{a}	88
		200	30, 60, 90	1.057 ± 0.426^{ab}	79
		300	30, 60, 90	1.147 ± 0.614^{ab}	77
		400	30, 60, 90	1.393 ± 0.171^{ab}	72
		500	30, 60, 90	2.000 ± 0.720^{b}	60
		600	30, 60, 90	3.289 ± 1.498^{c}	34
	70°	−10 (C)	30, 60, 90	5.000 ± 0.000^{d}	0
		50	30, 60, 90	0.390 ± 0.345^{a}	90
		100	30, 60, 90	0.602 ± 0.121^{a}	88
		200	30, 60, 90	1.036 ± 0.013^{ab}	79
		300	30, 60, 90	1.164 ± 0.091^{ab}	77
		400	30, 60, 90	1.434 ± 0.162^{ab}	71
		500	30, 60, 90	2.025 ± 0.807^{b}	60
		600	30, 60, 90	3.163 ± 1.495^{c}	37

(C) represents the windward control point of wind speed. Wind velocity (m/s) is given with corresponding standard deviation values. Superscripts with different letters for wind velocity denote identical groups of the average wind velocity for each inclination of the wind barrier (90°, 80°, and 70°) classified using Duncan analysis (significant at $p < 0.05$).

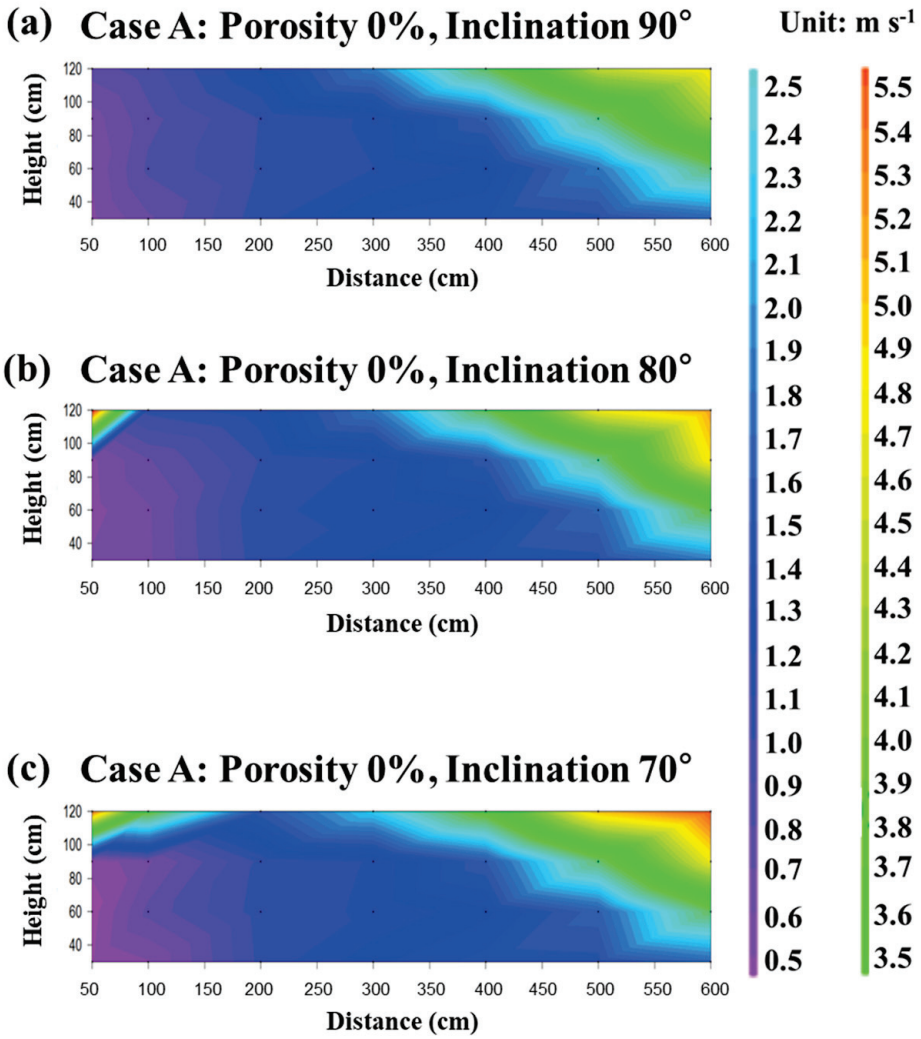


Figure 4. Visualization of the spatial distribution of the average wind velocity according to distance for Case A with a wind barrier porosity of 0% and an inclination of (**a**) 90°, (**b**) 80°, and (**c**) 70°.

3.2. Case B (Porosity of 25% with Inclinations of 90°, 80°, and 70°)

Table 2 shows the change in the average decrease in wind velocity according to distance for a porosity of 25% of a wind barrier with different inclinations (90°, 80°, and 70°), and Figure 5 shows the visualization of the spatial distribution of the average wind velocity according to distance. For each inclination, the correlation between the distance and decrease in average wind speed was statistically significant at $\alpha = 0.05$ (90°: F-value = 17.851, $p < 0.001$; 80°: F-value = 25.882, $p < 0.001$; 70°: F-value = 22.817, $p < 0.001$). Similar to the wind barrier with a porosity of 0%, the decreasing wind velocity effect for all inclinations was found to be up to six times greater. The reduction ratio of the wind velocity for each inclination of the wind barrier with a porosity of 0% decreased with increasing distance. In contrast, the reduction ratio for each inclination of the wind barrier with a porosity of 25% increased with increasing distance and then gradually decreased (Table 2, Figure 5). This indicates that the wind velocity differs with porosity. The wind velocity differed slightly from each measured point, according to the inclinations. The range of the reduction ratio varied with the inclination of the wind barrier, 38–69% for 90°, 33–67% for 80°, and 42–62% for 70°, indicating that inclinations played a considerable role in affecting wind velocity. The highest protection against wind was found to be provided by the inclination of 90°.

Table 2. Case B—average wind velocity at 25% porosity and three different inclinations of wind barriers (90°, 80°, and 70°) for every measuring point.

Porosity (%)	Inclination (°)	Distance (cm)	Height (cm)	Velocity (m/s)	Wind Reduction Ratio (%)
25%	90°	−10 (C)	30, 60, 90	5.000 ± 0.000^{c}	0
		50	30, 60, 90	3.077 ± 1.207^{b}	38
		100	30, 60, 90	2.180 ± 0.319^{a}	56
		200	30, 60, 90	1.673 ± 0.020^{a}	67
		300	30, 60, 90	1.570 ± 0.117^{a}	69
		400	30, 60, 90	1.603 ± 0.289^{a}	68
		500	30, 60, 90	1.675 ± 0.398^{a}	66
		600	30, 60, 90	1.801 ± 0.568^{a}	64
	80°	−10 (C)	30, 60, 90	5.000 ± 0.000^{d}	0
		50	30, 60, 90	3.350 ± 1.114^{c}	33
		100	30, 60, 90	2.553 ± 0.284^{b}	49
		200	30, 60, 90	1.818 ± 0.065^{ab}	64
		300	30, 60, 90	1.695 ± 0.185^{a}	66
		400	30, 60, 90	1.644 ± 0.306^{a}	67
		500	30, 60, 90	1.695 ± 0.354^{a}	66
		600	30, 60, 90	1.852 ± 0.540^{ab}	63
	70°	−10 (C)	30, 60, 90	5.000 ± 0.000^{c}	0
		50	30, 60, 90	2.409 ± 1.101^{ab}	52
		100	30, 60, 90	2.883 ± 0.635^{b}	42
		200	30, 60, 90	1.992 ± 0.211^{a}	60
		300	30, 60, 90	1.902 ± 0.312^{a}	62
		400	30, 60, 90	1.886 ± 0.450^{a}	62
		500	30, 60, 90	1.939 ± 0.560^{a}	61
		600	30, 60, 90	1.997 ± 0.618^{a}	60

(C) represents the windward control point of wind speed. Wind velocity (m/s) is given with corresponding standard deviation values. Superscripts with different letters for wind velocity denote identical groups of the average wind velocity for each inclination of the wind barrier (90°, 80°, and 70°) classified using Duncan analysis (significant at $p < 0.05$).

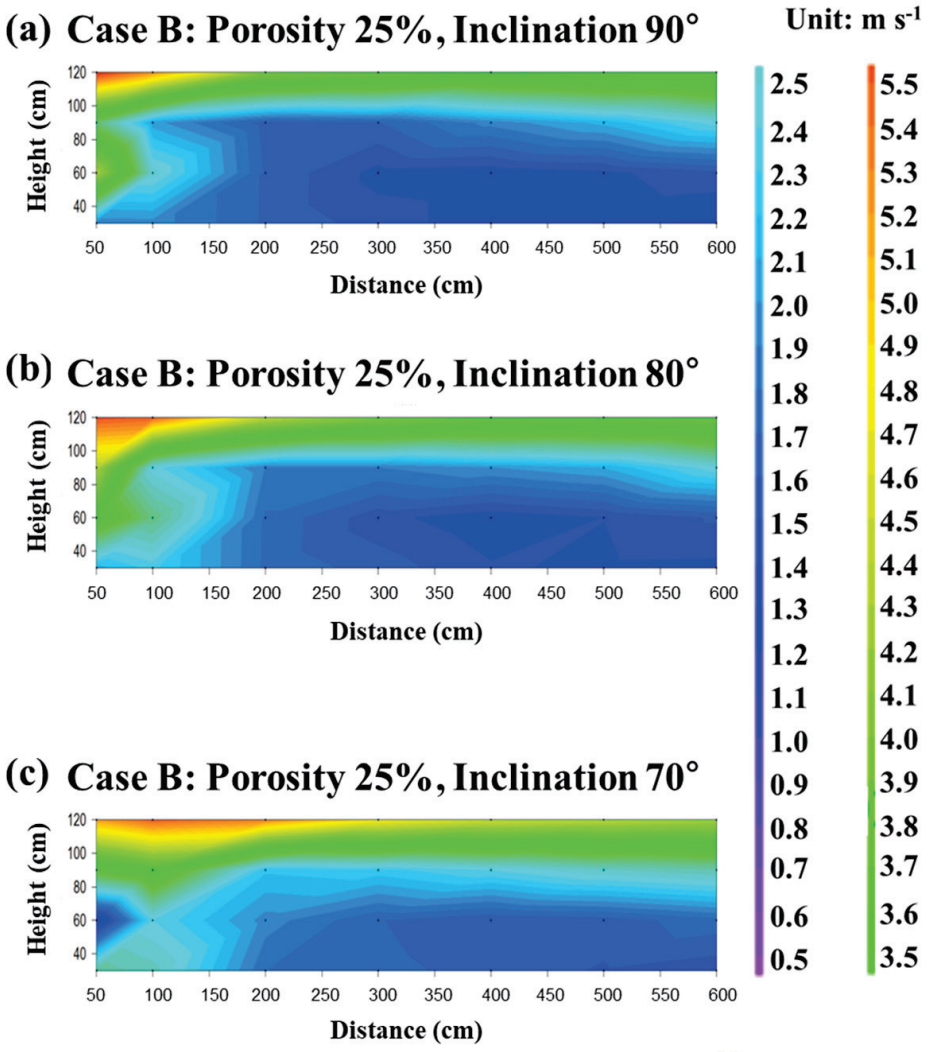


Figure 5. Visualization of the spatial distribution of the average wind velocity according to distance for Case B with a wind barrier porosity of 25% and an inclination of (**a**) 90°, (**b**) 80°, and (**c**) 70°.

3.3. Case C (Porosity of 50% with Inclinations of 90°, 80°, and 70°)

Table 3 presents the change in the average decrease in wind velocity according to distance for a porosity of 50% with different inclinations (90°, 80°, and 70°), and Figure 6 shows the visualization of the spatial distribution of the average wind velocity according to distance. For each inclination, the correlation between the distance and decrease in average wind speed was statistically significant at $\alpha = 0.05$ (90°: F-value = 59.605, $p < 0.001$; 80°: F-value = 50.356, $p < 0.001$; 70°: F-value = 55.659, $p < 0.001$). The effect of reducing wind velocity with a 50% porosity increased six-fold as the inclination decreased. The reduction ratio for each inclination increased and then gradually decreased as the distance increased (Table 3, Figure 6). The reduction ratios ranged from 71% to 87% at 90°, 69% to 86% at 80°, and 65% to 88% at 70°. Among the different inclinations, the reducing effect was greatest at 90° within 300 cm and greatest at 70° from 400 to 600 cm. This suggests that the wind velocity is affected by the inclination of the wind barrier.

Table 3. Case C—average wind velocity at 50% porosity and three different inclinations of wind barriers (90°, 80°, and 70°) for every measuring point.

Porosity (%)	Inclination (°)	Distance (cm)	Height (m)	Velocity (m/s)	Wind Reduction Ratio (%)
50%	90°	−10 (C)	30, 60, 90	5.000 ± 0.000^{d}	0
		50	30, 60, 90	1.336 ± 0.209^{bc}	73
		100	30, 60, 90	1.151 ± 0.015^{abc}	77
		200	30, 60, 90	0.673 ± 0.306^{a}	87
		300	30, 60, 90	0.675 ± 0.429^{a}	87
		400	30, 60, 90	0.831 ± 0.666^{ab}	83
		500	30, 60, 90	1.224 ± 0.466^{abc}	76
		600	30, 60, 90	1.469 ± 0.611^{c}	71
	80°	−10 (C)	30, 60, 90	5.000 ± 0.000^{c}	0
		50	30, 60, 90	1.568 ± 0.070^{b}	69
		100	30, 60, 90	1.208 ± 0.059^{ab}	76
		200	30, 60, 90	0.678 ± 0.316^{a}	86
		300	30, 60, 90	0.768 ± 0.316^{a}	85
		400	30, 60, 90	0.773 ± 0.372^{a}	85
		500	30, 60, 90	1.036 ± 0.618^{ab}	79
		600	30, 60, 90	1.315 ± 0.661^{ab}	74
	70°	−10 (C)	30, 60, 90	5.000 ± 0.000^{d}	0
		50	30, 60, 90	1.735 ± 0.614^{c}	65
		100	30, 60, 90	1.395 ± 0.160^{c}	72
		200	30, 60, 90	0.710 ± 0.339^{ab}	86
		300	30, 60, 90	0.613 ± 0.306^{a}	88
		400	30, 60, 90	0.628 ± 0.432^{a}	87
		500	30, 60, 90	0.749 ± 0.397^{ab}	85
		600	30, 60, 90	1.325 ± 0.682^{bc}	74

(C) represents the windward control point of wind speed. Wind velocity (m/s) is given with corresponding standard deviation values. Superscripts with different letters for wind velocity denote identical groups of the average wind velocity for each inclination of the wind barrier (90°, 80°, and 70°) classified using Duncan analysis (significant at $p < 0.05$).

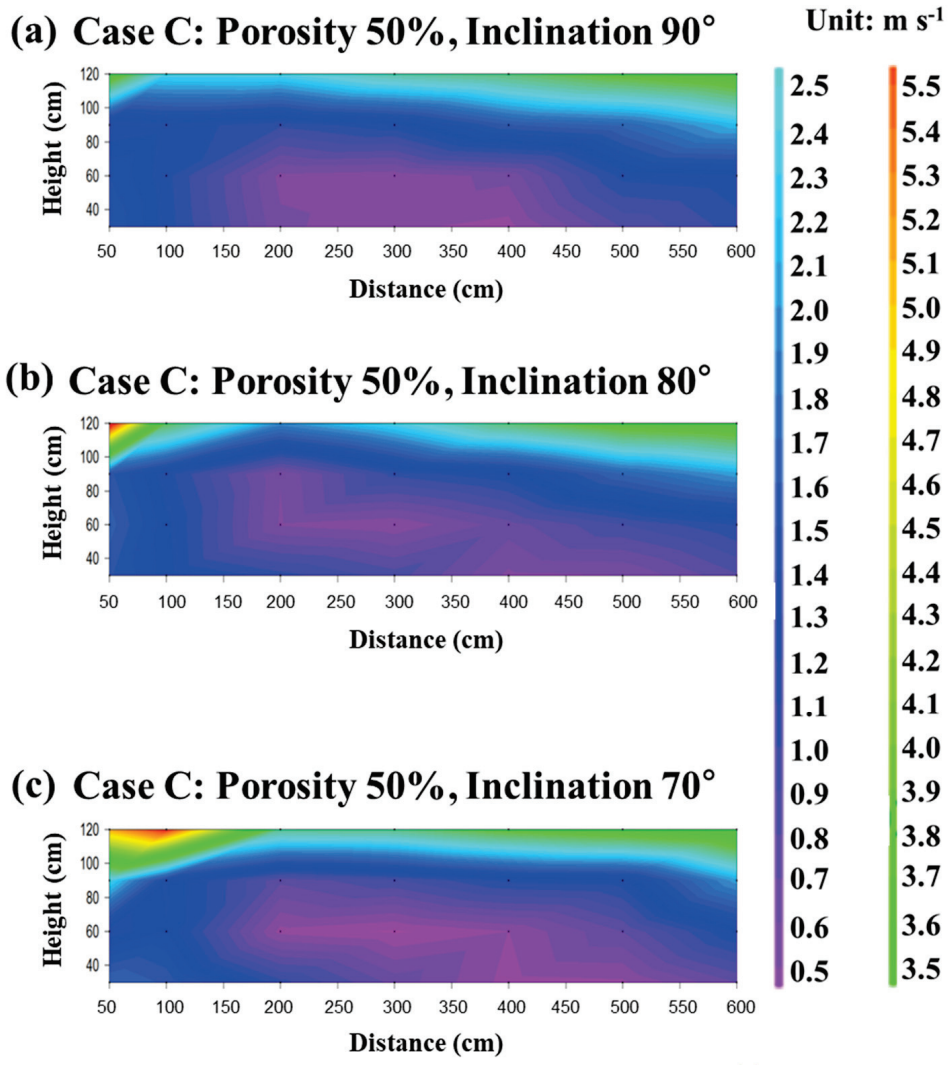


Figure 6. Visualization of the spatial distribution of the average wind velocity according to distance for Case C with a wind barrier porosity of 50% and an inclination of (**a**) 90°, (**b**) 80°, and (**c**) 70°.

3.4. Effects of Porosity and Inclination on Wind Speed

Figure 7 shows the variations in average wind velocity (m/s) with respect to distance (cm) at the windward and leeward sides of the wind barriers for three different cases: Case A (porosity of 0% with inclinations (90°, 80°, and 70°)), Case B (porosity of 25% with inclinations (90°, 80°, and 70°)), and Case C (porosity of 50% with inclinations (90°, 80°, and 70°)). In Case A, the average wind velocity (m/s) decreased significantly at a distance of 50 cm behind the wind barriers and gradually increased as the distance from the wind barrier increased. In contrast, Cases B and C exhibited a gradual decrease up to a distance of 300 cm, followed by a slight increase. These results suggest that changes in wind flow behind wind barriers are influenced by both porosity and inclination. Notably, Case C outperformed Cases A and B, demonstrating a significantly higher wind speed reduction. Specifically, a wind barrier with a porosity of 50% and an inclination of 70° exhibited better performance, providing an ample wind protection range.

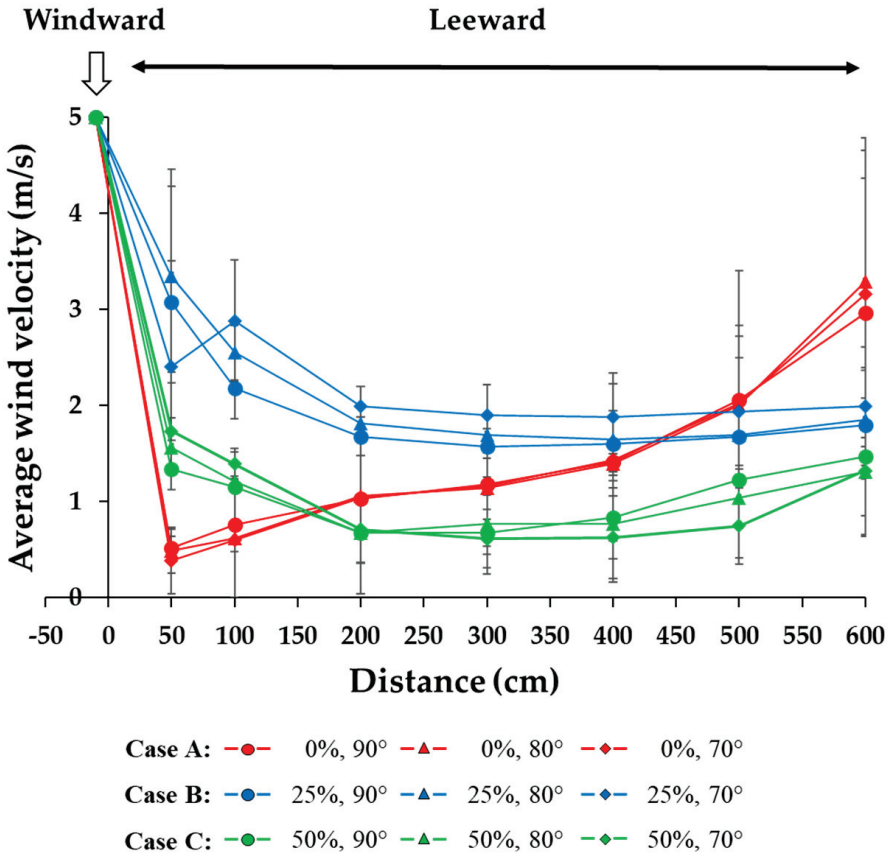


Figure 7. The relationship between average wind velocity (m/s) and distance (cm) on the windward and leeward sides of the wind barriers. The percentages (%) and degrees (°) in the legend represent the porosity and inclination of the wind barriers, respectively. The bars represent the standard deviation.

4. Discussion

Previously, the porosity of the wind barrier was regarded as the key factor influencing its effectiveness in protecting against wind (reviewed by [8,18]). To further advance the understanding of the wind flow characteristics and determine the effectiveness of wind barriers, this study examined the effects of inclinations and porosity on the effectiveness of the following wind barriers based on a wind tunnel experiment.

The reduction in wind speed varied among the three cases. For Case A, although all inclinations showed a six-fold decrease in wind velocity at the last measuring distance (Table 1), wind flow could reattach and recirculate at the leeward side of the wind barrier. Kang [33] reported that a reattachment point occurred at a distance of approximately 10–15 times the height of a wind barrier. The reattachment point and recirculation of wind flow may damage tree saplings as sea breezes with salinity, sand, and dust in coastal areas are particularly harmful to vegetation [2,9,16,17], resulting in lower growth rates [15]. Thus, when establishing a windbreak forest within a distance equal to or less than 10 times the height of the wind barriers, it is advisable to use a non-porous wind barrier in an embanked area rather than on flat land.

For Case B, the reduction ratio of wind velocity for each inclination increased with increasing distance (Table 2, Figure 5), whereas the opposite trend was observed for Case A (Table 1, Figures 4 and 7). This could be explained by the increase in porosity from 0% to 25% [18,32]. Although the change in the reduction ratio of wind velocity was similar between 90° and 80°, there was an abrupt decrease between 50 cm and 100 cm at 70°, probably (Table 2, Figure 7) due to the recirculation of wind flow [26]. Overall, the effect of wind protection was weak within 200 cm. Thus, to attain protection of over 60% with wind

barriers of 25% porosity, it is recommended to utilize vertical 90° wind fences. Further saplings should not be planted immediately behind the wind barriers.

Following a previous review that reported porosity as one of the influential factors on wind speed reduction alongside other factors such as the type, shape, and height of wind barriers [18], numerous earlier studies primarily focused on porosity [8,9,24,26,28]. Previous studies generally concluded that windbreaks with lower porosity had a higher reducing effect on wind velocity. However, the construction of wind barriers with lower porosities is expensive in practical applications [28]; therefore, the optimal porosity range is from 30% to 50% [24,25]. Wu et al. [8] reviewed recent studies that examined wind barrier porosity for wind protection effectiveness and reported that the highest sheltering efficiency of wind fences was achieved at a porosity within the range of 20% to 40%. In contrast, in this study, the wind barrier of Case C, with the highest porosity of 50%, substantially decreased the wind velocity and showed relatively stable reduction ratios for each inclination at varying distances relative to Cases A and B (Table 3, Figures 6 and 7). In addition, the effectiveness of Case C was higher than that of Case B in this study. This implies that a lower porosity does not always result in a greater wind velocity reduction. The different results of this study from the previous studies reviewed by Wu et al. [8] may be attributed to the inclinations that were not examined in the previous studies. Among the different inclinations, the decreasing effect was the greatest at 90° within 300 cm; however, the counterpart was largest at 70° from 400 to 600 cm (Table 3, Figures 6 and 7). This implies that the inclination may have a considerable effect on the range of wind protection, resulting in greater wind barrier efficacy. Therefore, the effectiveness of wind barriers may depend not only on their porosity but also on their inclination.

Our results suggest that a wind barrier with a porosity of 50% and an inclination of 70° may provide the most effective protection for pre-maturity saplings against wind in vegetative windbreak forests, although, overall, all wind barriers with varying porosities and inclinations performed well. Despite our findings, several avenues of this study remained unexplored, which should be considered in future research. As the wind tunnel section in this study was relatively small, the height of the wind barriers was not tested, although past studies have reported that height significantly affects shelter efficiency (e.g., [9,19,41]). Wind barriers with lower porosity are laborious, time-consuming, and costly, although they exhibit a higher reducing effect on wind velocity [28]. To achieve an optimal and cost-effective wind barrier, it is recommended to explore a wider range of porosities and inclinations beyond those tested in this study while keeping the material cost similar. An array of wind barriers can facilitate the reduction in wind velocity for vegetative windbreak forest construction [9]. Single and multiple rows of vegetation can also considerably reduce wind velocity, depending on the vegetation species used, such as shrubs, coniferous species, and broad-leaved species [9,10], or when combined with wind barriers [8,42]. Thus, combining an array of wind barriers with structurally varying windbreak trees with different porosities and inclinations could further advance our understanding of the change in wind flow caused by different porosities and inclinations, and optimize vegetative windbreak forest management strategies for various environmental conditions.

5. Conclusions

In a wind tunnel experiment, we examined the simultaneous effect of wind barrier porosity and inclination on wind speed reduction. The key findings of this study were as follows:

- The wind barriers tested in this study, which varied in porosity and inclination, exhibited different effects on wind speed reduction at various distances. This suggests that both the porosity and inclination of wind barriers play important roles in providing wind protection.
- All wind barriers provided up to six times more wind protection on the leeward side than on the windward side. However, the wind velocity reduction ratio varied at each distance for all wind barriers, indicating different levels of wind protection.

- Among the evaluated wind barriers, a wind barrier with a porosity of 0% and an inclination of 90° demonstrated the highest reduction in wind velocity. However, this wind barrier had a very limited wind protection range and could potentially cause wind flow recirculation on the leeward side, posing a risk of sapling damage.
- In contrast, a wind barrier with a porosity of 50% and an inclination of 70° sufficiently decreased wind velocity and prevented the recirculation of wind flow, thereby improving sapling protection and reducing material costs.

Our findings offer novel insights into the influence of wind barriers in terms of not only their porosity, which has been primarily examined as a key factor affecting wind speed reduction, but also their inclination. However, there are additional aspects that warrant further exploration beyond the scope of this study. Specifically, future investigations should explore the impact of wind barrier height, which was not evaluated in this study because of the limited size of the wind tunnel section. The height of wind barriers also plays a crucial role in determining shelter efficiency. Additionally, it is essential to investigate the integration of wind barriers with windbreak vegetative species (e.g., shrubs and trees), which exhibit diverse structural characteristics, porosities, and inclinations. Such comprehensive studies will facilitate the optimization of management strategies for vegetative windbreak forests under a range of environmental conditions.

Author Contributions: S.-H.L.: conceptualization, formal analysis, writing—original draft preparation, writing—review and editing, supervision, project administration, and funding acquisitions. H.K.: formal analysis, data duration, and writing—review and editing. H.M.: writing—review and editing. H.-S.K.: methodology, investigation, and writing—review and editing. S.-S.H.: writing—review and editing. S.J.: conceptualization, methodology, investigation, formal analysis, data curation, writing—original draft preparation, writing—review and editing, and visualization. All authors have read and agreed to the published version of the manuscript.

Funding: This work was supported by the Forest Science & Technology Development Project funded by Korea Forest Service (grant number S111111L050130), and the research grant of the Gyeongsang National University in 2022.

Institutional Review Board Statement: Not applicable.

Informed Consent Statement: Not applicable.

Data Availability Statement: The data in this study are available on reasonable request from the corresponding author.

Acknowledgments: The authors acknowledge the staff of the Korea Engineering Development Collaboratory Management Institute (KOCED) for their help in the set-up of wind barriers. We thank the editor and five anonymous reviewers for their constructive comments on the manuscript.

Conflicts of Interest: The authors declare no conflict of interest.

References

1. Wang, H.; Hua, J.; Kang, M.; Wang, X.; Fan, X.-R.; Fourcaud, T.; de Reffye, P. Stronger wind, smaller tree: Testing tree growth plasticity through a modling approach. *Front. Plan Sci.* **2022**, *13*, 971690. [CrossRef] [PubMed]
2. Ancelin, P.; Courbaud, B.I.T.; Fourcaud, T. Development of an individual tree-based mechanical model to predict wind damage within forest stands. *For. Ecol. Manag.* **2004**, *203*, 101–121. [CrossRef]
3. de Langre, E. Effects of wind on plants. *Annu. Rev. Fluid Mech.* **2008**, *40*, 141–168. [CrossRef]
4. Gardiner, B.; Peltola, H.; Kellomäki, S. Comparison of two models for predicting the critical wind speeds required to damage coniferous trees. *Ecol. Model.* **2000**, *129*, 1–23. [CrossRef]
5. Niklas, K.J.; Spatz, H.-C. Wind-induced stresses in cherry trees: Evidence against the hypothesis of constant stress level. *Trees-Struct. Funct.* **2000**, *14*, 230–237. [CrossRef]
6. Gardiner, B.; Berry, P.; Moulia, B. Review: Wind impacts on plant growth, mechanics and damage. *Plant Sci.* **2016**, *245*, 94–118. [CrossRef]
7. Jo, H.K.; Park, H.M. Effects of windbreak planting on crop productivity for agroforestry practices in a semi-arid region. *J. For. Environ. Sci.* **2017**, *33*, 348–354. [CrossRef]

8. Wu, X.; Guo, Z.; Wang, R.; Fan, P.; Xiang, H.; Zuo, X.; Yin, J.; Fang, H. Optimal design for wind fence based on 3D numerical simulation. *Agric. For. Meteorol.* **2022**, *323*, 109072. [CrossRef]
9. Bitog, J.P.; Lee, I.-B.; Shin, M.-H.; Hong, S.-W.; Hwang, S.-H.; Seo, I.-H.; Yoo, J.-I.; Kwon, K.-S.; Kim, Y.-H.; Han, J.-W. Numerical simulation of an array of fences in Saemangeum reclaimed land. *Atmos. Environ.* **2009**, *43*, 4612–4621. [CrossRef]
10. Jeong, S.; Lee, S.-H. Effects of windbreak forest according to tree species and planting methods based on wind tunnel experiments. *For. Sci. Technol.* **2020**, *16*, 188–194. [CrossRef]
11. Lyu, J.; Wang, C.M.; Mason, M.S. Review of models for predicting wind characteristics behind windbreaks. *J. Wind Eng. Ind. Aerodyn.* **2020**, *199*, 104117. [CrossRef]
12. Bitog, J.P.; Lee, I.-B.; Hwang, H.-S.; Shin, M.-H.; Hong, S.-W.; Seo, I.-H.; Mostafa, E.; Pang, Z. A wind tunnel study on aerodynamic porosity and windbreak drag. *For. Sci. Technol.* **2011**, *7*, 8–16. [CrossRef]
13. Bitog, J.P.; Lee, I.-B.; Hwang, H.-S.; Shin, M.-H.; Hong, S.-W.; Seo, I.-H.; Kwon, K.-S.; Mostafa, E.; Pang, Z. Numerical simulation study of a tree windbreak. *Biosyst. Eng.* **2012**, *111*, 40–48. [CrossRef]
14. Wu, T.; Yu, M.; Wang, G.; Wang, Z.; Duan, X.; Dong, Y.; Cheng, X. Effects of stand structure on wind speed reduction in a *Metasequoia Glyptostroboides* shelterbelt. *Agrofor. Syst.* **2013**, *87*, 51–257. [CrossRef]
15. Kim, J.H.; Lim, J.H.; Seo, K.W.; Jeong, Y.H. Effect of wind break on the early growth of *Pinus thunbergii* at Saemangeum sea-wall. *Korean J. Agric. For. Meteorol.* **2013**, *15*, 210–218. [CrossRef]
16. Munns, R. Comparative physiology of salt and water stress. *Plant Cell Environ.* **2002**, *25*, 239–250. [CrossRef] [PubMed]
17. Zhu, J.K. Plant salt tolerance. *Trends Plant Sci.* **2001**, *6*, 66–71. [CrossRef]
18. Heisler, G.M.; Dewalle, D.R. 2. Effects of windbreak structure on wind flow. *Agric. Ecosyst. Environ.* **1988**, *22–23*, 41–69. [CrossRef]
19. Li, B.; Sherman, D.J. Aerodynamics and morphodynamics of sand fences: A review. *Aeolian Res.* **2015**, *17*, 33–48. [CrossRef]
20. Manickathan, L.; Defraeye, T.; Allegrini, J.; Derome, D.; Carmeliet, J. Comparative study of flow field and drag coefficient of model and small natural trees in a wind tunnel. *Urban For. Urban Green.* **2018**, *35*, 230–239. [CrossRef]
21. Duniway, M.C.; Pfennigwerth, A.A.; Fick, S.E.; Nauman, T.W.; Belnap, J.; Barger, N.N. Wind erosion and dust from US drylands: A review of causes, consequences, and solutions in a changing world. *Ecosphere* **2019**, *10*, e02650. [CrossRef]
22. Yang, H.; Lu, Q.; Wu, B.; Yang, H.; Zhang, J.; Lin, Y. Vegetation diversity and its application in sandy desert revegetation on Tibetan Plateau. *J. Arid Environ.* **2006**, *65*, 619–631. [CrossRef]
23. Wu, T.; Zhang, P.; Zhang, L.; Wang, J.; Yu, M.; Zhou, X.; Wang, G.G. Relationship between shelter effects of optical porosity: A meta-analysis for tree windbreaks. *Agric. For. Meteorol.* **2018**, *259*, 75–81. [CrossRef]
24. Chen, G.; Wang, W.; Sun, C.; Li, J. 3D numerical simulation of wind flow behind a new porous fence. *Powder Technol.* **2012**, *230*, 118–126. [CrossRef]
25. Lee, S.J.; Lim, H.C. A numerical study on flow around a triangular prism located behind a porous fence. *Fluid Dyn. Res.* **2001**, *28*, 209–221. [CrossRef]
26. Lee, S.J.; Park, K.C.; Park, C.W. Wind tunnel observations about the shelter effect of porous fences on the sand particle movements. *Atmos. Environ.* **2002**, *36*, 1453–1463. [CrossRef]
27. Perera, M.D.A.E.S. Shelter behind two-dimensional solid and porous fences. *J. Wind Eng. Ind. Aerodyn.* **1981**, *8*, 93–104. [CrossRef]
28. Raine, J.K.; Stevenson, D.C. Wind protection by model fences in a simulated atmospheric boundary layer. *J. Wind Eng. Ind. Aerodyn.* **1977**, *2*, 159–180. [CrossRef]
29. Ranga Raju, K.G.; Garde, R.J.; Singh, S.K.; Singh, N. Experimental study on characteristics of flow past porous fences. *J. Wind Eng. Ind. Aerodyn.* **1988**, *29*, 155–163. [CrossRef]
30. Wang, T.; Qu, J.; Ling, Y.; Xie, S.; Xiao, J. Wind tunnel test on the effect of metal net fences on sand flux in a Gobi Desert, China. *J. Arid Land.* **2017**, *9*, 888–899. [CrossRef]
31. Zhou, X.; Zhang, T.; Ma, W.; Quan, Y.; Gu, M.; Kang, L.; Yang, Y. CFD simulation of snow redistribution on a bridge deck: Effect of barriers with different porosities. *Cold Reg. Sci. Technol.* **2021**, *181*, 103174. [CrossRef]
32. Yu, Y.P.; Zhang, K.C.; An, Z.S.; Wang, T.; Hu, F. The blocking effect of the sand fences quantified using wind tunnel simulations. *J. Mt. Sci.* **2020**, *17*, 2485–2496. [CrossRef]
33. Kang, K. Wind-tunnel simulation on the wind fence effect. *J. Korean Environ. Sci. Soc.* **1998**, *7*, 20–26, (In Korean with English Abstract).
34. Naaim-Bouvet, F.; Naaim, M.; Michaux, J.L. Snow fences on slopes at high wind speed: Physical modelling in the CSTB cold wind tunnel. *Nat. Hazards Earth Syst. Sci.* **2002**, *2*, 137–145. [CrossRef]
35. Chen, T.Y.; Liou, L.R. Blockage corrections in wind tunnel tests of small horizontal-axis wind turbines. *Exp. Therm. Fluid Sci.* **2011**, *35*, 565–569. [CrossRef]
36. He, R.; Sun, H.; Gao, X.; Yang, H. Wind tunnel tests for wind turbines: A state-of-the-art review. *Renew. Sust. Energy Rev.* **2022**, *166*, 112675. [CrossRef]
37. Jeong, U.Y.; Park, T.K. Experimental Investigation of the Shelter Effect of Porous Wind Fences. *KSCE* **2002**, *22*, 1481–1490, (In Korea with English Abstract).
38. Jeong, H.; Lee, S.; Kwon, S.D. Blockage corrections for wind tunnel tests conducted on a Darrieus wind turbine. *J. Wind Eng. Ind. Aerodyn.* **2018**, *179*, 229–239. [CrossRef]
39. Korea Meteorological Administration. Open MET Data Portal. Available online: https://data.kma.go.kr/resources/html/en/aowdp.html (accessed on 4 January 2023). (In Korean).
40. Duncan, D.B. Multiple range and multiple F tests. *Biometrics* **1955**, *11*, 1–42. [CrossRef]

41. Dong, Z.; Luo, W.; Qian, G.; Wang, H. A wind tunnel simulation of the mean velocity fields behind upright porous fences. *Agric. For. Meteorol.* **2007**, *146*, 82–93. [CrossRef]
42. Wang, T.; Qu, J.; Ling, Y.; Liu, B.; Xiao, J. Shelter effect efficacy of sand fences: A comparison of systems in a wind tunnel. *Aeolian Res.* **2018**, *30*, 32–40. [CrossRef]

Disclaimer/Publisher's Note: The statements, opinions and data contained in all publications are solely those of the individual author(s) and contributor(s) and not of MDPI and/or the editor(s). MDPI and/or the editor(s) disclaim responsibility for any injury to people or property resulting from any ideas, methods, instructions or products referred to in the content.

applied sciences

MDPI

Article

Stabilization of Road Embankments on Peat Soils Using Oil Shale Ash and Pozzolanic Additives

Vello Pallav [1,*], Tõnis Teppand [1], Andrus Leinpuu [1], Merrit Shanskiy [2], Mait Mets [1], Hugo Mändar [3], Ergo Rikmann [4] and Jüri Liiv [1,4]

[1] Institute of Forestry and Engineering, Estonian University of Life Sciences, 51014 Tartu, Estonia; tonis.teppand@emu.ee (T.T.); andrus.leinpuu@emu.ee (A.L.); mait.mets@emu.ee (M.M.); jyriliiv@ut.ee (J.L.)
[2] Institute of Agricultural and Environmental Sciences, Estonian University of Life Sciences, 51014 Tartu, Estonia; merrit.shanskiy@emu.ee
[3] Institute of Physics, Tartu University, 51014 Tartu, Estonia; hugo.mandar@ut.ee
[4] Institute of Chemistry, Tartu University, 51014 Tartu, Estonia; ergo.rikmann@ut.ee
* Correspondence: vello.pallav@emu.ee

Abstract: Using kukersite oil shale ash for the stabilization of organic-rich soils has been extensively studied but without much success. The main reason for this is the retarding effect of humic acids present in organic-rich soils on the formation of the C–S–H (calcium–silicate–hydrate) phase, which effectively prevents the solidification of cementitious materials in peat soils. Based on the studies performed at the University of Tartu, we have developed a novel method for the in situ mass stabilization of peat soils using waste materials (calcareous fly ash and silica fume). In this manner, the perfect hardening of peat–ash mixtures (to each 1 m^3 of soil, 150–400 kg ash, 25–50 L pozzolanic additives, and 2.5–5 kaNaOH were added) can be achieved. A test road embankment was constructed under extremely hard conditions in a peat quarry that is currently in use.

Keywords: peatlands; peat soils; stabilization; sustainable construction; oil shale ash; pozzolanic

Citation: Pallav, V.; Teppand, T.; Leinpuu, A.; Shanskiy, M.; Mets, M.; Mändar, H.; Rikmann, E.; Liiv, J. Stabilization of Road Embankments on Peat Soils Using Oil Shale Ash and Pozzolanic Additives. *Appl. Sci.* **2023**, *13*, 8366. https://doi.org/10.3390/app13148366

Academic Editors: Dibyendu Sarkar, Rupali Datta, Itzhak Katra, Prafulla Kumar Sahoo and Mohammad Mahmudur Rahman

Received: 11 May 2023
Revised: 5 July 2023
Accepted: 14 July 2023
Published: 19 July 2023

Copyright: © 2023 by the authors. Licensee MDPI, Basel, Switzerland. This article is an open access article distributed under the terms and conditions of the Creative Commons Attribution (CC BY) license (https://creativecommons.org/licenses/by/4.0/).

1. Introduction

Since the 1970s, scientists in many parts of the world have explored ways to build "floating" foundations, roads, and railway embankments by mixing unstable soils with binders on site instead of excavating all the soft soil beneath the road embankment down to the bedrock and replacing it with mineral fill. This makes it possible to significantly reduce the volume and cost of excavation and ensure the linear movement of the construction front. This approach is economically attractive and more environmentally friendly than traditional methods. The lifetimes of the bases obtained in this way are generally several times longer than those of filled bases [1].

The most problematic scenario is the stabilization of peat soils. This is being actively investigated (especially in Malaysia, Indonesia, and other peat-rich countries), but current solutions are expensive and require the use of large amounts of high-quality cement [2]. The use of lime (including lime-containing fly ash) is not possible on peat soils due to their low silicate and aluminate contents. Low pH values caused by organic acids (incl. humic and fulvic acids) can prevent the dissolution of clay minerals [3]. Additionally, the effect of humic acids on the setting process of cement is not fully understood.

In Estonia, improvements in the geotechnical properties of organic-rich soils have been investigated mostly by mixing or covering organic soils with filling soils and by compacting the organic soil. In 1979, a 4 m thick peat layer at a construction site was covered with a 4 m thick filling layer. Within 3 months, the thickness of the peat layer decreased by 60%, the undrained shear strength C_u doubled, and the water content decreased twofold. The 5 m high partition walls built on the peat subsided 3–6 mm, and the floors subsided 1–2 mm in the subsequent 5 years.

In Estonia, the most attractive binding agent for stabilizing road embankments on soils containing humic substances is oil shale ash [3,4], which is domestically produced in power and oil plants in excess of 7 million tons per year (before the reduction in power generation by the incineration of oil shale) [5].

Since 2014, geotechnical studies on soil stabilization to build road embankments have been carried out on the Võõbu polygon. In a particular experiment, organic-rich soil was loaded with a pressure of 42–97 kPa. At maximum pressure, the relative consolidation was 51%, and at lower pressure, it was 35%. The C_u of peat soil increased by 7 kPa to 28 kPa. After removing the load, the secondary consolidation ranged between 23 and 44 mm. In laboratory tests, soil samples taken from the Võõbu polygon were mixed with cement, oil shale ash, limestone screenings, and sand. Satisfactory results were only obtained when the soil was mixed with cement at a volumetric cement ratio exceeding 10%, and additional compaction under the influence of vertical loads was used. This made the methodology expensive. Mixing oil shale ash and peat generated no satisfactory results and even caused a reduction in the compressive strength of the peat [6].

This phenomenon has been observed before; floors made of oil shale ash have decayed due to the action of organic matter in previous studies.

However, road construction projects which utilize the removal and replacement of organic soil with backfilling showing an adequate load-bearing capacity or with the dense compacting of organic soil are time-consuming and costly as well as ecologically unsustainable [2].

The promoters of this project have previously (KIK 11048 "Reuse of secondary polymer waste and oil shale ash as building material raw material. Peat-based composite material with spatially prestressed polymer reinforcement") and successfully solved all problems related to chemical processes and developed a composite material of peat and oil shale ash [4].

A similar methodology can also be used to stabilize road embankments on peat soil because the chemical processes taking place are analogous. In this case, only the upper geotechnically necessary minimum part of the subsoil (down to 1–2 m) is stabilized. The rest of the subsoil (deeper than 1–2 m) is left untouched without disturbing the existing water regimes in ecosystems [7].

Initially, lime and materials containing it were mainly used to harden floating roadbeds, but in the 1980s, it was found that cement or cement–lime mixtures where cement has partially been replaced with lime are considerably more effective (but also more expensive). Soil stabilization with lime is possible only if its mineral part contains a sufficient amount of pozzolanic components (silicate clay particles) [1].

The stabilization of soils containing peat is expensive and requires the use of large amounts of high-quality cement [2]. The common use of lime (including lime-containing fly ash) is not possible on peat soils due to its low silicate content and the humic acids present in soil [1].

Humic acids have a strong chemical affinity for group II metal ions ($Ca^{2+,}$ $Mg^{2+,}$ etc.) [8], so they react with lime to form insoluble calcium and magnesium humates which can be adsorbed on the surface of the cementing particles, preventing the hydration of silicates and pozzolanic reactions [9].

Similar problems have also been described in studies dealing with the stabilization of peat soils with cement:

(1) Humic acids actively bind Ca^{2+}, forming insoluble humates and thus decreasing the amount of available Ca^{2+} ions to form C–S–H gel, while fulvic acids more selectively attack Al-containing particles, covering them with an adsorbed layer of fulvates and inhibiting further reactions. Fulvic acids can also disrupt the crystallization of calcium aluminate hydrate, calcium sulfate aluminate hydrate, and calcium ferrite aluminate hydrate [9].

(2) The dissolution of acidic compounds causes the pH level in the pore water to drop close to or below the threshold, above which secondary cementation products can form (pH~9), thus slowing down or preventing hardening [9].
(3) A high water-binding capacity, as well as high moisture content, slows down the hardening processes [9].

In Estonia, studies have been carried out to strengthen road embankments using oil shale ash [10–12], but their implementation was based on incomplete assumptions. These studies aimed to achieve the stabilization of soil at the expense of the hydraulic hardening of oil shale ash, but due to its low pozzolanic content, solidification occurs only when lime reacts with atmospheric carbon dioxide; in the deeper layers, it would require hundreds of years [13]. Additionally, the inhibitory effect of humic acids on hardening processes and their lime-degrading effect were not taken into account [6]. However, it has been proven that these problems can be successfully addressed with relatively cheap additives and a suitable treatment regime, which allows the bearing capacity of a road embankment to exceed 100 kPa. The aim of this study is to apply the results of earlier chemical studies performed at the University of Tartu [3,4,14] for the in situ mass-stabilization of peat soil areas, allowing the retarding effect of humic acids to be minimized.

2. Materials

2.1. Peat Soil

Soil sampling took place in January 2019 at the Järvselja Training and Experimental Forest Centre of the Estonian University of Life Sciences (58°16′ N, 27°19′ E) in four different locations. The soil at the test site is peat with a layer thickness of 0–3 m. Below this, in turn, lies a moraine layer and Devonian sediments. Due to the geology, it is a very good place for the formation of peat soils (the water-holding layers below the moraine layer). Additionally, this small area shows high variation in soil types [15]. The humidity and contents of organic and inorganic matter in percent by weight are shown in Table 1.

Table 1. Humidity, organic, and mineral matter concentrations (% of dry weight) of soil samples from the Järvselja test site.

Test Site	Depth, cm	Humidity, %	Organic Matter, %	Mineral Matter, %
1	0–22	181.7	34.4	65.6
	22–47	218.5	53.8	46.2
	47–111	146.9	22.2	77.8
	111–130	87.6	9.4	90.6
2	0–47	300.0	53.2	46.8
	47–77	192.4	55.6	44.4
	77–90	84.5	17.2	82.8
3	0–10	130.4	25.6	74.4
	10–37	200.3	42.0	58.0
	37–52	331.0	72.4	27.6
4	0–10	254.6	82.6	17.4
	10–37	246.0	59.9	40.1
	46–86	243.6	80.8	19.2
	92–114	100.8	24.7	75.3
	122–144	44.7	4.9	95.1

In sampling areas 1 and 4, the thickness of the peat layer and the deposition depth of the mineral subsoil are slightly more than one meter. In areas 2 and 3, the peat layer is thinner. In area 2, the subsoil is approximately 85 cm deep, and in area 3, it is less than half a meter deep.

2.2. Oil Shale Ash

EestiEnergia (an Estonian national energy company) generates millions of tons of oil shale ash every year, and approximately 5% of this is reused as a raw material; the majority of the ash is deposited in landfills [5].

The organic component of oil shale usually does not exceed 40% of the total mass (usually less)[1]. The composition of the mineral part, i.e., oil shale ash, which remains after burning is quite variable depending on the type of layer the oil shale used for heating derives from, and even more so on how many intermediate layers are left in the oil shale during sorting. The main part of the intermediate layers is made up of calcium carbonate or limestone. During firing, it decomposes into quicklime CaO and carbon dioxide.

In power plants, finely ground oil shale is burned floating in air (pulverized firing PF, older energy blocks) or in circulating fluidized bed boilers (CFB, newer energy blocks).

PF fly ash, consisting of the mineral part of oil shale, is separated from combustion gases using cyclones and electric filters. Fly ash is suitably fine for use as a binder and has the best hardening properties. It can have different mineral and elemental compositions depending on where it is obtained (cyclone or electrostatic precipitator).

Fluidized bed burning takes place at a lower temperature, and thus some of the calcium carbonate present in oil shale remains intact. At the same time, some toxic components of burning gas (phenoles, sulfur oxides) are trapped in the same ash, forming calcium sulfate and other substances.

The third type of oil shale ash is $DeSO_x$ ash, obtained from the desulfurization system of power plants. CaO from boilers is used in semidry $DeSO_x$ systems to remove sulfur oxides from emission gases. This ash has a high sulfate content.

The compositions of ashes used in the experiments are described in Table 2.

Table 2. Crystalline phases of oil shale ashes used in experiments, in percent by weight.

Component		CFB [1] Ash, %	Cyclone PF [2] Ash, %	$DeSO_x$ [3] Ash, %
Quartz	SiO_2	16.8	9	12.2
Orthoclase	$KAlSi_3O_8$	12.5	2.3	0.4
Illite + Illite–Smectite	$Na,K_x(Al,Mg)_2Si_4O_{10}(OH)_2 \cdot xH_2O$	13.8		0.4
Belite	Ca_2SiO_4	5.3	15.3	12.5
Merwinite	$Ca_3Mg(SiO4)_2$	5.7	11.9	13.1
C3A	$3CaO \cdot Al_2O_3$			1.6
Periclase	MgO	2.3	3.2	2.5
Melilite	$(Ca,Na)_2(Mg,Al)(Si,Al)_3O_7$	1.2	6.7	2
Anhydrite	$CaSO_4$	9.5	7.5	8.7
Lime	CaO	10.8	34.5	11
Calcite	$CaCO_3$	13.5	4.7	13.4
Portlandite	$Ca(OH)_2$		2.9	4.8
Hematite	Fe_2O_3	4.3	0.7	
Pseudowollastonite	$CaSiO_3$	3.6	0.6	1.7
Bassanite	$CaSO_4 \cdot 0.5(H_2O)$			1.5
Hannebachite	$Ca_2(SO_3)_2 \cdot H_2O$			13.4

[1]—circulating fluidized bed. [2]—pulverised firing. [3]—desulphurization.

2.3. Silica Fume

Silica fume (fine silica SiO_2) is one of the best pozzolanic agents[2]. Two different types of silica fume were used: microscale SiO_2 of Egyptian origin (manufactured by Efaco) and nanoscale SiO_2 (manufactured by Cabot) with a microscale particle diameter. Later, a ready-made suspension of nanosilica fume produced by TamCem was also introduced. The main silica fume data are shown in Table 3.

Table 3. Characteristics of three types of silica fume used in the study.

Silica Type	Particle Size, nm	SiO_2 Content, %
CAB-O-SIL H5	200–300	99.8
Efaco silica fume	1000	92
TamCem NanoSilica	10–15	20

2.4. Other Reagents

Caustic soda (potassium hydroxide, NaOH) and waterglass (sodium silicate, $(Na_2O)_x \cdot (SiO_2)_y$, 20% solution) were obtained from Keemiakaubandus AS technical grade.

2.5. Bog Water

Bog water with high acidity (pH 3) was collected from the same area as the soil, i.e., the Järvselja Experimental Centre. The organic content of the water was appr. 3%.

3. Experimental Procedure

3.1. Initial Lab Tests

Initially, 20 test specimens with different recipes were prepared for each soil type; later, the number of test specimens in each series increased to 57.

To prepare each test piece, 200 g of peat soil was mixed with 100–200 g of ash and additives. No pretreatment of peat was applied (except for the removal of green plant residues) so that its natural water content could be preserved. Additives included silica fume (SiO_2), NaOH for pH adjustment, and waterglass (20% Na_2SiO_3 aqueous solution). The use of additives in different test mixtures was varied (in most cases, not all additives were used together), and the data on the composition of specific test objects are shown in Table 4 (for the abbreviations, see Section 3.2).

Table 4. Composition of test specimens.

Specimen	Soil, g	Water, g	Cement, g	$DeSO_x$ [3] Ash, g	CFB [1] Ash, g	PF [2] Ash, g	Efaco Silica, g	CAB-O-SIL Silica, g	20% Waterglass, g	NaOH, g	Hardening in 7 Days
1	200		100								No
2	200		100							30	Yes
3	200			100			100				No
4	200					100	100				No
5	200			100			100			30	Yes
6	200					100	100			30	Yes
7	200			100							No
8	200					100					No
9	200			100			100		100		Yes
10	200					100	100		100		Yes
11	200	-			100	-	50	-	30	30	Yes
12	200	50			200	-	50	-	30	30	Yes
13	200	100			100	-	-	50	30	30	Yes
14	200	-			100	-	50	-	-	30	Yes
15	200	-			100	-	-	50	-	30	Yes
16	200	-			-	100	50	-	30	30	Yes
17	200	50			-	200	50	-	30	30	Yes
18	200	100			-	100	-	50	30	30	Yes
19	200	-			-	100	50	-	-	30	Yes
20	200	-			-	100	-	50	-	30	Yes

[1]—circulating fluidized bed. [2]—pulverised firing. [3]—desulphurization.

First, the hardening of the test pieces was checked after the first 7 days of mixing. Preliminary testing of the hardening of the specimens was performed using cone apparatus (Figure 1a). Samples that did not show any hardening were marked "No" in the "Hardening within 7 Days" cell in Table 4 and were excluded from further studies. The samples that showed hardening are indicated as "Yes" in Table 4, and 12 recipes were selected for the compression–strain analysis. The test specimens were prepared in standard containers (Figure 1b) for the compressive strength measuring apparatus.

The water content was determined on natural material (soil) and its composite mixtures. Water content (w) is the mass of water in the test sample expressed as a percentage of the weight of the dry test sample (EVS-EN 1097-5:2008).



(**a**) (**b**)

Figure 1. (**a**) Preliminary testing of the hardening of the specimens with the cone apparatus; (**b**) test specimens placed in containers.

3.2. Initial Field Tests

The preparation of pilot-scale test specimens took place at the Järvselja test site. Two 1 × 1 × 1 m pits were dug in the soil, in each of which a 1 m^3 bigbag made of water-permeable material was placed. The excavated soil was mixed with fly ash, silica fume, waterglass, and NaOH (Table 5) and used for backfilling bags (Figure 2). The recipe of the laboratory test specimen T17 was chosen as the basis for the pilot-scale test specimens, and it was identical to Table 5.

Table 5. Composition of the mixture used in field tests, as weighted.

Specimen	Soil, kg	CFB Ash, kg	Efaco Silica, kg	NaOH, kg	Waterglass, kg
AT	20	8	4	0.6	0.6

After the mixture was prepared and filled, the bigbag was sealed to prevent the mixture from drying too quickly.

The specimens were allowed to harden for 4 months from mid-June to mid-October 2019. During this period, the evolution of the mechanical properties of the test specimens was monitored. In October 2019, sampling took place.



(**a**) (**b**)

Figure 2. (**a**) mixing the soil with ash and additives; (**b**): bigbags partially filled with soil mix (labelled as Bag 1 on the (**a**) and Bag 2 on the (**b**)).

3.3. Construction of Test Roads

The concept was to build an experimental road on soil with the lowest possible bearing capacity to test the methodology under critical conditions to the extent possible. We chose a partially mined peat deposit at the Elva E.P.T. company in Sangla (58°30′ N, 26°25′ E) for two reasons:

- Easy access with large trucks (a car carrying shale ash);
- Possibility to use Elva E.P.T.'s heavy machinery.

The locations of the roads were marked, and the soil was loosened to the working depth (Figure 3, top left). The working depth was about 1 m. The upper peat layer had already been removed during the peat mining operations.

Five recipes of different thicknesses and compositions were tested (including one containing wood chips for reinforcing; Figure 3 top right and Table 6). All components (except oil shale ash) were added to the soil surface and then mechanically mixed with peat to a depth of 1 m. The PF oil shale ash was spread separately (Figure 3 bottom right) and immediately mixed with the soil (the hardening process began). The road was leveled and compacted (Figure 3 bottom left). The road, completed in the autumn of 2021, was left to stand over the winter. Load tests were carried out after the snow melted in the spring of 2022. The tests were carried out by OÜ REI Geotehnika (Figure 4).

Table 6. Composition of test specimens (field studies). PF ash from electrostatic precipitators and silica suspension from TamCem were used.

Specimen	Thickness, cm	Volume, m^3	Soil, m^3	Wood Chips, m^3	Ash, kg	Silica, l	NaOH kg	Waterglass l
1	100	10	10		2000	450	50	50
2	100	10	10		4000	450	50	50
3	100	10	7	3	2000	450	50	50
4	75	7.5	7.5		2250	337.5	37.5	37.5
5	50	5	5		1500	225	25	25



Figure 3. Clockwise from top left: preparatory work in Sangla bog; adding components; spreading of oil shale ash; road surface leveling.



Figure 4. Equipment for the road embankment load test on the test site.

3.4. Mechanical Testing of the Specimens

3.4.1. Uniaxial Compression Tests

After 14 and 28 days of hardening, the compression–strain diagrams of the test specimens were recorded (Figure 5). Uniaxial compression tests were performed using an Instron model 3369 universal testing machine (maximum load 50 kN).



Figure 5. Placement of the test specimen in the Eijkelkamp displacement apparatus.

The preparation of specimens for triaxial tests is costly and labor-intensive. Thus, monoaxial compression tests were selected for the studies of stabilized organic-rich soils. The density and water content were examined. For uniaxial compression tests, test specimens with dimensions of 50 × 50 × 50 mm and 150 × 150 × 150 mm were used.

Before the experiments, the samples were weighed on a Kern 578 electronic balance with an accuracy of 0.05 g. The surfaces of the test specimens were leveled and ground so that the difference in surface smoothness did not exceed 0.1 mm per side with a length of 100 mm and were then placed evenly on the loading plates. A mechanical load was applied to the test specimens with a continuously increasing force until failure or an exact displacement of 16 mm was reached. The maximum force exerted on the test objects in kN and the time of application of the maximum force were recorded, and the compressibility of the test objects in millimeters was measured depending on the force exerted on them. The q_u values were determined at compression tests, and then using the q_u values, shear strength and the expected load limit q_o were calculated. The compressive strength fc [N/mm^2] was calculated as the quotient of the maximum compressive force Fc [N] and the total area of the loaded surface [mm^2].

3.4.2. Shear Strength Tests

The tests were carried out as part of Andrus Leinpuu's master's thesis and were considered indicative, enabling the selection of the optimized composition of the mixture used in the final field tests (see Sections 4.3 and 4.5). In this regard, the solidified test specimens were treated not as mass-stabilized soil, but as lightweight concrete with organic fillers, and the tests were performed according to the national standard "EVS-EN 12390-3:2019 Testing hardened concrete—Part 3: Compressive strength of test specimens", using the equipment available in the research group's laboratory. The standard allows the use of cube or cylinder-shaped specimens or drill cores as test pieces. The corresponding ISO standard is "ISO 1920-6 Testing of concrete—Part 6: Sampling, preparing and testing of concrete cores". The water-saturated samples were weighed on a KERN FKB electronic scale, where the mass of the samples was determined together with the cutting ring and filter paper. The specimens were placed in an electronically controlled Eijkelkamp shear apparatus, and plane shear tests were performed (Figure 5). Load levels of 100, 200, 300, and 500 kPa were used. The duration of the test cycles was 36 min. The pressure apparatus stopped automatically when the yield point was reached.

3.4.3. Compressibility Tests

The compressibility test, or oedometer test, was prepared based on "EVS-EN 12390-3:2019 Testing hardened concrete—Part 3: Compressive strength of test specimens".

During the compression tests, load levels of 0.005, 0.01, 0.02, 0.04, 0.08, 0.16, and 0.32 MPa were used. At all load levels, the duration of loading was 12 h. Decompression was carried out at a load level of 0.005 MPa, and the duration of decompression was 2 h.

With oedometer cutting rings, the correct size specimens were taken to perform the compression test. The specimens were weighed together with the oedometer cutting ring and plates (Figure 6). The specimens were placed in the oedometer KP, with the number of lever press transmissions n = 10. An initial reading was taken from the gauge, and then the first load level was placed on the test pieces. All load levels were kept for 12 h. After reading the last load stage, the specimens were decompressed for 2 h. Specimens were removed from the oedometer and reweighed with an electronic scale to determine the mass of the specimen after the test. The tested specimens were placed in a drying oven to determine their water content and dry bulk density.



Figure 6. Preparation of specimens for the oedometer tests.

3.5. XRD/XRF Measurements

XRD/XRF tests were performed to determine the phase and elemental composition of the samples.

XRD was performed on a SmartLab^{TM} diffractometer (Rigaku, Tokyo, Japan), tube power 8.1 kW, using Cu rotating anode working at 45 kV and 180 mA, coordinate sensitive 1D detector D/teX Ultra and Bragg–Brentano optical setup. The diffraction pattern was measured between diffraction angles of 8 and 90° with a step size of 0.01° (2θ) and a scan speed of 4 deg/min. PDXL software (Rigaku) and database PDF-2 (International Centre of Diffraction Data, 2018) were used for phase identification. TOPAS 6 Academic software was used for the analysis of mass concentrations of crystalline and amorphous phases implementing the Rietveld refinement method.

The initial structural parameters of phases required for the refinements were taken from the database ICSD 2019 (FIZ Karlsruhe, Germany).

The concentration of the amorphous phase was estimated by a quantitative XRD analysis method using zircon ($ZrSiO_4$) as an external standard material for the calculation of calibration constants.

The quantities of Rwp and Rwp' (given in tables below) were defined as the overall residual error of the Rietveld approximation, i.e., the weighted difference between the

theoretically calculated and measured diffraction patterns of the phases found, taking into account the background and excluding the background, correspondingly.

XRF was performed on a spectrometer (ZSX 400, Rigaku, Tokyo, Japan) using an Rh X-ray tube working at a power of 3 kW.

4. Results and Discussion

4.1. Initial Lab Tests

The results of stress–strain tests are shown in Table 7 and Figure 7.

Table 7. Parameters and results of compression–strain tests.

	Specimen	Compressibility at Maximum Force, mm	Maximum Force, kN	Time on Max Force, s
1	T-6	16.08	7.53	482.54
2	T-10	16.04	12.01	481.26
3	T-11	16.02	7.38	480.56
4	T-12	16.07	7.42	482.18
5	T-13	16.34	3.19	490.26
6	T-14	16.02	8.35	480.51
7	T-15	16.01	4.9	480.44
8	T-16	16.13	20.01	483.81
9	T-17	16.01	1.25	480.26
10	T-18	16.03	3.74	480.76
11	T-19	17.78	2.33	533.52
12	T-20	16.47	0.53	494.22

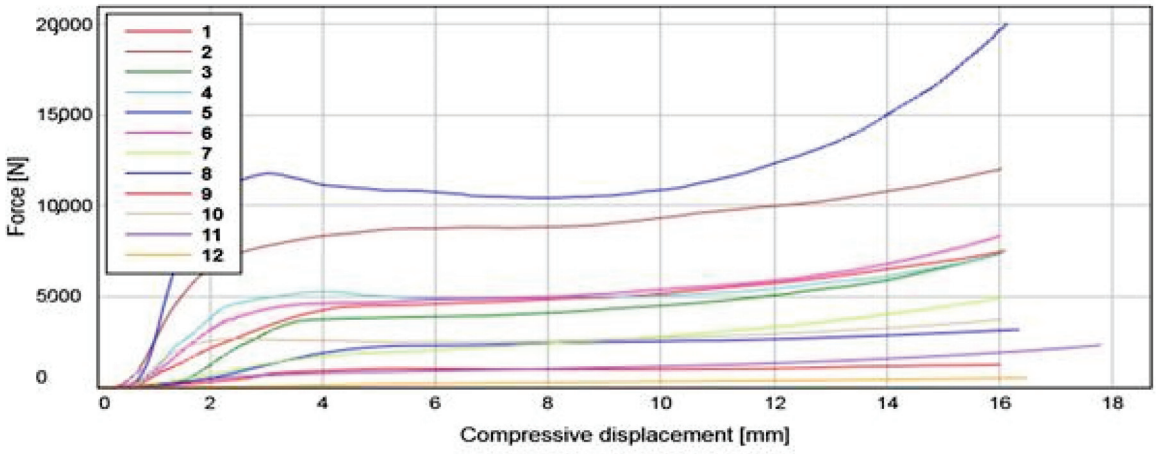


Figure 7. Compression–strain curves of test specimens listed in Table 7.

The results of the phase composition analysis for crystalline and semi-amorphous phases determined by the X-ray diffraction (XRD) method are presented in Table 8.

The elemental compositions of samples T10, T11, and T17 determined by X-ray fluorescence spectroscopy (XRF) (spectrometer ZSX 400, Rigaku, Tokyo, Japan) are given in Table 9.

The results of compression–deformation tests show that naturally occurring fibers in peat perform mechanically similarly to steel reinforcement or glass fiber admixtures in conventional cement-based concrete, with a difference appearing when compression occurs. The reinforcement effect and plasticity provided by the peat fiber to the composite are better, and the mechanical pressure exerted on the peat–ash composite is higher. Figure 8 shows that the compressive strength of the composite increases again under load after crossing the "plateau", unlike normal concrete. This may be due to the effect of heat from mechanical stress on the lignin contained in the naturally occurring fibers in the peat,

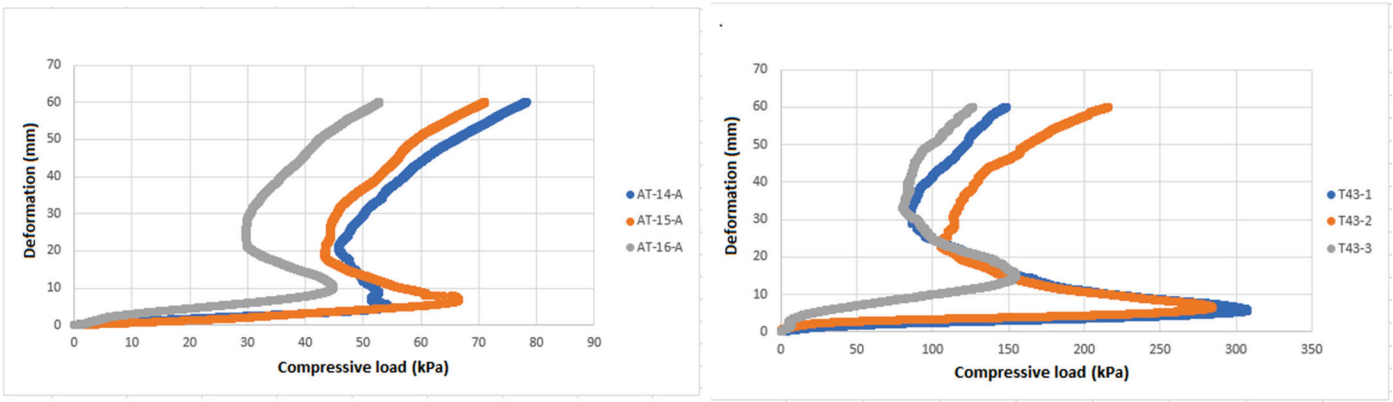
creating an additional "glue effect" in the composite. This described phenomenon requires further research.

Table 8. Mineral composition of the test specimen in per cents by weight.

Component		T10	T11	T17
		Rwp = 2.9%; Rwp′ = 9.2%	Rwp = 2.4%; Rwp′ = 12.4%	Rwp = 2.7%; Rwp′ = 15.7%
Quartz	SiO_2	33.6(1)	10.3(1)	6.8(1)
Anorthoclase	$KAlSi_3O_8$	1.4(2)	1.4(2)	1.1(1)
Orthoclase	$KAlSi_3O_8$	2.3(1)	3.8(2)	1.1(1)
Microcline	$(K,Na)(AlSi_3O_8)$	4.1(2)	1.3(2)	0.7(1)
Albite	$Na(AlSi_3O_8)$	2.2(1)	0.5(1)	0.4(1)
Arcanite	$K_2(SO_4)$	2.6(1)	3.2(1)	3.3(1)
Dolomite	$CaMg(CO_3)_2$		0.7(1)	
Belite	Ca_2SiO_4			2.4(1)
Periclase	MgO		0.6(1)	1.0(1)
Akermanite	$Ca_2MgSi_2O_7$		2.2(1)	0.4(1)
Calcite	$CaCO_3$	4.0(1)	5.0(1)	3.7(1)
Hematite	Fe_2O_3	0.7(1)	0.3(1)	
CSH, semi-amorphous phase		10(1)	24(2)	37(1)
Amorphous phase		40(1)	46(2)	42(1)

Table 9. Elemental composition of crystalline phases of samples T10, T11, and T17 (percent of total weight) with standard deviations.

Element	T10	T11	T17
Al	1.607 ± 0.046	1.252 ± 0.057	0.552 ± 0.036
C	0.808 ± 0.018	1.272 ± 0.043	0.819 ± 0.020
Ca	6.912 ± 0.198	15.960 ± 0.227	19.666 ± 0.110
Cl	0.108 ± 0.021	0.349 ± 0.039	0.085 ± 0.026
Fe	0.319 ± 0.038	0.849 ± 0.036	0.343 ± 0.048
K	3.655 ± 0.065	4.309 ± 0.128	3.296 ± 0.060
Mg	0.071 ± 0.017	1.187 ± 0.055	1.153 ± 0.035
Na	0.340 ± 0.016	0.092 ± 0.014	0.069 ± 0.012
O	50.562 ± 0.036	48.945 ± 0.083	49.409 ± 0.046
S	0.782 ± 0.010	1.089 ± 0.030	1.035 ± 0.014
Si	34.836 ± 0.128	24.696 ± 0.072	23.572 ± 0.070



(**a**) (**b**)

Figure 8. Graphs of compressive strength of 150 × 150 × 150 mm specimens of AT mixture (**a**); graphs of compressive strength of 150 × 150 × 150 mm specimens of T43 mixture (**b**).

As shown in Table 8, the content of the semi-amorphous CSH phase (hydrated semi-amorphous calcium silicate) increased almost four-fold in the order of T17 > T11 > T10, while the content of non-hydrated quartz showed the opposite trend. The quartz content decreased in the order of T10 > T11 > T17 from 33.6% in T10 to 10.3% in T11 and 6.8% in T17. The high SiO_2 content of specimen T10 also indicates that SiO_2 was added in excess, and its hydration and the rate of CSH gel (amorphous and semi-amorphous calcium silicate) formation were limited by the Ca^{2+} ion content, resulting in lower plasticity of the specimen compared to other specimens. For specimens T10 and T11, which had a lower content of CSH gel (amorphous and semi-amorphous calcium silicate), the crystallization of alkaline feldspars proceeded faster, while for specimen T17, it proceeded significantly slower. The crystallization of alkaline feldspars was also described in our previous work[3].

Among all samples, a relatively similar amount of the fully amorphous phase, which includes both the organic matter and a portion of the CSH gel, was present. Belite was detected only in specimen T17. The crystal phases of specimen T11 containing CFB ash also showed higher amounts of Mg- and Fe-bearing minerals.

4.2. Simulation of the Natural Conditions in the Lab

Based on the test results, it can be seen that the water content mixtures are 2–3 times lower than those of natural soil under the same conditions. As a result, we can say that mixtures do not absorb water and stay relatively dry.

4.3. Initial Tests in Nature

Five samples were taken, the phase composition and mineral compositions of which are outlined in Tables 10 and 11. The formation of crystalline phases proceeds relatively slowly under swamp conditions, and amorphous phases still make up approximately half of the total mass after 4 months.

Table 10. Mineral compositions of the crystalline and semi-amorphous phases of the pilot test specimens, percent by total weight. Samples are taken from different depths of test specimens prepared in bigbags and matured in soil in natural conditions for 4 months.

Mineral		Bag 1, 0–20 cm	Bag 1, 21–40 cm	Bag 1, 41–60 cm	Bag 1, below 60 cm	Bag 2, 0–20 cm
Quartz	SiO_2	8.58 ± 0.05	9.03 ± 0.06	12.97 ± 0.10	36.48 ± 0.31	8.65 ± 0.06
Calcite	$CaCO_3$	6.52 ± 0.05	6.26 ± 0.05	5.69 ± 0.06	0.59 ± 0.06	9.54 ± 0.07
CS anhydrite	$CaSO_4$	0.45 ± 0.05	0.65 ± 0.05	0.75 ± 0.04	0.00 ± 0.08	0.50 ± 0.05
Anorthoclase	$KAlSi_3O_8$	1.52 ± 0.12	1.18 ± 0.13	1.11 ± 0.09	2.44 ± 0.21	0.98 ± 0.15
Orthoclase	$KAlSi_3O_8$	3.55 ± 0.13	4.04 ± 0.14	3.71 ± 0.14	5.22 ± 0.18	4.62 ± 0.13
Microcline	$KAlSi_3O_8$	1.92 ± 0.23	1.89 ± 0.23	1.89 ± 0.19	10.90 ± 0.32	1.63 ± 0.22
Hematite	α-Fe_2O_3	0.92 ± 0.02	1.01 ± 0.02	0.74 ± 0.02	0.36 ± 0.05	1.00 ± 0.02
Akermanite	$MgAl.Ca_2Mg(Si_2O_7)$	0.85 ± 0.08	0.95 ± 0.08	0.85 ± 0.07	0.12 ± 0.07	1.74 ± 0.06
Periclase	MgO	0.67 ± 0.03	0.78 ± 0.03	0.26 ± 0.03	0.18 ± 0.03	0.67 ± 0.03
Mervinite	$Ca_3Mg(SiO_4)_2$	0.24 ± 0.03	0.31 ± 0.04	0.10 ± 0.03	0.11 ± 0.04	0.29 ± 0.06
Halite	NaCl	0.57 ± 0.02	0.50 ± 0.03	0.19 ± 0.02	0.20 ± 0.05	0.02 ± 0.02
Gelenite	$Ca_2Al[AlSiO_7]$	0.78 ± 0.11	0.80 ± 0.11	0.55 ± 0.09	0.04 ± 0.08	0.21 ± 0.04
$CSH_{0.5}$	$CaSO_4 \cdot \frac{1}{2} H_2O$	1.19 ± 0.06	1.35 ± 0.06	1.67 ± 0.05	0.41 ± 0.07	0.46 ± 0.07
Illite 2M1	$(K.H_3O)(Al.Mg.Fe)_2(Si.Al)_4O_{10}[(OH)_2.(H_2O)]$	2.26 ± 0.17	1.97 ± 0.19	2.04 ± 0.18	15.28 ± 0.25	0.68 ± 0.14
Illite 2M1 001	$(K.H_3O)(Al.Mg.Fe)_2(Si.Al)_4O_{10}[(OH)_2.(H_2O)]$	–	–	–	–	0.30 ± 0.11
Chloritoid 2M	$(Fe.Mg.Mn)_2Al_4Si_2O_{10}(OH)_4$	0.08 ± 0.07	0.07 ± 0.06	0.10 ± 0.06	0.77 ± 0.11	0.06 ± 0.06
Melilite	$(Ca.Na)_2(Al.Mg.Fe^{2+})[(Al.Si)SiO_7]$	0.83 ± 0.15	1.23 ± 0.18	0.73 ± 0.14	0.04 ± 0.04	0.75 ± 0.12
C2S belite α	$2CaO{\cdot}SiO_2$	1.47 ± 0.10	1.30 ± 0.10	0.25 ± 0.05	0.00 ± 0.06	0.83 ± 0.09
C2S belite β (larnite)	$2CaO{\cdot}SiO_2$	0.99 ± 0.10	0.83 ± 0.10	0.23 ± 0.09	0.00 ± 0.05	0.10 ± 0.04
Albite	Albiit. $NaAlSi_3O_8$	BDL	BDL	0.75 ± 0.06	7.93 ± 0.13	0.39 ± 0.07
Kaolinite	$Al_2Si_2O_5(OH)_4$	BDL	BDL	0.9 ± 0.13	3.83 ± 0.25	0.87 ± 0.12
CSH semi-amorphous	$xCaO{\cdot}ySiO_2{\cdot}zH_2O$	17.4 ± 1.0	16.3 ± 1.0	12.3 ± 1.0	0.37 ± 0.34	11.2 ± 0.8
Crystalline and semi-amorphous phases		51	50	48	85	45
Amorphous phases		49	50	52	15	55

Table 11. Elemental compositions of the mineral part of samples presented in Table 10 in percent by weight.

	Bag 1 0–20 cm	**Bag 1 21–40 cm**	**Bag 1 41–60 cm**	**Bag 1 >60 cm**	**Bag 2 0–20 cm**
O	37.1	48.2	47.8	47.3	28.5
C	30.2	6.28	9.29	6.88	12.8
Ca	12.7	29.2	31.0	28.5	5.75
Si	9.78	0.814	0.891	2.50	29.3
K	3.54	3.47	0.905	1.46	1.91
Al	1.24	0.244	0.239	3.37	3.88
Mg	1.11	2.08	2.19	1.94	0.687
P	0.987	0.941	0.992	0.856	0.379
Fe	0.984	0.205	0.208	0.430	2.91
Mn	0.702	0.766	0.764	0.781	0.137
S	0.646	0.415	0.184	0.375	0.240
Cl	0.401	0.141	0.0513	0.0770	0.0287
Ba	0.188	0.765	0.563	0.575	0.101
Na	0.173	6.18	4.55	4.61	1.08
Zn	0.0777	0.147	0.0896	0.243	0.0354
Ti	0.0764	0.0720	0.168	0.0758	0.182
Zr	0.0355	0.0619	0.0616	0.0654	0.0182
Cr	0.0197	BDL	BDL	BDL	BDL
Zr	0.0129	BDL	BDL	BDL	0.0228
Rb	0.0127	0.0089	TR	TR	0.0067
Cu	0.0062	0.0108	0.0107	0.0108	TR
Ni	0.0044	0.0072	TR	TR	0.0078

Several elements, such as C, Si K, Al, Fe, and S Cl, are concentrated in the upper layer, but the contents of O, Ca, Mg, Ba, and Na are higher in deeper layers. The contents of P and Mn do not change significantly with depth.

4.4. Mechanical Testing of the Specimens

All the results of mechanical tests are summarized in Table 12 (see below).

Table 12. Undrained shear strength cu, undrained residual shear strength c_u, and residual and bearing capacity q obtained as a result of uniaxial compression tests of 50 × 50 × 50 mm specimens.

Specimen	**w** [1] **%**	**ρ** [2] **g/cm^3**	**ρ_d** [3] **g/cm^3**	**q_u** [4] **kPa**	**c_u** [5] **kPa**	**$q_{u,res}$** [6] **kPa**	**$c_{u,res}$** [7] **kPa**	**q** [8] **kPa**
Soil-1	181.4	0.8	0.29	14	7	14	7	22
Soil-2	181.6	0.75	0.27	12	6	12	6	19
Soil-3	168.5	0.84	0.31	30	15	30	15	47
AT-1	109.9	1.09	0.52	17	8	16	8	25
AT-2	80	1.11	0.61	60	30	42	21	94
AT-3	108	1.02	0.49	38	19	24	12	60
T41-1	138.9	1.18	0.5	17	8	16	8	25
T41-2	139.5	1.08	0.45	11	5	8	4	16
T41-3	109.2	1.25	0.6	43	21	34	17	66
T42-1	171.6	1.07	0.39	45	22	45	22	69
T42-2	175.7	1.08	0.39	34	17	34	17	53
T42-3	164.4	1.03	0.39	42	21	42	21	66
T44-1	166.4	1.04	0.39	40	20	38	19	63
T44-2	131.8	1.14	0.49	66	33	50	25	104
T44-3	130.5	1.1	0.48	42	21	34	17	66

[1]—water content (of dry mass). [2]—density. [3]—dry density. [4]—undrained bearing capacity. [5]—undrained shear strength. [6]—residual undrained bearing capacity. [7]—residual undrained shear strength. [8]—bearing capacity.

During the compression tests, the water content and density of the test body were determined. The density of the soil is characterized by the compression index C_c. The water

content and density were determined before and after compression, and the parameter C_C was calculated.

Based on the graph, $\Delta h/h = f(\mathfrak{e})$, the overconsolidation ratio $\mathfrak{e}_p$ was determined. During the tests, the water content was changed, reducing it from 400% to 250%. The calculated deformation modules were in the range of 0.3–0.7 MPa (see Figure 9); therefore, they indicate that the behavior of the material was at a compression exceeding the creep limit. The value of $\mathfrak{e}_p$ was 90 kPa, slightly higher than that obtained from the plate load test (see below).

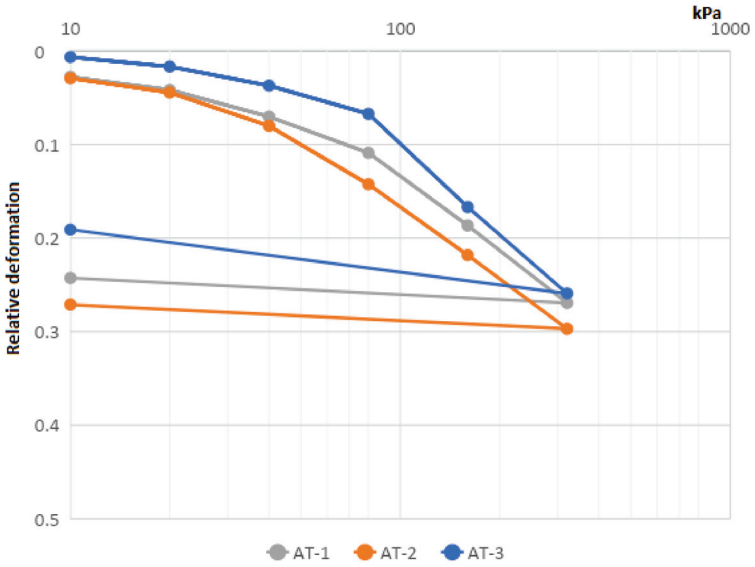


Figure 9. Uniaxial compression test load/deformation curves for specimens listed in Table 12.

Based on the results of the uniaxial compression test, it can be said that the compressive strength q_u of the soils used is in the range of 12–30 kPa (Table 12). The compressive strengths of different composites are in the range of 25–100 kPa.

In the graphs above (Figure 9), we can see a swan-neck-shaped curve that can be explained by the fact that after reaching a certain compression ratio, the peat fibers in the material behave like reinforcement structures (similar to steel or fiber reinforcement in concrete). Unlike concrete, the material is not broken, but after reaching a certain compression ratio, the compressive strength of the material increases again.

4.5. Investigation of Properties of Test Roads

Property determination results must always be verified with plate load tests in complicated cases such as the current one [16]. With these tests, we can assess distinctive points in the material under testing, where changes in physical processes occur which allows us to evaluate the actual load capacity of the material [17].

For weak materials, such as our improved peat, the load capacity is limited by the creep limit (the maximum stress that will cause less than a specified quantity of creep in a given time). Until it reaches this limit, the material can be compressed [18]. Beyond the creep limit, changes in the shape of the specimen occur, and it may flow out from under the plate. In our tests, we did not reach complete disintegration.

Previous laboratory studies showed that soil that improved with oil shale ash on a uniaxial test behaves differently from ordinary soil; its arrangements are mainly related to changes in form, and common compaction does not take place.

All tests provided are characterized by the development of low-intensity deformations up to the yield point as the load increases. At the creep limit, the intensity of deformations increases significantly, and the circumference of the specimens increases in the process. The formation of a larger surface area leads to a decrease in the intensity of the deformation

and apparent strengthening. If the new diameter is taken into account, this strengthening is practically absent, and the improved soil actually behaves like a liquid (Figure 10).

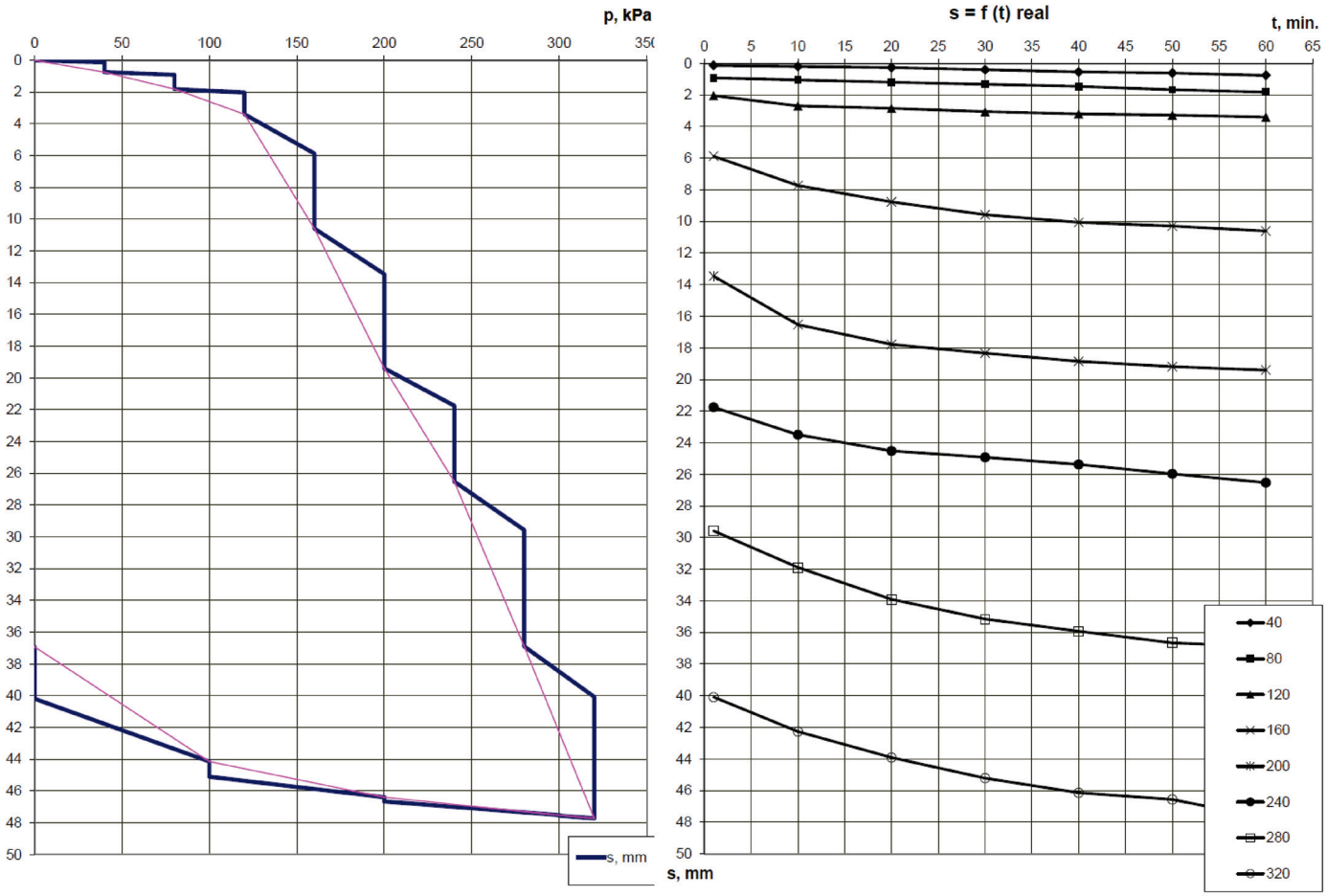


Figure 10. Dependence of plate subsidence on pressure; dependence of plate subsidence on time (field tests).

In the plate load test, the improved soil behaved similarly. On the graph S = f(q) (q—pressure), two segments can be separated, the first 0 to 120 kPa and the second 12 to 320 kPa. In both sections, there is a linear relationship between the pressure q and the settlement S.

In the first section, the size of the initial deformation at the load level is 0.1 to 0.2 mm. The creep index K (mm), which characterizes the intensity of the deformations, is determined by the following formula:

$$K = S_{60} - S_{20}/\lg (60\text{-}20)$$

which is relatively small—0.3 to 0.37 mm. S is the subsidence at the 60th and 20th minutes.

After reaching the creep limit, the initial deformations increased significantly from 2.5 to 3.2 mm, almost 10 times, and the creep index increased from 1.12 to 2.5 mm, almost 4 to 8 times. In the first section of the test, the deformation modulus calculated on the basis of test data was 13 MPa, and the deformation modulus considering time was 7 MPa. At pressures exceeding the yield strength, these numbers are 1.5 MPa and 0.5 MPa.

The average shear strength of the undrained unconsolidated improved soil calculated based on the results was 0.087 MPa. However, the creep limit value of 135 kPa calculated

by L. Jürgenson's formula [19] is somewhat higher than the 120 kPa determined by the plate load test.

$$q_Y = \pi \cdot c_u$$

q_Y—creep limit value.
c_u—undrained shear strength of soil.

5. Conclusions

Using kukersite oil shale ash to stabilize peat soils has been largely unsuccessful in studies published so far. However, the current study shows that excellent results can be achieved when the chemistry of the process is altered. For this purpose, two changes are necessary:

First, the pH of the mixture must be raised to over 13 to allow the retarding influence of humic acids to be eliminated.

Second, pozzolanic agents must be added to form the C–S–H phase which binds the organic fibers together and allows the organic fibers to function as a reinforcement.

Based on an experiment and tests, it can be said that the strength of the test embankment material is sufficient up to pressures of 100 kPa, and the arrangements accompanying its loading do not pose a threat to transport. The load-bearing capacity can be increased by using a geotextile, but this needs to be evaluated with corresponding plate load tests.

In any case, the achieved compression strength is sufficient for building roads with a moderate load capacity, such as roads serving natural reserves or military objects. The building costs of such roads are several times lower than those using traditional methods. For full-scale applications, a machine with a continuous mode of operation must be constructed. A matter of importance is also the significantly lower environmental impact of this method; the water regime of peat soils remains presumably unchanged, thus preventing GHG emissions and reducing negative impacts on biodiversity in comparison with traditional mass-stabilization methods. The tests were planned to be carried out sequentially in order to reach a satisfactory result with a minimum amount of time, labor, and material consumption. Each subsequent series of tests was based on the previous series, on the basis of which a limited number of test samples were selected for further studies; therefore, the results cannot be summarized.

Author Contributions: Conceptualization, V.P. and J.L.; methodology, E.R.; validation, M.S.; formal analysis, T.T.; investigation: field and lab testing V.P. and A.L.; XRD/XRF: H.M.; writing—original draft preparation, J.L. and V.P.; writing—review and editing, E.R.; supervision, J.L.; project administration M.M.; funding acquisition: T.T. and J.L. All authors have read and agreed to the published version of the manuscript.

Funding: This research was funded by project KIK-15401 "Stabilization of soil containing humic substances in roads with using oil shale ash".

Institutional Review Board Statement: Not applicable.

Informed Consent Statement: Not applicable.

Data Availability Statement: Not applicable.

Conflicts of Interest: The authors declare no conflict of interest. The funders had no role in the design of the study; in the collection, analyses, or interpretation of the data; in the writing of the manuscript; or in the decision to publish the results.

References

1. Janz, M.; Johansson, S.-E. The Function of Different Binding Agents. In *Deep Stabilization*; Swedish Deep Stabilization Research Centre: Linköping, Sweden, 2002.
2. Zulkifley, M.T.M.; Ng, T.F.; Raj, J.K.; Hashim, R.; Bakar, A.F.A.; Paramanthan, S.; Ashraf, M.A. A Review of the Stabilization of Tropical Lowland Peats. *Bull. Eng. Geol. Environ.* **2014**, *73*, 733–746. [CrossRef]
3. Rikmann, E.; Zekker, I.; Teppand, T.; Pallav, V.; Shanskiy, M.; Mäeorg, U.; Tenno, T.; Burlakovs, J.; Liiv, J. Relationship between Phase Composition and Mechanical Properties of Peat Soils Stabilized Using Oil Shale Ash and Pozzolanic Additive. *Water* **2021**, *13*, 942. [CrossRef]
4. Liiv, J.; Teppand, T.; Rikmann, E.; Tenno, T. Novel Ecosustainable Peat and Oil Shale Ash-Based 3D-Printable Composite Material. *Sustain. Mater. Technol.* **2018**, *17*, e00067. [CrossRef]
5. Arro, H.; Prikk, A.; Pihu, T. Calculation of Estonian Oil Shale and Its Combustion Products' Composition and Amounts Proceeding from Heat Value. *Oil Shale* **1998**, *15*, 329–340. [CrossRef]
6. Forsman, J.; Dettenborn, T.; Skepast, P.; Mets, M.; Olep, M.; Ellmann, A.; Vallas, I.; Tonts, T.; Kontson, K. Full Scale Reinforced Road Embankment Test Sections over Soft Peat Layer, Võõbu, Estonia. In Proceedings of the 13th Baltic Geotechnical Conference, Vilnius, Lithuania, 22–24 September 2016; pp. 1279–1288.
7. Liiv, J.; Zekker, I.; Tämm, K.; Rikmann, E. Greenhouse Gases Emissions and Climate Change—Beyond Mainstream. *MOJ Bioorg. Org. Chem.* **2020**, *4*, 10–16.
8. Sõukand, Ü. Simultaneous Adsorption of Cd^{2+}, Ni^{2+}, and Pb^{2+} on Peat. Ph.D. Thesis, University of Tartu, Tartu, Estonia, 2011.
9. Ma, C.; Chen, B.; Chen, L. Effect of Organic Matter on Strength Development of Self-Compacting Earth-Based Construction Stabilized with Cement-Based Composites. *Constr. Build. Mater.* **2016**, *123*, 414–423. [CrossRef]
10. Koroljova, A.; Talviste, P. *Põlevkivi Lendtuha Taaskasutamine Hüdraulilise Sideainena Pehmete Pinnaste Tugevdamisel IV*; Eesti Energia: Tallinn, Estonia, 2018.
11. Talviste, P.; Kirsimäe, K. *Põlevkivi Lendtuha Taaskasutamine Hüdraulilise Sideainena Pehmete Pinnaste Tugevdamisel II*; Eesti Energia: Tallinn, Estonia, 2018.
12. Talviste, P.; Kirsimäe, K. *Põlevkivi Lendtuha Taaskasutamine Hüdraulilise Sideainena Pehmete Pinnaste Tugevdamisel I*; Eesti Energia: Tallinn, Estonia, 2018.
13. Reinik, J.; Irha, N.; Koroljova, A.; Meriste, T. Use of Oil Shale Ash in Road Construction: Results of Follow-up Environmental Monitoring. *Environ. Monit. Assess.* **2018**, *190*, 59. [CrossRef] [PubMed]
14. Teppand, T.; Escuer, O.; Rikmann, E.; Liiv, J.; Shanskiy, M. Timber Structures and Prefabricated Concrete Composite Blocks as a Novel Development in Vertical Gardening. *Sustainability* **2022**, *14*, 14518. [CrossRef]
15. Błońska, E.; Lasota, J.; Tullus, A.; Lutter, R.; Ostonen, I. Impact of Deadwood Decomposition on Soil Organic Carbon Sequestration in Estonian and Polish Forests. *Ann. For. Sci.* **2019**, *76*, 102. [CrossRef]
16. Mets, M. Aja Mõju Arvestamine Plaatkoormuskatsel. In *Ehitusgeoloogia Kogumik III*; Valgus: Tallinn, Estonia, 1976.
17. Mets, M. Iseloomulike Punktide Meetod. In *Ehitusgeoloogia Kogumik V*; Valgus: Tallinn, Estonia, 1991.
18. Ashby, M.F.; Abel, C.A. Materials Selection to Resist Creep. *Philos. Trans. R. Soc. Lond. Ser. A Phys. Eng. Sci.* **1995**, *351*, 451–468. [CrossRef]
19. Jürgenson, L. *Dock Foundations on Soft Clays*; Massachusetts Institute of Technology: Cambridge, MA, USA, 1929.

Disclaimer/Publisher's Note: The statements, opinions and data contained in all publications are solely those of the individual author(s) and contributor(s) and not of MDPI and/or the editor(s). MDPI and/or the editor(s) disclaim responsibility for any injury to people or property resulting from any ideas, methods, instructions or products referred to in the content.

applied sciences

MDPI

Article

Development and Evaluation of Cow Dung Composting Equipment with Ventilation and Heating

Kailin Ren [1,†], Lide Su [1,†], Yong Zhang [1,*], Xiang He [1] and Hao Wu [2]

[1] College of Mechanical and Electrical Engineering, Inner Mongolia Agricultural University, Hohhot 010018, China; m17362908182@163.com (K.R.); sld@imau.edu.cn (L.S.); h17513207697@163.com (X.H.)
[2] Faculty of Mechanical Engineering and Mechanics, Ningbo University, Ningbo 315000, China; 2211090182@nbu.edu.cn
* Correspondence: yongz@imau.edu.cn; Tel.: +86-136-7474-8009
† These authors contributed equally to this work.

Abstract: Traditional cow manure composting equipment often lacks ventilation, heating, and real-time monitoring and adjustment capabilities, hindering manure maturation and proper utilization of compost, moisture reduction, and optimal environmental conditions for microbial activity. To address these limitations, we optimized and redesigned the structure and control elements of conventional composting equipment. In doing so, we developed a novel cow manure composting apparatus based on the target composting quantity method. The new design features a refined ventilation and heating structure, as well as an enhanced control system using PLC and MCGS. This equipment provides improved composting effects while offering real-time monitoring of composting data, effectively promoting the composting process. Further evaluation of the modified equipment was conducted using fermented cow dung, demonstrating its feasibility. The experiment yielded positive results, indicating that the composted cow manure satisfied all necessary standards across all evaluation parameters. These parameters included the moisture content of the compost, the duration of high temperature, the pH, and the seed germination index. The seed germination rate reaches 85%, and the water content of manure is 9.3%, which is much higher than the industry standard.

Keywords: composting equipment; ventilation heating device; control system; cow dung; standard assessments

Citation: Ren, K.; Su, L.; Zhang, Y.; He, X.; Wu, H. Development and Evaluation of Cow Dung Composting Equipment with Ventilation and Heating. *Appl. Sci.* **2023**, *13*, 8649. https://doi.org/10.3390/app13158649

Academic Editor: Francesca Scargiali

Received: 23 June 2023
Revised: 24 July 2023
Accepted: 26 July 2023
Published: 27 July 2023



Copyright: © 2023 by the authors. Licensee MDPI, Basel, Switzerland. This article is an open access article distributed under the terms and conditions of the Creative Commons Attribution (CC BY) license (https://creativecommons.org/licenses/by/4.0/).

1. Introduction

China's Inner Mongolia region encompasses 1.3 billion mu of natural grassland and 30 million mu of artificial grassland, creating unique advantages for the development of the dairy farming industry. With 66 major cattle and sheep farming counties in the region and approximately 95,000 large-scale cattle and sheep farms, it holds the highest number of cows in the country [1,2]. The herd size is steadily increasing year by year, resulting in a large volume of cow manure. Untreated cow manure can lead to massive environmental pollution [3–5]. The acceleration of China's urbanization and the rural population decline has created challenges in agricultural production, most significantly, the decrease in land fertility. Traditional agricultural production relies on the extensive use of chemical fertilizers and pesticides, causing environmental pollution, soil fatigue, and the imbalance of nature. Therefore, it is crucial to identify environmentally friendly and sustainable agricultural production methods.

Aerobic fermentation composting is one of the most effective methods to address environmental pollution and soil fatigue stemming from cow manure [6–8]. Composting organically converts waste into high-quality fertilizer through the decomposition of microorganisms. However, traditional composting methods face issues such as insufficient fermentation, long fermentation periods, and odor [9–11]. Consequently, more efficient and environmentally friendly composting equipment is necessary.

Cow manure is a prevalent organic waste, and its treatment and utilization play a significant role in environmental protection and agricultural production. Traditional cow manure treatment methodologies, including open-air composting [10,12], closed composting, and biogas fermentation, often results in odor interference, harmful gas generation, and low fertilizer efficiency. Recently, due to heightened environmental awareness and technological advancements, ventilation and heating of cow manure composting equipment have gained considerable attention. This equipment facilitates microbial activity in cow manure through heating and ventilation, accelerating compost decomposition and transformation [13–16], thereby enhancing fertilizer utilization efficiency and reducing odors and harmful gas emissions. However, current research on ventilated and heated cow manure composting equipment remains limited, necessitating the evaluation and optimization of such equipment, which holds significant theoretical and practical implications. This study aims to investigate the working principles, advantages, disadvantages, and factors affecting the performance of ventilated and heated cow manure composting equipment to provide a scientific basis for its promotion and application.

Conventional cow manure composting equipment design often lacks ventilation, heating, and real-time monitoring and adjustment functions, hindering effective manure maturation, compost utilization, moisture reduction, and providing suitable environmental conditions for microbial activities [17–19]. Based on these limitations, traditional composting equipment was optimized. Cow manure composting equipment employing the target composting method was developed, selecting appropriate air pumps and designing a heating box with a ventilation structure. The control system was optimized for real-time monitoring and adjustment capabilities, creating an effective device to promote the composting process. Subsequently, fermented cow dung equipment was evaluated.

Traditional manure composting equipment has long faced several challenges that have hindered optimal composting processes [20]. Chief among these drawbacks is the lack of ventilation and heating functions and the absence of a system for real-time composting data monitoring [21,22]. These limitations hinder the efficient maturation of livestock and poultry manure and obstruct comprehensive compost utilization. Additionally, the operational complexity of traditional composting equipment necessitates considerable manpower and resources, adding another layer of difficulty to the process [23,24]. In a bid to overcome these limitations and propel composting practices forward, this paper introduces a composting apparatus that checks all the boxes that traditional composting systems do not. This innovative device comes with integrated ventilation, heating, and real-time composting data monitoring capabilities [25].

Ventilation is crucial for supplying the necessary oxygen for proper composting [26]. The heating function maintains the ideal composting temperature, accelerating the breakdown of organic material. Real-time data monitoring allows for prompt adjustments and maintains ideal composting conditions [27,28]. Moreover, the apparatus inextricably links the aeration and heating devices. This linkage enhances the control of the entire composting process, optimizing operations and ensuring all components work in harmony. This new, integrated, and optimized equipment is a game-changer. It offers a solution conducive to the effective and efficient conversion of manure to valuable compost, marking a crucial progression in manure composting and organic waste management and, ultimately, more sustainable agriculture.

2. Materials and Methods

2.1. Structural Design of Ventilation and Heating Cow Manure Composting Equipment

2.1.1. Design of Cattle Manure Fermentation Tank Based on Target Compost Amount

In the operation of cow dung composting equipment, the design of inlet and outlet is very important. This paper believes cow dung import and export should be based on the fermentation tank's structural size and target compost amount. The fermentation tank of cow dung composting equipment is regarded as a cylinder, and the corresponding inner cavity diameter and height [29–31] can be further determined after the internal volume

is known. The study found that cow dung composting is most effective when the height–diameter ratio of the fermentation tank is greater than 2, which also minimizes heat loss during the process. With this in mind, the authors designed the fermentation tank cavity of the composting equipment to have a height diameter ratio greater than 2, taking into account the equipment's practical needs. To ensure optimal results, the inner cavity of the fermentation tank should meet the following expression:

$$h = \frac{h_{a1}}{h_{a2}} \geq 2 \tag{1}$$

Among them, h_{a1} represents internal height; h_{a2} refers to inner diameter. The authors designed the fermentation tank cavity of the composting equipment to have a height diameter ratio greater than 2 for optimal cow dung composting. To calculate the volume of the fermentation tank, the following expression should be used:

$$V = \frac{1}{4}\pi d^2 \frac{h_{a1}}{h_{a2}} \tag{2}$$

Among them, V represents the volume; d represents the diameter. Cattle manure composting equipment produces gases such as ammonia, methane, hydrogen sulfide, and carbon dioxide during the composting process. To accommodate these gases, a portion of the internal space in the fermentation tank needs to be reserved. The cow dung is in a loose accumulation state with large internal porosity [32]. To facilitate feeding and material collection, the fermentation tank is equipped with a feed inlet and a discharge outlet on the side and bottom, respectively. The feed inlet includes open and closed bin doors and a ramp feed channel to avoid mixer impact, achieve synchronous feeding and mixing, and improve mixing efficiency [33–35]. The bottom of the fermentation tank is funnel-shaped to allow for natural material falls, and the outlet is located in the middle. The structure diagram of the fermentation tank of cow dung composting equipment designed in this paper is shown in Figure 1.

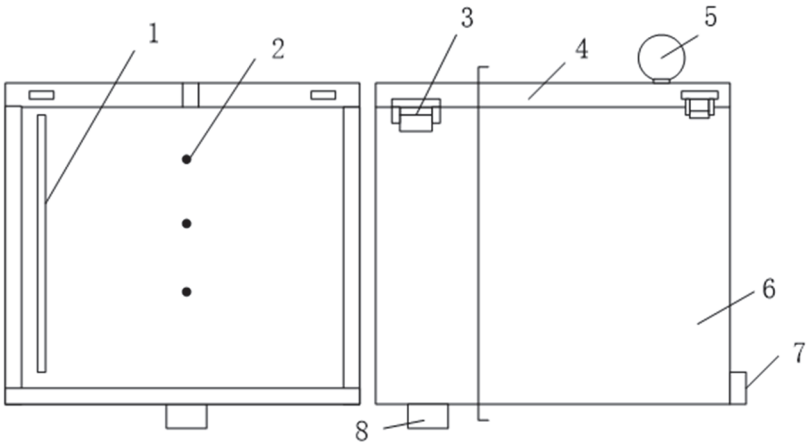


Figure 1. Structure diagram of fermentation tank of cattle manure composting equipment: 1 represents the inlet ring branch pipe of fermentation tank; 2 indicates temperature sensor; 3 represents upper cover buckle; 4 represents the upper cover; 5 refers to waste gas treatment device; 6 represents the reaction tank; 7 indicates fixed pin groove; 8 means drain outlet.

Cow dung composting is a relatively static and oxygen-consuming process. The amount and activity of microorganisms are different due to different fermentation processes of materials in different areas of composting, which affects the overall fermentation rate of materials [36]. Regular mixing and rotation of the reactor body can make the materials in the reactor body mix evenly and provide enough oxygen for the reactor body, which is conducive to the life activities of aerobic bacteria. During mixing, the temperature of each space area is evenly mixed [17]. Therefore, in the design of composting equip-

ment fermentation tanks, special attention should be paid to the rationality of its mixing section design.

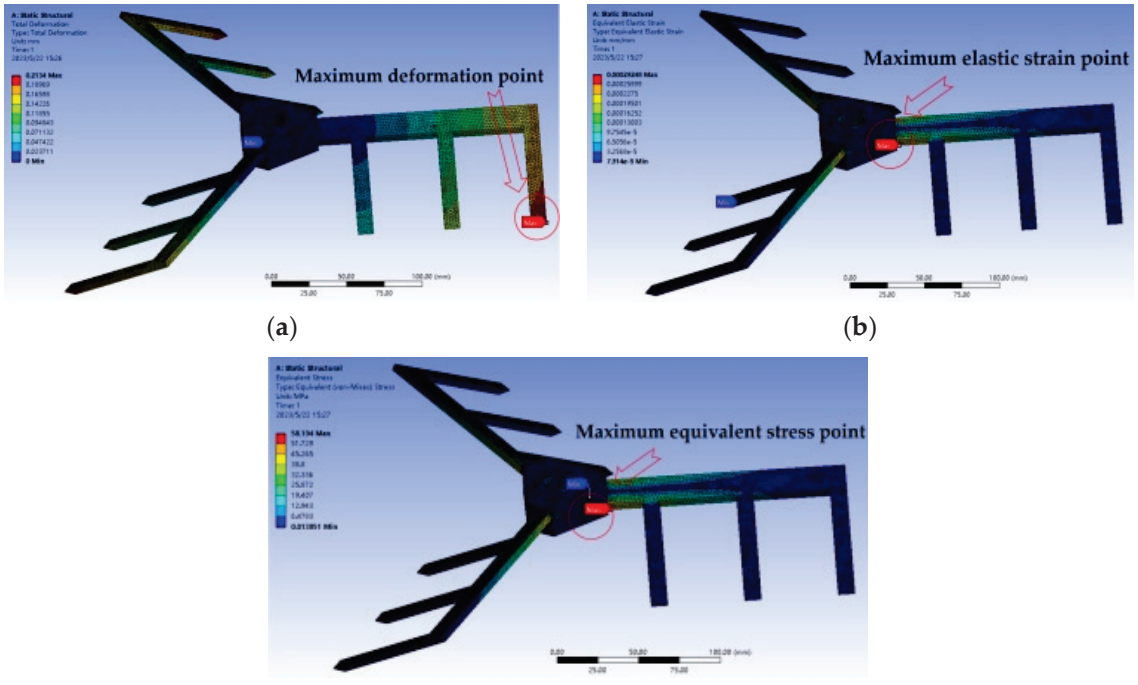
2.1.2. Reasonability Verification of Mixing Blades Based on ANSYS

The stirring blade design presented in this article comprises three transverse main blades and multiple oblique auxiliary blades. The main blade is welded to the middle support section at a 45° angle to the shaft's axial direction. The three transverse main blades are spaced 120° apart. Each transverse main blade has three parallel diagonal auxiliary blades fixed to it, with a 60° angle between them. Threaded holes are located on the middle support section's side, allowing it to be locked onto the shaft using set screws.

Three-dimensional solid modeling of the mixing blades in the mixing section was completed using SOLIDWORKS 2023, with a physical image displayed in Figure 2. During finite element analysis, the mixing device was idealized, and a 3D tetrahedral 4-node computational domain grid was generated using Workbench, featuring a mesh size of 2 mm and a total of 167,074 elements. According to material mechanical property estimates, the external load produced by the mixing device is approximately 120 N. Based on literature analysis [37], the maximum temperature of the aerobic composting pile can reach 70 °C. To better simulate the composting environment, the temperature is set at 70 °C. Analysis results are illustrated in Figure 3.



Figure 2. Physical image of mixing blade.



(**a**) (**b**)

(**c**)

Figure 3. ANSYS simulation results of unimproved blades. (**a**) Maximum deformation point; (**b**) maximum elastic strain point; (**c**) maximum equivalent stress point.

As shown in Figure 3, the maximum deformation of the three-blade E-shaped stirring blade is located at the tip of the E-shaped blade, while the maximum stress and elastic strain are located at the connection part between the blade and the fixed component. The maximum stress is 58.194 Mpa, which meets the standard and has strong firmness. Based on previous research [38], it can be seen that the stirring blade has stirring function, which is superior to most stirring structures on the market and will greatly improve the degree of fermentation maturity.

2.1.3. Selection of Air Pump for Composting Device

As an important part of the hot air device of the cow dung composting equipment, the air pump can provide the required air volume for the operation of the composting equipment and the working air pressure required by the agitator. The air pump design involves creating two separate ventilation pipelines using a y-shaped three-way interface. One of these pipelines delivers and heats the air, which is then dispersed into the fermentation tank through an aeration pipe. The other pipeline is connected to a pneumatic agitator with a cylinder-driven shaft. The speed of the agitator increases in proportion to the gas flow rate as long as the working pressure remains stable. Based on the above requirements, select the type of air pump commonly used in the market at present, and finally, determine the air pump model and working parameters for this equipment, as shown in Table 1.

Table 1. Model and working parameters of air pump for cattle manure composting equipment.

Number	Name	Technical Parameter
1	Air pump model	RB-53D-4
2	Volume of air storage tank/L	98
3	Voltage/V	220
4	Frequency/Hz	50
5	Input power/kW	0.28
6	Speed/r/min	2900

As shown in Table 1, the model and working parameters of the air pump of the cow dung composting equipment with vent heating designed in this paper, the ventilation volume of its air outlet meets the requirements of the ventilation volume required by the stack, and the exhaust pressure meet the requirements of the working pressure of the pneumatic mixer.

2.1.4. Structural Design of Heating Box with Vent

After completing the air pump selection and working parameter design of the above composting equipment, the next step is to comprehensively design the structure of the heating box with vents of the composting equipment. Before designing the structure of the heating box with vents, it is necessary to calculate the ventilation rate of the cattle manure composting equipment with vents.

Ventilation is an important factor affecting the quality of compost products. Part of the total ventilation is used to provide microbial degradation of organics, and part of it is used to remove water in compost [39]. Therefore, the total ventilation volume is determined by considering the oxygen consumption of physical and chemical reactions and the oxygen required for water removal. There are many organics in the pile, including about 15% nitrogenous organics, about 90% volatile solids, about 60% material moisture, and about 12% biodegradable organics [40]. The formula for calculating the ventilation rate of composting equipment is

$$V_a = \frac{M_0(1-W)V_m K_v}{Z_0 P_a} \tag{3}$$

Among them, V_a represents the ventilation volume of cow dung composting equipment; M_0 represents the total material mass of cow dung composting equipment; W

represents the material moisture content of cow dung composting equipment; V_m represents the amount of volatile solids in cow dung composting equipment; K_v represents the degradable organic matter of cow dung composting equipment; Z_0 represents the oxygen mass fraction in the air during the operation of the cow dung composting equipment; and P_a refers to the air density under standard atmospheric pressure when the cow dung composting equipment is running. According to the ventilation calculation results of the cow dung composting equipment, the ventilation distribution ring of the equipment vent is designed, and the structure diagram is shown in Figure 4.

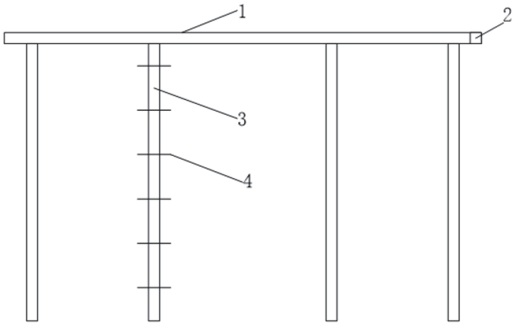


Figure 4. Structure diagram of ventilation and air distribution ring of cow manure composting equipment: 1 represents the main pipe of the air distribution ring at the vent; 2 represents the air inlet of the air distribution ring; 3 represents the branch pipe of gas distribution ring; 4 indicates the cloth hole.

There are two kinds of ventilation pipes used in this composting equipment; one is a PU hose, and the other is a stainless steel pipe. The parameters and function settings of the two ventilation pipes are shown in Table 2.

Table 2. Parameters and function settings of ventilation pipe.

Project	PU Hose	Stainless Steel Pipe
Function	PU hoses are commonly used in low and medium-pressure applications, such as pneumatic tools, spraying equipment, fluid transmission, etc. It has the characteristics of softness, good elasticity, light weight, and easy installation, making it suitable for occasions that require bending or folding. In addition, PU hoses also have excellent physical and chemical properties, such as wear resistance, oil resistance, and chemical corrosion resistance.	Stainless steel pipes are suitable for high-pressure and ultra-high-pressure applications, such as petrochemical, chemical, nuclear power plants, etc. Stainless steel pipes have excellent properties such as high strength, high pressure, corrosion resistance, and high-temperature resistance and can withstand the transportation of high-pressure, high-temperature, and highly corrosive media. In addition, stainless steel pipes also have the characteristics of beautiful appearance, easy cleaning, and hygiene.
Drift diameter	2–10 mm	10–50 mm
Texture of material	The material texture is relatively soft and has a certain elasticity, making it suitable for situations that require bending or folding.	The material is relatively hard and has good corrosion resistance, making it suitable for applications that require high strength and high pressure.
Installation position	For low and medium-voltage applications	Suitable for high voltage and ultra-high voltage applications

As shown in Table 2, this refers to the parameter and function settings of the vent pipe of composting equipment with vent heating. There are three modes of ventilation and oxygen supply: passive ventilation, natural ventilation, and forced ventilation [12]. Forced ventilation is to inject sufficient air into the reaction tank regularly and quantitatively through the mechanical agitator. The ventilation hole is arranged on the blade of the mixing shaft to allow air to enter during the mixing operation [36]. On this basis, the heating box with the vent of the composting equipment is designed as a rectangle, and the size of the heating box refers to the structure of the fermentation tank. This paper

describes the design of a heating box made of 304 stainless steel, with dimensions of 500 mm × 350 mm × 300 mm and vents [41]. The box consists of a top cover and a main structure, with an electric heating pipe installed in the middle of the top cover. Air inlets and outlets are located on both sides of the box, connected to the air inlet and outlet pipes. Air is pumped into the box through the pipe and heated by flowing through the electric heating pipe. Heat balance analysis is necessary to understand the heat transfer during air heating and determine the appropriate power of the electric heating tube. The selection of electric heating tubes is based on commonly used types in the market.

2.2. Control Design of Ventilation and Heating Cow Manure Composting Equipment

2.2.1. MCGS Touch Screen Design

Touch screens serve as crucial human–computer interaction tools and are vital components of automation control equipment. In the composting control system, the touch screen establishes communication with the PLC and sensors, allowing it to display real-time data collected by the sensors during the pile fermentation process and from the air within the tank. Simultaneously, it provides an operation interface, facilitating start and stop control of the air pump, electric heating tube, and motor. The chosen touch screen model is the Kunlun Tongtai TPC7062Ti, which is primarily designed for constructing the user window section. This section displays real-time data information on the stacking material and allows for automatic or manual operation. The primary monitoring interface of the user window is showcased in Figure 5.

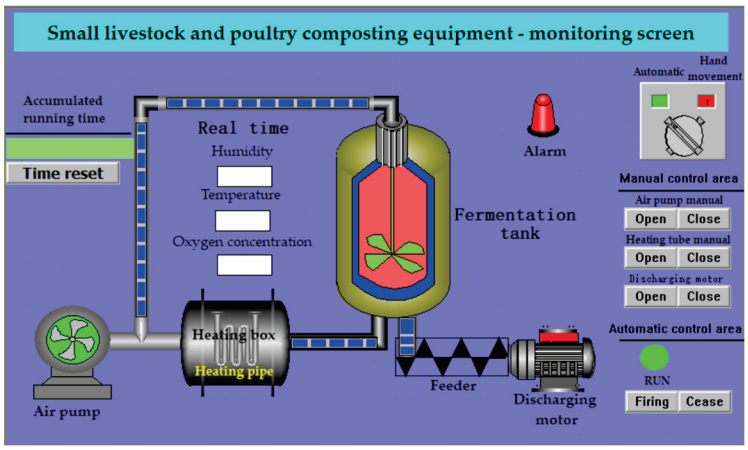


Figure 5. Monitoring screen.

2.2.2. PLC Programming

To achieve the high-temperature stage of composting, it is essential to maintain the compost material's temperature between 55 °C and 65 °C for as long as possible, promoting organic matter decomposition and enhancing the fermentation rate. If the stacking temperature falls below 55 °C, the control system activates the electric heating tube for preheating. Upon reaching the preheating time, the air pump is started for ventilation, and both the air pump and electric heating tube are turned off once the stacking temperature reaches 65 °C or above. Simultaneously, microorganisms decomposing organic matter will continuously consume oxygen, reducing the oxygen concentration in the fermentation tank. If the oxygen concentration drops below 15%, the control system starts the air pump to introduce room temperature air until the tank's oxygen concentration rises above 19% before turning off the air pump.

The Siemens S7-200/200 CN series PLC is programmable using V4.0 STEP7 MicroWIN SP9 software, which supports three programming methods: ladder diagram, function block diagram, and instruction table. Considering the control principles and conditions of this composting control system, using a ladder diagram for control program writing is more convenient and intuitive. The main program section is illustrated in Figure 6.

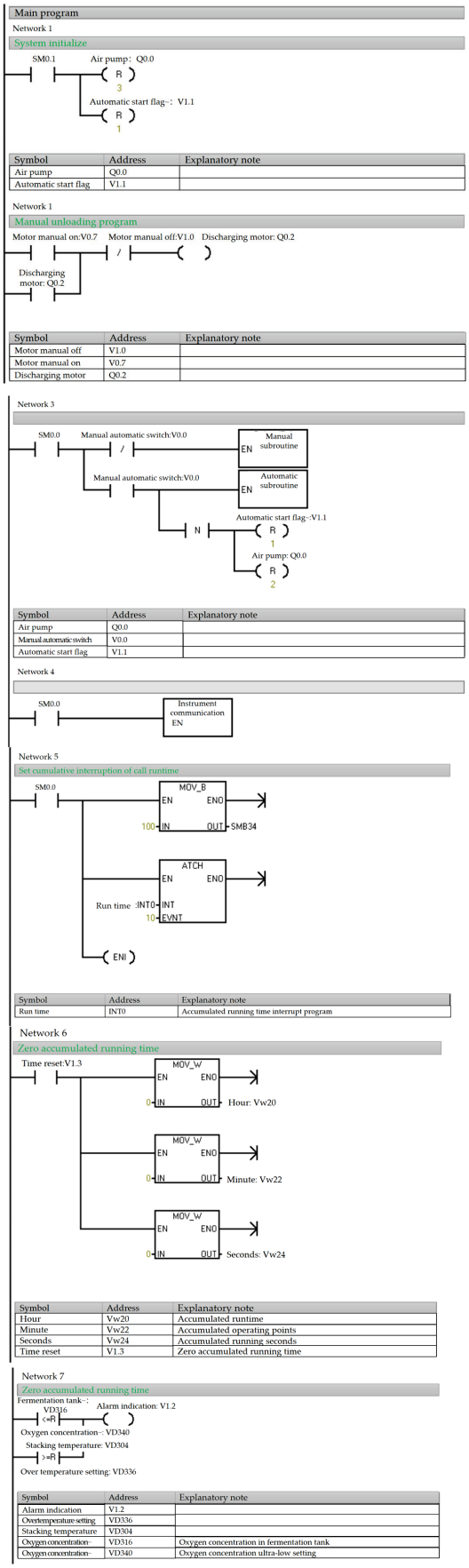


Figure 6. PLC main program section.

2.2.3. Touch Screen and PLC Communication Settings

The touch screen connects to the PLC via an RS485 serial port. During communication, it not only receives data information transmitted by sensors through the PLC but also sends control commands for the PLC to execute related operations. By utilizing configuration design software, data channels and connection variables are set within the window of the central and western gate PLC equipment, which allows for a one-to-one correspondence between data and instruction transmission. In the device editing window, corresponding data channels are added, and channel types, data types, channel addresses, and read/write methods are configured. Subsequently, variable objects and their connections from the database are specified, establishing a link between the touch screen and the PLC.

2.3. Experimental Verification of the Composting Effect of Cow Manure

2.3.1. Test Materials

The cow manure used in the composting experiment was taken from the modern dairy farming pasture in Inner Mongolia, China, as shown in Figure 7a; corn stalks are taken from the Agricultural Machinery Laboratory of the College of Inner Mongolia Agricultural University, which are crushed into 2–3 mm stalks, as shown in Figure 7b.



(**a**) (**b**)

Figure 7. Main raw materials for testing. (**a**) Cow dung; (**b**) corn stalks.

2.3.2. Test Equipment

When carrying out composting experiments, besides the necessary composting materials, additional experimental materials, supplies, and relevant testing instruments or equipment are required, as shown in Figures 8 and 9 The test materials and supplies primarily entail fermentation starter, activated carbon, mung bean seeds, farmland soil, seedling basins, glass measuring cylinders, and watering cans. The testing instruments mainly comprise electronic scales and small soil testers.

Before composting, it is necessary to add an appropriate amount of fermentation starter to the heap to increase the content of microbial flora and improve. The decomposition effect of organic matter promotes the composting of the heap. The additional amount of the fermentation starter is related to the actual composting amount, and they are added at the ratio of 1 kg: 1 mL (stack: fermentation starter). Activated carbon is placed in the deodorization device of the composting equipment to adsorb and filter the odor discharged from the fermentation tank; seedling pots, farmland soil, mung bean seeds, spray pots, etc., are used for determining the seed germination index of the compost samples taken during subsequent composting experiments, which is one of the evaluation indicators of the compost maturity.

The electronic scale is mainly used for weighing the quality of composting raw materials, such as cow manure and corn straw, and plays an accurate role in controlling the mixing ratio of materials in pre-composting experiments and actual composting experiments. The soil multi-element tester can detect indicators such as pH value, temperature and humidity, electrical conductivity EC, and nitrogen, phosphorus, and potassium content of the compost material. In subsequent composting experiments, this data can be used as one of the evaluation indicators for whether the compost material has completed its maturity.

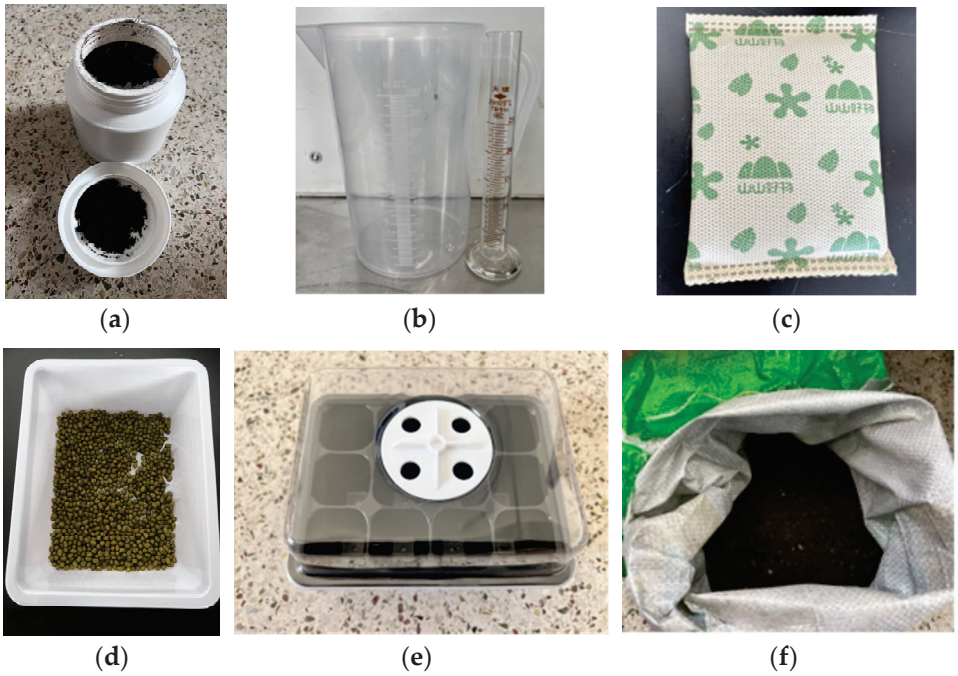


Figure 8. Partial testing equipment. (**a**) Starter; (**b**) glass measuring cylinder; (**c**) activated carbon; (**d**) mung bean seeds; (**e**) seedling pot; (**f**) farmland soil.



Figure 9. Part of test instruments. (**a**) Electronic scale; (**b**) soil integrated sensor.

2.3.3. Test Method

The most suitable initial moisture content for composting is 50% to 60%, while the original moisture content of cow manure raw materials cannot meet this requirement. Therefore, pretreatment is needed to improve the moisture content. At the same time, the relevant research results of livestock manure composting show that [42–44] adding crop straw can effectively improve the organic matter content of the compost and the levels of nitrogen, phosphorus, potassium, and other elements in the final manure are significantly increased. Referring to the research content of the previous literature and the production status of manure, the mixed stack of cow dung and corn straw was mixed at a mass ratio of 20:1, and then appropriate water was added to adjust the initial moisture content of the mixed stack to reach 50~60%.

During the actual composting experiment, the temperature, humidity, and oxygen concentration within the composting material's tank are recorded at 12 h intervals. This data collection continues until the end of the composting cycle. Based on previous research, it is determined that compost can decompose within a few days after three ventilation–heating cycles. Therefore, the experiments designed in this article all feature three ventilation–

heating treatments. When placing the processed pile material into the fermentation tank, daily unloading and sampling of the pile material are performed.

A portion of the stacked samples is combined with a specific amount of farmland soil, and 36 mung bean seeds are spread across the mixture. Regular watering simulates the actual planting effect, allowing the observation of seed germination. Another portion of the sample is poured into a bucket, and a soil comprehensive sensor is used to detect the pile material and collect data. By utilizing the MCGS data report function and experimental test data, graphs illustrating fermentation temperature changes, seed germination index, oxygen concentration changes within the tank, and stack humidity changes can be generated. The acquired graphs can be further discussed and analyzed.

3. Results and Analysis

3.1. Temperature Changes in Composting

Figure 10 illustrates the temperature changes during the composting process of cow manure composting equipment. According to the composting material's temperature change chart, the total duration of this composting experiment is 13 days, with the high-temperature stage lasting about 8 days under ventilated heating conditions. The composting material's maximum temperature can reach 69.9 °C. The time interval between two adjacent ventilation and heating operations in this experiment is approximately 48 h, indicating that the insulation time of the fermentation tank designed in this article is around 48 h.

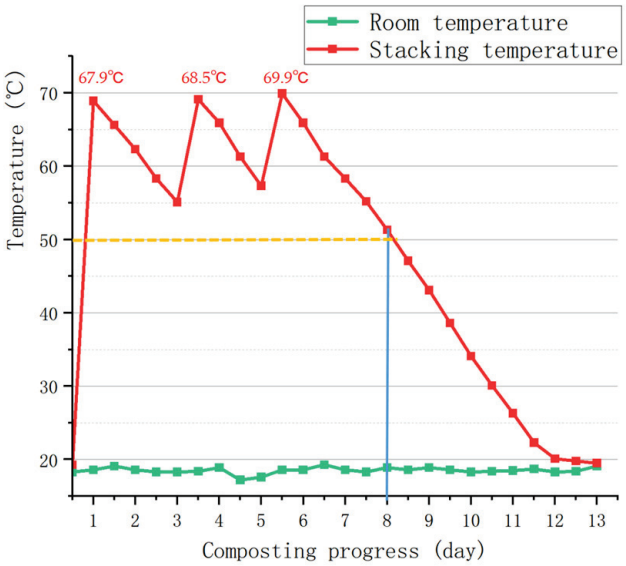


Figure 10. Temperature changes during composting process.

The national standard document "Technical Specification for Harmless Treatment of Livestock and Poultry Manure" specifies requirements for solid livestock and poultry manure treatment: the pile temperature must be maintained above 50 °C for no less than 7 days or above 45 °C for no less than 14 days. With a high-temperature stage duration of 8 days, this experiment satisfies the national standard requirements.

3.2. Humidity Changes in Composting

Figure 11 displays the changes in humidity during the composting process. As composting progresses, the humidity of the compost continuously decreases, with the rate of decrease being faster during the high-temperature stage. During the cooling stage, the rate of decrease gradually slows down and ultimately stabilizes at around 9%.

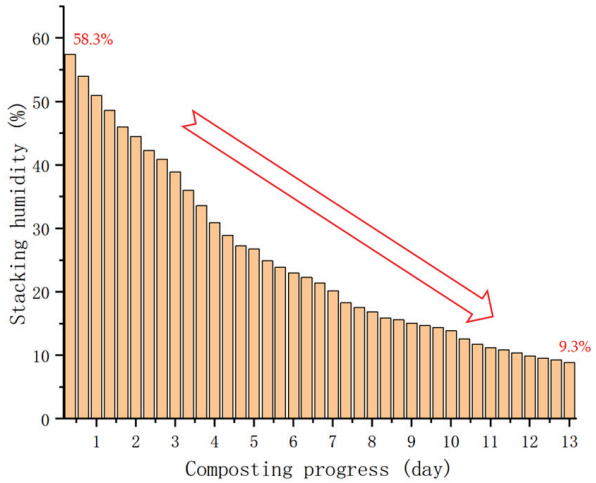


Figure 11. Process of moisture change in the stack material.

The industry standard document organic fertilizer stipulates that the moisture content of composted organic fertilizer shall be less than 30%. After 13 days of composting, the moisture content decreased from 58.3% to 9.3%, meeting national requirements.

3.3. PH Value Changes in Composting

Once the artificial heating phase starting on the 8th day of the composting process is completed, the pH value of the composting material is sampled and tested. Figure 12 shows the changes in pH value during the composting process. From the graph, it can be seen that the pH value of compost changes from weakly alkaline to weakly acidic in the middle and later stages of composting, both before and after improvement. This observation is consistent with the results of the natural fermentation composting experiment.

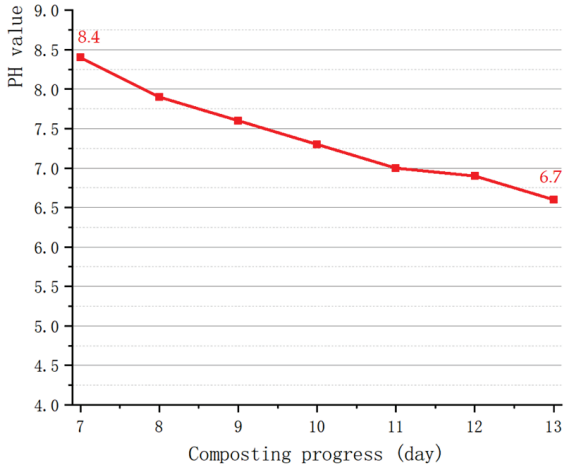


Figure 12. Test result of pH value.

The industry standard document organic fertilizer (NY 525-2012) stipulates that the pH of composted organic fertilizer should be between 5.5 and 8.5. The pH value after composting is 6.7, which meets the requirements of national standards.

The composting process often witnesses a decrease in pH value during the mature or stable stage, primarily due to the interplay between the production and consumption of organic acids. Initially, microorganisms decompose organic matter, generating a significant volume of organic acids and, consequently, lowering the pH value. As the process progresses, these microorganisms further break down these acids while converting ammonia nitrogen—a major component of compost—into nitrate. Both these processes consume hydrogen ions within the compost heap, facilitating an increase in pH value. However,

during the compost's mature stage, the generation of organic acids declines as most materials have been decomposed. Consequently, hydrogen ion concentrations rise within the compost heap, causing the pH value to decrease once more. This pH transition not only signifies compost maturity but also aids in suppressing the proliferation of harmful microorganisms, thereby enhancing the compost's safety and stability.

3.4. Seed Germination Index Changes in Composting

The Germination Index (GI) is an indicator used to evaluate the degree of harmless and stable composting by assessing the compost's inhibitory effect on plant germination. This index can detect the level of plant toxicity in compost samples and predict changes in plant toxicity within the compost.

The changes in seed germination rate during the composting process are shown in Figure 13. After the heating stage, the seed germination index (GI) of the pile material was sampled and tested in this experiment.

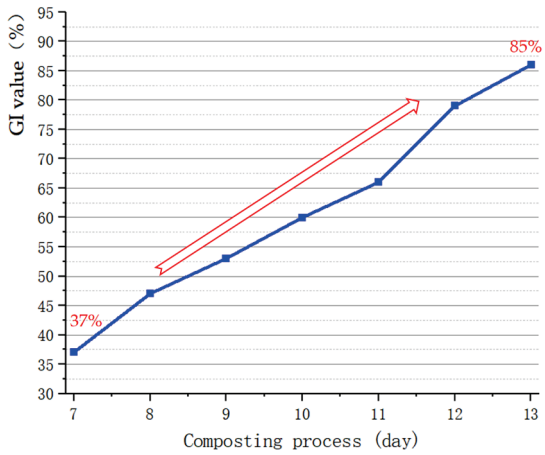


Figure 13. Test result of seed germination index.

According to Figure 13, the germination index (GI) significantly increased during the composting process. From 37% at the beginning to 85% at the end of composting. According to the standard, when the GI is greater than 80%, it indicates that the pile material has completed decomposition and is basically free from plant toxicity. After composting, the GI value of cow dung manure is increased to about 85%, which meets the requirement of low plant toxicity for organic fertilizer.

4. Discussion

Cow dung, an abundant byproduct of dairy farming, carries a dichotomous potentiality—it can manifest as a source of pollution or serve as organic fertilizer. Its transformation hangs in the balance, subject to the effectiveness of composting management. Ineffective composting management or insufficient utilization of cow dung often culminates in dung accumulation, leading to environmental pollution. Hence, devising an efficient cow manure composting system is critical to optimizing its use as organic fertilizer and minimizing its environmental impact.

Traditional cow manure composting methods, while practical, often grapple with operational inefficiencies and practical application issues. These issues undermine the effectiveness of composting and, consequently, the quality of the resulting product. Recognizing these challenges, this article introduces an innovative cow manure composting device designed to improve traditional composting equipment.

The new composting device posits enhancements that address the deficiencies of traditional equipment. Notably, it incorporates ventilation, heating, and real-time monitoring and adjustment capabilities—functions untypically seen in traditional composting methods. Ventilation ensures optimal aeration, which is crucial to accelerating microbial activity and,

consequently, the composting process. Simultaneously, integrated heating expedites the composting process by providing an environment conducive to microbial degradation of organic matter. Real-time monitoring and adjustment mechanisms imbue users with the capability to monitor key composting parameters such as temperature and moisture and make real-time adjustments in response to disturbances. Such improvements hold immense potential to boost the efficiency of the composting process and enhance the quality of the resulting compost.

The research conducted and presented in this article has precipitated the development of this cow manure composting system—a system that synergizes ventilation, heating, and real-time monitoring. The implementation of these features has resulted in significant improvement in the efficiency and fermentation quality of cow manure composting.

The resulting compost, following the improved composting process, meets and often exceeds the requisites of pertinent composting standards. These standards include parameters such as high-temperature duration, water content, pH, and a seed germination indicator referred to as the GI value. The composted cow manure complies with high-temperature duration norms, signifying that it has undergone sufficient processing to eliminate disease-causing pathogens. The compost also maintains appropriate water content, which is necessary for controlling moisture-dependent processes such as microbial activity and nutrient availability. Moreover, the compost registers acceptable pH and GI values, indicating its neutrality and non-phytotoxicity, respectively.

More importantly, the quality of the resulting compost provides conducive conditions for the survival and catabolism of microorganisms and aerobic organisms—an often overlooked yet crucial aspect of composting. The presence of these organisms ensures the continuous breakdown of organic matter within the compost even after its application to the soil. This ensures that nutrients are made available at a rate conducive to plant uptake, further enhancing the value of the compost as an organic fertilizer.

In conclusion, efficient management and utilization of cow manure through composting are essential to harnessing its potential as a valuable organic fertilizer while simultaneously averting its potential as an environmental pollutant. The introduction of the enhanced cow manure composting system, as presented in this study, marks significant advances in composting technology. It signifies a move towards enhancing composting efficiency, improving compost quality, and ultimately moving towards more sustainable and environmentally friendly agricultural practices.

5. Conclusions

This study provides compelling evidence that the cow manure composting equipment proposed herein significantly enhances the efficiency of livestock manure composting while yielding high-quality organic fertilizer. Through our thorough analysis, we derive two key conclusions:

1. The incorporation of efficient ventilation and heating systems, complemented by increased automation, augments the overall composting process efficiency. This advancement harbors the potential to be transformative in the realm of agricultural sustainability and offers solutions to the longstanding challenges faced in livestock manure management;
2. Compiled data confirms that the newly developed cow dung composting equipment successfully upholds the high-temperature duration of composting materials, aligning with industry-established norms. Moreover, the technology consistently produces organic fertilizer presenting desirable parameters: satisfactory water content, optimal acidity levels, and favourable seed germination rates.

In summary, the research findings underscore the feasibility and potential benefits of the proposed composting equipment, pointing towards a promising future for improved livestock manure management and sustainable agricultural practices.

Author Contributions: Conceptualization, methodology, writing—original draft preparation, and investigation, K.R. and L.S.; validation, formal analysis, and writing—review and editing, X.H. and H.W.; writing—review and editing and supervision, Y.Z. All authors have read and agreed to the published version of the manuscript.

Funding: This research was funded by The Innovation Team of Higher Education Institutions in Inner Mongolia Autonomous Region, grant number NMGIRT2312 and Modern Agriculture and Inner Mongolia Grassland Talent Innovation Team, grant number No. [2018] 19.

Institutional Review Board Statement: Not applicable.

Informed Consent Statement: Not applicable.

Data Availability Statement: Not applicable.

Conflicts of Interest: The authors declare no conflict of interest.

Abbreviations

MCGS	Monitor and Control Generated System
PLC	Programmable logic Controller
°C	Anders Celsius
GI	Germination index
PH	Potential of hydrogen

References

1. Li, S.; Dang, Y.Q.; Tang, F.B.; Meng, Y.J. Optimization research on evaluation index of aerobic compost based on ventilation frequency control. *Soil Fertil. Sci. China* **2020**, *3*, 182–188.
2. Zhang, Z.H.; Zhang, D.H.; Liu, H. Overview of International Dairy Industry Development in 2020 and Analysis and Prospect of China's Dairy Industry Situation. *Chin. Cows* **2021**, *5*, 51–54.
3. Lu, Y.; Chadwick, D.; Norse, D.; Powlson, D.; Shi, W. Sustainable intensification of China's agriculture: The key role of nutrient management and climate change mitigation and adaptation. *Agric. Ecosyst. Environ.* **2015**, *209*, 1–4. [CrossRef]
4. Antonious, G.F.; Turley, E.T.; Gyawali, B.R.; Freeman, A.C. Influence of Biochar and Animal Manures Application on Ammonia and Nitrate Concentrations in the Root and Shoot of Three Varieties of Turnips. *Agriculture* **2023**, *13*, 137. [CrossRef]
5. Shuang, Q.; Wang, Y.L.; Zhong, J.W. The Development History and Current Situation of Inner Mongolia Dairy Industry. *China Dairy Ind.* **2018**, *46*, 32–35+60.
6. Soliman, Y.M.; Soliman, W.S.; Abbas, A.M. Alley Cropping and Organic Compost: An Efficient and Sustainable Agro-Ecological Strategy for Improving Turmeric (*Curcuma longa* L.) Growth and Attributes. *Agriculture* **2023**, *13*, 149. [CrossRef]
7. Rehman, S.U.; De Castro, F.; Marini, P. Vermibiochar: A Novel Approach for Reducing the Environmental Impact of Heavy Metals Contamination in Agricultural Land. *Sustainability* **2023**, *15*, 9380. [CrossRef]
8. Więckol-Ryk, A.; Pierzchała, Ł.; Bauerek, A. Minimising Coal Mining's Impact on Biodiversity: Artificial Soils for Post-Mining Land Reclamation. *Sustainability* **2023**, *15*, 9707. [CrossRef]
9. Lambu, Z.N.; Shamsuddeen, U.; Yahaya, S. Production of Bio-Fertilizer through Composting of Tannery Wastes with Cow Dung and Rice Bran. *UMYU J. Microbiol. Res.* **2021**, *6*, 1–10. [CrossRef]
10. Malewski, T.; Borowik, P.; Olejarski, I.; Rutkiewicz, A.; Okorski, A.; Oszako, T. Addition of Organic Matter to Pine Plantations on Agricultural Land Positively Alters the Mycobiome of Agricultural Soils. *Appl. Sci.* **2023**, *13*, 5800. [CrossRef]
11. Patricia, W.; Kerstin, B.; Yin, T. Microscopic differential cell count and specific mastitis pathogens in cow milk from compost-bedded pack barns and cubicle barns. *J. Dairy Res.* **2021**, *88*, 413–419.
12. Siswati, L.; Nizar, R.; Ariyanto, A. Manfaatkan Kotoran Sapi Menjadi Kompos Untuk Tanaman Masa Pandemi Di Kelurahan Umbansari Kota Pekanbaru. *Din. J. Pengabdi. Kpd. Masy.* **2021**, *5*, 531–537. [CrossRef]
13. Patra, R.K.; Behera, D.; Mohapatra, K.K. Juxtaposing the quality of compost and vermicompost produced from organic wastes amended with cow dung. *Environ. Res.* **2022**, *214 Pt 4*, 114119. [CrossRef] [PubMed]
14. Magotra, V.K.; Kang, T.W.; Kim, D.Y. Urea fuel cell using cow dung compost soil as a novel biocatalyst for power generation applications. *Energy* **2022**, *239*, 122357.1–122357.12. [CrossRef]
15. Gorasiya, T.; Faldu, N. Exploring floral waste into bio-compost using microbial consortium from cow dung: A review. *J. Food Agric. Environ.* **2021**, *19*, 71–74.
16. Zailani, S.N.; Shaheen, A.; Noor, A.Z. Compost Bed Size Influences the Co-Composting of Cow Dung and Spent Mushroom at Mesophilic Stage. *IOP Conf. Ser. Earth Environ. Sci.* **2021**, *765*, 012074. [CrossRef]
17. Utami, A.; Hidayat, B. Mukhlis Study of some chemical properties of ultisol soil applied by biochar and compos from some biomasses and incubation time. *IOP Conf. Ser. Earth Environ. Sci.* **2021**, *782*, 042040. [CrossRef]

18. Kakihara, H.; Ogura, S. Effect of soil acidification on regrowth of orchardgrass (Dactylis glomerata) under application of grazing cattle dung, cattle manure compost, and chemical fertilizer. *Grassl. Sci.* **2022**, *68*, 255–262. [CrossRef]
19. Nurmas, A.; Rakian, T.C.; Asdari, N. Evaluation of plant distance and composition of goat manure in okra (Abelmoschus esculentus l.) plant in supporting food security. *IOP Conf. Ser. Earth Environ. Sci.* **2021**, *681*, 012026. [CrossRef]
20. Chi, W.H.; Ren, Y.X.; Chen, W.; Chen, R.; Liu, Y.Z.; Wang, X.C. Development and application of a pyriform rotating drum reactor for aerobic composting. *Chin. J. Environ. Eng.* **2013**, *7*, 3561–3566.
21. Makan, A.; Fadili, A.; Oubenali, M. Interaction of physicochemical parameters during pressurized in-vessel composting of food waste. *Bioresour. Technol. Rep.* **2020**, *10*, 100350. [CrossRef]
22. Xiong, J.; Ma, S.; He, X.; Han, L.; Huang, G. Nitrogen transformation and dynamic changes in related functional genes during functional-membrane covered aerobic composting. *Bioresour. Technol.* **2021**, *332*, 125087. [CrossRef] [PubMed]
23. Schneider, J.; Burg, J.M.; Theilen, U. Towards optimized drum composting: Evaluation of the radial mixing performance of a model substrate on the laboratory scale. *Environ. Technol.* **2020**, *41*, 1606–1613. [CrossRef] [PubMed]
24. Yang, Y.; Liang, W.; Hu, K. Simulated Ammonia Nitrogen Wastewater Treated with Spent Mushroom Compost in a Laboratory Bioreactor. *Pol. J. Environ. Stud.* **2016**, *25*, 2197–2203. [CrossRef] [PubMed]
25. Jain, M.; Paul, S.; Kalamdhad, A.S. Kinetics and physics during composting of various organic wastes: Statistical approach to interpret compost application feasibility. *J. Clean. Prod.* **2020**, *255*, 120324. [CrossRef]
26. Yu, P.; Chen, J. Performance test on the composting process of food wastes in a small composting reactor. *J. Hunan Agric. Univ. Nat. Sci.* **2021**, *47*, 351–355.
27. Sobieraj, K.; Stegenta-Dąbrowska, S.; Luo, G.; Koziel, J.A.; Białowiec, A. Biological treatment of biowaste as an innovative source of CO—The role of composting process. *Front. Bioeng. Biotechnol.* **2023**, *11*, 1126737. [CrossRef]
28. Yan, C.; Cao, L.P.; Liu, Y.H. Effect of new high temperature aerobic composting device on maturation of chicken manure and rice chaff. *Chin. J. Environ. Eng.* **2021**, *15*, 1103–1111.
29. Malik, K.; Rani, S.; Ahlawat, S. Bioconversion process for compost production from agricultural residue. *Int. J. Chem. Eng.* **2021**, *9*, 827–830. [CrossRef]
30. Zhang, J.; Zhang, T.; Ying, Y. Effects of different additives on the chemical composition and microbial diversity during composting of Camelliaoleiferashell. *Bioresour. Technol.* **2021**, *330*, 124990. [CrossRef] [PubMed]
31. Kuddus, M.A.; Alam, M.J.; Datta, G.C. Climate resilience technology for year round vegetable production in northeastern Bangladesh. *Int. J. Agric. Res. Innov. Technol.* **2021**, *11*, 29–36. [CrossRef]
32. Sukariawan, A.; Febrianto, E.B. Sakiah Ganoderma boninense control in palm oil plantations using Trichoderma harzianum in various Media. *IOP Conf. Ser. Earth Environ. Sci.* **2021**, *819*, 012001. [CrossRef]
33. Thakur, A.; Kumar, A.; Chava, V. A Review on Vermicomposting: By-Products and Its Importance. *Plant Cell Biotechnol. Mol. Biol.* **2021**, *22*, 156–164.
34. Sultana, M.; Jahiruddin, M.; Islam, M.R. Nutrient Enriched Municipal Solid Waste Compost Increases Yield, Nutrient Content and Balance in Rice. *Sustainability* **2021**, *13*, 1047. [CrossRef]
35. Huang, S.; Ma, Q.; Hou, Q. Identification and quantitative chemical analysis of betaines in different organic wastes and their bioconversion composts. *Bioresour. Technol.* **2021**, *328*, 124857. [CrossRef]
36. Komolafe, A.F.; Adejuyigbe, C.O.; Babalola, O.A. Fertilizer values of composts as affected by plant materials and composting duration on maize (*Zea mays*) performance. *Agro-Science* **2021**, *20*, 87–94. [CrossRef]
37. Wang, Y.; Pang, L.; Liu, X. Using thermal balance model to determine optimal reactor volume and insulation material needed in a laboratory-scale composting reactor. *Bioresour. Technol.* **2016**, *206*, 164–172. [CrossRef]
38. Wang, F. Design and Experiment of Small Composting Equipment for Fecal Matter of Livestock and Poultry Based on Heating by Aeration. Master's Thesis, Inner Mongolia Agricultural University, Hohhot, China, 2021.
39. Yusnaini, S.; Niswati, A.; Aini, S.N. Changes in soil respiration after application of in situ soil amendment and phosphate fertilizer under soybean cultivation at Ultisol South Lampung, Indonesia. *IOP Conf. Ser. Earth Environ. Sci.* **2021**, *724*, 012002. [CrossRef]
40. Wang, Q.; Awasthi, M.K.; Zhao, J.; Ren, X.; Li, R.; Wang, Z.; Wang, M.; Zhang, Z. Improvement of pig manure compost lignocellulose degradation, organic matter humification and compost quality with medical stone. *Bioresour. Technol.* **2017**, *243*, 771–777. [CrossRef]
41. Sobieraj, K.; Stegenta-Dąbrowska, S.; Zafiu, C.; Binner, E.; Białowiec, A. Carbon Monoxide Production during Bio-Waste Composting under Different Temperature and Aeration Regimes. *Materials* **2023**, *16*, 4551. [CrossRef]
42. Petric, I.; Selimbašić, V. Composting of poultry manure and wheat straw in a closed reactor: Optimum mixture ratio and evolution of parameters. *Biodegradation* **2008**, *19*, 53–63. [CrossRef] [PubMed]
43. Strenner, M.; Chmelíková, L.; Hülsbergen, K.J. Compost Fertilization in Organic Agriculture—A Comparison of the Impact on Corn Plants Using Field Spectroscopy. *Appl. Sci.* **2023**, *13*, 3676. [CrossRef]
44. Kujawa, S.; Niedbała, G.; Czekała, W.; Pentoś, K. Neural Image Analysis for the Determination of Total and Volatile Solids in a Composted Sewage Sludge and Maize Straw Mixture. *Appl. Sci.* **2023**, *13*, 3363. [CrossRef]

Disclaimer/Publisher's Note: The statements, opinions and data contained in all publications are solely those of the individual author(s) and contributor(s) and not of MDPI and/or the editor(s). MDPI and/or the editor(s) disclaim responsibility for any injury to people or property resulting from any ideas, methods, instructions or products referred to in the content.

applied sciences

MDPI

Article

Multi-Indicator Weighted Robustness Analysis of Planktonic Community Systems under Different Destructive Factors

Danfeng Zhao [1], Tao Zhang [1], Tianwen Chen [1], Qi He [1] and Dongmei Huang [2,*]

[1] College of Information Technology, Shanghai Ocean University, Shanghai 201306, China; dfzhao@shou.edu.cn (D.Z.); m210901457@st.shou.edu.cn (T.Z.); ccctw0825@163.com (T.C.); qihe@shou.edu.cn (Q.H.)
[2] College of Electronic and Information Engineering, Shanghai University of Electric Power, Shanghai 200090, China
* Correspondence: dmhuang_dz@163.com

Abstract: Marine plankton communities play a vital role in global carbon and nutrient cycles. Ensuring the robustness of these intricate ecosystems is critical for sustainable environmental management. In this paper, we apply complex network analysis to assess plankton community resilience against disturbances. We construct ecological interaction networks and simulate disruptions using four attack strategies targeting vertices and edges. Our multi-indicator evaluation scheme provides a more nuanced measure of robustness compared to single metrics. Our experiments revealed varying vulnerabilities across networks. Targeted attacks caused abrupt collapse, while random failures led to gradual decline. Identifying critical species and linkages is key to guiding protection efforts. Overall, plankton networks proved fragile, especially against deliberate attacks on central hubs. In our simulations, betweenness-based attacks were the most destructive. The multi-indicator robustness coefficient achieved better performance than individual metrics, with under 3% variance. This network methodology reveals hidden topological vulnerabilities and complements traditional plankton research. The quantitative insights provided in this paper can support marine conservation and governance.

Keywords: marine plankton; interaction; complex networks; multi-indicator weighted; robustness analysis

Citation: Zhao, D.; Zhang, T.; Chen, T.; He, Q.; Huang, D. Multi-Indicator Weighted Robustness Analysis of Planktonic Community Systems under Different Destructive Factors. *Appl. Sci.* **2023**, *13*, 8742. https://doi.org/10.3390/app13158742

Academic Editors: Mohammad Mahmudur Rahman, Dibyendu Sarkar, Rupali Datta and Prafulla Kumar Sahoo

Received: 6 June 2023
Revised: 26 July 2023
Accepted: 27 July 2023
Published: 28 July 2023

Copyright: © 2023 by the authors. Licensee MDPI, Basel, Switzerland. This article is an open access article distributed under the terms and conditions of the Creative Commons Attribution (CC BY) license (https://creativecommons.org/licenses/by/4.0/).

1. Introduction

Marine plankton play a crucial role in sustaining and balancing the health of marine food webs, making them essential for the sustainability of environmental technologies [1,2]. They exhibit diverse species, abundant populations, and wide distribution. Their contributions include the production of nutrients and oxygen, which are vital for maintaining ecosystem health. Additionally, they facilitate the decomposition and cycling of organic matter within water bodies. Marine plankton serve as valuable biological indicators, enabling the monitoring of ecological changes and ecosystem health [3]. Ensuring the stability of plankton communities is of the utmost importance, as it supports biogeochemical cycles and enables the proper functioning of marine ecosystems [4]. A decline in plankton abundance can have far-reaching consequences, disrupting the entire food web and negatively impacting the health of fish, marine mammals, and other marine populations. Conversely, rapid increases in phytoplankton populations can result in harmful algal blooms such as red tides, which pose risks to both humans and marine life. Moreover, the decomposition of these blooms consumes large amounts of oxygen, leading to the formation of underwater hypoxic zones [5]. Through study of the resilience of marine plankton communities against environmental disturbances and human activities, we can gain insights that can help to improve and restore marine ecosystems. This knowledge can inform actions such

as implementing sustainable harvest practices, utilizing biological controls, and adopting strategies to mitigate harmful algal blooms.

Recent studies have investigated the potential relationship between environmental changes and plankton stability. Gökçe et al. [6] developed an oxygen–plankton diffusion model that incorporated a time delay parameter, enabling analysis of the stability of the coexistence equilibrium of dissolved oxygen concentration and plankton density, and the detection of Hopf bifurcations. While facilitating numerical simulations, this comes at the expense of a rapidly decreasing solution speed with increasing parameters. Vallina et al. [7] examined how phytoplankton functional diversity influences ecosystem productivity and stability under fluctuating environments. They discovered that phytoplankton communities with greater functional diversity exhibited higher and more stable ecosystem productivity. On the other hand, they found that the positive influence of biodiversity on ecosystem function depended primarily on the type of environmental gradient. Thakur et al. [8] developed a nutrient–plankton interaction model to investigate the effects of phytoplankton toxin release on other plants. Their study analyzed the local stability conditions of the time-delayed system and determined critical parameter values for the influence of toxin release delay on phytoplankton community stability. Morozov et al. [9] constructed a generalized integral–differential equation-based plankton model. They proposed a method of finding the equilibrium boundary of ecosystem stability by incorporating both nutrient levels in the water body and zooplankton predatory behavior. A key advantage of their technique is the small deviation range in predicting outcomes for normal water bodies (no more than 20%); however, a different modeling approach is required for atypical environments such as red tide outbreaks.

In summary, traditional research schemes tend to discuss problems by building complex mathematical models with high solution accuracy. However, setting their many parameters can become unwieldy when multiple influential factors are involved. In contrast, complex network modeling and analysis can simplify highly complex systems to help grasp the essence of a problem, offering an effective methodology for studying such systems. The robustness of a complex network refers to how network performance changes under perturbations. and can serve as a key indicator of complex system reliability [10–12].

The network perspective on plankton stability reveals fragilities and connectivity patterns overlooked by traditional methods. Mapping these vulnerabilities enables preventive interventions to bolster resilience. Pinpointing keystone species and critical habitat linkages, for instance, can guide ecosystem conservation approaches. Simulating disruption scenarios quantifies robustness in a dynamic context and provides early warning of imminent regime shifts. Comparing network topologies exposes those designs that are most resilient against failures. These findings allow improvements to be implemented prior to collapse. For example, adding modularity with redundancies to the power grid can help to prevent large-scale blackouts. Increasing heterogeneity in cropland landscapes slows transmission of crop diseases. Thus, maintaining network robustness is critical for managers of natural ecosystems, physical infrastructure, supply chains, and human systems. Network approaches transition the analysis from simple dyadic ties to complex system interdependencies. The related methodologies reveal fragilities that are concealed when studying components in isolation. Quantifying network robustness can aid governance by enhancing robustness.

The utility of complex network robustness analysis has been demonstrated across many terrestrial and marine environments. Applications include studying pollination networks [13], trophic interactions in food webs [14], and symbiotic relationships between species [15]. Important discoveries have been made regarding ecosystem stability in forests, coral reefs, and animal gut microbiomes [16]. However, complex network robustness analysis has not been applied to study zooplankton communities. Extending robustness analysis to illuminate zooplankton community dynamics would similarly enhance understanding of this vital biome. The resulting insights can inform conservation strategies to protect marine ecosystems facing growing environmental pressures.

In this paper, we argue that analyzing the robustness of complex ecological networks has become an extremely valuable tool for comprehending the stability and resilience of natural communities. Applying complex network approaches to study interactions between zooplankton species can provide unique insights unavailable with traditional methods [17]. In a community, robustness refers to the ability to maintain characteristic behavior under influences such as species extinction and environmental disturbance [18]. Viewing zooplankton communities as complex networks allows critical species that contribute disproportionately to overall ecosystem stability to be identified. The loss of these highly connected "hub" species can precipitate catastrophic collapse. In addition, network analysis allows us to model how perturbations might propagate through the system.

In order to effectively evaluate marine plankton community resilience, this paper provides insight into different network structures' roles and patterns of robustness development. Specifically, plankton data are used to construct interaction networks of plankton communities. Various network attack strategies are then selected to simulate different types of network damage. We propose a multi-indicator weighted evaluation scheme, namely, the robustness coefficient, to analyze plankton community robustness across diverse network structures under simulated network damage scenarios. For this purpose, we selected three exemplary biological communities for robustness analysis based on continuous plankton recorder monitoring data. These communities exhibit different levels of biomass and interaction. Moreover, by comparing the robustness coefficient with other existing robustness evaluation metrics and analyzing the standard deviations, our comparative experiments provide additional evidence that using a weighted combination of multiple metrics (our proposed robustness coefficient) results in better performance than reliance on any single metric alone.

2. Materials and Methods

2.1. Materials

The data in this paper were obtained from the Australian Integrated Marine Observing System (IMOS) continuous plankton recorder (CPR) data. These plankton data are classified by genus and the time range is from January, 2009 to September 2022. We analyzed data from three marine plankton communities, with descriptive statistics shown in Table 1.

Table 1. Statistical data on each plankton community.

Plankton Community ID	Number of the Genus	Average Biomass (mg/m^3)
a	62	29,872.03
b	62	12,055.91
c	63	76,150.55

2.2. Methodology

The methodology in this paper consists of two main parts: (1) constructing complex networks using marine plankton community data, and (2) conducting a robustness analysis based on complex network theory, which includes selecting network attack strategies and developing network robustness evaluation schemes. Figure 1 shows the flow chart.

2.2.1. Complex Network Construction

This paper explores the application of complex network theory to model marine plankton community structures [19]. The resulting networks, referred to as marine plankton interaction networks, provide a comprehensive representation of the complex interactions between different plankton species within the marine ecosystem. The network consists of vertices and edges, where the vertices represent plankton community organisms and the edges represent interactions between them.

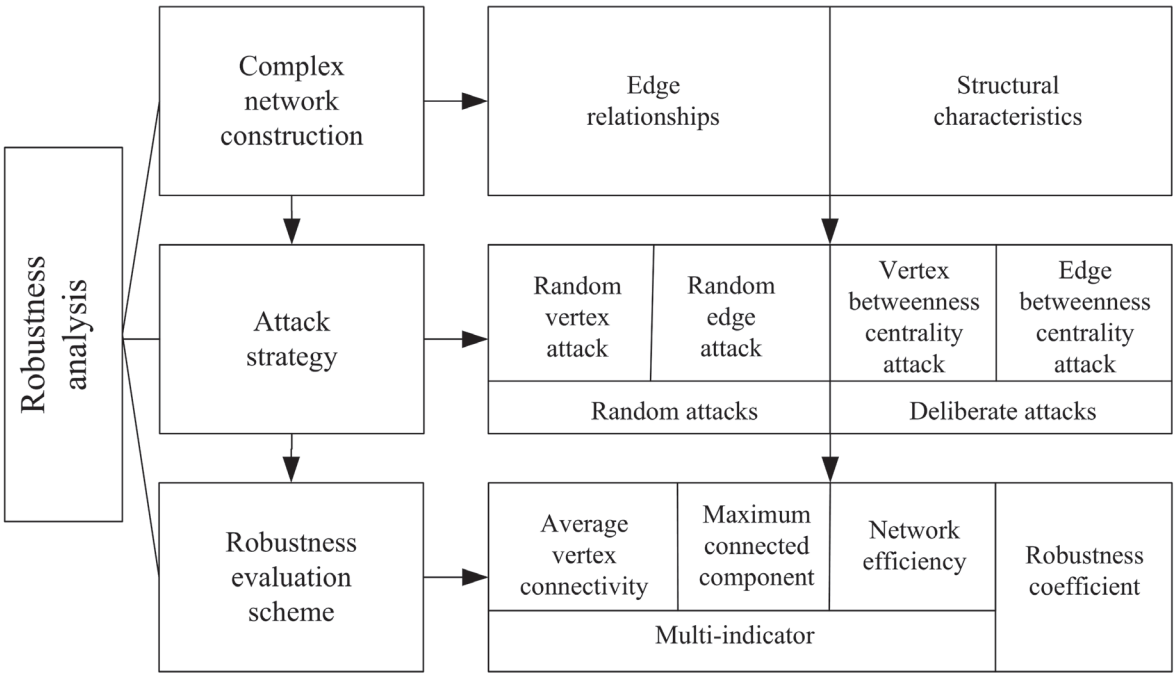


Figure 1. The approach to robustness analysis described in this paper consists of three essential components. First, the construction of a complex network relies on derived edge relationships. Second, attack strategies include two types of attacks, namely, random and deliberate. Finally, a robustness assessment scheme is derived from multi-indicator weighting.

The marine plankton interaction network can be represented as an undirected weighted network $G = (V, E)$, where $V = v_1, v_2, v_3, \ldots, v_n$ constitutes the set of vertices, n denotes the number of vertices, $E = e_1, e_2, e_3, \ldots, e_m$ constitutes the set of edges, and m represents the number of edges for any edge $e =< u, v >\in E$, where $u, v \in V$ and $u \neq v$

The Spearman rank correlation coefficient (Spearman coefficient) is a statistical measure used to calculate the correlation degree between two variables. It is commonly used in marine biology to determine the correlation between different plankton types. Suppose that two variables X and Y represent two plankton abundance datasets, each with h observations; X_i and Y_i denote the ith values of X and Y ($1 \leq i \leq H$), respectively. We sort both X and Y in ascending or descending order, yielding the two variables x and y. The element x_i is the rank of X_i in X, while y_i is the rank of Y_i in Y. The Spearman rank correlation coefficient between X and Y can be obtained by the following formula:

$$r_s = \rho_{x,y} = \frac{\sum_{i=1}^{h}(x_i - \bar{x})(y_i - \bar{y})}{\sqrt{\sum_{i}^{h}(x_i - \bar{x})^2 \sum_{i}^{h}(y_i - \bar{y})^2}} \tag{1}$$

where $\bar{x} = \frac{1}{h}\sum_{i=1}^{h} x_i$ is the mean value of x and $\bar{y} = \frac{1}{h}\sum_{i=1}^{h} y_i$ is the mean value of y.

In the marine plankton interaction network defined in this paper, each plankton type is represented as a network vertex. Edge weights are determined by the Spearman rank correlation coefficient between two vertices X and Y. No edges exist between X and Y if the p-value is <0.05. The weights w_{XY} of edges $< X, Y >$ between vertices X and Y are defined as follows:

$$w_{XY} = \left|\rho_{x,y}\right| \tag{2}$$

In addition, this paper proposes that the shortest path between vertices i and j has path weights d_{ij}, defined as follows:

$$d_{ij} = \frac{w_{v_i v_1} + w_{v_1 v_2} + \cdots + w_{v_{t-1} v_t} + w_{v_t v_j}}{t+1} \tag{3}$$

where $v_1, v_2, \ldots, v_t$ are the vertices on the shortest path between i and j.

Complex networks often possess intricate structures and numerous relationships, making their detailed structural modeling a challenge. Network structural characteristics are often used to concisely describe networks effectively. In this section, three common network metrics, namely, the average degree, average path length, and network diameter, are utilized to describe the overall topology of the marine plankton interaction network.

(1) Average degree: the degree of a vertex describes its connectivity, referring to its associated edge number; the higher the degree, the stronger its connection to other vertices. The average degree of network G is $K(G)$, defined as the average of all vertex degrees:

$$K(G) = \frac{\sum_{i=1}^{n} k(v_i)}{n} \tag{4}$$

where $k(v_i)$ denotes the degree of vertex i, or the number of connected edges.

(2) Average path length: in network theory, the path length describes the distance between two vertices, i.e., the minimum edge number a vertex passes through to reach another. A shorter path length indicates higher efficiency and greater information dissemination, while a smaller path length between two vertices indicates higher efficiency. The average path length of network G, denoted $L(G)$, is

$$L(G) = \frac{\sum_{i=1}^{n} \sum_{j=1}^{n} l_{ij}}{n(n-1)}, i \neq j \tag{5}$$

where l_{ij} is the minimum edge number between vertices i and j and n is the vertex number of network G.

(3) Network diameter: a network's diameter refers to the maximum distance between any two vertices, and is used to measure its efficiency and information transfer speed; more specifically, the network diameter refers to the worst link path length. The diameter of network G, denoted $D(G)$, is

$$D(G) = Max(l_{ij}). \tag{6}$$

2.2.2. Attack Strategies

Robustness analysis aims to analyze network performance under various attacks [20]. Network attacks can simulate removing members based on different strategies [21].

Attacks are currently divided into random attacks and deliberate attacks [22]. Random attacks involve random vertex or edge failures, and can be used to simulate natural disasters or climate effects. Deliberate attacks involve deliberate vertex or edge failures, which can simulate human activities or toxic substances that destroy communities. By using different attack strategies, network robustness can be evaluated from multiple perspectives. In this paper, we selected four attack strategies considering possible destruction of marine plankton communities: two random attacks (random vertex attack [23,24], and random edge attack [25]) and two deliberate attacks (betweenness centrality attack and edge betweenness centrality attack [26]).

(1) Random vertex attack: in the random vertex attack strategy, vertices are randomly deleted from the network [27]. When a vertex is deleted, its connected edges are deleted accordingly. The attack order q_{v_i} of vertex v_i is

$$q_{v_i} = Rand(n),\ 1 \leq i \leq n \tag{7}$$

where n is the network's vertex number and $Rand(n)$ generates a single random natural number within $[1, n]$ each time. $Rand(n)$ generates n numbers without repetition.

(2) Random edge attack: in the random edge attack strategy, edges are randomly deleted from the network [28]. When all edges connected to a vertex are deleted, that vertex is deleted accordingly [29]. The attack order q_{e_i} of edge e_i is

$$q_{e_i} = Rand(m),\ 1 \leq i \leq m \tag{8}$$

where m is the network's edge number and $Rand(m)$ generates a single random natural number within $[1, m]$ each time. $Rand(m)$ generates m numbers without repetition.

(3) Vertex betweenness centrality attack: this attack strategy sequentially attacks vertices based on betweenness centrality in order from largest to smallest. Two non-neighboring connected vertices' interaction depends mainly on the other vertices along the path. These vertices act as bridges forthe interaction of edge vertices. The vertex betweenness centrality $vbet_p$ is used to measure these vertices' importance:

$$vbet_p = \sum_{i \neq j \neq p} \frac{path_{ij}^p}{path_{ij}} \tag{9}$$

where $path_{ij}$ is the path number between vertices i and j and $path_{ij}^p$ is the path number between vertices i and j passing through vertex p.

(4) Edge betweenness centrality attack: this attack strategy sequentially attacks edges based on betweenness centrality in order from largest to smallest. If an edge frequently appears on the path between any two vertices, it is in a relatively central network position with high betweenness centrality. The betweenness centrality $ebet_{st}$ of edge e_{st} is

$$ebet_{st} = \sum_{i \neq j} \frac{path_{ij}^{e_{st}}}{path_{ij}} \tag{10}$$

where $path_{ij}^{e_{st}}$ is the path number between vertices i and j passing through edge e_{st} and $path_{ij}$ is the path number between vertices i and j.

2.2.3. Robustness Evaluation Scheme

In this paper, we adopt the average vertex connectivity, maximum connectivity component, and network efficiency as evaluation indicators, drawing on complex network theory and plankton community structure. However, these traditional single indicators present limitations in terms of robustness analysis and measurement. To address this issue, we introduce a novel multi-indicator weighted robustness evaluation scheme.

(1) Average vertex connectivity: vertex connectivity measures the ability of network vertices to remain connected after deleting some number of vertices [30] based on connectivity [31]. In marine plankton communities, a plankton type's steady-state biomass is closely related to the nutrients it can uptake. If a plankton type feeds only on one food type, any sharp population decline risks severe harm, as a reduction in food availability threatens this food source. Feeding on varied foods reduces this risk, as loss of one food source can be replaced with others. From an energy transfer perspective, fewer bioenergy sources are easily lost through disturbance and destruction. Community stability is often related to interaction diversity, and vertex connectivity measures a similar network property.

In network G, the vertex connectivity rm_{ij} between vertices i and j denotes the minimum vertex number needed to disconnect vertices i and j. Then, the average vertex connectivity AC is

$$AC = \frac{\sum_{i,j \in V} rm_{i,j}}{\binom{n}{2}}, \quad i \neq j. \tag{11}$$

Generally, higher AC indicates better network robustness. To eliminate dimensional influence on the robustness analysis, the value can be normalized as follows:

$$AC' = \frac{AC - \min(AC)}{\max(AC) - \min(AC)}. \tag{12}$$

(2) Maximum connected component: the maximum connected component refers to the largest subnetwork formed by vertices and edges. In robustness analysis, it reflects a network's damage degree [32]. When the removed vertex or edge ratio reaches a critical

value, the maximum connected component changes [33]. Plankton interactions play a critical role in shaping community characteristics and functions. However, disrupting plankton interaction clusters and hindering material transfer between them significantly changes characteristic functions, leading to collapse of the original plankton community. The maximum connected component change effectively reflects the network structure's tolerance to attack, providing a good evaluation of the network cluster structure.

In network G, the initial vertex number is N. After attack, the largest connected subnetwork's vertex number is N'. Then, the largest connected component's relative value is

$$MP = \frac{N^{'}}{N} \tag{13}$$

Here, MP reflects the network structure's tolerance degree to attacks. To eliminate dimensional influence on the robustness analysis, the values can be normalized as follows:

$$MP^{'} = \frac{MP - \min(MP)}{\max(MP) - \min(MP)}. \tag{14}$$

(3) Network efficiency: network efficiency refers to the efficiency of information exchange throughout the network [34,35]. Energy transfer between plankton often involves losses. The narrower the energy transfer path between any two plankton, the less conducive it is to gaining energy and the more prone it is to being disconnected under disturbances and destruction. In contrast, a wide path is clearly more conducive to maintaining the community in its steady state. Given the shortest path weight d_{st} in network G, the network efficiency NE is

$$NE = \frac{\sum_{s,t \in V} d_{st}}{\binom{n}{2}}, \quad s \neq t. \tag{15}$$

Generally, a higher NE indicates better network robustness. To eliminate dimensional influence, the value can be normalized as follows:

$$NE^{'} = \frac{NE - \min(NE)}{\max(NE) - \min(NE)} \tag{16}$$

(4) Robustness coefficient: three indicators (average vertex connectivity, maximum connected component, and network efficiency) have been introduced above. Below, we propose a multi-indicator weighted robustness evaluation scheme, called the robustness coefficient, by balancing the weights of these three indicators.

First, let the robustness coefficient be

$$R = f\left(AC^{'}, MP^{'}, NE^{'}\right), \tag{17}$$

where AC', MP', NE' represents the three normalized indicators in the robustness evaluation and f denotes the algorithm.

Next, calculate the indicators $r_k (k = 1, 2, 3; r_1 = AC^{'}, r_2 = MP^{'}, r_3 = NE^{'})$ when the marine plankton interaction network is destroyed. For each indicator, we obtain a changed dataset $\Delta r_k = \{\Delta r_{k_1}, \Delta r_{k_2}, \Delta r_{k_3}, \ldots, \Delta r_{k_{t-1}}, \Delta r_{k_t}\}$ of quantity t. Now, compute the data mean

$$\overline{\Delta r_k} = \frac{\sum_{i=1}^{t} \Delta r_{ki}}{n}, \quad k = 1, 2, 3. \tag{18}$$

Next, calculate the indicator variation variance

$$S_k^2 = \frac{\sum_{i=1}^{t} \left(\Delta r_{k_i} - \bar{\Delta r_k}\right)^2}{t}, \quad k = 1, 2, 3. \tag{19}$$

Repeat the experimental steps P times to calculate the mean variance $\overline{S_k^2}$. Then, determine each indicator's weight in the robustness coefficient using $\overline{S_k^2}$, as follows:

$$w_k = \frac{\sum_{k=1}^{3} \overline{S_k^2}}{\overline{S_k^2}}, \quad k = 1, 2, 3 \tag{20}$$

Using the normalization method ($w_1' + w_2' + w_3' = 1$),

$$w_k' = \frac{w_k}{\sum_{k=1}^{3} w_k}, \quad k = 1, 2, 3. \tag{21}$$

The robustness coefficient can now be summarized as follows:

$$R = \sum_{k=1}^{3} w_k' \frac{r_k - \min(r_k)}{\max(r_k) - \min(r_k)}. \tag{22}$$

3. Results

3.1. Network Construction

Take the examples of three plankton communities a, b, and c. We can calculate the correlation coefficients among organisms in communities a, b, and c and construct corresponding networks according to the network construction scheme, as shown in Figures 2–4.

The results of characterization and comparison of the structural properties of plankton interaction networks constructed from the three plankton communities (a, b, c) are shown in Table 2. All three networks have similar vertex numbers, while their edge numbers differ. Network b has substantially fewer edges compared to networks a and c, while networks a and c have comparable edge numbers. Additionally, network b has an average degree of only 5.55, indicating a sparse connection density.

Table 2. Characteristics indicators of the network.

Network ID	Number of Vertices	Number of Edges	Average Path Length	Average Degree	Network Diameter
a	62	388	12.52	2.05	4
b	62	172	5.55	2.93	5
c	63	333	10.57	2.15	4

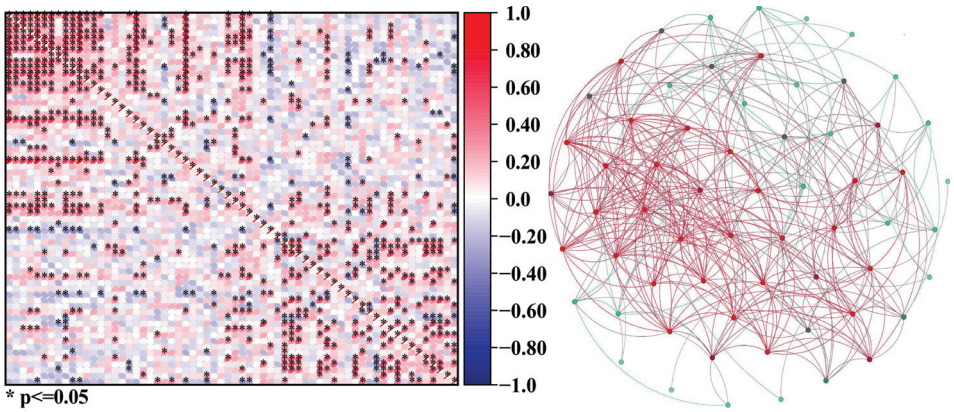


Figure 2. The correlation matrix of community a and its network a constructed based on the matrix; in the correlation matrix, the colors represent the strength of correlation, with * indicating $p \leq 0.05$. In the network, the colors represent the tightness of connections, with red vertices having tighter connections than blue vertices.

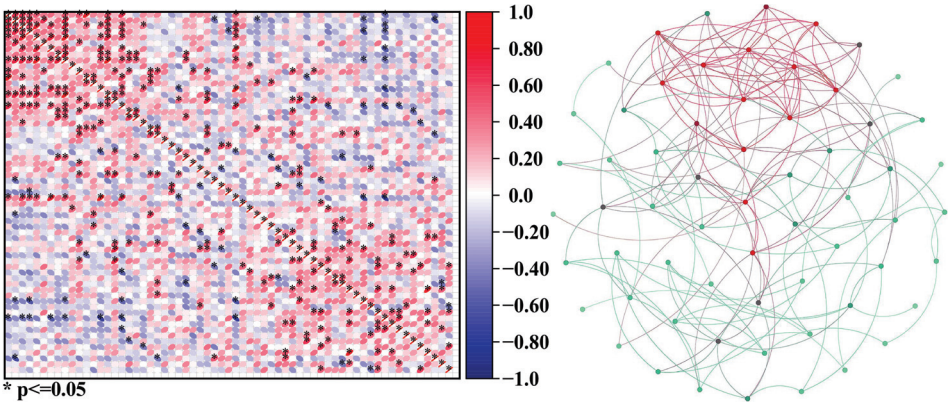


Figure 3. The correlation matrix of community *b* and the network *b* constructed based on the matrix.

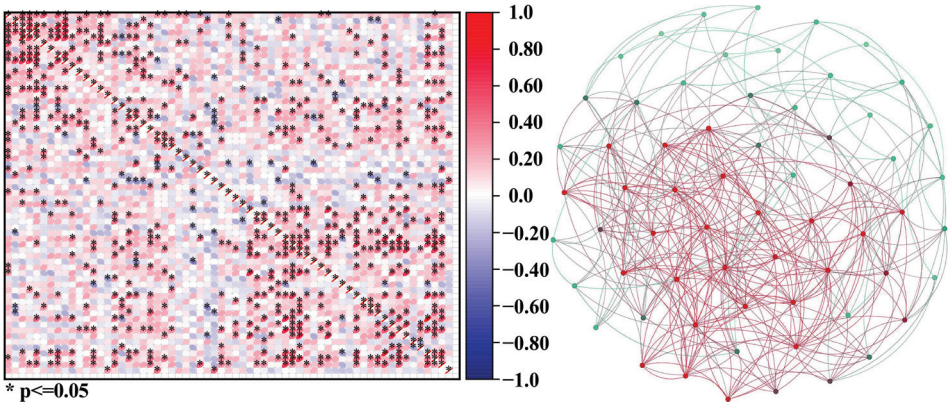


Figure 4. The correlation matrix of community *c* and the network *c* constructed based on the matrix.

3.2. Network Robustness Analysis

We performed the plankton interaction network robustness analysis according to the network attack strategies and robustness evaluation schemes presented in Section 2.2. First, the number of different plankton types (*1, 2, 3, ..., n*) by genus was set before starting the experiment. Then, attacks were carried out in certain proportions following different attack strategies. During network attacks, both the structure and characteristics of the network change. To assess the impacts of attacks on the network, we calculated the robustness evaluation indicators for the network at different attack degrees. Variations in the robustness evaluation indicators for the three networks under four attack strategies are shown through the curves in Figures 5–8, and changes in the robustness coefficients are displayed in Figure 5.

In Figure 6, the evaluation indicators decrease rapidly under random vertex attacks for all three networks. Although the changes in the indicators differ across networks, their robustness is similar. This suggests that plankton communities can undergo dangerously rapid collapse when certain organisms disappear regardless of their community structure. Furthermore, the maximum connected component of all three networks decreases the most slowly, followed by the average vertex connectivity, while the network efficiency declines the fastest. This shows that even though the community remains structurally sound under random vertex attacks, its function is severely damaged.

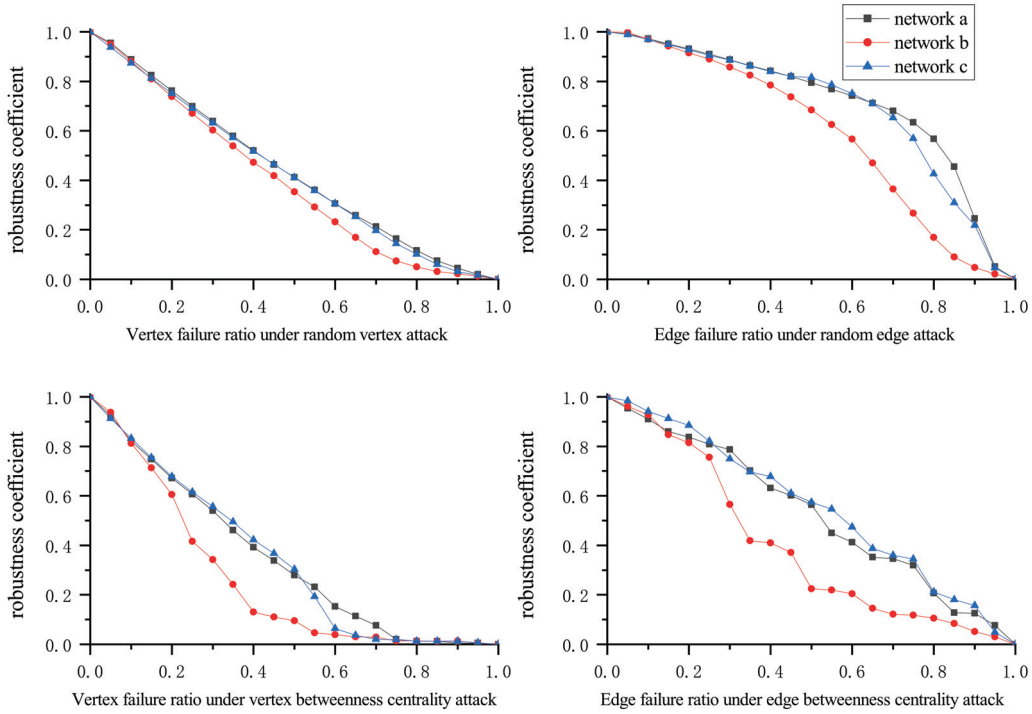


Figure 5. Changes in the robustness coefficient under different attack strategies.

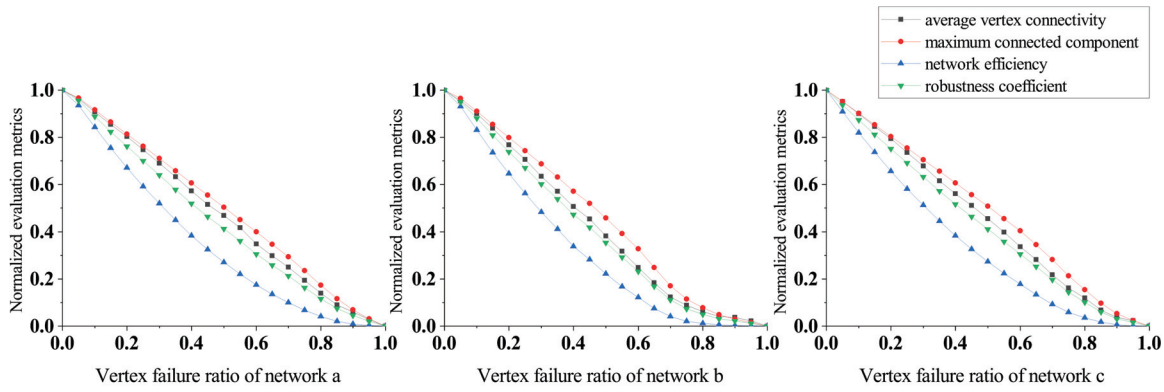


Figure 6. Changes in indicators under random vertex attack.

In Figure 7, the evaluation indicators perform better under random edge attacks for all three networks as compared to random vertex attacks. Networks *a* and *c* exhibit slow early stage declines, while network *b* is slightly less robust than networks *a* and *c*; however, this difference is insignificant. These results suggest that random edge attacks have weaker destructive power than random vertex attacks. In the early attack stages, networks with more edges, such as *a* and *c*, are less affected. This shows that plankton communities can resist natural disruptions well, especially highly interconnected communities such as *a* and *c*.

In Figure 8, the evaluation indicators decrease rapidly under vertex betweenness centrality attacks for all three networks, especially network *b*. In network *b*, when the vertex failure rate reaches 60%, the values of the average vertex connectivity and the network efficiency both drop to almost 0. At this point, the maximum connected component value is only about 10% of the original network. This shows that plankton communities can rapidly collapse under vertex betweenness centrality attacks, and that degradation of function is inevitable even if community biomass remains high.

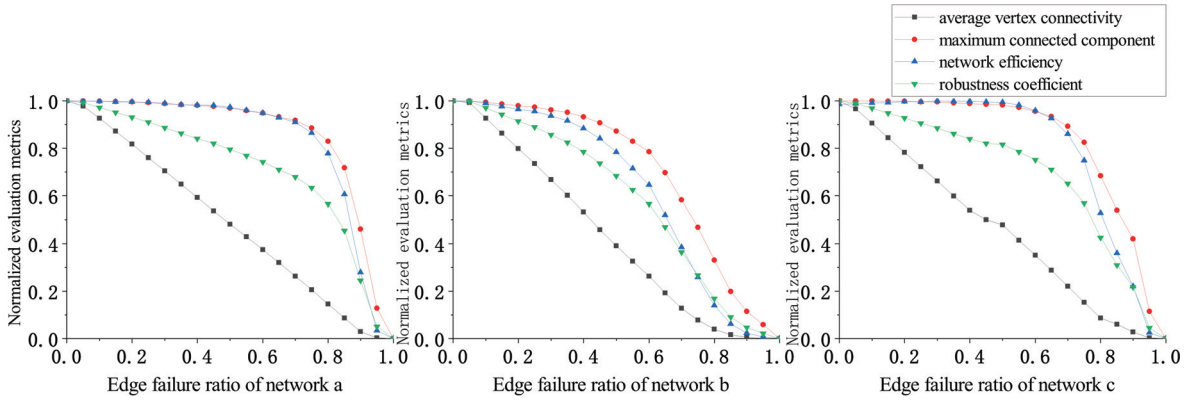


Figure 7. Changes in indicators under random edge attack.

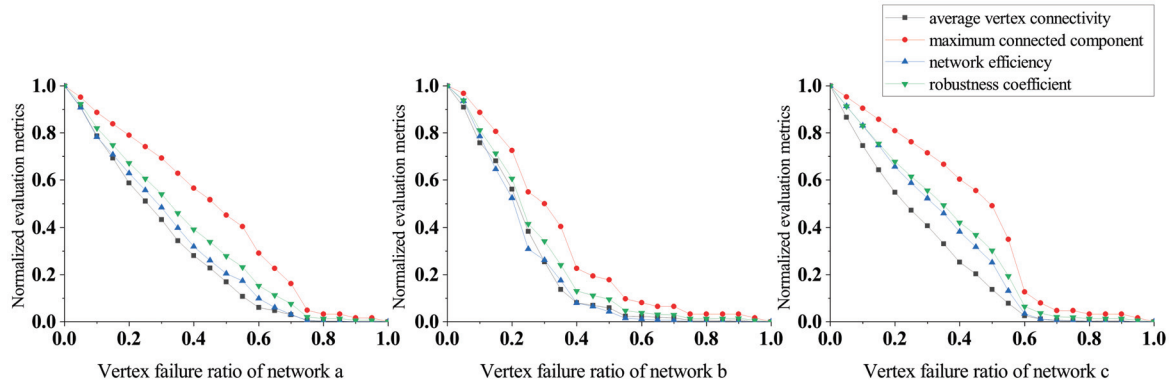


Figure 8. Changes in indicators under vertex betweenness centrality attack.

In Figure 9, the evaluation indicators under edge betweenness centrality attacks perform better than under vertex betweenness centrality attacks for all three networks. The maximum connected components and the network efficiency of networks *a* and *c* exhibit show slow decreases, while network *b* decreases more rapidly, which is likely related to its having fewer edges. This suggests that more interspecies connections confer higher plankton community robustness. However, the intensity of damage under edge betweenness centrality attacks is greater compared to random edge attacks, despite both attack types targeting edges. This shows that deliberate attacks, whether on vertices or edges, consistently cause more damage than random failures.

In Figure 5, the robustness coefficient intuitively expresses the overall network robustness under different attack strategies. Analysis of the robustness coefficients for the three networks shows that network robustness is greater under random attacks, especially random edge attacks. In the early and middle attack stages, little damage occurs to any network. Under random vertex attacks, the rate at which network robustness is degraded is higher than under random edge attacks, though the rate remains relatively gradual. However, network robustness decreases rapidly under deliberate attacks, rendering networks more vulnerable than under random attacks. Deliberate attacks exhibit greater global impact, are targeted more strategically, and disrupt networks faster than random attacks, conferring stronger attack capability. Furthermore, in both random and deliberate attacks, vertex attacks have greater destructive power than edge attacks; this is because the edges removed in edge attacks often have alternative paths for replacement, while vertex attacks eliminate both connected edges and alternative paths.

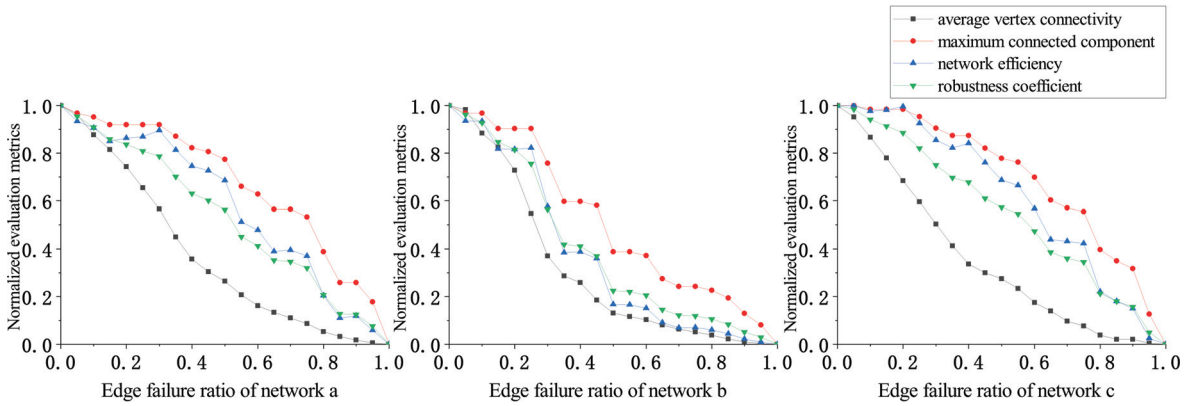


Figure 9. Change in indicators under edge betweenness centrality attack.

Finally, we specifically investigated the top five genera of planktonic organisms that exerted the most significant influence on robustness within each network, as visually represented in Figure 10. The outcomes of our analysis reveal noteworthy findings, as we observed crucial genera shared among the three networks that exhibited extensive interconnections. Additionally, we identified distinct variations between the networks, highlighting unique characteristics and dynamics. The findings of this study possess direct implications for advancing sustainable technological research, and can offer substantial assistance in this critical domain.

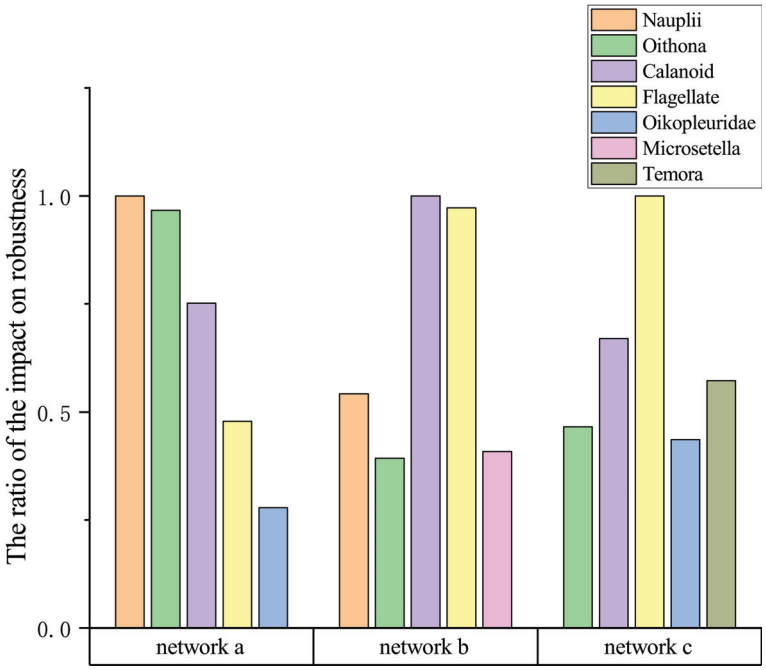


Figure 10. The top five genera of planktonic organisms with significant impacts on network robustness.

4. Discussion

This paper has applied complex network analysis to assess the robustness of marine plankton communities, providing insights relevant to sustainable environmental technology. Our findings reveal how different attack strategies impact network topology and performance. Several key points warrant further discussion.

4.1. Ecological Significance of the Results

The results preented in this paper demonstrate that plankton interaction networks exhibit varying robustness to disturbances. Identifying crucial hub genera and critical

linkages can guide protection efforts for at-risk marine environments. However, connectivity alone does not determine robustness. Even highly interconnected networks such as community *c* proved vulnerable to targeted attacks on central vertices. This highlights the complex interplay of structure, dynamics, and perturbations in ecological network analysis.

4.2. Methodological Advantages

Network approaches offer distinct advantages over traditional techniques for studying community robustness. Representing communities as networks enables the modeling of component interdependencies. Dynamic simulations can assess responses to perturbations in a way that is impossible with static methods. Moreover, our proposed multi-indicator weighted evaluation provides a more nuanced appraisal of robustness than single metrics such as connectivity.

Comparing our network-based approach to existing plankton community robustness assessment methods reveals many advantages of our method. Specifically, our technique can be compared to the plankton population dynamics model developed by Cropp et al. [36]. The Cropp model uses a series of nonlinear equations to simulate fluctuations in plankton biomass under various environmental conditions. Compared to the Cropp model, our network approach has the following strengths:

- It captures the intricate relationships between plankton types, rather than treating genera in isolation, helping to assess robustness at the ecosystem scale;
- It can simulate community dynamics during response to perturbations through different attack strategies;
- Its computational efficiency allows rapid investigation of multiple scenarios;
- The proposed multi-metric evaluation enables more nuanced measurement of robustness;
- Visual network representations provide intuitive understanding of topological vulnerabilities.

However, the Cropp model has more detailed biological characterizations of individual genera and their behaviors. Thus, the network technique offers higher-level robustness assessments that complement the individual-based modeling insights. In the future, an integrated framework combining both approaches may provide a more comprehensive perspective on plankton community resilience. While no single technique can provide all the answers, network analysis reveals community-scale phenomena that reductionist approaches cannot. Further synergistic application of systems and traditional methods can advance our understanding of these vital marine ecosystems.

In addition, we computed the standard deviation between the multi-metric weighted evaluation indicators we proposed and the single metrics, demonstrating that our multi-metric approach has better stability across the evaluation indicators compared to relying on any individual metric. A single metric may be susceptible to noise, and may fail to capture key aspects of ecosystem dynamics. In contrast, a composite indicator based on multiple metrics helps to smooth over variability in individual measurements and integrate diverse aspects of stability. The lower standard deviation that we obtained verifies that our multi-metric technique yields more consistent evaluations of plankton community robustness.

The calculated variation in the standard deviation for the evaluation indicators under the four attack strategies is shown Table 3. The standard deviation values in Table 3 show that the proposed multi-indicator weighting evaluation scheme, that is, the robustness coefficient, achieves more stable measurement than the other evaluation indicators under different attack strategies. The maximum standard deviation value is 0.33 and the minimum is 0.32, fluctuating by only about 3%, which is significantly less than the other evaluation indicators. In addition, the average standard deviation is the lowest among the different evaluation indicators.

Table 3. Comparison of the standard deviation of the evaluation indicators under different attack strategies.

Name	Average Vertex Connectivity	Maximum Connected Component	Network Efficiency	Robustness Coefficient (Ours)
Random vertex attack	0.33	0.33	0.33	0.33
Random edge attack	0.34	0.30	0.35	0.32
Vertex betweenness centrality attack	0.33	0.36	0.34	0.33
Edge betweenness centrality attack	0.34	0.31	0.35	0.32
Mean standard deviation	0.335	0.325	0.343	0.325

Overall, based on the differences in the trend lines and standard deviations of the different indicators, the robustness coefficient proposed in this paper demonstrates better stability and reliability.

4.3. Limitations

While this study presents several valuable contributions, it has certain limitations that should be acknowledged.

First, while the plankton dataset encompasses a broad scope, it primarily considers the relationships between plankton, and does not include all relevant genera and species. In addition, it does not account for the influence of varying external biotic factors.

Second, the simulated attack experiments make a number of simplifying assumptions, and may not fully reflect real-world complexity.

In light of these limitations, the findings presented in this paper should be interpreted as indicative rather than definitive. Within this delimited scope, however, these findings make a valuable contribution that can inform future research. The complex systems approach holds significant potential advantages for elucidating ecosystem dynamics.

4.4. Future Research Directions

While the network modeling approach presented in this paper represents an important initial foray towards the application of complex systems techniques to elucidate plankton community stability, there remain ample opportunities to expand upon this foundation and augment the utility of these methods.

One potential area for future work is incorporating additional biological detail into the network construction process, for instance, by weighting edges based on the strength of trophic interactions or distinguishing between symbiotic and competitive relationships. This could reveal how network topology is related to underlying population dynamics.

More sophisticated simulation studies could be conducted as well, such as modeling cascading extinctions or evaluating different recovery and restoration interventions. Transitioning from descriptive robustness analyses to utilizing network models predictively is a critical next frontier.

By capitalizing on these future opportunities, network analysis of plankton communities can mature into an established methodology that provides critical support for evidence-based ocean management and sustainable environmental technologies. The present study provides a solid initial foundation to enable progress toward this goal.

5. Conclusions

This paper has demonstrated the application of complex network analysis to evaluate the robustness of marine plankton communities, providing a novel systems perspective relevant to sustainable environmental technology.

Our findings reveal that plankton interaction networks exhibit varying vulnerabilities to disturbances depending on topological structure. Random failures of vertices or links result in slower degradation than targeted attacks on central hubs. This highlights the need to identify and protect crucial species that sustain ecosystem connectivity. The proposed

multi-indicator evaluation scheme enables more comprehensive robustness assessment than reliance on single metrics. By capturing multiple aspects of network performance, the proposed robustness coefficient offers a more nuanced and stable characterization. The presented network modeling approach enables plankton community dynamics to be studied under real-world disruption scenarios that are difficult to replicate experimentally. This approach contributes quantitative insights that can complement field studies, allowing for a more complete understanding.

While this work has limitations in terms of the dataset scope and model assumptions, it represents an important step in applying complex systems techniques to plankton ecology. Extensions could include incorporating broader biological data and environmental variables into network construction and analysis.

Overall, the present paper demonstrates the utility of network science for investigating plankton community robustness, and is relevant for conservation and sustainable resource management. Quantifying fragilities in this vital biome can help to guide wise interventions for better maintenance of marine ecosystem health.

Author Contributions: Conceptualization, D.Z.; Data curation, T.Z.; Formal analysis, T.C. and Q.H.; Investigation, D.H.; Methodology, D.Z. and T.Z.; Resources, T.C., Q.H. and D.H.; Software, T.Z.; Validation, T.C.; Writing—original draft, D.Z., T.C. and Q.H.; Writing—review and editing, D.Z., T.Z., T.C., Q.H. and D.H. All authors have read and agreed to the published version of the manuscript.

Funding: This research was funded by the National Key Research and Development Project of China (No. 2021YFC3101602) and the Young Scientists Fund of the National Natural Science Foundation of China (No. 42106190).

Institutional Review Board Statement: Not applicable.

Informed Consent Statement: Not applicable.

Data Availability Statement: Existing datasets are available in a publicly accessible repository. Publicly available datasets were analyzed in this study. Data were sourced from Australia's Integrated Marine Observing System (IMOS). IMOS is enabled by the National Collaborative Research Infrastructure strategy (NCRIS) operated by a consortium of institutions as an unincorporated joint venture, with the University of Tasmania as Lead Agent. These data can be found at: https://portal.aodn.org.au/search (accessed on 26 July 2023).

Conflicts of Interest: The authors declare no conflict of interest.

References

1. Paerl, H.W. *Marine Plankton*; Springer: Dordrecht, The Netherlands, 2012; pp. 127–153. [CrossRef]
2. Brierley, A.S. Plankton. *Curr. Biol.* **2017**, *27*, R478–R483. [CrossRef]
3. Araujo, G.S.; Pacheco, D.; Cotas, J.; da Silva, J.W.A.; Saboya, J.; Moreira, R.T.; Pereira, L. *Plankton: Environmental and Economic Importance for a Sustainable Future*; IntechOpen: London, UK, 2022.
4. Falkowski, P. Ocean Science: The power of plankton. *Nature* **2012**, *483*, S17–S20. [CrossRef] [PubMed]
5. Pierella Karlusich, J.J.; Ibarbalz, F.M.; Bowler, C. Phytoplankton in the Tara Ocean. *Ann. Rev. Mar. Sci.* **2020**, *12*, 233–265. [CrossRef] [PubMed]
6. Gökçe, A.; Yazar, S.; Sekerci, Y. Stability of spatial patterns in a diffusive oxygen–plankton model with time lag effect. *Math. Comput. Simul.* **2022**, *194*, 109–123. [CrossRef]
7. Vallina, S.M.; Cermeno, P.; Dutkiewicz, S.; Loreau, M.; Montoya, J.M. Phytoplankton functional diversity increases ecosystem productivity and stability. *Ecol. Model.* **2017**, *361*, 184–196. [CrossRef]
8. Thakur, N.K.; Ojha, A.; Tiwari, P.K.; Upadhyay, R.K. An investigation of delay induced stability transition in nutrient-plankton systems. *Chaos Solitons Fractals* **2021**, *142*, 110474. [CrossRef]
9. Morozov, A.; Arashkevich, E.; Nikishina, A.; Solovyev, K. Nutrient-rich plankton communities stabilized via predator—Prey interactions: Revisiting the role of vertical heterogeneity. *Math. Med. Biol.* **2011**, *28*, 185–215. [CrossRef]
10. Albert, R.; Barabási, A.L. Statistical mechanics of complex networks. *Rev. Mod. Phys.* **2002**, *74*, 47. [CrossRef]
11. Albert, R.; Jeong, H.; Barabási, A.L. Error and attack tolerance of complex networks. *Nature* **2000**, *406*, 378–382. [CrossRef]
12. Ellens, W.; Kooij, R.E. Graph measures and network robustness. *arXiv* **2013**, arXiv:1311.5064.
13. Bascompte, J. Disentangling the web of life. *Science* **2009**, *325*, 416–419. [CrossRef]
14. Dunne, J.; Williams, R.; Martinez, N. Network structure and biodiversity loss in food webs: Robustness increases with connectance. *Ecol. Lett.* **2002**, *5*, 558–567. [CrossRef]

15. Faust, K.; Raes, J. Microbial interactions: From networks to models. *Nat. Rev. Microbiol.* **2012**, *10*, 538–550. [CrossRef] [PubMed]
16. Tylianakis, J.; Laliberte, E.; Nielsen, A.; Bascompte, J. Conservation of species interaction networks. *Biol. Conserv.* **2010**, *143*, 2270–2279. [CrossRef]
17. Whitacre, J.M. Biological robustness: Paradigms, mechanisms, and systems principles. *Front. Genet.* **2012**, *3*, 67. [CrossRef]
18. Kitano, H. Biological robustness. *Nat. Rev. Genet.* **2004**, *5*, 826–837. [CrossRef]
19. Parrend, P.; Collet, P. A Review on Complex System Engineering. *J. Syst. Sci. Complex.* **2020**, *33*, 1755–1784. [CrossRef]
20. Wang, H.; Huang, J.; Xu, X.; Xiao, Y. Damage attack on complex networks. *Phys. A* **2014**, *408*, 134–148. [CrossRef]
21. Shang, Y. Subgraph robustness of complex networks under attacks. *IEEE Trans. Syst., Man. Cybern. Syst.* **2017**, *49*, 821–832. [CrossRef]
22. Zhou, M.; Liu, J. A memetic algorithm for enhancing the robustness of scale-free networks against malicious attacks. *Phys. A* **2014**, *410*, 131–143. [CrossRef]
23. Béthoux, J.P.; Morin, P.; Ruiz-Pino, D.P. Temporal trends in nutrient ratios: Chemical evidence of Mediterranean ecosystem changes driven by human activity. *Deep. Sea Res. Part II Top. Stud. Oceanogr.* **2002**, *49*, 2007–2016. [CrossRef]
24. Jiang, Z.; Huang, Y.; Xu, X.; Liao, Y.; Shou, L.; Liu, J.; Chen, Q.; Zeng, J. Advance in the toxic effects of petroleum water accommodated fraction on marine plankton. *Acta Ecol. Sin.* **2010**, *30*, 8–15. [CrossRef]
25. Crucitti, P.; Latora, V.; Marchiori, M.; Rapisarda, A. Error and attack tolerance of evolving networks with local preferential attachment. *Phys. A Stat. Mech. Its Appl.* **2004**, *340*, 388–394. [CrossRef]
26. Borgatti, S.P. Centrality and network flow. *Soc. Netw.* **2005**, *27*, 55–71. [CrossRef]
27. Jackson, J.M.; Lenz, P.H. Predator-prey interactions in the plankton: Larval fish feeding on evasive copepods. *Sci. Rep.* **2016**, *6*, 33585. [CrossRef]
28. Francis, T.B.; Wolkovich, E.M.; Scheuerell, M.D.; Katz, S.L.; Holmes, E.E.; Hampton, S.E. Shifting regimes and changing interactions in the Lake Washington, USA, plankton community from 1962–1994. *PLoS ONE* **2014**, *9*, e110363. [CrossRef]
29. Lewis, D.; Bala, S. Plankton predation rates in turbulence: A study of the limitations imposed on a predator with a non-spherical field of sensory perception. *J. Theor. Biol.* **2006**, *242*, 44–61. [CrossRef]
30. Frank, H.; Frisch, I. Analysis and design of survivable networks. *IEEE Trans. Commun. Technol.* **1970**, *18*, 501–519. [CrossRef]
31. Boesch, F.; Frisch, I. On the Smallest Disconnecting Set in a Graph. *IEEE Trans. Circuit Theory* **1968**, *15*, 286–288. [CrossRef]
32. Gazit, H. An optimal randomized parallel algorithm for finding connected components in a graph. *SIAM J. Comput.* **1991**, *20*, 1046–1067. [CrossRef]
33. Zhang, J.l.; Fu, Y.j.; Cheng, L.; Yang, Y.y. Identifying multiple influential spreaders based on maximum connected component decomposition method. *Phys. A* **2021**, *571*, 125791. [CrossRef]
34. Latora, V.; Marchiori, M. Efficient behavior of small-world networks. *Phys. Rev. Lett.* **2001**, *87*, 198701. [CrossRef] [PubMed]
35. Tran, V.H.; Cheong, S.A.; Bui, N.D. Complex Network Analysis of the Robustness of the Hanoi, Vietnam Bus Network. *J. Syst. Sci. Complex.* **2019**, *32*, 1251–1263. [CrossRef]
36. Cropp, R.; Norbury, J. Parameterizing plankton functional type models: Insights from a dynamical systems perspective. *J. Plankton Res.* **2009**, *31*, 939–963. [CrossRef]

Disclaimer/Publisher's Note: The statements, opinions and data contained in all publications are solely those of the individual author(s) and contributor(s) and not of MDPI and/or the editor(s). MDPI and/or the editor(s) disclaim responsibility for any injury to people or property resulting from any ideas, methods, instructions or products referred to in the content.

energies

MDPI

Article

Life Cycle Assessment of Four Floating Wind Farms around Scotland Using a Site-Specific Operation and Maintenance Model with SOVs

Iain A. Struthers [1,*], Nadezda Avanessova [2], Anthony Gray [3], Miriam Noonan [3], R. Camilla Thomson [1] and Gareth P. Harrison [1]

[1] School of Engineering, University of Edinburgh, Edinburgh EH9 3FB, UK
[2] Industrial CDT in Offshore Renewable Energy (IDCORE), University of Strathclyde, Glasgow G1 1XQ, UK
[3] Research and Disruptive Innovation, ORE Catapult, Glasgow G1 1RD, UK
* Correspondence: iain.struthers@ed.ac.uk

Abstract: This paper presents a life cycle assessment (LCA) of the International Energy Agency (IEA) 15 MW Reference Wind Turbine (RWT), on floating platforms, deployed in commercial-scale arrays at multiple locations around Scotland in the ScotWind leasing round. Site-specific energy production and vessel operations are provided by a dedicated offshore wind farm operations and maintenance (O&M) model, COMPASS, allowing service operation vessel (SOV) O&M impacts to be assessed with increased confidence. For climate change, the median global warming impact varied from 17.4 to 26.3 gCO_2eq/kWh across the four sites within a 95% confidence interval using an uncertainty assessment of both foreground and background data. As is common with other offshore renewable energy systems, materials and manufacture account for 71% to 79% of global warming impact, while O&M comprise between 9% and 16% of the global warming impacts. High-voltage direct current (HVDC) export cables, floating platforms, and composite blades are significant contributors to the environmental impacts of these arrays (by mass and material choice), while the contributions from ballast, vessel transportation emissions, and power-train components are lower. The results suggest that material efficiencies, circularity, and decarbonizing material supply inventories should be a priority for the Scottish floating wind sector, followed by minimizing vessel operations and the decarbonization of vessel propulsion, while avoiding burden shifting to other impact categories.

Keywords: floating wind; life cycle assessment; operation and maintenance; offshore wind; environmental impact

Citation: Struthers, I.A.; Avanessova, N.; Gray, A.; Noonan, M.; Thomson, R.C.; Harrison, G.P. Life Cycle Assessment of Four Floating Wind Farms around Scotland Using a Site-Specific Operation and Maintenance Model with SOVs. *Energies* **2023**, *16*, 7739. https://doi.org/10.3390/en16237739

Academic Editors: Dibyendu Sarkar, Rupali Datta, Prafulla Kumar Sahoo and Mohammad Mahmudur Rahman

Received: 29 September 2023
Revised: 10 November 2023
Accepted: 16 November 2023
Published: 23 November 2023



Copyright: © 2023 by the authors. Licensee MDPI, Basel, Switzerland. This article is an open access article distributed under the terms and conditions of the Creative Commons Attribution (CC BY) license (https://creativecommons.org/licenses/by/4.0/).

1. Introduction

Electricity generation from floating offshore wind (FOW) turbines has a significant global potential [1] and is expected to make a major contribution to the electricity sector from around 2030 [2]. However, bottom-fixed offshore wind (BFOW) technologies currently make up 99.7% of all offshore wind installed capacity: in 2022, the global installed capacity of offshore wind was 64.3 GW, of which only 188 MW was floating [3].

In 2022, the UK was the second largest operator of offshore wind globally, with nearly a quarter of all operating capacity, after China with 46%. The UK offshore wind installed capacity of 13.7 GW delivered 45 TWh, or around 14% of all UK electricity generation in 2022 [4]. Of this, only 78 MW, or 0.6%, of the UK's total offshore wind capacity is floating. While nascent, this is around 41% of all floating wind generation globally, making the UK the single largest operator of floating wind in 2022 [3].

All of these installed capacities are expected to grow significantly to achieve the UK's climate targets: in 2022, the UK government stated its ambition to deploy up to 50 GW of offshore wind by 2030 [5]. For the UK, FOW is expected to be located primarily in the Celtic Sea and Scottish waters, at around 4.5 GW [6] and 7 GW, respectively. The ScotWind seabed

leasing round is expected to achieve 10 GW of offshore wind around 2030, of which more than 70% (7 GW) may use FOW technologies [7], subject to ongoing commercial development.

In the UK, the Committee on Climate Change has identified that FOW could cut costs and improve the diversity of the UK's energy mix by 2050, and so play a greater role in the power sector decarbonization [8]. FOW can be constructed in water depths that are cost-prohibitive for BFOW, increasing the spatial distribution of wind generation across the grid, and potentially reducing the variability of aggregate wind power generation. Furthermore, additional wind power is likely to further reduce the carbon intensity of power generation operating on the British grid [9], which stood at 182 gCO_2/kWh in 2022 [10]. However, to avoid unintended burden shifting from climate change to other environmental impacts, the significant expansion of FOW installed capacity should merit a proportional interest in not just the operational emissions impacts, but the wider life cycle environmental impacts of these emerging technologies.

1.1. Methodology of Life Cycle Assessment

The environmental impacts of products and systems, including floating wind farms, can be quantified using life cycle assessment (LCA). LCA is a scientific method to address the use of resources, and the environmental consequences of releases, throughout a product's life cycle—from raw material acquisition through production, use, end-of-life treatment, recycling, and final disposal [11].

Life cycle assessment is a relatively young discipline with its beginnings around 1970 in the United States [12]. Subsequent efforts emerged across Europe, undergoing a surge in interest in the late 1980s, codification in the early 1990s, and international standardization of the scientific method in the late 1990s [13]. Today, the methodology and applications continue to innovate and mature, with increasing numbers of publications annually in the last two decades [14]. Accordingly, LCA is now widely recognized and increasingly applied in diverse fields including industry, academia, and policy development [15].

The basic process of an LCA is to collate a material and process inventory of the product life cycle; represent the inventory using data selected from an appropriate environmental impact database; aggregate the flows of material and energy to and from the environment manually or automatically; and report the environmental impacts using pre-defined life cycle impact assessment (LCIA) algorithms ("Methods"). Specifically, however, the basic structure of a life cycle assessment according to internationally standardized LCA principles and framework (ISO 14040), and general requirements and guidelines (ISO 14044) [11,16], comprises four phases [13]:

1. Goal and scope definition: The goal definition is the first phase of an LCA study, which sets out the context of the LCA study and determines the purpose of the study in detail. The scope determines the specific technical terms, limits, and characteristics of the analysis to be executed.
2. Inventory analysis: In the second phase of an LCA study, a system model is constructed according to the requirements of the goal and scope definition [17]. This is the central phase of an LCA, the core activity of which is the development and collation of data on the physical (material and energy) flows which make up the life cycle model of the system in question [13]. An assessment of uncertainty can be initiated in this phase [13] and the output is the system Life Cycle Inventory (LCI) which is often cached within specialized LCA software using dedicated LCI databases, which contain the "building blocks" of the life cycle model that the LCA practitioner can draw upon.
3. Impact assessment: This phase transforms the LCI data of physical flows and inventories of the product system into environmental impacts via impact models and pathways (LCIA "Methods"), developed by environmental science [13]. The selected impact categories are defined in the study scope, which classifies and assigns a characterization factor to each physical flow, enabling aggregation of all contributing harms from diverse chemical species into a single score for a given impact category.

4. Interpretation: In the final phase, the LCA practitioner interprets the results of the assessment in accordance with the goal and scope. Often, an iterative approach is required to judge the appropriate robustness of the conclusions, and may include uncertainty or sensitivity assessments [17] to fully evaluate the findings.

Developing a life cycle model of an artefact as large and complicated as a floating wind farm requires a sound understanding of the manufacturing, installation, maintenance, decommissioning, and disposal processes, as well as a significant application of effort to obtain representative inventory data. This is particularly challenging for future technologies, where engineering judgement must be applied throughout the assessment, to determine the modelled level of detail and appropriateness of available data. This challenge can be mitigated by the appropriate use of uncertainty assessment and sensitivity studies as set out in the international standards [11,16].

1.2. Life Cycle Assessments of Floating Wind Technologies

The number of LCA studies for floating wind is not large. A literature review published in 2018 [18] collated 148 wind energy LCA studies, of which 32 were for offshore wind farms, and only 2 for floating wind—perhaps reflecting the relative maturity of these technologies. The authors of this study have identified ten floating wind LCA studies of interest [19–28] (Table 1). In general terms, life cycle models have tended to increase incrementally in representation and sophistication, particularly around different configurations of farm and floating substructure. The rated power of the turbines assessed is also increasing (broadly), as is the popularity of semi-submersible substructure designs, somewhat mirroring real-world technological trends. A key area of opportunity, however, remains around the representation of operation and maintenance, which has tended to be (understandably) represented by simple assumptions from the literature, apart from a recent exception [25].

Transparently condensing and communicating the high level of detail, assumptions, and references required to generate a life cycle model inventory is not trivial, and this can be further exacerbated by the proprietary nature (or technology readiness) of the turbine, cable, substation, and substructure technologies themselves, to say nothing of the commercially sensitive maintenance burdens. Accordingly, it can occasionally be difficult to fully interrogate the assumptions behind some of the literature. This, along with the differences in each practitioner's style, model granularity, and the choice of life cycle impact assessment method, combine to make inter-study comparison difficult and potentially misleading. To combat this, considering multiple arrays within a single study can be insightful.

The studies identified here focus on a mix of hypothetical, planned, pre-constructed, and constructed sites, with array sizes ranging from a single turbine to 190 turbines, mostly in Europe and North America, with a single instance in China. A variety of floating substructure (platform) designs are considered, covering a range of water depths from 60 to 450 m in near-shore and distant offshore sites (3 to 230 km). For large arrays where substations are necessary, they are included, with examples of both floating and bottom-fixed jacket substructures. Where present, nearly all substation types utilize high-voltage alternating current (HVAC) designs, with only one example of a high-voltage direct current HVDC [28]. The capacity factor varies significantly from 23 to 54% across the studies, and this is the predominant method of energy calculation, with [24,25,28] augmenting this process using site-specific metocean data and, only in one example [25], linking this to a dedicated operations and maintenance (O&M) model to determine turbine availability. This is problematic given the inherently high sensitivity of the results to the functional unit of lifetime energy production, kWh [24], where assuming array availability and vessel impacts without a robust O&M model could lead to incomplete results.

Table 1. Selected characteristics of floating wind farm LCA. * The Supporting Information in the study by Tsai references a floating foundation in [19] which is a Sway design. Abbreviations: tension leg buoy (TLB); semi-submersible (Semi-sub); tension leg platform (TLP); megavolt-amp (MVA); high-voltage alternating current (HVAC); high-voltage direct current (HVDC); service operation vessel (SOV); cumulative energy demand (CED); global warming potential (GWP).

	Weinzettal (2009) [19]	**Raadal (2014) [20]**	**Tsai (2016) [21]**	**Elginoz (2017) [22]**	**Bang (2019) [23]**	**Poujol (2020) [24]**	**Yildiz (2021) [26]**	**Garcia-Teruel (2022) [25]**	**Yuan (2023) [27]**	**Brussa (2023) [28]**
Publication type	Journal paper	Journal paper	Journal paper	Journal paper	Master's Thesis	Journal paper	Journal paper	Journal paper	Journal paper	Journal paper
Turbine rated power (MW)	5	5	3	5	8	6	2	6; 9.5	6.7	15
No. turbines	40	100	100	77	75	4	1	5; 5	100	190
Array scale (MW)	200	500	300	385 (wind), 265.5 (wave)	600	24	Single turbine	30; 47.5	670	2800
Substructure design	Sway	Spar; TLB; Sway; Semi-sub; TLP	Sway *	Multi-use offshore platform (integrated wave power)	Spar	Semi-sub	Barge-type	Spar; Semi-sub	Semi-sub (Wind Float, Gen 3)	Semi-sub
Location	Dogger Bank area, England	Not stated	Great Lakes, US	Cantabria, Spain	California, US	Leucate, France	FLOATGEN, France	Hywind; Kincardine, Scotland	China	West of Sicily, Italy
Water depth (m)	Concept suitable for 100–300 (not stated)	200	60–140	Not stated (est. 100)	450	Not stated	Not stated	95–129; 60–80	60–80	200
Distance to shore (km)	50	200	5–30	3–13	35	16	Not stated	25; 15	12–20	230
Design life (years)	20	20	20	25	25	20	20	25	25	30
Site status	Hypothetical	Hypothetical	Hypothetical	Hypothetical	Hypothetical	Pre-construction	Constructed	Constructed	Hypothetical	Pre-construction
Energy calculation	Capacity Factor	Capacity Factor	Site-specific	Capacity Factor	Capacity Factor	Site-specific	Capacity Factor	Site-specific, O&M model	Capacity Factor	Site-specific
Capacity factor (%)	53	46	28–35	23 (wind)	50	34	Not stated	50.2 (tow), 49.4; 40.5 (tow), 39.7	53.8	34.35
Array voltage (kV)	Not stated	30–36	33	33	Not stated	Not stated	Not stated	33	33	66
Export voltage (kV)	170	145	132	132	Not stated	Not stated	Not stated	33	132 (HVDC)	500 (HVDC)

Table 1. *Cont.*

	Weinzettal (2009) [19]	Raadal (2014) [20]	Tsai (2016) [21]	Elginoz (2017) [22]	Bang (2019) [23]	Poujol (2020) [24]	Yildiz (2021) [26]	Garcia-Teruel (2022) [25]	Yuan (2023) [27]	Brussa (2023) [28]
Substation (substructure)	250 MVA (Floating)	500 MVA (Not stated)	Yes (Floating)	Yes (Jacket)	1000 MVA (Floating)	No	No	No	Yes (Jacket)	Yes (Floating)
Reference flow	Up to the end of the subsea export cable	Up to the end of the subsea export cable	Up to the end of the subsea export cable	Up to the end of the subsea export cable	Up to the end of the subsea export cable	Up to the end of the subsea export cable	Floating unit only: no export cable	Up to the end of the subsea export cable	Up to the end of the subsea export cable	Includes onshore HVDC cable
Life cycle stages	Materials, manufacturing, transport, O&M, dismantling, end-of-life credits	Production of raw materials, transport, installation, decommissioning, disposal	Manufacturing and assembly, installation, O&M, and decommissioning	Manufacturing and processing, transportation, installation; O&M; end-of-life	Manufacturing, transportation, installation, operation, decommissioning, and end-of-life treatment (credits)	Materials, manufacture, transport, offshore installation, grid connection, maintenance, end-of-life	Manufacture, transportation, erection, O&M, disposal, and recycling	Materials, manufacturing, installation (including transport), O&M, decommissioning, disposal	Components manufacturing and transport, wind farm construction, O&M, decommissioning, disposal	Raw materials supply, manufacturing and transport of components, assembly and offshore installation, O&M, dismantling, end-of-life including transportation
Manufacturing processes	Yes	No	Yes (excludes capital goods)	Yes	No	Yes	No	Yes	No	No
Component transportation and installation	Trucks, vessels	Vessels only	Trucks, vessels	Trucks, vessels	Trucks, vessels	Trucks, vessels	Trucks, vessels	Trucks, multiple vessel types	Lorry, barge	Lorry, ship, vessels
Vessel representation	t.km process (barge)	Fuel consumption	Fuel consumption data for shipping	t.km process (barge)	t.km process (transoceanic shipping)	Diesel (market for)	t.km process (not stated)	t.km process (ferry), scaled to vessel fuel consumption	t.km/direct fuel use	t.km/fuel consumption
Maintenance vehicles	Helicopter, towing boat	Not stated	Vessel, jack-up, crane	Barge, helicopter	Small boat, helicopter, specialized vessel, crane vessel	Not stated	Multiple vessel types	Multiple vessel types, road vehicles	Not stated	Excluded

Table 1. *Cont.*

	Weinzettal (2009) [19]	Raadal (2014) [20]	Tsai (2016) [21]	Elginoz (2017) [22]	Bang (2019) [23]	Poujol (2020) [24]	Yildiz (2021) [26]	Garcia-Teruel (2022) [25]	Yuan (2023) [27]	Brussa (2023) [28]
Maintenance frequency	Assumed	Assumed	Assumed	Assumed	Assumed	Assumed	Assumed	Modelled	Assumed	Excluded
LCA software	SimaPro 7.1	SimaPro (version not stated)	SimaPro 7.3.2	GaBi	No (Excel)	SimaPro 8.4	Gemis 5	SimaPro 9.1	eFootprint	SimaPro 9.3
LCI database	ecoinvent v1.3	ecoinvent (version not stated)	ecoinvent v2.0	GaBi	ecoinvent v3	ecoinvent v3.3	Europa	ecoinvent v3.6	Chinese core life cycle database (CLCD)/ecoinvent v3.5	ecoinvent v3.7.1
LCIA method/Impact category	CML 2 baseline 2000 V2.03	CED	TRACI; CED	CML 2001	GWP	ILCD 2011, AWARE, ReCiPe 2016 Midpoint (H), CED	GWP, AP, ADPF, EPT	ReCiPe Midpoint (H) 2016; CED	CML 2002	EPD; CED
Uncertainty assessment	No	No	No	No	Monte Carlo (input data)	Background	No	Background	Foreground and background	No
GWP (gCO2eq/kWh)	11.5	25.3; 18.0; 20.9; 31.4; 19.2; 18.9	38.1; 32.9; 33.0; 33.8; 35.5; 33.1; 33.9; 35.5	18.1	22.3	15.4	18.6	32.4–45.2 (tow), 30.2–32.7; 27.7–39.4 (tow), 25.6–27.6	25.8 (tow)	31.3

The life cycle inventories also differ significantly. Component transportation (trucks and vessels) and manufacturing processes (for example, sandblasting, welding, and paint application) are variously present and modelled in different ways and levels of detail. The maintenance life cycle stage also varies significantly. Vessels (and helicopters) are represented by different processes, for example, per ton-kilometre (t.km) transportation of various vessel types, direct fuel consumption, or scaling existing transportation processes to represent appropriate vessels. The actual maintenance burden itself is typically modelled by assumptions from the literature or, most recently, utilizing dedicated O&M models.

1.3. Research Opportunities

There are several research opportunities for floating wind LCA, specifically: modelling turbines with rated power greater than 10 MW, with HVAC and HVDC architecture in arrays far from the grid connection; using site-specific wind resource data to assess annual energy production; incorporating dedicated O&M model outputs; including an assessment of uncertainty for foreground and background data; and modelling real-world, planned sites that are of interest to policymakers.

This study was completed in response to these opportunities, as an LCA of a 15 MW reference wind turbine, developed by the National Renewable Energy Laboratory (NREL) and the International Energy Agency (IEA). Here, these turbines have been considered as forming four very large floating wind farms, located in the ScotWind leasing round, using a mix of HVAC and HVDC transmission systems, using data from a dedicated O&M model, COMPASS [29]. The O&M modelling and other foreground data have been prepared with expert input from the Offshore Renewable Energy (ORE) Catapult in Glasgow, Scotland.

2. Materials and Methods

This section describes the methodology of the LCA procedure followed in this study, with complete details provided in the Supplementary Materials. This study uses an attributional, process-based LCA, employing SimaPro 9.1 software, with background data sourced from the ecoinvent database v3.6 [30]. As introduced in Section 1.1, the LCA procedure used in this study was aligned with internationally standardized LCA principles and framework (ISO 14040), and general requirements and guidelines (ISO 14044) [11,16], comprising goal and scope definition, inventory analysis, impact assessment, and interpretation.

2.1. Goal and Scope

The goals of this study were to (i) address the opportunities identified in the literature review and (ii) quantify the environmental impacts of multiple, real-world representative floating wind farms using site-specific metocean data, very large turbines, HVAC and HVDC architecture, and dedicated O&M modelling, including an assessment of foreground and background data uncertainty. The outputs of the study are intended for researchers, project developers, and policymakers.

The scope of the study is a cradle-to-grave, attributional LCA of the 15 MW reference wind turbine and platform from IEA and the University of Maine (Figure 1) in four representative sites from the ScotWind leasing round: East 3, North East 1, North East 7 and North 3 (E3, NE1, NE7, and N3). These sites were selected for their range of relevant characteristics: electrical export system design; distance to grid connection point; distance to operating ports; water depth; number of turbines; and metocean conditions. Note that these sites represent general wind farm designs only, not the specific, commercial designs under development [31]. Five life cycle stages were defined: materials and manufacturing (M&M); transport and installation (T&I); operation and maintenance (O&M); decommissioning and removal (D&R); and landfill and recycling (L&R).

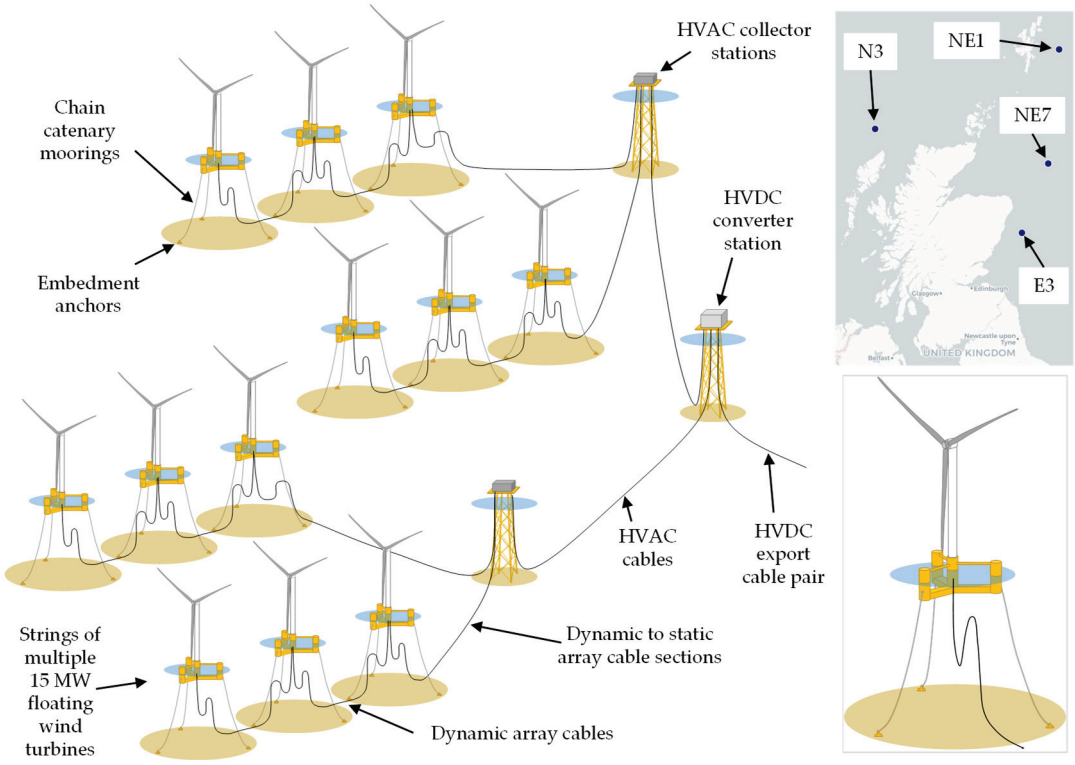


Figure 1. Overview of components included within the floating wind farms' reference flows; map of sites considered and general arrangement of the 15 MW reference wind turbine with platform. Diagrams adapted from [32,33], map adapted from [34]. Sites are labelled North 3, North East 1, North East 7 and East 3 (N3, NE1, NE7 and E3).

2.1.1. System Boundary

Figure 2 shows a schematic of the cradle-to-grave life cycle model. The system boundary was set as the landward end of the offshore transmission system, creating the reference flow of a single, complete floating wind farm: all floating wind turbine units, array cables, HVAC collector stations, and HVDC converter stations, through its raw material acquisition, production, installation, design life, decommissioning, and recycling. Onshore works were not considered, nor were spare parts, detailed manufacturing processes, or minor components. Throughout, the cut-off criteria were based on the availability of representative data and acceptable granularity.

2.1.2. Allocation Approach

Allocation by the 'Recycled Content' or 'Cut-off by classification' system model was used, as recommended in the European Product Environmental Footprint guideline [13], where the recycling of waste material is outside the system boundary. Thus, recycling impacts are only included for input materials; no credits are applied to the environmental impacts.

2.1.3. Functional Unit

The functional unit for this study was selected as a kilowatt hour (kWh) of electricity supplied to the grid. The energy production was determined using site-specific wind data and the array availability computed by COMPASS.

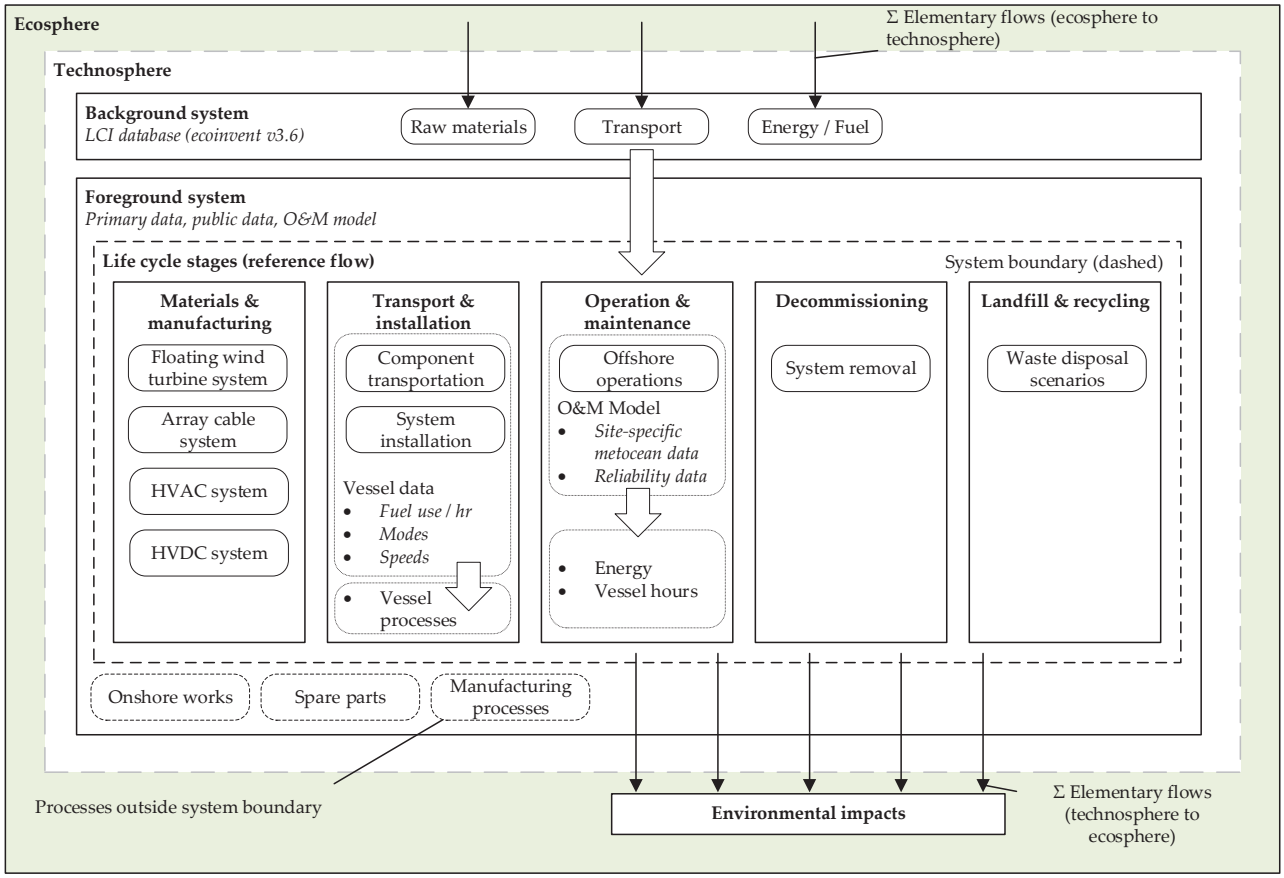


Figure 2. Schematic of the life cycle model, system boundary, life cycle stages, inventory assemblies, and processes, and the relationship with the COMPASS O&M model. White arrows indicate flows of data within the model, black arrows indicate elementary flows in the LCI.

2.2. Inventory Analysis

2.2.1. Site Parameters

Parameters were developed to represent the four floating wind farms using expert input and in-house models from ORE Catapult and publicly available data. E3 is the shallowest site, with a 40 km export route, and with the lowest installed capacity, using an HVAC export system. NE1 is located 48 km east of Lerwick, in deep water, east of Shetland, with a HVDC system. NE7 is defined as 3 GW in 110 m with an HVDC system. N3 is the largest site considered (3.3 GW) and in the deepest water, with an HVDC system. However, these data is are aggregated from a number of sources and do not precisely represent the commercial project awards announced in January 2022 [31]. Further, the scale of port activities assumed at certain locations (for example, Methil) would require development of the existing infrastructure. Full inventory data and assumptions for each site are provided in the Supplementary Materials.

2.2.2. Systematic Breakdown Structure

Each floating wind farm reference flow was divided into four primary systems: the floating wind turbine unit (turbine, floating platform, and moorings); the array cable system (all dynamic and static sections); the HVAC collector station system and HVDC converter station system (both comprising a station topside, jacket substructure, pile foundations, and transmission cables, albeit with different bodily properties).

2.2.3. Vessel Representation

The transportation, installation, and decommissioning of each system, subsystem, assembly, or component by vessel were modelled explicitly in each life cycle stage, where required. Hours of vessel use were modelled in SimaPro using simple, parameterized equations which included vessel type, speed, operating mode, and site/port locations. The ecoinvent database does not contain processes representing the fleet required throughout the floating wind farm life cycle so an appropriate process within ecoinvent was modified to emulate representative vessels. Representative vessel types were informed by input from ORE Catapult and the COMPASS O&M model. By obtaining fuel consumption data for each vessel mode, the process 'Diesel, burned in fishing vessel GLO—diesel, burned in fishing vessel—Cut-off, U' (MJ) was scaled by inspection of diesel density (kg/m^3), specific energy (kg/MJ), and volumetric fuel consumption (l/hr), converting the process to represent hours of vessel operation. In this way, the study included anchor handling tug supply (AHTS) vessels, tugs, high-speed heavy cargo vessels (HSHCVs), semi-submersible heavy cargo vessels (SSHCVs), crane vessels, cable lay vessels (CLVs), offshore subsea construction vessels (OSCVs), and service operation vessels (SOVs).

2.2.4. Materials and Manufacture (M&M)

The inventory for the floating wind turbine unit (FWTU) was taken from primary data [32,35], with mooring length calculations performed by engineers at ORE Catapult. The reference wind turbine is a Class IB direct-drive machine, with a rotor diameter of 240 m and a hub height of 150 m. The blade composition, array cable lengths, cable compositions, and HVAC collector station and HVDC converter station properties were similarly provided by ORE Catapult data and modelling. Electrical equipment was represented where appropriate using Environmental Product Declarations. Allowances for material transport and energy use are provided by the unit processes in ecoinvent, in accordance with the study scope and in line with the approach in [20,26–28].

2.2.5. Transport and Installation (T&I)

The hours of vessel use for the transportation of major components were modelled directly in SimaPro using simple, parameterized equations to represent the site-specific distances travelled during transport and installation. The distances travelled by each vessel were developed using historical floating wind projects as examples, current and future supply chains, local content, and site capabilities. For every journey, an appropriate vessel was selected, using the scaled vessel processes created for this study.

2.2.6. Operation and Maintenance (O&M)

O&M has been identified as an important life cycle stage affecting the environmental impacts of floating wind farms [25]. Each site was modelled using the COMPASS O&M model to determine hours of SOV use, and overall array annual energy production (AEP), based on site-specific wind resource and weather windows. In addition, the industrial literature was reviewed to input other array-scale vessel interventions: 0.0205 maintenance interventions per turbine per year by crane vessel (1.4 days for 'Vessel for replacement of large parts (jack up) (O&M)' and 0.2 days for 'Jack-up for replacement of heavy components (O&M)' for 78 turbines; (1.4 + 0.2)/78 = 0.0205 days, where each day is 24 h) [36] and cable servicing at 1 km per hour, every 2 years using an OSCV [23].

2.2.7. Decommissioning and Removal (D&R)

Decommissioning and removal were modelled as the reverse of installation but with the transportation of the disassembled subsystems removed on the basis of the high uncertainty around disposal location. Cable laying and pile removal operations were omitted to represent cable abandonment and pile cutting at the end of life.

2.2.8. Landfill and Recycling (L&R)

A recycling rate of 90% was assumed for steel [21,25,37], copper, and plastic [38]. Any waste streams remaining after separation were variously recycled, incinerated, or sent to landfill as per the ecoinvent process 'Waste (waste scenario) {ENG} | treatment of waste | Cut-off, U'.

2.3. Data Quality

To enable the goal and scope of the LCA to be met, data quality was addressed in accordance with international standards [11]. Data quality was addressed as follows:

1. Time-related coverage: assessed in Supplementary Materials under additional uncertainty data quality indicators.
2. Geographical coverage: as above.
3. Technology coverage: as above.
4. Precision: Data sourced directly from the reference wind turbine and platform definition literature are assumed to be precise, although the turbine is by definition a generic design, and thus not completely representative of a real-world, commercially designed machine. ORE Catapult data are assumed to be similarly precise.
5. Completeness: the authors assess that the primary, public and industrial partner data result in an acceptably complete representation of the sites of interest.
6. Representativeness: qualitatively assessed by the authors that the data do reflect the true population of interest.
7. Consistency: qualitatively assessed by the authors that the study methodology is applied uniformly to the various components of the analysis.
8. Reproducibility: qualitatively assessed by the authors that the data presented in the Supplementary Materials would allow an independent practitioner to reproduce the result reported in this study.
9. Sources of the data: provided in the Supplementary Materials.
10. Uncertainty of the information: assessed for foreground and background systems [39].

All input data, assumptions, and uncertainty estimates developed according to the pedigree matrix method set out in the ecoinvent data quality guidelines [39] are detailed in the Supplementary Materials.

2.4. Life Cycle Impact Assessment

Two life cycle impact assessment (LCIA) methods were used: the multi-criteria ReCiPe 2016 v1.1, midpoint method, Hierarchist version with global normalization, and the single-criterion Cumulative Energy Demand (CED) v1.11. ReCiPe computes 18 impact categories, providing a detailed picture of environmental impacts. CED calculates the embodied energy of the arrays. Both were selected to broadly align with similar, recent studies [25].

2.5. Interpretation

The environmental impacts are assessed with reference to the functional unit of 1 kWh electricity produced. Median values within a 95% confidence interval are reported here using a Monte Carlo uncertainty analysis of the foreground and background data (SimaPro 9.1 default settings: 1000 step, 0.005 stop factor). The results are not compared to ecoinvent processes of other generation technologies directly due to the inevitable, inherent methodological differences. The four sites are, however, compared to each other, assuming (reasonably) that the methodological differences between sites within this work are negligible. The contributions from each life cycle stage and the sensitivity of the results to key site parameters are considered for all impact categories. The main opportunities to mitigate global warming impacts are identified and discussed. The results are discussed in relation to perspectives from the literature and contextualized by comparison to two unit processes of British electricity.

2.6. Operation and Maintenance Model: COMPASS

COMPASS is a strategic O&M simulation tool which can model the full lifetime of a wind farm and estimate key performance indicators associated with its operation [29]. The energy production used in the environmental impact calculation is taken from the availability modelling from COMPASS.

3. Results and Discussion

3.1. Default Uncertainty Results for All Four Sites

In accordance with the goal and scope of this study, the inventory analysis was developed with an assessment of basic and additional uncertainty according to [39], enabling the results to be reported as a median value within a 95% confidence interval (Table 2).

The median results show that E3 was typically the site with the lowest environmental impacts, despite having the lowest turbine AEP. The vessel travelling distances for E3, in almost every case, were the shortest of all the sites, and the site has no HVDC transmission equipment (reducing its material requirements). It also has the lowest total SOV usage time. In contrast, site N3 has the highest impact in every category, driven by its remoteness from port facilities, HVDC system, and relatively low turbine AEP. The uncertainty across the four sites is typically within an order of magnitude, but not for all categories; ionising radiation (IR) and water consumption (WC) show the largest uncertainty. WC is so uncertain as to vary from environmental harm (positive impact) to environmental benefit (negative impact), as noted in other studies [25]. The median global warming (GW) impacts and 95% confidence interval for the E3, NE1, NE7, and N3 sites were 17.4 (13.0–23.6), 20.0 (14.9–27.8), 20.5 (15.4–28.2), and 26.3 (20.2–35.4) gCO2eq/kWh, respectively.

3.2. Contributions from Life Cycle Stages, Processes, and Components

As with other studies in the literature [19–28], life cycle impacts are dominated by the materials and manufacturing life cycle stage. For the four sites considered, the materials and manufacturing account for 71% to 79% of the global warming impact (Figure 3). O&M is commonly the second most impactful across the impact categories, with L&R dominating in the freshwater and marine ecotoxicity metrics. Component-wise, the most massive typically have the highest impact, including wind turbine platforms and other massive steel components such as the nacelle housing and turbine tower. The carbon-fibre-reinforced plastic (CFRP) of the turbine blades is also prominent due to its high primary energy requirement (heat and electricity). Relative to site N3, the environmental impacts of E3 are lower due to its proximity to the grid connection point and the HVAC export system design. For N3, the very long HVDC cables (connecting the farm in the east of Shetland to the GB grid at Dounreay) dominate these selected impacts. Each impact category is driven by different processes; for example, for GW, LU, MRS, and CED the most influential are steel, copper, lead, and polyethylene. O&M is significant for a number of impact categories (OFHH, FPMF, OFTE, TA, FRS, CED, and GW). For GW, this ranges from 9% to 16% (with distant sites showing higher impacts); however, this is not as significant as in a recent study [25]. This is possibly due to the optimization of turbine availability (and hence, AEP) in COMPASS and the use of in-field SOVs for a broad range of interventions (dramatically reducing the number of vessel transit journeys to the site relative to port-based crew transfer vessels, CTVs), as well as the influence of array-scale components in this study. The contributions to global warming are examined in more detail in Section 3.4 for each site.

Table 2. ReCiPe and CED results for all four sites using default uncertainty parameters (global warming impact shown in bold).

Impact Category/Attribute	Abbreviation	E3			NE1			NE7			N3			Units
		2.5%	Median	97.5%	2.5%	Median	97.5%	2.5%	Median	97.5%	2.5%	Median	97.5%	
Global warming	GW	13.0	**17.4**	23.6	14.9	**20.0**	27.8	15.4	**20.5**	28.2	20.2	**26.3**	35.4	g CO2eq/kWh
Stratospheric ozone depletion	SOD	5.7	7.7	11.0	5.9	8.2	11.7	6.7	9.3	13.9	9.6	13.8	21.3	µg CFC11 eq/kWh
Ionizing radiation	IR	0.1	0.4	3.2	0.1	0.4	4.0	0.1	0.4	3.2	0.2	0.6	4.4	Bq Co-60 eq/kWh
Ozone formation, Human health	OFHH	0.1	0.1	0.2	0.1	0.1	0.3	0.1	0.2	0.3	0.1	0.2	0.3	g NOx eq/kWh
Fine particulate matter formation	FPMF	0.0	0.1	0.1	0.1	0.1	0.1	0.1	0.1	0.1	0.1	0.1	0.2	g PM2.5 eq/kWh
Ozone formation, Terrestrial ecosystems	OFTE	0.1	0.1	0.2	0.1	0.2	0.3	0.1	0.2	0.3	0.1	0.2	0.3	g NOx eq/kWh
Terrestrial acidification	TA	0.1	0.2	0.2	0.1	0.2	0.3	0.2	0.2	0.3	0.2	0.3	0.5	g SO2 eq/kWh
Freshwater eutrophication	FE	8.5	13.5	23.3	8.0	13.1	24.5	11.3	17.6	28.8	22.1	34.7	59.1	mg P eq/kWh
Marine eutrophication	ME	2.5	3.5	5.0	0.4	3.5	5.3	2.8	3.9	5.8	4.3	5.9	8.9	mg N eq/kWh
Terrestrial ecotoxicity	TEX	0.2	0.4	0.9	0.2	0.3	0.8	0.3	0.5	1.3	0.5	1.1	3.2	kg 1,4-DCB/kWh
Freshwater ecotoxicity	FEX	14.0	18.6	25.6	12.6	16.5	22.4	21.5	28.6	38.2	49.4	65.9	90.1	kg 1,4-DCB/kWh
Marine ecotoxicity	MEX	17.2	22.8	31.3	15.5	20.2	27.4	26.4	35.0	46.7	60.3	80.4	110.4	kg 1,4-DCB/kWh
Human carcinogenic toxicity	HCT	3.5	7.1	17.6	3.8	7.6	18.0	3.8	7.6	18.4	5.9	11.2	25.3	kg 1,4-DCB/kWh
Human non-carcinogenic toxicity	HNCT	0.1	0.1	0.2	0.1	0.1	0.2	0.1	0.2	0.2	0.2	0.3	0.5	kg 1,4-DCB/kWh
Land use	LU	2.5	3.5	5.0	2.5	3.5	5.3	2.8	3.9	5.8	4.3	5.9	8.9	cm2a crop eq/kWh
Mineral resource scarcity	MRS	0.5	0.8	1.2	0.5	0.8	1.2	0.7	1.0	1.4	1.3	1.8	2.5	kg Cu eq/kWh
Fossil resource scarcity	FRS	3.4	4.6	6.2	4.0	5.3	7.4	4.1	5.6	7.7	5.6	7.3	9.8	kg oil eq/kWh
Water consumption	WC	−29.7	0.3	22.4	−29.9	1.3	24.6	−39.3	1.9	26.5	−61.1	3.3	47.7	l/kWh
Cumulative energy demand	CED	180.9	236.9	321.7	206.4	273.1	386.6	210.1	286.1	402.6	285.9	381.9	519.6	kJ/kWh
Turbines	-		94			154			200			220		-
Turbine AEP (including availability)	-		68.7			70.8			71.5			68.9		GWh/yr
Lifetime array energy production (20 years)	-		129.2			218.1			285.8			303.3		TWh



Figure 3. The relative contribution of life cycle stages to environmental impact categories: materials and manufacturing (M&M); transport and installation (T&I); operation and maintenance (O&M); decommissioning and removal (D&R); landfill and recycling (L&R).

3.3. Sensitivity Analysis

3.3.1. Lifetime Energy Production

Due to the functional unit, the environmental impacts will always scale in inverse proportion to the lifetime energy production [24]. This applies to many common parameters of interest: availability, capacity factor, and turbine AEP, obviating the requirement to include these in a sensitivity study. Extending the design life will also have an impact, but this would not be a pure inverse relationship due to the increased annual requirement for O&M, as described below.

3.3.2. Site and Engineering Design Parameters

The life cycle impact category results were reviewed for their sensitivity to site and engineering design parameters, which can be somewhat controlled during development. Five relevant parameters were identified: blade mass, wind turbine platform mass, export cable length (HVAC or HVDC), SOV use, and design life. The sensitivity of the life cycle impacts to these parameters was quantified by scaling the parameters by 10% and reviewing the change relative to the basic results without uncertainty, assuming no other changes to the life cycle model.

Firstly, the results for all sites were consistently improved by increasing design life, reflecting other sensitivity studies of this parameter [24]. Across all impact categories, this reduction was −4.9% (OFHH) to −9.1% (multiple) (Figure 4). Life extension improves every environmental impact almost linearly, bar the additional yearly requirement for O&M. Accordingly, ozone formation metrics show the least improvements due to these

increased vessel emissions. This approach excludes additional impacts from increased structural materiality or O&M consumables necessary to maintain turbine life, which are expected to be relatively minor in most categories [25]. This aligns with typical cost reduction approaches, where extending design life aims to maximize developer return on investment, and—for this parameter—suggests synergy between project cost engineering and environmental impacts.

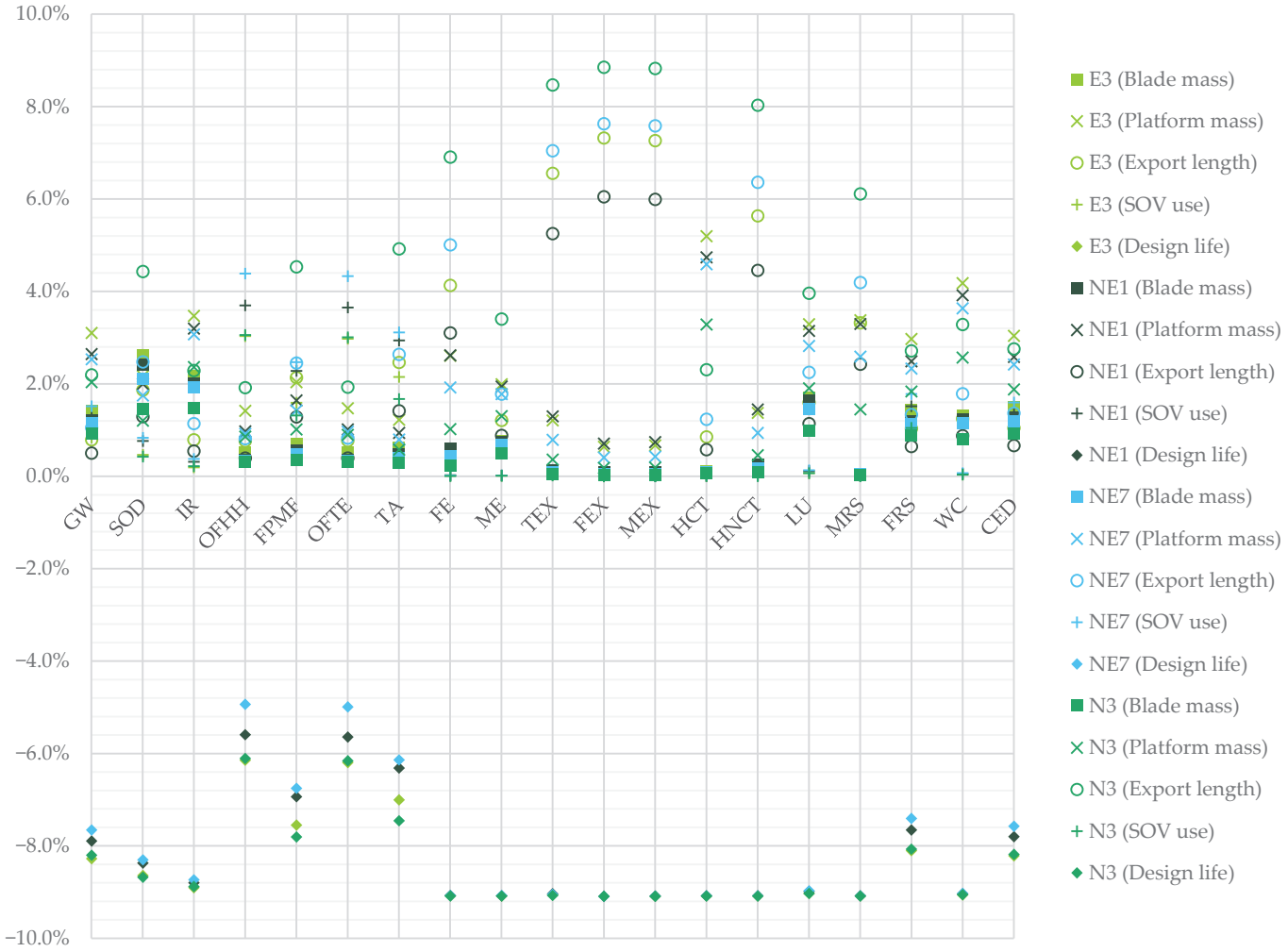


Figure 4. Sensitivity of impact categories to 10% increase in selected site and engineering design parameters for all four sites.

The results were relatively insensitive to 10% increased blade mass (0.02 to 2.6% across all categories) and platform mass (0.2 to 5.2% across all categories). However, the impact categories sensitivity to increased HVAC and HVDC export cable length was more pronounced, with some categories observing small differences (including global warming, GW at 0.5% to 2.2%) while others observed significant changes (up to 8.8% for terrestrial, freshwater, and marine ecotoxicity metrics: TEX, FEX, and MEX at N3). This pattern was found for all sites, but especially for N3 with the most HVDC converter stations (4, Table A1) and the second longest export cable route (149 km, Table A1) resulting in the longest total cable length of the sites considered.

Increases in SOV use (transit to site and station-keeping infield) saw the largest increases in categories associated with diesel combustion (up to 4.4% in OFHH at site NE7, which has the longest distance to O&M port (105 km, Table A1)). However, multiple impact categories were insensitive to increased SOV use. Notably, the 10% increase in SOV use

resulted in only a 0.8% to 1.5% increase in GW impacts, reflecting the dominance of other life cycle stages in climate change impacts.

These results show that the environmental impacts of these very large floating wind farms are primarily affected by design life, making life extension a crucial priority for the environmental impacts of these arrays. Material use—not vessel use—is, on balance, the next most significant contribution, suggesting that "greening" the supply of materials (via recycled materials, or alternative low-impact processes) should be the first priority, followed by decarbonizing vessel propulsion. However, there is already broad support for an accelerated transition to clean maritime operations in North Sea wind farm O&M [40].

3.4. Opportunities to Mitigate Global Warming Impact

Figure 5 shows the main contributions to GW for all four sites, split by assembly, process, and vessel operation, with a cut-off resolution of around 5%, in order to include ordinates for all arrays. As discussed previously, steel use is the single largest contribution to the GW impact for every farm. The turbine platform (steel alone; ballast was typically only around 1%) is the next most significant, which permits the opportunity for platform designers to significantly affect the climate impact of their products. Then, diesel combustion at around a fifth of the impact—also significant for contemporary efforts at vessel propulsion decarbonization. For N3, export cables are also significant given the site's second-longest distance-to-site and the large number of export-connected HVDC stations.

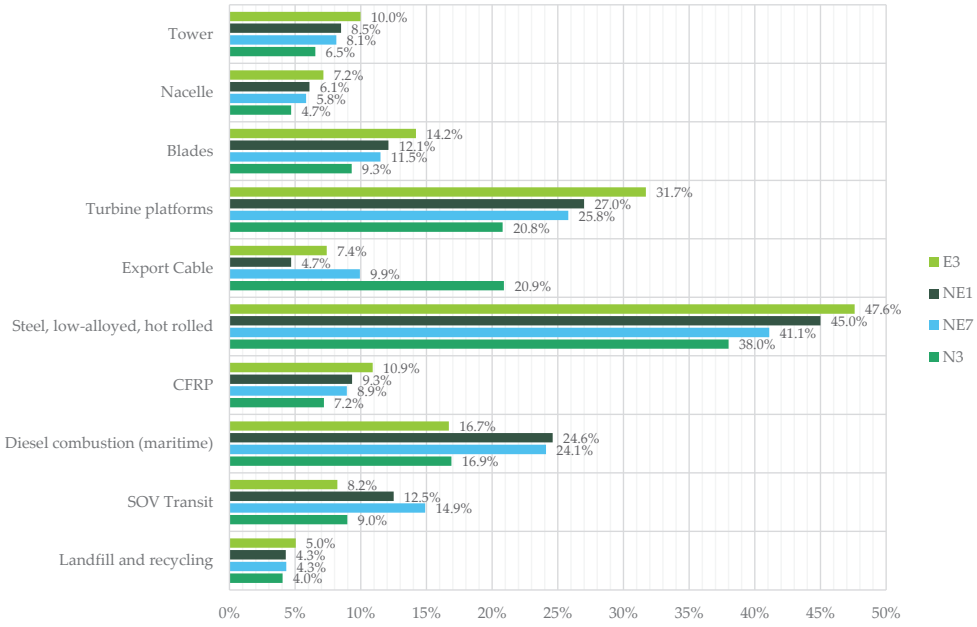


Figure 5. Main contributions to global warming by assemblies, processes, and vessel operations for all four sites.

3.5. Comparison with Literature

3.5.1. Contribution from Life Cycle Stages across Impact Categories

Material production and manufacture was the most impactful life cycle stage on global warming in all the studies reviewed [19–28], ranging from 49% [21] to a maximum of 94% [26]. The material supply of cables (typically containing aluminium or copper conductors and lead) also dominated, for example, in the ecotoxicity [25] and abiotic depletion [22,27,28] metrics. However, beyond the agreement on materials and manufacturing, the next most impactful stages vary according to the study and the impact category. O&M was often the next most frequently significant [21,25], for CED only. O&M was occasionally the most impactful stage for impact categories associated with fuel combustion (such as ozone depletion potential (ODP) at 59.41% [27]), in contrast to Figure 3. O&M is the most

impactful life cycle stage in multiple impact categories in only one study [25]: this study also uses inputs from a dedicated O&M model for the LCA but also includes the impact of spare parts. In one instance, O&M (using a transport by barge unit process) is not significant across all categories [22]. As found in this study, assembly, transportation, installation, and decommissioning were rarely significant [20,24,27,28]. This disparity reinforces the important effect of vessel representation on the life cycle environmental impacts. Lastly, the end-of-life stages are highly dependent on practitioner assumptions and are found to be both significant [19,22,23] and to make little contribution [24,28].

Overall, the results of this study align well with the literature regarding life cycle stages. As with the literature, Figure 3 reflects the dominance of M&M across most impact categories, but (as with the literature) also finds significant O&M and L&R impacts in selected instances, highlighting the need to accurately represent these stages in floating wind farm life cycle models.

3.5.2. Contribution from Processes/Materials

Across the literature, the largest contribution to all impact categories tends to arise from steel production [19,20,23,27], although fuel use is also significant in some studies, where it can be inferred in eight impact categories (FPMF, FRS, GW, OFHH, OFTE, SOD, TA, and CED) [25], again reinforcing the importance of the impact of O&M and vessel representation on the wider life cycle environmental impacts. Fossil fuel use is obviously relevant to global warming metrics, for example diesel at 20% of GWP [21] and diesel (and coal, not disaggregated) at 27% of GWP [23], but whether vessel use appears in this contribution tends to depend on the practitioner modelling choices for vessel representation. Cable conductor materials also contribute significantly to diverse impact categories, for example, FEX, FE, HNCT, ME, TEX, [25], eutrophication potential (EP) [27], and abiotic depletion of elements (AD el), [28]. This includes, in some cases, global warming [19,20], although this was occasionally not notable [21]. Glass fibre was also significant in the global warming results of some studies (for example 9% to 27% [20,25]), but not others [26,28].

Figure 5 in this study shows steel, diesel use, and CFRP as the three largest contributing unit processes to global warming at around 40%, 20%, and 10%, respectively, across the four arrays. The impact of copper cable conductors can be inferred from Figure 4, where varying the export length has a proportionate impact on select categories, especially FE, TEX, FEX, MEX, HNCT, and MRS, reflecting the results from recent studies [25,27,28].

3.5.3. Contribution from Components

The literature commonly finds that the massive (usually steel) floating platforms are the most significant contributors to most life cycle environmental impacts [22,24–26], beyond just global warming [20,23] and CED [21]. The next most significant component in the literature is typically the inter-array and export cables. As described, by virtue of their material composition, these components most commonly affect resource consumption metrics. For example, the abiotic depletion potential (ADP) of the manufacturing, transportation, and installation of all cables was found to be only slightly smaller than that of the platform (47% compared to 51%), via lead and copper use [22]. The power transmission system dominated FEX, FE, HNCT, MEX, and TEX [25], while cable manufacturing accounted for 64% of ADP (and 28% of EP) [27]. Most recently, cables were found to be the main contributor to abiotic depletion (52%), acidification (17%), and eutrophication (14%), again driven by the use of copper [28].

Sections 3.3 and 3.4 of this study align well with these perspectives from the literature. Figure 5 shows that the platforms are the component with the greatest impact on global warming for each array shown (20.8% to 31.7%). This is a smaller contribution than reported in some earlier studies (63%, 51%, 41%) [20,22,23] and comparable to more recent studies of larger turbines [25,28]. The sensitivity to platform mass and cable length in Figure 4 also reflects the attributions in the literature described above.

3.5.4. Contributions from O&M

Given the relatively novel use of outputs from a dedicated O&M model as inputs to a life cycle model, specific attention is given here to the contributions from O&M. A recent semi-submersible case study [25] finds that the O&M life cycle stage contributes 40.7% (after M&M at 46.6%). Of this, vessel processes comprise 30.0%, and the remainder is allocated to spare parts. This case study results in a life cycle global warming of 25.6 to 27.6 gCO_2eq/kWh, comparable to the 17.4 to 26.3 gCO_2eq/kWh found in this paper. However, this O&M contribution is quite different from Figure 3, which shows that O&M contributes only 9% to 16% to global warming, despite the likely more onerous metocean conditions at these remote sites. This may be due to the size of the array (demonstrator compared to utility-scale) and the assumptions underpinning the O&M model: further work would be required to resolve these model differences. Regardless, both these studies' O&M contributions contrast with some of the reviewed literature, where the overall O&M contribution to global warming is typically low. In other impact categories, O&M vessel processes are the single largest process contribution to FPMF, FRS, GW, OFHH, OFTE, SOD, TA, and CED [25]. Figure 3 in this paper reflects these trends, although the contribution of O&M to SOD is more similar to the proportion seen in [28].

3.5.5. General Comparability

It is usually challenging to compare studies because the methodical choices are different. Fundamentally, the system boundary selection issue is still a critical weakness in current LCA studies [41], as well as the various differences in inventory detail and representation, lifetime power generation, and array design life (Table 1). Section 3.3.1 and Figure 4 describe the respective significances of these parameters, which make it difficult to draw firm comparisons.

Generally, there will always be a tendency toward a decrease in environmental impacts with increased lifetime energy generation and life extension (Figure 4) [20,24]. For example, a related study with a comparable 190-turbine wind farm in Italy has a longer design life (30 years compared to 20, and hence more impact from each year of vessel operations), but a lower capacity factor (34.35%), resulting in a higher global warming impact of 31.3 gCO_2eq/kWh [28]. This compares to the capacity factors (52.3%, 53.9%, 54.4%, and 52.4%) and global warming results (17.4, 20.0, 20.5, and 26.3 gCO_2eq/kWh) for sites E3, NE1, NE7, and N3, respectively. When additional impacts from O&M are included to match a 30-year design life, and multiplied by the ratio of capacity factors between the studies (1.52, 1.57, 1.58, and 1.53), the global warming results from this study become 27.6, 33.1, 34.9, and 42.2 gCO_2eq/kWh, a difference of -12% to +35%, where any additional differences may be attributed to site characteristics, use of a dedicated O&M model as input, and vessel representation. This holds less well for the only other comparable impact category, CED, which becomes (376, 452, 487, and 607 kJ/kWh), in contrast with 410 kJ/kWh [28], a difference of -8% to +48%.

Conversely, alignment is observed with the literature on certain specific site characteristics, where shallow-water, close-to-shore sites can outperform more remote sites with higher average power generation. This is found to be the case with site E3 (Section 3.1, Figure 3), which tends to have the lowest environmental impacts, reflecting [21], but generally illustrates the relative importance of the ratio of life cycle model inventory to lifetime energy production [24].

3.6. Comparison with the Historical British Electricity Mix

The environmental performance of these arrays can also be considered by comparison with the life cycle impacts of the current British electricity mix. It is important to note that carbon intensity (182 gCO_2/kWh in 2022 [10]) only considers the operational (or direct) emissions from the power system generation mix, and so should not be compared with the life cycle global warming potential determined above. However, the LCI database, ecoinvent, does include a unit process suitable for this purpose ('Electricity, high voltage {GB}|market for|Cut-off, U') with data valid for the year 2016. This generation mix is primarily fossil gas, followed by nuclear, wind, and coal [30]. As a first approximation of contemporary

data, electricity generation statistics for 2022 were reviewed [42,43] and used to modify this unit process to represent the electricity generation in 2022. This new mix is characterized by a slight reduction in gas, very low generation from coal, and increased generation from solar and wind (both offshore and onshore) relative to 2016. Figure 6 shows that the median floating wind environmental impacts calculated in this study are generally significantly lower than the average 2016 mix, with only five exceptions: terrestrial ecotoxicity (166%), freshwater ecotoxicity (504%), marine ecotoxicity (408%), human carcinogenic toxicity (105%), and mineral resource scarcity (212%). These are primarily driven by copper production, copper disposal (for both freshwater and marine ecotoxicity), steel slag disposal, and the production of iron ore, ferronickel, and lead, respectively. The results of the modified 2022 electricity mix broadly follow the patterns between the 2016 mix and the median floating wind results, except across the freshwater, marine, and human toxicity metrics. This suggests that the floating wind LCI includes greater proportions of copper production and waste treatment allocation per functional unit. This is supported by inspection of the respective ecoinvent unit processes and again highlights the importance of detailed waste treatment representation for these technologies [19,21,22,25,28]. On balance, the median life cycle impact of these arrays is generally far lower than that of the contemporary electricity generation mix for most impact categories; however, it is important that impact categories other than climate change are considered, especially during material production and disposal.

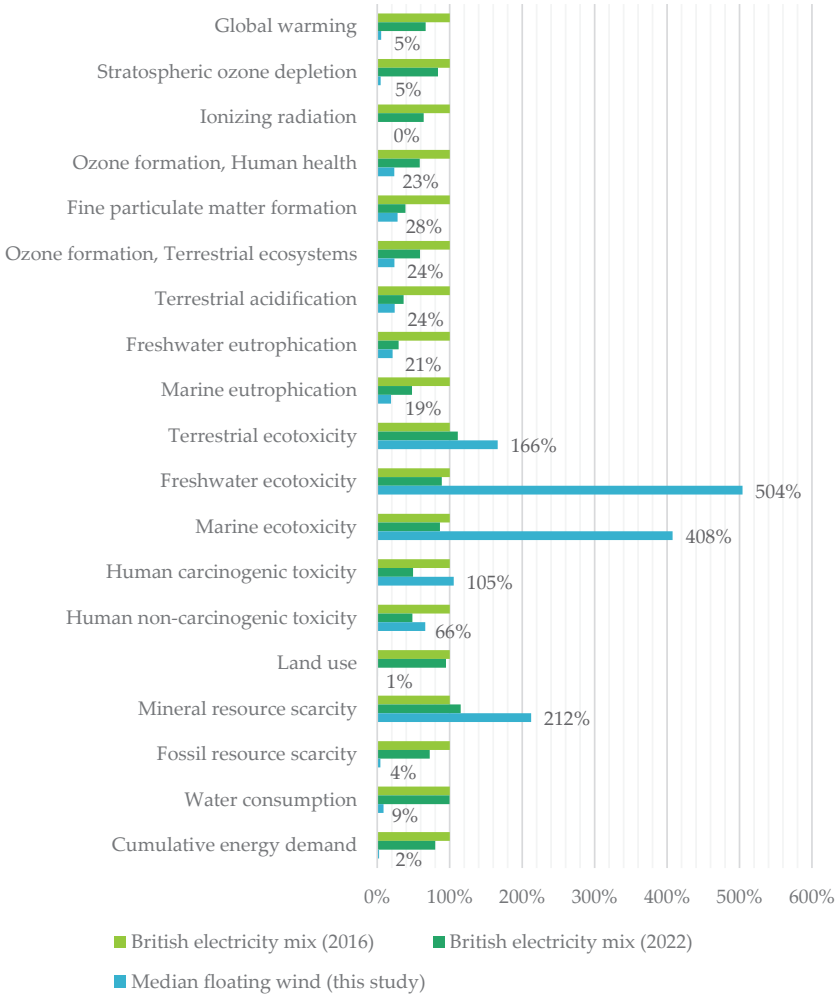


Figure 6. Comparison of the relative environmental performance of the ecoinvent unit process for 2016 British electricity mix [30], a modified process representative of 2022 generation by energy [42,43], and the median results of the four floating wind farms calculated in this study; 100% corresponds to the 2016 electricity mix results.

3.7. Limitations

As with any model, it is impossible to replicate exactly the complexity of the system under assessment, and approximations are essential for a tractable solution. Further, the more detailed a life cycle model, the more processes are included and typically the higher the impacts computed. This is observable in the literature where the inclusion of manufacturing processes and detailed O&M modelling tends to be associated with higher climate change impacts (Table 1).

This study attempted to address some gaps in the literature using modelling input from ORE Catapult. This gives good assurance on the foreground data for materials, vessel choice, and O&M inputs. However, a number of limitations remain. The O&M life cycle stage has only a nominal inclusion for cable inspection and major component replacement, with no allowance for other types of subsea inspection, such as moorings. Investigating tow-to-shore strategies from a life cycle perspective could also be instructive as state-of-the-art O&M practices for floating wind farms utilize tow-to-shore for major repairs, and novel crane vessel technologies necessary for on-site component exchange remain in development. Array losses have not been included in the lifetime energy production, which would have an inversely proportional effect on the environmental impacts (Section 3.3.1). Emission-causing activities during site development (such as vessel surveys) are also omitted. The turbine and platform models used are primarily intended as open benchmarks for new technologies or design methodologies and do not completely represent the LCI of an extant floating wind turbine design. Moreover, the site designs here are speculative and do not precisely represent the detailed designs of the commercial projects under development. Where export cables are shown to be impactful (at extreme site to landfall distances), greater assurance on the routing and cable length should be pursued. Fundamentally, future use of low-impact vessels and materials has the potential to significantly reduce the environmental impacts. Incremental benefits can also be achieved in the near term by technology maturation, such as optimizing platform, turbine, and transmission system designs to reduce mass and increase AEP.

4. Conclusions

This study assessed the life cycle impacts of a 15 MW reference wind turbine on floating platforms in sites representative of four floating wind farms in the ScotWind leasing round (E3, NE1, NE7, and N3) with a mixture of HVAC and HVDC transmission systems. The inventory data for this study used industry inputs for array materials and O&M vessel usage, giving assurance on the accuracy and representativeness of the results. The median global warming was 17.4 to 26.3 gCO2eq/kWh using default values for basic and additional uncertainty in the foreground data and background data. Across the four sites, materials and manufacturing account for 71% to 79% of the global warming impact, although the O&M burden was smaller than in other studies; O&M using SOVs comprised between 9% and 16% of the global warming impact.

This study has shown that the environmental impacts of these very large floating wind farms are fundamentally affected by design life, making life extension a crucial priority for the sustainability of these arrays. Following that, material use—not vessel use—is, on balance, the next most significant contribution, suggesting "greening" the supply of materials (via recycled materials, or alternative low-impact processes such as the use of hydrogen as a reducing agent in steel-making) should be a research priority, followed by decarbonizing vessel propulsion.

Supplementary Materials: The following supporting information can be downloaded at: https://www.mdpi.com/article/10.3390/en16237739/s1, original datasets describing the structure of the life cycle model and life cycle model parameters and data tables of the default uncertainty results, life cycle stage contributions, sensitivity study and global warming contributions.

Author Contributions: Conceptualization, R.C.T. and I.A.S.; investigation, I.A.S.; resources, N.A., M.N. and A.G.; data curation, I.A.S.; writing—original draft preparation, I.A.S.; writing—review and

editing, R.C.T., N.A., M.N., A.G. and G.P.H.; supervision, R.C.T. and G.P.H. All authors have read and agreed to the published version of the manuscript.

Funding: I.A.S. gratefully acknowledges funding from the Engineering and Physical Sciences Research Council through the EPSRC Centre for Doctoral Training in Wind and Marine Energy Systems, grant number EP/L016680/1.

Data Availability Statement: The data presented in this study are available in the Supplementary Materials.

Conflicts of Interest: The authors declare no conflict of interest.

Appendix A

Table A1 contains detailed site-specific parameters. Further site-specific inventory data are included in the Supplementary Materials.

Table A1. Site parameters, excluding site-specific inventory data.

Site	E3	NE1	NE7	N3
Number of turbines	94	154	200	220
Installed capacity (MW)	1410	2310	3000	3300
Turbine AEP (GWh/year)	68.7	70.8	71.5	68.9
Capacity factor	52.3%	53.9%	54.4%	52.4%
Assumed water depth (m)	60	130	110	150
Export system	HVAC	HVDC	HVDC	HVDC
Approximate export cable landfall route (km)	Aberdeen (40)	Sumburgh (72)	Montrose (207)	Dounreay (149)
Number of HVAC Collector Stations	3	3	4	4
Number of HVDC Converter Stations	-	2	2	4
O&M strategy	SOV (no tow-to-shore)	SOV (no tow-to-shore)	SOV (no tow-to-shore)	SOV (no tow-to-shore)
Number of SOVs	2	3	3	3
Lifetime (years)	20	20	20	20
FWTU Assembly Yard (km)	Methil, Scotland (145)	Nigg, Scotland (370)	Nigg, Scotland (220)	Nigg, Scotland (350)
Tower Origin (km)	Methil, Scotland (0)	Nigg, Scotland (0)	Nigg, Scotland (0)	Nigg, Scotland (0)
Nacelle Origin (km)	Esbjerg, Denmark (725)	Esbjerg, Denmark (820)	Esbjerg, Denmark (820)	Esbjerg, Denmark (820)
Blade Origin (km)	Hull, England (420)	Hull, England (670)	Hull, England (670)	Hull, England (670)
WT Platform Origin (km)	Methil, Scotland (0)	Nigg, Scotland (0)	Nigg, Scotland (0)	Nigg, Scotland (0)
Moorings Origin (km)	Bilbao, Spain (1910)	Bilbao, Spain (2170)	Bilbao, Spain (2170)	Bilbao, Spain (1815)
Mooring Load-out (km)	Methil, Scotland (145)	Nigg, Scotland (370)	Nigg, Scotland (220)	Arnish, Scotland (100)
Array Cable Origin (km)	Hartlepool, England (280)	Hartlepool, England (625)	Hartlepool, England (405)	Hartlepool, England (685)

Table A1. *Cont.*

Site	E3	NE1	NE7	N3
HVAC Topsides Origin (km)	Aalborg, Denmark (870)	Aalborg, Denmark (835)	Aalborg, Denmark (790)	Aalborg, Denmark (1140)
HVAC Jacket Origin (km)	Methil, Scotland (145)	Nigg, Scotland (370)	Nigg, Scotland (220)	Arnish, Scotland (350)
HVAC Piles Origin (km)	Methil, Scotland (0)	Methil, Scotland (0)	Methil, Scotland (0)	Arnish, Scotland (0)
HVAC Piles Load-out (km)	Methil, Scotland (145)	Methil, Scotland (510)	Methil, Scotland (295)	Arnish, Scotland (100)
HVAC Cable Origin (km)	Hartlepool, England (280)	Hartlepool, England (625)	Hartlepool, England (405)	Hartlepool, England (685)
HVDC Topsides Origin (km)	Aalborg, Denmark (870)	Aalborg, Denmark (835)	Aalborg, Denmark (790)	Aalborg, Denmark (1140)
HVDC Jacket Origin (km)	Methil, Scotland (145)	Methil, Scotland (510)	Methil, Scotland (295)	Arnish, Scotland (100)
HVDC Piles Origin (km)	Methil, Scotland (0)	Methil, Scotland (0)	Methil, Scotland (0)	Arnish, Scotland (0)
HVDC Piles Load-out (km)	Methil, Scotland (145)	Methil, Scotland (510)	Methil, Scotland (295)	Arnish, Scotland (100)
HVDC Cable Origin (km)	Hartlepool, England (280)	Hartlepool, England (625)	Hartlepool, England (405)	Hartlepool, England (685)
O&M Port (km)	Aberdeen, Scotland (40)	Lerwick, Scotland (55)	Fraserburgh, Scotland (105)	Stornoway, Scotland (100)
Major Repairs Port (km)	Aberdeen, Scotland (40)	Lerwick, Scotland (55)	Aberdeen, Scotland (155)	Nigg, Scotland (350)

References

1. IEA. *Offshore Wind Outlook 2019*; IEA: Paris, France, 2019.
2. IEA. *Net Zero by 2050 a Roadmap for the Global Energy Sector*; IEA: Paris, France, 2021.
3. Williams, R.; Zhao, F. Global Offshore Wind Report 2023. Global Wind Energy Council. August 2023. Available online: https://gwec.net/wp-content/uploads/2023/08/GWEC-Global-Offshore-Wind-Report-2023.pdf (accessed on 2 November 2023).
4. The Crown Estate. The Crown Estate Offshore Wind 2022. The Crown Estate. April 2023. Available online: https://assets.ctfassets.net/nv65su7t80y5/1Tr60ikvWdBncxjtySAgti/09121dae09f04dea907ee6a3ee2c043a/11720_owoperationalreport_2022_tp_020523plusaccessibility.pdf (accessed on 2 November 2023).
5. UK Government. Major Acceleration of Homegrown Power in Britain's Plan for Greater Energy Independence. GOV.UK. Available online: https://www.gov.uk/government/news/major-acceleration-of-homegrown-power-in-britains-plan-for-greater-energy-independence (accessed on 2 November 2023).
6. The Crown Estate. Offshore Wind Leasing Round 5 | The Crown Estate. Available online: https://www.thecrownestate.co.uk/our-business/marine/round-5 (accessed on 2 November 2023).
7. Gray, A. *Initial Predictions for Offshore Wind Farms in the ScotWind Leasing Round*; ORE Catapul: Glasgow, UK, 2021.
8. Stark, C.; Thompson, M.; Andrew, T.; Beasley, G.; Bellamy, O.; Budden, P.; Cole, C.; Darke, J.; Davies, E.; Feliciano, D.; et al. Net Zero Technical Report. Committee on Climate Change. 2019. Available online: www.theccc.org.uk/publications (accessed on 12 August 2019).
9. Thomson, R.C.; Harrison, G.P.; Chick, J.P. Marginal greenhouse gas emissions displacement of wind power in Great Britain. *Energy Policy* **2017**, *101*, 201–210. [CrossRef]
10. Britain's Electricity Explained: 2022 Review | ESO. Britain's Electricity Explained. 2022 Review. Available online: https://www.nationalgrideso.com/news/britains-electricity-explained-2022-review (accessed on 7 November 2023).
11. BSI. *Environmental Management—Life Cycle Assessment—Requirements and Guidelines*; British Standards Institution: London, UK, 2018.
12. Klöpffer, W. Life cycle assessment. *Environ. Sci. Pollut. Res.* **1997**, *4*, 223–228. [CrossRef] [PubMed]
13. Hauschild, M.Z.; Rosenbaum, R.K.; Olsen, S.I. *Life Cycle Assessment: Theory and Practice*; Springer: Berlin/Heidelberg, Germany, 2018.
14. Wulf, C.; Werker, J.; Ball, C.; Zapp, P.; Kuckshinrichs, W. Review of Sustainability Assessment Approaches Based on Life Cycles. *Sustainability* **2019**, *11*, 5717. [CrossRef]

15. Amahmoud, A.; Attar, M.M.E.; Meleishy, A. The Evolution of Life Cycle Assessment Approach: A Review of Past and Future Prospects. *IOP Conf. Ser. Earth Environ. Sci.* **2022**, *992*, 012002. [CrossRef]
16. BSI. *Environmental Management—Life Cycle Assessment—Principles and Framework*; British Standards Institution: London, UK, 2006; Volume 3, p. 20. [CrossRef]
17. Baumann, H.; Tillman, A.-M. *The Hitch Hiker's Guide to LCA*; Studentlitteratur AB: Lund, Sweden, 2004.
18. Mendecka, B.; Lombardi, L. Life cycle environmental impacts of wind energy technologies: A review of simplified models and harmonization of the results. *Renew. Sustain. Energy Rev.* **2019**, *111*, 462–480. [CrossRef]
19. Weinzettel, J.; Reenaas, M.; Solli, C.; Hertwich, E.G. Life cycle assessment of a floating offshore wind turbine. *Renew. Energy* **2009**, *34*, 742–747. [CrossRef]
20. Raadal, H.L.; Vold, B.I.; Myhr, A.; Nygaard, T.A. GHG emissions and energy performance of offshore wind power. *Renew. Energy* **2014**, *66*, 314–324. [CrossRef]
21. Tsai, L.; Kelly, J.C.; Simon, B.S.; Chalat, R.M.; Keoleian, G.A. Life Cycle Assessment of Offshore Wind Farm Siting: Effects of Locational Factors, Lake Depth, and Distance from Shore. *J. Ind. Ecol.* **2016**. [CrossRef]
22. Elginoz, N.; Bas, B. Life Cycle Assessment of a multi-use offshore platform: Combining wind and wave energy production. *Ocean Eng.* **2017**, *145*, 430–443. [CrossRef]
23. Bang, J.-I.; Ma, C.; Tarantino, E.; Vela, A.; Yamane, D. *Life Cycle Assessment of Greenhouse Gas Emissions for Floating Offshore Wind Energy in California*; University of California: Santa Barbara, CA, USA, 2019.
24. Poujol, B.; Prieur-Vernat, A.; Dubranna, J.; Besseau, R.; Blanc, I.; Pérez-López, P. Site-specific life cycle assessment of a pilot floating offshore wind farm based on suppliers' data and geo-located wind data. *J. Ind. Ecol.* **2020**, *24*, 248–262. [CrossRef]
25. Garcia-Teruel, A.; Rinaldi, G.; Thies, P.R.; Johanning, L.; Jeffrey, H. Life cycle assessment of floating offshore wind farms: An evaluation of operation and maintenance. *Appl. Energy* **2022**, *307*, 118067. [CrossRef]
26. Yildiz, N.; Hemida, H.; Baniotopoulos, C. Life cycle assessment of a barge-type floating wind turbine and comparison with other types of wind turbines. *Energies* **2021**, *14*, 5656. [CrossRef]
27. Yuan, W.; Feng, J.-C.; Zhang, S.; Sun, L.; Cai, Y.; Yang, Z.; Sheng, S. Floating wind power in deep-sea area: Life cycle assessment of environmental impacts. *Adv. Appl. Energy* **2023**, *9*, 100122. [CrossRef]
28. Brussa, G.; Grosso, M.; Rigamonti, L. Life cycle assessment of a floating offshore wind farm in Italy. *Sustain. Prod. Consum.* **2023**, *39*, 134–144. [CrossRef]
29. Avanessova, N.; Land, J.; Lee, A.; Lazakis, I.; Thomson, C. Comparison of Operation and Maintenance of Floating 14 MW Turbines and Twin 10 MW Turbines. *ASME Open J. Eng.* **2023**, *2*, 021031. [CrossRef]
30. Ecoinvent. Ecoinvent Centre. 2016. Ecoinvent Database (Version 3.6). [Allocation—Cut-off by Classification—Unit]. Retrieved from Simapro Software Version 9.1. December 2019. Available online: www.ecoinvent.org (accessed on 10 September 2023).
31. Crown Estate Scotland. ScotWind Offshore Wind Leasing Delivers Major Boost to Scotland's Net Zero Aspirations. Available online: https://www.crownestatescotland.com/news/scotwind-offshore-wind-leasing-delivers-major-boost-to-scotlands-net-zero-aspirations (accessed on 19 January 2022).
32. Allen, C.; Viselli, A.; Dagher, H.; Goupee, A.; Gaertner, E.; Abbas, N.; Hall, M.; Barter, G. *Definition of the UMaine VolturnUS-S Reference Platform Developed for the IEA Wind 15-Megawatt Offshore Reference Wind Turbine*; National Renewable Energy Laboratory: Golden, CO, USA, 2020.
33. Aqua-RET Project. Aqua-RET Project, Downloads and Resources', Downloads and Resources. Available online: https://aquaret.com/index3f8f.html?option=com_content&view=article&id=198&Itemid=50&lang=en (accessed on 26 May 2023).
34. Boniface, Y. uMap, an OpenStreetMap Project (Version 1.10.0). uMap. Available online: https://umap.openstreetmap.fr/en/ (accessed on 30 October 2023).
35. Gaertner, E.; Rinker, J.; Sethuraman, L.; Zahle, F.; Anderson, B.; Barter, G.; Abbas, N.; Meng, F.; Bortolotti, P.; Skrzypinski, W.; et al. Definition of the IEA Wind 15-Megawatt Offshore Reference Wind Turbine Technical Report; National Renewable Energy Laboratory. March 2020. Available online: www.nrel.gov/publications (accessed on 29 May 2020).
36. Birkeland, C. Assessing the Life Cycle Environmental Impacts of Offshore Wind Power Generation and Power Transmission in the North Sea. Master's Thesis, Norwegian University of Science and Technology, Trondheim, Norway, 2011.
37. Thomson, R.C.; Chick, J.P.; Harrison, G.P. An LCA of the Pelamis wave energy converter. *Int. J. Life Cycle Assess.* **2019**, *24*, 51–63. [CrossRef] [PubMed]
38. Karan, H.; Thomson, R.C.; Harrison, G.P. Full life cycle assessment of two surge wave energy converters. *Proc. Inst. Mech. Eng. Part J. Power Energy* **2019**, *234*, 1–14. [CrossRef]
39. Weidema, B.P.; Bauer, C.; Hischier, R.; Mutel, C.; Nemecek, T.; Reinhard, J.; Vadenbo, C.O.; Wenet, G. *Data Quality Guideline for the Ecoinvent Database Version 3. Ecoinvent Report 1 (v3)*; Swiss Centre for Life Cycle Inventories: Dübendorf, Switzerland, 2013; Volume 3.
40. ORE Catapult and The Workboat Association. *Decarbonising Maritime Operations In North Sea Offshore Wind O&M*; Innovation Roadmap produced for the UK Government DfT and FCDO; ORE Catapult and The Workboat Association: Glasgow, UK, 2021.
41. Li, T.; Zhang, H.; Liu, Z.; Ke, Q.; Alting, L. A system boundary identification method for life cycle assessment. *Int. J. Life Cycle Assess.* **2014**, *19*, 646–660. [CrossRef]

42. Martin, V. DUKES 2023 Chapter 5: Electricity. Department for Energy Security and Net Zero. July 2023. Available online: https://assets.publishing.service.gov.uk/media/64c23a300c8b960013d1b05e/DUKES_2023_Chapter_5.pdf (accessed on 7 November 2023).
43. UK Energy in Brief 2023. *Department for Energy Security and Net Zero*; Department for Energy Security and Net Zero: London, UK, 2023.

Disclaimer/Publisher's Note: The statements, opinions and data contained in all publications are solely those of the individual author(s) and contributor(s) and not of MDPI and/or the editor(s). MDPI and/or the editor(s) disclaim responsibility for any injury to people or property resulting from any ideas, methods, instructions or products referred to in the content.

MDPI AG
Grosspeteranlage 5
4052 Basel
Switzerland
Tel.: +41 61 683 77 34

MDPI Books Editorial Office
E-mail: books@mdpi.com
www.mdpi.com/books



Disclaimer/Publisher's Note: The title and front matter of this reprint are at the discretion of the Topic Editors. The publisher is not responsible for their content or any associated concerns. The statements, opinions and data contained in all individual articles are solely those of the individual Editors and contributors and not of MDPI. MDPI disclaims responsibility for any injury to people or property resulting from any ideas, methods, instructions or products referred to in the content.





Academic Open
Access Publishing

mdpi.com

ISBN 978-3-7258-3042-8